Deflection Behaviour of
FRP Reinforced Concrete Flexural Members

A thesis submitted for the degree of

Doctor of Philosophy

in the Faculty of Engineering of the University of Sheffield

by

Raed Akram Saliba Al-Sunna

B.Sc., Civil Engineering
M.Sc., Structural Engineering

Department of Civil and Structural Engineering
The University of Sheffield

June 2006

to my wife, Natalie
and my two sons, Akram and Laith

ABSTRACT

The design of fibre reinforced polymer (FRP) reinforced concrete (RC) can often be governed by the serviceability limit state of deflection. Currently, the evaluation of short-term deflection of FRP RC is undertaken using radically different approaches, in both research and codes of practice. This study investigates the short-term deflection behaviour of FRP RC, both experimentally and analytically, and examines the merits of those different approaches.

Experimentally, 28 RC beams and slabs with glass, carbon or steel rebars are tested under four-point loading. The main variables considered are the reinforcement ratio, modulus of elasticity and bond. In addition to measuring deflections, closely-spaced strain gauges are used to measure rebar strains between one forced crack at midspan and two naturally-occurring cracks on either side. This setup enables the investigation of rebar strains, tension stiffening and bond between flexural cracks. Furthermore, in connection with concrete strains at the extreme compressive concrete fibre, the flexural load-curvature relationship is evaluated experimentally and used to decompose the total deflection into flexural and shear-induced deflections.

Analytically two numerical analysis methods are used to provide further insight into the experimental results. Finite element analysis with smeared modelling of cracks is used to predict and examine the stress-displacement response in detail. Cracked section analysis is used to provide upper-bound deflections and strains.

This study also deals with the ACI and Eurocode 2 approaches for prediction of short-term deflection. The deflection prediction and tension stiffening expressions of these codes are evaluated against the experimental results of this and other studies.

The main conclusion is that deflection of FRP RC is essentially due to flexural curvatures, and can be reasonably evaluated by the tension stiffening model of Eurocode 2. However, with reinforcement of relatively low axial stiffness, and depending on the reinforcement bond characteristics, shear-induced deformations become significant and may need to be evaluated.

ACKNOWLEGEMENTS

To the Higher Council of Science and Technology (HCST) - Jordan for financially supporting this research project.

To the Royal Scientific Society (RSS) – Jordan, the Karim Rida Said Foundation (KRSF) – UK and the University of Sheffield for your sponsorship.

To Dr. Khaled Kahalleh: I am very grateful for your support along the way.

To Dr. Tareq Al-Hadeed: Thank you ever so much for introducing the concept of PhD-research at RSS, and for your persistence in pushing things forward.

To all my colleagues at RSS who contributed to my work, in particular, Eng. Issa Tarazi, Eng. Yehia Quraini and Mohammed Sami: Your help is very appreciated.

To my supervisor Professor Kypros Pilakoutas: I sincerely appreciate your advice, guidance and your dedication in discussing and reviewing my work, you always gave me something to think about. More importantly, you have been a true friend in need, and I will always cherish our invaluable friendship.

To Professor Peter Waldron: Thank you for your comments and thorough revision of the papers that I have written.

To Paul and Jonathan: Thank you for your assistance in testing my rebars.

To my mother and sisters, and to my wife's parents and brothers and sisters: Thank you very much for your confidence, and for your help in taking care of things at home.

To my wife and two sons: I realise that you went through a lot just for me, I love you so much as well.

Just a final word to my late father: I know you would have been very proud.

TABLE OF CONTENTS

CHAPTER 1

INTRODUCTION

1.1. INTRODUCTION

Steel reinforced concrete (RC) structures have been used successfully in all types of infrastructure for more than a century. The use of steel RC is currently governed by rather well established design guidelines and codes of practice, though these are continually reviewed to reflect latest developments and findings. Nonetheless, under aggressive exposure conditions such as marine environments, the steel reinforcement can corrode very rapidly, as typically shown in Figure 1-1. Corrosion can lead to costly repair and maintenance operations, reduced service life of the structure and, in severe cases, structural failure. Various measures and procedures have been developed to mitigate corrosion. However, none of these provides a comprehensive and cost-effective solution (ACI committee 440 1996, Pilakoutas 2000).

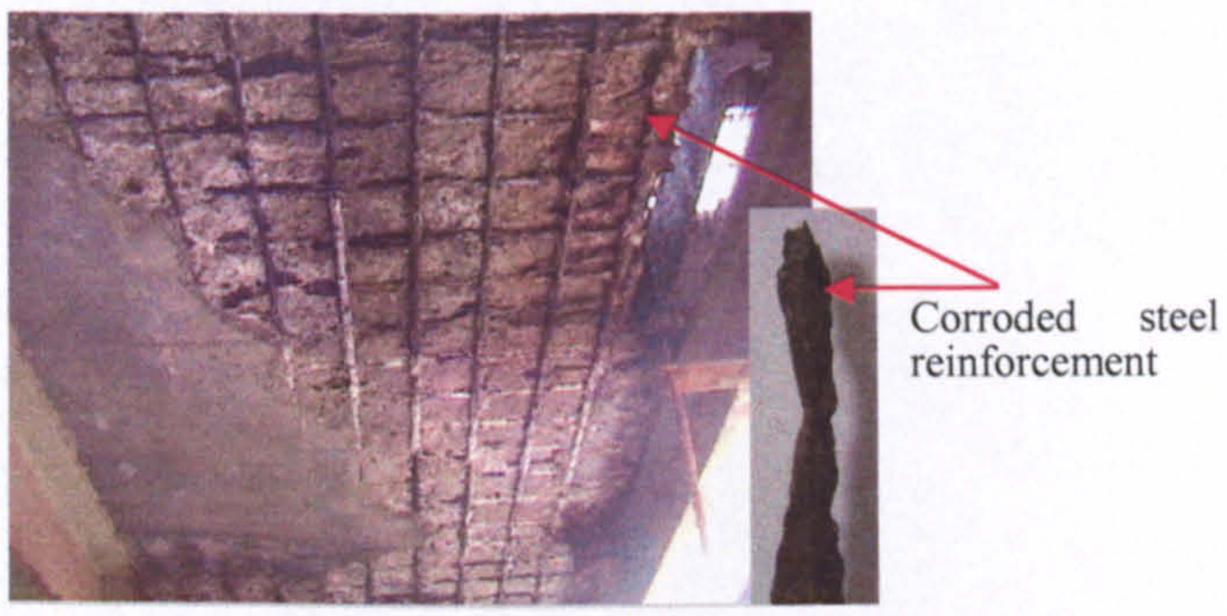

Figure 1-1: Corrosion of steel reinforcement on the soffit of a reinforced concrete slab.

In the last decade, non-ferrous reinforcement has been introduced in construction as a solution to the corrosion problem. Rebars are formed from a thermosetting resin matrix that is reinforced by various types of fibres; hence the name fibre reinforced polymer (FRP) rebars. Besides corrosion resistance, FRP can offer other advantages compared

to steel such as high tensile strength, light weight and electromagnetic transparency (Waldron et al 2000). The introduction of FRP RC in the construction industry has been associated with extensive scientific research to study the structural and durability behaviour of this new construction material. Results have been promising, and FRP has been used in many projects in North America, Japan and Europe (ACI Committee 440 1996).

Several design guidelines for FRP RC have already been developed. The most recent of these have been in Japan (JSCE 1997), USA (ACI Committee 440 2006), Canada (ISIS Canada 2001 and CSA 2002), and Europe/UK (IStructE 1999). All these guidelines have been produced by modifying the corresponding existing codes of practice for steel RC, despite the obvious differences in behaviour and failure modes.

The short-term structural behaviour of FRP RC is characterized by the low modulus of elasticity and the wide range of bond characteristics of the FRP reinforcement. The low modulus can lead to high reinforcement strains, hence wide cracks and large deflections. Therefore, the design of FRP RC may often be governed by the serviceability limit states of deflection and/or cracking. In other words, the design of FRP RC can be performance-controlled. Therefore, it is necessary to develop the understanding of the deflection and cracking behaviour of FRP RC and to refine their predictive models.

At the present time, the evaluation of short-term deflection of FRP RC has varying points of view and is not settled yet. For instance, ACI Committee 440 (2003) and ISIS Canada (2001) consider that serviceability of FRP RC is an area where further research is still required. Their formula for the effective flexural stiffness accounts for the FRP modulus of elasticity and includes a bond coefficient that needs to be test-determined for every specific type of FRP rebar. Preliminary values are adopted for this coefficient, until further research data become available. The latest ACI Committee 440 (2006) abandons the dependence of the effective flexural stiffness on bond, but relates it to the reinforcement ratio. On the European side, the IStructE (1999) and some researchers consider that the deflection approaches of steel RC are equally applicable to FRP RC.

1.2. RESEARCH OBJECTIVES

This study aims at investigating the short-term deflection behaviour of FRP RC flexural members, both experimentally and analytically. A comprehensive background and justification for this research are provided in the literature review on the flexural behaviour of steel and FRP RC (Chapter 2). To achieve the general aim of this research, the following more specific objectives are identified.

- To investigate, through literature, the flexural behaviour of FRP and steel RC members, and identify the key variables and different approaches involved. Flexural behaviour includes the topics of deflection, cracking, bond and tension stiffening.
- To investigate, through structural tests, the deflection behaviour of FRP RC members, as well as the behaviour of deflection-related parameters. These involve rebar strains at and between cracks, concrete strains, curvature, crack width and spacing, tension stiffening, and bond.
- To examine the numerical analysis techniques of cracked section analysis (CSA) and finite element (FE) analysis, and to evaluate their predictions of curvature and deflection, as well as rebar and concrete strains.
- To examine and evaluate the approaches for prediction of short-term deflection in major codes of practice on FRP RC.

Another objective is to investigate the failure modes and flexural capacity of FRP RC, since these are outcomes of the structural tests.

1.3. OUTLINE OF THE THESIS

In Chapter 2, a literature review is undertaken on the topics of flexural capacity, cracking, deflection, bond and tension stiffening; for both steel and FRP RC flexural members. Initially, the current state of knowledge of the flexural behaviour of steel RC members is reviewed, and the underlying assumptions, key parameters and various approaches are identified. This is followed by a similar revision for FRP RC. This chapter concludes by justifying the objectives and focus of this research, and by identifying the main variables that need to be considered for experimental investigation.

The experimental methodology is presented in Chapter 3. The layout and details of the test members are presented and discussed, and the experimental setup and

instrumentation are illustrated. The preparation methods, quality control and test procedure are also elaborated. The concrete and reinforcement material tests are presented at the end of this chapter.

The results of the structural tests are dealt with in Chapter 4. To start with, the modes of failure and load capacity are discussed. Then, the rebar and concrete strain, deflection and crack width and spacing are examined over the entire loading range. Subsequently, the experimental data are analysed to investigate other structural aspects that are related to the deflection behaviour. These involve the tension stiffening and bond behaviour between cracks, the experimental load-curvature response and the average depth of the neutral axis.

Chapter 5 deals with numerical analysis. FE analysis with smeared modelling of cracking and tension stiffening is presented, and its implementation in this study is elaborated. Then, FE analysis is used to predict the stress-displacement response of some test members. CSA is discussed next and is used to predict the failure load, rebar and concrete strain as well as curvature and deflection for all the tested RC members at their cracked state.

In Chapter 6, a comprehensive discussion is undertaken on the deflection behaviour of the tested FRP RC members. The predictions of rebar and concrete strain, curvature and deflection, made by FE analysis and CSA, are compared to the corresponding experimental results. The predictions of failure load are also briefly discussed. Further FE analyses are undertaken in connection with suspected shear lag in the carbon FRP rebars. Conclusions are drawn regarding the parameters that control the development and distribution of curvature in flexural FRP RC members and the adequacy of the numerical analysis techniques used.

The approaches of ACI and Eurocode 2 for evaluation of short-term deflection are examined in Chapter 7. Deflections predicted by these approaches are compared to the test measurements. A slight modification is proposed to the deflection formula of Eurocode 2 to refine its predictions for FRP RC.

In Chapter 8 the conclusions of this research are drawn, and recommendations are made for future research work.

CHAPTER 2

LITERATURE REVIEW

2.1. INTRODUCTION

This literature review deals with flexural behaviour of reinforced concrete (RC) members with internal reinforcement. Flexural behaviour entails the topics of flexural capacity, cracking, deformation as well as tension stiffening and bond. Initially, the current state of knowledge of flexural behaviour of steel RC members is reviewed and the key parameters are identified. This is necessary because the current trend dealing with fibre reinforced polymer (FRP) RC member design is to make comparisons and impose modifications to the steel RC design practice. State-of-the-art reports and codes of practice are used for this part of the literature review. Before considering the flexural design issues, FRP reinforcing materials are introduced. The types and constituents of FRP, and their physical and mechanical properties are presented and are compared with those of steel. Then, the research and current state of knowledge on flexural behaviour of FRP RC members are reviewed. Recently published state-of-the-art reports and codes of practice on FRP RC are also examined. Finally, justifications for the objectives of this research project are presented.

2.2. STEEL RC MEMBERS

Steel RC is a composite of two materials: concrete and steel reinforcing bars (rebars). Plain concrete possesses adequate resistance in compression, but has limited tensile strength. Steel, however, is capable of resisting both tension and compression. Hence, steel reinforcement is used to compensate for the deficient concrete tensile strength by

providing the tensile resistance in tension zones. Steel reinforcement is also used to enhance the concrete resistance in compression zones. As a composite, steel and concrete work well together for several reasons (Wang and Salmon 1985):

- Adequate bond may be developed between steel rebars and the surrounding concrete, which ensures proper composite action with insignificant slip of rebars.
- Concrete may provide adequate protection to steel rebars against corrosion.
- Concrete and steel have rather similar coefficients of thermal expansion, which diminishes internal stresses due to temperature changes.

The following sections deal with flexural behaviour of steel RC. Flexural capacity, cracking and deflection are considered first. Then, the related topics of bond and tension stiffening are presented.

2.2.1. Flexural Capacity

The ultimate limit state design of steel RC for flexure aims at achieving ductile failure under ultimate loading conditions, where steel yields prior to crushing of the concrete. Ductile behaviour is desirable because it gives ample pre-failure warning, in the form of noticeable cracking and deformation, and it allows for redistribution of internal stresses. The evaluation of flexural capacity of steel RC sections is based on the following four assumptions and idealisations (Park and Paulay 1975, Wang and Salmon 1985):

- Plane sections before bending remain plane after bending (Bernoulli's principle).
- The tensile strength of the concrete may be neglected.
- The steel tensile stress-strain relationship is known.
- The concrete compressive stress-strain relationship is known.

The first assumption has been verified by a large number of tests to be very nearly correct throughout the whole loading range up to failure, provided good bond exists between concrete and steel. In that regard, Bernoulli's principle is not perfectly applicable in the vicinity of a crack, because a crack implies that some slip has occurred between steel and the surrounding concrete. However, it is noted that Bernoulli's principle applies well when considering the average strain measured over several cracks. This assumption is not true for deep beams and in regions of high shear, where

shear deformations and effects are prominent. The second assumption is nearly exact at the ultimate limit state because any tensile stresses just below the neutral axis are small and have a small lever arm. The tensile stress-strain relationship for steel is usually idealized with a bilinear model. The concrete compressive stress-strain relationship may be idealized with a suitable concrete model, but is usually simplified at the instance of failure with a rectangular stress block (Park and Paulay 1975).

To evaluate the flexural response within the loading range, before failure, the aforementioned assumptions and analysis are equally applicable. Then, it is possible to make a distinction between two analysis options. Cracked section analysis (CSA) assumes that every section of the flexural member is cracked and does not allow for any tension in the concrete. CSA is expected to provide an upper-bound solution for rebar strains and deflections and is further discussed in Chapter 5. However, cracks in flexural members are spaced and not every section is cracked. To allow for tension in the concrete between cracks, a tension model can be assigned to the concrete below the neutral axis. Such more general analysis may be referred to as sectional analysis. Figure 2-1 compares CSA and sectional analysis for a steel RC section under pure flexure prior to failure.

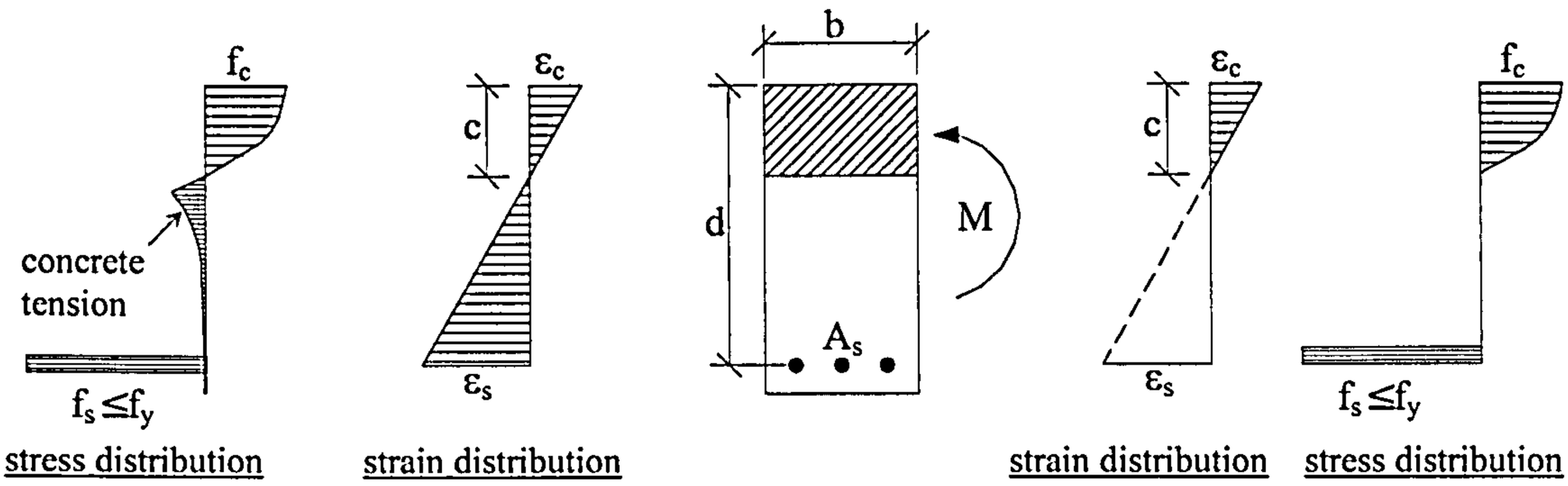

Figure 2-1: Cracked section analysis and sectional analysis.

2.2.2. Flexural Cracking

Cracking is an inherent property of the behaviour of reinforced concrete. The design to satisfy the serviceability limit state of cracking aims at controlling the width of cracks under service loads. Crack width control is generally required to ensure that the appearance of a structure is not harmed, specialized performance is not impaired (such as water-tightness) and risk of steel corrosion is mitigated (*fib* 1999b, CEB 1993). This study is only concerned with transverse cracks resulting from flexure. The mechanism of crack formation is considered next.

2.2.2.1. Mechanism of Crack Formation

The classical theory of cracking explains that tensile stresses are transferred from steel to concrete through bond. Before cracking, concrete and steel strains are compatible and no slip occurs. However, concrete tensile strength is limited and highly variable. A crack occurs when the tensile stress exceeds the tensile strength of concrete at a weak section. In a pure tension zone, the concrete becomes free from stress while the steel carries the tensile load at the crack. Strains in concrete and steel become incompatible and slip occurs on either side of the crack, within a distance known as the transmission length (L_t). The formation of the cracks, in this way, continues until their spacing reduces to between L_t and $2L_t$. Thereafter, no further cracks can develop and only crack widening occurs, in what is referred to as the stabilized cracking phase (*fib* 1999b, Park and Paulay 1975). Figure 2-2 shows the expected distribution of strains, stresses, bond and slip in the crack formation and stabilized cracking phases (*fib* 1999b, Balazs 1993).

As can be seen from Figure 2-2 , the first derivative of slip is equal to the difference between steel and concrete strains, while slip is equal to the difference of the integral of steel and concrete strains within the transmission length. Then, the crack width is equal to the sum of slip on either side. Furthermore, based on equilibrium requirements, the bond stress is linearly related to the first derivative of steel strain. Therefore, the distribution of tensile stresses and strains in the steel and concrete between cracks may be determined by a bond-slip relationship, which may be obtained experimentally or from bond-slip models (*fib* 1999b).

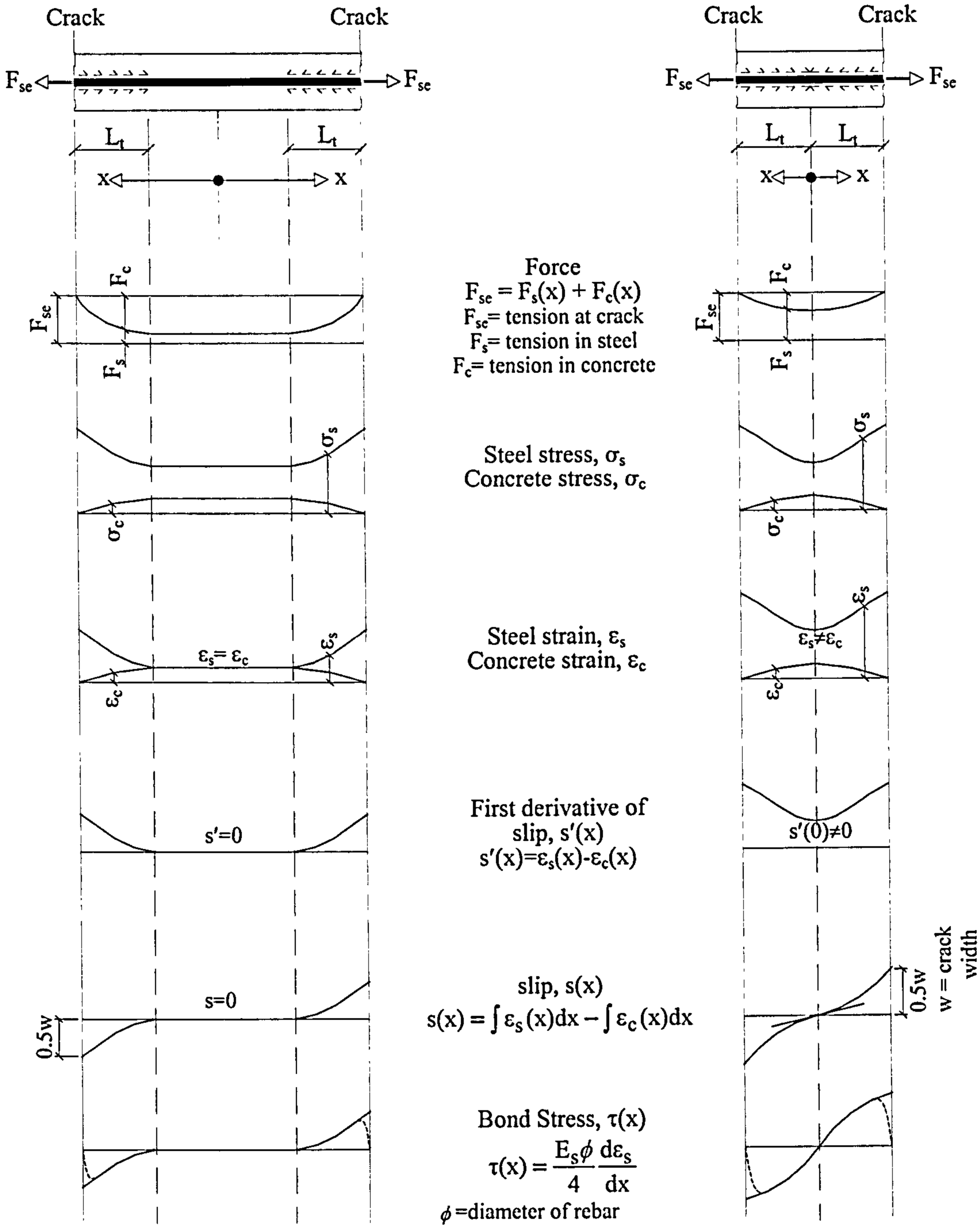

Figure 2-2: Expected distribution of strains, stresses, bond and slip in the crack formation and stabilized cracking phases (*fib* 1999b, Balazs 1993).

Alternatively, the contribution of concrete in carrying tensile stresses, or equivalently reducing stresses and strains in the reinforcement between cracks, may be viewed as causing an increase in the stiffness of the tensile reinforcement. This stiffening effect is commonly known as tension stiffening. Tension stiffening is actually a structural aspect of bond, and a tension stiffening relationship, whether experimental or analytical, may

be conveniently used to indirectly consider bond behaviour, without having to resort to a bond-slip relationship (*fib* 1999b). In other words, the use of a tension-stiffening or a bond-slip relationship may be interchangeable. However, the bond-slip approach is more direct when investigating bond splitting and anchorage of reinforcement. On the other hand, the tension stiffening approach may be more direct in dealing with flexural cracking and deformation.

By evaluating the crack width based on relative slip between the reinforcement and concrete, the assumption is made that the crack width at the surface of the concrete and at the surface of the rebar are equal. However, several studies have indicated that this is not the case, as crack widths tend to diminish at the surface of the rebar (Park and Paulay 1975, Beeby 2004). Therefore, on the other extreme, the no-slip theory of cracking assumes zero and maximum crack widths at the surfaces of rebar and member, respectively. The distribution of stress and strain in the concrete between the cracks may then be determined by the theory of elasticity (Park and Paulay 1975). ACI Committee 224 (1992) clarifies that two types of cracks are formed: primary and secondary cracks. Primary cracks are narrow on the surface of the rebar and wider on the surface. Secondary cracks, however, are similar to primary cracks but they close before reaching the surface. Therefore, formation of hidden cracks may explain why the cracks become narrower at the rebar surface.

Crack widths encountered in practice are highly variable, with a coefficient of variation of around 40% (ACI Committee 224 2001). This is mainly due to the high variability in the tensile strength of concrete. CEB (1993) estimates that, for the same grade of concrete, the mean characteristic tensile strength has lower and upper bounds within 35%. ACI 224 (1992) estimates that the crack formation phase along the length of a tension member occurs within 90% to 110% of the average tensile strength. *fib* (1999a) also emphasizes that the tensile concrete strength varies along the length of tension and flexural members, and estimates a ratio of 1.3 between the loads at which the final and first cracks form.

2.2.2.2. *Provisions in Codes of Practice*

The provisions for evaluation and control of cracking, in different prominent codes of practice on steel RC, are presented below. This is useful in identifying the different approaches and the key variables involved.

2.2.2.2.1 CEB-FIP Model Code 1990

CEB-FIP Model Code 1990 (CEB 1993) requires that the characteristic crack width (w_k) be less than a nominal value, which depends on exposure conditions (0.3mm for usual exposure). For all stages of cracking (formation and stabilized cracking), w_k is calculated as the relative slip between steel and concrete on either side of the crack, as follows.

$$w_k = l_{s,max}(\varepsilon_{sm} - \varepsilon_{cm} - \varepsilon_{cs}) \qquad (2\text{-}1)$$

where:

$l_{s,max}$ is the length over which slip between steel and concrete occurs,

ε_{sm} is the average steel strain within $l_{s,max}$,

ε_{cm} is the average concrete strain within $l_{s,max}$,

ε_{cs} is the strain of concrete due to shrinkage.

At stabilized cracking, an average crack width is estimated using an average crack spacing of $0.67 l_{s,max}$. $l_{s,max}$ is evaluated using equilibrium of the rebar between a crack and the point of zero slip midway between cracks, as follows.

$$l_{s,max} = 2\frac{\sigma_{s2} - \sigma_{sE}}{4\tau_{bk}}\phi_s \qquad (2\text{-}2)$$

where:

σ_{s2} is the steel stress at the crack,

σ_{sE} is the steel stress at the point of zero slip,

τ_{bk} is the lower fractile of the average bond stress,

ϕ_S is the steel rebar diameter.

τ_{bk} is evaluated as $(1.8 f_{ctm})$ for short-term loading and deformed rebars, where f_{ctm} is the mean concrete tensile strength. Then, the equation of $l_{s,max}$ simplifies as follows.

$$l_{s,max} = \frac{\phi_s}{3.6\rho_{s,ef}} \qquad (2\text{-}3)$$

in which, $\rho_{s,ef}$ is the effective reinforcement ratio within an effective reinforced concrete tension tie around the reinforcement. Moreover, an empirical factor (β) is used to evaluate the average values of the actual steel and concrete stress distributions between cracks. β is taken as 0.6 for deformed steel rebars and short-term loading. The CEB (1993) approach is further clarified in Figure 2-3.

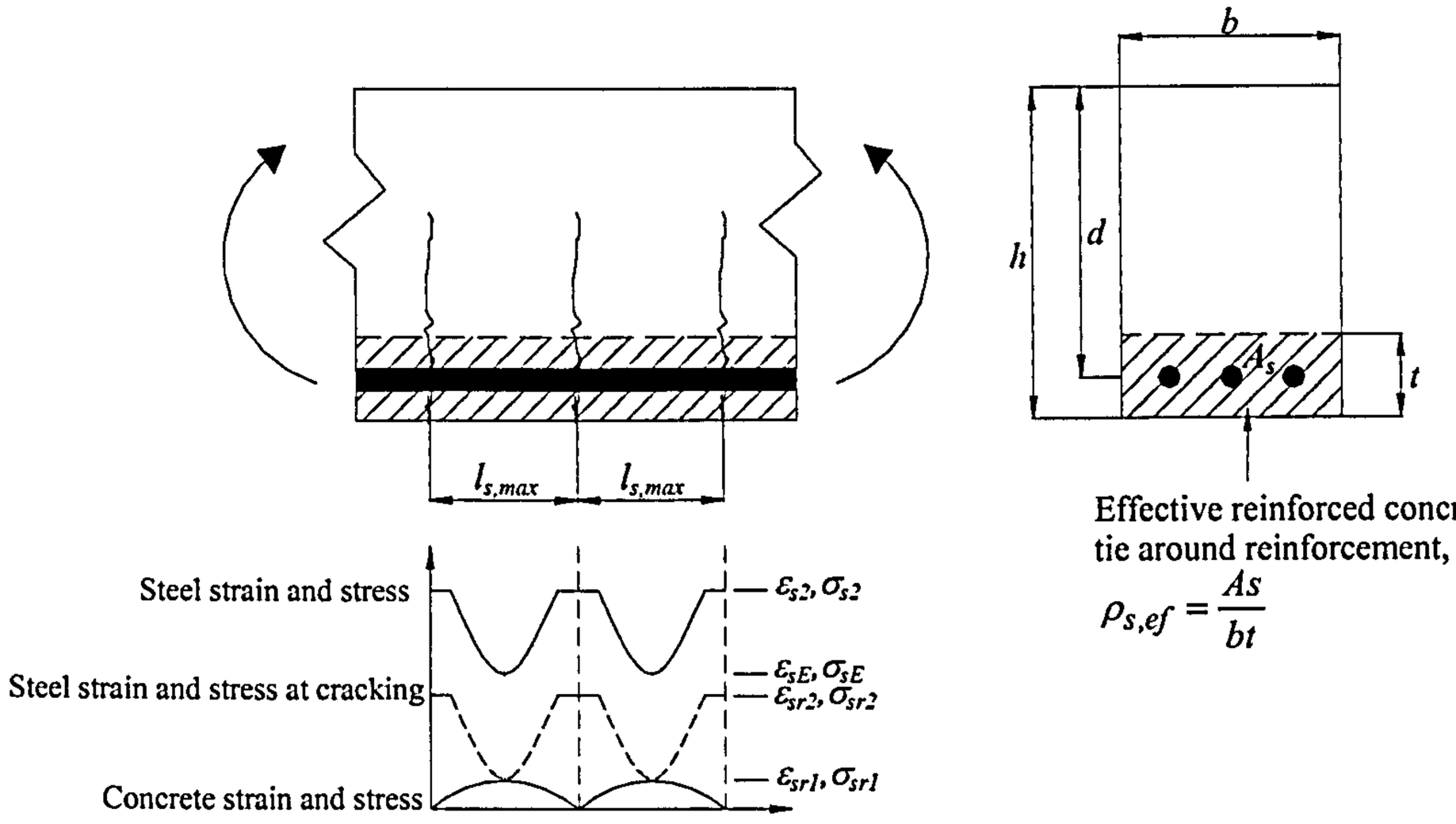

Figure 2-3: Crack spacing, strain and stress distributions and effective reinforced concrete tie according to CEB (1993).

It can be concluded that cracking of steel RC is dependent on several key parameters, namely, average reinforcement strain, reinforcement modulus, rebar diameter, concrete tensile strength, bond characteristics and effective reinforcement ratio. Moreover, the CEB (1993) treatment of flexural cracking is based on fundamentals, and only two assumptions are made. The tension stiffening factor (β) is given a constant empirical value. Also, a constant average bond is assumed and taken as a function of the concrete tensile strength. These assumptions are particular to steel RC, and may need to be modified for FRP RC.

2.2.2.2.2 *Eurocode 2*

Eurocode 2, EN 1992-1-1:2004 (CEN 2004), calculates the surface crack width (w_k) based on the CEB (1993) approach. However, the maximum crack spacing ($s_{r,max}$) is modified as follows.

$$s_{r,max} = k_3 c + k_1 k_2 k_4 \phi_s / \rho_{s,ef}, \text{ for } s \leq 5(c+\phi_s/2) \quad (2\text{-}4)$$

$$s_{r,max} = 1.3(h-x), \text{ for } s > 5(c+\phi_s/2) \quad (2\text{-}5)$$

where:

k_1 is a bond coefficient (0.8 for high bond rebars and 1.6 for plain rebars),

k_2 is a strain distribution coefficient (0.5 for bending and 1.0 for pure tension),

k_4 is recommended as 0.425,

c is the concrete cover to the longitudinal reinforcement,

k_3 is recommended as 3.4,

s is the spacing of rebars,

h is the overall member depth,

x is the neutral axis depth.

The second term in Equation (2-4) can be evaluated as 60% of the corresponding CEB (1993) expression [Equation (2-3)]. In other words, this term gives the average crack spacing recommended by CEB (1993). The first term introduces the concrete cover as an additional variable, which recognises the fact that the crack width is larger at the concrete surface than at the surface of the rebar (Beeby 2004).

2.2.2.2.3 *ACI*

The ACI building code for structural concrete, ACI 318-95 (ACI committee 318 1995), does not calculate crack widths explicitly, but rather uses a factor (z) derived from a crack width formula. This has been done in order not to give too much weight to crack widths, as these are highly variable in practice. However, for better comparison with other codes, the underlying crack width approach is shown below. ACI committee 224 (2001) on cracking explains that statistical analysis of maximum crack width data by Gergely and Lutz (1968) led to a formula for the maximum probable crack width. This

formula has been simplified and rewritten by using rebar strain instead of stress, as follows.

$$w = 2.2\beta\varepsilon_s \sqrt[3]{d_c A} \qquad (2\text{-}6)$$

where:

w is the maximum probable crack width at the bottom surface,

ε_s is the steel reinforcement strain,

A is the concrete area symmetric with reinforcement divided by the number of rebars,

d_c is the thickness of cover from the extreme tension fibre to the centre of closest rebar,

β is the ratio of the distance between neutral axis and tension face to the distance between neutral axis and centre of reinforcement.

In Equation (2-6), the ratio of maximum crack width at the surface to that at the reinforcement level is proportional to the ratio of strain at the surface and the reinforcement strain. The steel stress was rated as the most important variable. The concrete cover thickness and the area of concrete surrounding the rebars were also considered as two important variables. The rebar diameter was not considered to be a major variable. The ACI approach is further clarified in Figure 2-4.

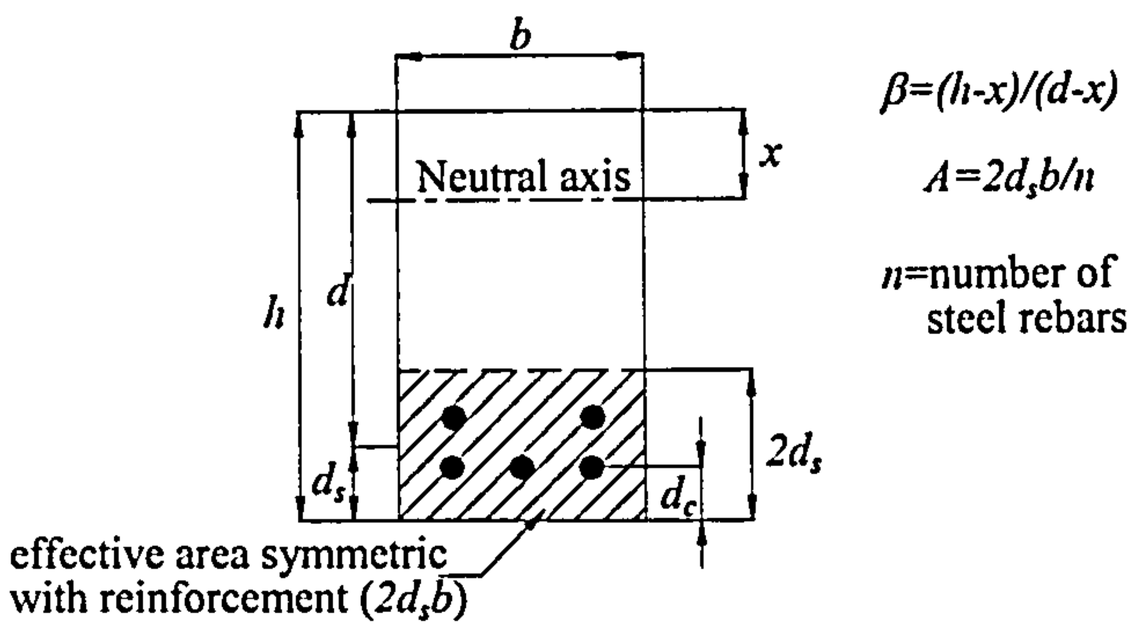

Figure 2-4: Notation of the ACI 318 crack width formula.

The ACI approach involves only some of the key parameters identified in CEB (1993). It does not explicitly allow for the concrete tensile strength, tension stiffening or bond characteristics. These parameters may be implicit in the formulation, but then their role needs to be identified before adapting the ACI approach to FRP RC.

ACI 318-02 and ACI 318-05 (ACI Committee 318 2002 and 2005) control cracking under normal exposure conditions by limiting the spacing of the steel reinforcement (s). However, this approach is again based on a crack width formula that was proposed by Frosch (1999), as follows.

$$w = 2\beta\varepsilon_s \sqrt[3]{d_c^{\,2} + \left(\frac{s}{2}\right)^2} \qquad (2\text{-}7)$$

in which, all the terms are as defined for the earlier crack width Equation (2-6).

ACI Committee 224 (1992) provides general guidance on crack spacing. The maximum crack spacing in tension-only members is estimated as four times the cover thickness; measured to the centre of reinforcement. For flexural members, the maximum crack spacing is estimated to be less than tension members by more than 20%.

2.2.2.2.4 BSI

BS 8110-2:1985 (BSI 1985) also specifies a maximum crack width of 0.3mm for usual exposure. The crack width at a particular point on the surface depends on the average surface strain at that point and on its proximity to the neutral axis and rebars, as follows.

$$w_{cr} = \frac{3a_{cr}\varepsilon_m}{1 + 2\left(\frac{a_{cr} - c_{\min}}{h - x}\right)} \qquad (2\text{-}8)$$

where:

w_{cr} is the maximum crack width at the point considered.

a_{cr} is the distance of the point considered to the surface of the nearest rebar.

$c_{\min}$ is the minimum cover.

h is the overall depth of the member.

x is the neutral axis depth.

ε_m is the average strain at the level of the point considered.

To evaluate ε_m, the general method is to carry out elastic section analysis that does not neglect the concrete in tension, but rather considers a linear tensile stress distribution for the concrete; with a value of zero at the neutral axis and 1.0 MPa at the level of the tensile reinforcement. This indirectly accounts for tension stiffening. It is worth noting

that, at a point on the tension face directly beneath a rebar, a_{cr} is equal to $c_{\min}$. Then, w_{cr} reduces to $3c_{\min}\varepsilon_m$, which means that the crack spacing is equal to three times the cover thickness. The approach of BSI (1985) is further clarified in Figure 2-5.

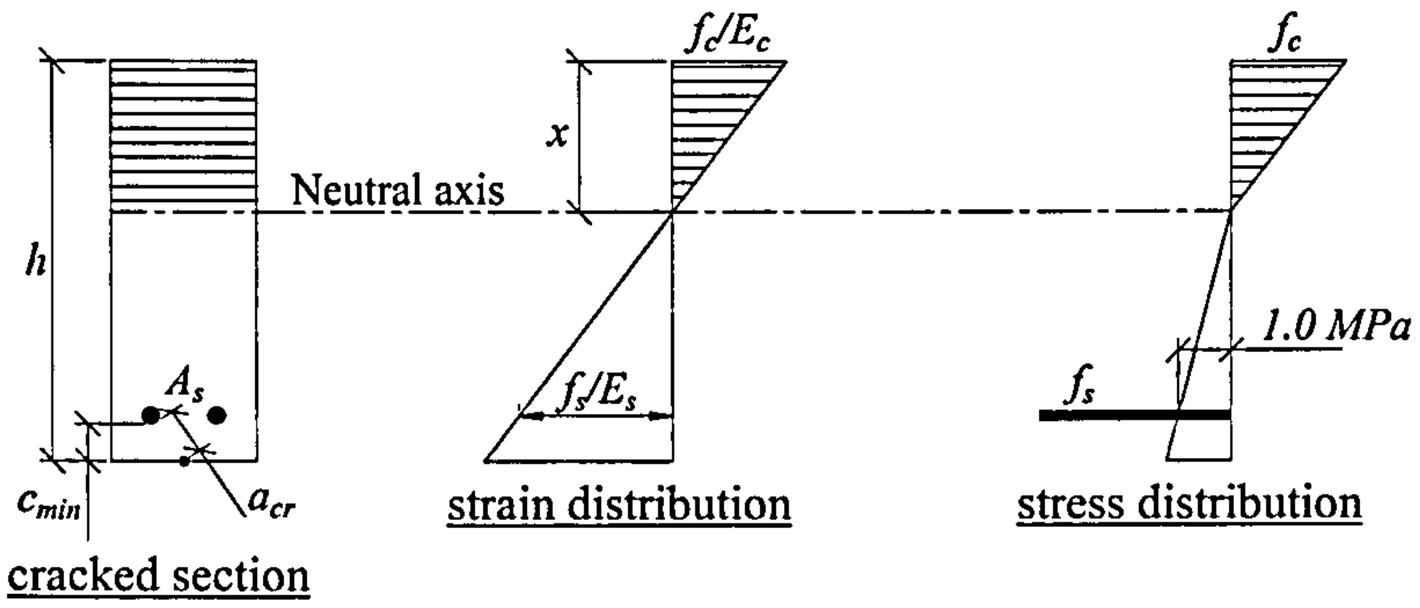

Figure 2-5: Crack width evaluation by BSI (1985).

The key parameters in the approach of BSI (1985) are the average reinforcement strain and concrete cover. The tension stiffening is given a fixed effect that may be particular to steel RC, and may need to be modified to allow for different bond and tension stiffening characteristics of the FRP reinforcement.

2.2.3. Flexural Deflection

The design for the serviceability limit state of deflection aims at limiting deflection under service conditions to within acceptable limits. Deflection control is generally required to ensure that the appearance of the structure is not impaired, the non-structural components are not harmed and the proper function of the structure or its equipment is not adversely affected (*fib* 1999b, CEB 1993).

The general approach in evaluating deflection due to flexure can be based on the basic relationship between curvature (κ) and deflection (δ), where:

$$\kappa = \frac{d^2\delta}{dx^2} \qquad (2\text{-}9)$$

Equation (2-9) is applicable for any flexural member of any material; as it is derived from purely geometric considerations. The only limitation is that deflections should be small, which is normally the case in RC members at their serviceability limit state. To

solve the differential equation for deflection, the curvature-area theorems in association with numerical techniques can be used (Timoshenko and Gere 1972).

However, dealing with short-term deflection of RC members is not as straightforward. Concrete cracking and nonlinear bond between the reinforcement and concrete have a direct impact on curvature, and should be properly accounted for. Codes of practice on steel RC attempt to account for cracking and bond by simplified methods. These methods apply when shear effects are negligible and assume pure flexure conditions; where plane sections remain plane midway between the cracks. The interaction of the reinforcement and concrete between cracks is considered by a tension stiffening relationship, which interpolates a certain deformation parameter between its extreme values at the cracked and uncracked states. The provisions for evaluation of short-term deflection, in different prominent codes of practice on steel RC, are presented and discussed next. Similar to the treatment of cracking, this is useful in identifying the various approaches and the key variables involved.

2.2.3.1. Provisions in Codes of Practice

2.2.3.1.1 CEB-FIP Model Code 1990

The general approach of CEB (1993) is to calculate deflections from curvatures. The mean curvature (instantaneous or long term) at a section is given by:

$$\frac{1}{r} = \frac{\varepsilon_{s,m} - \varepsilon_{c,m}}{d} \qquad (2\text{-}10)$$

where:

$\varepsilon_{s,m}$ is the mean reinforcement strain; evaluated by a tension stiffening relationship for an effective RC tension tie around the tensile reinforcement,

$\varepsilon_{c,m}$ is the mean concrete strain at the top concrete fibre, and should account for the variation of the depth of the compression zone between adjacent cracks,

d is the lever arm.

Alternatively, CEB (1993) provides a tension stiffening expression, which interpolates the mean curvature ($1/r$) between the curvatures at the uncracked ($1/r_1$) and cracked states ($1/r_2$), as shown in the moment-curvature diagram in Figure 2-6 and as detailed in the following.

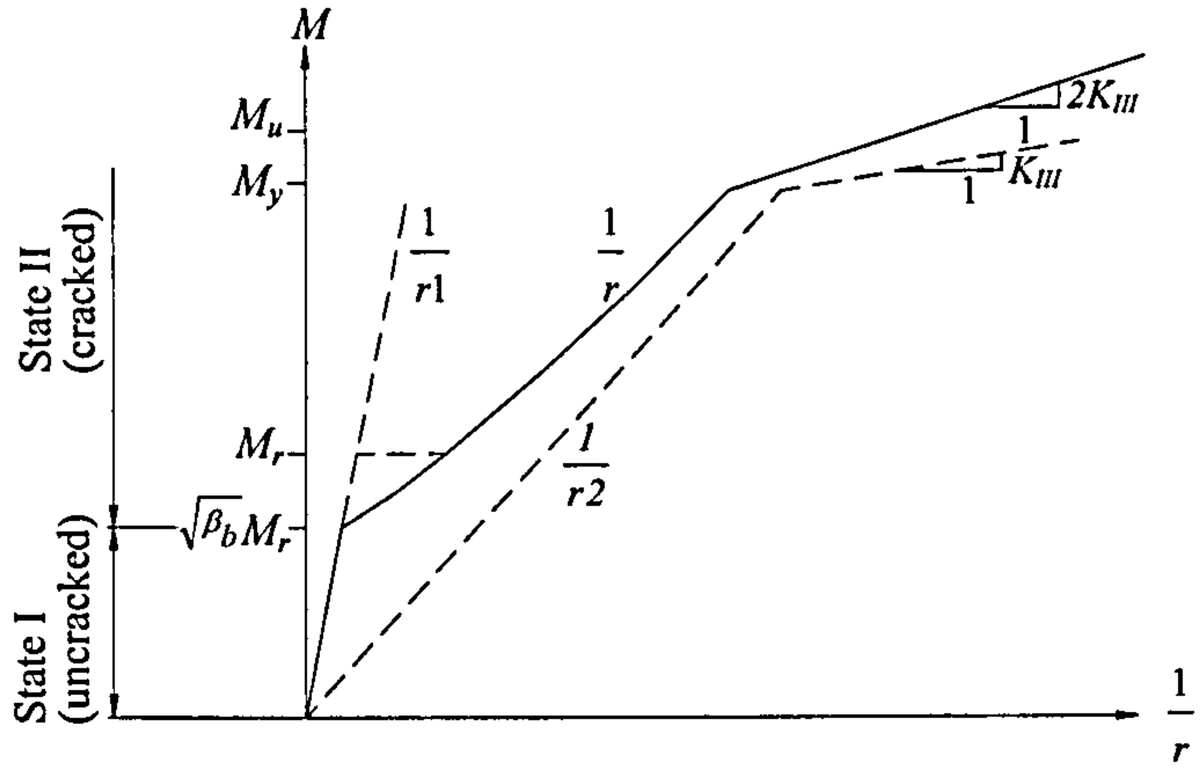

Figure 2-6: Moment-curvature relationship (CEB 1993).

$$\frac{1}{r} = \frac{1}{r_1} \text{ for state I (uncracked state)} \qquad (2\text{-}11)$$

$$\frac{1}{r} = \frac{1}{r_2} - \frac{1}{r_{ts}} = \frac{1}{r_2} - (\frac{1}{r_{2r}} - \frac{1}{r_{1r}})\beta_b(M_r / M) \text{ for state II (cracked state)} \qquad (2\text{-}12)$$

$$\beta_b = \beta_1 \beta_2 \qquad (2\text{-}13)$$

where:

M is the acting bending moment,

M_r is the cracking moment,

$\frac{1}{r_1}$ and $\frac{1}{r_{1r}}$ are curvatures in state I corresponding to M and M_r, respectively,

$\frac{1}{r_2}$ and $\frac{1}{r_{2r}}$ are curvatures in state II corresponding to M and M_r, respectively,

$\frac{1}{r_{ts}}$ is the tension stiffening effect on curvature,

β_1 is a bond quality coefficient (1 for high-bond rebars and 0.5 for smooth rebars),

β_2 is a duration or repetition of load factor (0.8 at first loading and 0.5 for long-term or cyclic loading).

It may be observed that the ratio of the tension stiffening effect at any load level to that at the cracking load level is taken as proportional to the ratio of the cracking moment to the applied moment (M_{cr}/M). Similar to cracking, CEB (1993) treatment of flexural deflection follows a general and fundamental approach. Only the tension stiffening relationship and bond factors may be particular to steel RC.

2.2.3.1.2 Eurocode 2

To evaluate deflection, Eurocode 2 (CEN 2004) interpolates a deformation parameter (α) between its values at the uncracked and cracked states, and then requires numerical integration to calculate deflection. For example, α may be strain, rotation or curvature. More simply, α may be taken as deflection directly, and is expressed as follows.

$$\alpha = \xi\alpha_{II} + (1-\xi)\alpha_{I} \qquad (2\text{-}14)$$

in which, α_I and α_{II} are the values of the deformation parameter considered at the uncracked and cracked states, respectively. ξ accounts for tension stiffening, and is given as follows.

$$\xi = 1-\beta\left(\frac{M_{cr}}{M}\right)^2 \qquad (2\text{-}15)$$

in which, M_{cr} and M are the cracking and applied moment, and β is a duration or repetition of load factor (1.0 for short-term loading and 0.5 for sustained or cyclic loading). In the earlier version of Eurocode 2 [ENV 1992-1-1:1992 (CEN 1992)], the factor β was termed β_2 and was multiplied by another bond factor (β_1), which was taken as 1.0 for high-bond rebars and 0.5 for plain rebars.

The tension stiffening expression (ξ) of Eurocode 2 is just a modified form that can actually be derived from the tension stiffening expression of CEB (1993). However, in Eurocode 2, it is applied to any deformation parameter. Moreover, the bond factor does not show in the latest Eurocode 2, but the use of such a factor may be required for FRP RC.

2.2.3.1.3 ACI

ACI 318-02 and ACI 318-05 (ACI Committee 318 2002 and 2005) calculate short-term deflection using elastic analysis. Tension stiffening is accounted for by using an effective moment of inertia (I_e), which also accounts for the spread of cracking along the flexural member. I_e is interpolated between the uncracked (I_g) and cracked (I_{cr}) values, as follows.

$$I_e = I_{cr} + \left(I_g - I_{cr}\right)\left[\frac{M_{cr}}{M_a}\right]^3 \le I_g \qquad (2\text{-}16)$$

in which, M_{cr} and M_a are the cracking and applied moment, respectively.

Conceptually, the ACI deflection approach is not different from that of CEB (1993) or Eurocode 2. All these codes use a tension stiffening expression that provides some form of transition between the uncracked and cracked states of a certain deformation parameter. However, the ACI tension stiffening expression does not allow for different bond characteristics, as may be the case for FRP RC.

2.2.3.1.4 BSI

BS 8110-2:1985 (BSI 1985) evaluates deflection from curvature. Similar to CEB (1993), the general approach is to calculate curvatures at successive sections along the span, and then numerical integration is used to calculate deflection. In a simplified approach, deflection is calculated as follows.

$$a = Kl^2(1/r_b) \qquad (2\text{-}17)$$

in which, a is the deflection, l is the effective span, K is a constant that depends on the shape of the bending moment diagram, and $1/r_b$ is the curvature at the midspan section or, for cantilevers, at the support section. $1/r_b$ is evaluated by elastic section analysis that accounts for tension stiffening by allowing the concrete below the neutral axis to carry some tension. A linear concrete tensile stress distribution is assumed, which is identical to that used for crack width calculation, as shown in Figure 2-5 in Section 2.2.2.2.4. Again, tension stiffening is given a fixed effect, which may be very particular to steel RC and may need to be modified to become suitable for FRP RC.

2.2.4. Bond

All behavioural aspects of RC members are influenced by bond. Crack width and spacing, deformation, and even the ultimate load carrying capacity are bond dependent (*fib* 1999a). Bond of steel to concrete is generated by adhesion, mechanical actions and friction, which are activated at different levels of stress in the reinforcement. Bond stresses are also accompanied by relative slip of the reinforcement. Figure 2-7 shows a typical bond-slip relationship that may be described in four stages, as follows (*fib* 1999a, *fib* 2000).

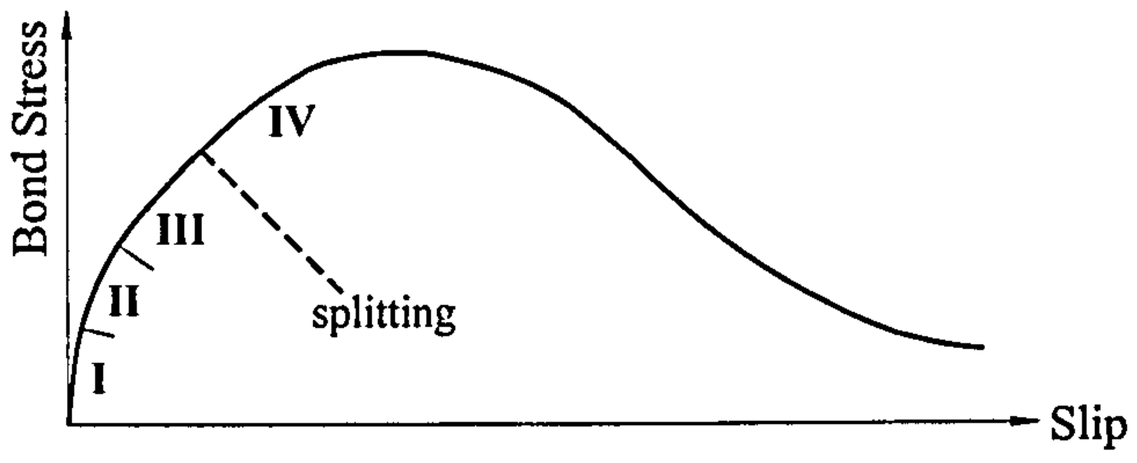

Figure 2-7: Typical bond-slip relationship (*fib* 1999a)

- In Stage I, bond is due to adhesion. Bond stresses are very low and slip is negligible. Adhesion breaks at the end of this stage.
- In Stage II, bond is due to bearing of the steel ribs against the concrete, which causes transverse micro-cracks originating at the ribs, bending of the concrete keys between the ribs as well as crushing of the concrete in front of the ribs, as shown in Figure 2-8. The Rib wedging action is not mobilized yet.

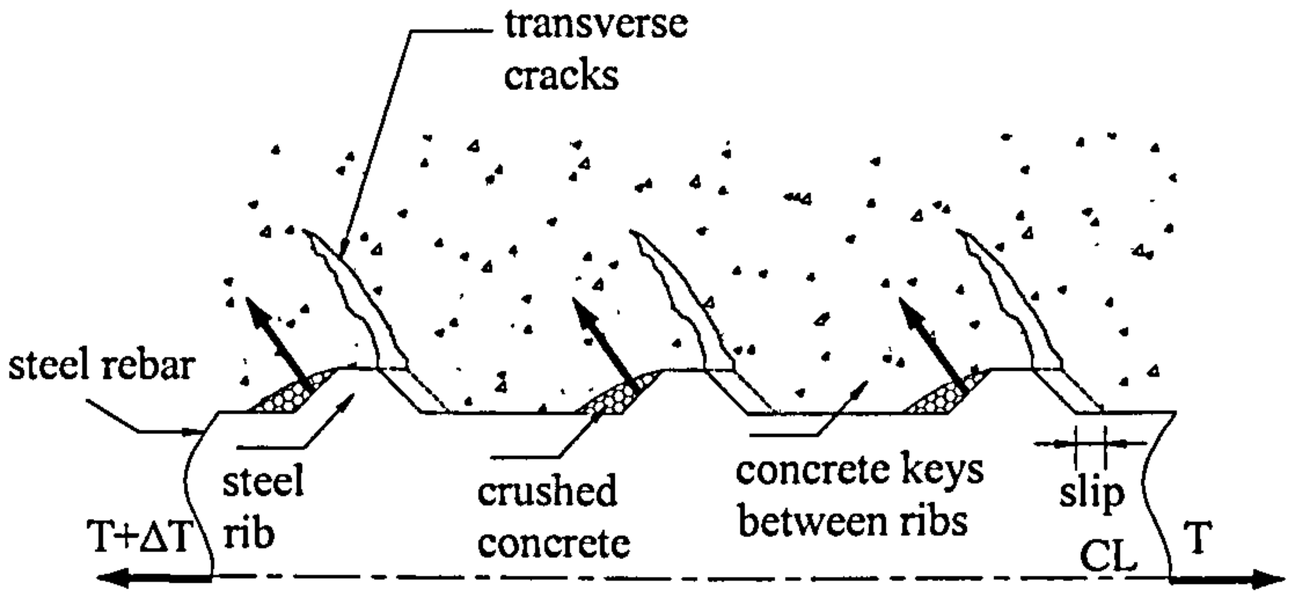

Figure 2-8: Stage II-bearing of ribs on concrete and transverse micro-cracks (*fib* 2000).

- In Stage III, wedging of the ribs is mobilized and causes longitudinal splitting cracks that spread radially. If the concrete is not confined conveniently or if the concrete cover is not sufficient, these splitting cracks propagate through the entire concrete cover and appear on the surface. Then, a splitting bond failure occurs.
- In Stage IV, if splitting is prevented, pull-out failure occurs at higher bond stresses. The concrete keys between the ribs shear off and a friction mechanism is activated along a sliding plane around the rebar, with significantly reduced bond stresses.

Bond action in steel is mainly dependent on the geometry of the rib pattern. Reinforcement with an optimized rib pattern generates better bond, with reduced transfer length, hence, reduced crack spacing and width. Bond action is also affected by transverse contraction of the reinforcement at higher stress levels (particularly after yield). However, this is only important when the friction mechanism is activated. On the other hand, bond resistance is mainly dependent on the concrete tensile strength and state of stress, level of confinement, concrete cover, rebar spacing and rebar diameter (*fib* 1999a, *fib* 2000).

CEB (1993) adopts a simplified local bond-slip model, as shown in Figure 2-9. This model is based on a statistical mean of a broad range of experimental results. It may be used to calculate the distribution of bond stress over the transfer length and to predict crack formation and elongation of a steel RC tie. Also, it may be used to study anchorage of rebars (*fib* 1999a, CEB 1993).

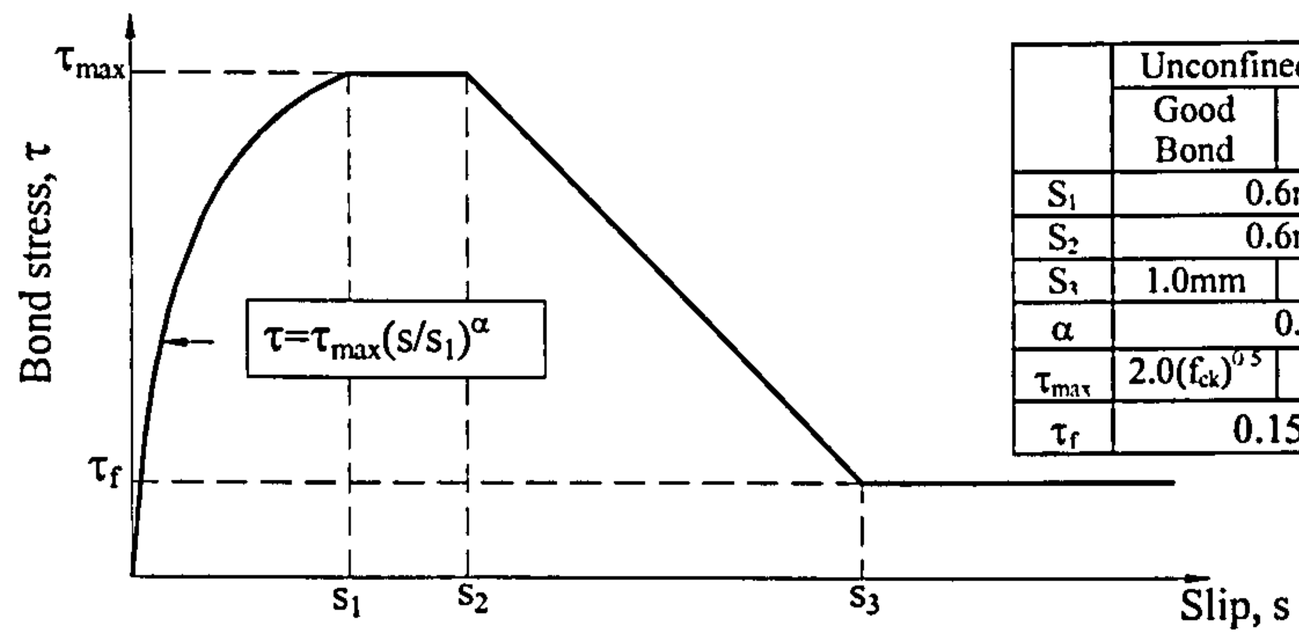

	Unconfined Concrete		Confined Concrete	
	Good Bond	Other cases	Good Bond	Other cases
S_1	0.6mm		1.0mm	
S_2	0.6mm		3.0mm	
S_3	1.0mm	2.5mm	Clear rib spacing	
α	0.4		0.4	
τ_{max}	$2.0(f_{ck})^{0.5}$	$1.0(f_{ck})^{0.5}$	$2.5(f_{ck})^{0.5}$	$1.25(f_{ck})^{0.5}$
τ_f	$0.15\tau_{max}$		$0.40\tau_{max}$	

Figure 2-9: Bond-slip model (CEB 1993).

Different regions of RC elements have different bond conditions, as shown in Figure 2-10. Therefore, researchers use various test methods to assess bond behaviour. Several versions of the pull-out test with short anchorages are usually used to obtain bond-slip relationships. Beam tests have closer proximity to the actual structural conditions. Strain gauging of reinforcement is useful in studying long anchorages, splices and tension stiffening. However, the test methods for bond are not standardized (*fib* 2000).

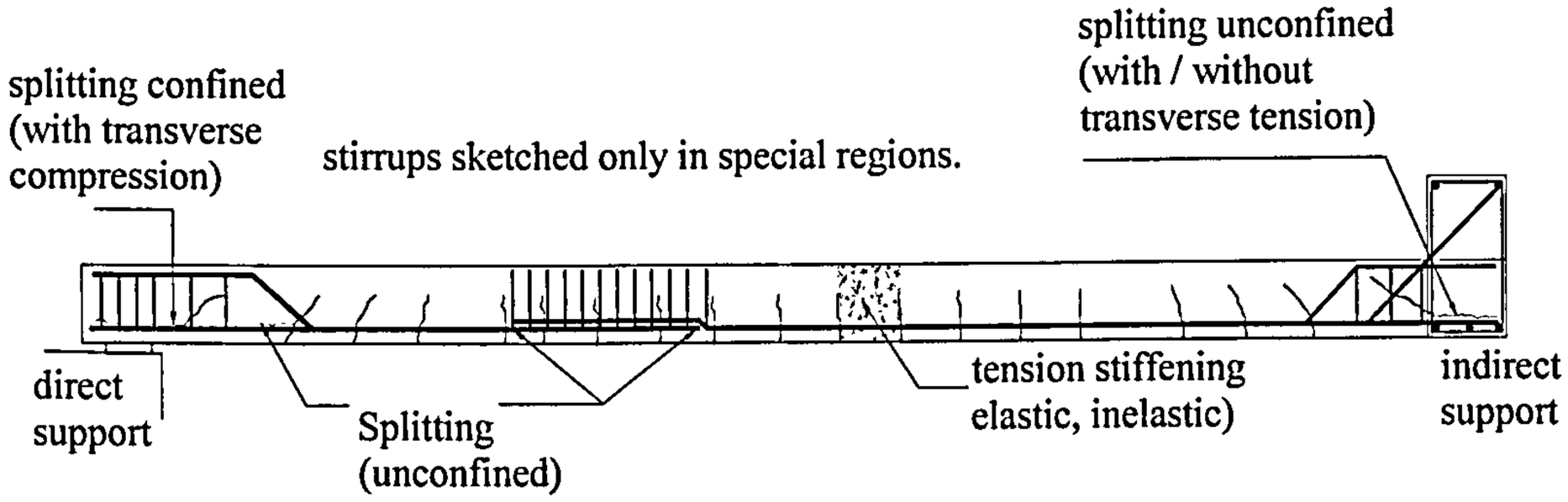

Figure 2-10: Typical bond problems in RC beams (*fib* 2000).

2.2.5. Tension Stiffening

The tension stiffening effect has been introduced previously. To recapitulate, tension stiffening is a term that accounts for the effect of bonded concrete, acting in tension between cracks, on the reinforcement. At a crack, all the tensile force is carried by the reinforcement, whereas between cracks, some of the tensile force is transferred, through bond, to the surrounding concrete. This reduces the reinforcement stresses and strains, and causes the average reinforcement strain to be less than the reinforcement strain at the crack or of the bare reinforcement. Hence between cracks, the concrete stiffens the reinforcement and the reinforcement appears to have a higher effective modulus of elasticity (CEB 1993, *fib* 1999a, ACI committee 224 1992).

CEB (1993) and *fib* (1999a) provide a basically identical tension stiffening model for a steel RC tension tie; in the form of a stress-average strain relationship. The model with *fib* (1999a) terminology uses force instead of stress, and is shown in Figure 2-11. *fib* (2000) clarifies that such an approach smears cracking and slip of the reinforcement. Such a model can be used to calculate deflections of a flexural member, since the tension reinforcement and the surrounding concrete can be considered as a tension tie.

However, it is more common to consider the effects of tension stiffening by providing a transition between the uncracked and cracked states of a deformation parameter at the section or member levels, as explained earlier.

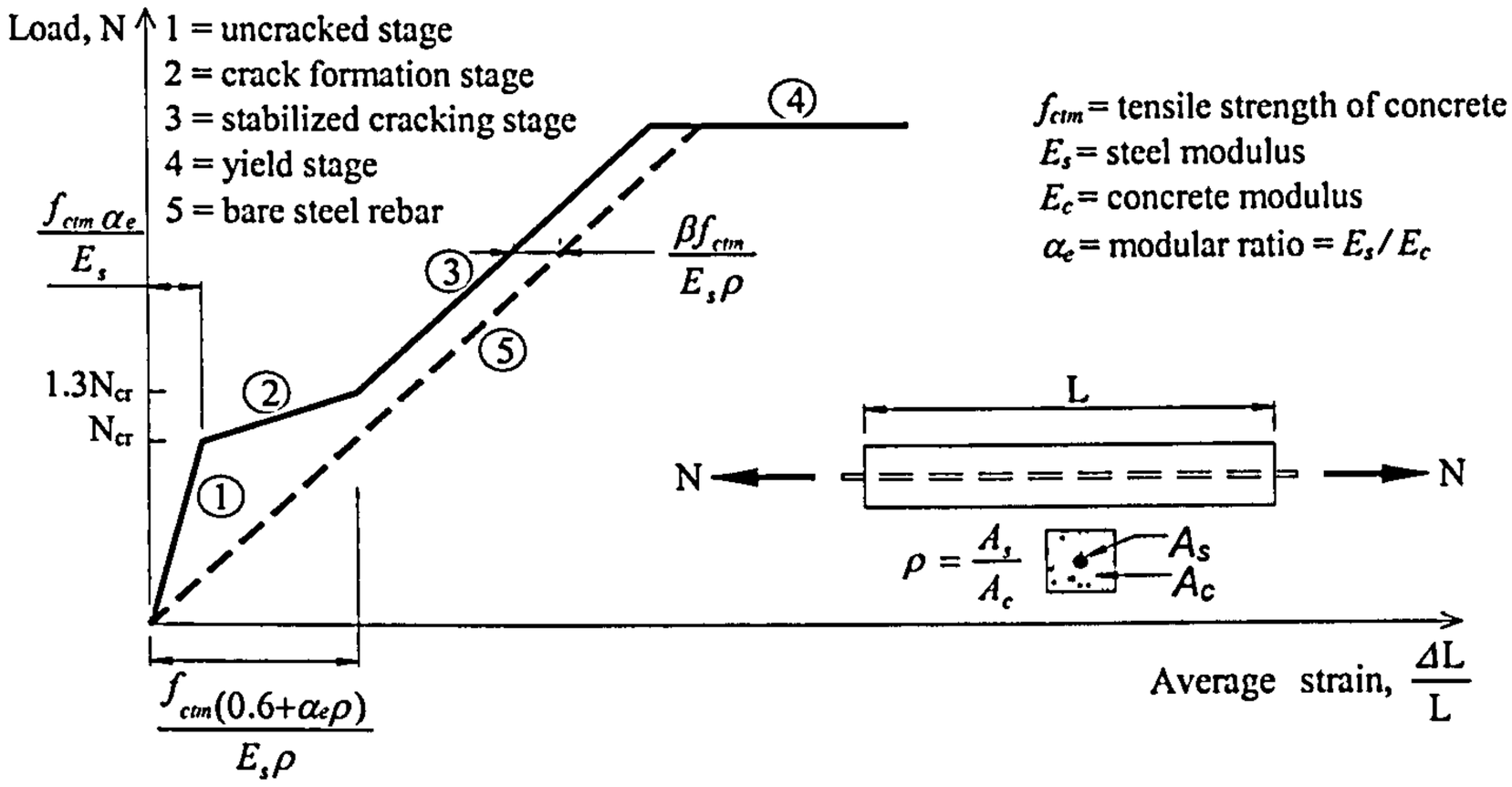

Figure 2-11: Load-strain relationship of an RC tension tie (*fib* 1999a).

Most important in Figure 2-11 is the tension stiffening factor (β), which defines the strain difference between the bare and embedded reinforcement. For steel RC, β is taken as 0.4 and 0.25 for short-term and long-term loading, respectively. The short term value of β (β=0.4) is based on two assumptions: the bond stress is constant regardless of slip, and the average crack spacing equals 1.5 times the crack transmission length. The assumption of a constant bond-slip relationship entails that the steel and concrete strain profiles between cracks are linear. It also entails a constant tension stiffening effect after cracking (CEB 1993, *fib* 1999a). With different modulus and surface characteristics of the FRP reinforcement, a different constant or variable β may apply.

ACI Committee 224 (1992) deals with tension stiffening of a steel RC tie by using a reduced effective concrete area; similar to the effective moment of inertia in the ACI deflection approach. In that document, the ACI and CEB approaches are shown to compare very well in terms of their prediction of average strain. Moreover, ACI Committee 224 (1992) reports that tension stiffening has been modelled rather successfully by both the discrete crack and smeared crack finite element formulations. Details of these may be found in the literature (ASCE 1982). The smeared crack approach is considered in Chapter 5.

2.3. FRP RC MEMBERS

2.3.1. General

FRP reinforcement is a composite of continuous fibres in a resin matrix. The commonly used fibres are glass, aramid or carbon (*fib* 2000, ISIS Canada 2001), while the resins are usually thermosetting resins, such as polyester, vinyl ester or epoxy. Fibres are the main load carrying constituent, while the matrix transfers stresses between the fibres, protects the fibres from environmental or mechanical damage, provides lateral support against fibre buckling under compression, and ensures interaction with the surrounding concrete. Fillers may be added to the matrix to impart desirable properties such as improvement of load transfer (ACI Committee 440 1996). For structural purposes, the matrix content typically ranges from 0.25 to 0.5 by weight (ACI Committee 440 1996), or equivalently, the fibre volume fraction ranges from 0.5 to 0.7 (ACI Committee 440 2003). The surface preparation of the FRP rebar has a direct impact on bond. Various surface conditions are commercially available, such as sand coated, ribbed, indented and braided (Figure 2-12). A combination of surface treatments is also used. However, there is no standardized classification of surface conditions (ACI Committee 440 2003).

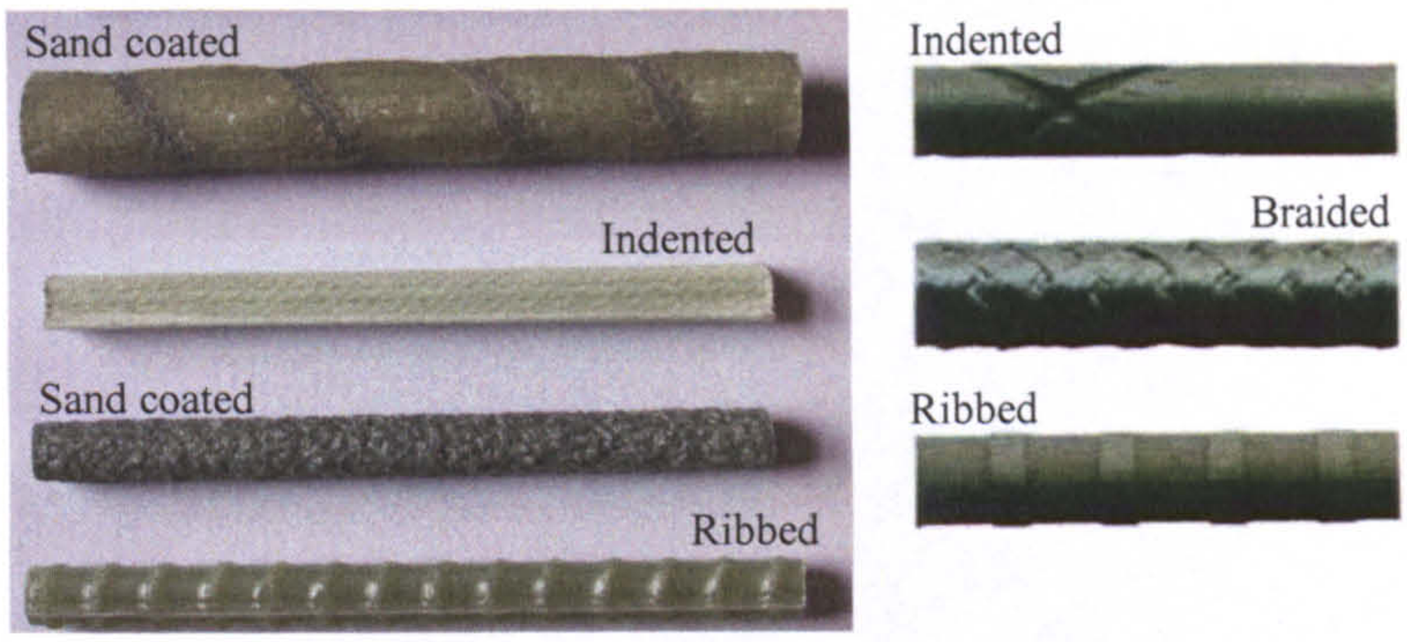

Figure 2-12: FRP rebars with various surface conditions.

FRP composites show linear stress-strain behaviour under tension up to failure. Compared to the ductile steel, FRP generally have brittle behaviour, with higher tensile capacity, limited strain range and lower modulus of elasticity. Table 2-1 and Figure 2-13 show typical tensile characteristics of glass, carbon and aramid FRP (GFRP, CFRP and AFRP) rebars compared to steel. Strength and modulus of elasticity of FRP are

weaker in compression than in tension. The shear strength of FRP is low. However, no standard test methods are yet available to characterise the FRP compressive and shear behaviour. FRP is more susceptible to creep rupture than steel; CFRP and GFRP being least and most susceptible, respectively. In general, FRP seem to have good fatigue resistance, as has been well established in the aerospace industry (ACI Committee 440 1996 and 2003, ISIS Canada 2001).

Table 2-1: Typical tensile properties of steel and FRP rebars (ACI Committee 440 2003)

	Steel	GFRP	CFRP	AFRP
Nominal yield stress, MPa	276 to 517	N/A	N/A	N/A
Tensile strength, MPa	483 to 690	483 to 1600	600 to 3690	1720 to 2540
Elastic Modulus, GPa	200	35.0 to 51.0	120.0 to 580.0	41.0 to 125.0
Yield strain, %	1.4 to 2.5	N/A	N/A	N/A
Rupture strain, %	6.0 to 12.0	1.2 to 3.1	0.5 to 1.7	1.9 to 4.4

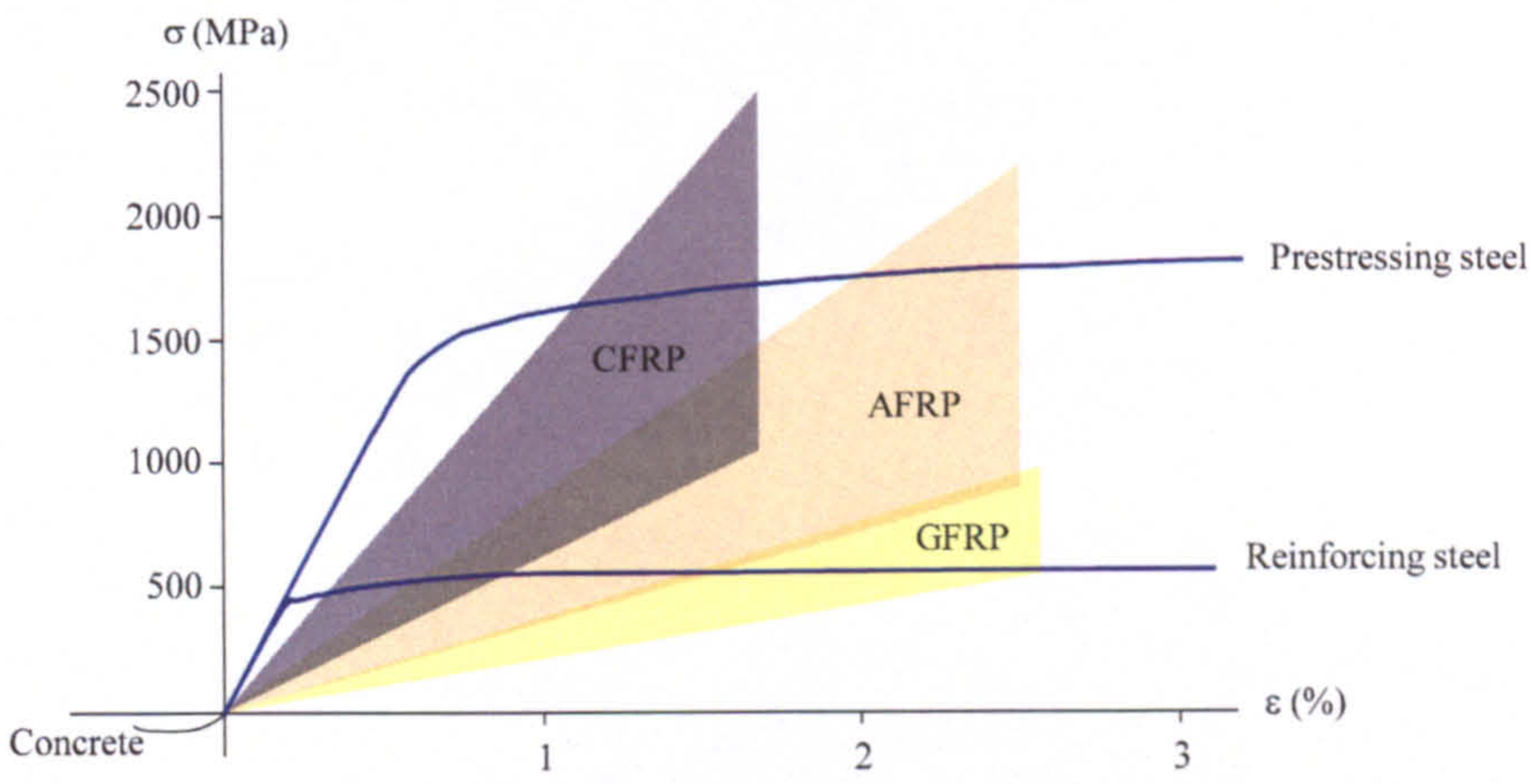

Figure 2-13: Tensile stress versus strain of FRP and steel materials (Pilakoutas 2000).

In addition to the high tensile strength, FRP offer several advantages in comparison to steel. FRP are corrosion resistant, which makes them ideal in situations where steel reinforcement suffers from corrosion, such as marine RC structures. FRP offer electromagnetic permeability, which is essential in specialized applications where steel causes electromagnetic interference, for example in the mobile telecommunications industry and MRI rooms in hospitals. Moreover, FRP are lighter than steel, which facilitates transportation and speeds construction (ACI Committee 440 1996, Waldron et al 2000).

The main disadvantage of FRP is their lower modulus of elasticity. Generally, this entails higher reinforcement strains in FRP RC compared to steel RC, together with wider and deeper cracks as well as higher deflections. Therefore, contrary to steel RC, serviceability may often govern the design of FRP RC (ISIS Canada 2001). Wider crack width limits may be tolerated in FRP RC because corrosion is no longer of concern. On the other hand, steel RC deflection limits should remain applicable to FRP RC because they are independent of the reinforcement (ISIS Canada 2001, ACI Committee 440 1996). In cases where the ultimate limit state controls the design, a ductile failure similar to that of steel RC cannot be attained. Two types of flexural failure may develop in FRP RC: failure by rupture of rebars or failure by crushing of concrete. Both failures are brittle in nature with the former being more sudden and catastrophic (ISIS Canada 2001, ACI Committee 440 2003). Another drawback may be the diverse bond characteristics of the different commercial FRP products; particularly that serviceability can be strongly influenced by bond (Pecce et al 2001).

Relatively little research was undertaken on FRP RC before 1990. Since that date, a substantial amount of research has been carried out on the structural and durability behaviour of FRP RC, and to improve the characteristics of FRP reinforcement. However, most of the applications have been in prestressed concrete structures, particularly bridges. The subsequent sections present a review of the relevant FRP RC research since 1990, in addition to the current knowledge and research needs as reported in state-of-the-art reports and codes of practice on FRP RC. For better comparison, the sections are arranged similarly to those on steel RC.

2.3.2. Flexural Capacity

The flexural capacity and modes of failure of FRP RC members were investigated experimentally by several researchers. Beams, and sometimes slabs, were tested under four-point loading. The theoretical prediction of flexural capacity was based on the basic assumptions of cracked section analysis (Section 2.2.1). The FRP reinforcement used was mostly GFRP; probably because GFRP has better commercial potential. The two modes of flexural failure; by concrete crushing and rupture of rebars, were encountered in those experiments. Figure 2-14 shows typical failure by concrete crushing.

Figure 2-14: Typical FRP RC concrete crushing (Euro-Projects 1997).

In general, the predictions of failure modes and flexural capacities were considered to compare well with the experimental results. Benmokrane et al (1996) reported experimental and predicted flexural capacities with 15% differences. These differences were attributed to variability of material. Masmoudi et al (1998) predicted the experimental flexural capacities to within 8%. The experimental results of Brown and Bartholomew (1993), Theriault et al (1998) and Alkhrdaji et al (2000) were always higher than predictions, but within a maximum of 20%. The differences were sometimes attributed to a higher ultimate compressive concrete strain than that assumed in the analysis. Faza and GangaRao (1993) reported a mean deviation of 10%, but recommended that the ultimate tensile strength of the rebars be taken as 80% of the test-determined value, to account for production variability and quality control. Duranovic et al (1997) confirmed experimentally that Bernoulli's principle is well applicable to FRP RC. Their predictions were always lower than the experimental results, but within a maximum of 25%. This was regarded as favourable for design.

Obviously, representative properties and failure limits of concrete and FRP can refine the prediction of flexural capacity. However, Nanni (1993) reported that identical reinforcement, but with better surface characteristics, resulted in higher flexural stiffness and capacity. Thus, it was proposed that flexural capacity of FRP RC could also depend on bond characteristics.

The flexural capacity was found to increase with an increase in reinforcement ratio (Masmoudi et al, 1998) and/or concrete strength (Theriault et al 1998), with the effect of the reinforcement ratio being more pronounced (Nanni 1993). However, this increase was always limited by the ultimate compressive concrete strain, which is typical of brittle overreinforced RC sections.

ACI Committee 440 (1996 and 2003) and ISIS Canada (2001) state that flexural behaviour of FRP RC can be well predicted by working from first principles, namely, compatibility of strains between FRP and concrete, plane sections and equilibrium of cross sections considering proper constitutive laws of FRP and concrete. However, more work is still required to develop a solid design philosophy and safety factors (Neocleous 1999). ACI Committee 440 (1996) also recommends further studies with varying reinforcement ratios to investigate the behaviour throughout the whole loading range, and to create a wider background database. IStructE (1999) emphasizes that developing sufficient structural bond is a prerequisite for working from first principles.

2.3.3. Flexural Cracking

Cracking moment, crack spacing and crack width were investigated within the tests of FRP RC flexural members, and were often compared with cracking behaviour of steel RC. Sometimes, the results were only qualitatively analysed and reported. At other times, equations to predict crack width and spacing of FRP RC were proposed by imposing modifications to the equations of steel RC. Numerical approaches were also attempted to predict the cracking behaviour.

The cracking moment could be adequately evaluated based on gross section properties, regardless of the type of reinforcement (Benmokrane et al 1996). Neglecting the reinforcement effect on the cracking moment was considered more justified for FRP because of their lower modulus of elasticity (Masmoudi et al 1998).

Crack spacing was reported as similar to that of steel RC at low loads (25% of the ultimate moment, M_u), but less than steel RC by about 35% at moderate and high loads (50% and 90% M_u) (Benmokrane et al 1996). Less spacing may indicate better bond. Masmoudi et al (1998) arrived at precisely identical conclusions, though rebars of different diameter and surface texture were used. Zhao et al (1997b, 1999) reported crack spacing less than steel RC by about 30% at any load level beyond cracking.

Contrary to steel RC, the reinforcement ratio was reported to have negligible effect on crack spacing (Masmoudi et al 1998, Theriault et al 1998). In contrast, Toutanji and Saafi (1999) reported that crack spacing reduced with the increase in reinforcement

ratio. The compressive strength was reported to have negligible effect on crack spacing (Theriault et al 1998).

Crack widths were reported to increase with the increase in concrete strength (Theriault et al 1998), which is opposite to what was reported by GangaRao and Faza (1991). The increase in reinforcement ratio was reported to reduce crack width (Theriault et al 1998, Toutanji and Saafi 1999).

Masmoudi et al (1998) reported that crack widths were three to five times larger than in steel RC. They proposed to calculate crack width by a modified Gergely-Lutz equation (section 2.2.2.2.3), as follows.

$$w = K_g f_s \beta \sqrt[3]{d_c A} \qquad (2\text{-}18)$$

The coefficient (K_g) was evaluated as $41\text{x}10^{-6}$ mm^2/N, for their particular tests. The predictions with this model compared well to the tests of Theriault et al (1998); similar GFRP rebars were used in both cases.

Faza and GangaRao (1993) clarified that crack width in FRP RC should differ from steel RC due to the differences in modulus of elasticity and bond characteristics. Crack width calculation incorporating the actual bond strength of FRP rebars was emphasized. Calculations for crack widths were proposed as follows, but this procedure did not compare well to their experiments involving sand-coated GFRP rebars that are characterized by high bond strength.

$$w_{max} = l\varepsilon_f \qquad (2\text{-}19)$$

$$l = \frac{(2f'_t A)}{\mu_m \pi D}, \text{ psi units} \qquad (2\text{-}20)$$

where, l is crack spacing, f'_t is the tensile strength of concrete, μ_m is the maximum bond stress, A is the effective tension area of concrete surrounding the tension reinforcement divided by the number of rebars, D is the rebar diameter and ε_f is the maximum strain in FRP reinforcement at the service load level.

In a different approach, Faza and GangaRao (1993) basically proposed the original Gergley-Lutz equation, by replacing the steel strain by the FRP strain, as follows.

$$w = 0.076\beta\frac{E_s}{E_f}f_f\beta\sqrt[3]{dcA}\text{ , ksi units} \qquad (2\text{-}21)$$

where, f_f/E_f is the FRP strain. It was realized again that equation (2-21) would only be true in the case of similar steel and FRP bond characteristics. The crack width predicted by this equation did not compare well to their tests using high-bond sand-coated rebars. However, the same equation was reported to make good prediction of crack width in the tests of Alkhrdaji et al (2000).

Zhao et al (1997b, 1999) made crack width predictions by using the approach of BSI (1985). These predictions were reported to be unconservative by about 20 to 40%. Modifications to the code approach to account for concrete characteristics, the higher strains of FRP reinforcement and the nature of bond of FRP to concrete were deemed necessary and further research was recommended. The crack width predictions by Eurocode 2 (CEN 1992) were considered to be accurate.

A numerical procedure based on an assumed bond-slip law was used to calculate crack widths and deflections by Ombres et al (2000). Their predictions compared well to the experimental results particularly under service conditions, which corresponded to a load level less than 50% of the ultimate load.

2.3.3.1. Provisions in Codes of Practice

The provisions for evaluation of cracking, in current codes of practice and state-of-the-art reports on FRP RC, are presented below. This is useful to further identify the different approaches, the key variables and the research needs in this particular area.

2.3.3.1.1 ACI

ACI 440R-96 (ACI Committee 440 1996) identifies that crack width is influenced by the bond characteristics and modulus of elasticity of FRP. The research summarised in that document concerns GFRP only, with no guidance for other FRP materials. The document, rather uniquely, refers to the work of Faza and GangaRao (1993) who proposed equation (2-19).

ACI 440.1R-03 (ACI Committee 440 2003) acknowledges that crack width is proportional to the reinforcement strain rather than stress, and adopts a modified form of the Gergley-Lutz equation as follows.

$$w = \frac{2.2}{E_f} \beta k_b f_f \sqrt[3]{dcA} \qquad (2\text{-}22)$$

The term k_b has been introduced to account for the bond between FRP and concrete, and should be determined experimentally. If the bond is similar to steel, then k_b is equal to one. If the bond is inferior to steel, then k_b is greater than one, and vice versa. If k_b is unknown, a value of 1.2 is recommended. ISIS Canada (2001) adopts the ACI formula and stresses the importance of a proper evaluation of k_b. The Canadian standard for design of buildings with FRP reinforcement, CAN/CSA-S806-02 (CSA 2002), also adopts the ACI approach, but deals with an indirect quantity (z) derived from the crack width formula.

ACI 440.1R-06 (ACI Committee 440 2006) introduces a major modification to the crack width formula. w is related to the concrete cover (d_c) and rebar spacing (s) based on the proposal by Frosch (1999), as follows.

$$w = 2\frac{f_f}{E_f} \beta k_b \sqrt{{d_c}^2 + \left(\frac{s}{2}\right)^2} \qquad (2\text{-}23)$$

If not determined experimentally, the recommended value for the bond coefficient (k_b) is increased and is taken as 1.4.

2.3.3.1.2 IStructE

Contrary to ACI and ISIS Canada, IStructE (1999) considers that crack widths of FRP RC may be predicted by existing formulae for steel RC. This conclusion has been based on mere comparison of few test-measured crack widths with the corresponding BSI (1985) predictions. The measured crack widths were generally higher than predicted by a maximum of about 40%. However, even for steel RC, the actual crack widths could be 20% higher than predicted. Hence, it was concluded that the BSI (1985) approach would be adequate, or could even be improved by applying a modification factor of about 1.2. However, this is considered an area that requires further research.

2.3.4. Flexural Deflection

Similar to cracking, the short-term deflection behaviour of FRP RC was investigated within tests of flexural members. Closed-form formulae to predict deflection of FRP RC were proposed by imposing modifications to the steel RC equations. Analytical approaches to evaluate deflections were also considered.

Theriault et al (1998) reported that beam stiffness was rather independent of concrete strength, but increased with reinforcement ratio. Zhongming et al. (1997) concluded that deflection was dependent on the sectional flexural stiffness, and in turn on the reinforcement ratio and modulus. Proper evaluation of the cracking moment was identified as more important for deflection prediction of FRP RC members; due to their relatively low ratio of service to cracking load (Pecce et al 2001).

Benmokrane et al (1996) concluded that the ACI 318 deflection approach overestimated the effective moment of inertia (I_e), hence underestimated the deflection of their FRP RC beams. A modified expression for I_e was proposed, as follows.

$$I_e = \alpha I_{cr} + \left(\frac{I_g}{\beta} - \alpha I_{cr}\right)\left(\frac{M_{cr}}{M_a}\right)^3 \qquad (2\text{-}24)$$

For those tests, α and β were evaluated as equal to 0.84 and 7, respectively. Zhao et al (1997a, 1999) found that Equation (2-24) overestimated the deflection of the Eurocrete FRP RC beams. On the contrary, the original ACI 318 expression, as well as the CEB (1993) approach, correlated well to the Eurocrete tests, without any modification.

The need to modify the ACI 318 equation for I_e was confirmed by Masmoudi et al (1998). Another modified expression was used as follows.

$$I_e = I_{cr} + (\beta I_g - I_{cr})\left(\frac{M_{cr}}{M_a}\right)^3 \qquad (2\text{-}25)$$

The reduction coefficient, β, was calibrated as equal to 0.6.

Toutanji and Saafi (1999) concluded, based on their and others tests, including those mentioned above, that the ACI 318 expression for I_e did underestimate FRP RC deflections, but only for low reinforcement ratios (less than 1%). Hence, it was

proposed to replace the constant exponent (3) in that expression with a variable exponent (m), which accounted for the effect of reinforcement ratio and modulus, as follows.

$$m = 6 - \frac{10E_f}{E_s}\rho_f \quad \text{for} \quad \frac{E_f}{E_s}\rho_f < 0.3 \qquad (2\text{-}26)$$

$$m = 3 \quad \text{for} \quad \frac{E_f}{E_s}\rho_f \geq 0.3 \qquad (2\text{-}27)$$

where, ρ_f is the reinforcement ratio in percent.

Pecce et al. (2001) carried out statistical analysis of tests with one common GFRP rebar type. The exponent in the ACI 318 equation for I_e was evaluated as equal to 5.4; instead of 3 for steel RC. Further experimental work considering other types of FRP rebars was deemed necessary. An exponent of 5 was also proposed by Brown and Bartholomew (1993) based on their tests. Pecce et al. (2000) reported that the Eurocode 2 deflection approach is adequate, but somewhat conservative.

Faza and GangaRao (1992) considered the pure-flexure zone, in four-point loading tests, as fully cracked, and the shear-span zone as partially cracked. Thereupon, a modified effective moment of inertia (I_m) was derived as follows.

$$I_m = \frac{23I_{cr}I_e}{8I_{cr} + 15I_e} \qquad (2\text{-}28)$$

Bischoff (2005 a,b) extensively analysed the ACI 318 expression for I_e from a tension stiffening standpoint. It was concluded that the ACI expression was not based on fundamentals to start with, and might not be applicable to GFRP RC. Bischoff proposed a different form for I_e, which was derived based on the tension stiffening provisions of CEB (1993). This expression for I_e was claimed to be equally applicable for FRP and steel RC, and was given as follows.

$$I_e = \frac{I_{cr}}{1 - \eta\left(\frac{M_{cr}}{M_a}\right)^2} \leq I_g \text{ , and } \eta = 1 - \frac{I_{cr}}{I_g} \qquad (2\text{-}29)$$

Analytically, the experimental moment-curvature relationship was shown to cross the elastic cracked-state moment-curvature line at a low load level, but it only converged to the nonlinear cracked-state moment–curvature curve. Therefore, the use of a nonlinear cracked section analysis was deemed necessary to evaluate deflection of FRP RC. However, more experimental and analytical work was recommended to evaluate the tension stiffening behaviour within the service load range (Cosenza et al 1997a). Zhao et al (1997a, 1999) showed that deflections of FRP RC could be well predicted with sectional and finite element analyses, but tension stiffening in those analyses was not based on a tension stiffening relationship. On a more fundamental level, Aiello and Ombres (2000) considered a linear sectional strain distribution between cracks together with an assumed nonlinear bond–slip relationship, as discussed by Cosenza et al (1997b), to predict the deflection behaviour of AFRP RC beams.

2.3.4.1. Provisions in Codes of Practice

2.3.4.1.1 ACI

ACI 440.1R-03 (ACI Committee 440 2003) adopts a modified expression for I_e, which accounts for the lower FRP modulus of elasticity (E_f) and different FRP bond characteristics. This modification was proposed by Gao et al (1998), as follows.

$$I_e = \left(\frac{M_{cr}}{M_a}\right)^3 \beta_d I_g + \left[1 - \left(\frac{M_{cr}}{M_a}\right)^3\right] I_{cr} \le I_g, \text{ and } \beta_d = \alpha_b \left[\frac{E_f}{E_s} + 1\right] \qquad (2\text{-}30)$$

where, α_b is a bond dependent coefficient, which equals 0.5 for steel reinforcement. For FRP reinforcement, α_b also equals 0.5 pending further research.

The latest ACI 440.1R-06 (ACI Committee 440 2006) abandons the reliance of β_d on bond, and takes β_d as proportional to the ratio of reinforcement ratio (ρ_f) to the balanced reinforcement ratio (ρ_{fb}), as follows.

$$\beta_d = \frac{1}{5}\left(\frac{\rho_f}{\rho_{fb}}\right) \qquad (2\text{-}31)$$

This equation inappropriately entails that deflection depends on the ultimate tensile stress of the FRP reinforcement!

2.3.4.1.2 ISIS Canada

ISIS Canada (2001) uses the same approach and modified I_e as in ACI 440.1R-03. It is emphasized, however, that the correction factor (β_d) was based on limited test data, with doubtful applicability to other loading and boundary conditions. Another equation for I_e, described as derived based on CEB (1993), is also provided as follows.

$$I_e = \frac{I_t I_{cr}}{I_{cr} + \left[1 - 0.5\left(\frac{M_{cr}}{M_a}\right)^2\right]}\left(I_t - I_{cr}\right) \qquad (2\text{-}32)$$

where, I_t is the moment of inertia of an uncracked section transformed to concrete. This equation was reported to work well with different types of FRP reinforcement.

2.3.4.1.3 Canadian Standards Association

CAN/CSA-S806-02 (CSA 2002) evaluates short-term deflection of FRP RC by integration of curvatures along the span. A tri-linear moment-curvature relationship is assumed. The flexural stiffness of the first linear segment is based on the uncracked moment of inertia (I_g), while the second segment has zero stiffness. The stiffness of the third segment is based on the elastic cracked moment of inertia (I_{cr}), which indicates that tension stiffening is neglected immediately after cracking. This approach can be very conservative when low reinforcement ratios are involved. Closed-form deflection formulae, derived from the adopted moment-curvature relationship, are also provided.

2.3.4.1.4 Japanese JSCE

The Japanese JSCE (1997) uses the same deflection approach used for steel RC. However, attention is drawn that where the FRP modulus is low compared to steel, and where the reinforcement ratio is low, the increased member deformations are expected to enhance and be associated with shear cracking. In such cases, it is required that shear cracking be properly allowed for in evaluating deformations.

2.3.4.1.5 IStructE

Contrary to ACI and ISIS Canada, IStructE (1999) considers that the short-term deflection of FRP RC can be predicted by the same approach of BSI (1985) for steel RC. It is explained that the underlying curvature approach automatically accounts for the type of reinforcement. Therefore, the only questionable variable would be the amount of concrete tensile strength at cracked locations, which is used to indirectly account for the stiffness of the uncracked zones. In that document, the comparison of measured and predicted deflections, by using the approach of BSI (1985), show generally good agreement. However, few measured deflections are significantly greater than predicted, while some are significantly lower. Moreover, the tests used for comparison were relatively few, and only cover a limited range of behaviour (most beams have a span to depth ratio of about 8, and service deflections not exceeding 8 mm). Also, the comparison of results is made at an assumed service load level only, and not considering the entire loading path. Therefore, the recommendation of ISructE (1999) may require further verification by considering a wider range of test conditions.

2.3.5. Bond

Similar to steel RC, all aspects of structural performance of FRP RC are expected to depend on the bond developed between FRP and concrete (Nanni et al 1995, *fib* 2000). However, bond behaviour is expected to vary between FRP and steel rebars because several key parameters are different, mainly, the lower FRP modulus and shear strength of the surface resin matrix (*fib* 2000).

Bond of FRP RC was investigated, in general, by pull-out tests and beam tests. Sometimes, bond was investigated within structural members. Key parameters, levels of bond stresses and bond-slip relationships were identified, but the research work mostly aimed at establishing safe anchorage length equations.

The pull-through mode of failure was found to depend on the shear strength of the surface fibre-resin system, with the concrete strength being immaterial (Achillides and Pilakoutas 2004, Nanni et al 1995), particularly when the concrete strength was more

than 30 MPa (Achillides and Pilakoutas 2004). The surface characteristics were reported to have the major effect on bond, and a lower modulus of elasticity seemed to give a lower bond capacity (Zhongming et al 1997). The type of fibre did not seem to affect bond (Achillides and Pilakoutas 2004), opposite to what was concluded by Zhongming et al (1997). The maximum average bond stress was shown to decrease with increase in embedment length. Square rebars were found to develop better bond strength than round rebars. A minimum height of deformations was found to be necessary for developing satisfactory bond to concrete (Achillides and Pilakoutas 2004). Larger size rebars were found to develop less bond strength (Achillides and Pilakoutas 2004, Tighiourat et al 1998). The level of GFRP and CFRP bond strength compared to steel was estimated at the order of 72% (Achillides and Pilakoutas 2004). Comparatively, Tighiouart et al (1998) and Brown and Bartholomew (1993) reported ratios of 50% and 67%, respectively, for GFRP. Nanni (1993) concluded that bond of a deformed FRP rod was generally lower than that of an equivalent diameter steel rod, except when sand-coating was used, then the opposite became true. Ehsani et al (1996) suggested new critical free-end and loaded-end slip values as 0.064 and 0.38mm, respectively (the corresponding values for steel are 0.05 and 0.25mm).

Achillides et al (1997) investigated the splitting bond failure in FRP beams under four-point loading. Strains measured along the rebars were converted into average bond stresses. CFRP and GFRP developed 85% and 60%, respectively, of the characteristic bond strength proposed for steel. The bond characteristics of FRP rebars were considered suitable for structural purposes.

fib (2000) describes the FRP rebar to concrete interaction with reference to bond-slip curves from short-embedment pull-out tests (Figure 2-15). Qualitatively, the behaviour in the different stages is similar to steel, except that the pull through failure surface at the end of stage IV occurs within the relatively soft surface deformations of the FRP rebar. However, the pull through shear surface may occur in weak concrete. Another pull through possibility is by squeezing of the rebar due to its low stiffness in the transverse direction. Quantitatively, the document recognizes that the development of general code provisions for bond of FRP might be a complex task due to the large number of possible combinations of fibres, resins and shapes of reinforcement.

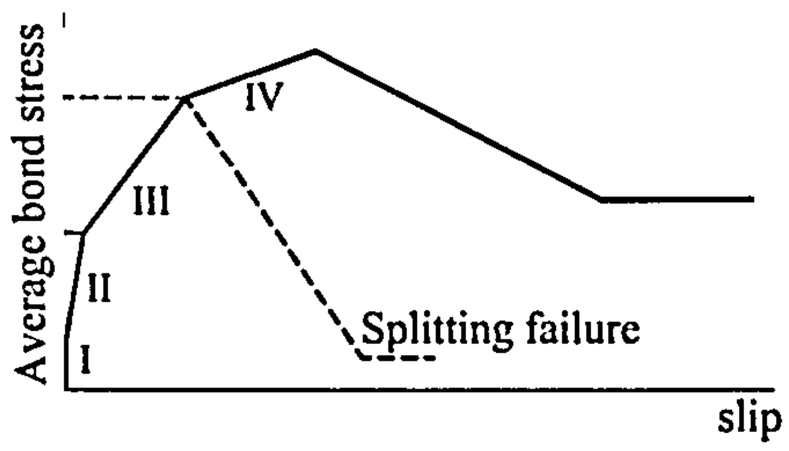

Figure 2-15: Bond-slip relationship for FRP RC (*fib* 2000).

2.3.6. Tension Stiffening

At the present time, codes of practice do not adopt any specific model for the behaviour of FRP RC tension ties. Bischoff and Paixao (2004) tested steel and GFRP RC tension ties. It was emphasized that shrinkage is an important parameter that should be taken into consideration. With similar reinforcement ratios, the GFRP RC ties exhibited more tension stiffening than the steel RC ties.

Sooriyaaracchchi et al. (2005) investigated tension stiffening of RC tension ties with GFRP reinforcement. It was concluded that tension stiffening increased with an increase in the concrete strength and/or a reduction in reinforcement ratio, but was not affected by the rebar diameter. Tension stiffening was overestimated by the provisions of both ACI 224.2R-92 and CEB (1993), but the CEB approach compared better to the experimental results.

2.4. CONCLUDING REMARKS

The design of FRP RC members may often be governed by the serviceability limit state. Nonetheless, the evaluation of cracking and short-term deflection of FRP RC is still an area with differing points of view and requires further research. In their formulae for crack width and effective moment of inertia, the previous ACI 440.1R-03 and ISIS Canada (2001) account for the FRP modulus of elasticity and include a bond coefficient that needs to be test-evaluated. In the latest ACI 440.1R-06, the effective moment of inertia is related to the reinforcement ratio, and surprisingly, to the ultimate reinforcement stress, but with no allowance for bond effects. The Canadian CAN/CSA-

S806-02 conservatively assumes zero tension stiffening after cracking. The Japanese JSCE (1997) is the only code to bring up the issue of shear-related deformations for cases with low reinforcement ratio and modulus. On the European side, the IStructE (1999), as well as some researchers, consider that crack width and deflection provisions for steel RC are equally applicable to FRP RC without any modification, though unconservative by about 20% in the case of cracking. However, their conclusions were based on comparing predictions with relatively few test results, most of which fall within a narrow range of behaviour. Another relevant issue is the inadequate distribution of FRP RC research. Most of this research has involved GFRP reinforcement. However, developing reliable design guidelines requires an equal investigation of other types of FRP reinforcement.

To deal with short-term deflection of FRP RC members, further fundamental research is necessary. This research should consider three main variables: the reinforcement ratio, modulus of elasticity and bond characteristics. The first two variables control the level of strain in the reinforcement, and as such have the largest contribution to curvature or deflection. In qualitative terms, reducing the reinforcement ratio and/or modulus of elasticity increases the reinforcement strain at a certain load, and therefore increases curvature and deflection. Assuming an adequate level of composite action, the bond characteristics affect the spacing of cracks, as well as the distribution of strains between cracks. In that sense, the effect of bond on deflection is expected to be much less pronounced compared to the reinforcement ratio or modulus. The three variables together define the tension stiffening characteristics at the rebar level. In that regard, an experimental approach where tension stiffening is evaluated in the structural member itself, and not in a separate setup, can be more valuable. Other parameters such as the rebar diameter, concrete cover and concrete grade are included in the bond variable, and are of direct relevance to crack width and spacing only.

This study investigates the short-term deflection behaviour of FRP RC flexural members, both experimentally and analytically, considering the main variables identified. In doing so, the flexural capacity is automatically involved, and can be investigated further. In addition, the database of experimental results of FRP RC will be enhanced by the outcomes of this research.

CHAPTER 3

EXPERIMENTAL METHODOLOGY

3.1. INTRODUCTION

The experimental work undertaken in this research comprised structural tests of FRP and steel RC beams and slabs. It aimed at investigating deflection, cracking and tension stiffening behaviour of those flexural elements. In addition, material tests were carried out to determine the mechanical properties of concrete and rebars, which were used in constructing the structural elements. This chapter presents the structural tests, including details of test elements, experimental parameters, preparation methods, instrumentation, experimental setup, and testing procedure. The concrete and rebar tests are also presented, together with their results.

3.2. STRUCTURAL TESTS

The focus of the structural tests was to investigate the deflection behaviour of FRP RC flexural elements. Hence, a simultaneous investigation of cracking and tension stiffening behaviour was necessary. To ensure a good coverage of flexural elements, both beams and slabs were considered. Moreover, both GFRP and CFRP were used for the main FRP flexural reinforcement. Steel RC elements were used for comparison purposes. A total of 28 RC beams and slabs with GFRP, CFRP or steel rebars were tested.

3.2.1. Details of test elements

The layouts of the beams and slabs, and their geometric and reinforcement details are shown in Appendix A. They are also given in Figures 3-1 and 3-2, and are further described as follows.

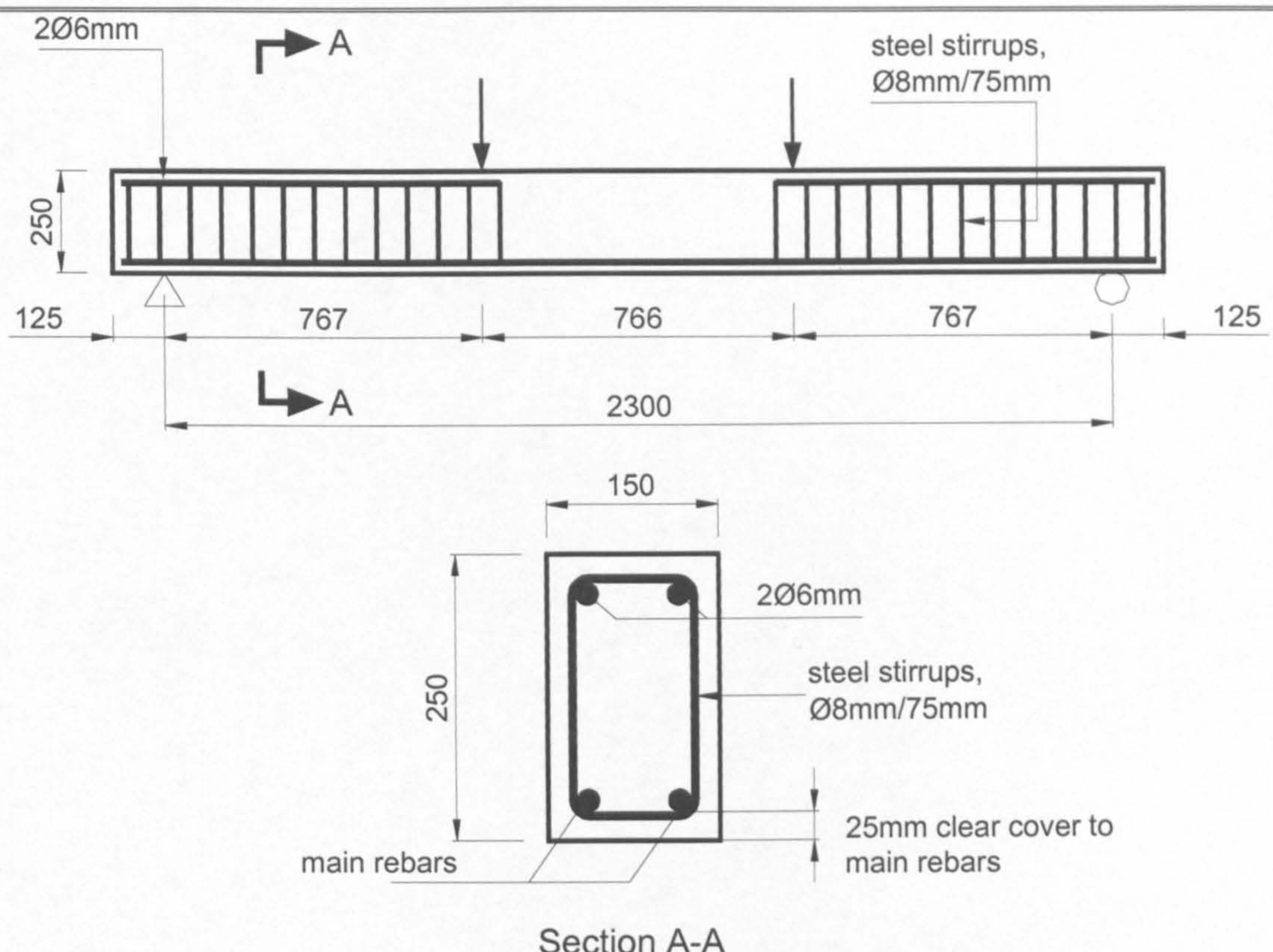

Rebar type	Series designation	Beam designation	Main rebar details	Reinforcement ratio	Relation to control steel beam
GFRP	BG1	BG1a	2Ø9.53	0.0043	Equal flexural capacity
		BG1b			
	BG2	BG2a	2Ø12.7	0.0077	Equal area of rebars
		BG2b			
	BG3	BG3a	4Ø19.05[(1)]	0.0393	Equal stiffness of rebars
		BG3b			
CFRP	BC1	BC1a	3Ø6.35	0.0029	Equal flexural capacity
		BC1b			
	BC2	BC2a	3Ø9.53	0.0065	Equal area of rebars
		BC2b			
	BC3	BC3a	3Ø12.7	0.0116	Equal stiffness of rebars
		BC3b			
Steel	BS	BSa	2Ø12	0.0069	-
		BSb			

(1) Two layers, with 25 mm clear spacing between them.

Figure 3-1: Layout, and geometric and reinforcement details of the beams.

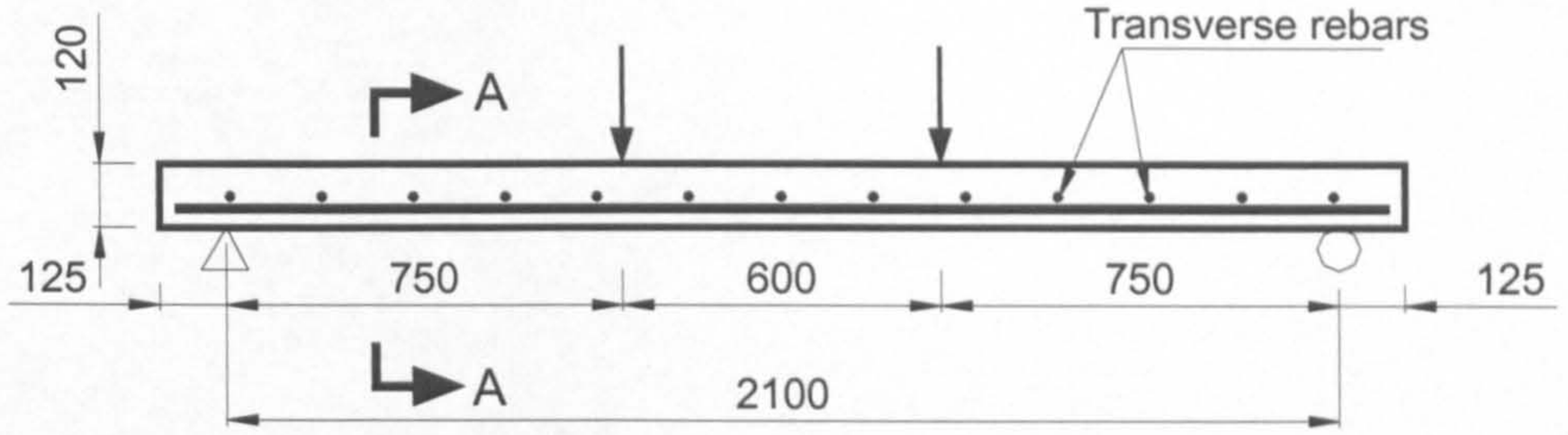

Note: The mesh of some GFRP and CFRP RC slabs floated during casting. Therefore, the cover to the main rebars was confirmed after every test. The actual cover values are given in Chapter 4.

Rebar type	Series designation	Slab designation	Main Rebar details	Transverse Rebar details	Reinforcement ratio	Relation to control steel slab
GFRP	SG1	SG1a	5∅6.35	7∅9.53 /m	0.0035	Equal flexural capacity
		SG1b				
	SG2	SG2a	5∅9.53	7∅9.53 /m	0.0079	Equal area of rebars
		SG2b				
	SG3	SG3a	5∅19.05	7∅9.53 /m	0.0333	Equal stiffness of rebars
		SG3b				
CFRP	SC1	SC1a	4∅6.35	6∅6.35 /m	0.0028	Equal flexural capacity
		SC1b				
	SC2	SC2a	4∅9.53	6∅6.35 /m	0.0063	Equal area of rebars
		SC2b				
	SC3	SC3a	4∅12.7	6∅6.35 /m	0.0114	Equal stiffness of rebars
		SC3b				
Steel	SS	SSa	4∅10	5∅8 /m	0.0070	-
		SSb				

Figure 3-2: Layout, and geometric and reinforcement details of the slabs.

Three GFRP, three CFRP and one steel RC beam series were prepared. The beam series were designated as BG#, BC# or BS#. B stands for beam; G, C and S refer to GFRP, CFRP and steel rebars, respectively; while # is the series number. To ensure repeatability, each series comprised two identical beams. These were identified by adding a or b to the series name. The layout of the slabs was identical to that of the beams; only the series letter S (for slab) was used instead of the letter B. In total, the structural tests comprised 14 beams and 14 slabs.

The beams were of medium scale. They were 150 mm wide, 250 mm deep and 2550 long. All the beams were tested under four-point loading. The span between the supports was 2300 mm. The shear span was 767 mm (one third of the span). To avoid shear failure, steel stirrups were used, but only in the shear span. Two nominal 6mm GFRP, CFRP or steel rebars were used as top reinforcement within the shear span to hold the stirrups. The dimensions of the beams and the four-point loading arrangement were similar to those of the beams tested during the Eurocrete Project (Euro-Projects 1997).

The slabs were also of medium scale. They were 500 mm wide, 120 mm deep and 2350 mm long. Similar to the beams, all the slabs were tested under four-point loading. The span between the supports and the shear span were 2100 mm and 750 mm, respectively.

In all the beams and slabs, the clear concrete cover to the main flexural rebars was set as 25 mm. This cover was expected to avoid splitting bond failure. However, the mesh of some GFRP and CFRP RC slabs floated during casting. Therefore, the cover to the main rebars was confirmed after every test. The actual cover values are given in Chapter 4.

The GFRP and CFRP RC beams and slabs were designed to have approximately equal flexural capacity; equal area of rebars or equal stiffness of rebars to their steel RC control elements. Therefore, for each type of FRP rebar, a wide range of reinforcement ratios was required and several rebar diameters were used. The resulting RC sections were under-reinforced, near balanced or over-reinforced, with failure expected to occur either by rupture of rebars or crushing of concrete.

3.2.2. Experimental parameters

It was concluded in the review of the literature that the investigation of deflection, cracking, and tension stiffening behaviour of FRP RC involves three main variables: the reinforcement ratio, modulus of elasticity of the rebars and their bond characteristics. All these variables were considered in the design of the beams and slabs.

The modulus of elasticity and the bond characteristics were accounted for by using different types of rebars: steel, GFRP and CFRP. The FRP rebars used were manufactured by Hughes Brothers, Inc., USA. The GFRP rebars were known as Aslan 100. The surface treatment of these rebars is characterized by helically over-wound fibres and sand coating. During the experimental program, the CFRP rebars were still under development and then became commercially available as Aslan 200. They have indented peel-ply surface treatment applied helically. Figure 3-3 shows the GFRP and CFRP rebars used. The mechanical properties of all the rebars will be discussed later in this chapter.

A wide range of reinforcement ratios was covered, as explained and shown in the previous section. To achieve these ratios, it was necessary to use several rebar diameters, which ranged from 6.35 mm to 19.05 mm. Therefore, the rebar diameter was incorporated as an additional variable.

CFRP rebar **GFRP rebar**

Figure 3-3: GFRP and CFRP rebars.

3.2.3. Preparation Methods

3.2.3.1. Reinforcement

The FRP and steel rebars were cut to the appropriate lengths. While cutting the steel rebars required using power disc cutters or steel scissors, it was possible to cut the FRP rebars with a simple steel saw. The steel stirrups were also cut and bent to the appropriate dimensions. Plastic ties (zip ties) or galvanized coated wire were used to assemble the FRP reinforcement cages and meshes, whereas the steel reinforcement was assembled with conventional steel wire. Figure 3-4 shows a completed FRP reinforcement beam cage and slab mesh.

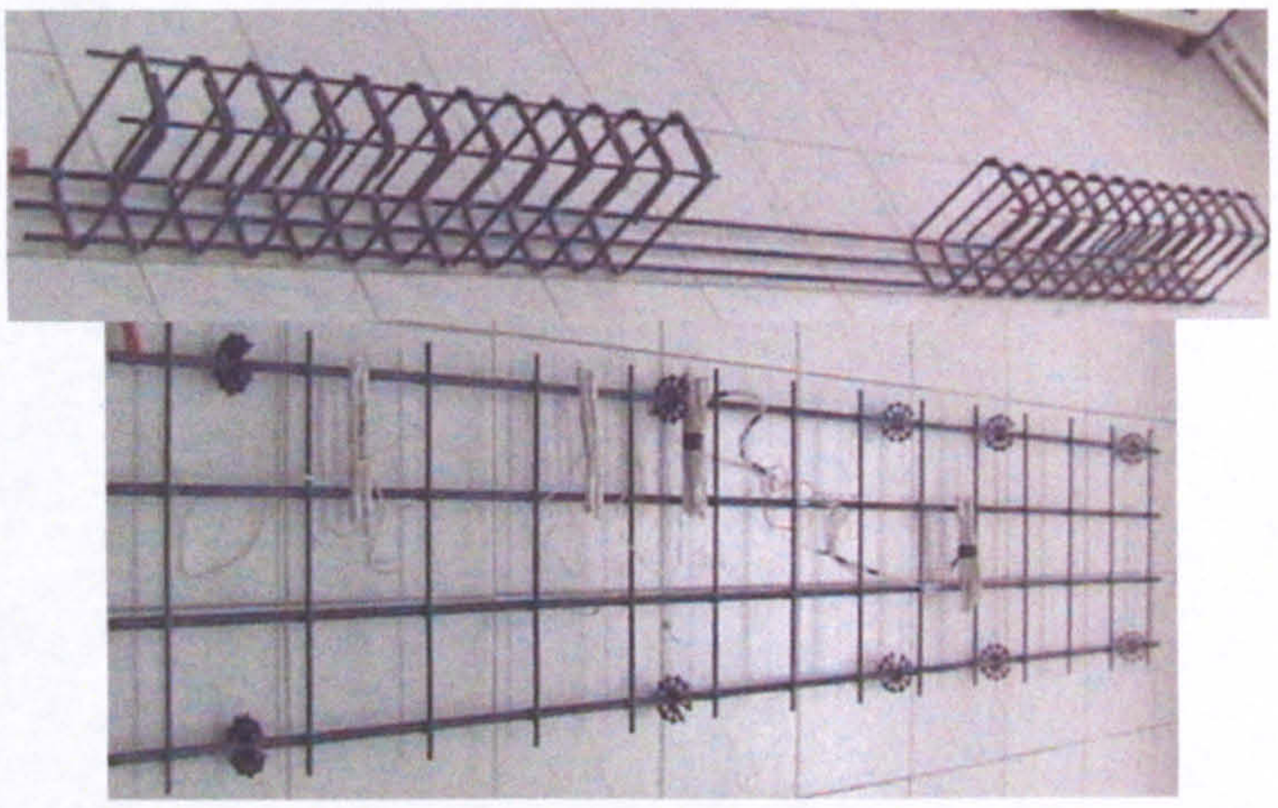

Figure 3-4: FRP reinforcement beam cage and slab mesh.

3.2.3.2. Moulds

The moulds were made of plywood, with metal fasteners. Each mould could accommodate two beams or two slabs. The mould was cleaned and its inside edges were sealed with silicon. To act as a crack inducer, a steel angle, 18 x 18 x 0.6 mm, was glued with silicon across the mid-length of the bottom mould surface (Figure 3-5). To ease de-moulding, the inside surfaces of the mould were covered with a thin layer of oil.

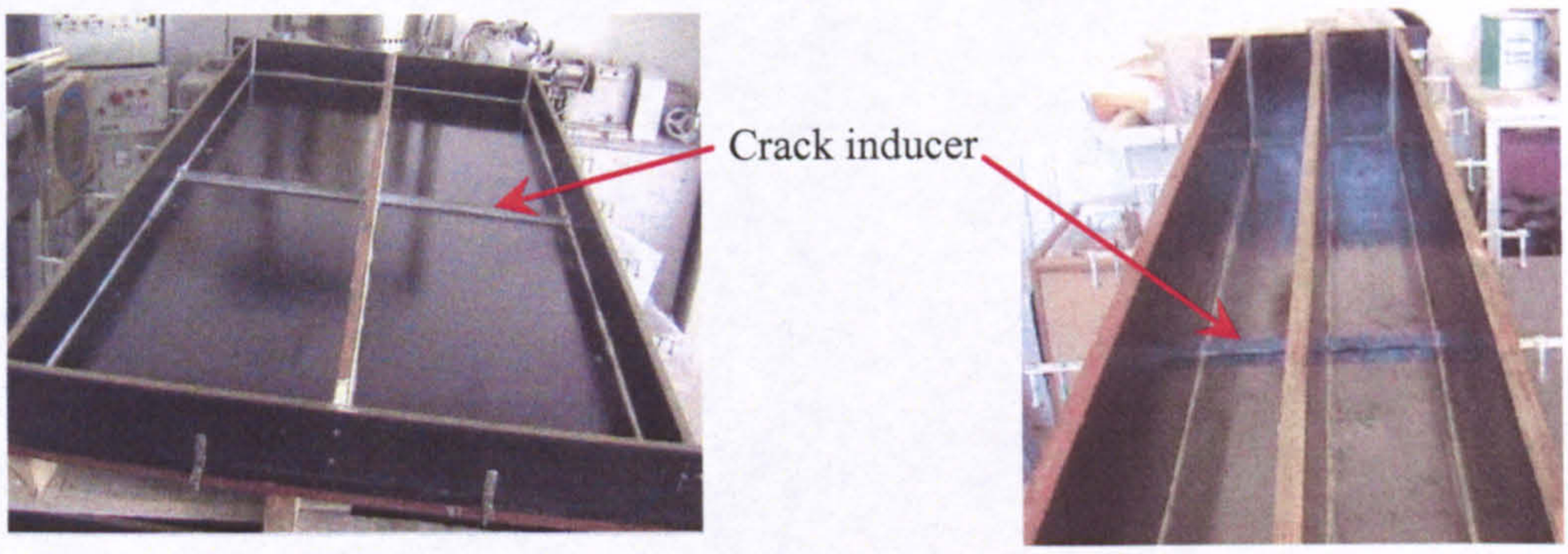

Figure 3-5: Beam and slab moulds showing crack inducers.

The reinforcement cage or mesh was instrumented with strain gauges, and then carefully placed in the mould. Appropriate size plastic spacers were used to fix the reinforcement cage or mesh at the correct bottom and side covers. Due attention was paid to ensure the correct location of the crack inducer relative to the strain gauges at midspan. Figure 3-6 shows reinforcement cages and meshes positioned in the moulds and ready for casting.

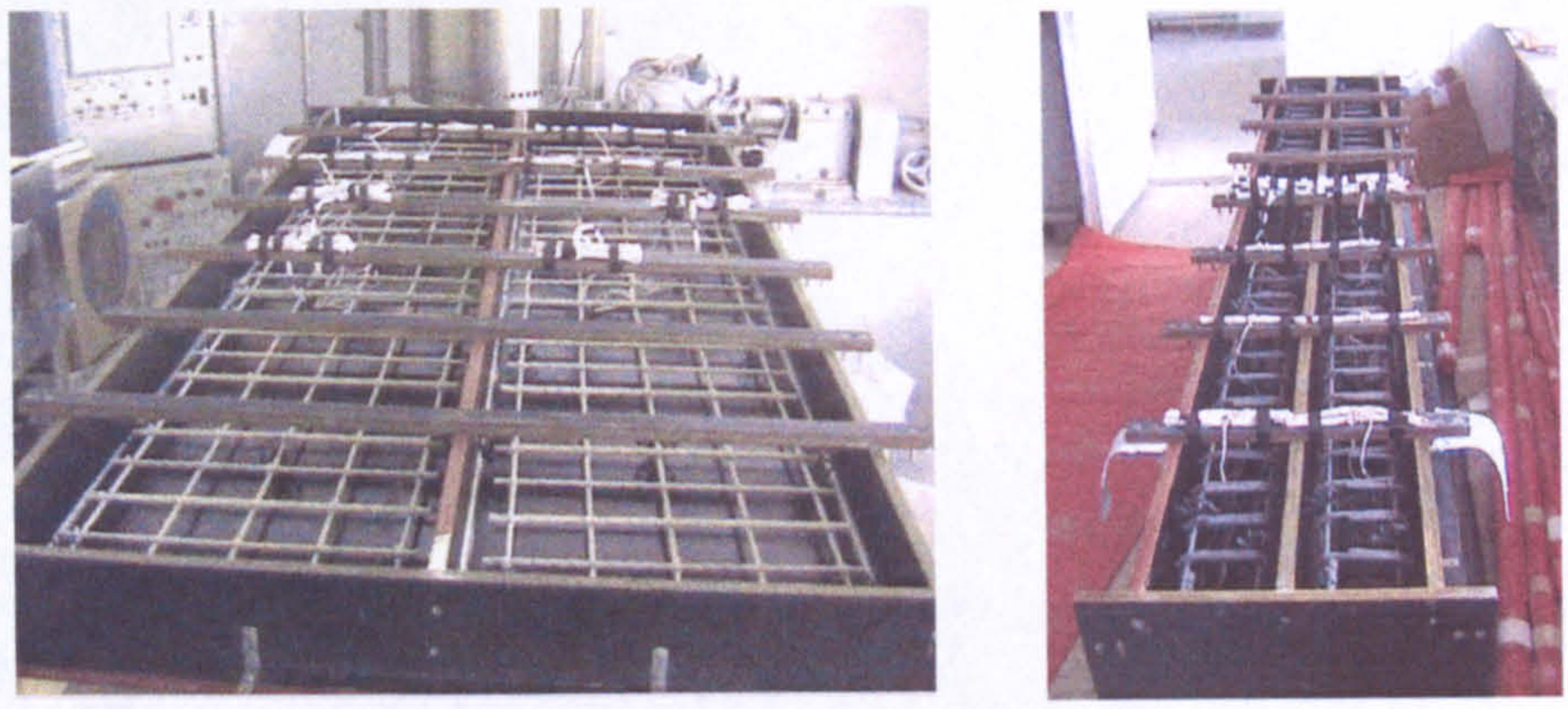

Figure 3-6: Beam and slab moulds with reinforcement, ready for casting.

3.2.3.3. Casting and Curing

Two beam series (4 beams) and two slab series (4 slabs) were cast in a day. The two identical beams or slabs of each series were cast from the same batch of concrete. The mould was placed on two vibrating steel beams that could furnish external vibration to the concrete (Figure 3-7). Casting and vibration were performed in three layers for the beams, and two for the slabs. For every beam or slab, four control 150 mm cubes and three 150 x 300 mm cylinders were prepared from the same concrete batch. After casting, the top concrete surface was levelled as best as possible. An overhead crane was used to carefully lift the mould off the vibrating beams and place it on the ground. One hour later, the cast elements and control specimens were covered with nylon sheets.

Figure 3-7: Vibrating steel beams used for vibration of concrete.

The next day, the cast elements were labelled and covered with wet hessian and nylon sheets. The control specimens were de-moulded, labelled and covered similarly to the elements. These curing conditions were maintained for one week. At the end of the week, concrete strength development was assessed by testing one of the control cubes. The elements were then de-moulded and stored together with their control specimens until the date of testing.

3.2.4. Instrumentation

Internal and external instrumentation were used for every beam and slab. Internally, fourteen strain gauges were used to measure rebar strains. Externally, five linear variable displacement transducers (LVDTs) were used to measure deflections, two dial gauges to measure support settlements, one LVDT to measure crack width and average surface strain, and one strain gauge to measure concrete strain.

3.2.4.1. Strain Gauges

One rebar of every beam or slab was instrumented with a total of fourteen strain gauges, as shown in (Figure 3-8). Four strain gauges were used to measure rebar strains within one of the shear spans: one at the support, one at the load location and two at the third points. These gauges will enable the evaluation of strain development and average bond stresses within the shear span, and will also give an indication of any rebar slip at the support. The other ten strain gauges were concentrated around the crack inducer at midspan. These gauges will enable the investigation of strains, tension stiffening and bond profiles between one induced crack at the location of the crack inducer at midspan and the two naturally-occurring contiguous cracks on either side. It was assumed that the crack spacing would be in the range of three to four times the clear cover thickness (75 to 100 mm). Therefore, the strain gauges were distributed within 90 mm on either side of the location of the crack inducer: every 18 mm on one side and 22.5 mm on the other side.

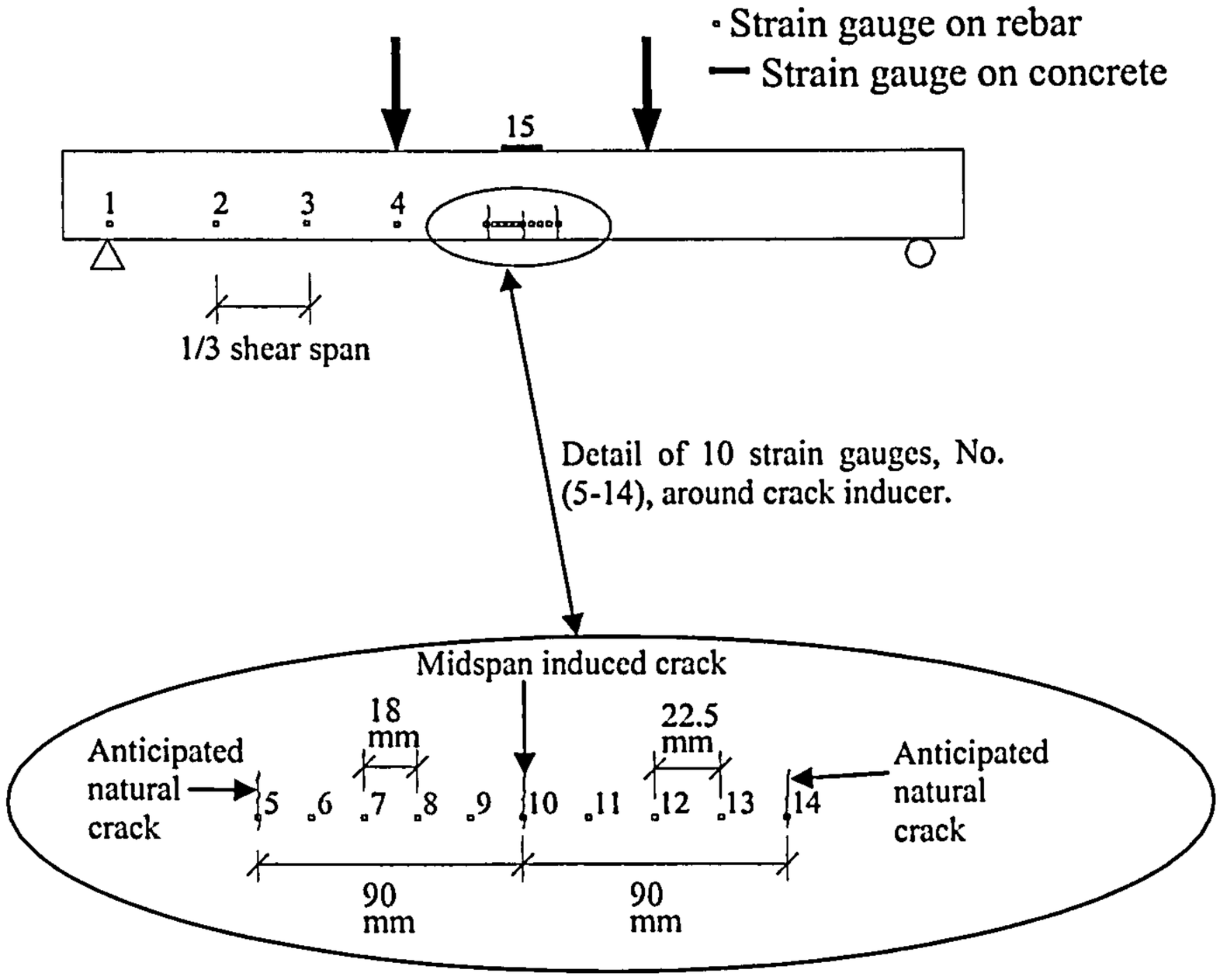

Figure 3-8: Arrangement of rebar and concrete strain gauges.

The strain gauges used were foil-type, three-wired temperature-compensating, with a resistance of 120 ohm, gauge length of 6 mm and base material dimensions of 3.4×10 mm. They were bonded to the surface of the rebar with adhesive. Specialized silicon was used to cover the strain gauges to protect them during casting, and to prevent moisture uptake. The free ends of the extension wires were labelled for later identification. It was realized that the strain gauges in the midspan zone would have some effect on the rebar-concrete interaction, because they were closely spaced. Therefore, due attention was paid to minimise the rebar area disturbed by each strain gauge. In that regard, using strain gauges with factory installed jumper leads and extension wires proved to be useful. Moreover, two arrangements were used in the replicate elements. For the elements designated with the letter a, the strain gauges were placed along the bottom fibre of the rebar, while for those designated with the letter b, they were placed helically around the rebar (90° rotation between the locations of the successive strain gauges). These arrangements could not be literally adhered-to in the case of FRP rebars, GFRP in particular, because of the nature of the rebar surface. Figure 3-9 shows the two strain gauge arrangements at the midspan zone.

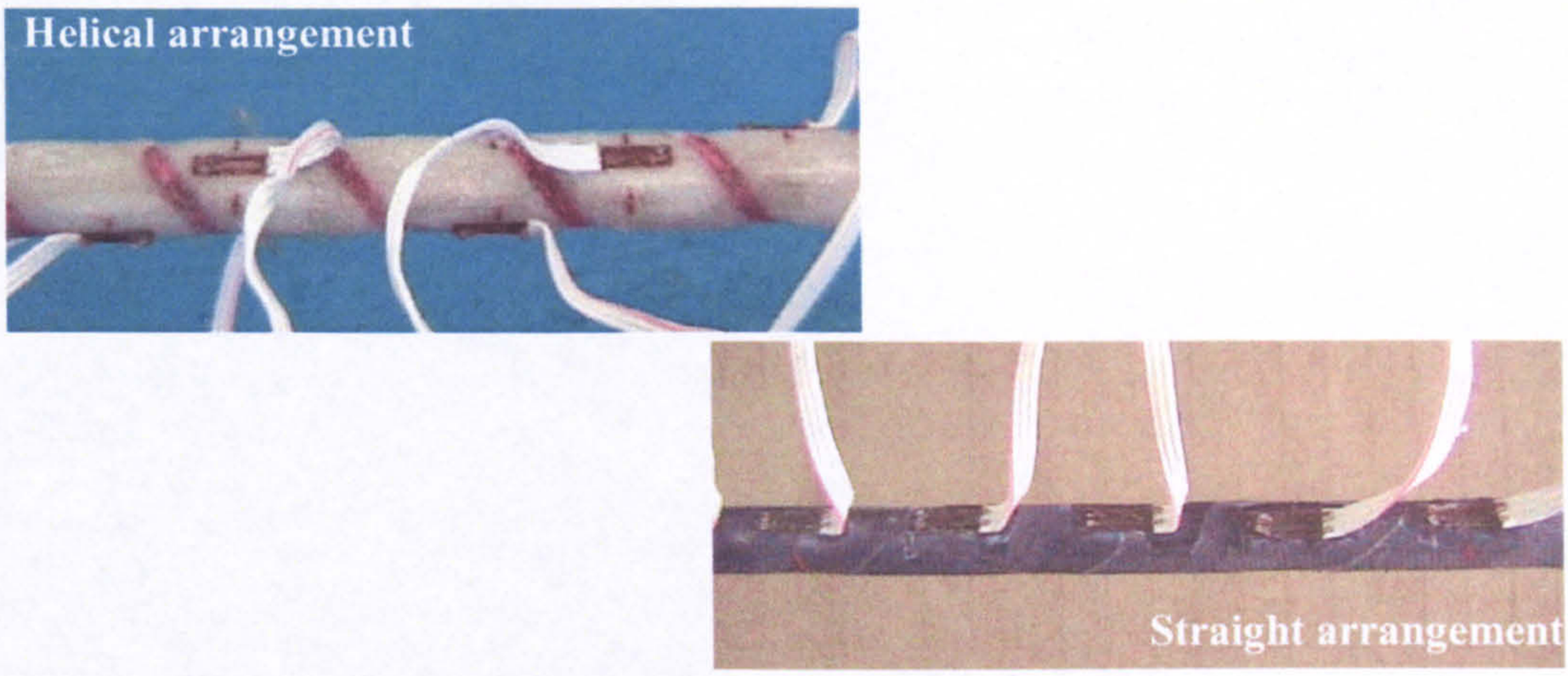

Figure 3-9: Arrangements of rebar strain gauges at the midspan zone.

Externally, one strain gauge was bonded to the top concrete surface of every beam or slab, at midspan (Figure 3-8). This gauge would enable measuring the average compressive strain along the top concrete fibre around the midspan crack. The concrete strain gauge used was wire-type, three-wired, with a resistance of 120-ohm, gauge length of 67 mm and base material dimensions of 10×80 mm. It was bonded to the concrete surface with adhesive. Specialized silicon was used to cover the strain gauge to prevent moisture uptake. The concrete strain gauge is shown in Figure 3-10.

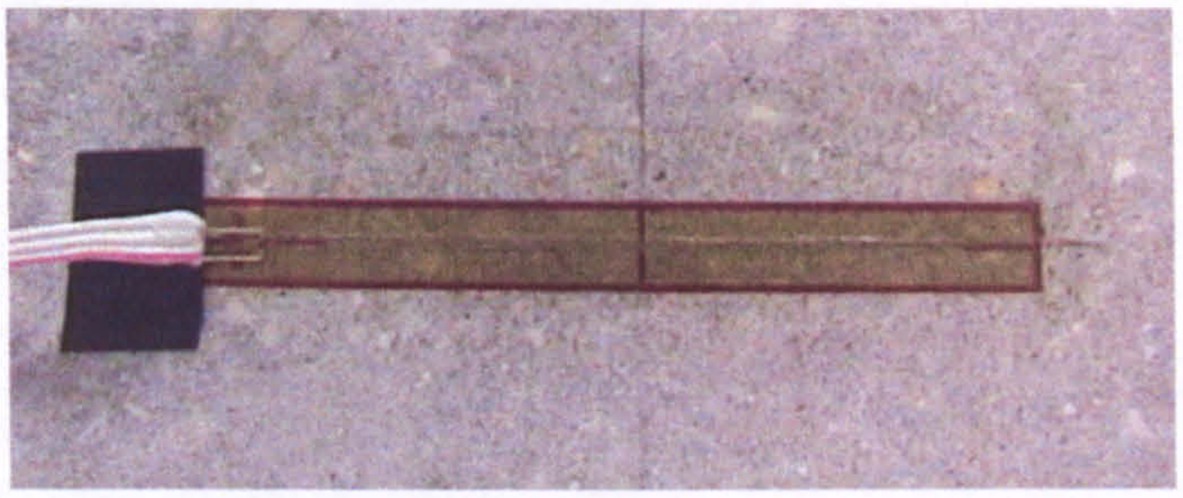

Figure 3-10: Strain gauge glued at the top concrete surface at midspan.

3.2.4.2. Linear Variable Displacement Transducers (LVDTs)

Five LVDTs were used to measure vertical deflections at midspan, the two loading points and the third-points of one shear span. Two dial gauges were used to measure settlements at the supports. Dial gauges were used because the data acquisition system could not accommodate additional LVDTs. The LVDTs were held by magnetic stands, which were attached to ground-supported purpose-built frame around the test element.

The needles of the LVDTs were positioned on the top surface of the concrete, after smoothing it, or on aluminium angles glued to the side of the test element; as appropriate. Additionally, one LVDT was used to measure the crack width and the average surface strains at midspan, at the level of the tension reinforcement, over a gauge length of 100 mm. Figure 3-11 shows the arrangement of LVDTs and dial gauges. Figure 3-12 shows a photograph of an LVDT and its support.

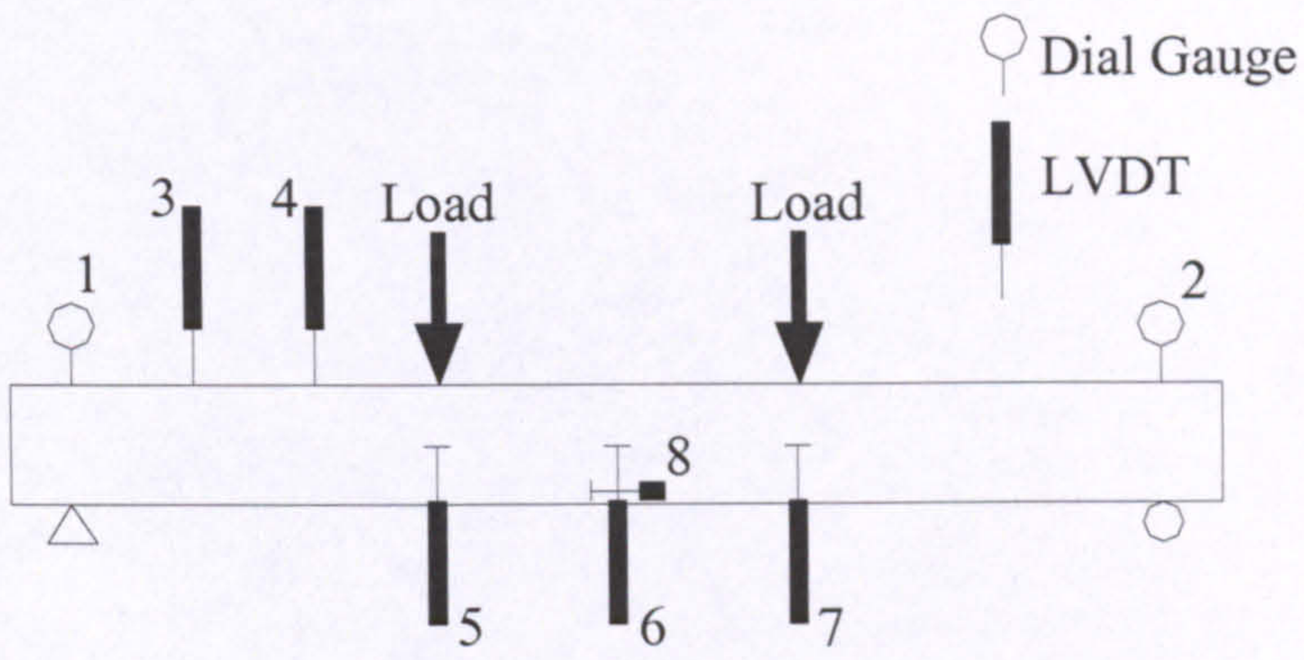

Figure 3-11: Arrangement of LVDTs and dial gauges.

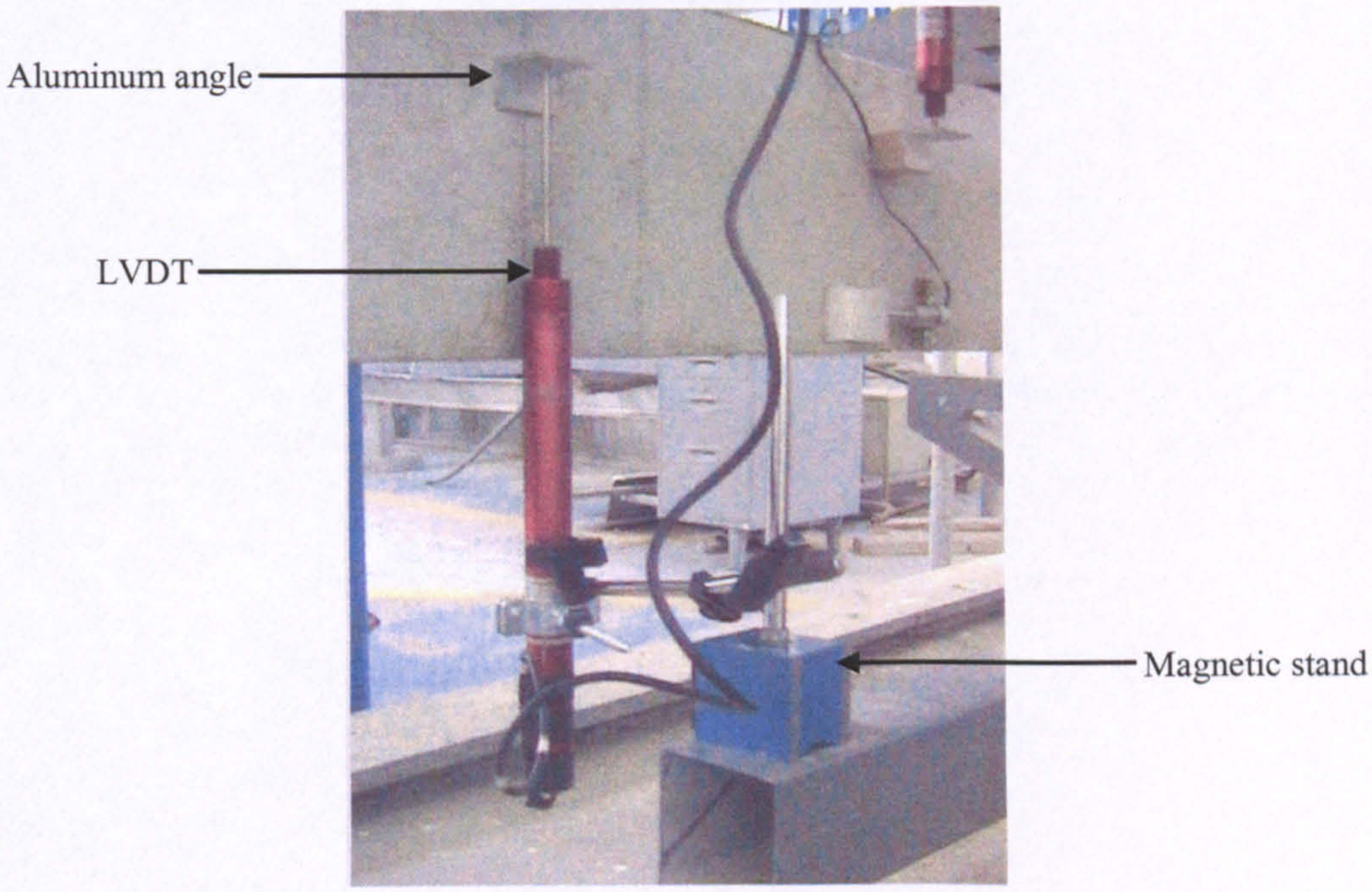

Figure 3-12: LVDT at the back of a beam.

3.2.5. Test Setup

All beams and slabs were tested under four-point loading, as shown in Figure 3-13. The load was applied at midspan by a hydraulic actuator acting against a reaction frame. The actuator had 400 mm stroke and 600 kN load capacity. A stiffened steel I-beam was used to distribute the actuator load to the slab or beam through two steel loading blocks, over 80mm-wide contact plates. By using rollers in two perpendicular directions, the loading blocks allowed for unconstrained longitudinal translation and rotation, as well as transverse rotation, which was necessary to eliminate torsion effects in the relatively wide slabs. Steel supports with 80mm-wide contact plates were used to support the beam or slab at its ends. One support allowed for the same degrees of freedom as the loading blocks. The other support only allowed for free longitudinal rotation. Some details of the loading blocks and supports are shown in Figure 3-13.

The tests were carried out in load control mode. A data acquisition system connected to a personal computer was used to control the actuator load and loading rate through a pressure transducer. All test data: load, deflections and strains were collected by the data acquisition system and downloaded to the computer.

3.2.6. Pre-test Preparations

To facilitate the identification and marking of cracks during testing, the front face of the beam or slab was white-washed with gypsum slurry, and a grid was drawn on the front face. The grid dimensions were 100×100 mm and 100×40 mm for beams and slabs, respectively. Aluminium angles and clamps for the LVDTs were fixed to the back face with epoxy adhesive. Locations for measuring deflections at the top concrete surface were smoothed and clearly marked. The beam or slab was then carefully placed on its supports and positioned in the testing frame. A small pre-load of about 1.5 kN was applied to maintain the positioning. The LVDTs and dial gauges were fixed to their supporting frame, and their needles were accurately positioned while ensuring verticality. Finally, all the wires of the strain gauges and LVDTs were connected to the data acquisition system. The beam or slab was then ready for testing.

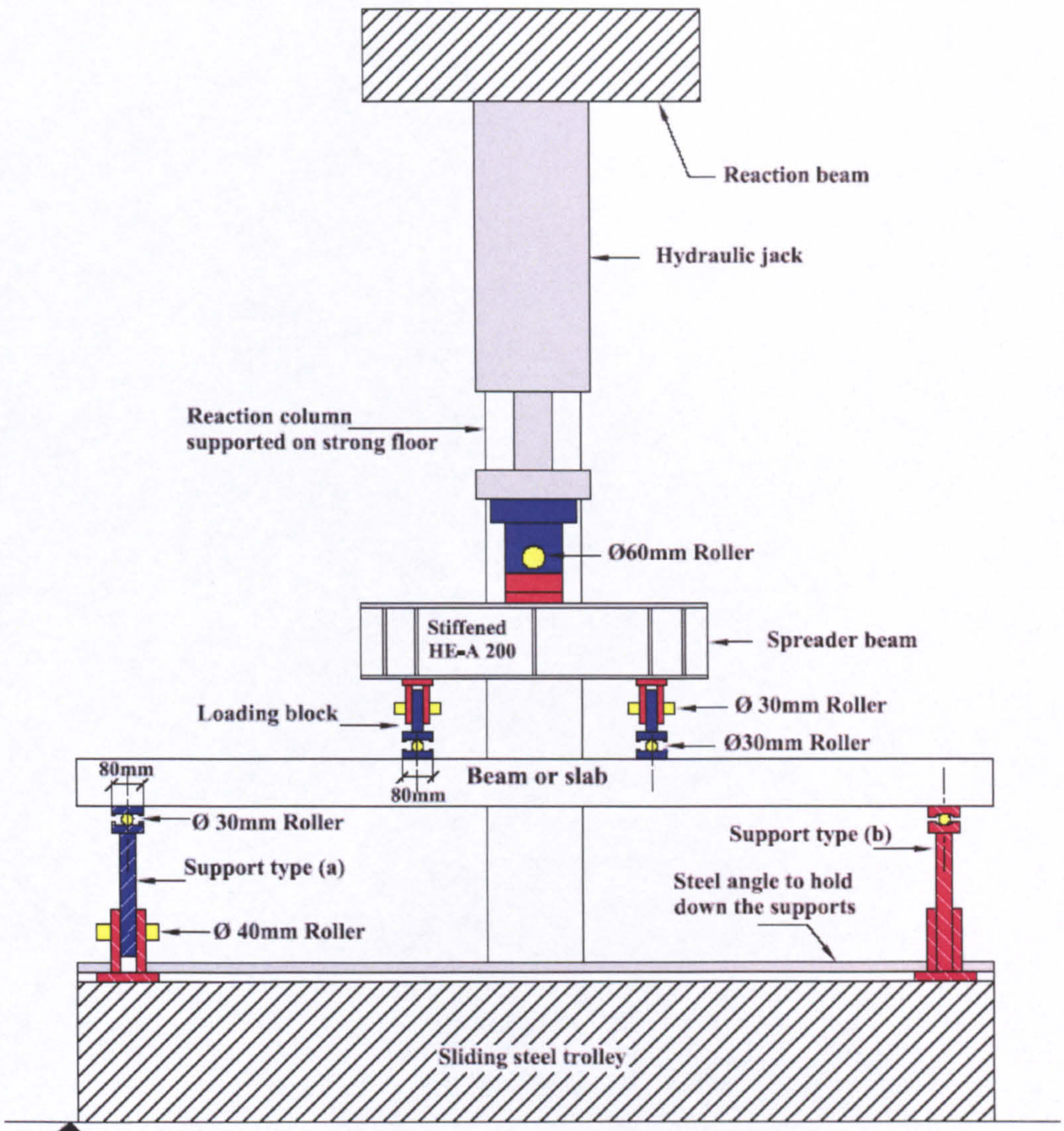

Notes:
- Support type (a) and loading blocks accommodate longitudinal rotation and translation, as well as transverse rotation.
- Support type (b) accommodates only longitudinal rotation.

Figure 3-13: Test setup.

3.2.7. Testing procedure

All the instrumentation (strain gauges and LVDTs) were automatically initialized by the data acquisition system. The test was carried out in load control at a rate of 1 kN/min. The load was paused at about 5 kN intervals to mark and measure the cracks, and to take notes and photographs. Two load cycles were performed. In the first cycle, the load was increased to a "service" load, which corresponded to a stress level in the top concrete fibre of about 40% of the concrete compressive strength. In the second cycle, the load was increased until failure occurred, either by rupture of rebars or crushing of concrete. All test data: force, strains and deflections were collected by the data acquisition system. The data were monitored graphically in real-time, and were downloaded digitally to the personal computer every second.

An optical microscope with an accuracy of 0.02 mm, shown in Figure 3-14 , was used to measure crack width at the bottom concrete fibre. Several cracks within the constant flexure zone, and sometimes within the shear spans, were measured at every load pause. The cracks, crack width and corresponding load level were marked on the front face of the beam or slab. In some tests the sequence of crack formation was recorded. In addition, the locations of the cracks relative to the grid were measured and photographs were taken. The documentation of cracks was carried out up to a load of about 75% of the expected failure load. It was considered unsafe to get near the test element beyond that load level.

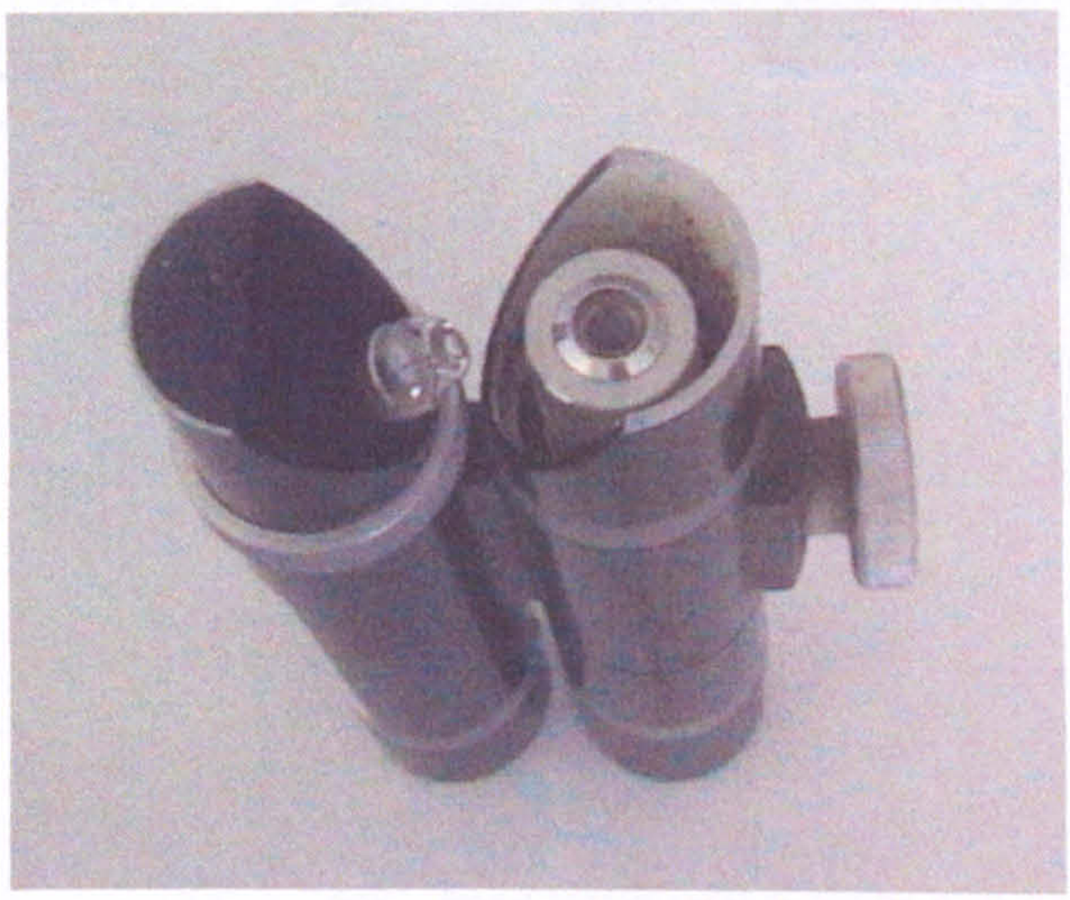

Figure 3-14: Optical microscope used in measuring crack width.

After test completion, a closer examination of the mode of failure was conducted. The cracks and failure pattern were documented, and additional photographs were taken. Sometimes, the crack patterns at the back and underside were investigated. The beam or slab was then removed from the testing frame and turned upside down. The concrete cover was carefully chiselled out to expose the strain gauges on both sides of the crack inducer. Then, it was possible to confirm the exact location of the crack inducer relative to the strain gauges, and the cover to the rebars in the centre zone. The cover was also confirmed at the ends. This was necessary, particularly for some slabs, because it was suspected that their reinforcement mesh moved or floated during casting.

3.3. MATERIALS

In addition to the structural tests, material tests were carried out to determine the mechanical properties of the concrete and rebars that were used in the beams and slabs. These tests and their results are presented next.

3.3.1. Concrete

The concrete was produced insitu using crushed limestone aggregate and CEM II/A-L 42.5 Portland-limestone cement (according to BS EN 197-1/2000 CEM II/A-L). The concrete was designed to have a slump of 75 mm, and a 28-day cube compressive strength of 35 MPa not including any factors of safety, with 25 mm maximum aggregate size, 0.48 free water-cement ratio and 380 kg/m^3 cement content.

As explained in Section 3.2.3.3, four control 150 mm cubes and three 150×300 mm cylinders were cast with every beam or slab. The three cylinders and three of the cubes were tested on the same day of testing the beam or slab that they represented. The fourth cube was tested either at 7 days or at 28 days, for purposes of quality and curing control. The cubes were used to determine the compressive strength of the concrete according to BS1881-P116 (Testing Concrete, Method for Determination of Compressive Strength of Concrete), while the cylinders were used to determine the split cylinder tensile strength of the concrete according to ASTM C496-96 (Standard Test

Method for Splitting Tensile Strength of Cylindrical Concrete Specimens). Figure 3-15 shows the concrete cube and cylinder tests.

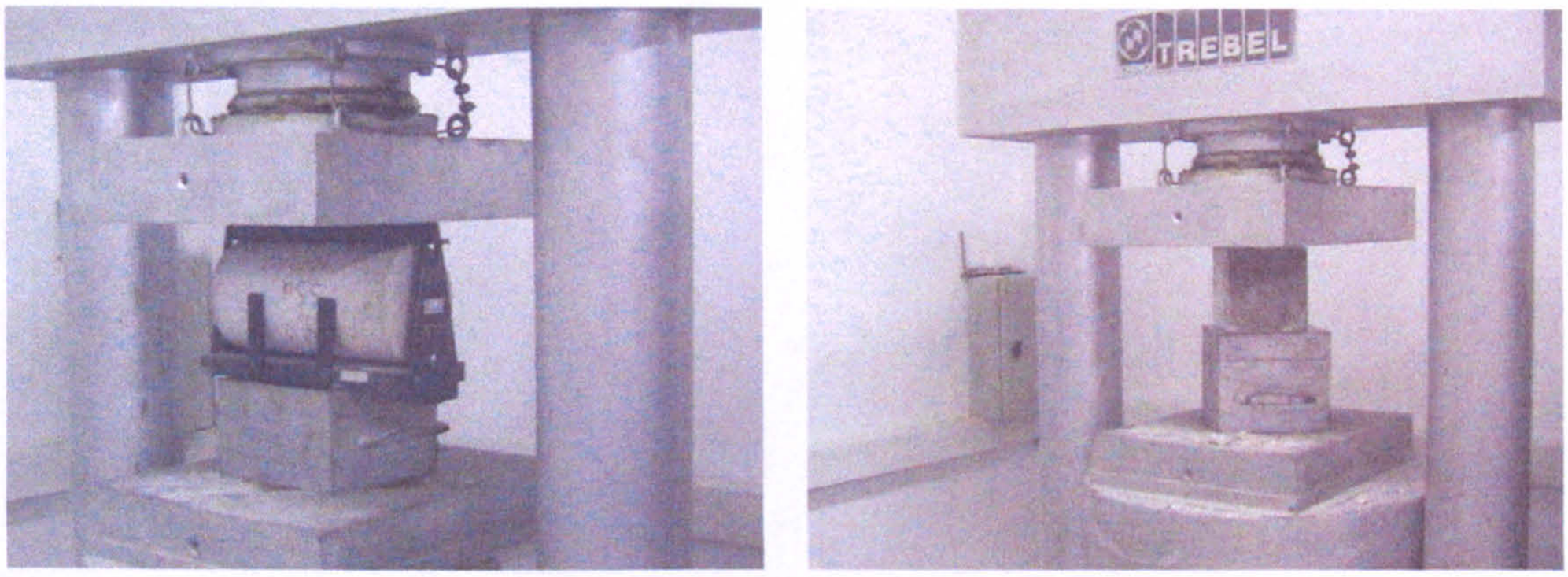

Figure 3-15: Concrete cube and cylinder tests.

All structural and accompanying concrete specimen tests had to be carried out beyond one year of casting, by which age the concrete properties had almost stabilized. The concrete test results are detailed in Table 3-1. The table shows that the mechanical properties of the concrete are consistent with insignificant statistical variation, which reflects very good quality control and production procedures.

Table 3-1: Mechanical properties of the concrete

Beam or Slab Series	Cube Compressive Strength, MPa		Split Cylinder Tensile Strength, MPa	
	Average	Standard Deviation	Average	Standard Deviation
SS	50.6	2.56	3.6	0.24
BS	52.0	1.40	4.1	0.28
SG1	51.0	1.44	3.9	0.23
SG2	46.2	1.55	3.4	0.24
SG3	45.9	2.02	3.8	0.17
BG1	47.7	3.56	4.1	0.29
BG2	47.7	3.56	3.8	0.15
BG3	46.5	0.92	3.6	0.08
SC1	50.1	2.50	3.9	0.21
SC2	51.0	2.41	3.4	0.11
SC3	49.8	3.95	3.8	0.24
BC1	55.4	2.86	3.9	0.20
BC2	52.6	2.38	3.6	0.05
BC3	51.8	2.59	3.6	0.19

This study deals with deflection and cracking. Hence, it was important to properly evaluate the concrete modulus of elasticity. For that purpose, additional cylinders tests were required for every beam and slab, but these were not possible. Instead, stringent quality control was exercised on the production of concrete so that all batches would be identical as far as practicable. The homogeneity of the concrete was confirmed by the cubes tested at 7 and 28 days, and later by all the cube and cylinder tests (Table 3-1). Then, three concrete cylinders from one of the concrete batches were tested to determine the concrete compressive modulus of elasticity, according to BS 1881-121:1983 (Method for Determination of Static Modulus of Elasticity in Compression). In these tests, the measurements of strains were duplicated by using both strain gauges and LVDTs, as shown in Figure 3-16. This test-determined modulus of elasticity was expected to provide a means to decide on which recognized modulus formula to be adopted for the evaluation of the modulus for all the other concrete batches. An average experimental modulus of 31500 MPa was obtained for an average cube compressive strength of 52.5 MPa, as shown in Figure 3-17. The corresponding moduli according to ACI Committee 318 (2002) and CEN (2004) were 31200 MPa and 30800 MPa, respectively. Both predictions were good but the ACI formula was slightly closer to the experimental modulus. Therefore, it was decided to use the ACI formula to evaluate the concrete modulus of elasticity in all cases.

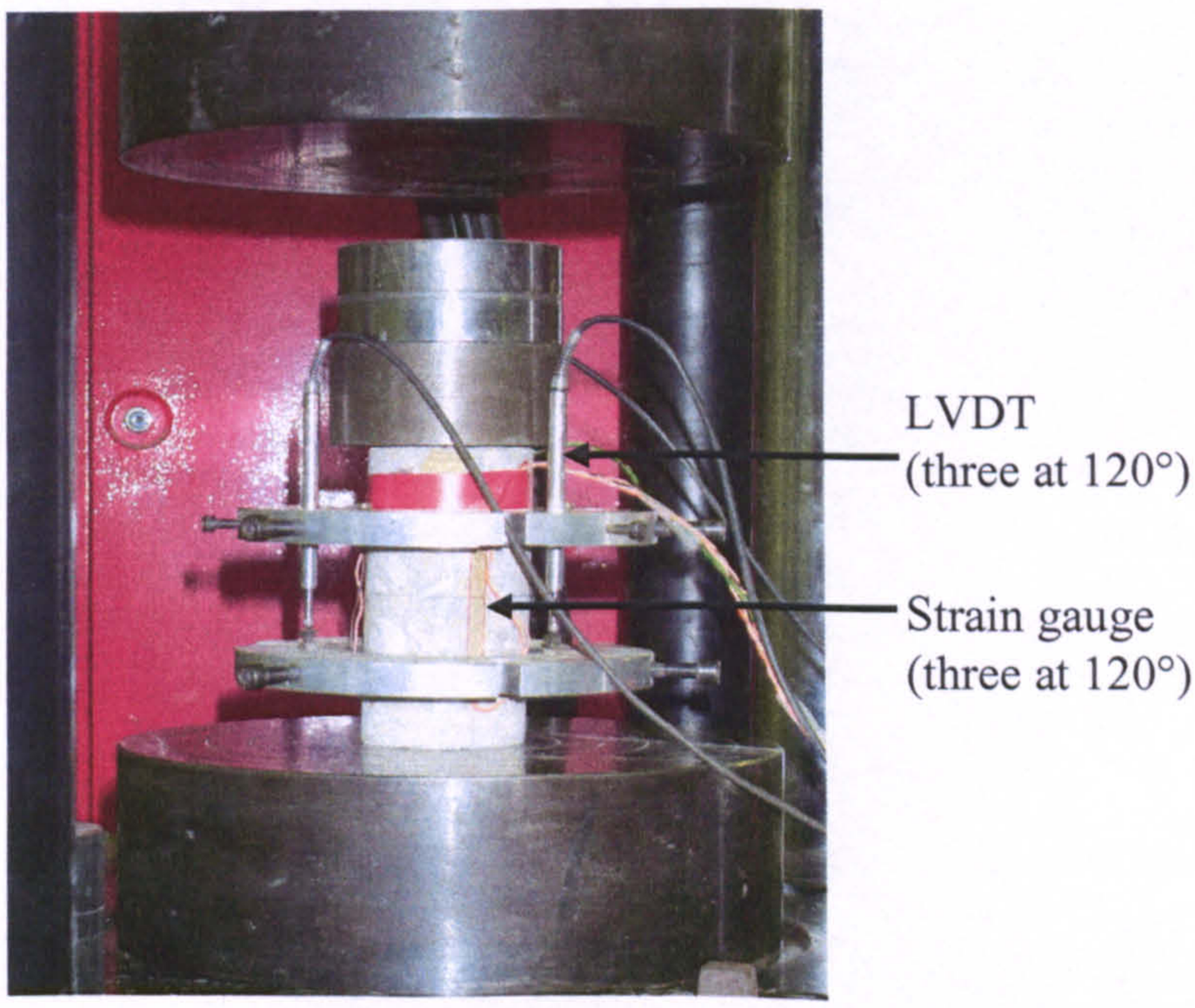

Figure 3-16: Test for the concrete compressive modulus of elasticity.

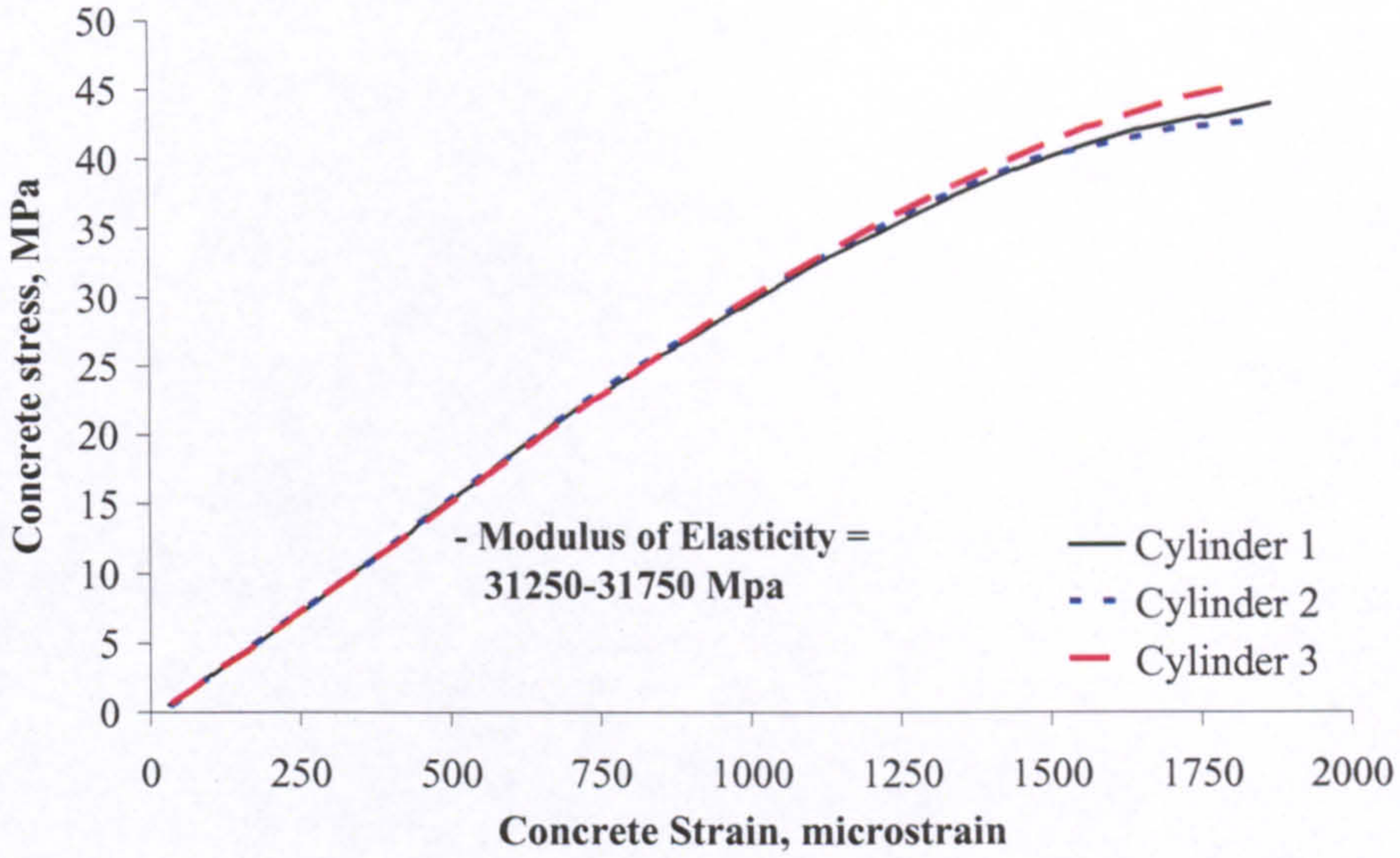

Figure 3-17: Concrete stress vs. strain.

3.3.2. Reinforcement

The modulus of elasticity of the reinforcement is one of the main variables of this research. Hence, representative FRP rebar specimens were tested in uniaxial tension to determine their modulus of elasticity, as well as their ultimate stress and strain. Representative steel rebars were also tested for their yield and ultimate strength in tension.

3.3.2.1. FRP Reinforcement

FRP rebars are sensitive to transverse pressure. Hence, the steel grips of the tension machine can damage the rebar. Normally, such damage would not affect the modulus of elasticity, but would undermine the tensile capacity. To overcome this problem, steel tube end-anchorages were used at the grips (Figure 3-18). This method is not standardized, so the anchorage had to be designed and pre-evaluated. It was realized that intricate analysis of a complex state of stresses was involved. However, simplified preliminary design was made, and then checked by testing. In simple terms, the steel tube had to be thick enough to accommodate the transverse pressure from the grips, as well as the longitudinal tensile stresses transferred to it from the rebar. In the first case, transverse deformations should be diminished. In the second case, the steel material

should not yield. Low viscosity epoxy was used to adequately fill the annular gap between the tube and rebar without entrapping air. The tube length necessary to transfer the tension force in the rebar was determined based on the shear capacity of the epoxy, as well as the shear-friction capacity at the epoxy-FRP and epoxy-steel interfaces. Hence, different tube lengths were used for the various types and diameters of FRP rebars, as shown in Figure 3-18. In some cases, it was necessary to induce one or two steps in the inner diameter to enhance the shear resistance and to prevent slippage. The clear length of rebar between the anchorages was taken as a multiple of the rebar diameter, and in general ranged from 30 to 45 times the diameter. At the ends of the tubes, the rebar was centred by using round plastic locators. These were fabricated with an outer diameter equal to the outer diameter of the tube, and an inner hole-diameter equal to the diameter of the rebar.

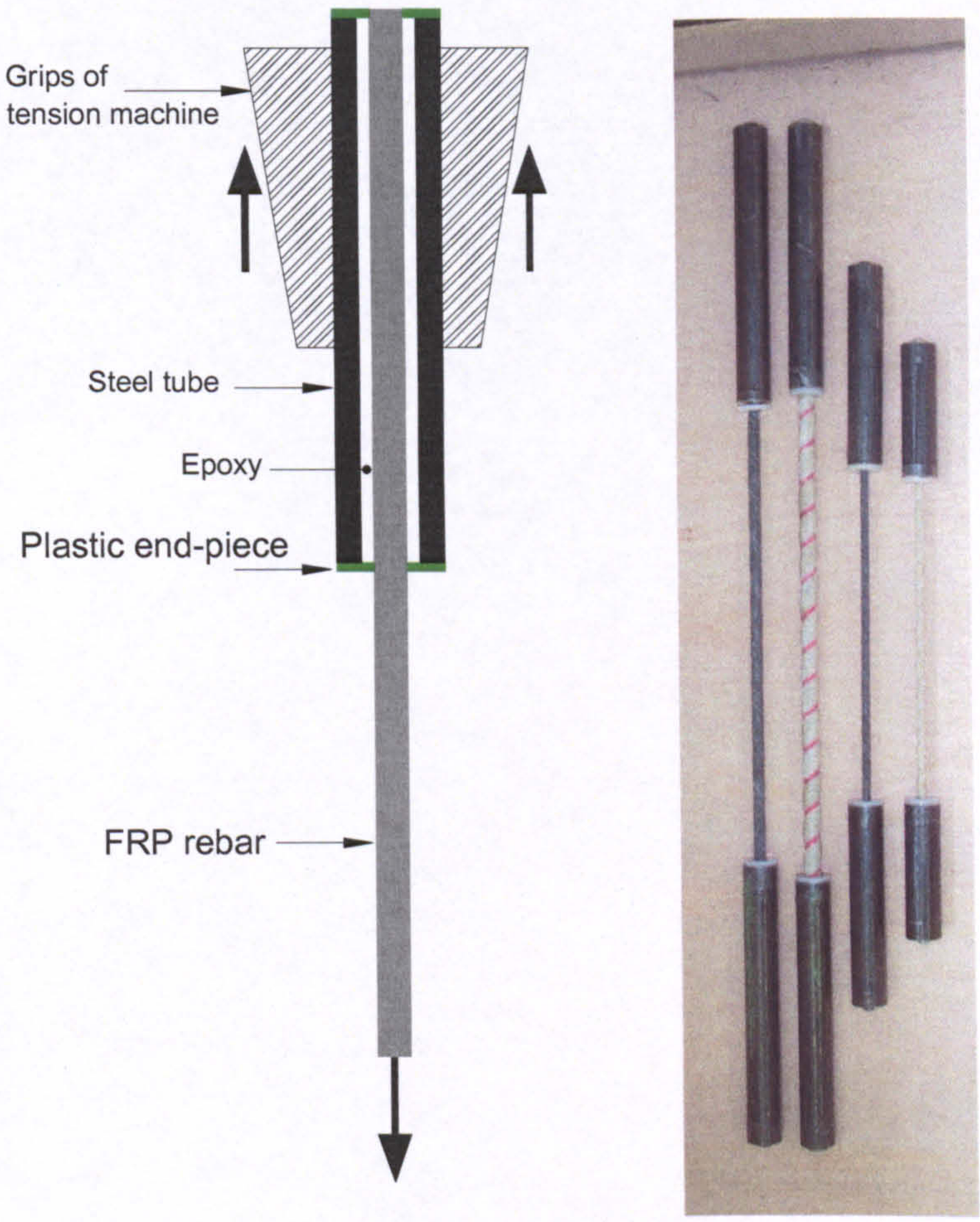

Figure 3-18: Steel tube end-anchorages for tensile tests of FRP rebars.

Five representative specimens were tested for each type and diameter of FRP rebar. The tensile tests involved load and strain measurements. The strains were measured by both strain gauges and LVDTs. Two strain gauges, on opposite sides at 180°, were used to measure local strain at mid-length over a gauge length of 6mm. Three LVDTs, every 120° around the rebar, were used to measure the average strain over a gauge length of 160 mm in the middle region. Typical rebar instrumentation is shown in Figure 3-19.

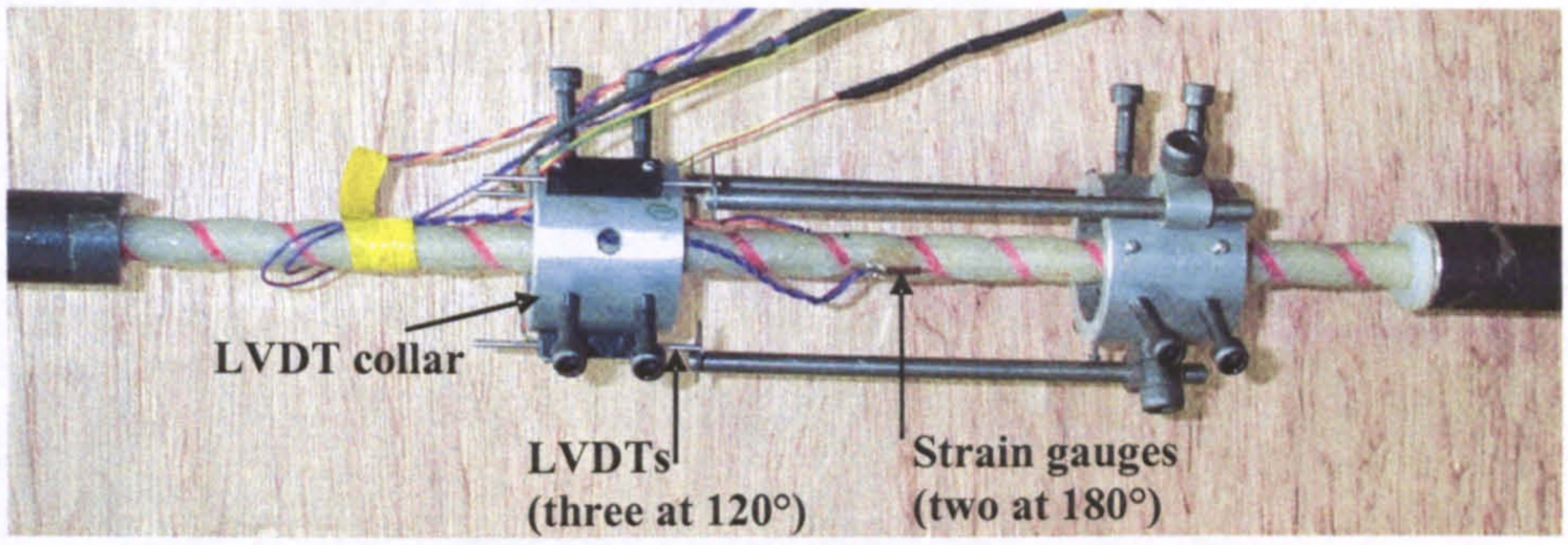

Figure 3-19: Instrumentation of FRP rebar in tensile test.

The tensile stress-strain diagrams were linear up to failure, as typically shown in Figure 3-20. Figure 3-21 shows typical tension failure of GFRP and CFRP rebars. The results of the tensile tests of all the FRP rebars are summarized in Table 3-2. The mechanical properties of the GFRP and CFRP rebars as published and provided by the manufacturer, at the time of the investigation, are also shown in Table 3-2.

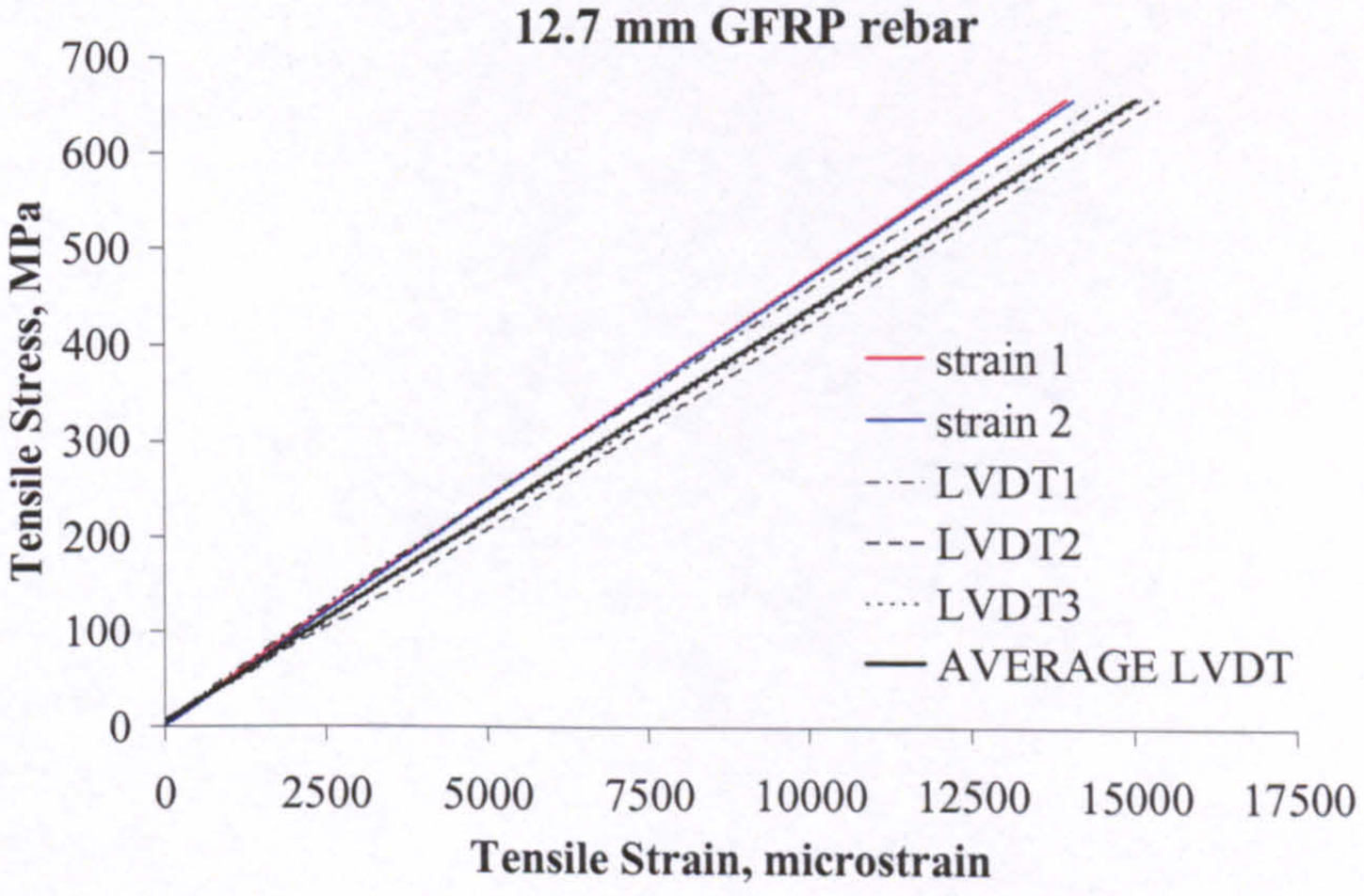

Figure 3-20: Typical FRP stress-strain diagram.

Figure 3-21: Failure of FRP rebars in tension.

Table 3-2: Tensile mechanical properties of FRP rebars

Rebar type	Nominal Diameter, mm	Modulus of Elasticity, E, MPa	Rupture Strain, microstrain	Rupture Stress, f_{fu}, MPa	Coefficient of Variation, %		Manufacturer Mechanical Properties[1]	
					E [2]	f_{fu}	E	f_{fu}
GFRP	6.35	38850	15450	600	3.03	11.6	40800	830
	9.53	42750	15550	665	2.87	5.48	40800	760
	12.7	41600	14900	620	4.55	6.11	40800	690
	19.05	41950	15950	670	3.39	1.80	40800	620
CFRP	6.35	133000	10900	1450	4.25	2.77	119250	1450
	9.53	131750	10050	1325	4.94	13.05	122500	1350
	12.7	118600	12450	1475	3.09	3.89	111700	1230

[1] Manufacturer mechanical properties as published for the GFRP rebars, and as provided for the used batch of CFRP rebars, at the time of the investigation.

[2] The rebar modulus was evaluated based on the average strains measured by LVDTs for the GFRP rebars, and based on the local strains measured by strain gauges for the CFRP rebars.

3.3.2.2. Steel Reinforcement

The tensile mechanical properties of the steel rebars were also determined by testing representative samples. These tests were carried out according to ASTM A370-97a (Standard Test Methods and Definitions for Mechanical Testing of Steel Products). The yield strength, ultimate strength and elongation were measured, and are shown in Table 3-3.

Table 3-3: Tensile mechanical properties of steel rebars

Rebar Type	Nominal Diameter, mm	Elongation, microstrain	Yield Strength, f_y, MPa	Ultimate Strength, MPa	Coefficient of Variation of f_y, %
Steel	10	80000	590	675	1.9
	12	114000	590	670	0.8

During the analysis of experimental data, more detailed knowledge of the stress-strain properties of the 12-mm steel rebar were needed. These were determined by uniaxial tensile testing; similarly to the FRP rebars, but without end anchorages and only strain gauge measurements. The stress-strain results are shown in Figure 3-22.

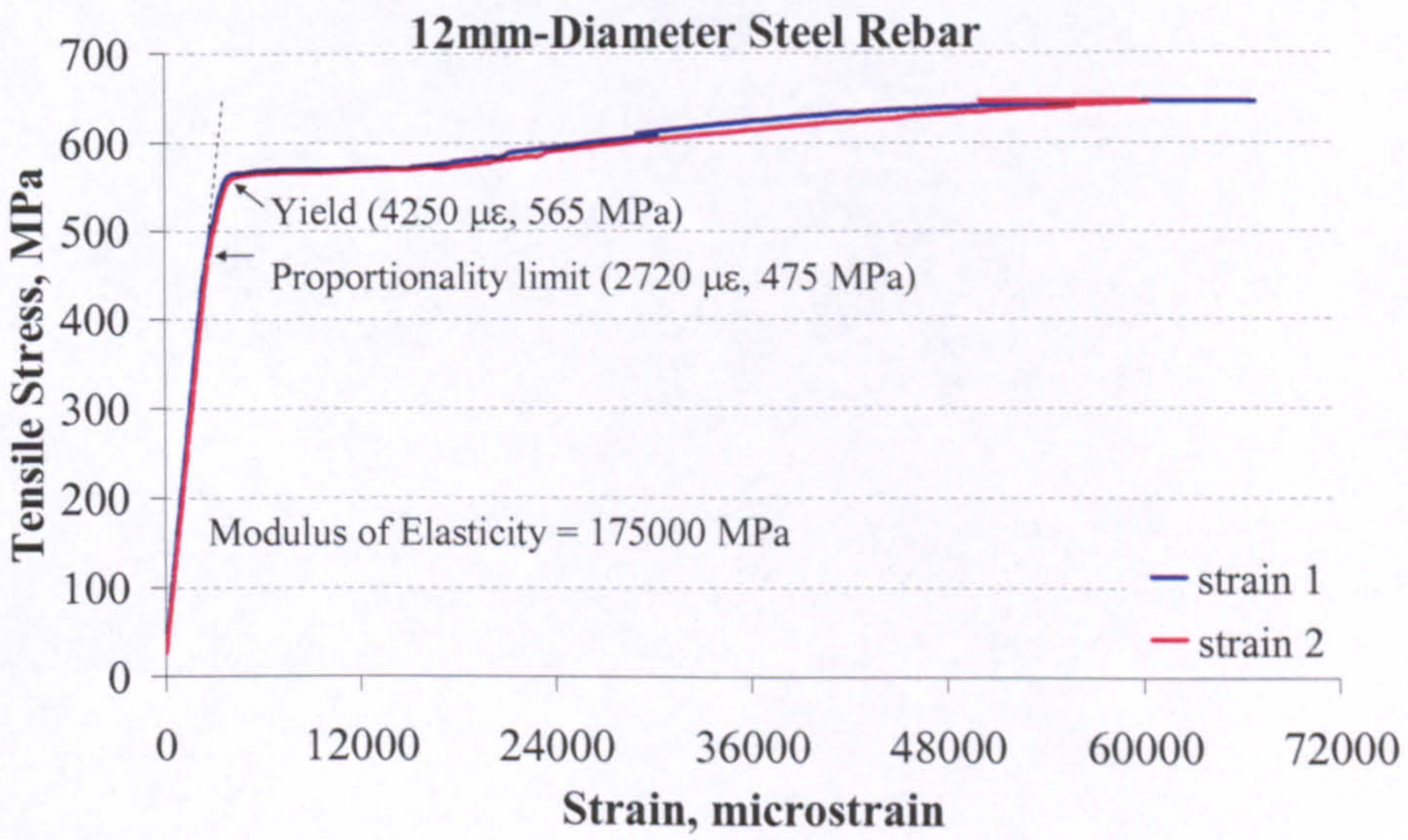

Figure 3-22: Stress vs. strain relationship for 12mm-diameter steel rebar.

CHAPTER 4

EXPERIMENTAL RESULTS AND DATA ANALYSIS

4.1. INTRODUCTION

This chapter deals with the experimental data acquired in the beam and slab tests. The data are not considered for each individual test on its own. Instead, the various categories of data are presented and typical types of behaviour are identified. Any deviations from the general behaviour are explained. Initially, the modes of failure and load capacity are discussed. Then, the rebar and concrete strain, deflection, and crack width and spacing are examined over the entire loading path. The results of the steel RC elements are always used for comparison purposes. Subsequently, some of the experimental data are analysed in order to investigate other structural aspects that are related to deflection behaviour. Hence, the rebar strain data around the crack inducer are used to look into tension stiffening and bond. Furthermore, rebar strain data are utilised, in conjunction with concrete strain, to experimentally derive the load-curvature relationship between flexural cracks, as well as the average neutral axis depth.

4.2. EXPERIMENTAL DATA

A large amount of data was gathered during the structural tests. An appropriate common link for the data is the load. Therefore, the experimental load-rebar strain, load-concrete strain, load-deflection and load-crack width relationships were prepared for every test, and are shown in Appendix B. In the following sections, only typical experimental relationships are presented and investigated to identify typical types of

behaviour. Discrepancies and peculiarities are not ignored; they are pointed out and discussed. The modes of failure and load capacity are examined first.

4.2.1. Modes of Failure and Load Capacity

Two modes of failure were encountered during the beam and slab tests, namely, rupture of the rebars and compressive failure of the concrete, which is also referred to as concrete crushing. Near balanced conditions were also encountered; where the compressive concrete failure commenced but was followed, almost immediately, by rupture of the rebars.

In the rebar rupture mode of failure, the rebars are ruptured at one of the flexural cracks within the constant flexure zone, or less frequently, at the crack directly beneath one of the loading blocks. Due to the absence of top flexural reinforcement, rupture of the rebars causes the crack to penetrate through the entire section. Hence, the element is literally cut into two separate segments and it collapses. The rupture of the rebars occurs suddenly and instantaneously, which makes the collapse catastrophic. Figure 4-1 shows a typical rebar rupture mode of failure.

Figure 4-1: Typical failure by rupture of rebars (Beam BG1a).

The compressive concrete failure also occurs above the location of a crack within the constant flexure zone. A tiny concrete arc-segment pops upwards at the unconfined top surface above the crack where the compressive strains are highest. This is followed by further successive breaking-up of bigger concrete segments at the weakened section, while the crack becomes wider. The width of an adjacent crack also increases, but to a lesser extent. In the mean time, the load drops from its maximum level at a continuously increasing rate, while the other cracks close. The compressive concrete failure is brittle and fairly quick, though more gradual compared to the rebar rupture failure. In load control mode, complete failure occurred in no more than approximately 20 seconds. In few tests, the compressive failure occurred explosively and almost instantaneously. Figure 4-2 shows a typical concrete compressive failure.

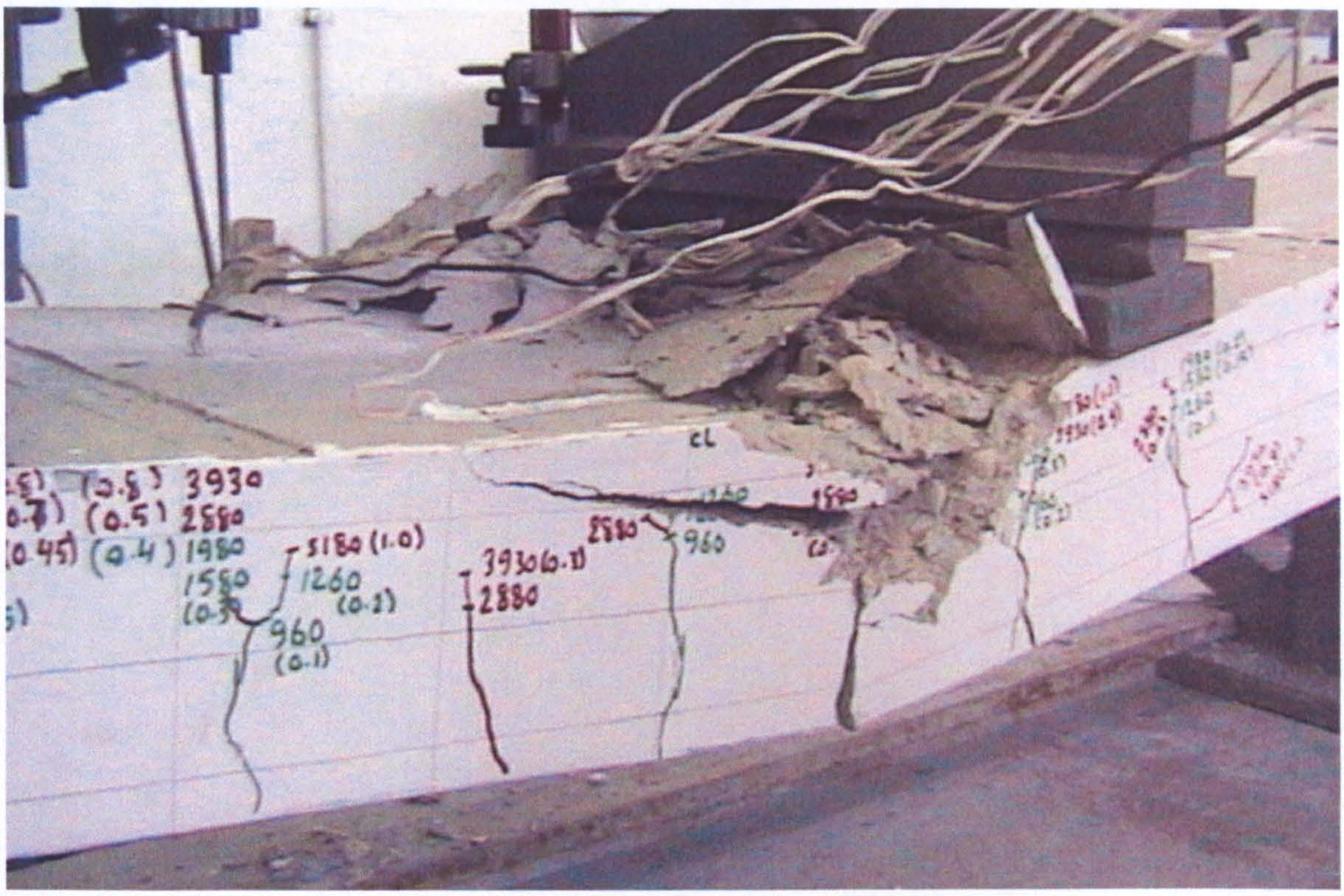

Figure 4-2: Typical concrete compressive failure (slab SC3a).

The steel RC elements also fail by compressive concrete failure, similarly to the FRP RC elements. However, the compressive failure process is preceded by a yielding phase that gives the sense of ductility to the failure. In the yielding phase, the load increases, but only marginally. The flexural cracks grow progressively wider while the steel reinforcement yields at several cracks within the constant flexure zone. The yielding

may concentrate more across one or two critical cracks, where the concrete and/or the steel rebars are weaker. The deflection also increases progressively. Eventually, the compressive concrete failure occurs at the critical crack as described earlier. After failure, the cracks maintain higher residual width because of the unrecoverable yield of the steel reinforcement.

The modes of failure and load capacity results of the beams and slabs are shown in Table 4-1. The replicate elements within each series have almost identical load capacity, which reflects very good quality control and repeatability of the tests. A greater deviation is noticed in the case of the slabs. Slab SG1a fails at a higher load, but this is because its rebars rupture at higher strains. Slabs SG2a and SG2b have an almost balanced reinforcement ratio. While slab SG2a fails by rupture of rebars, the rebars in slab SG2b sustain higher strains that increase the load capacity and cause compressive concrete failure. In that regard, the tests indicate that the rupture strain has some variability and can be less than the value obtained in the uniaxial tension test, which may be caused by the concentration of bond stresses at the cracks. On the other hand, the flotation of the reinforcement during casting resulted in different cover values in the slabs SC3a and SC3b, which caused these slabs to have differing load capacities. However, it is worth emphasizing again that the cover values were measured after every test. The actual cover values are shown in Table 4-1, and are taken into account in the analysis of the results.

The results also indicate that the relation between the FRP RC and their reference steel RC elements, as initially designed, is not maintained. This is due to the differences between the material properties considered in the design and the actual material properties. All the elements were tested beyond an age of one year after casting, hence the concrete compressive strength increased by about 40%. Also, the common (for Jordan) grade 400-steel had unexpectedly high yield strength of 590 MPa. Nonetheless, the steel RC elements are still useful for comparison purposes.

Table 4-1: Modes of failure and load capacity results

Rebar Type	Beam/ Slab	Cover, mm	Reinforcement Ratio	Cube Concrete Strength, MPa	Load Capacity, kN	Mode of Failure
BEAMS						
GFRP	BG1a	25	0.00432	47.7	45.1	Rupture of rebars
	BG1b				44.6	Rupture of rebars
	BG2a	25	0.00772	47.7	80.7	Concrete crushing[1]
	BG2b				77.8	Concrete crushing[1]
	BG3a	25	0.03928	46.5	112.1	Concrete crushing
	BG3b				117.4	Concrete crushing
CFRP	BC1a	25	0.00286	55.4	73.7	Rupture of rebars
	BC1b				77.0	Rupture of rebars
	BC2a	25	0.00648	52.6	104.8	Concrete crushing[1]
	BC2b				103.2	Concrete crushing[1]
	BC3a	25	0.01159	51.8	122.8	Concrete crushing
	BC3b				124.6	Concrete crushing
Steel	BSa	25	0.00688	52.0	73.7	Yielding[2]
	BSb				75.0	Yielding[2]
SLABS						
GFRP	SG1a	27.5	0.003547	51.0	20.7	Rupture of rebars
	SG1b	27.5			18.2	Rupture of rebars
	SG2a	31	0.008471	46.2	40.3	Rupture of rebars
	SG2b	31			45.0	Concrete crushing[1]
	SG3a	40	0.040459	46.0	62.6	Concrete crushing
	SG3b	40			63.4	Concrete crushing
CFRP	SC1a	31	0.00295	50.1	38.0	Rupture of rebars
	SC1b	33	0.00302		37.5	Rupture of rebars
	SC2a	38.0	0.00739	51.0	56.3	Concrete crushing[1]
	SC2b	35.0	0.00711		56.7	Concrete crushing[1]
	SC3a	42.5	0.01424	49.8	61.3	Concrete crushing
	SC3b	36	0.01305		71.2	Concrete crushing
Steel	SSa	25	0.00698	50.6	47.8	Yielding[2]
	SSb	25			46.3	Yielding[2]

[1] Crushing almost immediately followed by rupture of rebars, which is very close to balanced failure.

[2] Yielding followed by crushing of concrete.

4.2.2. Strain in the Rebars

A typical experimental load-rebar strain relationship is shown in Figure 4-3. The rebar strains are at and around the crack inducer at midspan (Figure 3-8). Before cracking, the strains in the reinforcement are compatible with the strains in the surrounding concrete, and are therefore of negligible magnitude. When the first crack forms at the crack inducer, the strains increase considerably. The magnitude of the increase in strain is highest at the crack, and gradually reduces away from the crack as the tension carried by the uncracked concrete increases. A similar increase in rebar strains occurs with the formation of the two contiguous cracks on either side of the crack inducer. Thereafter and with no major intermediary cracks developing, the strains between the cracks follow an almost linear relationship with load until failure occurs either by rupture of the rebars or crushing of the concrete somewhere within the constant flexure zone. Generally, the lines that represent the individual strains between the cracks deviate away from, or at least do not converge to, the line that represents the maximum strain at the crack. In other words, the difference between the maximum strain at the crack and the minimum strain between the cracks continues to increase as the load increases.

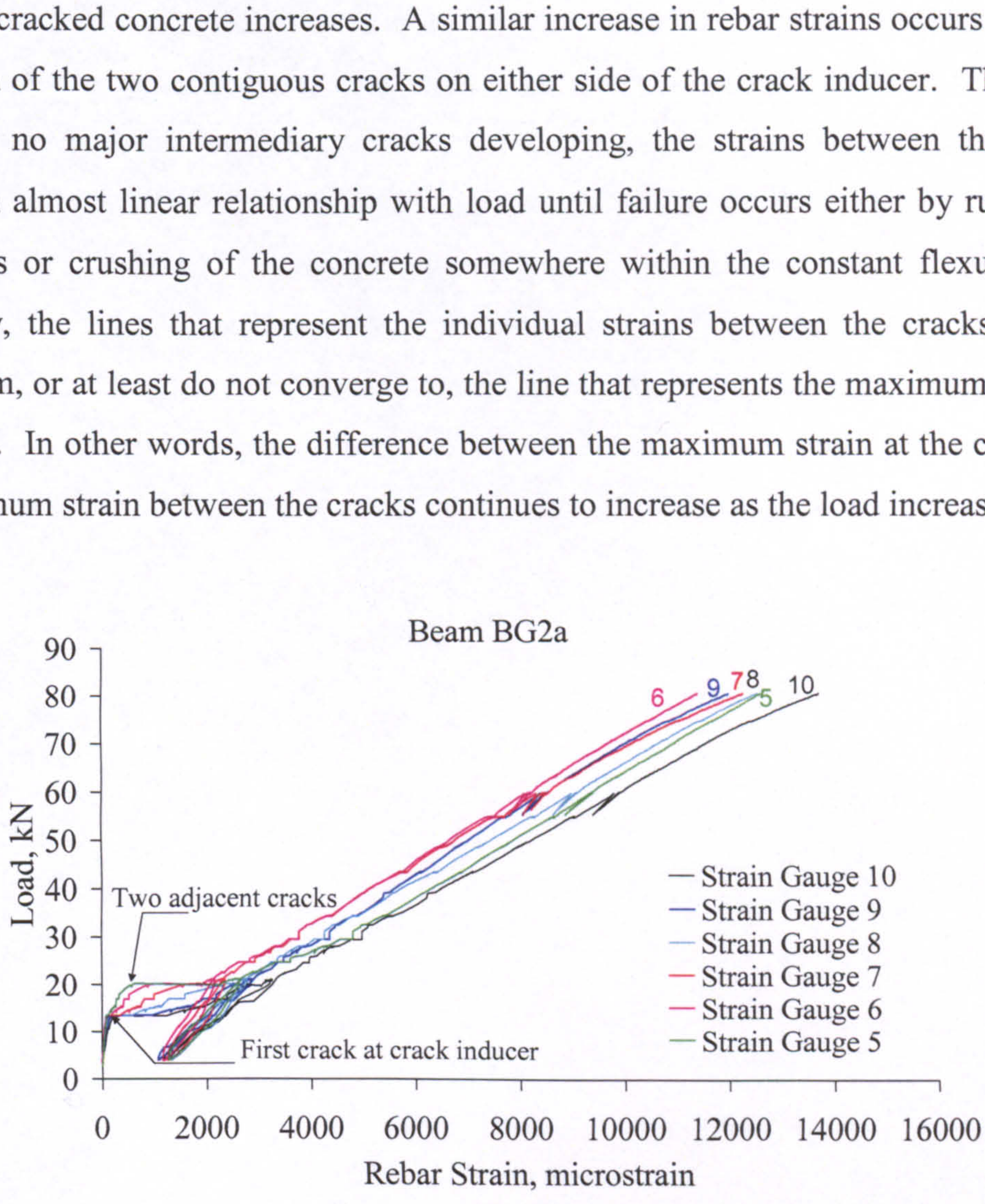

Figure 4-3: Typical experimental load vs. rebar strain relationship.

Figure 4-4 shows diagrammatically the development of strain profiles between cracks with increasing load. This strain behaviour indicates that the average bond between the rebar and the concrete, in the constant flexure zone, continues to increase or at least

does not drop below its level when the cracks have formed. A diagrammatic development of bond profiles and average bond with load is also shown in Figure 4-4.

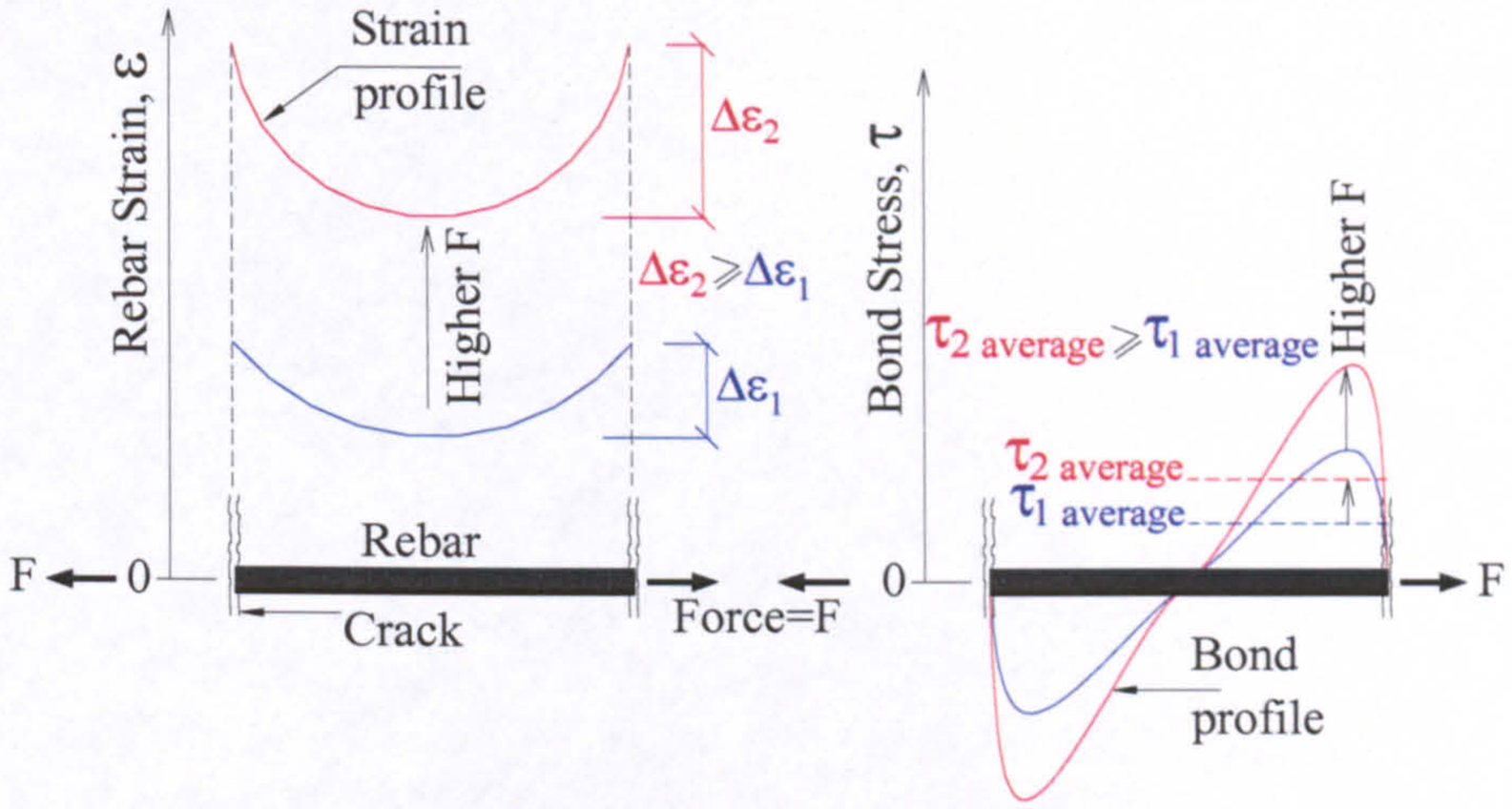

Figure 4-4: Development of strain and bond profiles with increasing force in the rebar.

Figure 4-5 shows a typical profile of strains around a crack inducer and along a rebar, which further clarifies the development of rebar strains in association with cracking around the crack inducer, as explained earlier. The negligible strains at the support indicate that the rebar is adequately anchored, with effectively no slip at its end. In tests: BG3, BC2 and BC3, the rebar strain at the support reached noticeable values at the maximum load, but did not exceed 450 microstrains. However, this strain can be adequately anchored by the 100 mm rebar extension beyond the centre of the support, as the average bond stress over that length would not exceed 1.8 MPa in the worst case. Hence, no rebar end-slip is suspected.

Figure 4-5 also shows that the reinforcement undergoes additional strains, in excess of the strains due to flexure, within the shear span and at the location of the load. In some tests mostly involving GFRP rebars (BG1b, BG2a, BG2b, BG3b, SG2a and SC1a), the rebar strain at the location of the load exceeded the rebar strain at midspan. In steel RC, the interaction of flexure and shear within the shear span is known to cause additional strains in the reinforcement in excess of the requirements of flexure. However, the resulting maximum rebar strain in the shear span does not exceed the maximum strain at a crack within the constant flexure zone. To allow for the increase in reinforcement strains within the shear span, CEN (2004) requires a horizontal shift in the bending

moment diagram, thereby the flexural strains that are developed in the absence of shear where the maximum bending moment occurs are not exceeded. This issue needs further shear-oriented research; possibly considering all the shear resistance mechanisms and slip of the reinforcement at the shear cracks, the deformation and failure characteristics of the concrete teeth between the shear cracks, and the deformation of the concrete compression zone on top of these cracks, which is beyond the scope of this thesis.

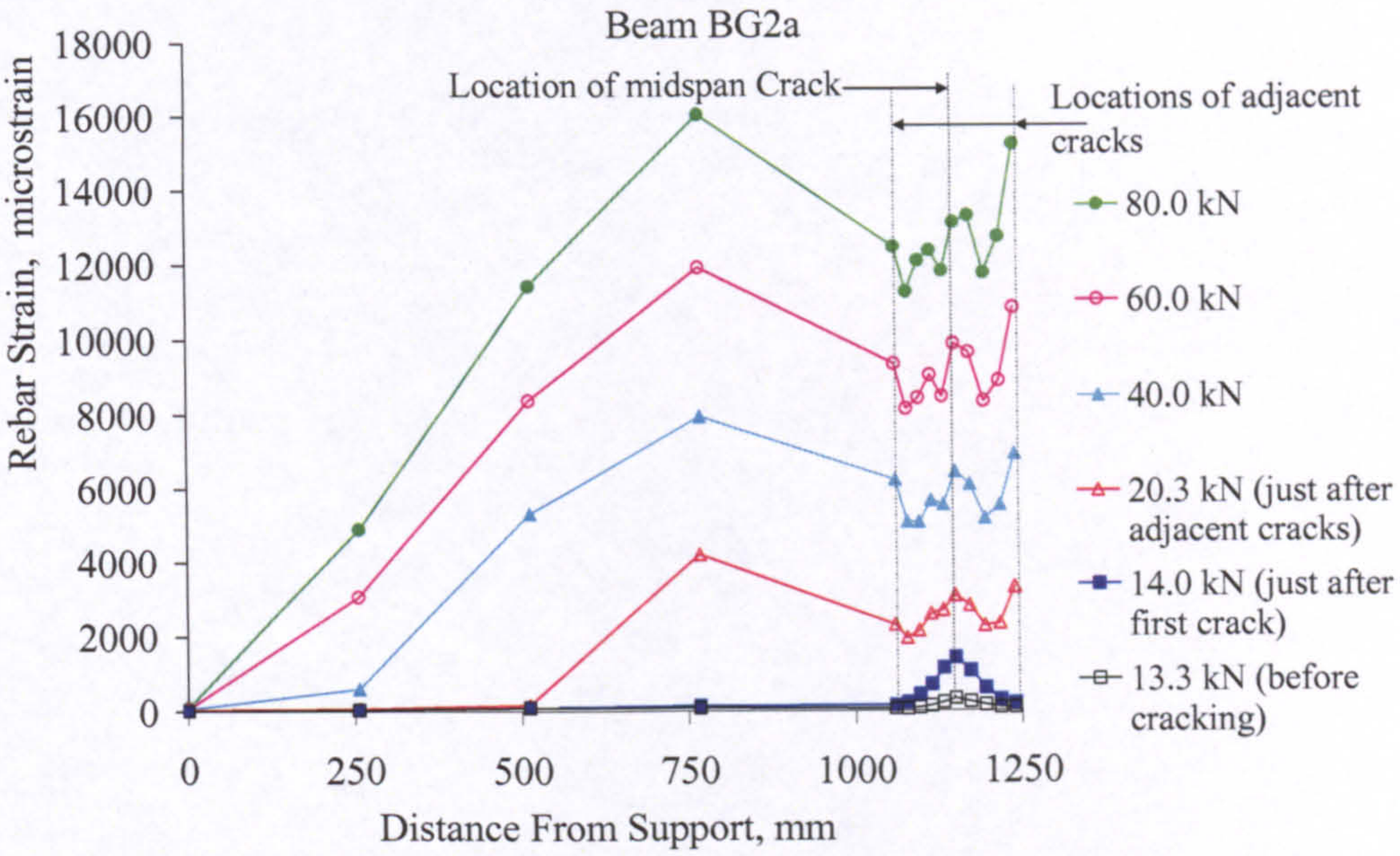

Figure 4-5: Typical experimental profile of strains along a rebar.

As explained, any noticeable increase in rebar strain is caused by the development of a nearby crack. Therefore, the strain profile in Figure 4-5 reflects the spread of cracking at the corresponding load level. However, closer strain measurements along the rebar would be required for refined strain profiles.

4.2.3. Strain in the Concrete

A typical experimental load-concrete strain relationship is shown in Figure 4-6. The concrete strain shown was measured at the top concrete fibre at midspan. Similar to the development of strains in the rebar, the concrete strain is negligible before cracking. With the formation of the first crack at midspan, the concrete strain increases noticeably. It then increases with load at a somewhat fast rate, while the midspan crack

widens and penetrates deeper into the section. Another noticeable increase in the concrete strain occurs with the formation of the two adjacent cracks. The concrete strain then follows a curved relationship with load up to failure.

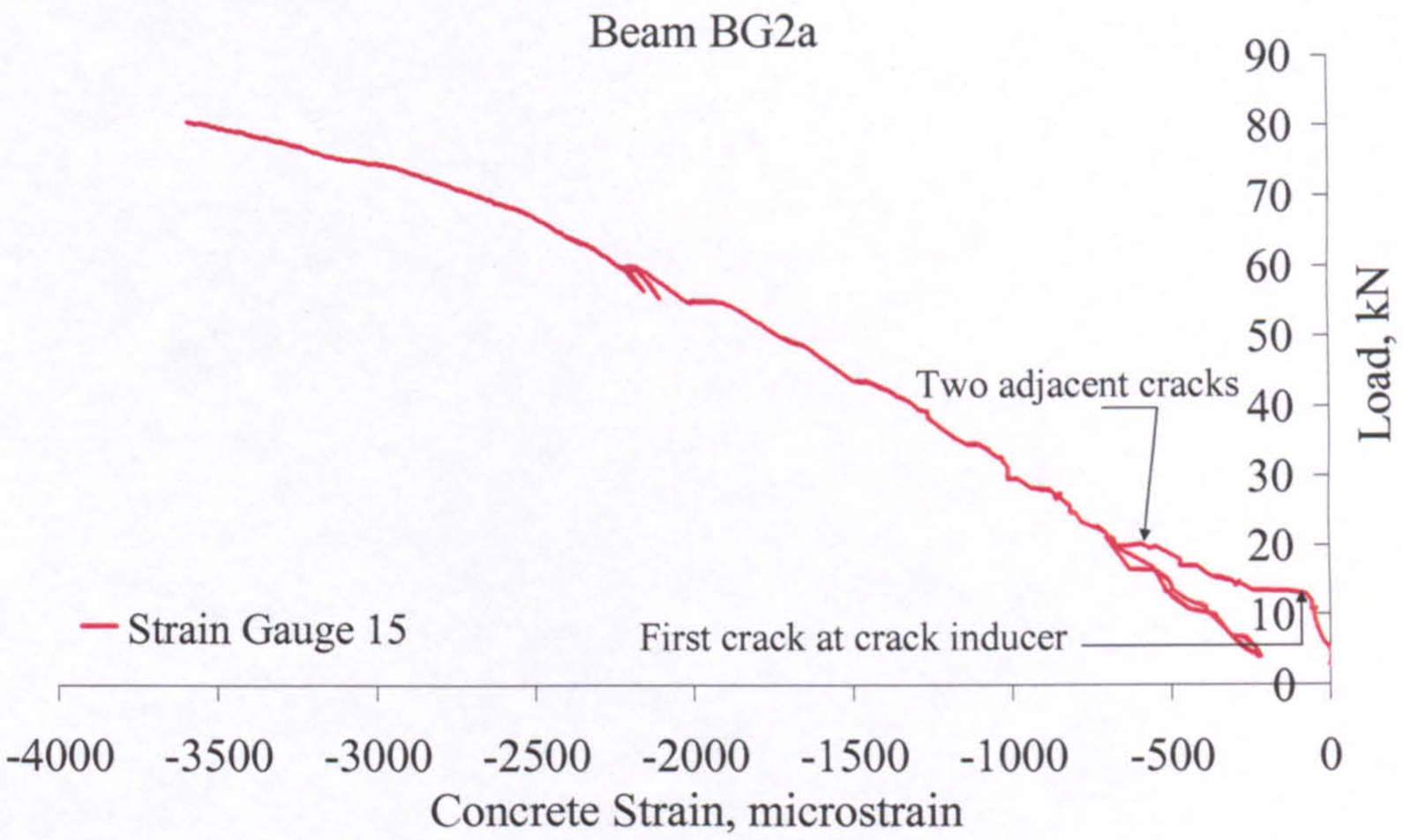

Figure 4-6: Typical experimental load vs. concrete strain relationship.

4.2.4. Deflection

A typical experimental load-deflection relationship is shown in Figure 4-7. The deflection shown was measured at midspan. Before any cracking occurs, the load-deflection relationship is linear, and the deflection is almost negligible as the member possesses a relatively high stiffness that is associated with the uncracked concrete section. A rapid reduction in the member stiffness occurs with the formation of the first crack at midspan. A subsequent considerable reduction in stiffness (in this particular case, almost a horizontal plateau in the load-deflection curve) is associated with the formation of several other flexural cracks within the constant flexure zone. Thereafter, the deflection follows an almost linear relationship with load up to failure, while the existing cracks widen and propagate, and additional cracks form within the shear span.

In general, beyond the first crack, the load-deflection curve can be idealized by an essentially bilinear relationship. The first linear segment has a lower stiffness than the second, and represents a phase of formation of cracks in and possibly slightly outside the constant flexure zone. This segment is expected to be horizontal if the tensile

properties of the concrete were homogeneous. The second linear segment continues up to failure, and represents a stabilized cracking phase for the already developed cracks, and new phases of crack formation and stabilized cracking within the shear span. Another simpler and adequate idealization is to use a linear load-deflection relationship from the point of first cracking up to failure.

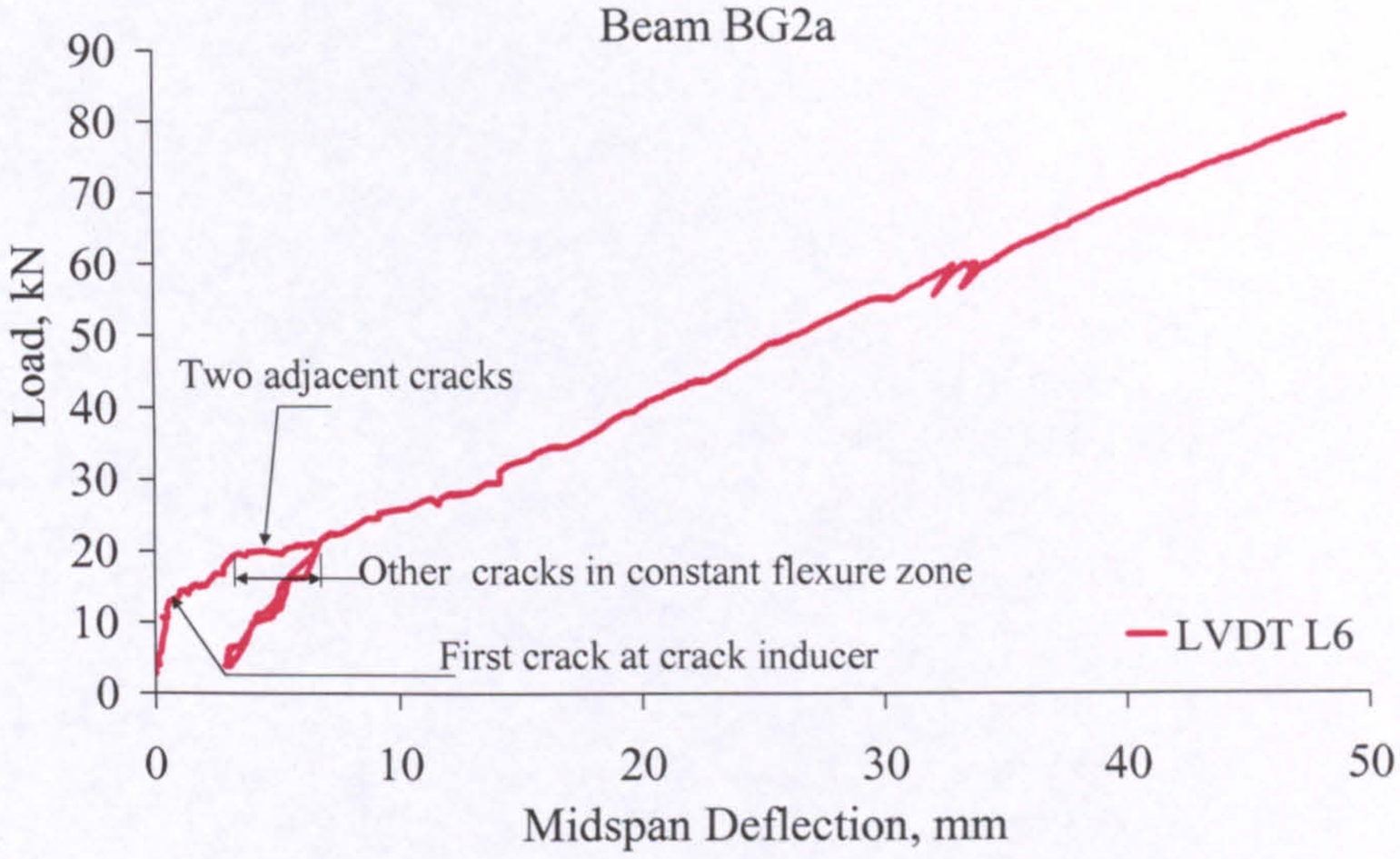

Figure 4-7: Typical experimental load vs. midspan deflection relationship.

The prediction of deflection in codes of practice always involves the cracking moment. In the tests carried out here, the formation of the first crack occurs at a reduced cracking load because of the crack inducer. However, the other cracks within the constant flexure zone develop at the usual cracking load, and are not affected by the crack inducer. In other words, the presence of the crack inducer only lowers the first crack point and has no other consequence on the load-deflection plot. Figure 4-8 shows that the first crack load without a crack inducer can be estimated from the load-deflection plot; at the intersection point of the extension of the uncracked and crack-formation segments. The figure also emphasizes the localized and transient effect of the crack inducer.

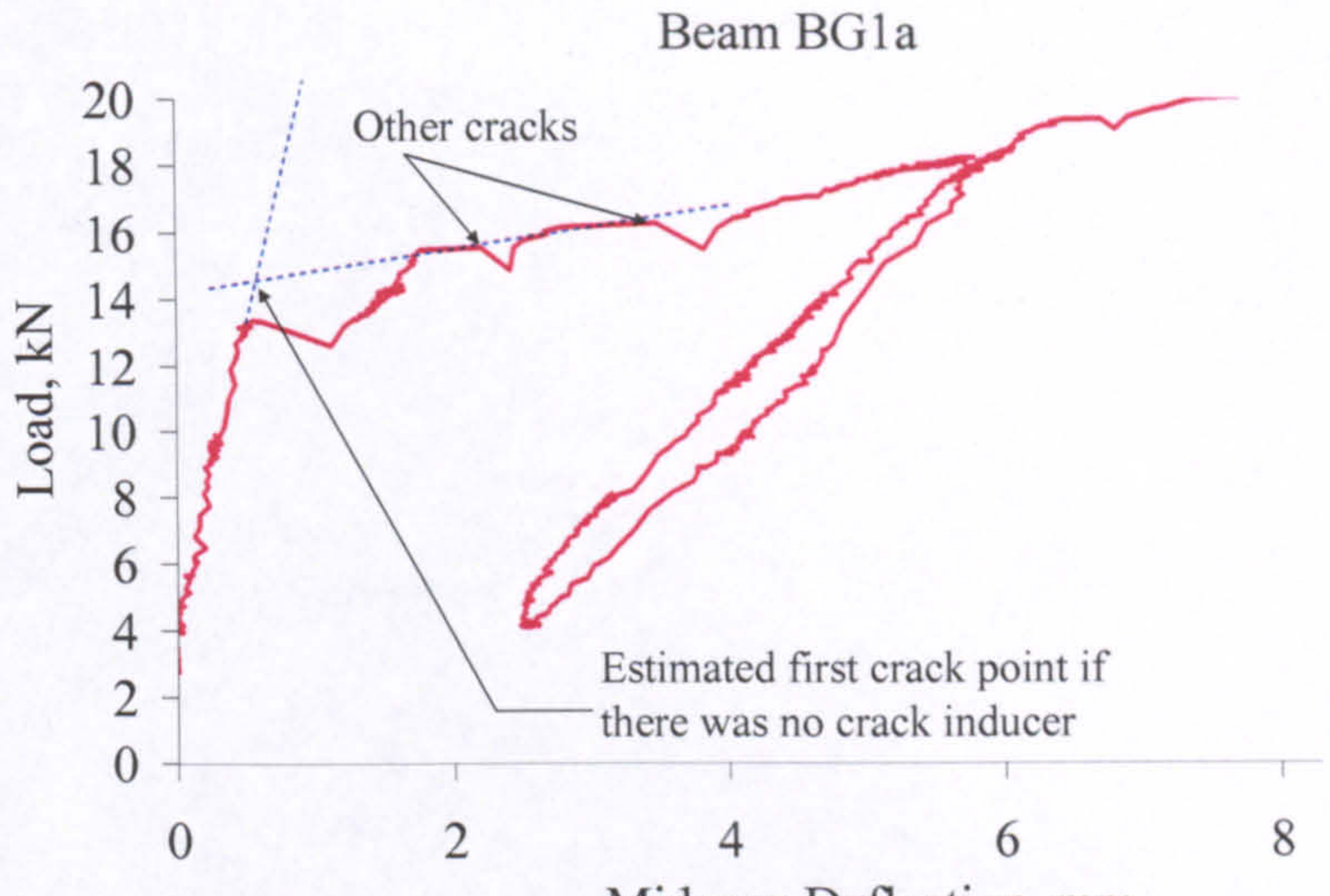

Figure 4-8: Effect of the crack inducer on the load-deflection plot.

The load-deflection behaviour of the GFRP and steel RC beams is compared in Figure 4-9. Contrary to steel RC, the GFRP RC beams exhibit brittle non-ductile behaviour, irrespective of the reinforcement ratio or the mode of failure. However, the ultimate deflections are comparable in both cases, which may compensate for ductility and serve to provide ample warning before failure. After cracking, the load-deflection curves are similar in shape to the constitutive law of the corresponding reinforcement, which reflects the fact that the reinforcement strains have more influence than those of the concrete on the overall behaviour. Within the range where the steel reinforcement is not yielding, the deflection of the GFRP RC beams are much higher than those of the steel RC beams. Deflection reduces with increasing reinforcement ratio, but very high GFRP reinforcement ratios are required to make the deflection within that range comparable to steel RC, which emphasizes that the design of FRP RC can be controlled by the serviceability limit state. Figure 4-9 also shows almost identical deflections and failure loads of the replicate beams within each series, which indicates appropriate quality control in the construction of the test elements. A small deviation is noticed in the deflections of the steel RC beams, but this is due to the fact that one of those beams was accidentally loaded and pre-cracked before the actual test. The load-midspan deflection plots of the GFRP RC slabs and the CFRP RC beams and slabs compare similarly, and are shown in Appendix B.

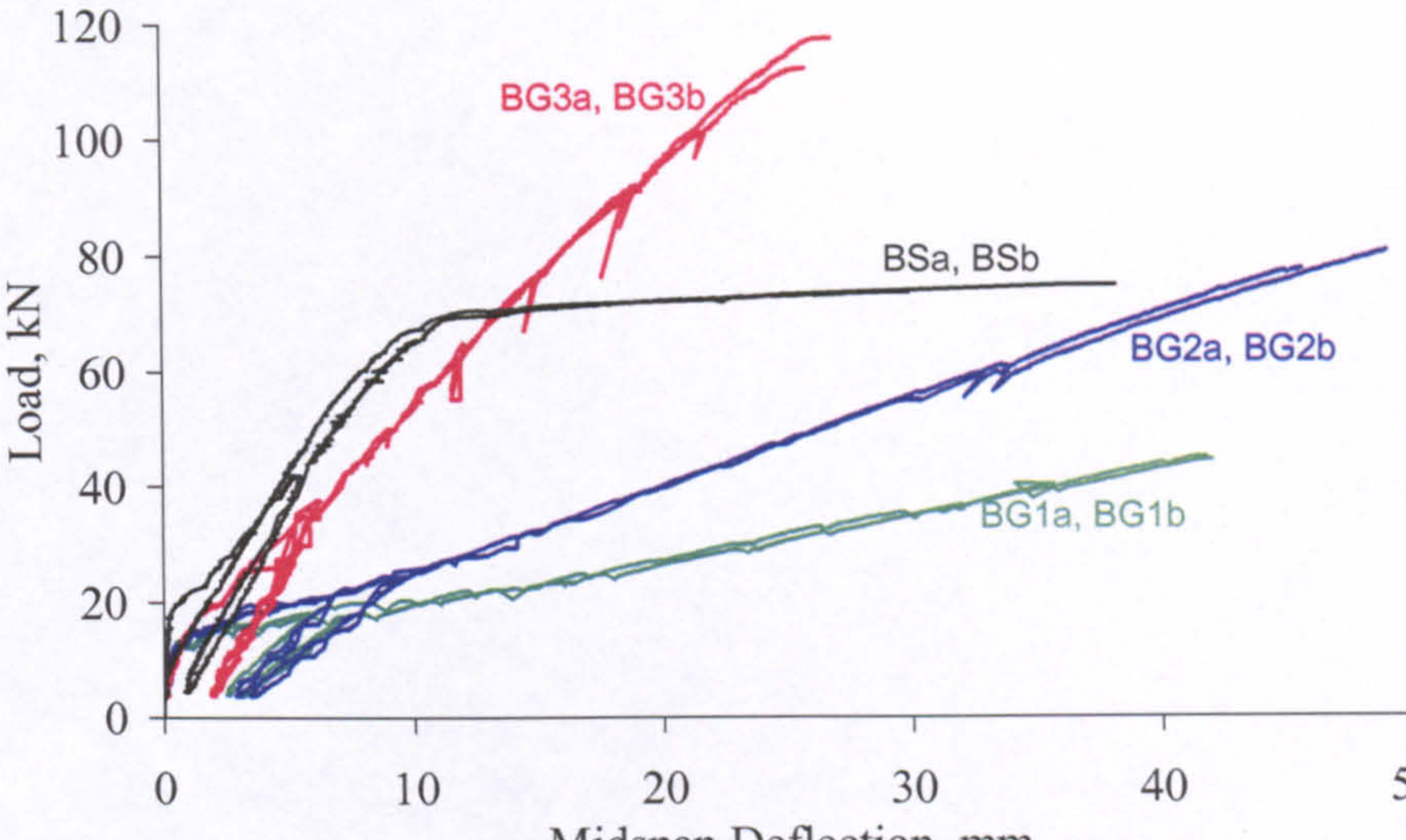

Figure 4-9: Load vs. midspan deflection for the GFRP and steel RC beams.

4.2.5. Crack Width

A typical load-crack width relationship is shown in Figure 4-10. The crack width shown was measured by an LVDT, at the crack inducer at midspan, at the level of the steel reinforcement, over a gauge length of 100 mm. The LVDT measurement has actually two components: the crack width and the elongation in the concrete at the surface. However, the elongation in the concrete is negligible. For instance, at a concrete strain of 125 με, which approximately corresponds to the concrete tensile strength, the elongation would be only 0.0125 mm. The load-crack width behaviour is somewhat similar to that of the load-rebar strain, as explained earlier. The first crack forms at midspan with a considerable width, which reduces with an increase in the reinforcement ratio and/or modulus of elasticity. The crack width increases at a fast rate while the crack penetrates deeper. The two contiguous cracks then form, but their effect on the width of the midspan crack is minimal. Thereafter, the crack width increases almost linearly with load until failure. Figure 4-10 shows also distinct widths of the midspan crack at different load levels, which were measured by an optical instrument at the bottom concrete fibre. The crack widths measured by the two methods compare reasonably, with those measured at the bottom concrete fibre being slightly wider.

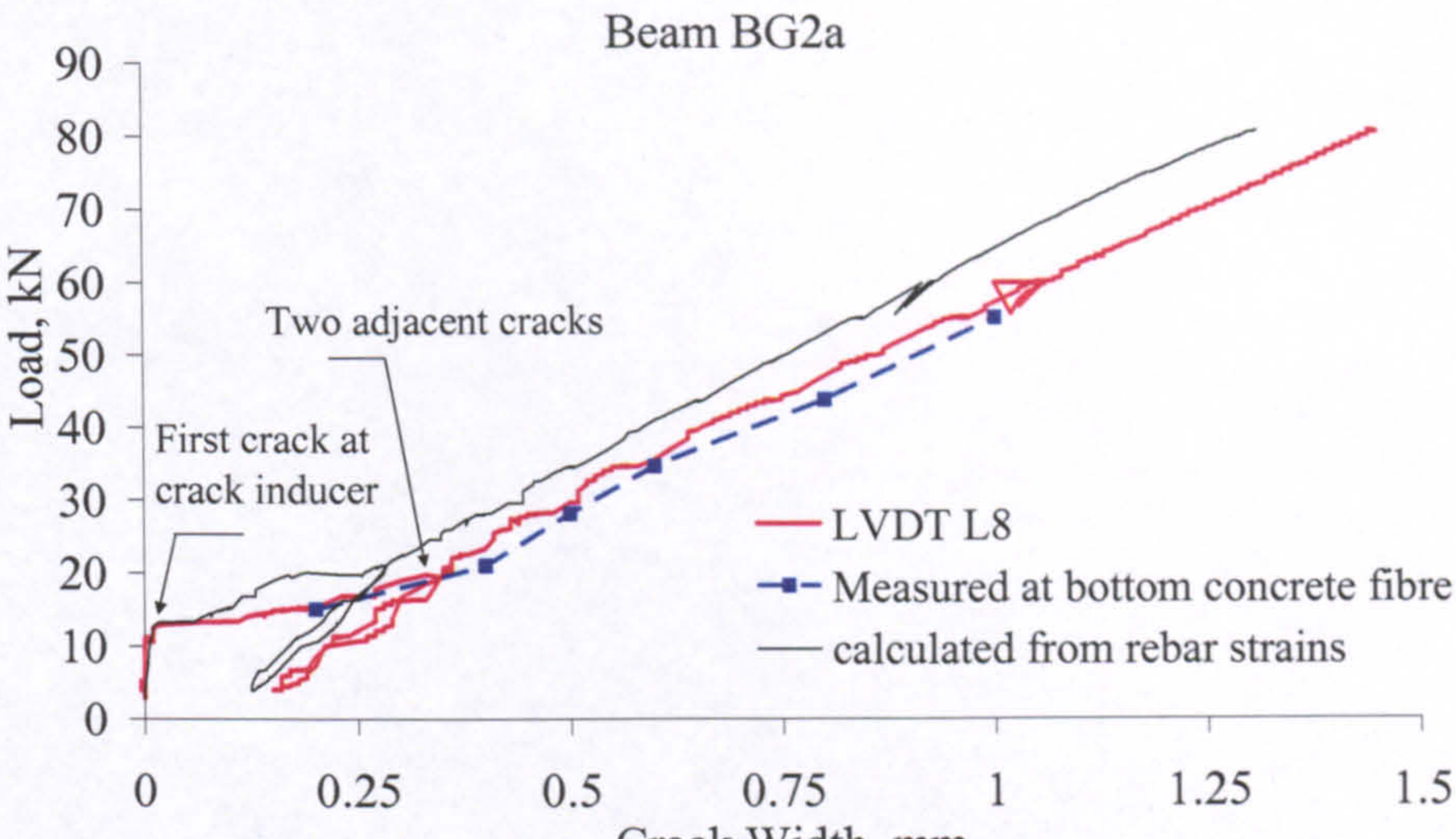

Figure 4-10: Typical load vs. midspan crack width relationship.

Following the general approach of CEB (1993), but neglecting the strain in the concrete and shrinkage strain, the midspan crack width can be estimated by multiplying the average of the distances between the midspan crack and the two adjacent cracks, which were measured in the tests, by the average of the rebar strains between the cracks. The average rebar strain is calculated by numerical integration of the experimental rebar strains between the cracks. The estimated midspan crack width compares well with the measured values, as typically shown in Figure 4-10. The difference can be attributed to the fact that the no-slip points do not have to be precisely midway between cracks since the bond and slip conditions are not necessarily ideal or symmetrical around the cracks. The estimated midspan crack width is shown together with the load-midspan crack width plot for all the tests in Appendix B.

Figure 4-11 shows a comparison of the midspan crack width of the GFRP and steel RC beams. The comments made on the deflection behaviour are equally applicable to the crack width behaviour. Hence, the GFRP RC beams exhibit brittle non-ductile behaviour commensurate with the constitutive law of the GFRP reinforcement. The ultimate crack width of GFRP and steel RC can be comparable. Within the range where the reinforcement is not yielding, very high GFRP reinforcement ratios are required to make the crack width comparable to steel RC, which emphasizes again that the design of FRP RC can be controlled by the serviceability limit state. Figure 4-11 also reflects good repeatability of the crack width behaviour in the replicate beams. The load versus

midspan crack width plots of the CFRP RC beams compare similarly, and are shown in Appendix B.

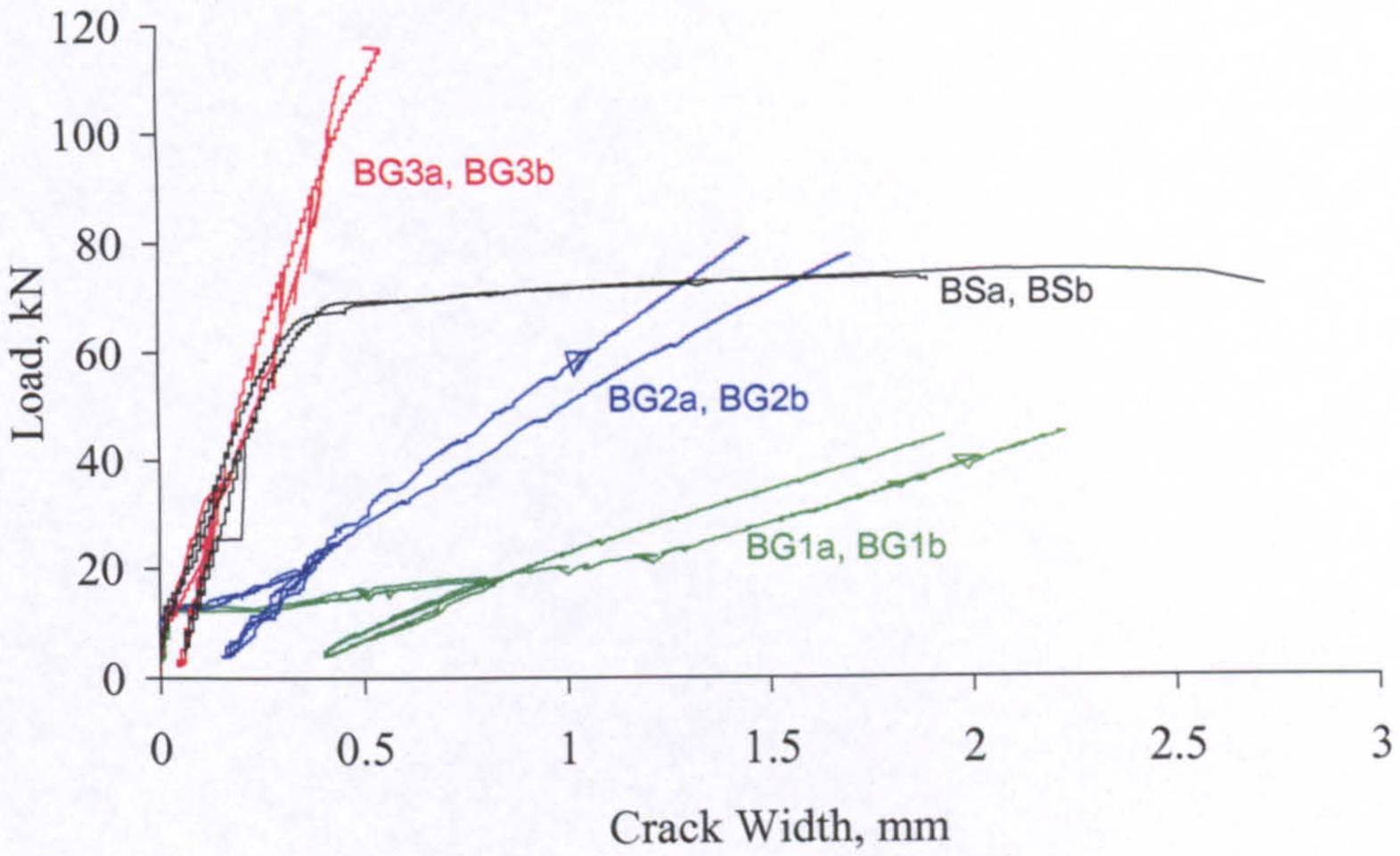

Figure 4-11: Load vs. midspan crack width for the GFRP and steel beams.

In addition to the crack width at midspan, the widths of other cracks within the constant flexure zone were measured at discrete load levels at the bottom concrete fibre. Moreover, the crack patterns and spacing were documented along the whole length of the elements. Figure 4-12 shows typical crack patterns and their development with increasing load for an FRP beam. The figure also shows simple statistical analysis of the crack width data in the constant flexure zone. At the early stages of loading, vertical flexural cracks develop in, and sometimes a little outside, the constant flexure zone, penetrating high into the section. In general, these cracks form over a limited range of load, which reflects the homogeneity of the concrete tensile strength within the constant flexure zone; the narrower the load range is, the better the homogeneity. With increasing load, these cracks become progressively wider, while they penetrate deeper. However, the rate of penetration reduces continuously, until it becomes hardly noticeable. The cracks in the shear spans develop after the flexural cracks. These cracks start out vertically in the vicinity of the two loading blocks, but then start to incline towards these blocks due to the effect of shear forces. With increasing load, these cracks spread towards the end supports, while increasing in width and penetrating deeper in the section. Failure occurs within the constant flexure zone, as explained

earlier. The statistical analysis of crack widths in the flexure zone shows relatively high standard deviation values, which emphasizes the high variability of cracking behaviour.

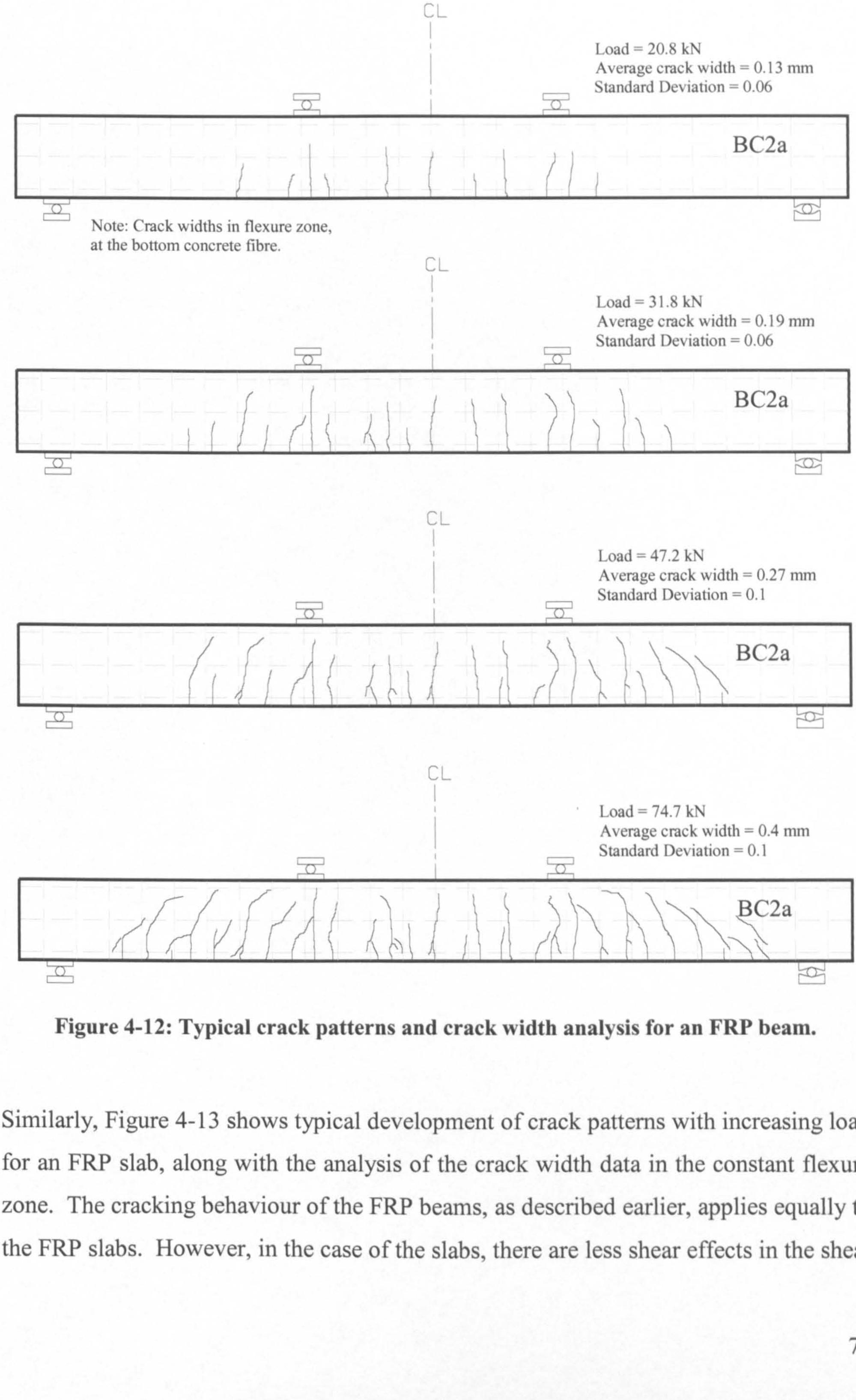

Figure 4-12: Typical crack patterns and crack width analysis for an FRP beam.

Similarly, Figure 4-13 shows typical development of crack patterns with increasing load for an FRP slab, along with the analysis of the crack width data in the constant flexure zone. The cracking behaviour of the FRP beams, as described earlier, applies equally to the FRP slabs. However, in the case of the slabs, there are less shear effects in the shear

span, which is due to their significantly higher shear span to depth ratio. Furthermore, a wider scatter of the crack widths in the constant flexure zone is observed. This may be expected because the slabs can have higher concrete variability along their width than the relatively narrow beams. The variability in the concrete affects the transverse path of the cracks as well as their spacing, which therefore affects the crack widths.

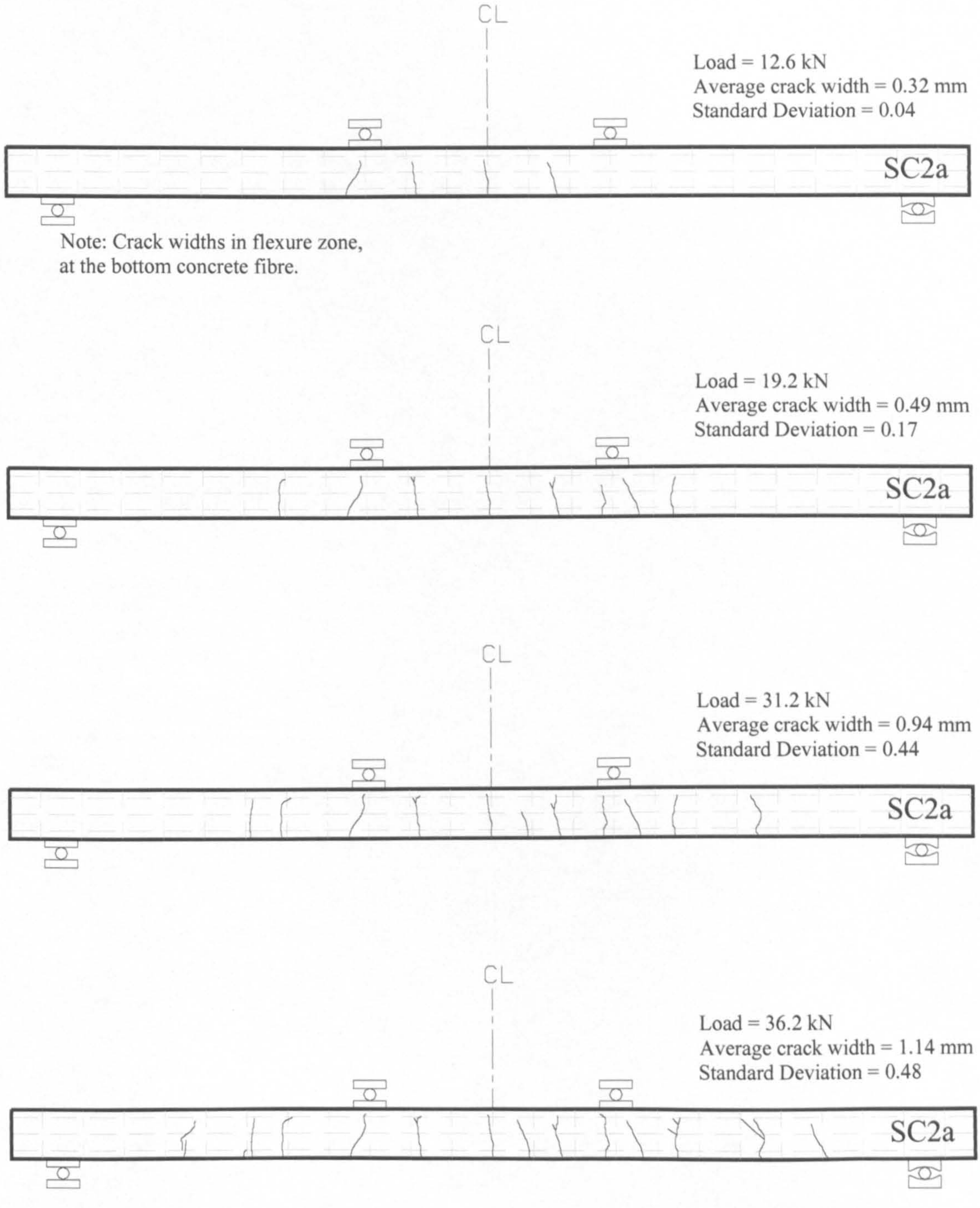

Figure 4-13: Typical crack patterns and crack width analysis for an FRP slab.

4.2.6. Crack Spacing

The average spacing of the cracks in the constant flexure zone is shown in Figure 4-14, for all the elements. In all the cases, cracks did form beneath or very close to the two loading blocks. Therefore, the spacing is averaged by dividing the length of the constant flexure zone by the number of cracks in that zone less one. Obviously, the crack spacing for the FRP RC and steel RC elements are of the same order of magnitude. The repeatability of the crack spacing appears to be an issue. However, in theory, the cracks can be spaced anywhere from one to two times the transmission length, which reduces the chances for the average crack spacing to be repeatable.

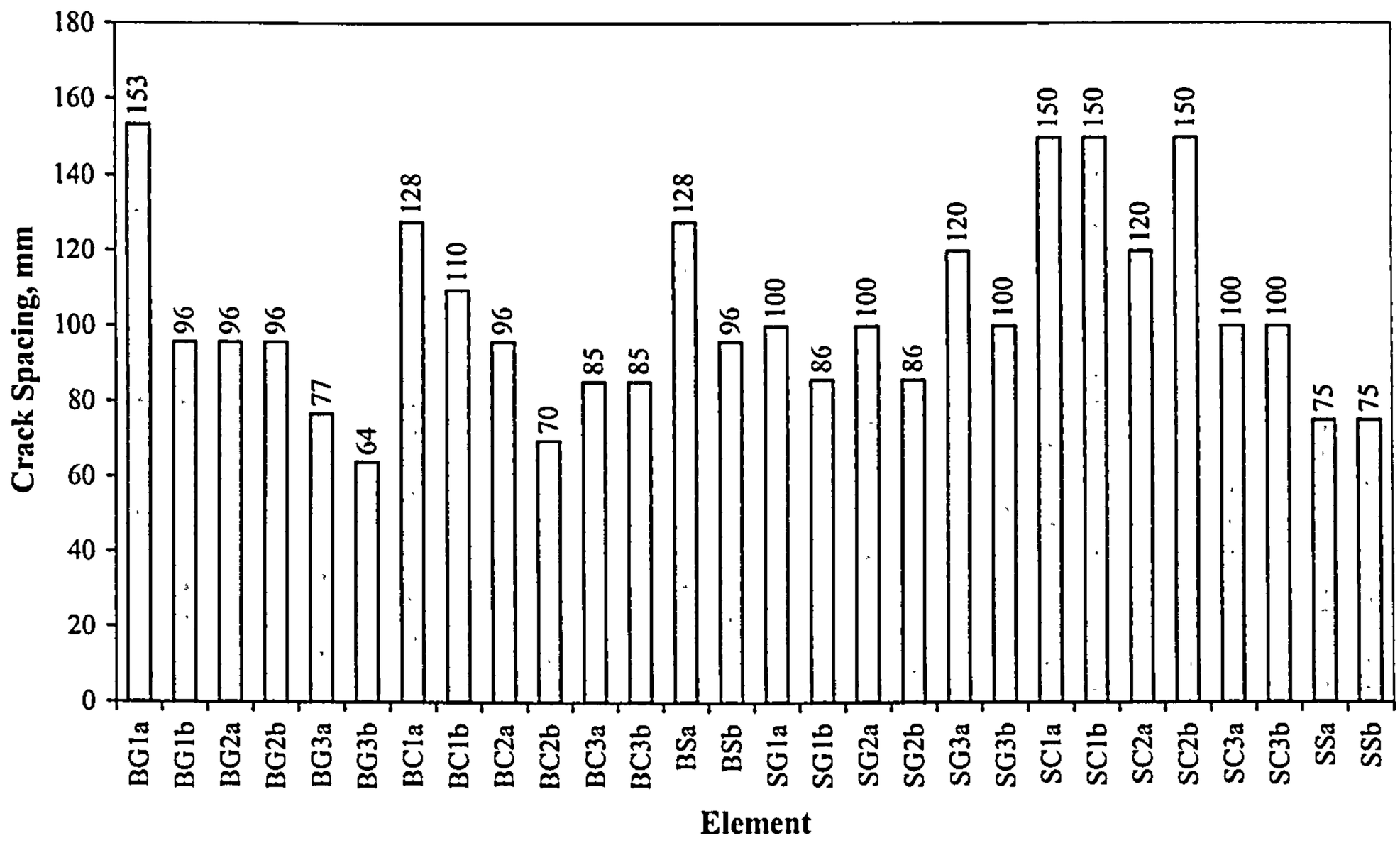

Figure 4-14: Average spacing of the cracks in the constant flexure zone.

4.3. DATA ANALYSIS

The focus of this research is on the deflection behaviour. Therefore, the rebar strain data around the crack inducer are analyzed and used to investigate other structural aspects that are related to the deflection behaviour. Tension stiffening is examined by correlating the average strain between the cracks to the strain at the crack. The bond between the cracks is also investigated. Bond profiles are constructed from the average bond between the strain gauges. Moreover, the average bond and average strain

between the cracks are correlated. The rebar strain data are further utilized, in conjunction with the concrete strain, to experimentally derive the load-curvature relationship between the flexural cracks, which is then used to predict and filter out the flexural component of the deflection. The average depth to the neutral axis is also evaluated. The results of all the data analyses for every beam and slab test are shown with the data measured directly during the tests in Appendix B.

4.3.1. Tension Stiffening

Tension stiffening is usually investigated in pure tension tests of RC tie elements. In such tests, the rebar stress or strain at the crack is calculated from the measured tensile load, and the average strain in the rebar is calculated from the total elongation of the element, which typically involves several cracks. In this section, tension stiffening is evaluated from the experimental rebar strain profiles between the midspan crack and the two contiguous cracks. The strain at the crack is obtained directly from the strain profile, while the average rebar strain between the cracks is evaluated by numerical integration. This experimental approach has the advantage that tension stiffening is evaluated in the structural test itself, and not in a different test setup. Nevertheless, it can involve several drawbacks. The strain at the crack may be underestimated because the strain is measured over a gauge length that is larger than the width of the crack, and the precise path of the crack is not definite at the location of the reinforcement. Moreover, concrete does not allow for any symmetry. Hence, the cracks and their location, and the strain and slip in the reinforcement may not be symmetric around the crack at midspan. At the same time, the strain gauges could not be placed more frequently within the measurement zone in order to minimize the disruption to bond. Moreover, only three cracks are involved, which is the minimum possible to have measurements on both sides of a crack. Therefore, some judgement is necessary in the utilization and interpretation of the experimental data.

Figure 4-15 compares a typical rebar strain at a crack to the average strain between cracks for a GFRP RC element. Similar to a pure tension RC tie, at a crack, all the tensile force is carried by the reinforcement, whereas between cracks, some of the tensile force is transferred to the surrounding concrete through bond. This results in a

reduction of the reinforcement stresses and strains. Hence, between cracks, the concrete stiffens the reinforcement, and causes the reinforcement to have an average strain that is less than the strain at a crack.

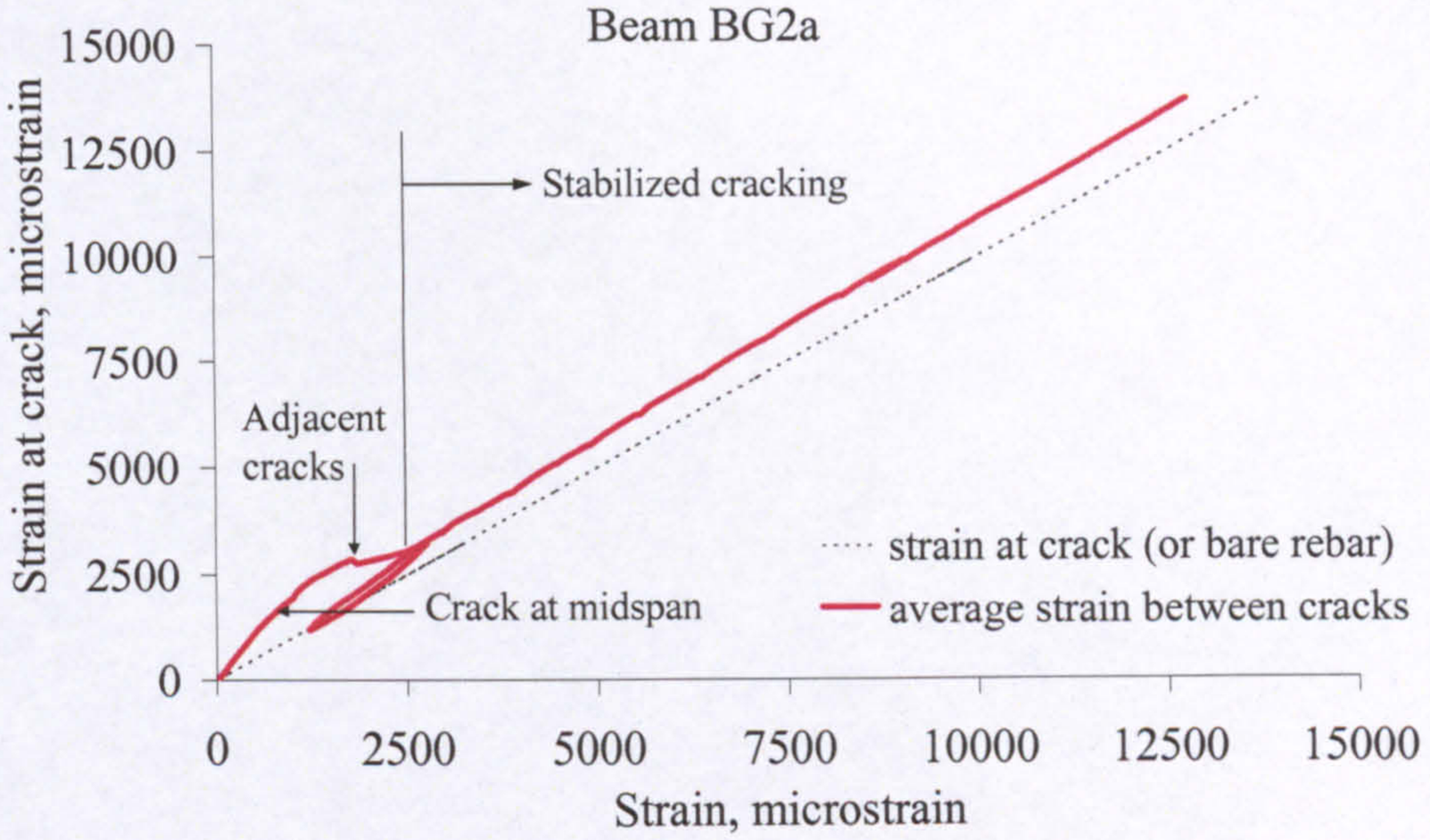

Figure 4-15: Typical GFRP RC crack strain vs. average strain relationship.

In a flexural member, a tension tie develops progressively with cracking. A more or less proper tie is formed only shortly after the end of the crack formation phase. Hence, in Figure 4-15, in the pre-cracking and crack formation phases, the relationship between the crack strain and average strain does not have any resemblance with that of a tension tie. It is merely a curve that shows reduction of stiffness with the formation of cracks. However, the end of the curve clearly identifies the beginning of an essentially linear relationship throughout the stabilized cracking phase. As in the case of rebar strains, the stabilized cracking line is noticed to deviate away from the line representing the crack strain or bare rebar response, which again indicates that the average bond continues to build up in that phase.

The crack strain versus average strain relationship for the CFRP RC and steel RC members is similar to that of the GFRP RC members, as typically shown in Figures 4-16 and 4-17, respectively. The steel RC plot is only shown up to the point where the reinforcement yields at the crack.

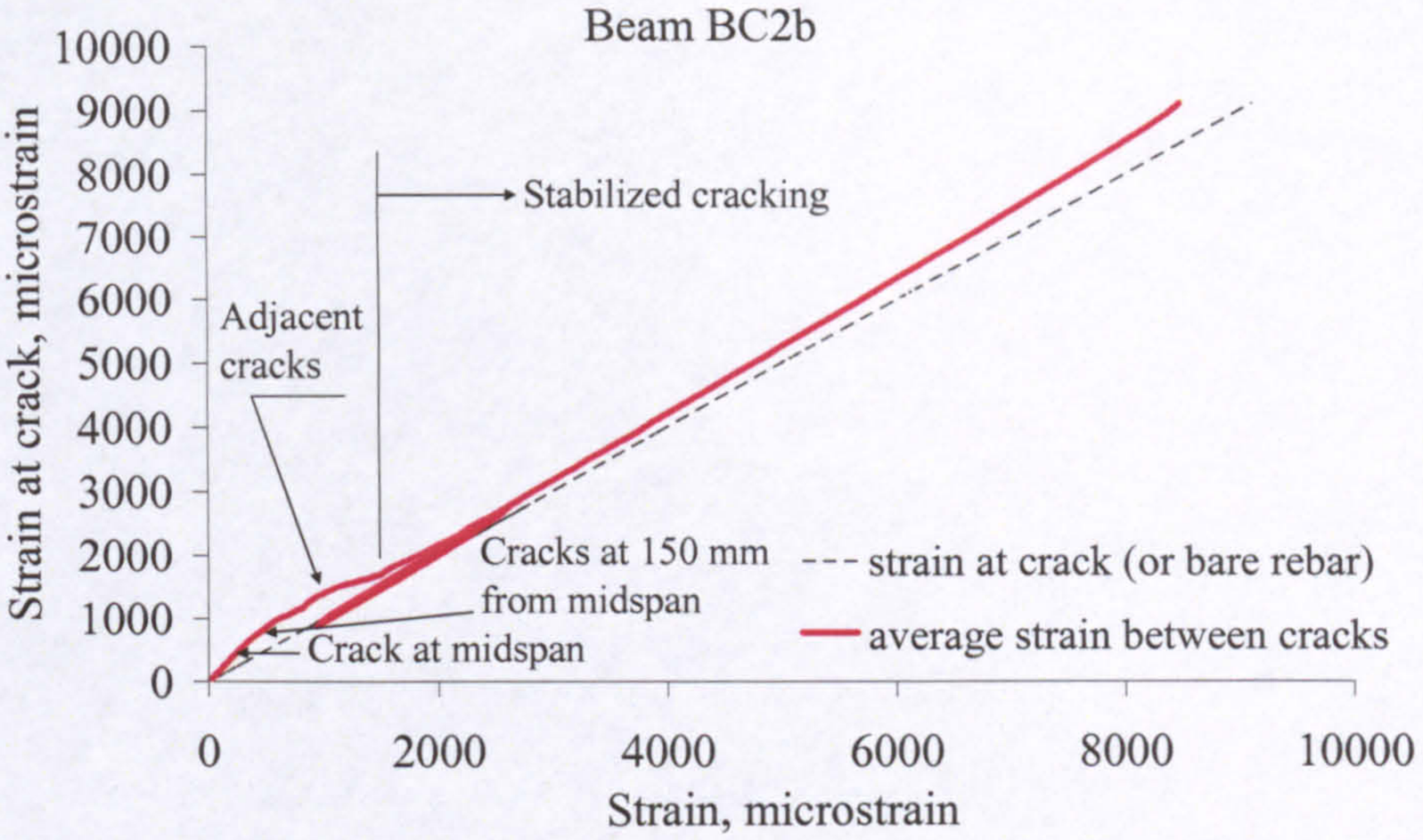

Figure 4-16: Typical CFRP RC crack strain vs. average strain relationship.

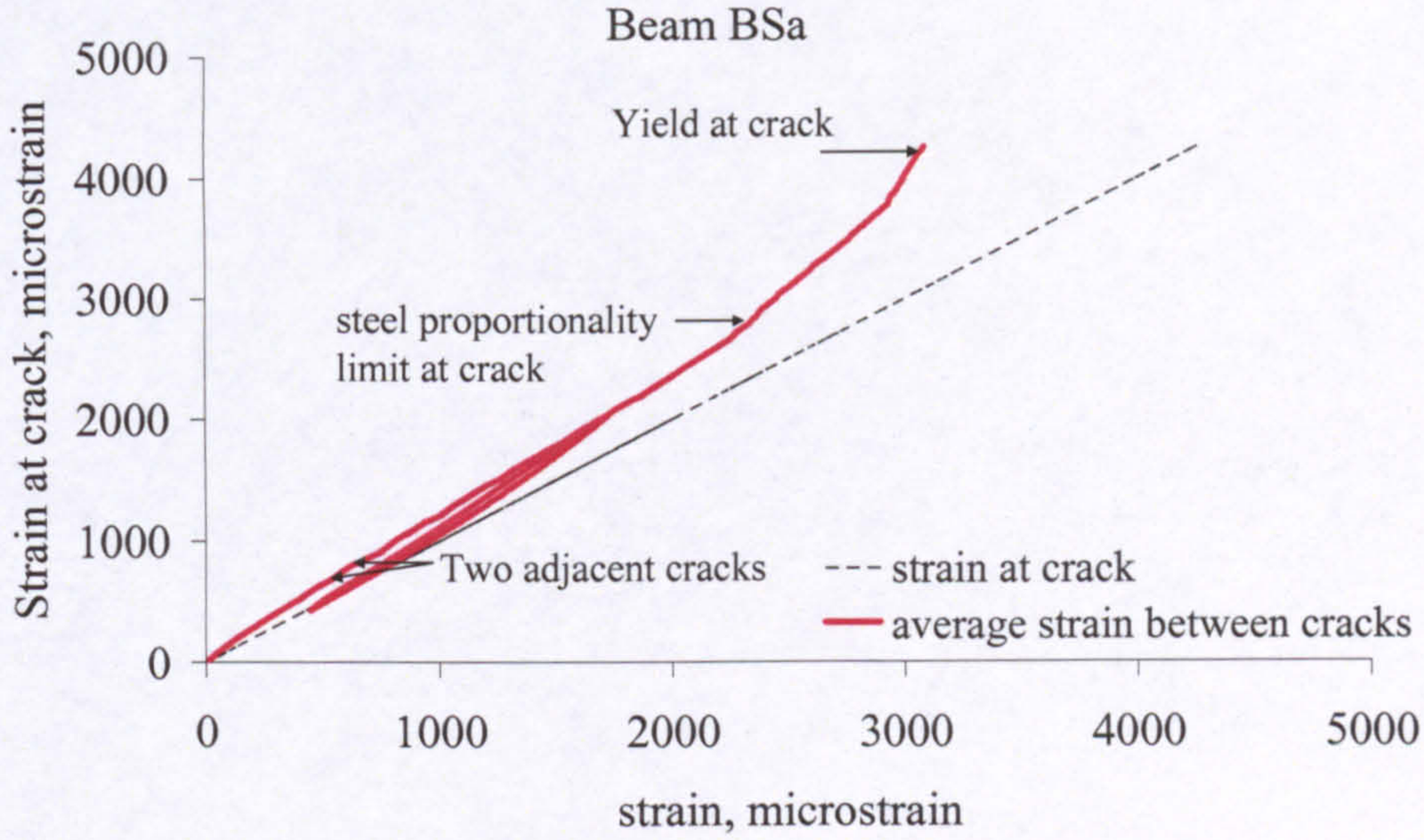

Figure 4-17: Steel RC crack strain vs. average strain relationship.

The increase in the difference between the crack and average strains may indicate that tension stiffening is increasing. However, tension stiffening is better visualised as an increased effective modulus of elasticity of the reinforcement. An effective reinforcement modulus (E_{eff}) can be defined as the ratio of the stress at a crack (σ_{cr}) to the average strain between cracks (ε_{ave}), while the actual modulus (E) is the ratio of stress to strain (ε_{cr}) at the crack. Therefore, the following equation can be written.

$$\frac{E_{eff}}{E} = \frac{\varepsilon_{cr}}{\varepsilon_{ave}} \qquad (4\text{-}1)$$

The ratio of effective to actual reinforcement modulus (E_{eff}/E) provides a rational measure of tension stiffening after cracks have formed. For the GFRP, CFRP and steel RC elements, E_{eff}/E reduces tending to a value of 1.0 as the average strain increases in the stabilized cracking phase, as shown in Figures 4-18 to 4-20, which means that tension stiffening is effectively reducing. For steel RC, the increase in the value of E_{eff}/E after an average strain of 2360 microstrain may be attributed to a reduction in the modulus of elasticity past the steel proportionality limit.

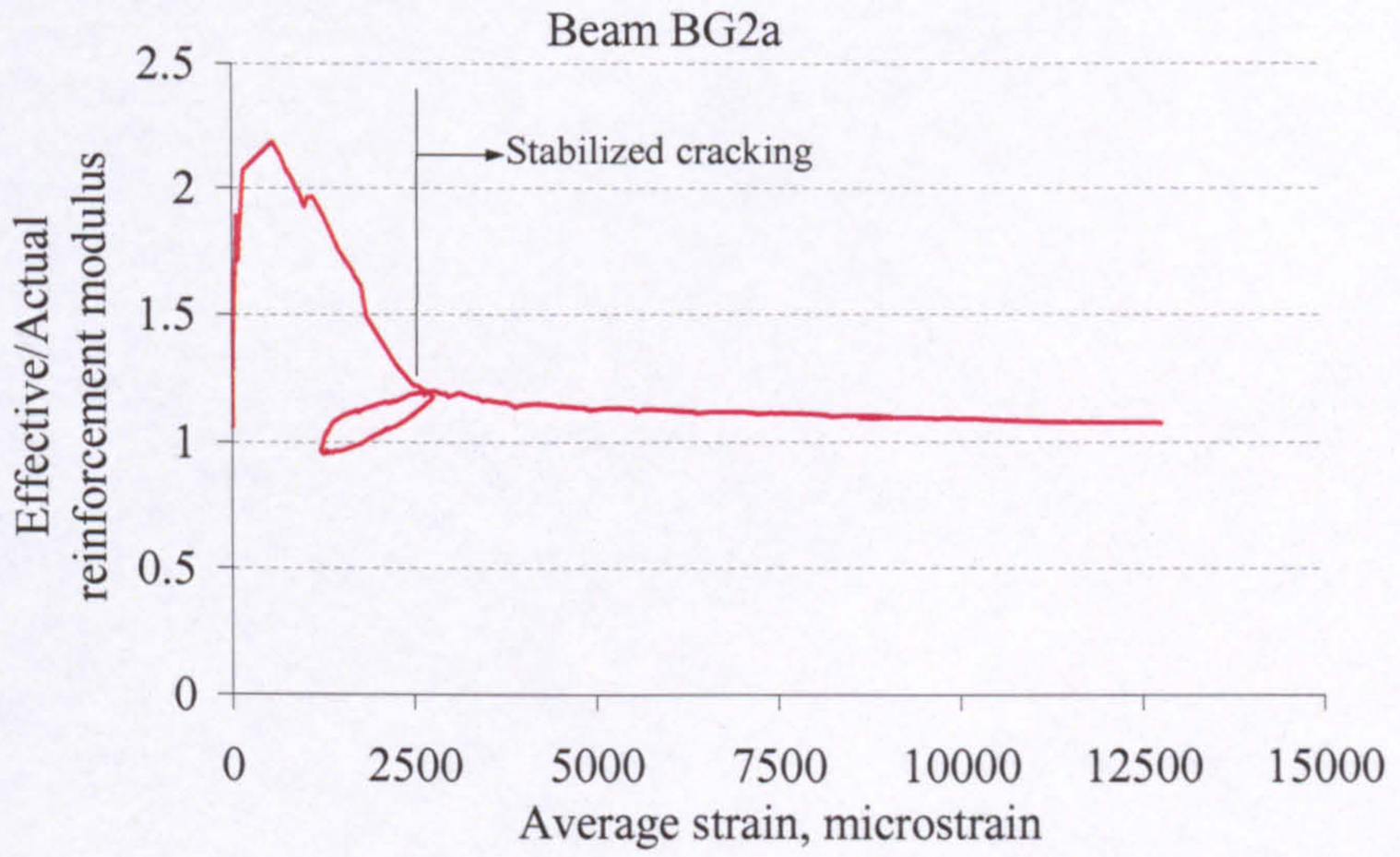

Figure 4-18: Typical GFRP RC effective/actual reinforcement modulus vs. average strain.

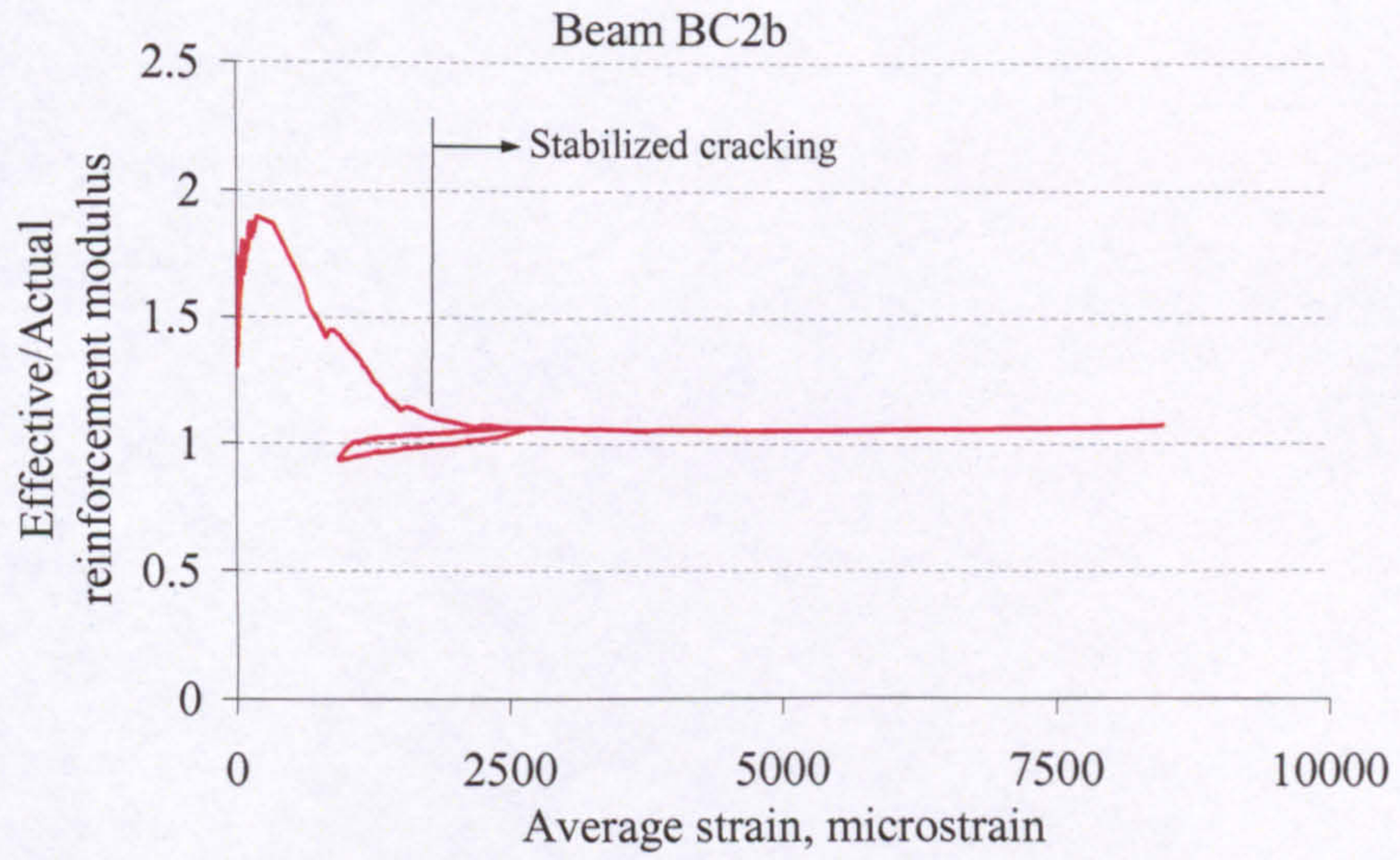

Figure 4-19: Typical CFRP RC effective/actual reinforcement modulus vs. average strain.

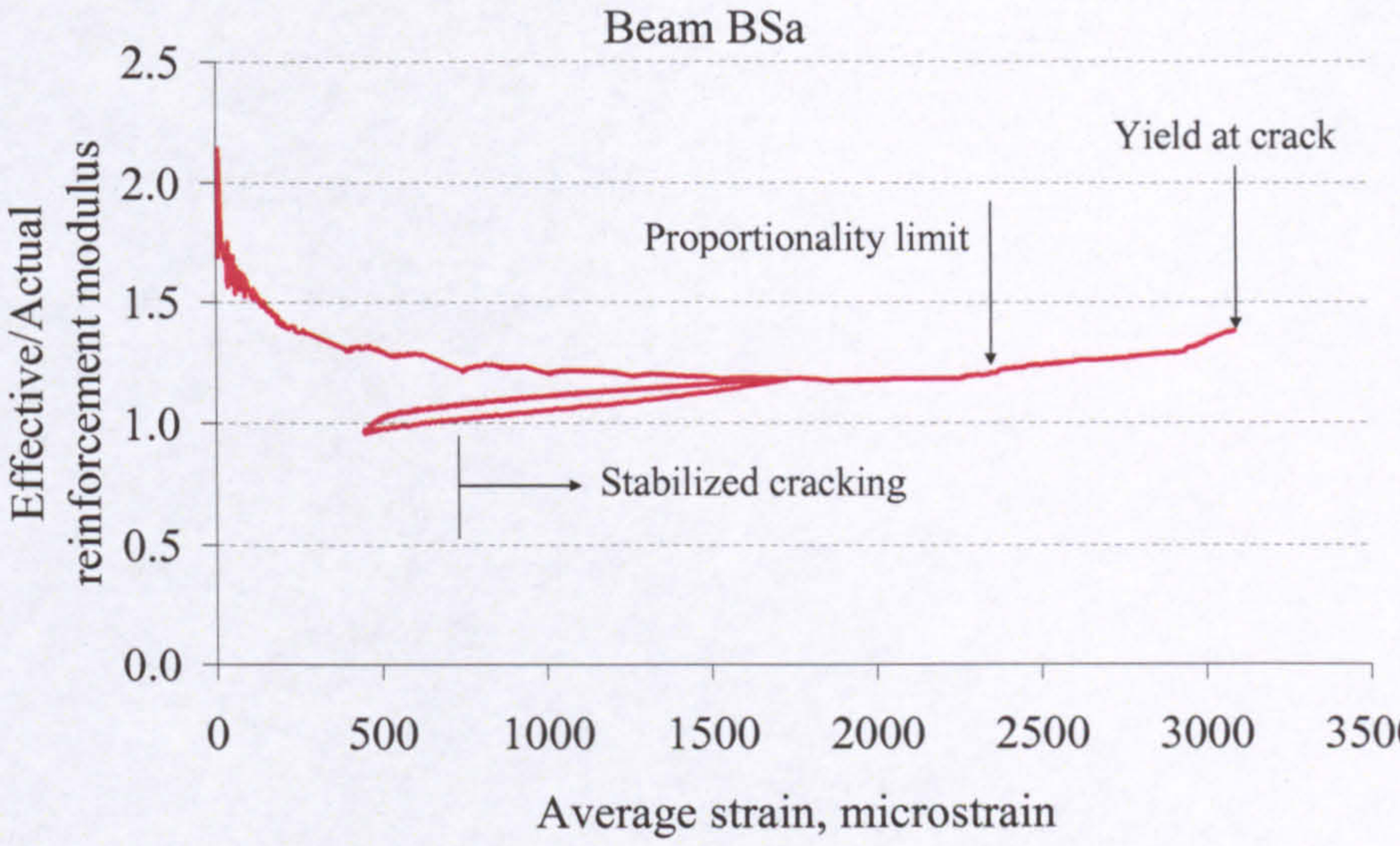

Figure 4-20: Steel RC effective/actual reinforcement modulus vs. average strain.

4.3.2. Bond

The closely spaced rebar strain data between the midspan and the two adjacent cracks enable some investigation of the bond development and bond profiles between these cracks. Considering the equilibrium of a rebar segment as shown in Figure 4-21, the average bond stress (τ) on the surface of the rebar can be expressed as follows.

$$\tau = \frac{E\phi(\varepsilon_2 - \varepsilon_1)}{4\Delta_L} \qquad (4\text{-}2)$$

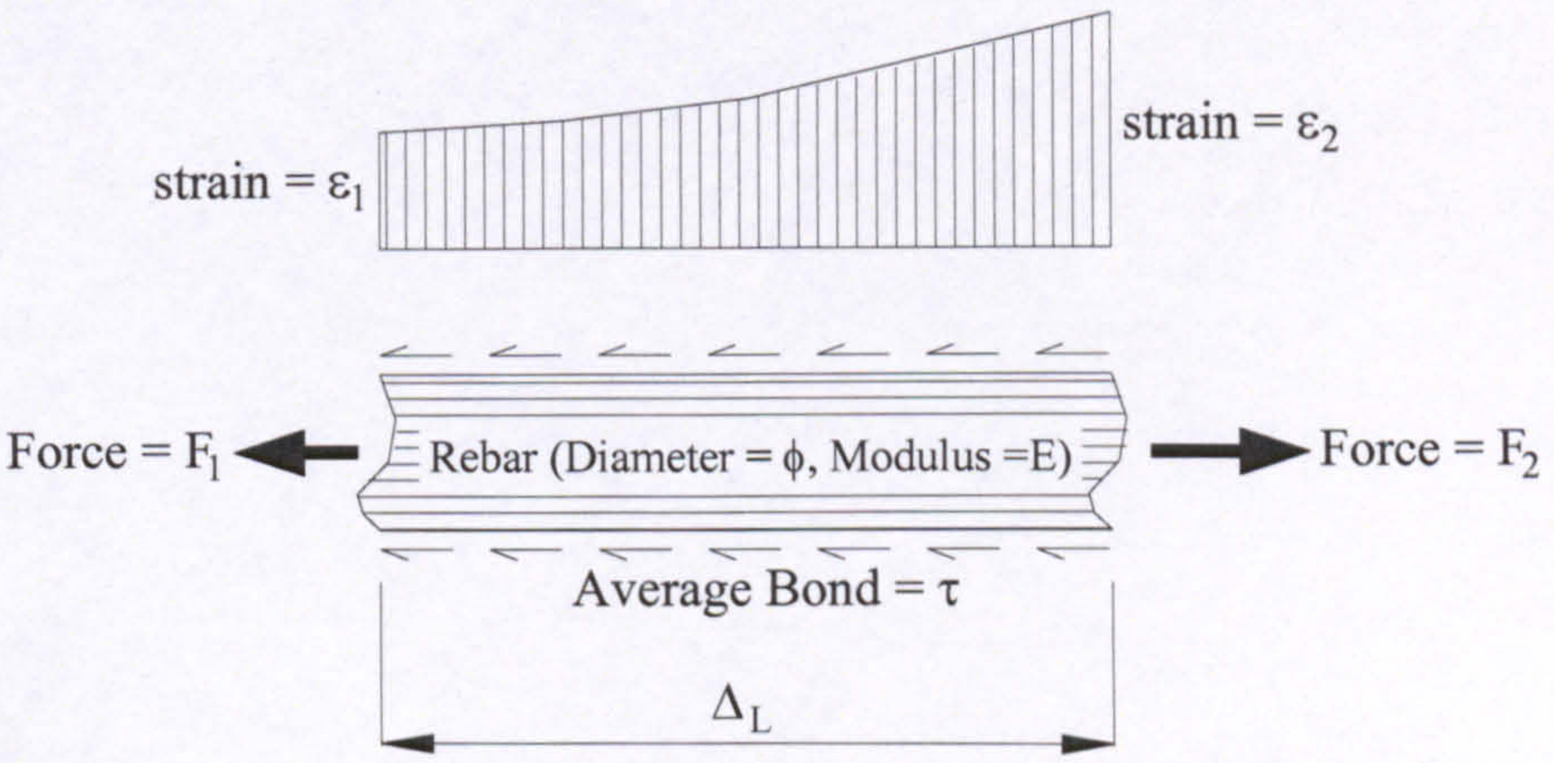

Figure 4-21: Equilibrium of a segment of rebar.

Figure 4-22 shows bond profiles between the midspan and adjacent cracks at discrete load levels for a GFRP RC element. At a load of 10 kN, before any cracking, the bond stresses around the crack inducer at midspan are negligible and fairly symmetric. At a load of 13 kN, the first crack formed exactly at the location of the crack inducer at midspan. The bond stresses increase on either side of the crack until they reach a maximum value at about 30 mm from the crack, but then reduce with increasing distance. At a load of 20 kN, the adjacent cracks are in the process of developing. Also, an intermediate crack is developing about 30mm to the left of the midspan crack. At a load of 22 kN, the adjacent cracks have formed. At a load of 34 kN, the intermediate crack has formed about 32 mm to the left of the midspan crack, but in the tests this crack was not visible on the surface. At loads of 55 kN and higher, the bond profile maintains the same shape, and the maximum bond stresses at the various locations increase with load. Exceptional to this is the maximum bond stress to the left of the intermediate crack which, at a load of 80 kN, shifts its location further left by about 20mm. Figure 4-22 shows that the no-slip point between the cracks can shift its location as well. The maximum average bond stress is around 15 MPa, within a short distance less than 22.5 mm from the crack.

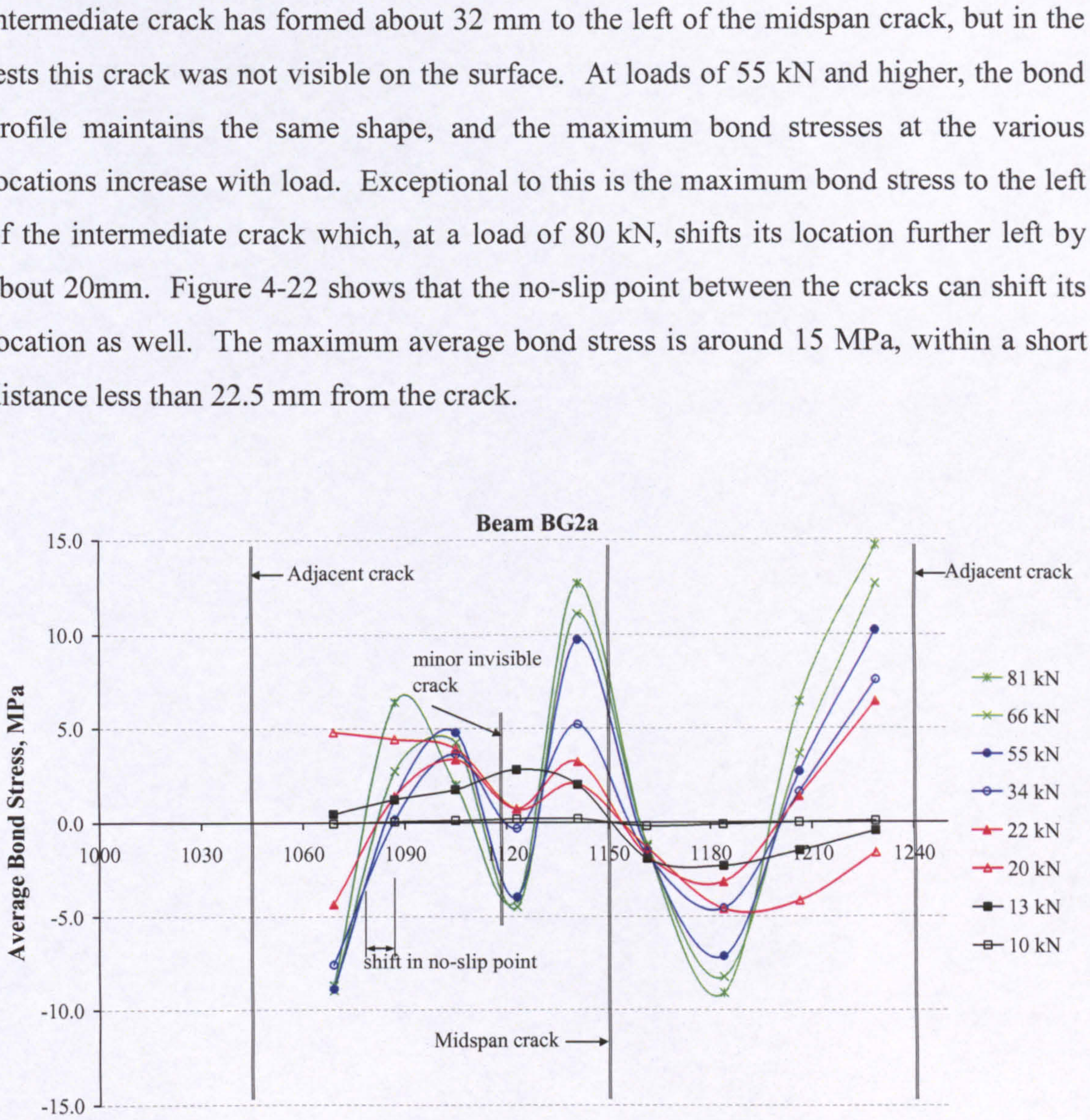

Figure 4-22: GFRP RC bond profiles between midspan and adjacent cracks.

Similarly, Figure 4-23 shows bond profiles between the midspan and adjacent cracks at discrete load levels for a CFRP RC element. At a load of 15 kN, before any cracking, the bond stresses around the crack inducer at midspan are negligible and fairly symmetric. At a load of 17 kN, the first crack formed just to the left of the crack inducer. Subsequently, other cracks formed at about 145 mm left and 150 mm right of the crack inducer, but these do not seem to affect bond stresses around the midspan crack. At a load of 24 kN, a crack developed 52 mm to the right of the midspan crack. In the test, this crack was visible on the front face at 87 mm from the midspan crack. At a load of 34 kN, another crack formed 50 mm to the left of the midspan crack. At loads of 50 kN and higher, the bond profile maintains the same shape and the maximum bond stresses at the various locations increase with load. Contrary to the GFRP RC element, Figure 4-23 shows that the no-slip point between the cracks maintains well its location. Also, the maximum bond stress is around 30 MPa, which is about twice that of the GFRP RC element, within a short distance less than 22.5 mm from the crack.

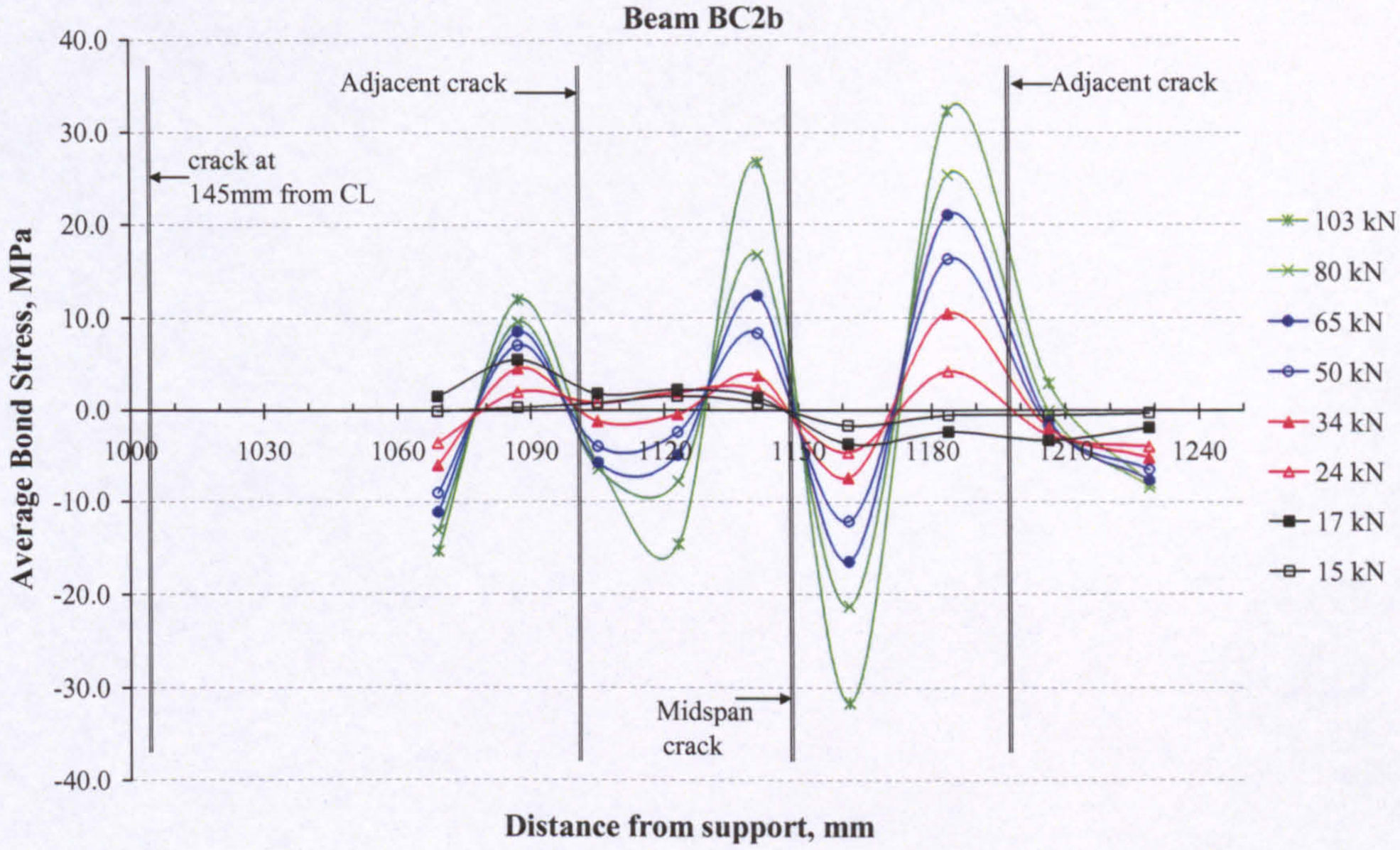

Figure 4-23: CFRP RC bond profiles between midspan and adjacent cracks.

The rebar strain data of only one steel RC element (BSa) allow for a similar bond analysis to be undertaken; but not over its entire loading range. As mentioned earlier, the elements were tested beyond one year of age, which may have affected the glue of the strain gauges on the steel rebars. Nonetheless, the adequacy of the strain gauge data of BSa were validated up to a load of 44 kN, while the steel proportionality limit was reached at the crack at a load of 55 kN, and the yield followed at a load of 66 kN. The bond behaviour of BSa is shown in Figure 4-24. It is obviously very asymmetric around the midspan crack, but nothing more can be added to the previous discussion.

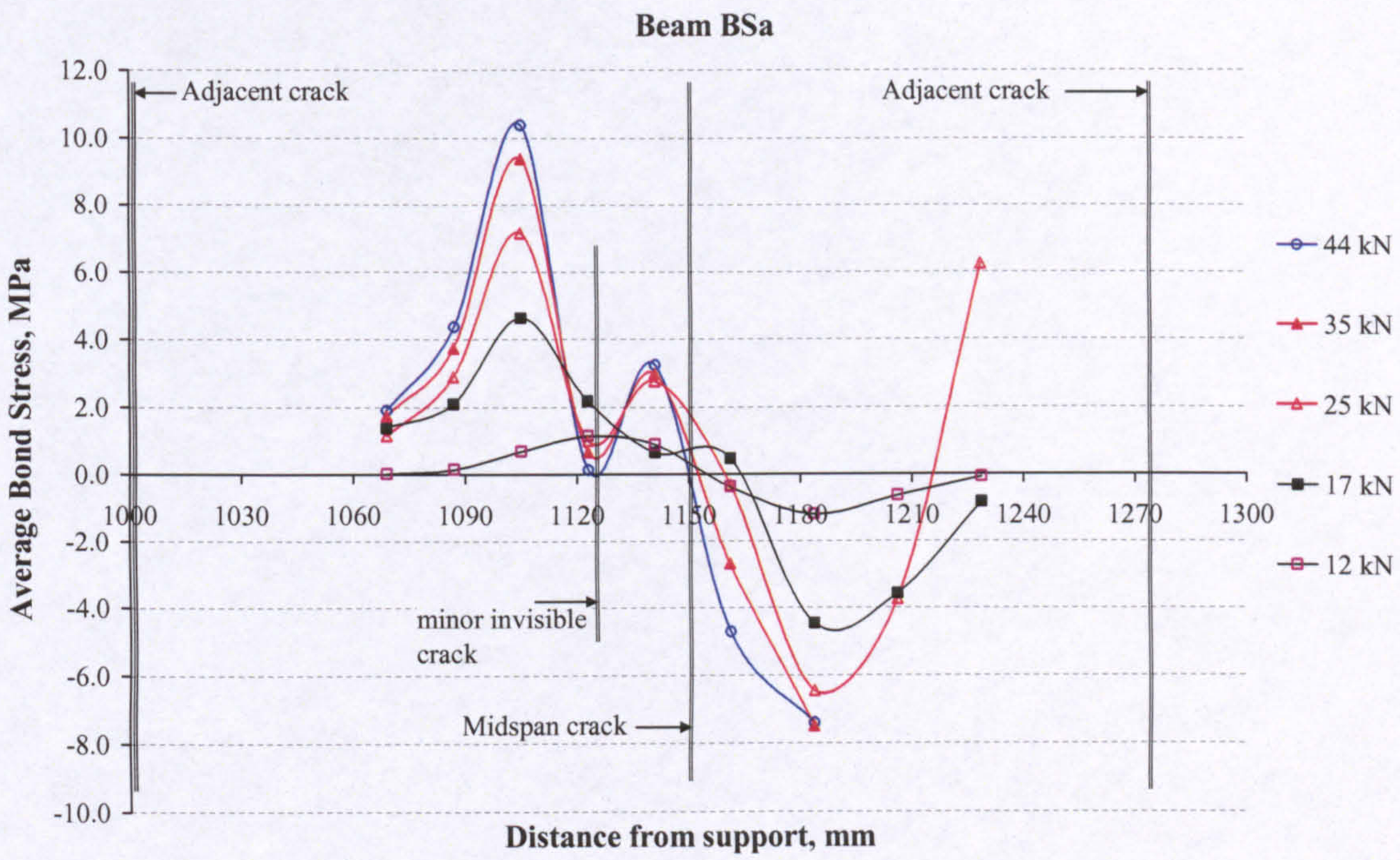

Figure 4-24: Steel RC bond profiles between midspan and adjacent cracks.

It is obvious that the bond conditions around the cracks are highly unsymmetrical. Furthermore, it is not the purpose of this research to investigate bond-strain or bond-slip models. For that purpose, it is believed that additional cracks and more strain measurements between the cracks are more representative. Nevertheless, the available data are adequate to evaluate the average bond between cracks.

Numerical integration of the absolute values of the average bond between the individual strain gauges is used to calculate the average bond between the cracks. Figure 4-25 shows a typical experimental GFRP RC relationship between the average bond and average strain between cracks. The average bond increases almost linearly with average strain even beyond the formation of the midspan crack. However, before the formation of the adjacent cracks, the average bond softens until it reaches a peak value. When the adjacent cracks form, the average bond drops. Beyond that, the stabilized cracking phase commences, in which the average bond-average strain relationship is slightly curved, reflecting slight softening of bond, but is not far from linearity. Therefore, the earlier conclusion that the average bond continues to build up with increasing load up to failure is further confirmed.

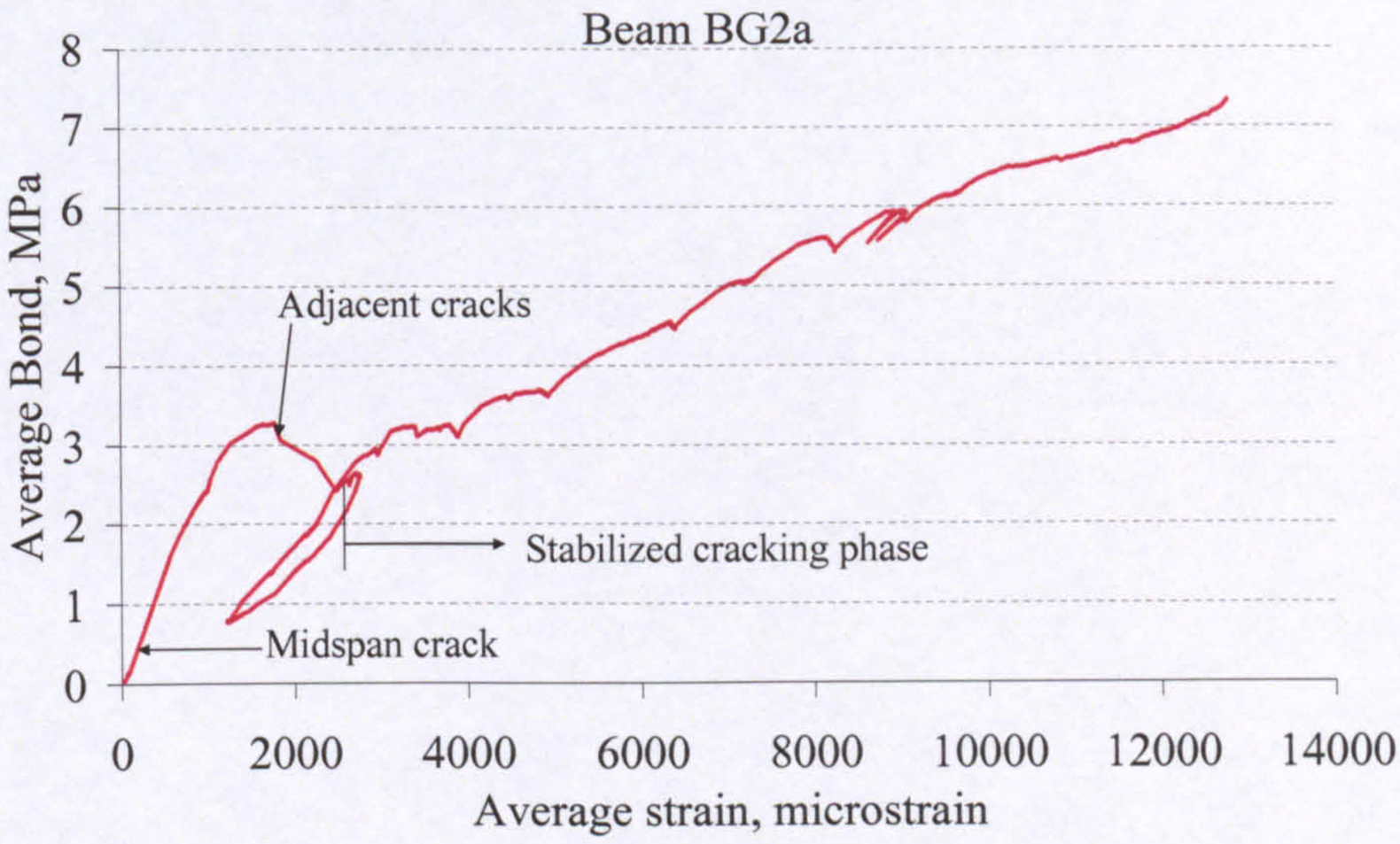

Figure 4-25: Typical GFRP RC average bond vs. average strain relationship.

The average bond versus average strain behaviour of CFRP RC is similar to that of GFRP RC, as shown in Figure 4-26. However, despite the similarity in rebar diameter, the average bond of CFRP RC follows a stiffer path in the stabilized cracking phase, and almost double the bond is developed at failure. The average bond versus average strain behaviour of steel RC shows higher bond stresses at low strains, but the stiffness of bond after cracking is similar to that of CFRP RC, as shown in Figure 4-27.

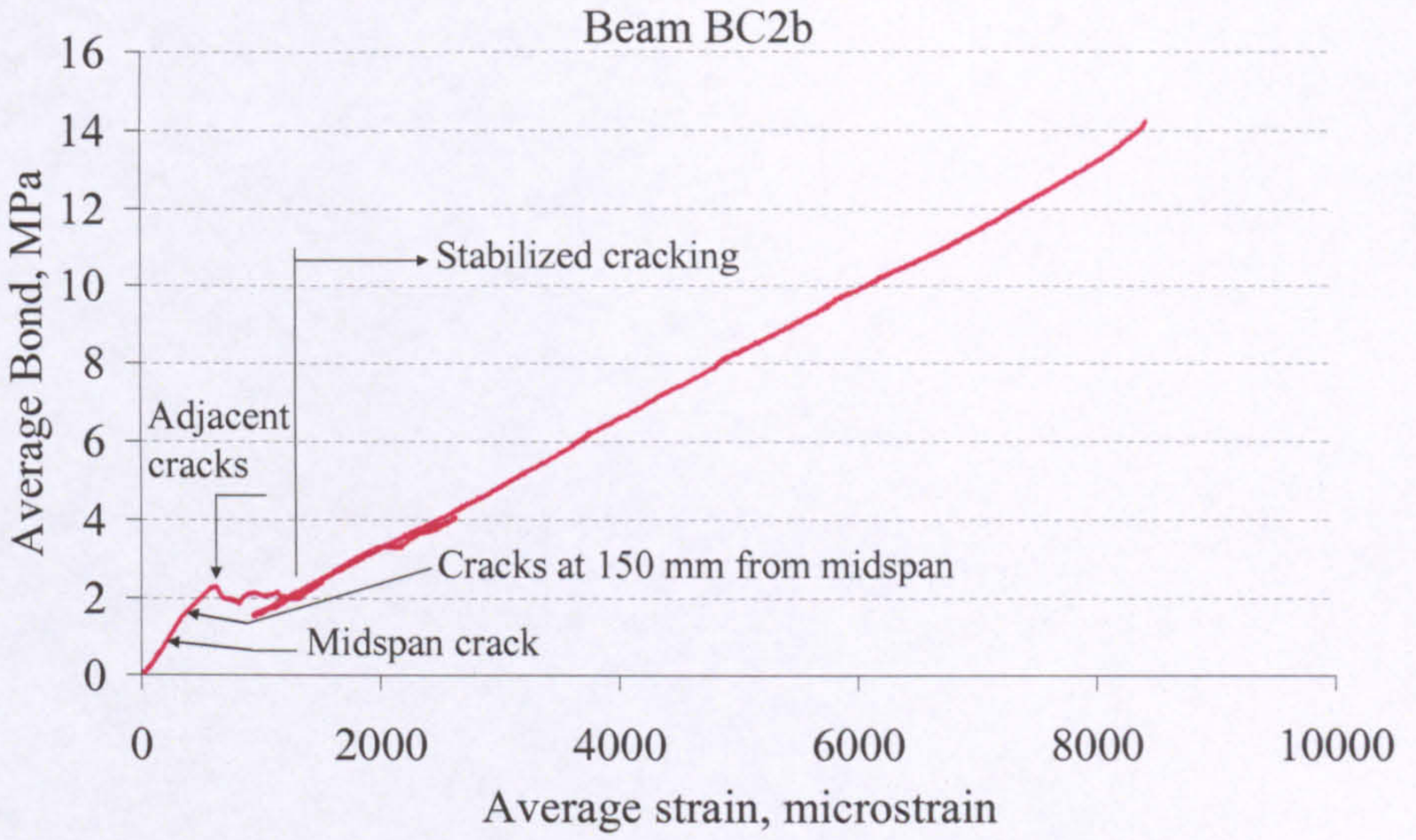

Figure 4-26: Typical CFRP RC average bond vs. average strain relationship.

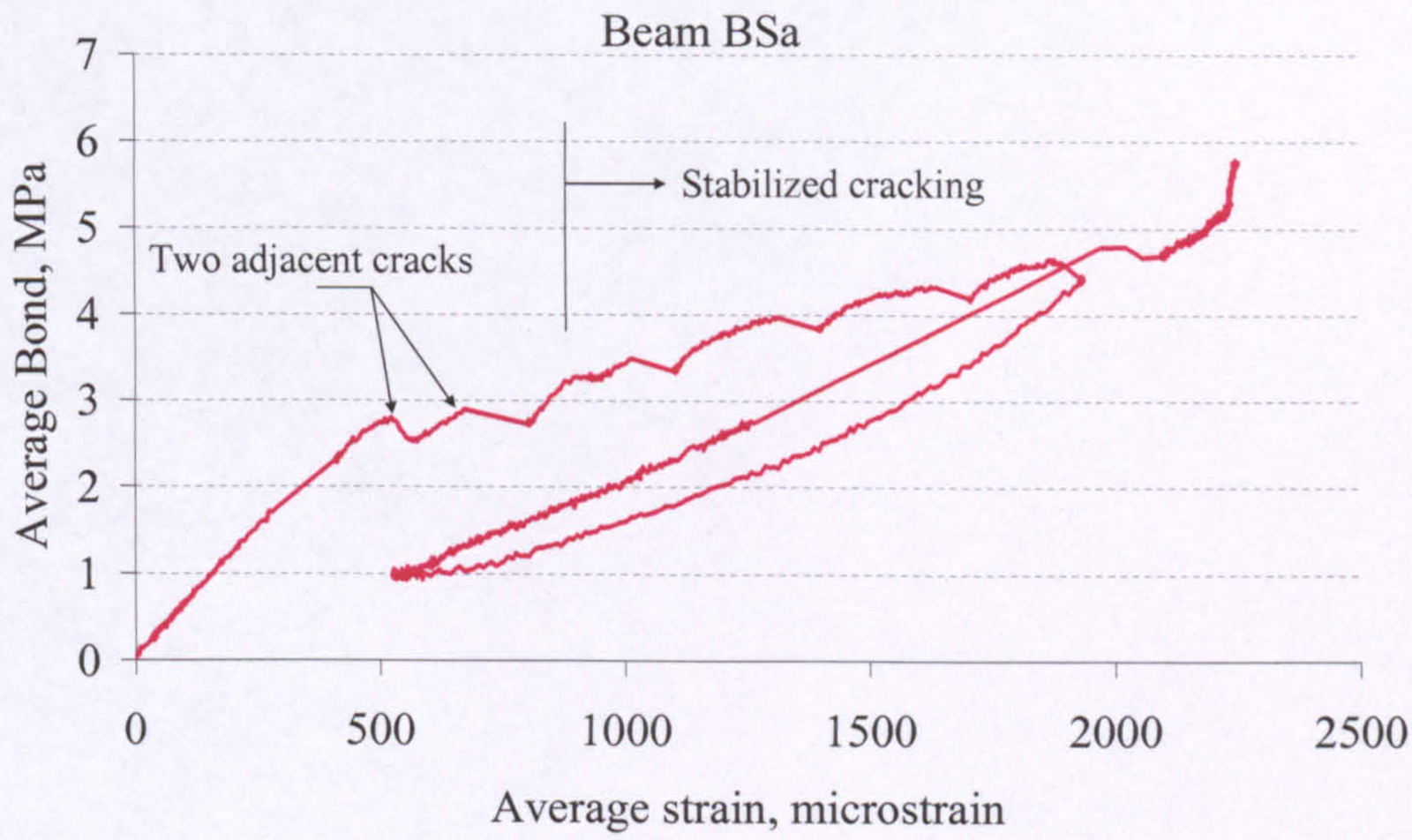

Figure 4-27: Steel RC average bond vs. average strain relationship.

Figure 4-28 relates the average bond between cracks to tension stiffening as defined in the previous section (ratio of effective to actual reinforcement modulus) for GFRP and CFRP RC elements. The figure shows that, after the cracks have formed, tension stiffening reduces tending to 1.0 while the average bond increases. To summarize, once cracks have stabilized and with further increase in load, the difference between the crack strain and average strain between cracks increases, the average bond also increases, but tension stiffening effectively reduces.

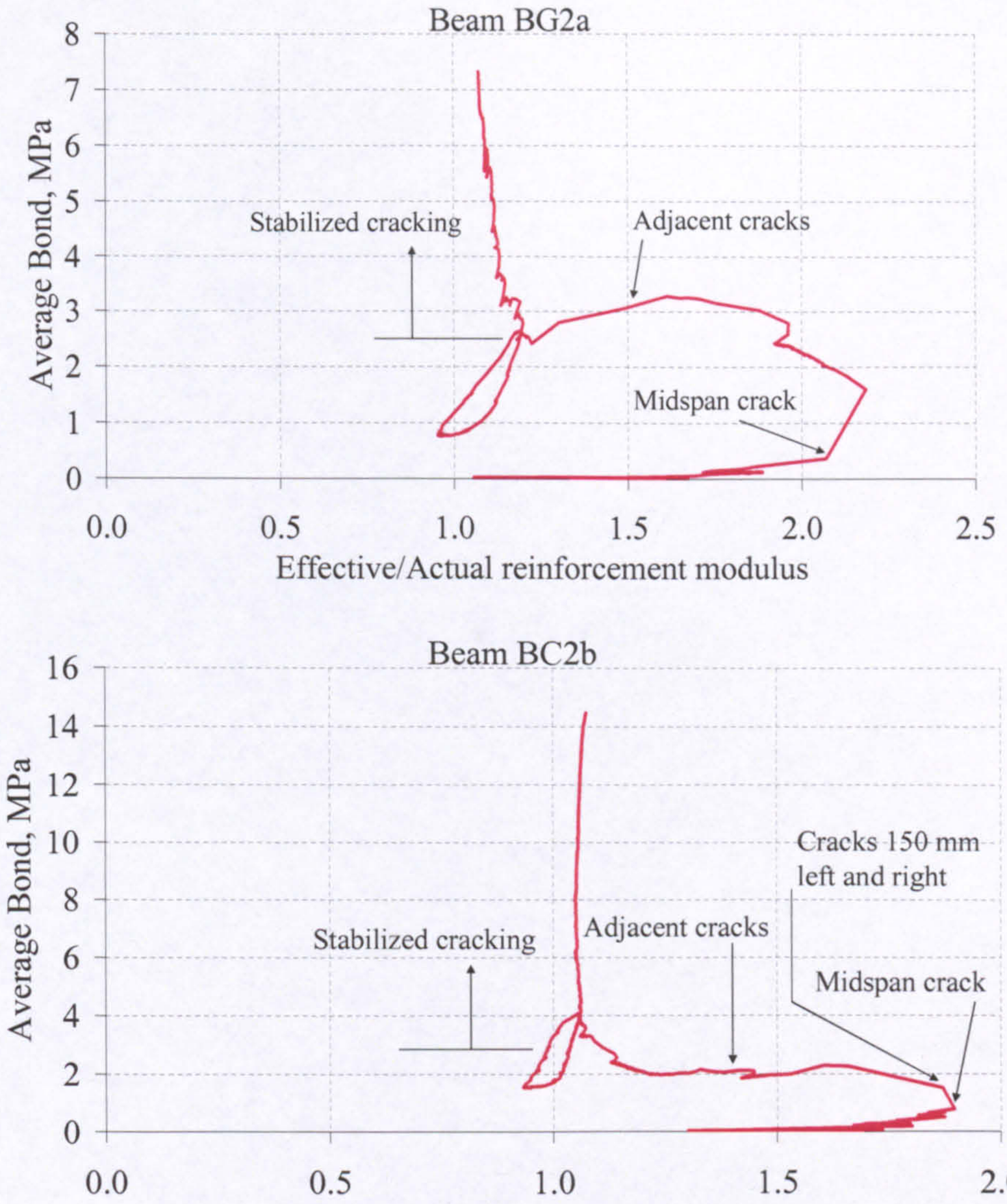

Figure 4-28: Typical average bond vs. tension stiffening relationships.

4.3.3. Load-Curvature

Using the top fibre average concrete strain at midspan (ε_c), the average rebar strain around the crack inducer (ε_{fave}) and the effective reinforcement depth (d), the curvature (φ) at every load (or moment) level is evaluated according to the general approach of CEB (1993), as follows.

$$\varphi = \frac{|\varepsilon_c| + |\varepsilon_{fave}|}{d} \qquad (4\text{-}3)$$

As explained earlier, (ε_{fave}) is calculated by numerical integration of the rebar strain data between the midspan crack and the two adjacent cracks. The load-curvature relationship thus calculated includes the effect of tension stiffening. Literally, it reflects the behaviour of the concrete block that is centred on the crack inducer. However, it should equally represent the behaviour of the other concrete blocks within the constant flexure zone, particularly those that are not too close to the external loads. In the shear span, concrete blocks are created between inclined cracks; as a result of the interaction between flexure and shear. However, it is generally recognized that shear-induced deformations are negligible. In that case, the load-curvature relationship is reasonably applicable within the shear span. If shear-induced deformations were sizeable, then the load-curvature relationship would provide a sensible means of "filtering" the curvature due to flexure out of the total actual curvature.

Figures 4-29 and 4-30 show typical GFRP and CFRP RC experimental load-curvature relationships. The formation of the first crack at midspan causes a considerable increase in curvature. Another sizeable increase occurs with the formation of the two adjacent cracks. Thereafter, the curvature increases almost linearly with load until failure. The load-curvature behaviour is similar to that of rebar strain. Obviously, after cracking the rebar strain has a much larger contribution towards curvature than the concrete strain.

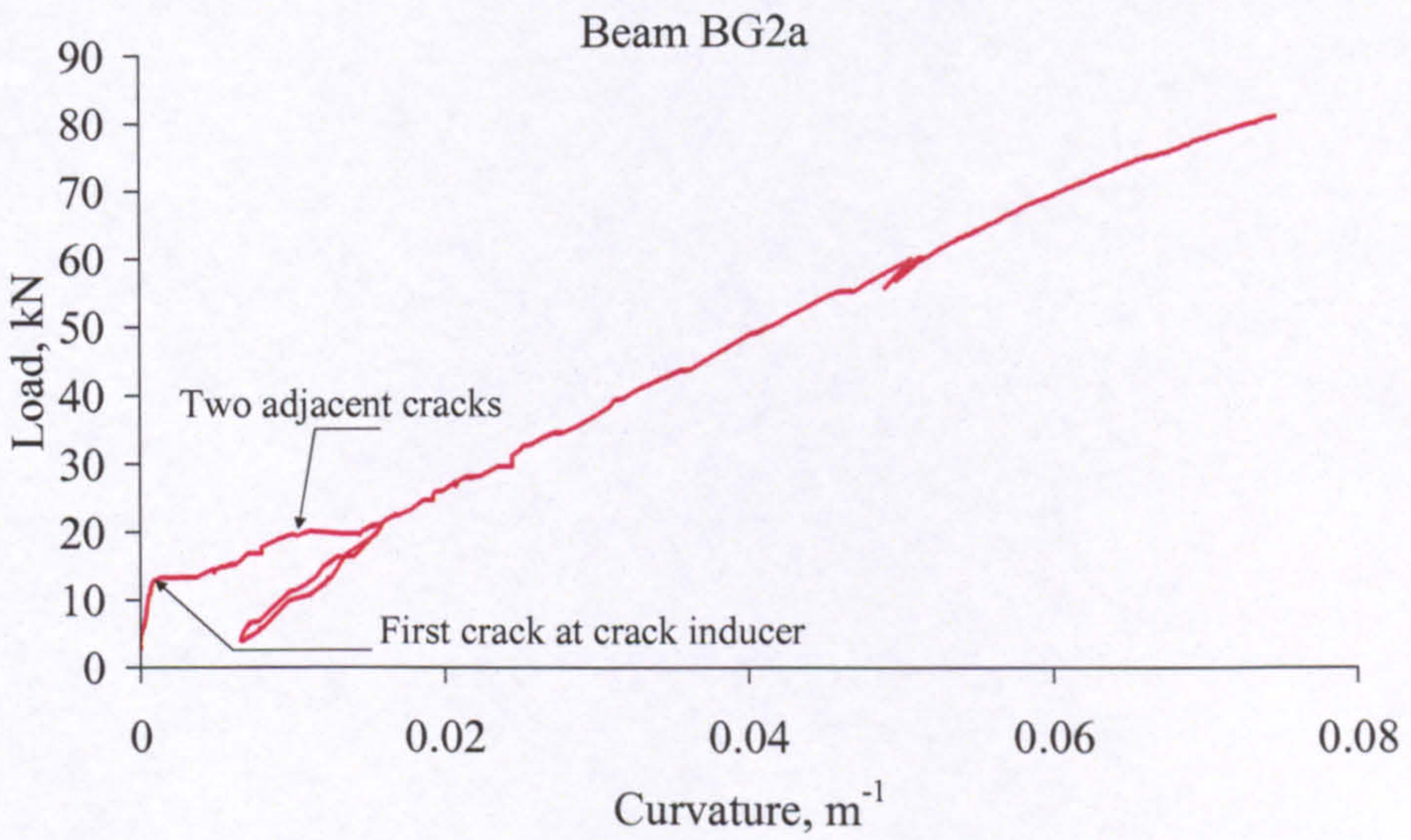

Figure 4-29: Typical GFRP RC experimental load vs. curvature relationship.

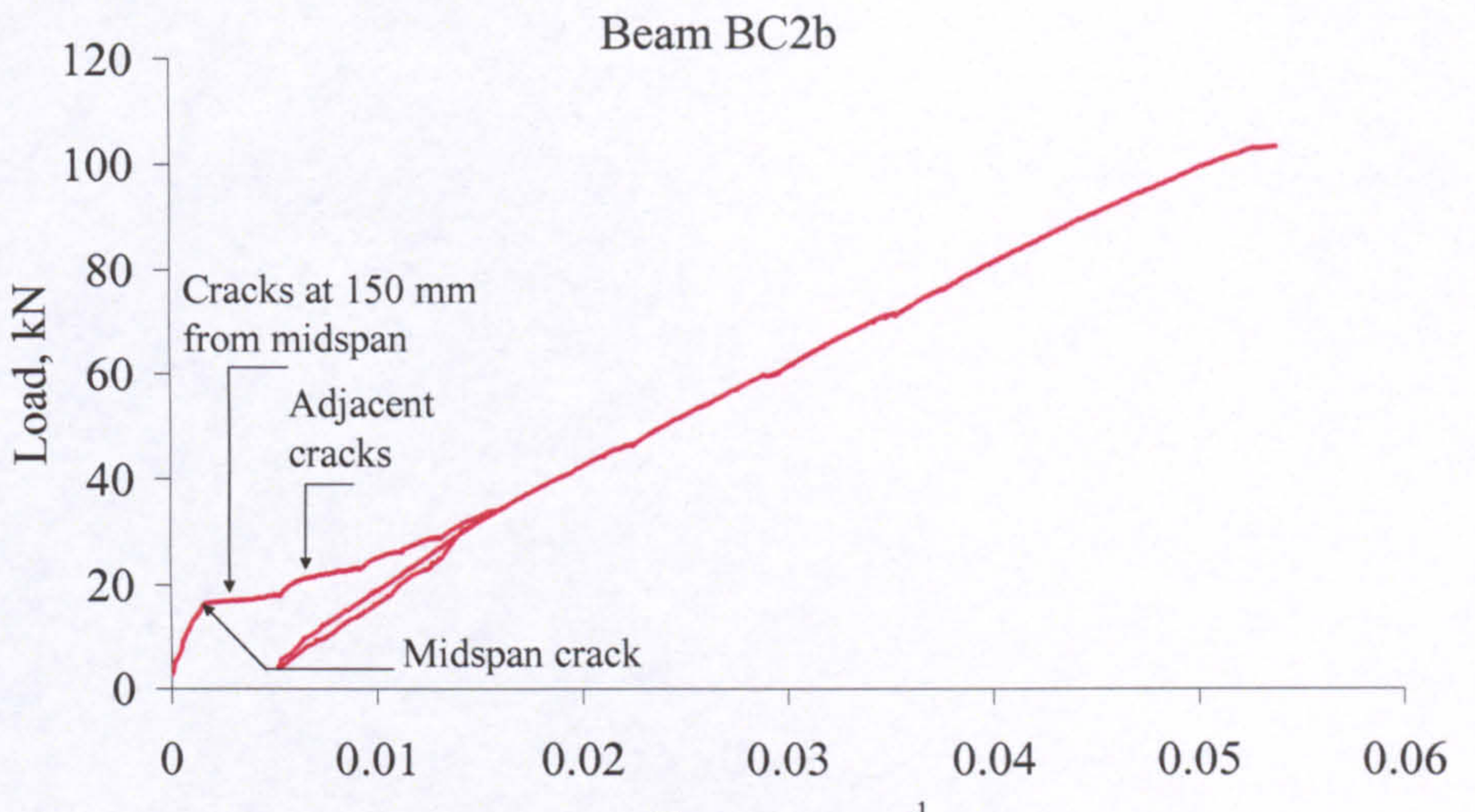

Figure 4-30: Typical CFRP RC experimental load vs. curvature relationship.

Figure 4-31 shows a typical steel RC load-curvature relationship. Beyond the formation of the first crack at midspan, curvature increases at a faster rate. The transition from the uncracked to cracked states is smooth due to the high stiffness of steel reinforcement. The formation of adjacent cracks causes only a slight increase in curvature. Thereafter, the curvature increases almost linearly with load until the reinforcement commences to yield. While the steel rebars are yielding, the curvature increases very rapidly with load until failure occurs by concrete crushing.

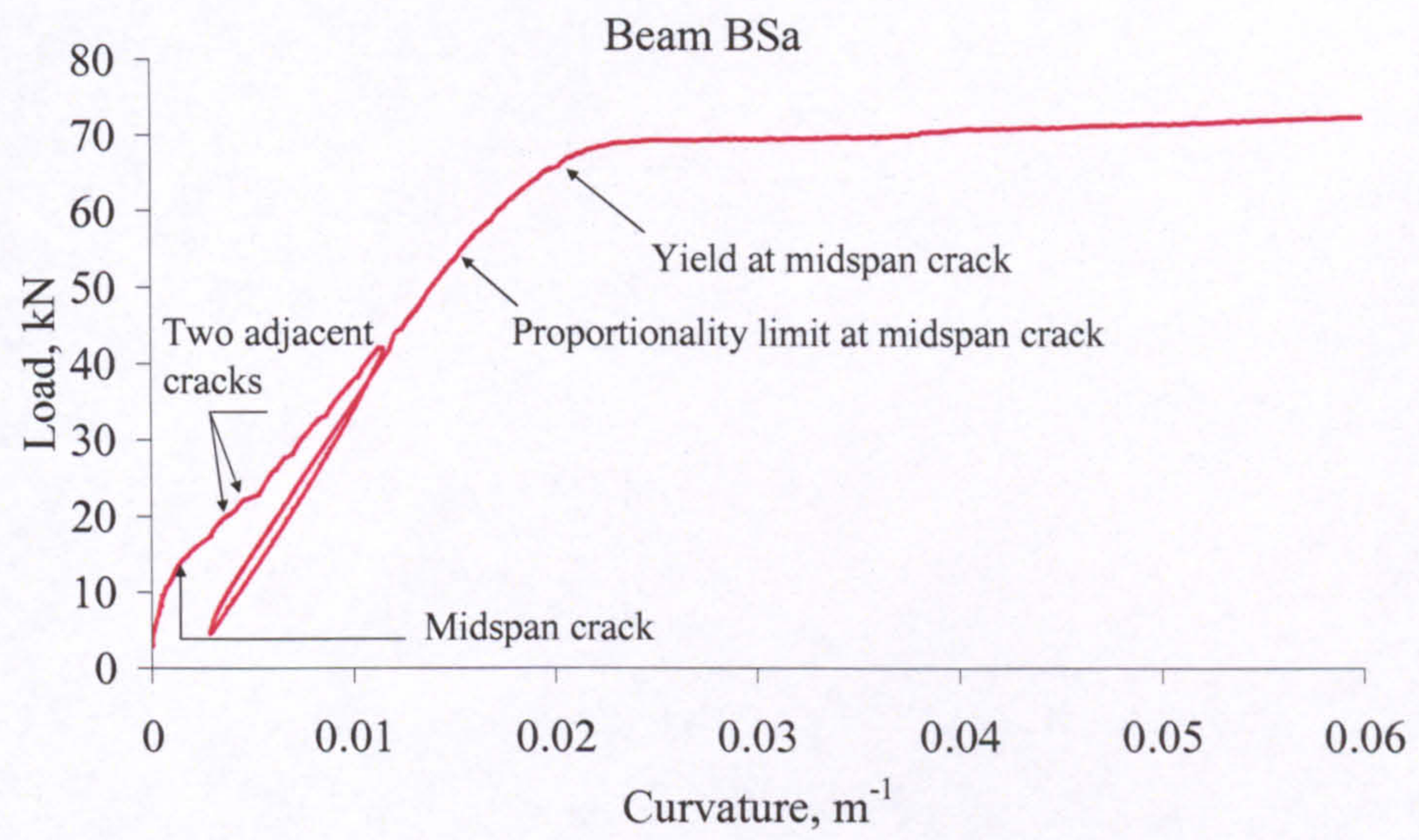

Figure 4-31: Typical steel RC experimental load vs. curvature relationship.

As explained, the derived experimental load-curvature relationship applies to a block of concrete between the cracks. The localized effect of a crack is included and smeared in the behaviour of the concrete block. From the curvature profile at any load level, the curvature-area theorems can be used to calculate the deflection due to flexure at any point along the flexural member. The flexural deflection at midspan was predicted by using this approach for all the beams and slabs. The predicted deflections compare very well with the measured deflections, and are effectively spot on in almost 50% of the tests, as typically shown in Figure 4-32 for GFRP RC and CFRP RC elements.

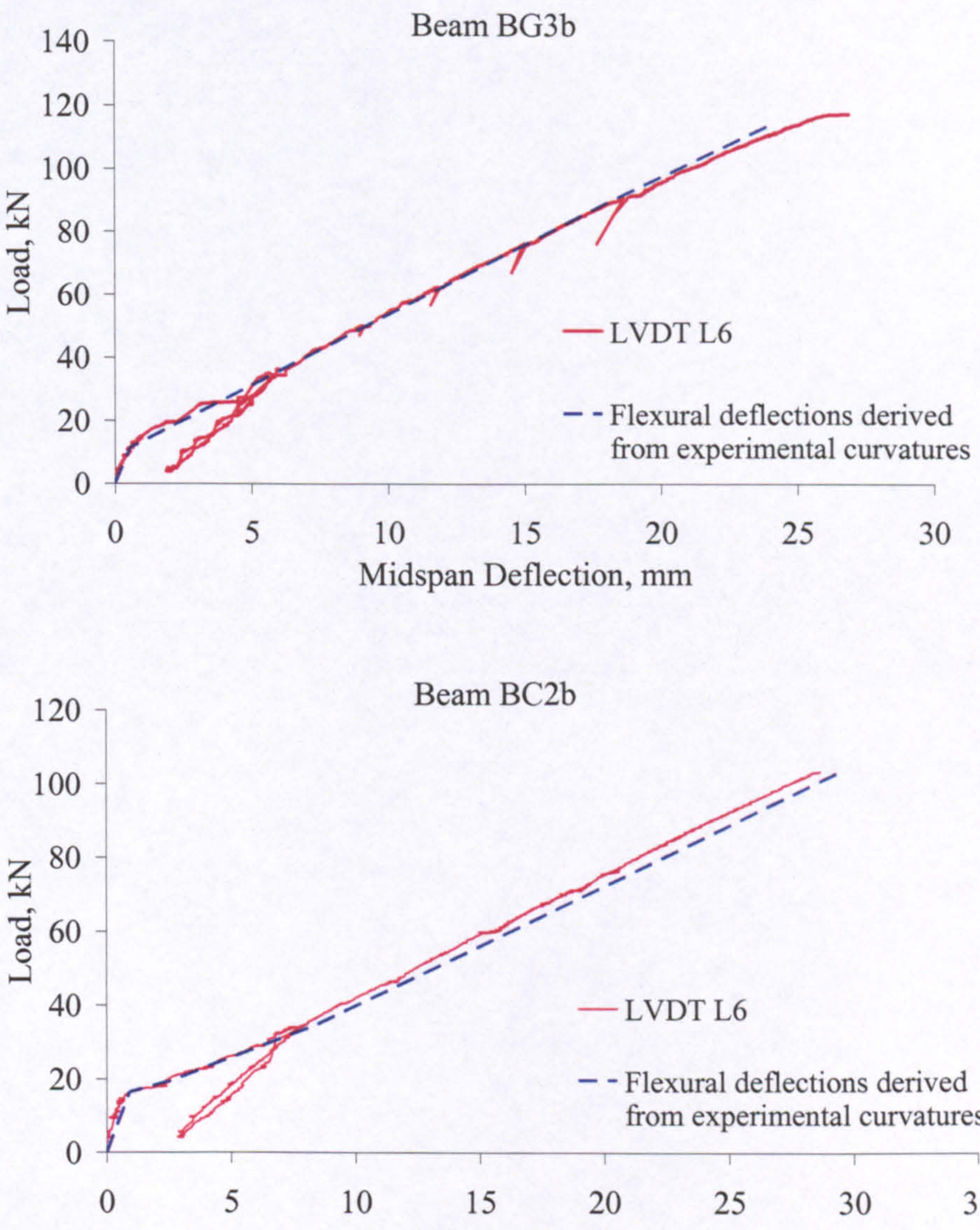

Figure 4-32: Midspan deflection; measured and predicted from experimental curvatures.

4.3.4. Average Neutral Axis Depth

The calculated curvature (φ) and the top fibre average concrete strain at midspan (ε_c) can also be used to obtain a reasonable estimate of the average neutral axis depth (x) within the concrete block around the midspan crack, as follows.

$$x = \frac{\varepsilon_c}{\varphi} \qquad (4\text{-}4)$$

Figures 4-33 and 4-34 show typical experimental load versus average neutral axis depth relationships for GFRP and CFRP RC members. The neutral axis depth decreases considerably just after formation of the first crack at midspan and the two adjacent cracks. Thereafter, a minor decrease is observed, followed by a minor but continuous increase until the maximum load level.

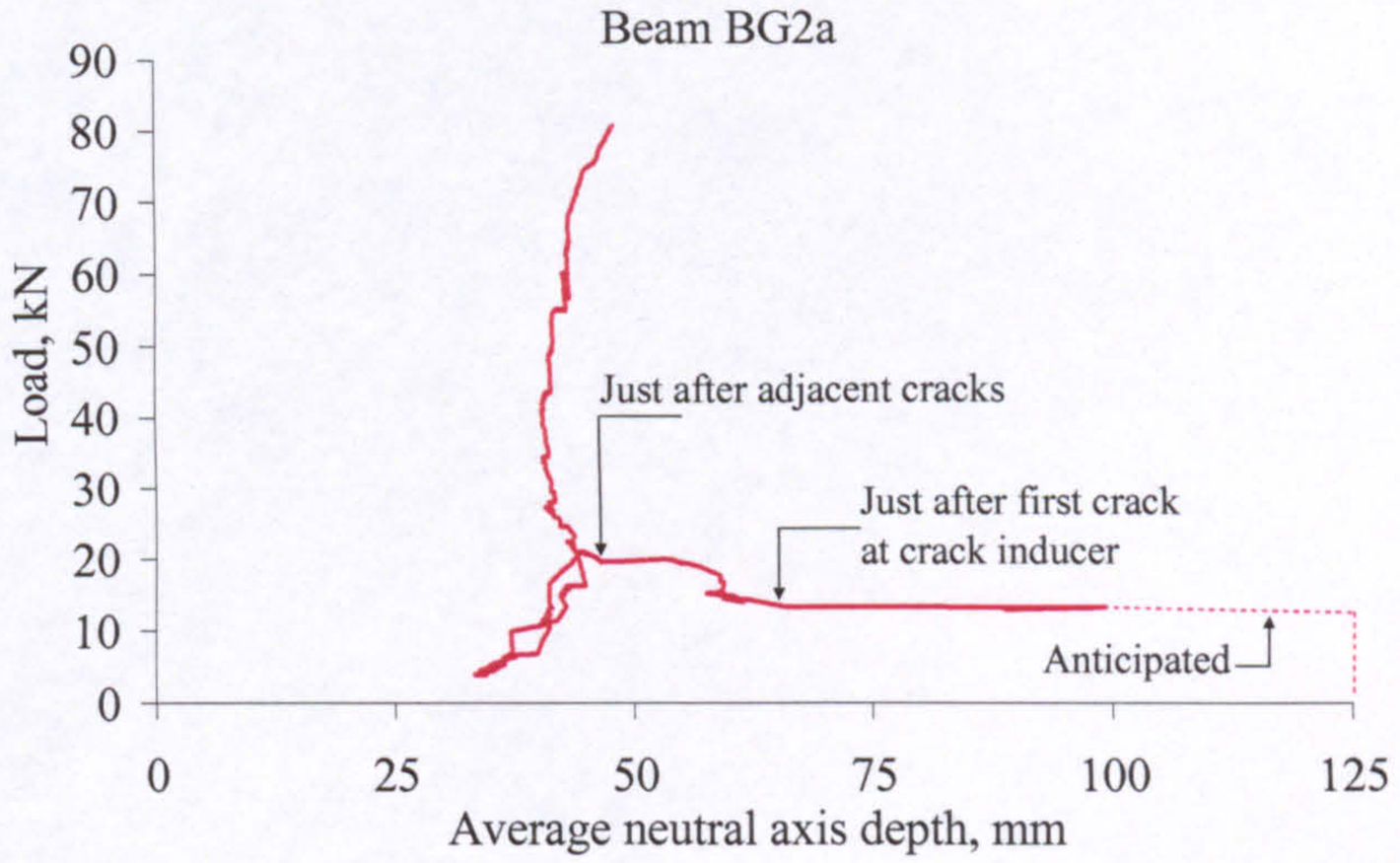

Figure 4-33: Typical GFRP RC load vs. average neutral axis depth relationship.

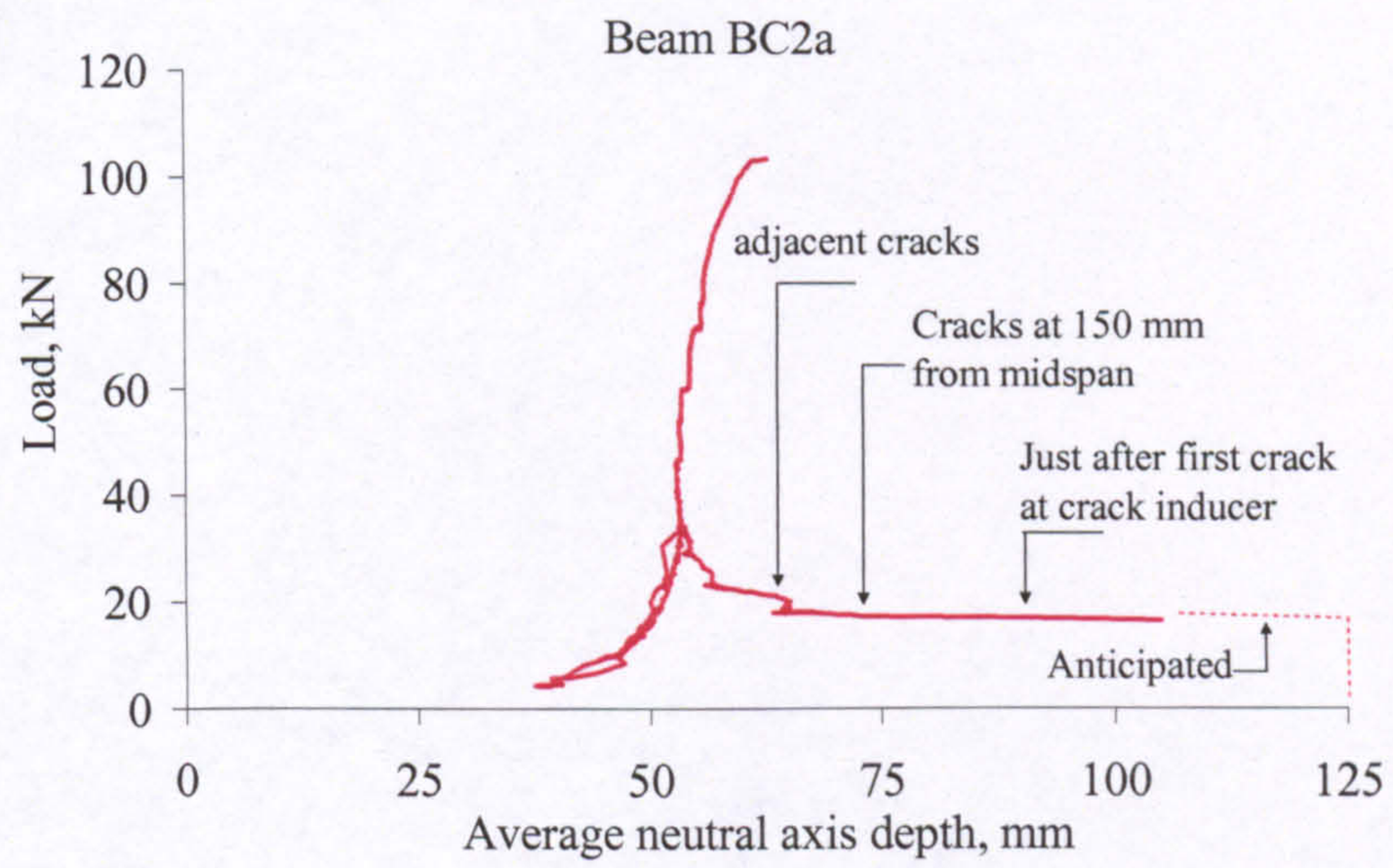

Figure 4-34: Typical CFRP RC load vs. average neutral axis depth relationship.

Figure 4-35 shows typical load versus average neutral axis depth relationship for a steel RC member. In contrast to the FRP RC members, the neutral axis depth decreases considerably just after the formation of the first crack at midspan, but then reduces at a slower rate. The formation of the two adjacent cracks per se does not seem to have much of an effect. Thereafter, the neutral axis depth almost stabilizes until the reinforcement commences to yield. While the reinforcement is yielding, the neutral axis depth reduces at a very fast rate until failure occurs.

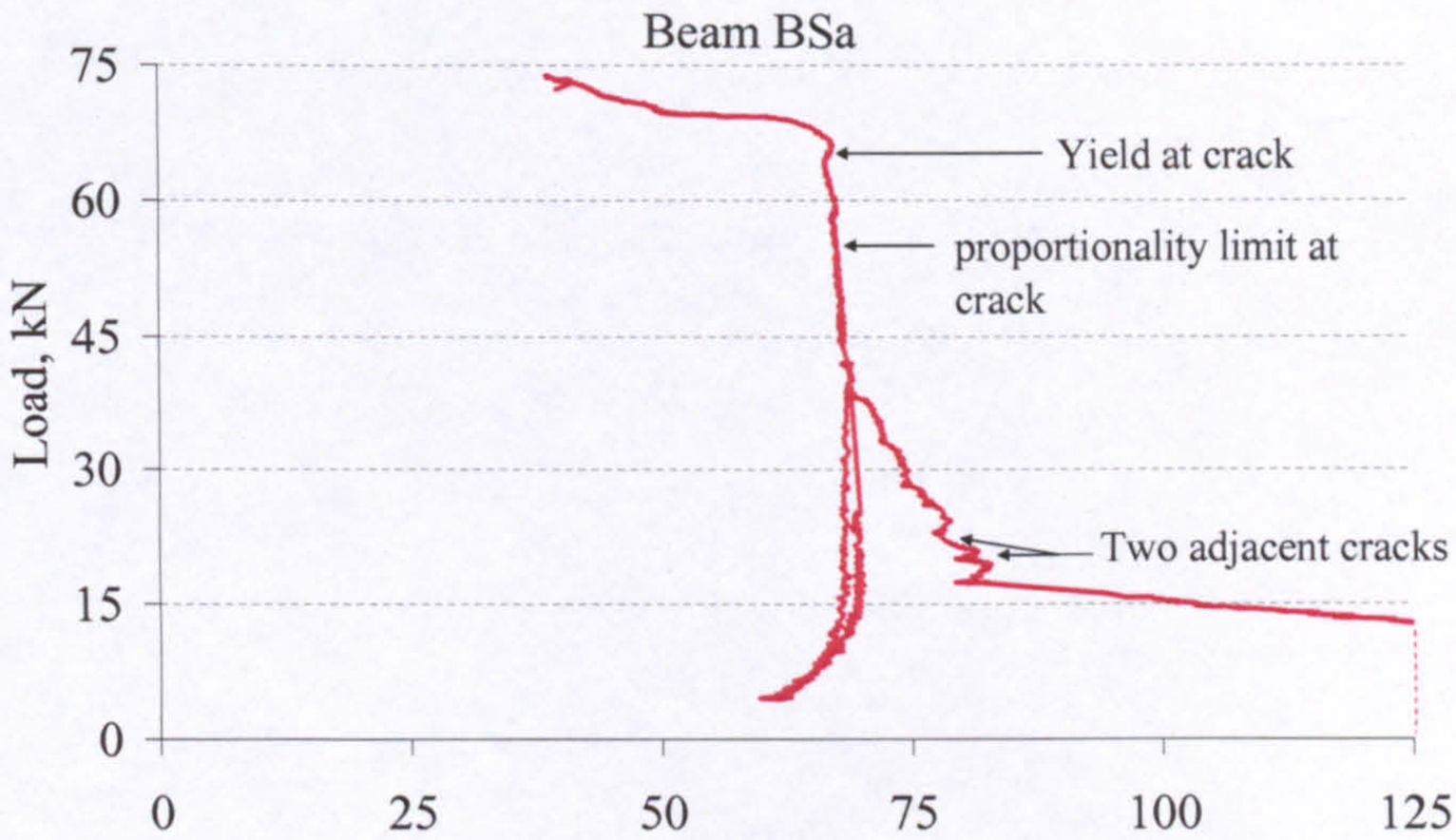

Figure 4-35: Typical steel RC load vs. average neutral axis depth relationship.

CHAPTER 5

NUMERICAL ANALYSIS

5.1. INTRODUCTION

Besides the experimental work, numerical analysis was carried out to investigate deflections of the tested flexural members, together with the associated tension stiffening and rebar and concrete strains. One objective was to provide further insight into the experimental results. Another aim was to evaluate the adequacy of the corresponding theoretical predictions. Two numerical analysis methods were employed. Finite element (FE) with smeared crack modelling of cracking and tension stiffening was used to predict and examine the stress-displacement response in detail. Cracked section analysis is a simple analysis tool that was used to provide an upper-bound prediction of deflections. This chapter presents the background of the two approaches and elaborates on their implementation in this study. Sample analytical results are presented and briefly discussed, while a comprehensive comparison of the experimental and theoretical results is undertaken in the next chapter.

5.2. FINITE ELEMENT ANALYSIS

Reinforced concrete poses a highly nonlinear stress-displacement analysis challenge that involves many complications. In compression, the concrete behaviour is nonlinear. In tension, concrete has a very limited tensile strength and then it cracks. Cracking creates complex bond conditions between the reinforcement and the surrounding concrete, which involve invisible micro and secondary cracks, relative slip between concrete and reinforcement, as well as splitting transverse stresses in the concrete. The

problem is further complicated in the presence of high shear forces when other mechanisms are activated, such as dowel action and aggregate interlock.

FE analysis is currently the most reliable numerical analysis tool available. ABAQUS version 6.5 (ABAQUS, Inc. 2004) is a renowned FE package that is based on sound and state-of-the-art theoretical background. Among numerous capabilities, ABAQUS can deal with a wide range of stress-displacement analysis problems allowing for almost any structural material. For reinforced concrete, ABAQUS uses the smeared crack approach to model cracking and tension stiffening. It offers nonlinear analysis techniques designed for unstable local or global collapse situations but may be appropriate to deal with the sudden release of strain energy due to cracking of concrete. The following sections present the geometric and material models and nonlinear analysis techniques in ABAQUS. Model parameters are then investigated, and ABAQUS is used to analyse representative beam and slab tests. The detailed discussion of the analytical results in comparison to the corresponding test results is undertaken in the next chapter.

5.2.1. Model

The following sections present the approach of ABAQUS for modelling and analysing RC members. Topics covered include the different meshing elements and their characteristics, reinforcement and concrete models and nonlinear analysis techniques.

5.2.1.1. Meshing Elements

The structural member is modelled as a mesh of finite elements. A wide range of elements is available in ABAQUS. Among these, continuum elements are the most comprehensive; as they can be used in almost any linear/nonlinear stress-displacement analysis and to model nearly any shape.

Both two- and three- dimensional (2D and 3D) continuum elements are available in ABAQUS library. However, the behaviour of the beams and slabs in this research can be adequately investigated by 2D continuum models. The 2D continuum elements in

ABAQUS can be either plane-strain or plane-stress elements. The plane-strain theory assumes zero out-of-plane normal and shear strains, which is ideal when the out-of-plane dimension is large compared to the in-plane dimensions, as in dams or tunnels. The plane-stress theory assumes zero out-of-plane normal and shear stresses, which is ideal when the out-of plane dimension is small relative to the in-plane dimensions. Obviously, the beams and slabs fall under the plane-stress category.

The 2D plane-stress elements can be either triangular (3 or 6 nodes) or quadrilateral (4 or 8 nodes). However, reinforcement cannot be used with triangular elements. Besides, the triangular geometry is not ideal to mesh the rectangular beams or slabs. Therefore, the choice is narrowed down to quadrilateral elements.

Continuum elements only have translational degrees of freedom at their nodes, and the displacements are calculated at the nodes. 4-node quadrilateral elements, also known in ABAQUS as linear or first order elements, use linear interpolation to obtain displacements at other points. This implies that the edges of these elements cannot curve under bending. Therefore, pure bending causes shear rather than bending deformation in these elements, a phenomenon referred to as shear locking, which causes the element to be too stiff in bending. On the other hand, 8-node quadrilateral elements, also known in ABAQUS as quadratic or second order elements, use quadratic interpolation to obtain displacements away from the nodes. Therefore, the edges of these elements can curve, which diminishes the effect of shear locking.

In ABAQUS, the various response quantities are evaluated at integration points within the element. Fully-integrated 4-node quadrilateral elements use two integration points in each direction, while fully-integrated 8-node quadrilateral elements use three integration points in each direction. To deal with the problem of shear locking, ABAQUS has reduced integration-elements, which have one fewer integration point in each direction. Hence, 4-node quadrilateral reduced integration elements do not suffer from shear locking. However, unless a very fine mesh is used, they can show a numerical problem, referred to as hourglassing, where a zero-energy mode is created in the element along with unrealistic deformations under bending. Therefore, 4-node quadrilateral elements are disregarded.

The above elimination process limits the element choice to continuum 2D plane-stress 8-node quadrilateral element with either full or reduced integration, referred to in ABAQUS as CPS8 and CPS8R, respectively. These elements are compared in Figure 5-1. CPS8R has the advantage that it is not susceptible to shear locking, while CPS8 can develop some shear locking if the bending stress has a gradient or when subjected to complicated states of stress. On the other hand, CPS8 has more integration points, which means better accuracy for the same mesh size. Furthermore, shear locking is not an issue for 8-node elements to start with, and it effectively disappears as the mesh becomes finer. After some trials, it was found that the convergence of the analysis algorithm is much better with CPS8 than with CPS8R. Therefore, CPS8 was adopted in all the FE analyses carried out.

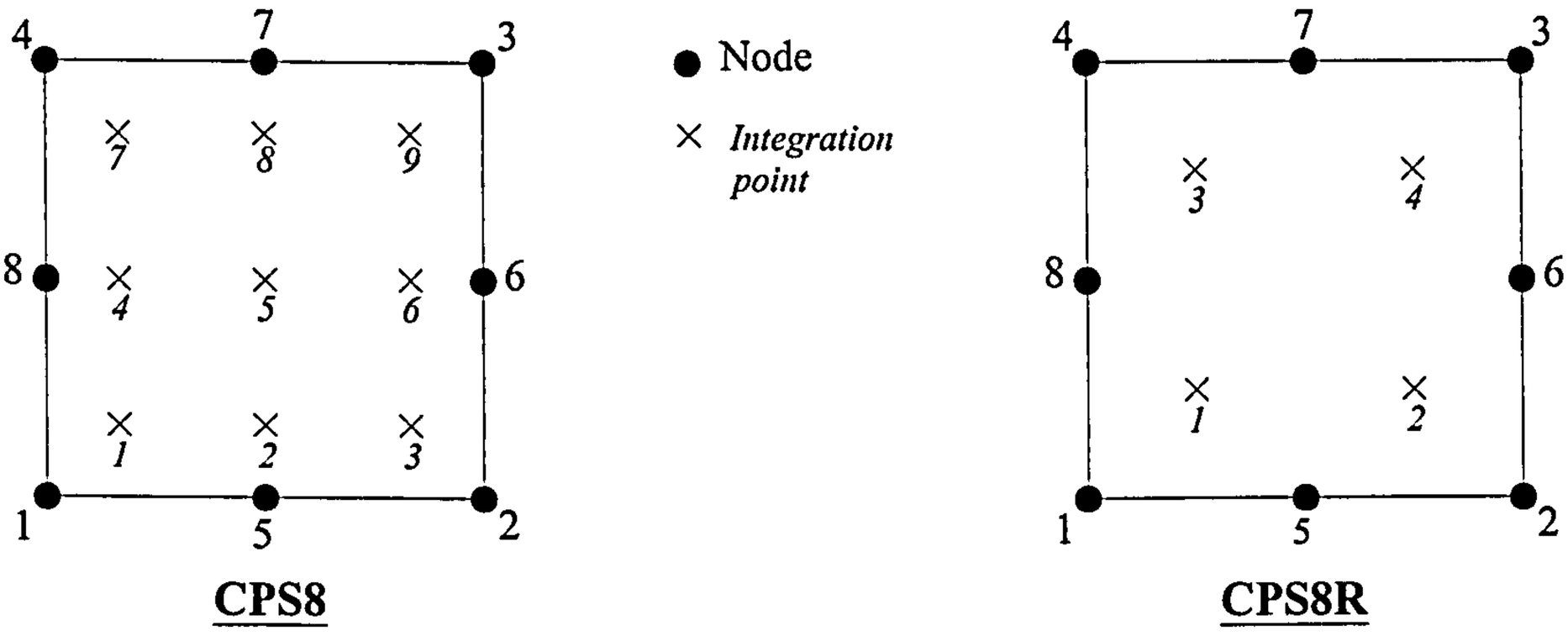

Figure 5-1: CPS8 and CPS8R continuum elements.

5.2.1.2. Reinforcement

ABAQUS has two methods for defining reinforcement in continuum 2D plane-stress elements. In the first method, beam or truss elements are used to represent the reinforcement, and these are embedded in "host" continuum elements. Embedding means that the translational degrees of freedom at the nodes of the embedded element are eliminated and become constrained to the corresponding interpolated values in the host continuum element. In the second method, the reinforcement is defined in one or more layers of uniformly spaced rebars. The rebars within each layer lie in a surface that intersects the plane of the model at right angles. The orientation of the rebars within the surface can de defined if not parallel to the plane of the model. The

reinforcement layer is treated as a smeared layer within the volume of the element, with a constant thickness equal to the area of each rebar divided by the rebar spacing.

The reinforcement-concrete interaction is not accounted for, but is indirectly considered in the concrete model. The second method with smeared reinforcement implies perfect bond along the reinforcement within the continuum element, whereas, the first method with embedded reinforcement assumes perfect bond only at the embedded nodes. Hence, if the embedded element has nodes at the edges of the host element only, then the reinforcement becomes free within the host element. If multiple embedded nodes are used with the host element, then perfect bond is assumed at these nodes. The second method is more in-line with the smeared crack concrete model, and is therefore adopted.

The material of the reinforcement is defined based on the stress-strain results of the uniaxial tensile tests (Chapter 3). The elastic part of the behaviour is defined by the longitudinal elastic modulus. The plastic part is defined by (stress, plastic strain) data pairs. The rupture of the FRP reinforcement was defined by specifying a plastic part where the rupture stress drops to zero at a negligible plastic strain.

5.2.1.3. Concrete

The smeared crack concrete model in ABAQUS is intended for the analysis of plain or reinforced concrete with low confining pressures under essentially monotonic straining. At the material point, the model allows for either tensile cracking or concrete crushing. Structural aspects of the rebar-concrete interaction, like bond-slip and tension stiffening, are indirectly considered by modifying the softening behaviour of plain concrete. The model also allows for the reduction in shear stiffness due to cracking. The concrete model is presented in the following.

- Cracking

Cracking and post-cracking behaviour are the most important aspects of the concrete model. Cracking is assumed to occur when the biaxial state of stress reaches a failure surface, referred to as crack detection surface, as shown in Figure 5-2.

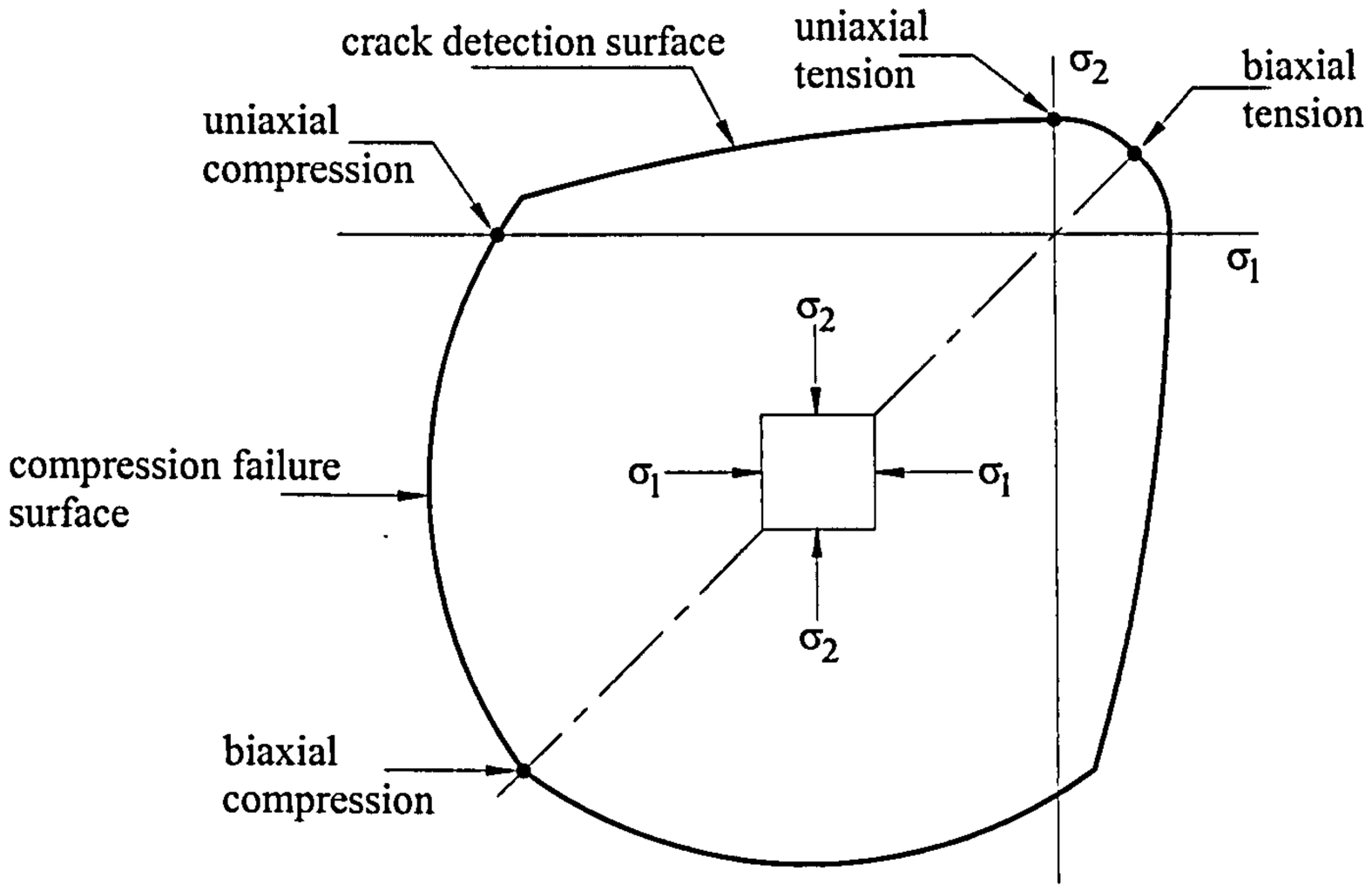

Figure 5-2: Crack detection and compression failure surfaces in plane stress (ABAQUS, Inc 2004).

The plain concrete model is a smeared crack model, meaning that the model does not physically generate individual macro cracks. Cracks are indirectly accounted for by the way their presence affects the stress and material stiffness. The post-cracking behaviour is described by a concrete softening relationship. Cracks are allowed to close without any remaining strain, which implies that the elastic stiffness reduces as cracks open. Therefore, the concrete softening model is also referred to as a damaged elasticity model.

Two concrete softening models are available in ABAQUS, as shown in Figure 5-3. One model is a stress-strain softening relationship, while the other is a stress-(crack opening) relationship. Stress-strain softening may lead to mesh sensitivity, meaning that the analysis does not converge to a unique solution as the mesh is refined, because mesh refinement results in narrower crack bands. However, it is considered that mesh size is of concern only when few cracks physically develop in the structure. If, on the other hand, as in the beams and slabs under investigation, the cracks are reasonably distributed, then mesh sensitivity is considered to be of little concern (ABAQUS, Inc 2004).

The stress-(crack opening) model is based on brittle fracture energy concepts, where the fracture energy ($G_f=0.5u_o\sigma_{cr}$) required to form a unit area of crack surface is viewed as a

material property that is independent of the mesh size (ABAQUS, Inc 2004). In the implementation of this approach, ABAQUS relates crack opening to strain via a characteristic length. The characteristic length is defined as the square root of the area associated with an integration point. Hence, a crack opening is associated with differing strains depending on the mesh size. This model is essentially tailored for plain or lightly reinforced concrete applications, but is considered herein for the sake of completeness.

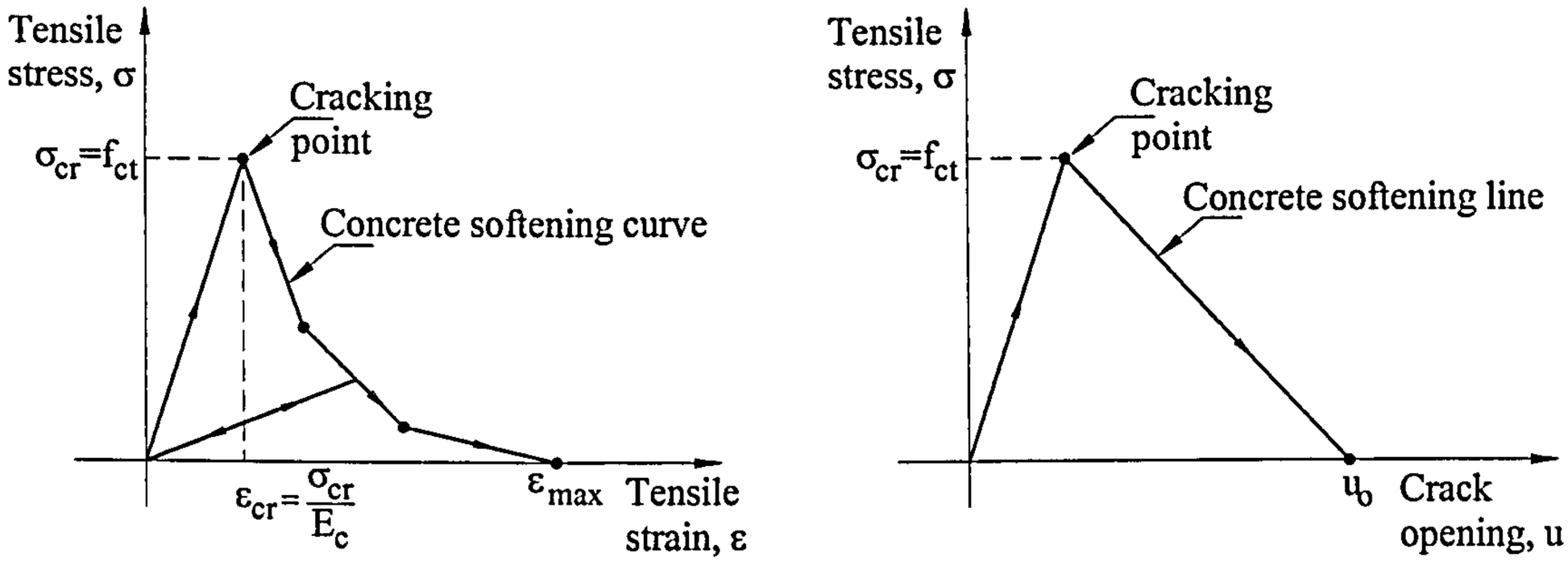

Note: For RC, concrete softening is modified to account for tension stiffening.

Figure 5-3: Concrete softening models (ABAQUS, Inc 2004).

Concrete softening models, in general, apply to cracking of plain concrete. As mentioned earlier, structural effects associated with reinforcement-concrete interaction around cracks, such as tension stiffening and bond-slip, are indirectly considered in ABAQUS in the concrete model. It is stipulated that the concrete softening branch can be modified to account for these effects; depending on the reinforcement ratio, bond characteristics, aggregate size, as well as the mesh size. Very little guidance is provided in ABAQUS for that purpose. For instance, for heavily reinforced concrete with a fine mesh, ABAQUS estimates that stress reduces linearly to zero at a total strain of about 10 times the concrete strain at cracking (0.001 approximately). In the fracture energy approach, it is estimated that stress reduces linearly to zero at a maximum crack opening (u_o) of 0.05 mm and 0.08 mm for normal and high strength plain concrete, respectively. In fact, ABAQUS advises that the concrete softening model be calibrated based on the experimental results. Both the strain and fracture energy softening models were considered in the FE analyses carried out.

- *Compression*

In compression, ABAQUS requires the user to input a uniaxial compressive stress-strain relationship for concrete. This uniaxial compressive model is then used with concepts of isotropic hardening and associated flow to determine response and compressive failure surface in plane stress, as shown in Figure 5-2. A "Failure Ratios" command is included in ABAQUS to control the shape of the failure surface. The FE analyses were carried out based on the uniaxial compressive concrete model of Eurocode 2 (CEN 2004), as shown in Figure 5-4. However, the elastic concrete modulus was based on ACI 318-02 (ACI Committee 2002), as explained in Chapter 3.

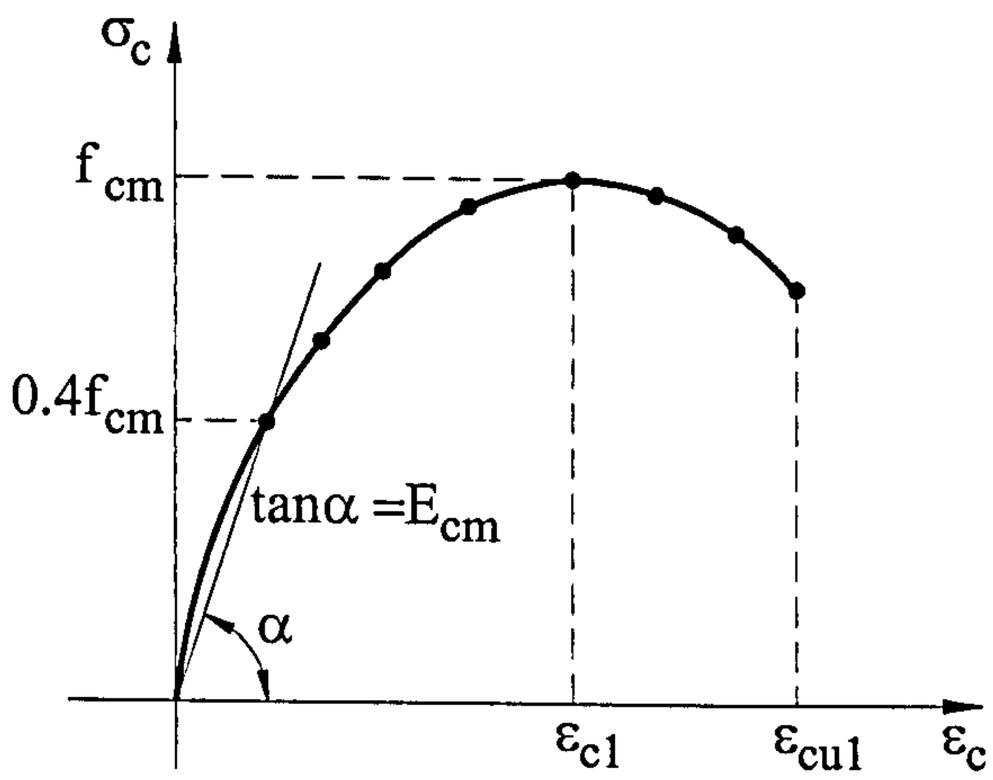

$$\sigma_c = f_{cm}\frac{k\eta - \eta^2}{1+(k-2)\eta}$$

$$\eta = \varepsilon_c/\varepsilon_{c1}$$

$$\varepsilon_{c1} = 0.0007 f_{cm}^{\ 0.31} < 0.0028$$

$$k = 1.05 E_{cm}\frac{\varepsilon_{c1}}{f_{cm}}$$

$$E_{cm} = 22\left[\frac{f_{cm}}{10}\right]^{0.3} \times (0.9)$$

"0.9 factor for limestone aggregate"

$$\varepsilon_{cu1} = 0.0035, \text{ for fcm} < 58 \text{ MPa}$$

Figure 5-4: Uniaxial compressive stress-strain concrete model (CEN 2004).

- *Shear Stiffness*

ABAQUS has a "shear retention" model that accounts for the reduction in shear stiffness due to cracking by multiplying the elastic shear modulus of uncracked concrete (G) by a reduction shear retention factor (ρ). ρ is assumed to reduce linearly with increasing strain across a crack (ε), until it reaches zero at a maximum strain value (ε_{max}), as follows.

$$\left[\rho = (1-\varepsilon/\varepsilon_{max}), \text{for } \varepsilon < \varepsilon_{max}\right] \text{ and } \left[\rho = 0, \text{for } \varepsilon \geq \varepsilon_{max}\right] \qquad (5\text{-}1)$$

Furthermore, the model allows for the definition of a shear retention factor for closed cracks, as follows.

$$\rho = \rho_{close}, \text{ for } \varepsilon < 0 \qquad (5\text{-}2)$$

If the effect of cracking on shear stiffness is insignificant (full shear retention), ρ_{close} is equal to 1.0 and ε_{max} is equal to a large value. Otherwise, both ρ_{close} and ε_{max} need to be estimated. ABAQUS considers it reasonable, as a starting point, to take ε_{max} equal to the maximum strain value in the tension stiffening model. The effect of the shear retention factor was investigated in the FE analyses carried out.

5.2.1.4. Nonlinear Analysis

Due to material nonlinearity, solving RC problems requires nonlinear analysis. Furthermore, when cracks develop, strain energy is suddenly released, meaning that kinetic effects are generated and the analysis becomes highly unstable. ABAQUS offers two specialized algorithms to deal with unstable nonlinear problems: the modified RIKS algorithm and the STABILIZE algorithm.

The RIKS method is designed for geometrically nonlinear collapse and global post-buckling analysis, but can include nonlinear materials. The load is treated as an unknown, and the solution is carried out for the load and displacement simultaneously. The progress and increment of the solution is measured by an arc length over the static equilibrium path (ABAQUS, Inc 2004). The "STABILIZE" algorithm is suitable for cases where the instabilities are local, in which case global load control becomes inappropriate. Stabilization is effected by applying damping (dashpots) throughout the model such that the viscous forces are sufficiently large to prevent instantaneous buckling or collapse, but small enough so as not to affect stable behaviour (ABAQUS, Inc 2004). Both methods were considered in the FE analyses carried out.

5.2.2. Investigation of Model Parameters

Having decided on the appropriate meshing element (CPS8) and identified the material models and analysis techniques, the various modelling parameters were investigated. To start with, the size of the mesh that would diminish mesh sensitivity was determined. Then, the effect of shear retention was evaluated, and tension stiffening was investigated in some detail to enable proper prediction of deflections.

5.2.2.1. Mesh Size

ABAQUS does not consider mesh sensitivity to be a prominent issue for RC with reasonably distributed cracks. Nevertheless, mesh sensitivity was investigated. For that purpose, GFRP and steel beams and slabs were considered in order to cover the reinforcement modulus range. Beam and slab series BG2 and SG2 were chosen because their reinforcement ratios were not extreme, but within the investigated range. The stress-strain concrete softening relationship was considered to be linear. Too little tension stiffening can result in unstable behaviour, whereas too much tension stiffening makes it easier to obtain a numerical solution; though at the expense of a stiffer response. Therefore, at this stage, maximum strain (ε_{max}) and crack opening (u_o) in the concrete softening models were chosen at the lowest values that would enable a numerical solution, though not necessarily the correct values to predict the response. However, mesh sensitivity was confirmed to follow similar trends as those obtained herein for the realistic tension stiffening levels that were identified later.

Different mesh sizes were considered for each beam and slab, keeping the individual elements as close to square as possible in every case, as detailed in Figure 5-5. The beam mesh sizes ranged from a coarse mesh (~250 mm square) to a fairly detailed mesh (~62.5 mm square). Similarly, the slab mesh sizes ranged from a coarse mesh (~120 mm square) to a fine mesh (~40 mm square).

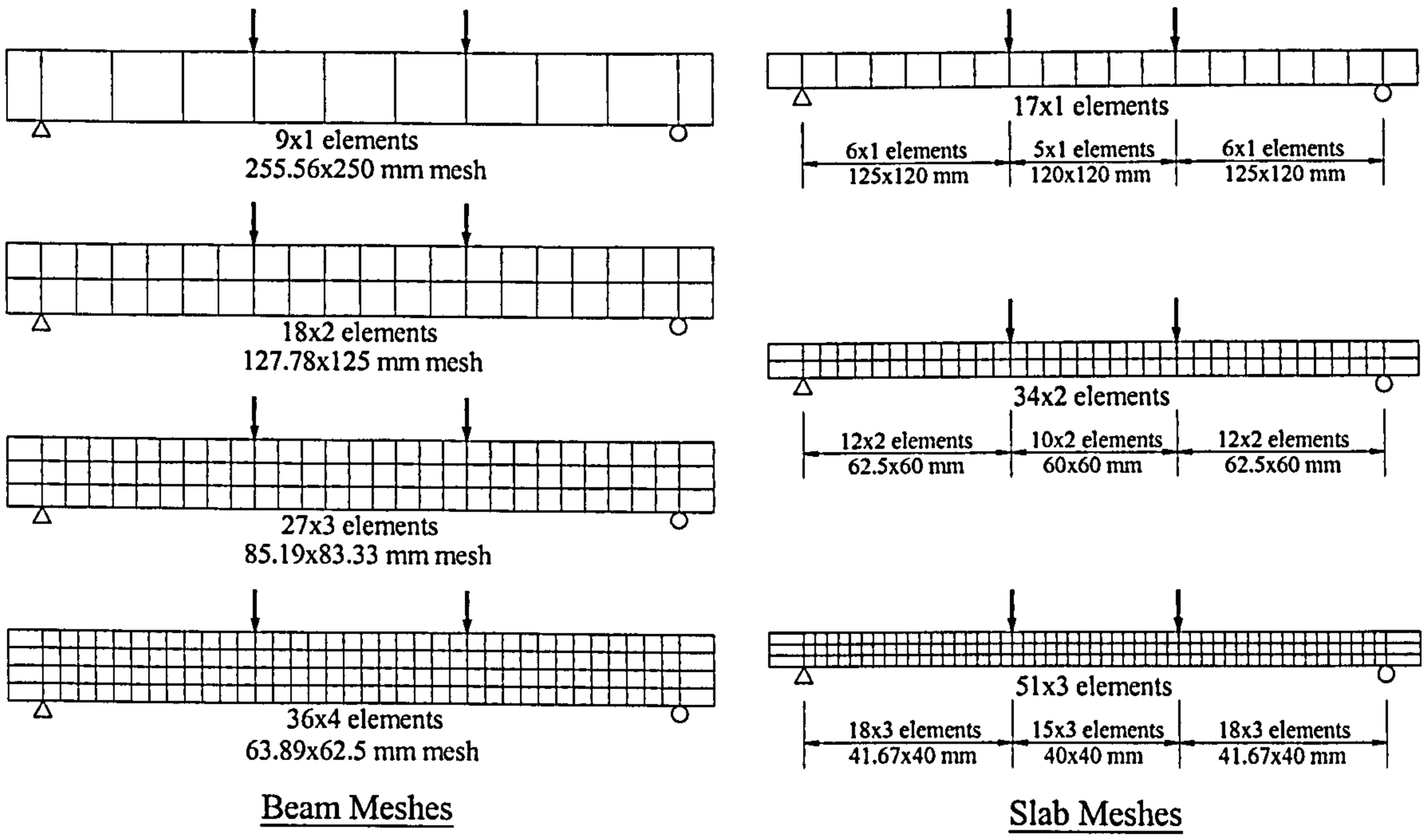

Figure 5-5: Meshes of beams and slabs.

The choice of the appropriate mesh size was based on the load-midspan deflection response. To start with, mesh sensitivity was evaluated for beam BG2 using the fracture energy concrete softening approach, setting u_o=0.22, as shown in Figure 5-6. The results show that, in this application, mesh sensitivity is an issue. Apparently, the energy approach is more suited for the applications for which it was originally designed, such as plain and lightly reinforced concrete, as mentioned earlier. Mesh sensitivity may be diminished with a finer mesh. However, with the finest mesh used, the solution starts to suffer from numerical convergence problems. Therefore, the fracture energy concrete softening approach was discarded.

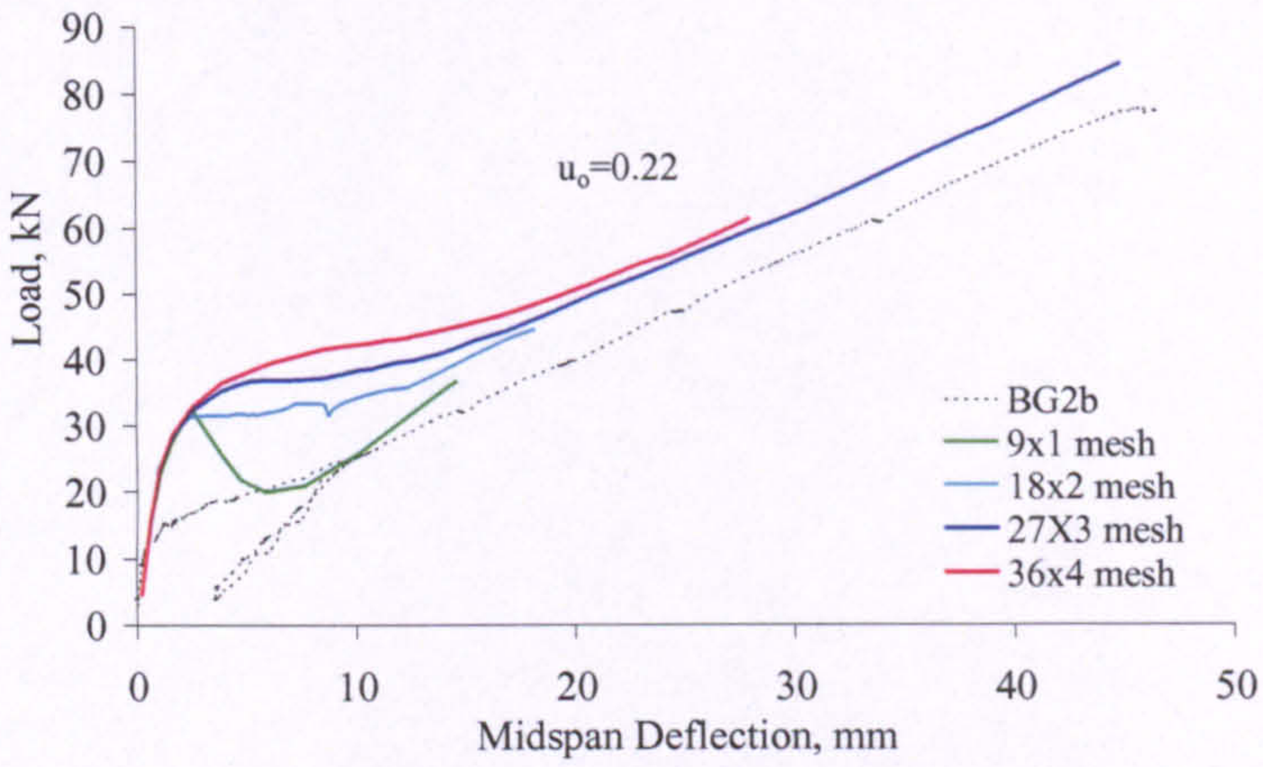

Figure 5-6: Mesh sensitivity of beam BG2- fracture energy concrete softening.

Subsequently, mesh sensitivity was evaluated for the same beam BG2, using the stress-strain concrete softening approach, setting ε_{max}=0.0054, as shown in Figure 5-7. Meshes that are finer than the relatively coarse 18x2 mesh converge to effectively the same solution. However, the finest 36x4 mesh shows numerical problems, whereas the 27x3 mesh shows numerical stability, enabling the solution to proceed to a higher load.

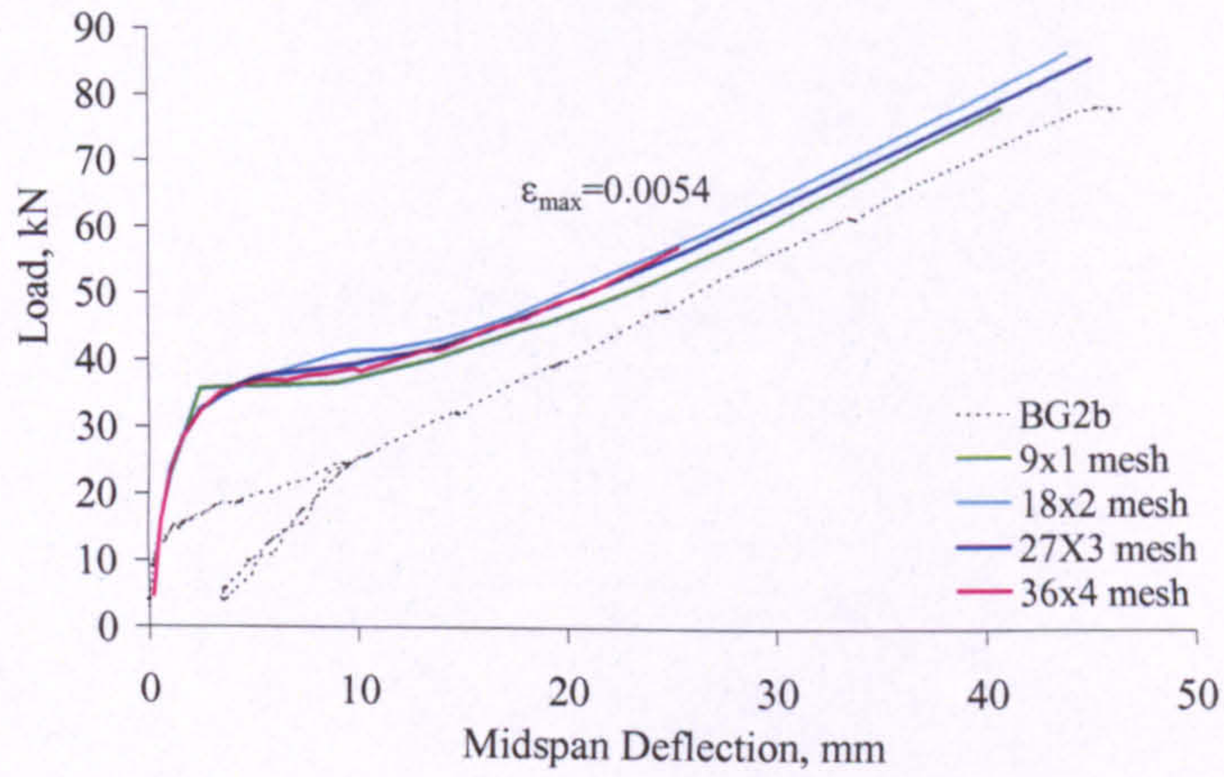

Figure 5-7: Mesh sensitivity of beam BG2- stress-strain concrete softening.

A similar mesh sensitivity analysis was carried out for the other extreme case (beam BS), using the stress-strain concrete softening approach and setting ε_{max}=0.0013, as shown in Figure 5-8. The effect of the mesh size was similar to that of beam BG2. Therefore, a 27x3 mesh (~83.3 mm square) was considered satisfactory for all the beams.

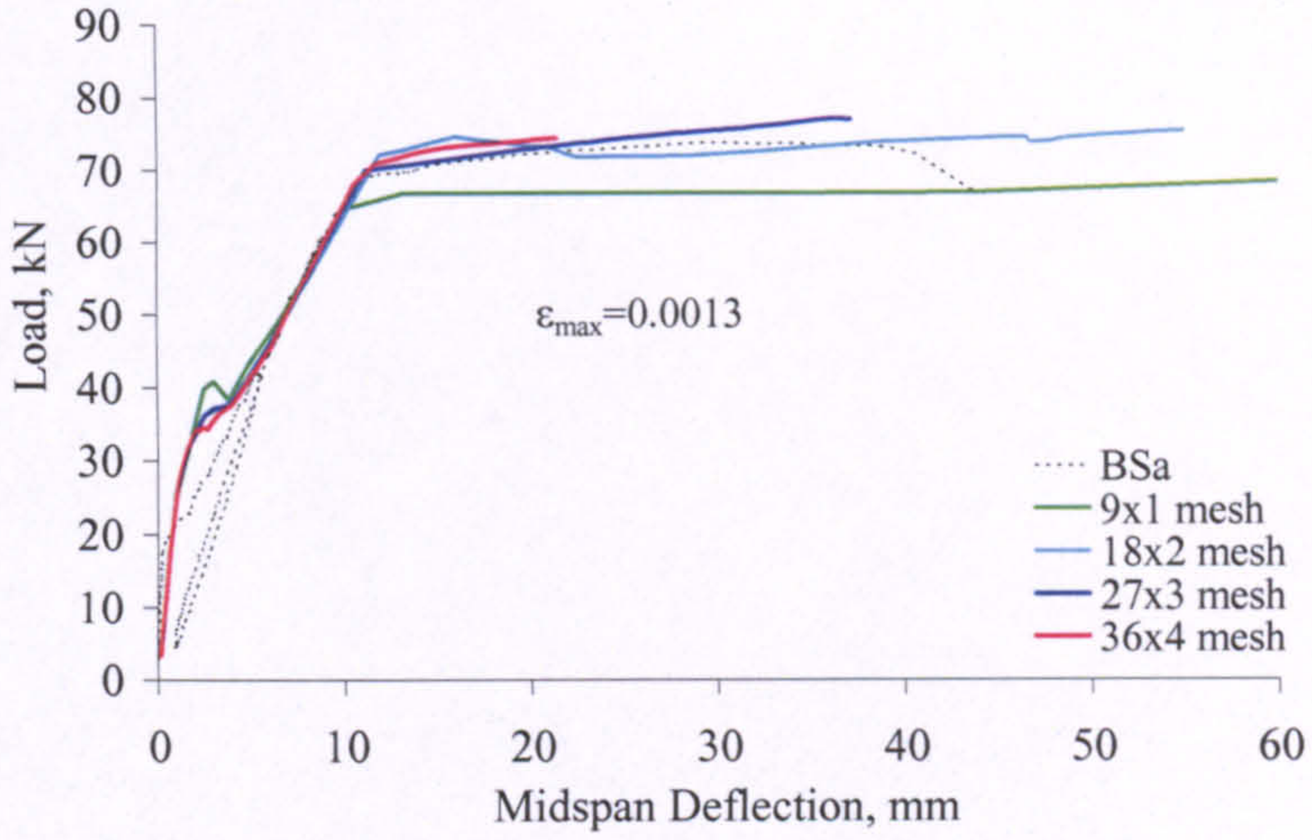

Figure 5-8: : Mesh sensitivity of beam BS- stress-strain concrete softening.

Another similar mesh sensitivity analysis was carried out for the slabs. The results are shown in Figures 5-9 and 5-10 for slabs SG2 and SS, respectively. The 34x2 mesh (~62.5 mm square) appears to be suitable to diminish mesh sensitivity and to provide numerical stability, and was therefore considered appropriate for all the slabs.

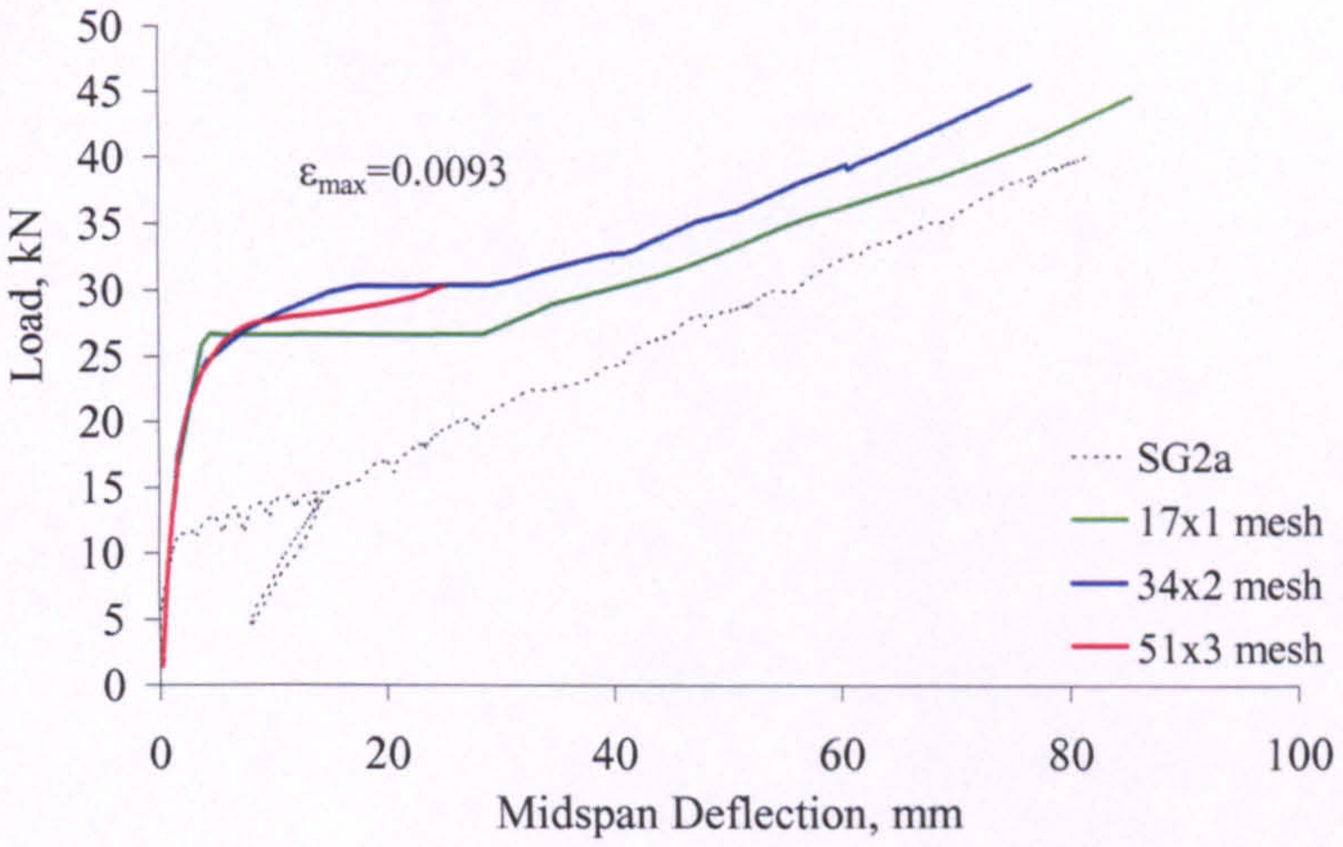

Figure 5-9: Mesh sensitivity of slab SG2- stress-strain concrete softening.

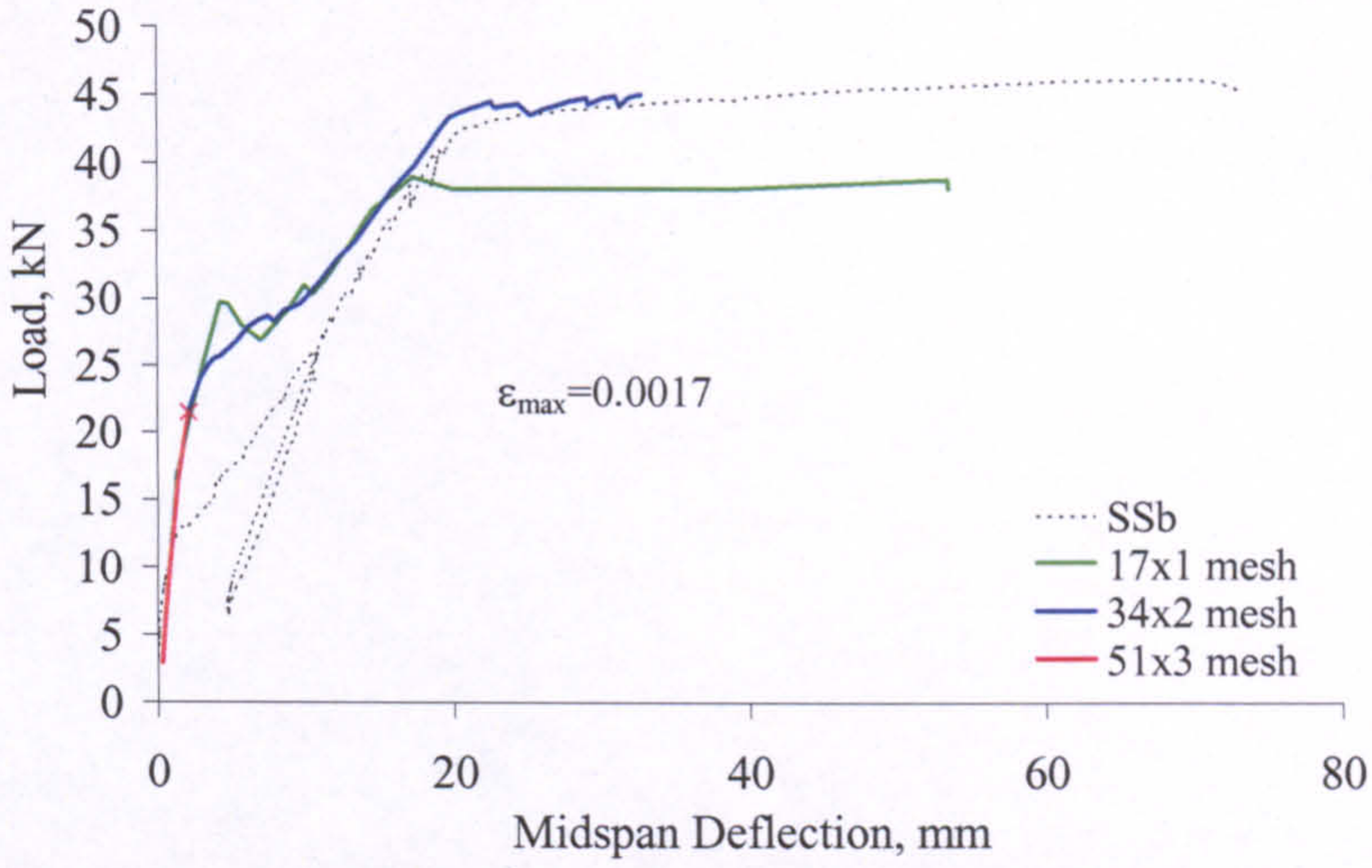

Figure 5-10: Mesh sensitivity of slab SS- stress-strain concrete softening.

5.2.2.2. Shear Retention

In the tests carried out, GFRP RC members develop the widest cracks because GFRP reinforcement has the lowest modulus of elasticity. Moreover, shear deformations are expected to be more prominent in beams than in slabs, as beams have lower span to depth ratio. Therefore, the effect of the shear retention factor was investigated for beam BG2, as shown in Figure 5-11. Again, the analysis was based on a linear concrete stress-strain softening model with the lowest ultimate strain that would enable a numerical solution (ε_{max}=0.0054). Three values were used for the maximum strain in the shear retention model (ε_{max}=0.0035, 0.0054 and 0.009), in addition to the full retention case.

The results show that shear retention has negligible effect on the load-deflection response, indicating that either shear deformations are insignificant or the shear retention approach is inadequate to deal with shear cracking. In fact, no stirrups were used in the model in the shear span, which physically should have resulted in premature failure due to shear. However, this was not the case as the solution proceeded to develop the full flexural capacity. Moreover, identical solutions were obtained with or without stirrups in the model, as shown in Figure 5-11. The transverse strains in the shear span did not exceed a very low value of 200 microstrains, as shown in Figure 5-12. Therefore, it was concluded that ABAQUS formulation is flexure-based and is

inappropriate to deal with shear effects. On the other hand, the convergence of the solution becomes more difficult as shear retention is reduced. Therefore, only full shear retention was considered in all FE analyses.

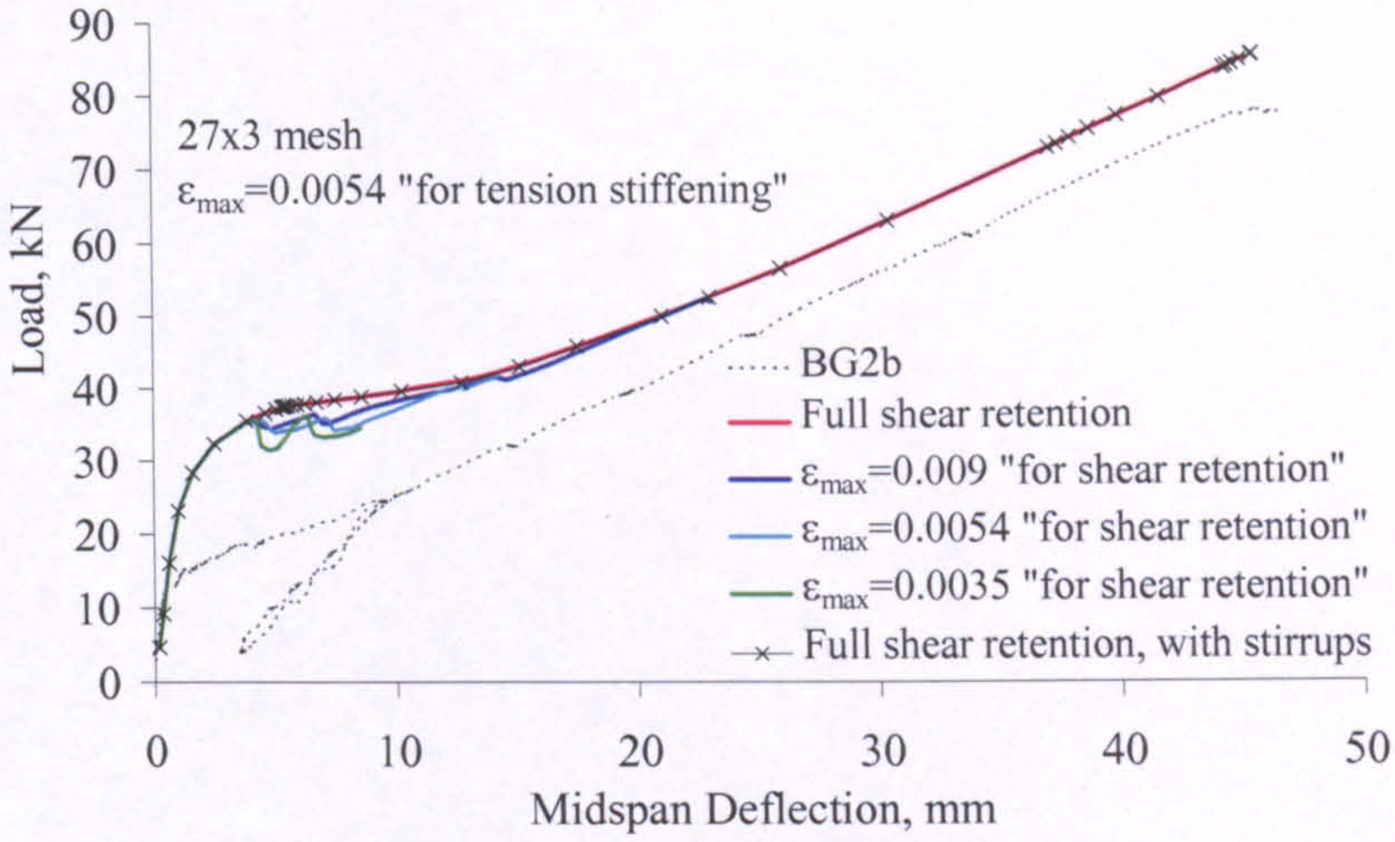

Figure 5-11: Effect of shear retention for beam BG2.

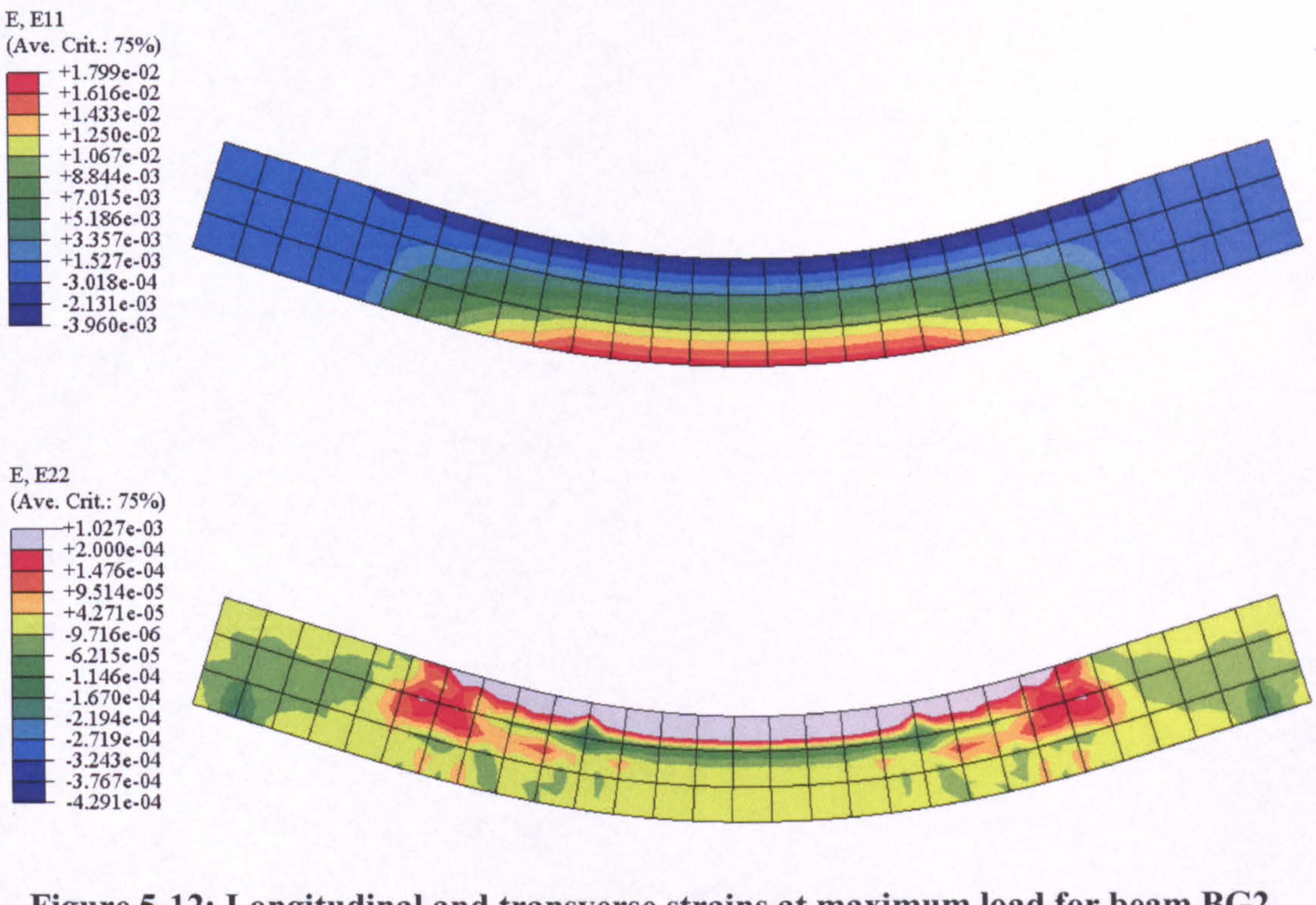

Figure 5-12; Longitudinal and transverse strains at maximum load for beam BG2 (ε_{max}=0.0054, full shear retention with stirrups).

5.2.2.3. Tension Stiffening

As explained earlier, ABAQUS allows for tension stiffening by modifying the concrete softening behaviour. However, ABAQUS has effectively no guidance either on the path of the stress-strain concrete softening curve or on the value of ε_{max} (the maximum strain with zero tensile stress). Therefore, it was necessary to investigate tension stiffening in some detail. GFRP RC beam BG2 was considered for that purpose because, whilst evaluating mesh sensitivity, it became evident that unrealistically high tension stiffening levels were required to obtain a numerically stable solution.

Initially, the predicted load-midspan deflection response of beam BG2 was evaluated against the corresponding experimental behaviour considering a linear concrete softening relationship with a range of ε_{max}, as shown in Figure 5-13. At ε_{max}=0.0054, the solution converges easily, but the tension stiffening introduced is too high, which enormously stiffens the response. By using lower values for ε_{max} the predicted response improves slightly, but the solution becomes increasingly unstable while tension stiffening remains too high. On the other hand, the predicted first crack load is effectively increased as a result of the exaggerated tension stiffening. In contrast, the experimental first crack load can be predicted very well by using first principles and employing the measured concrete split cylinder tensile strength. This means that the concrete strength variability of the member cannot be responsible for the apparent discrepancy in the first crack load.

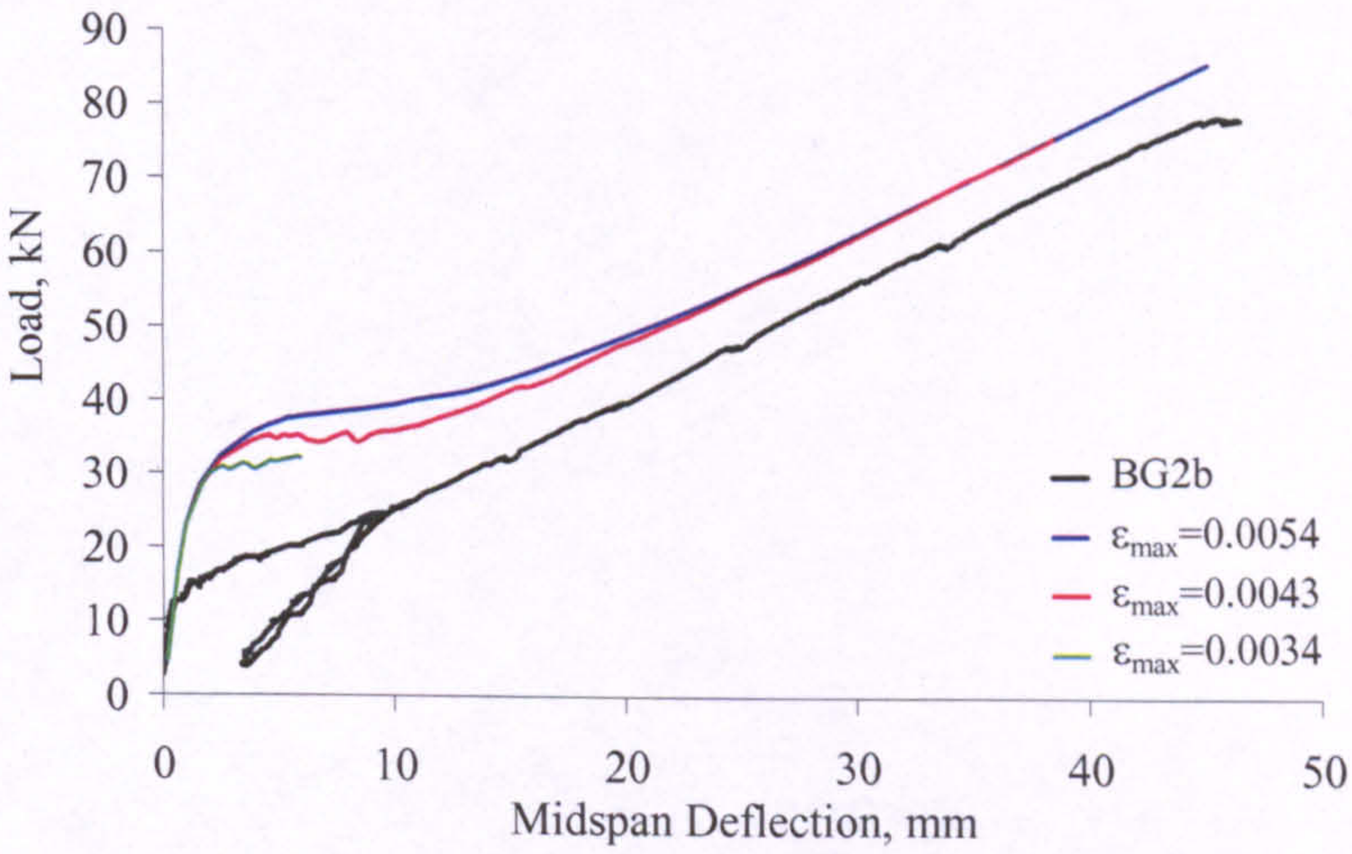

Figure 5-13: Effect of tension stiffening – beam BG2.

All the previous FE analyses were undertaken with the RIKS nonlinear analysis algorithm. The STABILIZE algorithm was investigated at this point to find if it can enable lower tension stiffening values, which it did to a good extent, as shown in Figure 5-14. An almost complete response was obtained at $\varepsilon_{max} = 0.002$, and the load-deflection prediction now compares rather well with the test results. However, the response by the STABILIZE option is very "noisy", which raises questions as to how much impact this solution algorithm has on the predicted results. Besides, similar to the RIKS algorithm, the convergence of the solution becomes increasingly worse as tension stiffening is further reduced. Therefore, the use of the STABILIZE algorithm was not considered any more.

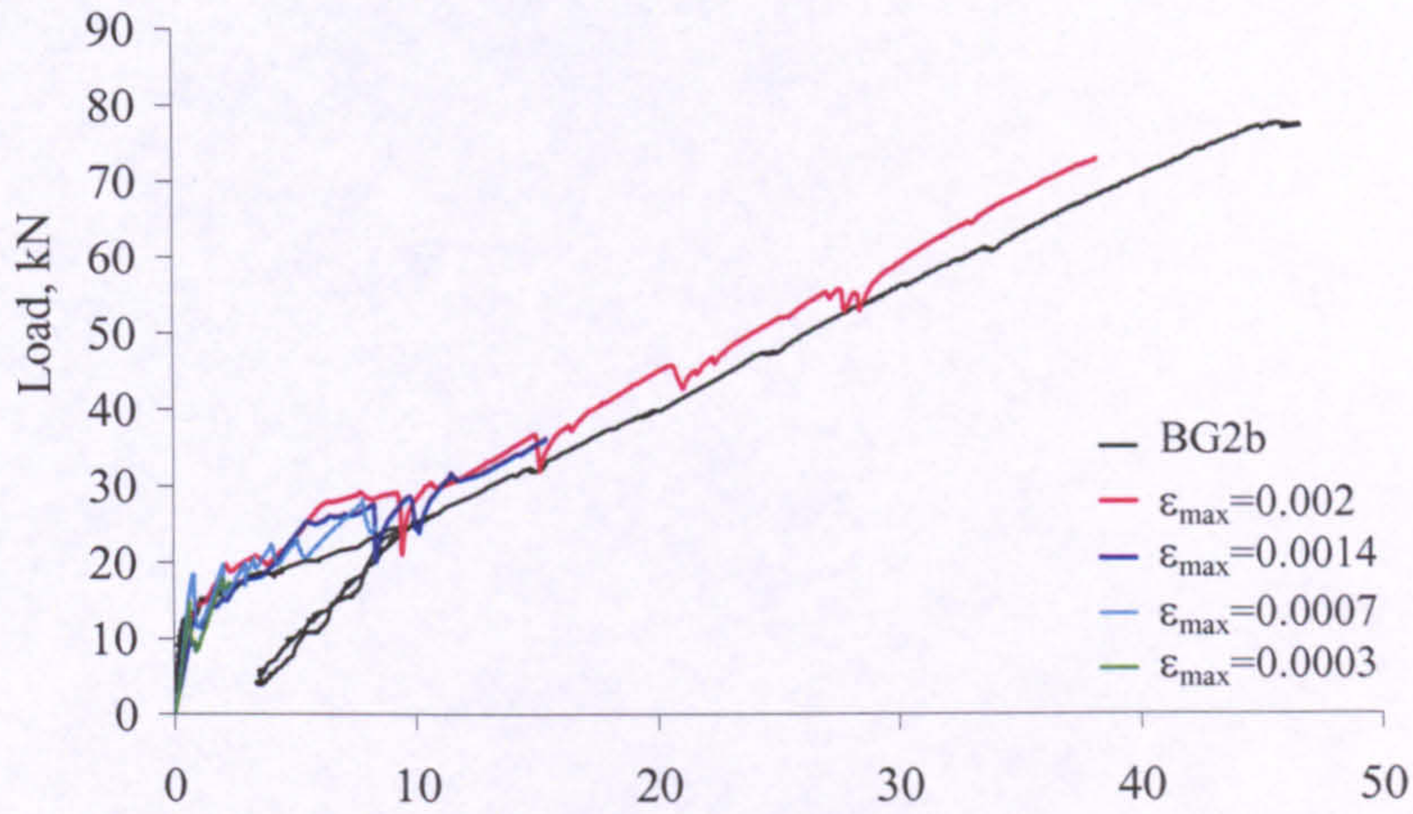

Figure 5-14: STABILIZE nonlinear solution – beam BG2.

An exponential-decay curve is more realistic to represent concrete softening, but leads to worse instability as the crack energy is released at a faster rate. The only remaining option was to reduce tension stiffening by lowering the actual concrete tensile strength ($\sigma_{cr}=f_{ct}$). The concrete softening branch could then be poly-linear or curved. In terms of post-cracking energy, all three tension stiffening approaches can be equivalent, and are clarified in Figure 5-15. Physically, lowering the concrete tensile strength can have some effect on shear behaviour, but this is immaterial because ABAQUS formulation has been discussed to be flexure-dominated. A lower concrete tensile strength can also soften the response by reducing the cracking load and increasing the extent of cracking along the member. However, softened behaviour may be compensated by tension stiffening.

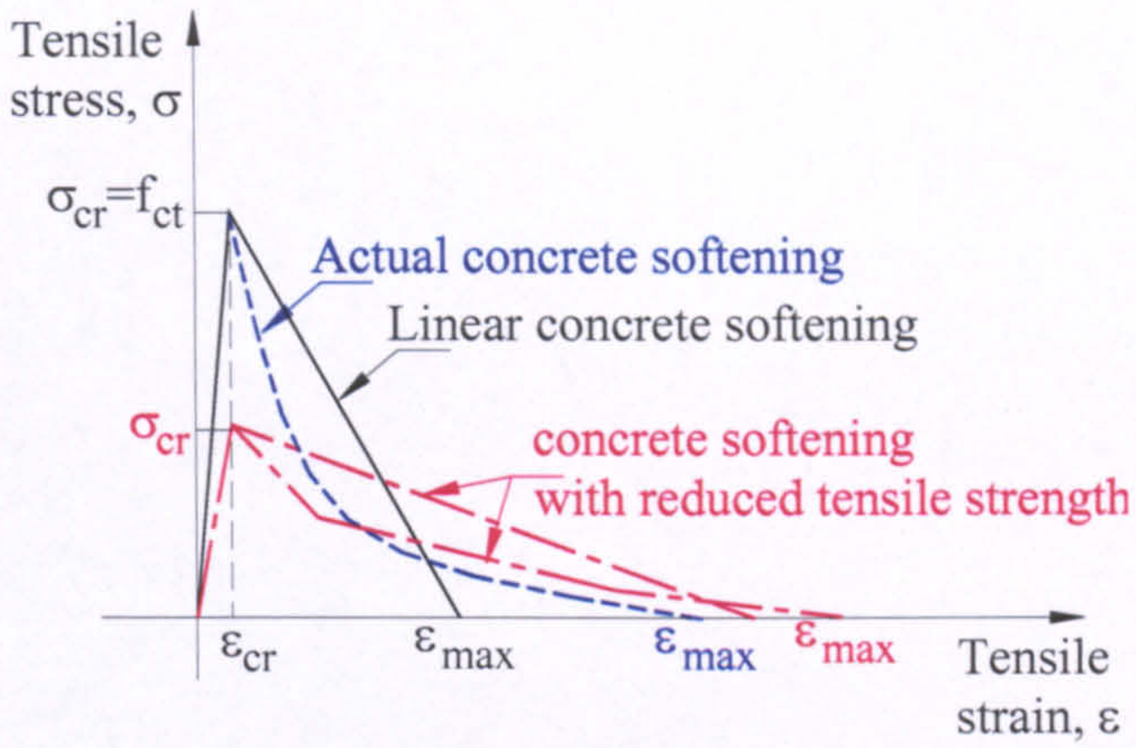

Figure 5-15: Alternatives of implementing tension stiffening.

The approach of tension stiffening with reduced tensile concrete strength was used in the FE analyses of beams and slabs. Either a linear or bilinear concrete softening branch was used, as appropriate. Tension stiffening was "calibrated" based on the load-deflection response of each test. If such tension stiffening is compared between different tests, it may be helpful in formulating a proper theoretical tension stiffening model that is based on physical variables. This latter methodology is not attempted in this study.

5.2.3. Investigation of Beams and Slabs

Having considered all FE modelling and analysis aspects, ABAQUS was used to investigate all the tested GFRP RC and representative CFRP RC beams and slabs (BC2 and SC2). Tension stiffening was chosen to predict the experimental load-deflection response as close as possible. The predicted rebar and concrete strains were then examined against the corresponding test results. The FE analysis predictions are discussed together with the experimental results in the next chapter. Sample FE analysis results are presented as follows, while all results are shown in Appendix B.

Figure 5-16 shows an almost spot-on prediction by ABAQUS of the load-midspan deflection response of beam BG2. Tension stiffening was defined by ε_{max}=0.003 and a reduced tensile concrete strength σ_{cr} =0.035f_{cm}, where f_{cm} is the average uniaxial compressive strength. Figure 5-17 shows that, soon after formation of the induced and adjacent cracks, ABAQUS overestimates the average strain between cracks. As the

load increases, tension stiffening reduces and the predicted strain tends to the maximum strain at the crack. ABAQUS prediction of concrete strain at the top concrete fibre at midspan was very good in this particular case, as shown in Figure 5-18. The prediction of central curvature compares well with the curvature derived from experimental strains up to a load of about 23 kN, just beyond formation of the cracks, as shown in Figure 5-19. At higher loads, the curvature is overestimated. Therefore, how could ABAQUS do such a good prediction of the experimental deflection if curvatures or rebar strains are overestimated? By examining the strain profiles along the span at discrete load levels, as shown in Figure 5-20, it is evident that ABAQUS underestimates the actual rebar strains in the shear span. The larger shear span strains are associated with shear-flexure interaction and may have compensated for the overestimated strains, hence curvatures, in the constant flexure zone. As mentioned, these issues will be discussed in more detail in the next chapter.

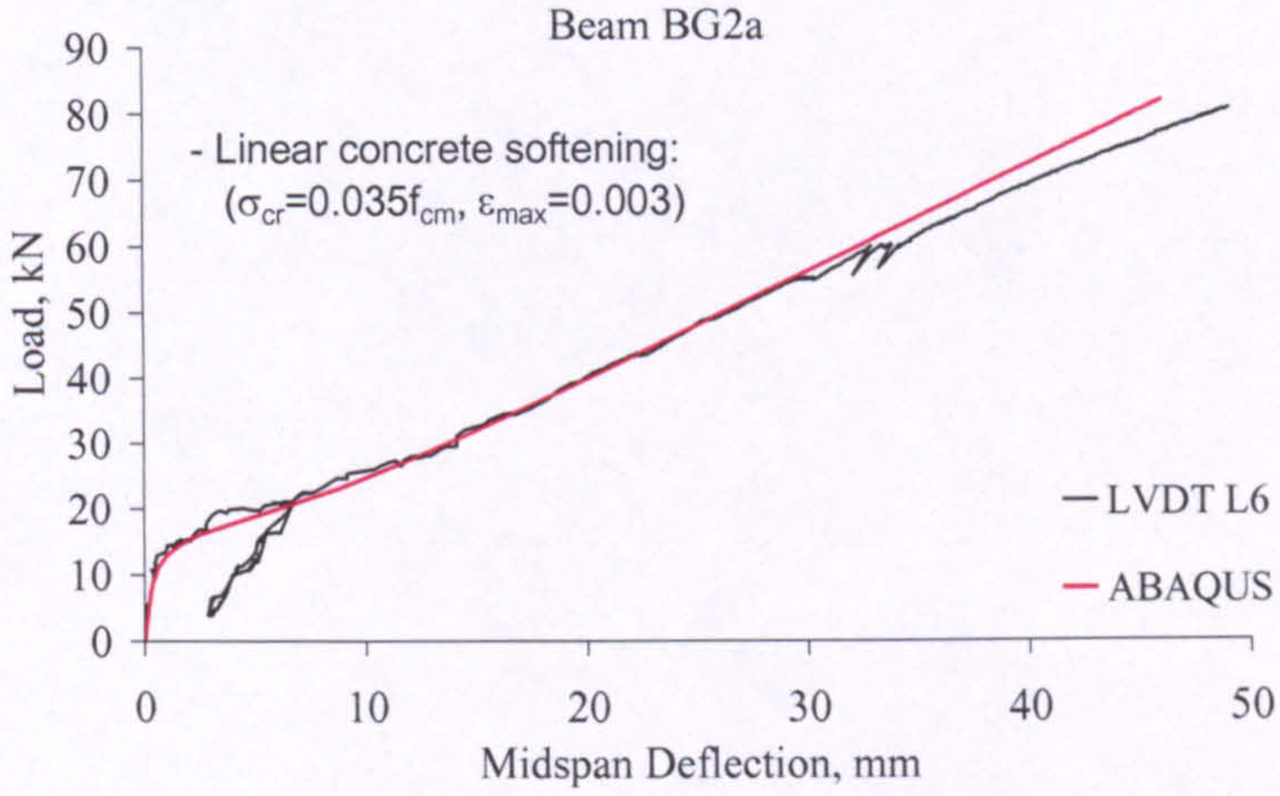

Figure 5-16: ABAQUS prediction of load-midspan deflection.

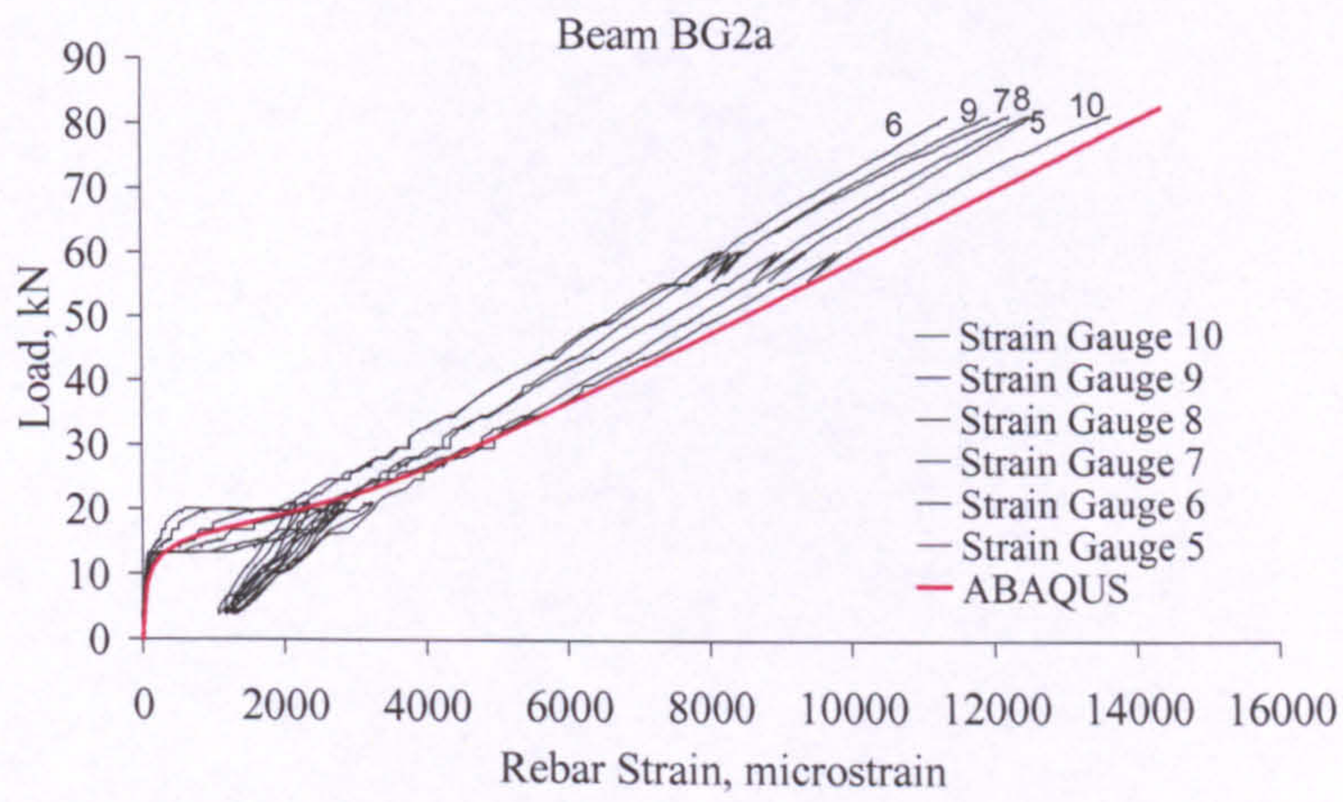

Figure 5-17: ABAQUS prediction of load-rebar strain.

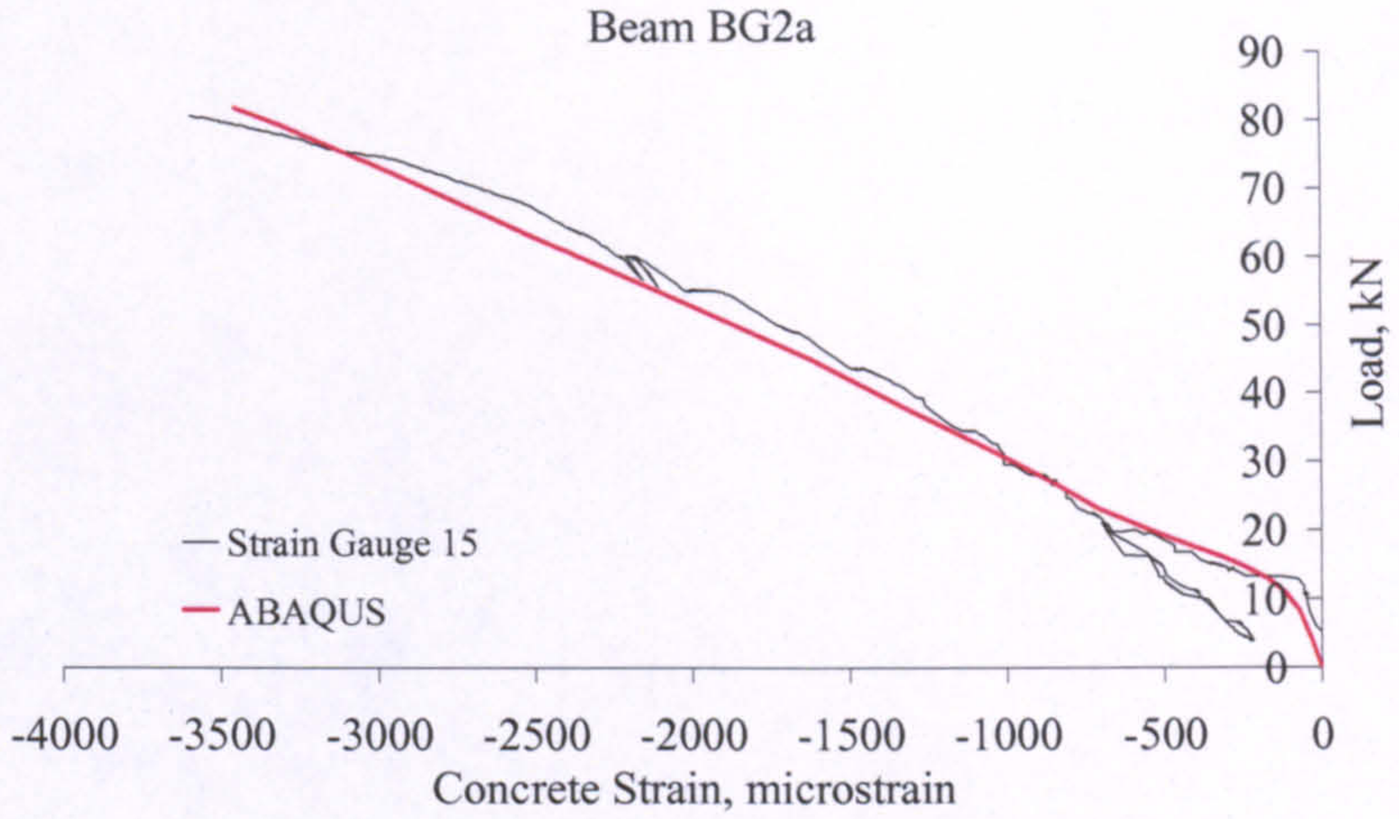

Figure 5-18: ABAQUS prediction of load-concrete strain.

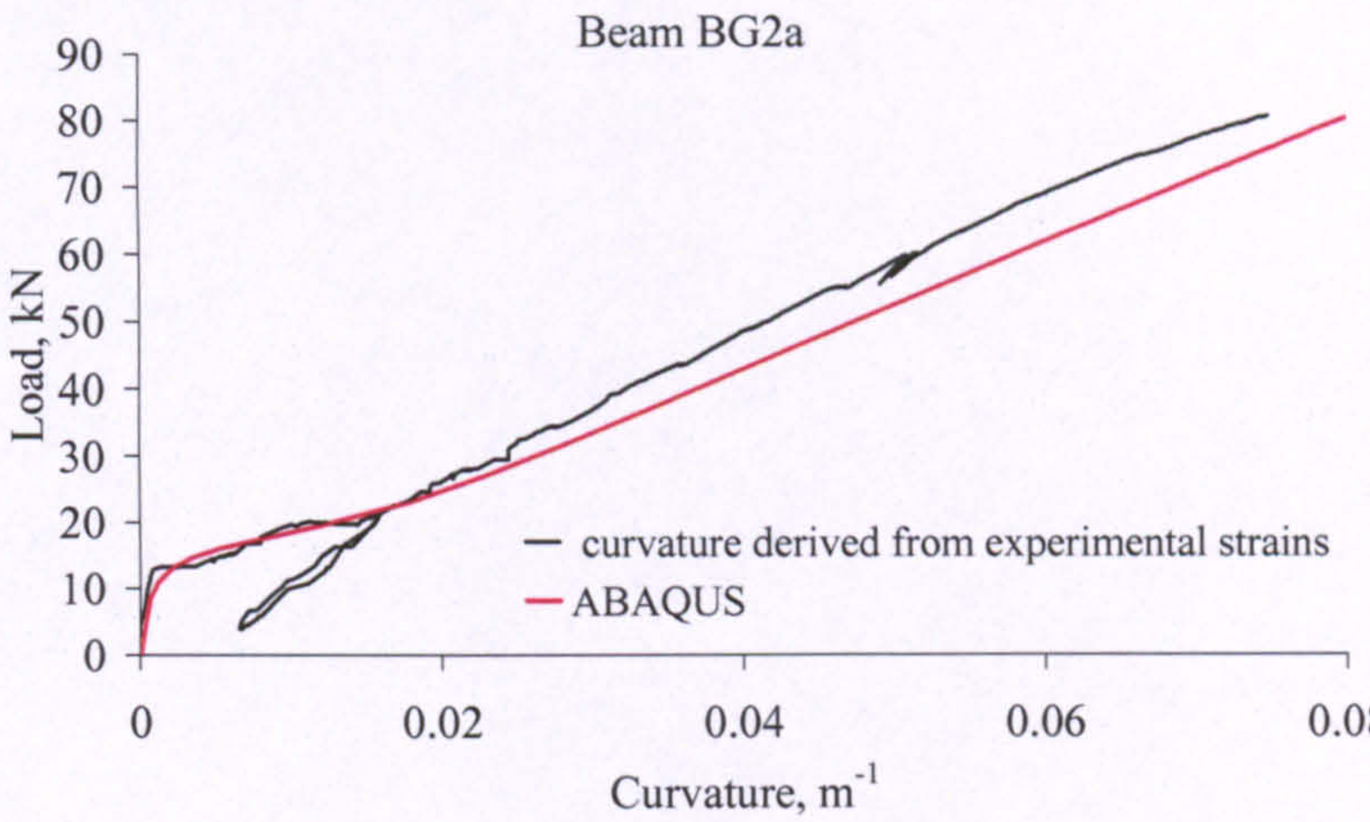

Figure 5-19: ABAQUS prediction of load-curvature.

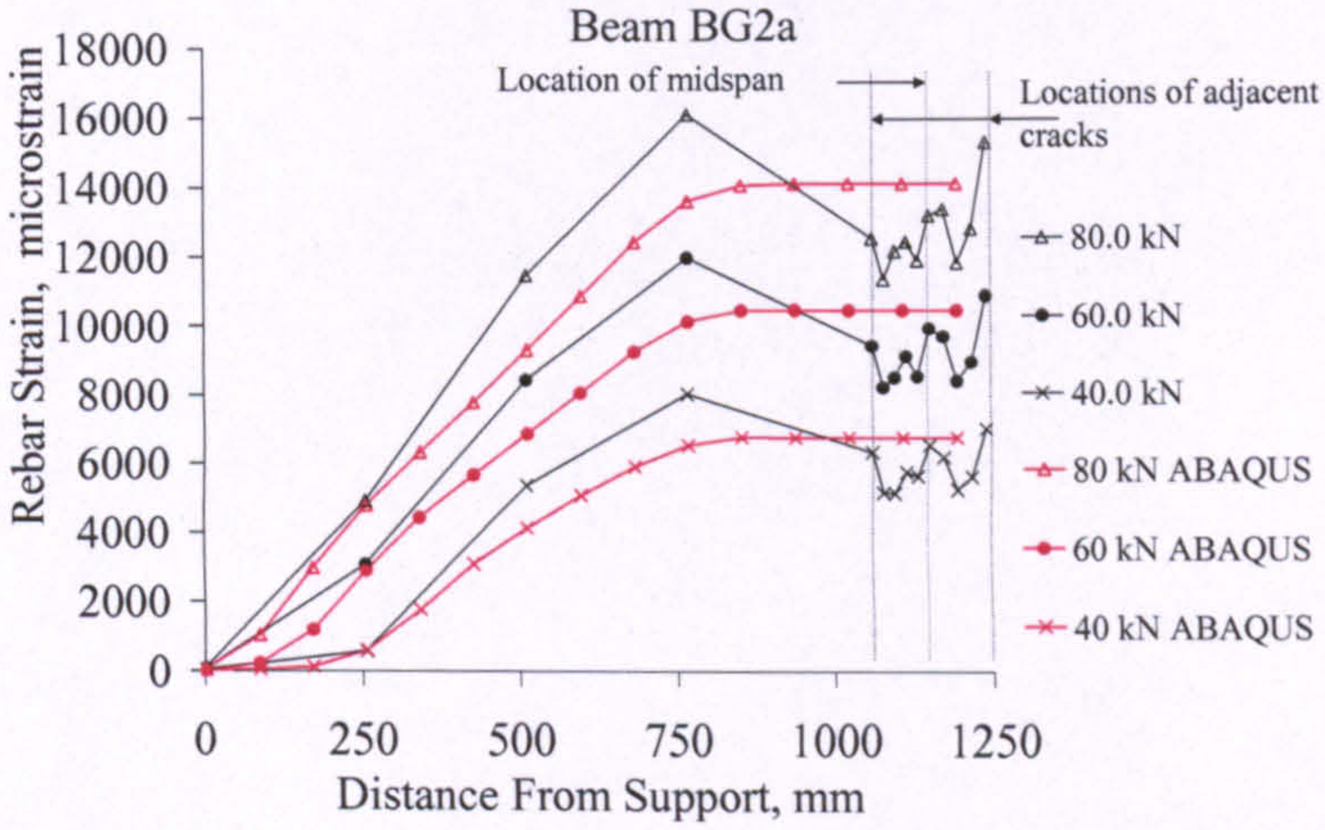

Figure 5-20: ABAQUS prediction of rebar strain profiles.

5.3. CRACKED SECTION ANALYSIS

Cracked section analysis (CSA) was briefly introduced in Chapter 2 in connection with prediction of flexural capacity. To recapitulate, this analysis assumes that plane sections remain plane, with linear distribution of strains across a cracked section and perfect bond between reinforcement and concrete. It also assumes tension-free concrete below the neutral axis, and uses one dimensional material constitutive laws for both concrete and reinforcement. In the following sections, CSA is closely examined and its implementation in this study is explained. CSA is then used to predict the behaviour of all the tested beams and slabs. Similar to FE analysis, only sample CSA results are shown herein, whereas the detailed discussion of the analytical results in comparison to the corresponding test results is undertaken in the next chapter.

5.3.1. Discussion of Cracked Section Analysis

This discussion aims at relating CSA, which is usually considered on a sectional level, to the behaviour of a concrete block between cracks. Figure 5-21 shows the behaviour stipulated by CSA (in red) and the expected behaviour (in blue) of an RC block centred on a vertical crack in a pure flexure zone. The behaviour is illustrated by the likely profiles of reinforcement and concrete strain, neutral axis and bond stress.

CSA assumes that plane sections remain plane and perfect bond exists between the reinforcement and concrete. These two assumptions actually apply to the section midway between cracks, in deformation terms, and follow from pure geometric considerations in an ideal flexure zone (Bernoulli's principle). The reinforcement at the midway point between cracks does not undergo any slip with the concrete, and this condition is equivalent to perfect bond.

CSA also assumes that the concrete beneath the neutral axis carries no tension, which is equivalent to neglecting the interaction between the concrete and reinforcement. In so doing, CSA neglects tension stiffening and equates the strain along the rebar to its maximum level at the crack.

By imposing a linear strain distribution for the entire depth of the cracked section, CSA smears the effect of the crack and assumes some constant strain at any level in the tension and compressive concrete zones together with a constant neutral axis depth. Ignoring the variation in the tensile strain has no implications because the tension in the concrete is neglected anyhow. However, by using a constant compressive concrete strain, CSA considerably simplifies the actual strain distribution in connection with the variable neutral axis depth along the concrete block.

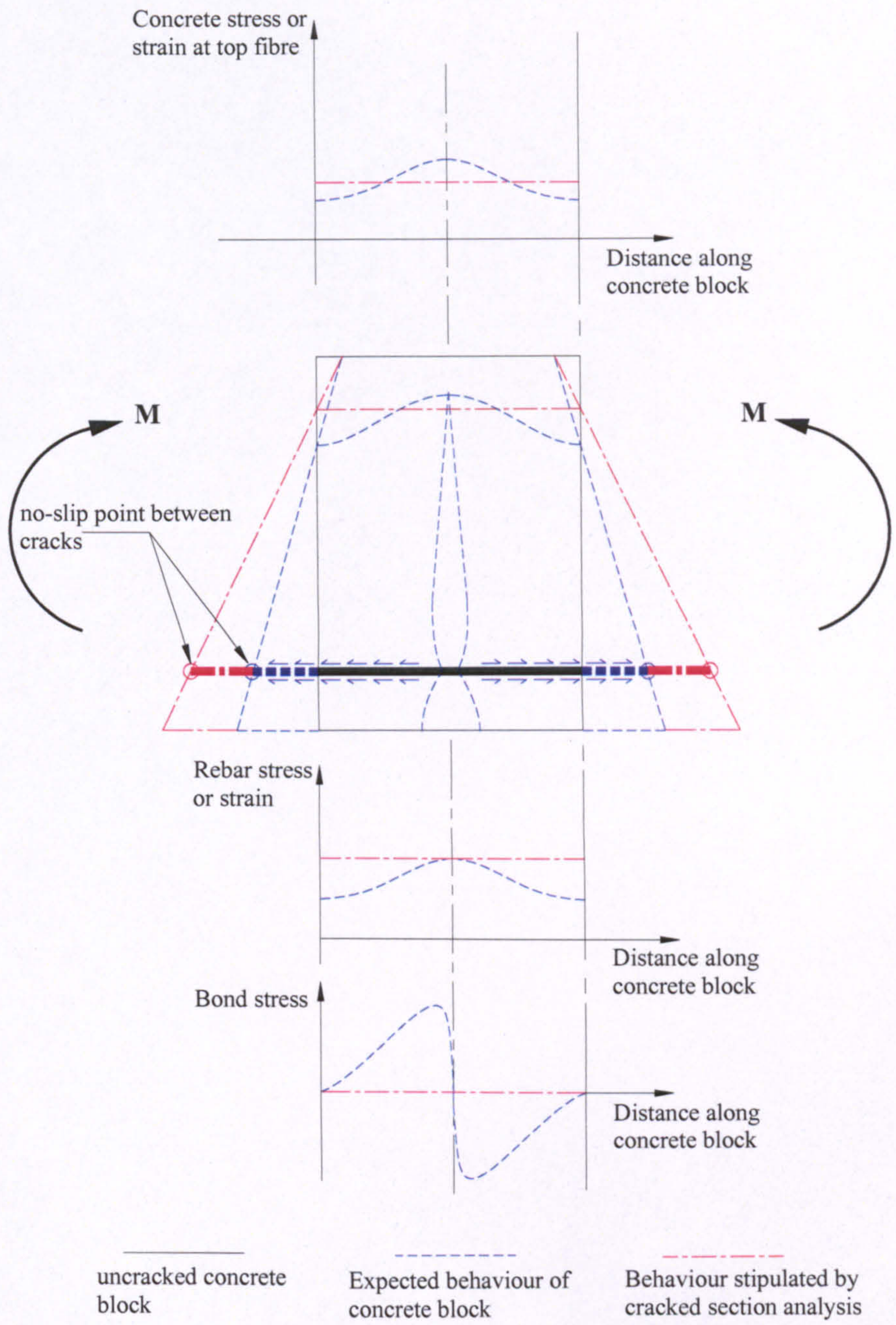

Figure 5-21: Expected behaviour of a concrete block under pure flexure versus prediction of cracked section analysis.

Therefore, when considered on a block level, it can be argued that CSA predicts the maximum rebar strain at a crack but some average strain in the compressive concrete zone. This hypothesis is valid given that plane sections are violated at the cracked sections. Provided the strain distribution of the compressive concrete zone is not too different from the assumed average conditions, CSA is expected to provide an upper-bound solution for flexural curvature and deflection, as well as an almost accurate prediction of flexural capacity. On the contrary, if the assumed average concrete conditions are very different from the actual conditions at the crack, CSA may underestimate the flexural capacity, but may still provide an adequate limiting deflection, because deflection is more dependent on rebar strains. In fact, the prediction of the actual compressive concrete behaviour involves further complications as it may be influenced by other factors, such as the size and long term effects as well as the use of a one-dimensional model for the concrete stress-strain behaviour.

The limiting deflection predicted by CSA may be exceeded if the assumptions of CSA are not satisfied in the first place. This may occur, for instance, in flexural members with high shear stresses, where plane sections do not remain plane and sizeable shear-induced deformations occur. Exceptionally weak bond between the concrete and reinforcement can also result in increased deflection, because this causes some level of non-composite behaviour. A tied arch is one such extreme case.

5.3.2. Implementation of Cracked Section Analysis

Excel spreadsheets were used to computerize CSA, which also enabled a parametric investigation. The implementation of CSA is clarified in Figure 5-22, and is briefly explained as follows.

One-dimensional concrete and reinforcement models, similar to those described in the previous section on FE analysis, were used. At any concrete strain at the extreme compression fibre (ε_{ci}), two unknowns are required to define the strain profile across the entire section, namely, the neutral axis depth (x) and the strain in the reinforcement (ε_{fi}). Two equations are used to solve for these two unknowns: geometric similarity of triangles in the strain diagram and equilibrium of internal concrete and reinforcement

forces, C_c and T_f. A centroidal factor, α, and a location factor, γ, are used to define the magnitude and point of application of C_c. α and γ are determined from the concrete stress-strain constitutive law. Subsequently, the curvature (φ) is determined from the strain profile, and is used to calculate deflection based on the curvature-area theorems. To cover the entire loading range, this process is repeated for ε_{ci} values ranging from zero to the maximum ultimate concrete compressive strain (ε_{cu1}). If the reinforcement ruptures, the analysis is terminated at the corresponding ε_{ci}, which is less than ε_{cu1}.

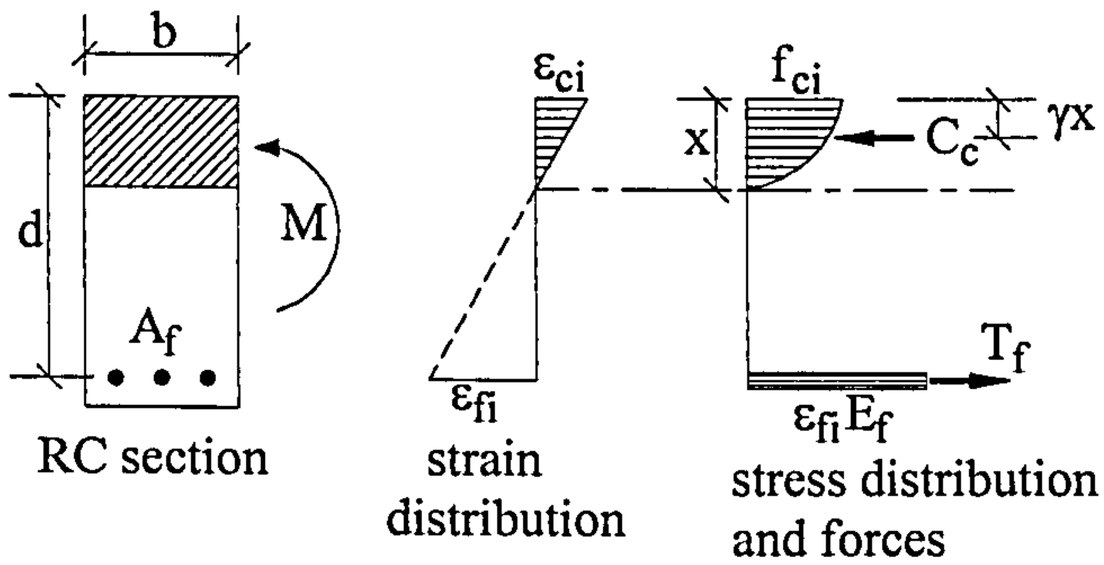

$$\alpha = \frac{\int_0^{\varepsilon_{ci}} f_c d\varepsilon_c}{f_{cm}\varepsilon_{ci}}$$

$$\gamma = 1 - \frac{\int_0^{\varepsilon_{ci}} \varepsilon_c f_c d\varepsilon_c}{\varepsilon_{ci}\int_0^{\varepsilon_{ci}} f_c d\varepsilon_c}$$

$$\varepsilon_{fi} = \varepsilon_{ci}\frac{(d-x)}{x}$$

$$[C_c = \alpha f_{cm} x b] = [T_f = A_f E_f \varepsilon_{fi}]$$

$$M = C_c(d - \gamma x)$$

$$\varphi = \frac{\varepsilon_{ci}}{x}$$

Figure 5-22: Cracked section analysis.

5.3.3. Investigation of Beams and Slabs

CSA was used to investigate the behaviour of all the tested beams and slabs over their entire loading history, by predicting their failure load, rebar and concrete strain at cracked sections as well as upper-bound flexural curvature and deflection. The CSA predictions are discussed together with the corresponding experimental results in the next chapter. Sample results are presented in the following, whereas all results are shown in Appendix B.

Figure 5-23 shows a very good prediction by CSA of the maximum rebar strain at a crack. Figure 5-24 shows that CSA somewhat underestimates the maximum concrete strain at the extreme compression fibre. Figure 5-25 shows that CSA provides an upper-bound curvature, while Figure 5-26 shows less success in predicting an upper-

bound deflection. Once again, increased rebar strains resulting from shear-flexure interaction in the shear span, as shown in Figure 5-27, can be associated with additional deflections. The load capacity is reasonably predicted in this particular case. As mentioned, these issues will be discussed in greater detail in the next chapter.

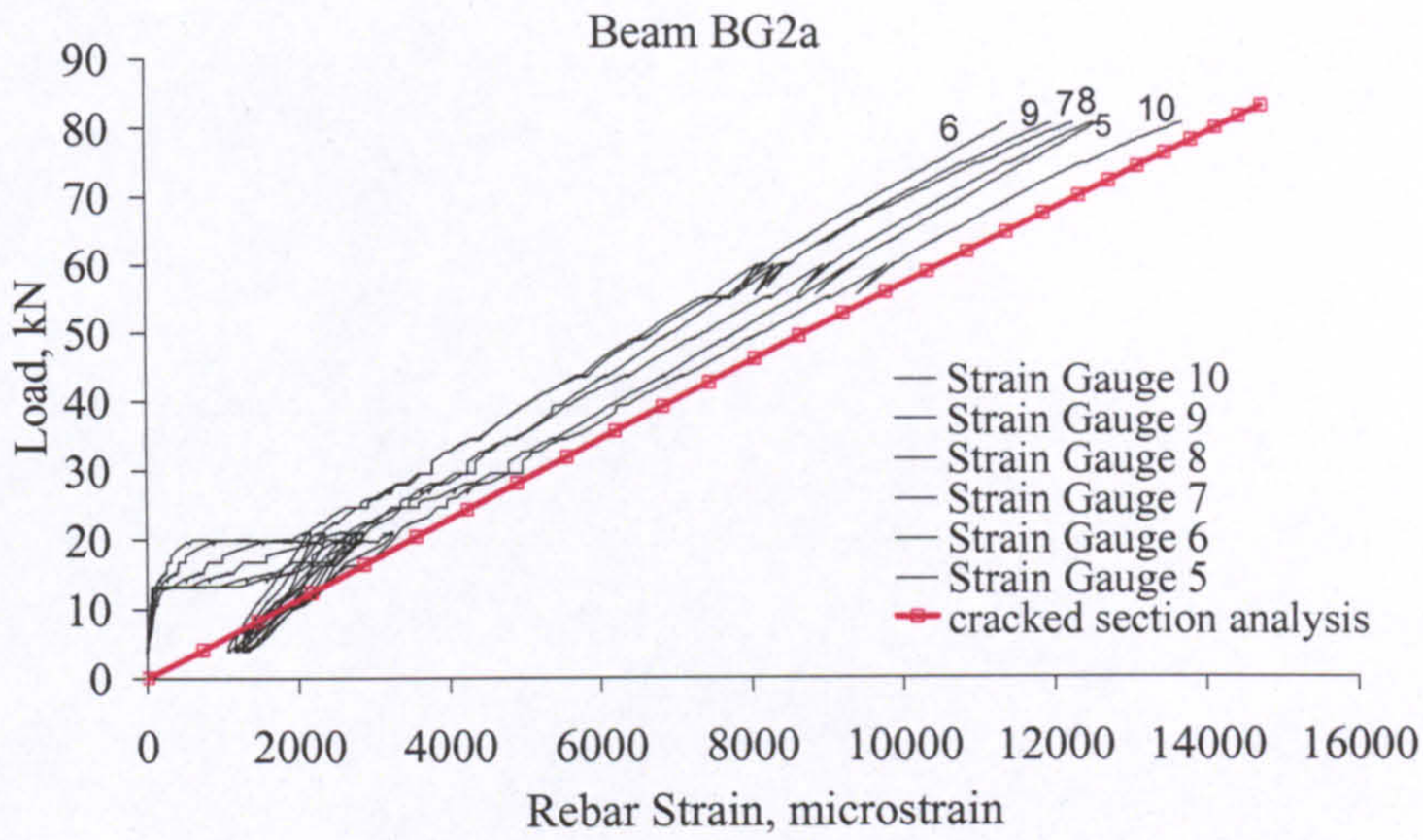

Figure 5-23: CSA prediction of load-rebar strain.

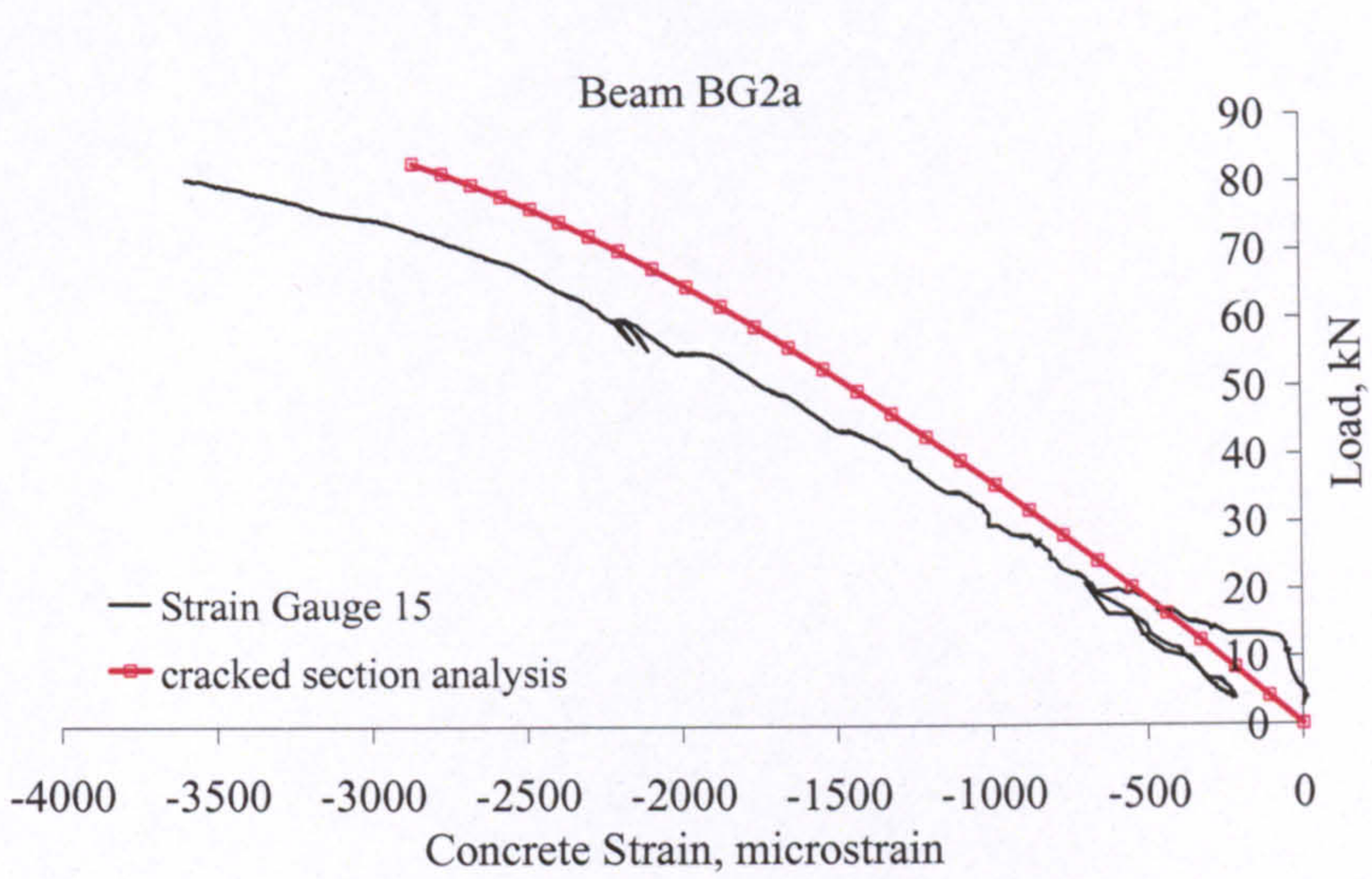

Figure 5-24: CSA prediction of load-concrete strain.

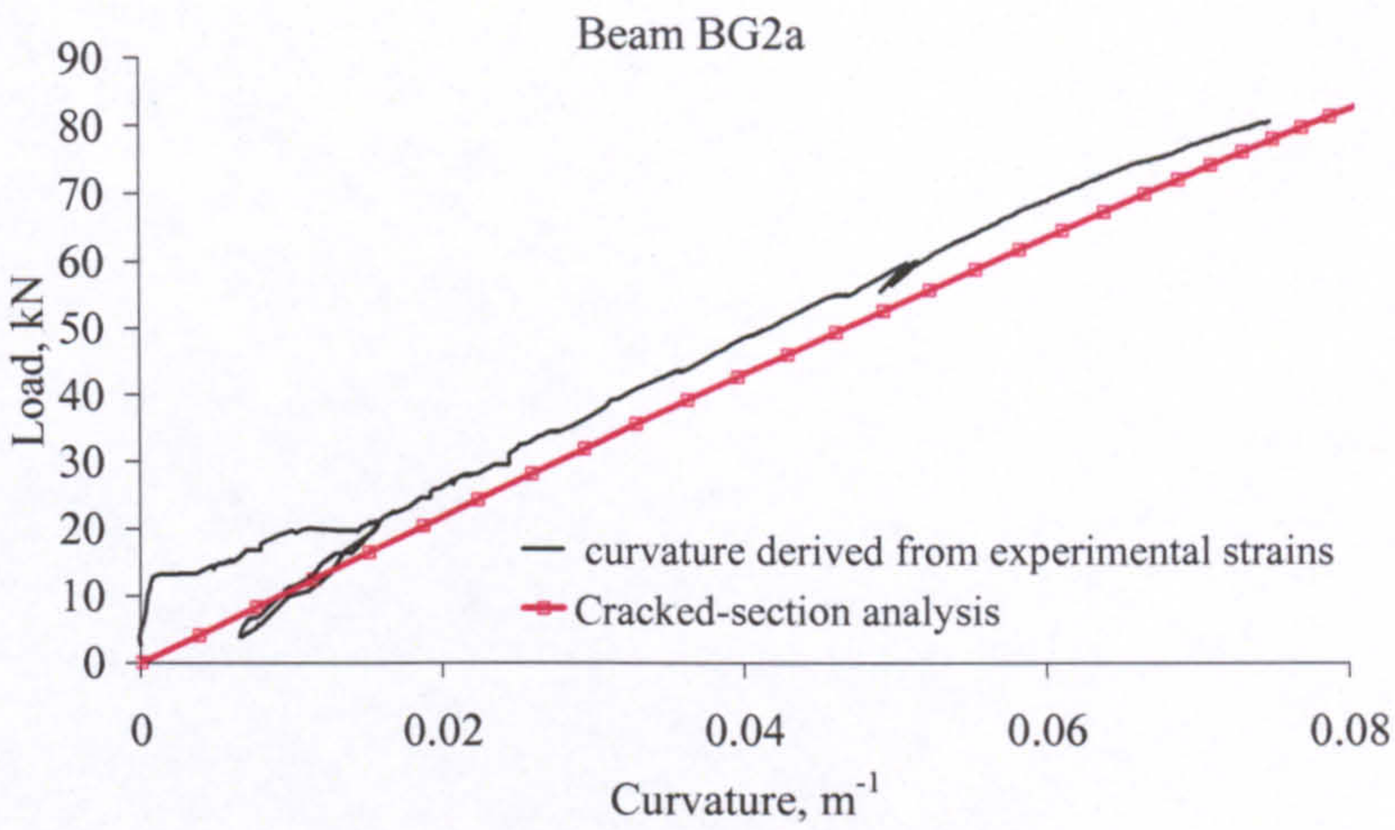

Figure 5-25: CSA prediction of load-curvature.

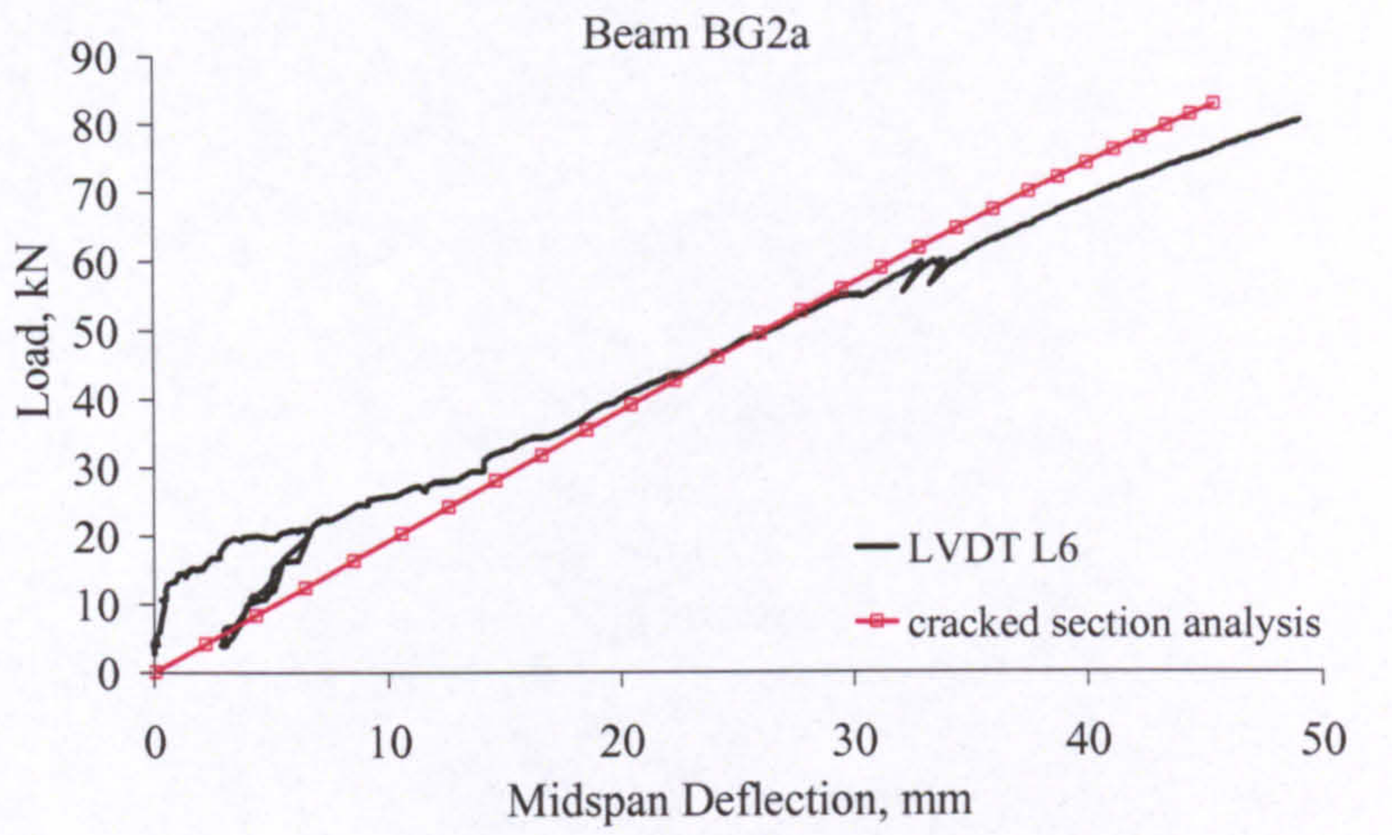

Figure 5-26: CSA prediction of load-deflection.

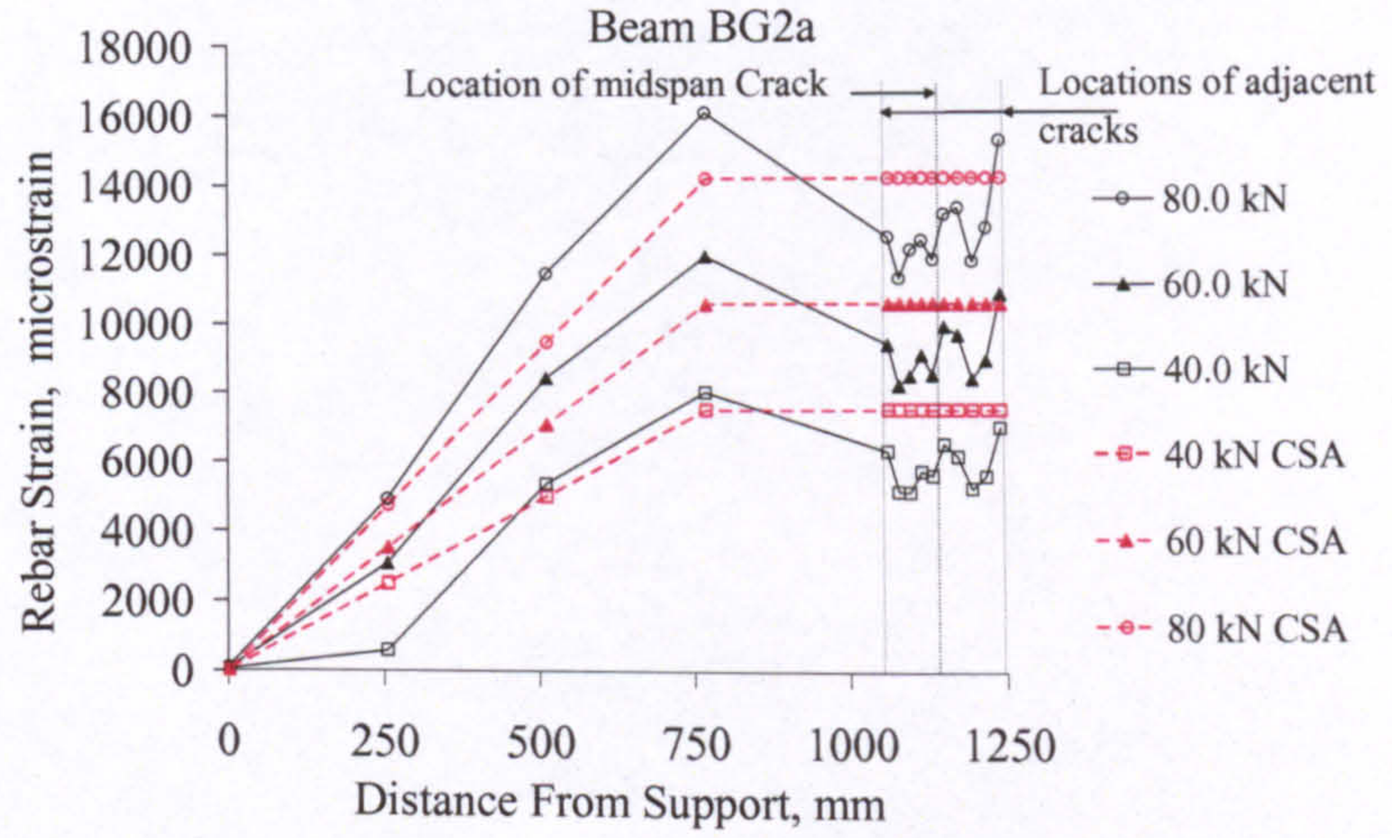

Figure 5-27: CSA prediction of rebar strain profiles.

CHAPTER 6

DISCUSSION ON DEFLECTION

6.1. INTRODUCTION

This chapter discusses the deflection behaviour of the tested FRP RC beams and slabs. The deflections predicted by FE analysis and CSA are also investigated and compared to the experimental results. Flexural deflection is essentially a consequence of curvature along the member, which in turn is a function of longitudinal strains. Therefore, the experimental and predicted rebar and concrete strains are considered initially, whereas curvature and deflection are discussed later in detail. The prediction of failure load is also considered briefly. All through the discussion, the recognised behavioural aspects and practice of steel RC are used as a reference.

The GFRP and CFRP RC members are dealt with separately, because the CFRP RC tests showed some unexpected behaviour that needs to be addressed on its own. Additional FE analyses are undertaken in connection with the particular behaviour of CFRP RC members.

The discussion on deflection concludes with a summary of the factors that affect the development and distribution of curvature along the member, as well as the adequacy of the numerical analysis techniques used.

6.2. GFRP RC MEMBERS

6.2.1. Strain in the Rebars

- CSA

It has been explained in Chapter 5 that, after cracking, CSA is expected to predict the maximum rebar strain at a crack. For the GFRP RC beams and slabs, the prediction of CSA does compare very well with the experimental rebar strains at and around the midspan crack, as typically shown in Figure 6-1. Exceptionally, in slab series SG1, CSA considerably overestimates the rebar strain. This may indicate a large tension force transferred across the cracked concrete section. However, this cannot be the case because, at failure, the rebar strain reached a high level of about 10000 microstrains, which is associated with a very wide midspan crack (> 1.2 mm).

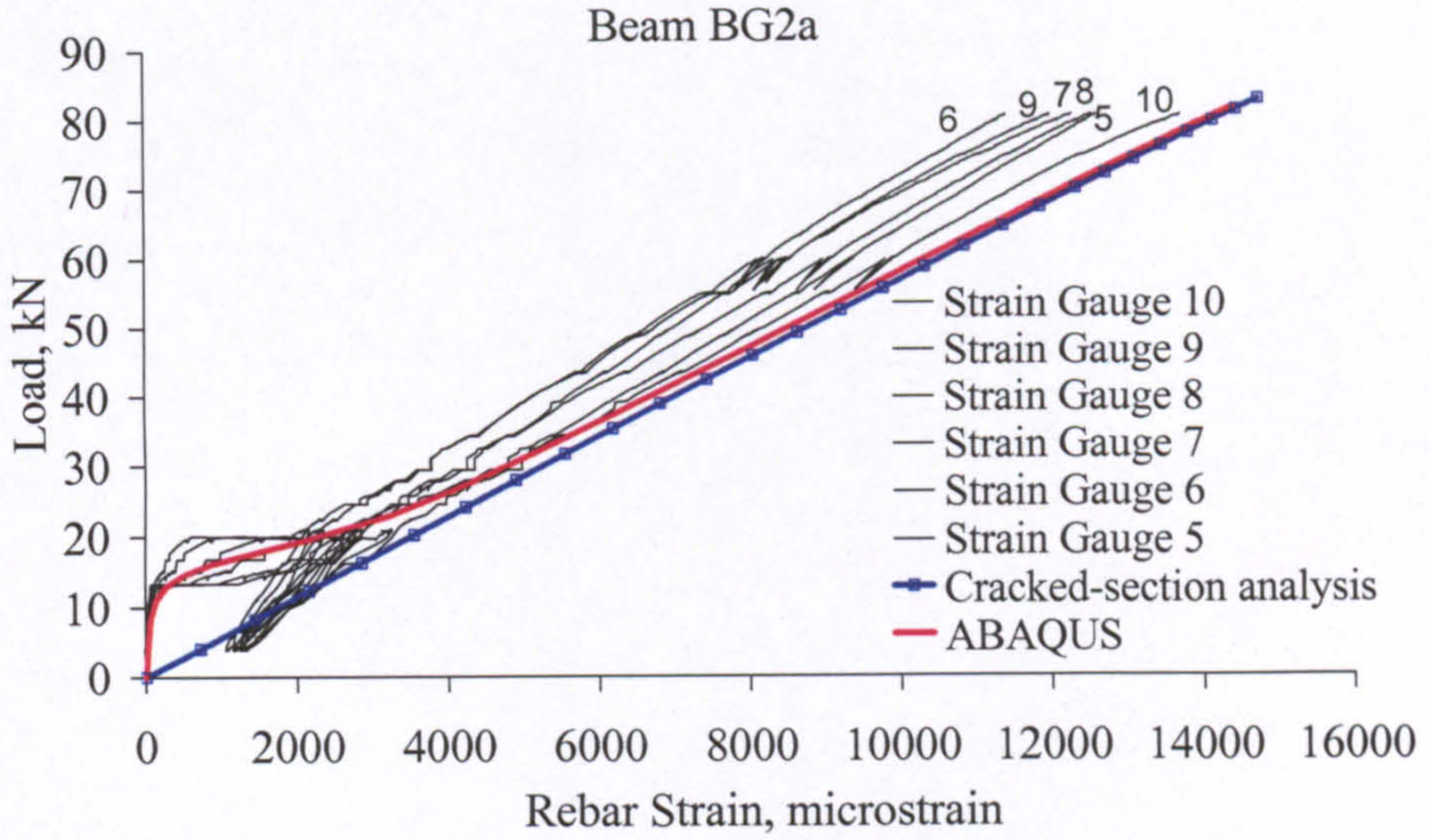

Figure 6-1: Typical GFRP RC experimental and predicted load vs. rebar strain.

The apparent discrepancy of strains in slab SG1 may be attributed to the special shape of the GFRP rebars used. At their surface, these rebars are not straight but curved, as shown in Figure 6-2, which means that the rebar area varies along its length. Therefore, when a GFRP rebar is under tension, strains will also vary at different sections along the rebar. The effect of the curved rebar surface becomes more pronounced as the rebar diameter reduces. In the tests carried out, rebar strains were measured at the apex of the curves where the strains are at their lowest values. Moreover, slab series SG1 were

reinforced with the smallest 6.35 mm-diameter GFRP rebars. In the uniaxial tensile tests of these rebars, the ratio between the local surface strain (measured with strain gauges at the apex of the curves) and the average strain (measured with LVDTs) was around 60%. Therefore, for slab series SG1, the measured rebar strains should be increased by a factor of up to 1.6 to convert them to average rebar strains. The average strains can then be compared to the strains predicted by CSA, since the rebar modulus in CSA was evaluated, in the uniaxial tensile tests, based on average rebar strain together with a nominal rebar area. Corrected rebar strains using a factor of 1.45 match very well with the measured deflections of slab SG1.

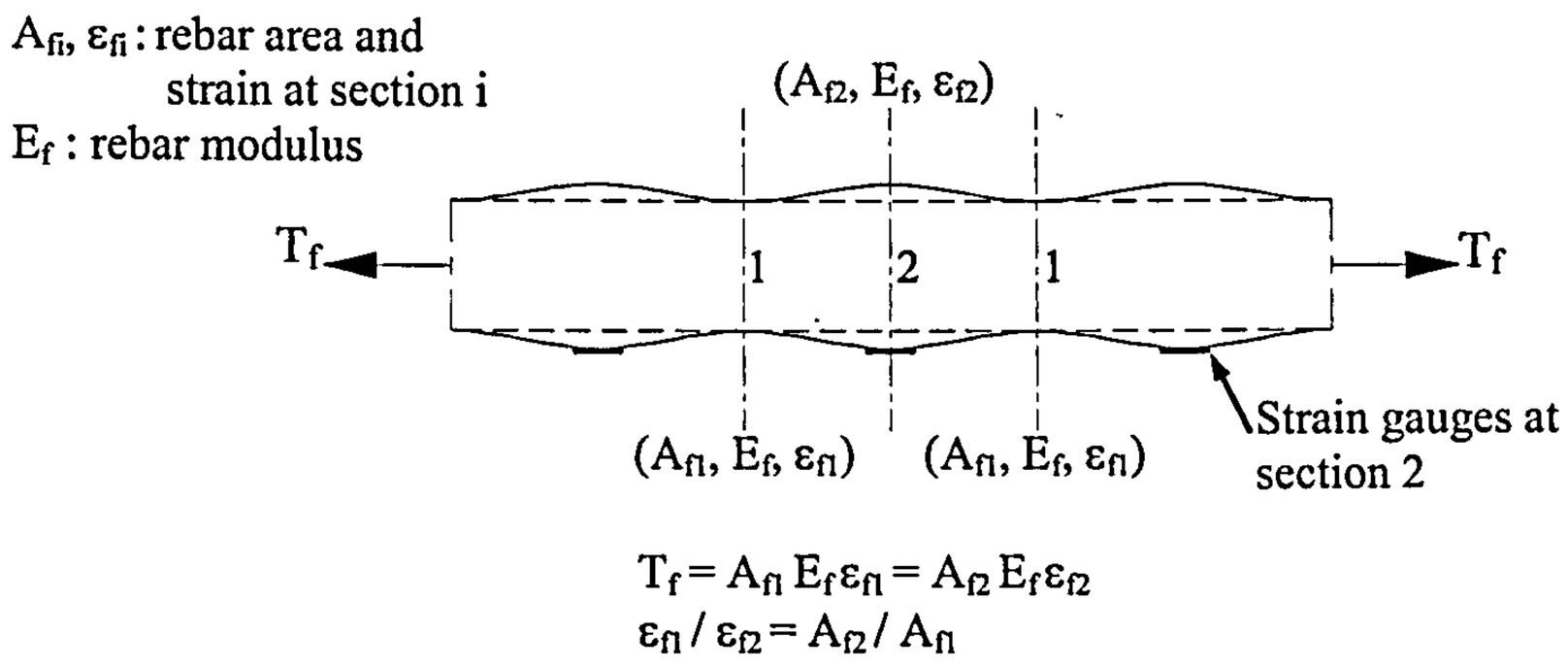

Figure 6-2: GFRP rebar profile and variation of tensile strain.

- FEA

On the other hand, FE analysis smears the effect of a crack and, as such, does not distinguish between cracked and uncracked sections. The level of tension stiffening in FE analysis was chosen to obtain the best possible prediction of the experimental deflection. Therefore, FE analysis is expected to predict the average rebar strain between cracks. However, it does not. As typically shown in Figure 6-1, the rebar strain predicted by FE analysis converges very quickly to the maximum crack strain predicted by CSA, thus overestimating the actual average rebar strain. Only for slab SG3 does FE analysis predict reasonably well the average rebar strain between cracks. In that particular case, the concrete cover was relatively high (40 mm) and the rebar strains were relatively low (< 6000 microstrains), which necessitated exceptionally high tension stiffening to predict the experimental deflection.

The fact that FE analysis overestimates the average rebar strain in the pure flexure zone must be associated with a simultaneous underestimate of other deflection or curvature-related factors; otherwise, the deflection predicted by FE analysis would not have matched the experimental deflection. Flexural curvature may be defined as the summation of average rebar and extreme-fibre compressive concrete strains divided by the effective depth. Therefore, if FE analysis underestimates the concrete strain in the central span, then this may counterbalance, partially or totally, the overestimate of the rebar strains. The prediction of concrete strains is discussed in the next section.

Another probable parameter may be identified by investigating the rebar strains in the shear span. Figure 6-3 shows typical GFRP RC measured and predicted profiles of rebar strains at discrete load levels. The figure shows again that FE analysis overestimates the average rebar strain between cracks, but at the same time, the rebar strains within the shear span are underestimated. Realizing that FE analysis only predicts flexural effects, the additional rebar strains may be attributed to the interaction of shear and flexure. Furthermore, the additional rebar strains indicate that additional curvatures in excess of flexural curvatures predicted by FE analysis develop in the shear span. This will be further considered in the discussion on deflection in Section 6.2.4.

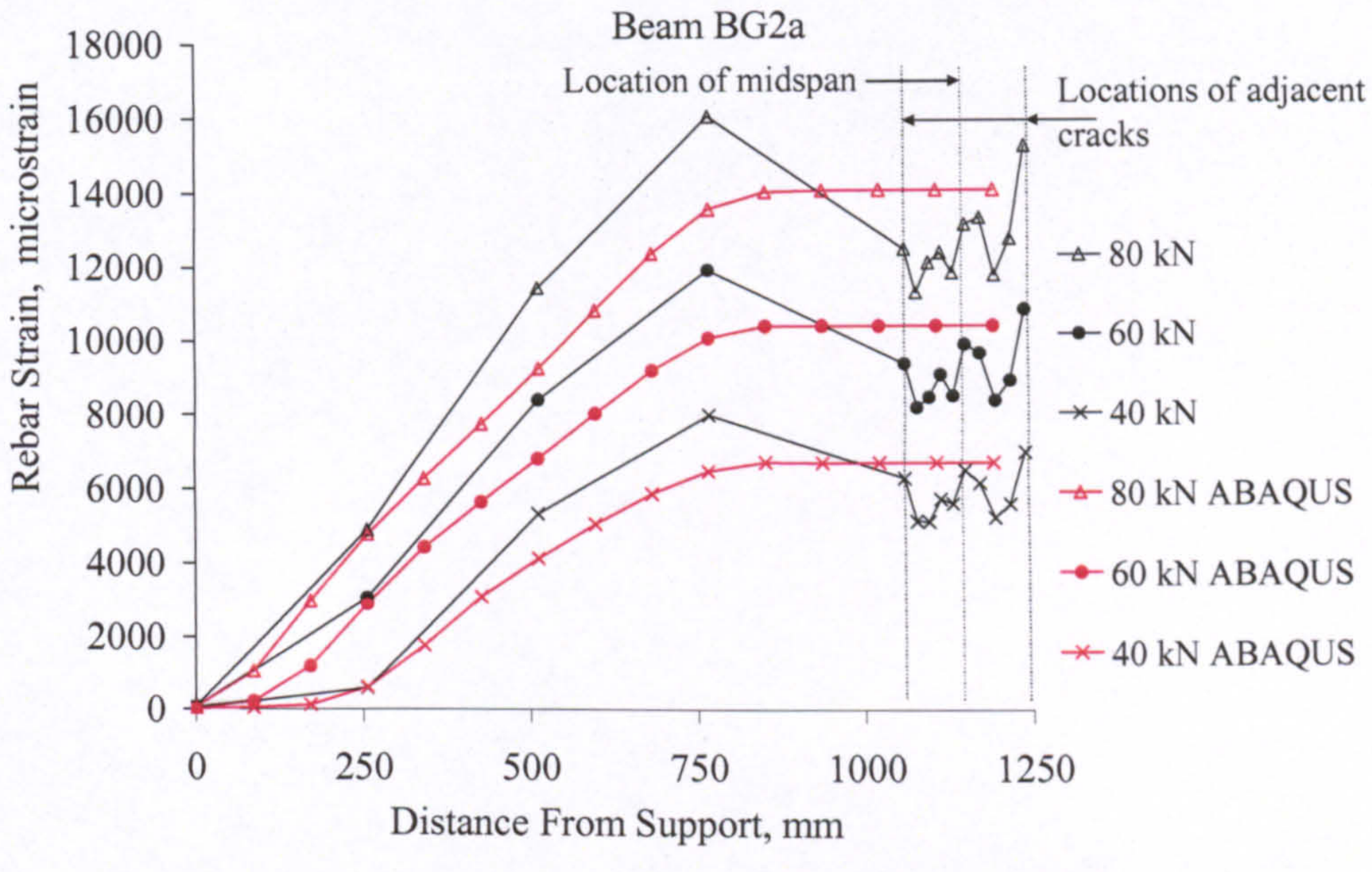

Figure 6-3: Typical GFRP RC experimental and FE analysis rebar strain profiles.

6.2.2. Strain in the Concrete

As explained in Chapter 5, CSA is expected to provide some average estimate of the compressive concrete strain and neutral axis depth between cracks. For the GFRP RC beams, CSA considerably underestimates the maximum compressive concrete strain at the extreme concrete fibre at midspan, as typically shown in Figure 6-4. On the contrary, the maximum compressive concrete strain is considerably underestimated for the GFRP slabs (Figure 6-5). The concrete strains predicted by FE analysis, which is based on a two-dimensional formulation, are not far off from those predicted by CSA. Exceptionally, FE analysis predicts reasonably well the measured concrete strains for beam BG2 (see Appendix B)!

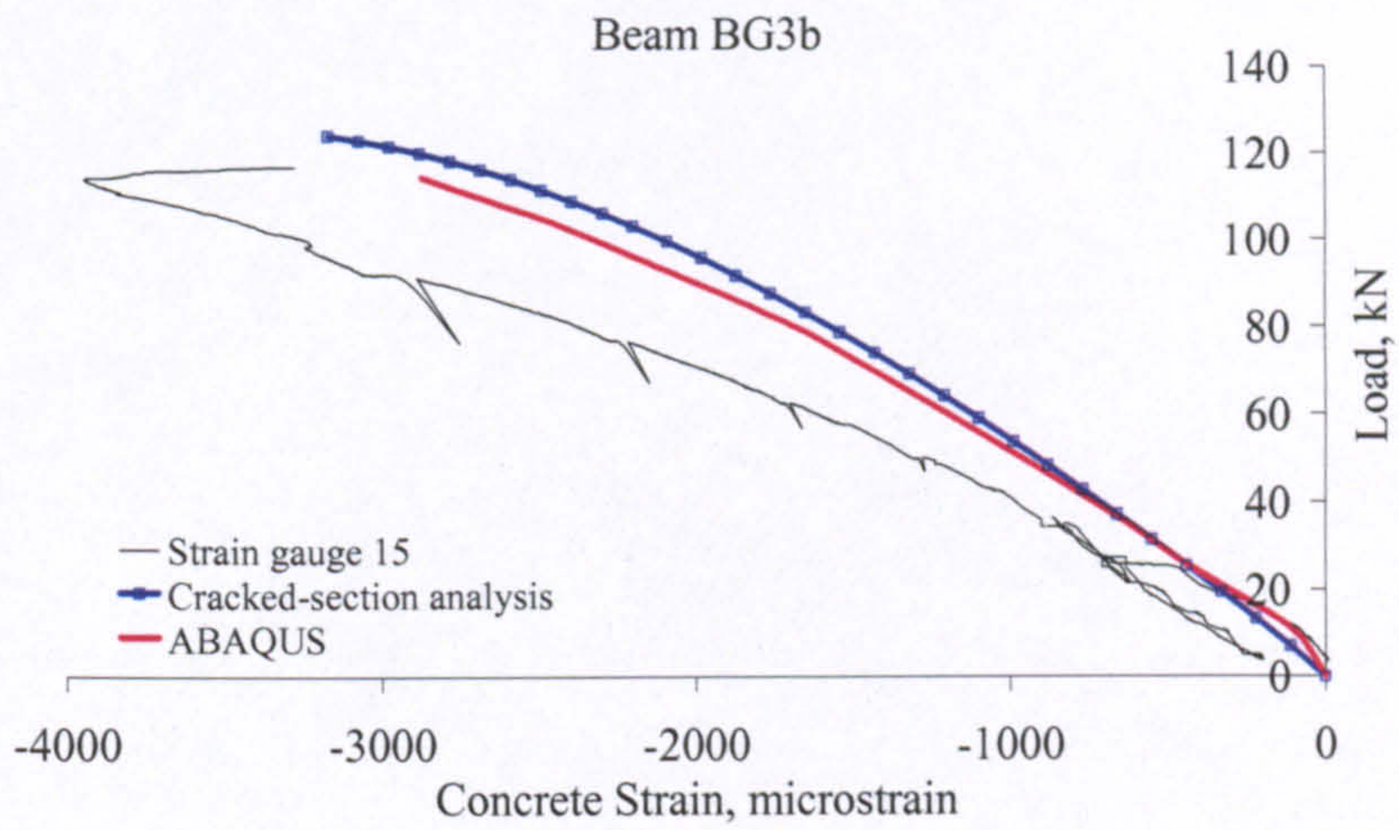

Figure 6-4: Typical GFRP RC beam experimental and predicted load vs. concrete strain.

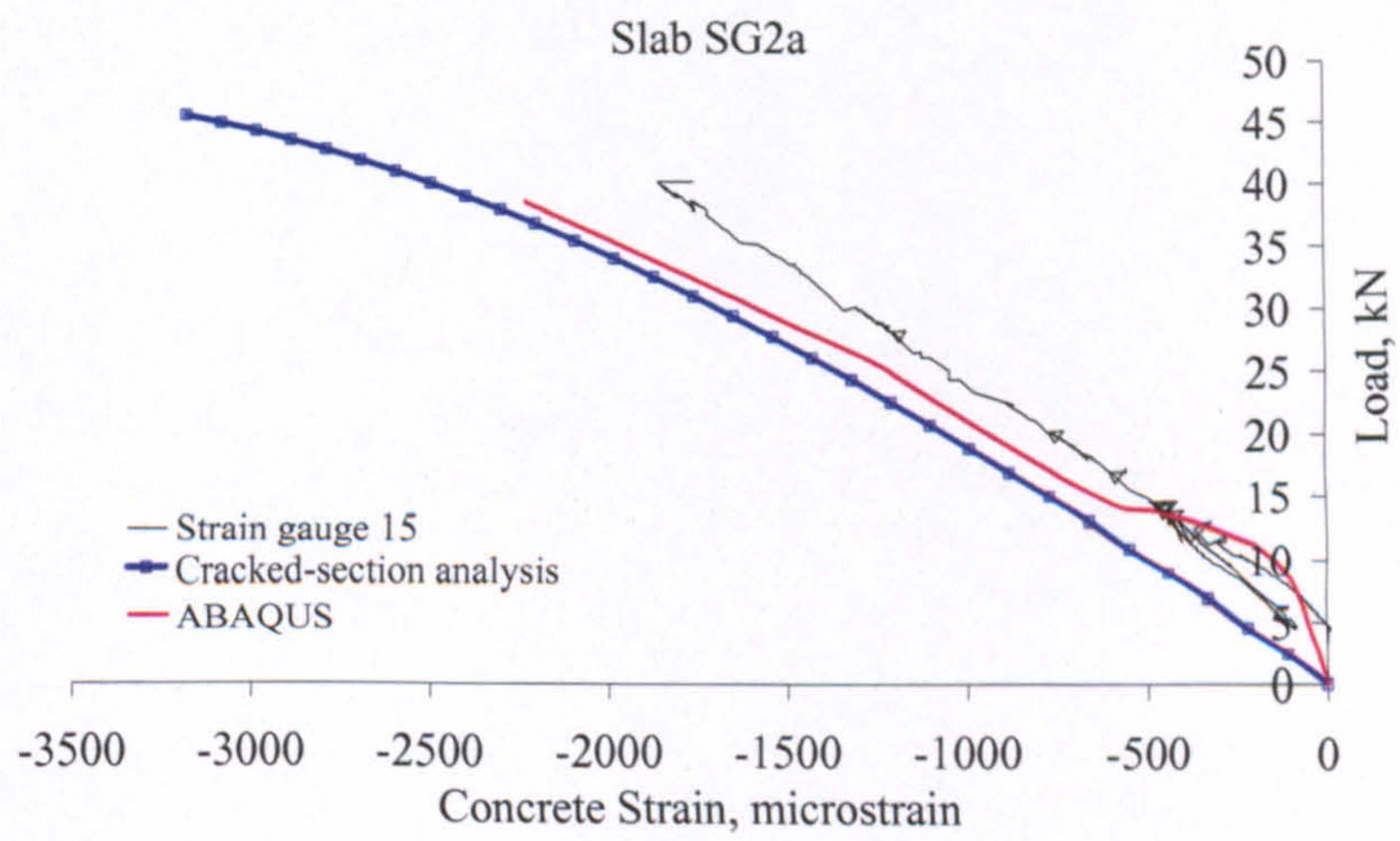

Figure 6-5: Typical GFRP RC slab experimental and predicted load vs. concrete strain.

The major contributor to the variation in concrete strains may be the penetration of cracks and their opening. With deeper penetration and wider cracks, concrete strains are expected to be more localized around a crack, and strain variation may be very different from the average conditions assumed in CSA. Nevertheless, the extreme fibre concrete strain predicted by CSA can never exceed that expected at the extreme fibre at the crack location. Hence, while concrete strains measured in the beams may be sensible, those in the slabs need further consideration.

Several factors may contribute to the discrepancy in concrete strains. At the forefront of these factors is concrete homogeneity. The concrete has been judged to be homogeneous on a global or member scale. However locally, which is how concrete strains are measured, heterogeneity of the concrete is expected to be more prominent. This is particularly true for the relatively wide slabs.

Another factor may be the concrete model and size effect. The concrete model is based on concentric compressive conditions, while the strain profile due to flexure has a high strain gradient that creates an eccentrically compressed zone. Park and Paulay (1975) consider that the strain gradient improves the properties of the compressive concrete zone, in the sense that a higher peak stress may be achieved at a higher strain, and the appearance of longitudinal cracks may be delayed. Park and Paulay (1975) also report that, depending on the concrete grade, the maximum cylinder strength may reduce in the member, but no more than about 10%. Hence, the concrete model and size effect may not be responsible for the measured concrete strains in the slabs, and the discrepancy is attributed to the lack of homogeneity of concrete.

So, how sensible are the measured concrete strains in the beams? This study is not designed to investigate the behaviour of the compressive concrete zone. However, it has been shown in the analysis of experimental data in Chapter 4 that the deflection prediction involving the measured concrete strains was generally very good for many tests. Furthermore, the effect of the penetration and width of cracks on the response of the compressive zone may be more pronounced in FRP RC than in steel RC because, in general, the lower modulus of the FRP reinforcement causes higher rebar strains, hence wider and deeper cracks. In contrast, it is only after the steel yields that the cracks in steel RC may become comparable to those in FRP RC. Therefore, the measured concrete strains are considered representative.

The response of the compressive concrete zone is directly related to curvature and is further considered in discussing the deflection results (6.2.4). However, it is necessary first to investigate if there are any consequences on the prediction of failure load, or flexural capacity, which is discussed in the following section.

6.2.3. Failure Load

For the compressive concrete failure mode, CSA relates the flexural capacity to a maximum usable compressive strain at the extreme concrete fibre (ε_{cu1}). Following the steel RC practice, ACI 440.1R-03 (ACI committee 440 2003) takes ε_{cu1} as 0.003. For the concrete grade used herein, Eurocode 2 (CEN 2004) adopts a higher value for ε_{cu1} of 0.0035. It is worth pointing out that the flexural capacity of steel RC is controlled by the yield of the reinforcement and is only marginally affected by the value of ε_{cu1}. However, ε_{cu1} is of prime importance when considering ductility of steel RC.

For sections with high crack penetration and width, as in GFRP RC, CSA may considerably underestimate the measured concrete strain at the extreme compressive fibre, as discussed in the previous section. Nevertheless, CSA prediction of flexural capacity is generally good. Table 6-1 shows that, for the concrete crushing failure mode, the failure load predicted by CSA is within 12% of the actual failure load. Moreover, a value of ε_{cu1} of 0.003 seems to be more appropriate.

Table 6-1 shows also that it may be more difficult to predict the failure load when failure occurs due to rupture of rebars. Beam BG2 failed by concrete crushing while a rupture failure is predicted. This may be attributed to an underestimate of the tensile capacity of the GFRP rebar. On the contrary, Beam BG1 and slab SG1 show premature rupture of rebars, which may be attributed to the concentration of bond stresses around cracks having a more pronounced effect on rebars with small diameters.

Table 6-1: Experimental and CSA prediction of load capacity and failure modes

Series	Beam or Slab	Test		CSA			Load Capacity Ratio, (CSA/Test, ε_{cu1}= 0.003)
		Load Capacity, kN	Failure Mode	Load Capacity, kN		Failure Mode	
				ε_{cu1}= 0.003	ε_{cu1}= 0.0035		
BG1	BG1a	45.1	Rupture	52.3	52.3	Rupture	1.16
	BG1b	44.6	Rupture			Rupture	1.17
BG2	BG2a	80.7	Crushing[1]	83.0	83.0	Rupture	1.03
	BG2b	77.8	Crushing[1]			Rupture	1.07
BG3	BG3a	112.1	Crushing	125.0	127.5	Crushing	1.11
	BG3b	117.4	Crushing			Crushing	1.06
SG1	SG1a	20.7	Rupture	21.8	21.8	Rupture	1.05
	SG1b	18.2	Rupture			Rupture	1.20
SG2	SG2a	40.3	Rupture	45.2	47.0	Crushing	1.12
	SG2b	45.0	Crushing[1]			Crushing	1.00
SG3	SG3a	62.6	Crushing	56.2	57.9	Crushing	0.90
	SG3b	63.4	Crushing			Crushing	0.89

[1] Crushing almost immediately followed by rupture of rebars, which is very close to balanced failure.

6.2.4. Deflection

In addition to measuring deflections during the tests, the midspan deflection was predicted by several approaches. In Chapter 4, the rebar and concrete strains within the two blocks of concrete around the midspan crack were used to establish a flexural moment-curvature relationship, which was then used to calculate the deflection due to beam-action or flexure. In Chapter 5, the level of tension stiffening in FE analysis was chosen to make the best possible prediction of the load-midspan deflection response. Moreover, CSA was used to provide an upper-bound solution for both curvature and deflection.

Flexural deflection is a result of curvature along the span. The curvature of a concrete block can be estimated as the summation of average rebar strain, which includes the tension stiffening effect, and extreme-fibre compressive concrete strain within the block divided by the effective depth. In the discussion on rebar and concrete strain of FRP RC in this chapter, it became evident that besides rebar strain and tension stiffening,

curvature may be considerably affected by the behaviour of the compressive concrete zone. Moreover, additional rebar strains in excess of flexural requirements within the shear span were attributed to shear-flexure interaction. The additional strains indicate additional curvatures that may increase the deflection along the member.

In this section, all the deflection-relevant GFRP RC experimental and analytical results are examined together to try to firm-up on the deflection behaviour of these structural elements, as well as the analytical approaches used. Rebar and concrete strains have already been considered individually. However, an overestimate of rebar strains may be compensated by an underestimate of concrete strain to give the same curvature. Therefore, strains are further considered jointly through curvatures. The following discussion considers individual GFRP tests. The behaviour is categorized and summarised at the end. The discussion is undertaken for the GFRP RC beams and slab SG2.

- Beam BG1

Figure 6-6 shows the relevant experimental results and data analysis of beam BG1. The corresponding predictions by FE analysis and CSA are also shown in the figure.

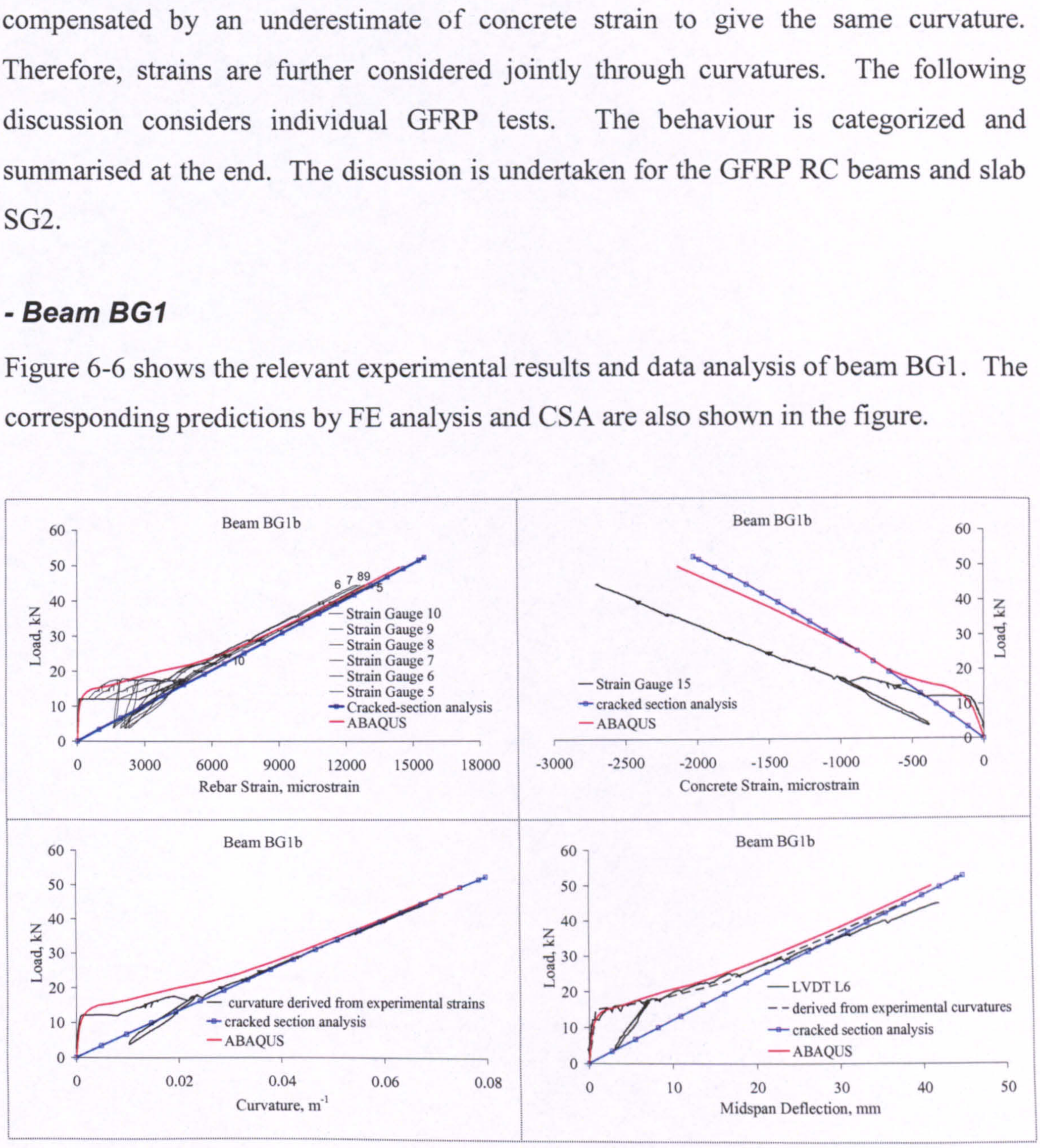

Figure 6-6: Measured and predicted strains, curvature and deflection of Beam BG1.

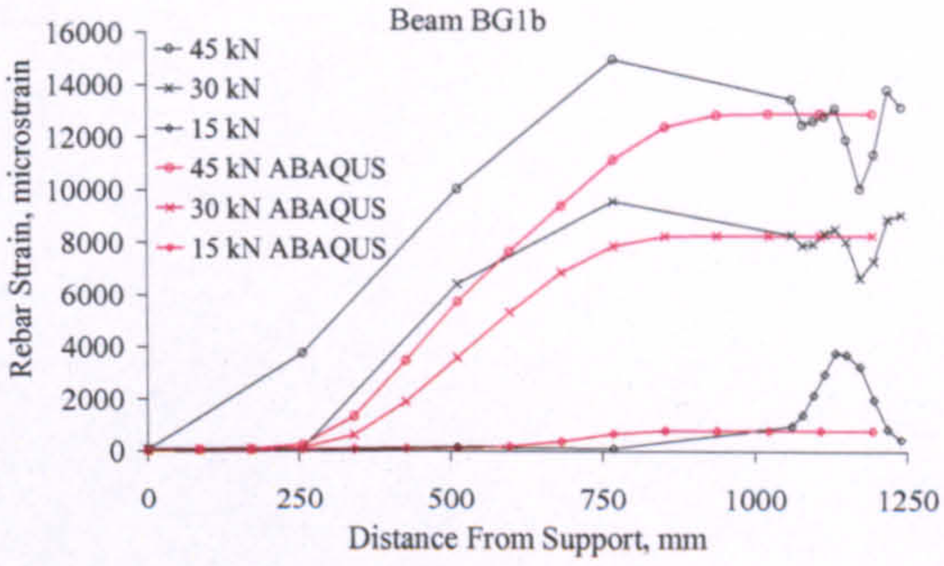

Figure 6-6 cont.: Measured and predicted strains, curvature and deflection of Beam BG1.

The deflection predicted based on the experimental curvature compares very well with the measured deflection up to a load of about 25 kN. Beyond that load, the measured deflection increases at a faster rate. At failure, the measured deflection is about 12% higher than predicted.

The onset and development of the additional deflection coincides with the formation and spread of cracks within the shear span. By investigating the rebar strain profiles within the shear span, it is obvious that the rebar strains exceed the flexural requirements. Hence, the additional deflection may be attributed to the interaction of flexure with shear causing increased curvature within the shear span, and possibly within a region disturbed by the load in the central span, and can therefore be referred to as "shear-induced" deflection. However, it is important to confirm if this shear-induced deflection can measure-up to the additional measured deflections. For that purpose, a numerical analysis is not feasible, but a rough estimate may be made of the additional deflection at the failure load, due to the difference between the measured and flexural strains. Firstly, it is assumed that the flexure and shear effects can be decoupled. Moreover, it is assumed that the flexural curvature profile at any load level can be modified proportionally to the additional strains within the shear span. For instance, at failure, the measured rebar strain beneath the load is about 10% larger than the maximum rebar strain at midspan, so the additional curvature is taken to be 10% of the flexural curvature at that location. The implementation of this approach is further clarified in Figure 6-7.

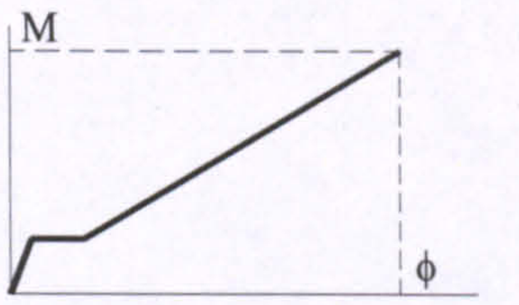

Idealized Moment-Curvature

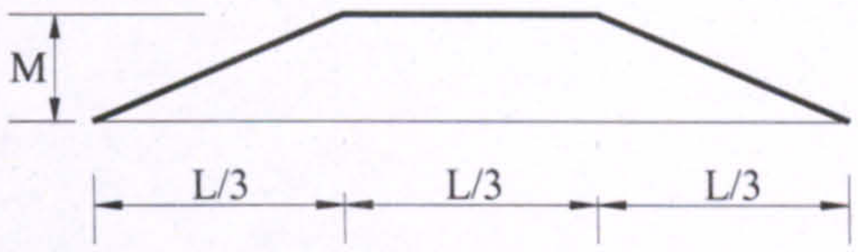

Bending Moment Diagram

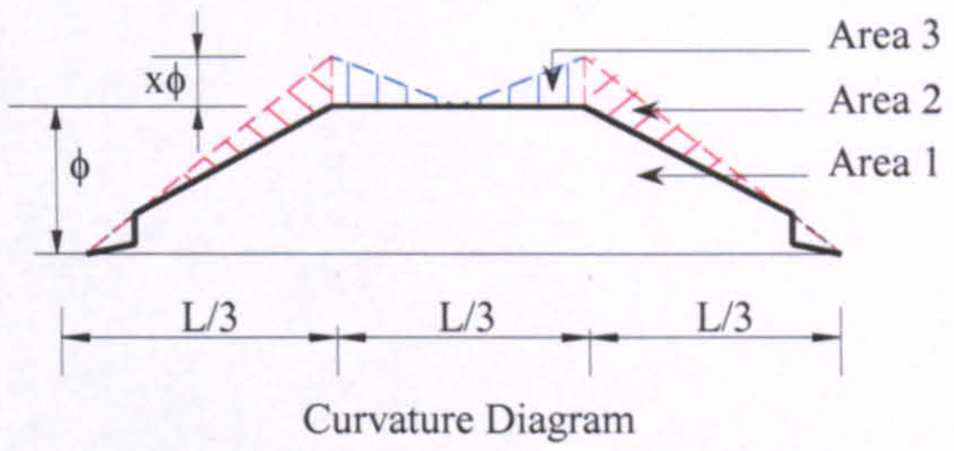

Curvature Diagram

Area 1: curvature due to flexure
Area 2: additional curvature
Area 3: additional curvature

Area	x	Midspan Deflection	Ratio of additional deflections
1	0.1	$0.106\ \phi L^2$	-
2		$0.037\ x\phi L^2$	3.5%
3		$0.032\ x\phi L^2$	3.0%

Figure 6-7: Estimation of additional deflection due to shear-flexure interaction.

Figure 6-7 shows that, at failure, the shear-induced deflection due to the additional rebar strains may be somewhere between 3.5% and 6.5% of the flexural deflection. The actual additional deflection is larger than the estimate, but it has to be emphasized that only rebar strains were considered to estimate the additional curvatures. Other curvature-contributing parameters may have also been involved. For instance, the strain in the concrete contributes more to the curvature as the load increases, which is a mere consequence of the concrete being a nonlinear material. Furthermore, tension stiffening may not be constant along the beam due to variation of crack spacing. As crack spacing increases, tension stiffening is expected to increase and vice versa.

The above treatment of the shear-induced deformations is very crude and stems from the approach of flexural curvatures where the assumption of plane sections is fundamental. A more intricate approach would be to investigate the behaviour of concrete blocks between inclined cracks, normally referred to as "teeth", as shown in Figure 6-8 (Park and Paulay 1975). For such teeth, the shear resistance mechanisms (dowel action, aggregate interlock and resistance of the stirrups and compressive concrete zone) are incorporated. The interaction of the longitudinal reinforcement and the surrounding concrete is also involved. One very important consideration may be the deformation and failure characteristics of the concrete teeth between the shear cracks,

and the deformation of the compressive concrete zone on top of these cracks. The teeth are like tied cantilevers hanging from the compressive concrete zone. In FRP RC the cracks penetrate deeper than steel RC, which makes these cantilevers longer and with less rigid fixation at the shallower compressive concrete. Therefore, the teeth in FRP RC can undergo more rotation, which may result in increased deflections such as those observed in the GFRP RC tests. The penetration of the cracks and the stiffness of the concrete teeth and the compressive concrete zone are issues that require a specifically tailored research, which is beyond the scope of this thesis. In any case, for beam BG1 the shear-induced deflections are not significant within the "service" range of behaviour.

V_{ai} : aggregate interlock

V_{di} : dowel resistance

V_{ci} : shear resistance in compressive zone

T_i : tension in reinforcement

S_i : tension in stirrups

C_i : Compressive concrete forces

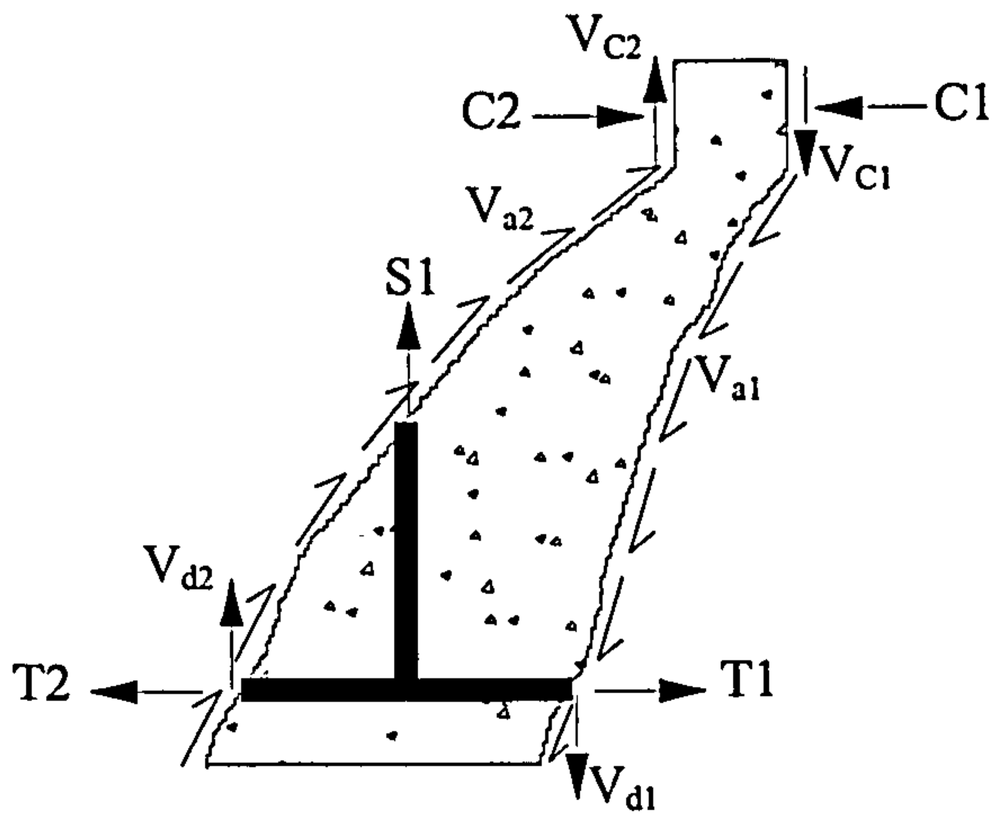

Figure 6-8: Concrete teeth in the shear span and the internal resistance mechanisms (after Park and Paulay 1975).

In FE analysis, the level of tension stiffening was calibrated to obtain the best possible fit to the experimental deflection. Figure 6-6 shows that the deflection predicted by FE analysis matches the measured deflection up to a load of about 25 kN, but beyond that load the predicted deflection follows a stiffer path. In fact, the deflection predicted by FE analysis compares very well with the deflection predicted from the experimental load-curvature relationship. The additional deflection due to shear induced deformation could not have been predicted by FE analysis anyway, because as explained, ABAQUS formulation is flexure-based. It has to be emphasized though, that while FE analysis predicts well the flexural deflection or curvature, it imbalances to some degree the relative contribution of rebar and concrete strains to the curvature. So, the rebar strains

are overestimated while the concrete strains are underestimated. In other words, FE analysis does not perfectly reflect the actual state of flexural strains in the member.

CSA provides an appropriate upper limit for flexural deflection, since the deflections predicted by FE analysis and those based on the experimental curvatures tend to the CSA solution. However, the measured deflection slightly exceeds the CSA limit, but then CSA does not allow for any shear-induced deformations.

- Beam BG2

Figure 6-9 shows the experimental results and data analysis of beam BG2 together with the corresponding predictions by FE analysis and CSA.

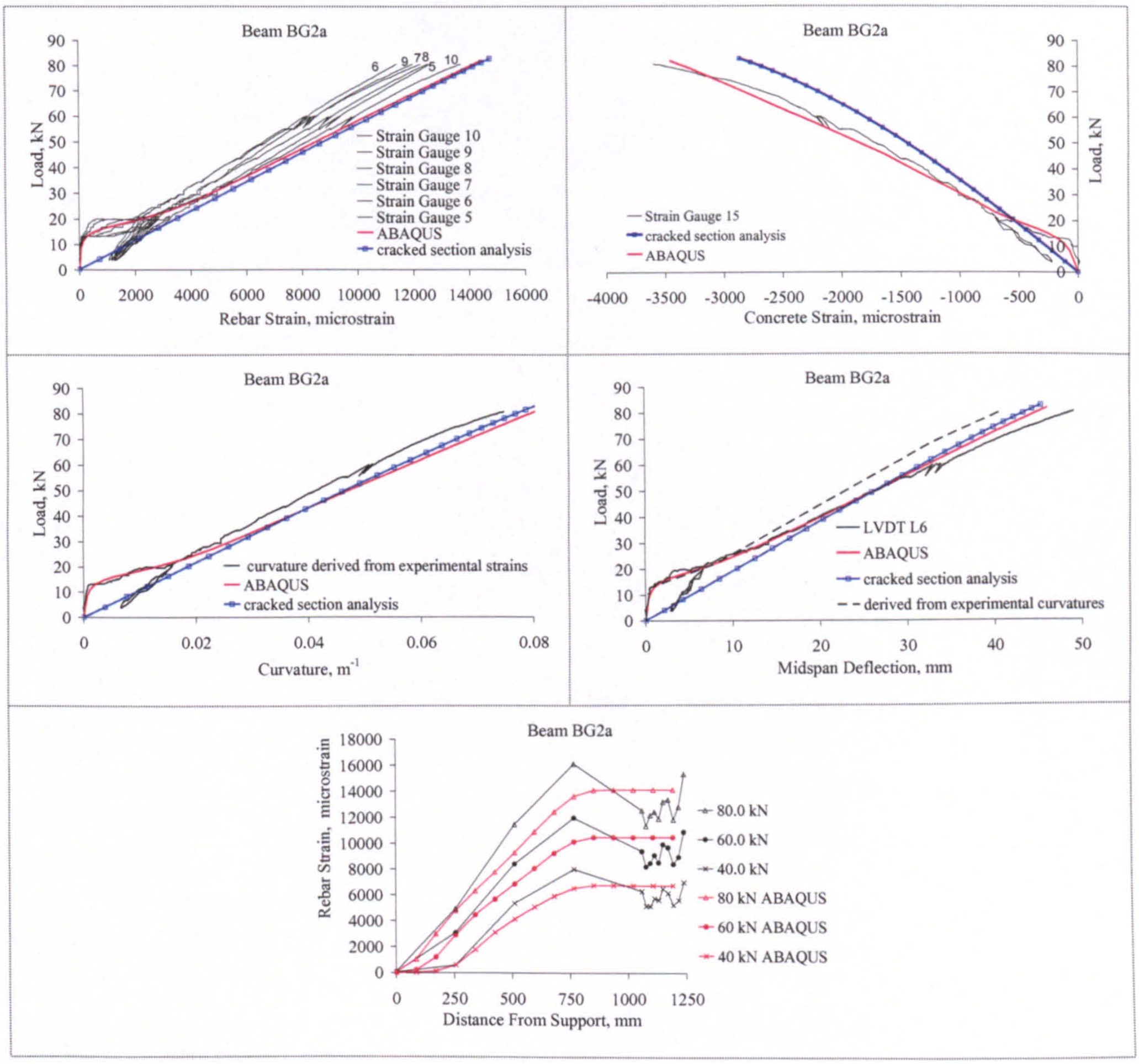

Figure 6-9: Measured and predicted strains, curvature and deflection of Beam BG2.

Similar to beam BG1, the deflection predicted based on the experimental curvature compares very well with the measured deflection up to a load of about 25 kN. Beyond that load, the measured deflection increases at a faster rate. At failure, the measured deflection is about 19% higher than predicted.

Again, the onset and development of the additional deflections coincide with the formation and spread of cracks within the shear span. Furthermore, the rebar strains measured within the shear span substantially exceed the flexural rebar strains, thus indicating shear-induced deformations. Following the crude approach explained for Beam BG1, x in Figure 6-7 is around 0.2, and the shear-induced deflection may be somewhere between 7% and 13 % of the flexural deflection.

For beam BG2 the failure was almost balanced. Therefore, compared to beam BG1, higher shear levels were reached together with increased additional strains within the shear span. This may help to support the concept of shear-induced deflections. Figure 6-10 shows profiles of measured deflections at discrete load levels and corresponding flexural deflections derived from experimental curvatures. Both cases are essentially identical up to the load level where the cracks start to form within the shear span. However, with the formation and propagation of cracks in the shear span, the measured deflections become increasingly larger than the flexural deflections. The difference between every pair of profiles with common load level is seen to arise within the shear span only, while the profiles are essentially parallel within the central span.

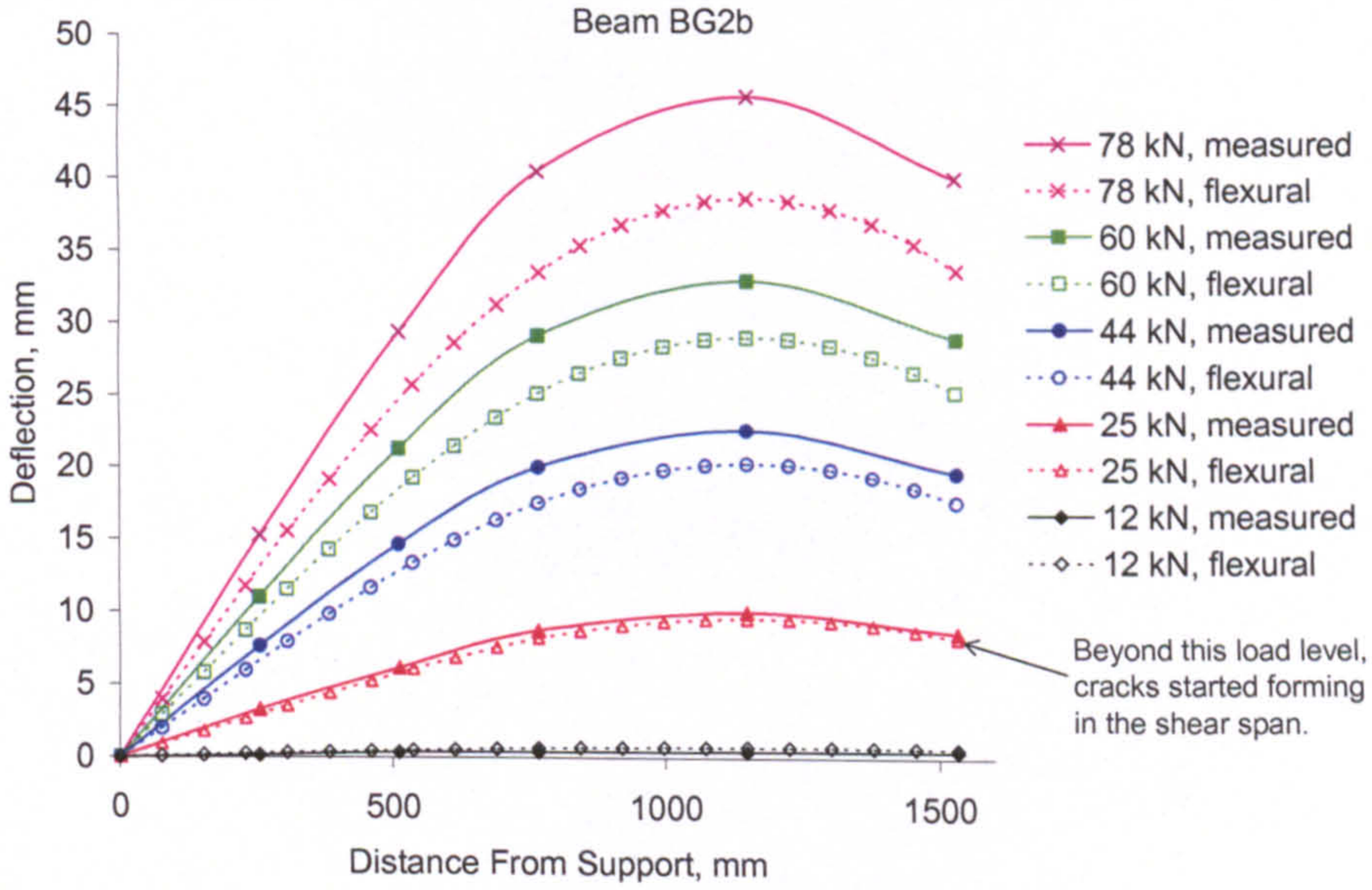

Figure 6-10: Measured versus derived flexural deflection profiles.

Figure 6-9 shows that the deflection predicted by FE analysis matches the measured deflection up to a load of about 55 kN, but beyond that load the predicted deflection follows a stiffer path, which may be attributed to shear-induced deformations. Unexpectedly, the deflection predicted by FE analysis diverges from and exceeds the deflection predicted by the experimental load-curvature relationship, reaching a maximum difference of about 10% at failure. However, these differences are within the tolerances expected from experimental measurements and material variability.

As expected, the deflection predicted by FE analysis and CSA converge towards failure. The ability of CSA to provide a limiting deflection solution is affected by shear-induced deformations to a greater extent than for beam BG1.

- Beam BG3

Figure 6-11 shows the experimental results and data analysis of beam BG3 together with the corresponding predictions by FE analysis and CSA.

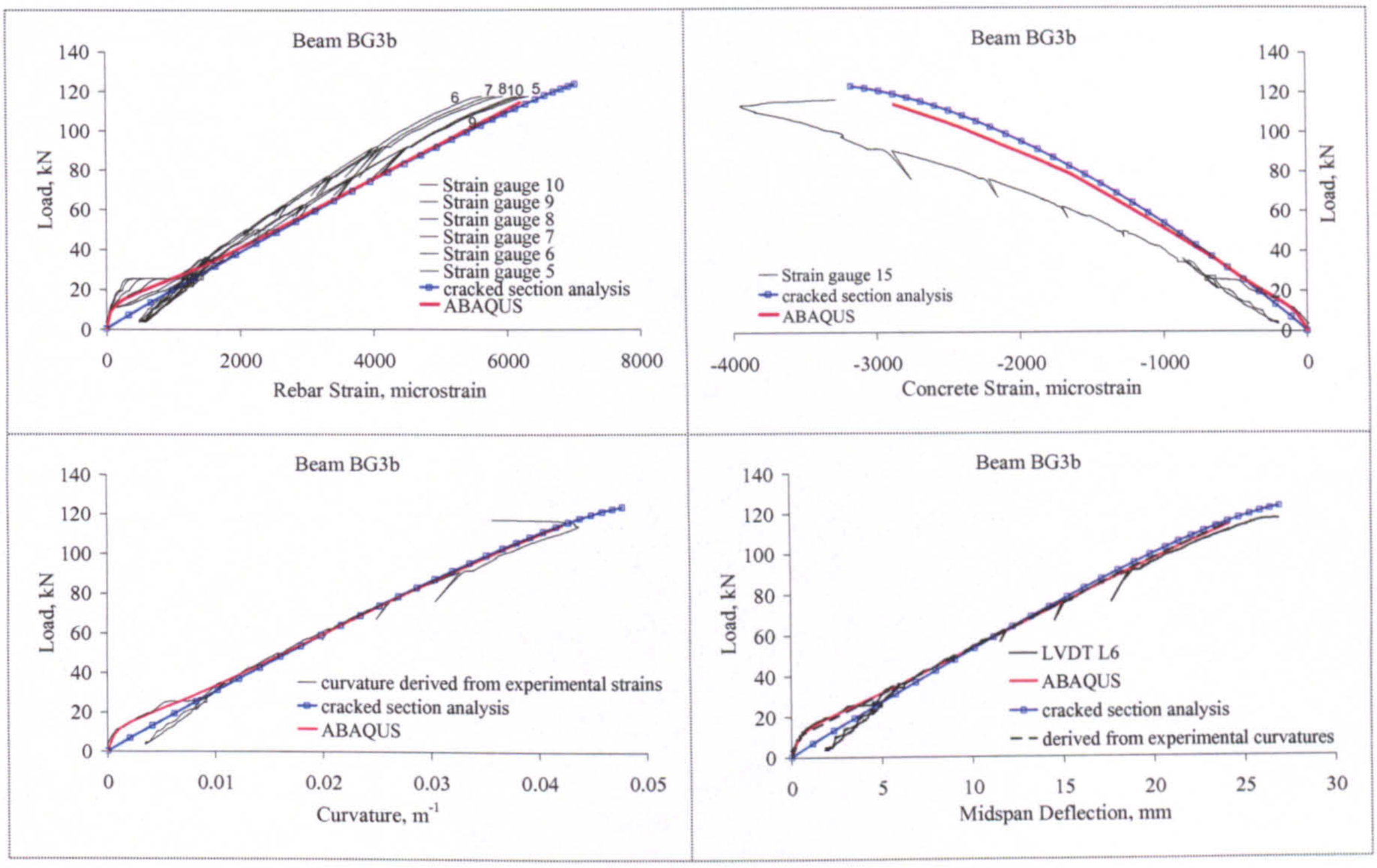

Figure 6-11: Measured and predicted strains, curvature and deflection of beam BG3.

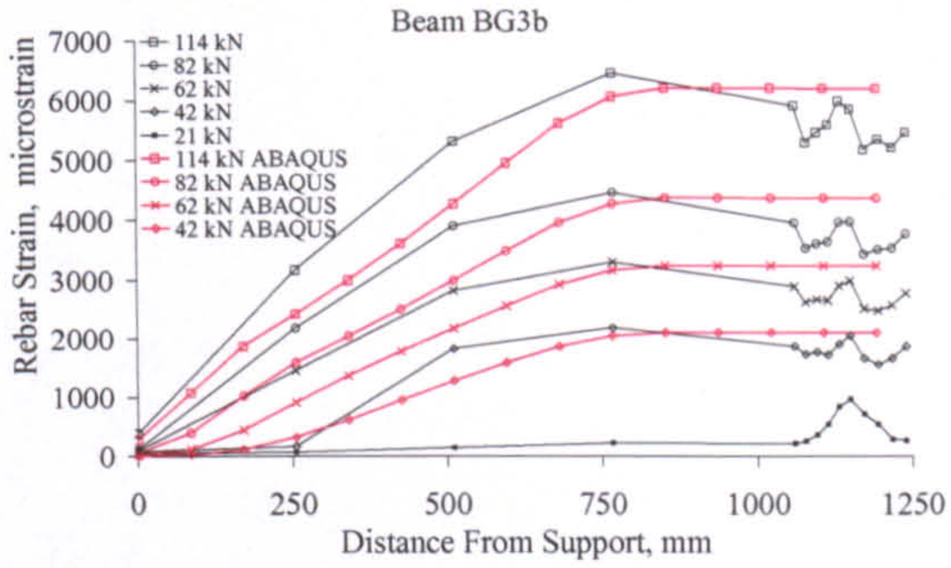

Figure 6-11 cont.: Measured and predicted strains, curvature and deflection of beam BG3.

The flexural deflections derived by the experimental load-curvature and by FE analysis coincide with the measured deflection, which indicates negligible shear-induced deformations. However, additional rebar strains are obvious in the rebar strain profiles. Moreover, the applied shear force levels reached are much higher than in beams BG1 and BG2. Nonetheless, shear induced deformations are much less apparent, which may be explained by the magnitude of rebar strains. Beam BG3 has a very high reinforcement ratio. Therefore, its rebar strains are much less than those in beams BG1 and BG2, even at the higher failure load. With lower rebar strains, the width and penetration of the cracks, within the central zone as well as the shear span, are reduced. Hence, it may be in line with the argument presented while discussing beam BG1 that shear-induced deformations are more associated with deeper and wider cracks than normal. This may also be in line with the fact that shear-induced deformations are not noticed in similar steel RC beams, where before any yielding occurs, relatively very low rebar strains are reached, with narrow cracks that do not penetrate deep in the section.

- Slab SG2

Slab SG2 had an almost balanced flexural failure together with high rebar strains. With similar conditions, beam BG2 was discussed to undergo the highest shear-induced deformations among the GFRP RC beam series. Figure 6-12 shows the experimental results and data analysis of slab SG2 together with the corresponding predictions by FE analysis and CSA.

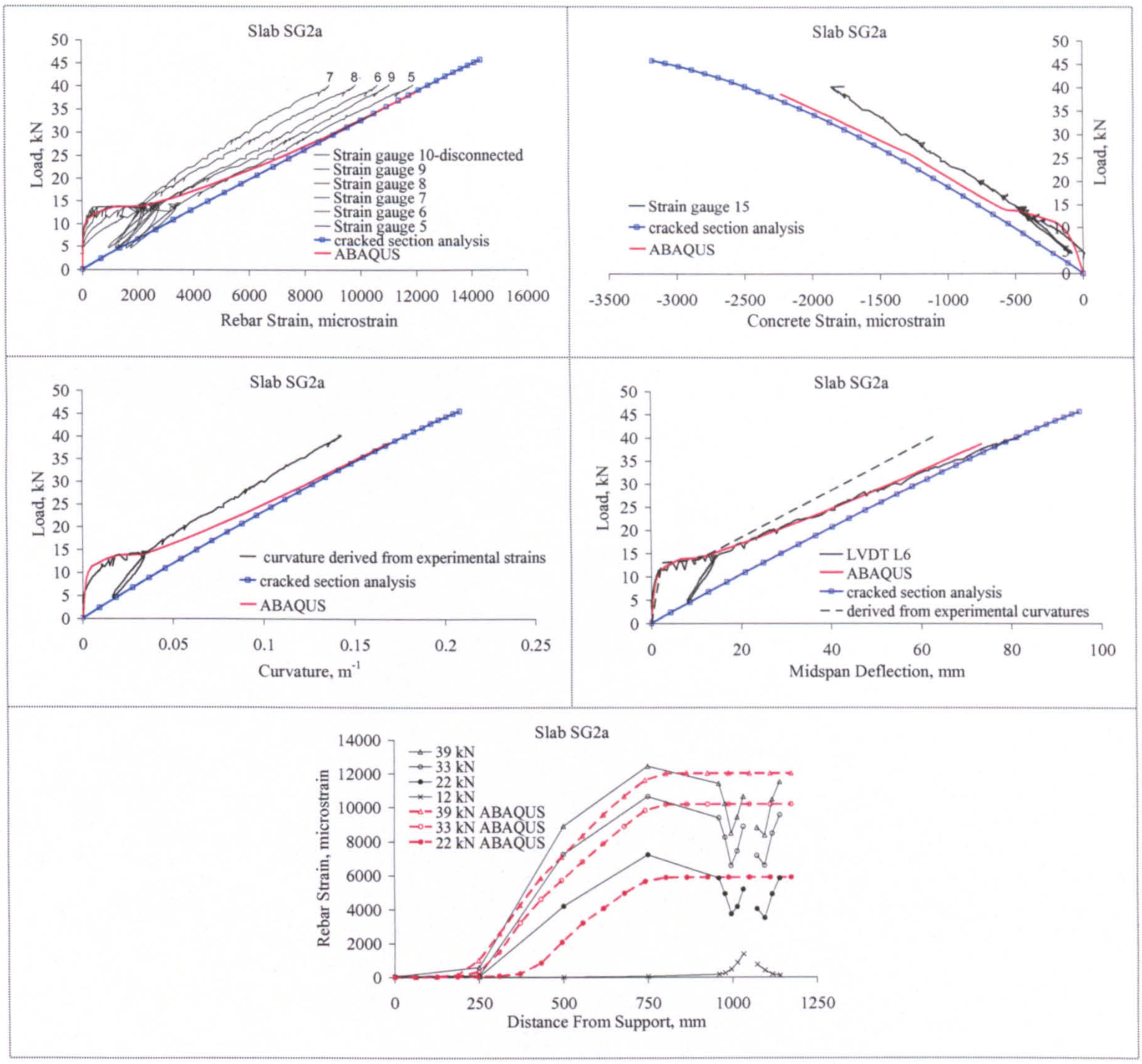

Figure 6-12: Measured and predicted strains, curvature and deflection of slab SG2.

Almost immediately after the formation of cracks within the central zone, the deflection predicted by the experimental load-curvature follows a much stiffer path than the measured deflection. Moreover, this predicted deflection does not converge with the FE analysis or CSA prediction despite the high rebar strains reached close to failure. This may raise questions as to how representative is the experimental load-curvature relationship in this case. It was discussed earlier that the measured concrete strain might be underestimated, but it would require three times as much to justify the difference in deflections, which is highly improbable. The rebar strains between the cracks indicate a very high tension stiffening effect, but are believed to be representative of other concrete blocks because the spacing of cracks along the span is nearly uniform, which indicates more or less similar tension stiffening. Therefore, the load-curvature relationship is believed to be reasonably representative, which may be further supported

by the fact that the experimental results of the two replicate slabs, SG2a and SG2b, compare well. Similar to the GFRP RC beams, the difference between the measured and predicted deflection is suspected to arise from shear-induced deformations in the shear span.

On the contrary, the flexural deflection predicted by FE analysis almost matches the measured deflection along the entire loading path. Moreover, the predicted rebar strains near failure compare reasonably well to those measured in the central span, which means that there is no reason to suspect material variability. CSA also does well in providing an upper-bound deflection along the entire loading path.

The apparent discrepancy between the experimental and numerical analysis results may be attributed to the relatively high level of rebar tension stiffening, which may be observed for the GFRP slabs, but not the beams. High tension stiffening gives sufficient margin for CSA to always provide a limiting solution; hence the measured deflection does not exceed that predicted by CSA. In FE analysis, much lower tension stiffening, as evident from the rebar strains, was necessary to accurately, but not necessarily correctly, predict the measured deflection. Therefore, the concept of shear-induced deformations may still be sustained.

6.2.5. Conclusions

The fairly detailed discussion of the GFRP RC deflection-related results may be conducive to some important aspects of the behaviour of GFRP RC elements, and concerning the numerical analysis techniques used, which may be summarised as follows.

- Deflection of GFRP RC is mainly caused by flexural curvatures, but shear-induced curvatures may not be negligible for low reinforcement ratios and deep-penetrating wide cracks.
- Flexural curvature of a concrete block may be defined as the summation of average flexural rebar and extreme-fibre concrete strains divided by the effective depth. The rebar strains have the major contribution towards curvature, and require a proper

evaluation of tension stiffening at the rebar level. However, the contribution of concrete strains is not negligible and is enhanced by the increased localised effect of the wide and deep cracks of GFRP RC.

- Shear-induced curvatures may initiate due to the interaction of flexure with shear. Such curvatures may be sizeable and are believed to increase with wider and deeper cracks, or equivalently with the increase in rebar strain. In other words, shear-induced curvatures are expected to reduce with increasing reinforcement ratio and/or modulus. Hence, for GFRP RC where the reinforcement modulus is very low, a very high reinforcement ratio is required to limit shear-induced curvatures, as for instance was the case for beam BG3.

- The proper evaluation of shear-induced effects and the response of the compressive concrete zones require a further specially-tailored research.

- As expected, CSA predicts the maximum rebar strain at a crack in the pure flexure zone, but can underestimate the maximum concrete strain at the extreme compressive fibre. Moreover, CSA does not account for the additional rebar strains and shear-induced deformations. Therefore, CSA may not perfectly provide an upper-bound curvature and deflection, but may still do so if high tension stiffening is maintained up to failure, as for instance in slab SG2. It may be worthwhile to note that though CSA may sizeably underestimate actual curvature and deflection at the failure load level, the underestimate is only marginal at the service load level.

- Though CSA underestimates the maximum concrete strain at the extreme compressive fibre, its prediction of failure load is within a reasonable tolerance.

- The level of tension stiffening can be calibrated in the smeared-crack approach of FE analysis to almost match the actual deflection. However, the FE solution is flexure based, which necessitates unrealistically low values of tension stiffening to allow for curvatures originating from sources other than flexure, such as the shear induced-deformations. In doing so, FE analysis overestimates the average rebar strain and converges very quickly to the solution of CSA. Moreover the smeared-crack approach cannot account for localization of concrete strains due to penetration of cracks, which may cause higher flexural curvatures. Again, unrealistically low tension stiffening is used to account for these curvatures. The use of a two-dimensional concrete theory did not prove to offer much of an advantage in that regard. Probably FE analysis with discrete crack modelling can do better!

6.3. CFRP RC MEMBERS

6.3.1. Strain in the Rebars

Unexpectedly and contrary to GFRP RC, CSA underestimates rebar strains at and around the midspan crack for the CFRP RC members, as typically shown in Figure 6-13. Soon after cracking, the rebar strains predicted by CSA deviate away from the measured strains following a stiffer path. Only for slab series SC1 do the predicted and measured rebar strains compare reasonably!

The rebar strains predicted by FE analysis are not any better; as they converge very quickly to those predicted by CSA. Moreover, the measured deflections could not be matched by FE analysis in the first instance as in the case of GFRP RC, and the deflections were underestimated.

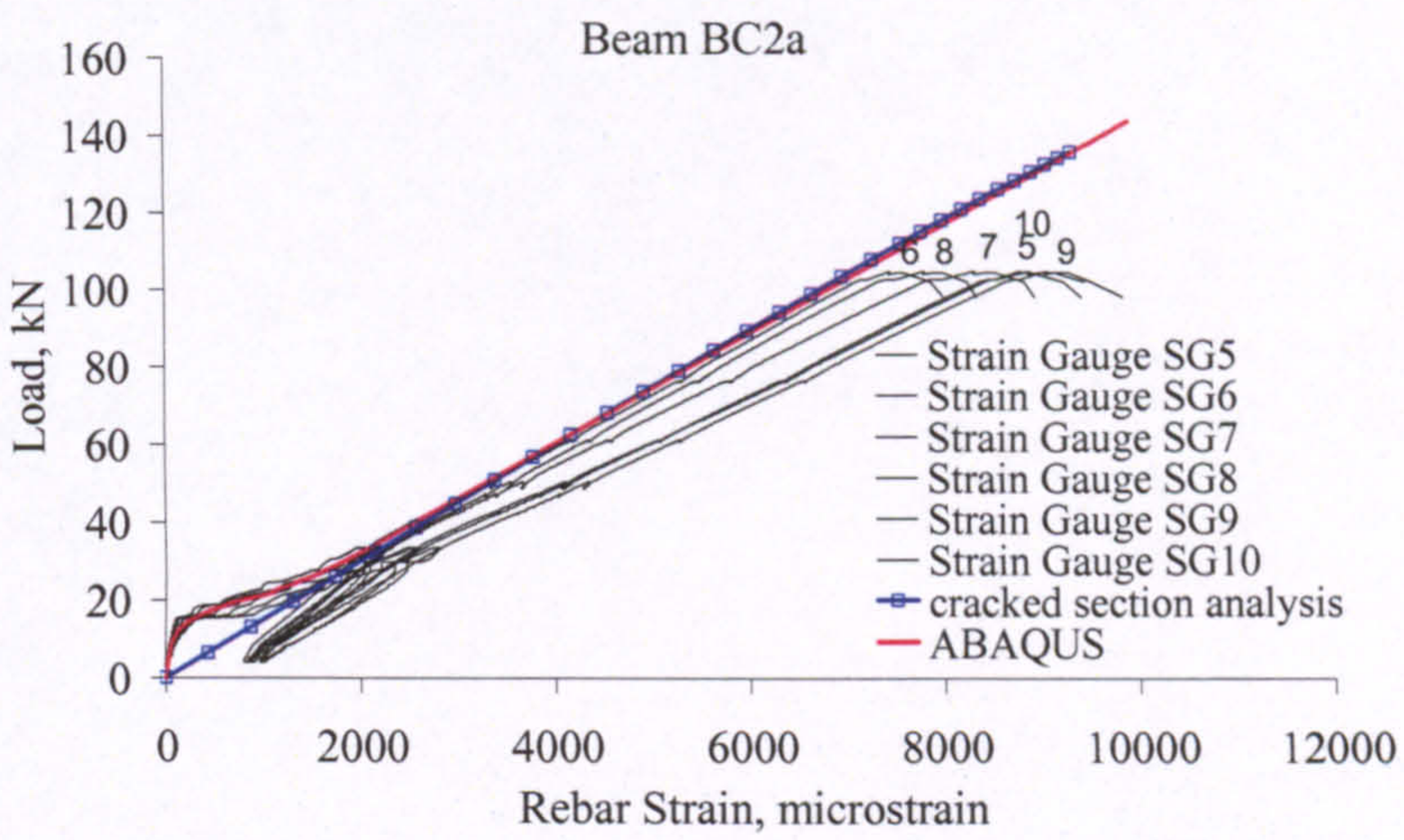

Figure 6-13: Typical CFRP RC experimental and predicted load vs. rebar strain.

Conceptually, there is no fundamental reason for CFRP RC to behave differently from GFRP RC. Hence, to figure out what may have caused or contributed to the unexpected rebar strains in the tested CFRP RC members, it is necessary to consider basic internal equilibrium and compatibility at the section and block (between cracks) levels, as discussed in the following.

- Cracked section

At a cracked section in a pure flexure zone, the internal resisting moment (M) is furnished by a couple of tensile force in the rebars (T_f) and an equal compressive force in the concrete (C_c) separated by a distance (z). M can be expressed as follows.

$$M = T_f z = \varepsilon_f E_f A_f n z \qquad (6\text{-}1)$$

in which ε_f, E_f and A_f are the rebar tensile strain, modulus of elasticity and nominal area, respectively, and n is the number of rebars.

Figure 6-13 indicates that, at a particular strain after cracking, M predicted by CSA considerably exceeds the measured applied M. To explain such a discrepancy it is necessary to examine the variables in Equation (6-1).

z depends on the actual distribution of concrete strains in the compressive concrete zone. At a cracked section, z is expected to be greater than predicted by the linear strain gradient of CSA. In other words, a better estimate of z would lead to an even higher prediction of M, meaning that z may not be the culprit.

A_f is a nominal rebar area that just needs to be used consistently with E_f; since what actually matters is the tensile stiffness (E_f A_f). E_f was determined by tensile tests of representative rebar specimens, where as explained in Chapter 3, average rebar strains were measured by LVDTs and local rebar strains were measured by strain gauges. In those tests, the local CFRP rebar strains were less scattered (less than 5% coefficient of variation)! Therefore, E_f was evaluated based on the local rather than average rebar strains. E_f values were also provided by the manufacturer for the batch of CFRP rebars used. These E_f values were evaluated based on average LVDT strains, and were less than the "local" E_f by no more than 12% (see section 3.3.2.1). Therefore, the "average" E_f of the CFRP rebars used may be lower than their measured "local" E_f.

On the other hand, the CFRP rebars used were still under development, while the final developed rebars are reported to have much better mechanical properties. These CFRP rebars are marketed with an E_f of 124 MPa, tensile strength of 2070 MPa along with nominal rebar areas that are about 90% of those used herein (Hughes Brothers, Inc 2005).

However, to predict the measured M at a particular ε_f in Equation (6-1), an unlikely low value of E_f is required. For beam BC2 (Figure 6-13), an E_f of 105000 MPa is required as opposed to a local E_f of 131750 MPa and the manufacturer average E_f of 122500 MPa. Therefore, a lower E_f may be suspected, but together with another issue that is related to ε_f, as discussed next.

The strains ε_f across a section in a tensioned rebar are assumed to be uniform. However, according to mechanics of materials principles (Gere 2001), these average or nominal strains occur only at sections that are sufficiently away from any disturbance. Depending on the type of disturbance; hole, change in geometry or applied load, disturbed regions undergo different concentrations of stress and strain.

Within a flexural RC member, bond stresses between concrete and reinforcement create disturbing forces on the outer rebar surface. These surface forces are maximised and reversed at cracks. Therefore, for rebar sections at and around cracks, concentration of strain may occur at the rebar surface, meaning that the surface rebar strain exceeds the average rebar section strain. A similar situation occurs close to end anchorages in the rebar tensile tests. This concentration of strains is caused by shear lag. If the shear modulus of elasticity is high, such as in steel rebars, the difference between the surface and average section strains is diminished. However, the shear modulus of FRP rebars is typically of the order of 5000 MPa (Taranu 2005), which makes these composite rebars more susceptible to shear lag effects.

Therefore, in FRP RC flexural members, shear lag may be significant at a crack due to reversal of bond shear stresses. This may have occurred in the CFRP RC tests, meaning that shear lag in the CFRP rebars may have caused the measured surface rebar strain to be higher than the average strain within the rebar section, as illustrated in Figure 6-14. In Equation (6-1), a lower average value of ε_f may obviously reduce the predicted M.

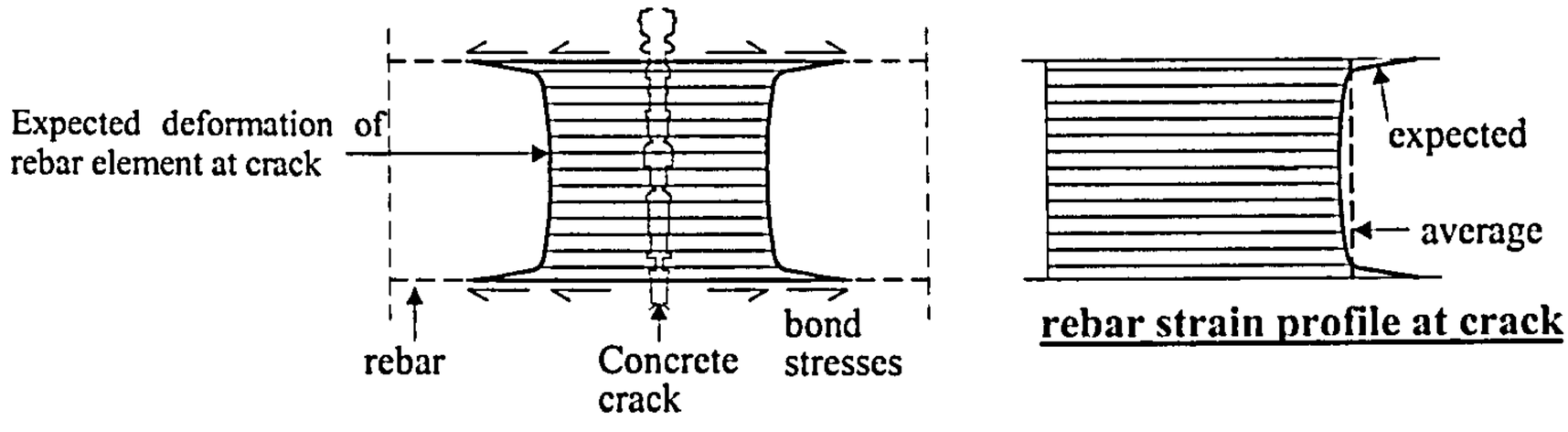

Figure 6-14: Expected and average FRP rebar strain profile at a crack.

Up to this point, the unexpected rebar strains in the CFRP RC members may be attributed either to shear lag in the CFRP rebars together with a lower CFRP rebar modulus or to shear lag on its own. To decide what is more likely, it is necessary to consider the rebar strains measured within the concrete blocks between cracks. Before going into that discussion, shear lag and rebar modulus are further considered at the rebar level.

- Shear Lag and Rebar Modulus of Elasticity

For the general case of a rebar cross section in tension, where the material is heterogeneous and with prominent shear lag effect, the resultant tensile force (T_f) may be expressed as shown in the general Equation (6-2).

$$T_f = \sum_{i=1}^{i=n} A_{fi} E_{fi} \varepsilon_{fi} \qquad (6\text{-}2)$$

in which, A_{fi}, E_{fi} and ε_{fi} are the area, modulus of elasticity and strain of element i, while n is the number of elements in the rebar cross section, as illustrated in Figure 6-15.

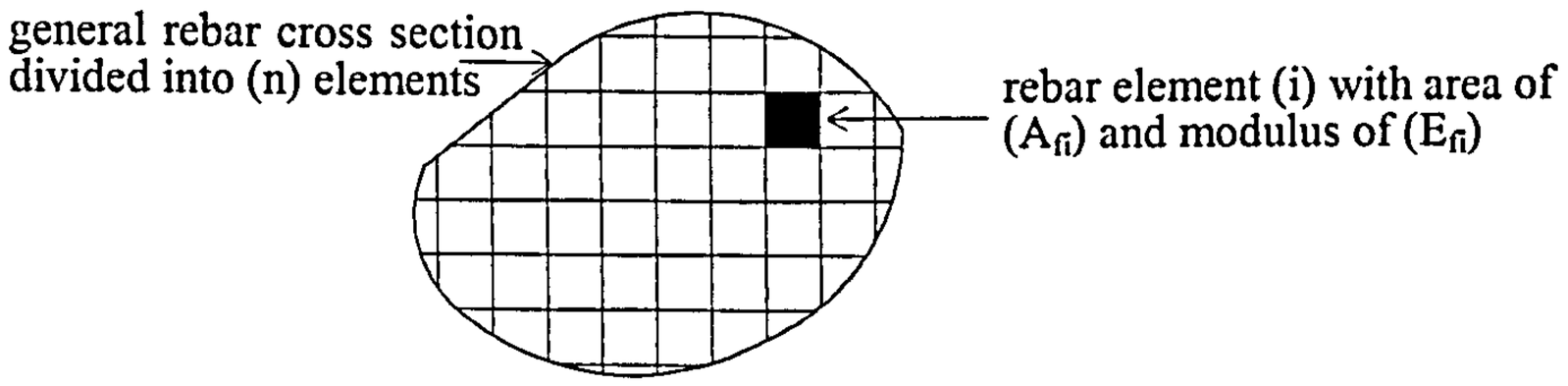

Figure 6-15: General discretised rebar cross section.

In uniaxial tensile tests, the rebar strains are measured in the central zone of the rebar away from the ends; where the shear lag effect is diminished. This creates a special loading condition with uniform sectional strain (ε_f), for which Equation (6-2) reduces to Equation (6-3).

$$T_f = \varepsilon_f \sum_{i=1}^{i=n} A_{fi} E_{fi} = \varepsilon_f A_f E_{f\,ave} \tag{6-3}$$

in which A_f is the nominal rebar area and $E_{f\,ave}$ is an average modulus of elasticity, which is the value normally determined by the tensile test.

In the case where the material is homogeneous and there is shear lag effect, such as in the rebar zone near the end anchorages, the modulus of elasticity is uniform and Equation (6-2) reduces to Equation (6-4).

$$T_f = E_f \sum_{i=1}^{i=n} A_{fi} \varepsilon_{fi} = E_f A_f \varepsilon_{f\,ave} \tag{6-4}$$

in which $\varepsilon_{f\,ave}$ is the average strain across the section considered.

CSA predicts a constant strain across a section at the location of a crack assuming a homogeneous material with no shear lag. When there is shear lag effect, Equation (6-4) becomes applicable, and CSA would then predict the average strain across a rebar section at the location of a crack, but not the maximum surface strain. If both shear lag and heterogeneity are present, the general Equation (6-2) applies, and all rebar variables; modulus of elasticity, area and strain are coupled.

Therefore, homogeneity across the rebar cross section is another issue that is connected with rebar modulus and shear lag. For steel, homogeneity is not of concern, but may be so for the composite FRP material. A basic investigation of homogeneity was carried out for a 9.53mm-diameter CFRP rebar by using Environmental Scanning Electron Microscopy (ESEM). The ESEM revealed that the distribution of carbon fibres is fairly uniform across the rebar cross section, with negligible voids, as shown in Figure 6-16. Hence, the suspicion of non-uniform modulus of elasticity across a CFRP rebar may be relaxed.

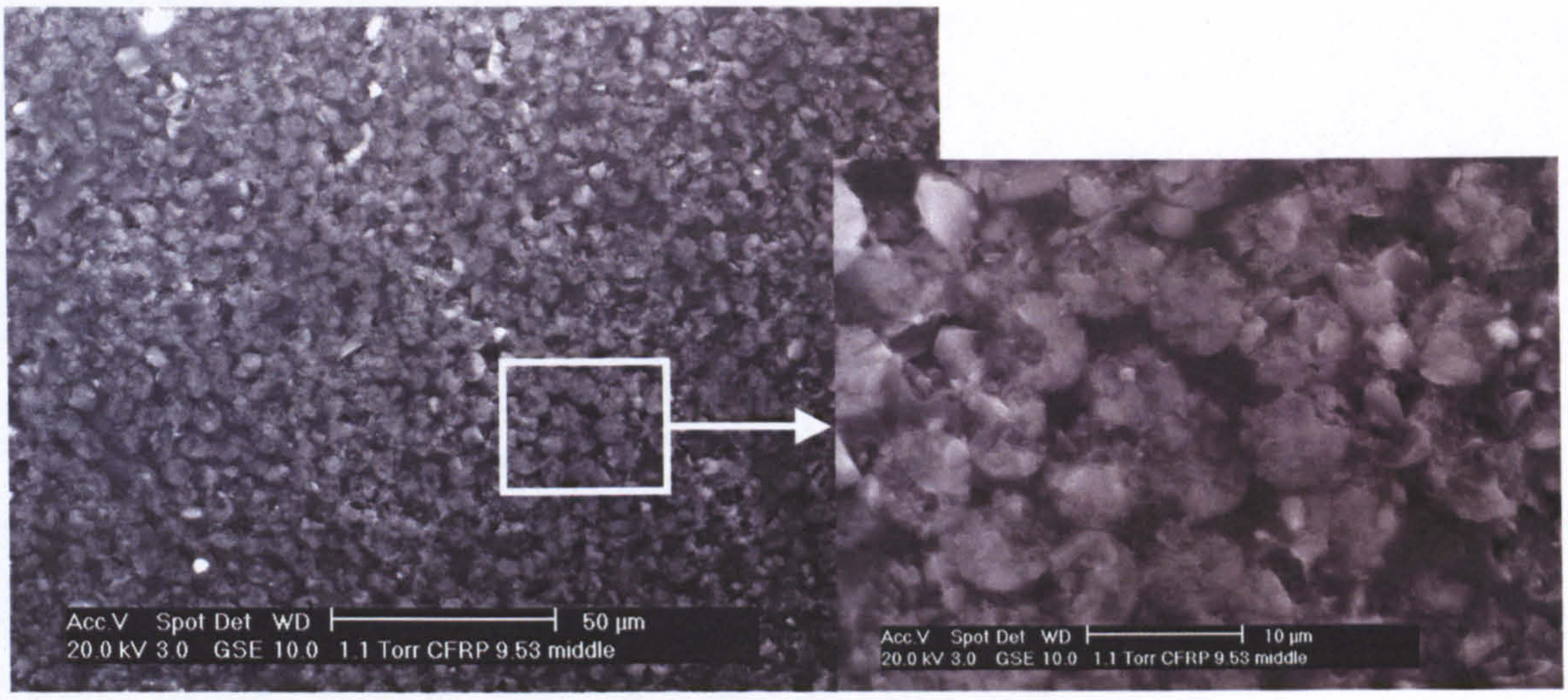

Figure 6-16: Environmental Scanning Electron Microscopy of a CFRP rebar.

- RC Block between Cracks

In an ideal pure flexure zone, cracked sections and sections midway between cracks are planes of symmetry for the rebars, meaning that the rebar cross section should not distort out of those planes after bending or cracking. Distortion can occur if some fibres rupture, which may happen close to failure at high rebar strain levels. Hence, between cracks, the rebar fibres undergo the same overall elongation whether they are surface or inner fibres. Shear lag would only disturb the distribution of strains along these fibres, but not their overall elongation. In other words, all fibres undergo the same average longitudinal strain (ε_{avel}) whether shear lag is present or not. Figure 6-17 illustrates the expected strain distribution across and along an FRP rebar with and without shear lag.

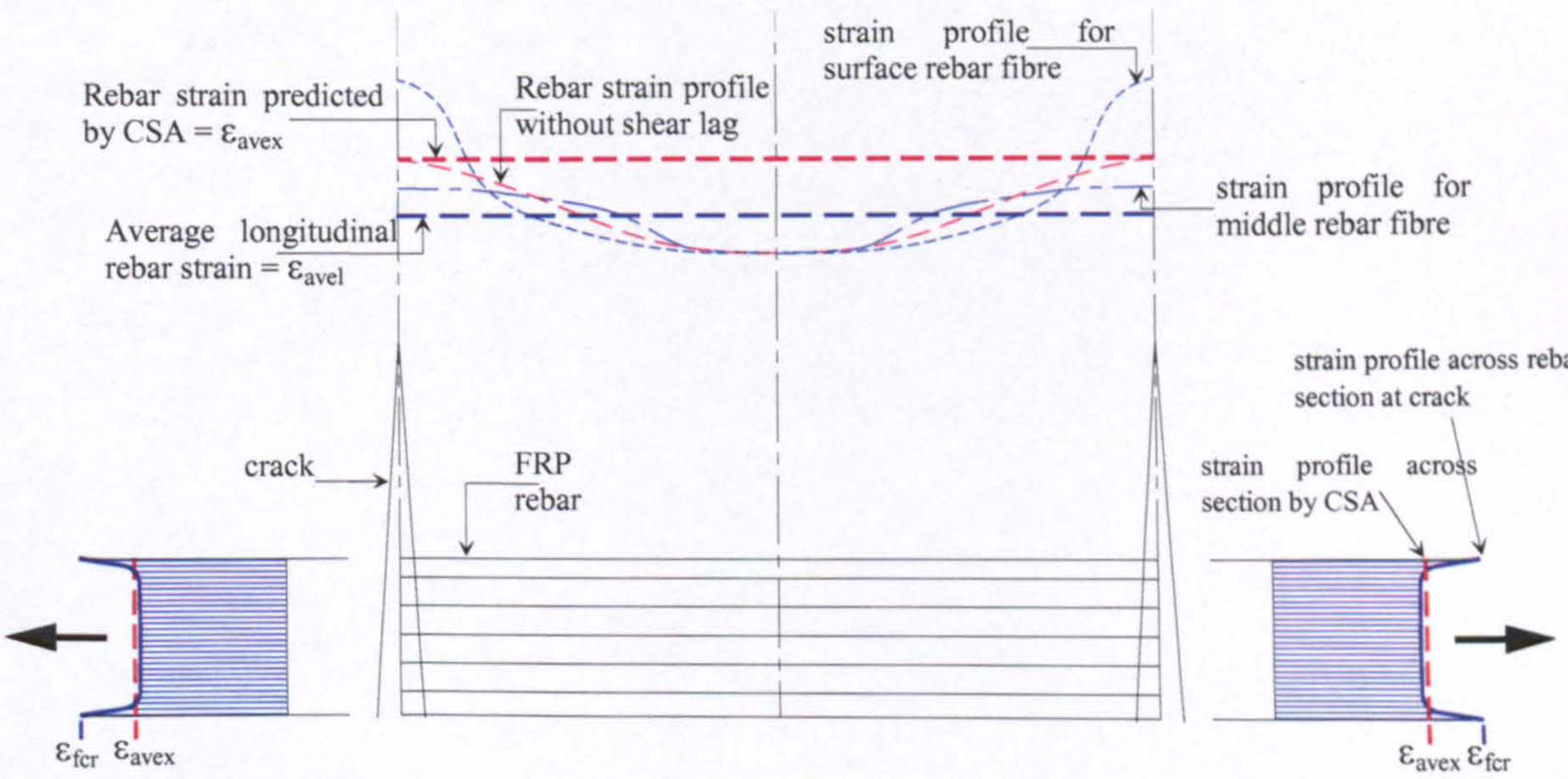

Figure 6-17: Expected strain distribution across and along an FRP rebar.

Figure 6-17 also shows the expected prediction of rebar strain by CSA. At the same force in the rebar, CSA predicts an average strain across the rebar section at the crack (ε_{avex}) that is less than the surface rebar strain at that section (ε_{fcr}). Due to tension stiffening between cracks, ε_{avex} is expected to be higher than ε_{avel}; otherwise the rebar between cracks would elongate more than a bare rebar, which is not possible. Therefore with shear lag, the difference between ε_{fcr} and ε_{avel} would be due to the combined effect of shear lag as well as tension stiffening, and ε_{avex} is expected to be somewhere between ε_{avel} and ε_{fcr}.

The argument on rebar strains and elongation between cracks with shear lag was investigated by a simplistic FE model, as shown in Figure 6-18. A 1080 mm-long, 10mm-diameter CFRP rebar was considered. Realising axisymmetric conditions, only a very thin circular sector of the rebar was considered. In the radial and longitudinal directions, the rebar was modelled by a fine (1x1)mm mesh. The concrete cover around the rebar was assumed to be circular with a thickness of 25mm, and was modelled similarly to the rebar by an (8.3x1)mm mesh in the radial and longitudinal directions. To simulate cracking, the concrete cover was separated every 90mm. Similar to the conditions in the four-point beam tests, two-thirds of the rebar were assumed to be in a shear span, while the remaining third was assumed to be in a pure flexure zone. In the shear zone, the rebar was subjected to drag forces to simulate the drag effect of the concrete on the rebar; as a result of the gradient in the bending moment. The concrete was rigidly connected to the rebar at their common nodes, and was assumed to be elastic in order to enable a stable solution. The interaction of the rebar and concrete between cracks was simulated by varying the modulus of the concrete (E_c). Two extreme E_c values were used; 30000 and 2500 MPa. The CFRP rebar was assumed to be elastic with a longitudinal modulus of 131750 MPa and a shear modulus of 5000 MPa.

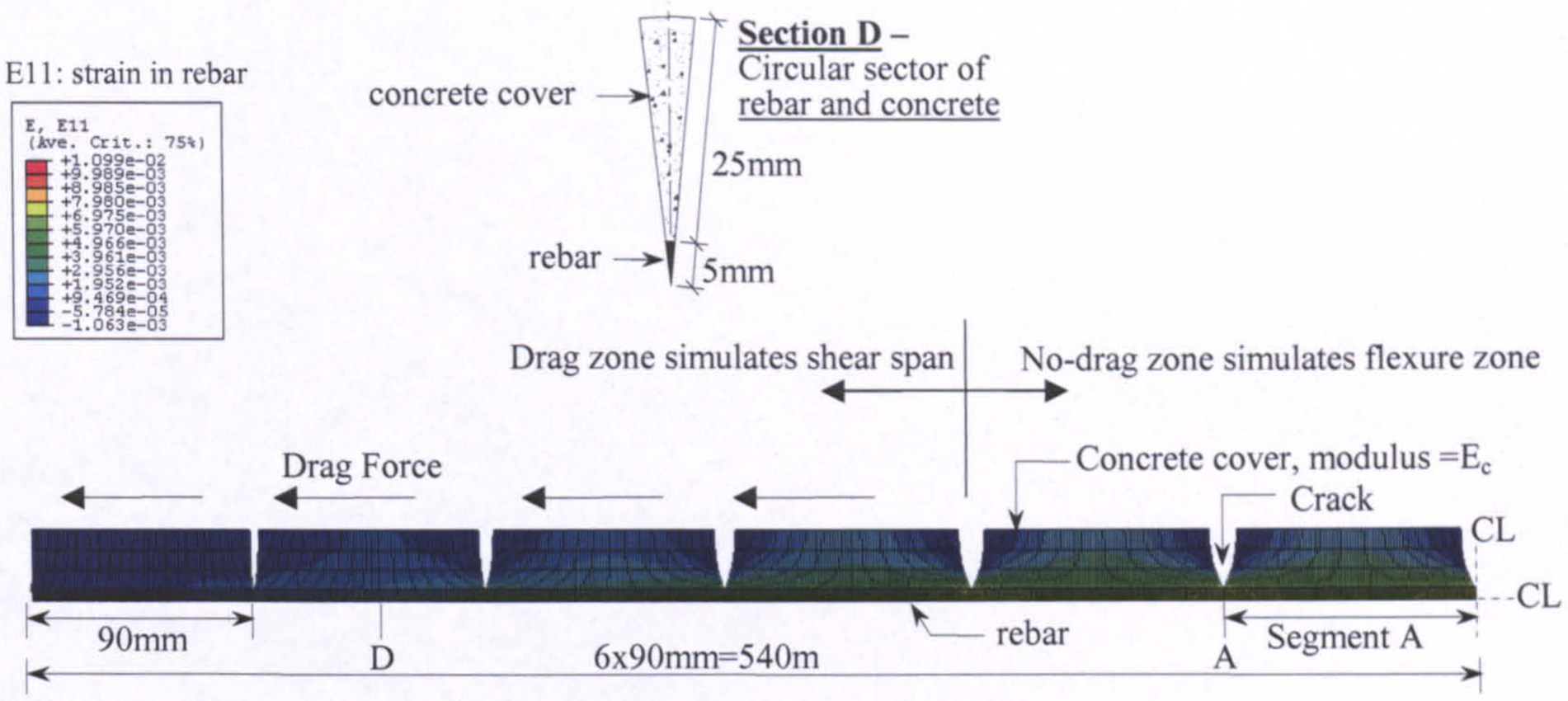

Figure 6-18: Simplified FE model to investigate shear lag in a CFRP rebar.

Rebar strain profiles across cracked section A and along rebar segment A (see Figure 6-18) are shown in Figures 6-19 and 6-20. With a rigid rebar-concrete interaction (E_c=30000 MPa), a massive increase in surface rebar strains can occur at the crack, but sharply drops within a very limited zone of few millimetres around the crack. However, with soft rebar-concrete interaction (E_c=2500 MPa), the effect of shear lag is tempered; as the increase in surface rebar strains is limited, and again drops within few millimetres around the crack. In both cases, the overall elongations of surface and centre elements within segment A are identical.

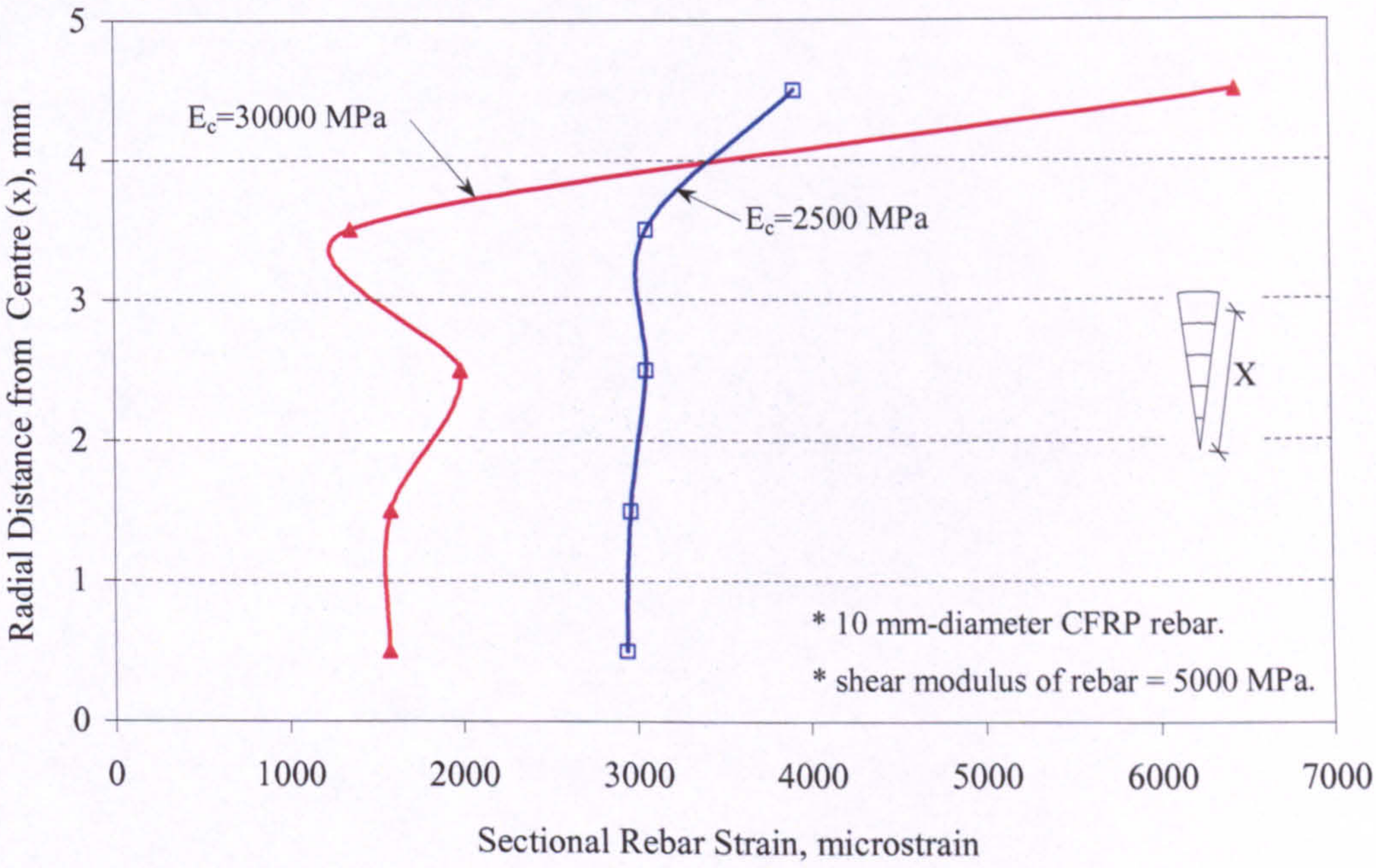

Figure 6-19: Rebar strain profiles at cracked section A.

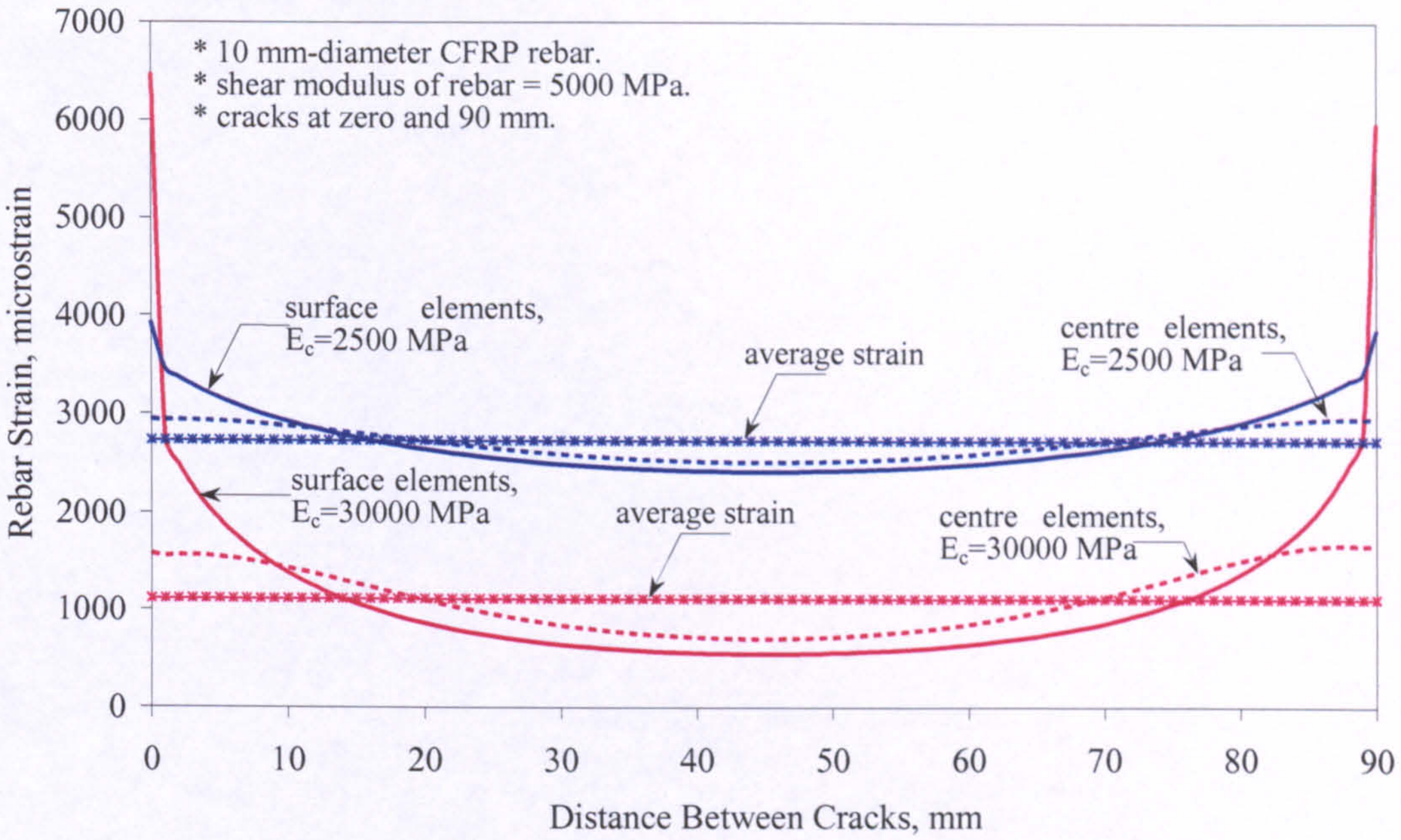

Figure 6-20: Longitudinal rebar strain profiles along segment A.

The previous arguments on shear lag and rebar modulus may be further clarified with reference to Figure 6-21, which compares the measured surface rebar strain at the midspan crack, the measured average rebar strain between cracks and the rebar strain predicted by CSA for beam BC2. At a certain rebar strain at a crack (ε_{fcr}), a measured load (point A) is overestimated by CSA (point B). Shear lag may explain the discrepancy in load prediction; as the measured surface strain (ε_{fcr}) may be greater than the average rebar strain across the cracked section (ε_{favex}), with both strain values corresponding to the same tension in the rebar at the crack, or equivalently to the same applied load (F). Hence with shear lag, point A may actually correspond to point C rather than point B. However at a force level (F), ε_{favex} needs to be somewhere between the average surface rebar strain between cracks (ε_{favel}) and ε_{fcr}; meaning that point C needs to slide somewhere between points D and A. This is only possible if the CFRP rebar had a lower modulus (E_f) than that used in CSA. In other words, shear lag may not explain the discrepancy of measured and predicted CFRP rebar strains on its own and may still be associated with a reduced rebar modulus. For beam BC2, the reduced rebar modulus would need to be in the range of 105000 to 113500 MPa, which is 80 to 86% of the measured local rebar modulus, or 86 to 92% of the manufacturer average rebar modulus. This also indicates that the combined effect of shear lag and tension

stiffening may be up to about 8%; taken as a ratio of the difference between surface and average sectional strains at the crack to the crack surface strain [(ε_{fcr}-ε_{favex})/ ε_{fcr}].

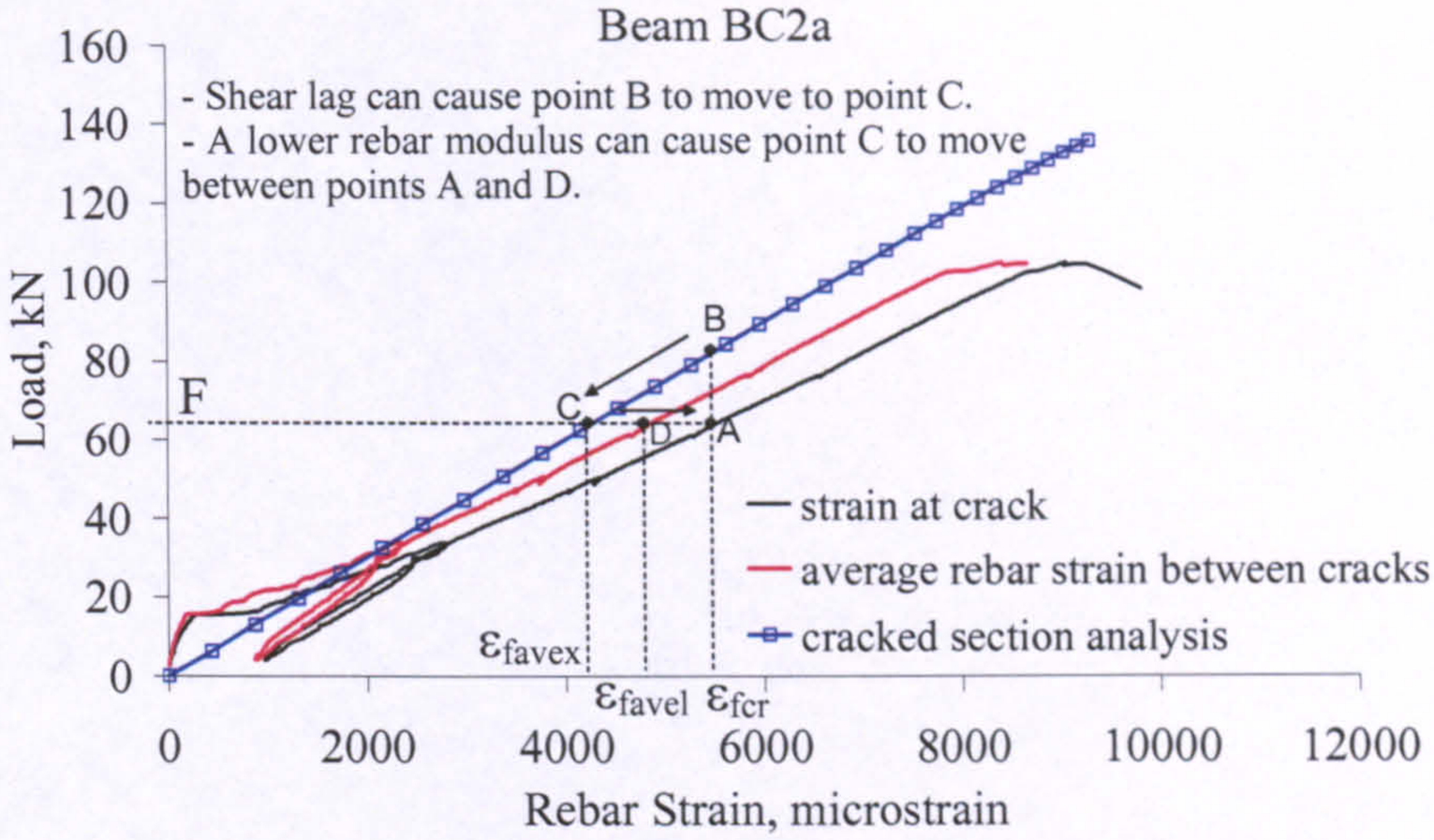

Figure 6-21: Measured crack rebar strain and average strain between cracks vs. prediction of CSA for beam BC2.

- Reduced Rebar Modulus

As will be shown in Section 6.3.4, the experimental load-curvature relationship evaluated using the measured rebar strains predicts very well the measured deflections in most of the tested CFRP beams and slabs; which indicates that the measured rebar strains may not be suspicious. A reduced rebar modulus not only matches with the measured rebar strains but also with the measured deflections. Furthermore, most of the CFRP RC tests indicate a lower rebar modulus as well. The maximum expected rebar modulus values that correspond to the measured average longitudinal rebar strain (ε_{favel}) were evaluated for every CFRP RC test, as shown in Appendix B, and are summarised in Table 6-2.

Table 6-2 may indicate some inconsistencies as well as trends. For beam BC1 and slab SC1 with the 6.35mm-diameter CFRP rebar, there seems to be no major problem with the rebar modulus; as the local rebar modulus predicts, at worst, the measured average rebar strain between cracks instead of the crack rebar strain. For beams BC2 and slabs SC2 with the 9.53mm-diameter CFRP rebar and for beams BC3 with the 12.7mm-

diameter CFRP rebar, a reduced rebar modulus compares better to the measured strains. Such a reduced modulus is of the order of 86% of the local modulus or 92% of the average modulus.

Table 6-2: Measured and maximum expected rebar modulus of elasticity for CFRP RC

CFRP RC Member	Rebar Diameter, mm	Locally Evaluated Modulus, MPa (1)	Manufacturer Average Modulus, MPa (2)	Maximum Expected Modulus, MPa (3)	Modulus Ratio, (3)/(1), %	Modulus Ratio, (3)/(2), %
BC1a	6.35	133000	119250	local modulus predicts average strain between cracks		
BC1b	6.35	133000	119250	measured strains not representative[1]		
BC2a	9.53	131750	122500	113250	86	92
BC2b	9.53	131750	122500	108000	82	88
BC3a	12.7	118600	111700	102000	86	91
BC3b	12.7	118600	111700	103250	87	92
SC1a	6.35	133000	119250	local modulus predicts strain at crack		
SC1b	6.35	133000	119250	local modulus predicts average strain between cracks		
SC2a	9.53	131750	122500	113250	86	92
SC2b	9.53	131750	122500	119900	91	98
SC3a	12.7	118600	111700	measured strains not representative[1]		
SC3b	12.7	118600	111700	measured strains not representative[2]		

[1] Measured strains indicate a reduced modulus for the rebar instrumented with strain gauges only; as these strains lead to deflections and/or crack width that are higher than measured.
[2] Slab was accidentally loaded and pre-cracked before the test. In such a case, the measured strains would be reduced by the amount of residual strains at the restart of the test.

A reduced rebar modulus may be attributed to poor quality control, but this does not seem to be the case. For one thing, the moduli of the tested rebar specimens show little scatter that does not raise any suspicion concerning material variability. Moreover, the local modulus evaluated in the uniaxial tensile tests is consistently higher than the average modulus provided by the manufacturer, and can be more representative of the smaller batch of rebars used in the CFRP RC tests.

It is believed that the issue of an effective reduced rebar modulus is a consequence of the presence of shear lag. Generally in Table 6-2, it may be observed that the reduced rebar modulus is only associated with the larger 9.53 and 12.7mm diameter rebars.

Shear lag is also expected to become more prominent as rebar diameter increases. Moreover, shear lag may be amplified in FRP rebars due to their relatively low shear modulus. As discussed earlier, an FRP rebar may undergo shear lag throughout a cracked zone within a flexural FRP RC member. In contrast, in a uniaxial tensile test, an FRP rebar may undergo shear lag only in limited zones at the end anchors. Nevertheless, it remains unexplained how shear lag may have caused the CFRP RC beams and slabs to show a reduced effective modulus of elasticity! This issue requires further dedicated research, which is beyond the scope of this thesis. However, it is advisable to minimise the shear lag effect through appropriate design and production of FRP rebars.

Other possibilities may be considered to envisage why a reduced rebar modulus is effective in the CFRP RC tests, though these may be less likely than shear lag. One possibility may be related to the fact that the RC beams and slabs were tested at an age of more than a year after casting. Hence, if the CFRP rebars used had deficient durability inside the concrete, then the rebar modulus might have deteriorated with aging. To check this possibility, a 9.53mm-diameter rebar was extracted from a CFRP RC member and was tested in uniaxial tension. The resulting rebar modulus compared very well with the local modulus, which indicates that there was no quantifiable durability effect on the rebar. Moreover, the smallest 6.35-mm diameter CFRP rebars should have been most affected if there was a rebar durability issue, which was not indicated by the flexural tests.

Another possibility may be that the surface fibres of the CFRP rebars were breaking; particularly at the cracks where bond stresses are at their maximum. This may lead to one scenario on how shear lag can result in a reduced rebar modulus. A low shear modulus reflects low cohesiveness within the rebar in its transverse direction, which may cause the surface fibres to be more vulnerable to breaking. However, the CFRP rebars were visually inspected after the tests and did not show any surface damage.

Before ending this section, it is important to consider two queries concerning shear lag. Firstly, can shear lag be quantifiable in the CFRP RC rebars used to start with? And if this is the case, are CFRP rebars more susceptible to shear lag than GFRP rebars? Again, these issues require specialised investigation, but are simplistically considered next.

- Quantifying Shear Lag in CFRP Rebars

An attempt was carried out to quantify shear lag in a 12.7 mm-diameter CFRP rebar in a uniaxial test setup, as shown in Figure 6-22. Besides the end-anchors that are necessary for a proper grip at the jaws of the tensile machine, additional intermediary steel tubes were glued close to one end anchor, as detailed in the figure. The space between the steel tubes may be equivalent to concrete cracks, and the steel tubes may stiffen the rebar similar to concrete between cracks. Therefore, strains measured between the tubes may be indicative of the surface strain at a crack, where the effect of shear lag is maximised. Moreover, strains measured at the centre of the free part of the rebar are far enough from any disturbance, and should be uniform across the rebar. Real reinforced concrete conditions are expected to be more severe in terms of shear lag than this simplified setup. For one thing, real cracks are much narrower than the gap between the tubes, which was dictated by a working distance necessary to glue the strain gauges. Furthermore, the concrete between cracks provides a much larger effective stiffening area around a rebar, which may enhance the shear lag effect.

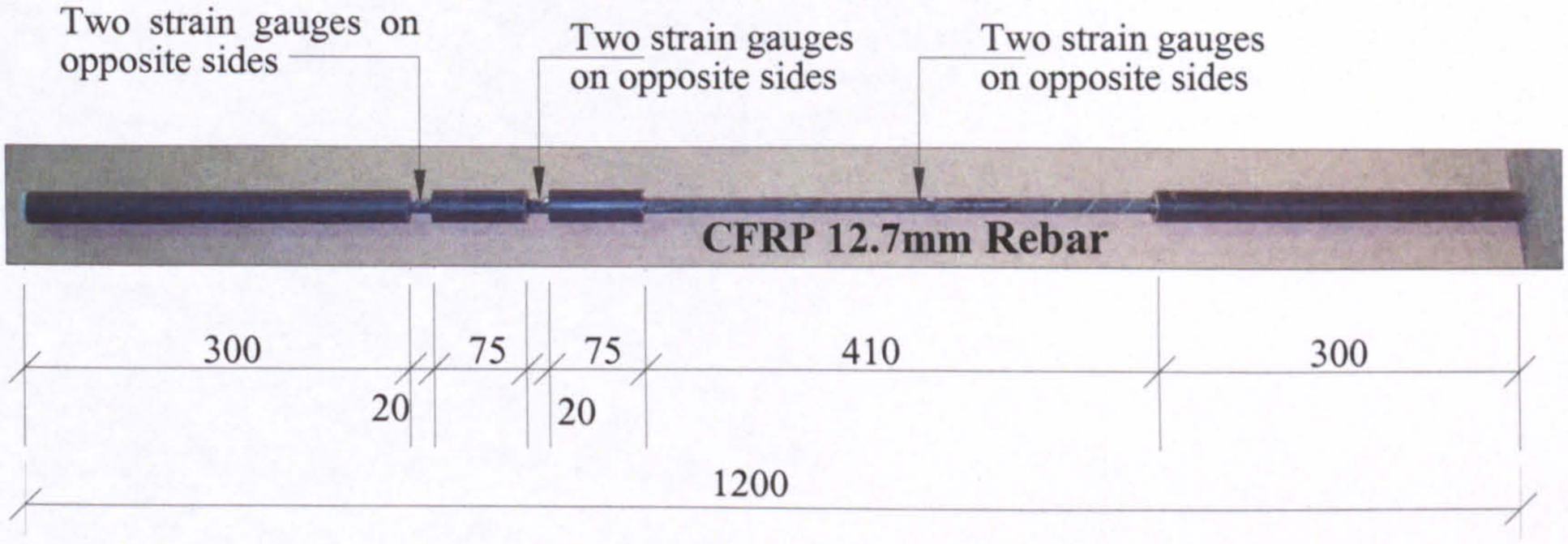

Figure 6-22: Uniaxial test setup to quantify shear lag in a CFRP rebar.

Two rebars were tested for shear lag, and the results were similar in both cases. Figure 6-23 compares the rebar strains measured in one of those tests. The average rebar strain is about 85 to 90% of the surface rebar strain between the steel grips. This indicates that the measured strains may include a shear lag effect as high as about 15%.

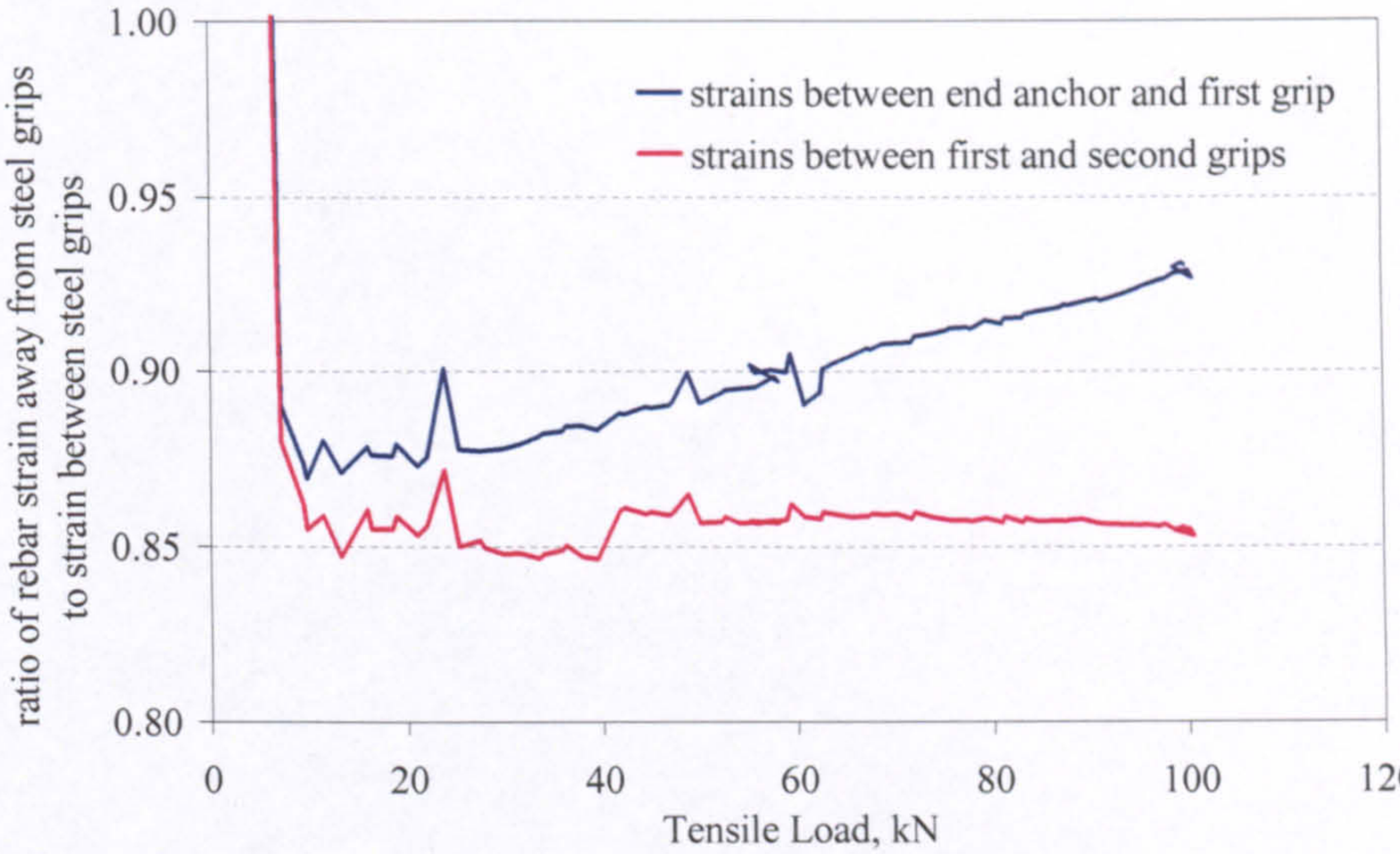

Figure 6-23: Results of CFRP rebar shear lag test.

- Shear Lag: CFRP versus GFRP

To verify if CFRP rebars may be more susceptible to shear lag than GFRP rebars, another simplistic FE analysis was undertaken, as shown in Figure 6-24. 600mm-long CFRP and GFRP rebars, with 7x10mm rectangular cross section, were modelled by a fine 1x1mm mesh. The rebars were subjected to uniaxial tension conditions with 50 kN tensile load at both ends. The tensile load was distributed uniformly over the outer nodes within a distance of 100mm at both ends; crudely simulating shear forces transferred by end anchors. The modulus of elasticity was taken as 40000 MPa and 130000 MPa for the GFRP and CFRP rebars, respectively. The shear modulus was taken as 5000 MPa for both rebars.

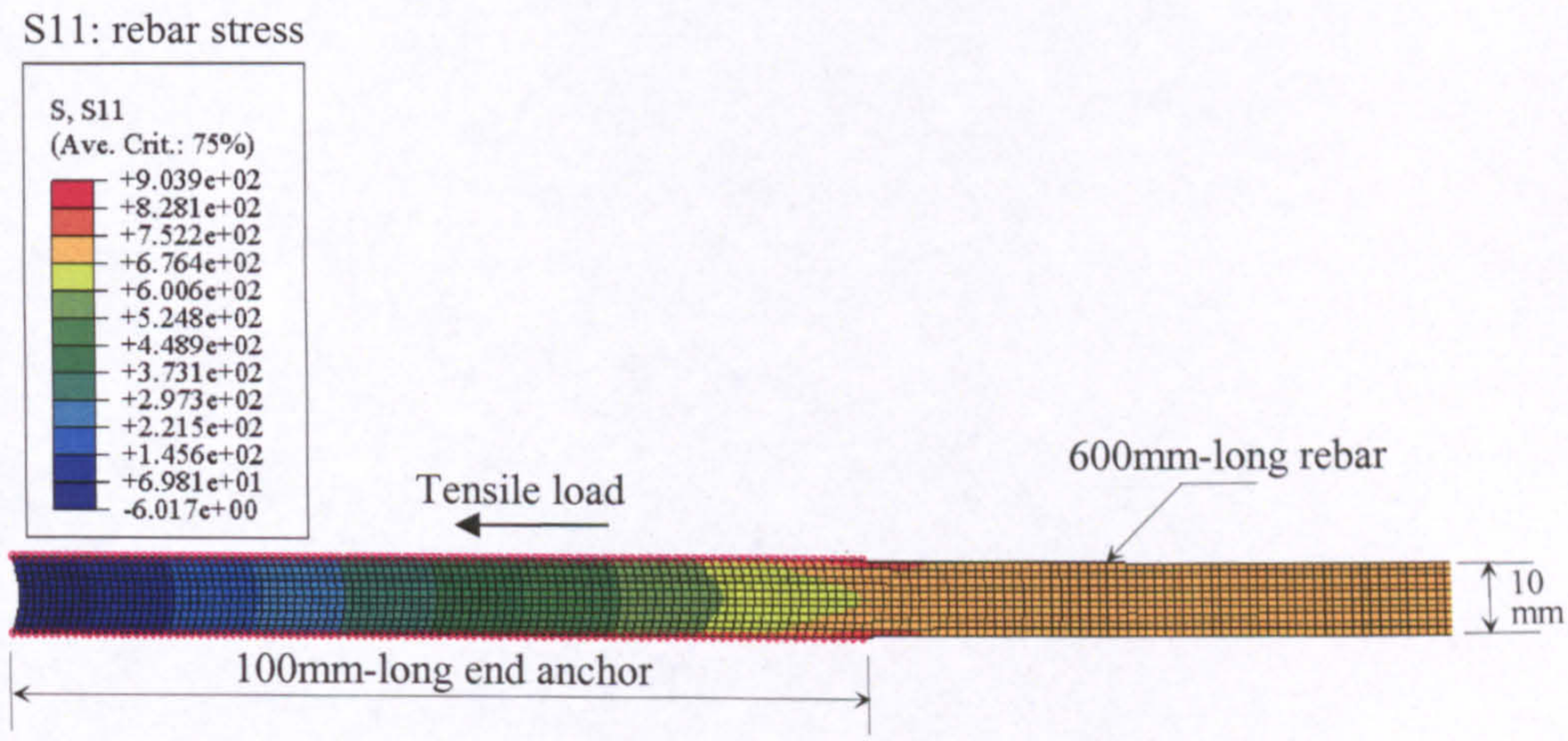

Figure 6-24: FE model and stress contours for an FRP rebar under uniaxial tension.

Due to the difference in rebar modulus, the FE results are considered in terms of rebar stresses rather than strains. Figure 6-25 compares stress profiles of rebar sections 1mm and 7mm outside one end anchor. At 1mm, both CFRP and GFRP rebars suffer from shear lag; as the surface stresses are significantly higher than the centre stresses. However, the ratio of surface to centre stresses is much higher for the CFRP rebar, which indicates that the shear lag effect is more pronounced for CFRP. At a distance of 7mm, the stresses are rather uniform in the GFRP rebar, while shear lag in the CFRP rebar is reduced but still noticeable. This indicates that the higher shear lag effects in CFRP require a longer distance to fade away.

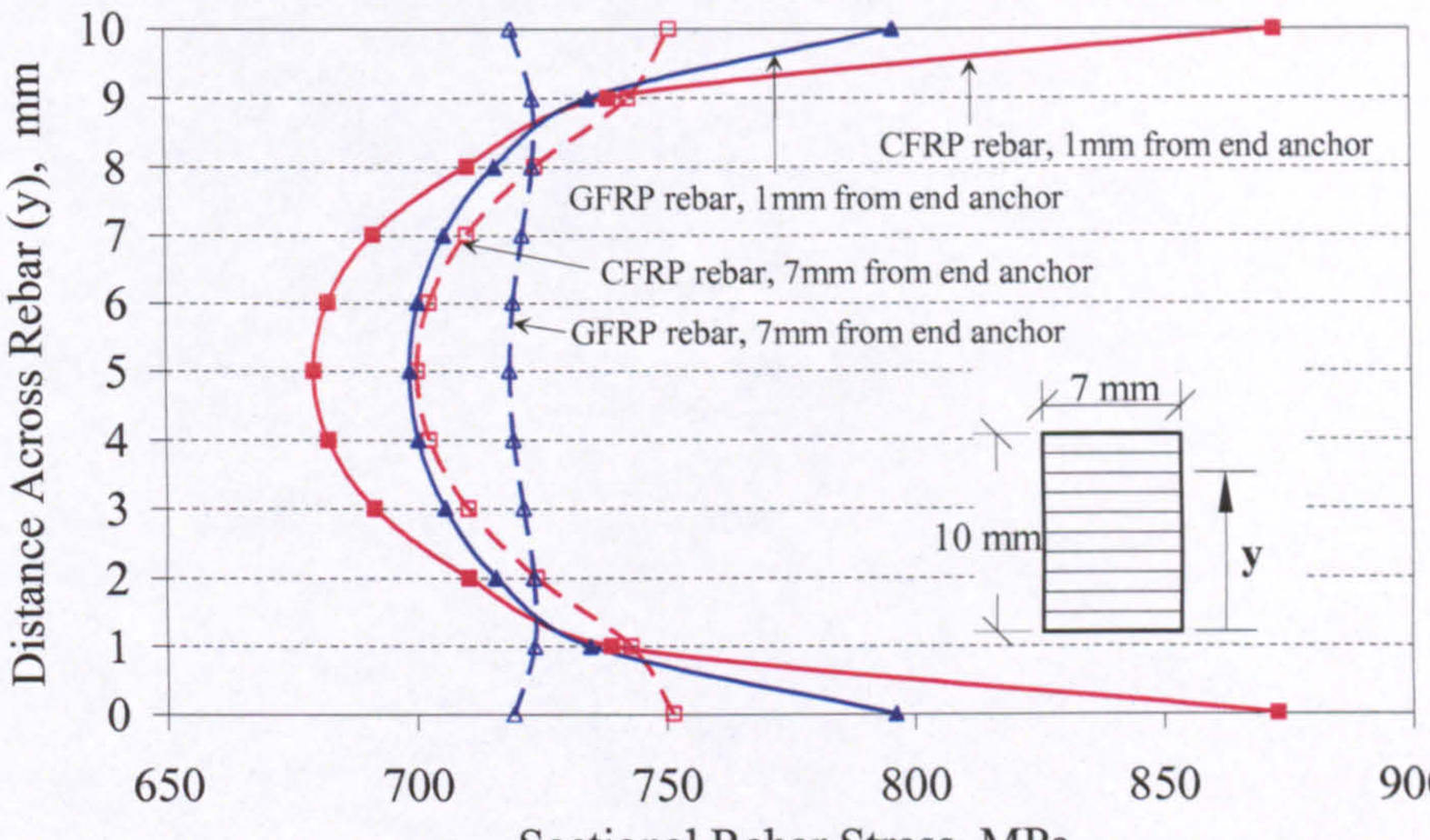

Figure 6-25: Sectional rebar stresses just outside an end anchor.

Similarly, Figure 6-26 compares the stress profiles at outer and centre fibres within a distance of 10mm from the end anchor. Again, both CFRP and GFRP rebars show noticeable shear lag just outside the end anchor; as the outer fibre stresses are higher than the inner fibre stresses. However, shear lag in the CFRP rebar is more significant. Moreover, the shear lag effect in the GFRP rebar disappears over a very short distance of about 5mm from the end anchor, whereas in the CFRP rebar, shear lag is still obvious at a distance of 10 mm.

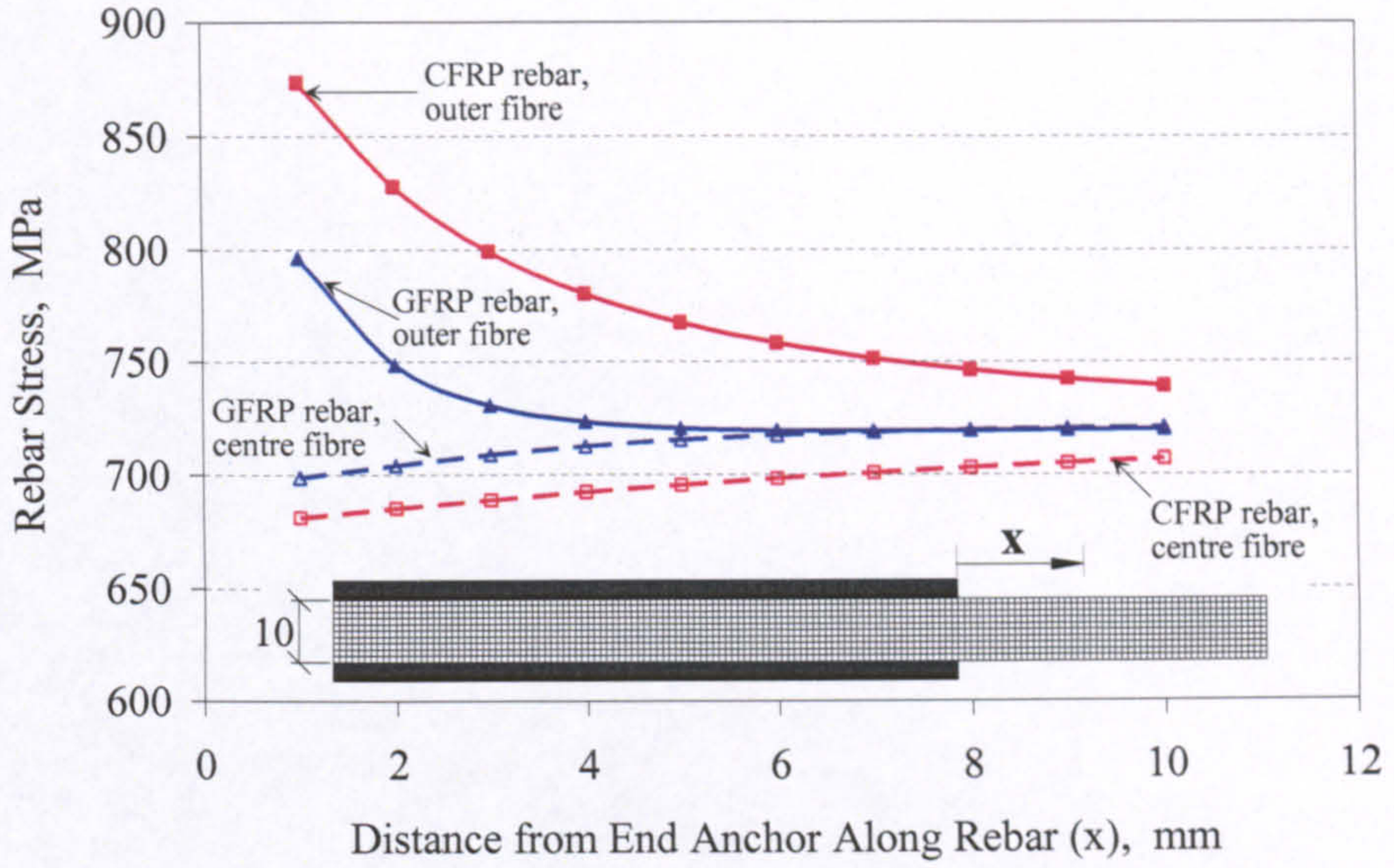

Figure 6-26: Longitudinal rebar stresses just outside end anchors.

Therefore, it may be concluded that, for the same tensile force and shear modulus, shear lag in CFRP rebars may be higher than in GFRP rebars, and may influence a longer distance along the rebar. Nevertheless, it is worth pointing out that shear lag effects are not generally very obvious in the CFRP RC strain profiles around the midspan crack. This may be due to the surface strain measurement being an average over a 6mm-gauge length, and to possible slip within few millimetres around the crack.

In the following sections, the prediction of CSA and FE analysis are based on both the local rebar modulus evaluated in the uniaxial tensile tests and the reduced effective rebar modulus evaluated in Table 6-2. This enables a further consideration of the effects of those two modulus values.

6.3.2. Strain in the Concrete

Similar to the GFRP RC beams and opposite to the GFRP RC slabs, CSA underestimates the maximum compressive concrete strain at the extreme concrete fibre at midspan for both the CFRP RC beams and slabs, as typically shown in Figures 6-27 and 6-28. This may further support the earlier argument that the unexpected concrete strains in the GFRP RC slabs might have been caused by lack of concrete homogeneity. The concrete strains predicted by FE analysis are somewhat better than those predicted by CSA.

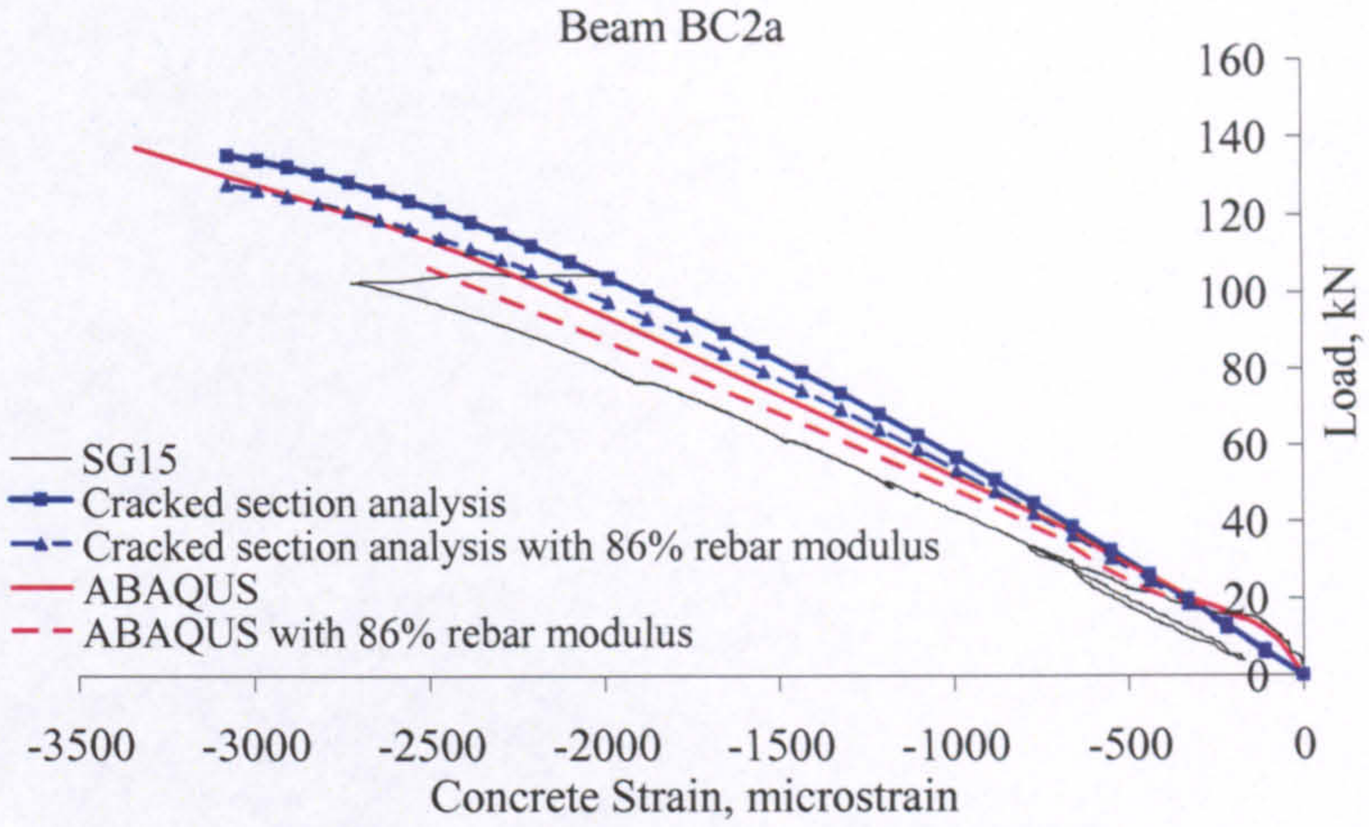

Figure 6-27: Typical CFRP RC beam experimental and predicted load vs. concrete strain.

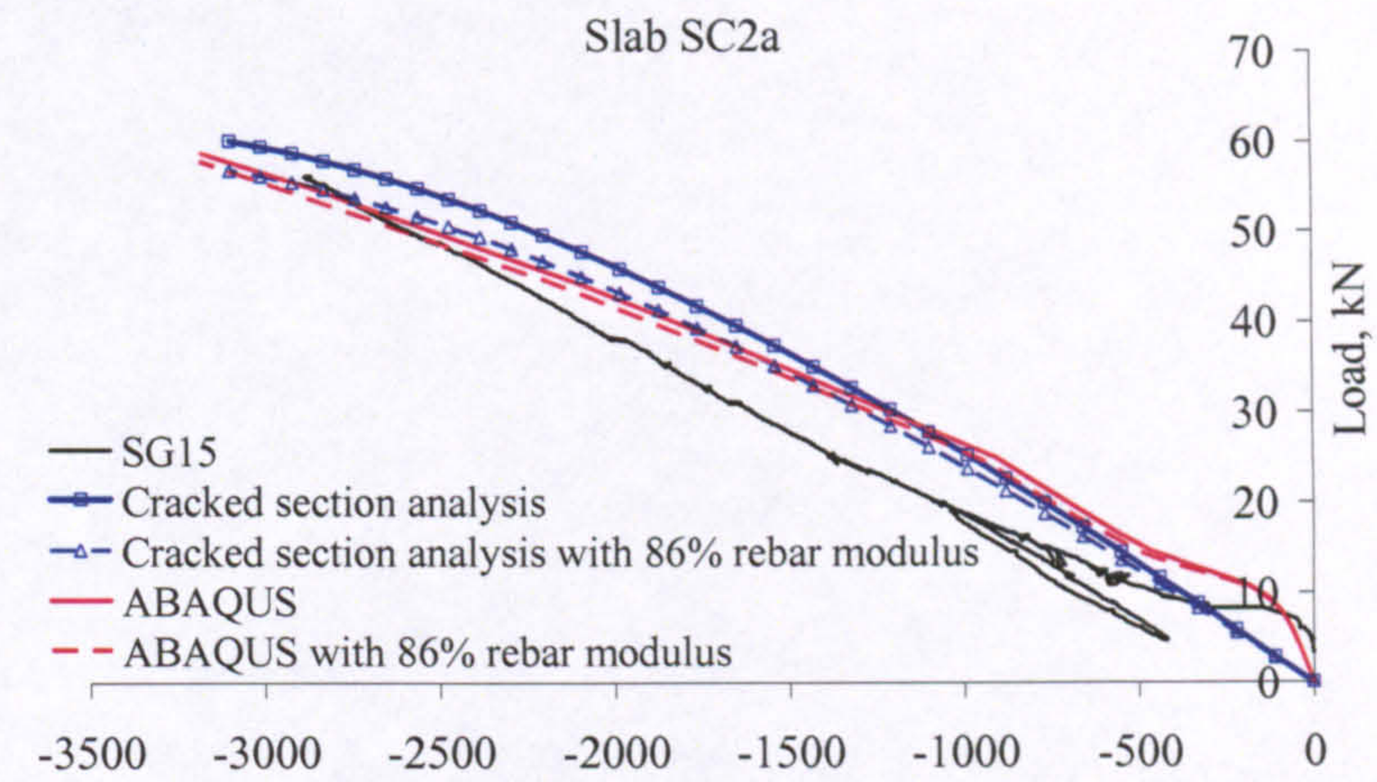

Figure 6-28: Typical CFRP RC slab experimental and predicted load vs. concrete strain.

Again, the variation in predicted and measured concrete strains may be related to the characteristics of cracks in terms of their width and penetration. The response of the compressive concrete zone may also be influenced by the suspected shear lag as it may enhance the localised effect of cracks. In both analyses, using a reduced effective rebar modulus improves the prediction of concrete strains, which further supports this concept.

6.3.3. Failure Load

Table 6-3 summarises the measured and CSA-predicted failure loads for the CFRP RC members, along with their modes of failure. When failure is by rupture of rebars, the failure load predicted by CSA is within only 4% of the actual failure load. The premature rupture of rebars indicated by the GFRP RC tests with small diameter rebars (6.35 mm) does not seem to be an issue for CFRP rebars with similar diameter. Apparently the difference in bond characteristics between the GFRP and CFRP rebars has some significance in that regard.

Table 6-3: Experimental and CSA prediction of load capacity and failure modes

Series	Beam or Slab	Cover, mm	Test		CSA[2]			Load Capacity Ratio, CSA/Test, (2)/(1)
			Load Capacity, kN, (1)	Failure Mode	Load Capacity, kN		Failure Mode	
					Measured Local, E_f[3], (2)	Reduced Effective E_f		
BC1	BC1a	25	73.7	Rupture	75.0	N.A.[4]	Rupture	1.02
	BC1b	25	77.0	Rupture				0.97
BC2	BC2a	25	104.8	Crushing[1]	135.6	127.9	Crushing	1.29
	BC2b	25	103.2	Crushing[1]				1.31
BC3	BC3a	25	122.8	Crushing	158.2	149.9	Crushing	1.29
	BC3b	25	124.6	Crushing				1.27
SC1	SC1a	31	38.0	Rupture	39.5	N.A.[4]	Rupture	1.04
	SC1b	33	37.5	Rupture	38.6		Rupture	1.03
SC2	SC2a	38	56.3	Crushing[1]	60.2	56.9	Crushing	1.07
	SC2b	35	56.7	Crushing[1]	62.7	60.5	Crushing	1.11
SC3	SC3a	42.5	61.3	Crushing	60.2	N.A.[4]	Crushing	0.98
	SC3b	36	71.2	Crushing	69.5		Crushing	0.98

[1] Crushing almost immediately followed by rupture of rebars, which is very close to balanced failure.
[2] Maximum usable concrete strain (ε_{cu}) = 0.003.
[3] E_f is the rebar modulus of elasticity.
[4] Refer to Table 6-2.

When failure is by crushing of concrete, a contradictory trend is indicated in Table 6-3. Similar to GFRP RC, CSA overestimates the actual failure load by up to 11% for the CFRP RC slabs. The use of an effective reduced modulus can even decrease such difference. However, for the CFRP RC beams, CSA greatly overestimates the actual failure load by about 30%. Again, the use of a reduced rebar modulus can decrease

such difference, but only by 7%. Such inappropriate failure load prediction may be attributed to weaker concrete in the compressive concrete zone than that evaluated by testing the control concrete specimens. Nevertheless, it may be worthwhile not to overlook shear lag, which was suspected in those CFRP RC beams. By causing higher than average surface strains at and around a crack, shear lag can enhance the localisation effect of a crack, which in turn may negatively influence the behaviour of the compressive concrete zone. Therefore, in addition to using a reduced rebar modulus for CFRP rebars, it may also be required to reduce the maximum usable strain in the concrete to about 0.0025; as a means of reducing the flexural capacity predicted by CSA. However, undermining the load capacity of CFRP RC members is a safety issue that may not be tolerated, and if shear lag was indeed the culprit, then it may be imperative to be able to evaluate and diminish shear lag in any FRP rebar product.

Stratford and Burgoyne (2002) discuss that the current strain-based analysis does not satisfy compatibility at a crack but is appropriate for steel RC because the ductile steel reinforcement allows for redistribution of stresses and the lower bound theorem may be applicable. For brittle FRP RC, redistribution of stresses cannot occur and it is considered necessary to simultaneously satisfy equilibrium and compatibility at a crack. Therefore, a crack-based analysis is proposed for FRP RC, where the response of the compressive concrete zone is related to the geometric characteristics of the crack opening as a stress-crack width relationship, as shown in Figure 6-29. Such an analysis also allows for the bond characteristics of the FRP reinforcement and its compatibility with the surrounding concrete. High bond is considered to be undesirable; as it may change the failure mode from compressive to rupture of rebars. It is emphasized that these issues should be fields for future research.

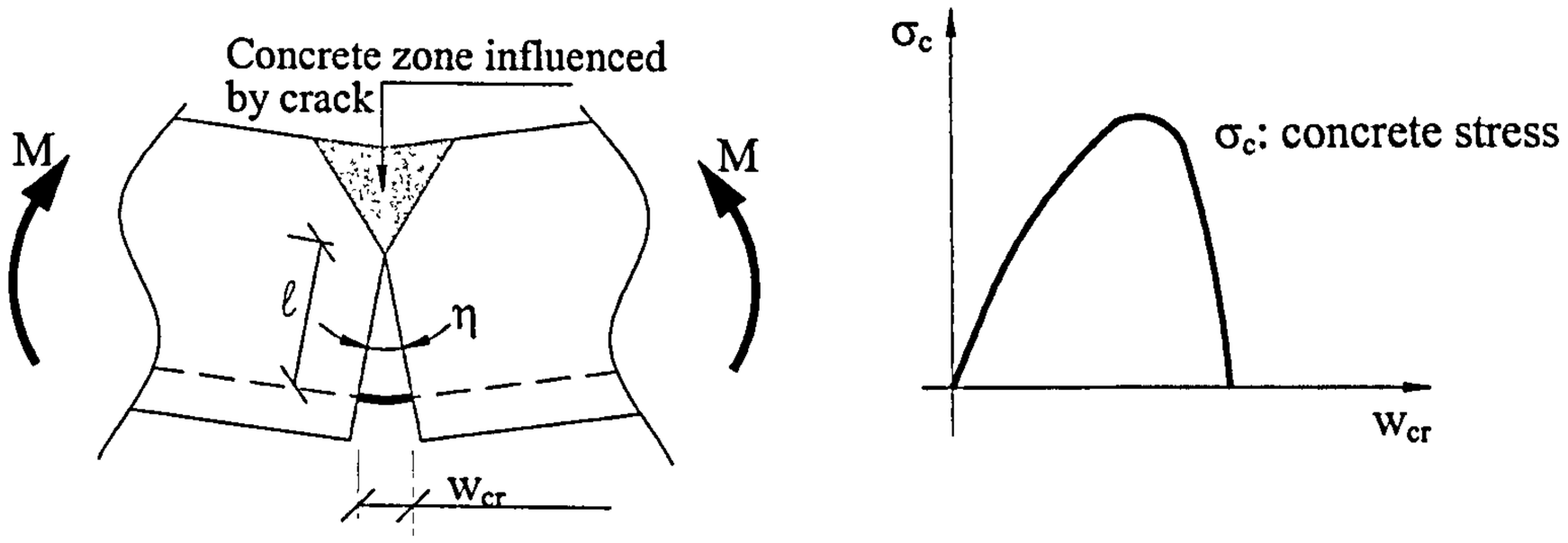

Figure 6-29: Crack-based flexural analysis of FRP RC (Stratford and Burgoyne 2002).

6.3.4. Deflection

Deflection of CFRP RC beams and slabs was dealt with similarly to GFRP RC. Hence, midspan deflection predictions were made based on the experimental load-curvature relationships and by numerical FE analysis and CSA. Both the measured local rebar modulus and estimated reduced rebar modulus were considered in the analysis.

Again, the deflection-relevant experimental and analytical results are examined together to try to firm-up on the deflection behaviour of these structural members, as well as the adequacy of the analytical approaches used. Most aspects may be covered by considering beam BC2, as discussed in detail next. Particulars of other CFRP RC tests are pointed out as well.

- Beam BC2

Figure 6-30 shows the relevant experimental results and data analysis of beam BC2a. The corresponding predictions by FE analysis and CSA are also shown in the figure.

The deflection predicted based on the experimental load-curvature matches the measured deflection up to the failure load. In fact, this is the case for all the CFRP RC beams and slabs, except for beam BC1b and slab SC3a! It follows that the rebar and concrete strain measurements have no major problem. Moreover and contrary to GFRP RC, shear-induced deformations seem to be insignificant within the entire loading range.

By examining the profiles of rebar strain at discrete load levels, it is obvious that additional strains in excess of flexural requirements do occur within the shear span, but to a much less extent than GFRP RC. Again, this is the case for all the tested CFRP RC beams and slabs, which indicates negligible shear-induced deformations for these members.

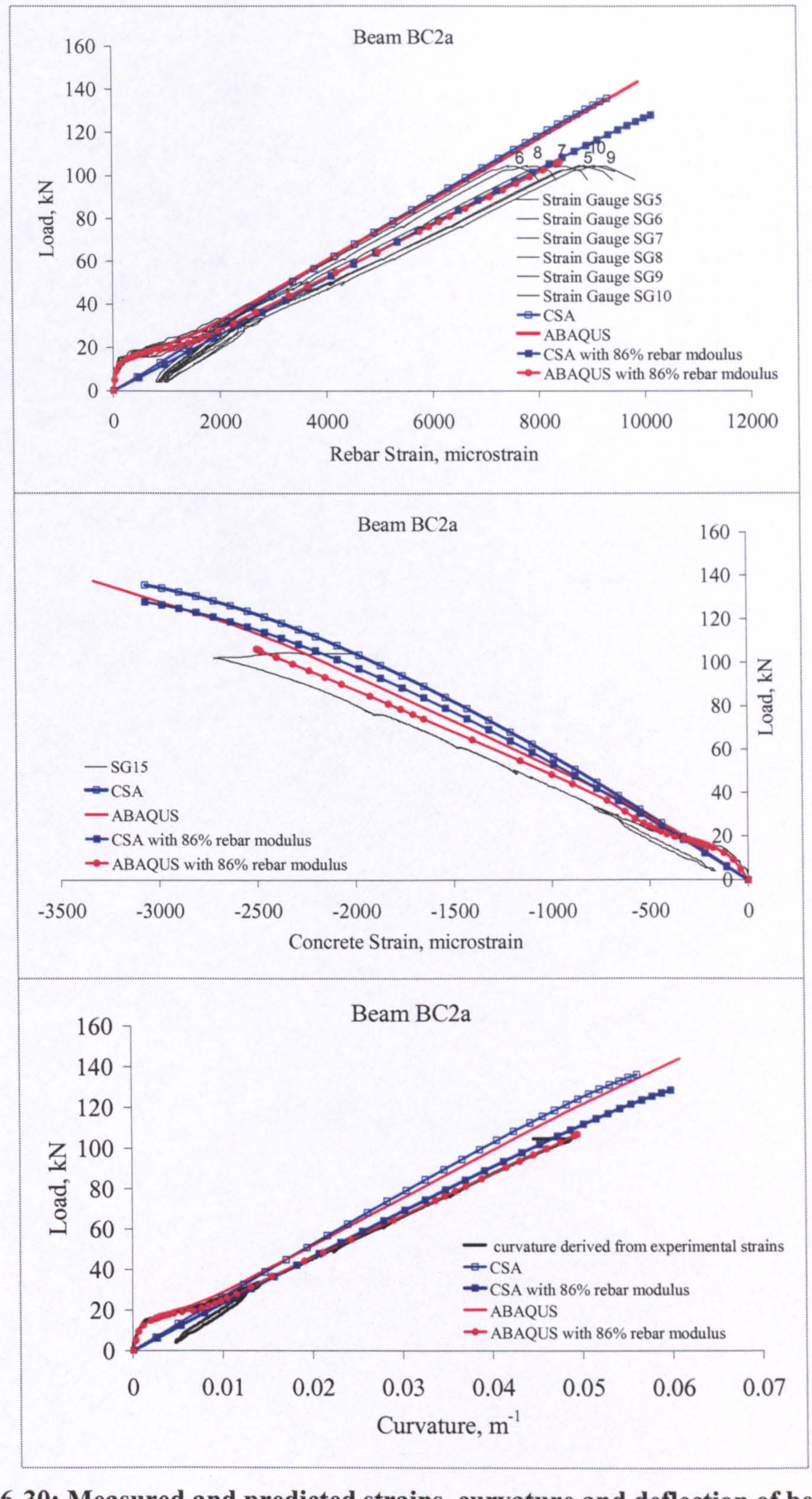

Figure 6-30: Measured and predicted strains, curvature and deflection of beam BC2.

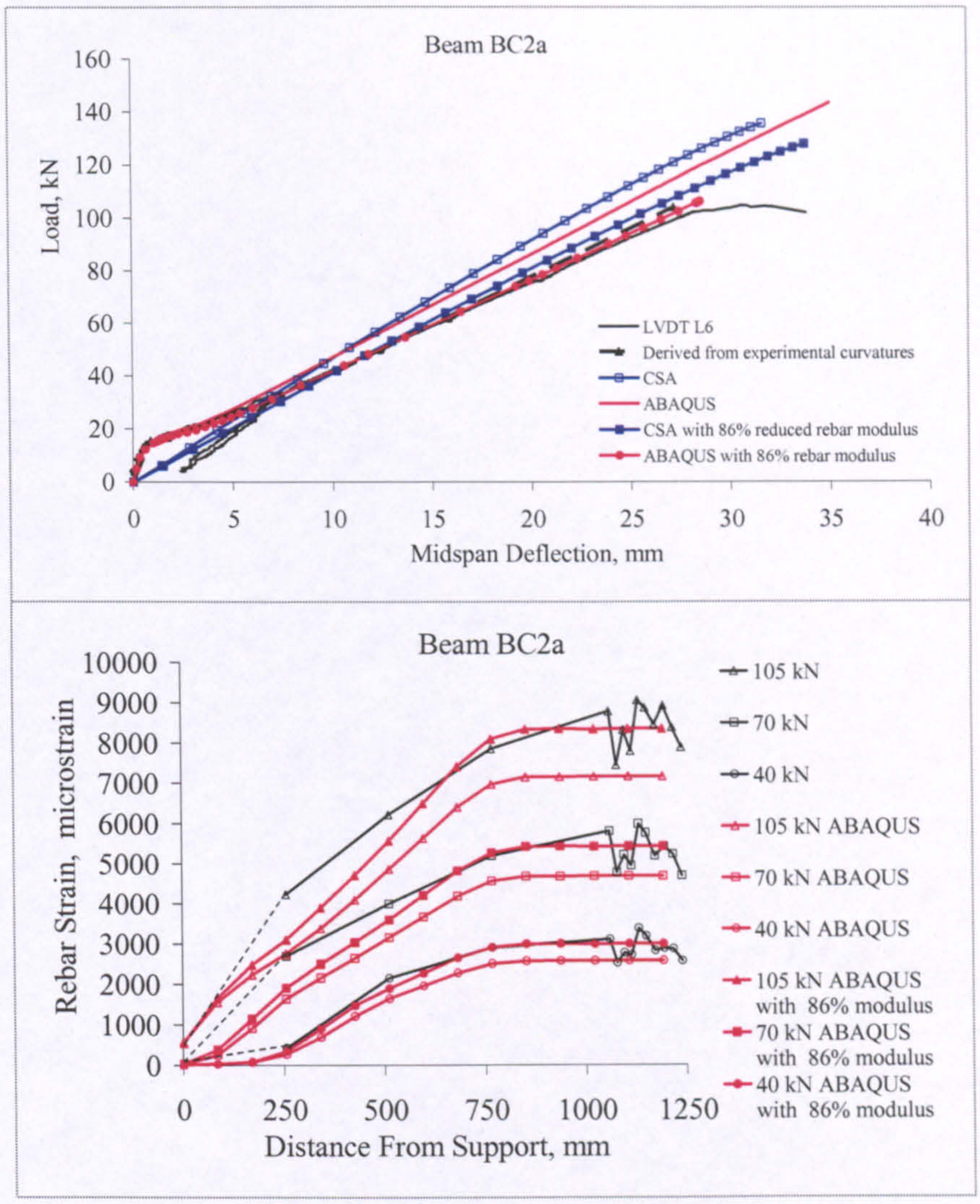

Figure 6-30-cont.: Measured and predicted strains, curvature and deflection of beam BC2.

In the discussion on GFRP RC, shear-induced deflections were related to the deformation characteristics of concrete teeth between cracks in the shear span, which were expected to be mainly influenced by the width and penetration of cracks. The width and penetration of a crack are expected to be dependent on the tensile stiffness of the reinforcement (E_fA_f), regardless of the type of reinforcement. However, CFRP RC beam BC1 and GFRP RC beam BG2 had almost equal E_fA_f. Moreover, both beams reached comparable shear levels in their shear span. Nonetheless, shear-induced deflections are obvious in beam BG2 but are insignificant in beam BC1. A similar situation applies for slabs SG1 and SC1, which also have almost equal E_fA_f. The difference in behaviour may be related to the difference in bond characteristics of the GFRP and CFRP rebars. With differing bond characteristics; crack spacing, width and penetration may differ as well. For instance, with better bond the spacing of cracks is

expected to reduce, which means that the crack width and penetration may also reduce. Therefore, insignificant shear-induced deflections in the CFRP RC members may have been associated with their higher rebar modulus as well as their bond characteristics. This highlights the importance of bond in the specialized research on shear-induced deformations that was recommended earlier.

As shown in Figure 6-30, when using the measured local rebar modulus, both CSA and FE analysis underestimate the measured deflection. The level of tension stiffening in FE analysis could not be calibrated to match the experimental deflection, as the predicted deflection always converged to the CSA solution. However, when using a reduced rebar modulus, the deflection predicted by FE analysis matches with the experimental deflection throughout the entire loading range, and CSA provides a reasonable upper-bound for deflection. Moreover, the reduced rebar modulus leads to better prediction of rebar strains, not only within the pure flexure zone but also within the shear span. Therefore, a reduced rebar modulus may be effective in beam BC2. A reduced modulus compares better with the deflections and rebar strains of beam BC3 and slab SC2 as well. For the other CFRP beams and slabs (BC1, SC1 and SC3), the deflections predicted by CSA using the measured local modulus values compare well with the measured deflection! Moreover, FE analysis can match the deflection of those CFRP RC members as it always converges to the CSA solution.

When discussing the CFRP rebar strains, shear lag was discussed rather extensively. However, it could not be resolved if or how or under what conditions shear lag may have caused a reduced rebar modulus to be effective within the CFRP RC members specified above. In addition, considerable work and time were spent trying to predict the measured rebar strains and deflections of beam BC2; without reducing the rebar modulus and by using various options offered by FE analysis. However, all these efforts always led to a dead end. It was sometimes possible to refine the deflection prediction, but at the expense of some unrealistic physical behaviour. Moreover, the rebar strains at midspan always converged to those predicted by CSA, which may be expected because these strains follow from simple equilibrium at a cracked section, as discussed earlier. Nevertheless, those FE attempts are very briefly presented next, as the experience gained may be useful.

- Truss reinforcement

The CFRP reinforcement was modelled as truss elements rigidly connected to the nodes of continuum elements at the level of reinforcement. This approach did not offer any noticeable advantage over the "REBAR" modelling of reinforcement.

- Springs

ABAQUS offers both linear and nonlinear spring elements. Hence, the CFRP reinforcement was modelled as truss elements, as above, but these were connected to the continuum nodes by springs. Results of rebar pull-out tests with short embedment lengths were used to develop some idea on the properties of these springs. In principle, springs should totally model the reinforcement-concrete interaction characteristics. In ABAQUS, the concrete-softening model indirectly accounts for this interaction, and may not be waived or replaced by springs. Therefore, the use of springs was additional to the concrete-softening model, and was expected to allow for possible additional slip of the reinforcement, particularly within the shear span.

The use of springs did allow for somewhat better prediction of deflection when low-stiffness springs were used, but prediction of rebar strains was never improved. This indicates that the predicted deflection was associated with an unrealistic mechanism. Low-stiffness springs resulted in large reinforcement slip within the shear span. In order for this to happen, bond should be in a degrading stage. However, the average bond between cracks was shown to increase up to failure, even reaching higher levels than the GFRP reinforcement, as shown in Chapter 4.

- Tied arch

The truss rebars were allowed to slip freely between the midpoints of the two shear spans, while of course deflecting with the concrete in the vertical direction. This solution simulates what may happen in a tied-arch situation. In this case, the measured deflection could be matched, but again not the rebar strains. The tied-arch option is actually an extreme case of slip and non-composite RC behaviour, which again was not indicated by the tests.

- Model with discrete cracks

In an attempt to simulate the discrete crack approach, vertical crack planes were introduced every 100mm within the centre span and part of the shear span, as shown in Figure 6-31. Again, the reinforcement was modelled as truss elements. Springs were introduced in some trial solutions as well. Tension stiffening could not be waived, but was less effective because it was interrupted at the cracks. The rebar strain and deflection response were not changed by using this model, other than they converged more quickly to the CSA solution as a result of the reduced tension stiffening.

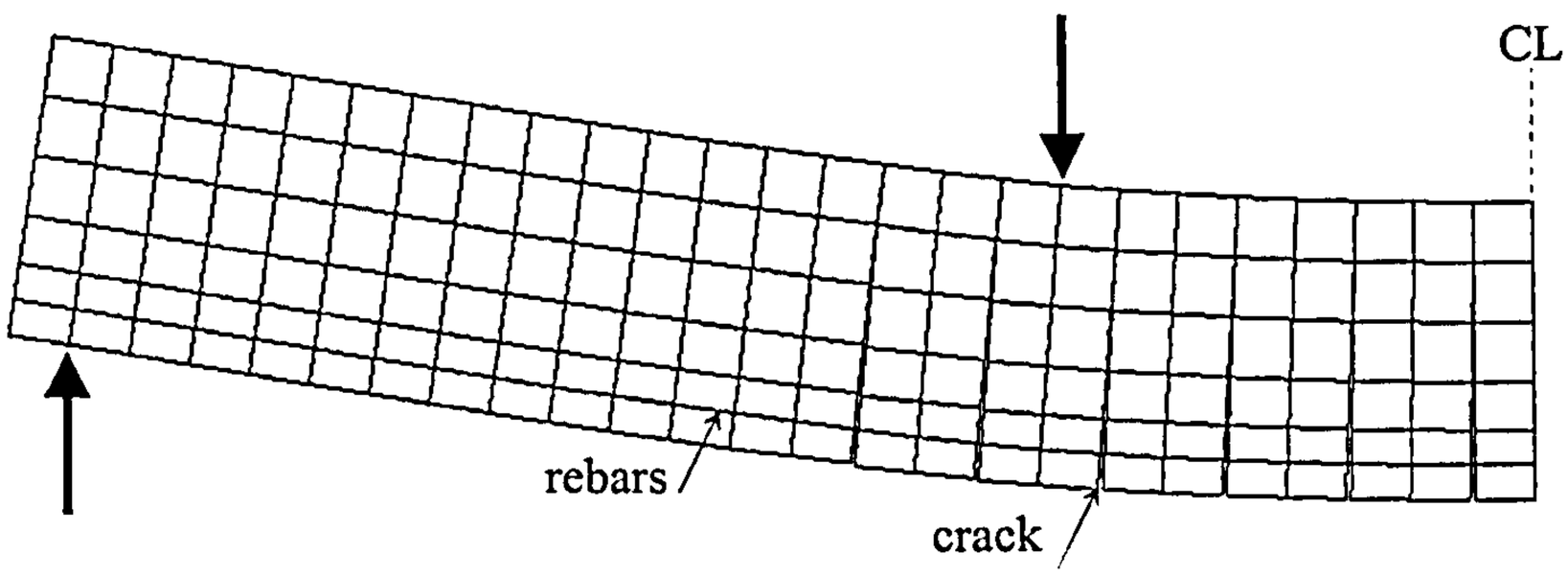

Figure 6-31: Model with discrete cracks.

Nevertheless, this model enabled some investigation of the localised effects of cracks, by comparing the concrete strains at a cracked section and a section midway between cracks, as shown for example in Figure 6-32. The figure shows a case where the extreme fibre compressive concrete strain above the crack is 23 % higher than that midway between cracks. Moreover, the compressive concrete zone has less depth at the cracked section. These results agree with what have been repeatedly pointed out in the previous discussions in that regard. Therefore, such a cracked model may be a valuable analytical tool for investigating the localised effect of cracks on the response of the compressive concrete zone.

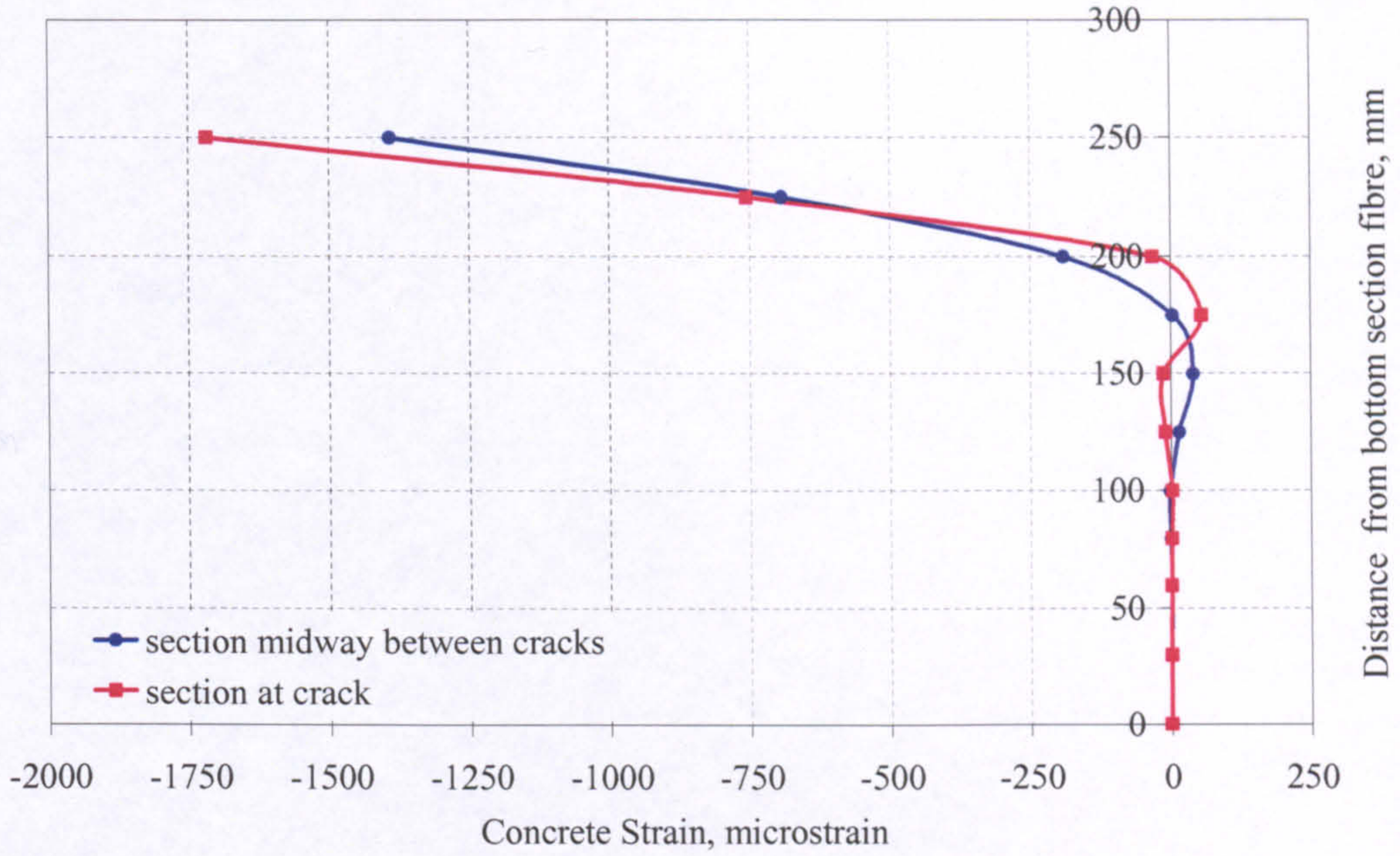

Figure 6-32: Strain profiles at a cracked section and a section midway between cracks.

6.3.5. Conclusions

In addition to the earlier conclusions regarding the behaviour of GFRP RC flexural members, the fairly detailed discussion of the CFRP RC results may be conducive to some additional important aspects of behaviour, which may be summarised as follows.

- Contrary to GFRP RC, shear induced deformations are insignificant for CFRP RC. In that case, deflections may be evaluated based on flexural curvatures, which require proper evaluation of tension stiffening at the rebar level. The localised effect of cracks on the compressive concrete strains may still be noticeable and needs to be considered as well.
- The rebar bond characteristics may be an important factor in limiting shear induced deformations, as it may affect the crack width and penetration.
- FE-analysis with discrete cracks may be valuable in investigating the response and extent of the compressive concrete zone.
- Some of the CFRP RC elements show an unexpected behaviour where the rebar strains and deflections exceed those predicted by CSA, despite the negligible shear induced deformations. Those members behave as though their reinforcement has a

lower effective reduced modulus. This is believed to be caused by shear lag in the rebars, but could not be physically explained and requires further dedicated research.

- Shear lag may enhance the localised effect of cracks, and may result in premature failure. Therefore, it is prudent to diminish shear lag in any FRP rebar product.
- Shear lag may be more prominent in CFRP than in GFRP rebars.
- Crack-based analysis of FRP RC may solve some of the issues that remain unresolved.

CHAPTER 7

SHORT-TERM DEFLECTION

7.1. INTRODUCTION

In the three previous chapters, the short-term deflection behaviour of FRP RC flexural members was investigated and discussed in detail. In general, deflection of FRP RC may be evaluated by using an analytical approach, such as sectional or FE analysis. Most importantly, such analyses require proper evaluation of tension stiffening, which may be achieved by a rebar tension stiffening relationship or a concrete softening model. Another consideration is the response of the compressive concrete zone in relation to the width and penetration of cracks. Shear-induced deformations may be significant and need to be evaluated, particularly for GFRP RC with low reinforcement ratios. For CFRP RC, a reduced rebar modulus may be effective, probably in connection with shear lag in the CFRP rebars.

To evaluate short-term deflection, steel and FRP RC codes of practice often adopt closed-form formulae, which only consider the flexural component of deflection within the elastic range of behaviour. In those formulae, a deformation parameter is interpolated between its minimum and maximum limits at the uncracked and cracked states. Various deformation parameters at different levels can be used, namely, strain at the rebar level, rotation or moment of inertia at the section level, curvature at the block level (between cracks) or even deflection at the member level. The interpolation is achieved by using a tension stiffening expression that allows for the effect of tension stiffening between cracks, and provides some form of transition between the uncracked and cracked states of the deformation parameter considered. When applied at the member level, the tension stiffening expression also allows for the spread of cracks

along the member. Deflection is then calculated by numerical integration along the member or by elastic deflection equations.

This chapter deals with the approaches of ACI and Eurocode 2 for evaluation of short-term deflection of RC flexural members. These codes are used to predict the deflection of the tested beams and slabs over their entire loading range, and then these predictions are evaluated and discussed against the test measurements. Only the GFRP RC tests are considered because the behaviour of some CFRP RC tests could not be justified and requires further research. Subsequently, the Eurocode 2 and ACI deflection approaches are examined in relation to FRP RC tests carried out by other researchers.

7.2. PREDICTION OF DEFLECTION

The ACI and Eurocode 2 short-term deflection approaches and formulae were explained in Chapter 2. For convenience, these formulae are summarised in common format and notation in Table 7-1. Moreover, the proposal of Bischoff (2005a, 2005b) for a modified form of the ACI effective moment of inertia (I_e) is worth considering and is also shown in Table 7-1.

Table 7-1: Predictive formulae for short-term deflection

<table>
<tr><th>Approach</th><th colspan="2">formulae</th></tr>
<tr><td>ACI 318 02; ACI 318 05</td><td rowspan="3">$I_e = \left(\frac{M_{cr}}{M}\right)^3 \beta_d I_g + \left(1 - \left(\frac{M_{cr}}{M}\right)^3\right) I_{cr} \le I_g$</td><td>$\beta_d = 1.0$</td></tr>
<tr><td>ACI440.1R-03</td><td>$\beta_d = \alpha_b \left(\frac{E_f}{E_s} + 1\right)$</td></tr>
<tr><td>ACI 440.1R-06</td><td>$\beta_d = 0.2 \left(\frac{\rho_f}{\rho_{fb}}\right) \le 1.0$</td></tr>
<tr><td>Bischoff</td><td colspan="2">$I_e = \frac{I_{cr}}{1 - \left(1 - \frac{I_{cr}}{I_g}\right)\left(\frac{M_{cr}}{M}\right)^2} \le I_g$</td></tr>
<tr><td>Eurocode 2 :
ENV 1992-1-1:1992</td><td rowspan="2">$\Delta = \beta \left(\frac{M_{cr}}{M}\right)^2 \Delta_g + \left(1 - \beta \left(\frac{M_{cr}}{M}\right)^2\right) \Delta_{cr}$</td><td>$\beta = \beta_1 \beta_2$</td></tr>
<tr><td>Eurocode 2:
EN 1992-1-1:2004</td><td>$\beta = \beta_1$</td></tr>
<tr><td colspan="3">Notation:
M_{cr}: cracking moment; M: applied moment; I_e: effective moment of inertia; I_g: uncracked moment of inertia;
I_{cr}: cracked moment of inertia; E_f: FRP rebar modulus; E_s: steel modulus; α_b: bond coefficient=0.5;
ρ_f: reinforcement ratio; ρ_{fb}: balanced reinforcement ratio; Δ: deflection, Δ_g: uncracked-state deflection,
Δ_{cr}: cracked-state deflection, β_1: 1.0 for short-term loading; β_2: 1.0 for high-bond or 0.5 for plain rebars.</td></tr>
</table>

The different approaches in Table 7-1 were used to predict the short-term midspan deflection for all the GFRP and steel RC beam and slab tests over their entire loading range. These were then compared to the test measurements, as shown in Appendix C. Typical measured and predicted load versus midspan deflection results of a GFRP RC beam and slab are reproduced in Figures 7-1 and 7-2. The predicted deflections are discussed next with reference to Appendix C.

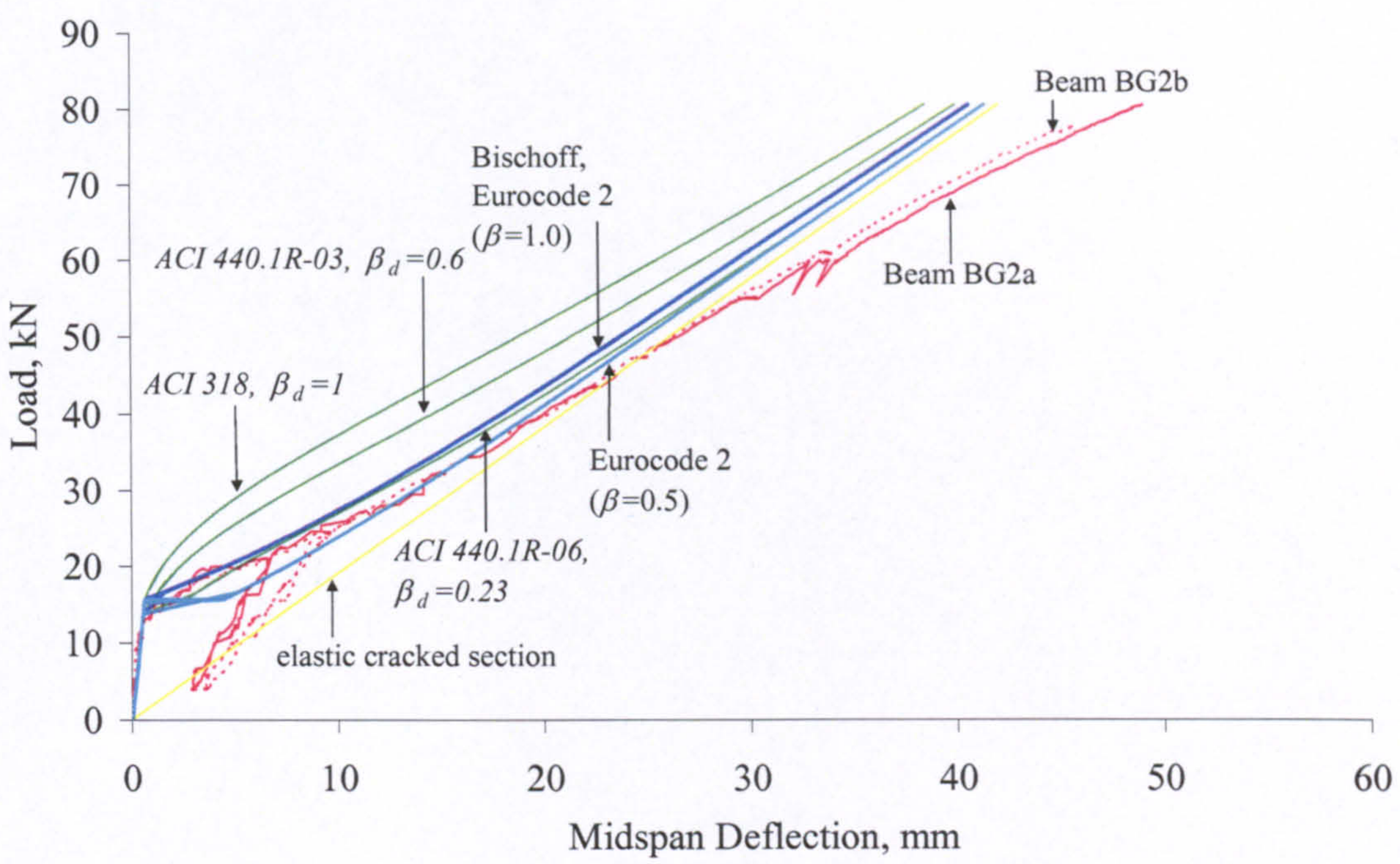

Figure 7-1: Typical measured and predicted load vs. midspan deflection – beam BG2.

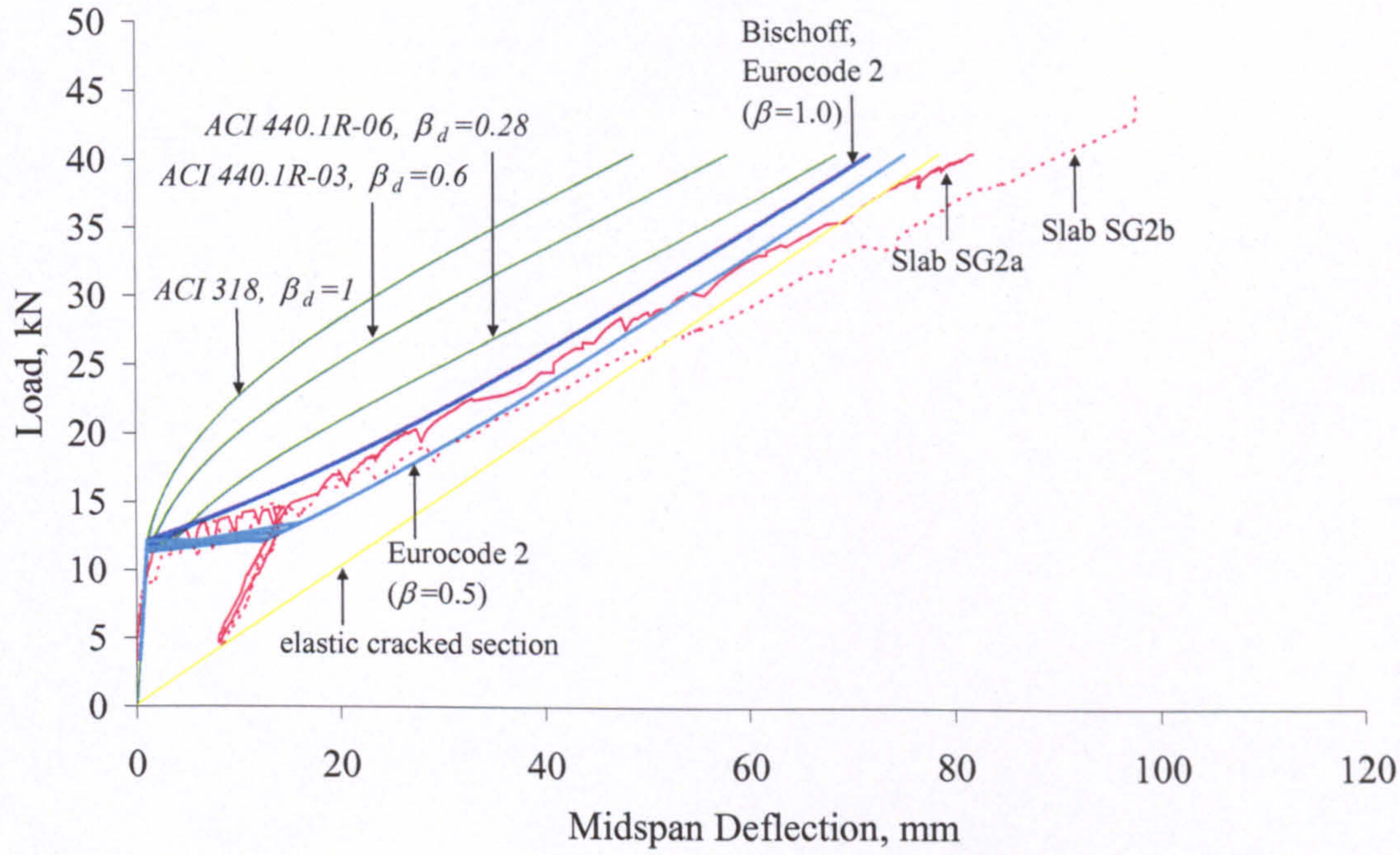

Figure 7-2: Typical measured and predicted load vs. midspan deflection – slab SG2.

7.2.1. ACI 318-05

ACI 318-05 (ACI Committee 318 2005) predicts deflection by using an effective moment of inertia (I_e), which accounts for tension stiffening as well as the spread of cracking along the member. For very low reinforcement ratios (beam BG1 and slab SG1), the predicted deflection is very stiff and greatly underestimates the measured deflection over the entire loading range, which means that I_e is greatly overestimated. As the reinforcement ratio increases (beam BG2 and slab SG2), the predicted deflection converges to the measured deflection. At very high reinforcement ratios (beam BG3 and slab SG3), the predicted deflection converges close to, but still underestimates the measured deflection over the entire loading range.

Table 7-2 illustrates the percentages of predicted to measured deflections at 50% of the failure load. It is obvious again that the prediction of deflection is inadequate, though it improves as the reinforcement ratio increases. Furthermore, the whole practical range of reinforcement ratios is covered, which means that the deflection approach of ACI 318-05 is not adequate for GFRP RC flexural members.

Table 7-2: Accuracy of deflections predicted by ACI 318-05

Beam or slab	Reinforcement ratio, ρ_f	I_g/I_{cr}	Ratio of predicted to measured deflection at 50% of the failure load, %
BG1	0.0043	22.4	15
BG2	0.0077	13.8	60
BG3	0.039	4.9	95
SG1	0.0036	50.3	10*
SG2	0.0085	23.6	25
SG3	0.040	10.8	75

* At 70% of failure load to avoid the crack formation load.

Bischoff (2005a) examines and discusses the ACI 318 equation rather extensively. It is explained that the form of this equation is empirical and was originally proposed by Branson (1977) by calibrating it to deflection results of rectangular steel RC beams;

with 1.65% reinforcement ratio and a corresponding gross to cracked stiffness ratio (I_g/I_{cr}) of 2.2, at a load level (M) of 2.5 times the cracking load (M_{cr}). Bischoff shows analytically that the tension stiffening evaluated by Branson's formula is not only dependent on the ratio of cracked to applied load (M_{cr}/M), but is also influenced by the reinforcement and modular ratios, or equivalently I_g/I_{cr}. Tension stiffening, hence I_e, is shown to be increasingly exaggerated as I_g/I_{cr} increases above 3, even for steel RC. Bischoff concludes that Branson's equation is inadequate for GFRP RC, which typically involves high I_g/I_{cr} values in the range of 5 to 25. The findings of Bischoff agree with Table 7-2, which shows that the predicted GFRP RC deflections increasingly underestimate the measured deflections with the increase of I_g/I_{cr}.

7.2.2. ACI 440.1R-03

ACI 440.1R-03 (ACI Committee 440 2003) modifies I_e by reducing I_g with a factor β_d. β_d is given as a function of the FRP rebar modulus (E_f) and a bond factor (α_b), which is taken as 0.5 pending further research. For the GFRP rebars used, E_f is about 40000 MPa and β_d is 0.6.

The equation of ACI 440.1R-03 improves the deflections predicted by ACI 318-05, but only slightly. For beam BG3 and slab SG3, the predicted deflections are very good. However, for the other GFRP RC beams and slabs with relatively low reinforcement ratios, the measured deflections are still significantly underestimated over the entire loading range, meaning that I_e is still considerably overestimated. Invoking the approach of Bischoff (2005a), the I_g/I_{cr} values of these members are reduced by 40% but are still very high, which means that the modified form of the ACI equation is also inadequate to predict the deflection of those GFRP RC members.

7.2.3. ACI 440.1R-06

ACI 440.1R-06 (ACI Committee 440 2006) abandons the idea of relating I_e to bond, but still attempts to reduce tension stiffening and I_e by reducing I_g with a factor β_d. β_d is given as a function of the member reinforcement ratio (ρ_f) and the balanced

reinforcement ratio (ρ_{fb}). For the GFRP beams and slabs, the factor β_d is variable and its values are evaluated as shown in Table 7-3.

Table 7-3: Coefficient β_d according to ACI 440.1R-06

Beam or slab	Reinforcement ratio, ρ_f	Balanced reinforcement ratio, ρ_{fb}	$\beta_d I_g/I_{cr}$	β_d
BG1	0.0043	0.0061	3.1	0.14
BG2	0.0077	0.0068	3.2	0.23
BG3	0.039	0.0058	4.9	1.00
SG1	0.0036	0.0071	5.0	0.10
SG2	0.0085	0.0060	6.6	0.28
SG3	0.040	0.0058	10.8	1.00

For beams BG1 and BG2, ACI 440.1R-06 improves noticeably the deflections predicted by ACI 440.1R-03. The predicted and measured deflections now compare reasonably, and the differences may be mainly attributed to shear-induced deformations, which are not accounted for in the first place. According to Bischoff (2005a), the ACI approach is expected to give reasonable predictions because $\beta_d I_g/I_{cr}$ is approximately equal to 3. For slabs SG1 and SG2, the predicted deflections are also noticeably improved, but still underestimate the measured deflections. For slab SG2, the underestimation of deflection is still significant, being about 35% at a load of 50% of the failure load. This is again commensurate with $\beta_d I_g/I_{cr}$ being significantly larger than 3, as shown in Table 7-3. For beam BG3 and slab SG3, the predicted deflections are back to those predicted by ACI 318-05 because β_d has a value of 1.0.

ρ_f can physically influence tension stiffening, which may justify its inclusion in the ACI 440.1R-06 equation for I_e. The balanced reinforcement ratio (ρ_{fb}) allows for another important variable that can affect tension stiffening, which is the rebar modulus. However, ρ_{fb} is also a function of the rebar rupture stress, which cannot be related to the deflection behaviour. The use of ρ_{fb} entails an unrealistic situation, where different deflections would be predicted for two identical flexural members with rebars that have the same axial stiffness, but only differ in their rupture stress. Furthermore, the

equation of ACI 440.1R-06 is totally inapplicable to steel RC because the maximum value of β_d would be 0.2 (when $\rho_f = \rho_{fb}$)! Appendix C shows a bizarre deflection response of the tested steel RC beam and slab when using a β_d value of 0.06.

Therefore, even though the I_e formula of ACI 440.1R-06 gives much better results than its predecessors, it does not seem to be based on fundamentals. In addition, it may significantly underestimate the actual deflections, as for instance in the case of the GFRP slabs. Hence, the ACI 440 formula still requires further consideration.

7.2.4. Eurocode 2 (ENV 1992-1-1:1992, EN 1992-1-1:2004)

Eurocode 2 [ENV 1992-1-1:1992 (CEN 1992) and EN 1992-1-1:2004 (CEN 2004)] initially evaluates tension stiffening for a deformation parameter, which may be strain, rotation or curvature. Then, short-term deflection may be calculated by numerical integration of curvatures along the member. As an acceptable simplification, the tension stiffening expression may be applied directly to deflection, as shown in Table 7-1. The approach of Eurocode 2 is based on CEB-FIP Model Code 1990 (CEB 1993), where the ratio of tension stiffening effect at a certain load after cracking (TS) to the tension stiffening effect at cracking (TS_{cr}) is proportional to the ratio M_{cr}/M, as clarified in Figure 7-3. Bischoff (2005a, 2005b) uses this tension stiffening approach in connection with curvature and deflection to derive another form for the effective moment of inertia (I_e) of the member, as shown in Table 7-1.

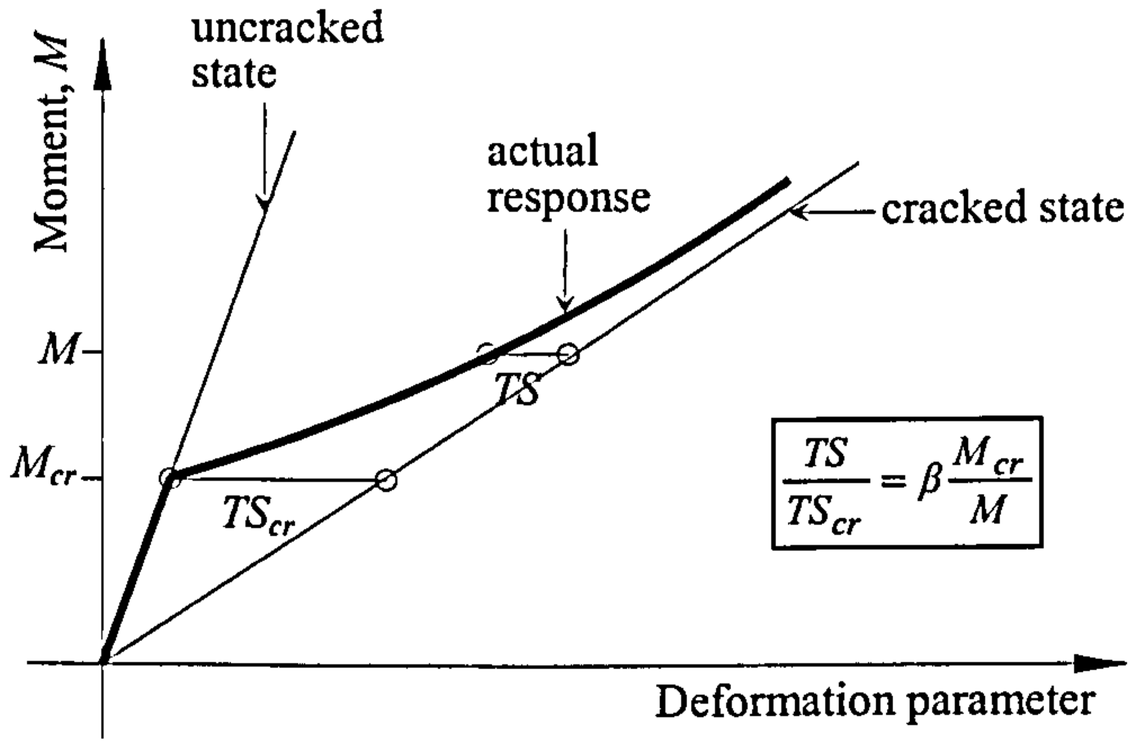

Figure 7-3: Tension stiffening according to Eurocode 2.

The Eurocode 2 approach was applied to the GFRP RC beams and slabs with a β_1 factor of 1.0 (for short-term loading) and a β_2 factor of 1.0 (for high-bond rebars). Bischoff does not allow for any of these factors in his proposed equation. M_{cr} evaluated by Eurocode 2 was about 89% of that evaluated by ACI, and both compare reasonably well with the experimental crack-formation load range. However, for a better comparison of the deflection formulae, M_{cr} was evaluated by the ACI expression in all the cases.

Interestingly, the deflections predicted by Eurocode 2 and the formula of Bischoff match perfectly over the entire loading range for all the GFRP and steel RC tests. Moreover, the predicted deflections compare very well with the measured deflections for all the GFRP RC beams and slabs. For beams BG1 and BG2, and slabs SG1 and SG2, the predicted deflections somewhat underestimate the measured deflections, but this may be attributed to shear-induced deformations in those members, which are not allowed for in the first place.

As explained, Eurocode 2 allows for the effect of bond on tension stiffening by a bond factor β_2, which is given a value of 0.5 for the low-bond plain steel rebars. Hence, deflections were also predicted by Eurocode 2 with a β_2 of 0.5, as shown in Appendix C. It may be observed that the predicted deflections are increased for all the GFRP RC beams and slabs. Despite the use of a supposedly lower-bound value of β_2, which is 50% less than that of the high-bond rebars, the increase in predicted deflection is generally little and only noticeable for beam BG1 and slab SG1. This may indicate that the effect of bond may be prominent only when very low reinforcement ratios are involved. Physically however, bond is a complicated issue that is not easy to represent with a single bond factor. At the level of bond, many factors may be effective such as the diameter and number of rebars, the rebar modulus and surface characteristics in addition to the tensile strength of the concrete and the concrete cover. The GFRP and CFRP rebars used herein show good levels of structural bond and adequate composite action, as discussed in Chapter 4. In other words, these rebars, at least, are not expected to require the use of a bond factor. Nonetheless, β_2 basically causes a horizontal shift in the load-deflection curve beyond cracking, which may provide a simplified means to account for shear-induced deflections. In that sense, a β_2 value of 0.5 provides a good

prediction of the measured deflection of the GFRP beams and a slightly conservative prediction for the GFRP slabs up to their service load range, as shown in Appendix C.

It may be concluded that the formulae of Eurocode 2 and Bischoff, with a β_2 of 1.0, have a sound form that can be used to predict tension stiffening and deflection of FRP RC flexural members. This is assuming FRP rebars with adequate structural bond and composite action. The value of β_2 may be reduced to 0.5; as an indirect and simplified means to account for cases where shear-induced deflections are noticeable at the service load level. For cases where shear-induced deformations are insignificant, such reduced value of β_2 can increase the predicted deflections but only slightly. In other words, a β_2 of 0.5 may be always applicable.

Another simplified but more appropriate means to account for shear-induced deflections in Eurocode 2 and Bischoff formulae may be achieved by softening the member cracked-state. For Eurocode 2, the cracked-state deflection (Δ_{cr}) may be increased by a factor of 1.1. For the formula of Bischoff, the cracked moment of inertia (I_{cr}) may be reduced by a factor of 0.9. The predicted deflections with these proposed modification factors compare better with the measured deflections, along the entire load range, as shown in Appendix C. Again, if shear-induced deformations are not present, then such a modification only has a slight conservative effect on the predicted deflection. It is worth pointing out that the difference between measured and predicted curves, for beam BG1 and slab SG3, may be reduced with a better estimate of M_{cr}. For all the other beams and slabs, the prediction of deflection is almost spot-on. Typical predicted load-deflection response of a GFRP beam and slab using this proposed modification are shown in Figures 7-4 and 7-5.

Nevertheless, it is emphasized that the proposed modification to Eurocode 2 and Bischoff formulae is empirical, and needs to be verified for a wide database of FRP RC research involving other FRP rebar products and experimental setup. Furthermore, this modification is by no means an alternative to a proper understanding of shear-induced deformations in FRP RC members or to a fundamental approach for evaluating such deformations, which still require dedicated research.

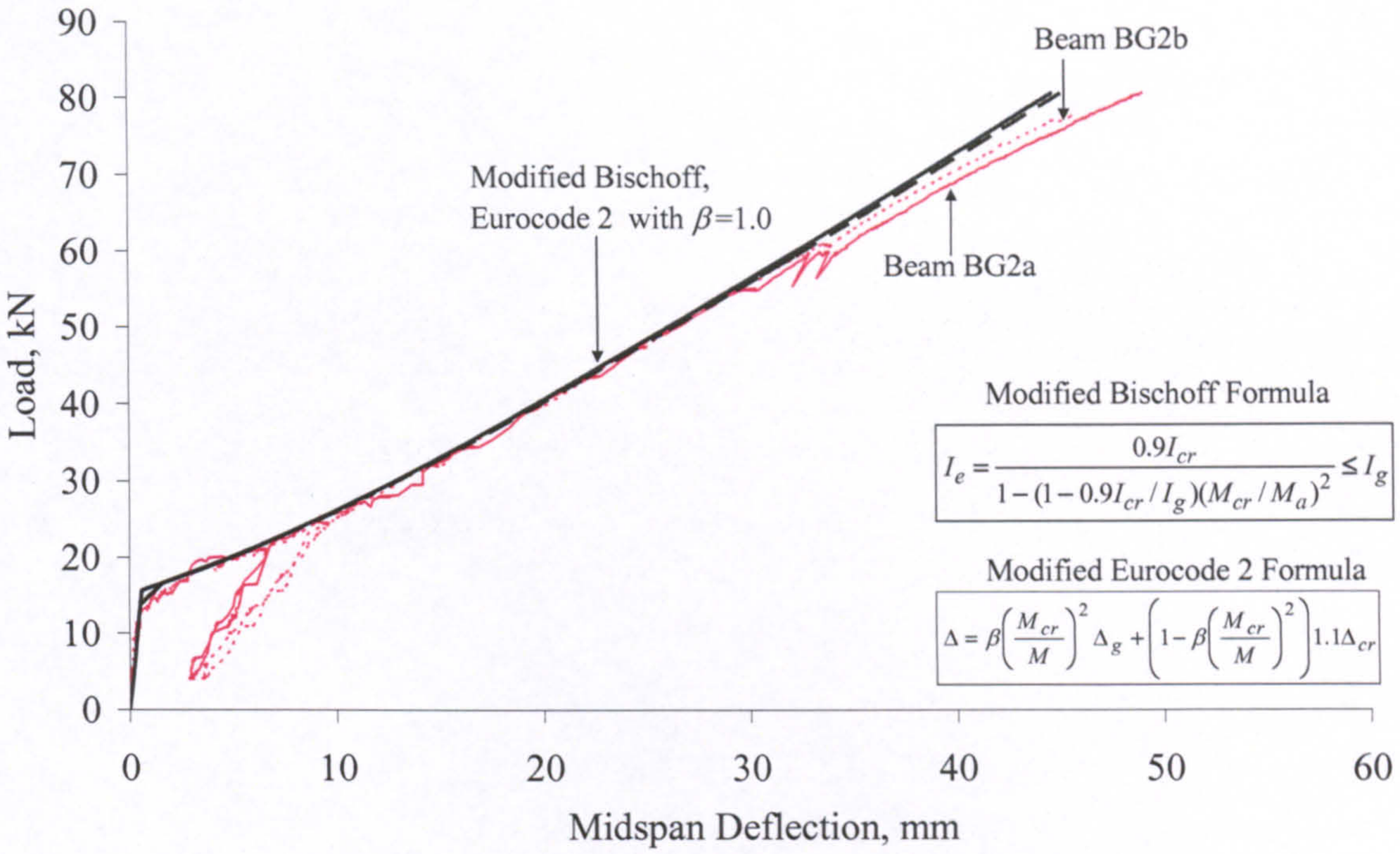

Figure 7-4: Predicted midspan deflection by proposed modification of Eurocode 2 and Bischoff formulae – Beam BG2.

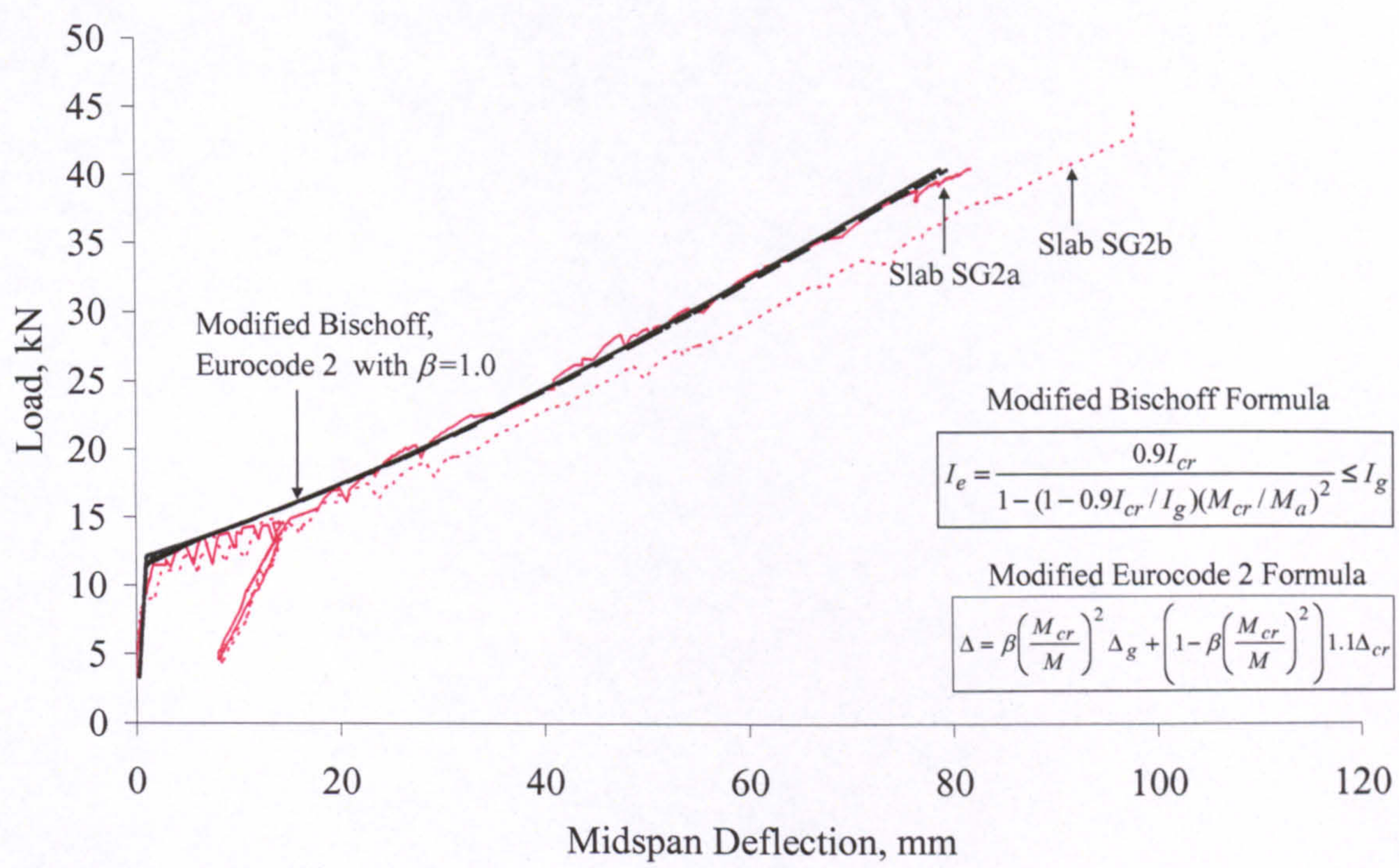

Figure 7-5: Predicted midspan deflection by proposed modification of Eurocode 2 and Bischoff formulae – Slab SG2.

7.3. TESTS IN THE LITERATURE

To confirm the adequacy of the Eurocode 2 approach for evaluating short-term deflection of FRP RC, this approach was used to predict the deflection results of other FRP RC tests carried out by various researchers. Three sets of tests with three different types of GFRP RC rebars (Isorod, C-Bar and Eurocrete) were considered. The details of these tests were obtained from the literature, and are summarised in Table 7-4. In what follows, the measured and predicted midspan deflections of these tests are discussed in view of the findings of this research. For further comparison, the deflections predicted by ACI 318-05 for steel RC are also considered.

Table 7-4: Details of FRP RC tests in the literature

Research	Beam	Dimensions, mm			f'_c, MPa	c, mm	Flexural Reinforcement					Loading	a, mm
		b	h	L			Type	Details	ρ, %	E_f, MPa	f_{fu}, MPa		
Benmokrane et al. (1996)	ISO1,2	200	300	3000	43	30	Isorod[(i)]	2ϕ19.1	1.1	45000	690	4-point	1000
	ISO3,4	200	550	3000	43	30	Isorod[(i)]	2ϕ19.1	0.56	45000	690	4-point	1000
Masmoudi et al. (1998)	CB2B	200	300	3000	52	30	C-Bar[(ii)]	2ϕ14.9	0.66	38000	773	4-point	1250
	CB3B	200	300	3000	52	30	C-Bar[(ii)]	3ϕ14.9	0.99	38000	773	4-point	1250
	CB4B	200	300	3000	45	30[(ii-a)]	C-Bar[(ii)]	4ϕ14.9	1.45	38000	773	4-point	1250
	CB6B	200	300	3000	45	30[(ii-a)]	C-Bar[(ii)]	6ϕ14.9	2.3	38000	773	4-point	1250
Eurocrete Project	GB5[(iv)]	150	250	2300	26	24	Eurocrete[(iii)]	3ϕ13.5	1.33	45000	750	4-point	767
	GB9[(iv)]	150	250	2300	33	24	Eurocrete[(iii)]	3ϕ13.5	1.33	45000	750	4-point	767

Legend: b: width, h: depth, L: span, f'_c: concrete cylinder compressive strength, c: clear concrete cover, ρ: reinforcement ratio, E_f: reinforcement modulus, f_{fu}: ultimate reinforcement tensile strength, a: shear span.
(i) GFRP rebars with helically over-wound fibres and sand coating.
(ii) GFRP rebars with ribbed surface; similar to epoxy-coated steel rebars.
(ii-a) Two layers of reinforcement with 30mm spacing.
(iii) GFRP rebars with peel-ply indented surface.
(iv) Beams GB5 and GB9 with GFRP links spaced at 35mm and 76.7mm, respectively.

- Eurocrete Tests

The measured and predicted midspan deflections of Beams GB5 and GB9 with the Eurocrete rebar are shown in Figure 7-6. The deflection behaviour of beam GB5 is similar to the GFRP RC beams and slabs of this research. Beyond a relatively low load,

the measured deflections exceed the limit of cracked-state deflections, which may be attributed to shear-induced deformations in addition to increased concrete strains in a less-deep compressive concrete zone. As explained, these additional effects are not accounted for by the cracked-state of the member. Beam GB9, which is identical to beam GB5 but with 50% less shear reinforcement, shows an even softer deflection response than beam GB5. This may further support the role of shear-induced deformations.

The deflections predicted by Eurocode 2 compare well but slightly underestimate the deflections of beam GB5 within the service load range. The deflections of beam GB9 are more underestimated. Compared to ACI 318, the deflection prediction by Eurocode 2 is better. However, it is obvious that the Eurocode 2 approach needs to allow for the abovementioned additional effects.

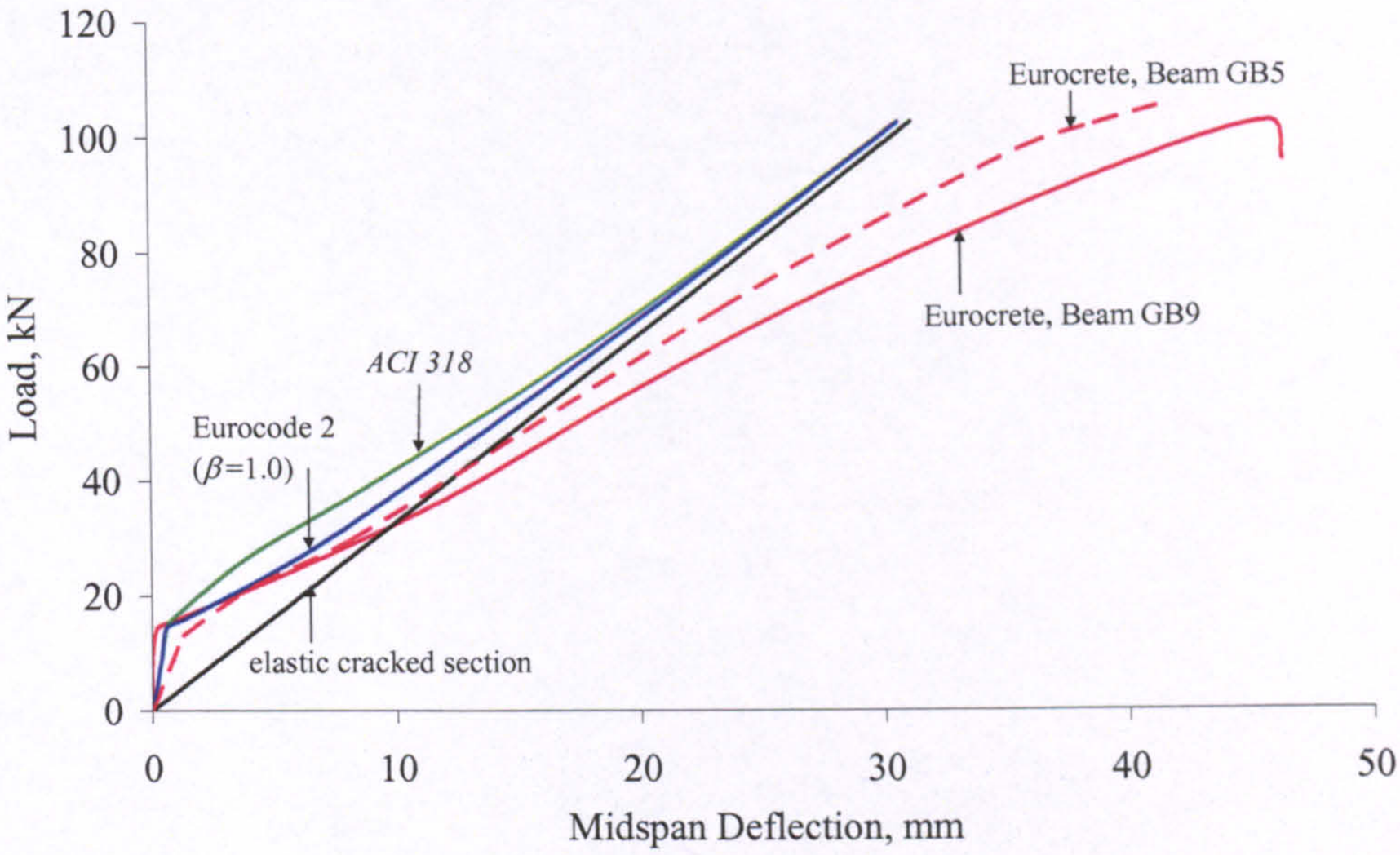

Figure 7-6: Measured and predicted midspan deflections – tests with Eurocrete rebar.

- Benmokrane et al. (1996) Tests

The measured and predicted midspan deflections of Benmokrane et al. (1996) tests with the Isorod rebar are shown in Figure 7-7. The results of these tests are also similar to the results of this research. The deflections of beams ISO3 and ISO4, which have a low reinforcement ratio, again indicate that additional effects are present and need to be taken into consideration. The deflections predicted by Eurocode 2 compare well but

somewhat underestimate the measured deflections within the service load range. These predicted deflections can be improved with a better estimate of the cracking moment. On the other hand, the deflections predicted by ACI 318 greatly underestimate the measured deflections. With double the reinforcement ratio in beams ISO1 and ISO2, the additional effects are insignificant. The deflections predicted by Eurocode 2 are almost spot-on, while the deflections predicted by ACI 318 are still on the conservative side.

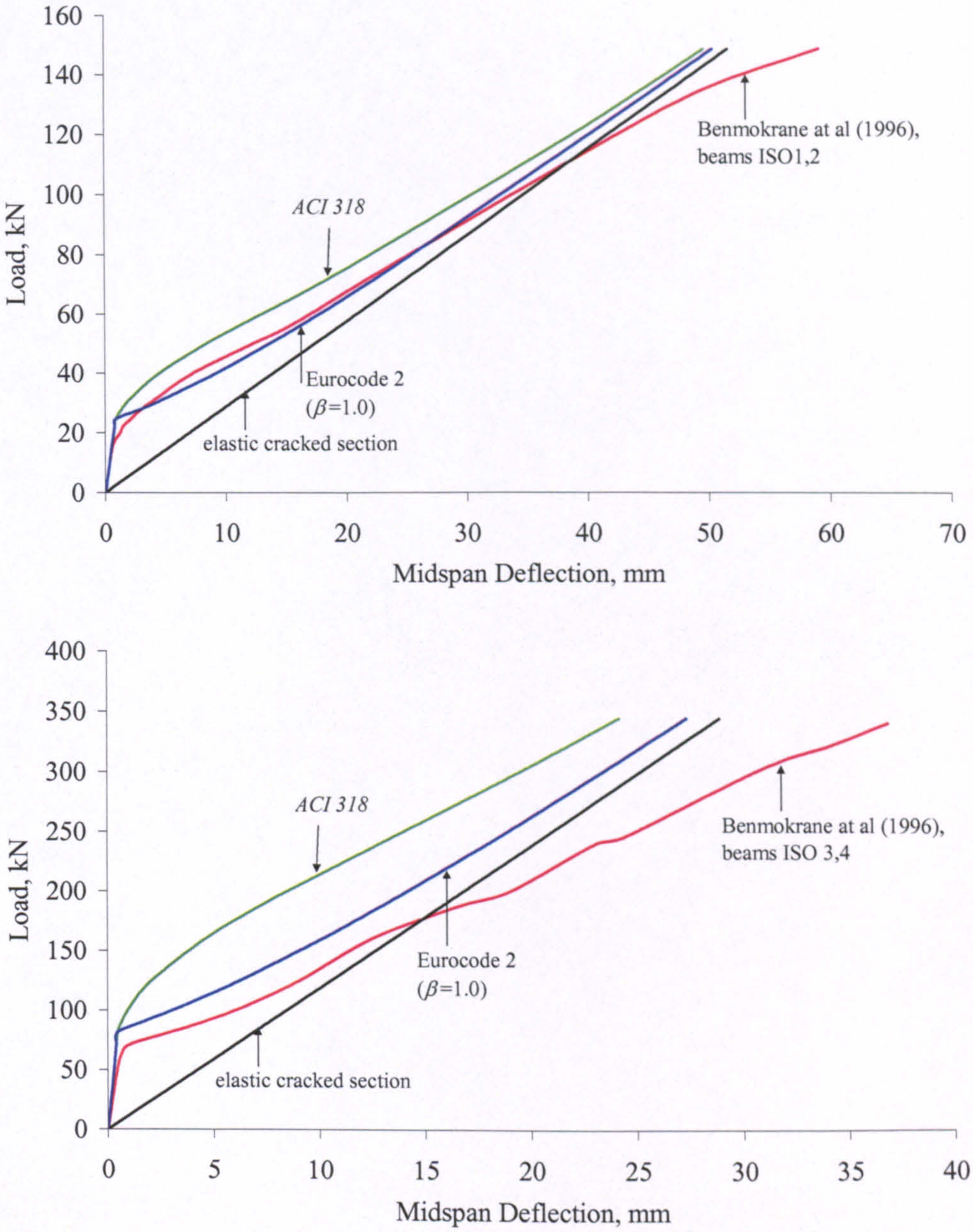

Figure 7-7: Measured and predicted midspan deflections – tests with Isorod rebar.

A probable influence of the bond characteristics on the shear-induced deformations was pointed out in this research, and may be further supported by comparing beams ISO1 and ISO2 with the Eurocrete beam GB5. All these beams have an almost equal reinforcement ratio and modulus. However, contrary to the Eurocrete beam, the results of the ISO beams do not indicate any shear-induced deformations, which may be associated with better bond of the Isorod rebar.

- Masmoudi et al. (1998) Tests

The effect of the bond characteristics may be more obvious in the tests of Masmoudi et al (1998) with the C-bar. In these tests and regardless of the reinforcement ratio, which ranged from as low as 0.66% to as high as 2.3%, the deflections of the cracked-state are never exceeded and the additional effects are always insignificant, as shown in Figure 7-8. This behaviour may be associated with better bond characteristics of the C-bar.

Figure 7-8 also shows that, with the absence of any additional effects, the deflections predicted by Eurocode 2 compare very well to the measured deflections in all the cases. This confirms that the tension stiffening model of Eurocode 2, which is intended for steel RC, is also essentially applicable for FRP RC. On the other hand, the ACI 318 always underestimates the measured deflections, though its predictions improve noticeably with the increase in reinforcement ratio.

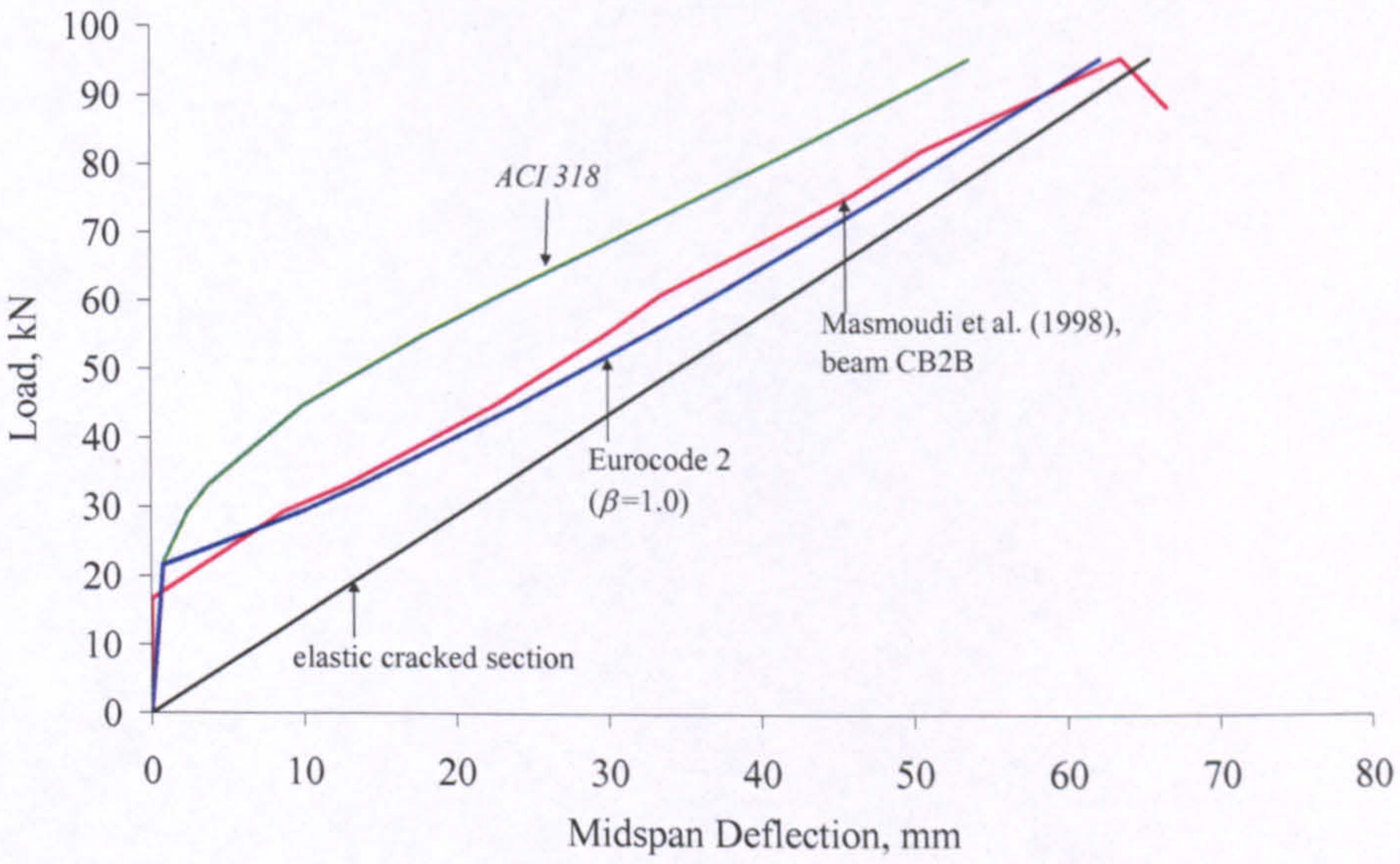

Figure 7-8: Measured and predicted midspan deflections – tests with C-bar.

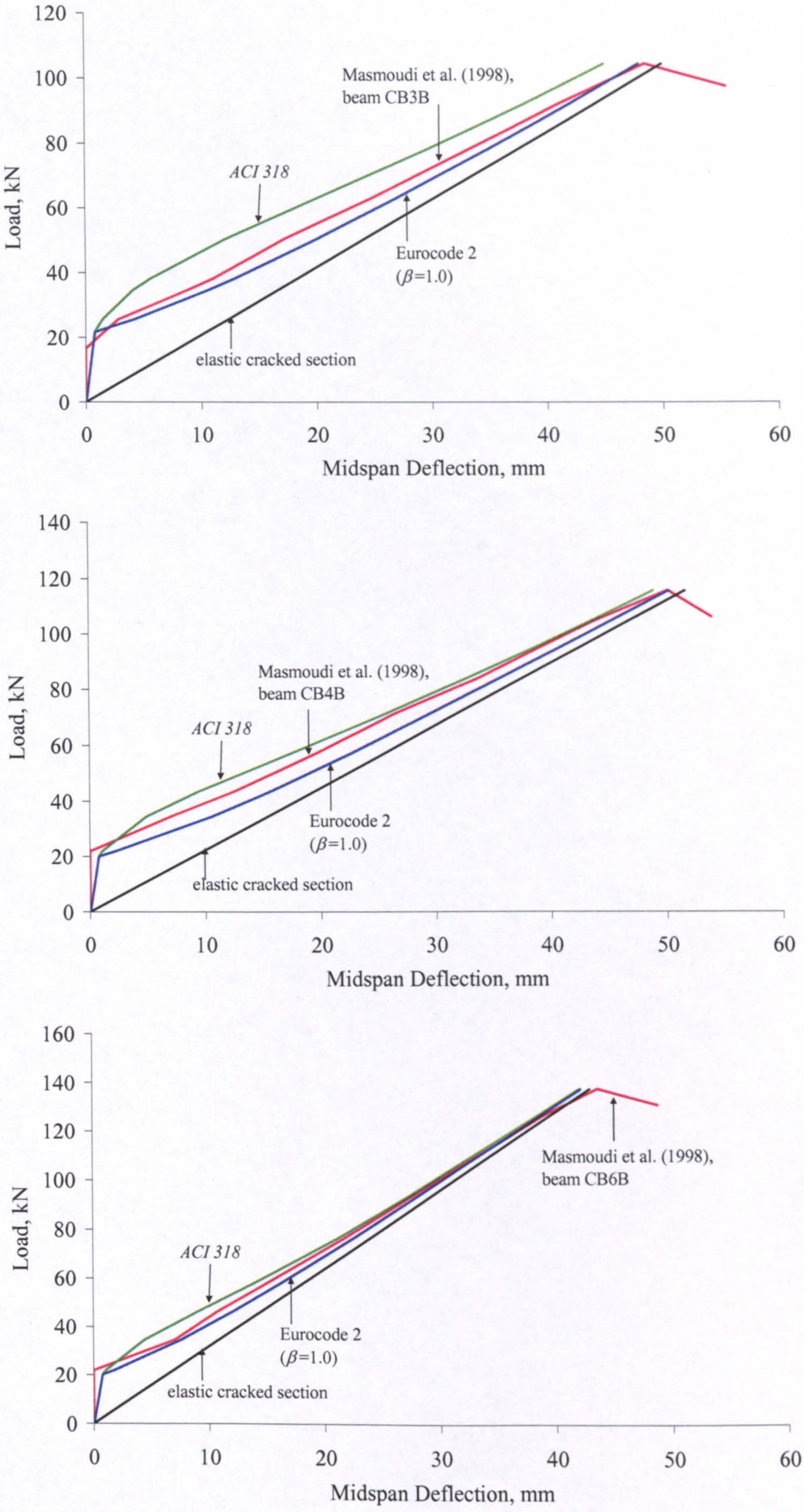

Figure 7-8 continued: Measured and predicted midspan deflections – tests with C-bar.

7.4. CONCLUSIONS

The discussion of Eurocode 2 and ACI deflection approaches in comparison to the test results of this and other research projects can lead to the following results.

- Bond characteristics can influence the deflection response of FRP RC.
- If the bond is structurally adequate and the bond characteristics are such that additional effects (shear induced deformations and increased strains of the compressive concrete zone) are diminished, the cracked-state provides a limiting deflection condition and the Eurocode 2 approach with a bond factor of 1.0 can be used to predict short-term deflections. In other words, the difference in tension stiffening characteristics between FRP RC and steel RC does not warrant a different tension stiffening model.
- If the bond is structurally adequate but the bond characteristics are such that additional effects are not diminished, the cracked-state does not provide a limiting deflection condition. In that case, the Eurocode 2 approach still applies, in the sense that the tension stiffening characteristics per se can still be reasonably represented by the tension stiffening model of Eurocode 2. However, the tension stiffening expression of Eurocode 2 needs to be modified to account for deflections due to the additional effects. This may be simplistically achieved with a different bond factor that is less than one (a value of 0.5 seems to be adequate), or in a better way by reducing the cracked-state stiffness or increasing the cracked-state deflection (about 10% on average seems to be adequate).
- Before firming-up on the above conclusions, it has to be emphasized again that two specialised investigations are necessary. One investigation should be designed to understand shear-induced deformations as well as the effect of bond on these deformations. The other investigation should be designed to investigate the response of the compressive concrete zone in connection with cracking. Proper predictive models are necessary for both cases.

CHAPTER 8

CONCLUSIONS AND RECOMMENDATIONS

8.1. CONCLUSIONS

This study investigated the short-term deflection behaviour of FRP RC flexural members, both experimentally and analytically. Experimentally, a total of 28 medium-scale RC beams and slabs with GFRP, CFRP or steel flexural reinforcement were tested under four-point loading. The main variables considered were the reinforcement ratio, modulus of elasticity and bond. The experimental study examined flexural deflection together with the deflection-related parameters, which comprised rebar strains at and between cracks, compressive concrete strains, flexural curvature, crack width and spacing, tension stiffening and bond.

All the tested beams and slabs were analysed by using cracked section analysis (CSA), while FE analysis with smeared modelling of cracks was used to analyse all the GFRP and representative CFRP RC members. The analytical part looked into the numerical analysis techniques used and evaluated their predictions of deflection, curvature, as well as rebar and concrete strains. Furthermore, FE analysis was used to investigate shear lag in the CFRP rebars.

This study also evaluated the prediction of short-term deflection in the ACI and Eurocode 2 codes of practice. Modes of failure and prediction of flexural capacity were addressed as well. The conclusions and recommendations of this study are presented in the following.

- Modes of Failure and Flexural Capacity

- Flexural failure in FRP RC can occur by rupture of rebars or crushing of concrete.
- Both failure modes are brittle, but concrete crushing is more gradual.
- When failure occurs by concrete crushing, CSA, with a value of 0.003 for the ultimate compressive concrete strain, predicts the flexural capacity within a reasonable tolerance, and generally tends to be on the unconservative side. For the GFRP RC members of this study, the predicted failure load was within 12% of the actual failure load.
- Noticeable shear lag in the FRP rebars may enhance the effect of cracks on the response of the compressive concrete zone, and may result in premature flexural failure by concrete crushing. For a 12.7mm-diameter CFRP rebar, shear lag was estimated to cause a difference of about 15% between the surface and average rebar strains. For beams BC2 and BC3, the predicted failure load overestimated the actual load by about 30%. Therefore, it is prudent to ensure that shear lag is diminished in any FRP rebar product.
- Premature rupture of rebars may occur, particularly for small diameter rebars, which may be attributed to the concentration of bond stresses at the cracks. For series BG1 and SG1 in this study, CSA underestimated the failure load by up to 20%. For series BC1 and SC1, premature rupture was not observed and the failure load was predicted within 4%. The difference in bond characteristics between the GFRP and CFRP rebars may have had an important role in that regard.

- Rebar Strain

- In the stabilised cracking phase, the FRP rebar strains increase almost linearly with load up to failure.
- In some cases, mostly involving GFRP rebars, the rebar strain at the location of applied load exceeds the maximum rebar strain at cracks within the pure flexure zone. The difference between these strains reached a maximum of 20% for beam BG2a. This behaviour could not be explained and requires further shear-oriented research.
- CSA predicts the maximum rebar strain at a crack in a pure flexure zone, and as such provides an upper-bound for the average rebar strain between cracks throughout the entire loading range.

- Concrete Strain

- In the stabilised cracking phase, the concrete strain at the extreme compressive concrete fibre increases nonlinearly with load up to failure.
- The response of the compressive concrete zone can be noticeably influenced by the width and penetration of cracks. Therefore, CSA and FE analysis can considerably underestimate the extreme fibre compressive concrete strain, as these analyses do not account for the localised effects of cracks. The difference between the measured and predicted concrete strains reached about 40% for beams BG1 and BC3.
- FE analysis with discrete modelling of cracks may be valuable in investigating the response of the compressive concrete zone above cracks as well as the extent of that zone.

- Cracking

- Within the service load range and depending on the rebar modulus, relatively high FRP reinforcement ratios can be necessary to reduce crack widths of FRP RC to become comparable to steel RC. For the GFRP and CFRP RC beams, reinforcement ratios of 5.7 and 1.7 times the steel reinforcement ratio were necessary to achieve the same cracking stiffness of BSa.
- In the stabilized cracking phase, crack width follows an almost linear relationship with load up to failure.
- Neglecting concrete strain, crack width can be reasonably estimated by multiplying the average reinforcement strain between cracks by the crack spacing. The accuracy of this approach depends on the exact locations of the no-slip points between cracks.
- Crack spacing of FRP RC and steel RC can be of the same order of magnitude.

- Tension Stiffening

- The stabilized cracking phase of FRP RC is characterized by an almost linear relationship between the rebar strain at a flexural crack and the average rebar strain between cracks. Moreover, the difference between the rebar crack strain and average strain between cracks increases with load, which indicates that the average bond between cracks continues to increase with load as well.

- The ratio of effective to actual reinforcement modulus provides a rational measure of tension stiffening. This ratio reduces tending to a value of 1.0 as the average strain increases in the stabilised cracking phase, which means that the tension stiffening effect progressively reduces throughout that phase.

- Bond

- The FRP rebars used developed adequate bond levels between flexural cracks. At failure and within a short distance of 22.5 mm from the midspan and adjacent cracks, average bond stresses reached 15 MPa and 30 MPa for beams BG2 and BC2, respectively.
- In the stabilised cracking phase, the average bond increases with average strain up to failure. The average bond-average strain relationship is somewhat nonlinear, which indicates some softening of bond, but it is not far from linearity. Close to the maximum strain capacity of the rebars, the average bond between flexural cracks was in the range of: 5.0 to 9.5 MPa for the GFRP RC members, 9.5 to 14 MPa for the CFRP RC beams, and 12.5 to 19.5 MPa for the CFRP RC slabs.

- Curvature and Deflection

- Within the service load range and depending on the rebar modulus, relatively high FRP reinforcement ratios are required to reduce deflections of FRP RC to become comparable to steel RC. For the GFRP and CFRP RC beams, reinforcement ratios of 5.7 and 1.7 times the steel reinforcement ratio could not achieve the same deflection stiffness of BSa.
- In the stabilised cracking phase, deflection and flexural curvature follow an almost linear relationship with load up to failure, which indicates that rebar strains have more contribution to curvature than concrete strains. The average neutral axis depth between flexural cracks increases slightly with load up to failure. This is contrary to steel RC where, after yield, the neutral axis depth reduces at a very fast rate.
- Deflection of FRP RC is mainly caused by flexural curvatures. However, depending on the reinforcement modulus and bond characteristics, shear-induced curvatures may not be negligible, particularly for low reinforcement ratios with deep-penetrating wide cracks. For beam BG2, the shear-induced deflections were estimated at 20% of the measured deflection at failure.

- An experimental load versus flexural curvature relationship can be evaluated from the rebar strains between flexural cracks and the average extreme fibre compressive concrete strain. Such a relationship smears the localised crack effect on the compressive concrete and accounts for tension stiffening of the rebars, and can therefore be used to calculate the deflections due to flexure. The shear-induced deflections can then be evaluated as the difference between the measured and flexural deflections.
- The rebar strains have the major contribution towards flexural curvature, and require a proper evaluation of tension stiffening at the rebar level. However, the contribution of concrete strains is not negligible, and can be increased by the localised effect of the wide and deep cracks of FRP RC.
- Shear-induced deformation may initiate due to the interaction of flexure with shear. Such deformations may not be negligible, and are believed to increase with wider and deeper cracks, or with the increase in rebar strain. In other words, shear-induced deformations are expected to reduce with increasing reinforcement ratio and/or modulus. Hence, for GFRP RC where the reinforcement modulus is very low, a very high reinforcement ratio, such as that of BG3, may be required to limit shear-induced deformations. For CFRP RC, shear induced deformations can be insignificant due to the relatively high modulus of elasticity of their rebars.
- The rebar bond characteristics may be an important factor in limiting shear-induced deformations, as they may affect the width and penetration of cracks.
- Even though CSA can underestimate the compressive concrete strains, tension stiffening can give sufficient margin for CSA to provide an upper-bound solution for flexural deflection and curvature. A high-enough tension stiffening, such as in the case of slab SG2, can allow CSA to provide an upper-bound solution for total deflection and curvature; including shear induced deformations.
- FE analysis with smeared modelling of cracks does not account for shear-induced deformations. Therefore, though the level of tension stiffening in FE analysis can be chosen to match the measured deflection, FE analysis may not predict the actual state of strain in the member. Hence, the average rebar strains and curvature in the pure flexure zone may be overestimated, while the rebar strains and curvature within the shear span may be underestimated.
- The proper evaluation of shear-induced effects and the response of the compressive concrete zones require specially-tailored research.

- CFRP RC Members

- Some of the CFRP RC members showed an unexpected behaviour where the rebar strains and deflections exceed those predicted by CSA, despite the negligible shear-induced deformations. Those members behave as though their reinforcement has a lower effective reduced modulus. Such a reduced modulus was of the order of 85% of the modulus determined by the uniaxial tensile tests. This behaviour is believed to be caused by shear lag in the rebars, but could not be physically explained and requires further dedicated research.
- FE analysis shows that, for the same tensile force and shear modulus, shear lag in CFRP rebars may be higher than in GFRP rebars, and may influence a longer distance around a crack.

- Codes of Practice

- The ACI approach for prediction of short-term deflection is not based on fundamentals, and is not appropriate for FRP RC without major modifications.
- With an adequate structural bond of the FRP rebars, the Eurocode 2 approach for prediction of short-term deflection is believed to be appropriate for FRP RC. In other words, the difference in tension stiffening characteristics between FRP RC and steel RC does not warrant a differing tension stiffening model. Nonetheless and depending on the bond characteristics of the rebars, the approach of Eurocode 2 may need to allow for the additional effects of shear-induced deformations and increased concrete strains in the compressive concrete zones in connection with wider and deeper cracks. This may be done simplistically via a bond factor or by softening the stiffness of the FRP RC member cracked-state. A bond factor of 0.5 and a 10% reduction of cracked stiffness seem to be appropriate based on the GFRP RC deflection results of this study.

8.2. RECOMMENDATIONS FOR FUTURE WORK

Based on the findings of this study, future research is recommended as follows.

- A specialised study is required to investigate the behaviour of concrete teeth between inclined cracks, under combined shear and flexure effects. An important consideration may be the deformation and failure characteristics of the concrete teeth between cracks, and the deformation of the compressive concrete zone on top of these cracks. Another key consideration may be the bond characteristics of the rebars. Predictive models to evaluate shear-induced deflections can then be developed.
- Another major investigation is required to investigate and predict the response and depth of the compressive concrete zone in connection with crack width and penetration. Such investigation falls within the broader context of crack-based analysis and FE analysis with discrete modelling of cracks, which need to be explored more extensively.
- The adequacy of the Eurocode 2 tension stiffening expression for FRP RC needs to be evaluated against a much wider database of experimental research work, with different test details and FRP rebars.
- Shear lag, particularly in CFRP rebars, requires more fundamental understanding and investigation. In that regard, shear lag standard tests and evaluation criteria should be devised to control shear lag in FRP rebars.
- The issue of why the CFRP RC members behaved as though their CFRP reinforcement had a lower effective reduced modulus could not be resolved and needs to be examined and understood.

REFERENCES

ABAQUS Inc. (2004), "ABAQUS Documentation - version 6.5," ABAQUS Inc., Providence, RI, USA.

ACI Committee 318 (1995), "Building Code Requirements for Structural Concrete (ACI 318-95) and Commentary (ACI 318R-95)," American Concrete Institute, Farmington Hills, Mich, 369 pp.

ACI Committee 318 (2002), "Building Code Requirements for Structural Concrete (ACI 318-02) and Commentary (ACI 318R-02)," American Concrete Institute, Farmington Hills, Mich, 443 pp.

ACI Committee 318 (2005), "Building Code Requirements for Structural Concrete (ACI 318-05) and Commentary (ACI 318R-05)," American Concrete Institute, Farmington Hills, Mich, 430 pp.

ACI Committee 224 (1992), "Cracking of Concrete Members in Direct Tension (ACI 224.2R-92, Reapproved 1997)," American Concrete Institute, Farmington Hills, Mich, 12 pp.

ACI Committee 224 (2001), "Control of Cracking in Concrete Structures (ACI 224R-01)," American Concrete Institute, Farmington Hills, Mich, 46 pp.

ACI Committee 440 (1996), "State-of-the-Art Report on Fiber Reinforced Plastic (FRP) Reinforcement for Concrete Structures (ACI 440R-96, Reapproved 2002)," American Concrete Institute, Farmington Hills, Mich, 68pp.

ACI Committee 440 (2003), "Guide for the Design and Construction of Concrete Reinforced with FRP Bars (ACI 440.1R-03)," American Concrete Institute, Farmington Hills, Mich, 42 pp.

ACI Committee 440 (2006), "Guide for the Design and Construction of Concrete Reinforced with FRP Bars (ACI 440.1R-06)," American Concrete Institute, Farmington Hills, Mich, 45 pp.

Achillides Z., Pilakoutas K., and Waldron P. (1997a), "Bond Behaviour of FRP Bars to Concrete," Proceedings of the Third International Symposium on Non-Metallic (FRP) Reinforcement for Concrete Structures, Sapporo-Japan, Oct. 1997, Vol. 2, pp. 341-348.

Achillides Z., Pilakoutas K., and Waldron P. (1997b), "Modelling of FRP Rebar Bond Behaviour," Proceedings of the Third International Symposium on Non-Metallic (FRP) Reinforcement for Concrete Structures, Sapporo-Japan, Oct. 1997, Vol. 2, pp. 423-430.

Achillides Z., and Pilakoutas K. (2004), "Bond Behaviour of Fibre Reinforced Polymer Bars Under Direct Pullout Conditions," Journal of Composites for Construction, ASCE, Vol. 8, No. 2, April 2004, pp. 173-181.

Aiello M. A., and Ombres L. (2000), "Load-Deflection Analysis of FRP Reinforced Concrete Flexural Members," Journal of Composites for Construction, ASCE, Vol. 4, No. 4, November 2000, pp. 164-171.

Alkhrdaji T., Ombres L., and Nanni A. (2002), "Flexural Behavior and Design of One-Way Concrete Slabs Reinforced with Deformed GFRP Bars," Proceedings, 3rd International Conference on Advanced Composite Materials in Bridges and Structures, Ottawa, Canada, Humar J. and Razaqpur A.G., Editors, 15-18 Aug. 2000, pp. 217-224.

ASCE (1982), "Finite Element of Reinforced Concrete," American Society of Civil Engineers (ASCE), New York, 1982, 545 pp., cited in ACI Committee 224 (1992).

Balazs G. L. (1993), "Cracking Analysis Based on Slip and Bond Stresses," ACI materials Journal, Vol. 90, No. 4, July-August 1993, pp. 341-348.

Beeby A. W. (2004), "The Influence of the Parameter $\varnothing/\rho_{eff}$ on Crack Widths," Structural Concrete, Thomas Telford and *fib*, Vol. 5, No. 2, pp. 71-83.

Benmokrane B., Chaallal O., and Masmoudi R. (1996), "Flexural Response of Concrete Beams Reinforced with FRP Reinforcing Bars," ACI Structural Journal, Vol. 93, No. 1, Jan.-Feb. 1996, pp. 46-55.

Bischoff P. H., and Paixao R. (2004), "Tension Stiffening and Cracking of Concrete Reinforced with Glass Fiber Reinforced Polymer (GFRP) bars," Canadian Journal of Civil Engineering, Vol. 31, 2004, pp. 579-588.

Bischoff P. H. (2005a), "Reevaluation of Deflection Prediction for Concrete Beams Reinforced with Steel and Fiber Reinforced polymer Bars," Journal of Structural Engineering, ASCE, May 2005, pp. 752-767.

Bischoff P. H. (2005b), "A rational Proposal for Predicting Beam Deflection," 33rd Annual Conference of the Canadian Society for Civil Engineering, Toronto, Ontario, Canada, 2-4 June 2005, pp. GC-299-- 1-10.

Branson D. E. (1977), "Deformation of Concrete Structures," McGraw-Hill, new York.

Brown V. L., and Bartholomew C. L. (1993), "FRP Reinforcing Bars in Reinforced Concrete Members," ACI Materials Journal, Vol. 90, No. 1, Jan.-Feb 1993, pp.34-39.

BSI (1985), "Structural Use of Concrete–Part 2 : Code of Practice for Special Circumstances (BS8110-2:1985), including ammendments No. 1 (1989) and 2 (2001)," British Standard Institution, 1985, 60 pp.

Burgoyne C. J. (2001), "Rational Use of Advanced Composites in Concrete," Proceedings of the Institution of Structural Engineers, Structures and Buildings 146, Issue 3, Aug. 2001, pp 253-262.

CEB (1993), "CEB-FIP Model Code 1990," Comite Euro-International du Beton, Thomas Telford Services Ltd., 1993, 437 pp.

CEN (1992), "Eurocode 2: Design of Concrete Structures – Part 1: General rules and rules for buildings (ENV 1992-1-1:1992)," Comite Europeen de Normalisation, Brussels, 176pp.

CEN (2004), "Eurocode 2: Design of Concrete Structures – Part 1-1: General rules and rules for buildings (EN 1992-1-1:2004)," Comite Europeen de Normalisation, Brussels, 225pp.

Cosenza E., Greco C., Manfredi G., and Pecce M. (1997a), "Flexural Behaviour of Concrete Beams Reinforced with Fibre Reinforced Plastic (FRP) Bars," Proceedings of the Third International Symposium on Non-Metallic (FRP) Reinforcement for Concrete Structures, Sapporo-Japan, Oct. 1997, Vol. 2, pp. 463-470.

Cosenza E., Manfredi G. and Realfonzo R. (1997b), "Behaviour and Modelling of Bond of FRP Rebars to Concrete," Journal of Composites for Construction, ASCE, Vol. 1, No. 2, May 1997, pp. 40-51.

CSA (2002), "Design and Construction of Building Components with Fibre-Reinforced Polymers (CAN/CSA-S806-02)," Canadian Standards Association, Mississauga, Ontario, Canada, 177 pp.

Duranovic N., Pilakoutas K., and Waldron P. (1997), "FRP Reinforcement for Concrete Structures: Design Considerations," Proceedings of the Third International Symposium on Non-Metallic (FRP) Reinforcement for Concrete Structures, Sapporo-Japan, Oct. 1997, Vol. 2, pp. 527-534.

Ehsani M. R., Saadatmansh H., and Tao S. (1996) "Design Recommendation for Bond of GFRP Rebars to Concrete," Journal of Structural Engineering, Vol. 122, No. 3, March 1996, pp. 247-257.

Euro-Projects (LTTC) (1997), "The development of non-ferrous reinforcement for concrete structures," Eurocrete Project Final Report, Loughborough, UK.

Faza S. S., and GangaRao H. V. S. (1993) "Theoretical and Experimental Correlation of Behaviour of Concrete Beams Reinforced with Fibre Reinforced Plastic Rebars," Fibre-Reinforced-Plastic Reinforcement for Concrete Structures (SP-138), A. Nanni and C. W. Dolan, eds, American Concrete Institute, Farmington Hills, Mich., pp. 599-614.

Faza S. S., and GangaRao H. V. S. (1992) "Bending and Bond Behaviour of Concrete Beams Reinforced with Fiber-Reinforced Plastic Rebars," WVDOH-RP-93 Phase I Report, West Virginia University, Morgantown, cited in ACI Committee 440 (1996).

fib (1999a), " Structural Concrete, Textbook on Behaviour, Design and Performance, Bulletin 1," Federation internationale du beton, Lausanne, Switzerland, 224pp.

fib (1999b), " Structural Concrete, Textbook on Behaviour, Design and Performance, Bulletin 2," Federation internationale du beton, Lausanne, Switzerland, 305 pp.

fib (2000), " Bond of Reinforcement in Concrete, Bulletin 10," Federation Internationale du Beton, Task Group Bond Models,Lausanne, Switzerland, 427 pp.

Gangarao H. V. S., and Faza, S. (1991), "Bending and Bond Behaviour in Design of Concrete Beams Reinforced with Fiber-Reinforced Plastic Rebars, " Final Rep. to Federal Highway Admin., West Virginia Univ, cited in Theriault and Benmokrane (1998).

Frosch R. J. (1999), "Another Look at Cracking and Crack Control in Reinforced Concrete," ACI Structural Journal, Vol. 96, No. 3, May-June 1999, pp. 437-442.

Gao D., Benmokrane B., and Masmoudi R. (1998a), "A Calculating Method of Flexural Properties of FRP Reinforced Concrete Beam: Part1: Crack Width and Deflection," Technical Report, Department of Civil Engineering, University of Sherbrooke, Sherbrooke, Quebec, Canada, 24 pp, cited in ACI Committee 440 (2001).

Gere J. M. (2001), "Mechanics of Materials," Brookes/Cole, 5th edition, 2001, 926 pp.

Gergely P., and Lutz L. A. (1968), "Maximum Crack Width in Reinforced Concrete Flexural Members," Causes, Mechanism, and Control of Cracking in Concrete (SP-20), American Concrete Institute, Farmington Hills, Mich., pp. 87-117, cited in ACI Committee 224 (2001).

Hughes Brothers, Inc. (2005), USA, 17 Nov. 2005, http://hughesbros.com.

ISIS Canada (2001), "Reinforcing Concrete Structures with Fibre Reinforced Polymers, Design Manual No. 3," Intelligent Sensing for Innovative Structures, Manitoba, Canada.

IStructE (1999), "Interim Guidance on the Design of Reinforced Concrete Structures Using Fibre Composite Reinforcement," SETO Ltd, London, 116 pp.

JSCE (1997), "Recommendation for Design and Construction of Concrete Structures Using Continuous Fiber Reinforcing Materials," Concrete Engineering Series No, 23, 325 pp.

Masmoudi R., Theriault,M., and Benmokrane B. (1998), "Flexural Behaviour of Concrete Beams Reinforced with Deformed Fiber Reinforced Plastic Reinforcing Rods," ACI Structural Journal, Vol. 95, No. 6, Nov.-Dec. 1998, pp. 665-676.

Nanni, A. (1993), "Flexural Behaviour and Design of Reinforced Concrete Using FRP Reinforcement," Journal of Structural Engineering, Vol. 119, No. 11, Nov., pp. 3344-3359.

Nanni A., Al-Zahrani M. M., Al-Dulaijan S. U., Bakis C. E., and Boothby T. E. (1995), "Bond of FRP Reinforcement to Concrete – Experimental Results," Proceedings of the Second International RILEM Symposium: Non-Metallic (FRP) Reinforcement for Concrete Structures (FRPRCS-2), L. Taerwe, editor, Ghent, Belgium, pp. 135-145.

Neocleous K. (1999), "Design and Safety Philosophy for Concrete Structures Reinforced with Fibre Reinforced Polymers (FRP)," PhD thesis, the University of Sheffield, Dec. 1999, 213 pp.

Ombres L., Alkhrdaji T., and Nanni A., (2000), "Flexural Analysis of One-Way Concrete Slabs Reinforced with GFRP Rebars," International Meeting on Composite Materials, PLAST 2000, Proc., Advancing with Composites 2000, Milan, Italy, May 9-11, I. Crivelli-Visconti, Editor, pp. 243-250.

Pecce M., Manfredi G., and Cosenza E. (2000), "Experimental Response and Code Models of GFRP RC Beams in Bending," Journal of Composites for Construction, ASCE, Vol. 4, No. 4, November 2000, pp. 182-190.

Pecce M., Manfredi G., and Cosenza E. (2001), "A Probabilistic Assessment of Deflections in FRP RC Beams ," Proceedings of the Fifth International Symposium on Fiber-Reinforced Plastics for Reinforced Concrete Structures, Cambridge, UK, 16-18 July, 2001, C. J. Burgoyne, editor, pp. 887-896.

Pilakoutas K. (2000), "Composites in Concrete Construction," Failure Analysis of Industrial Composite Materials, E. E. Gdoutos, K. Pilakoutas, and C. A. Rodopoulos, eds, McGraw-Hill, London, 449-497.

Pilakoutas K., Neocleous K., and Guadagnini M. (2002), "Design Philosophy Issues of Fiber Polymer Reinforced Concrete Structures," Journal of Composites for Construction, Vol. 6, No. 3, Aug. 2002, pp 154-161.

R. Park, and T. Paulay (1975), "Reinforced Concrete Structures," John Wiley and Sons, 1975, 769 pp.

Sooriyaarachchi K., Pilakoutas K., and Byars E. (2005), "Tension Stiffening Behavior of GFRP-Reinforced Concrete," Proceedings of the 7th International Symposium on Fiber-Reinforced Polymer (FRP) Reinforcement for Concrete Structures, ACI SP-230, Kansas City, Missouri, USA, November 2005, pp. 974-990.

Taranu N. (2005), "Composite Materials and Constitutive Relationships," lecture notes, FRP Composites in Construction course, University of Sheffield, 2005.

Theriault M., and Benmokrane B. (1998), "Effects of FRP Reinforcement Ratio and Concrete Strength on Flexural Behaviour of Concrete Beams," Journal of Composites for Construction, ASCE, Vol. 2, No. 1, Feb. 1998, pp. 7-16.

Tighiouart B., Benmokrane B., and Gao D. (1998), "Investigation of Bond in Concrete Member With Fiber Reinforced Polymer (FRP) Bars," Construction and Building Materials Journal, Elsevier, Vol. 12, Dec. 1998, pp. 453-462.

Timoshenko S. P., and Gere, J. M. (1972), "Mechanics of Materials," Van Nostrand Reinhold, 1972, 552 pp.

Toutanji H. A., and Saafi M. (1999) "Deflection and Crack Width Predictions of Concrete Beams Reinforced with Fiber Reinforced Polymer Bars," Proceedings, Fourth International Symposium on Fiber Reinforced Polymer Reinforcement for Reinforced Concrete Structures, Baltimore-USA, SP 188, Charles W. Dolan, Sami H. Rizkalla, and Antonio Nanni, editors, American Concrete Institute, Farmington Hills, Mich., 1999, pp.1023-1034.

Waldron P., Pilakoutas K., and Guadagnini M. (2000), "Composite Materials in Reinforced Concrete Repair and Construction," 6th International Conference on Deterioration and Repair of Reinforced Concrete in the Arabian Gulf, Bahrain, Nov. 2000, pp. 277-292.

Wang C. and Salmon C. G. (1985), "Reinforced Concrete Design," Harper and Row, New York, 947 pp.

Zhao W., Pilakoutas K., and Waldron P. (1997a), "FRP Reinforced Concrete: Calculations for Deflections," Proceedings of the Third International Symposium on Non-Metallic (FRP) Reinforcement for Concrete Structures, Sapporo-Japan, Oct. 1997, Vol. 2, pp. 511-518.

Zhao W., Pilakoutas K., and Waldron P. (1997b), "FRP Reinforced Concrete: Cracking Behaviour and Determination," Proceedings of the Third International Symposium on Non-Metallic (FRP) Reinforcement for Concrete Structures, Sapporo-Japan, Oct. 1997, Vol. 2, pp. 439-446.

Zhao W. (1999), "Crack and Deformation Behaviour of FRP Reinforced Concrete Structures," PhD thesis, the University of Sheffield, Oct., 236 pp.

Zhongming W., Yasuaki G., and Osamu J. (1997), "Bond Characteristics of FRP Rods and Effect on Long Term Deflection of Concrete Beams," Proceedings of the Third International Symposium on Non-Metallic (FRP) Reinforcement for Concrete Structures, Sapporo-Japan, Oct. 1997, Vol. 2, pp. 389-396.

Appendix A

Experimental Details and Instrumentation

Layout, Geometric and Reinforcement Details of the Beams

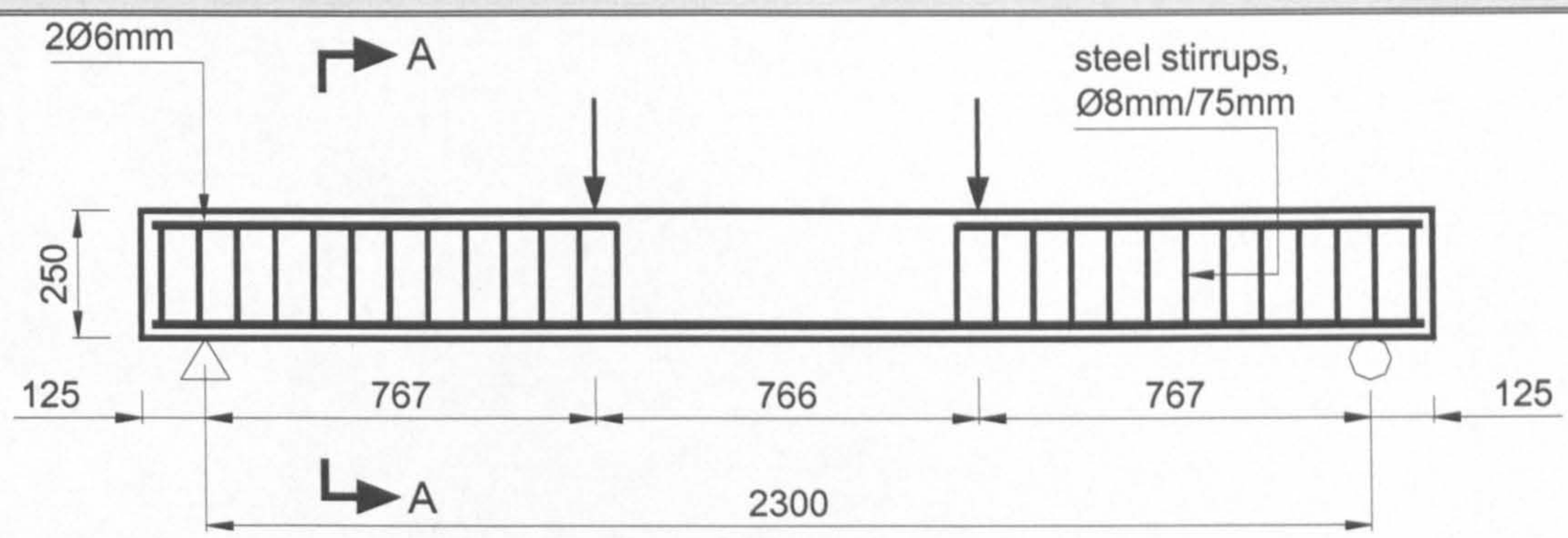

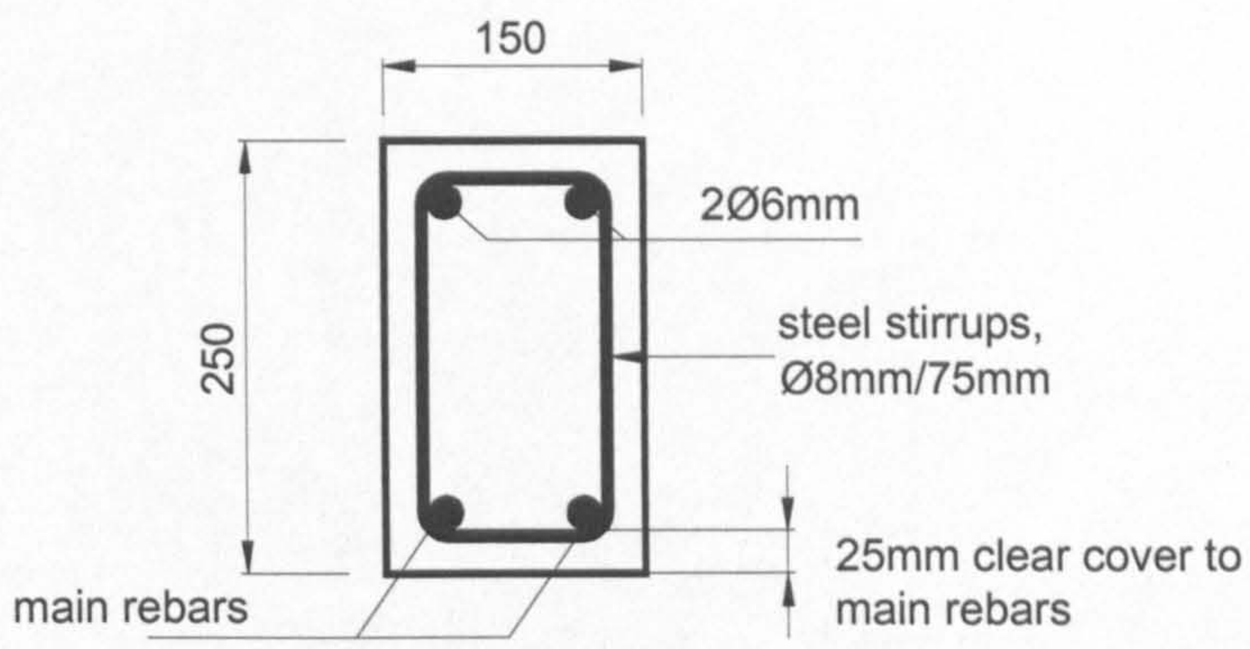

Section A-A

dimensions in mm

Rebar type	Series designation	Beam designation	Main rebar details	Reinforcement ratio	Relation to control steel beam
GFRP	BG1	BG1a	2Ø9.53	0.0043	Equal flexural capacity
		BG1b			
	BG2	BG2a	2Ø12.7	0.0077	Equal area of Rebars
		BG2b			
	BG3	BG3a	4Ø19.05[(1)]	0.0393	Equal stiffness of rebars
		BG3b			
CFRP	BC1	BC1a	3Ø6.35	0.0029	Equal flexural capacity
		BC1b			
	BC2	BC2a	3Ø9.53	0.0065	Equal area of rebars
		BC2b			
	BC3	BC3a	3Ø12.7	0.0116	Equal stiffness of rebars
		BC3b			
Steel	BS	BSa	2Ø12	0.0069	-
		BSb			

(1) Two layers, with 25 mm clear spacing between them.

Layout, Geometric and Reinforcement Details of the Slabs

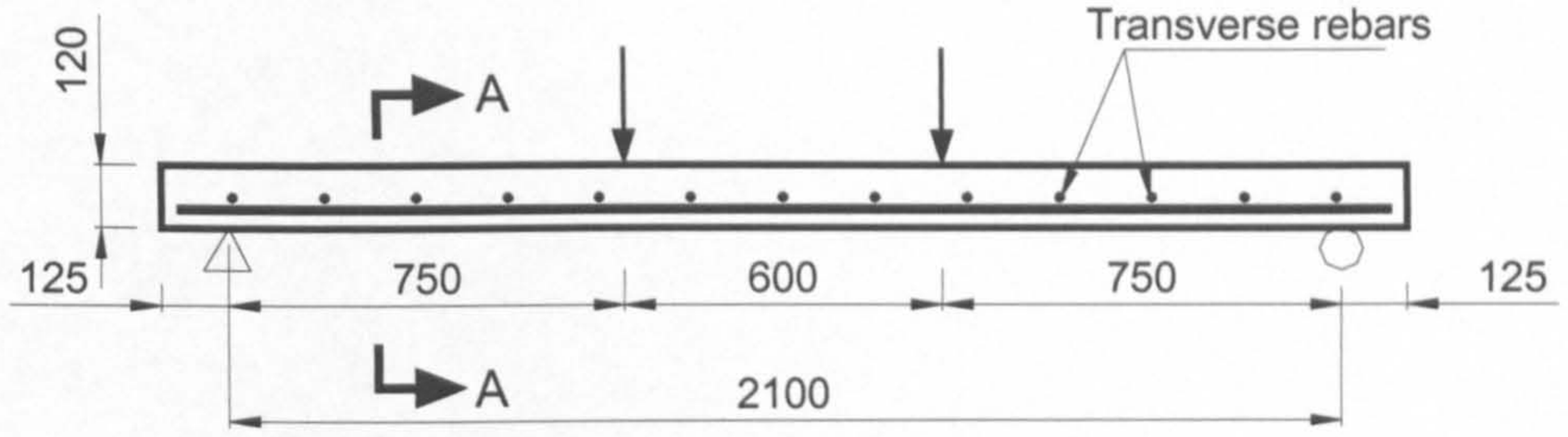

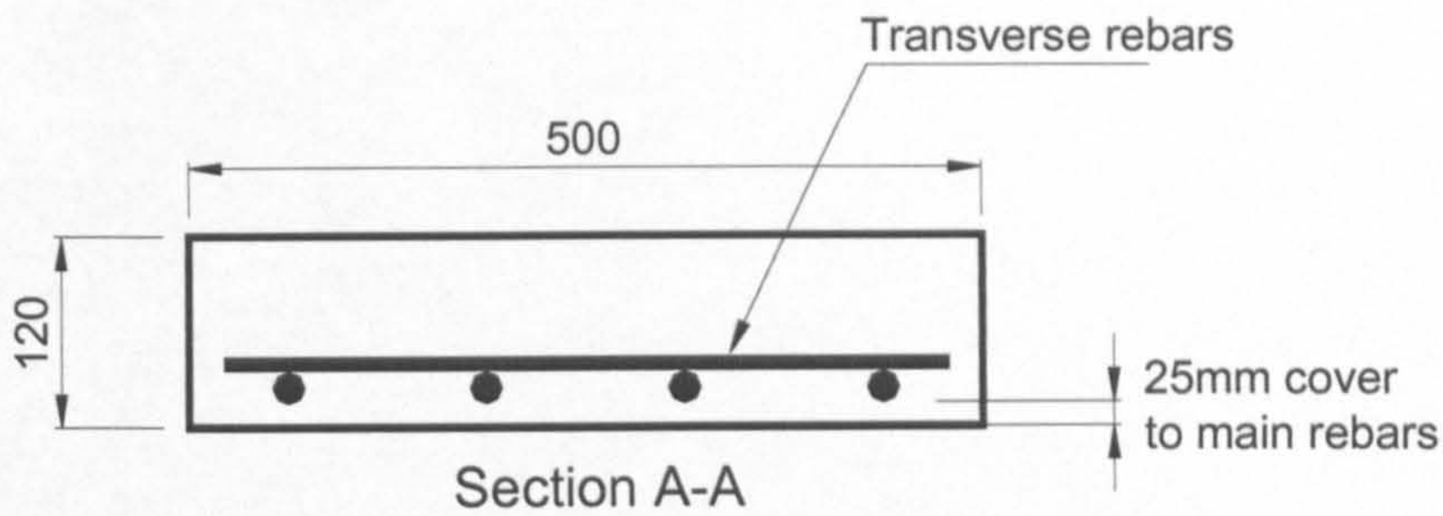

dimensions in mm

Section A-A

Note: The mesh of some GFRP and CFRP RC slabs floated during casting. Therefore, the cover to the main rebars was confirmed after every test. The actual cover values are given in Chapter 4.

Rebar type	Series designation	Slab designation	Main Rebar details	Transverse Rebar details	Reinforcement ratio	Relation to control steel slab
GFRP	SG1	SG1a	5∅6.35	7∅9.53 /m	0.0035	Equal flexural capacity
		SG1b				
	SG2	SG2a	5∅9.53	7∅9.53 /m	0.0079	Equal area of rebars
		SG2b				
	SG3	SG3a	5∅19.05	7∅9.53 /m	0.0333	Equal stiffness of rebars
		SG3b				
CFRP	SC1	SC1a	4∅6.35	6∅6.35 /m	0.0028	Equal flexural capacity
		SC1b				
	SC2	SC2a	4∅9.53	6∅6.35 /m	0.0063	Equal area of rebars
		SC2b				
	SC3	SC3a	4∅12.7	6∅6.35 /m	0.0114	Equal stiffness of rebars
		SC3b				
Steel	SS	SSa	4∅10	5∅8 /m	0.0070	-
		SSb				

Instrumentation

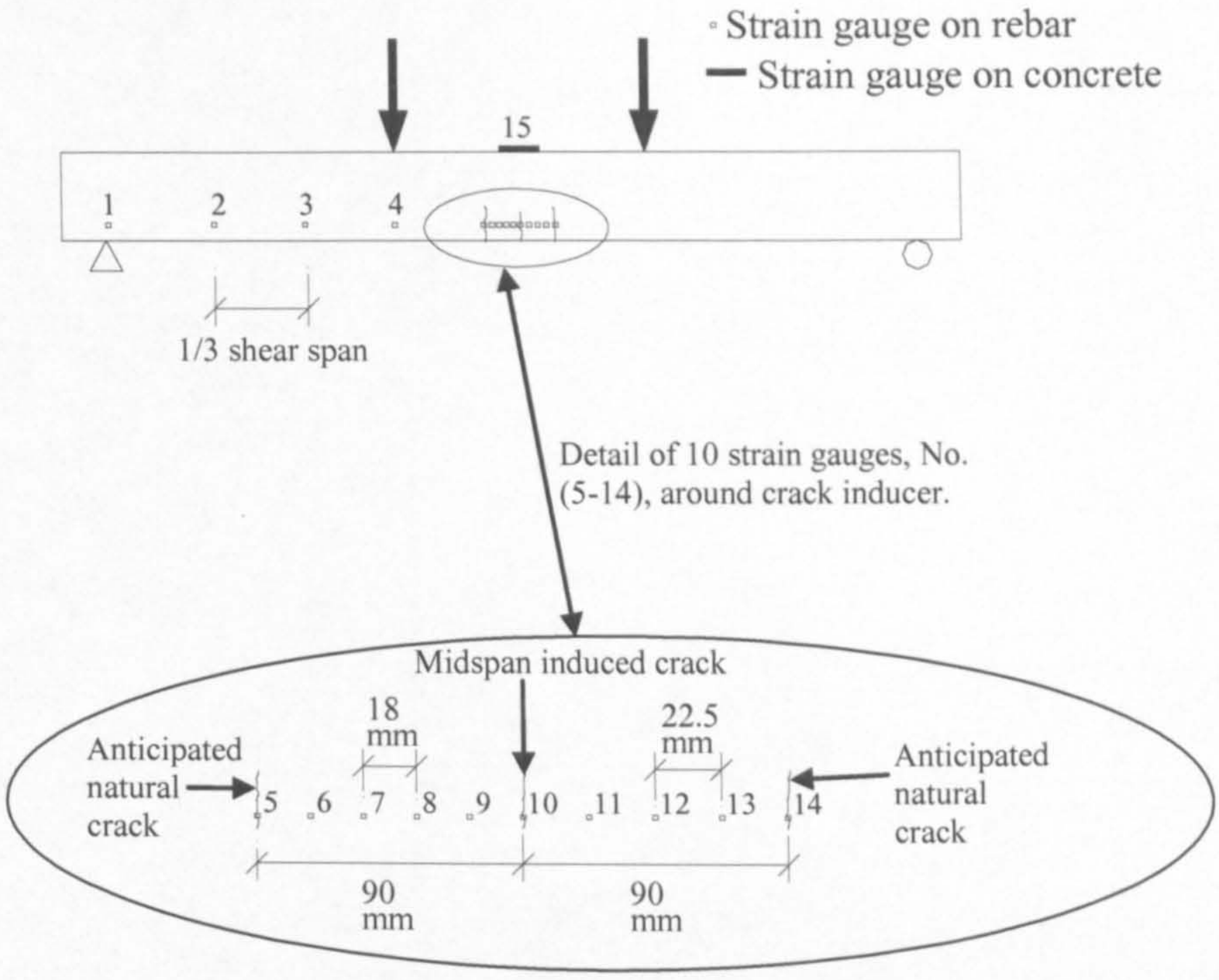

Arrangenement of Rebar and Concrete Strain Gauges

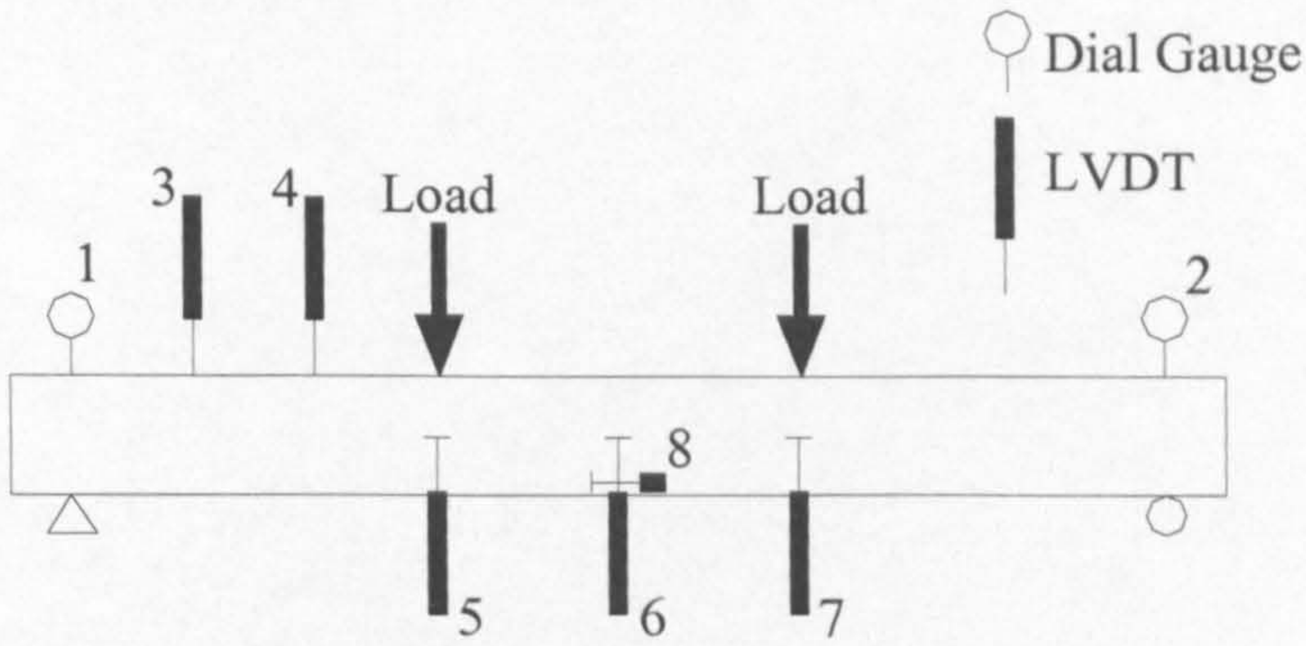

Arrangement of LVDTs and Dial Gauges

Appendix B

Experimental Results and Data Analysis, Cracked Section Analysis, Finite Element Analysis

BEAM BG1a

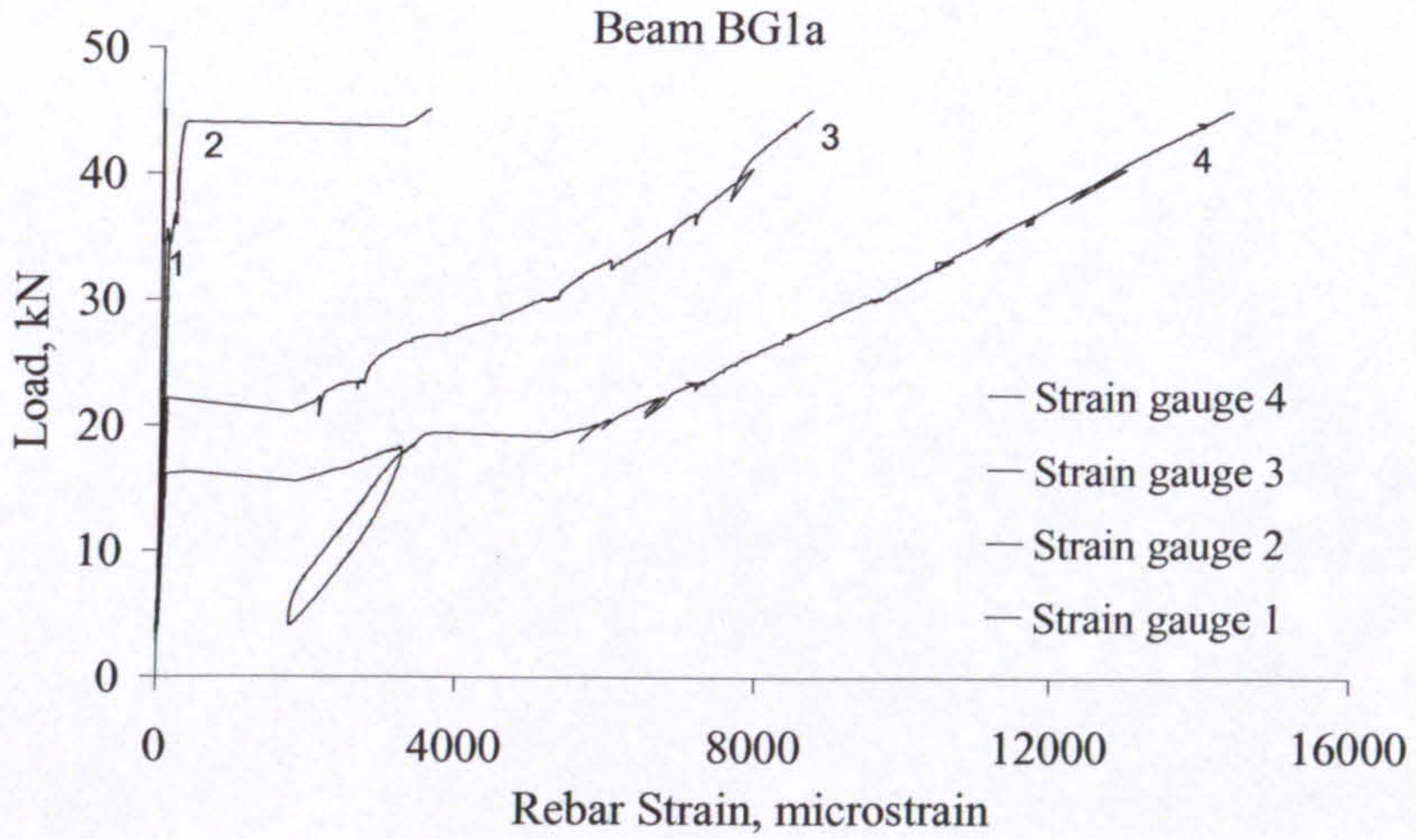
Beam BG1a
Load, kN
Rebar Strain, microstrain
Strain gauge 4
Strain gauge 3
Strain gauge 2
Strain gauge 1
1
2
3
4

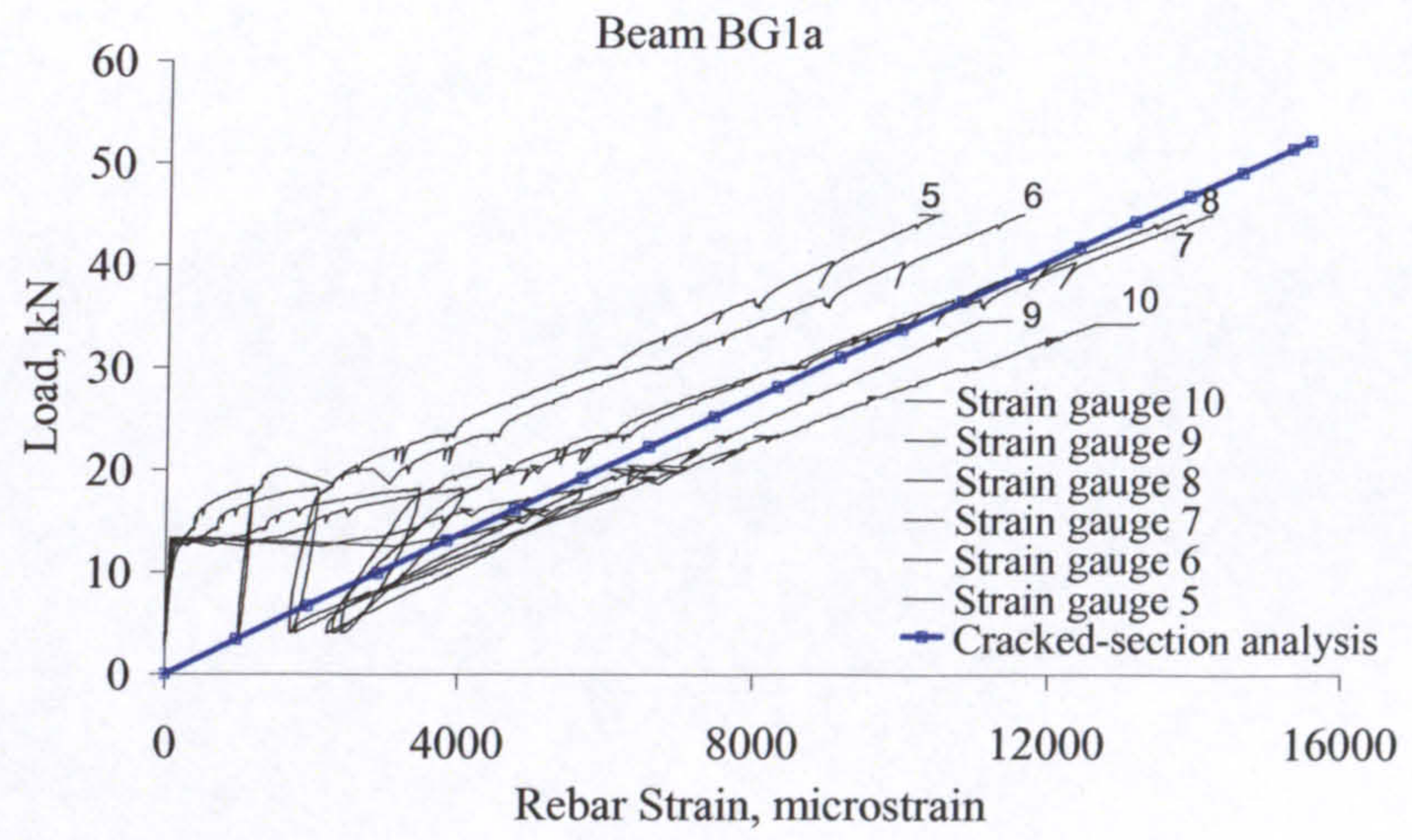
Beam BG1a
Load, kN
Rebar Strain, microstrain
Strain gauge 10
Strain gauge 9
Strain gauge 8
Strain gauge 7
Strain gauge 6
Strain gauge 5
Cracked-section analysis
5
6
7
8
9
10

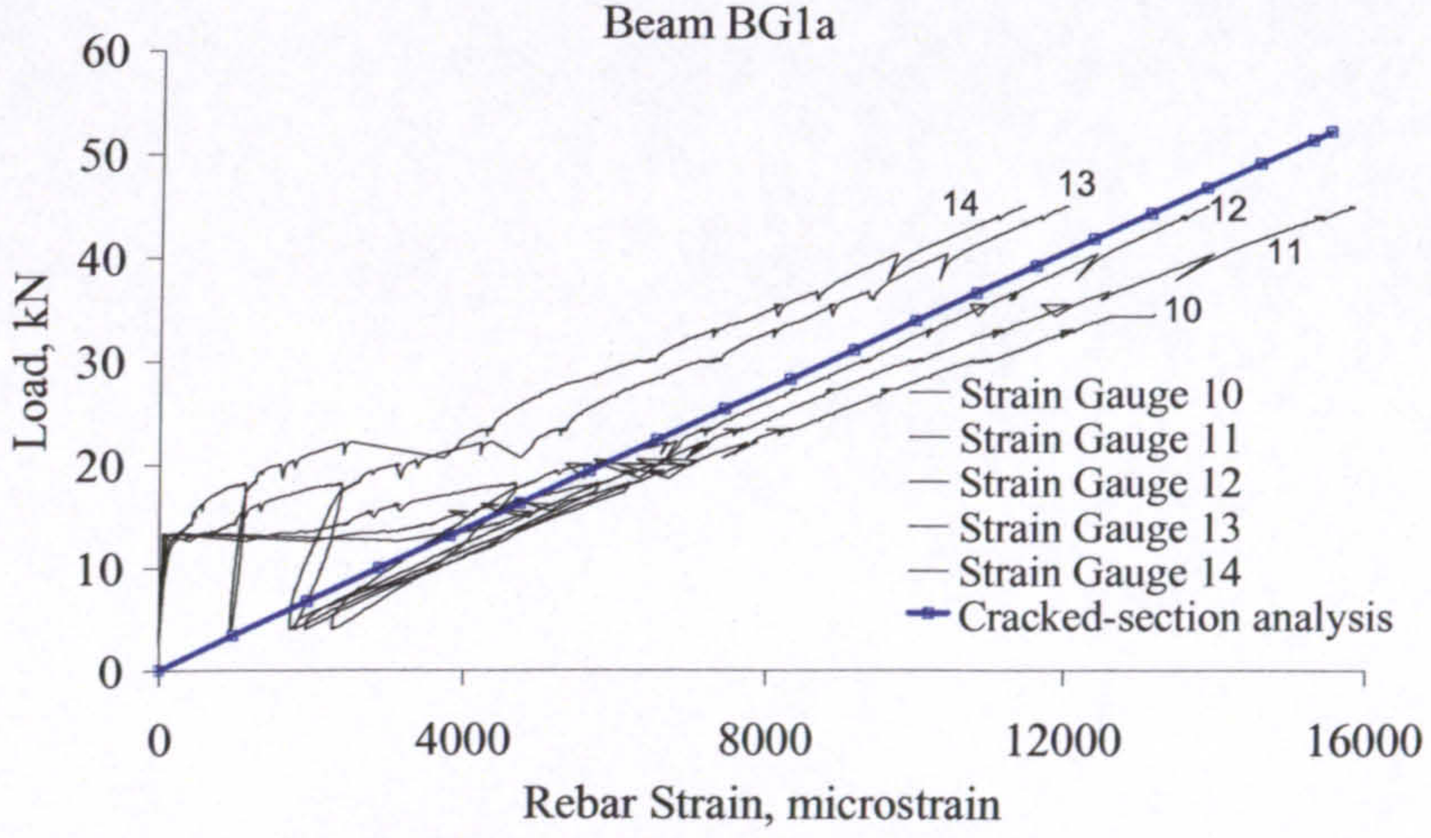
Beam BG1a
Load, kN
Rebar Strain, microstrain
Strain Gauge 10
Strain Gauge 11
Strain Gauge 12
Strain Gauge 13
Strain Gauge 14
Cracked-section analysis
10
11
12
13
14

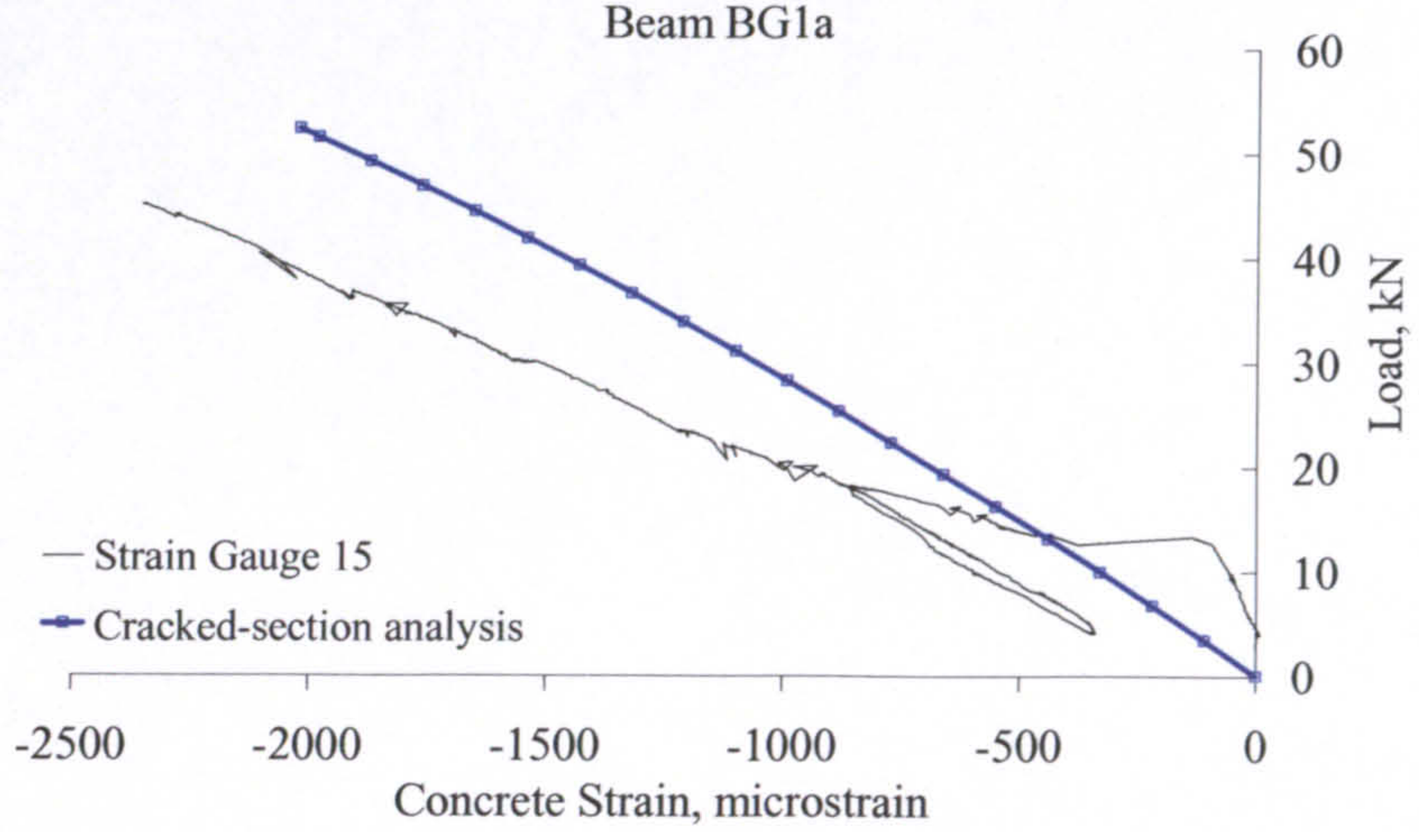
Beam BG1a
Load, kN
Concrete Strain, microstrain
Strain Gauge 15
Cracked-section analysis

BEAM BG1a

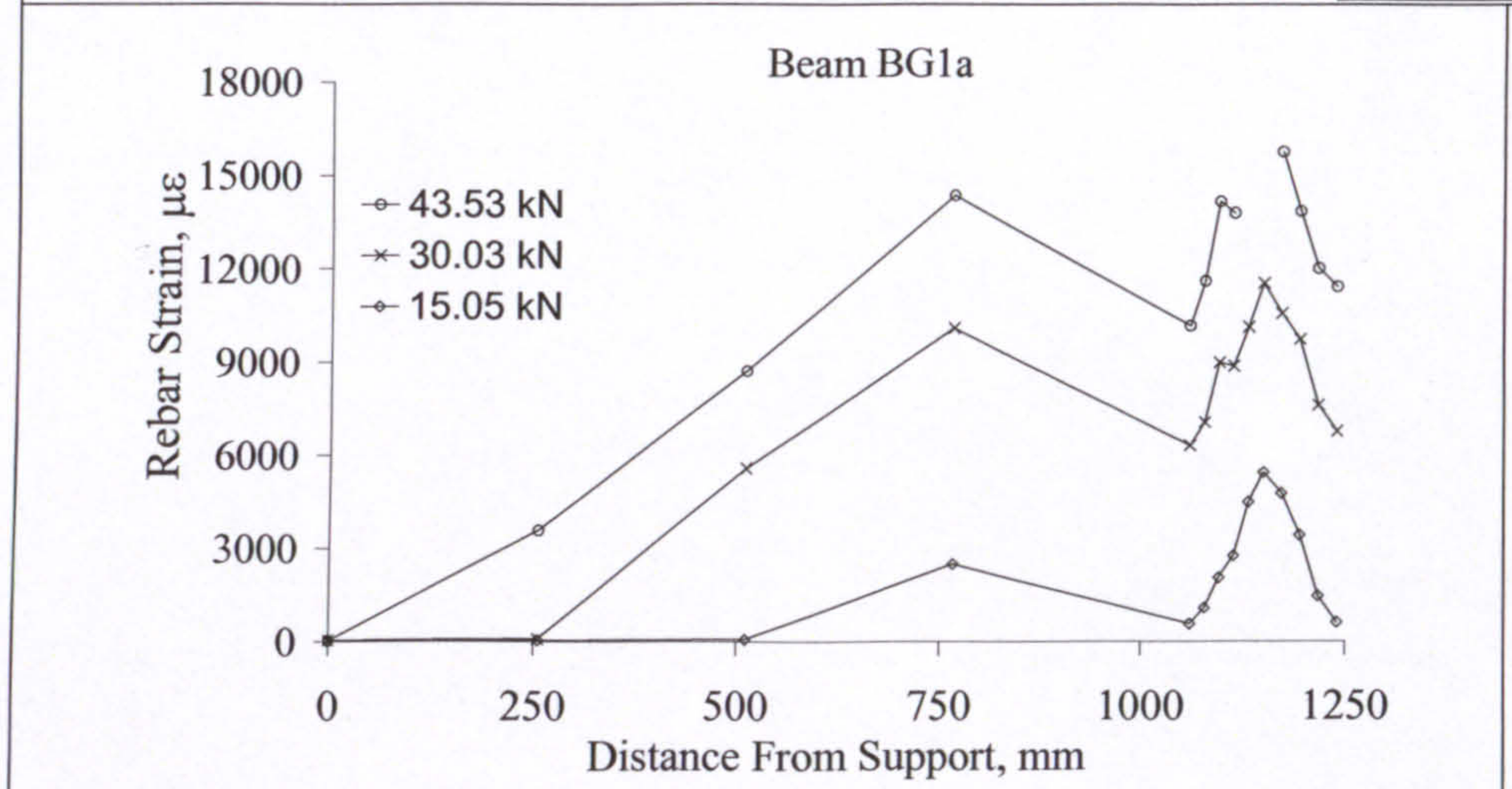
Beam BG1a
Rebar Strain, με
18000
15000
12000
9000
6000
3000
0
43.53 kN
30.03 kN
15.05 kN
0
250
500
750
1000
1250
Distance From Support, mm

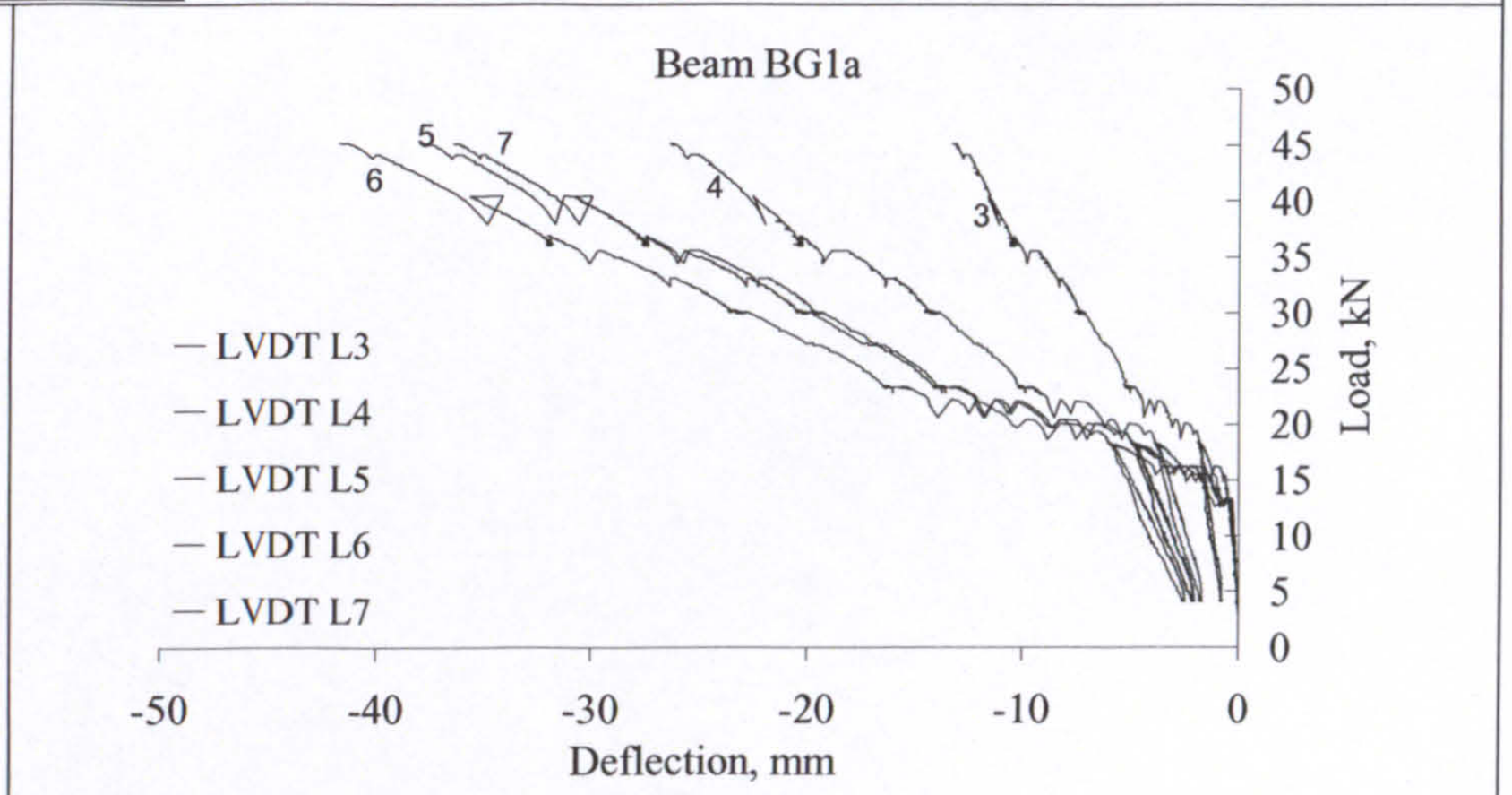
Beam BG1a
5
7
6
4
3
LVDT L3
LVDT L4
LVDT L5
LVDT L6
LVDT L7
50
45
40
35
30
25
20
15
10
5
0
Load, kN
-50
-40
-30
-20
-10
0
Deflection, mm

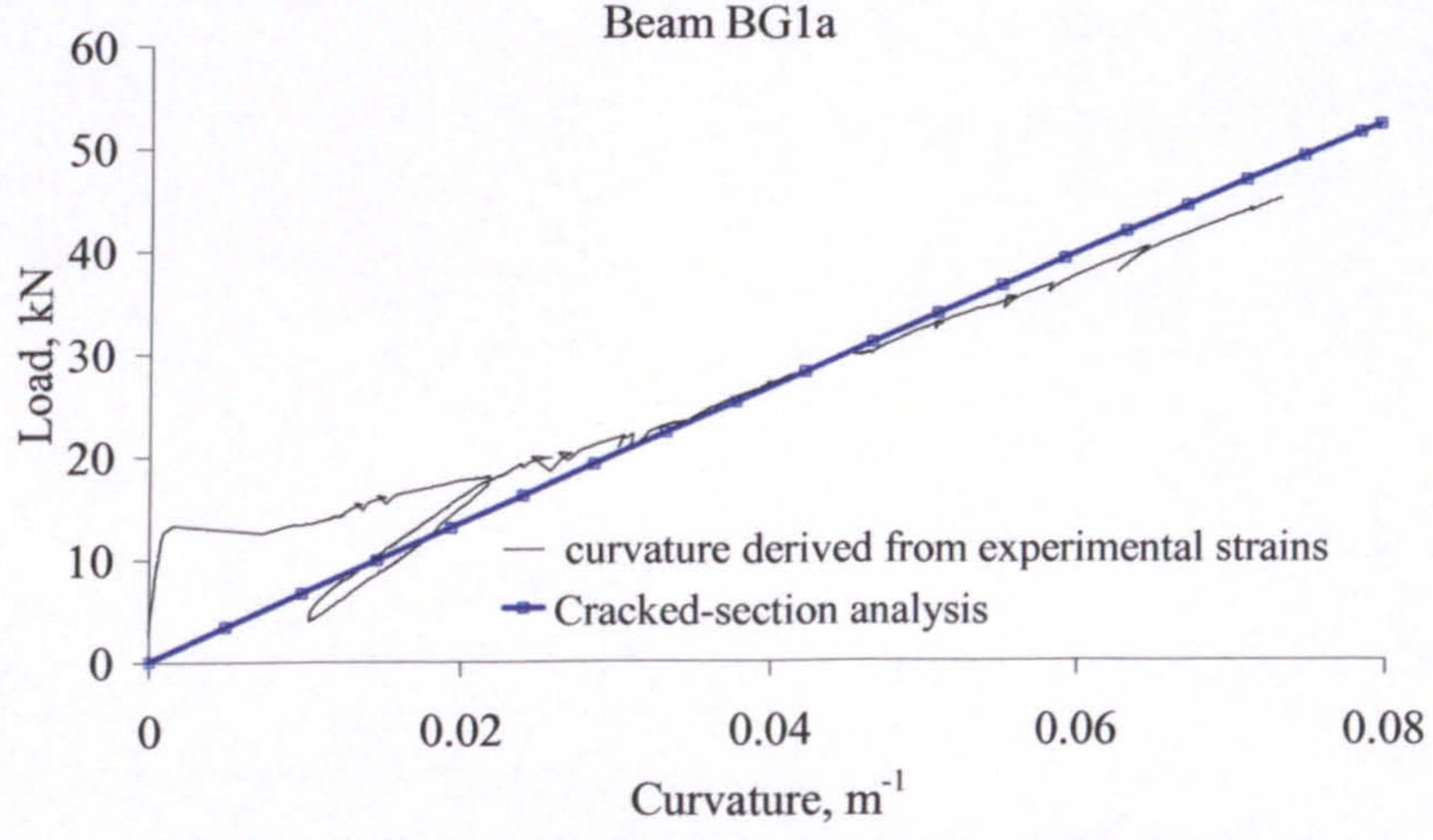
Beam BG1a
Load, kN
60
50
40
30
20
10
0
curvature derived from experimental strains
Cracked-section analysis
0
0.02
0.04
0.06
0.08
Curvature, m-1

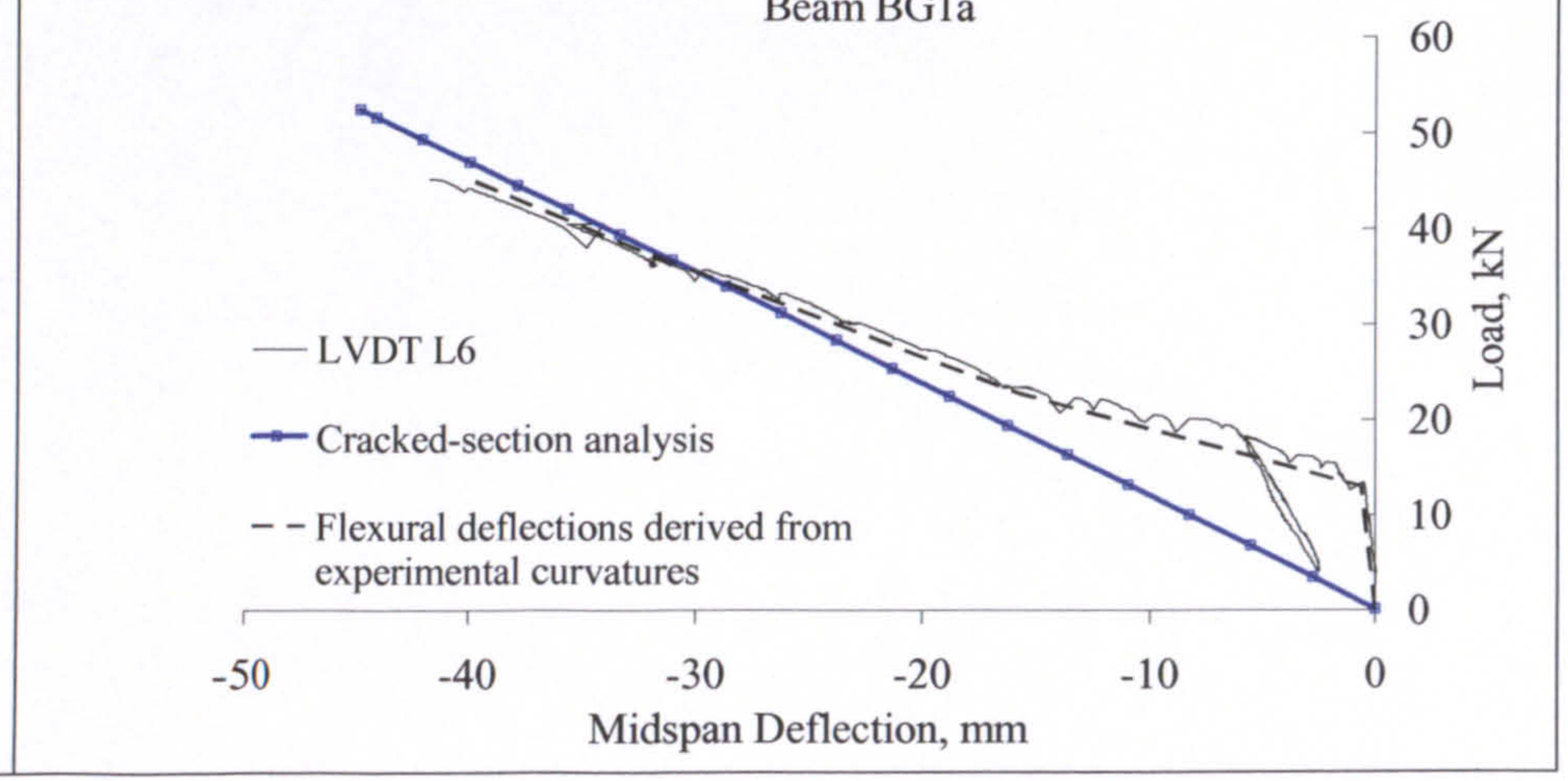
Beam BG1a
60
50
40
30
20
10
0
Load, kN
LVDT L6
Cracked-section analysis
Flexural deflections derived from experimental curvatures
-50
-40
-30
-20
-10
0
Midspan Deflection, mm

BEAM BG1a

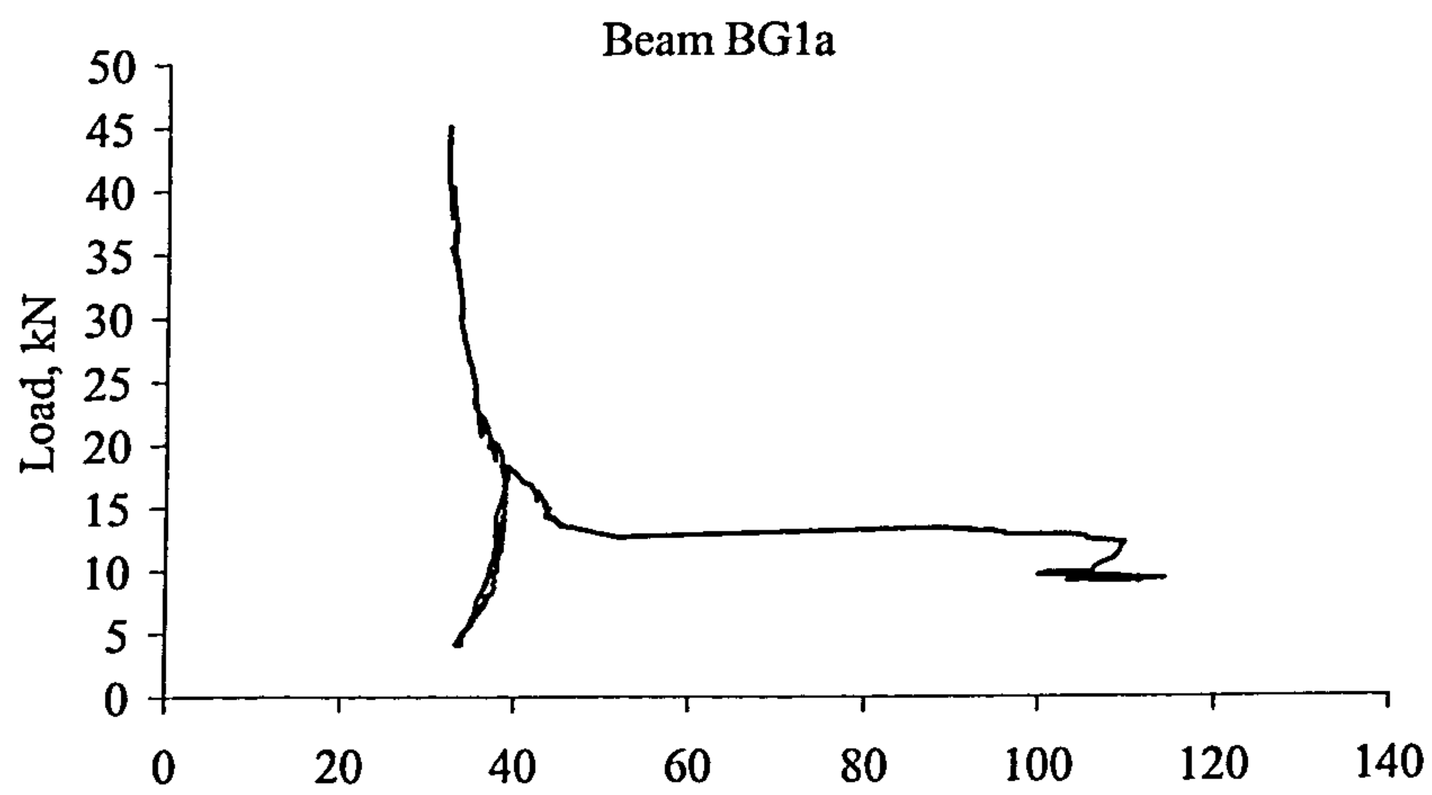
Beam BG1a
Load, kN
0
5
10
15
20
25
30
35
40
45
50
0
20
40
60
80
100
120
140
neutral axis depth, mm

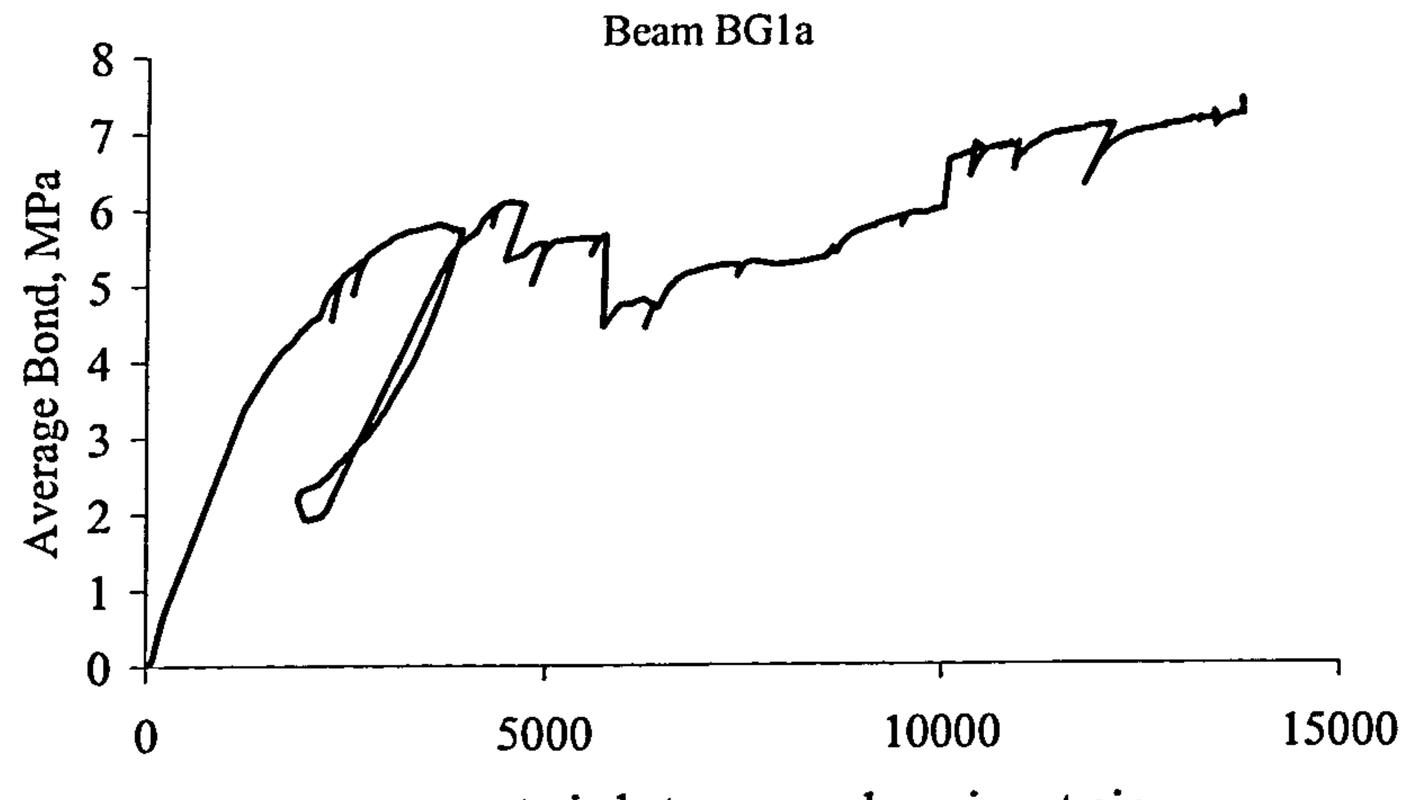
Beam BG1a
Average Bond, MPa
0
1
2
3
4
5
6
7
8
0
5000
10000
15000
average strain between cracks, microstrain

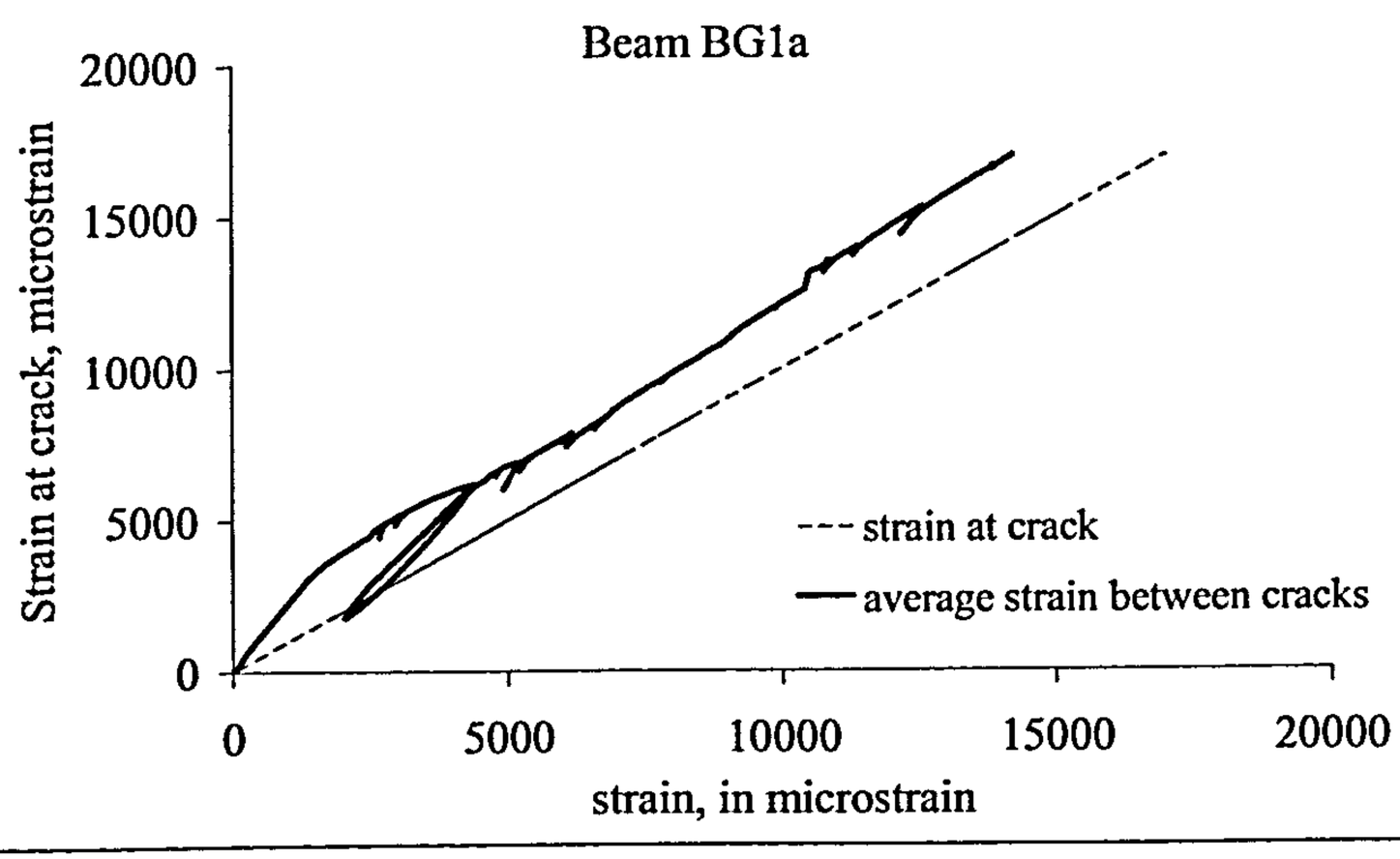
Beam BG1a
Strain at crack, microstrain
0
5000
10000
15000
20000
strain at crack
average strain between cracks
0
5000
10000
15000
20000
strain, in microstrain

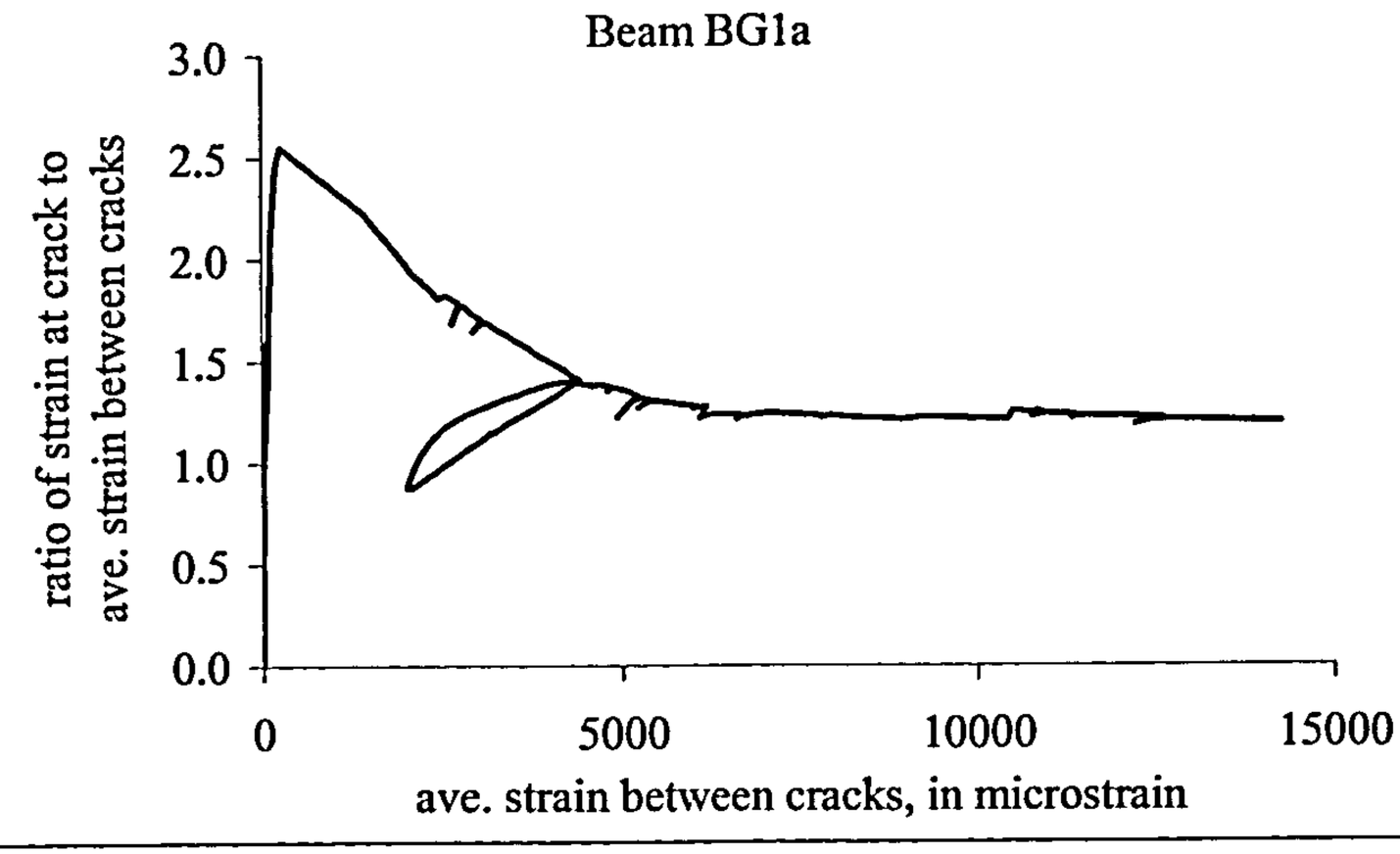
Beam BG1a
ratio of strain at crack to ave. strain between cracks
0.0
0.5
1.0
1.5
2.0
2.5
3.0
0
5000
10000
15000
ave. strain between cracks, in microstrain

BEAM BG1a

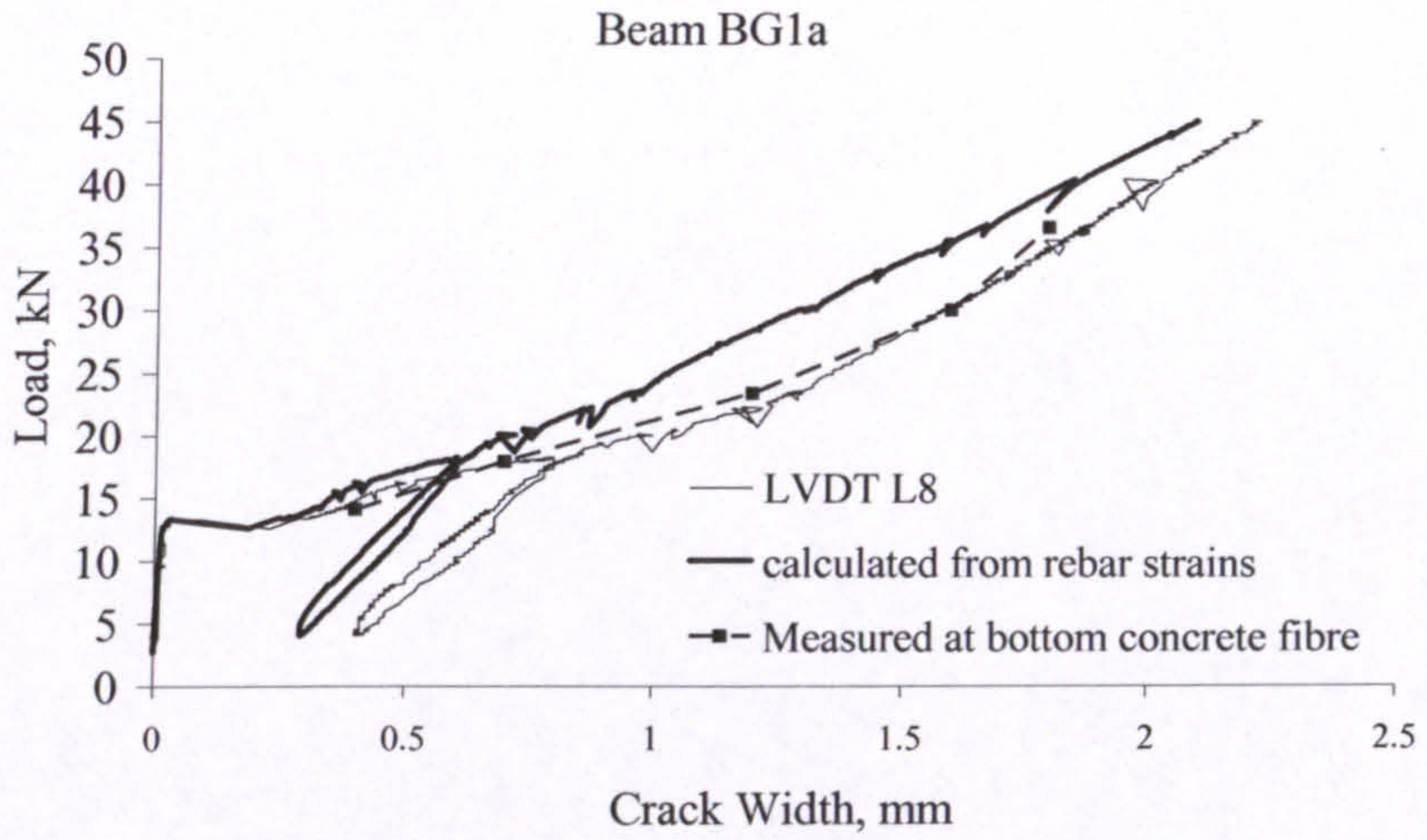

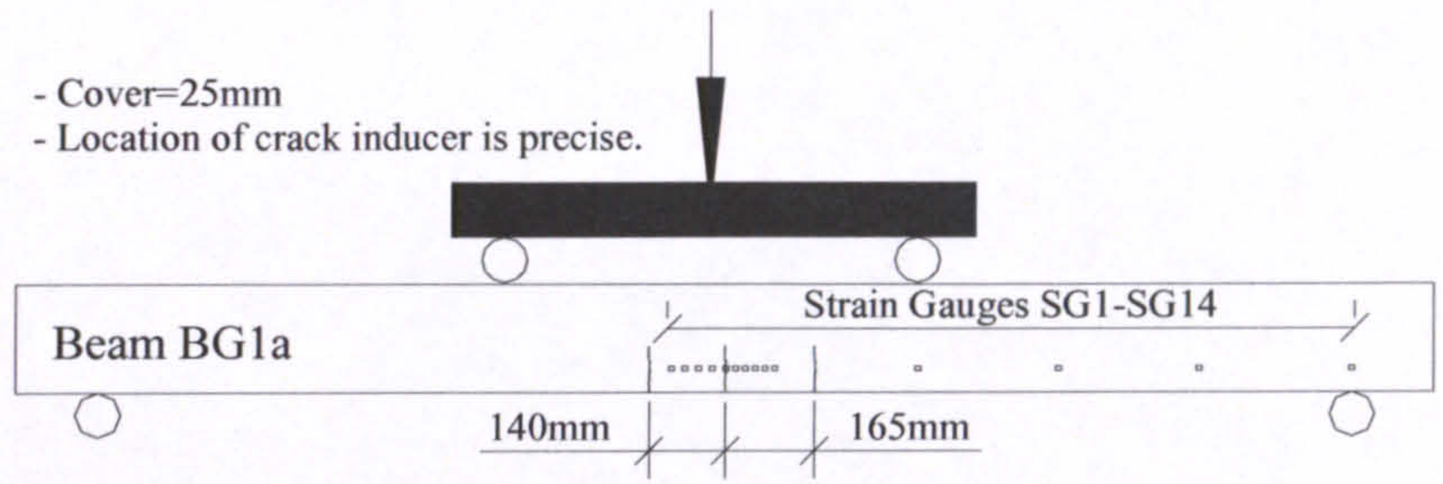

Cracks around Centre

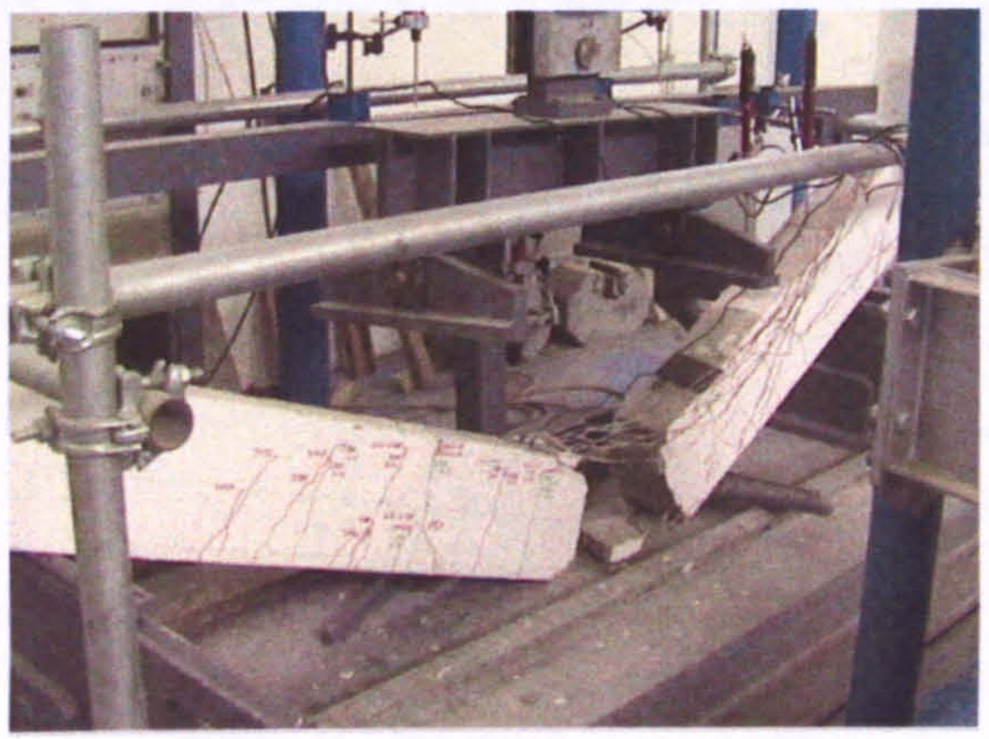

Failure by rupture of rebars

BEAM BG1b

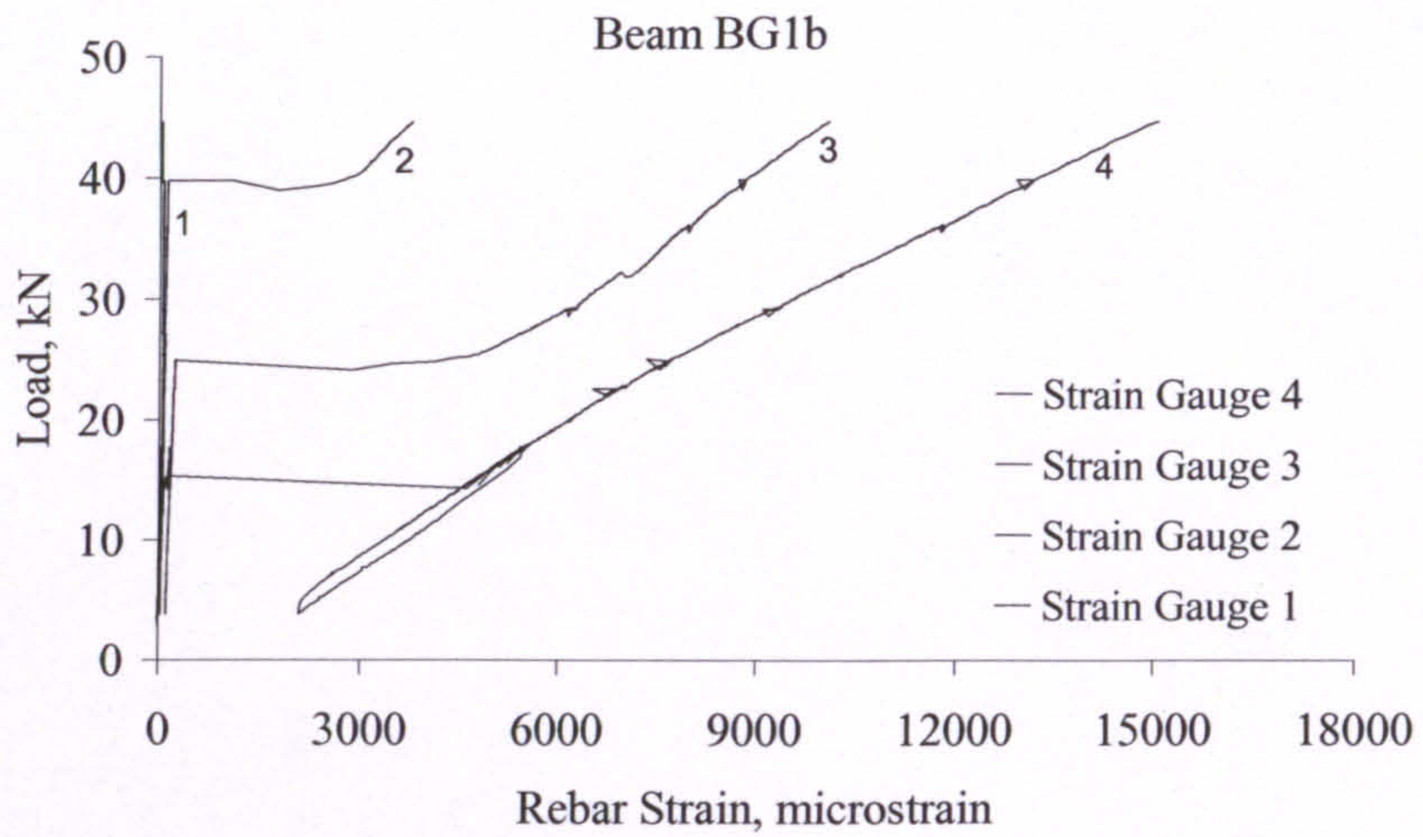
Beam BG1b
Load, kN
Rebar Strain, microstrain
1
2
3
4
Strain Gauge 4
Strain Gauge 3
Strain Gauge 2
Strain Gauge 1

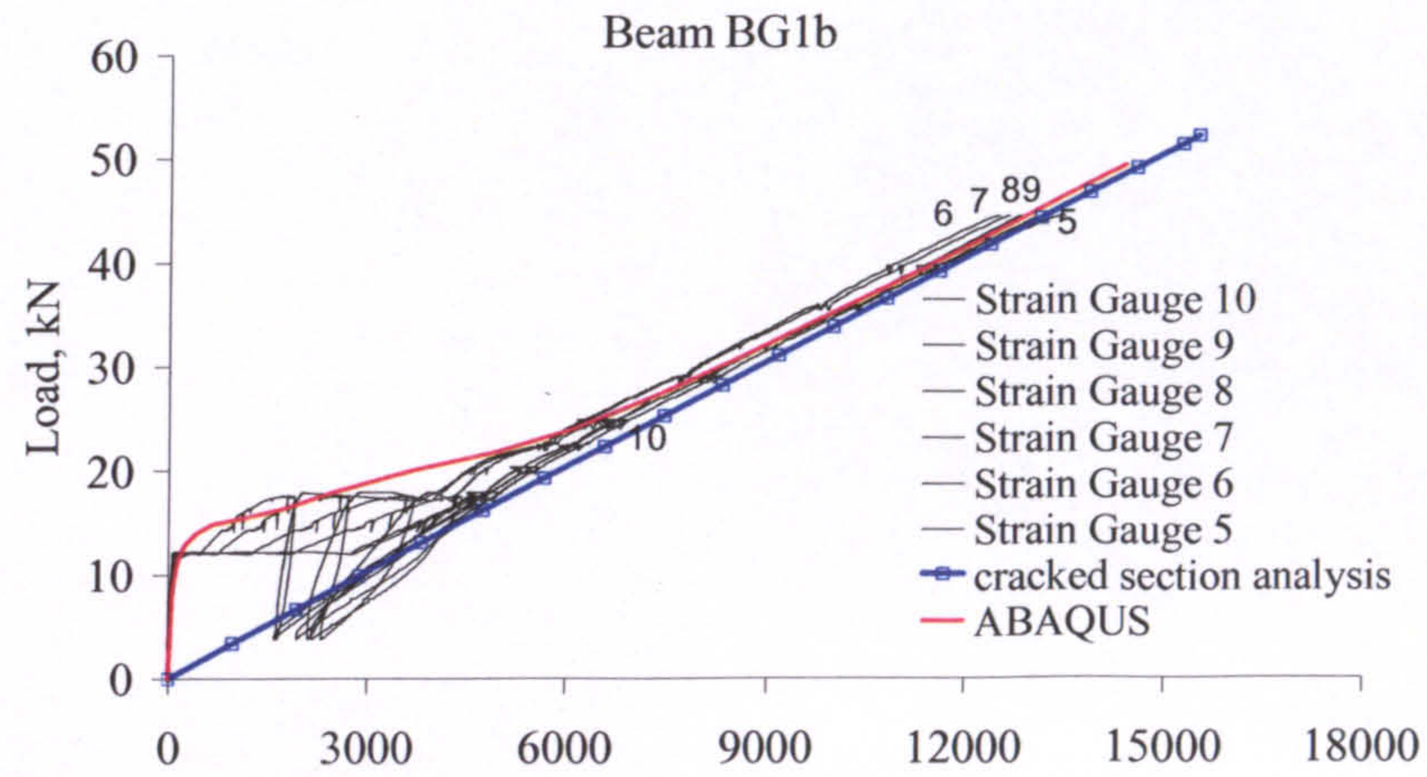
Beam BG1b
Load, kN
Rebar Strain, microstrain
5
6
7
8
9
10
Strain Gauge 10
Strain Gauge 9
Strain Gauge 8
Strain Gauge 7
Strain Gauge 6
Strain Gauge 5
cracked section analysis
ABAQUS

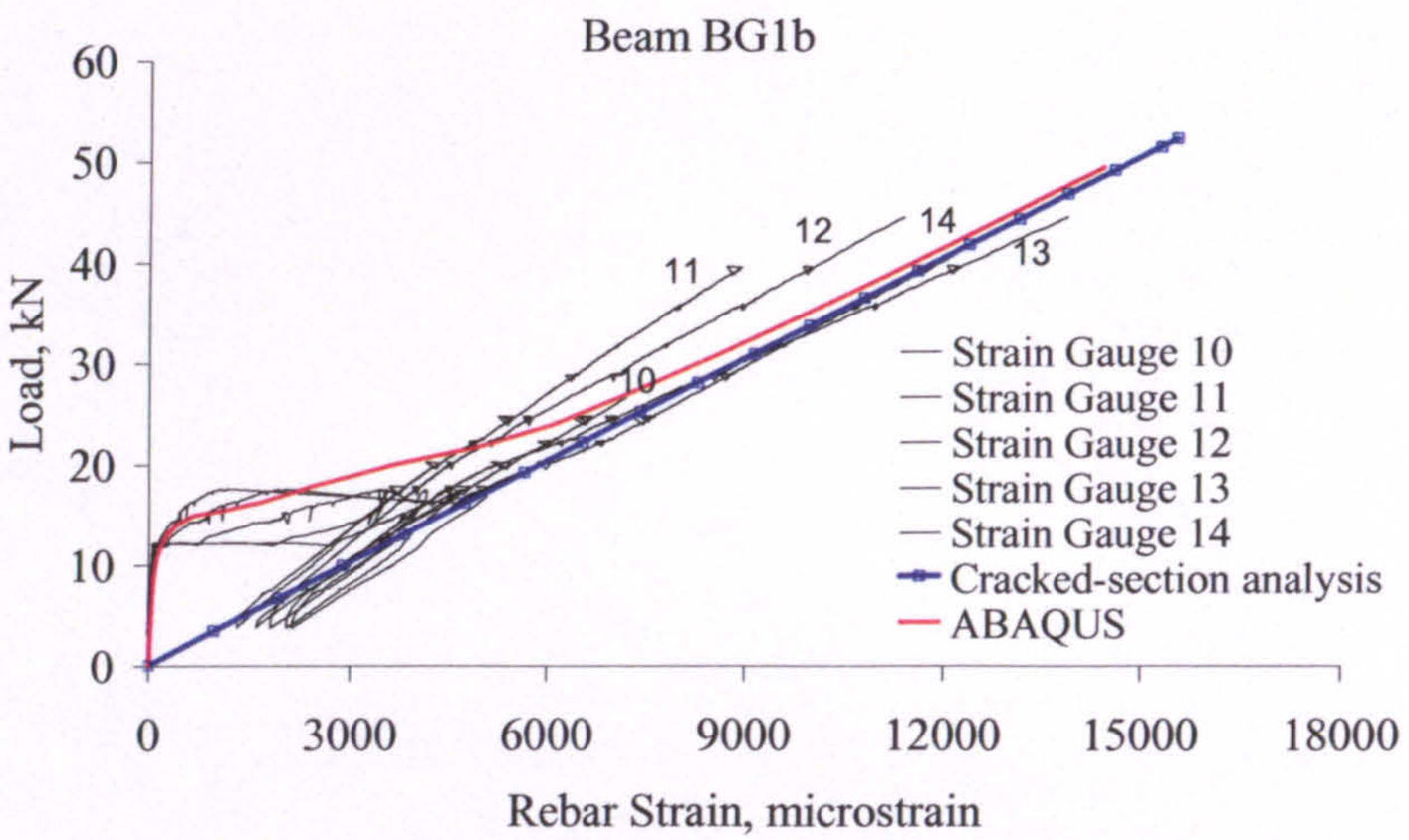
Beam BG1b
Load, kN
Rebar Strain, microstrain
10
11
12
13
14
Strain Gauge 10
Strain Gauge 11
Strain Gauge 12
Strain Gauge 13
Strain Gauge 14
Cracked-section analysis
ABAQUS

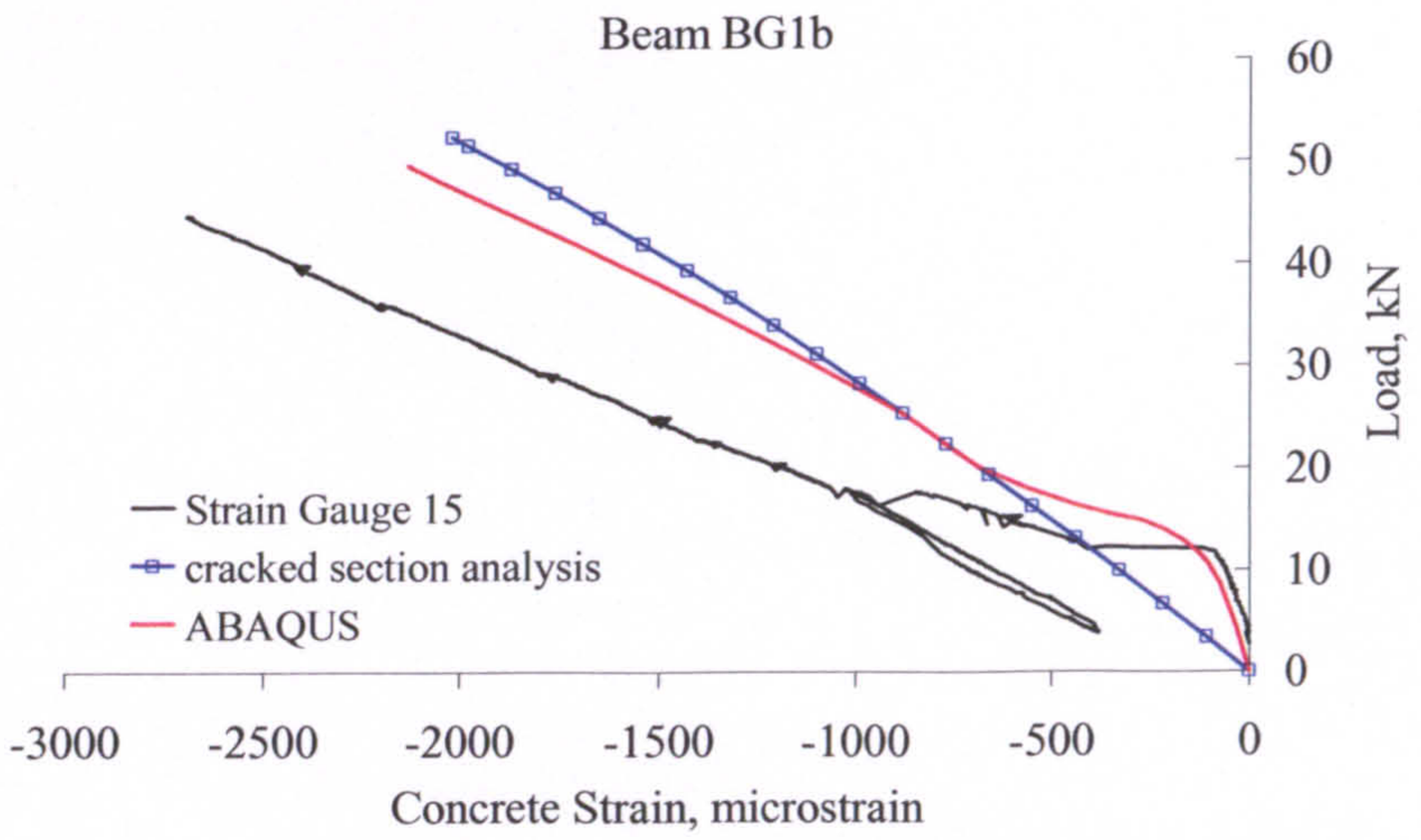
Beam BG1b
Load, kN
Concrete Strain, microstrain
Strain Gauge 15
cracked section analysis
ABAQUS

BEAM BG1b

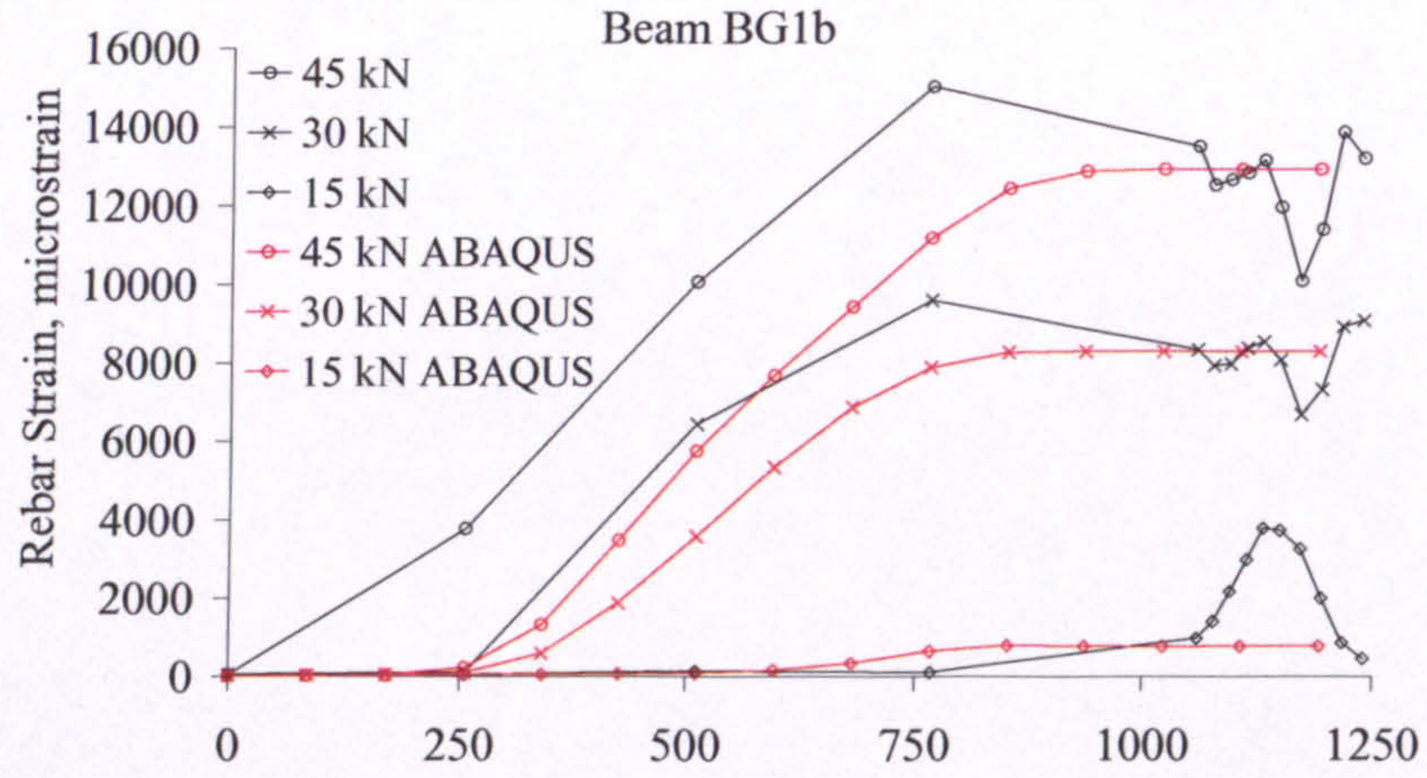
Beam BG1b
Rebar Strain, microstrain
16000
14000
12000
10000
8000
6000
4000
2000
0
45 kN
30 kN
15 kN
45 kN ABAQUS
30 kN ABAQUS
15 kN ABAQUS
0
250
500
750
1000
1250
Distance From Support, mm

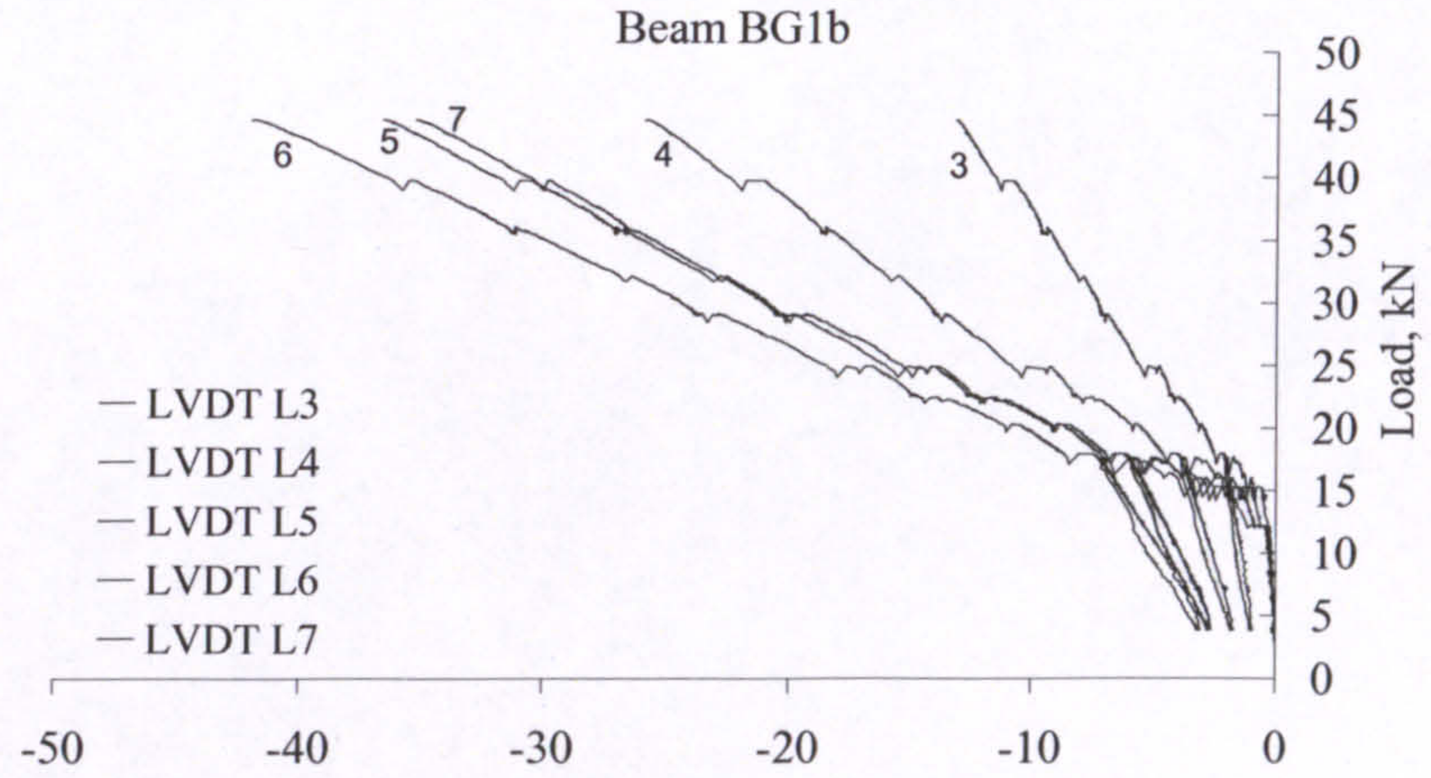
Beam BG1b
6
5
7
4
3
LVDT L3
LVDT L4
LVDT L5
LVDT L6
LVDT L7
50
45
40
35
30
25
20
15
10
5
0
Load, kN
-50
-40
-30
-20
-10
0
Deflection, mm

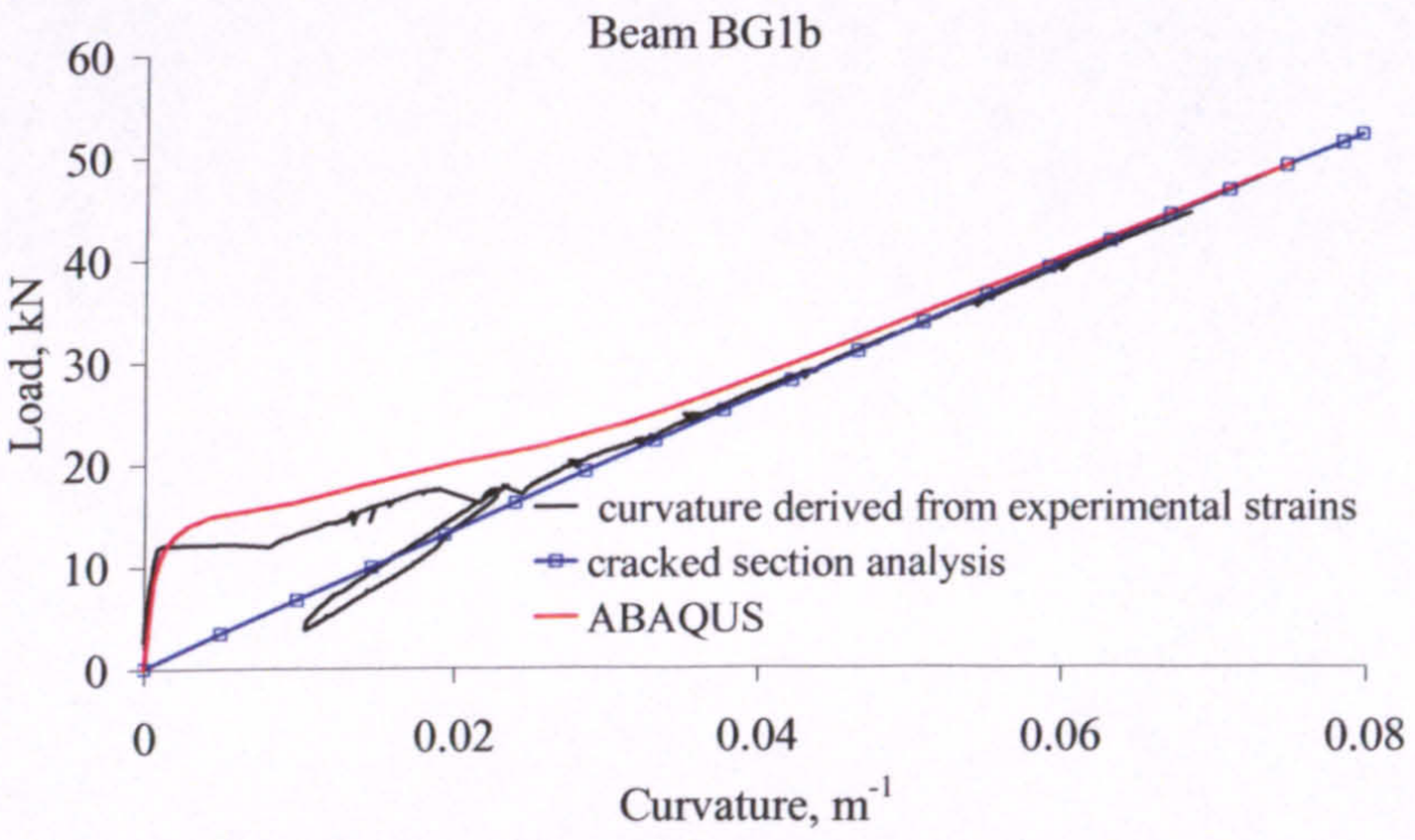
Beam BG1b
Load, kN
60
50
40
30
20
10
0
curvature derived from experimental strains
cracked section analysis
ABAQUS
0
0.02
0.04
0.06
0.08
Curvature, m-1

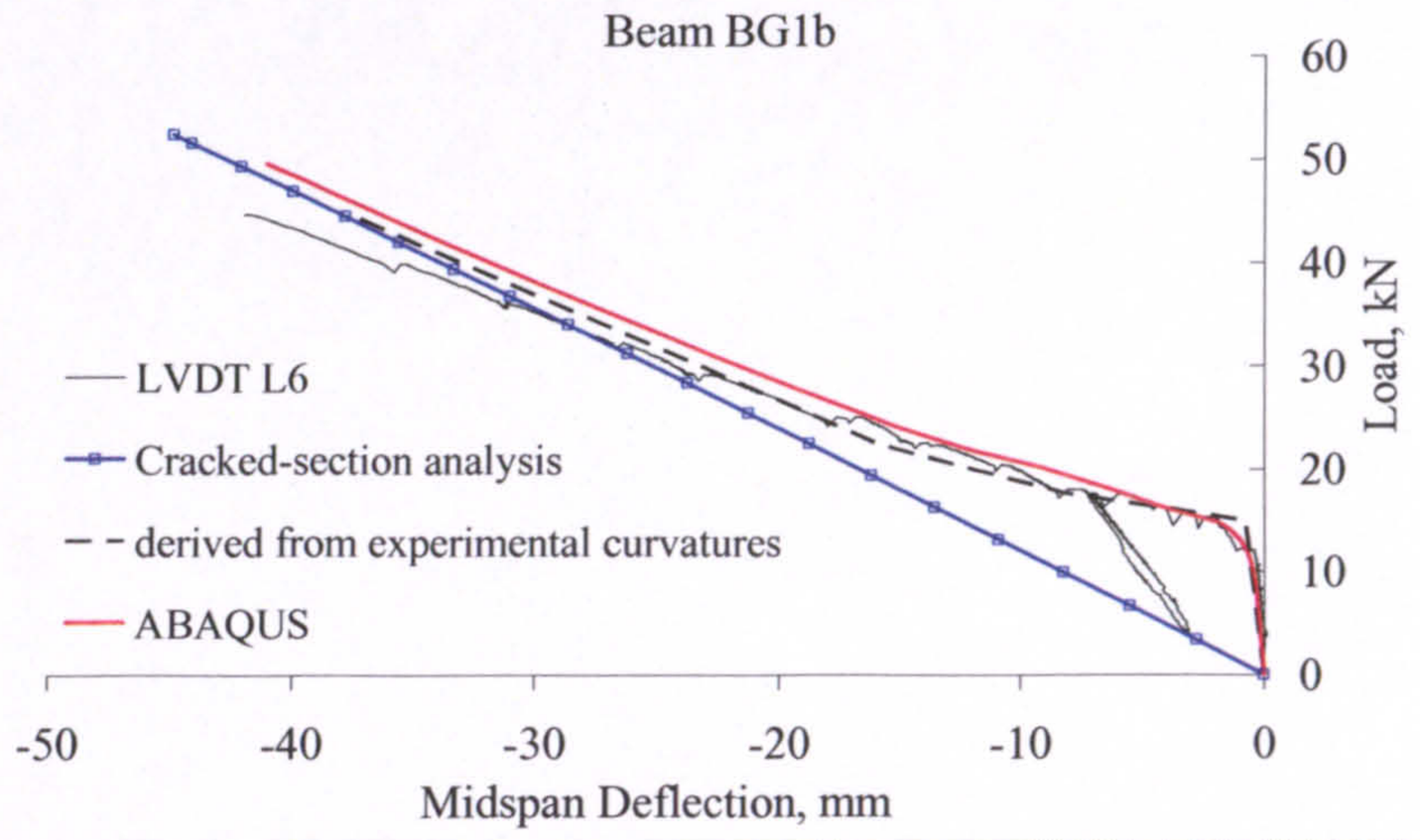
Beam BG1b
60
50
40
30
20
10
0
Load, kN
LVDT L6
Cracked-section analysis
derived from experimental curvatures
ABAQUS
-50
-40
-30
-20
-10
0
Midspan Deflection, mm

BEAM BG1b

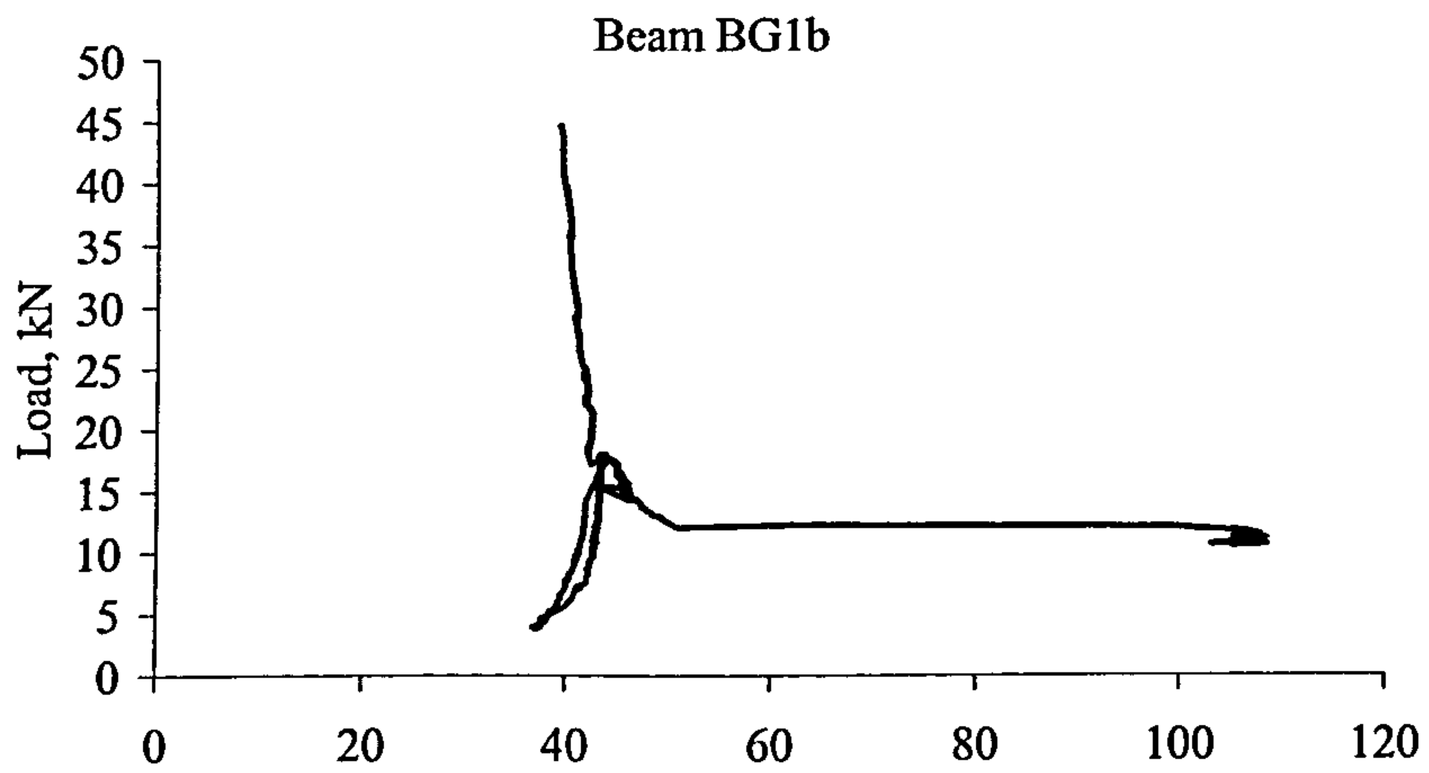
Beam BG1b
Load, kN
0
5
10
15
20
25
30
35
40
45
50
0
20
40
60
80
100
120
neutral axis depth, mm

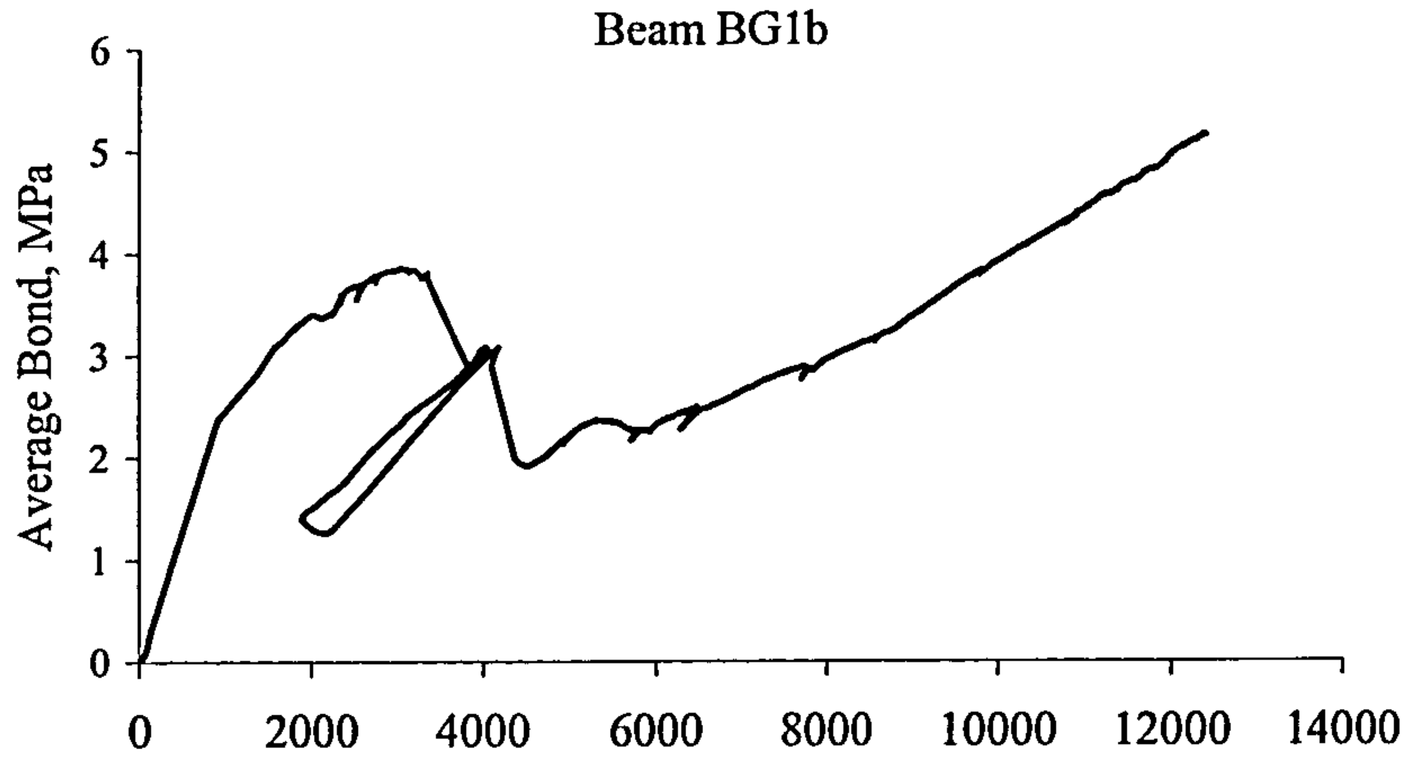
Beam BG1b
Average Bond, MPa
0
1
2
3
4
5
6
0
2000
4000
6000
8000
10000
12000
14000
Average Strain Between Cracks, microstrain

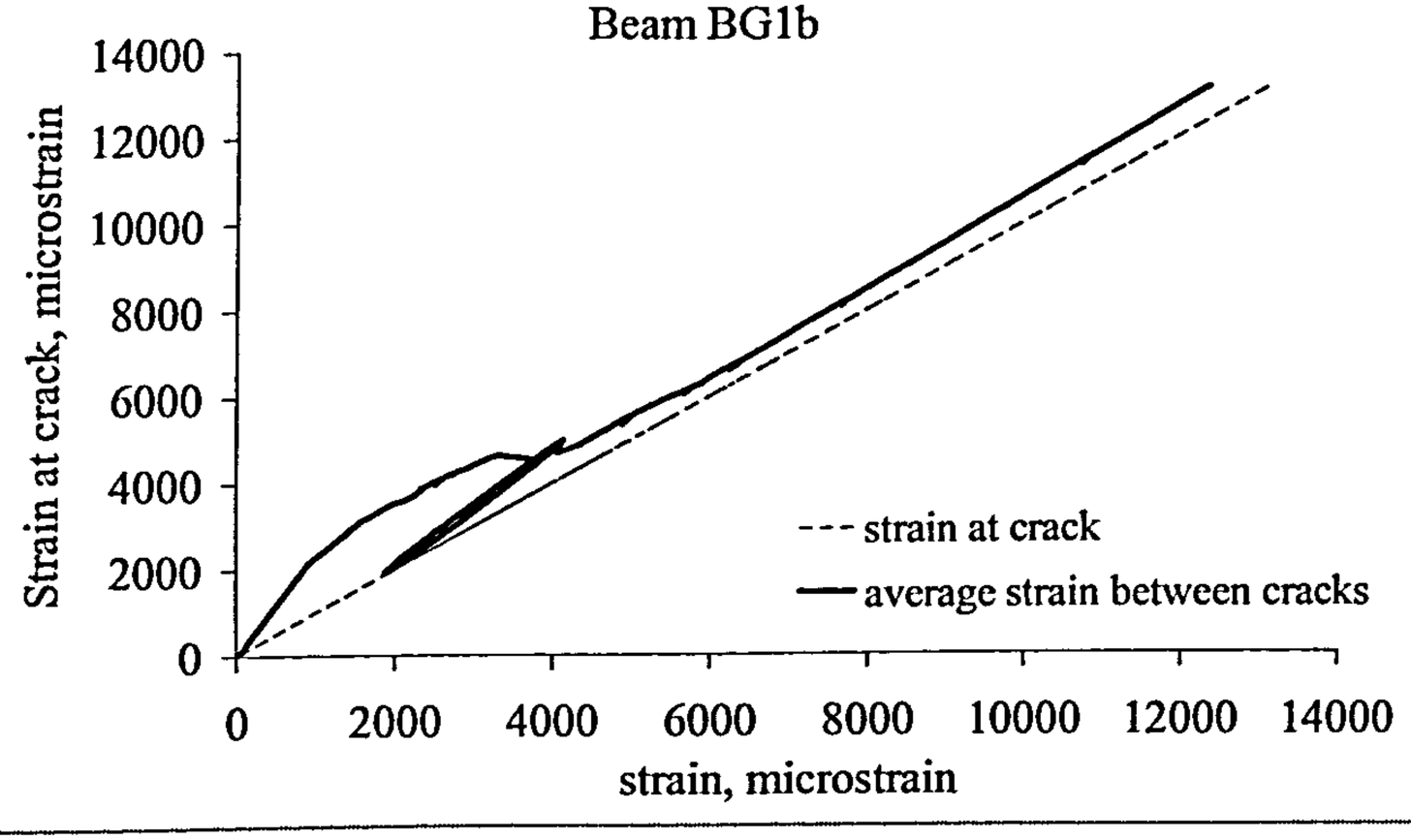
Beam BG1b
Strain at crack, microstrain
0
2000
4000
6000
8000
10000
12000
14000
strain at crack
average strain between cracks
0
2000
4000
6000
8000
10000
12000
14000
strain, microstrain

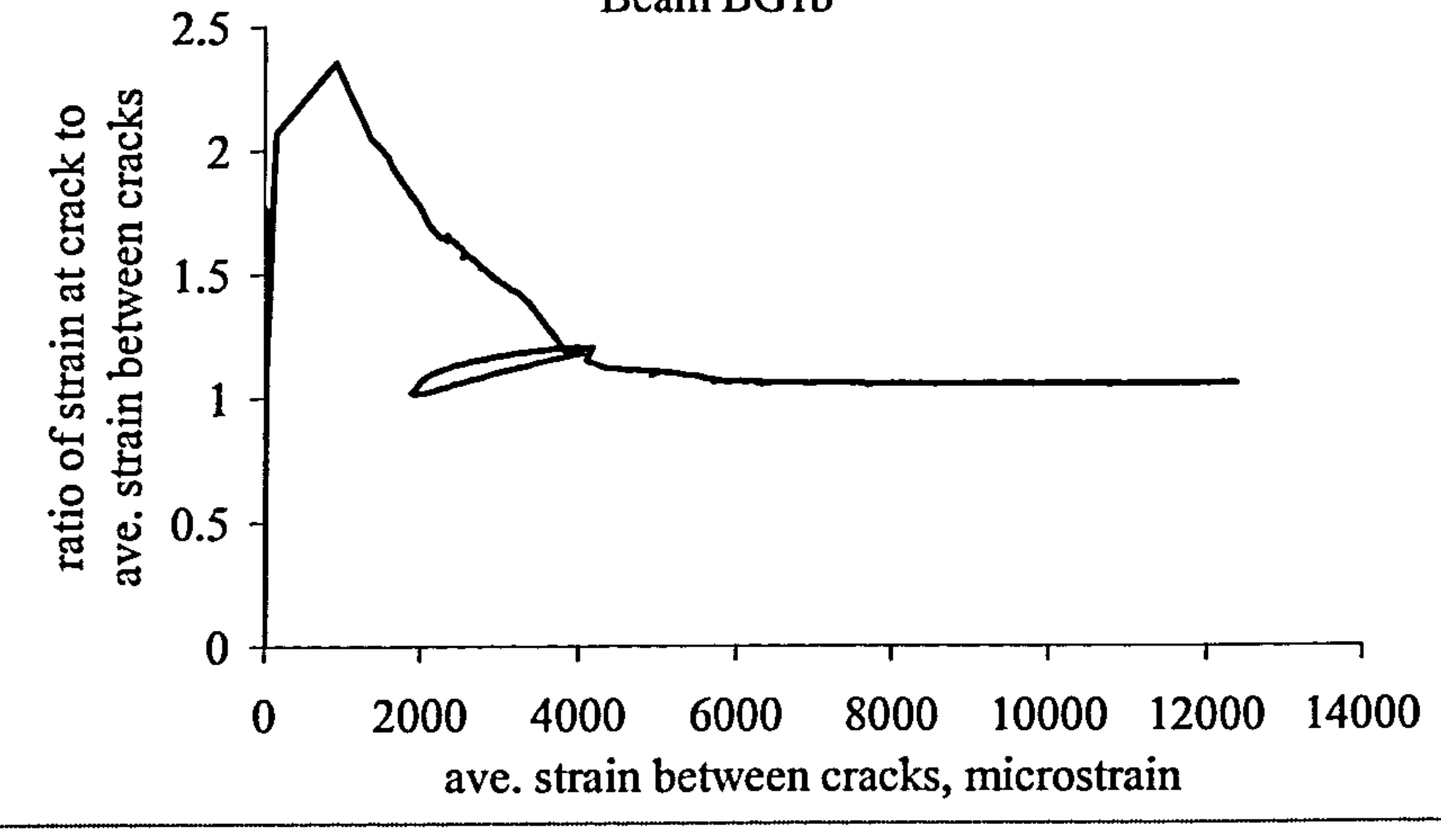
Beam BG1b
ratio of strain at crack to ave. strain between cracks
0
0.5
1
1.5
2
2.5
0
2000
4000
6000
8000
10000
12000
14000
ave. strain between cracks, microstrain

BEAM BG1b

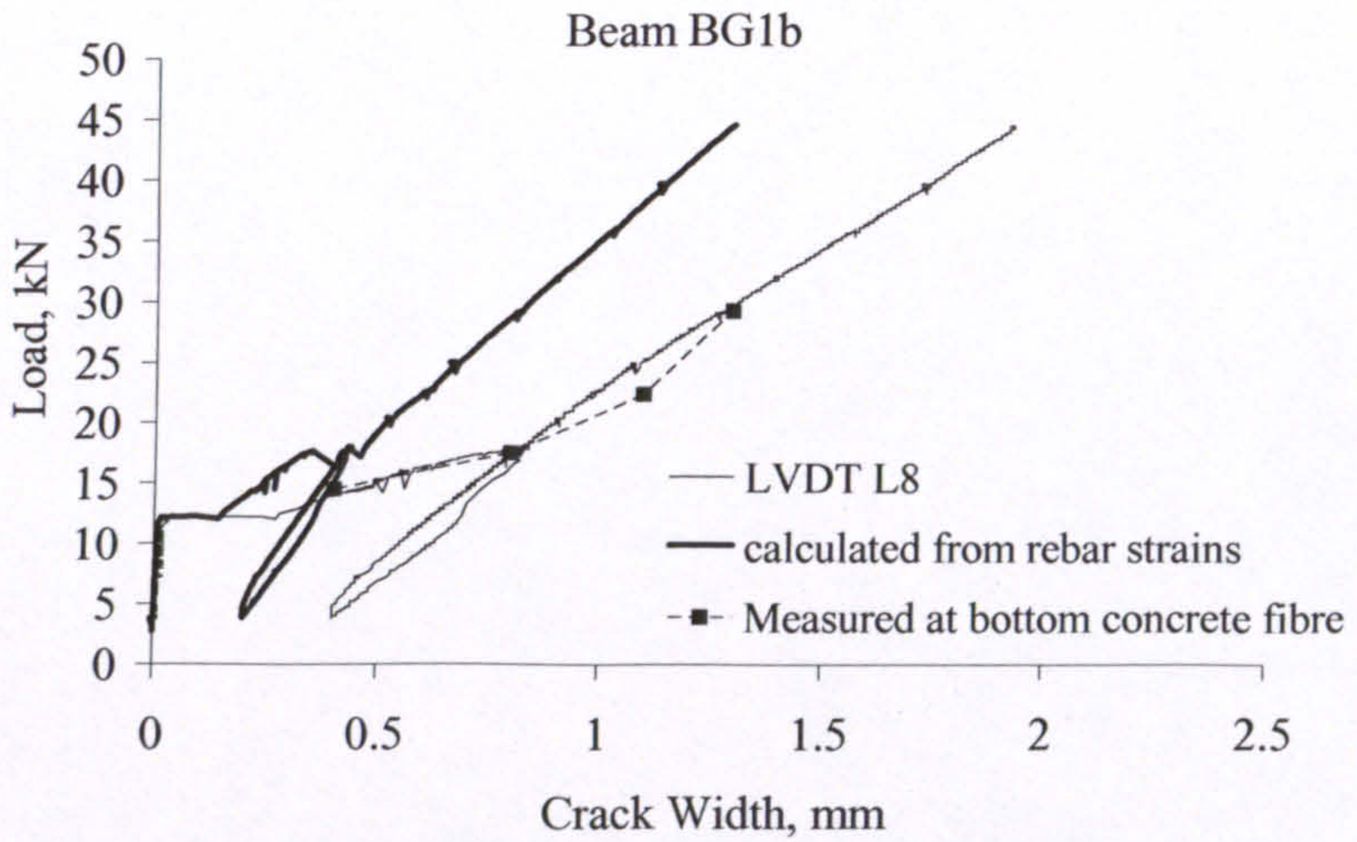

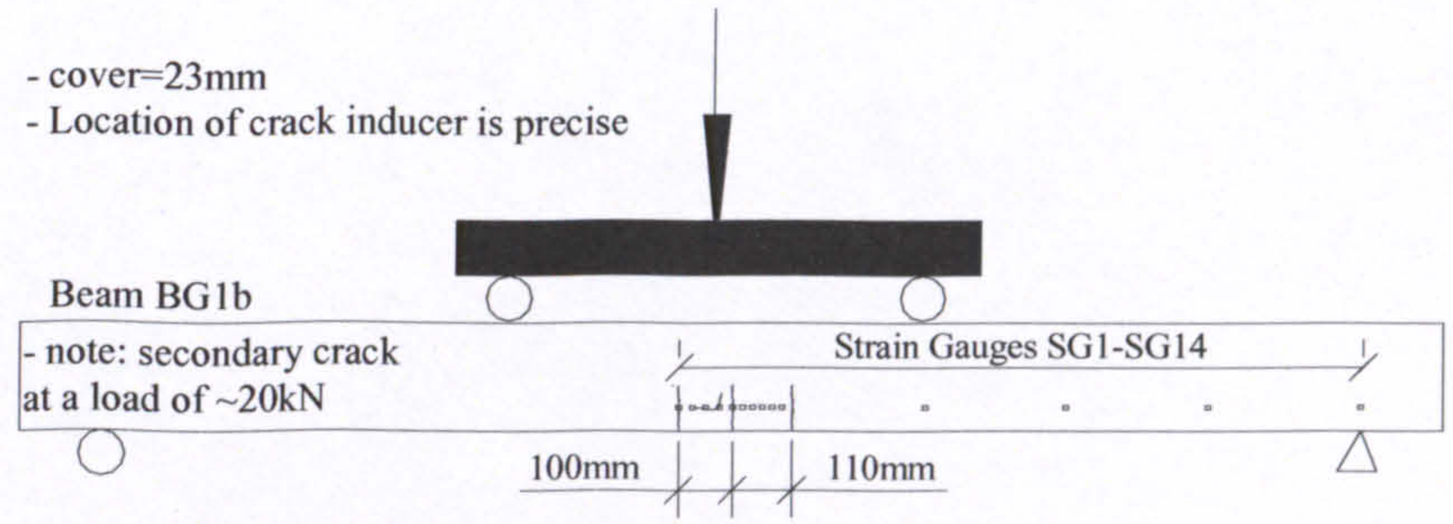

Cracks around Centre

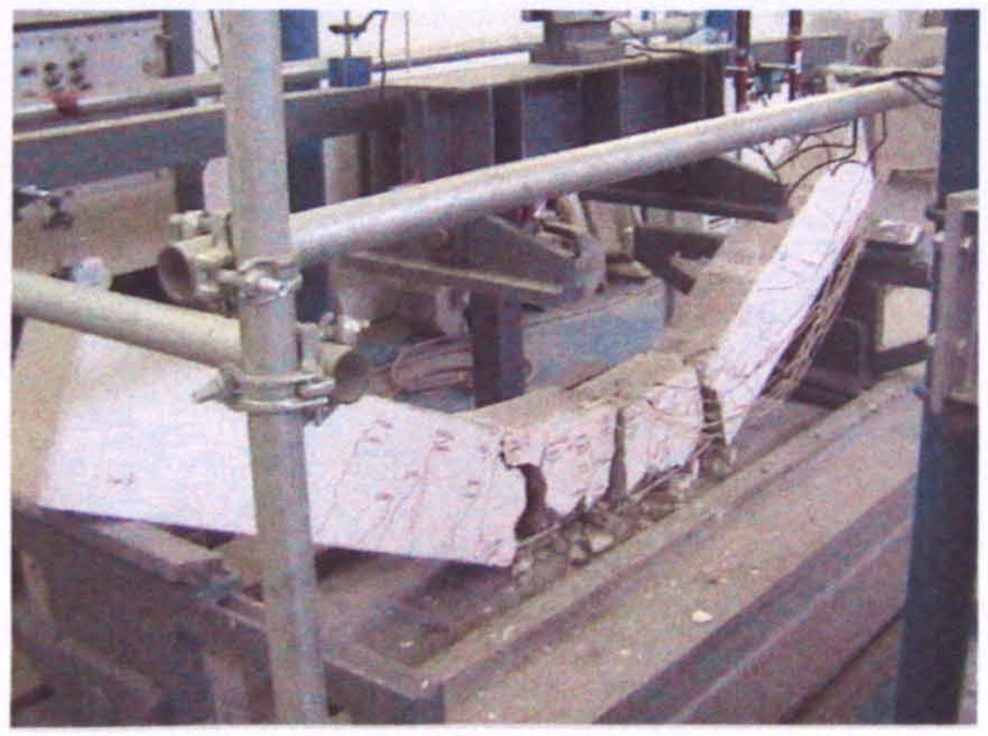

Failure by rupture of rebars

BEAM BG2a

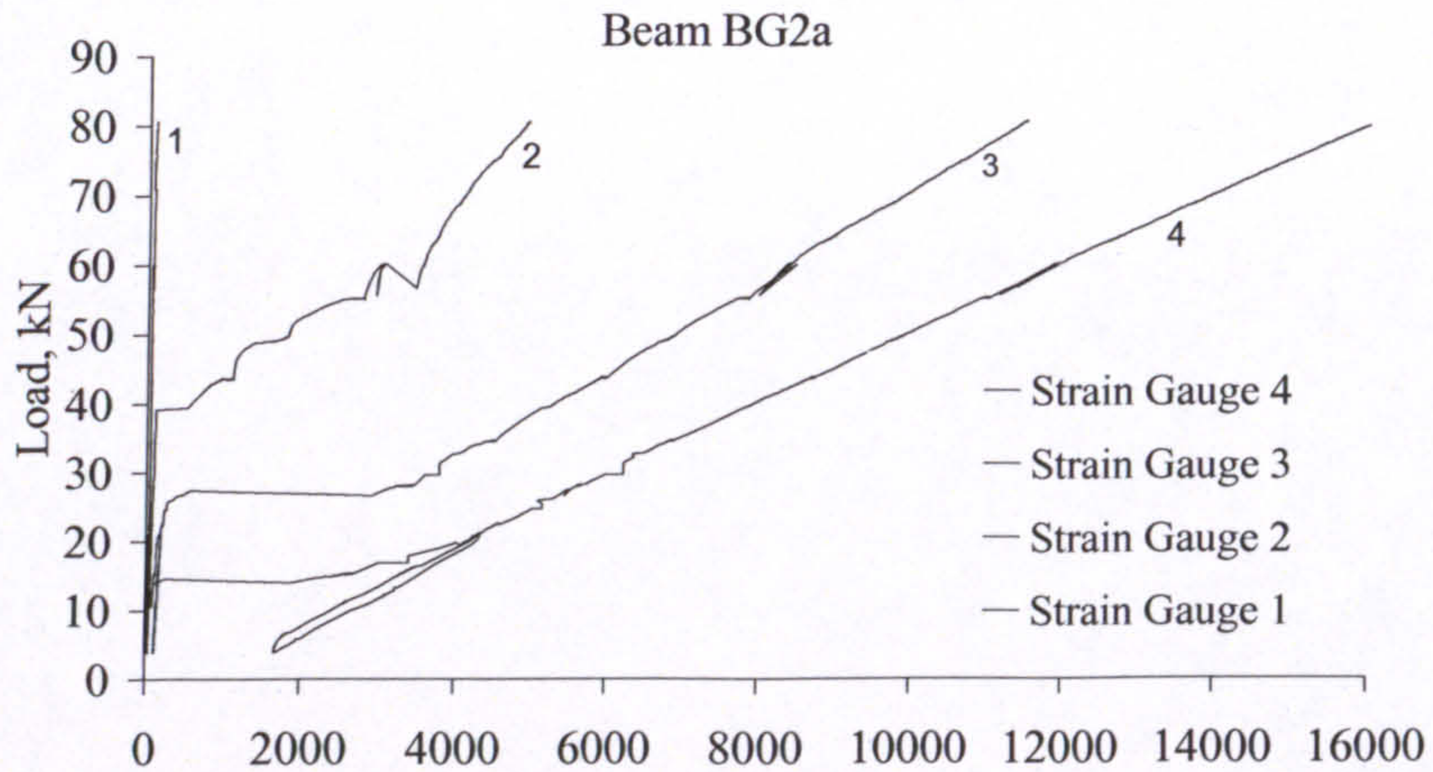
Beam BG2a
Load, kN
Rebar Strain, microstrain
1
2
3
4
Strain Gauge 4
Strain Gauge 3
Strain Gauge 2
Strain Gauge 1

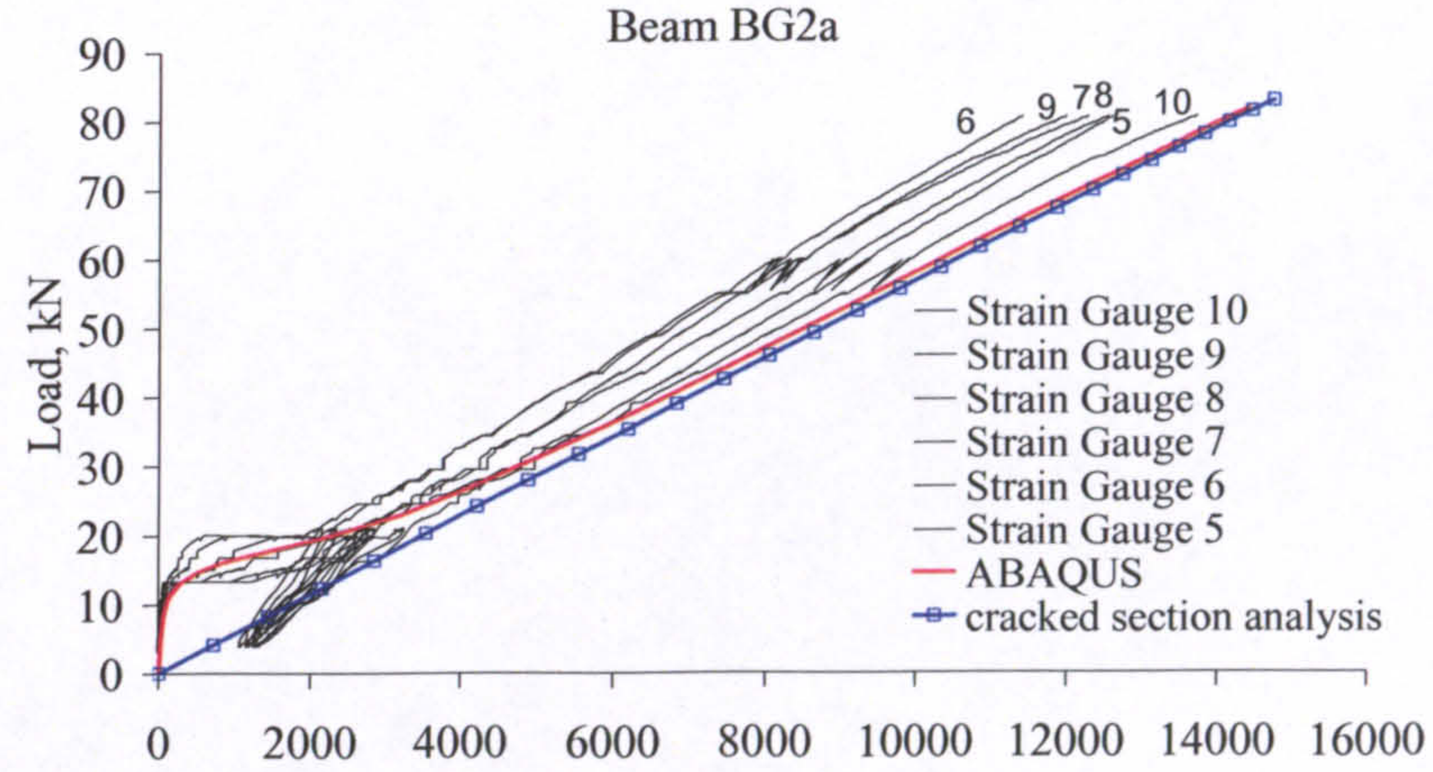
Beam BG2a
Load, kN
Rebar Strain, microstrain
6
9
7
8
5
10
Strain Gauge 10
Strain Gauge 9
Strain Gauge 8
Strain Gauge 7
Strain Gauge 6
Strain Gauge 5
ABAQUS
cracked section analysis

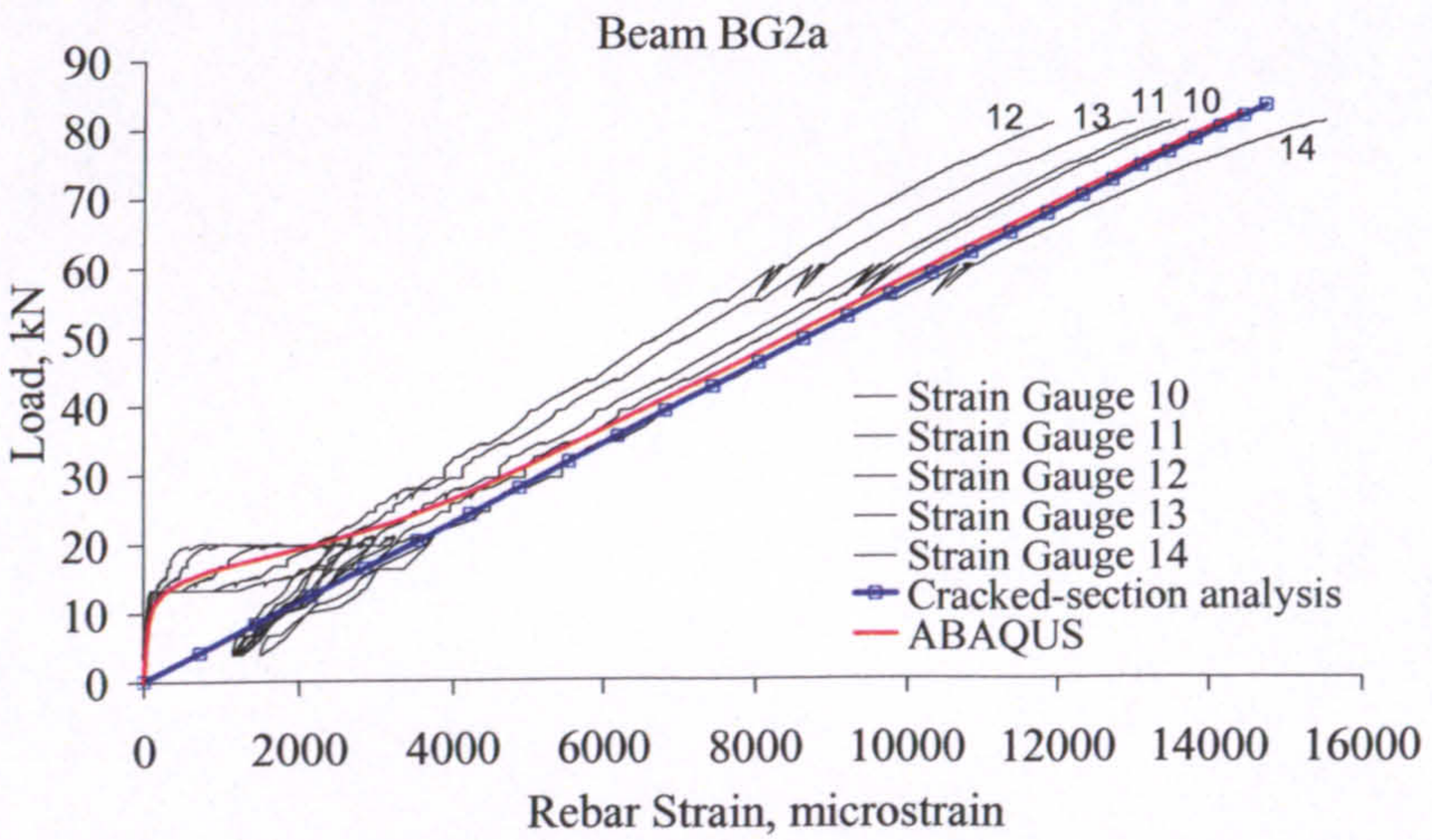
Beam BG2a
Load, kN
Rebar Strain, microstrain
12
13
11
10
14
Strain Gauge 10
Strain Gauge 11
Strain Gauge 12
Strain Gauge 13
Strain Gauge 14
Cracked-section analysis
ABAQUS

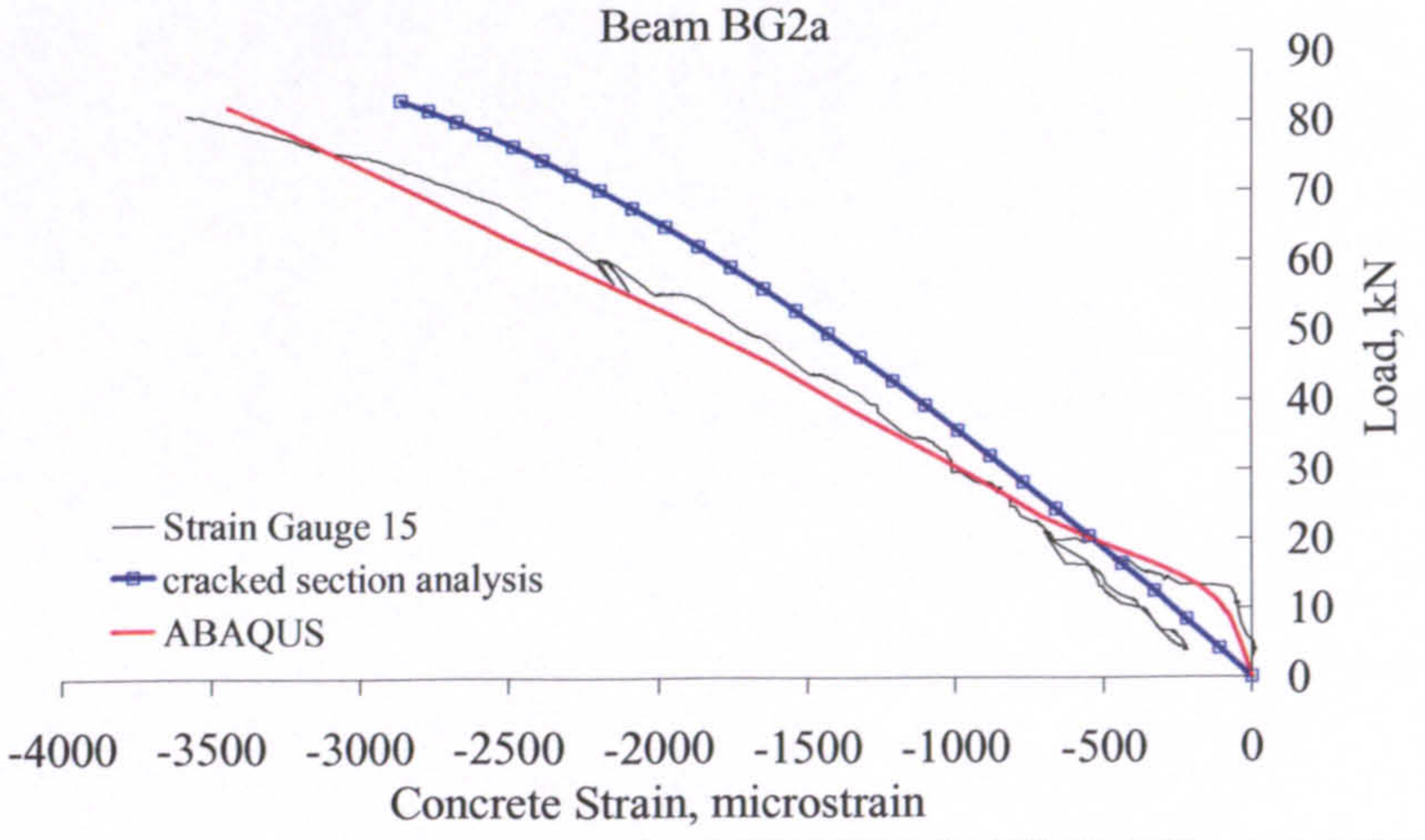
Beam BG2a
Load, kN
Concrete Strain, microstrain
Strain Gauge 15
cracked section analysis
ABAQUS

BEAM BG2a

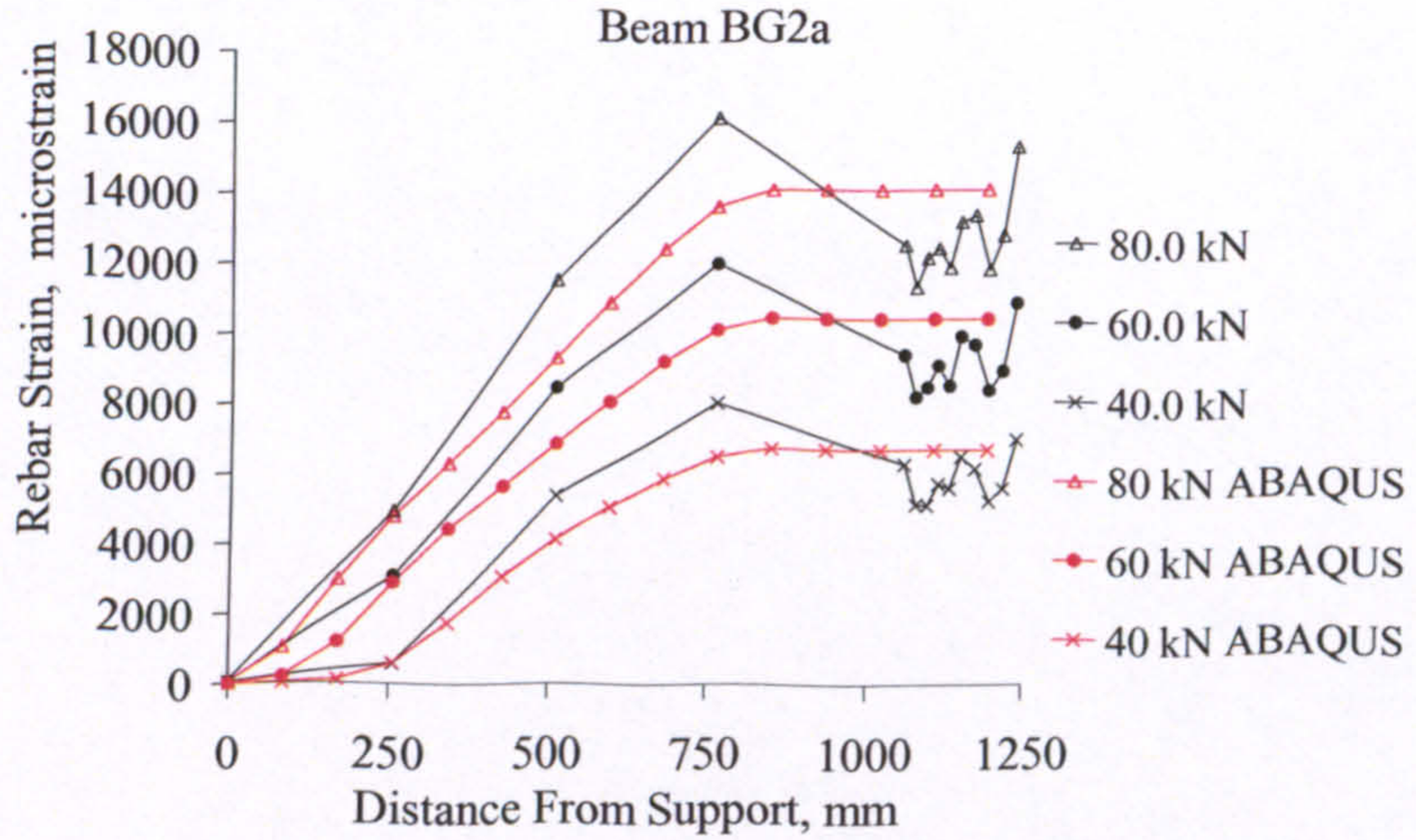
Beam BG2a
Rebar Strain, microstrain
18000
16000
14000
12000
10000
8000
6000
4000
2000
0
0
250
500
750
1000
1250
Distance From Support, mm
80.0 kN
60.0 kN
40.0 kN
80 kN ABAQUS
60 kN ABAQUS
40 kN ABAQUS

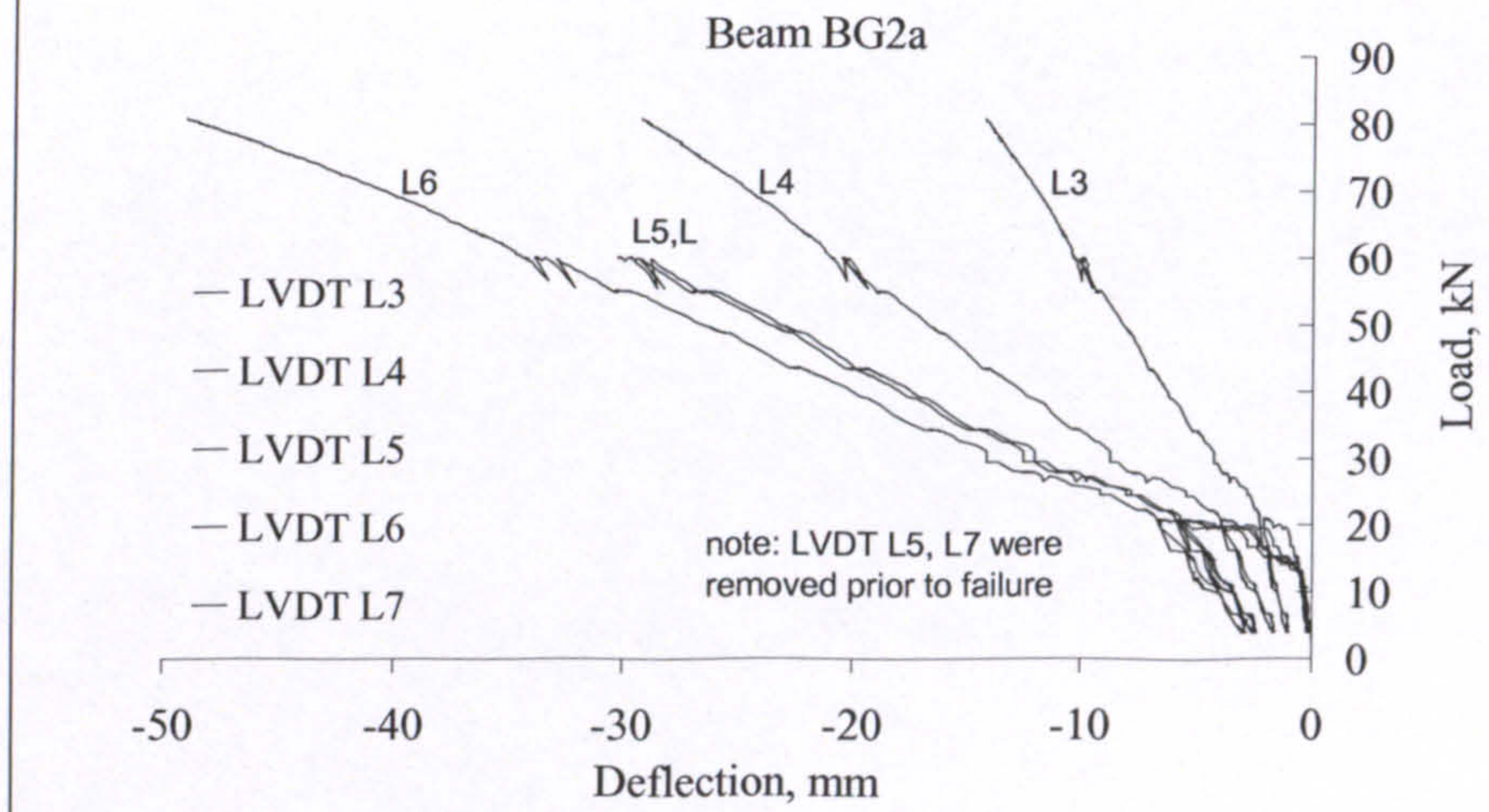
Beam BG2a
L6
L5,L
L4
L3
LVDT L3
LVDT L4
LVDT L5
LVDT L6
LVDT L7
note: LVDT L5, L7 were
removed prior to failure
90
80
70
60
50
40
30
20
10
0
Load, kN
-50
-40
-30
-20
-10
0
Deflection, mm

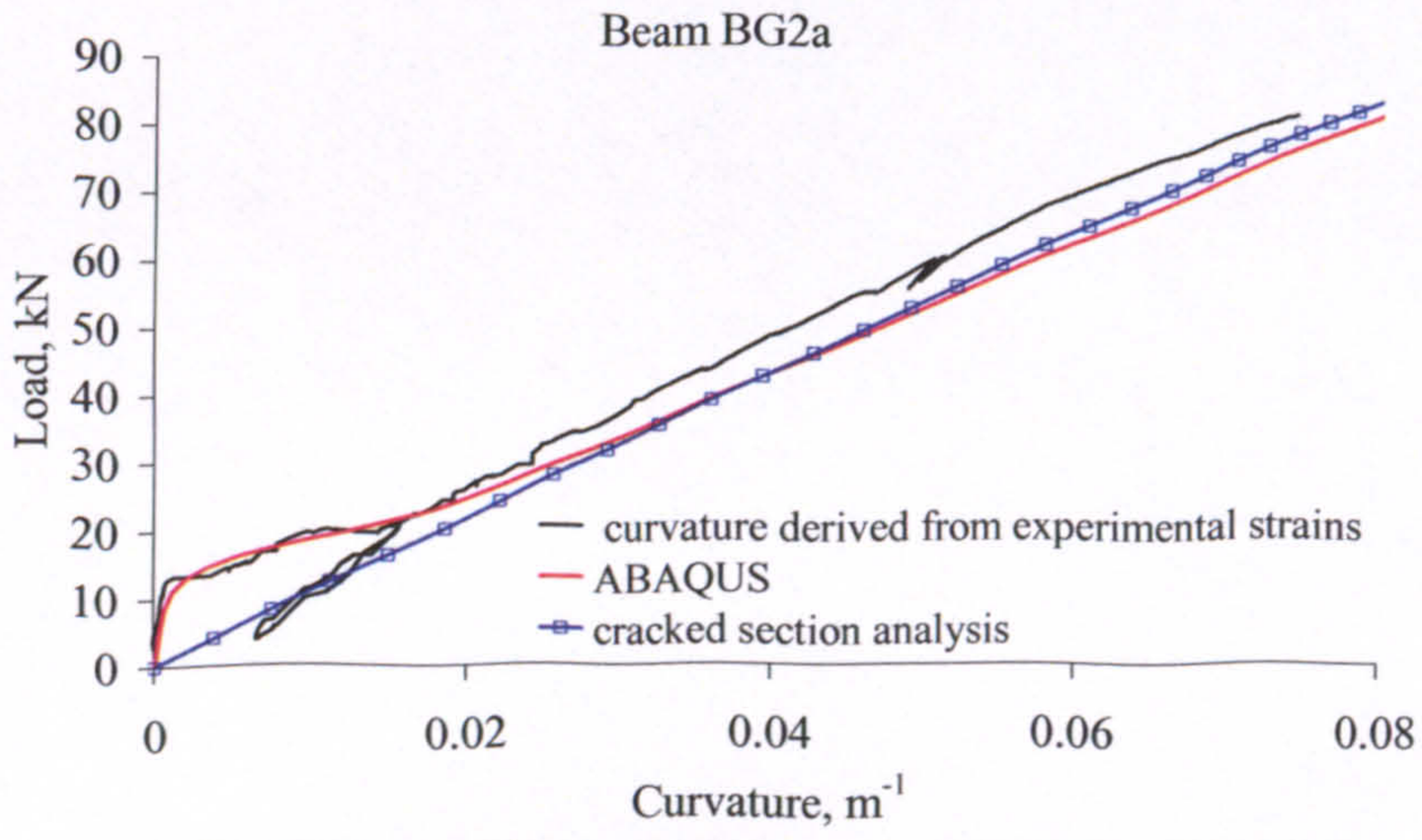
Beam BG2a
Load, kN
90
80
70
60
50
40
30
20
10
0
0
0.02
0.04
0.06
0.08
Curvature, m-1
curvature derived from experimental strains
ABAQUS
cracked section analysis

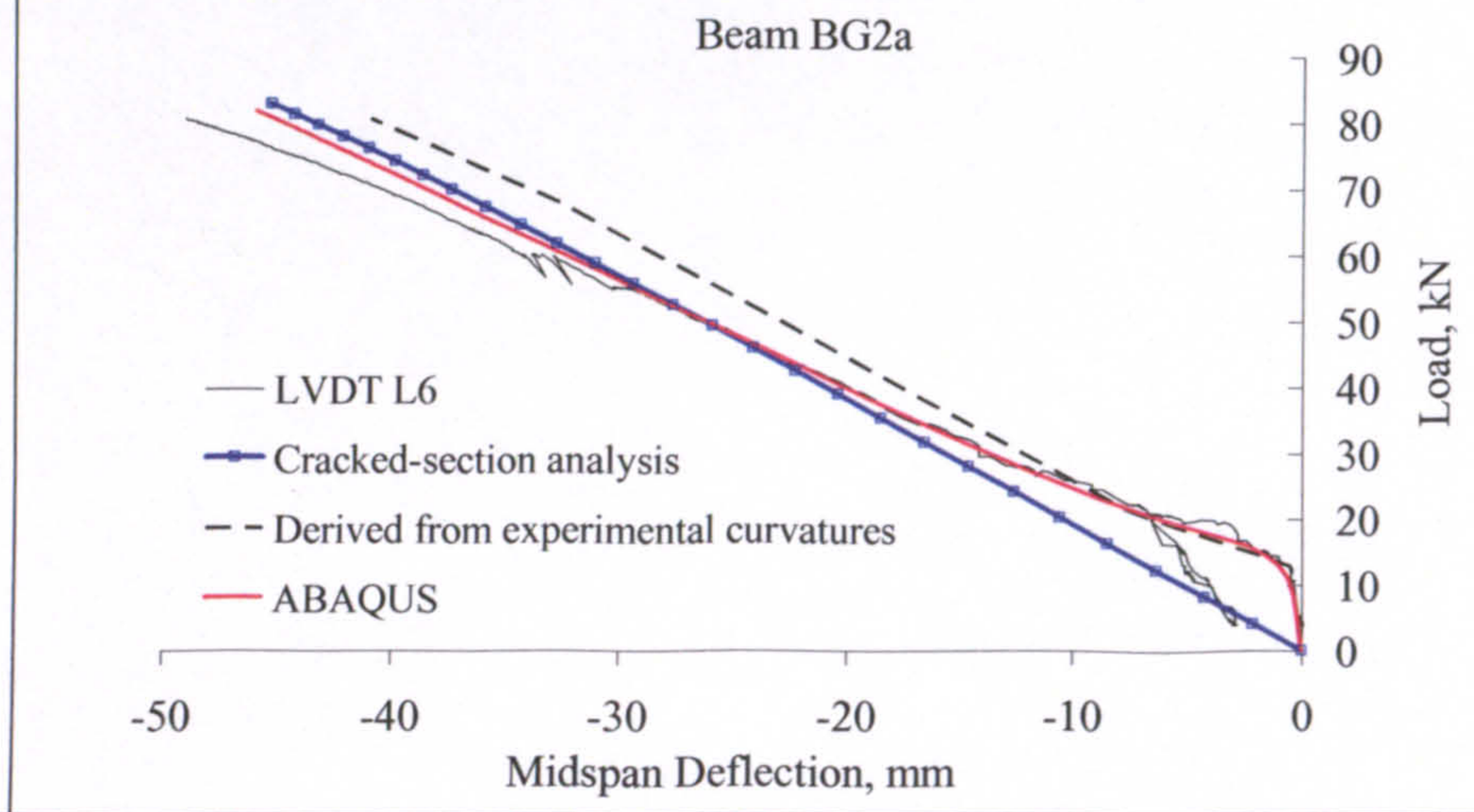
Beam BG2a
90
80
70
60
50
40
30
20
10
0
Load, kN
-50
-40
-30
-20
-10
0
Midspan Deflection, mm
LVDT L6
Cracked-section analysis
Derived from experimental curvatures
ABAQUS

BEAM BG2a

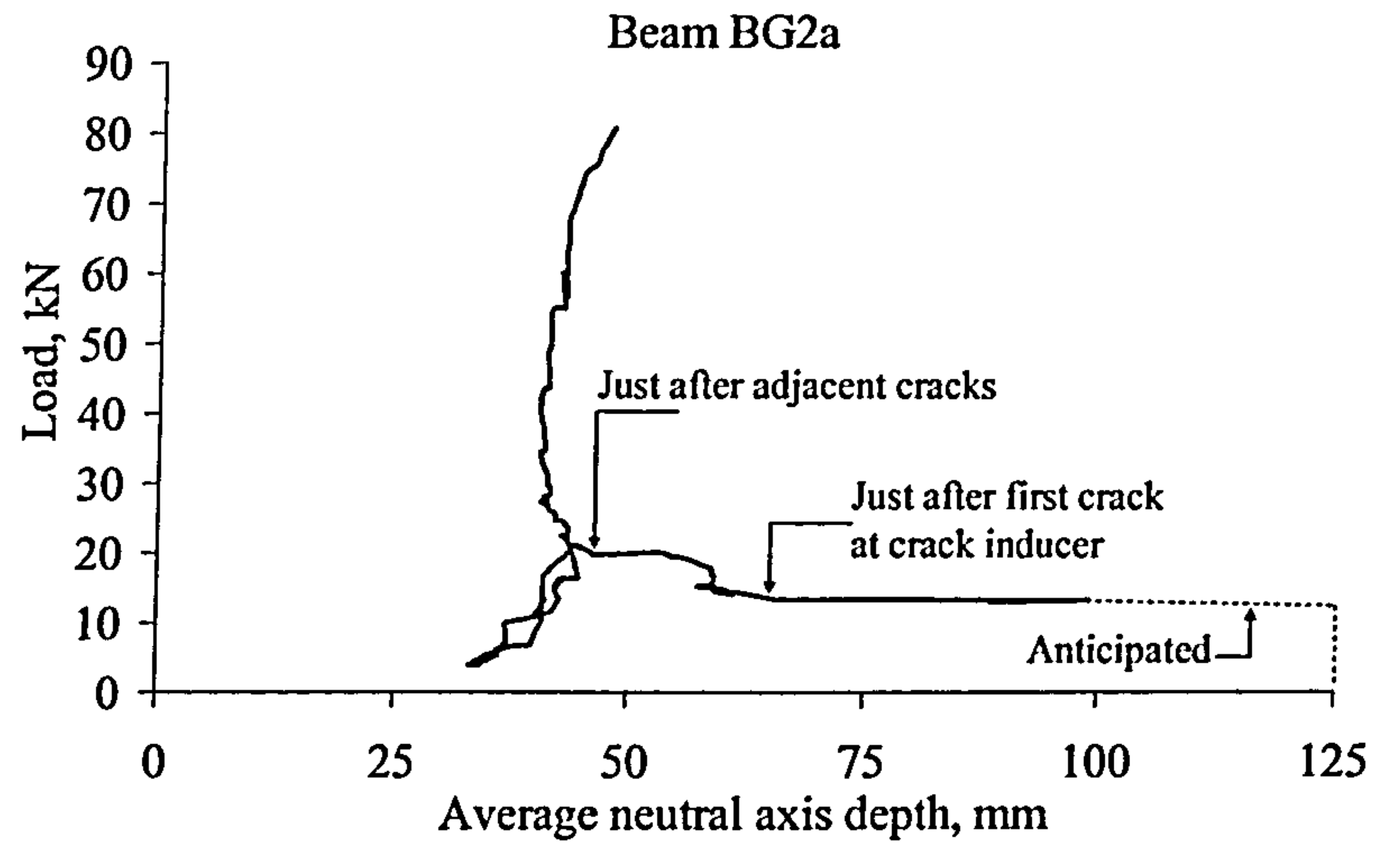
Beam BG2a
Load, kN
Average neutral axis depth, mm
Just after adjacent cracks
Just after first crack
at crack inducer
Anticipated
0
10
20
30
40
50
60
70
80
90
0
25
50
75
100
125

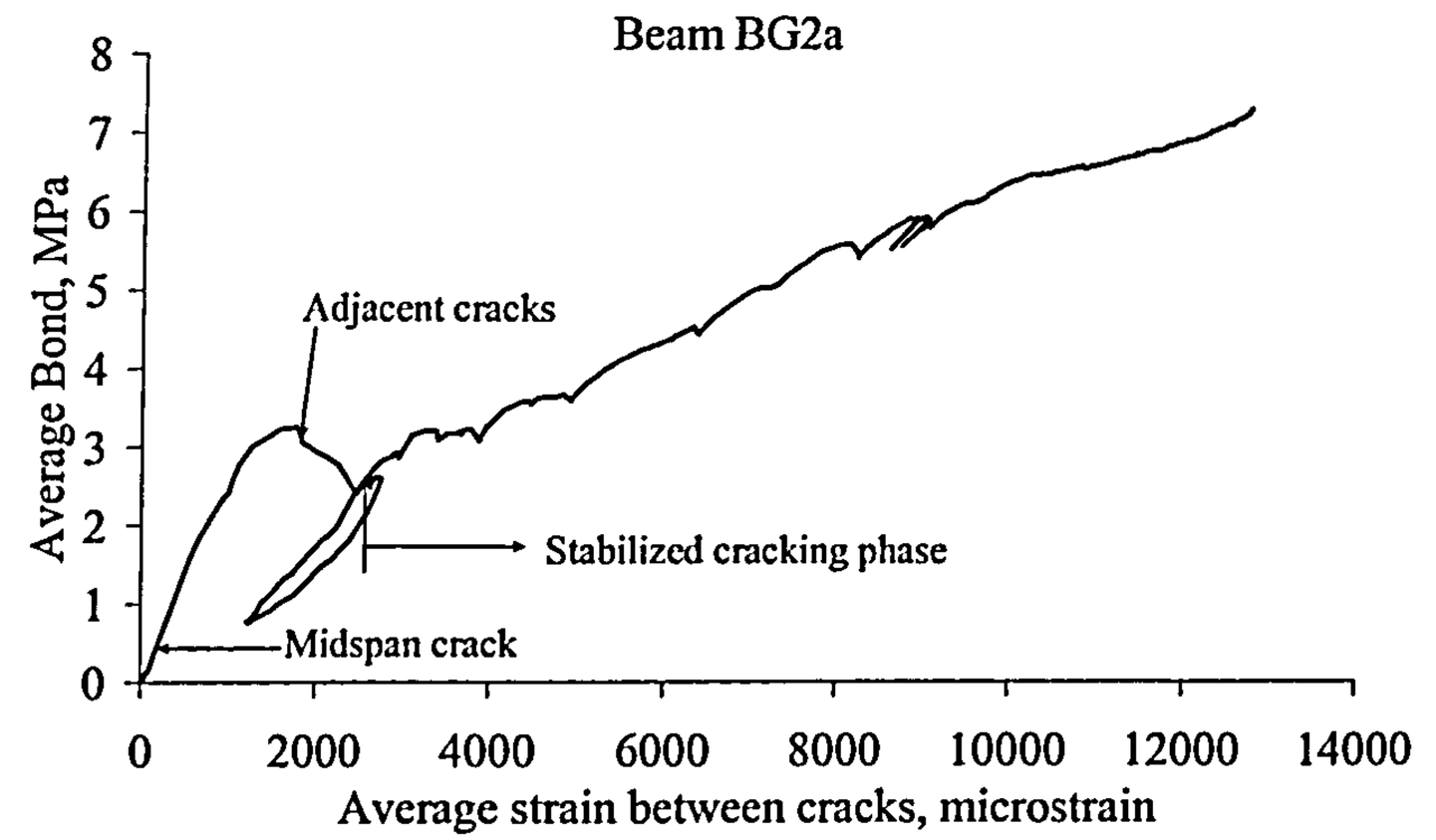
Beam BG2a
Average Bond, MPa
Average strain between cracks, microstrain
Adjacent cracks
Stabilized cracking phase
Midspan crack
0
1
2
3
4
5
6
7
8
0
2000
4000
6000
8000
10000
12000
14000

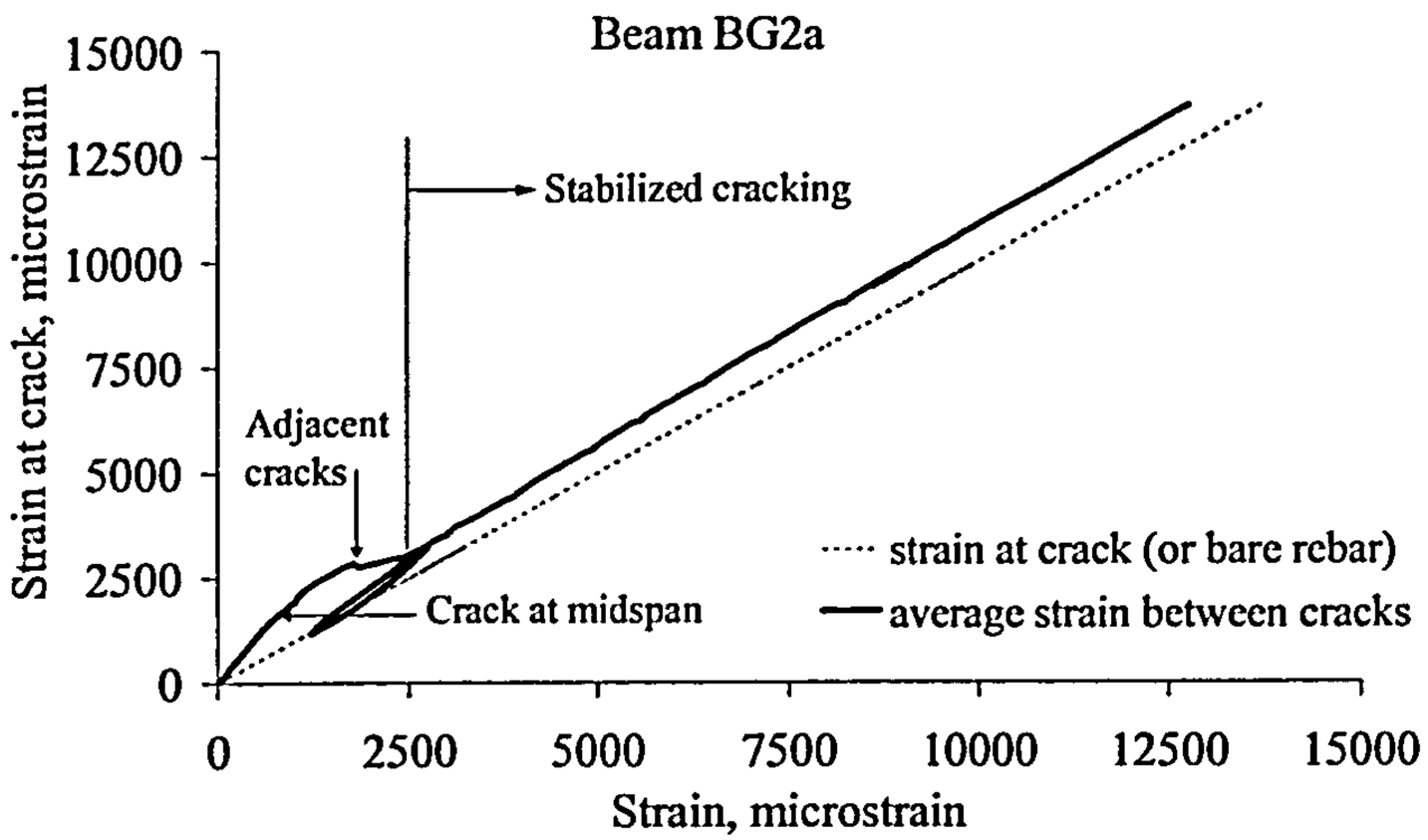
Beam BG2a
Strain at crack, microstrain
Strain, microstrain
Stabilized cracking
Adjacent
cracks
Crack at midspan
strain at crack (or bare rebar)
average strain between cracks
0
2500
5000
7500
10000
12500
15000
0
2500
5000
7500
10000
12500
15000

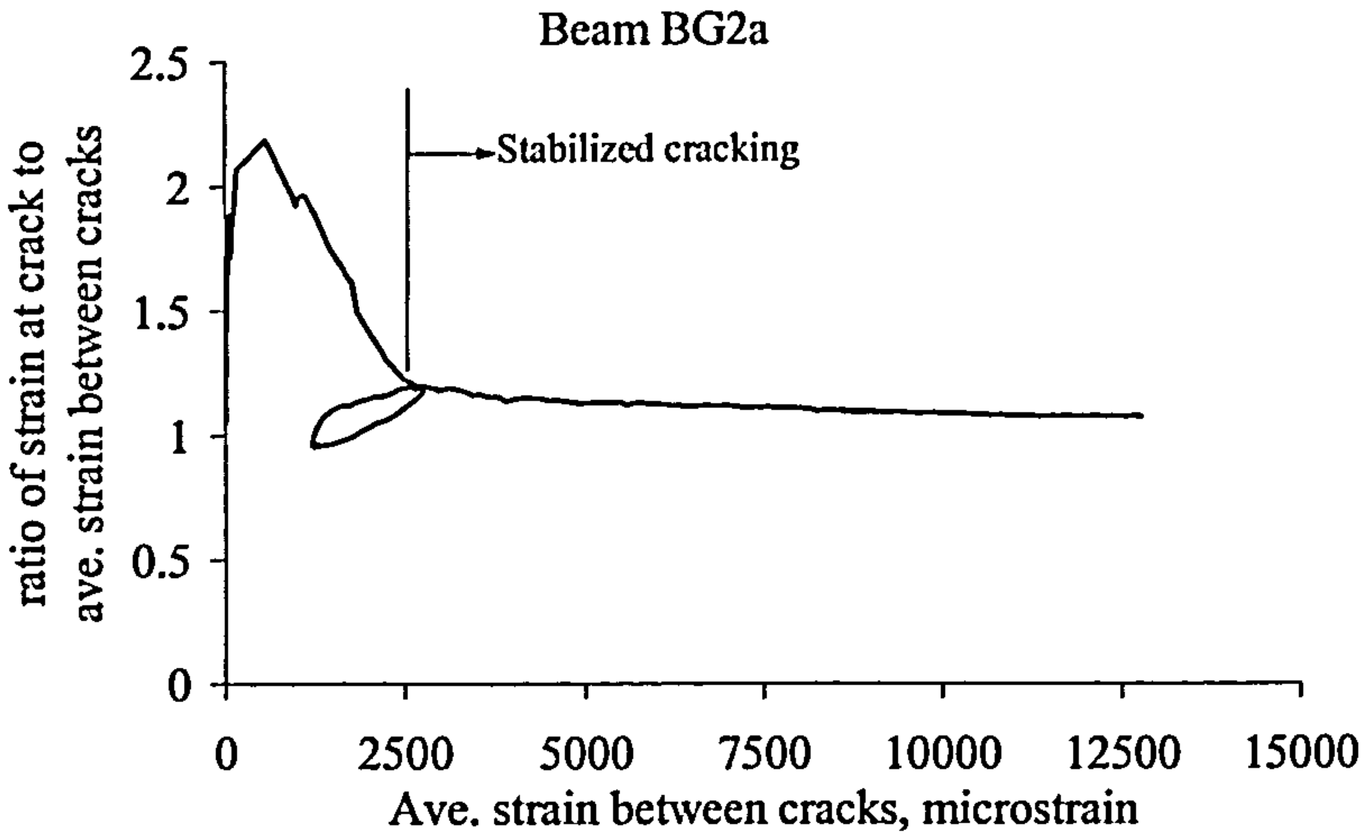
Beam BG2a
ratio of strain at crack to
ave. strain between cracks
Ave. strain between cracks, microstrain
Stabilized cracking
0
0.5
1
1.5
2
2.5
0
2500
5000
7500
10000
12500
15000

BEAM BG2a

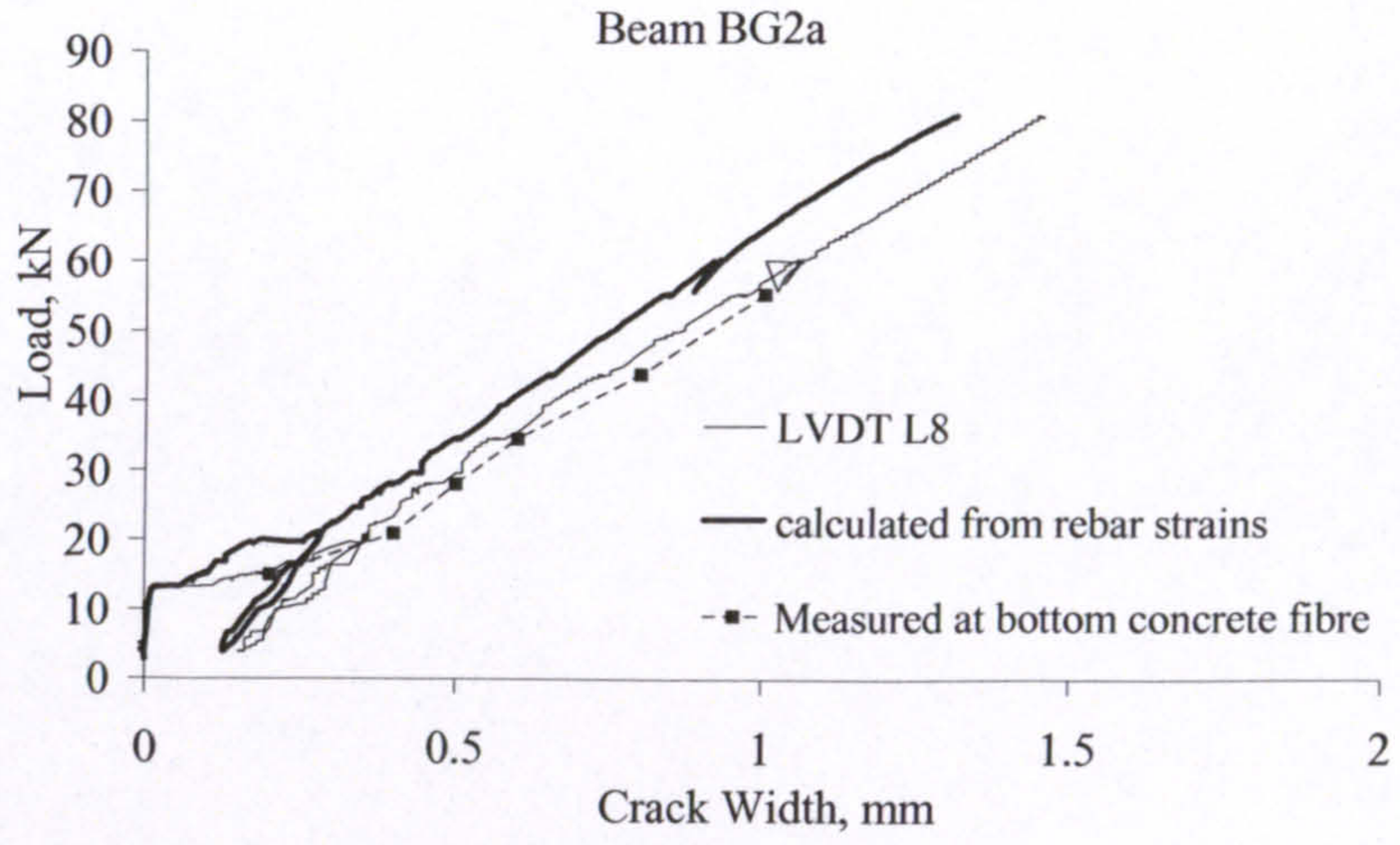

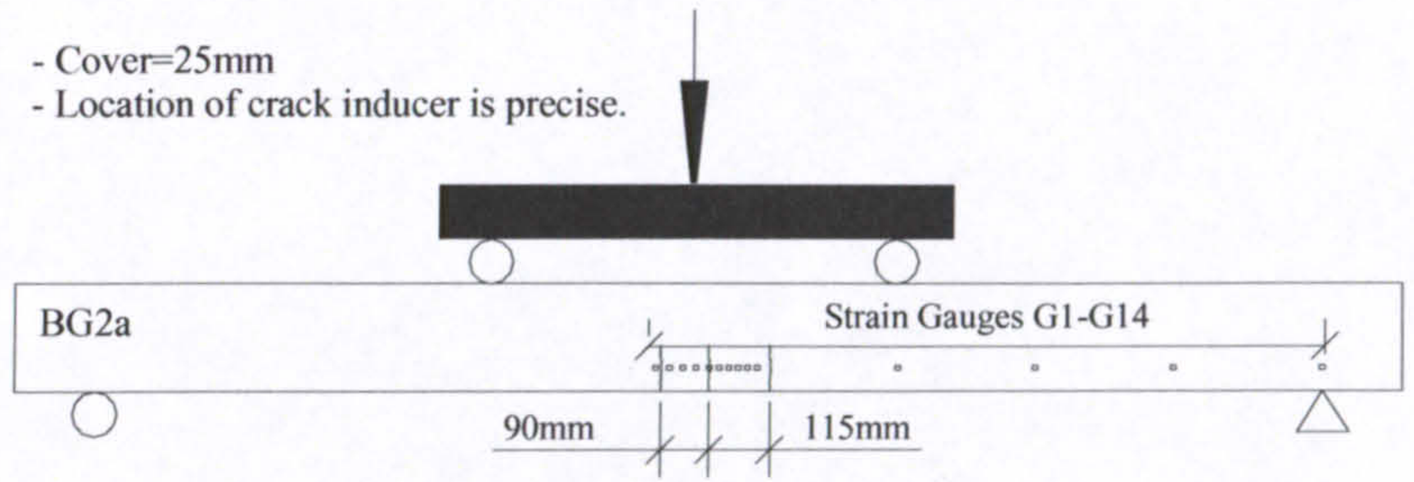

Cracks around Centre

Almost balanced failure

Rupture of rebars subsequent to concrete crushing

BEAM BG2b

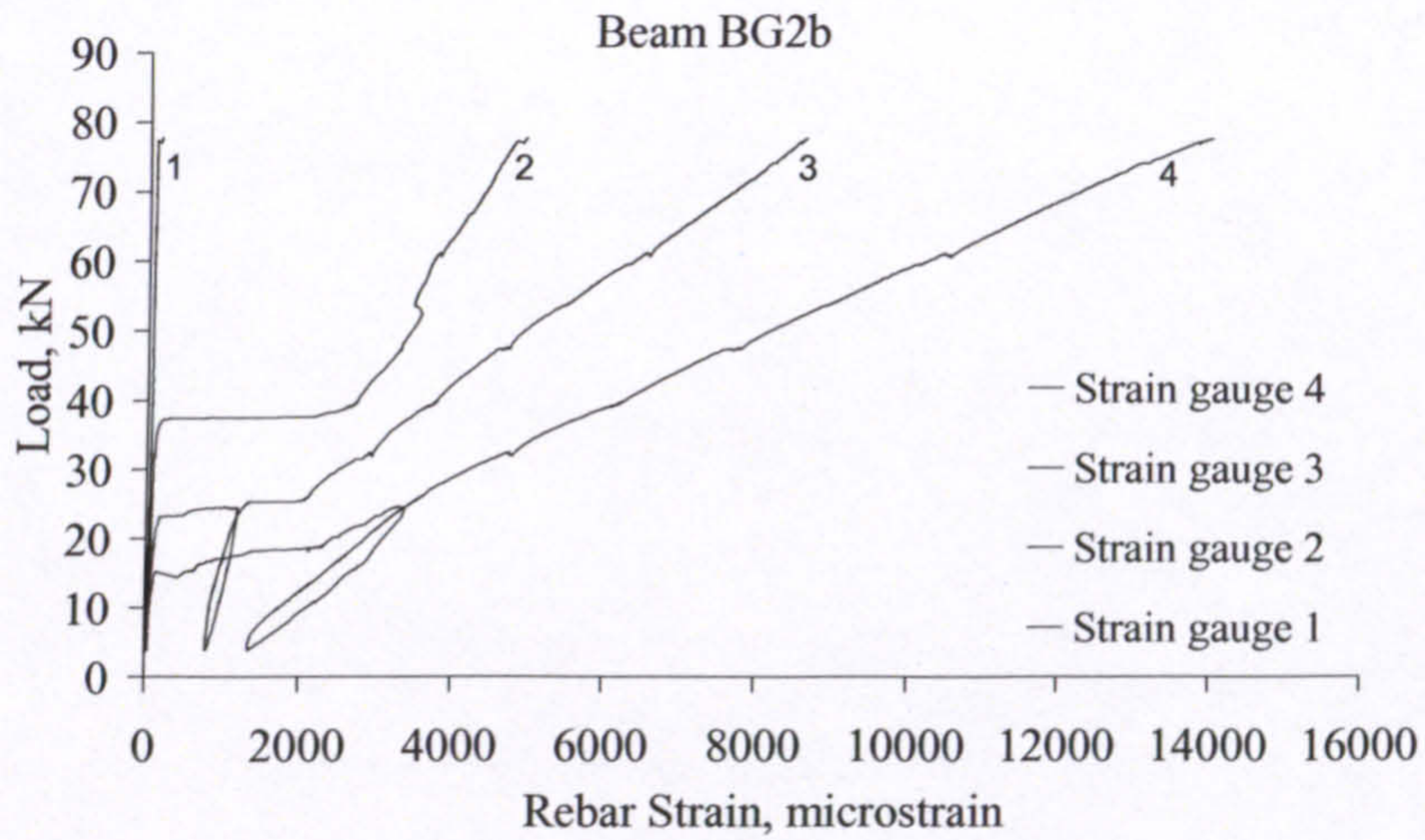
Beam BG2b
Load, kN
Rebar Strain, microstrain
1
2
3
4
Strain gauge 4
Strain gauge 3
Strain gauge 2
Strain gauge 1

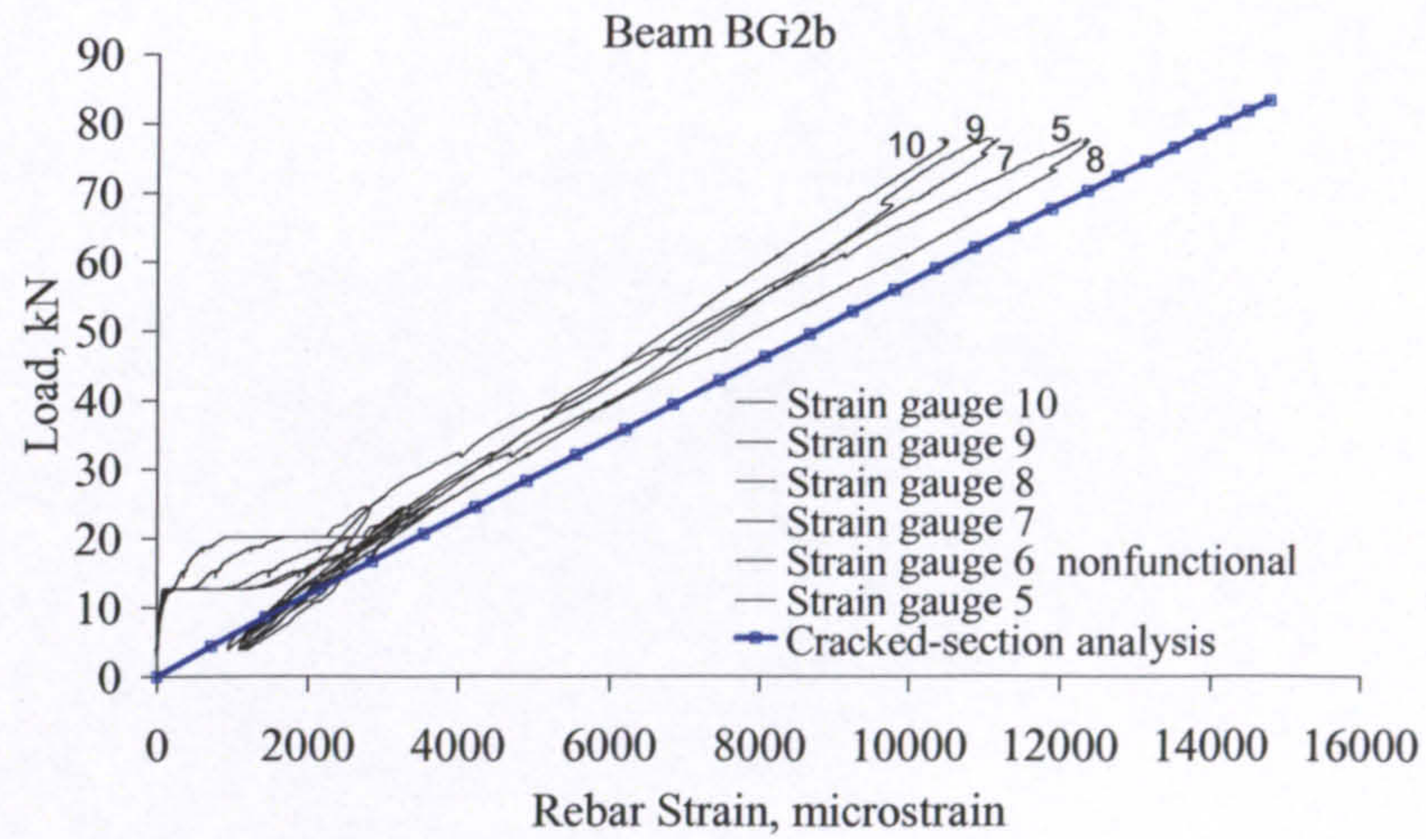
Beam BG2b
Load, kN
Rebar Strain, microstrain
10
9
7
5
8
Strain gauge 10
Strain gauge 9
Strain gauge 8
Strain gauge 7
Strain gauge 6 nonfunctional
Strain gauge 5
Cracked-section analysis

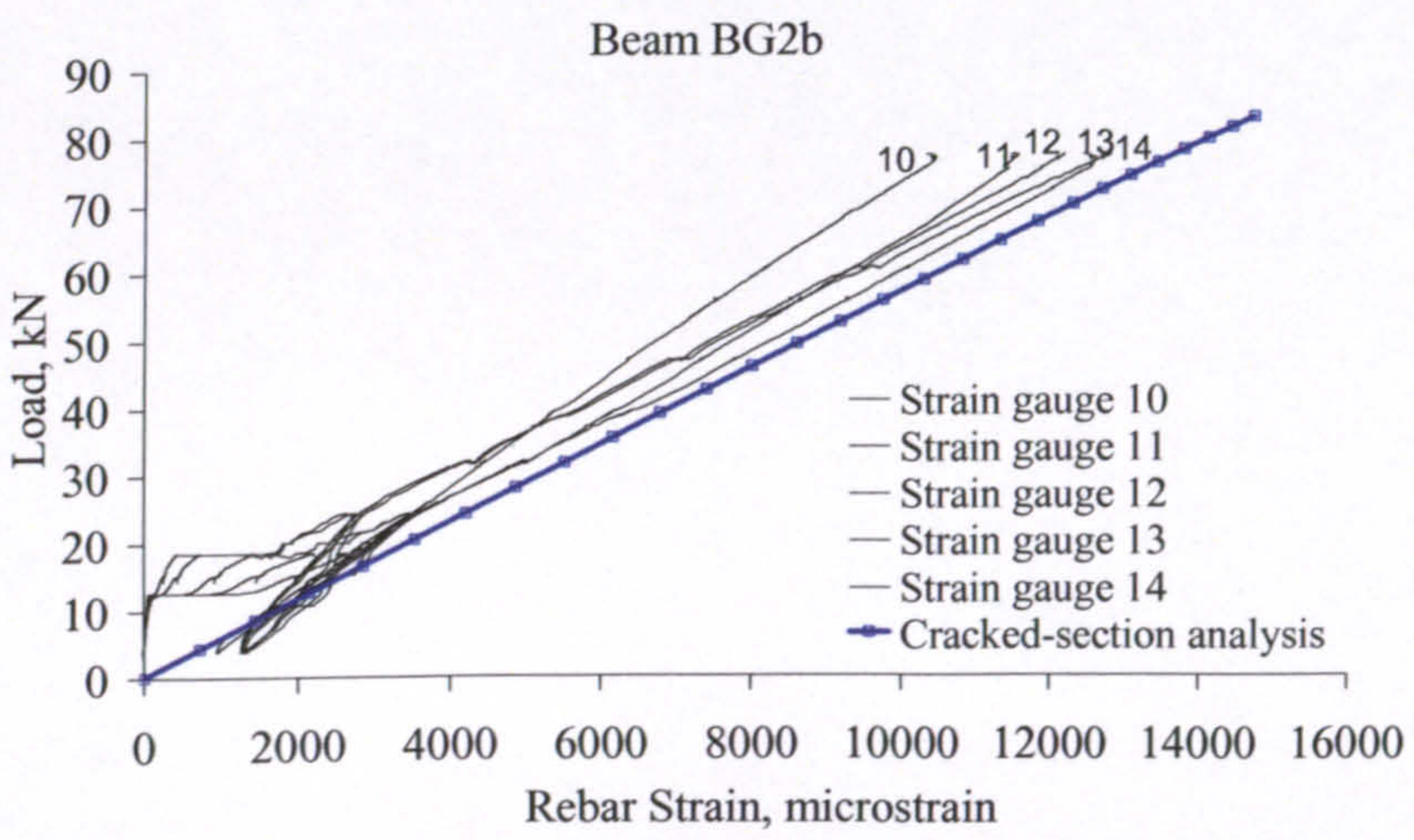
Beam BG2b
Load, kN
Rebar Strain, microstrain
10
11
12
13
14
Strain gauge 10
Strain gauge 11
Strain gauge 12
Strain gauge 13
Strain gauge 14
Cracked-section analysis

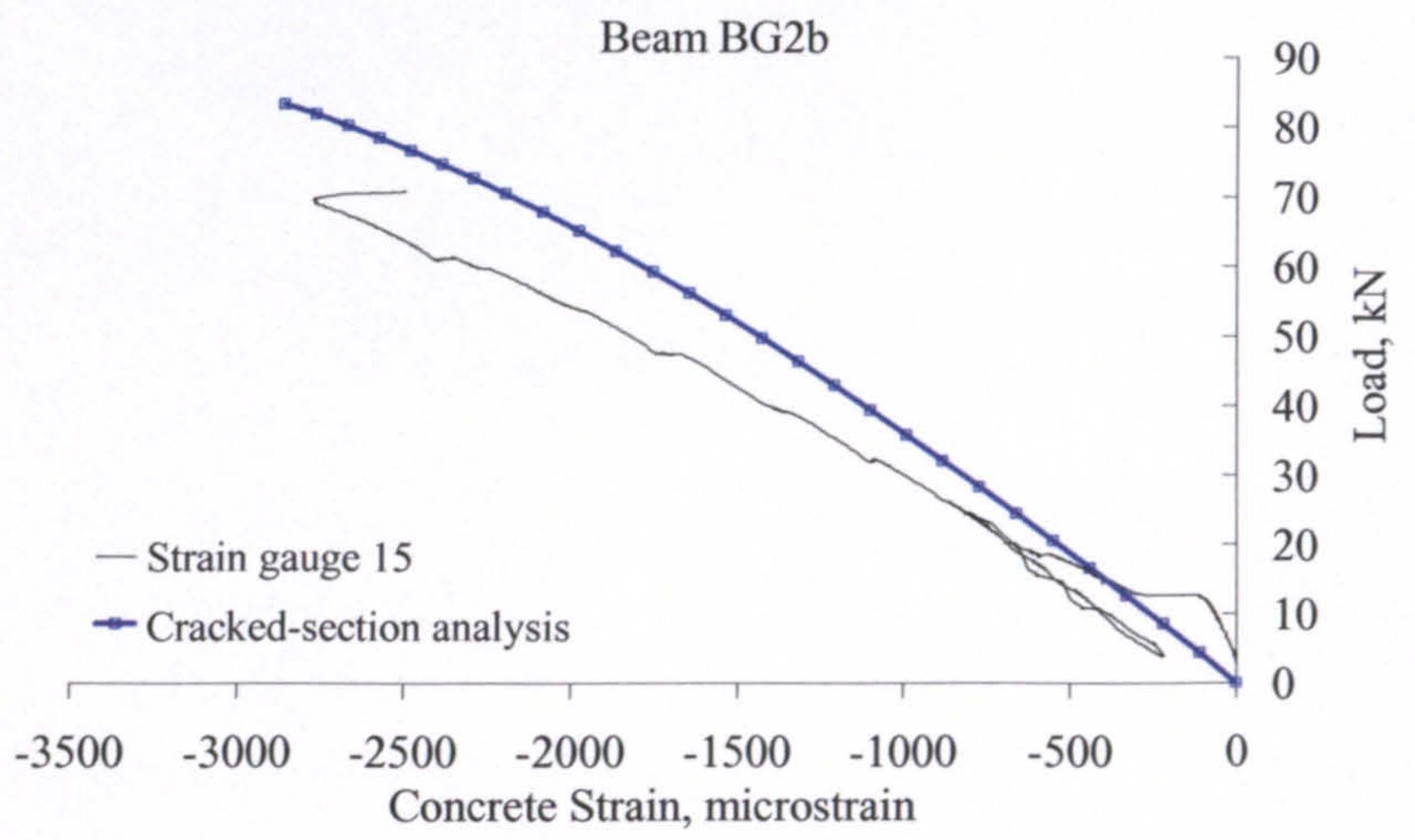
Beam BG2b
Load, kN
Concrete Strain, microstrain
Strain gauge 15
Cracked-section analysis

BEAM BG2b

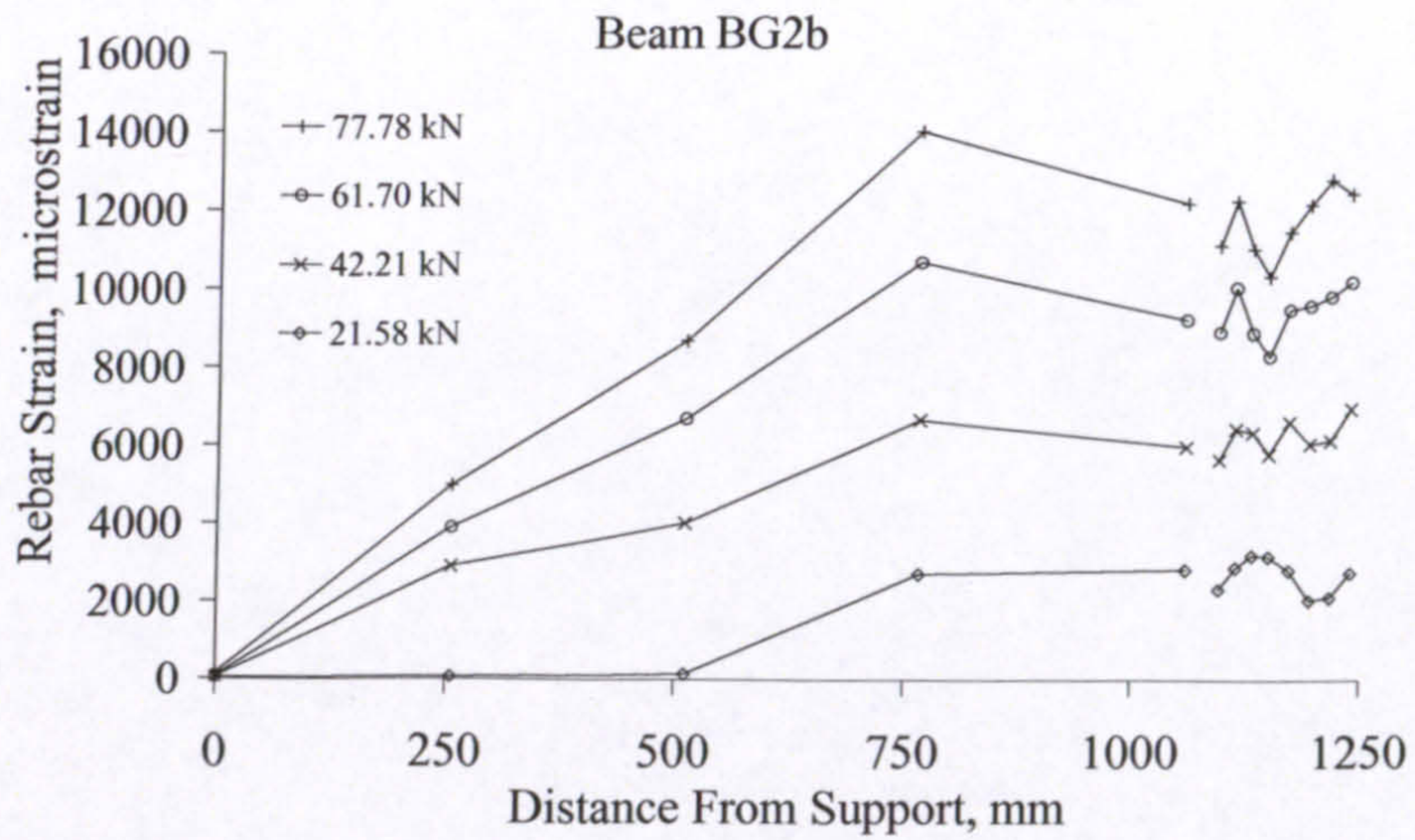
Beam BG2b
Rebar Strain, microstrain
16000
14000
12000
10000
8000
6000
4000
2000
0
77.78 kN
61.70 kN
42.21 kN
21.58 kN
0
250
500
750
1000
1250
Distance From Support, mm

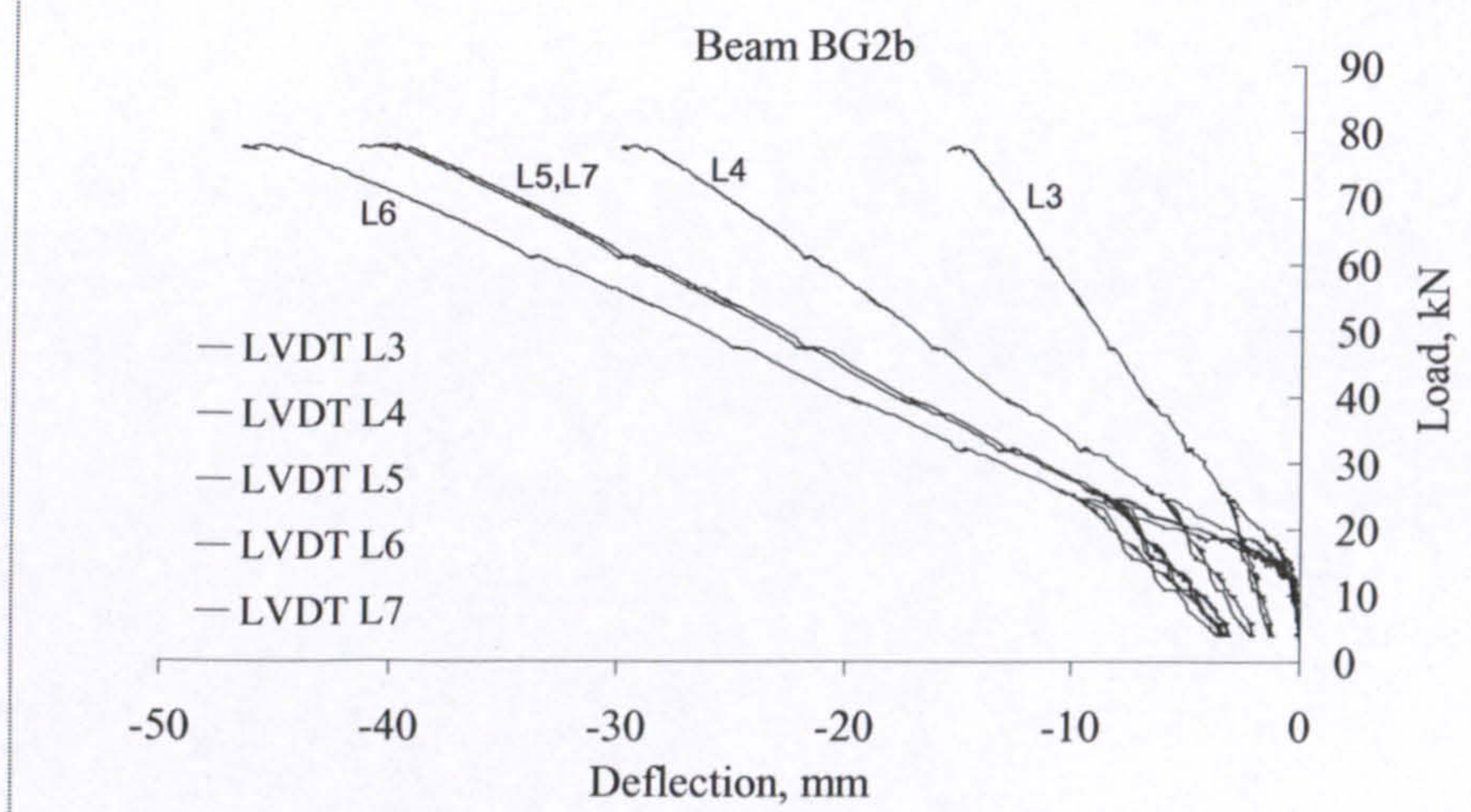
Beam BG2b
L6
L5,L7
L4
L3
LVDT L3
LVDT L4
LVDT L5
LVDT L6
LVDT L7
90
80
70
60
50
40
30
20
10
0
Load, kN
-50
-40
-30
-20
-10
0
Deflection, mm

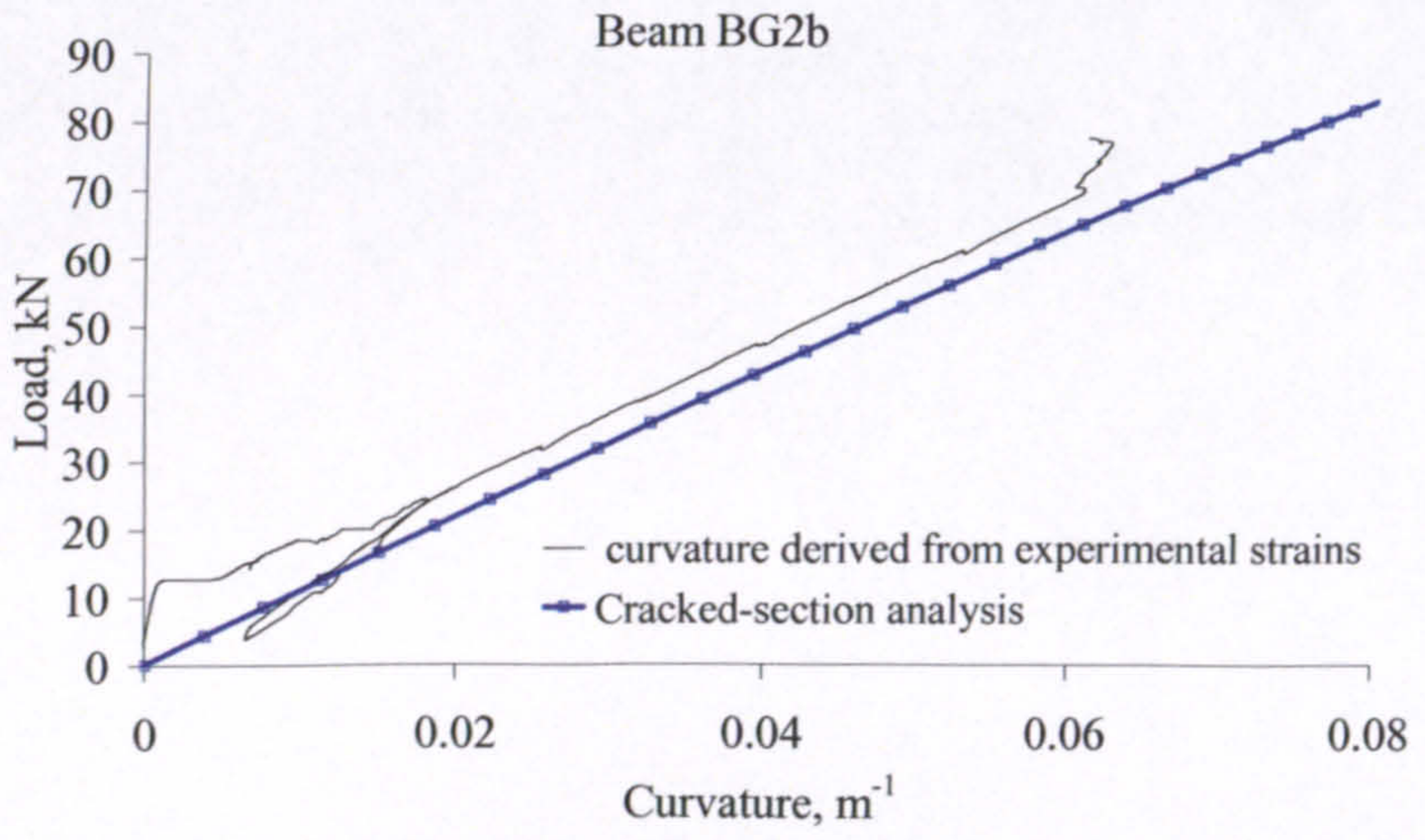
Beam BG2b
Load, kN
90
80
70
60
50
40
30
20
10
0
curvature derived from experimental strains
Cracked-section analysis
0
0.02
0.04
0.06
0.08
Curvature, m-1

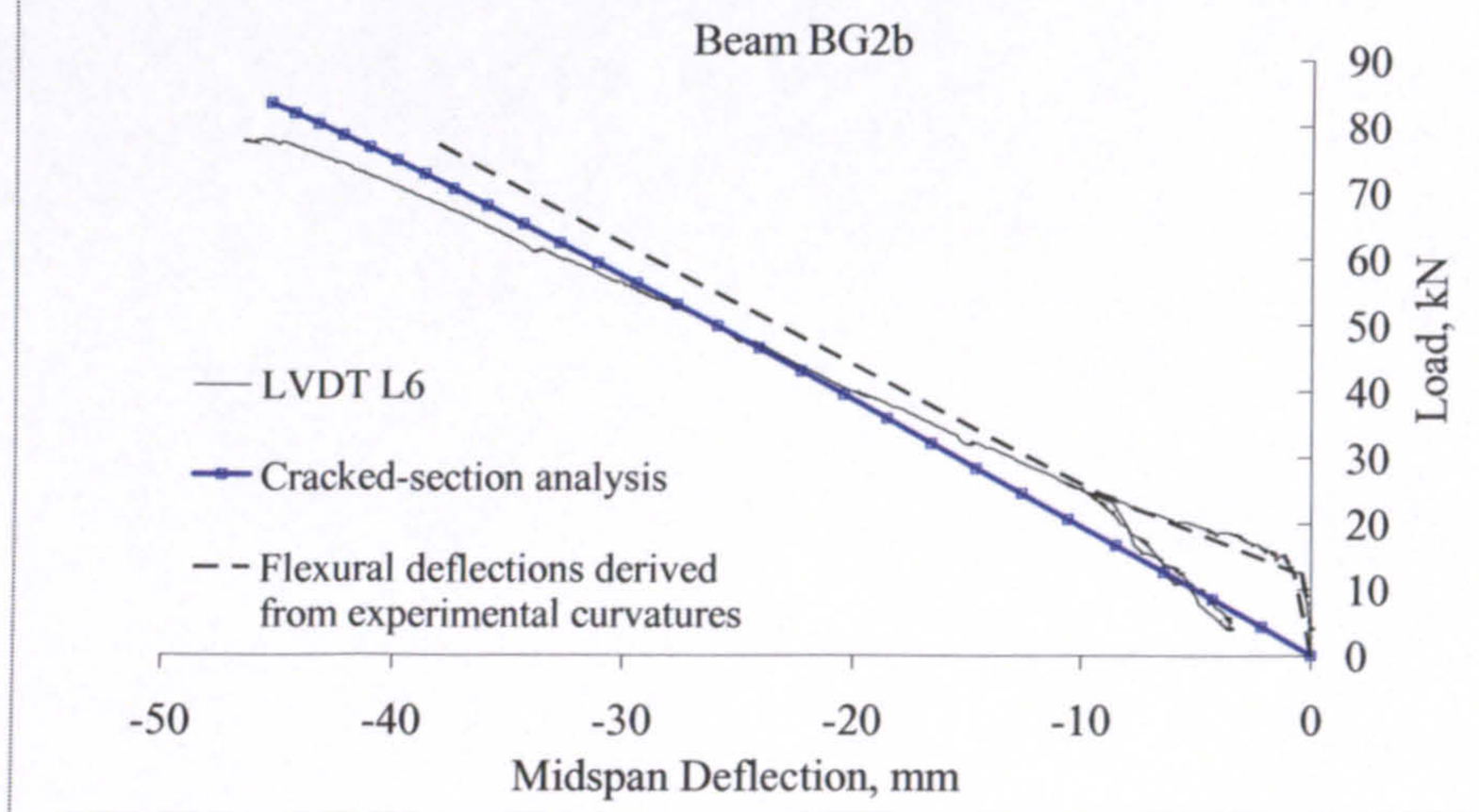
Beam BG2b
90
80
70
60
50
40
30
20
10
0
Load, kN
LVDT L6
Cracked-section analysis
Flexural deflections derived
from experimental curvatures
-50
-40
-30
-20
-10
0
Midspan Deflection, mm

BEAM BG2b

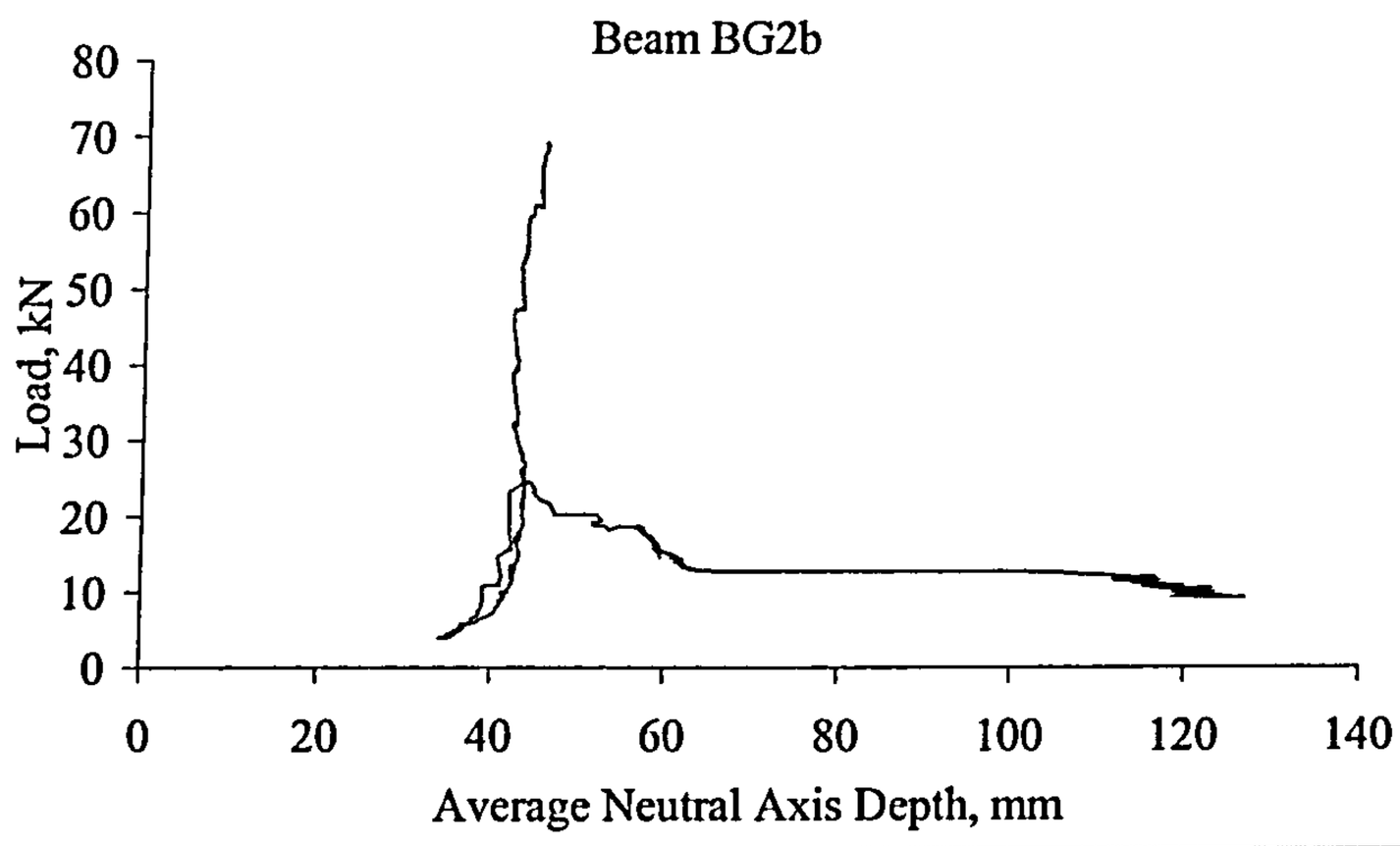
Beam BG2b
Load, kN
0
10
20
30
40
50
60
70
80
0
20
40
60
80
100
120
140
Average Neutral Axis Depth, mm

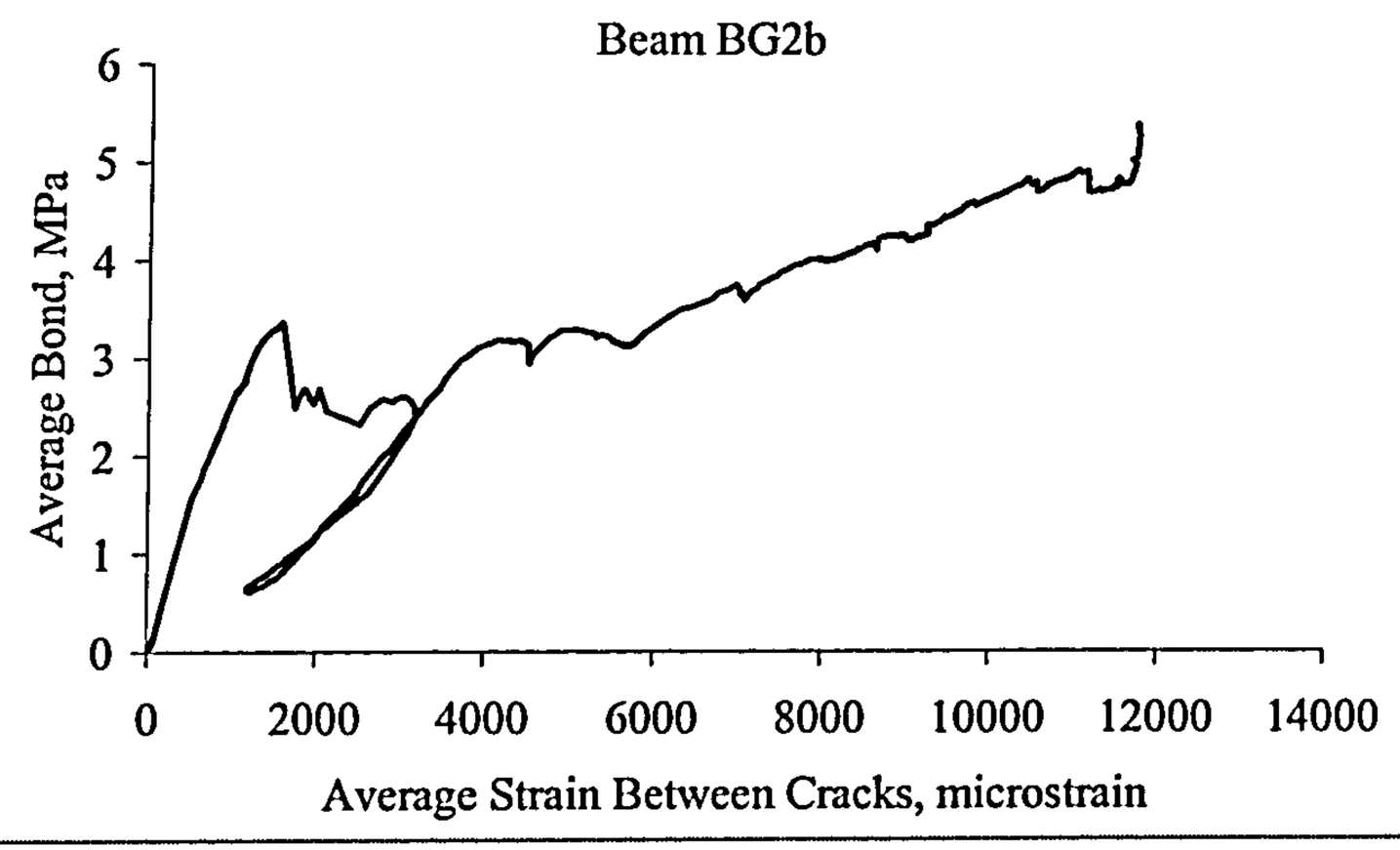
Beam BG2b
Average Bond, MPa
0
1
2
3
4
5
6
0
2000
4000
6000
8000
10000
12000
14000
Average Strain Between Cracks, microstrain

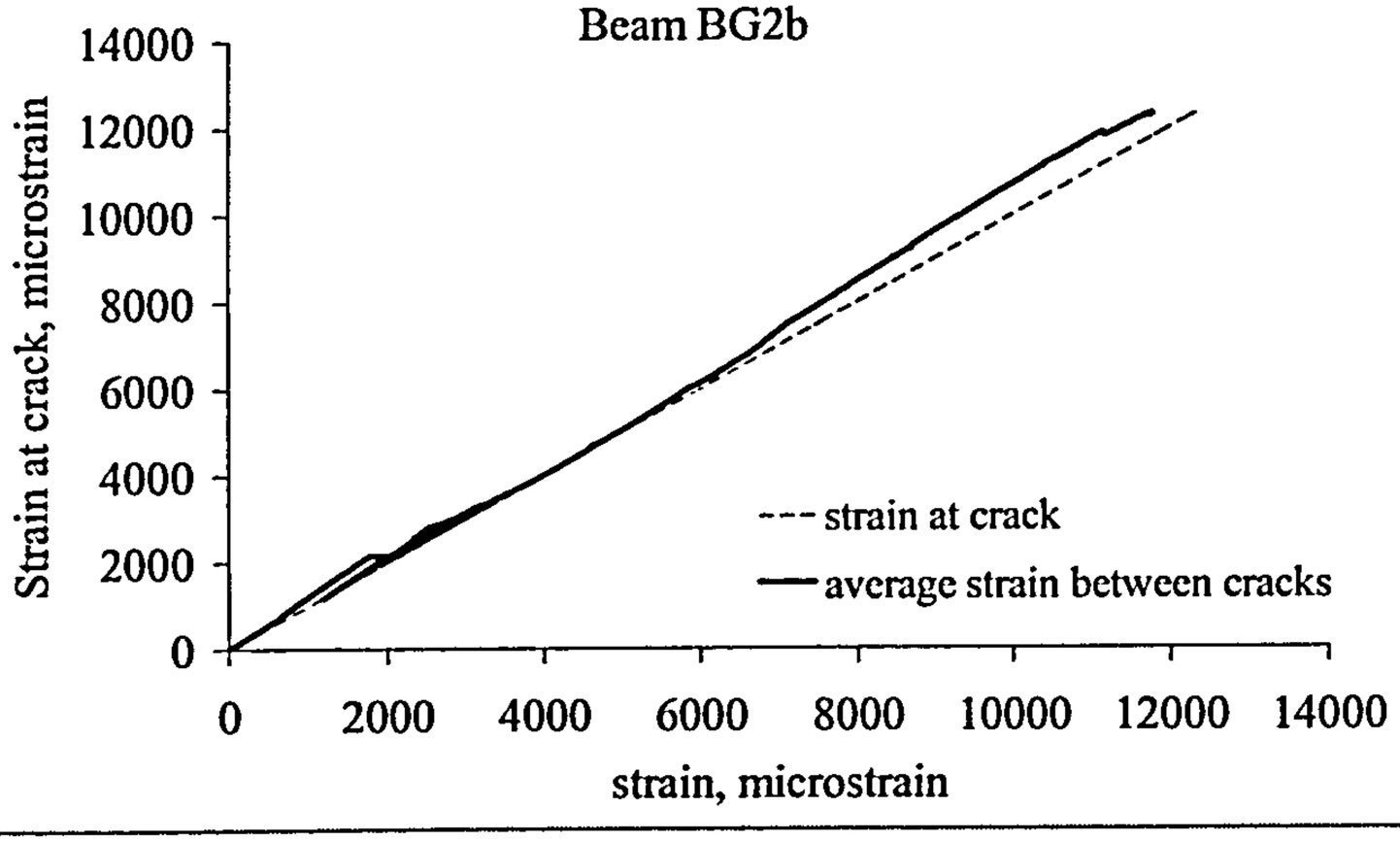
Beam BG2b
Strain at crack, microstrain
0
2000
4000
6000
8000
10000
12000
14000
strain at crack
average strain between cracks
0
2000
4000
6000
8000
10000
12000
14000
strain, microstrain

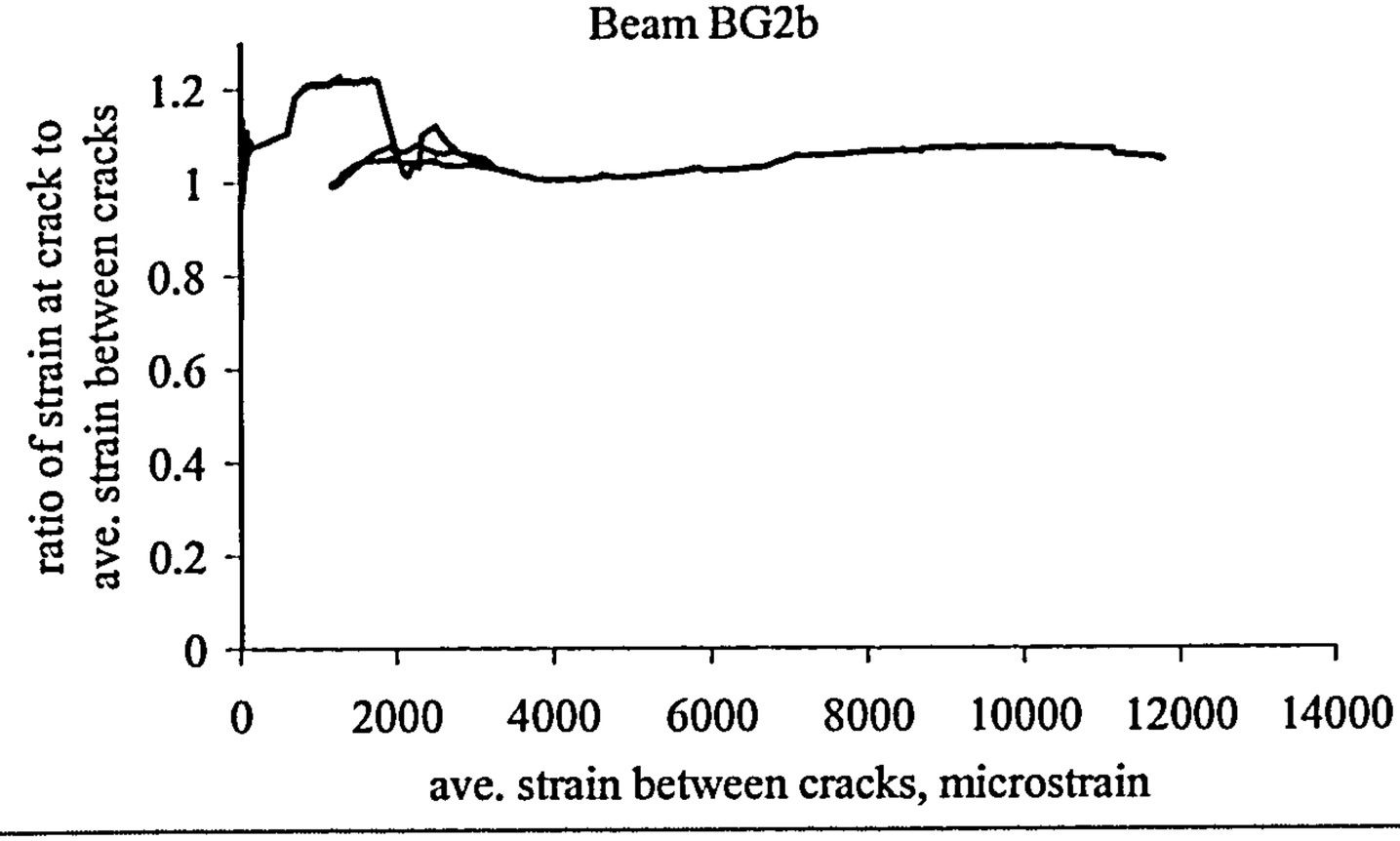
Beam BG2b
ratio of strain at crack to ave. strain between cracks
0
0.2
0.4
0.6
0.8
1
1.2
0
2000
4000
6000
8000
10000
12000
14000
ave. strain between cracks, microstrain

BEAM BG2b

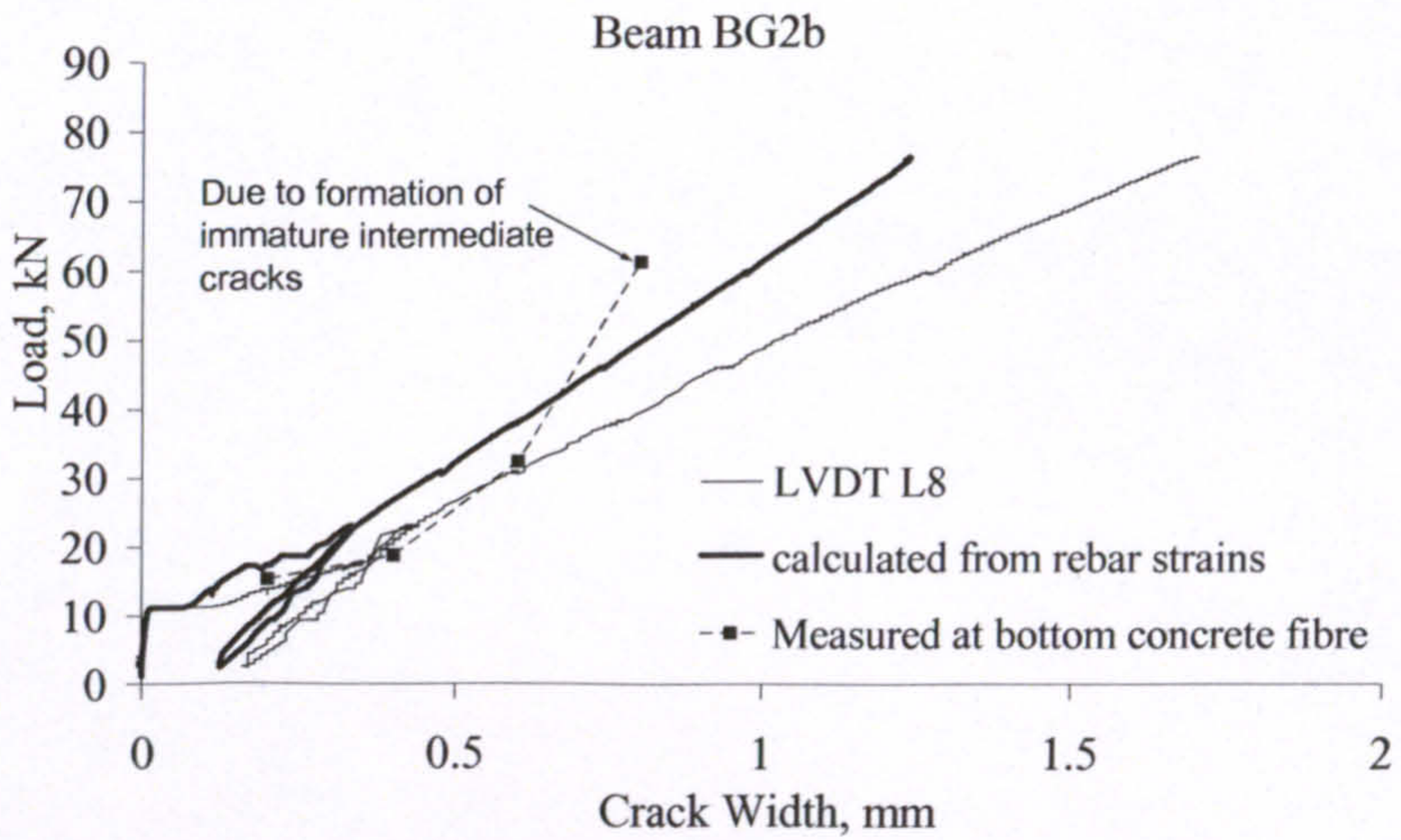

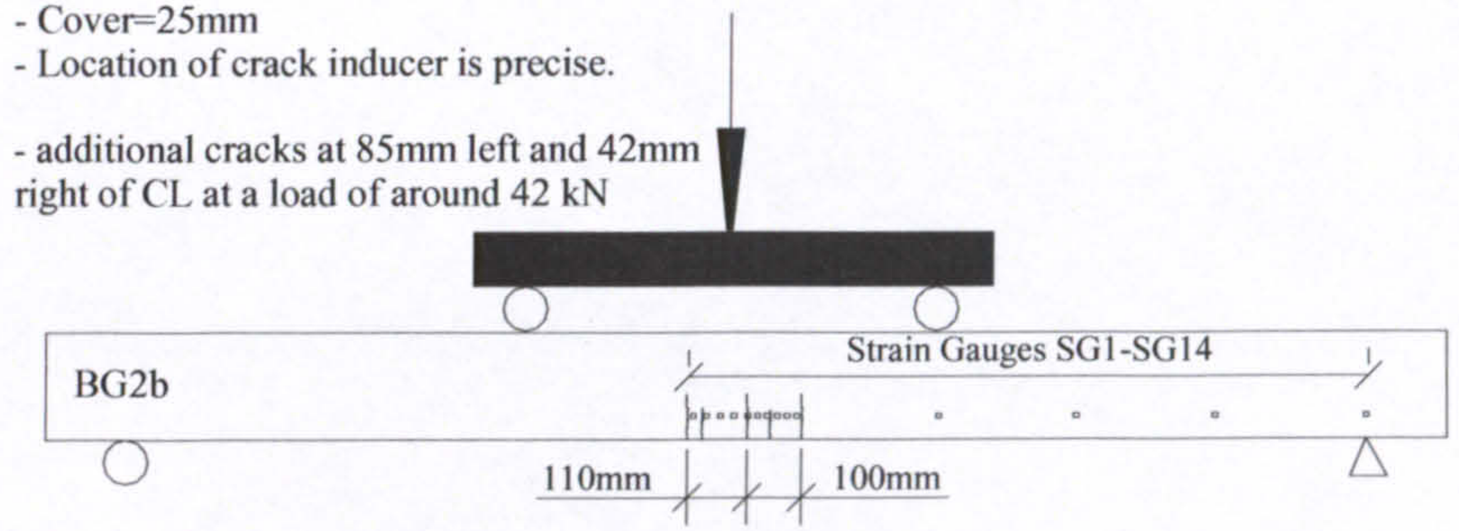

Cracks around Centre

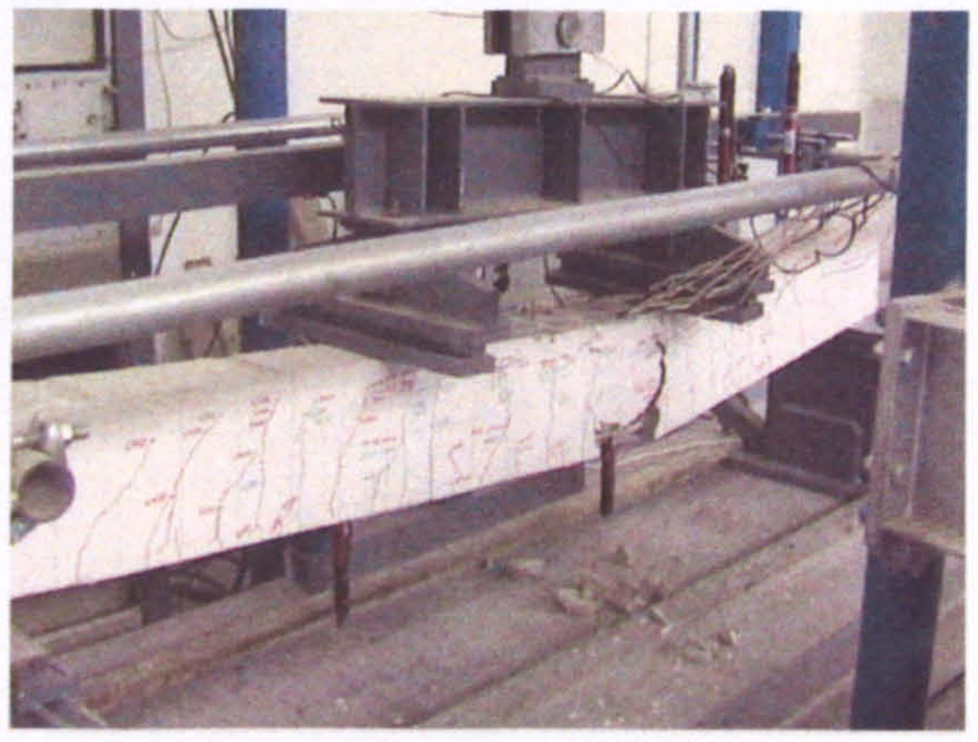

Almost balanced failure

Rupture of rebars following concrete crushing

BEAM BG3a

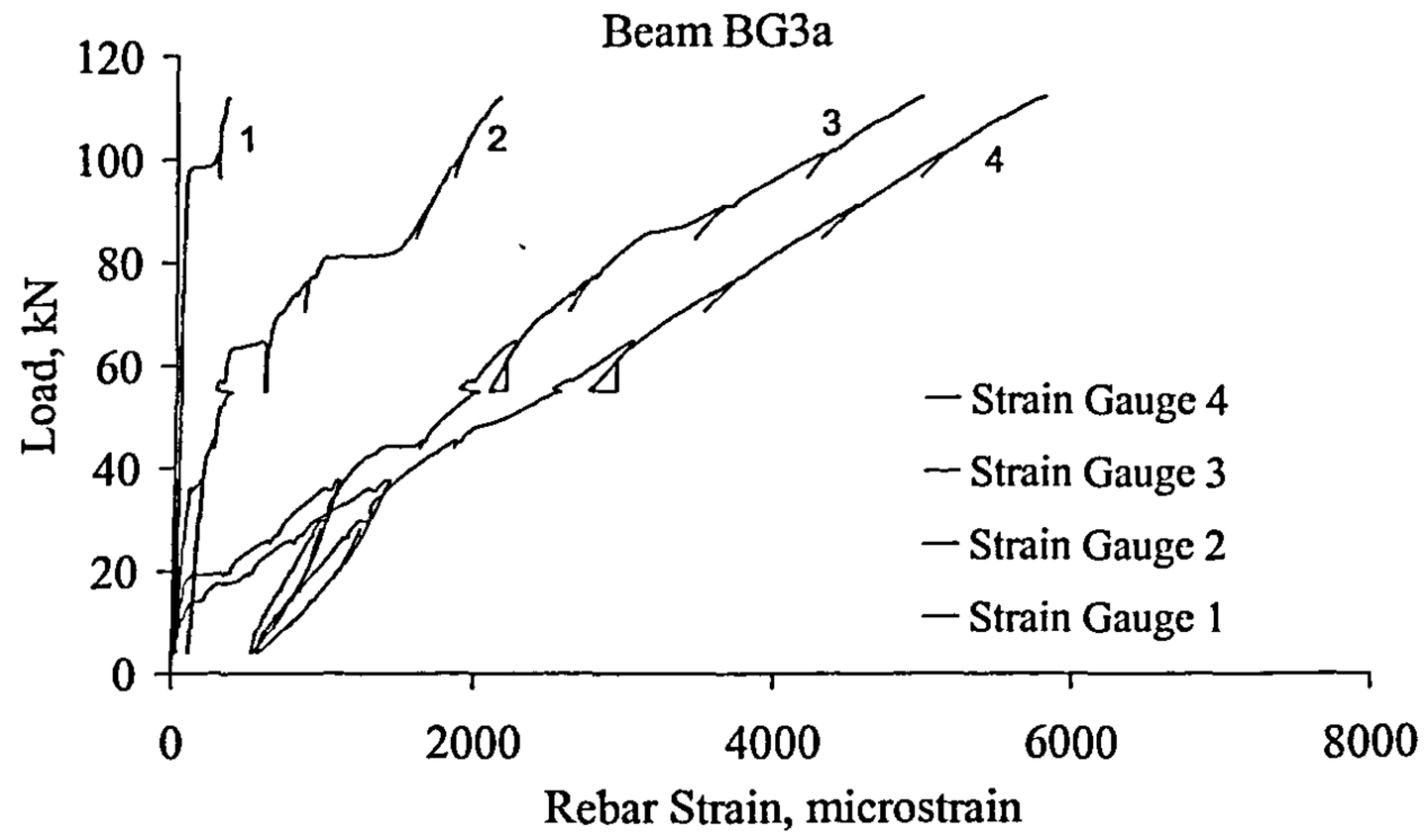
Beam BG3a
Load, kN
Rebar Strain, microstrain
1
2
3
4
Strain Gauge 4
Strain Gauge 3
Strain Gauge 2
Strain Gauge 1

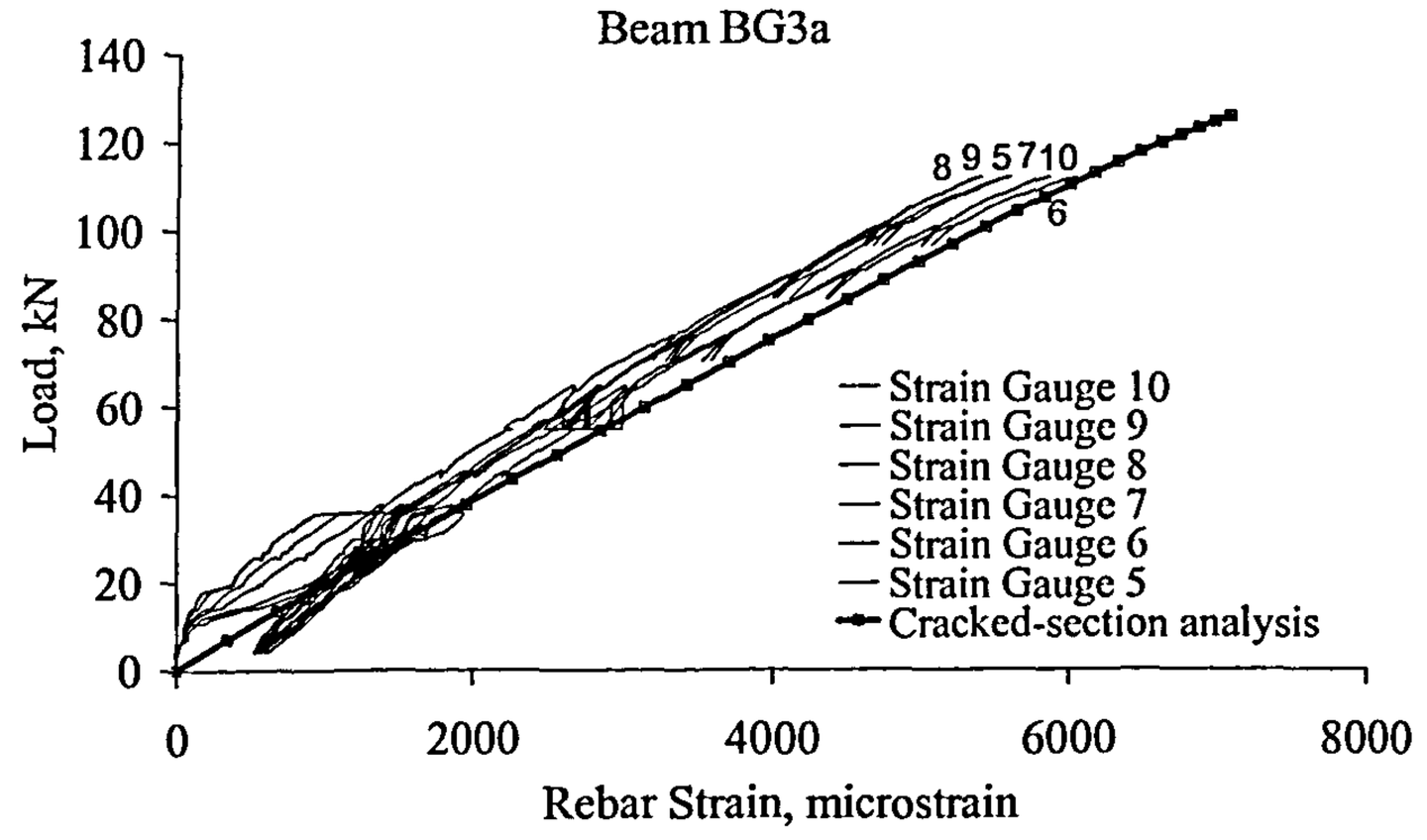
Beam BG3a
Load, kN
Rebar Strain, microstrain
8 9 5 7 10
6
Strain Gauge 10
Strain Gauge 9
Strain Gauge 8
Strain Gauge 7
Strain Gauge 6
Strain Gauge 5
Cracked-section analysis

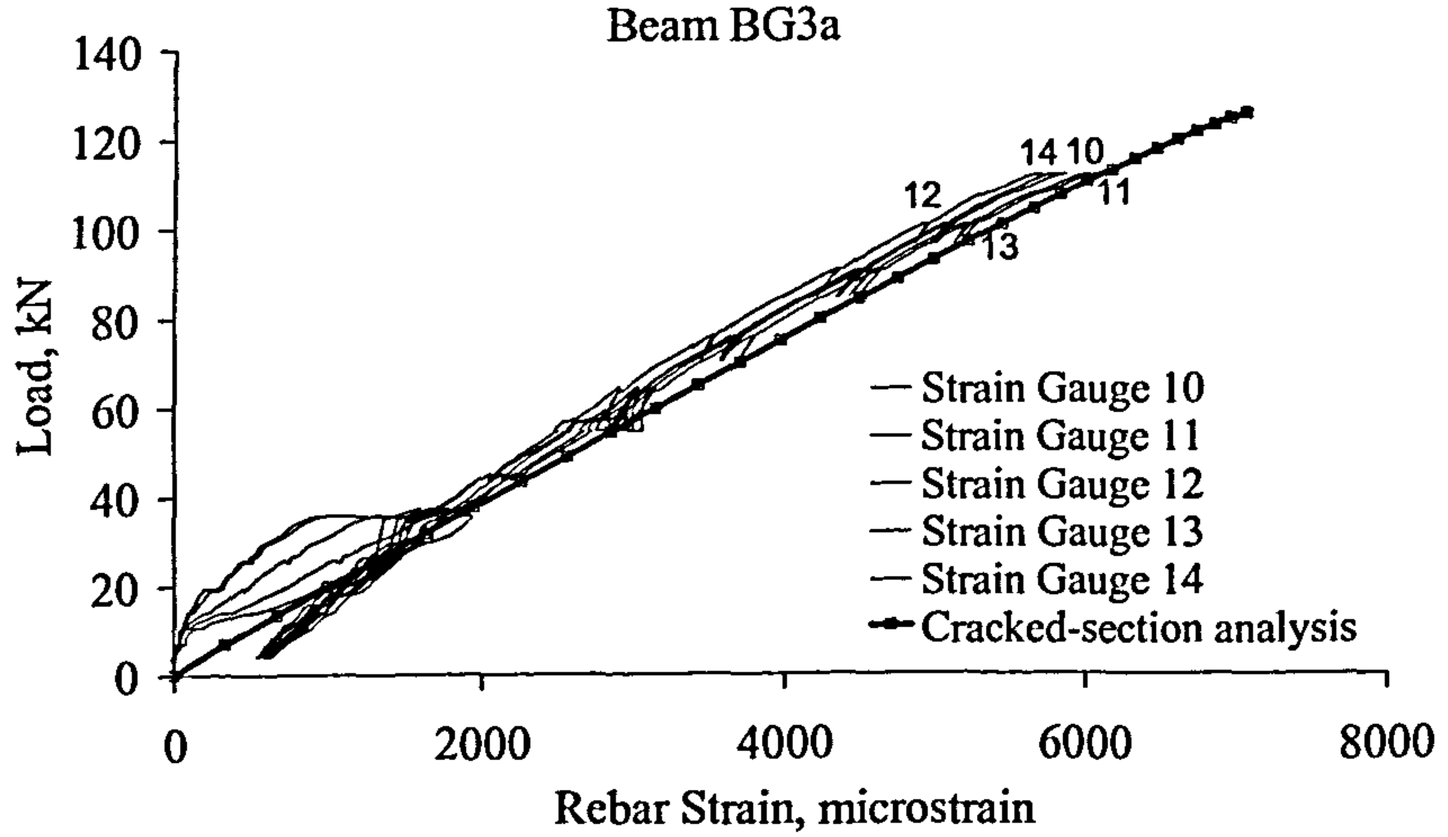
Beam BG3a
Load, kN
Rebar Strain, microstrain
14 10
12
11
13
Strain Gauge 10
Strain Gauge 11
Strain Gauge 12
Strain Gauge 13
Strain Gauge 14
Cracked-section analysis

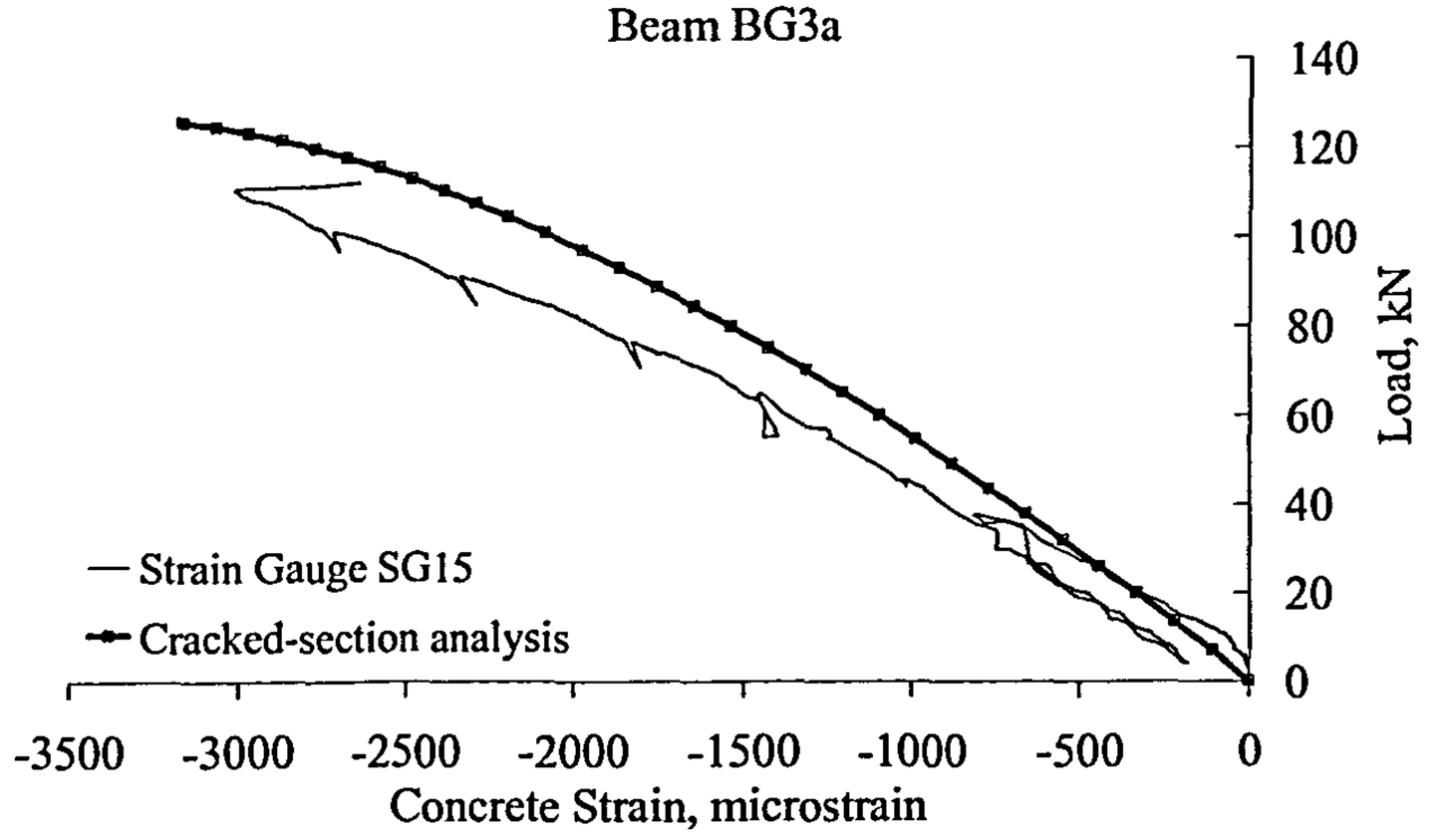
Beam BG3a
Load, kN
Concrete Strain, microstrain
Strain Gauge SG15
Cracked-section analysis

BEAM BG3a

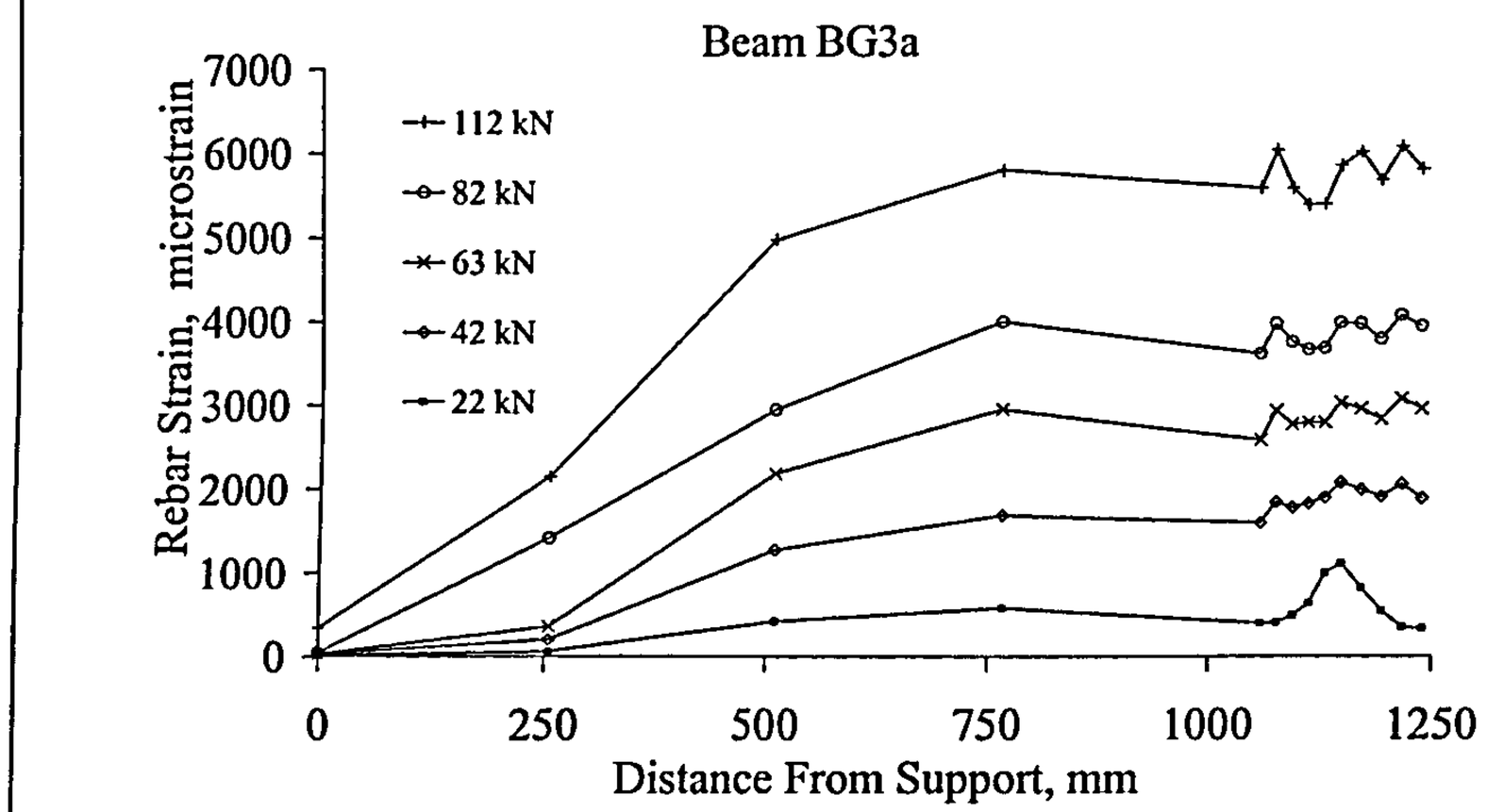
Beam BG3a
Rebar Strain, microstrain
7000
6000
5000
4000
3000
2000
1000
0
112 kN
82 kN
63 kN
42 kN
22 kN
0
250
500
750
1000
1250
Distance From Support, mm

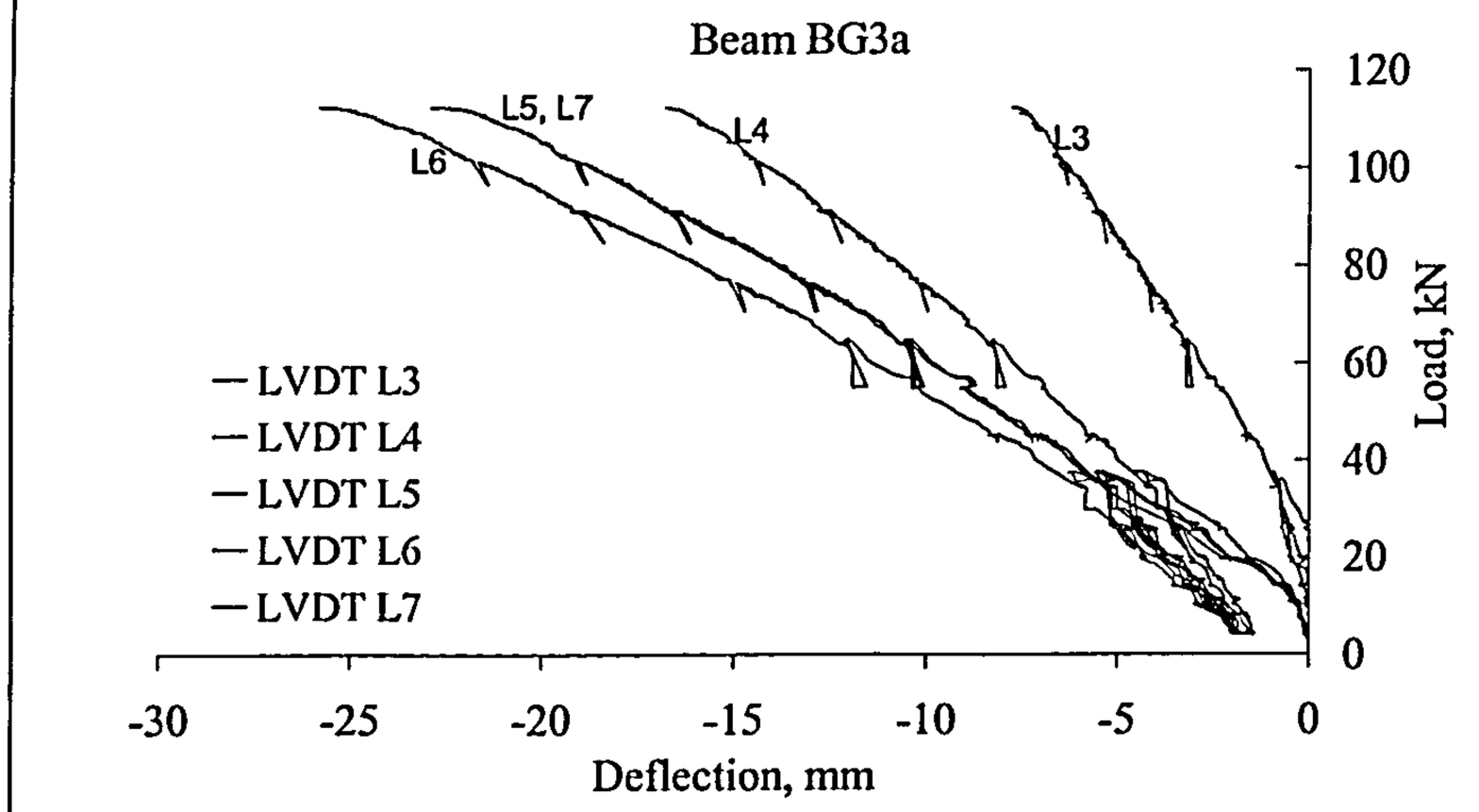
Beam BG3a
L5, L7
L6
L4
L3
LVDT L3
LVDT L4
LVDT L5
LVDT L6
LVDT L7
120
100
80
60
40
20
0
Load, kN
-30
-25
-20
-15
-10
-5
0
Deflection, mm

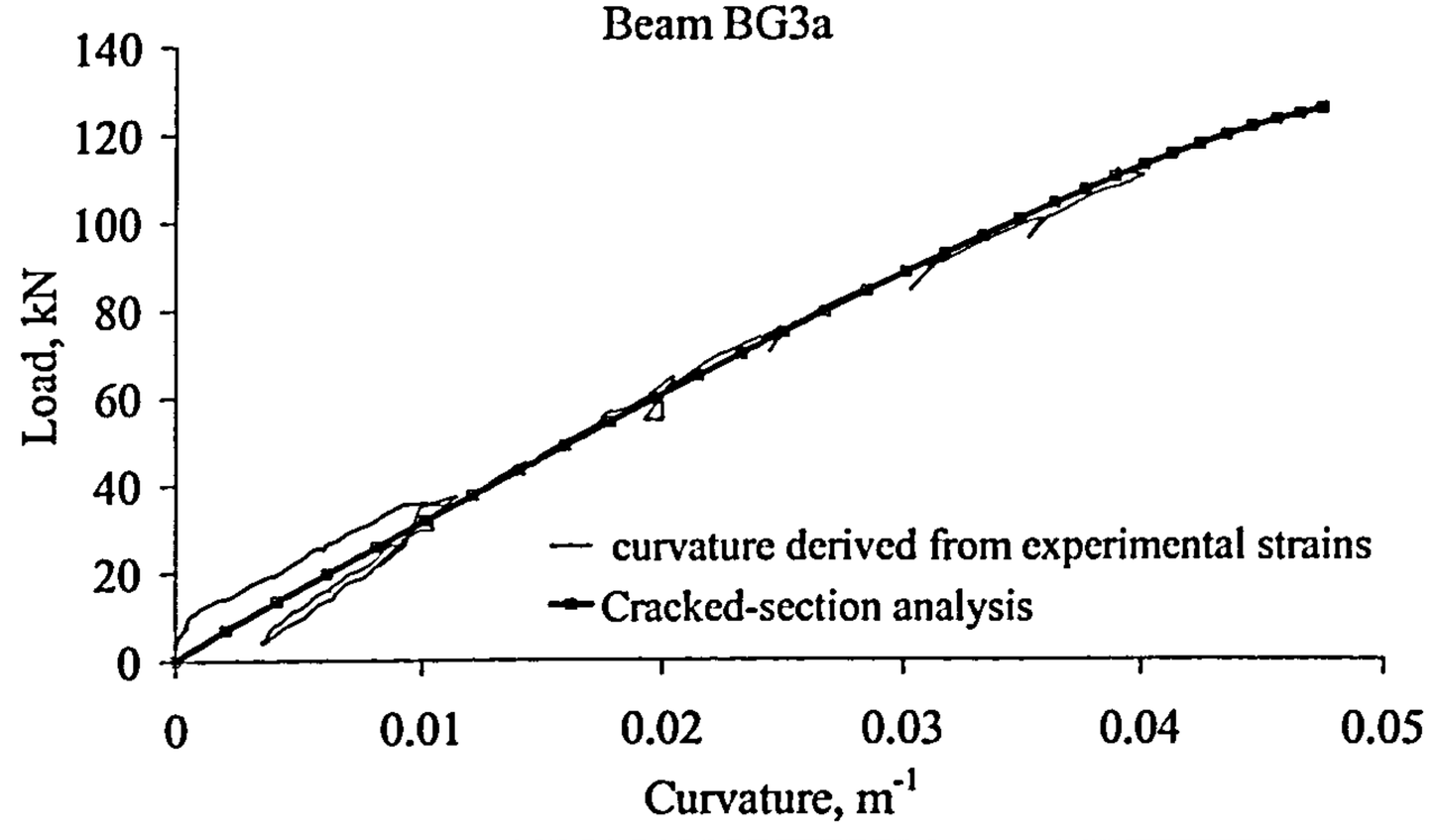
Beam BG3a
Load, kN
140
120
100
80
60
40
20
0
curvature derived from experimental strains
Cracked-section analysis
0
0.01
0.02
0.03
0.04
0.05
Curvature, m-1

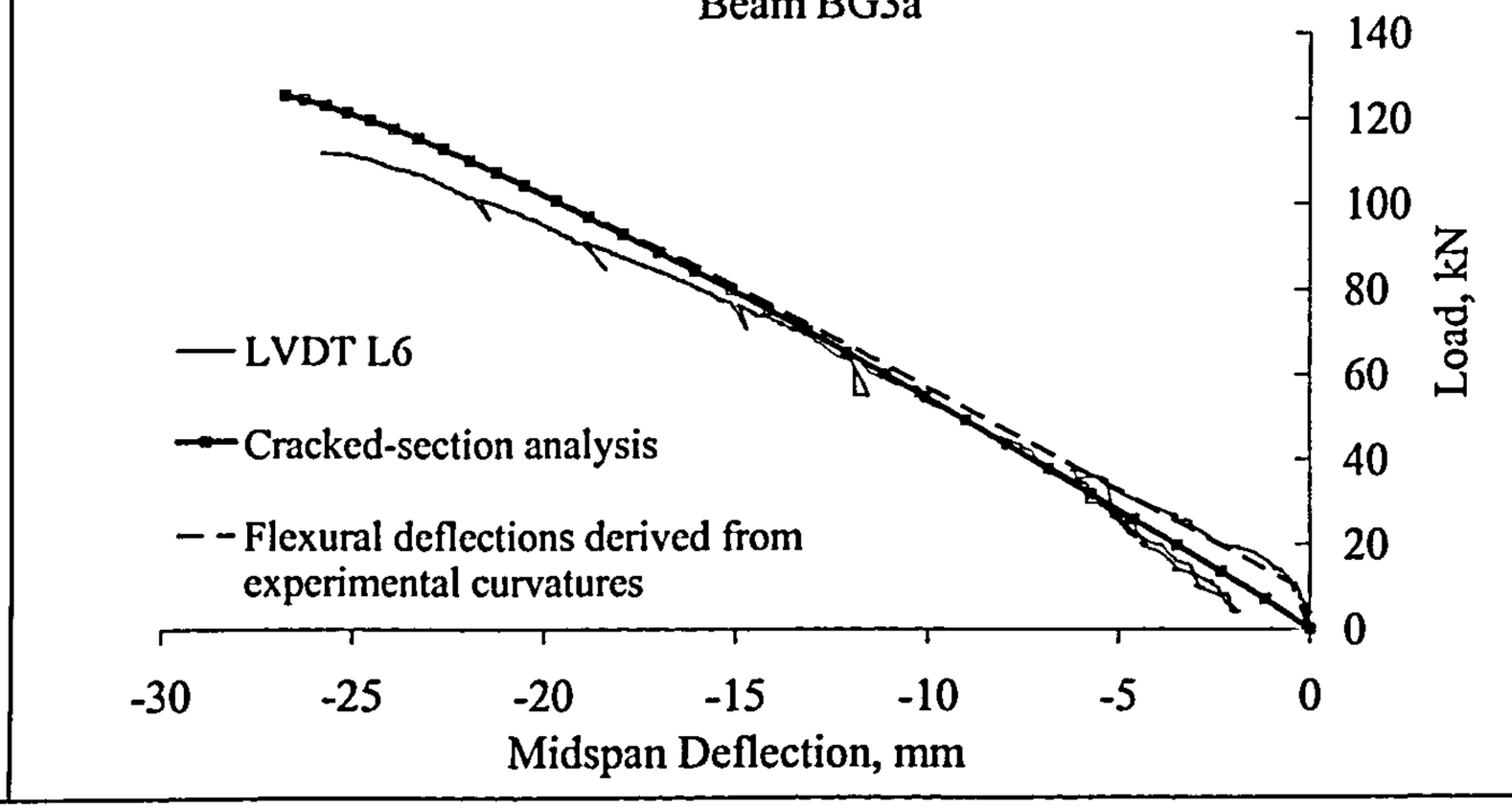
Beam BG3a
140
120
100
80
60
40
20
0
Load, kN
LVDT L6
Cracked-section analysis
Flexural deflections derived from experimental curvatures
-30
-25
-20
-15
-10
-5
0
Midspan Deflection, mm

BEAM BG3a

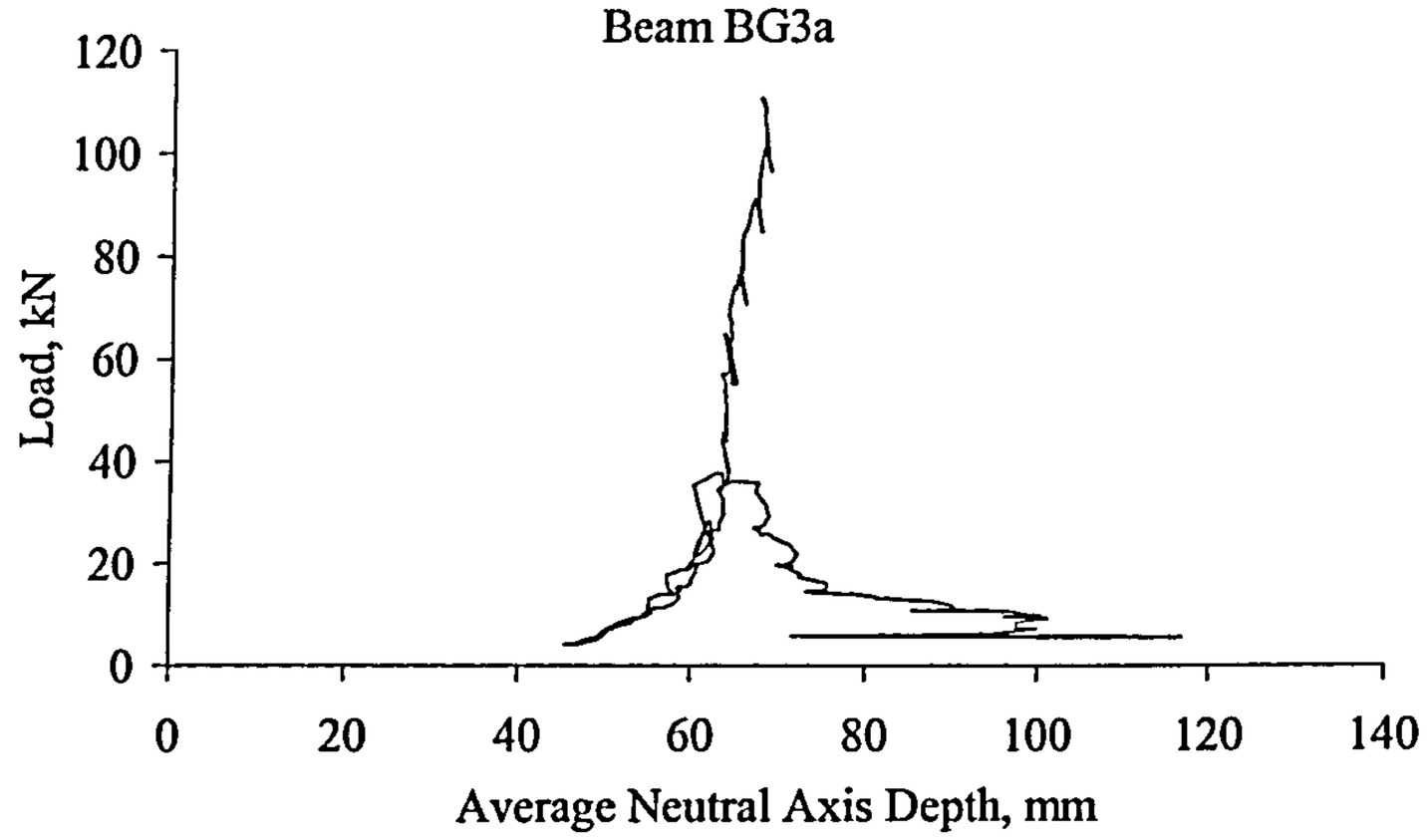
Beam BG3a
Load, kN
0
20
40
60
80
100
120
0
20
40
60
80
100
120
140
Average Neutral Axis Depth, mm

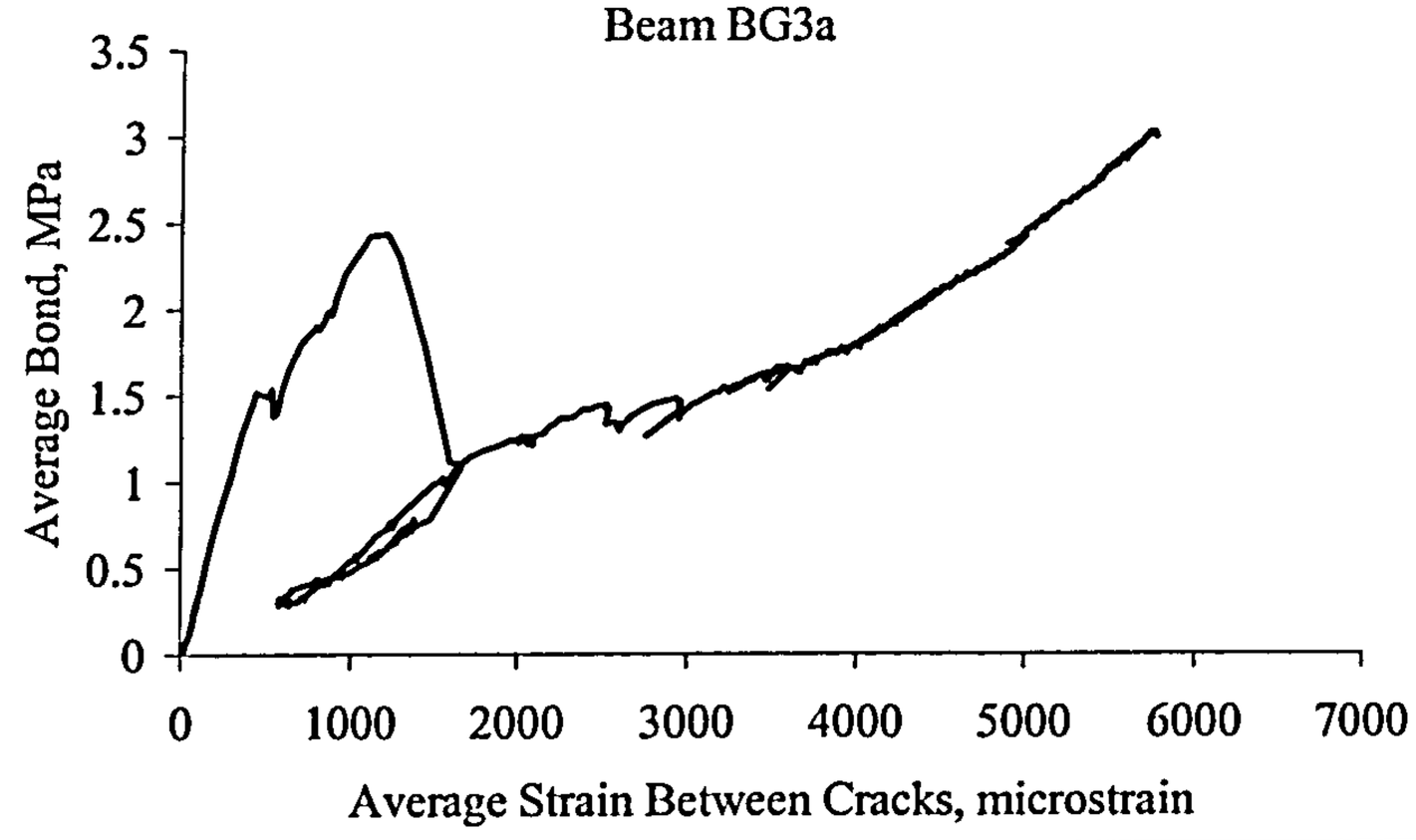
Beam BG3a
Average Bond, MPa
0
0.5
1
1.5
2
2.5
3
3.5
0
1000
2000
3000
4000
5000
6000
7000
Average Strain Between Cracks, microstrain

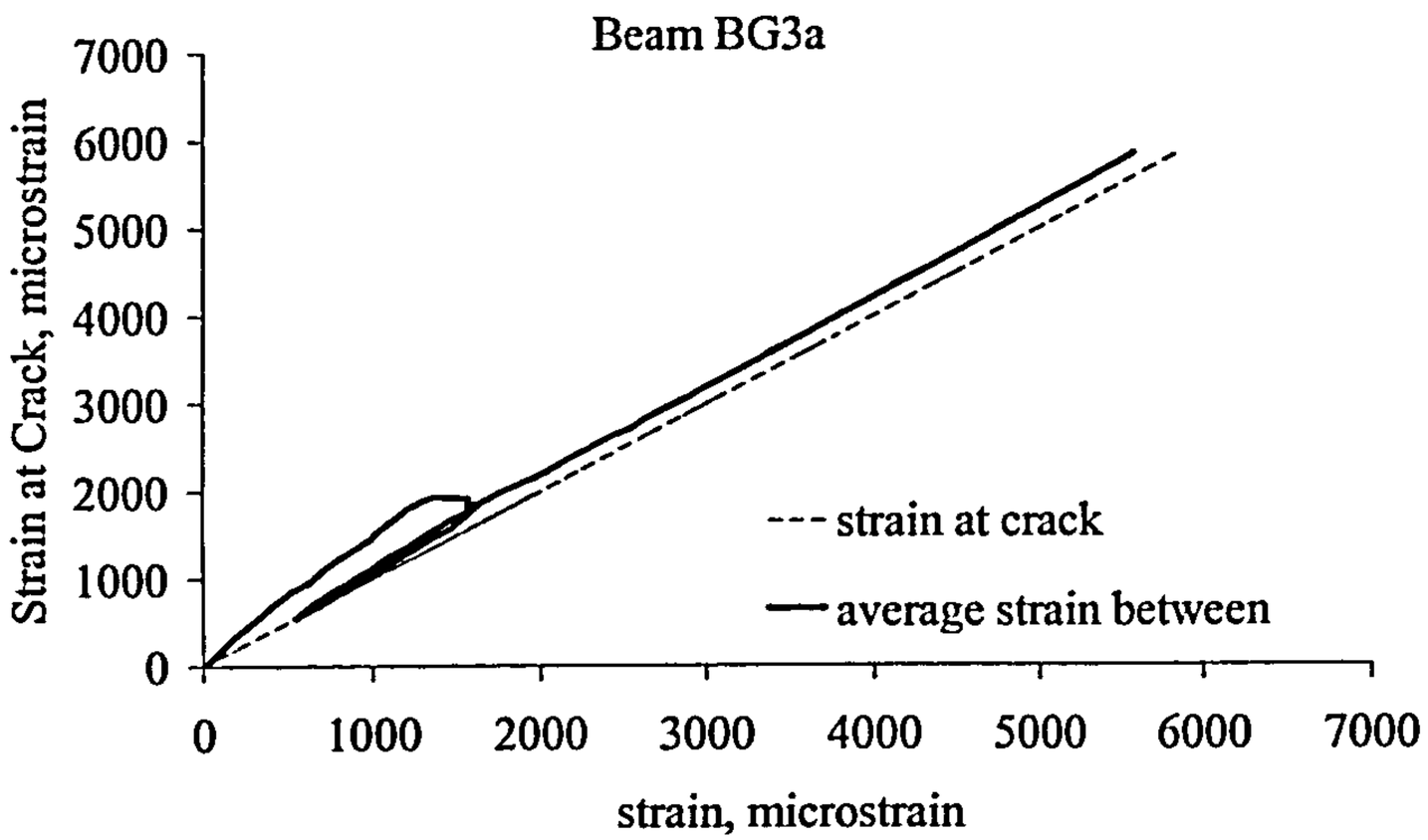
Beam BG3a
Strain at Crack, microstrain
0
1000
2000
3000
4000
5000
6000
7000
0
1000
2000
3000
4000
5000
6000
7000
strain, microstrain
strain at crack
average strain between

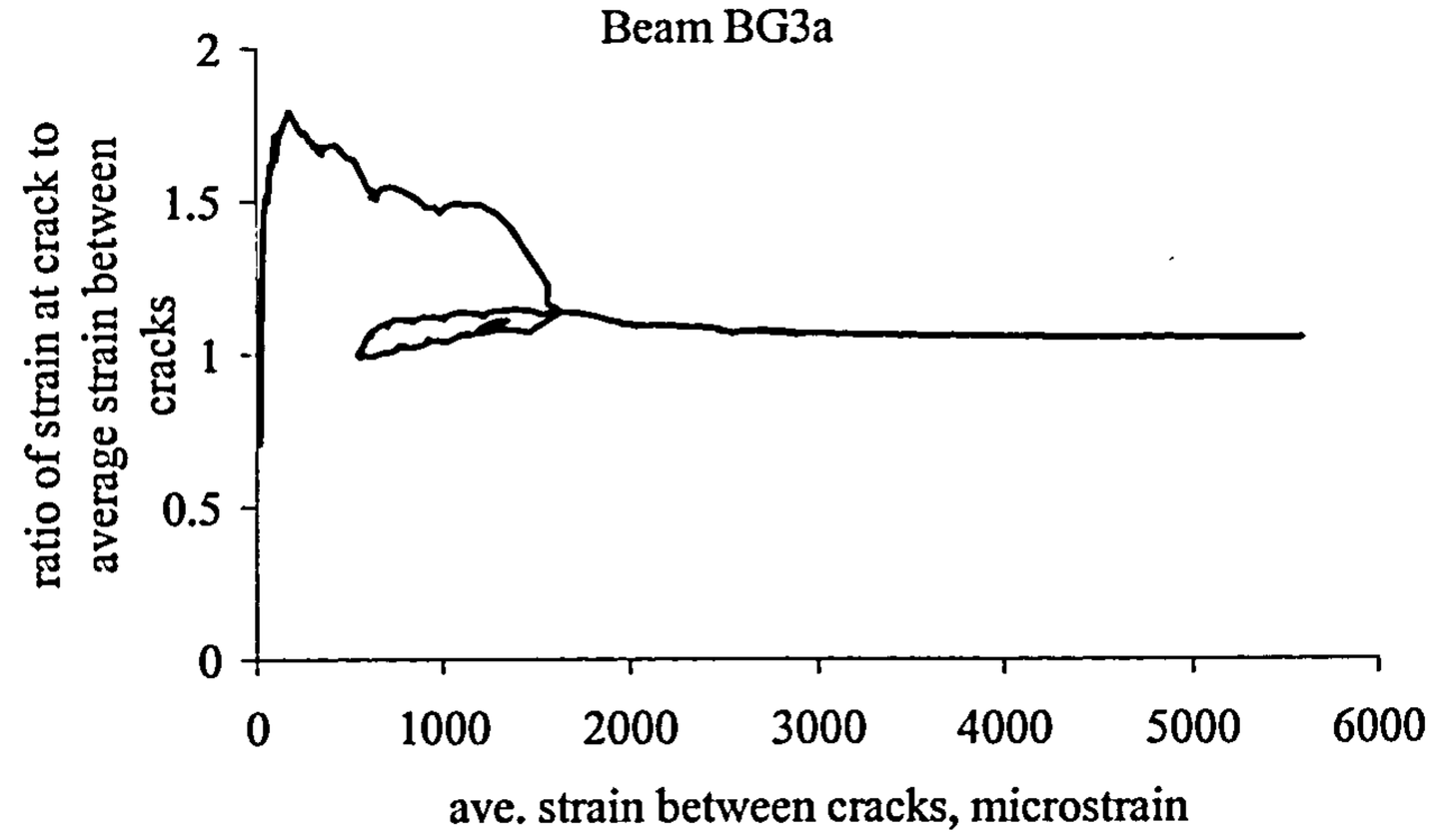
Beam BG3a
ratio of strain at crack to average strain between cracks
0
0.5
1
1.5
2
0
1000
2000
3000
4000
5000
6000
ave. strain between cracks, microstrain

BEAM BG3a

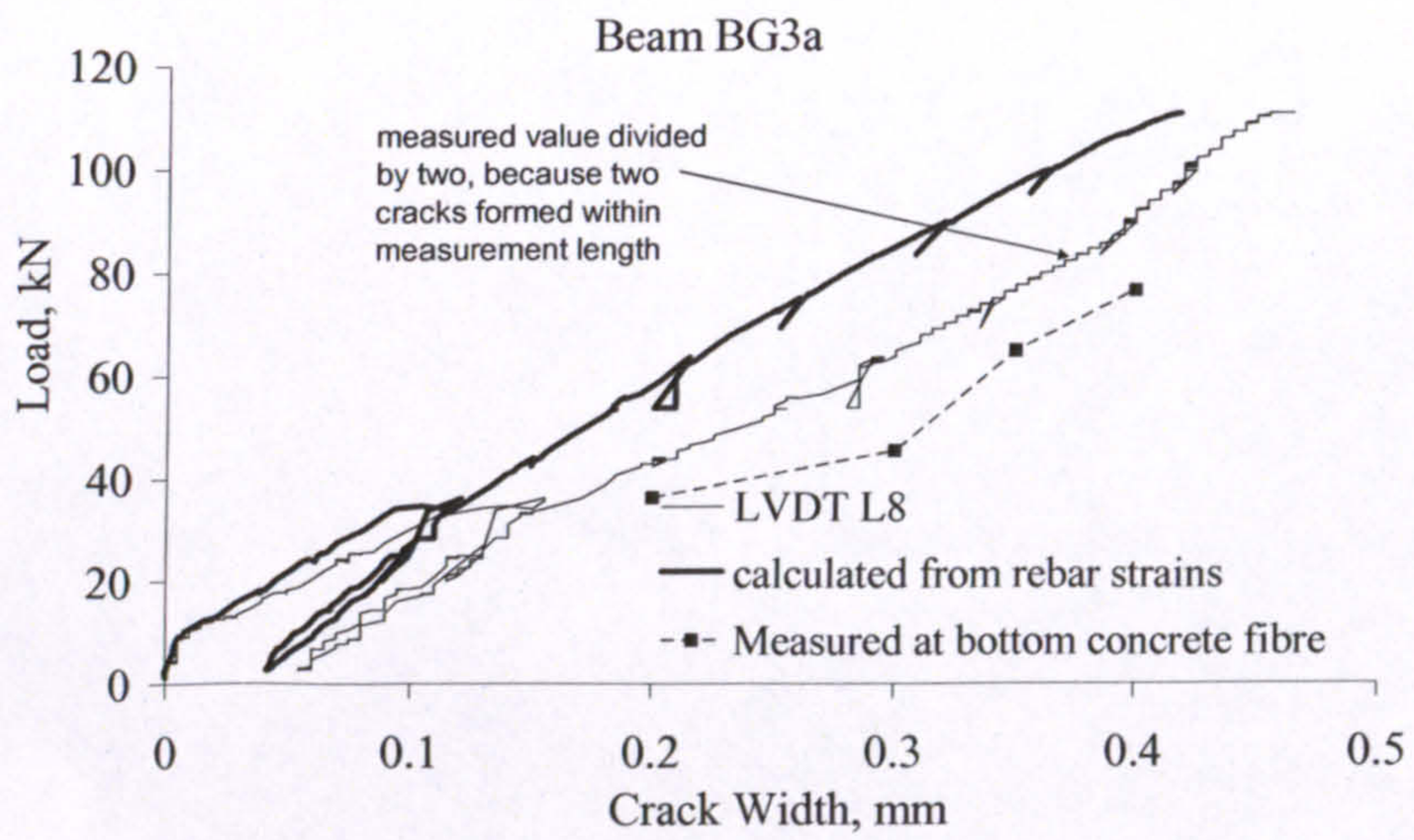

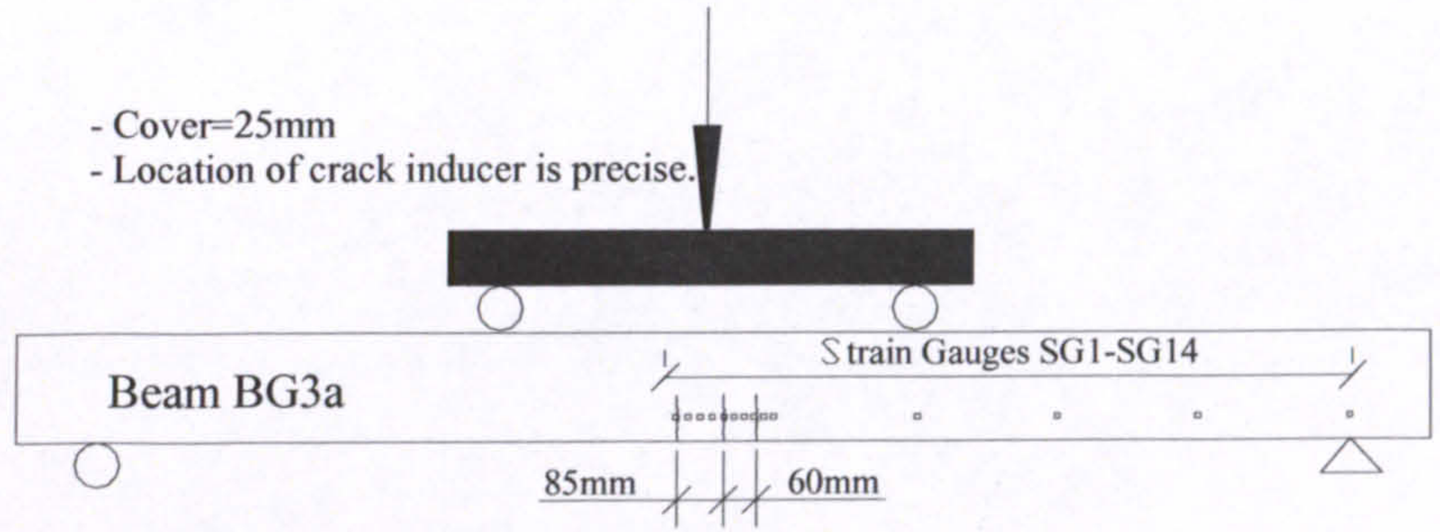

Cracks around Centre

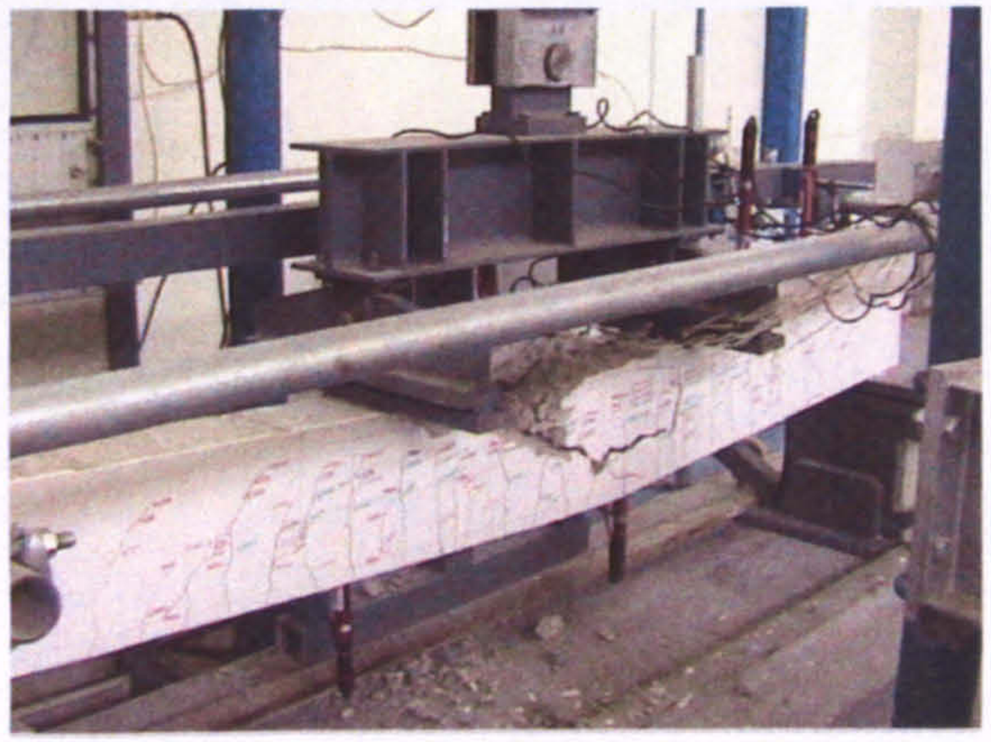

Compressive concrete failure

BEAM BG3b

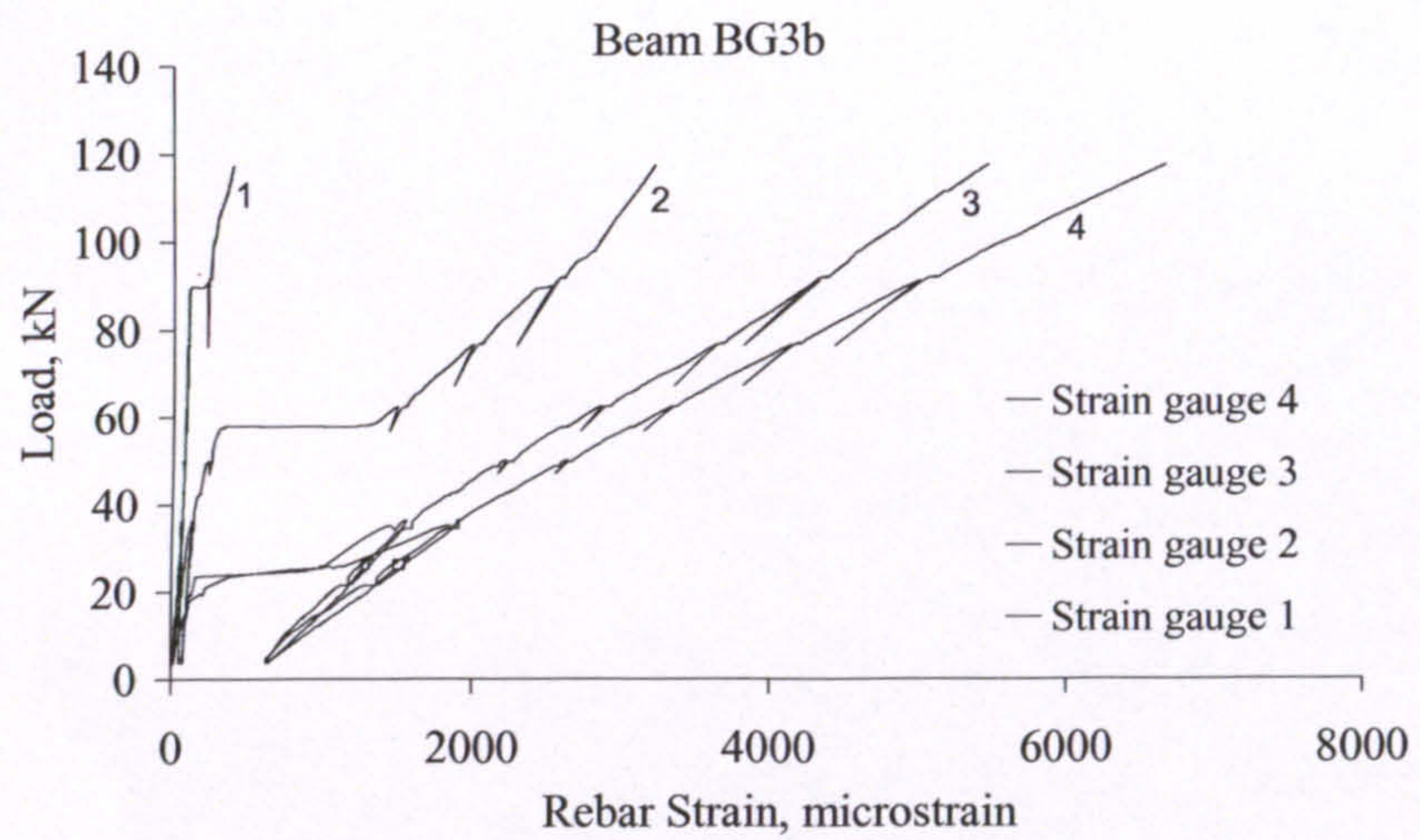
Beam BG3b
Load, kN
Rebar Strain, microstrain
1
2
3
4
Strain gauge 4
Strain gauge 3
Strain gauge 2
Strain gauge 1

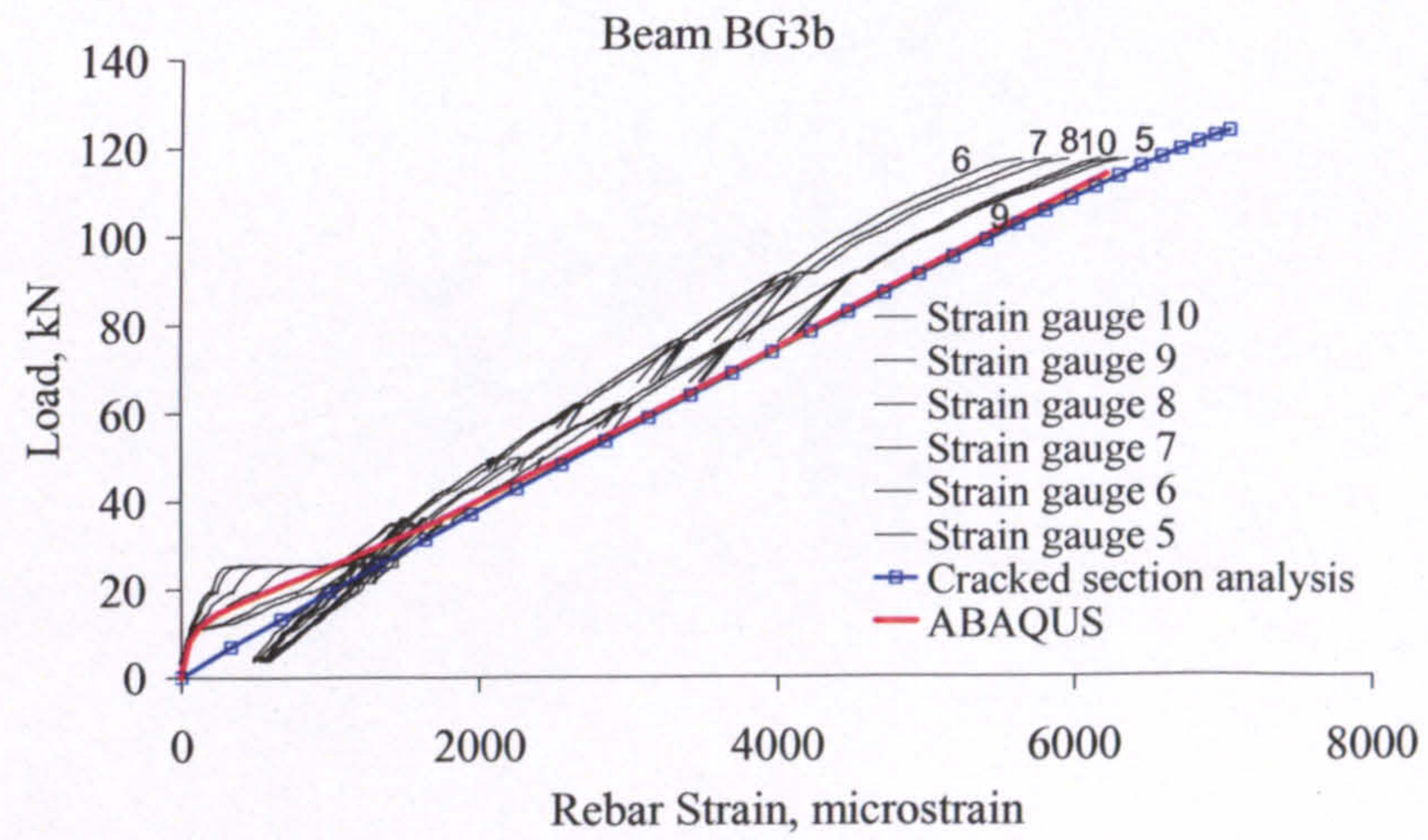
Beam BG3b
Load, kN
Rebar Strain, microstrain
5
6
7
8
9
10
Strain gauge 10
Strain gauge 9
Strain gauge 8
Strain gauge 7
Strain gauge 6
Strain gauge 5
Cracked section analysis
ABAQUS

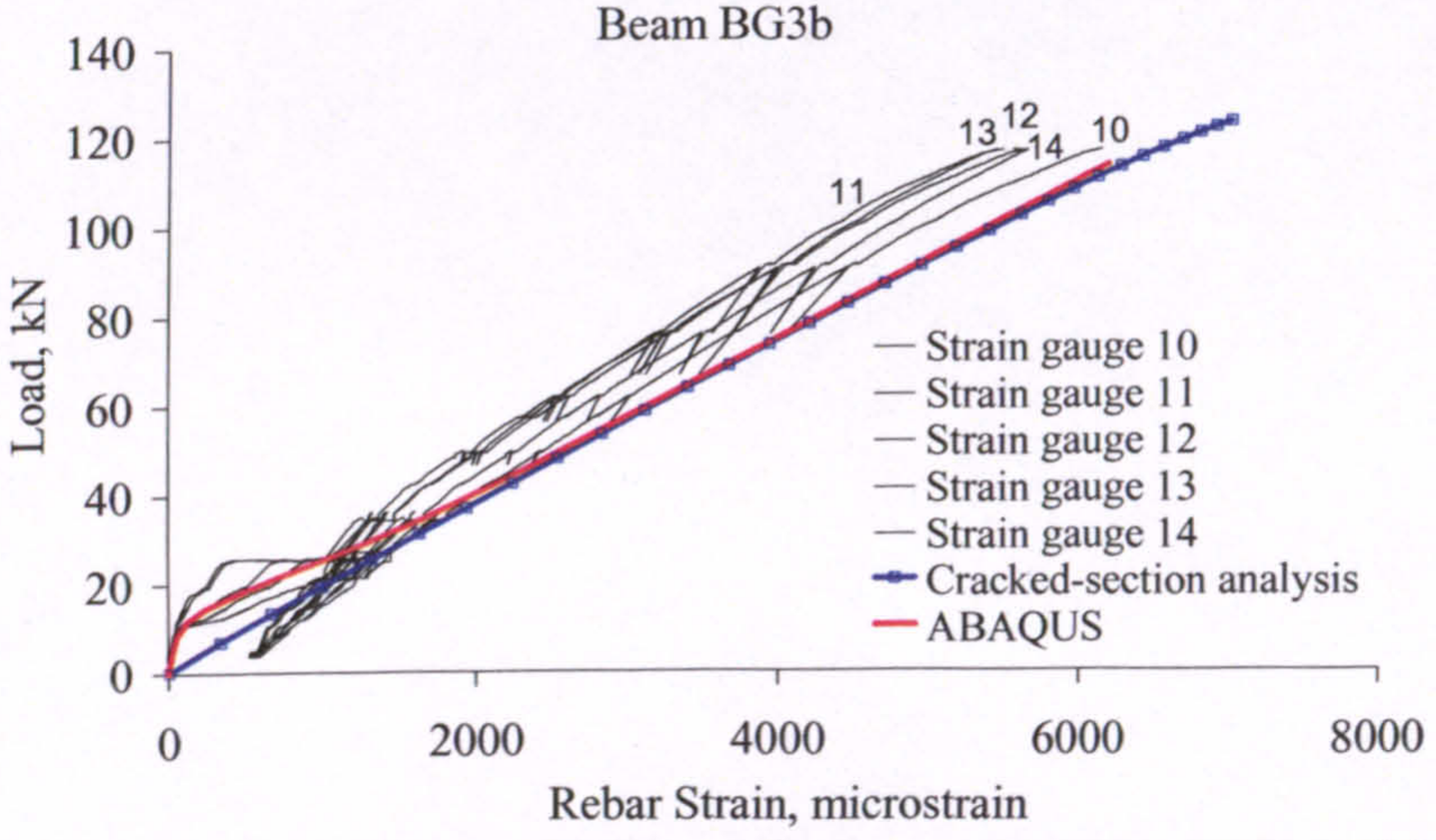
Beam BG3b
Load, kN
Rebar Strain, microstrain
10
11
12
13
14
Strain gauge 10
Strain gauge 11
Strain gauge 12
Strain gauge 13
Strain gauge 14
Cracked-section analysis
ABAQUS

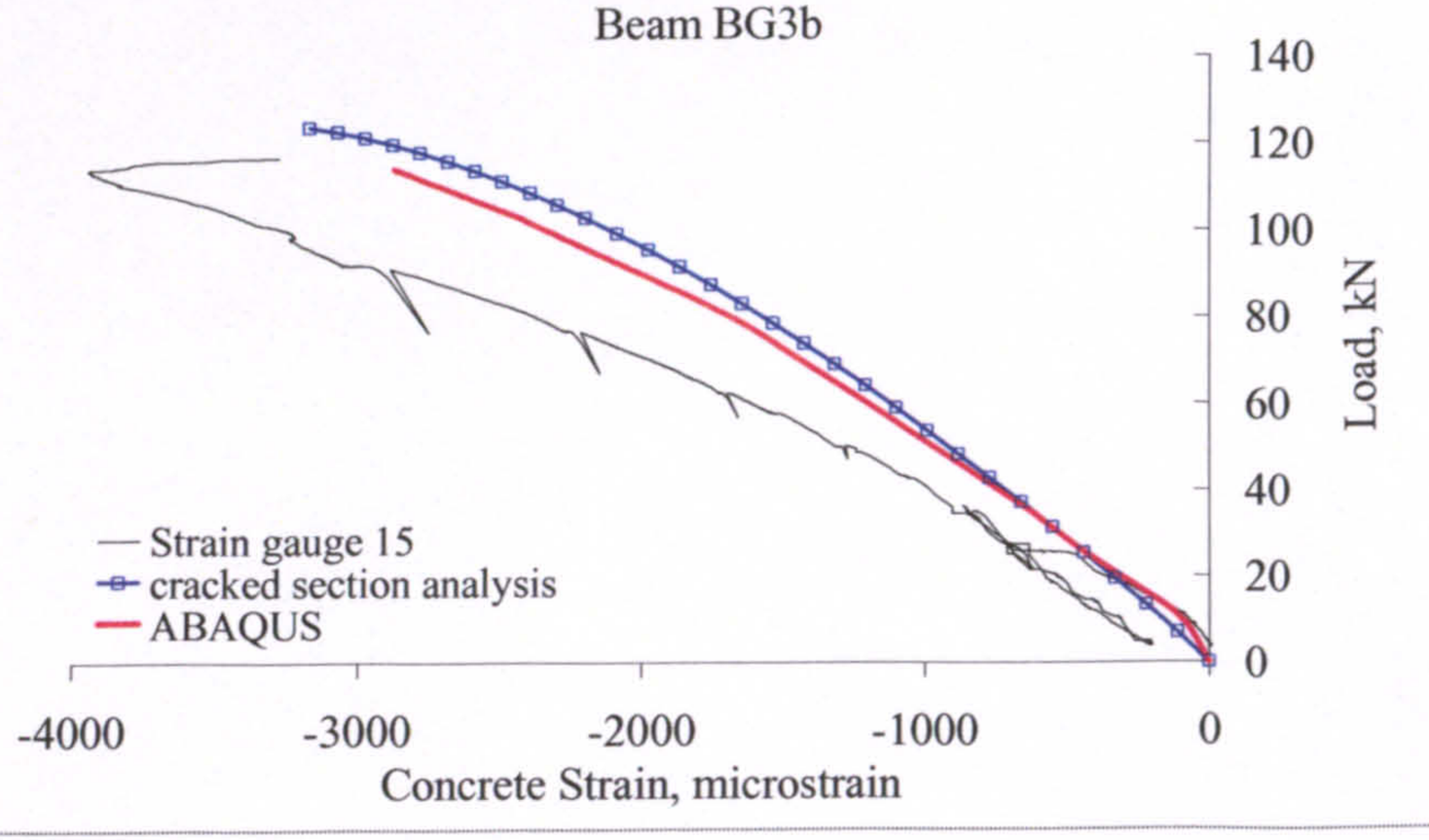
Beam BG3b
Load, kN
Concrete Strain, microstrain
Strain gauge 15
cracked section analysis
ABAQUS

BEAM BG3b

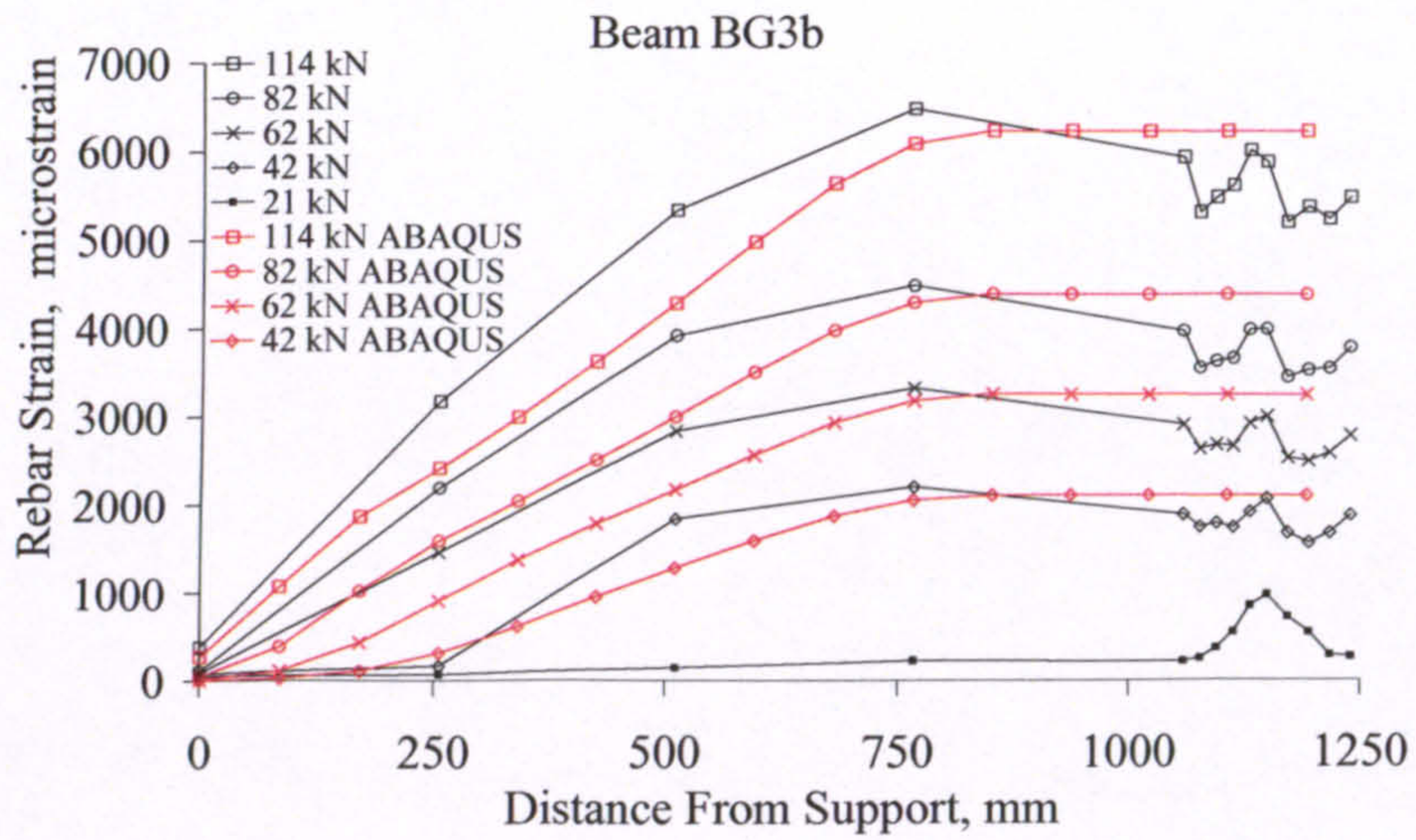
Beam BG3b
Rebar Strain, microstrain
7000
6000
5000
4000
3000
2000
1000
0
114 kN
82 kN
62 kN
42 kN
21 kN
114 kN ABAQUS
82 kN ABAQUS
62 kN ABAQUS
42 kN ABAQUS
0
250
500
750
1000
1250
Distance From Support, mm

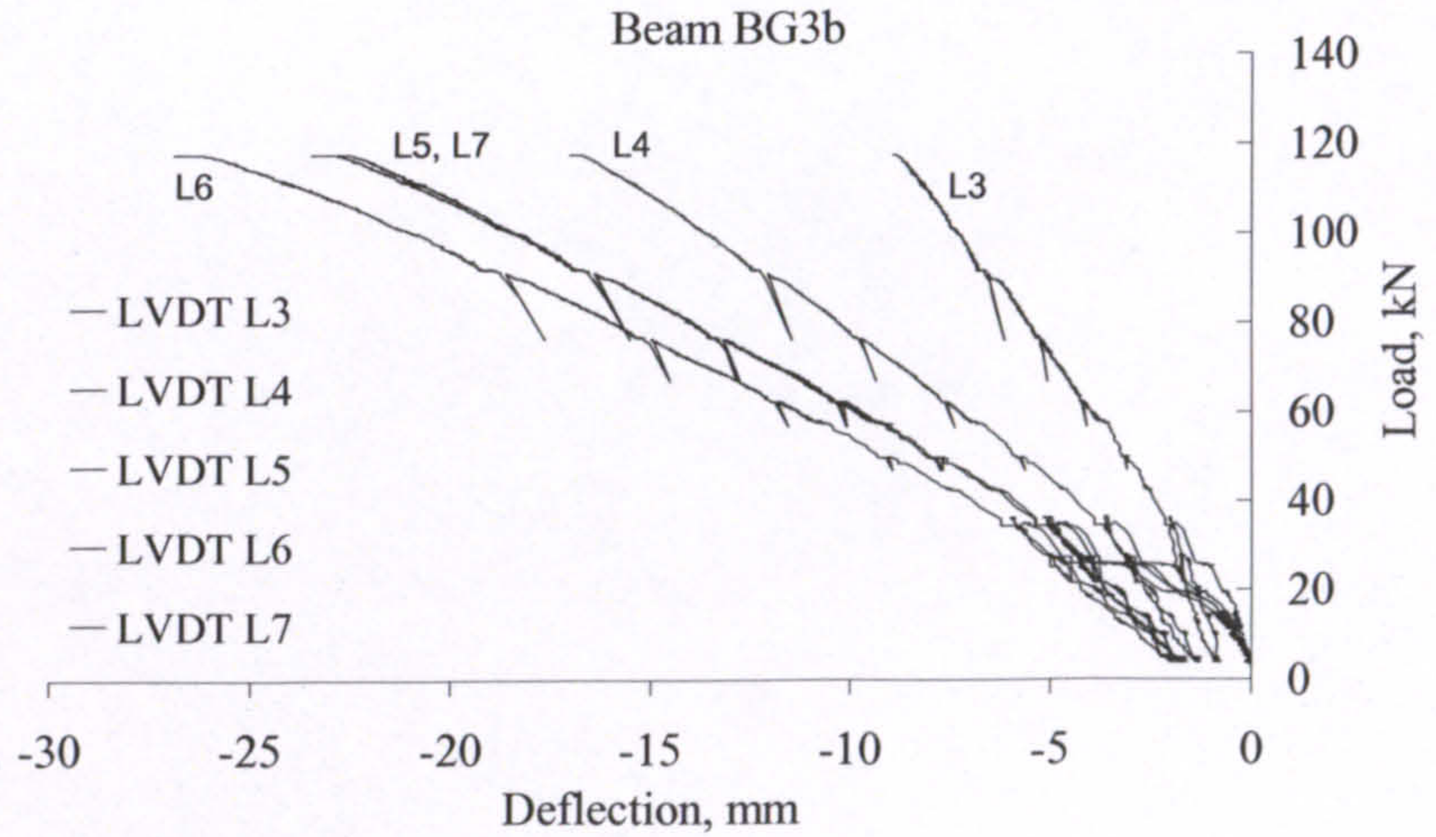
Beam BG3b
L6
L5, L7
L4
L3
LVDT L3
LVDT L4
LVDT L5
LVDT L6
LVDT L7
-30
-25
-20
-15
-10
-5
0
Deflection, mm
140
120
100
80
60
40
20
0
Load, kN

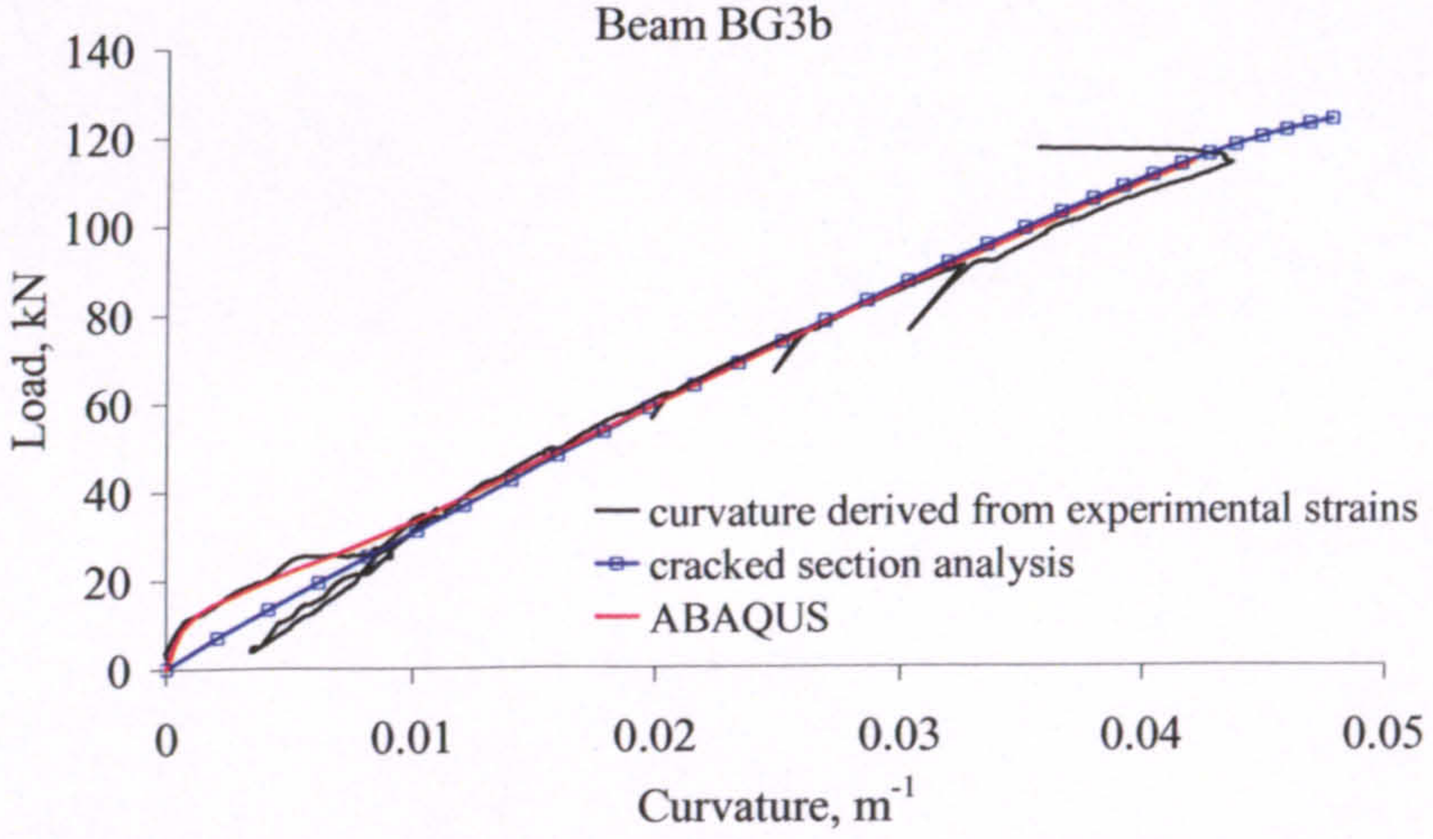
Beam BG3b
Load, kN
140
120
100
80
60
40
20
0
curvature derived from experimental strains
cracked section analysis
ABAQUS
0
0.01
0.02
0.03
0.04
0.05
Curvature, m-1

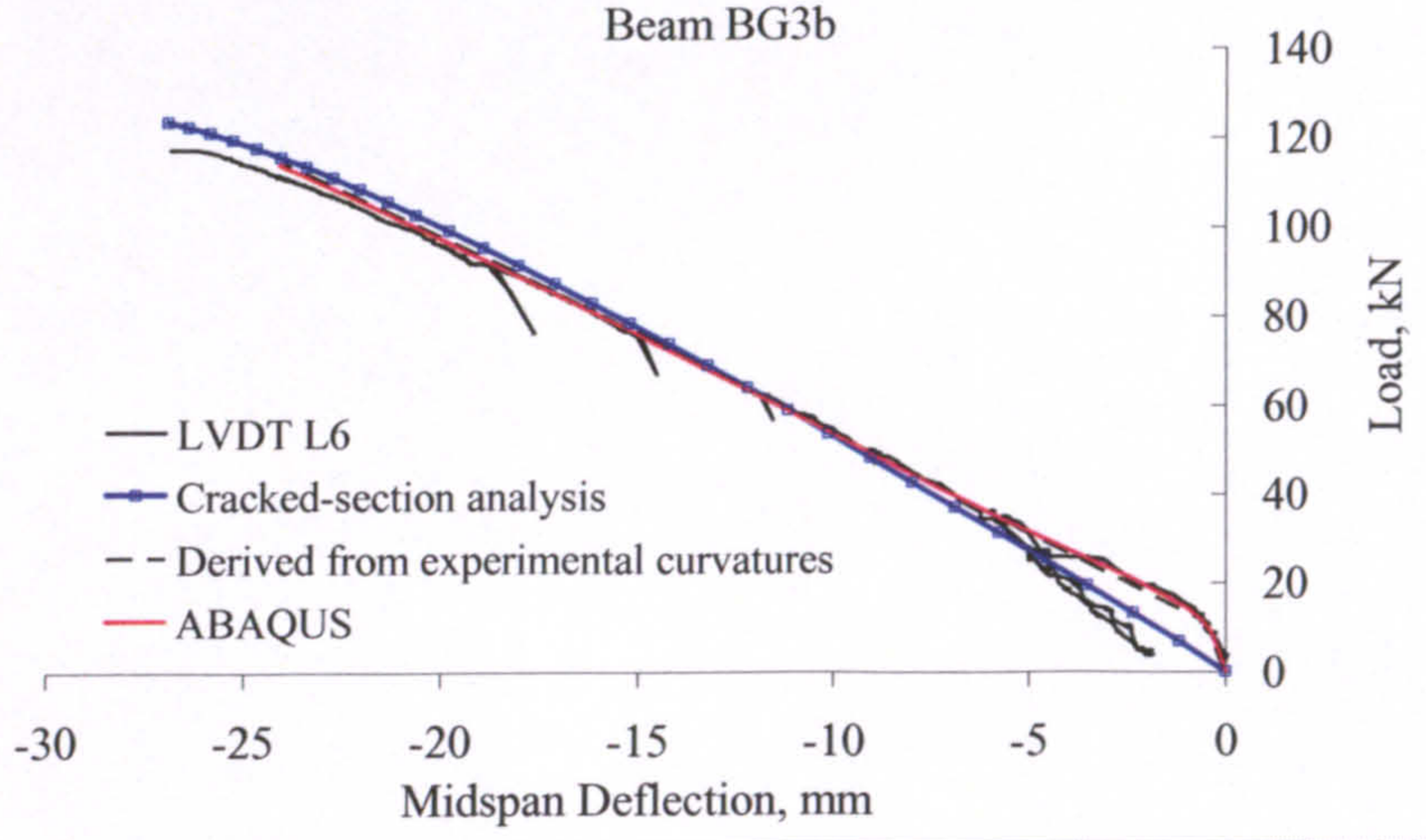
Beam BG3b
LVDT L6
Cracked-section analysis
Derived from experimental curvatures
ABAQUS
-30
-25
-20
-15
-10
-5
0
Midspan Deflection, mm
140
120
100
80
60
40
20
0
Load, kN

BEAM BG3b

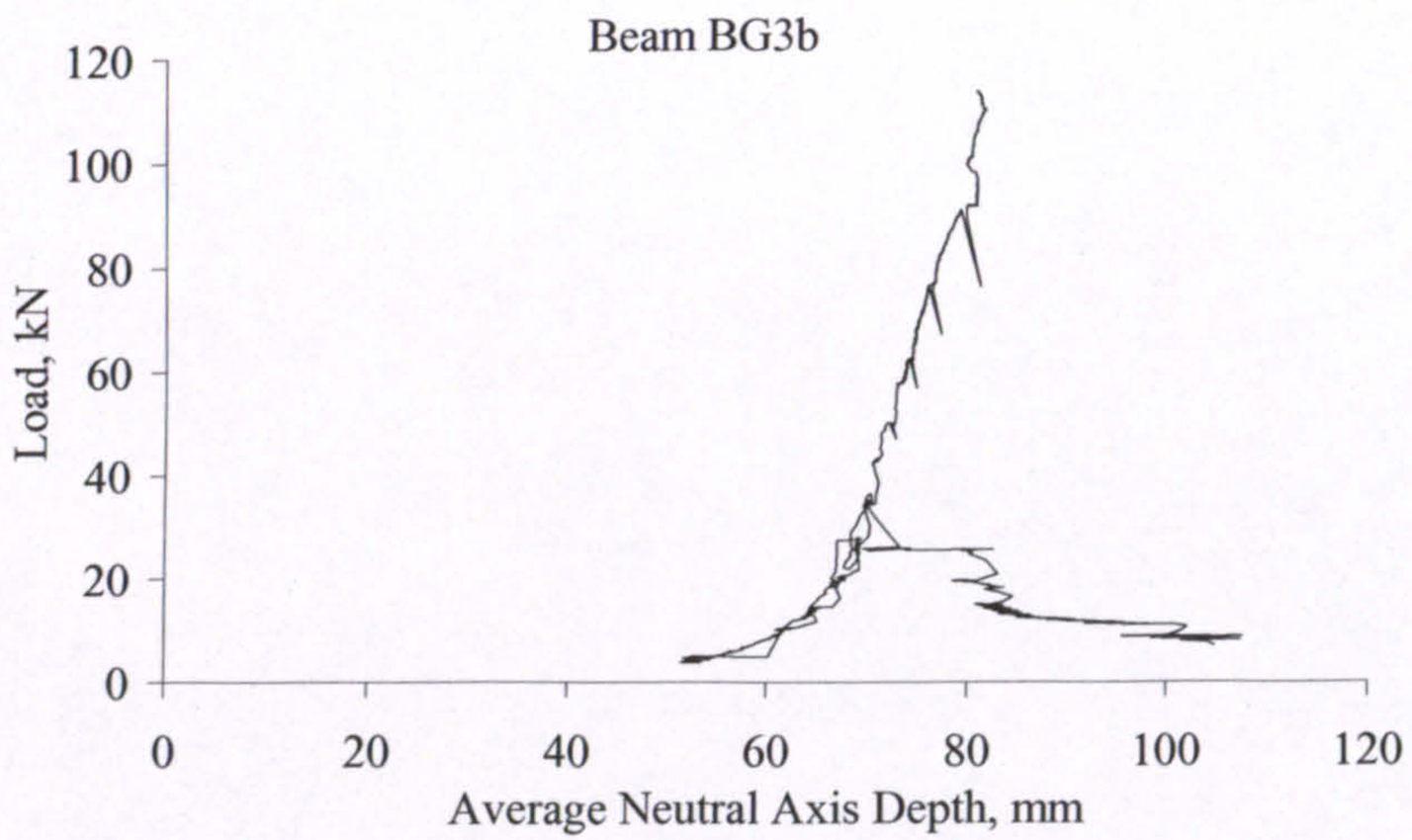
Beam BG3b
Load, kN
0
20
40
60
80
100
120
Average Neutral Axis Depth, mm

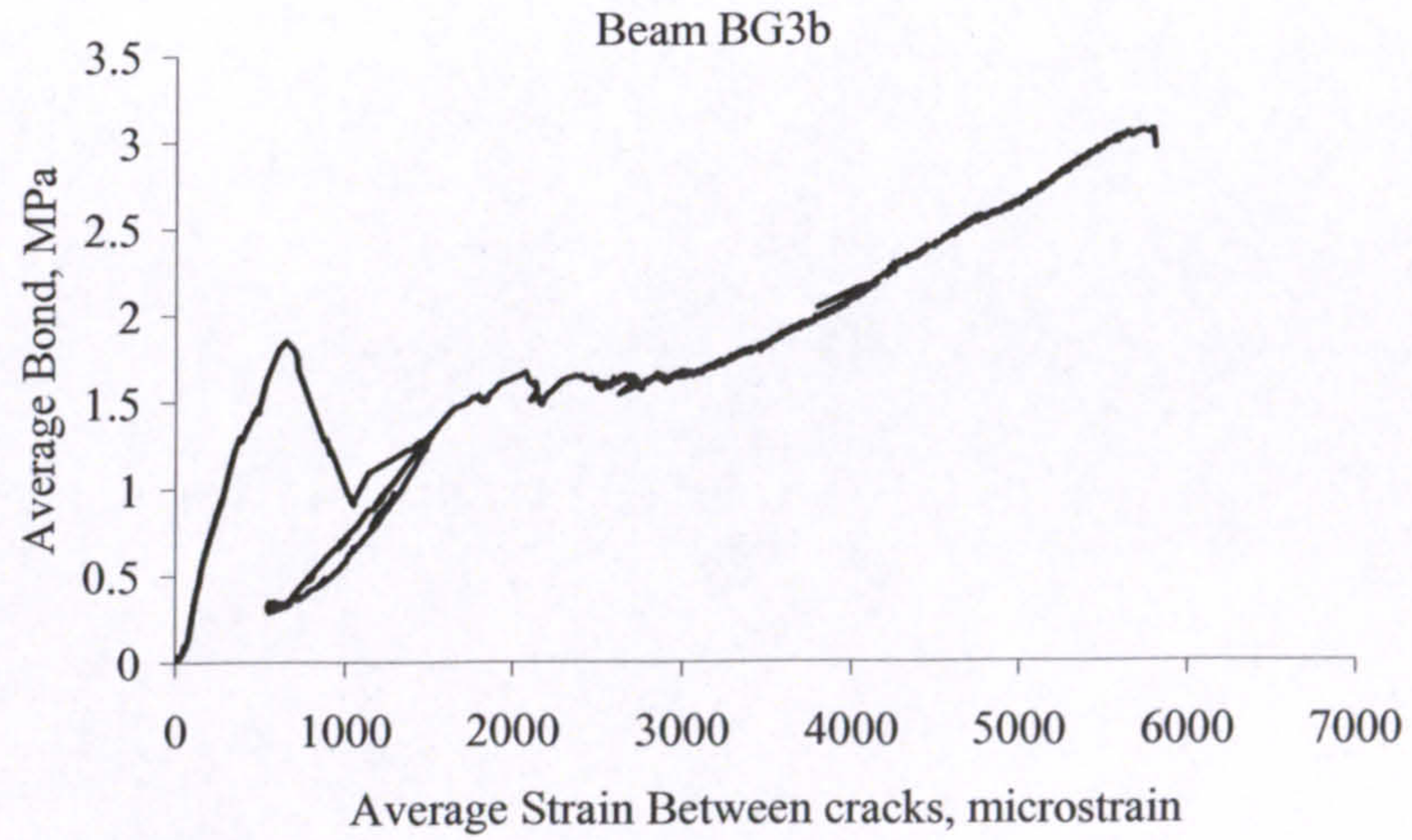
Beam BG3b
Average Bond, MPa
0
0.5
1
1.5
2
2.5
3
3.5
0
1000
2000
3000
4000
5000
6000
7000
Average Strain Between cracks, microstrain

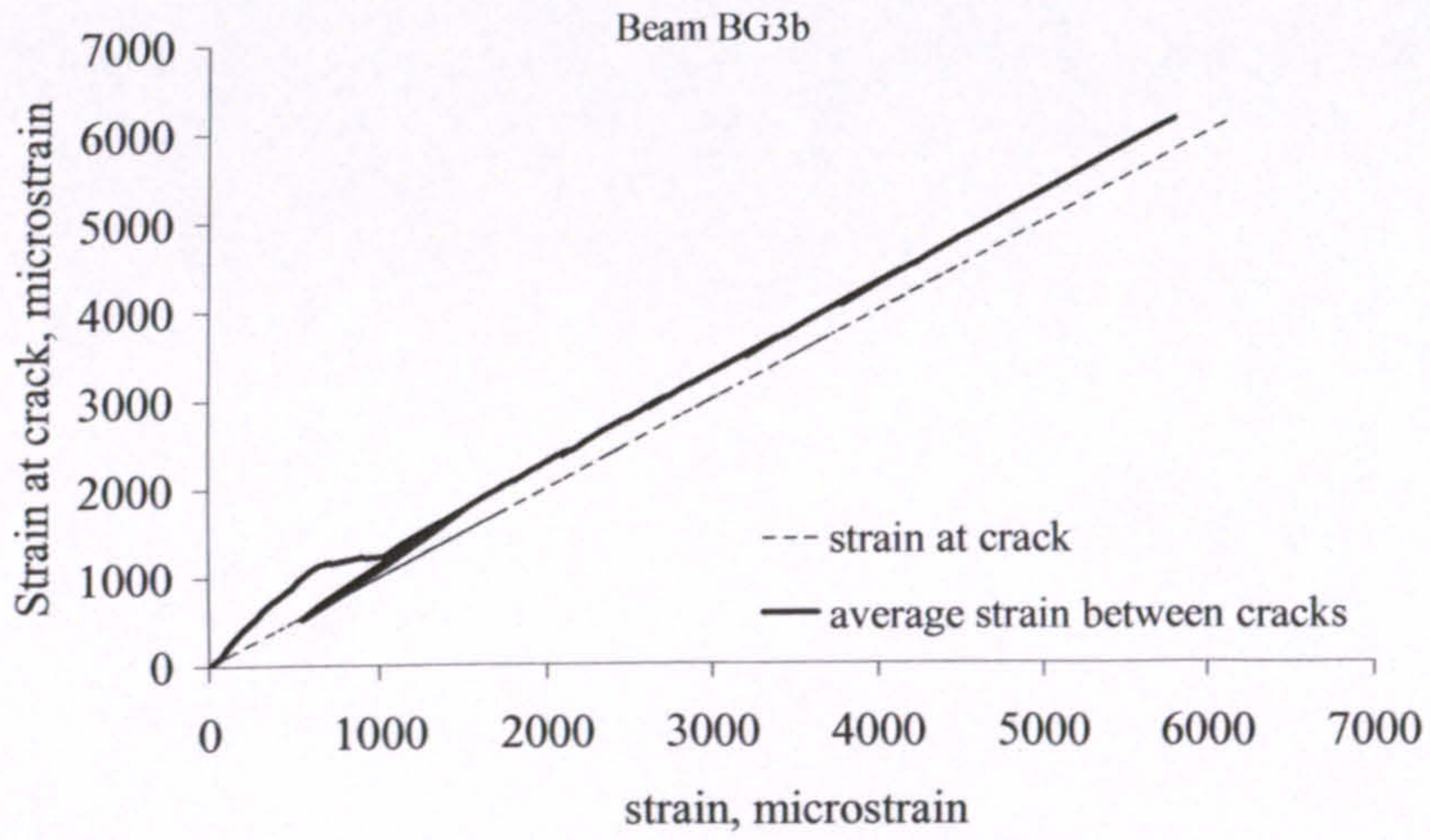
Beam BG3b
Strain at crack, microstrain
0
1000
2000
3000
4000
5000
6000
7000
strain at crack
average strain between cracks
strain, microstrain

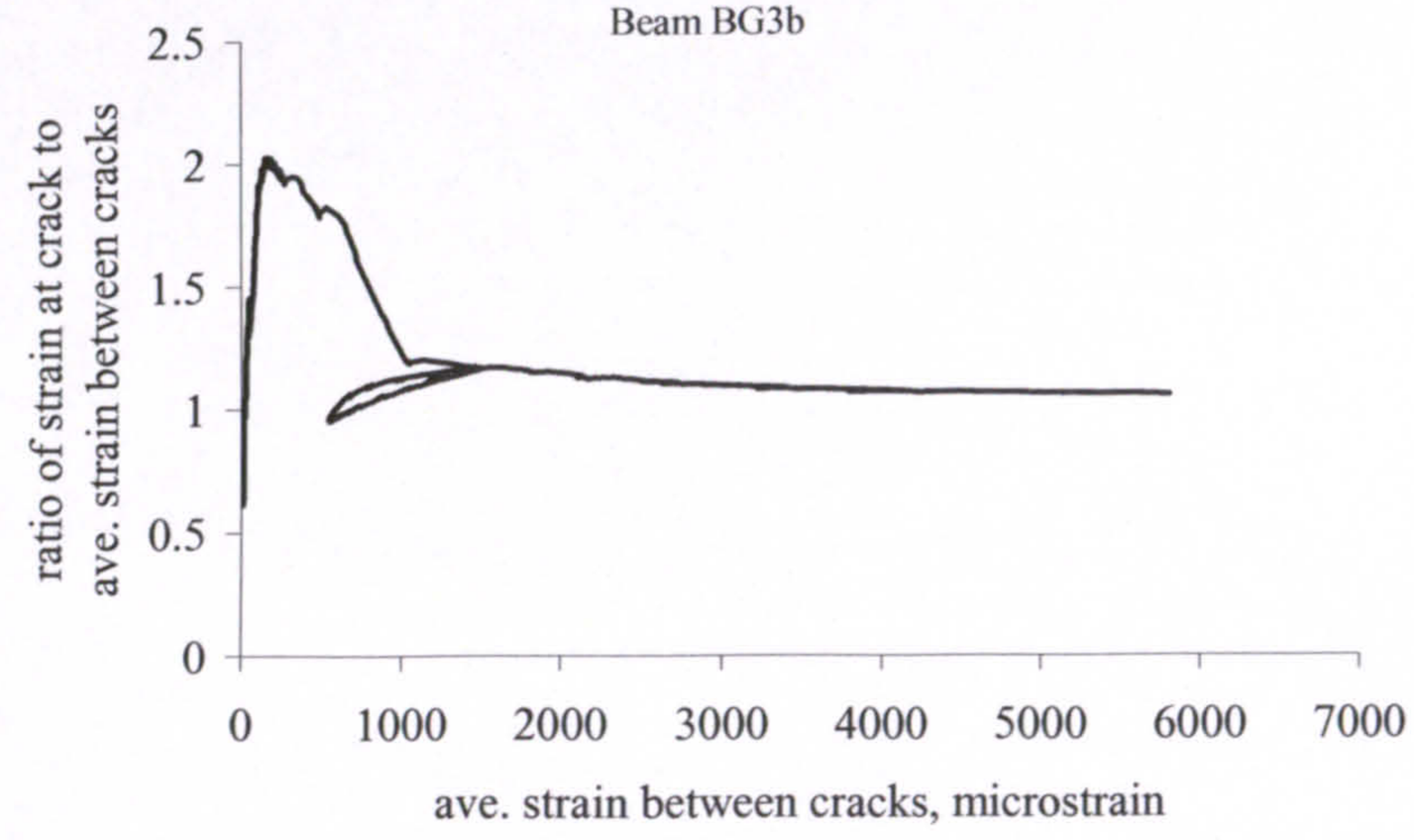
Beam BG3b
ratio of strain at crack to ave. strain between cracks
0
0.5
1
1.5
2
2.5
0
1000
2000
3000
4000
5000
6000
7000
ave. strain between cracks, microstrain

BEAM BG3b

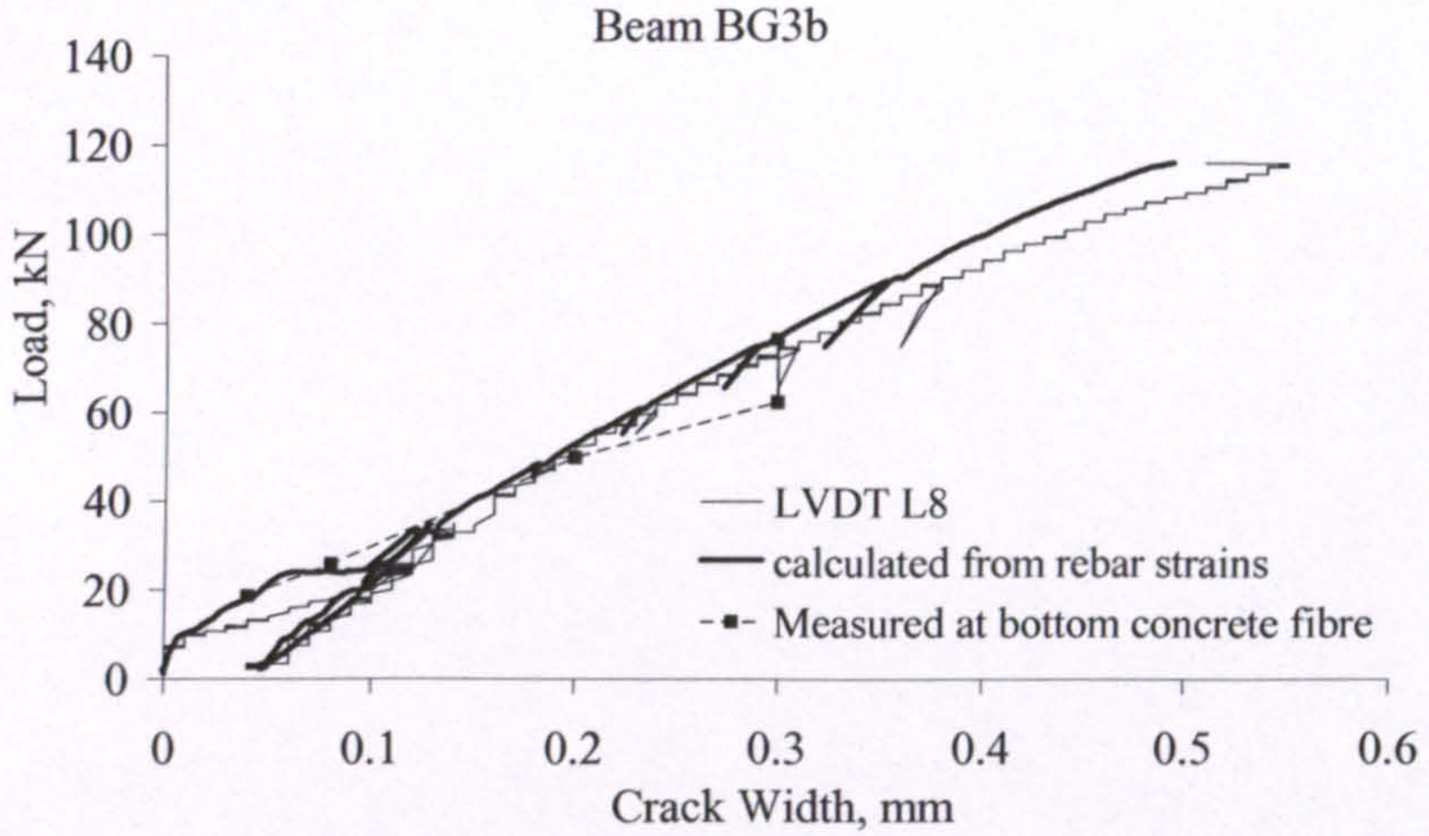

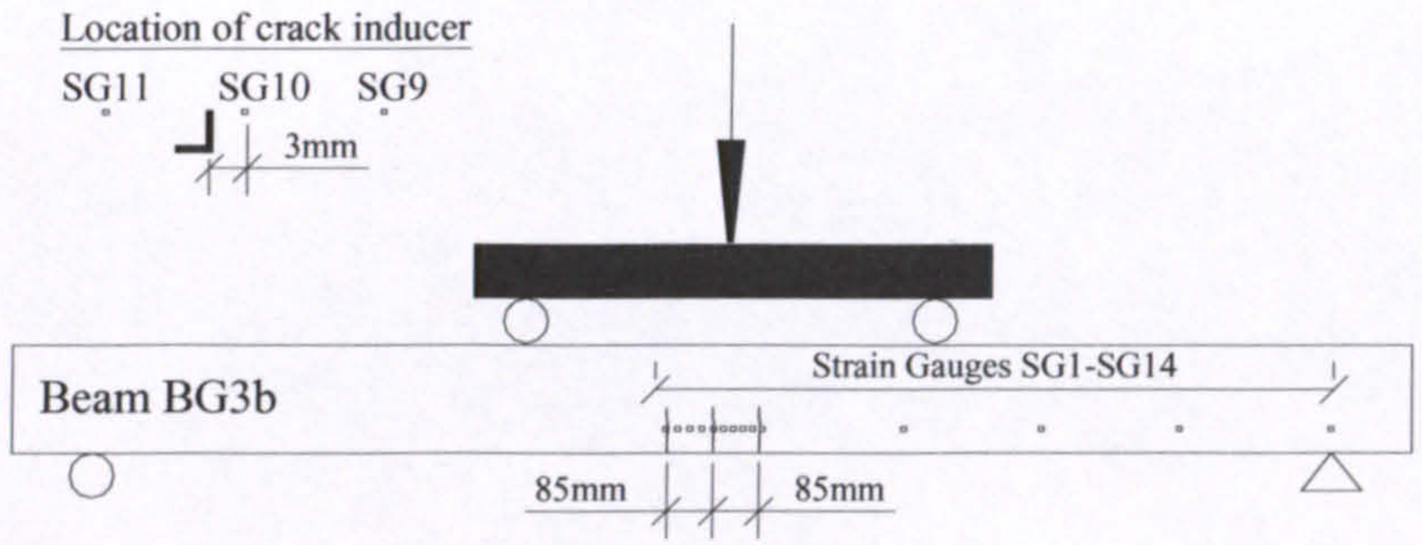

Cracks around Centre

Compressive concrete failure.

BEAM BC1a

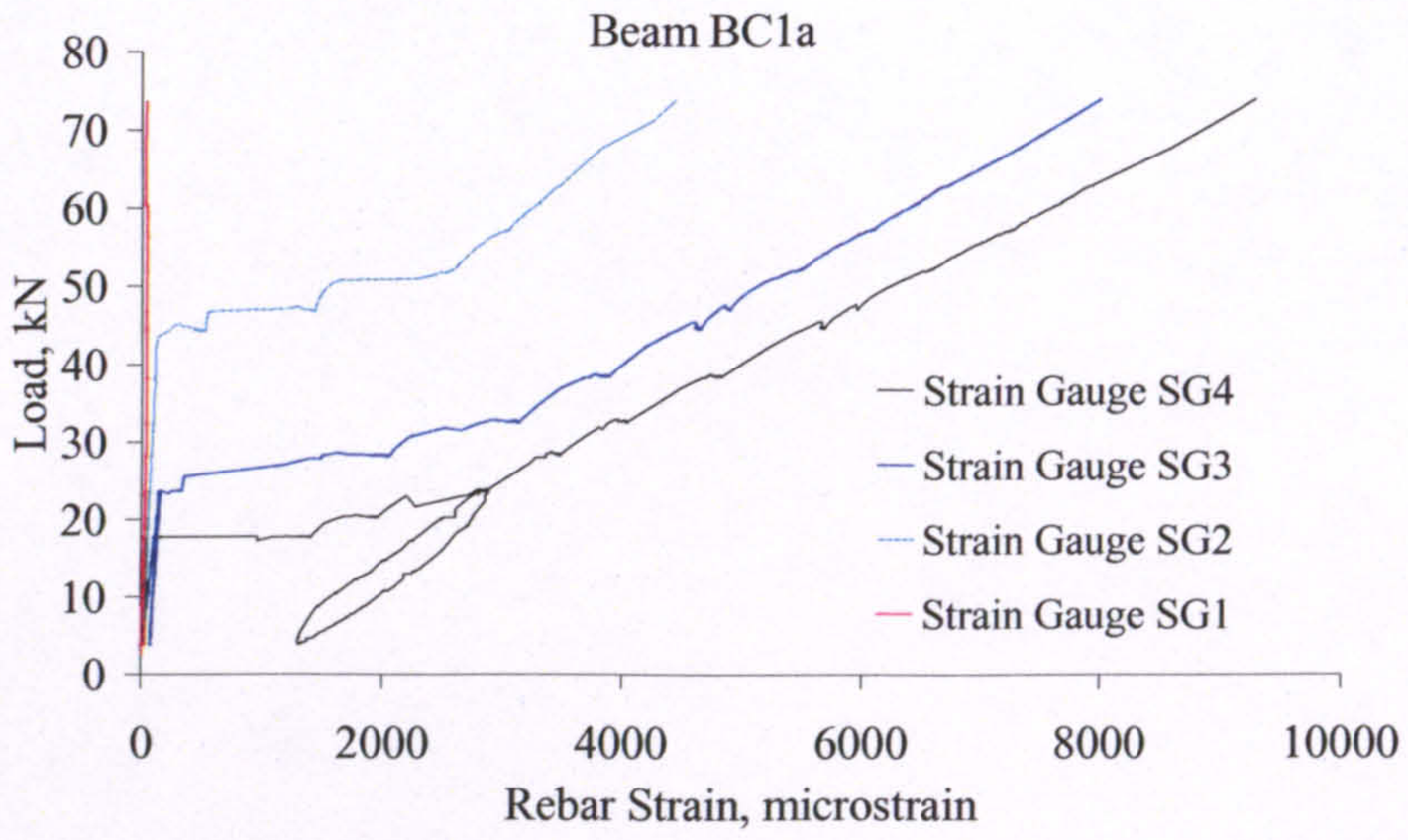
Beam BC1a
Load, kN
Rebar Strain, microstrain
Strain Gauge SG4
Strain Gauge SG3
Strain Gauge SG2
Strain Gauge SG1

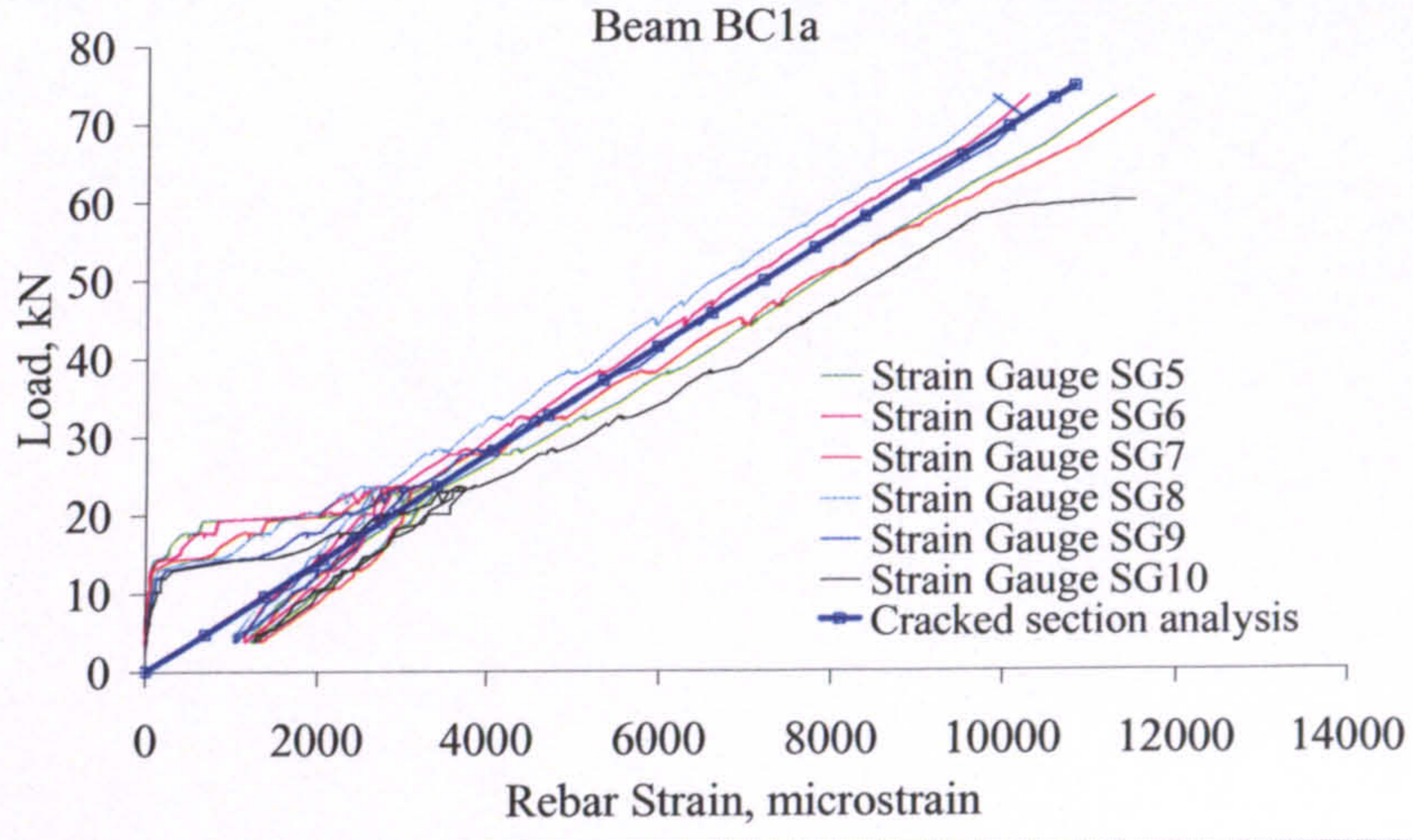
Beam BC1a
Load, kN
Rebar Strain, microstrain
Strain Gauge SG5
Strain Gauge SG6
Strain Gauge SG7
Strain Gauge SG8
Strain Gauge SG9
Strain Gauge SG10
Cracked section analysis

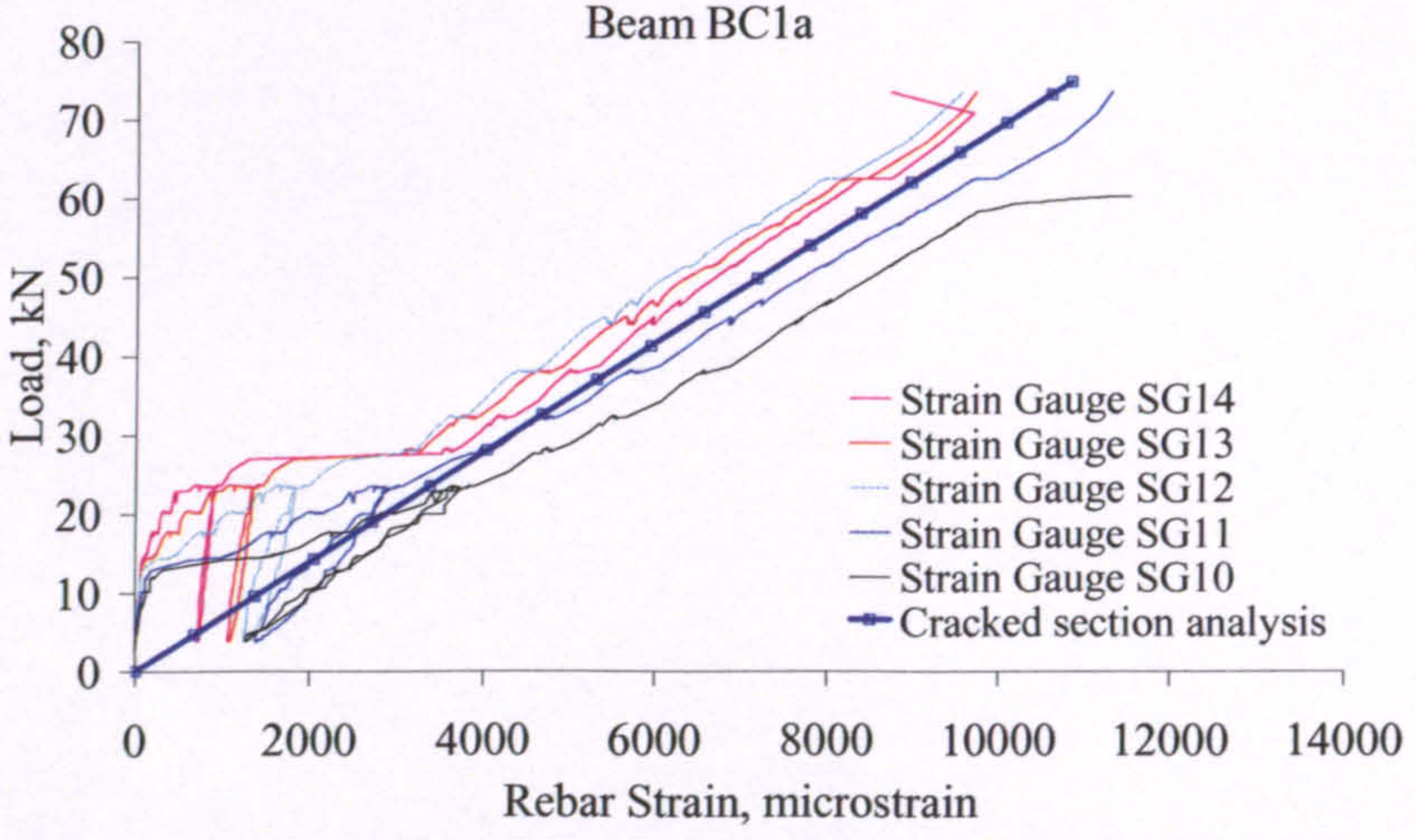
Beam BC1a
Load, kN
Rebar Strain, microstrain
Strain Gauge SG14
Strain Gauge SG13
Strain Gauge SG12
Strain Gauge SG11
Strain Gauge SG10
Cracked section analysis

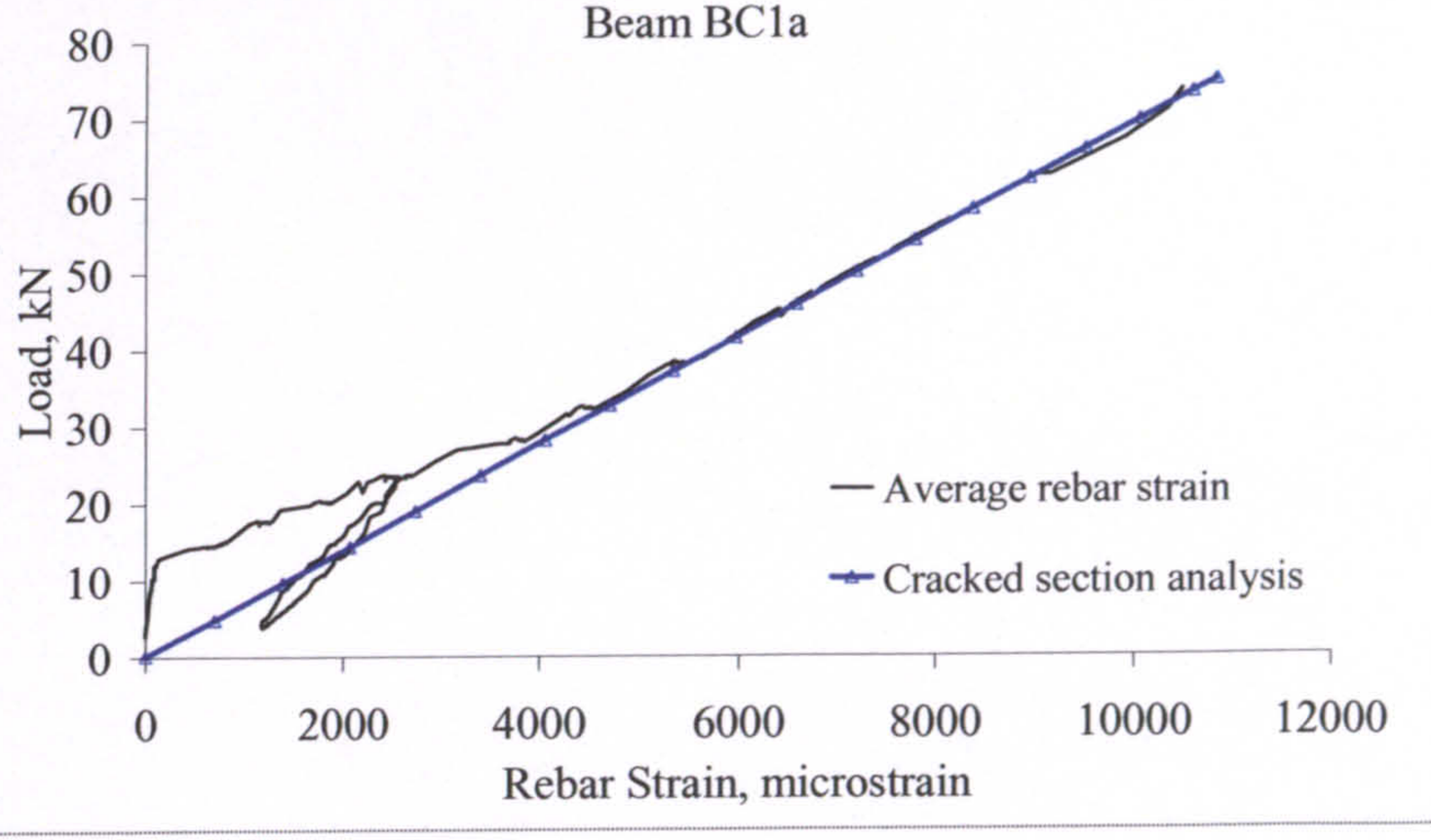
Beam BC1a
Load, kN
Rebar Strain, microstrain
Average rebar strain
Cracked section analysis

BEAM BC1a

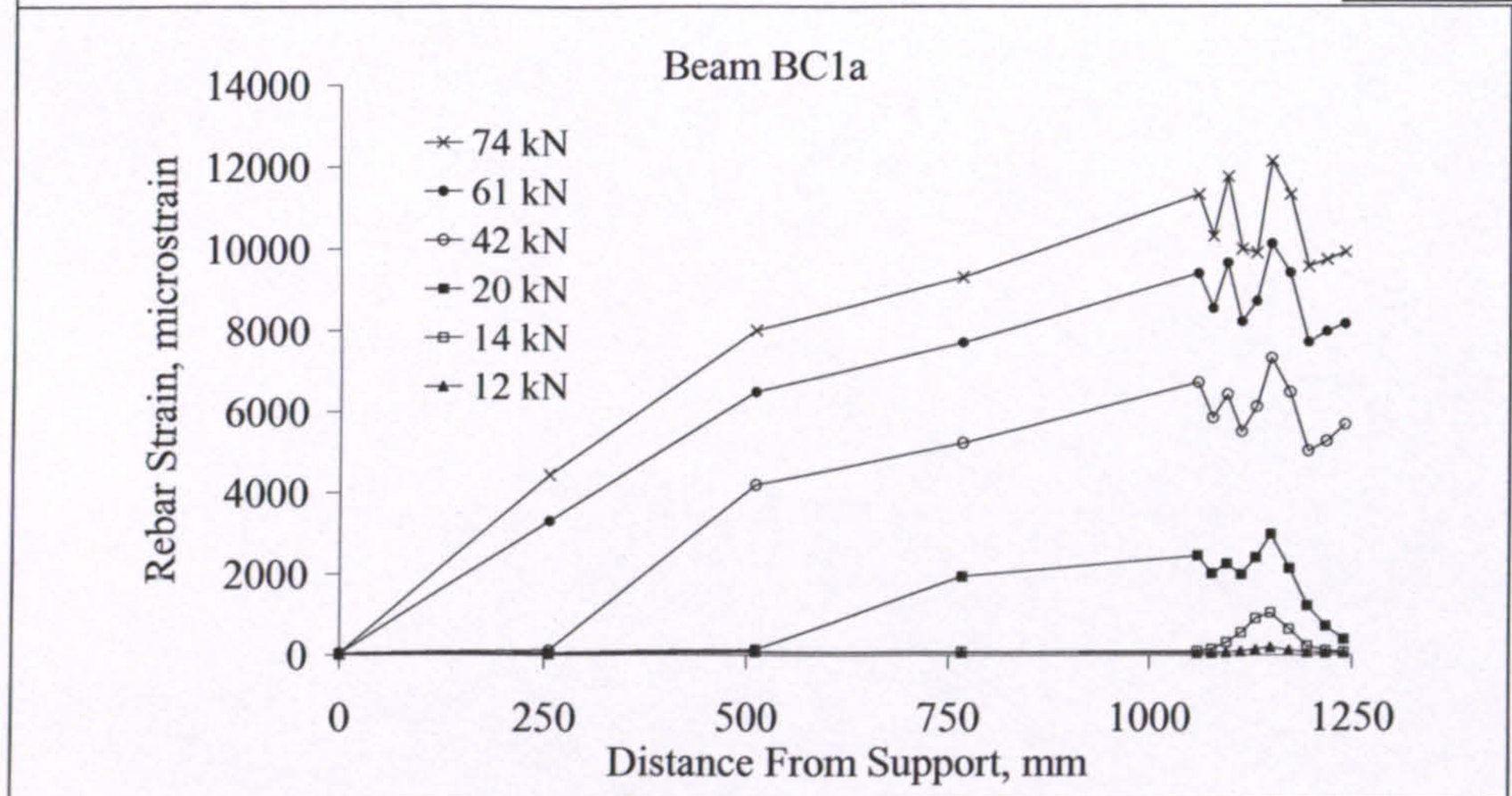
Beam BC1a
Rebar Strain, microstrain
14000
12000
10000
8000
6000
4000
2000
0
74 kN
61 kN
42 kN
20 kN
14 kN
12 kN
0
250
500
750
1000
1250
Distance From Support, mm

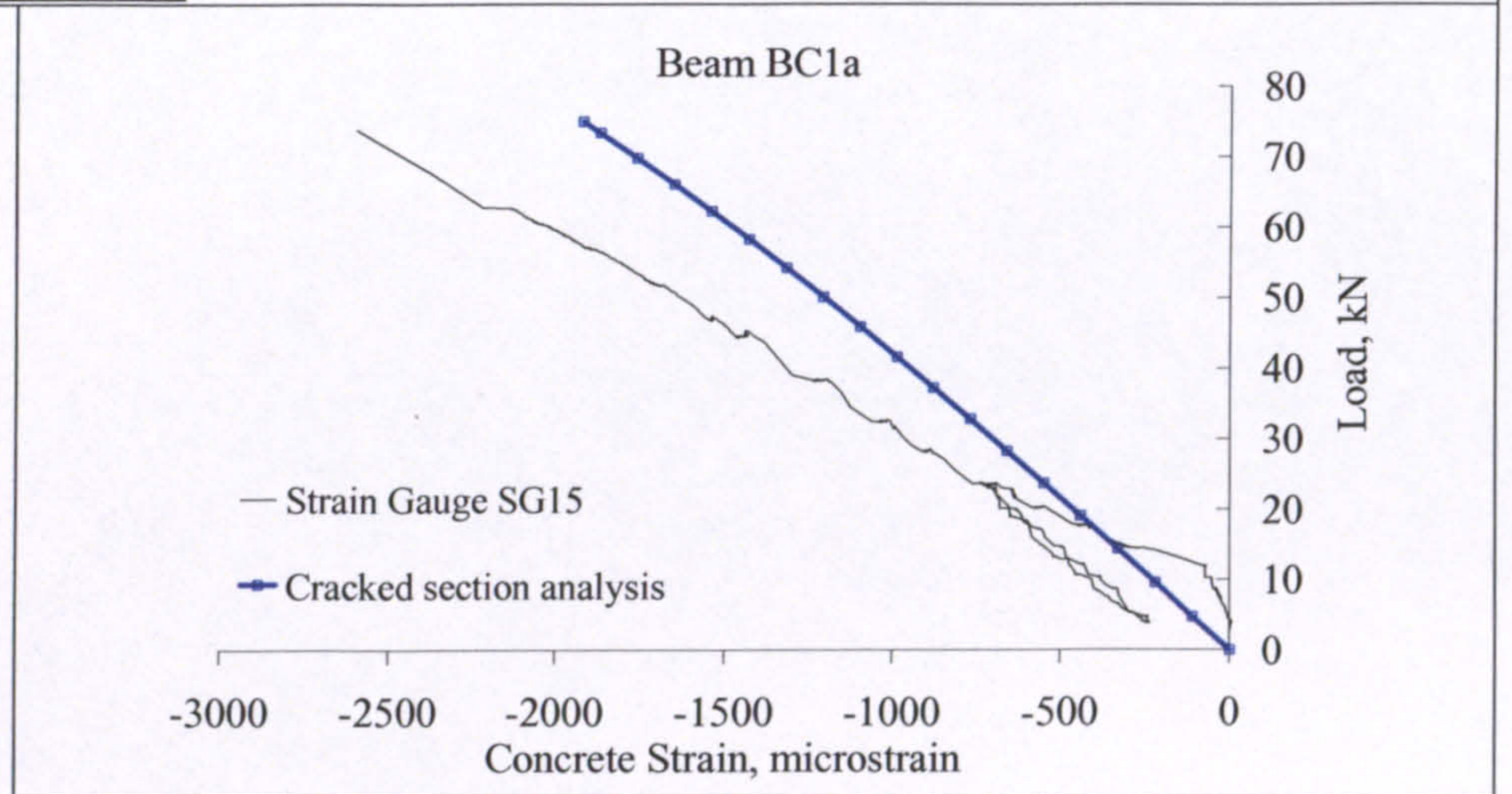
Beam BC1a
Load, kN
80
70
60
50
40
30
20
10
0
Strain Gauge SG15
Cracked section analysis
-3000
-2500
-2000
-1500
-1000
-500
0
Concrete Strain, microstrain

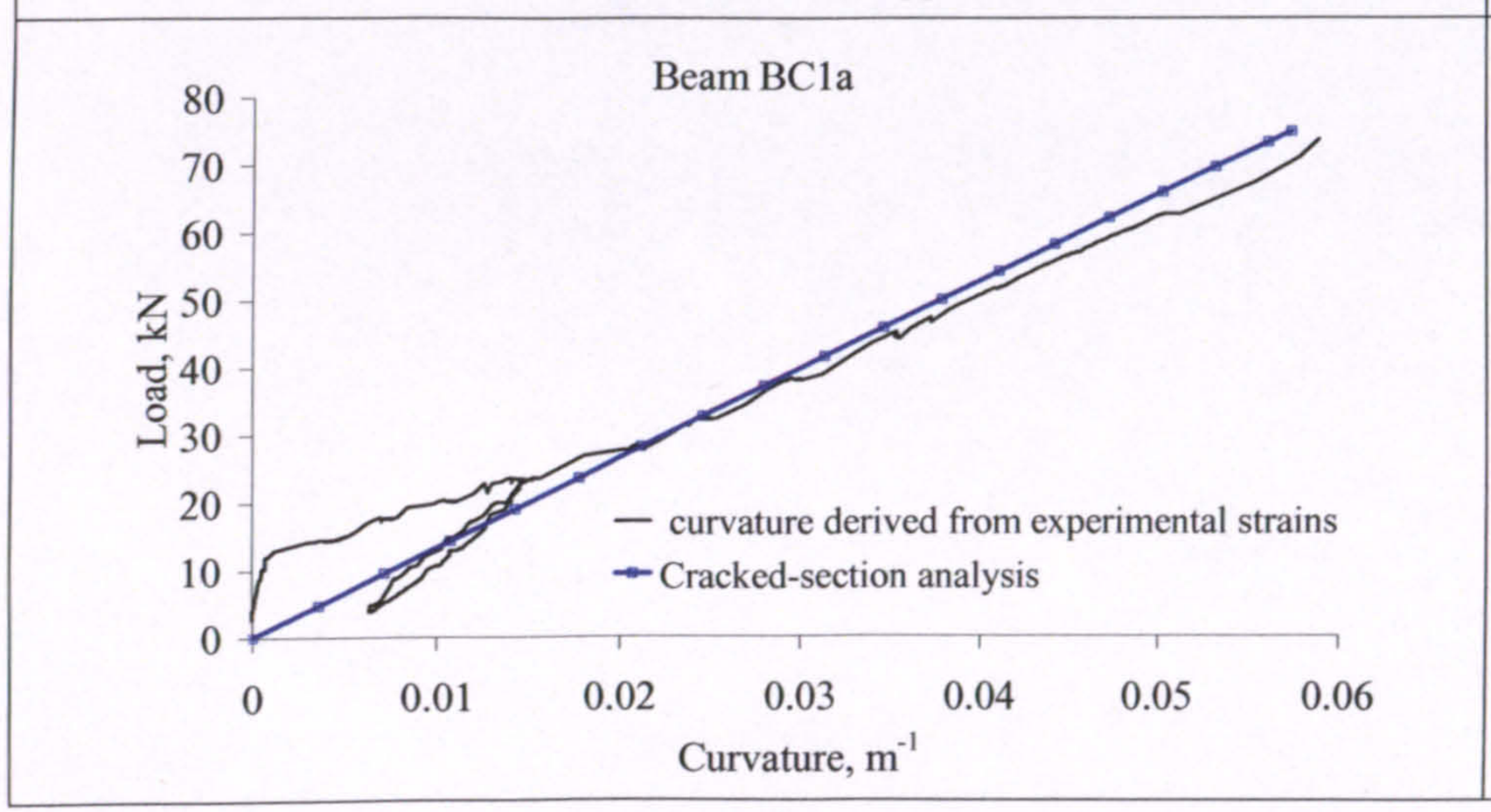
Beam BC1a
Load, kN
80
70
60
50
40
30
20
10
0
curvature derived from experimental strains
Cracked-section analysis
0
0.01
0.02
0.03
0.04
0.05
0.06
Curvature, m-1

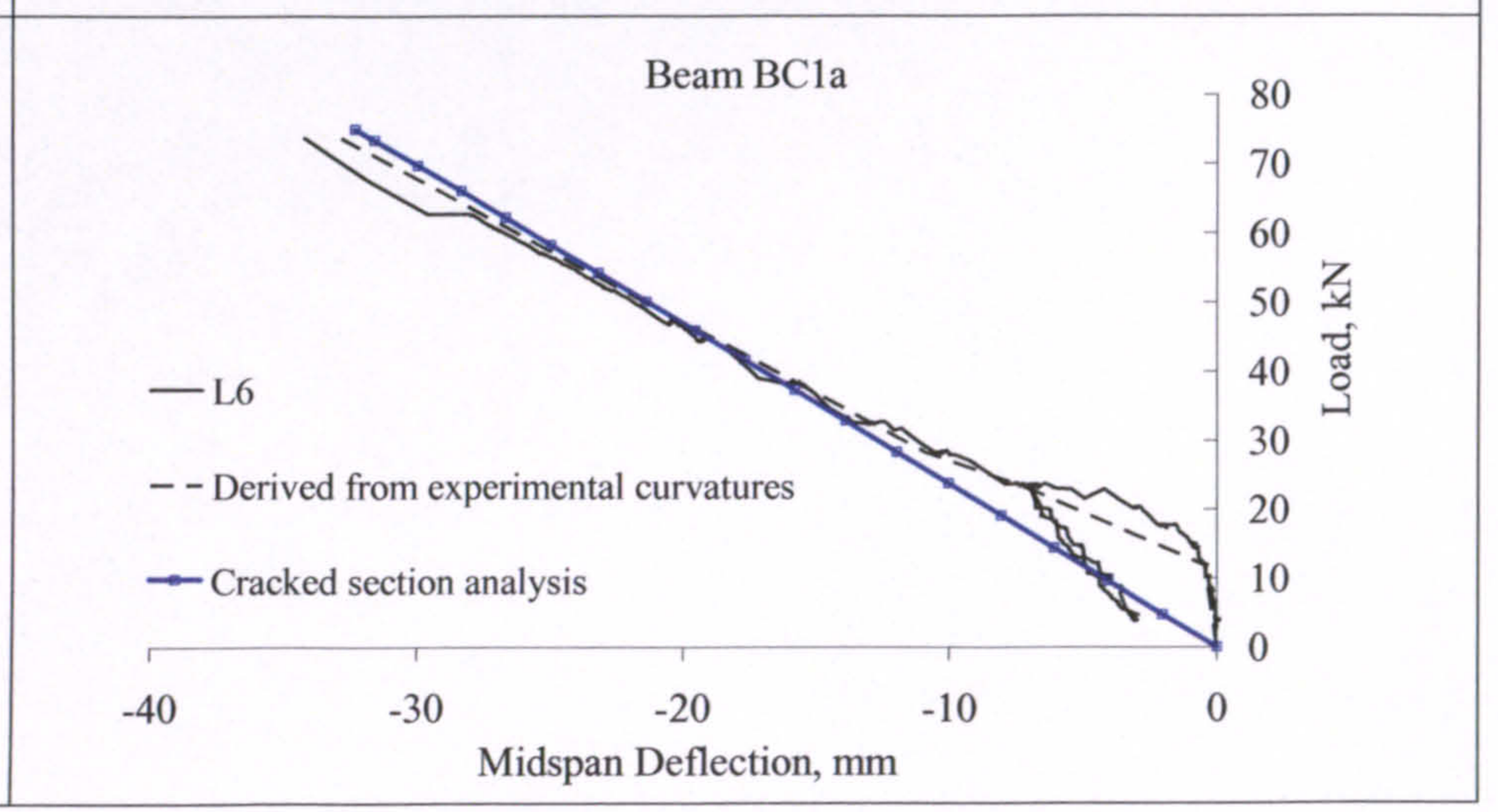
Beam BC1a
Load, kN
80
70
60
50
40
30
20
10
0
L6
Derived from experimental curvatures
Cracked section analysis
-40
-30
-20
-10
0
Midspan Deflection, mm

BEAM BC1a

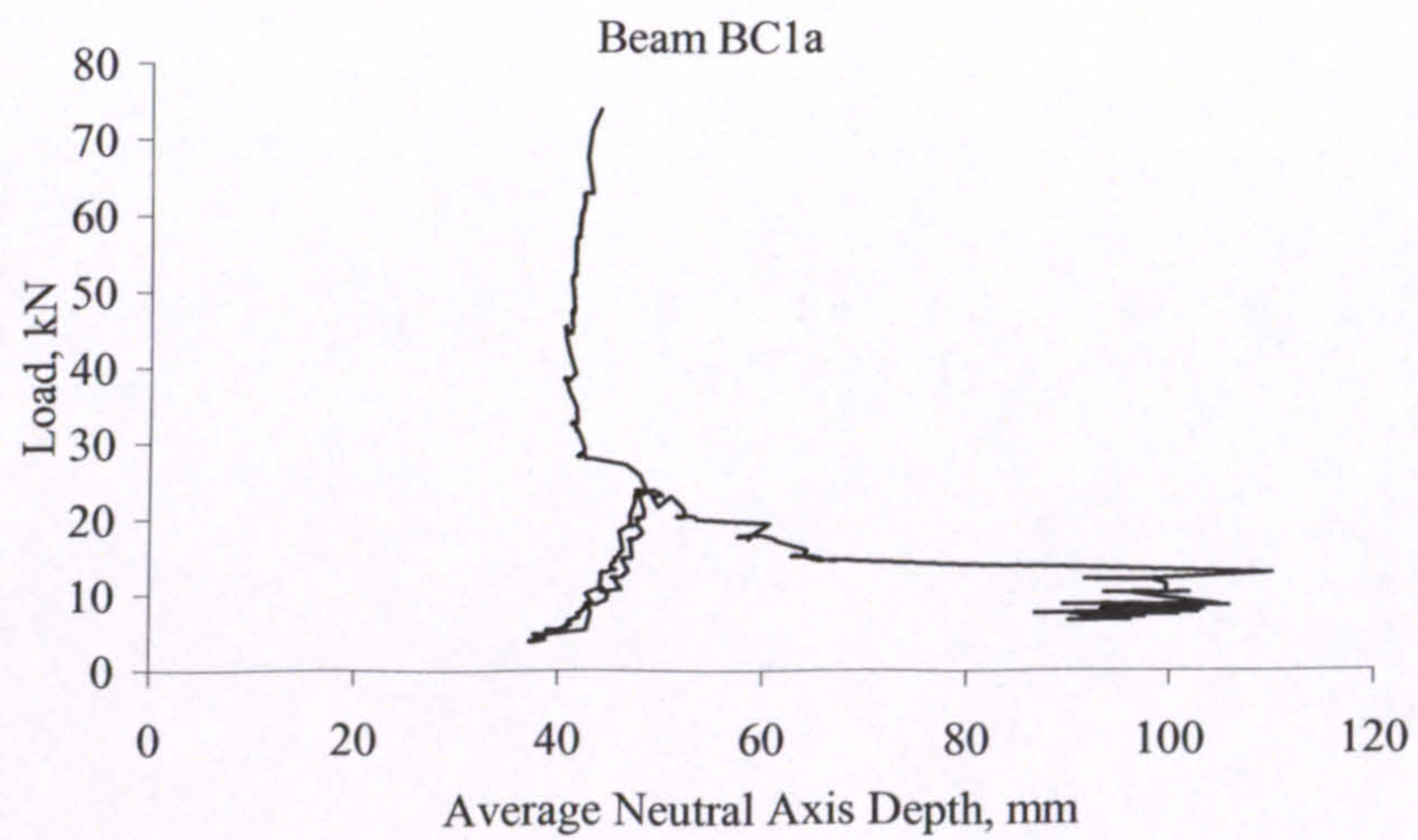
Beam BC1a
Load, kN
0
10
20
30
40
50
60
70
80
0
20
40
60
80
100
120
Average Neutral Axis Depth, mm

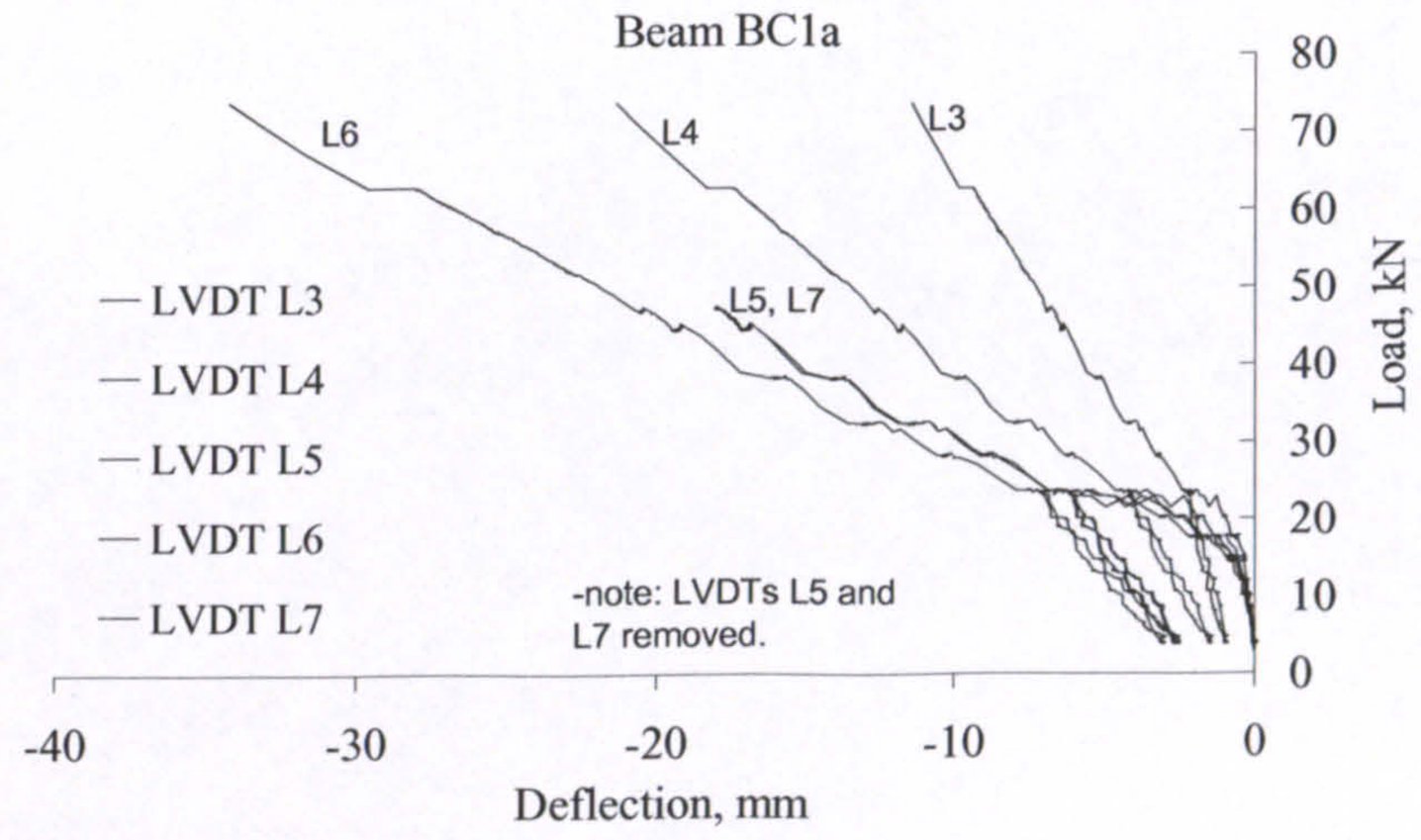
Beam BC1a
L6
L4
L3
L5, L7
— LVDT L3
— LVDT L4
— LVDT L5
— LVDT L6
— LVDT L7
-note: LVDTs L5 and L7 removed.
Load, kN
0
10
20
30
40
50
60
70
80
-40
-30
-20
-10
0
Deflection, mm

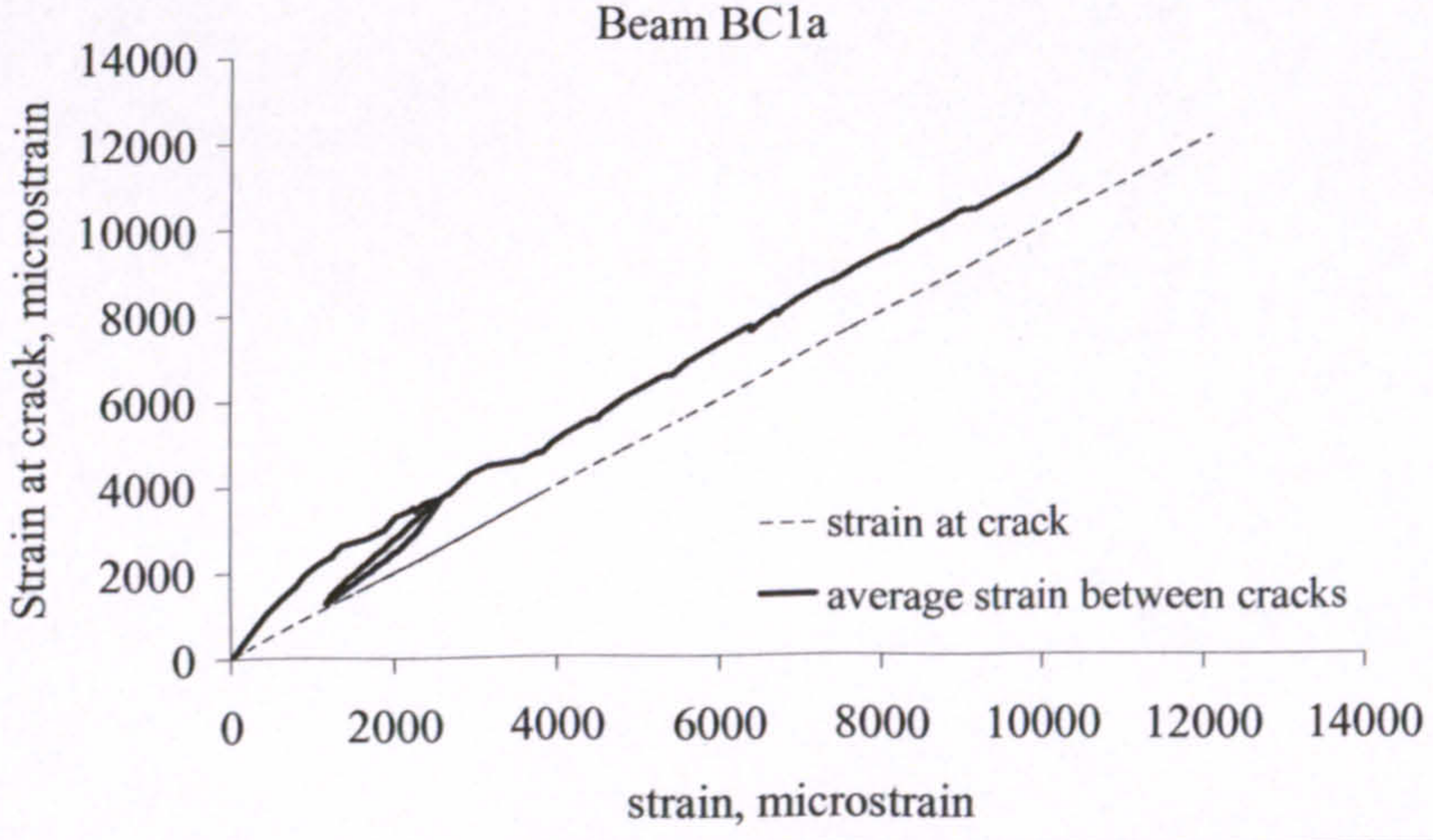
Beam BC1a
Strain at crack, microstrain
0
2000
4000
6000
8000
10000
12000
14000
--- strain at crack
— average strain between cracks
strain, microstrain

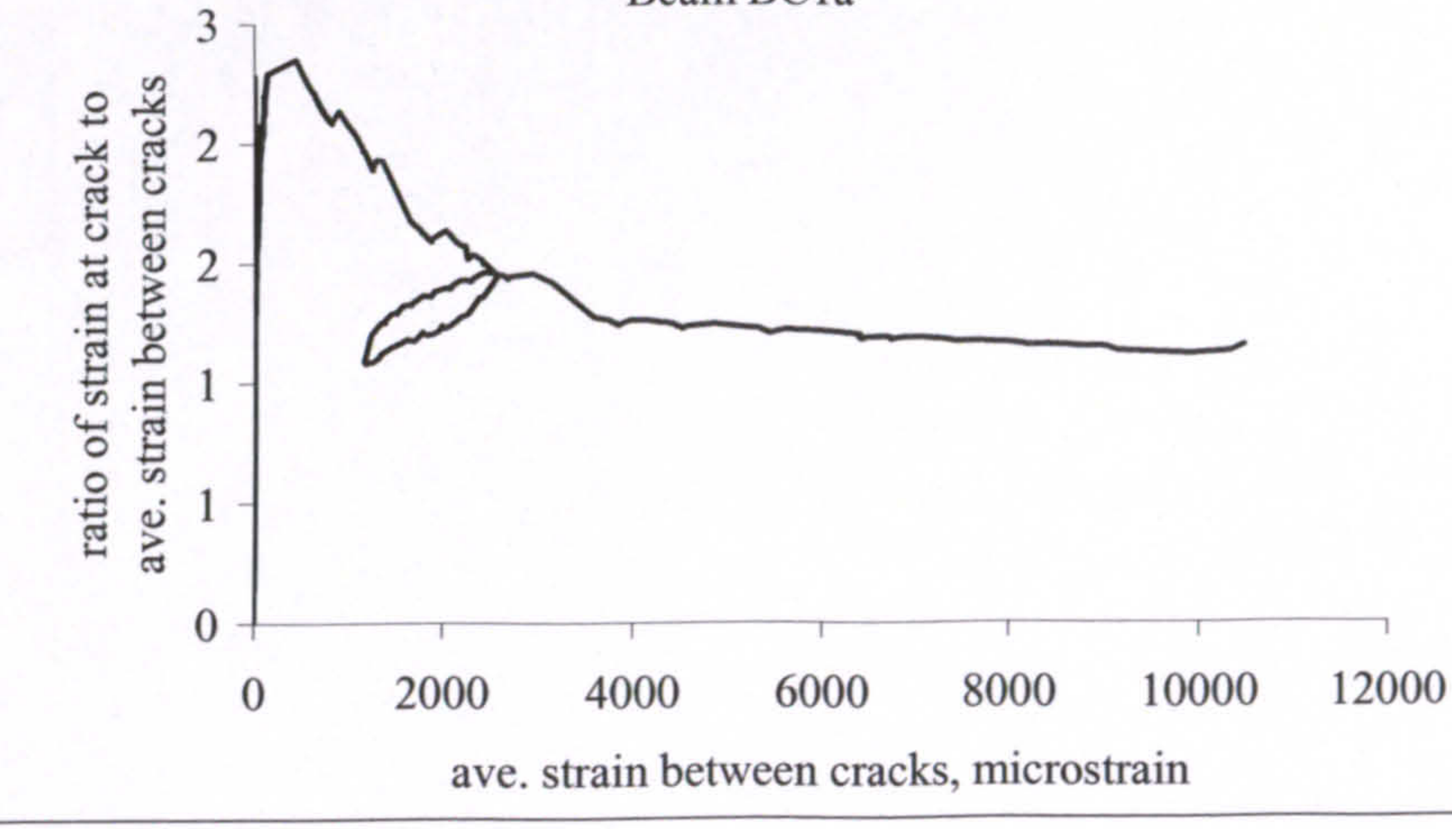
Beam BC1a
ratio of strain at crack to ave. strain between cracks
0
1
1
2
2
3
0
2000
4000
6000
8000
10000
12000
ave. strain between cracks, microstrain

BEAM BC1a

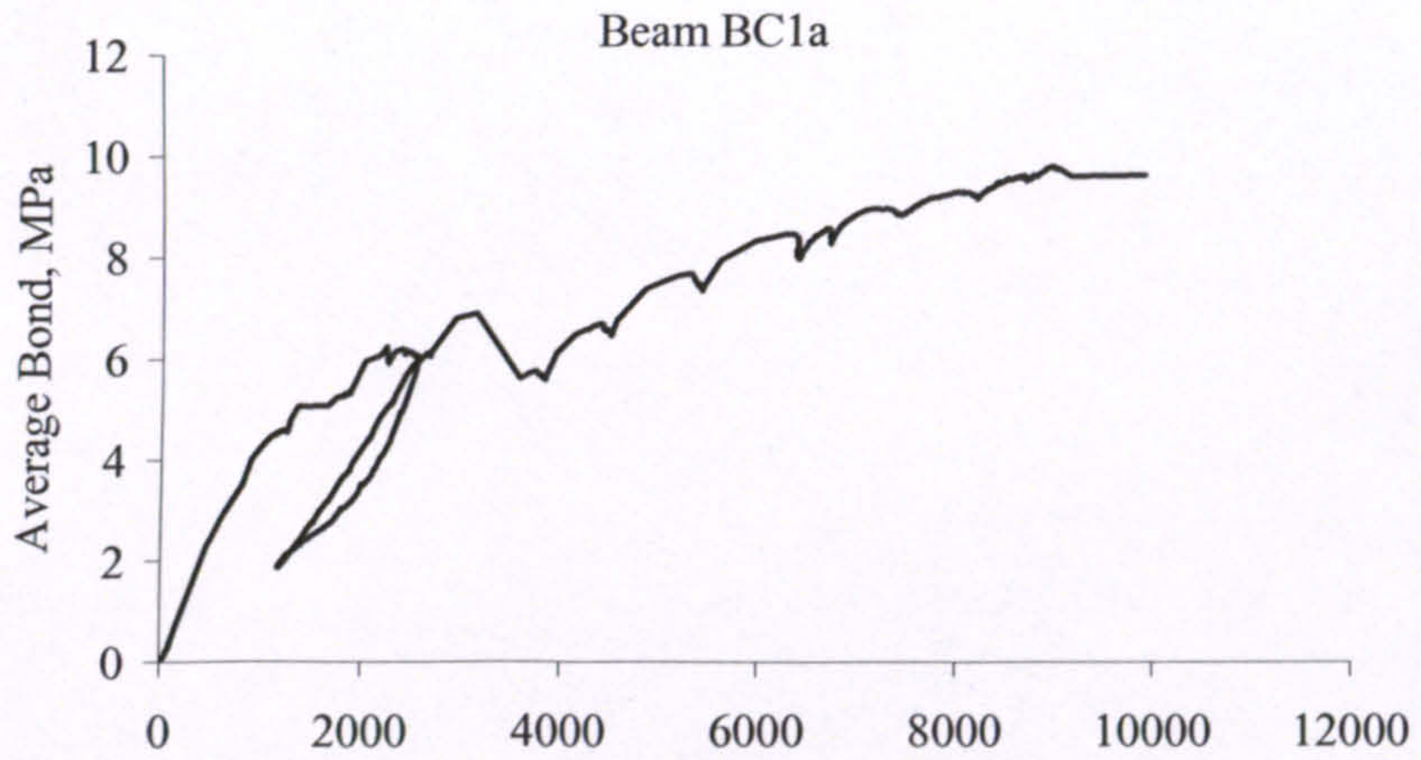

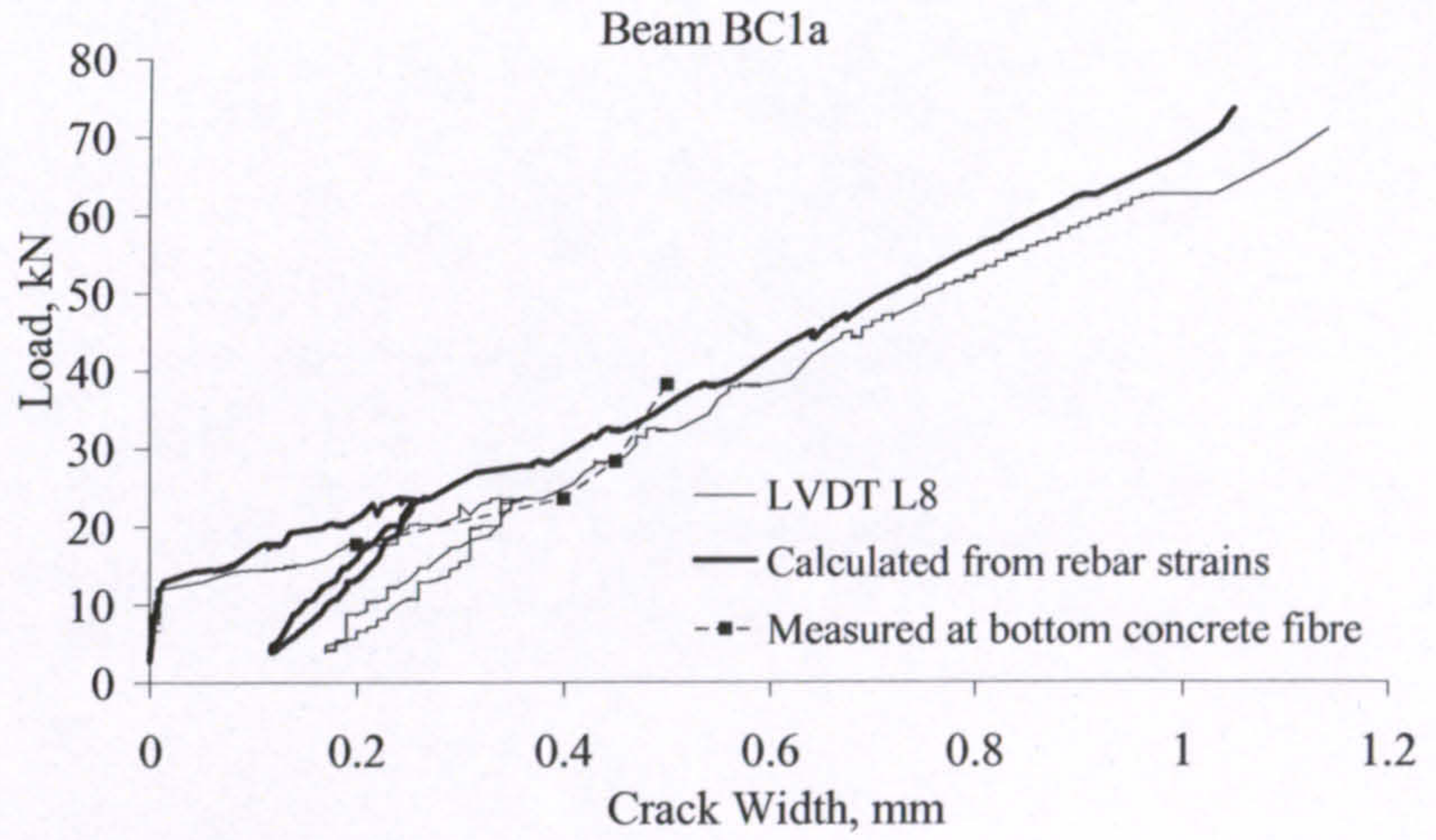

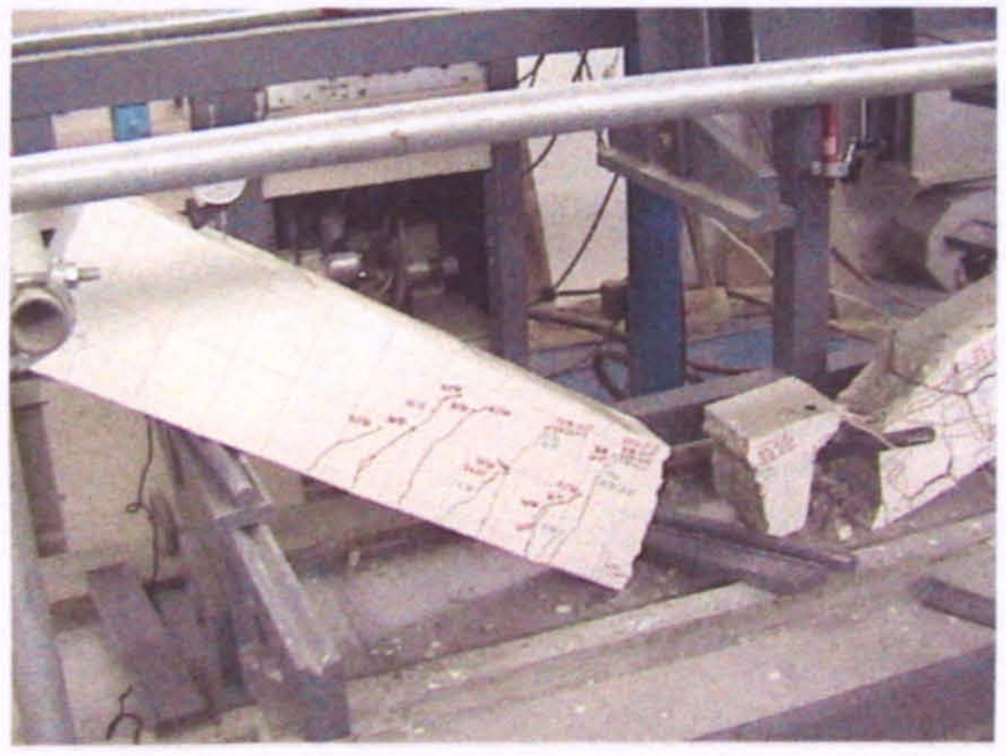

Failure by rupture of rebars

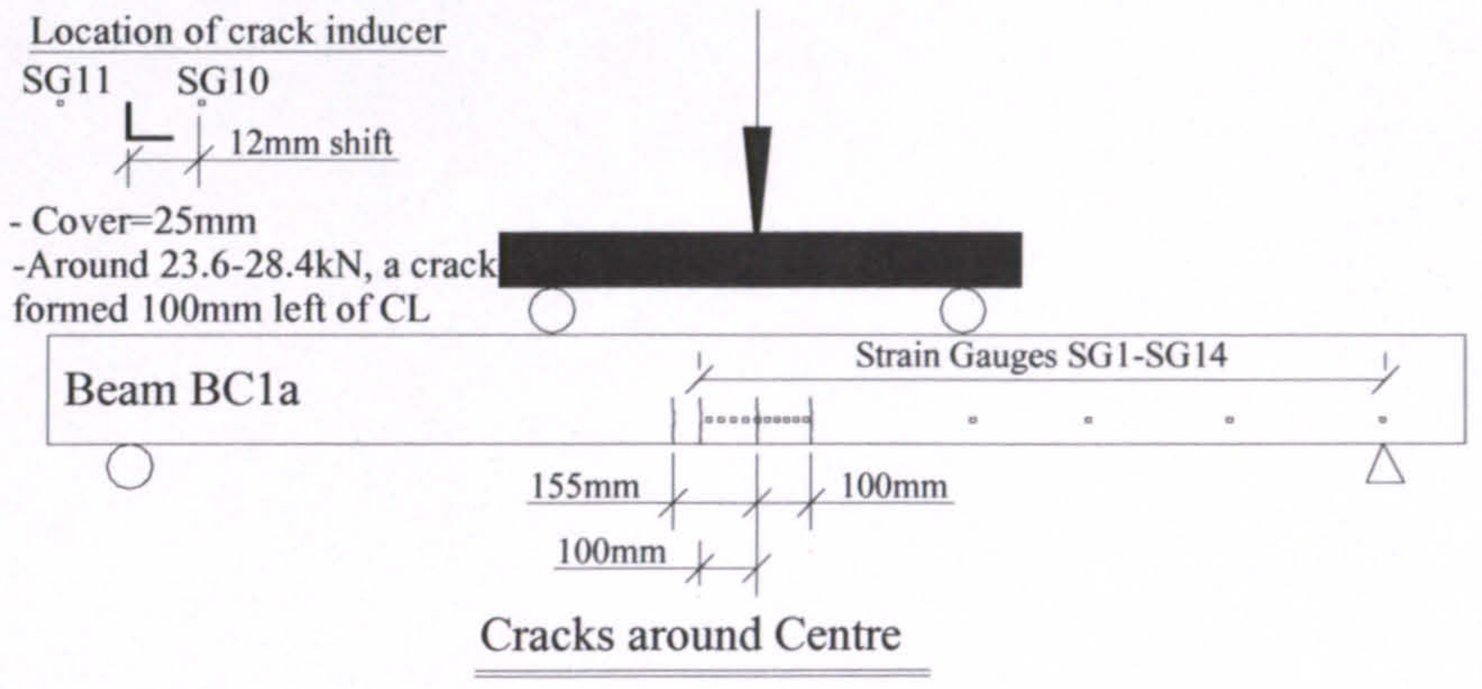

Cracks around Centre

BEAM BC1b

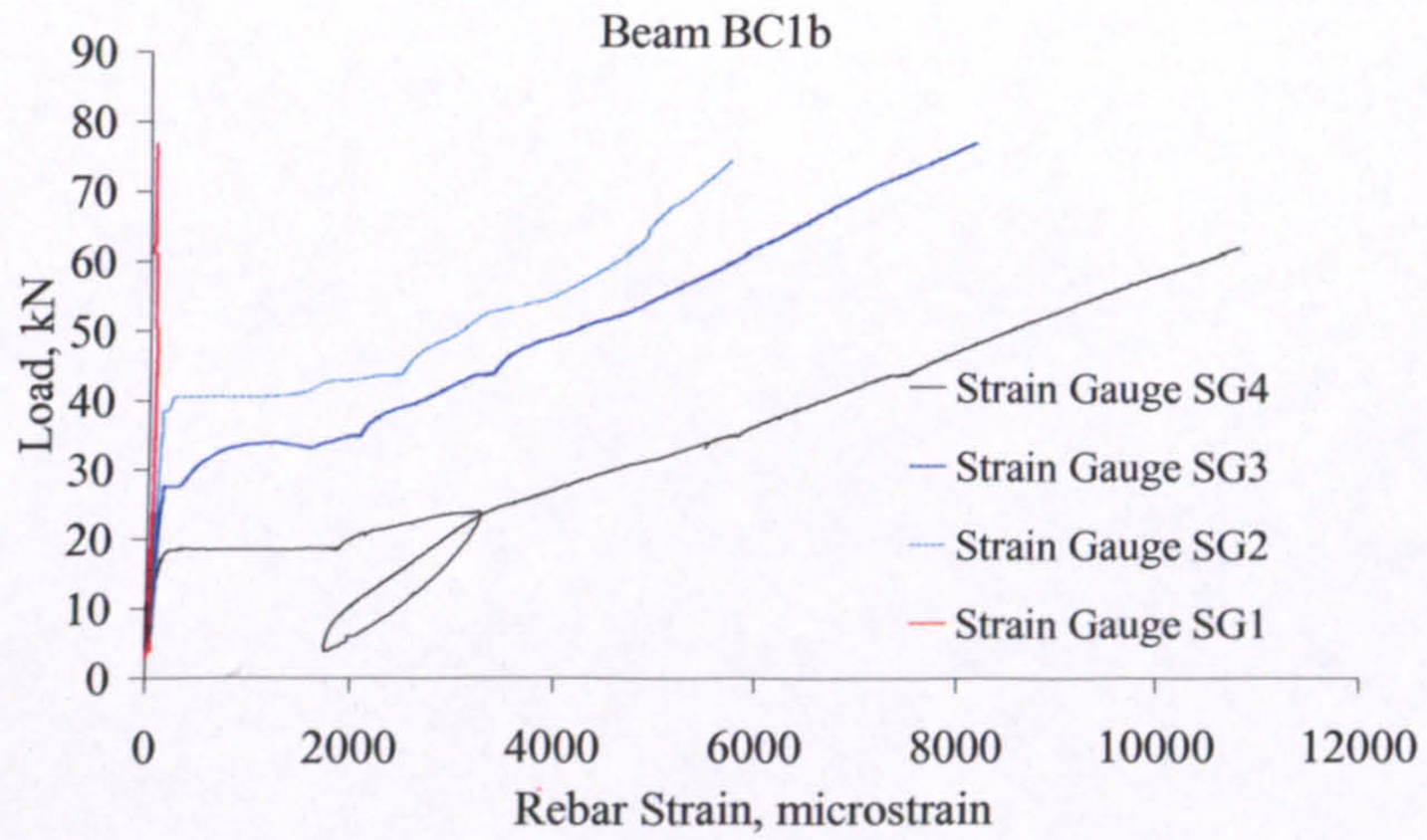
Beam BC1b
Load, kN
Rebar Strain, microstrain
Strain Gauge SG4
Strain Gauge SG3
Strain Gauge SG2
Strain Gauge SG1

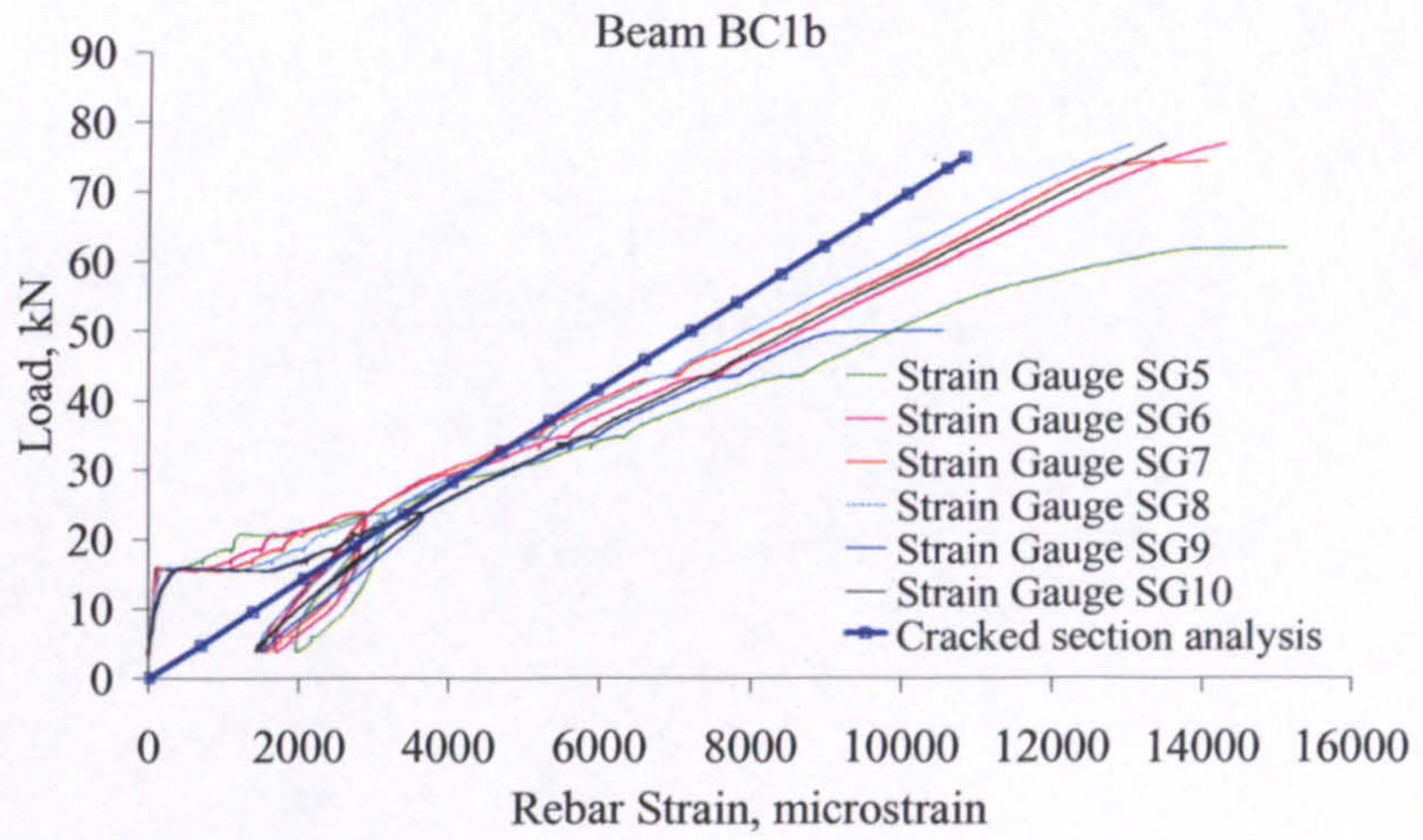
Beam BC1b
Load, kN
Rebar Strain, microstrain
Strain Gauge SG5
Strain Gauge SG6
Strain Gauge SG7
Strain Gauge SG8
Strain Gauge SG9
Strain Gauge SG10
Cracked section analysis

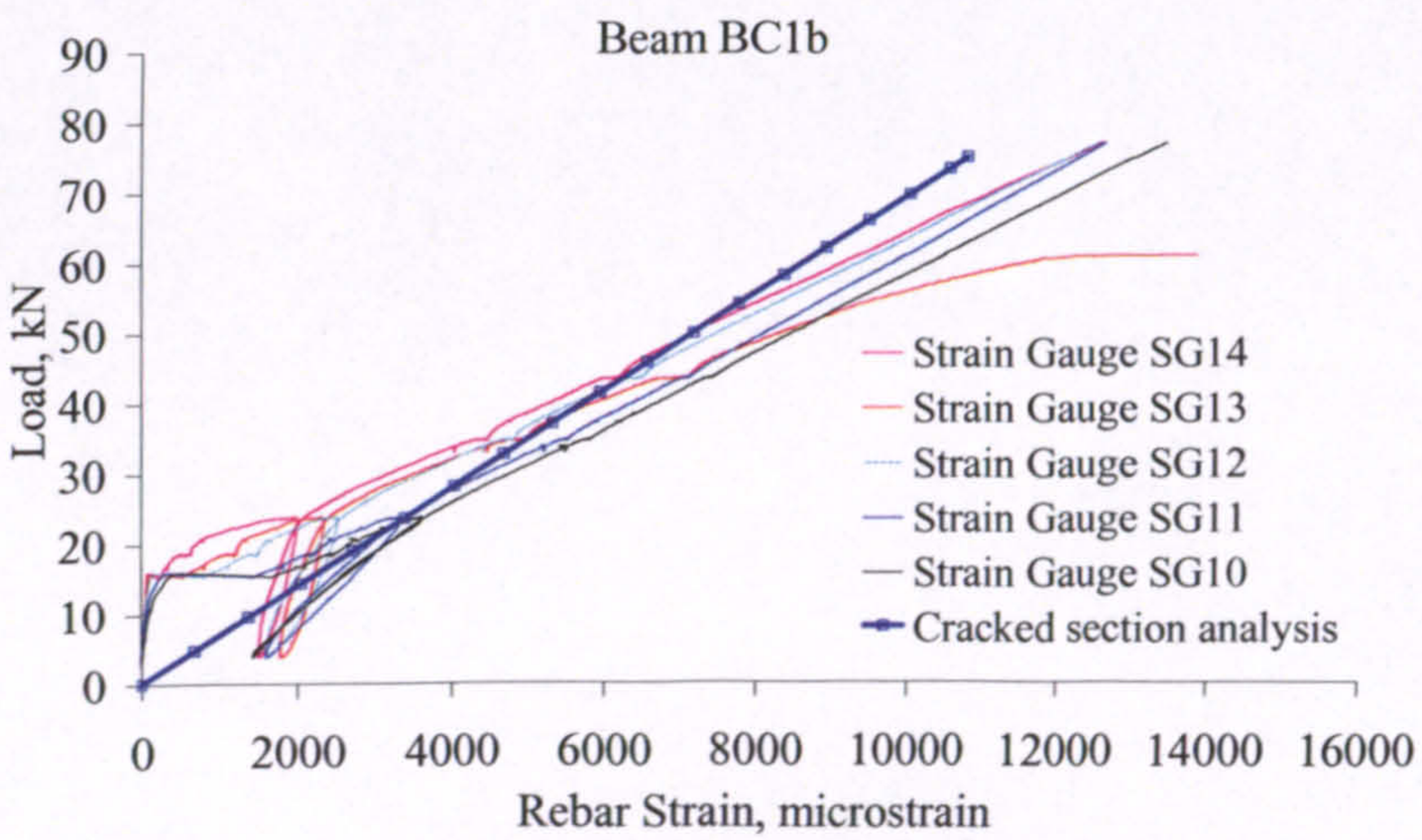
Beam BC1b
Load, kN
Rebar Strain, microstrain
Strain Gauge SG14
Strain Gauge SG13
Strain Gauge SG12
Strain Gauge SG11
Strain Gauge SG10
Cracked section analysis

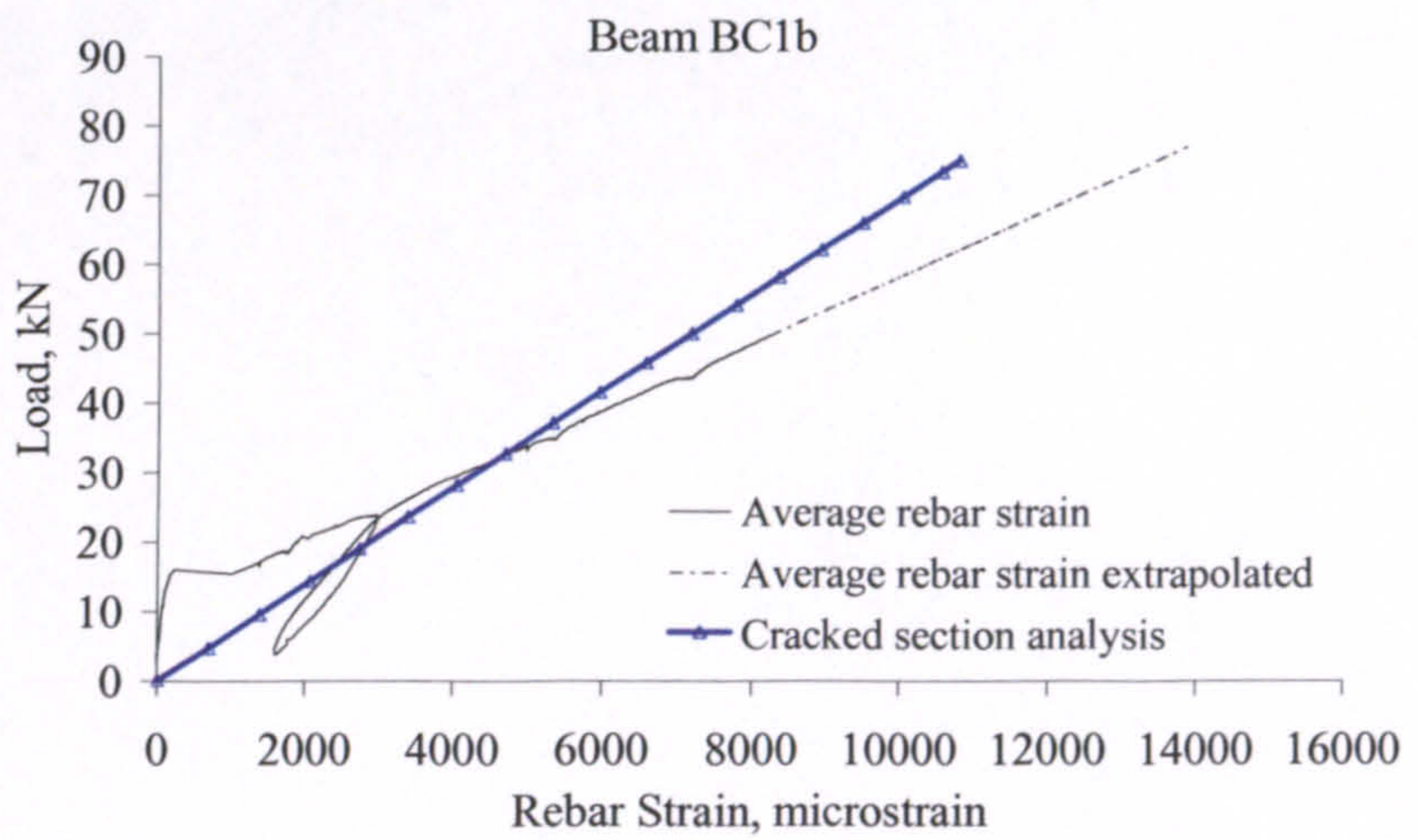
Beam BC1b
Load, kN
Rebar Strain, microstrain
Average rebar strain
Average rebar strain extrapolated
Cracked section analysis

BEAM BC1b

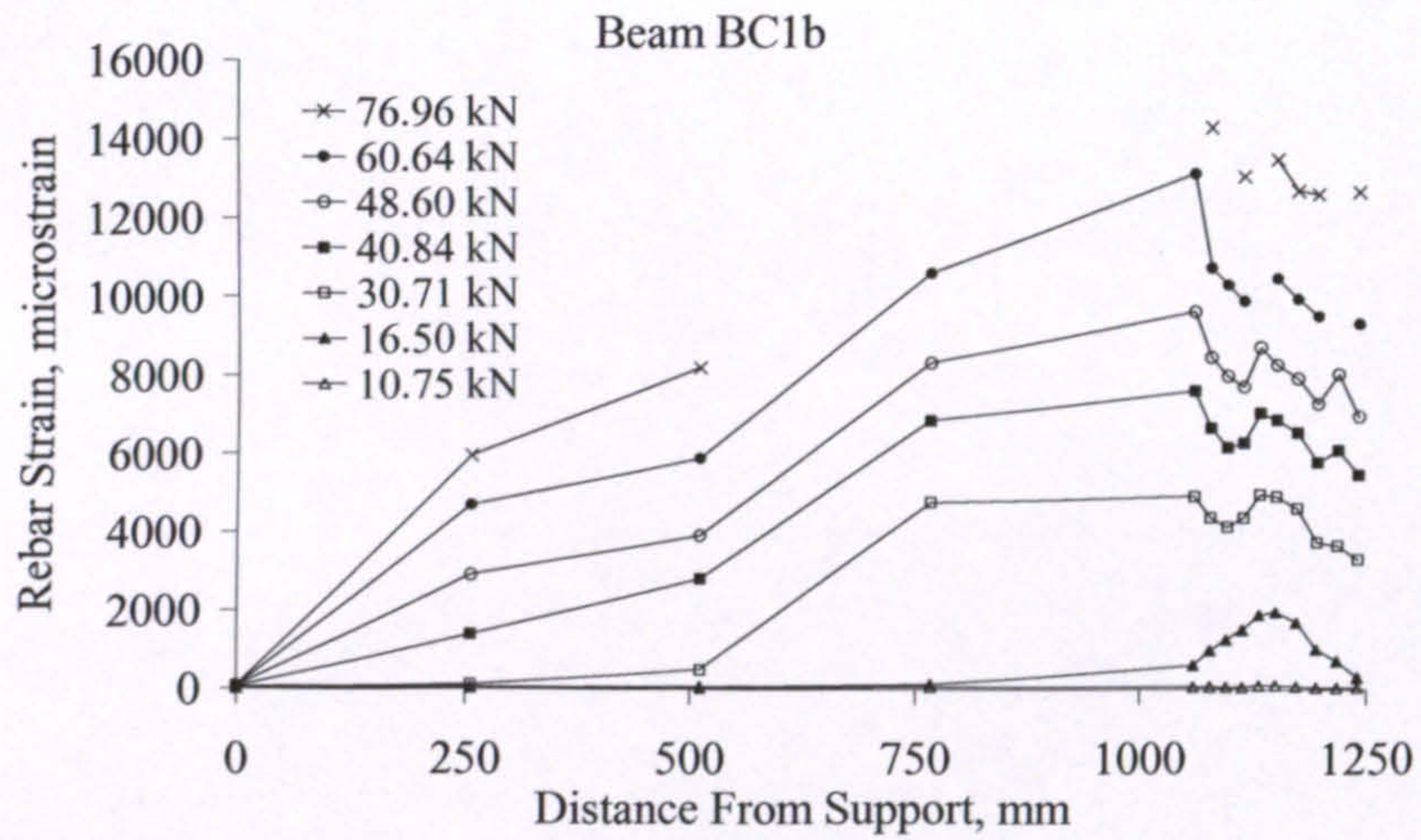
Beam BC1b
Rebar Strain, microstrain
16000
14000
12000
10000
8000
6000
4000
2000
0
76.96 kN
60.64 kN
48.60 kN
40.84 kN
30.71 kN
16.50 kN
10.75 kN
0
250
500
750
1000
1250
Distance From Support, mm

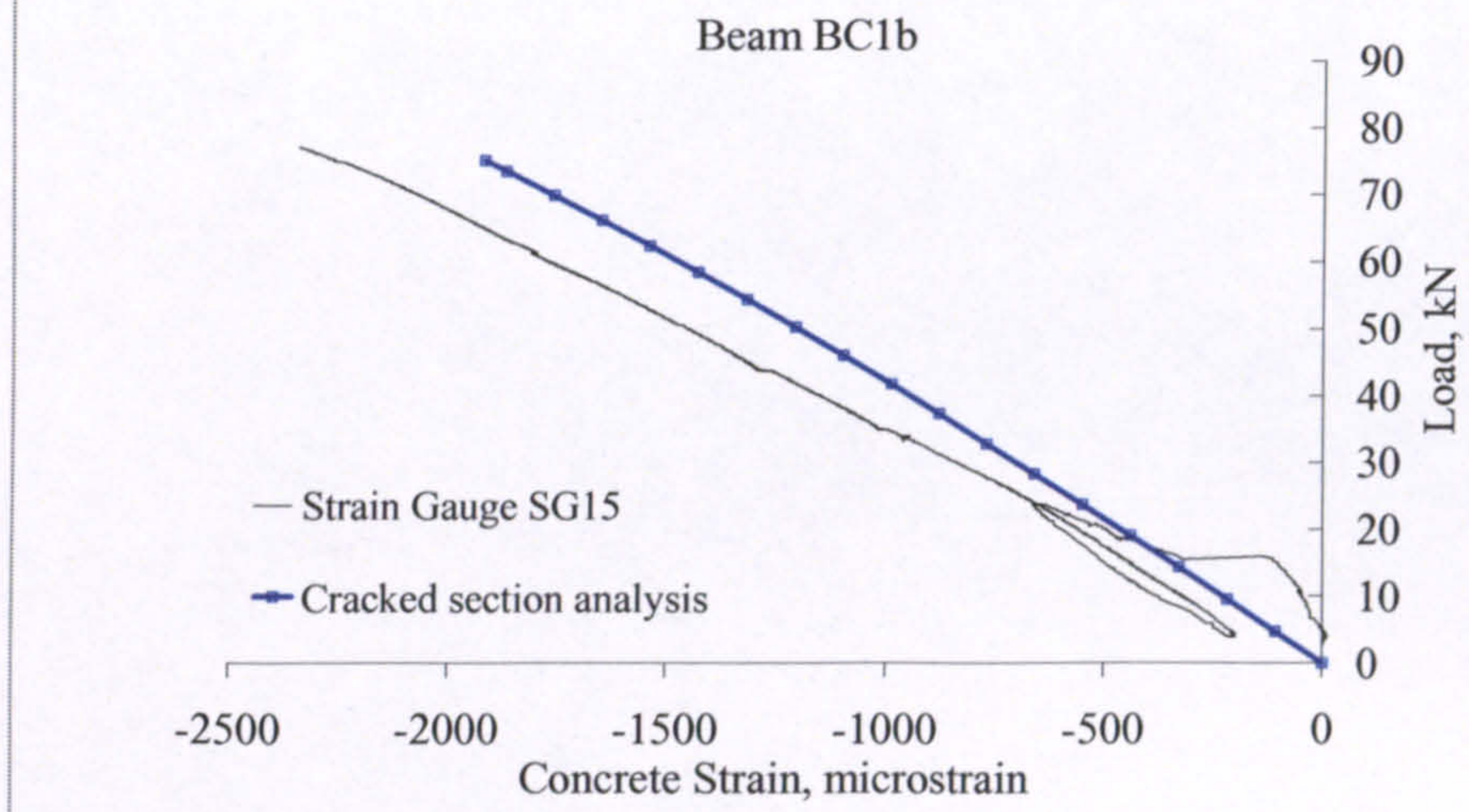
Beam BC1b
Load, kN
90
80
70
60
50
40
30
20
10
0
Strain Gauge SG15
Cracked section analysis
-2500
-2000
-1500
-1000
-500
0
Concrete Strain, microstrain

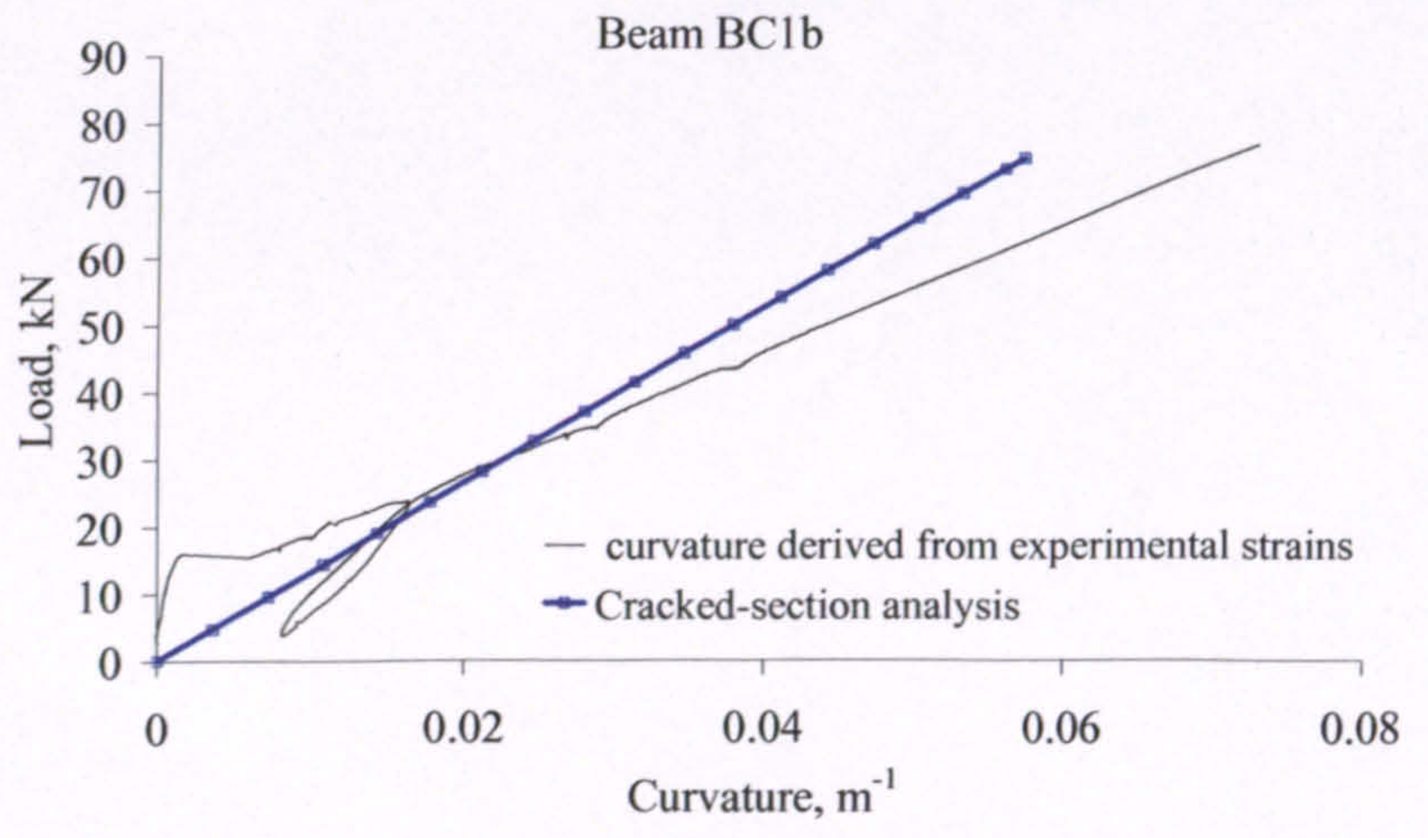
Beam BC1b
Load, kN
90
80
70
60
50
40
30
20
10
0
curvature derived from experimental strains
Cracked-section analysis
0
0.02
0.04
0.06
0.08
Curvature, m-1

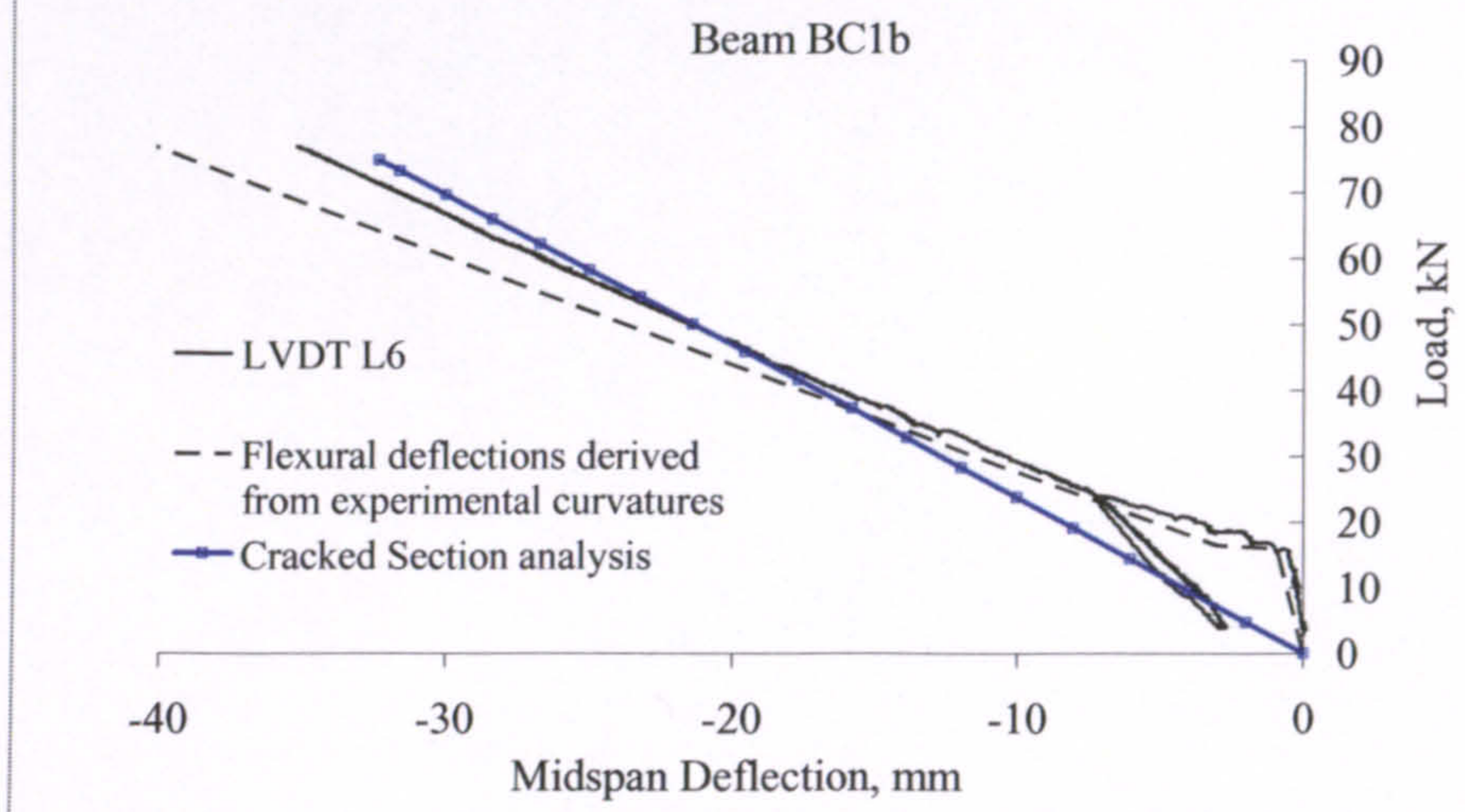
Beam BC1b
Load, kN
90
80
70
60
50
40
30
20
10
0
LVDT L6
Flexural deflections derived from experimental curvatures
Cracked Section analysis
-40
-30
-20
-10
0
Midspan Deflection, mm

BEAM BC1b

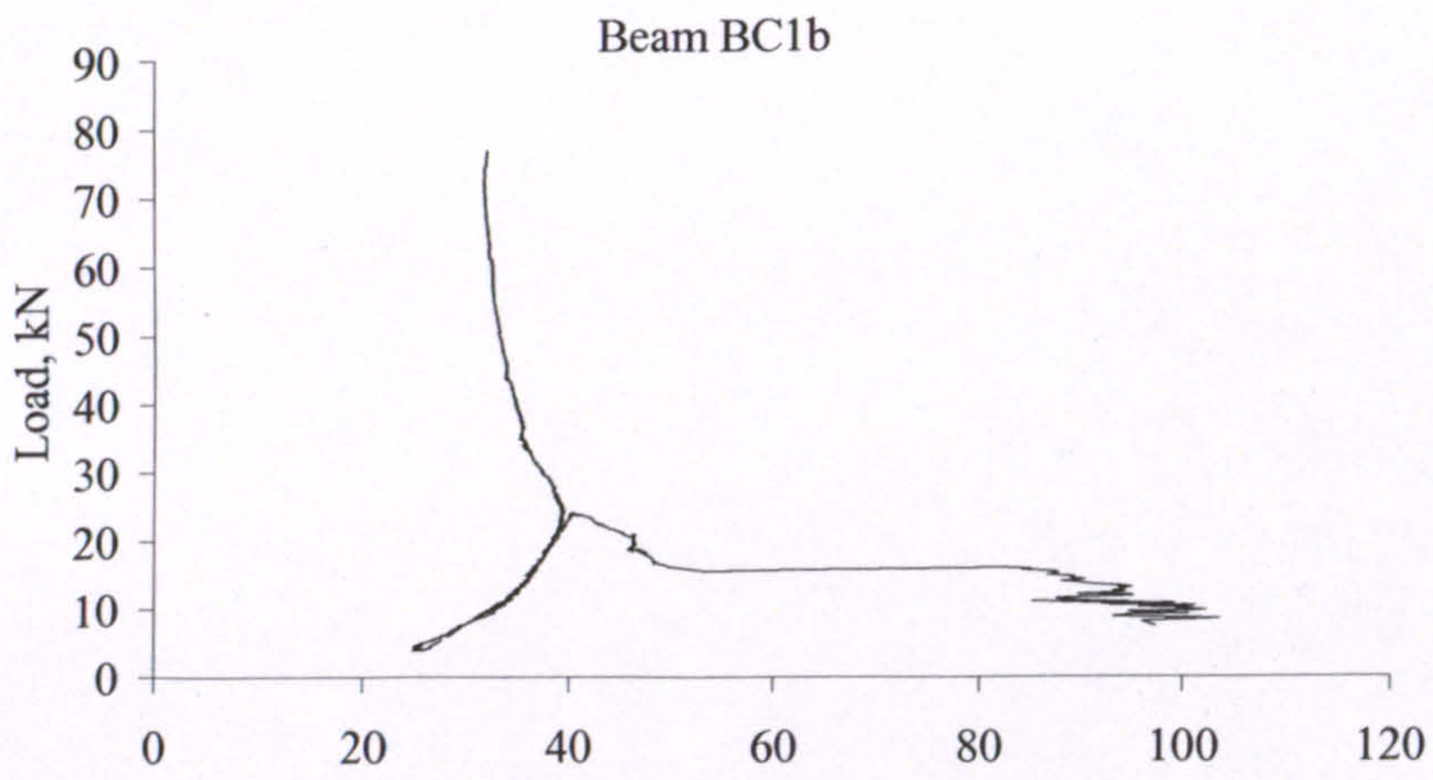
Beam BC1b
Load, kN
0
10
20
30
40
50
60
70
80
90
0
20
40
60
80
100
120
Average Neutral Axis Depth, mm

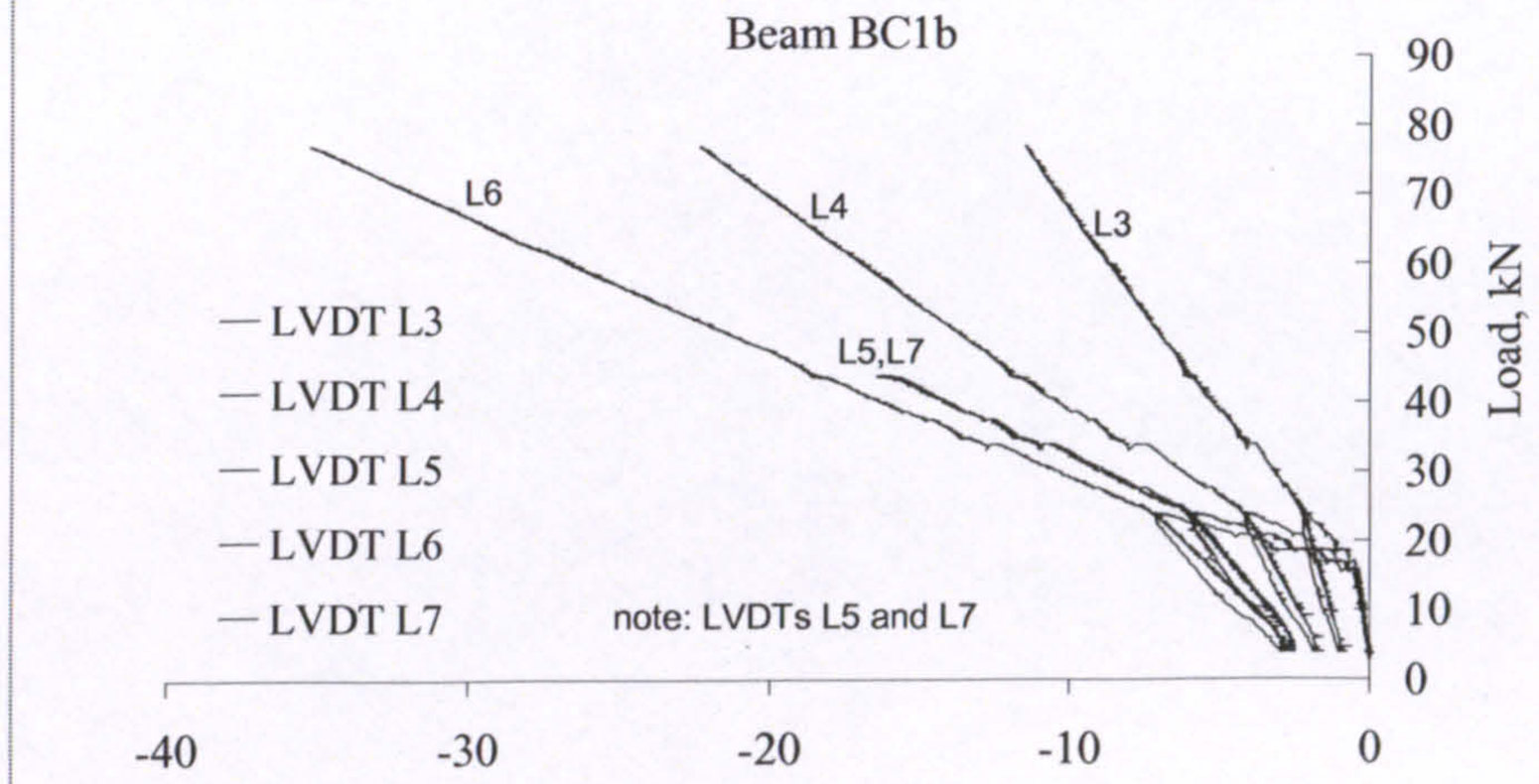
Beam BC1b
L6
L4
L3
L5,L7
— LVDT L3
— LVDT L4
— LVDT L5
— LVDT L6
— LVDT L7
note: LVDTs L5 and L7
Load, kN
0
10
20
30
40
50
60
70
80
90
-40
-30
-20
-10
0
Deflection, mm

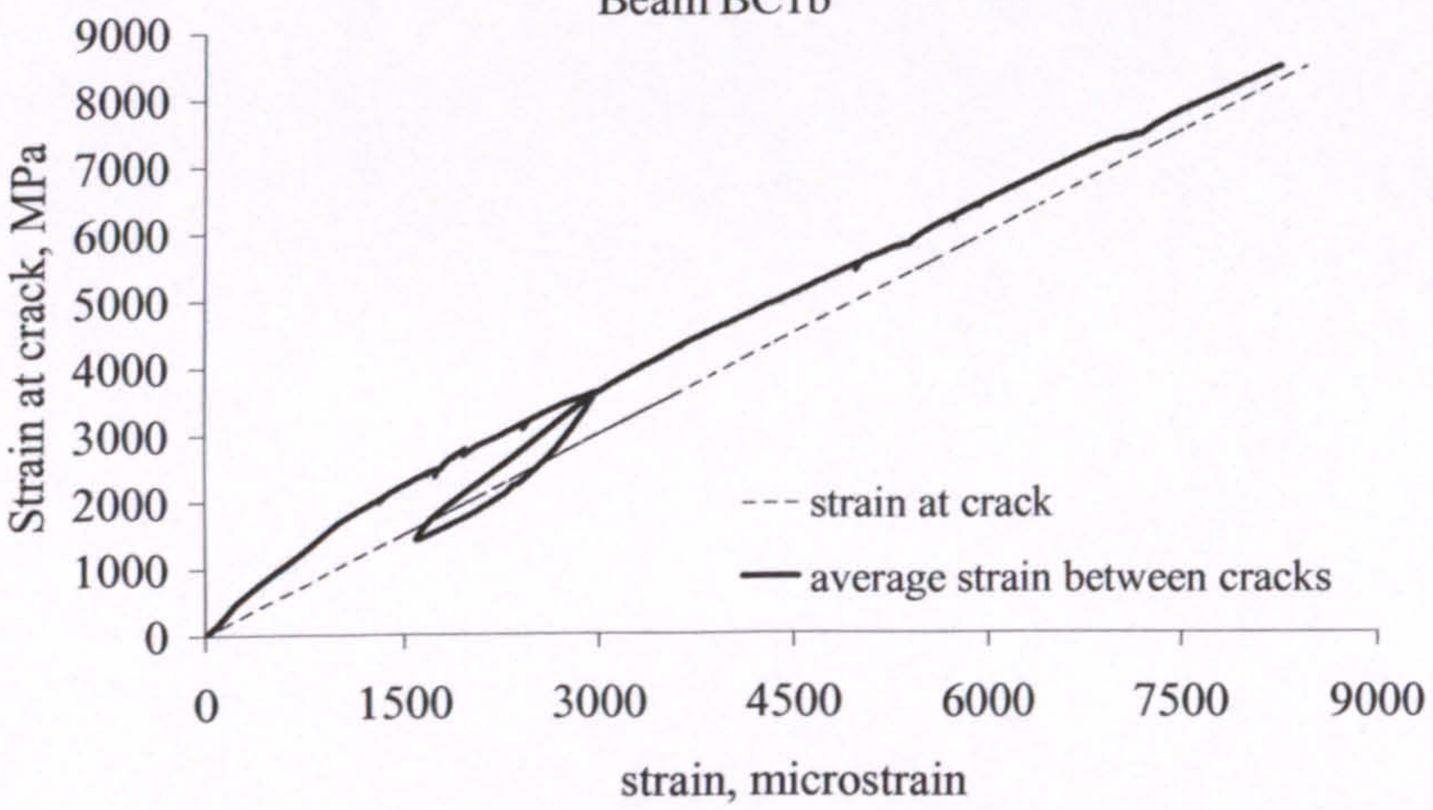
Beam BC1b
Strain at crack, MPa
0
1000
2000
3000
4000
5000
6000
7000
8000
9000
--- strain at crack
— average strain between cracks
0
1500
3000
4500
6000
7500
9000
strain, microstrain

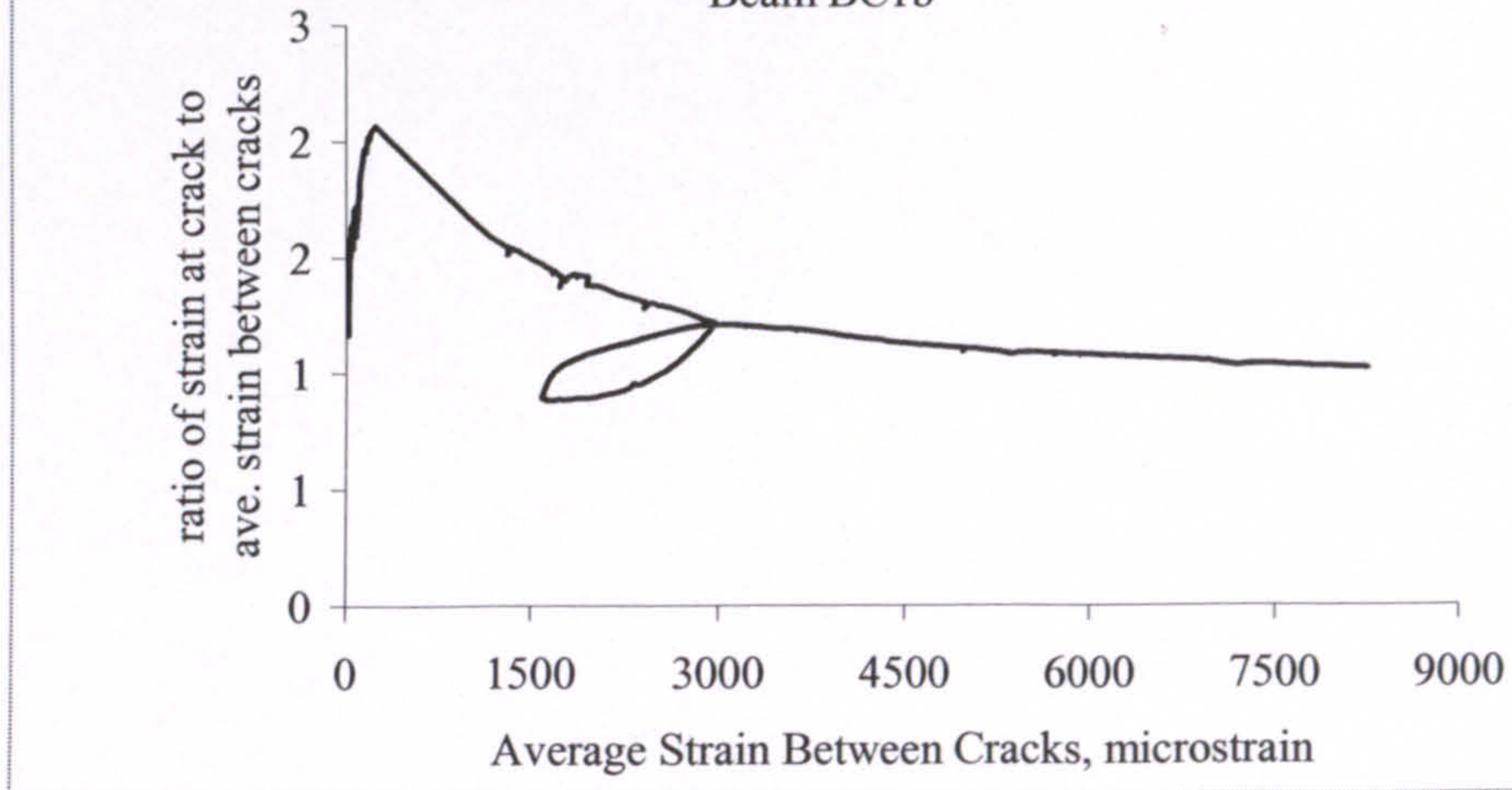
Beam BC1b
ratio of strain at crack to ave. strain between cracks
0
1
1
2
2
3
0
1500
3000
4500
6000
7500
9000
Average Strain Between Cracks, microstrain

BEAM BC1b

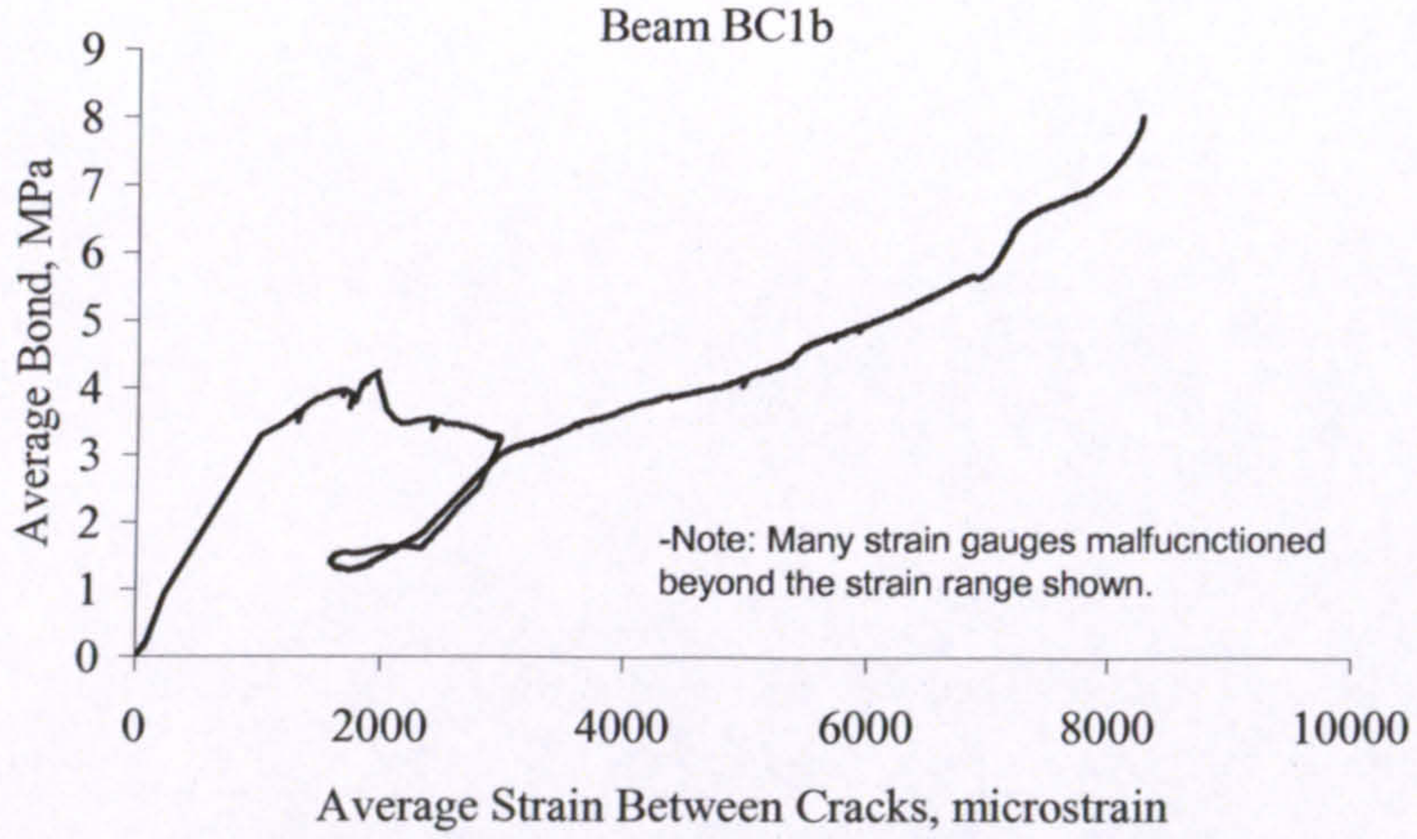

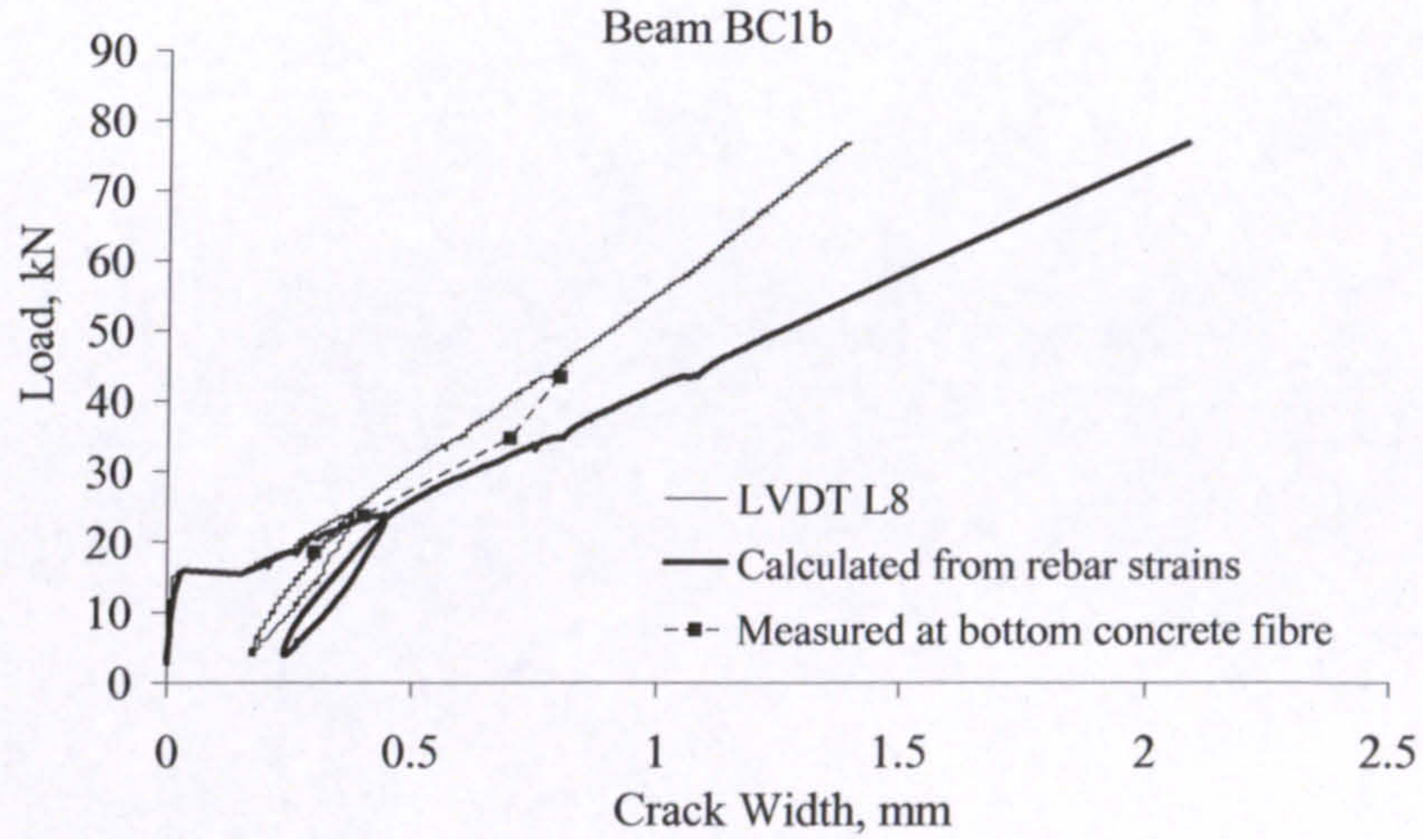

Failure by rupture of rebars

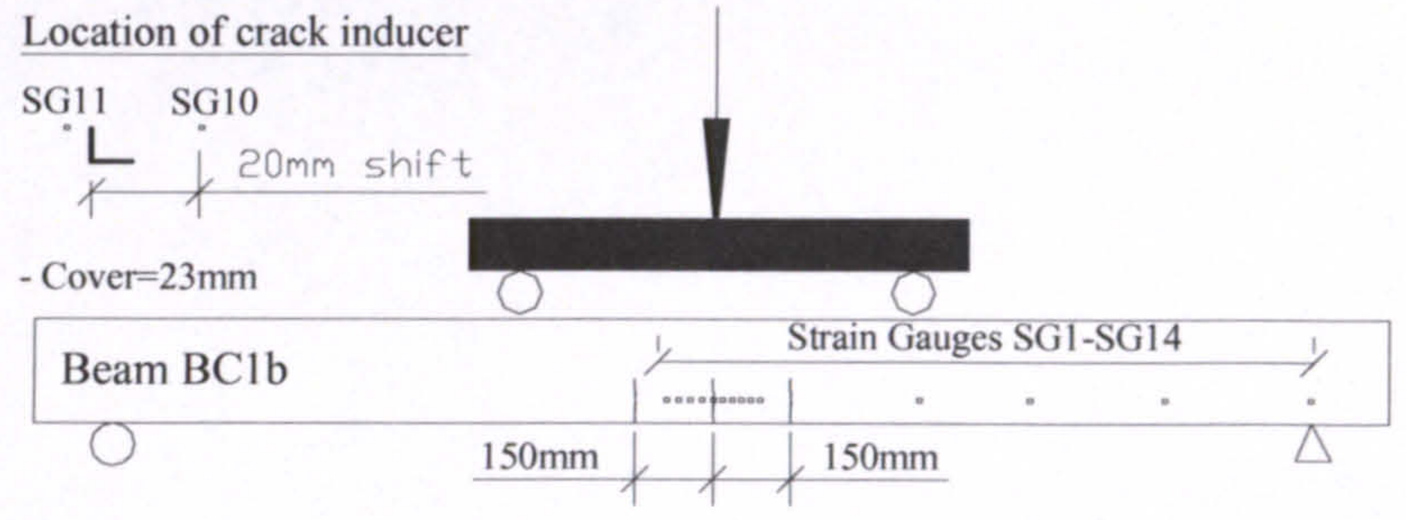

Cracks around Centre

BEAM BC2a

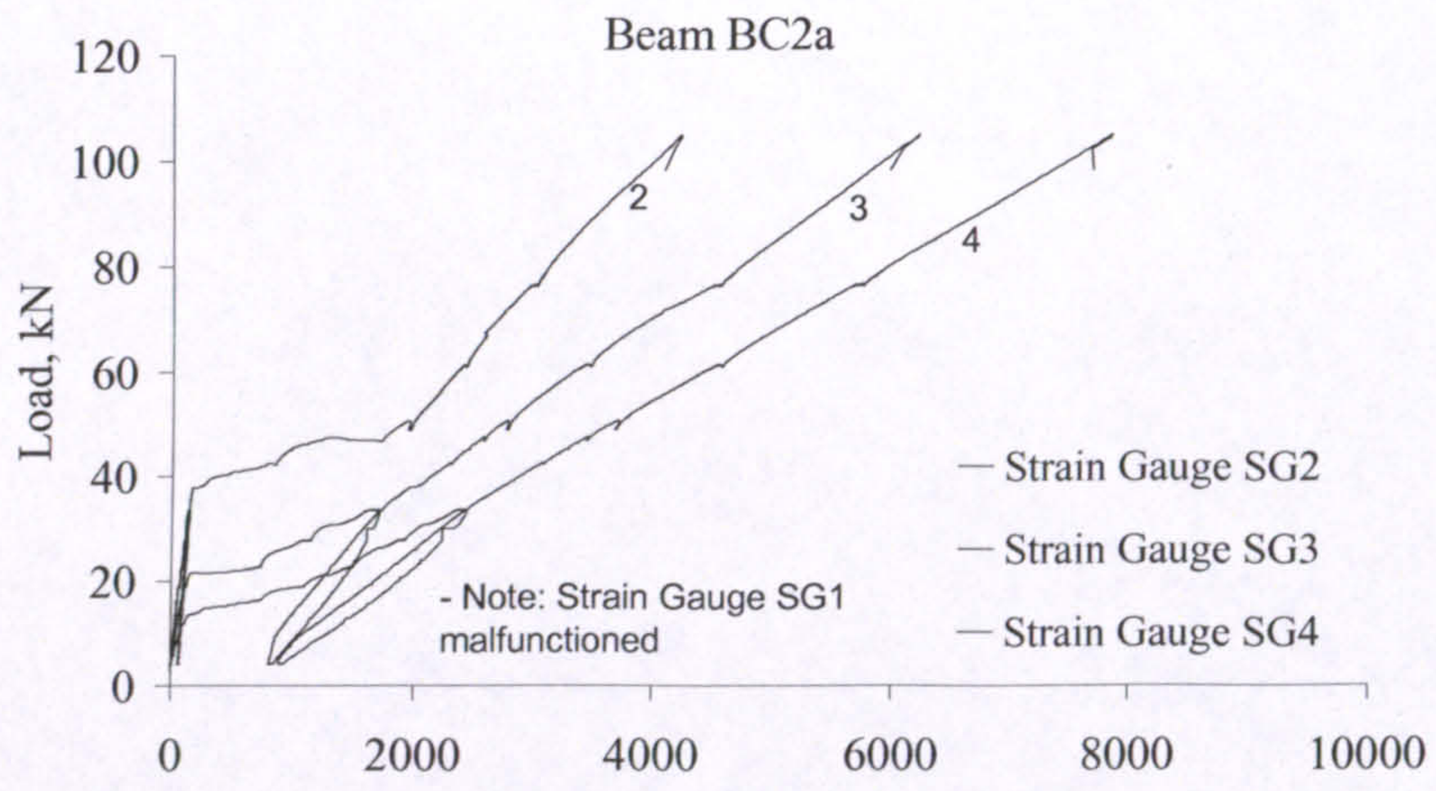
Beam BC2a
Load, kN
Rebar Strain, microstrain
2
3
4
1
- Note: Strain Gauge SG1 malfunctioned
Strain Gauge SG2
Strain Gauge SG3
Strain Gauge SG4

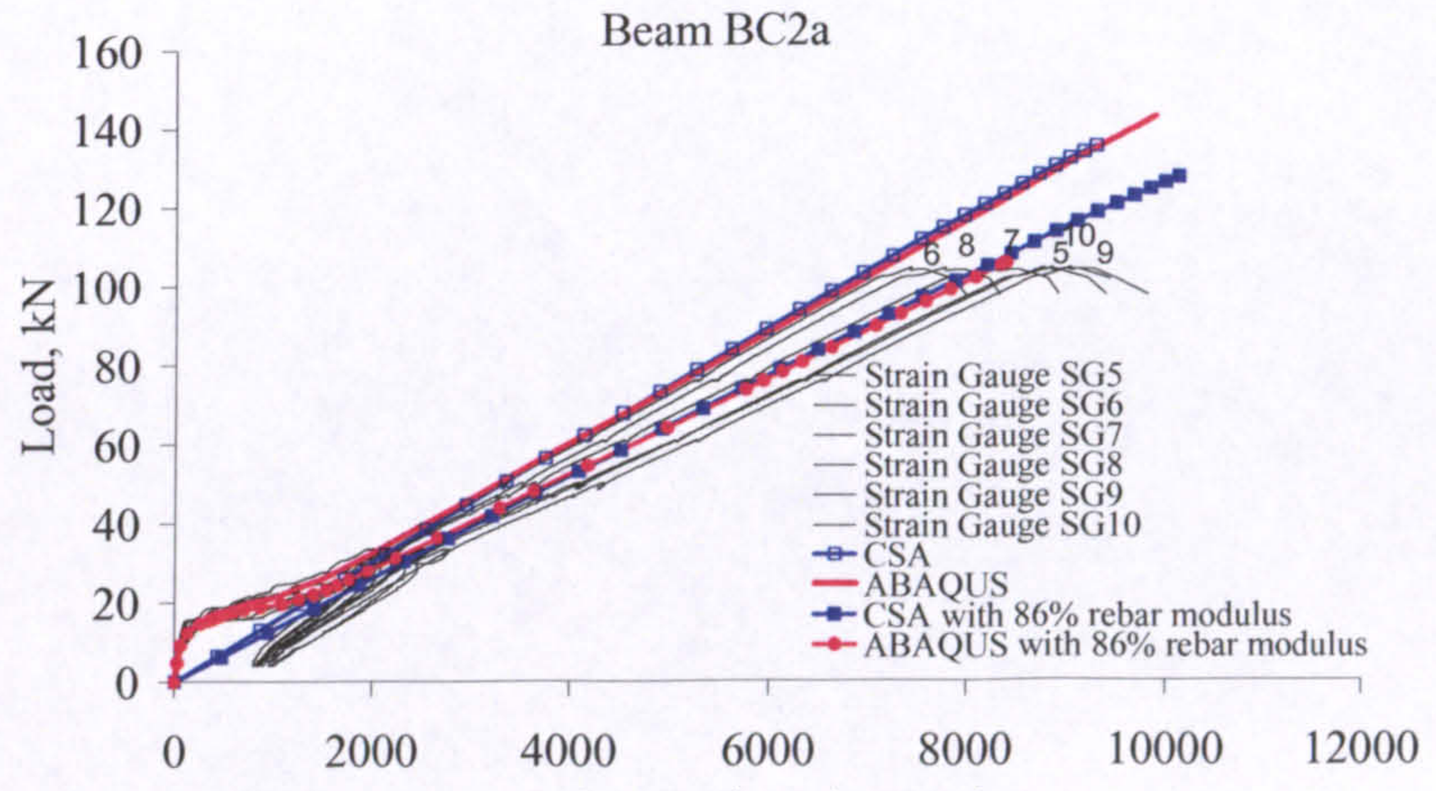
Beam BC2a
Load, kN
Rebar Strain, microstrain
6
8
7
5
10
9
Strain Gauge SG5
Strain Gauge SG6
Strain Gauge SG7
Strain Gauge SG8
Strain Gauge SG9
Strain Gauge SG10
CSA
ABAQUS
CSA with 86% rebar modulus
ABAQUS with 86% rebar modulus

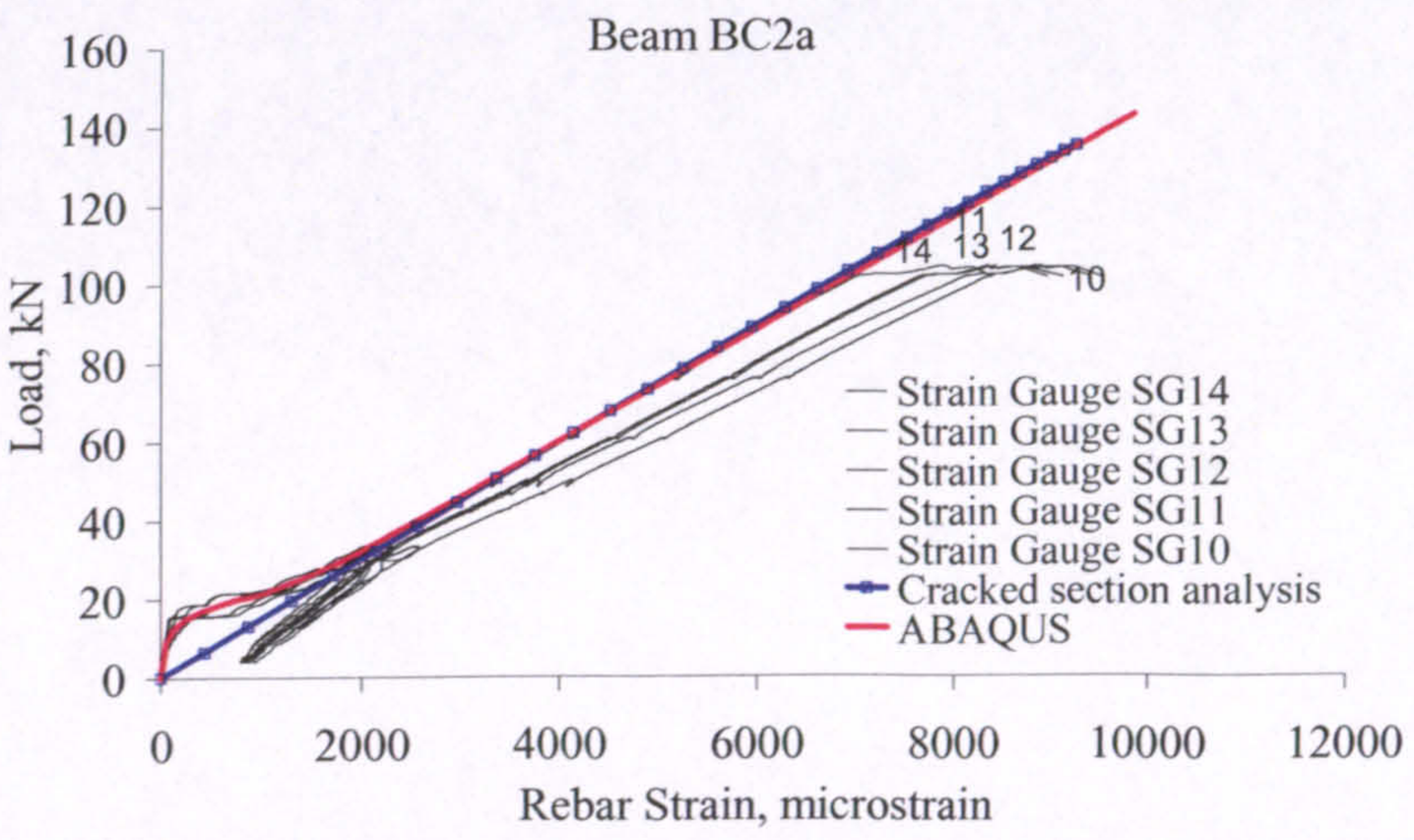
Beam BC2a
Load, kN
Rebar Strain, microstrain
11
14
13
12
10
Strain Gauge SG14
Strain Gauge SG13
Strain Gauge SG12
Strain Gauge SG11
Strain Gauge SG10
Cracked section analysis
ABAQUS

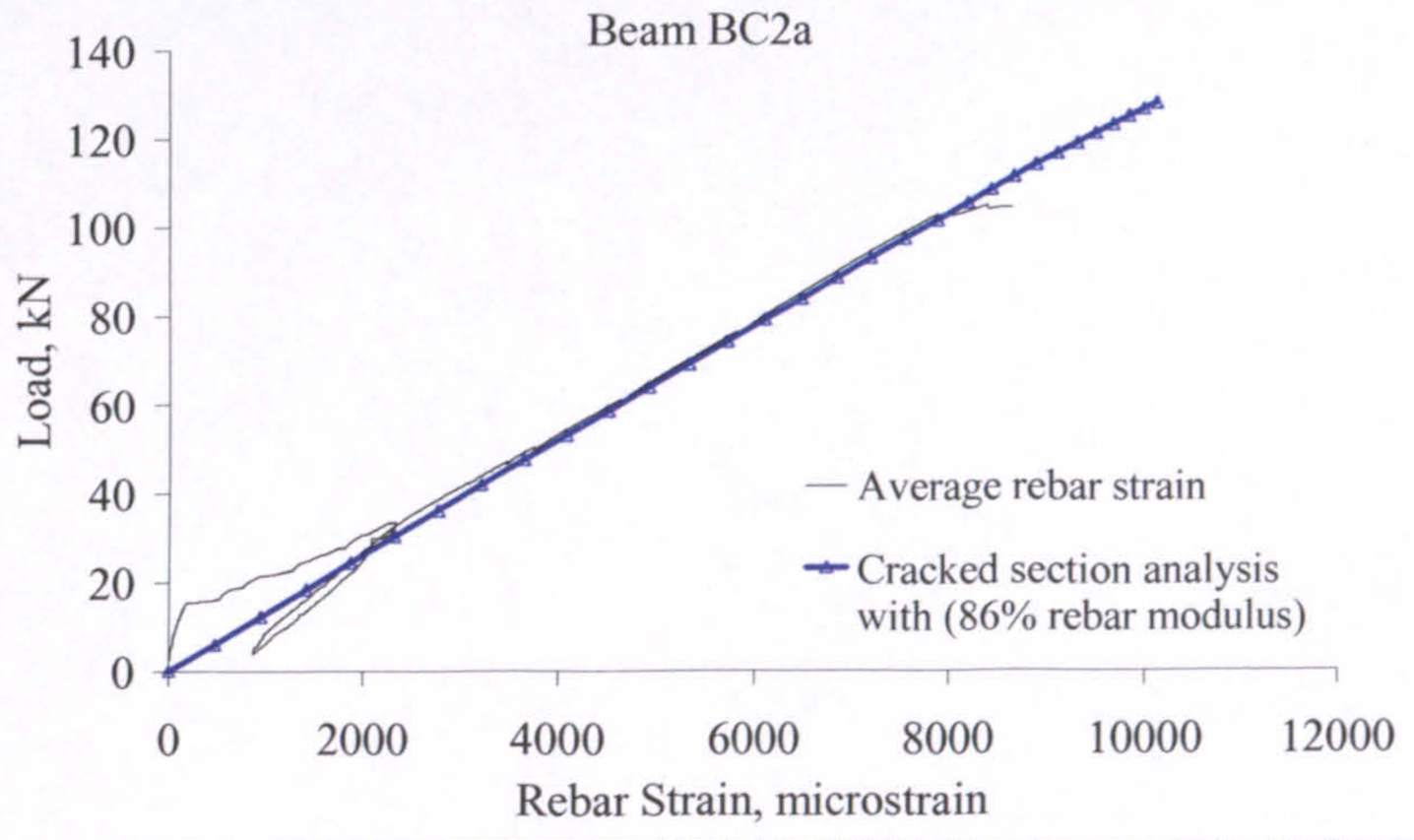
Beam BC2a
Load, kN
Rebar Strain, microstrain
Average rebar strain
Cracked section analysis with (86% rebar modulus)

BEAM BC2a

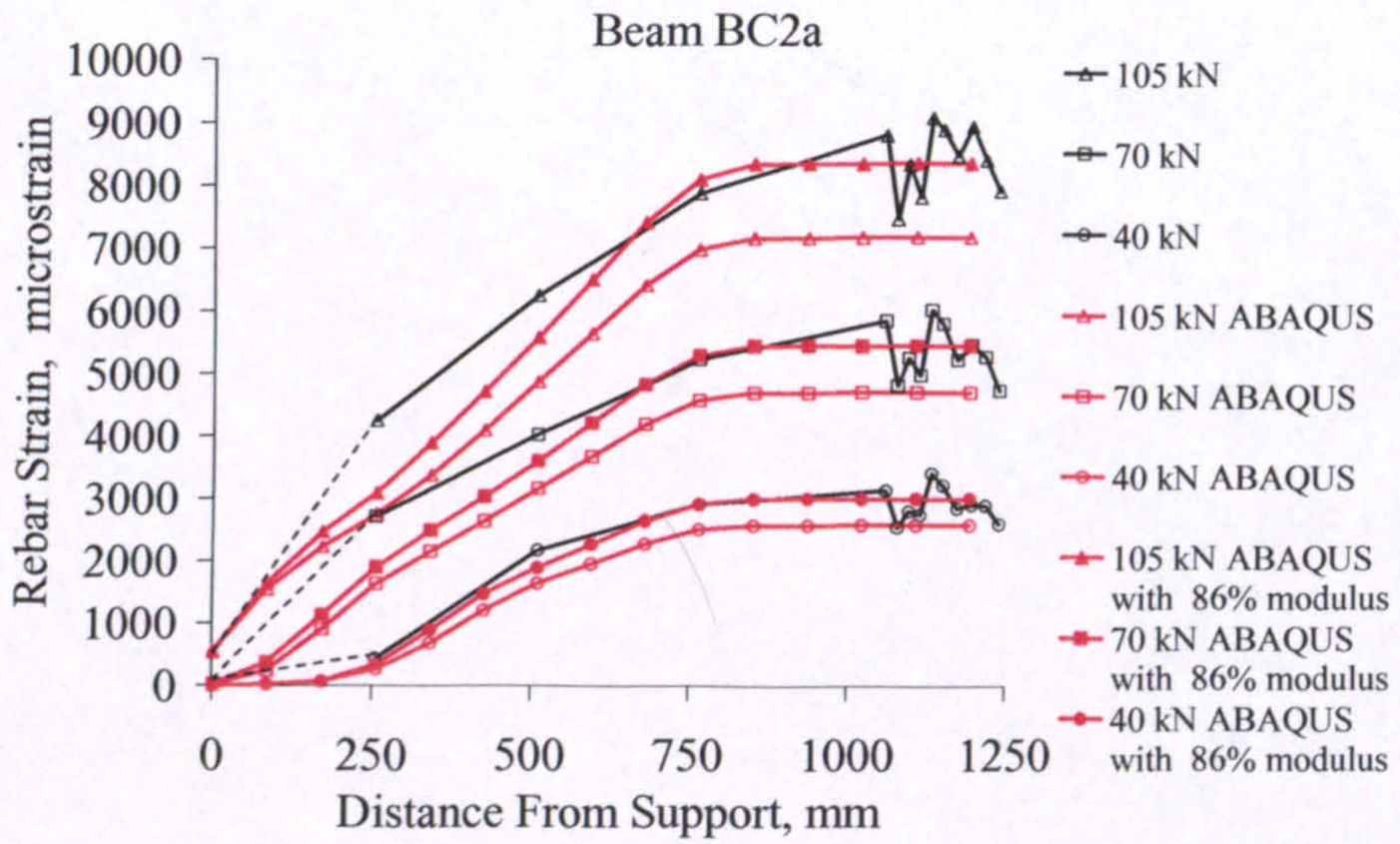
Beam BC2a
Rebar Strain, microstrain
10000
9000
8000
7000
6000
5000
4000
3000
2000
1000
0
0
250
500
750
1000
1250
Distance From Support, mm
105 kN
70 kN
40 kN
105 kN ABAQUS
70 kN ABAQUS
40 kN ABAQUS
105 kN ABAQUS with 86% modulus
70 kN ABAQUS with 86% modulus
40 kN ABAQUS with 86% modulus

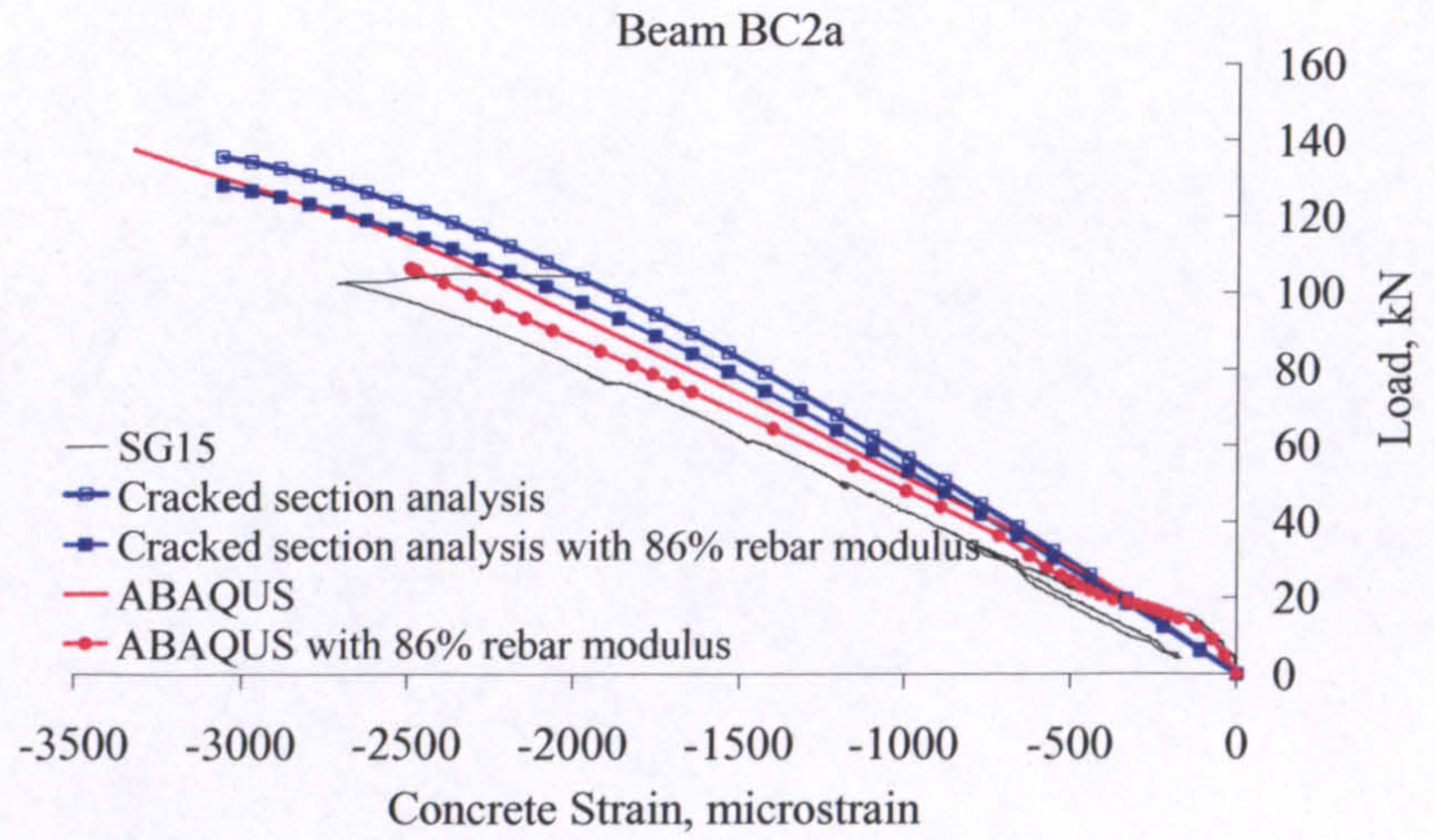
Beam BC2a
Load, kN
160
140
120
100
80
60
40
20
0
-3500
-3000
-2500
-2000
-1500
-1000
-500
0
Concrete Strain, microstrain
SG15
Cracked section analysis
Cracked section analysis with 86% rebar modulus
ABAQUS
ABAQUS with 86% rebar modulus

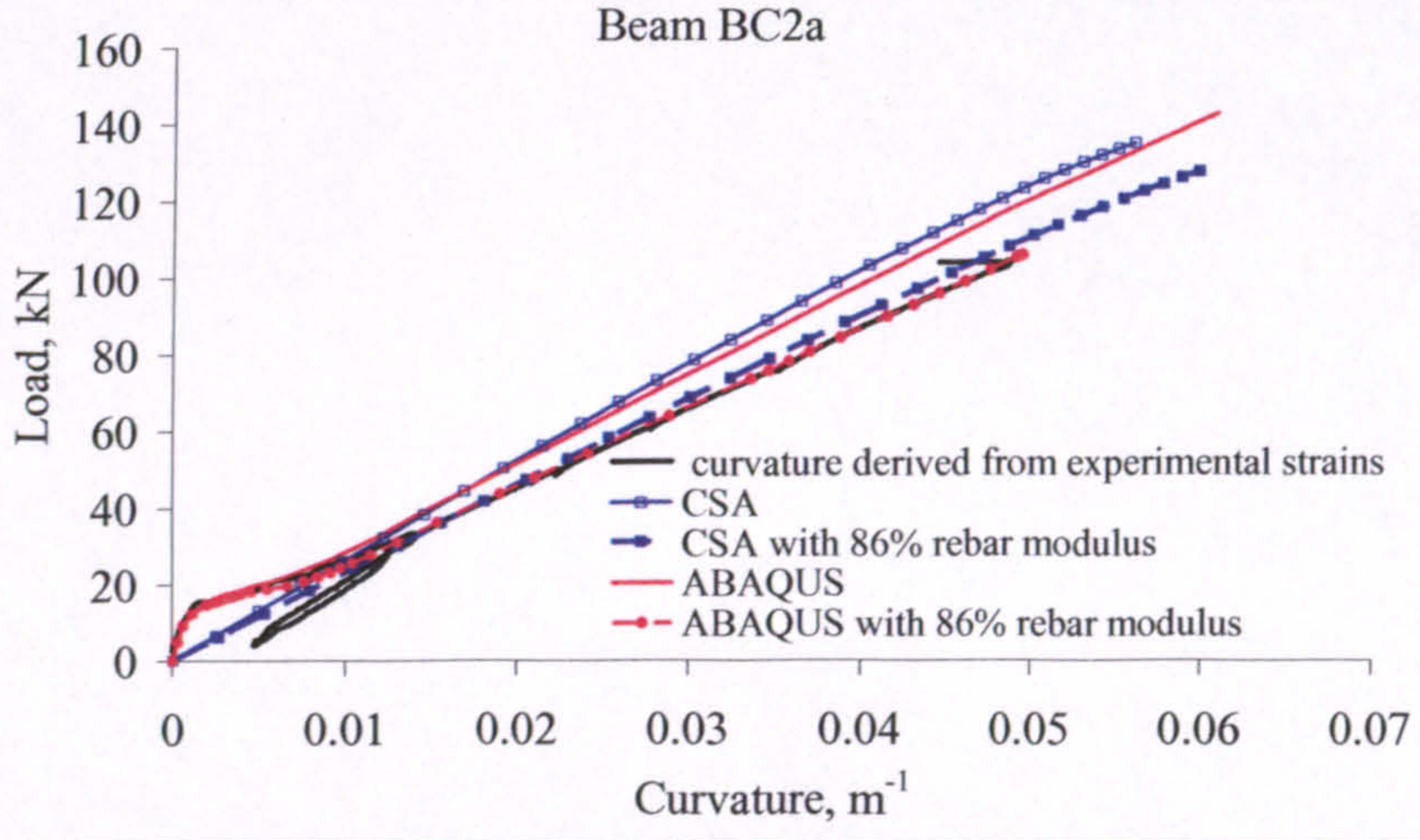
Beam BC2a
Load, kN
160
140
120
100
80
60
40
20
0
0
0.01
0.02
0.03
0.04
0.05
0.06
0.07
Curvature, m-1
curvature derived from experimental strains
CSA
CSA with 86% rebar modulus
ABAQUS
ABAQUS with 86% rebar modulus

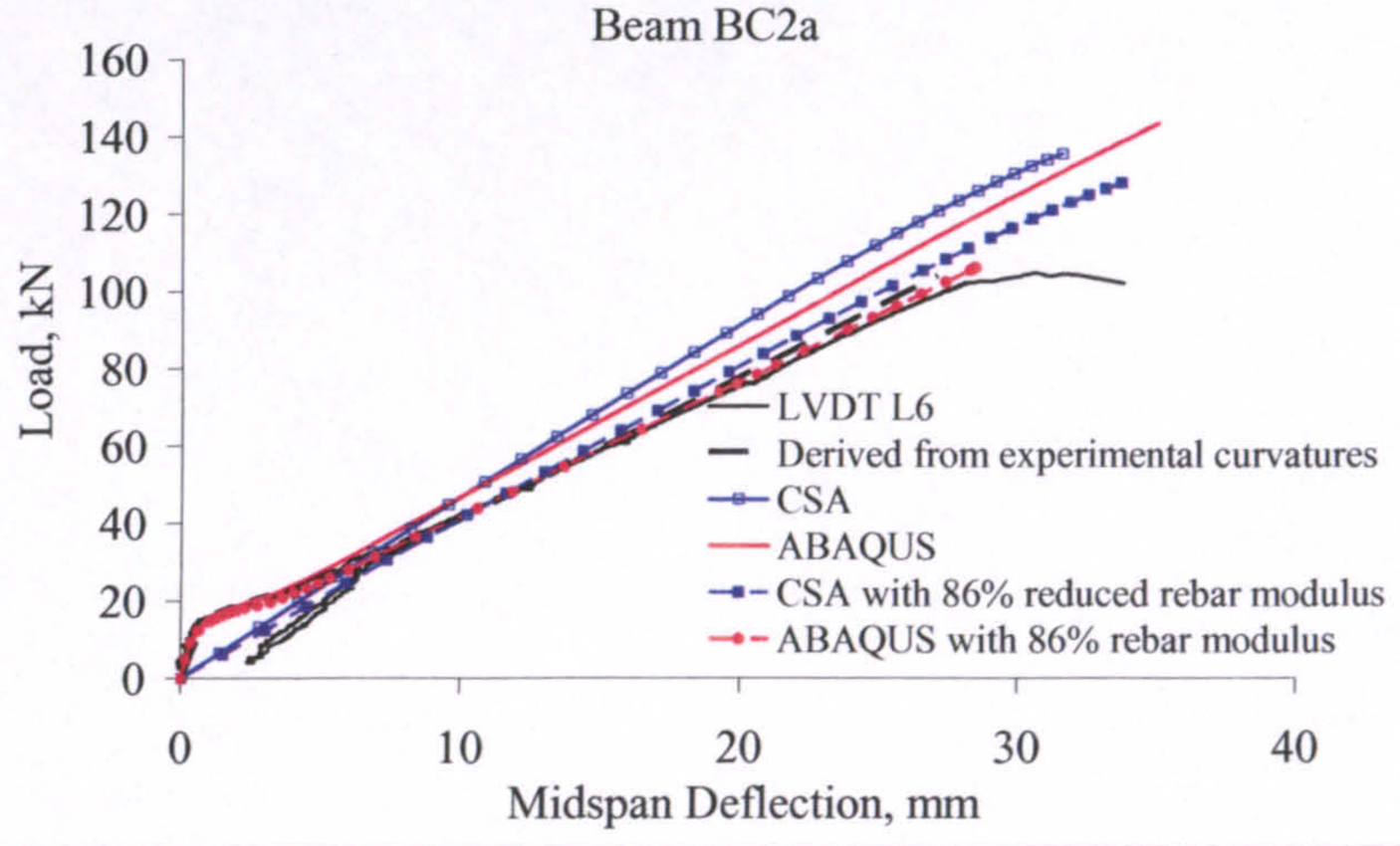
Beam BC2a
Load, kN
160
140
120
100
80
60
40
20
0
0
10
20
30
40
Midspan Deflection, mm
LVDT L6
Derived from experimental curvatures
CSA
ABAQUS
CSA with 86% reduced rebar modulus
ABAQUS with 86% rebar modulus

BEAM BC2a

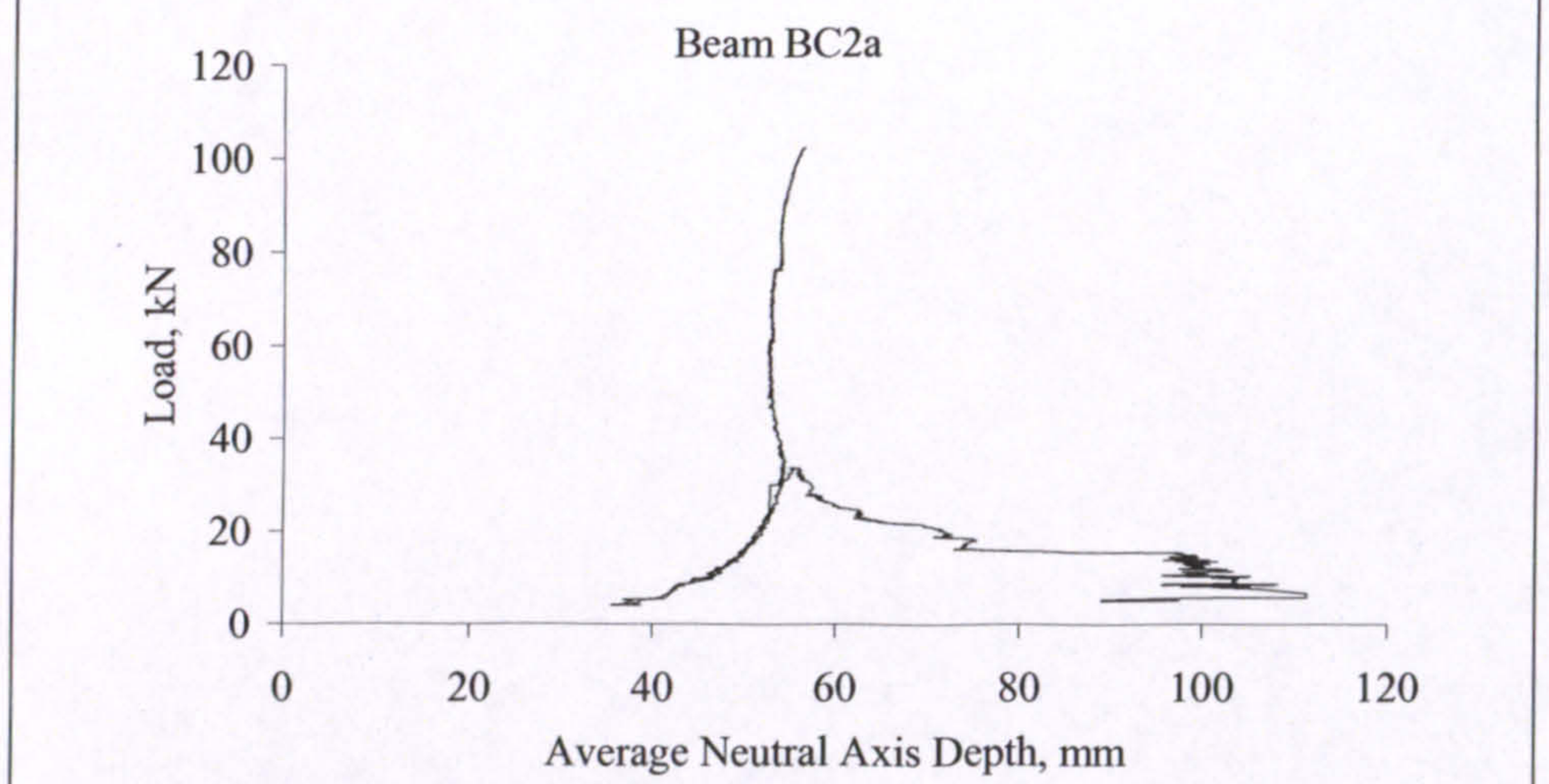
Beam BC2a
Load, kN
Average Neutral Axis Depth, mm
0
20
40
60
80
100
120

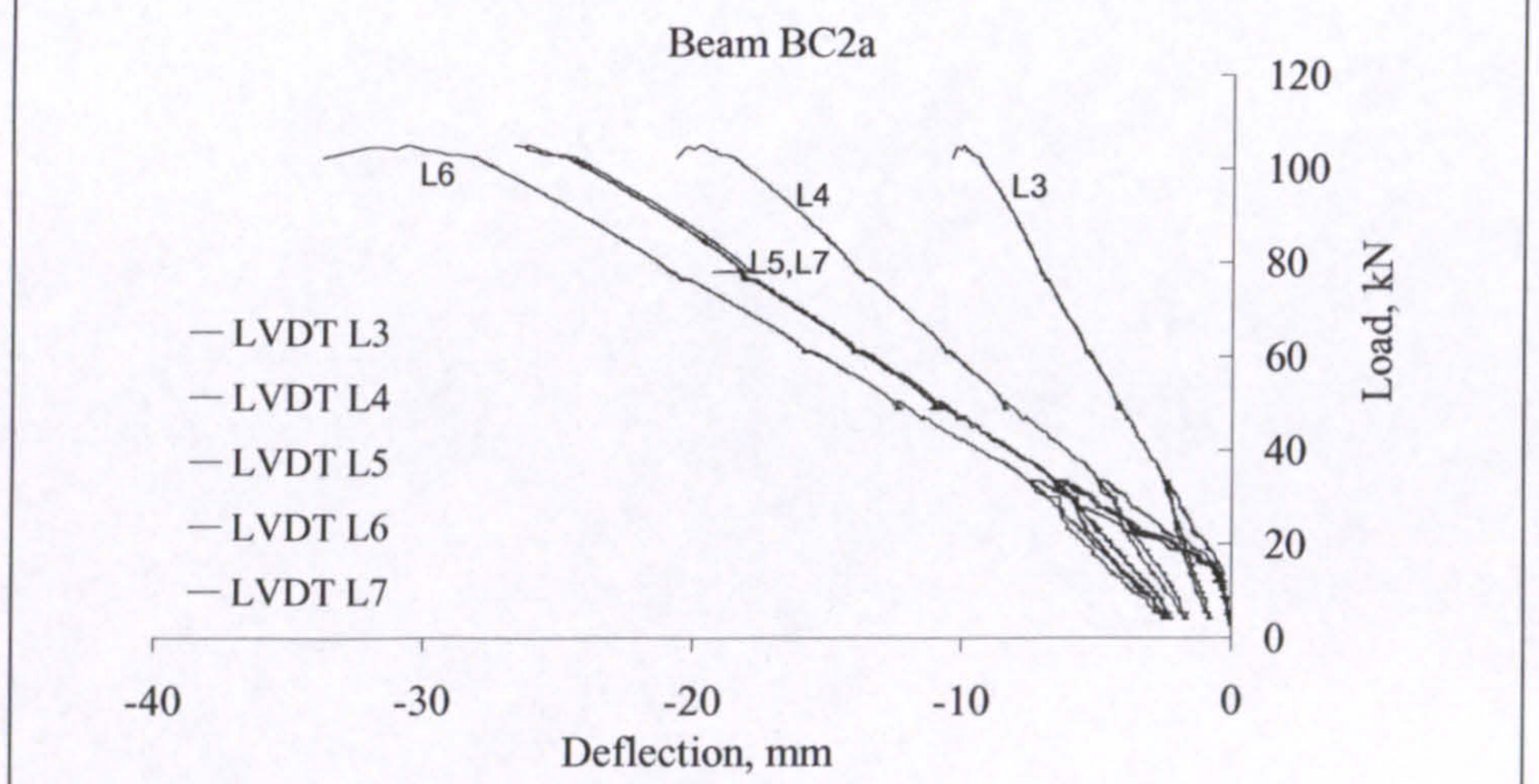
Beam BC2a
L6
L4
L3
L5,L7
LVDT L3
LVDT L4
LVDT L5
LVDT L6
LVDT L7
Load, kN
Deflection, mm
-40
-30
-20
-10
0

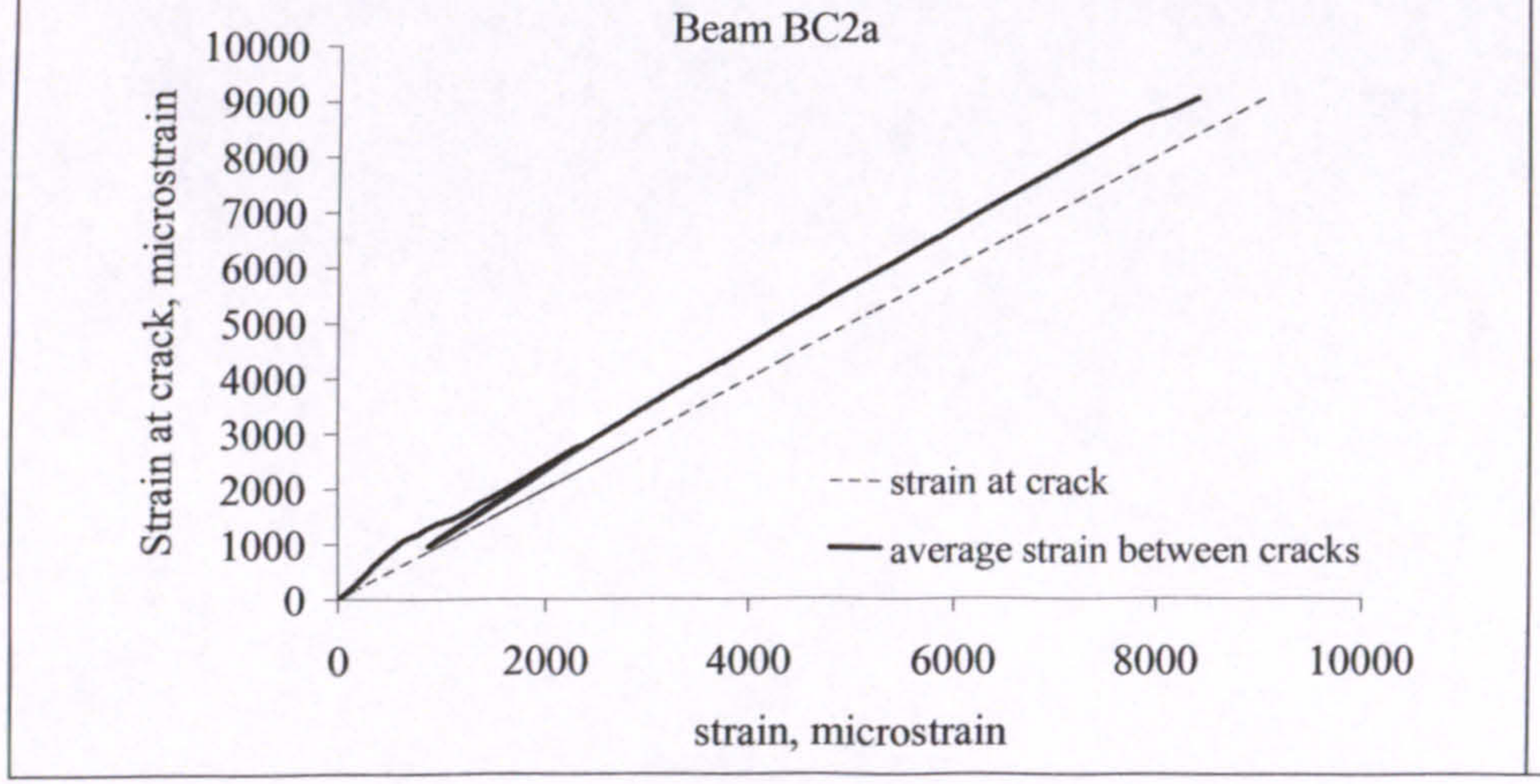
Beam BC2a
Strain at crack, microstrain
strain at crack
average strain between cracks
strain, microstrain
0
1000
2000
3000
4000
5000
6000
7000
8000
9000
10000

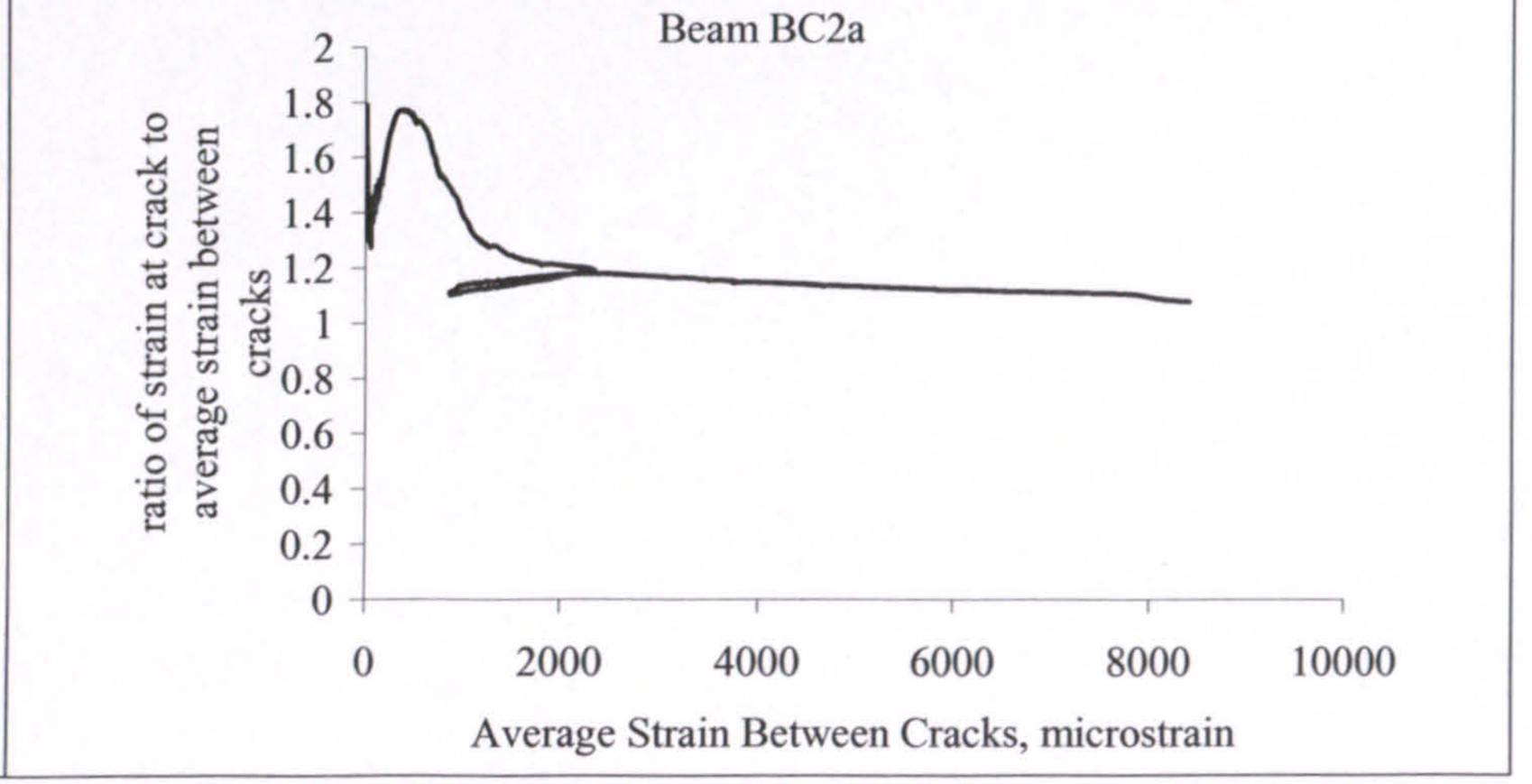
Beam BC2a
ratio of strain at crack to average strain between cracks
Average Strain Between Cracks, microstrain
0
0.2
0.4
0.6
0.8
1
1.2
1.4
1.6
1.8
2
0
2000
4000
6000
8000
10000

BEAM BC2a

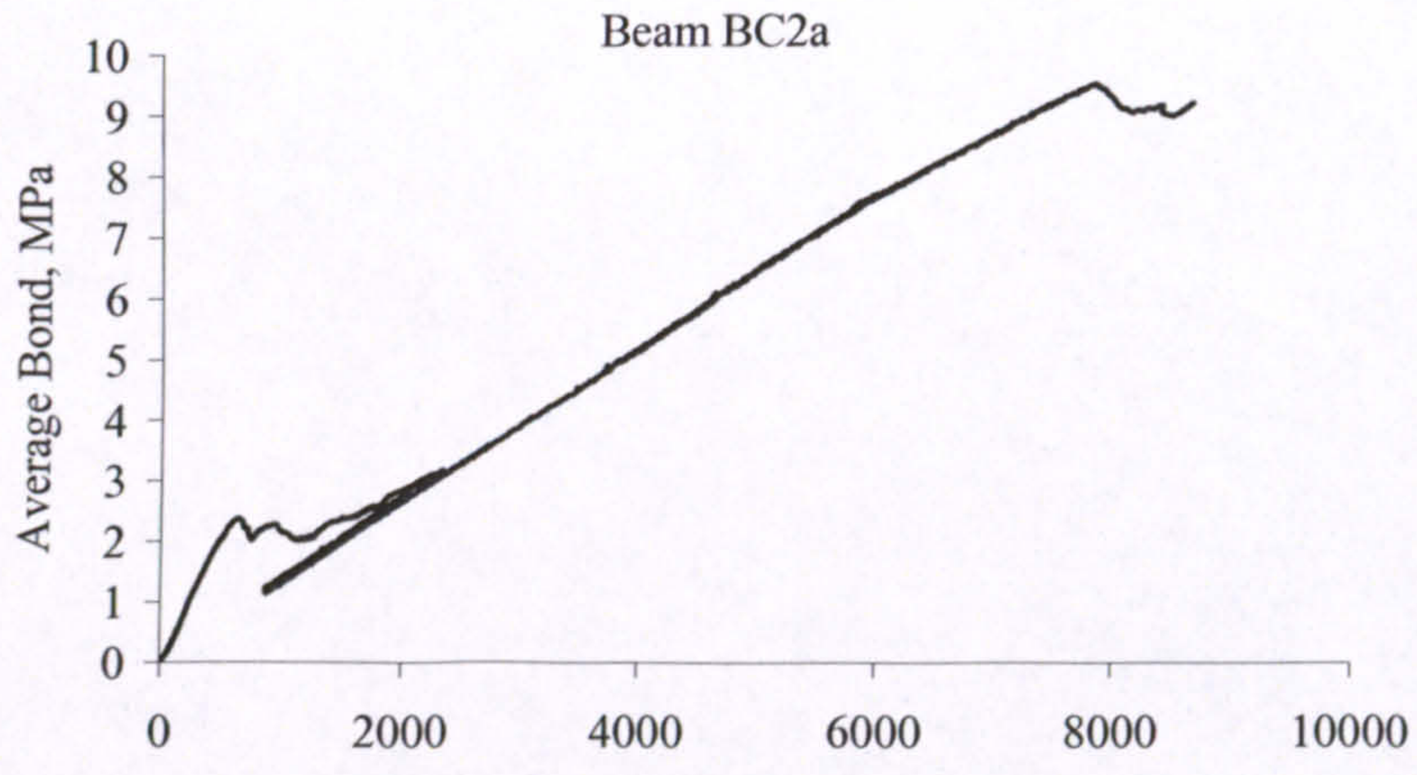

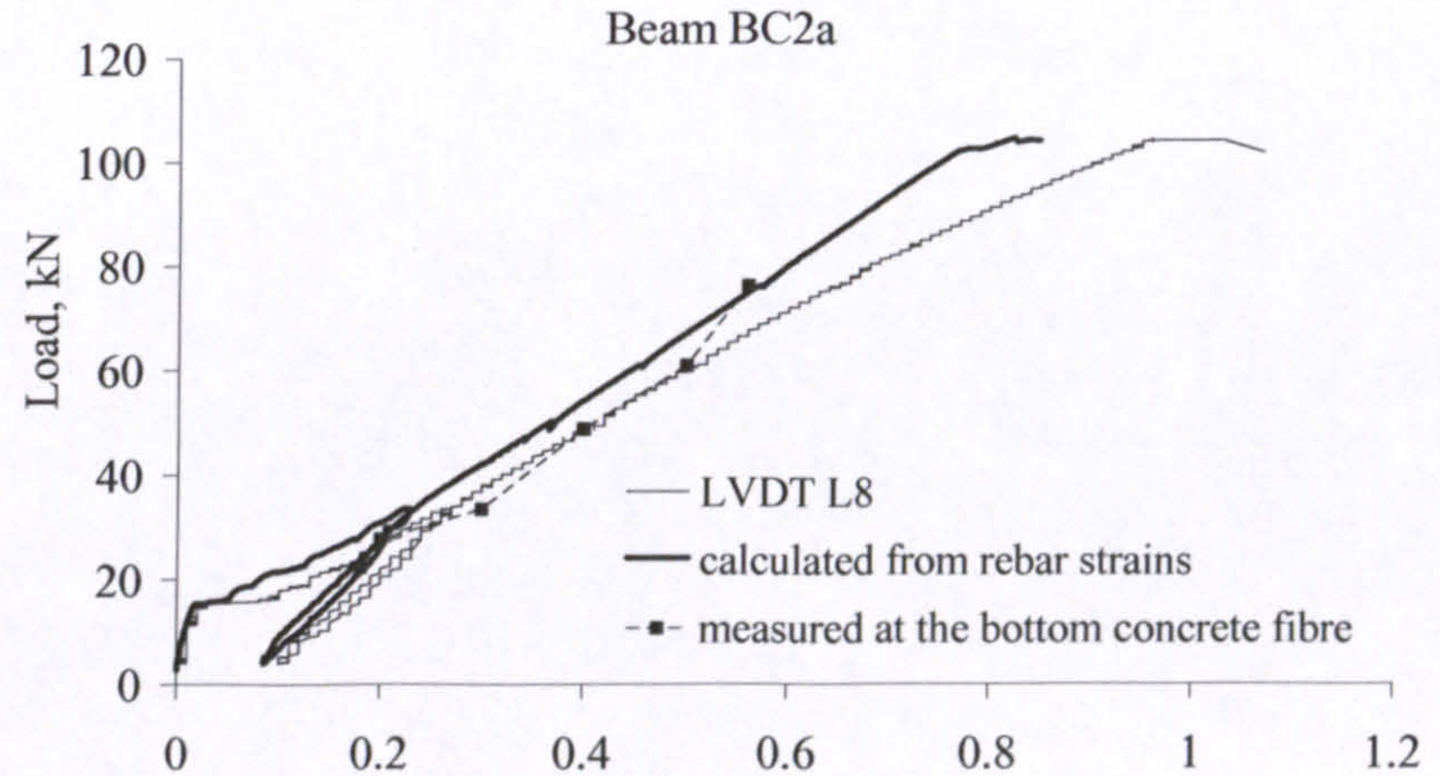

Rupture of rebars following concrete crushing.

- Cover=25mm
- Location of crack inducer is precise.
- crack at 66mm left of CL at a load of ~ 22.3-27.6kN.
- Immature crack 85mm right of CL at a load of ~ 60.9-76.2kN.

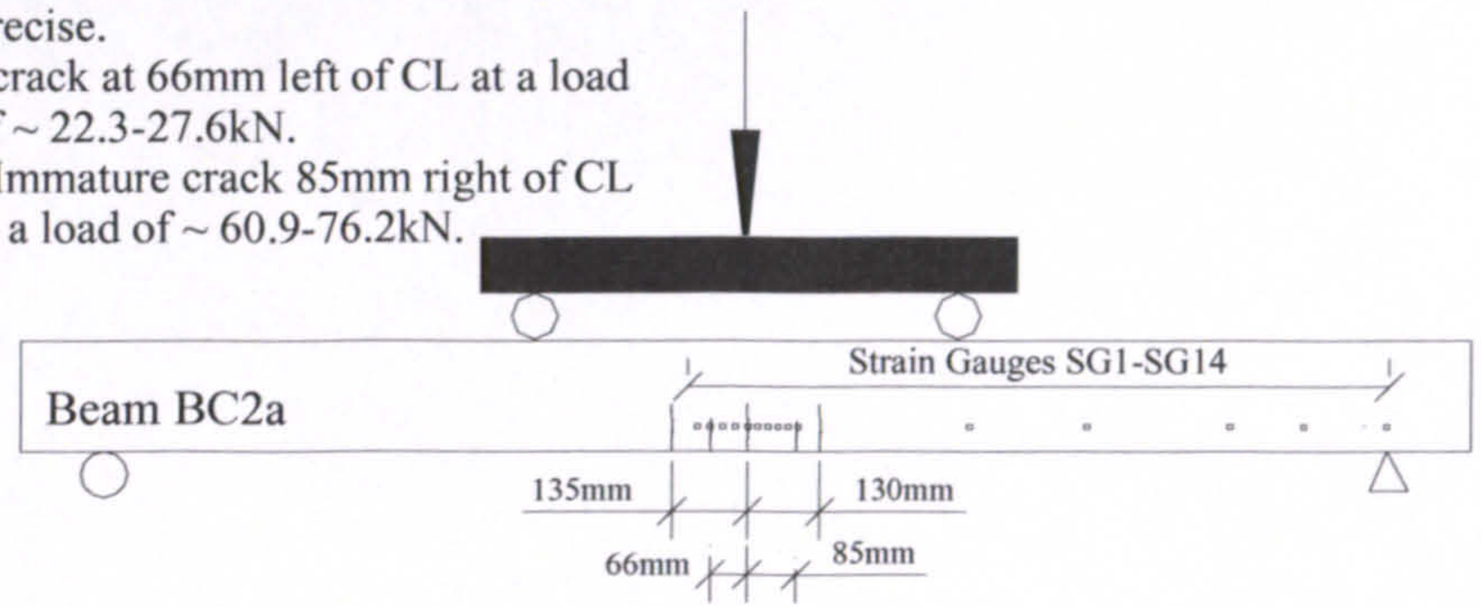

Cracks around Centre

BEAM BC2b

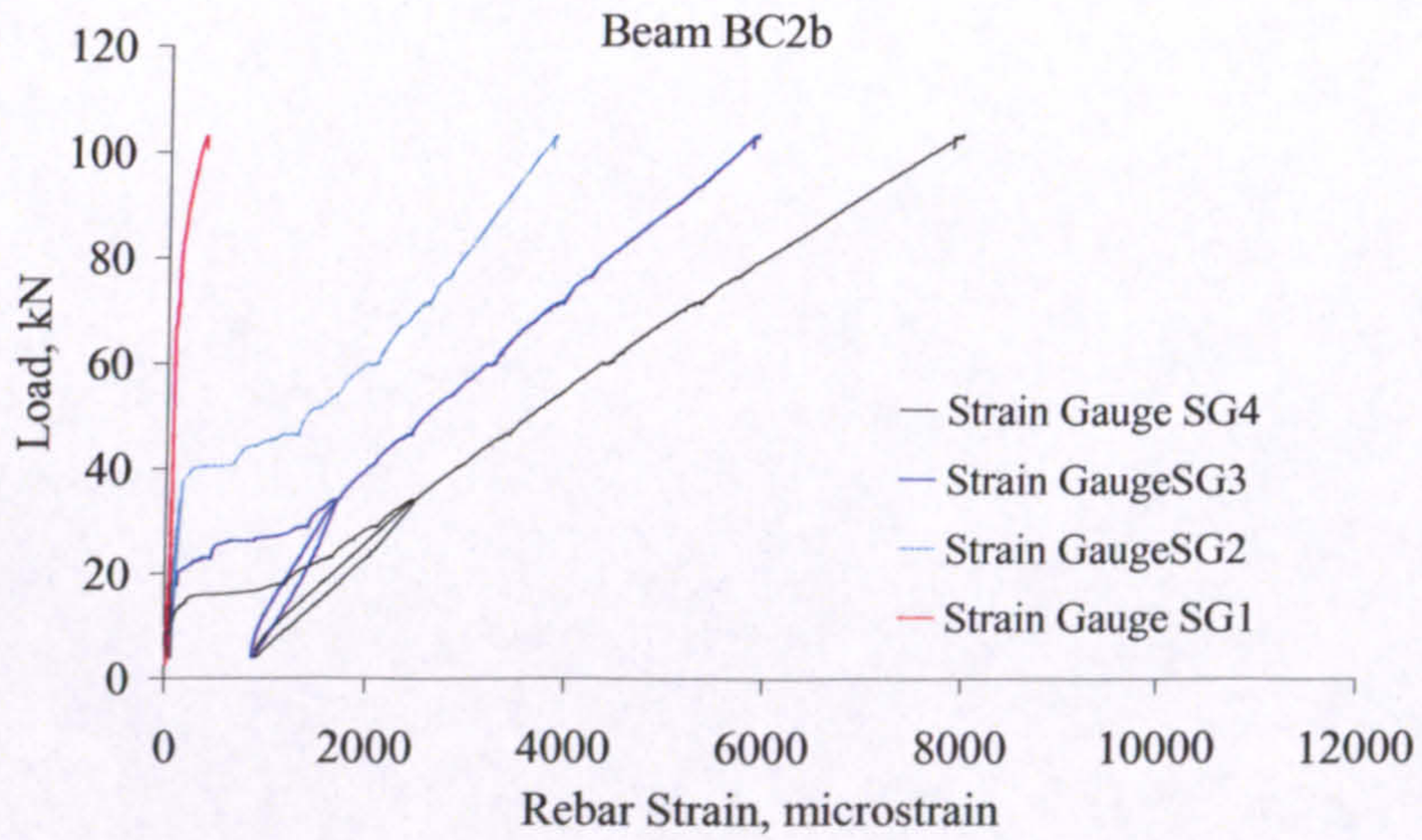
Beam BC2b
Load, kN
Rebar Strain, microstrain
Strain Gauge SG4
Strain GaugeSG3
Strain GaugeSG2
Strain Gauge SG1

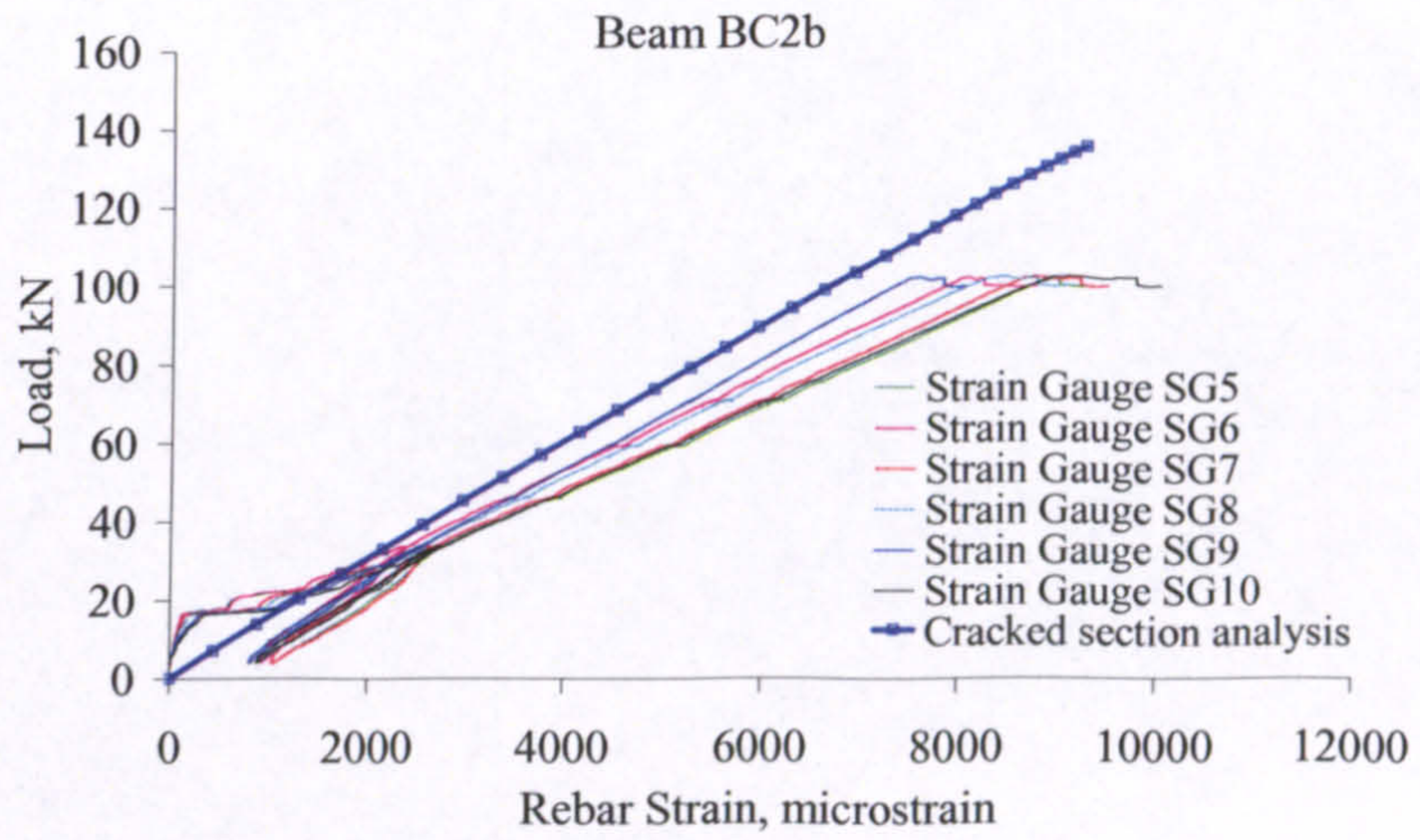
Beam BC2b
Load, kN
Rebar Strain, microstrain
Strain Gauge SG5
Strain Gauge SG6
Strain Gauge SG7
Strain Gauge SG8
Strain Gauge SG9
Strain Gauge SG10
Cracked section analysis

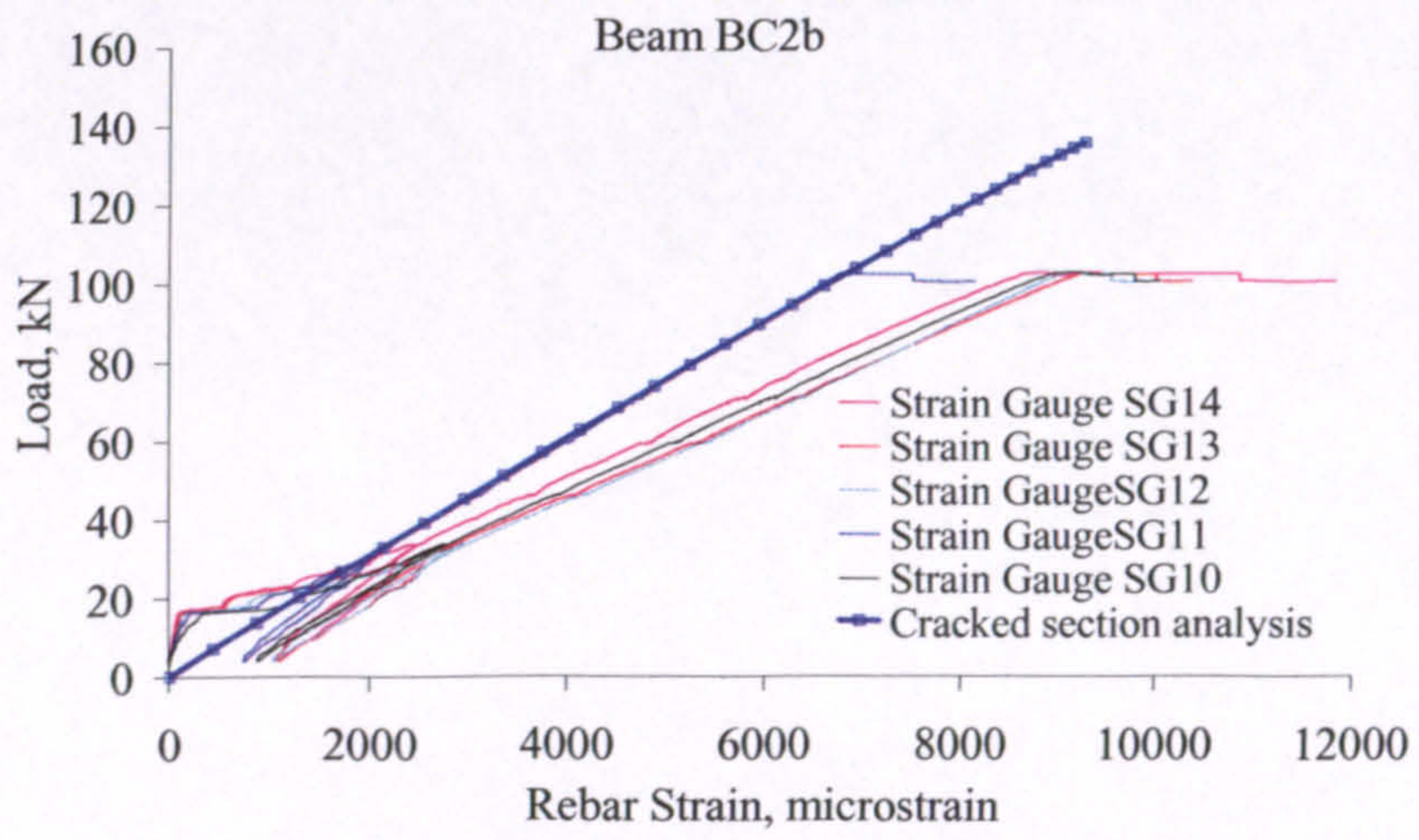
Beam BC2b
Load, kN
Rebar Strain, microstrain
Strain Gauge SG14
Strain Gauge SG13
Strain GaugeSG12
Strain GaugeSG11
Strain Gauge SG10
Cracked section analysis

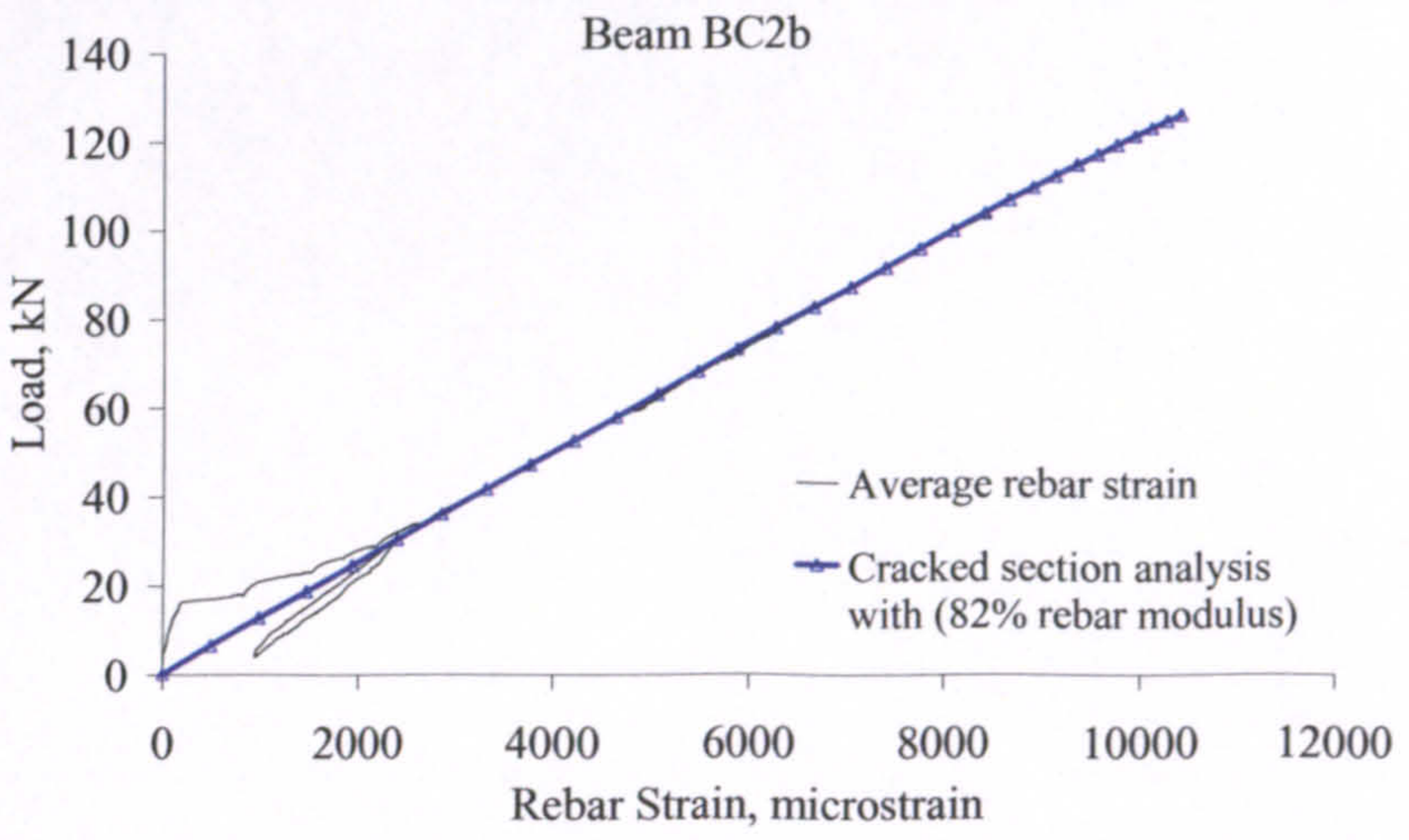
Beam BC2b
Load, kN
Rebar Strain, microstrain
Average rebar strain
Cracked section analysis
with (82% rebar modulus)

BEAM BC2b

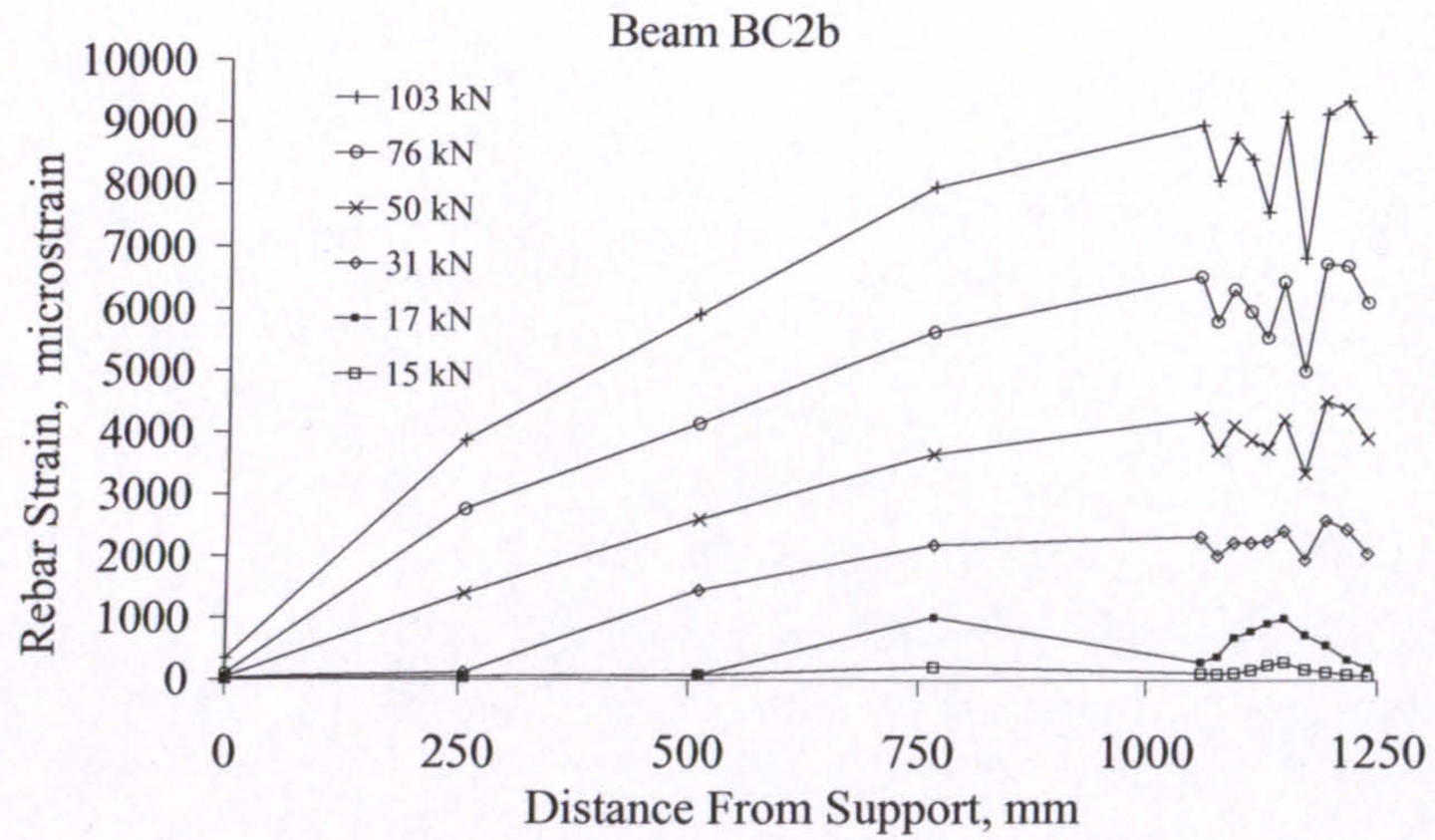
Beam BC2b
Rebar Strain, microstrain
10000
9000
8000
7000
6000
5000
4000
3000
2000
1000
0
103 kN
76 kN
50 kN
31 kN
17 kN
15 kN
0
250
500
750
1000
1250
Distance From Support, mm

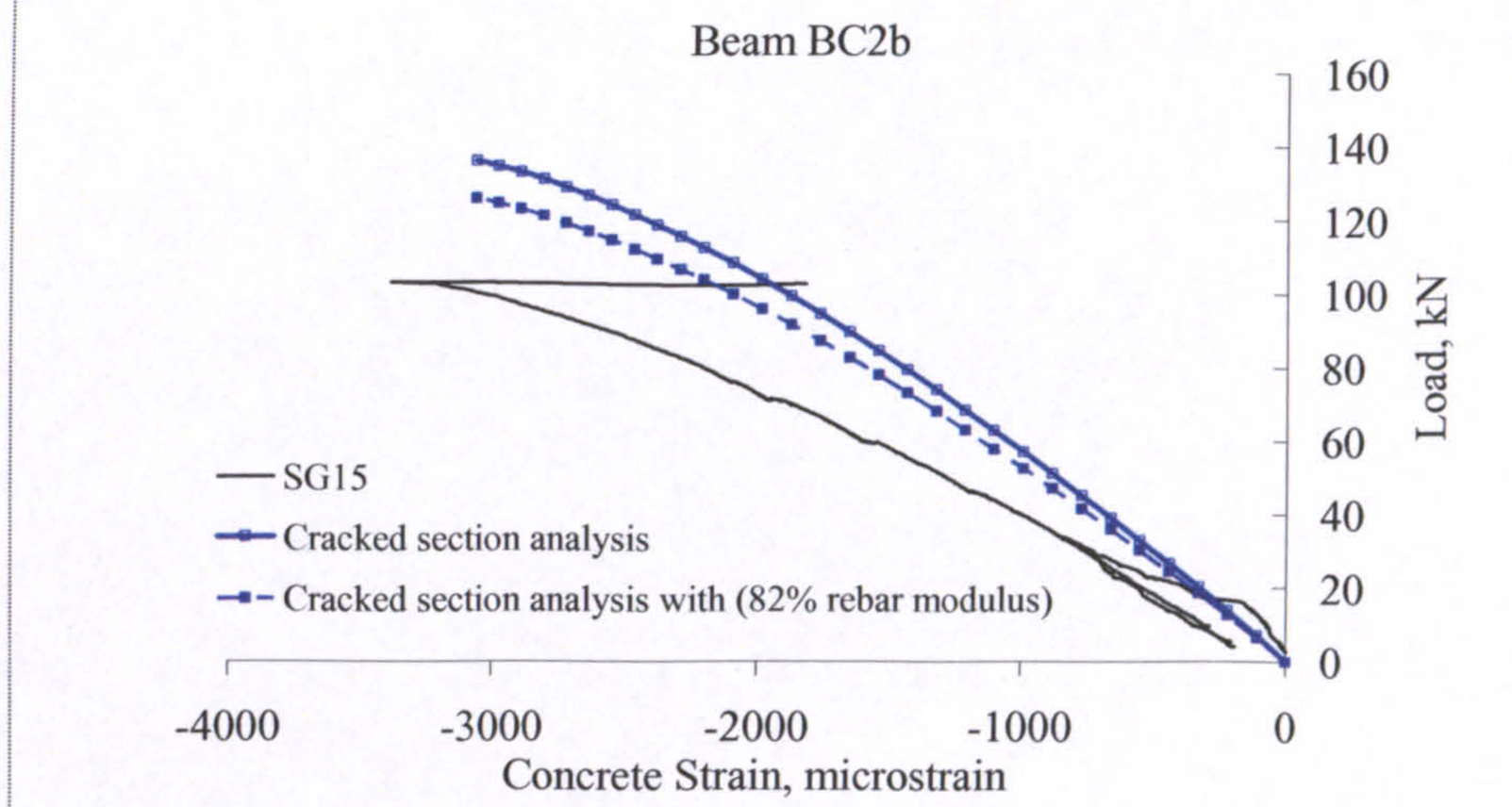
Beam BC2b
Load, kN
160
140
120
100
80
60
40
20
0
SG15
Cracked section analysis
Cracked section analysis with (82% rebar modulus)
-4000
-3000
-2000
-1000
0
Concrete Strain, microstrain

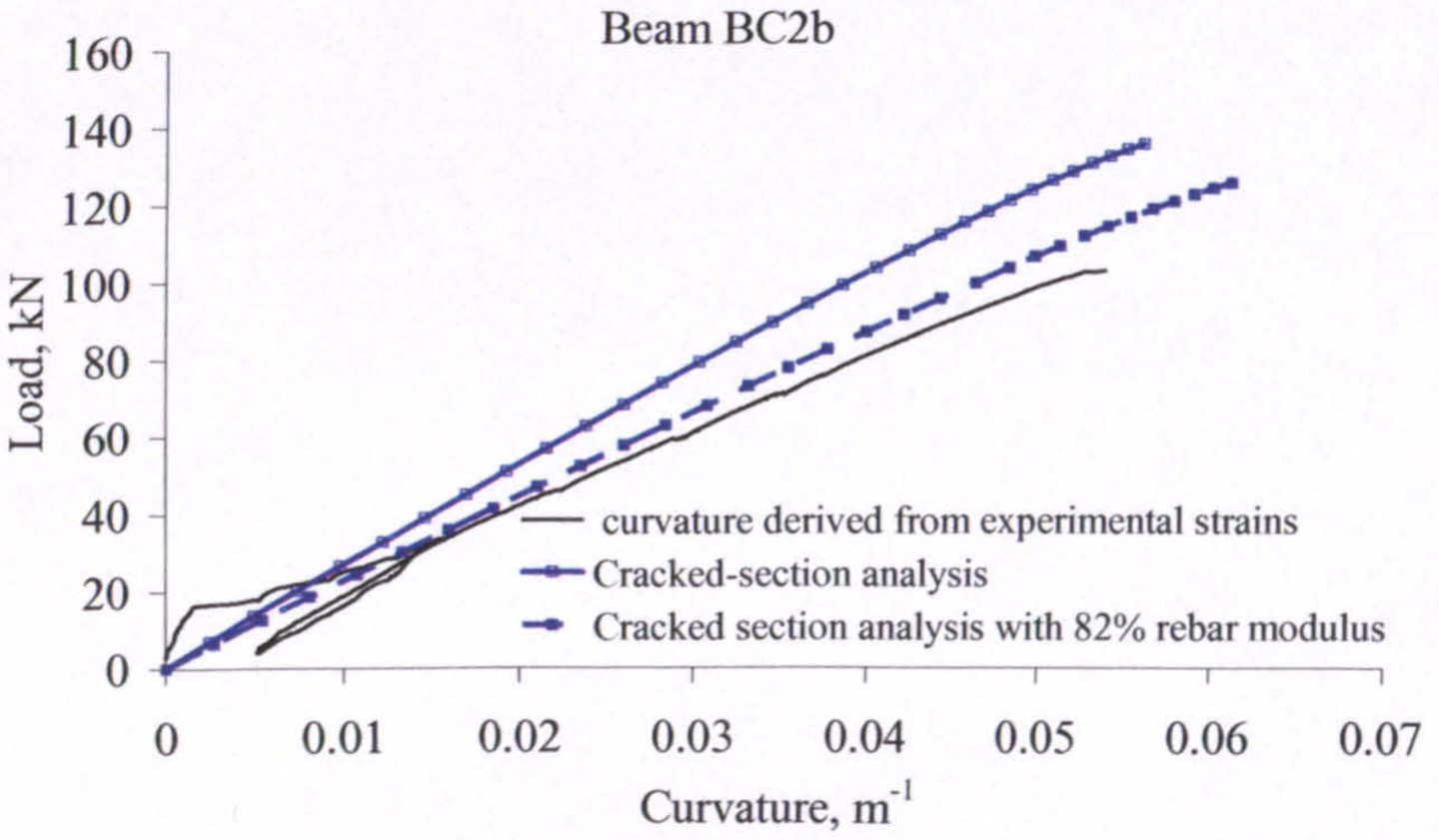
Beam BC2b
Load, kN
160
140
120
100
80
60
40
20
0
curvature derived from experimental strains
Cracked-section analysis
Cracked section analysis with 82% rebar modulus
0
0.01
0.02
0.03
0.04
0.05
0.06
0.07
Curvature, m-1

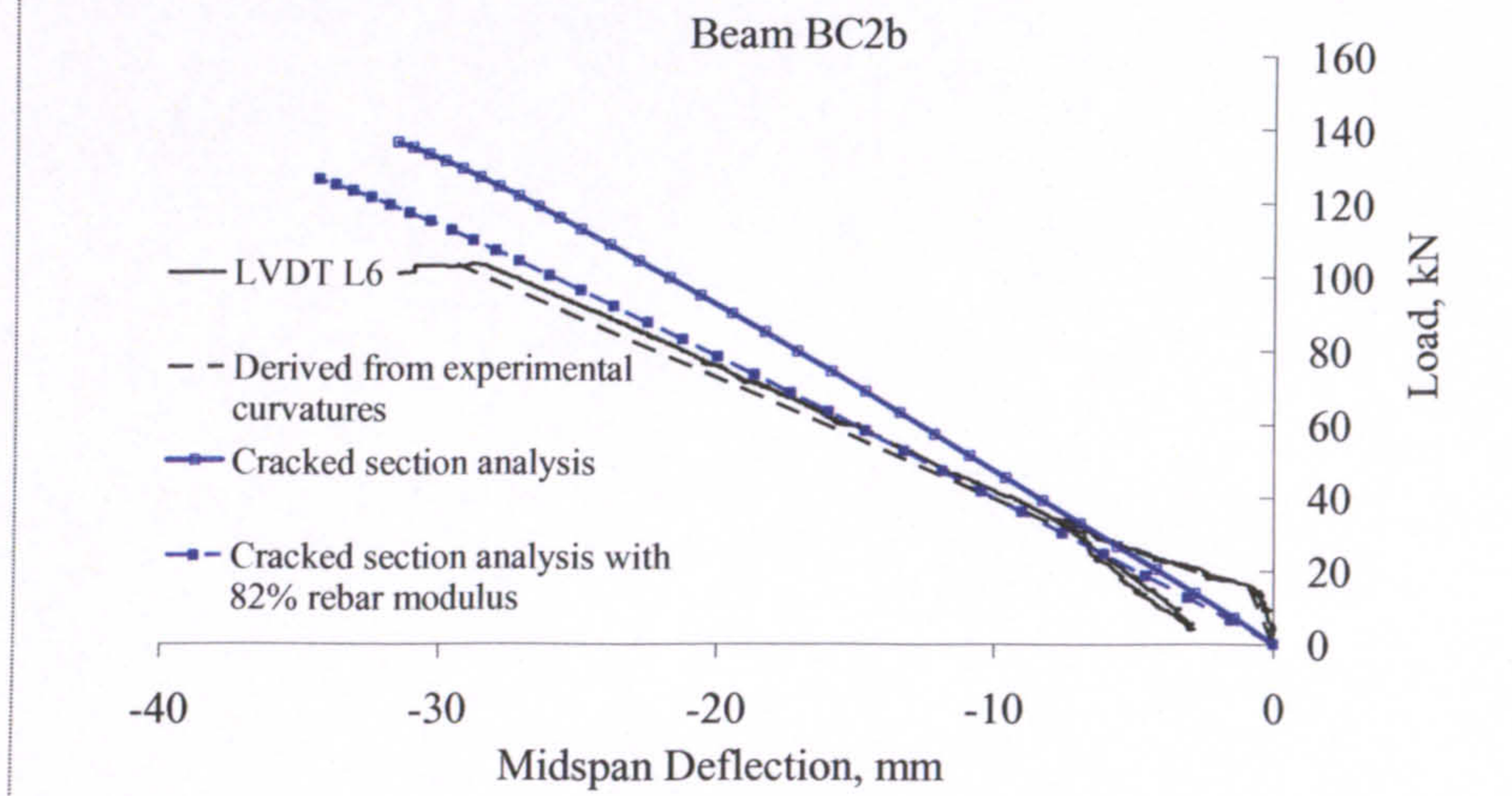
Beam BC2b
Load, kN
160
140
120
100
80
60
40
20
0
LVDT L6
Derived from experimental curvatures
Cracked section analysis
Cracked section analysis with 82% rebar modulus
-40
-30
-20
-10
0
Midspan Deflection, mm

BEAM BC2b

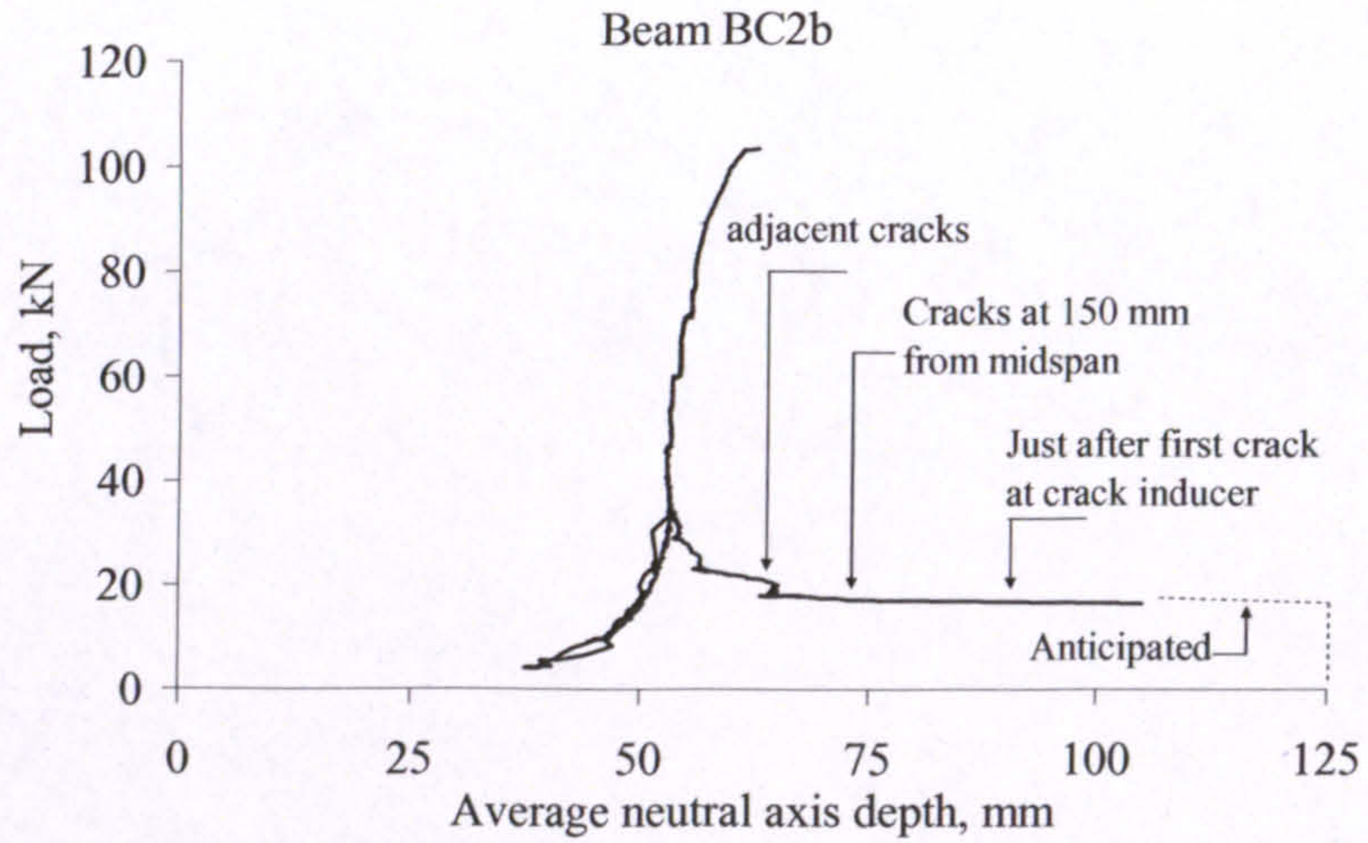
Beam BC2b
Load, kN
Average neutral axis depth, mm
adjacent cracks
Cracks at 150 mm from midspan
Just after first crack at crack inducer
Anticipated
0
20
40
60
80
100
120
0
25
50
75
100
125

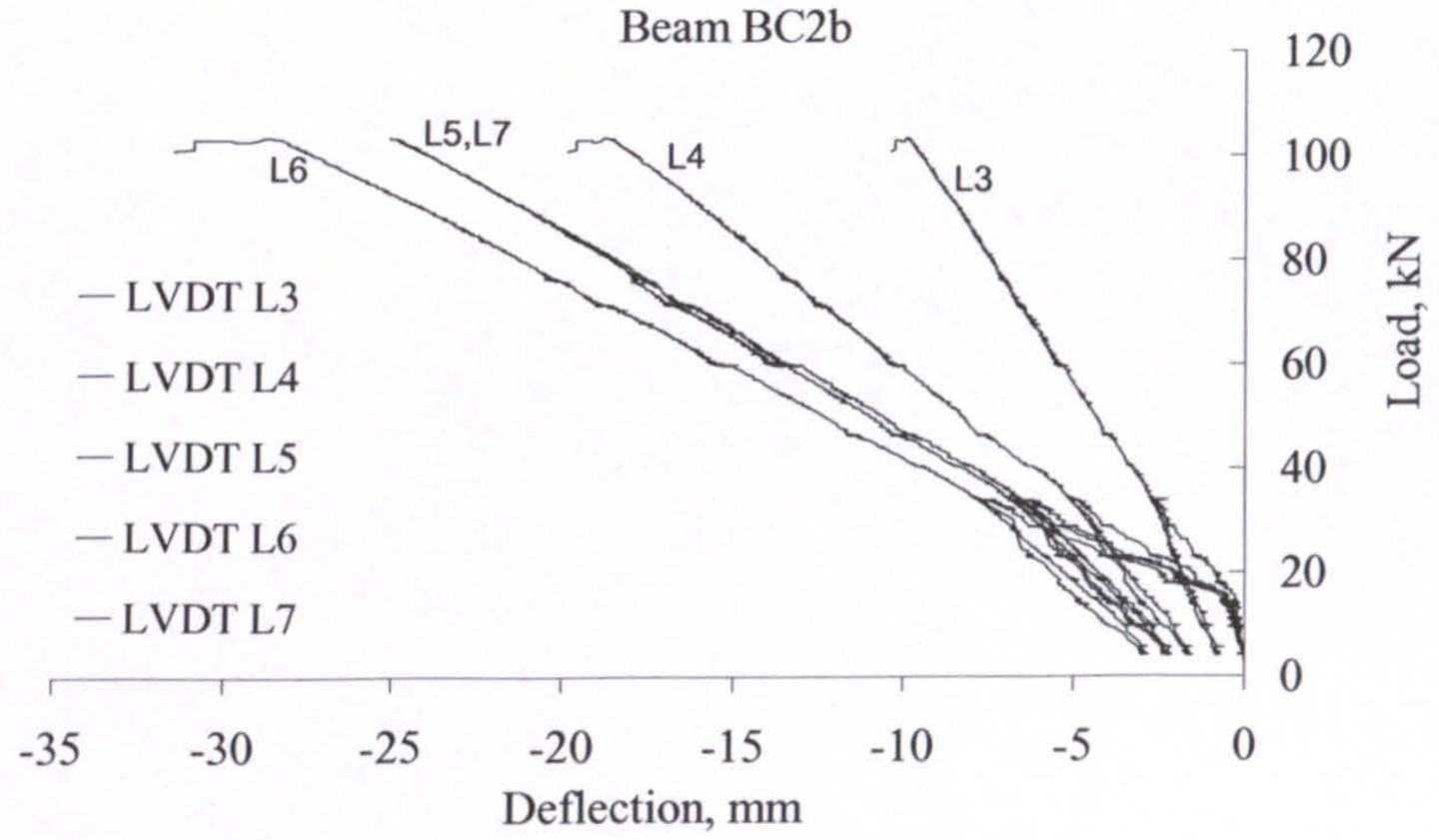
Beam BC2b
Load, kN
Deflection, mm
L6
L5,L7
L4
L3
LVDT L3
LVDT L4
LVDT L5
LVDT L6
LVDT L7
0
20
40
60
80
100
120
-35
-30
-25
-20
-15
-10
-5
0

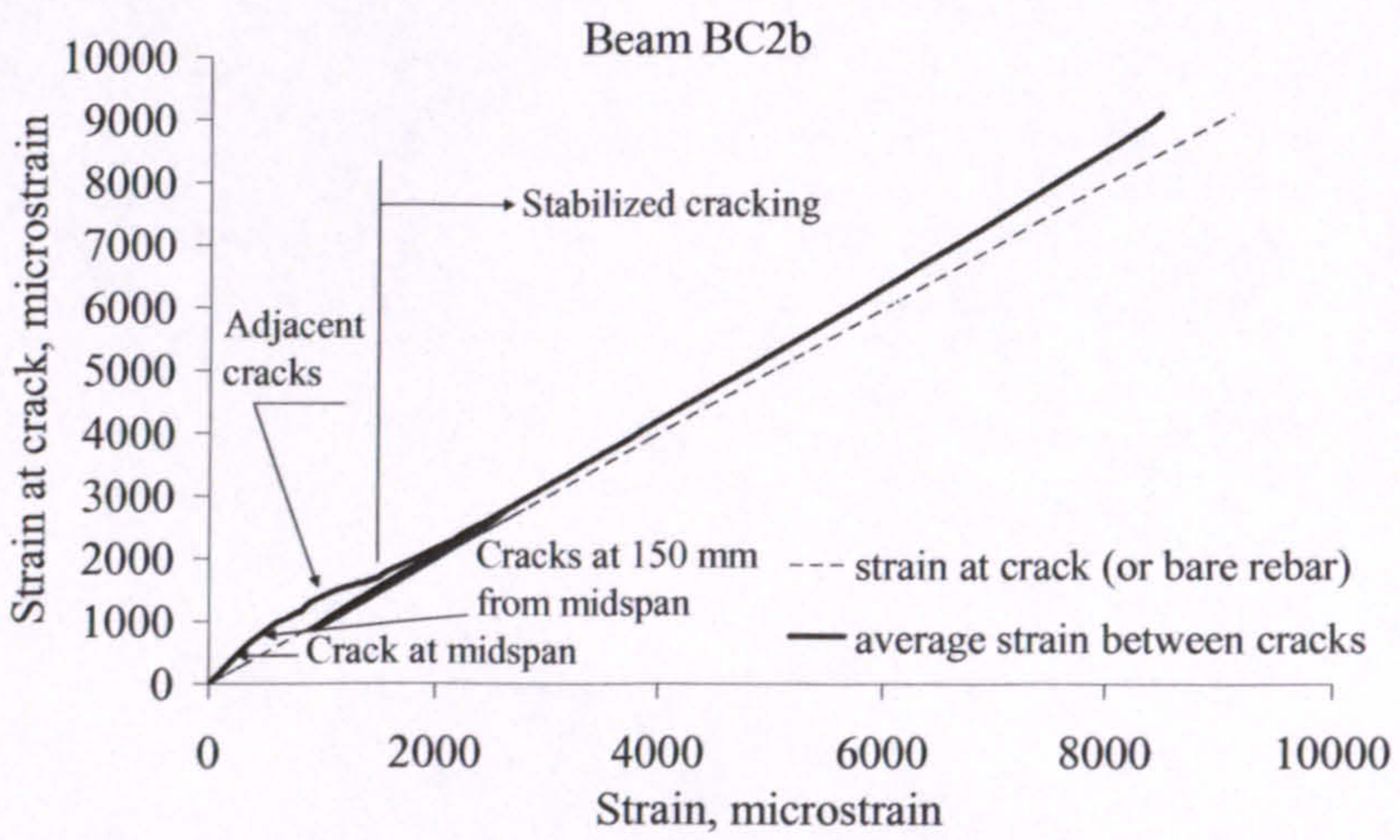
Beam BC2b
Strain at crack, microstrain
Strain, microstrain
Stabilized cracking
Adjacent cracks
Cracks at 150 mm from midspan
Crack at midspan
strain at crack (or bare rebar)
average strain between cracks
0
1000
2000
3000
4000
5000
6000
7000
8000
9000
10000
0
2000
4000
6000
8000
10000

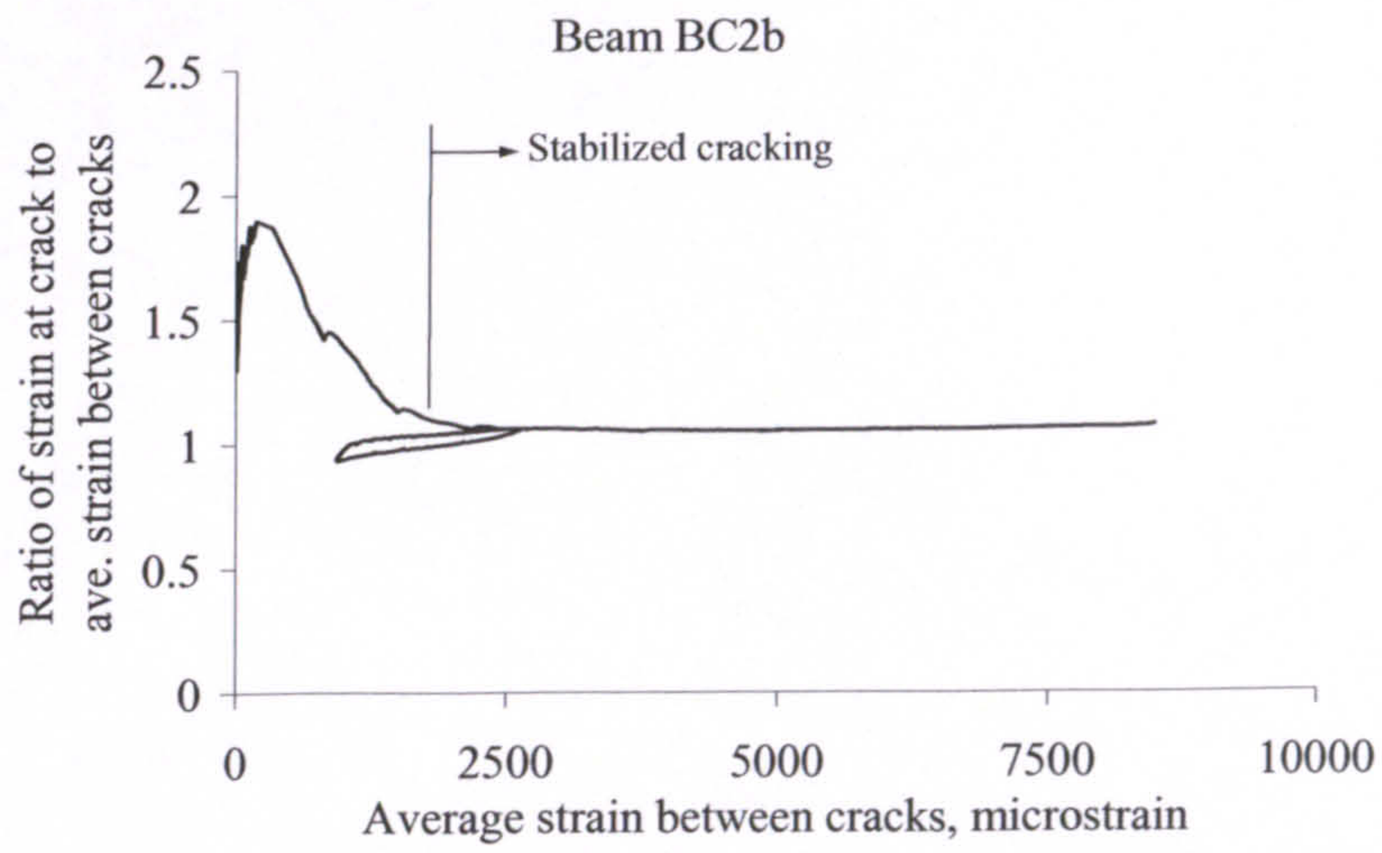
Beam BC2b
Ratio of strain at crack to ave. strain between cracks
Average strain between cracks, microstrain
Stabilized cracking
0
0.5
1
1.5
2
2.5
0
2500
5000
7500
10000

BEAM BC2b

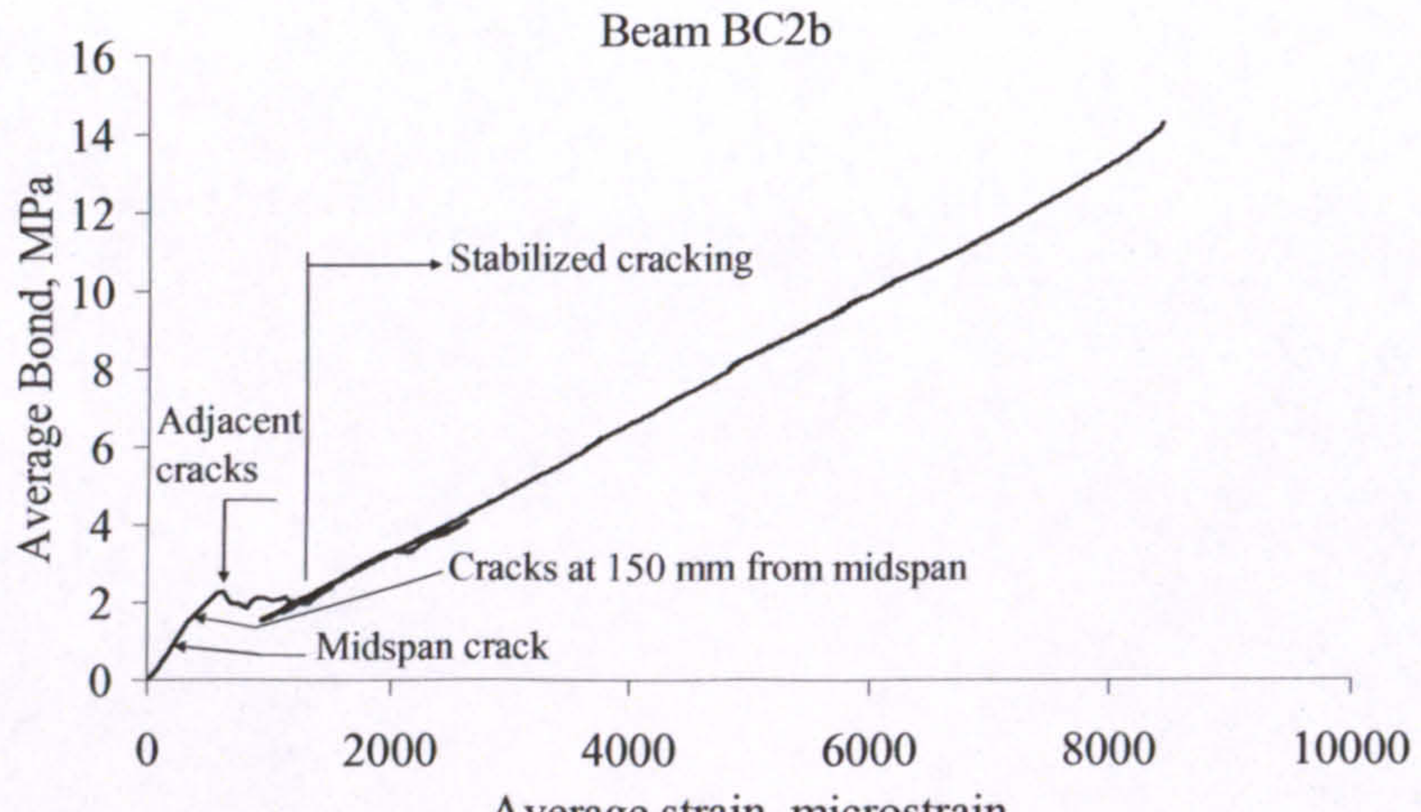

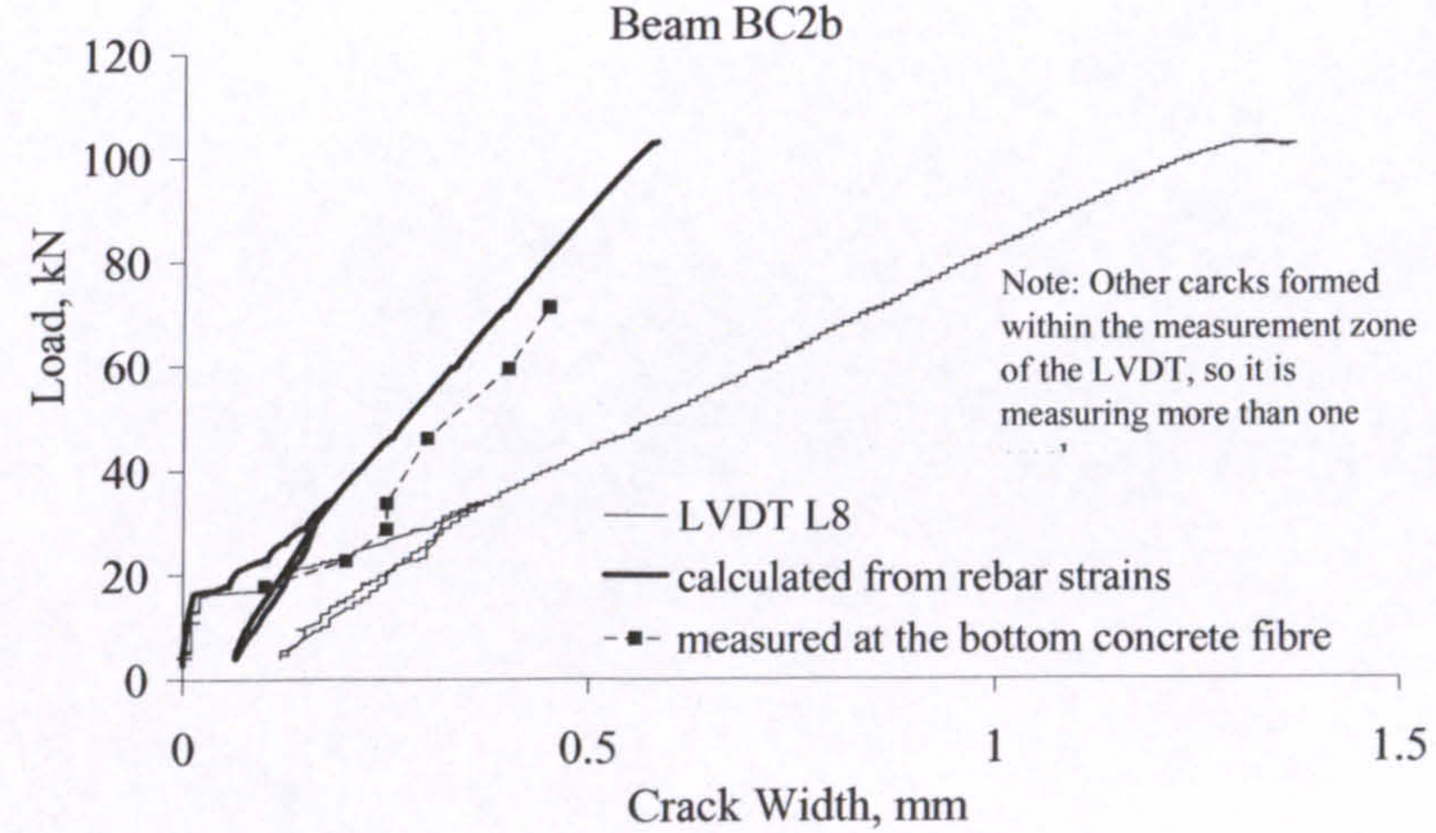

Rupture of rebars following concrete crushing

- Cover=25mm
- Location of crack inducer is precise.
- cracks at 50mm left and 87mm right of CL at a load of ~ 18.0-22.7kN.

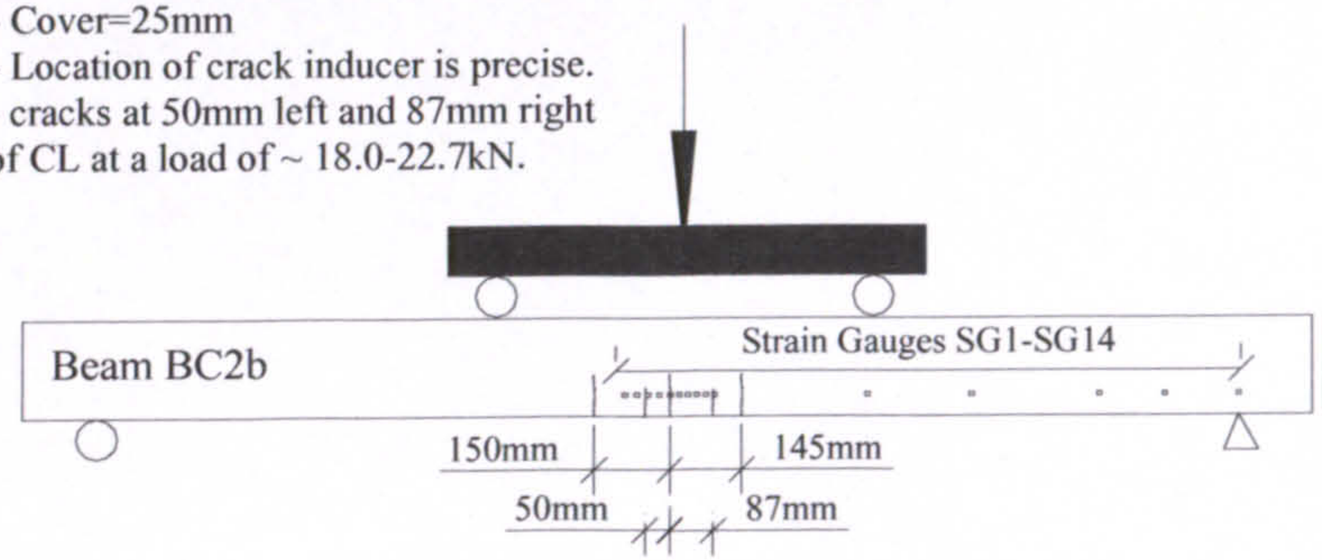

Cracks around Centre

BEAM BC3a

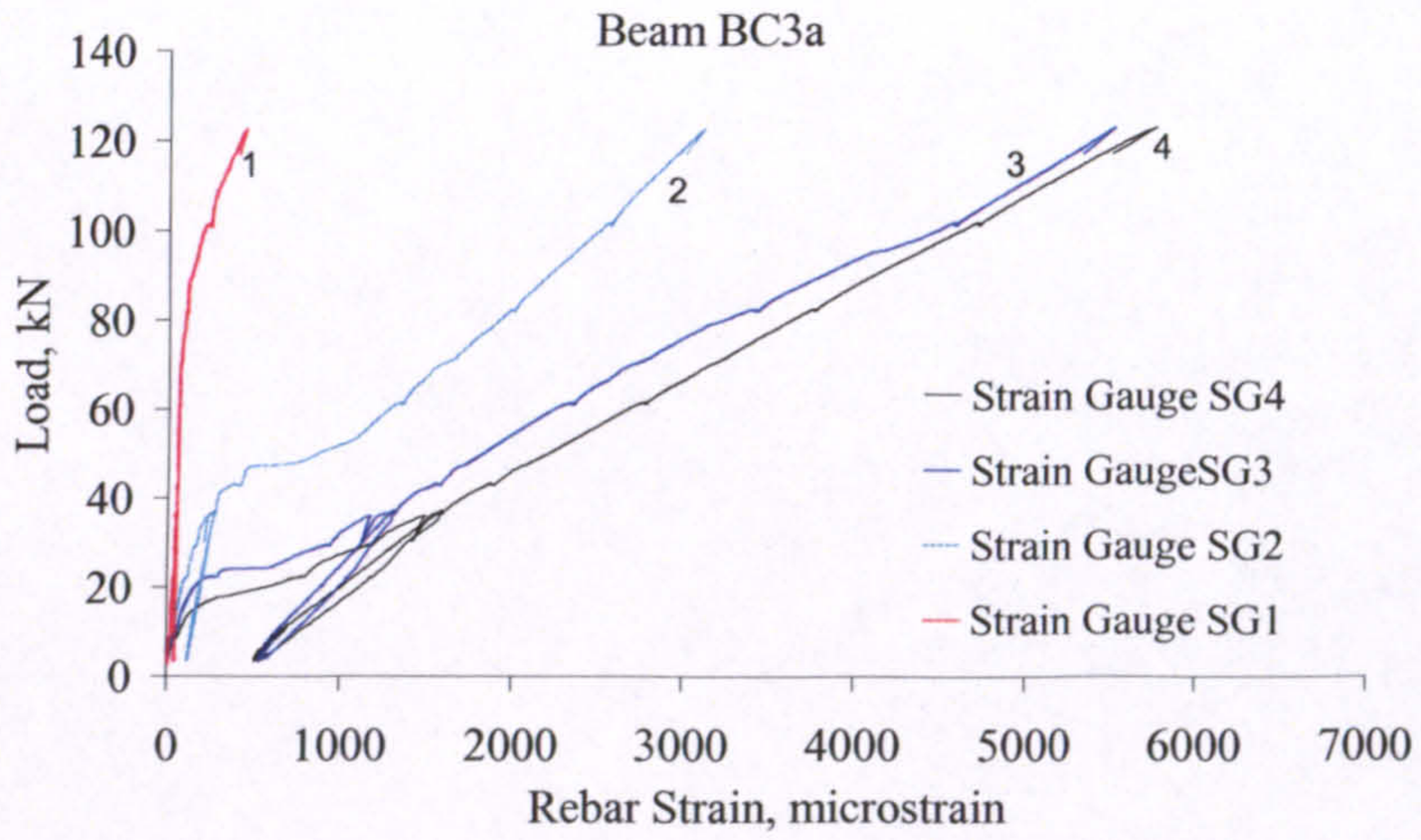
Beam BC3a
Load, kN
Rebar Strain, microstrain
0
20
40
60
80
100
120
140
0
1000
2000
3000
4000
5000
6000
7000
1
2
3
4
Strain Gauge SG4
Strain GaugeSG3
Strain Gauge SG2
Strain Gauge SG1

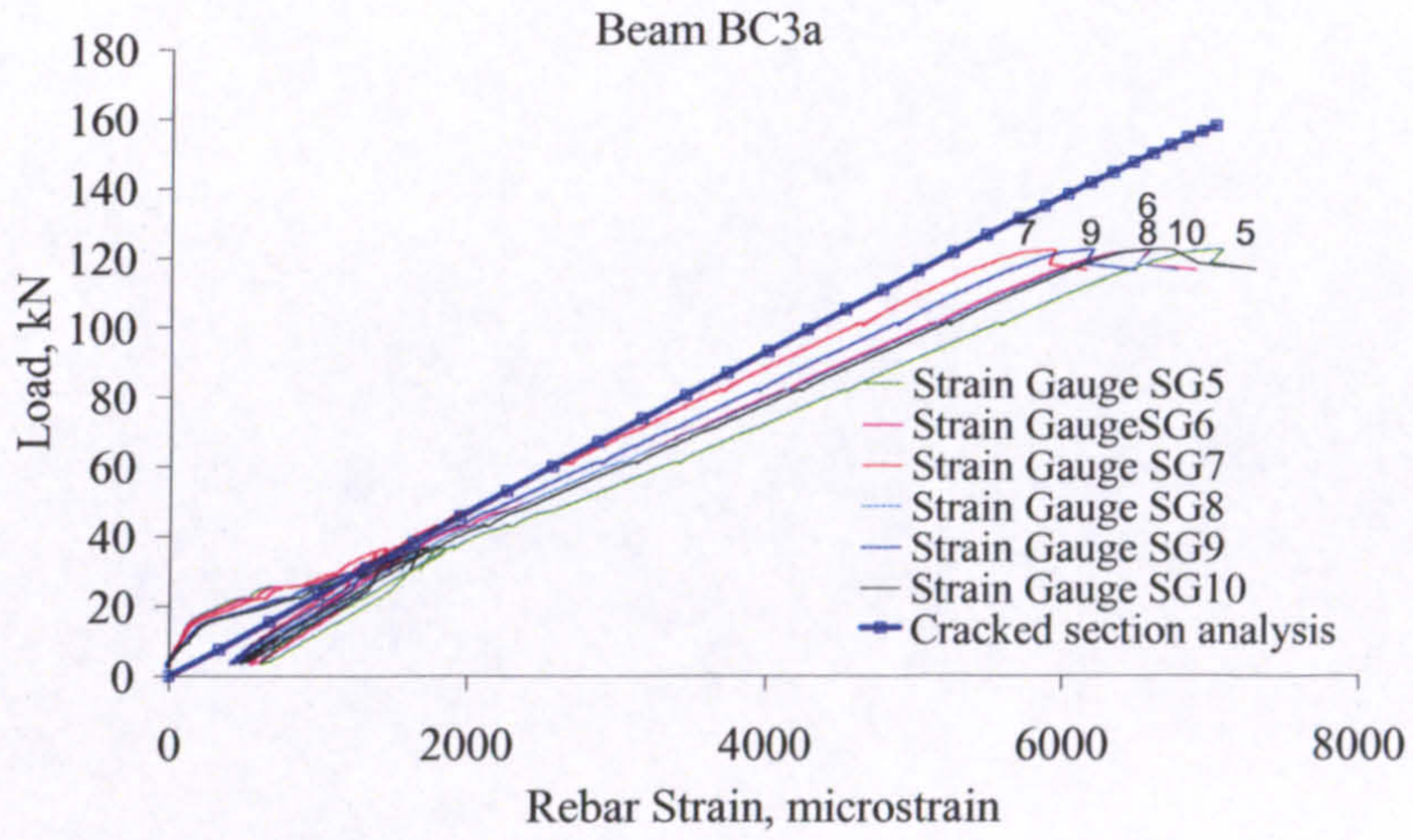
Beam BC3a
Load, kN
Rebar Strain, microstrain
0
20
40
60
80
100
120
140
160
180
0
2000
4000
6000
8000
6
7
9
8
10
5
Strain Gauge SG5
Strain GaugeSG6
Strain Gauge SG7
Strain Gauge SG8
Strain Gauge SG9
Strain Gauge SG10
Cracked section analysis

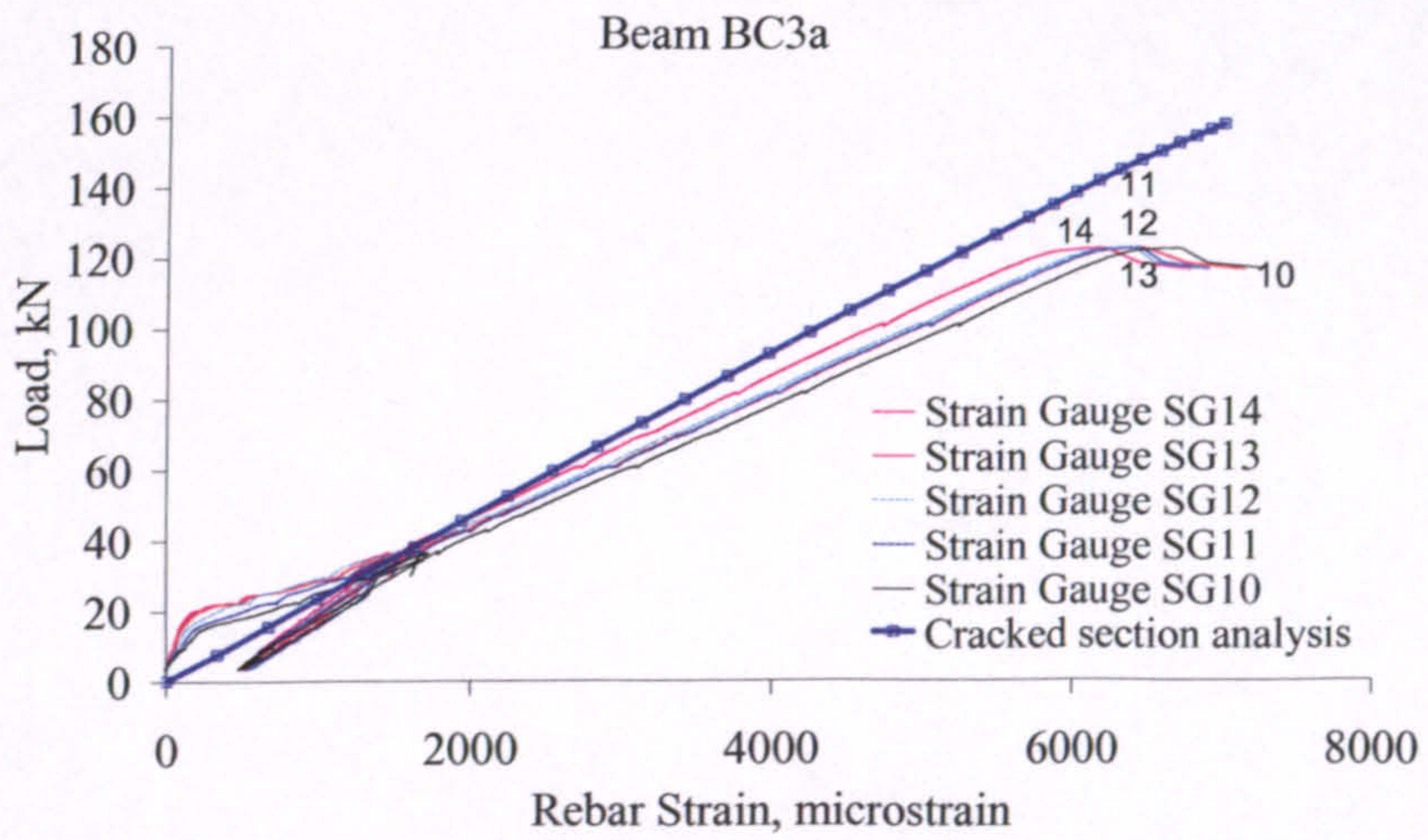
Beam BC3a
Load, kN
Rebar Strain, microstrain
0
20
40
60
80
100
120
140
160
180
0
2000
4000
6000
8000
11
14
12
13
10
Strain Gauge SG14
Strain Gauge SG13
Strain Gauge SG12
Strain Gauge SG11
Strain Gauge SG10
Cracked section analysis

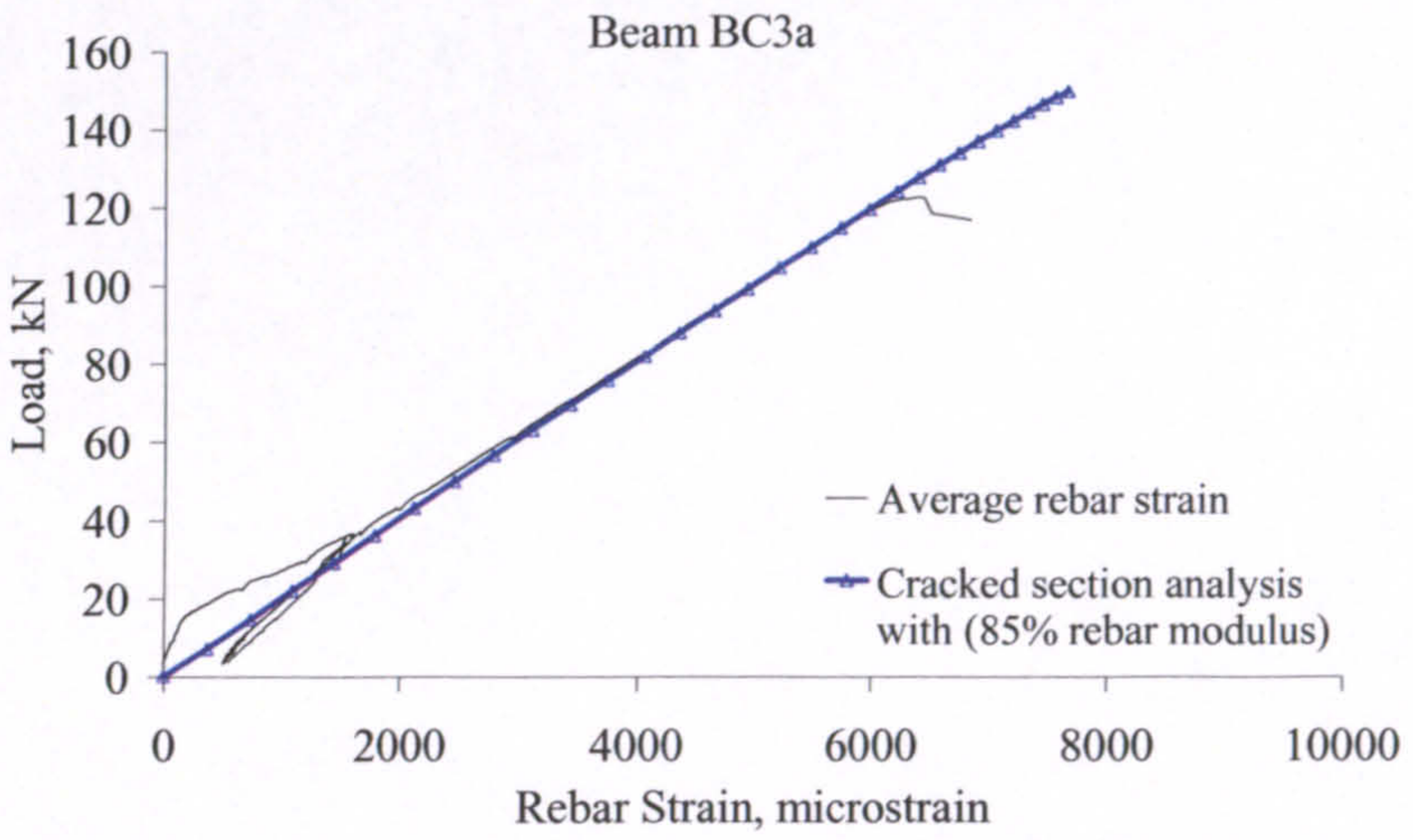
Beam BC3a
Load, kN
Rebar Strain, microstrain
0
20
40
60
80
100
120
140
160
0
2000
4000
6000
8000
10000
Average rebar strain
Cracked section analysis
with (85% rebar modulus)

BEAM BC3a

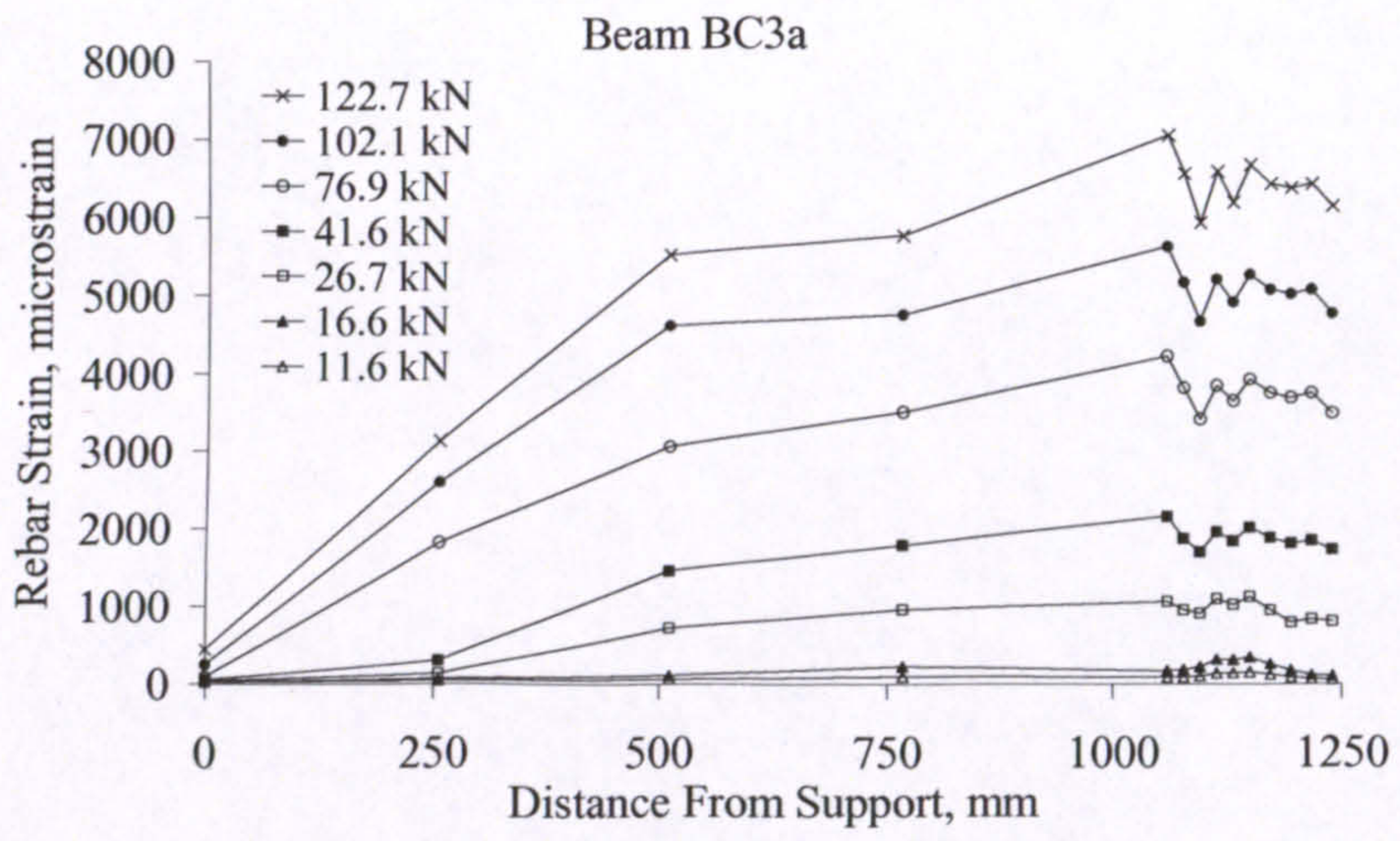
Beam BC3a
Rebar Strain, microstrain
8000
7000
6000
5000
4000
3000
2000
1000
0
122.7 kN
102.1 kN
76.9 kN
41.6 kN
26.7 kN
16.6 kN
11.6 kN
0
250
500
750
1000
1250
Distance From Support, mm

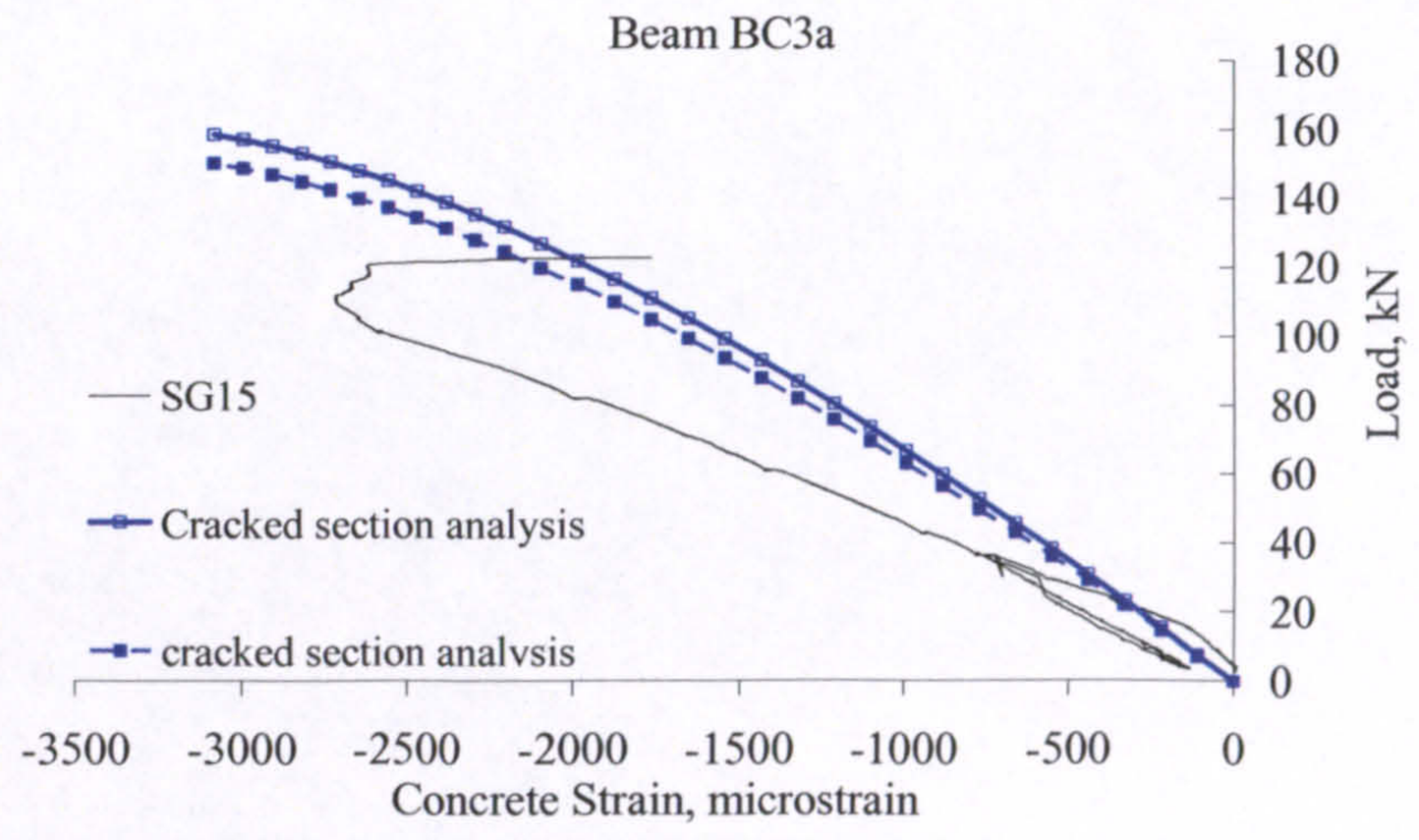
Beam BC3a
Load, kN
180
160
140
120
100
80
60
40
20
0
SG15
Cracked section analysis
cracked section analysis
-3500
-3000
-2500
-2000
-1500
-1000
-500
0
Concrete Strain, microstrain

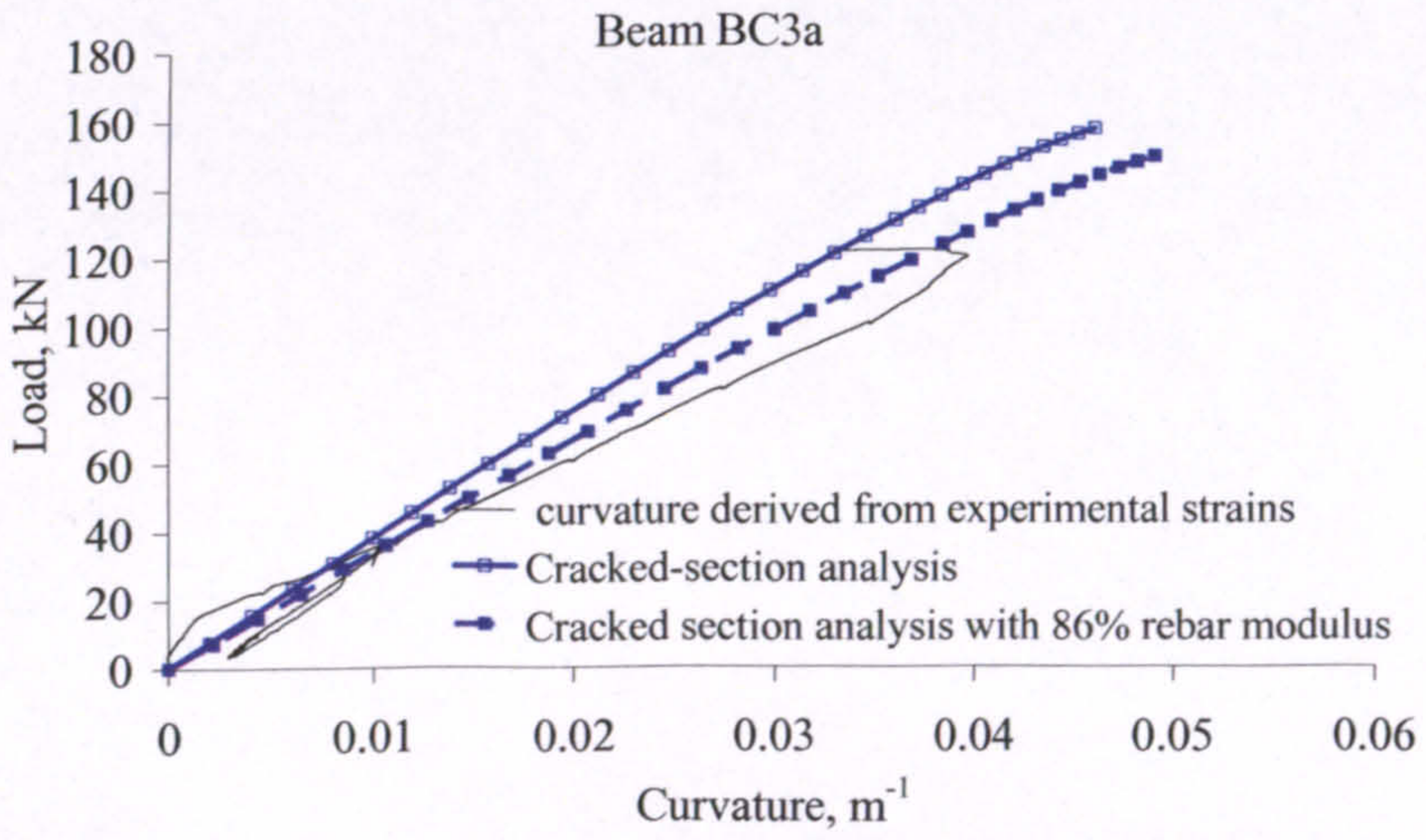
Beam BC3a
Load, kN
180
160
140
120
100
80
60
40
20
0
curvature derived from experimental strains
Cracked-section analysis
Cracked section analysis with 86% rebar modulus
0
0.01
0.02
0.03
0.04
0.05
0.06
Curvature, m-1

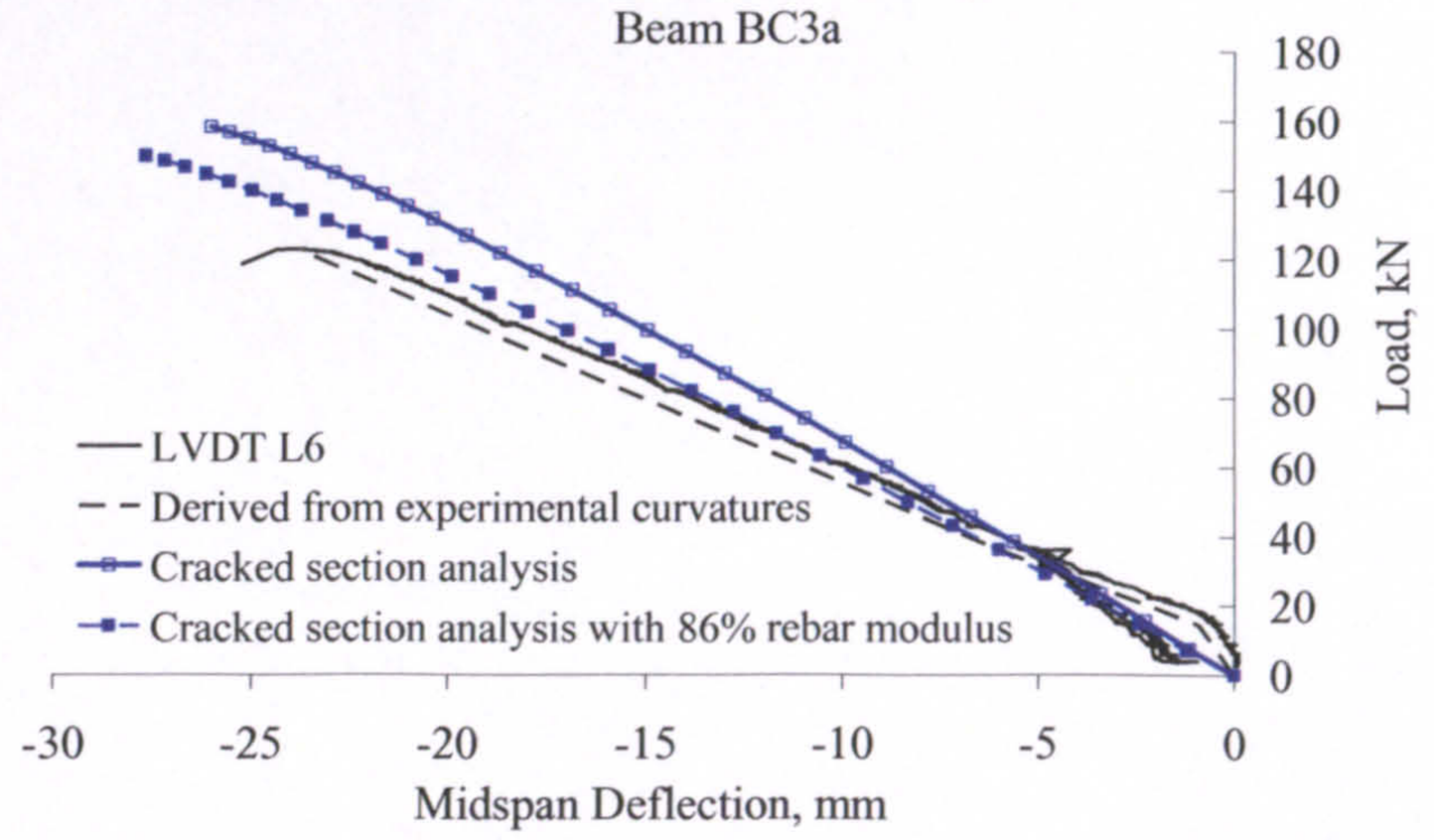
Beam BC3a
Load, kN
180
160
140
120
100
80
60
40
20
0
LVDT L6
Derived from experimental curvatures
Cracked section analysis
Cracked section analysis with 86% rebar modulus
-30
-25
-20
-15
-10
-5
0
Midspan Deflection, mm

BEAM BC3a

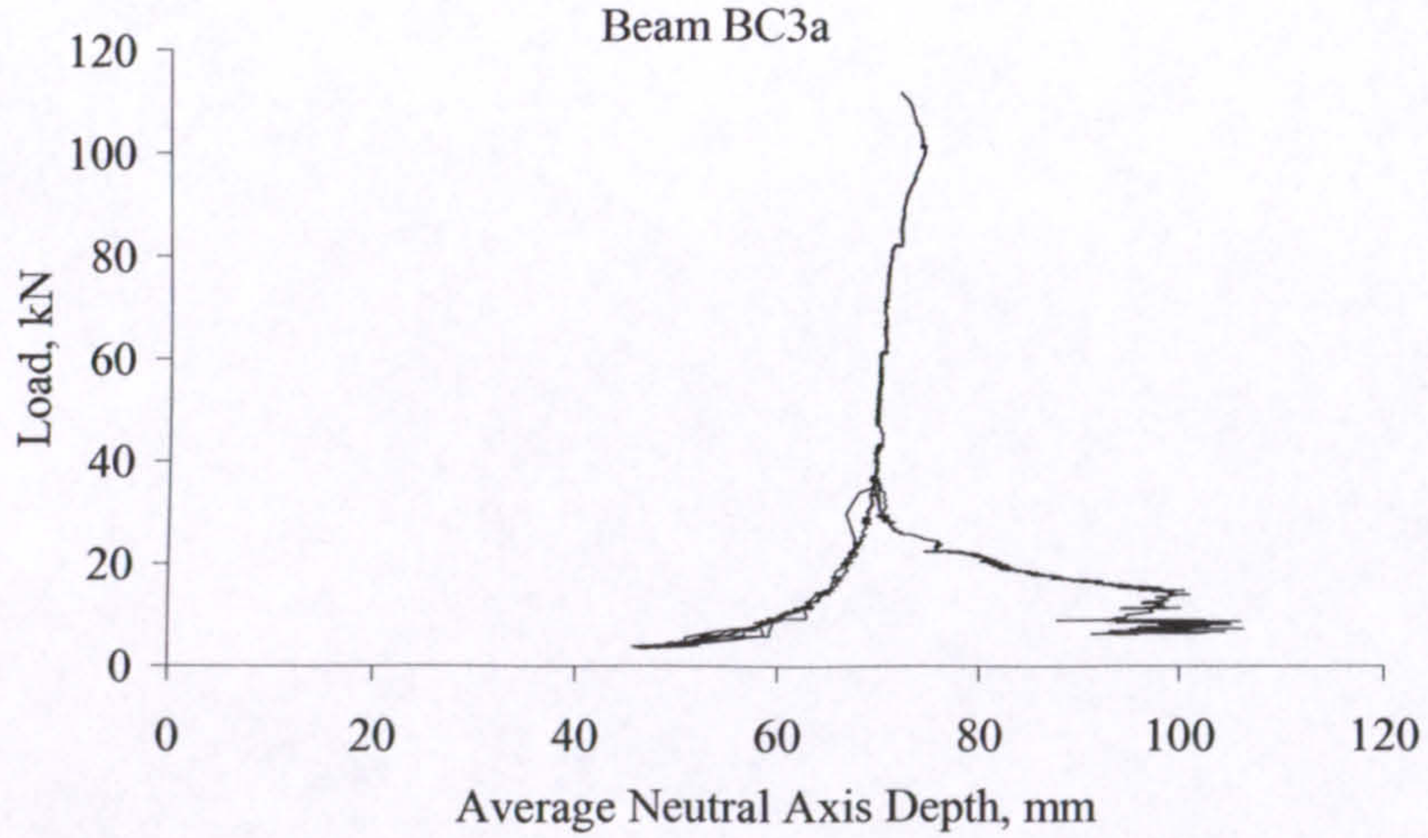
Beam BC3a
Load, kN
120
100
80
60
40
20
0
0
20
40
60
80
100
120
Average Neutral Axis Depth, mm

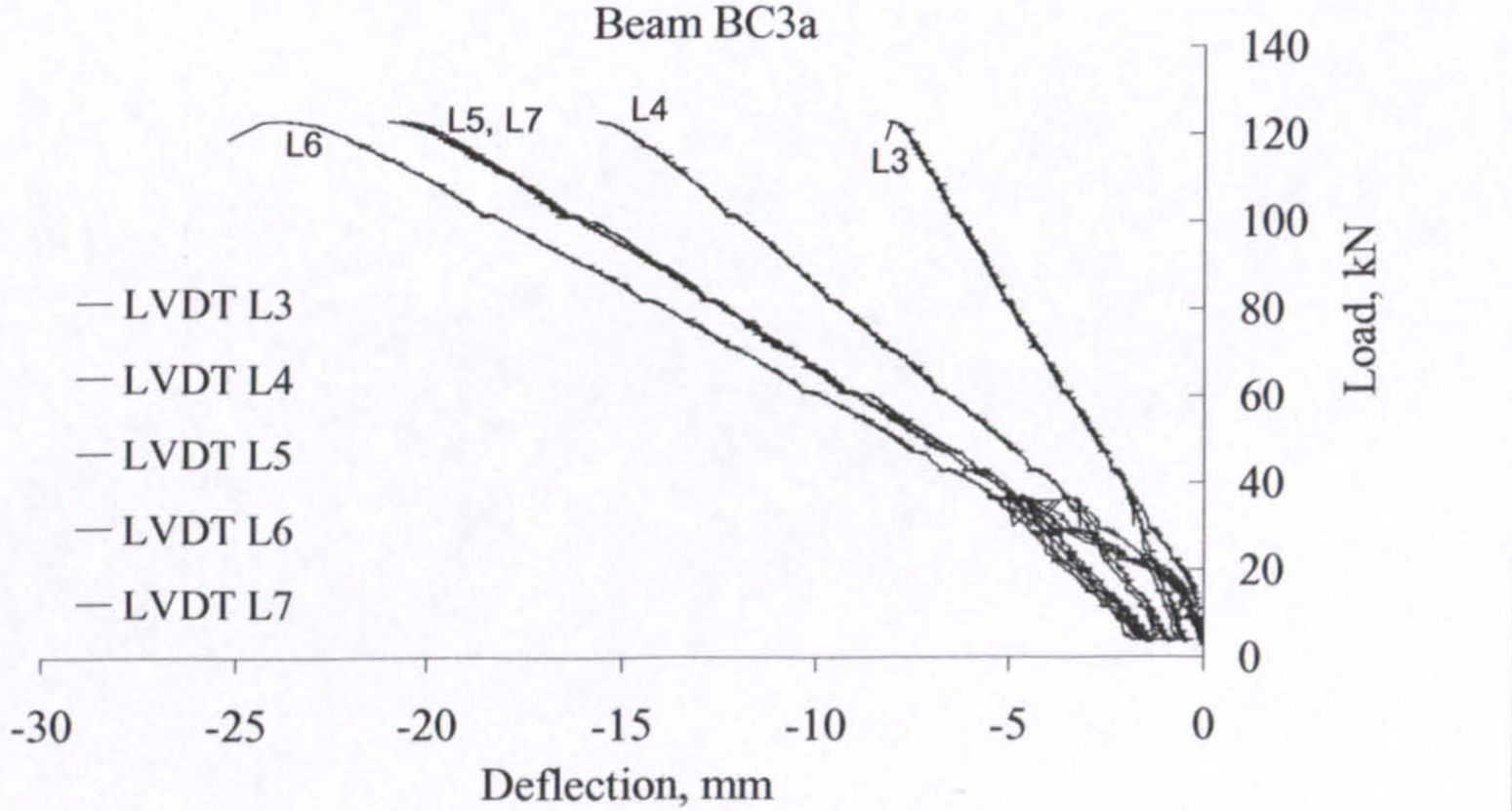
Beam BC3a
L6
L5, L7
L4
L3
— LVDT L3
— LVDT L4
— LVDT L5
— LVDT L6
— LVDT L7
140
120
100
80
60
40
20
0
Load, kN
-30
-25
-20
-15
-10
-5
0
Deflection, mm

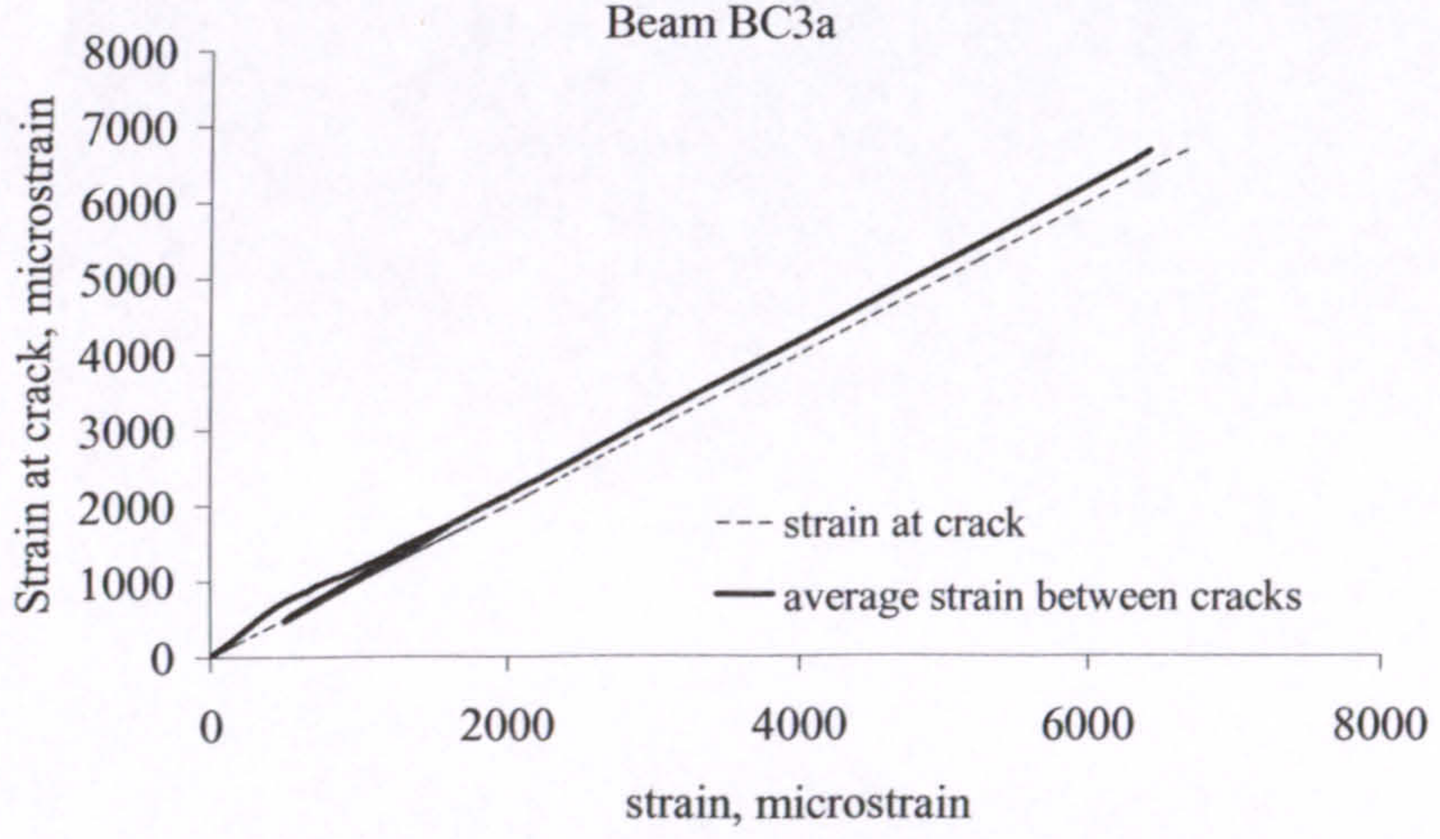
Beam BC3a
Strain at crack, microstrain
8000
7000
6000
5000
4000
3000
2000
1000
0
--- strain at crack
— average strain between cracks
0
2000
4000
6000
8000
strain, microstrain

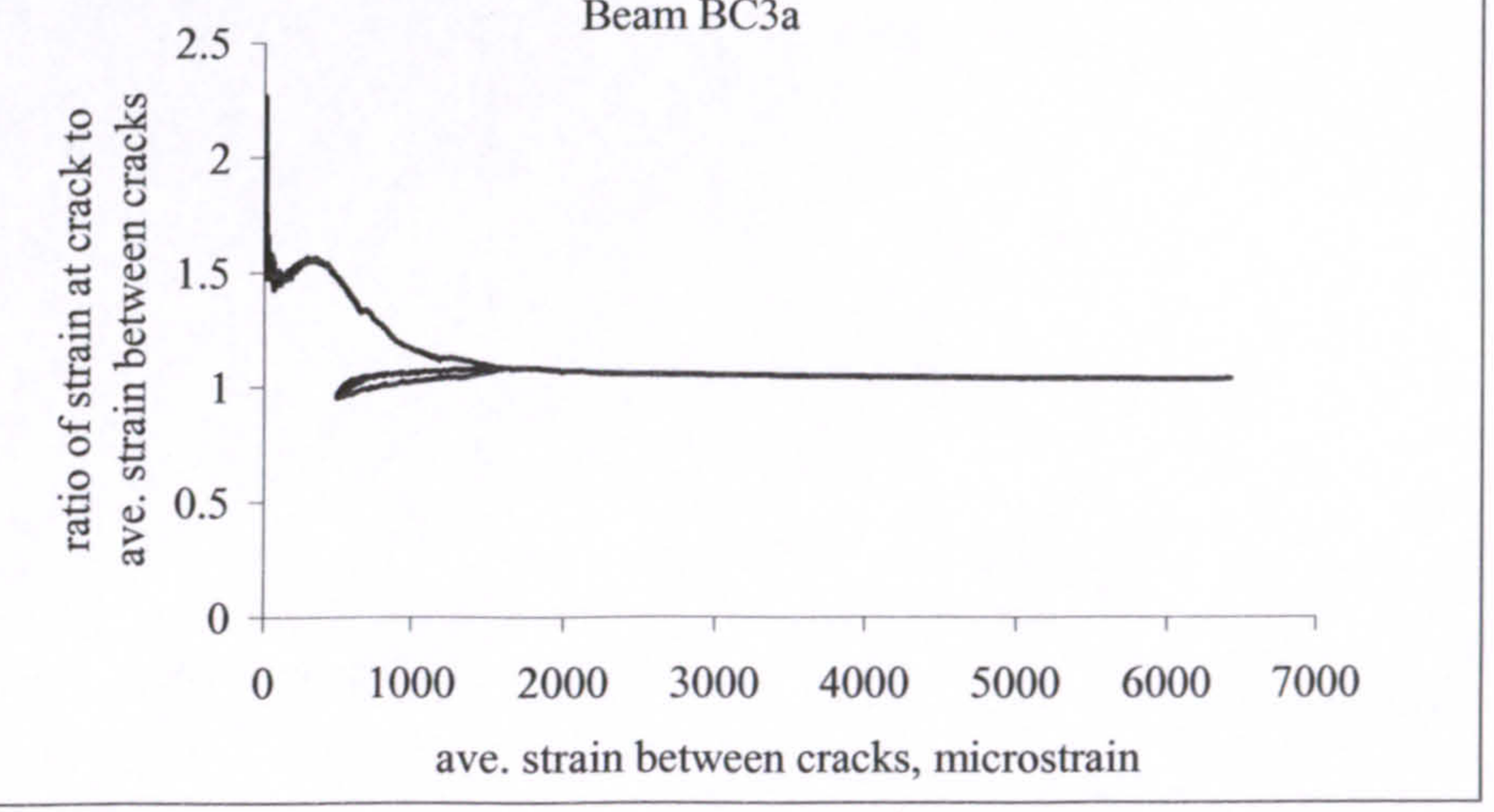
Beam BC3a
ratio of strain at crack to ave. strain between cracks
2.5
2
1.5
1
0.5
0
0
1000
2000
3000
4000
5000
6000
7000
ave. strain between cracks, microstrain

BEAM BC3a

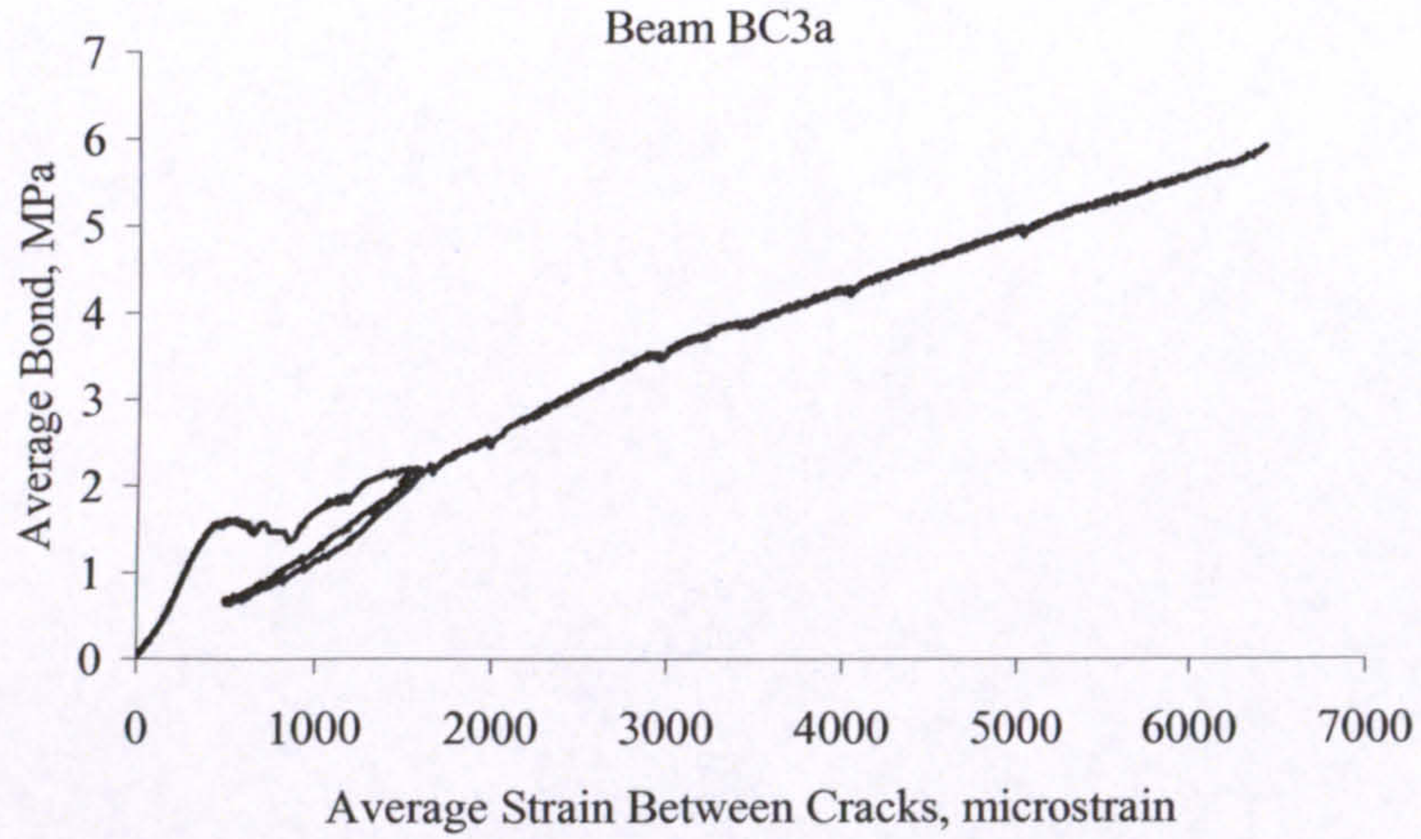

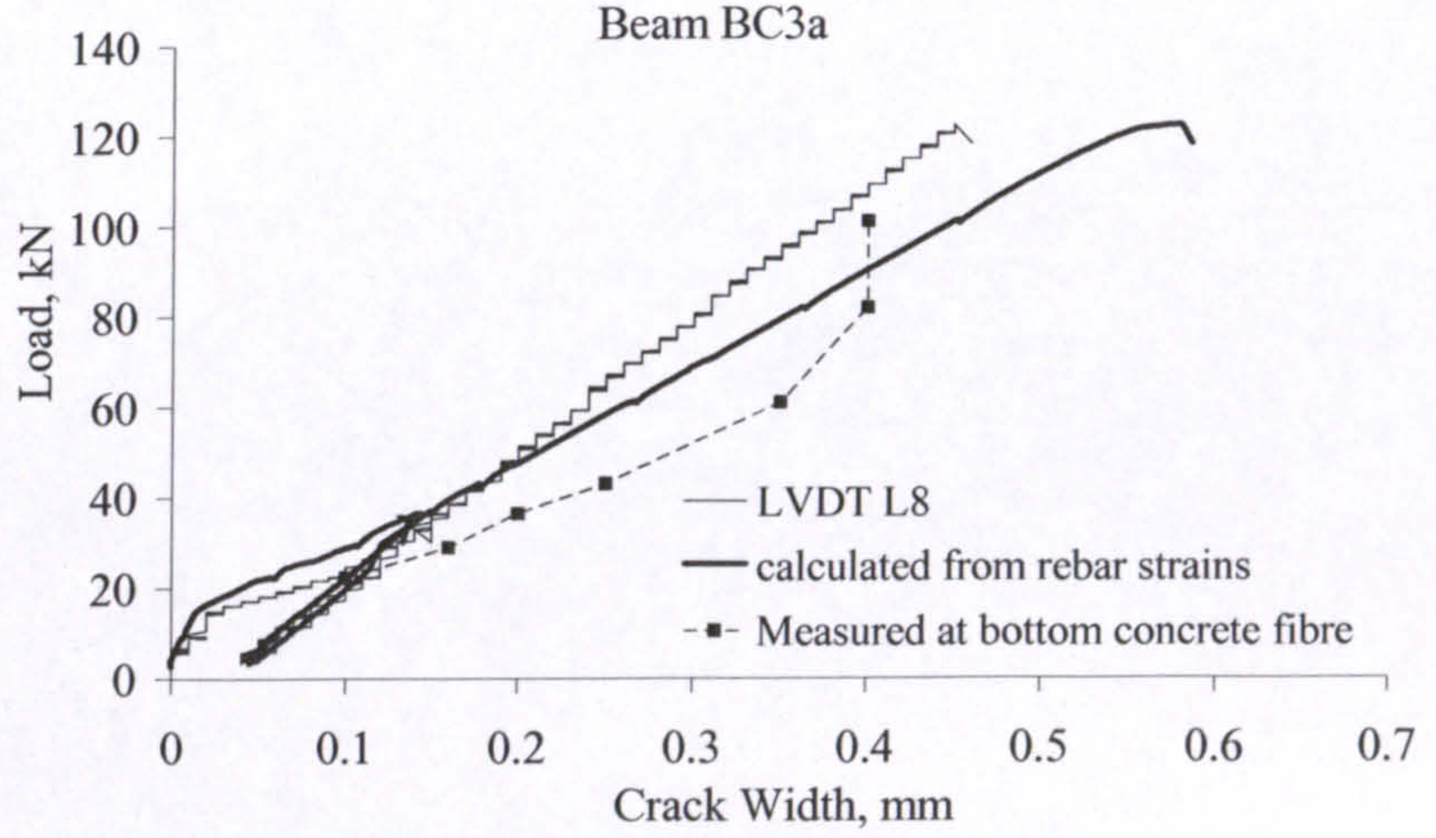

Failure by concrete crushing

- Location of crack inducer is precise.
- Cover=25mm

cracks at 95 mm left and 110 mm right of CL at a load of around 22.3-29.0 kN

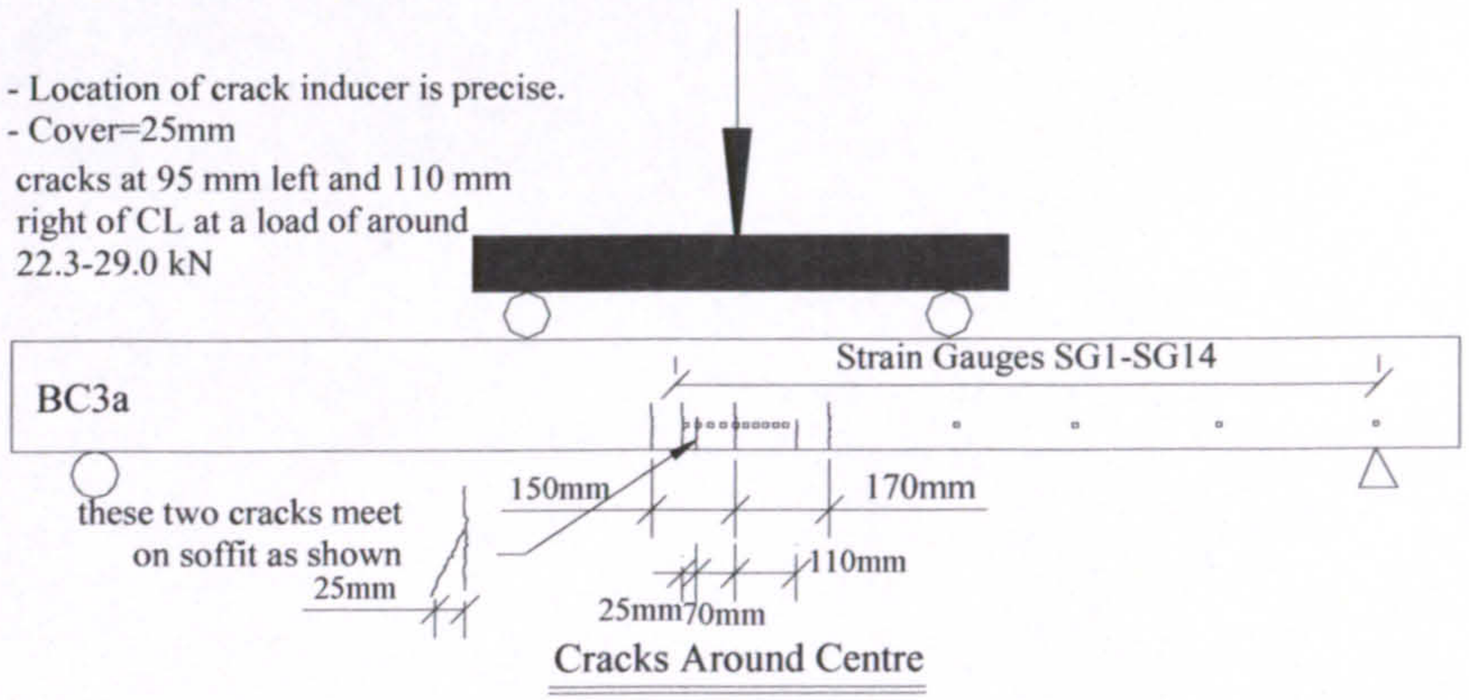

Cracks Around Centre

BEAM BC3b

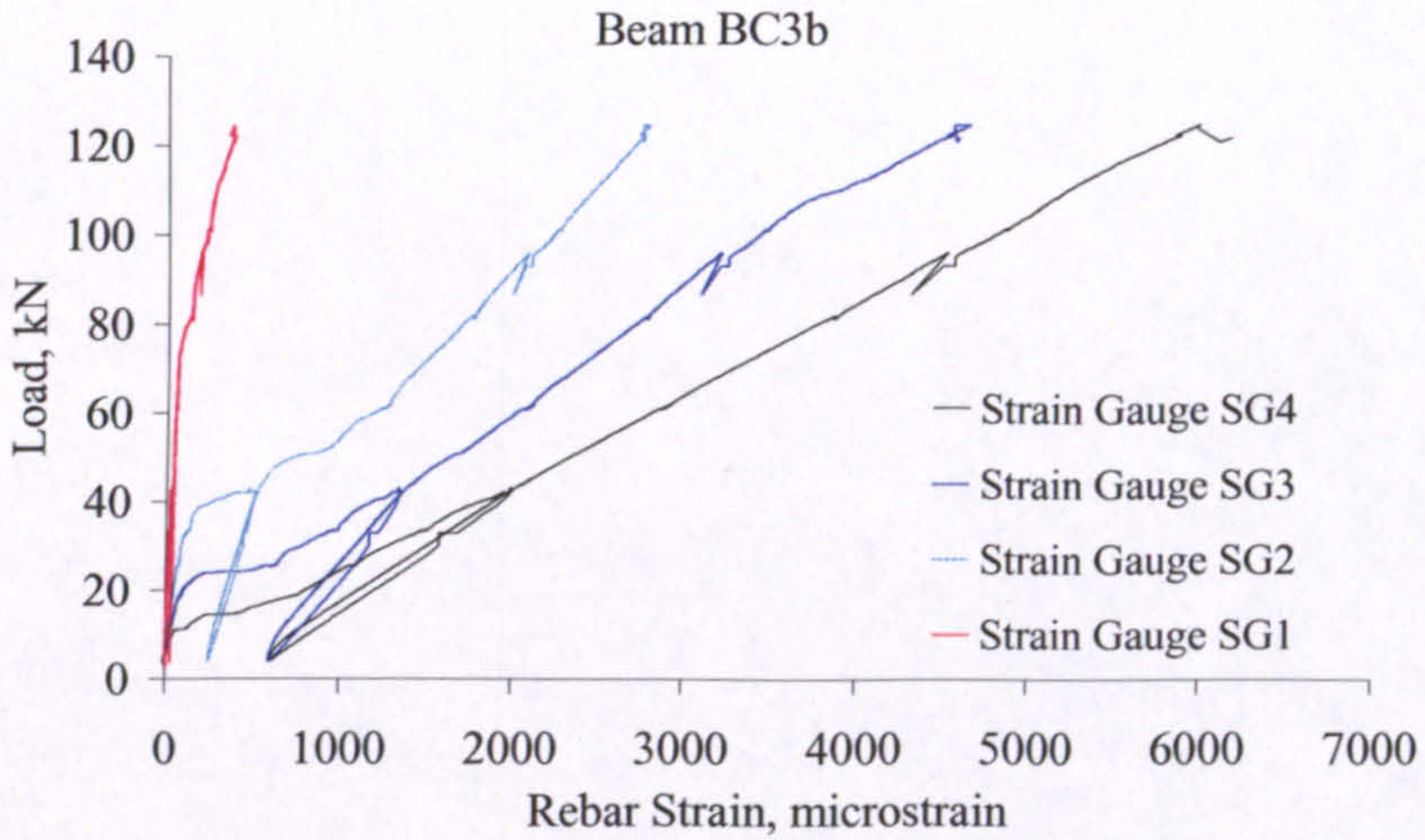
Beam BC3b
Load, kN
Rebar Strain, microstrain
Strain Gauge SG4
Strain Gauge SG3
Strain Gauge SG2
Strain Gauge SG1

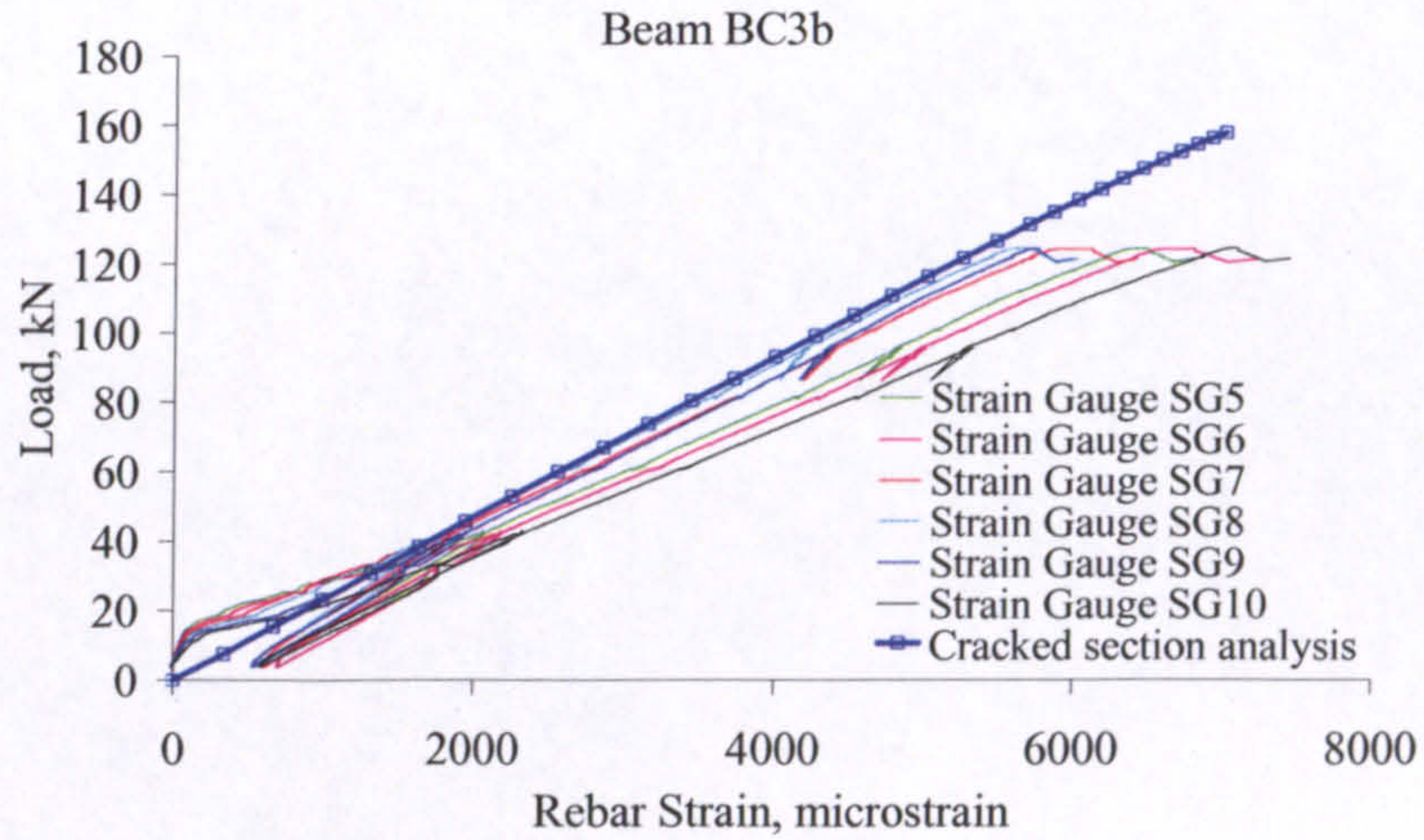
Beam BC3b
Load, kN
Rebar Strain, microstrain
Strain Gauge SG5
Strain Gauge SG6
Strain Gauge SG7
Strain Gauge SG8
Strain Gauge SG9
Strain Gauge SG10
Cracked section analysis

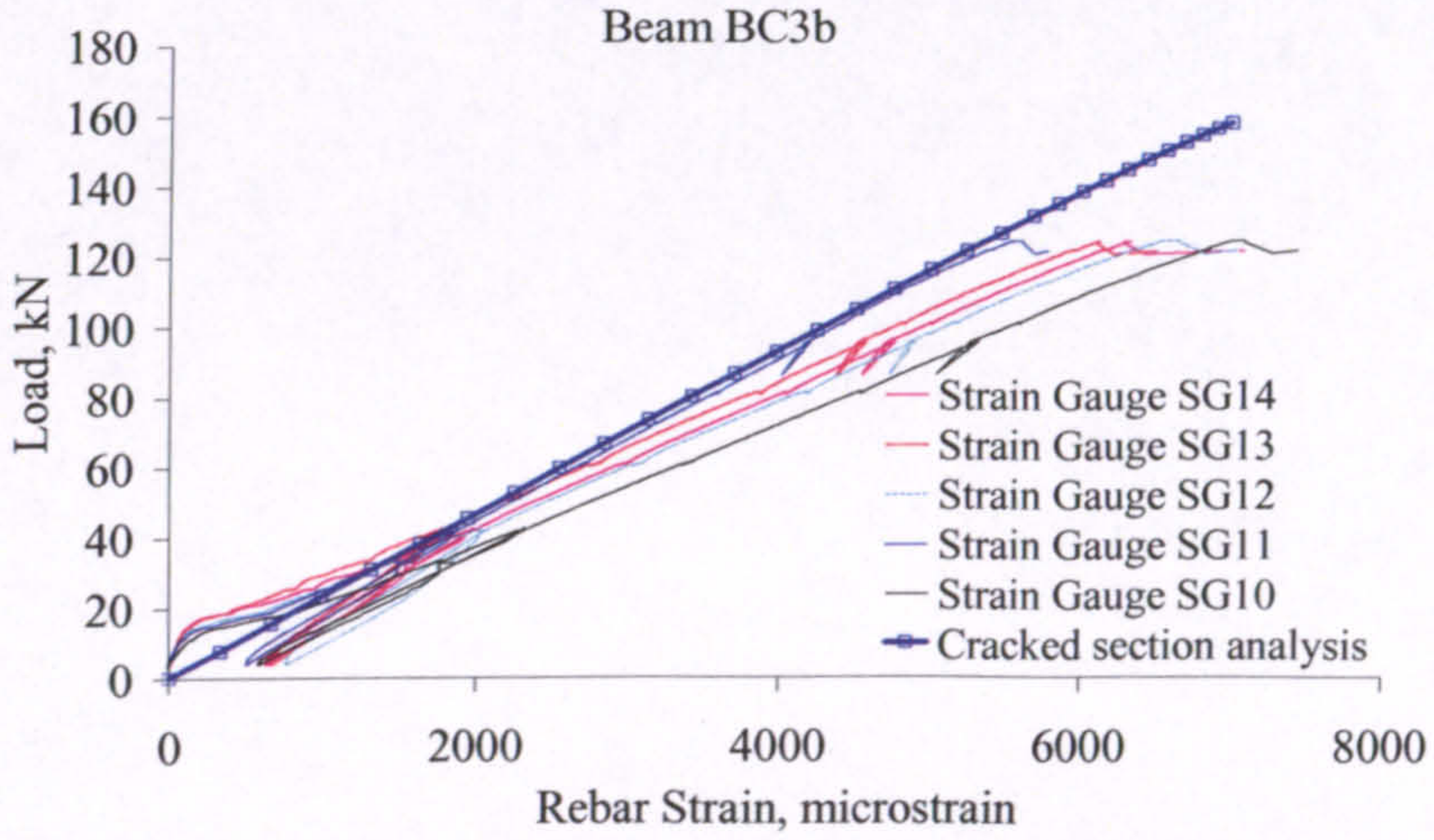
Beam BC3b
Load, kN
Rebar Strain, microstrain
Strain Gauge SG14
Strain Gauge SG13
Strain Gauge SG12
Strain Gauge SG11
Strain Gauge SG10
Cracked section analysis

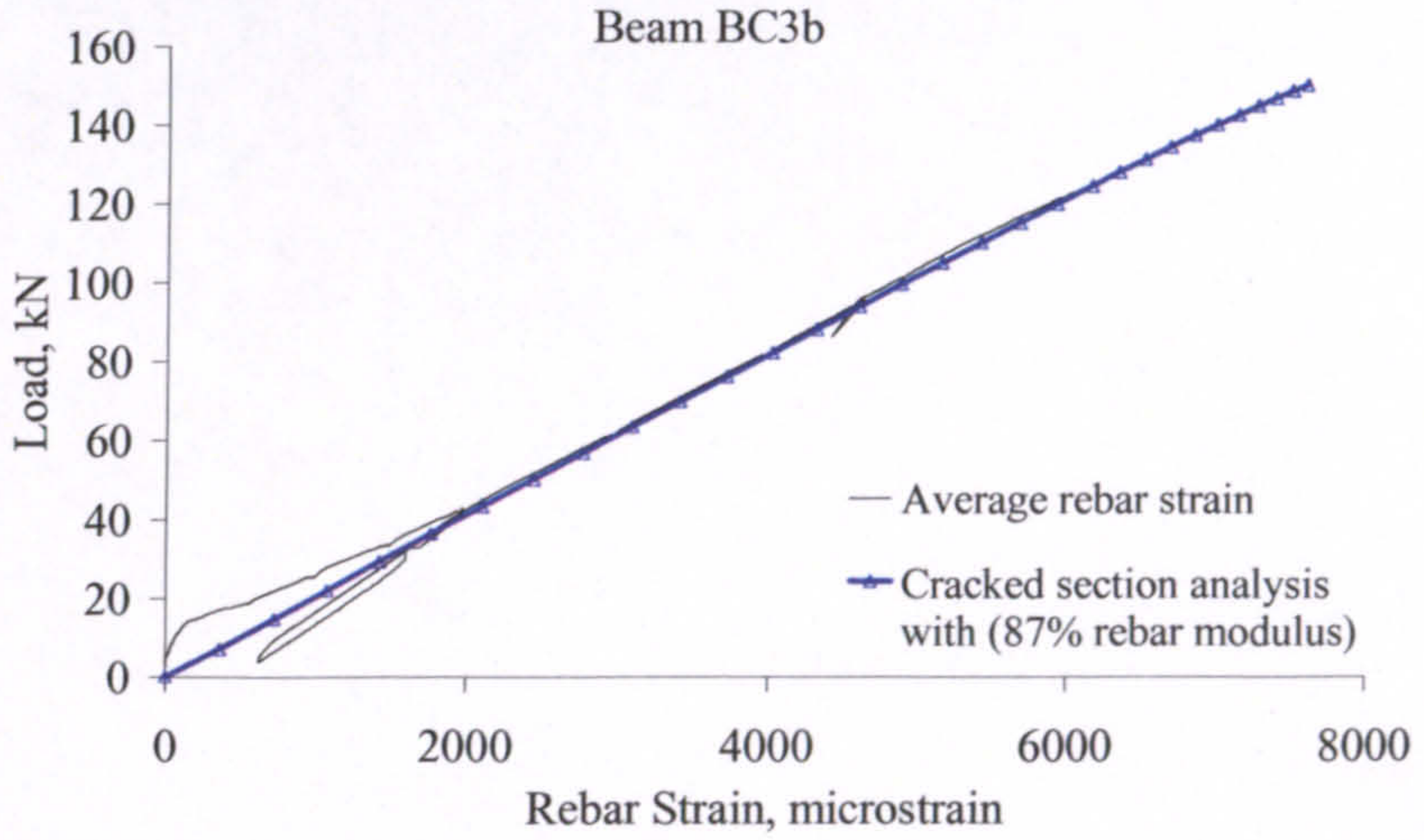
Beam BC3b
Load, kN
Rebar Strain, microstrain
Average rebar strain
Cracked section analysis
with (87% rebar modulus)

BEAM BC3b

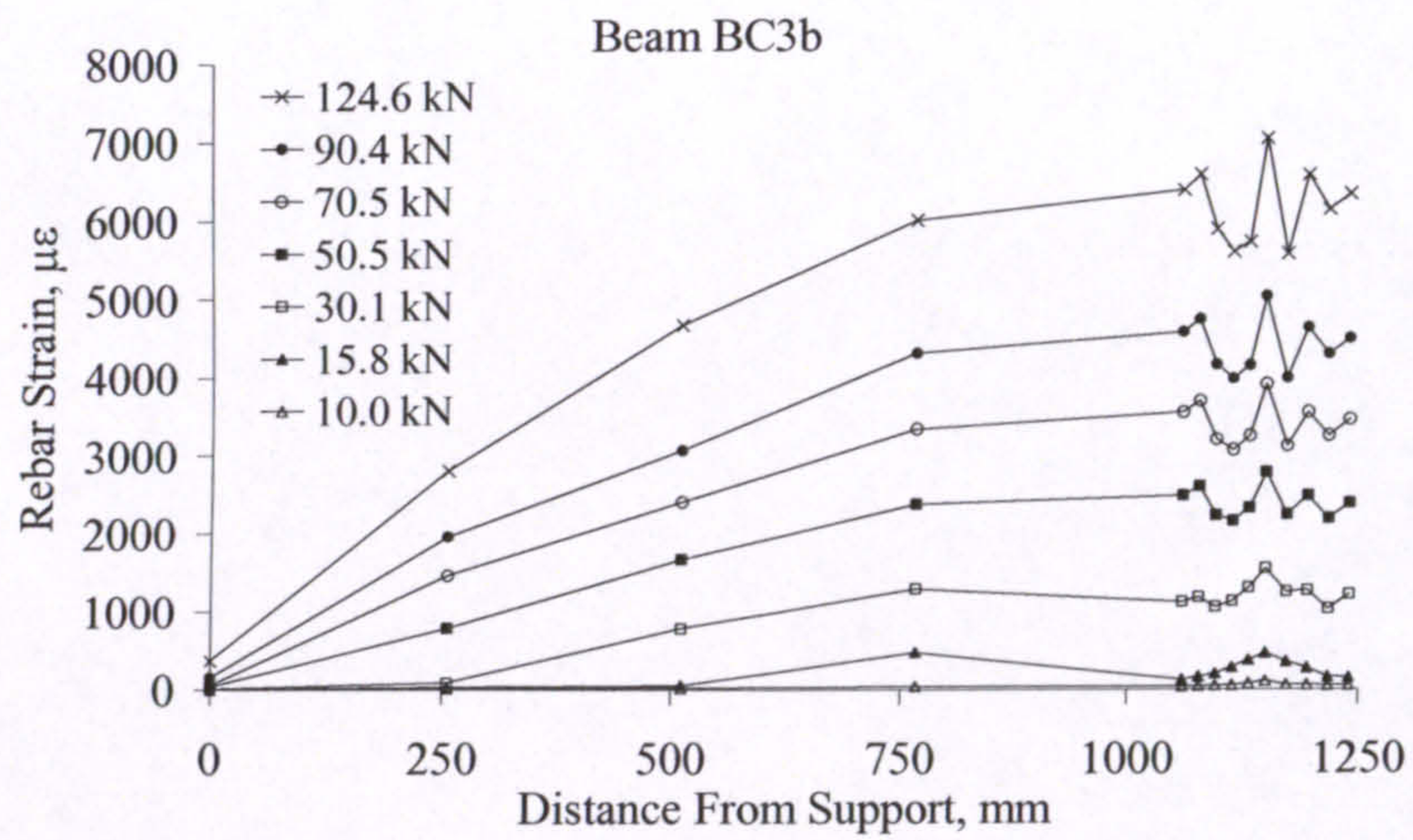
Beam BC3b
Rebar Strain, με
8000
7000
6000
5000
4000
3000
2000
1000
0
124.6 kN
90.4 kN
70.5 kN
50.5 kN
30.1 kN
15.8 kN
10.0 kN
0
250
500
750
1000
1250
Distance From Support, mm

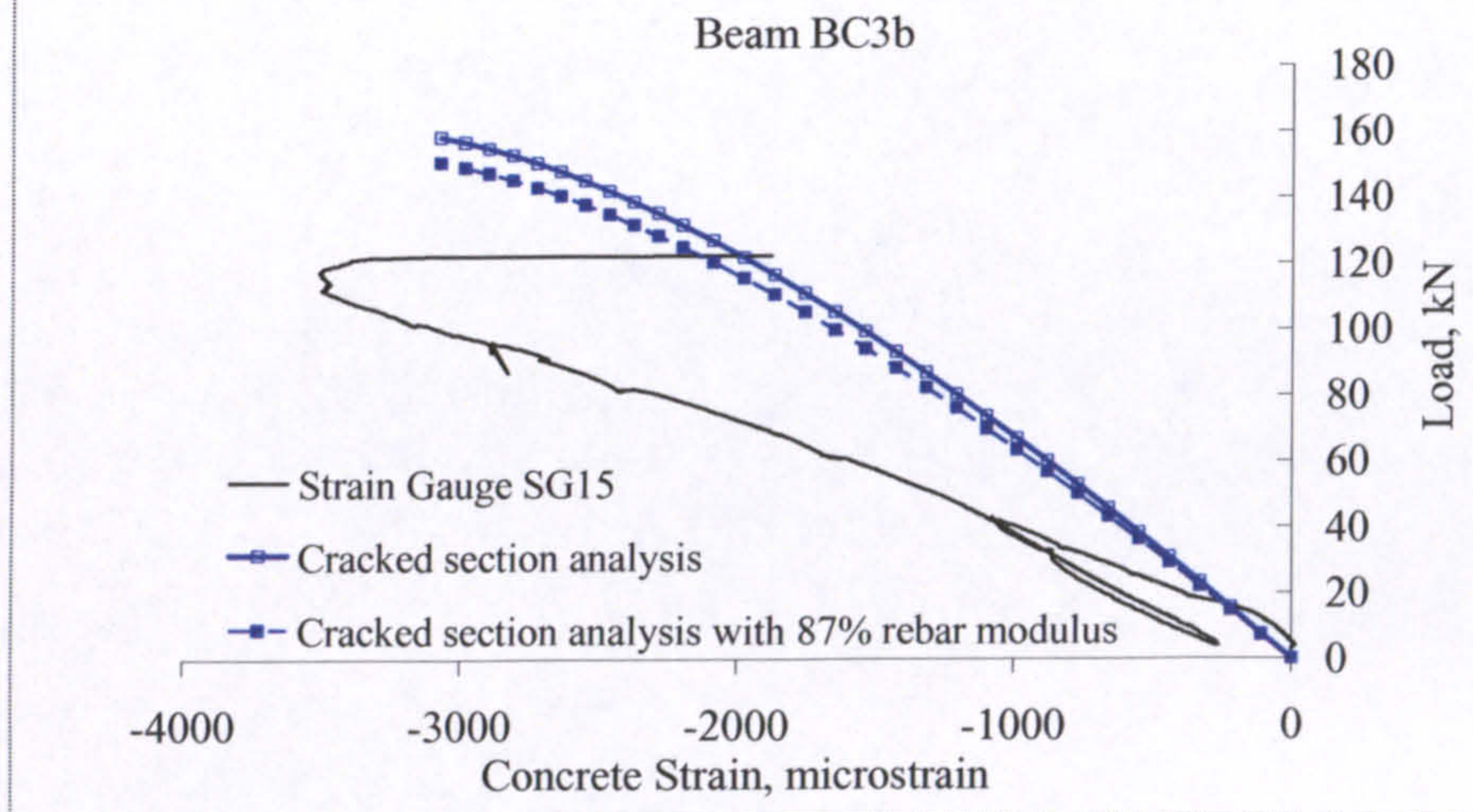
Beam BC3b
Load, kN
180
160
140
120
100
80
60
40
20
0
Strain Gauge SG15
Cracked section analysis
Cracked section analysis with 87% rebar modulus
-4000
-3000
-2000
-1000
0
Concrete Strain, microstrain

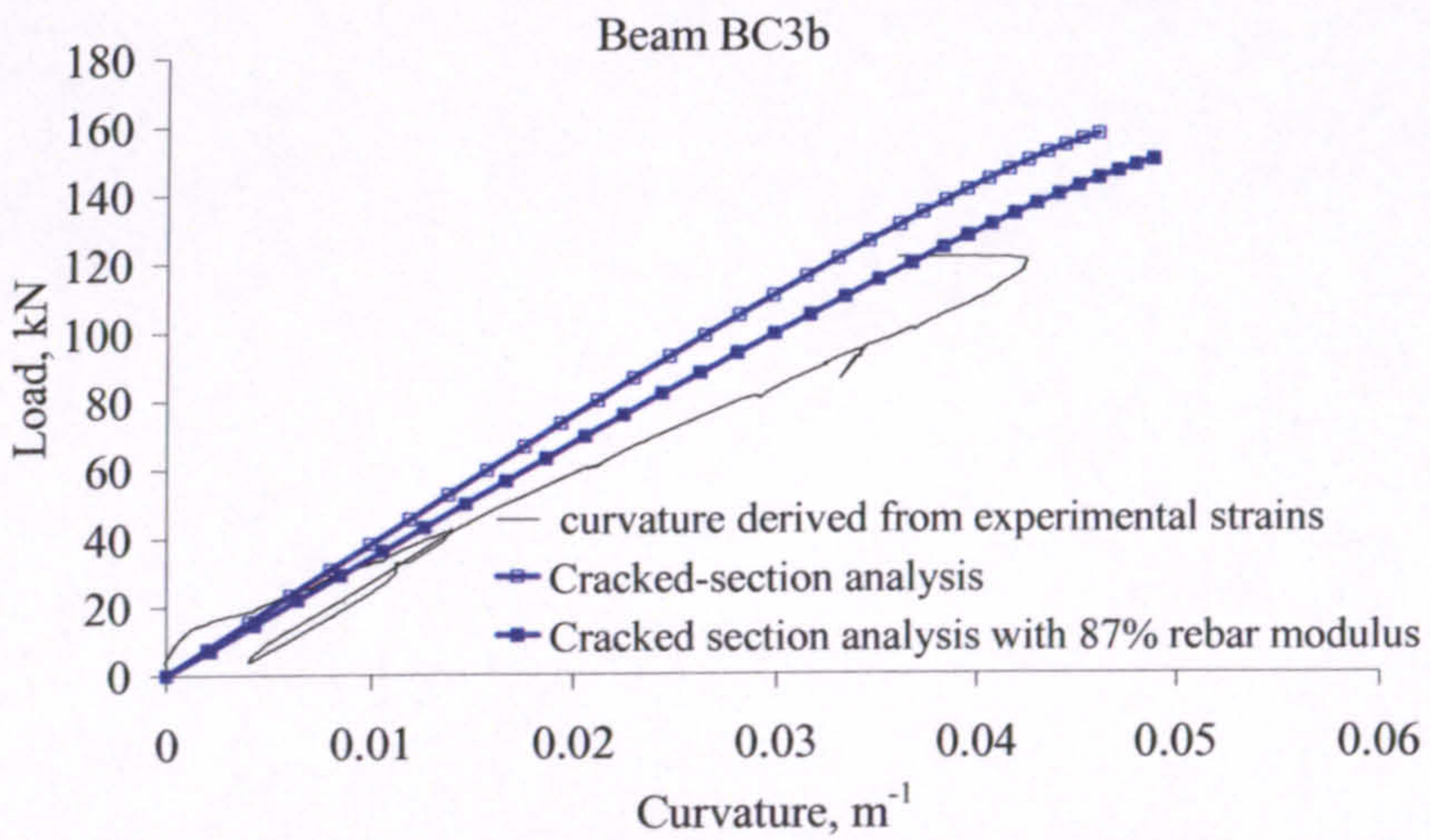
Beam BC3b
Load, kN
180
160
140
120
100
80
60
40
20
0
curvature derived from experimental strains
Cracked-section analysis
Cracked section analysis with 87% rebar modulus
0
0.01
0.02
0.03
0.04
0.05
0.06
Curvature, m-1

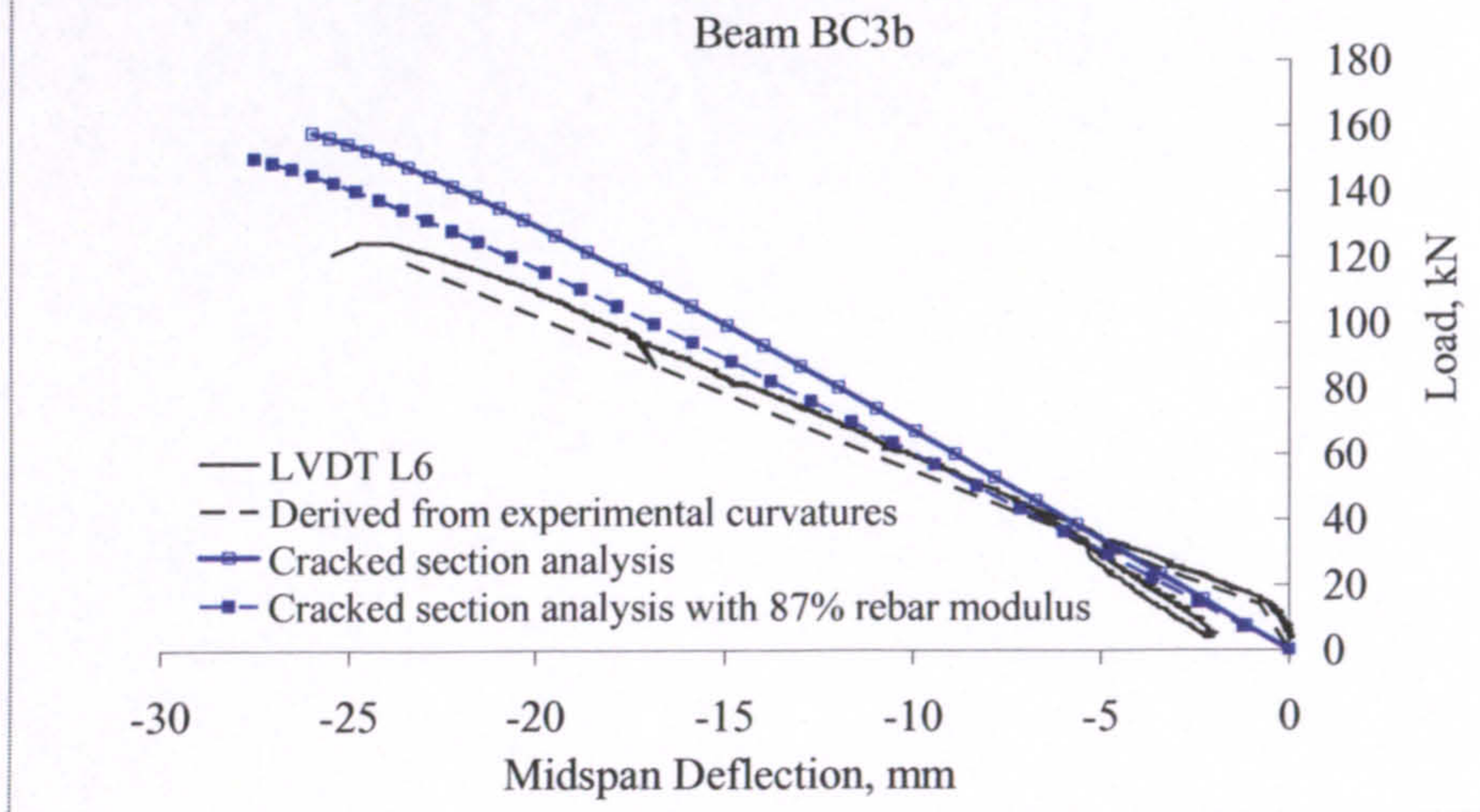
Beam BC3b
Load, kN
180
160
140
120
100
80
60
40
20
0
LVDT L6
Derived from experimental curvatures
Cracked section analysis
Cracked section analysis with 87% rebar modulus
-30
-25
-20
-15
-10
-5
0
Midspan Deflection, mm

BEAM BC3b

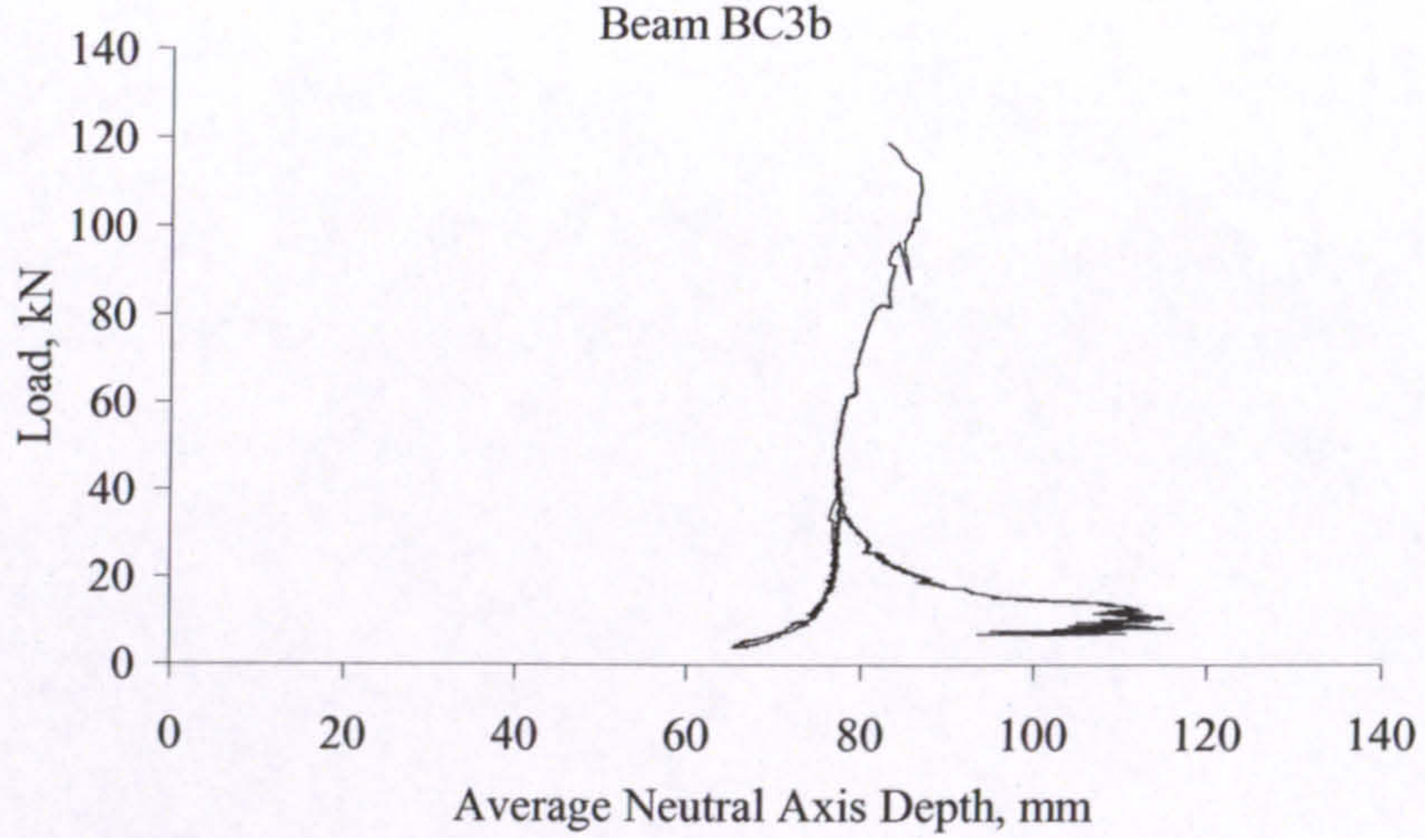
Beam BC3b
Load, kN
Average Neutral Axis Depth, mm
0
20
40
60
80
100
120
140

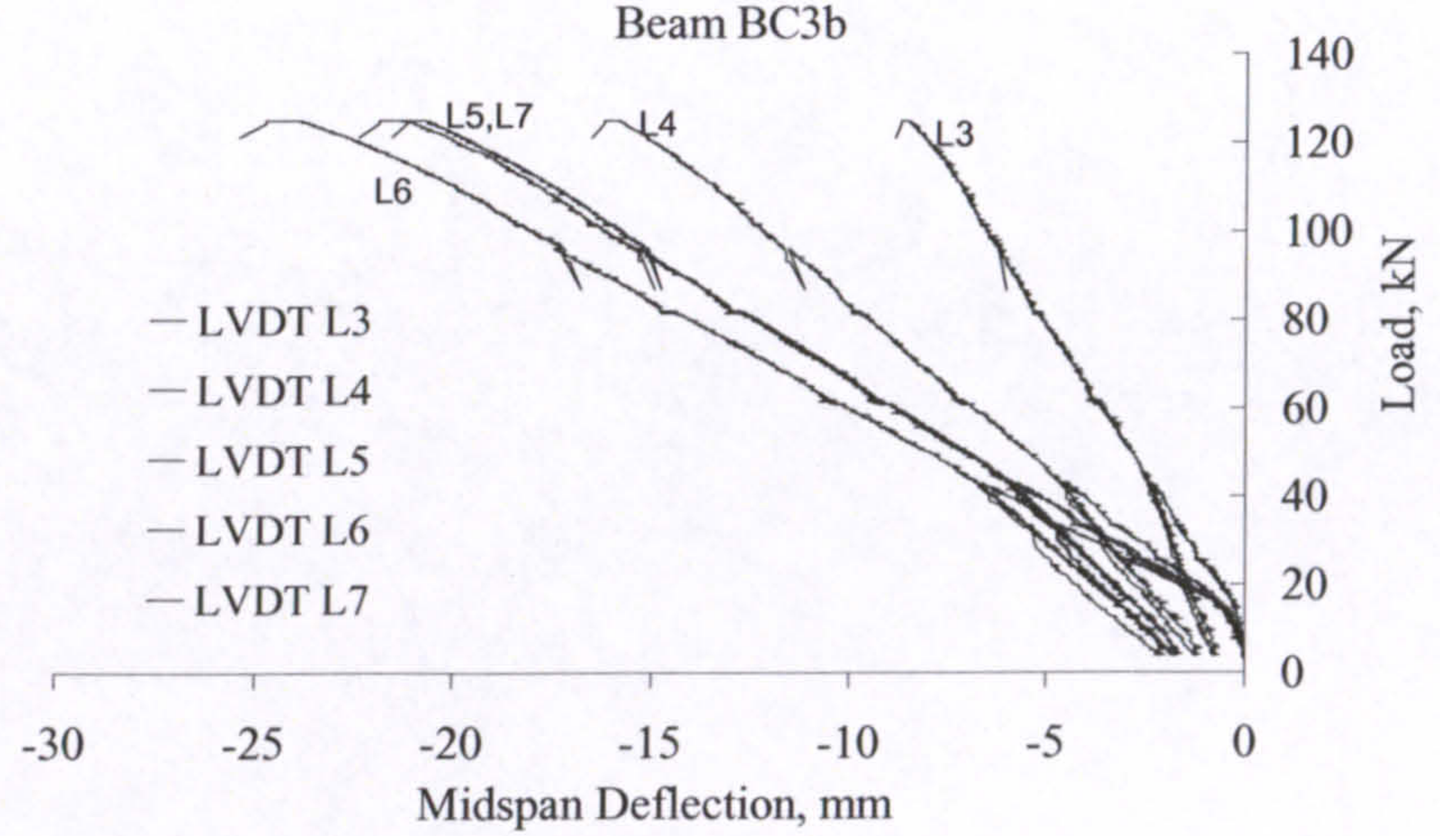
Beam BC3b
L6
L5,L7
L4
L3
— LVDT L3
— LVDT L4
— LVDT L5
— LVDT L6
— LVDT L7
Load, kN
Midspan Deflection, mm
-30
-25
-20
-15
-10
-5
0

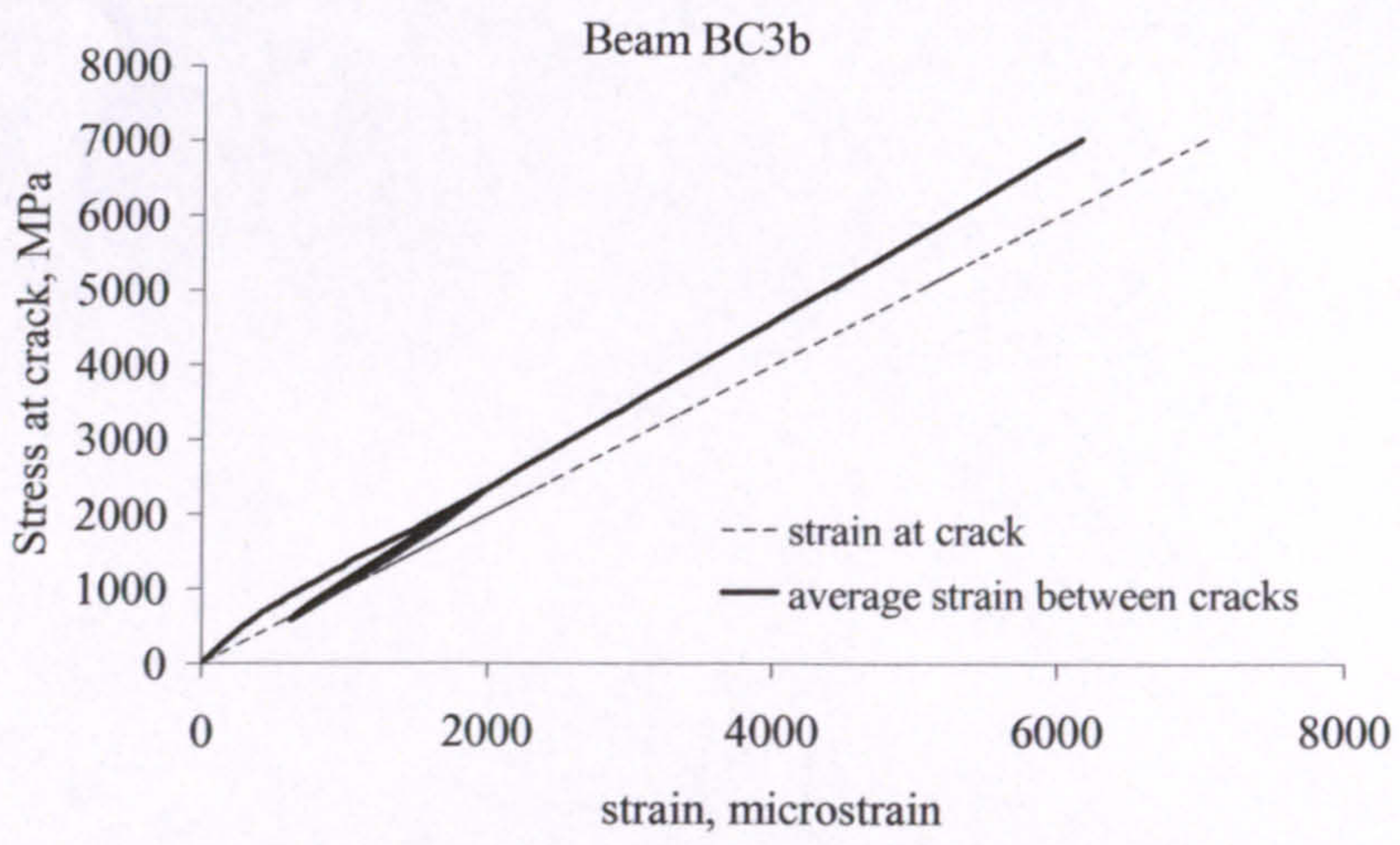
Beam BC3b
Stress at crack, MPa
strain, microstrain
--- strain at crack
— average strain between cracks
0
1000
2000
3000
4000
5000
6000
7000
8000

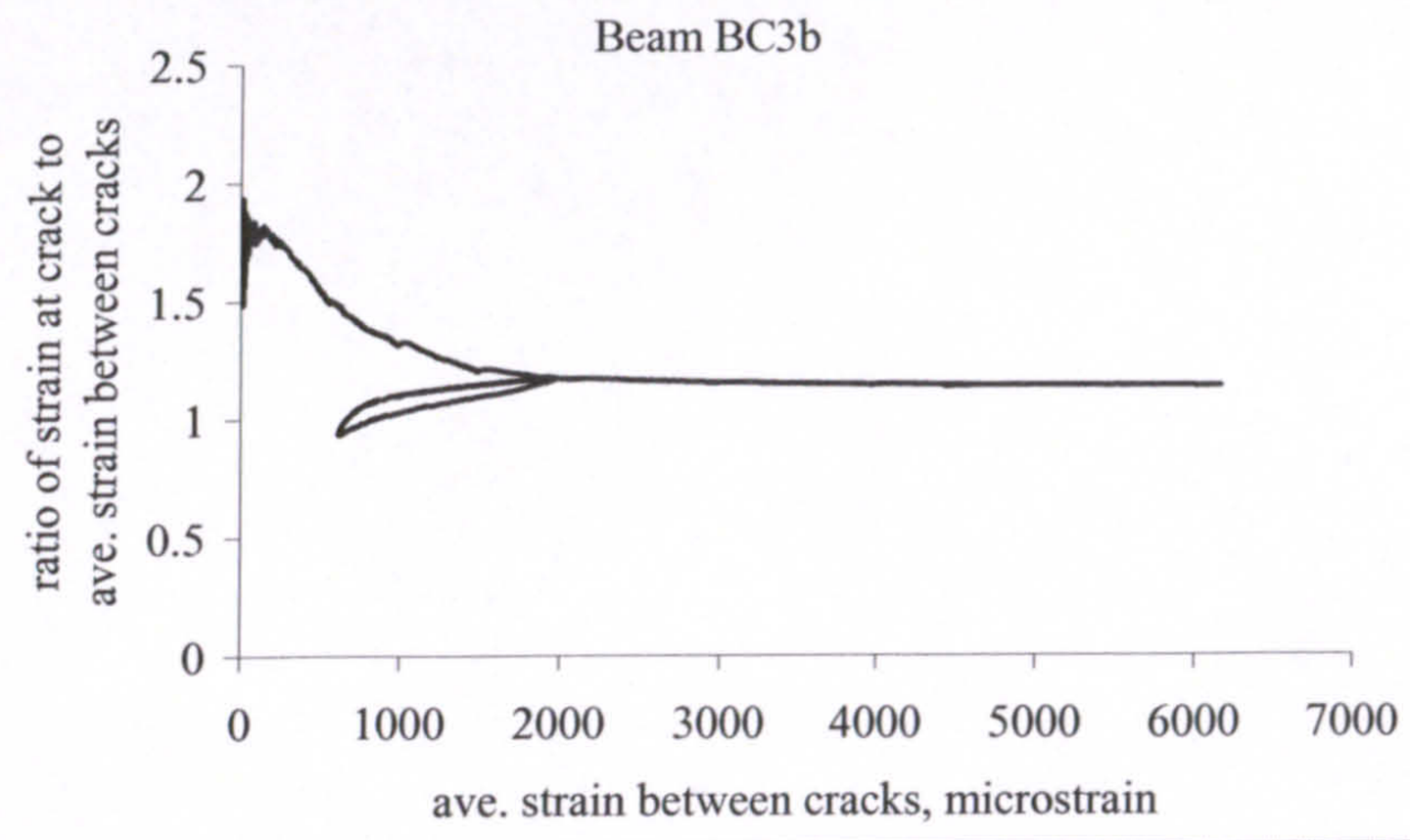
Beam BC3b
ratio of strain at crack to ave. strain between cracks
ave. strain between cracks, microstrain
0
0.5
1
1.5
2
2.5
1000
2000
3000
4000
5000
6000
7000

BEAM BC3b

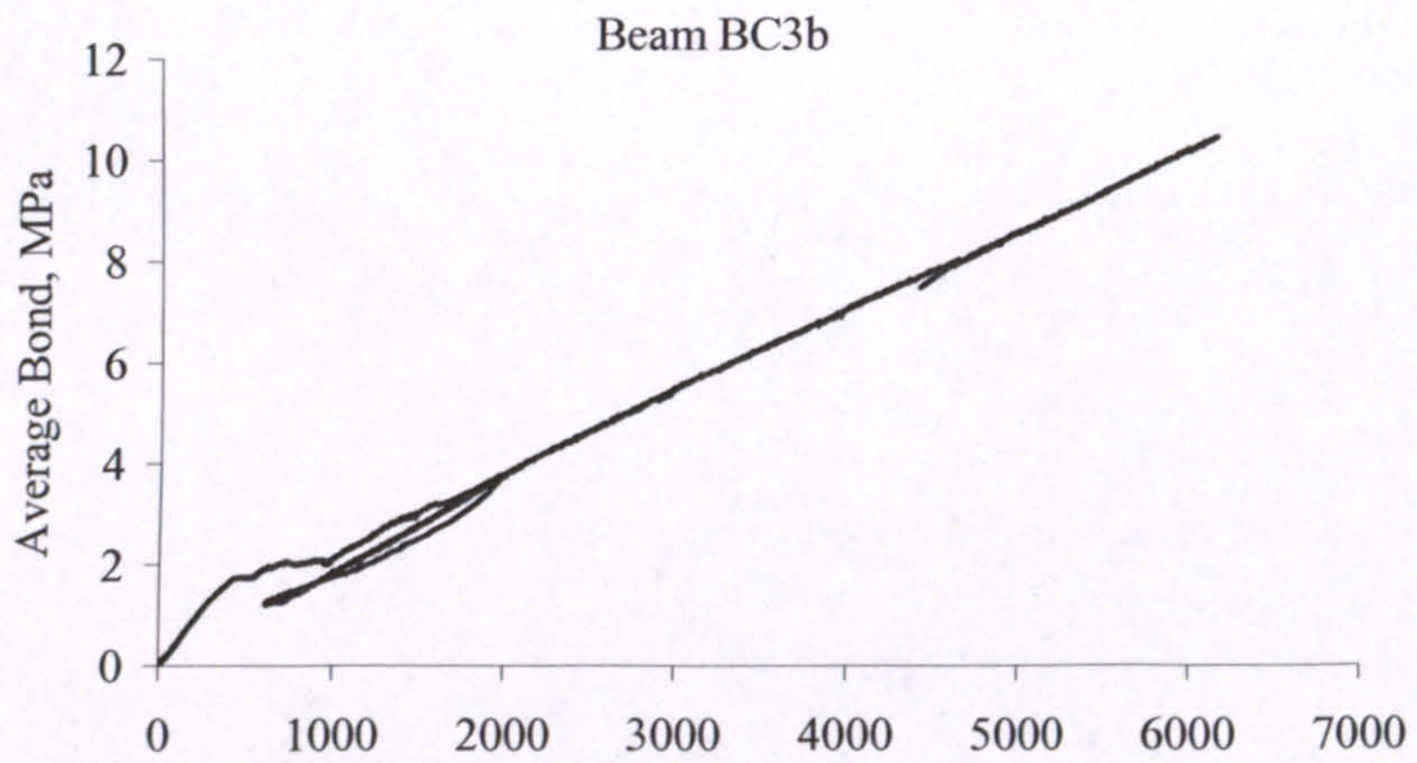

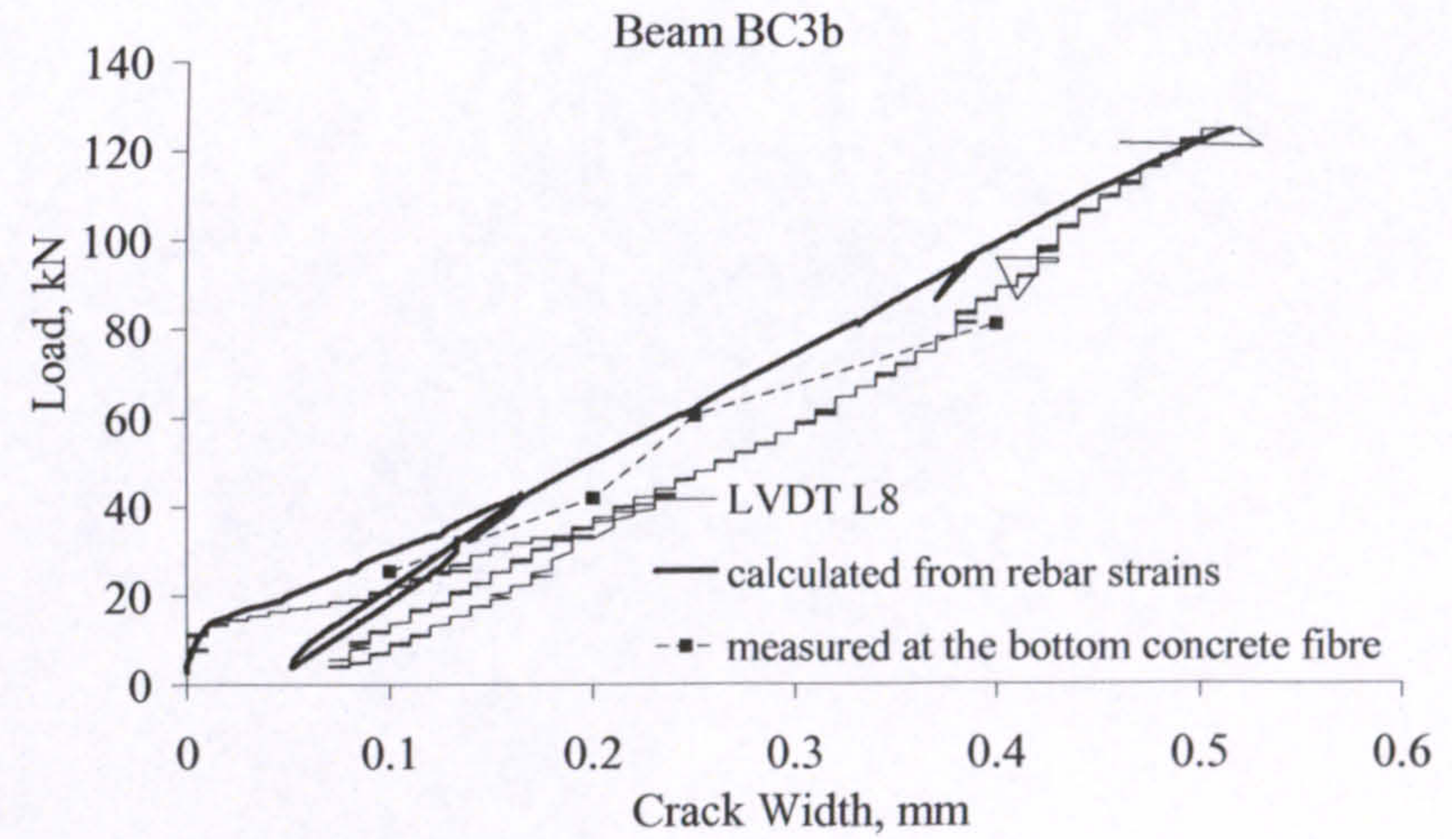

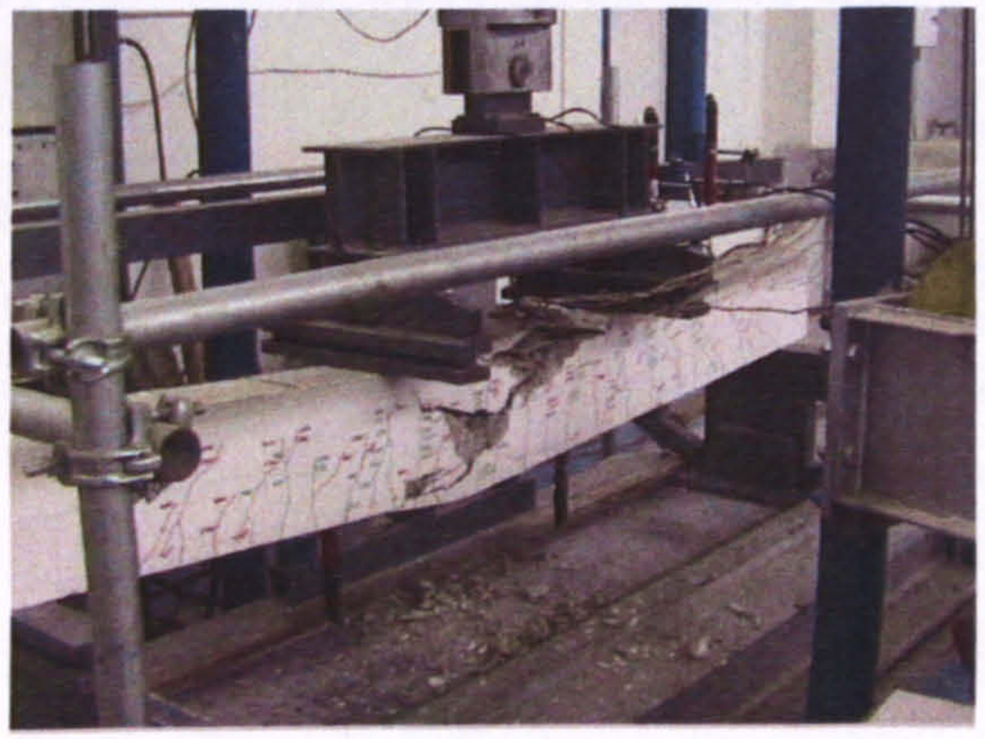

Failure by concrete crushing.

- Location of crack inducer is precise.
- Cover=25mm
- cracks at 100mm left and 67mm right of CL at a load of around 33.3-42.0 kN

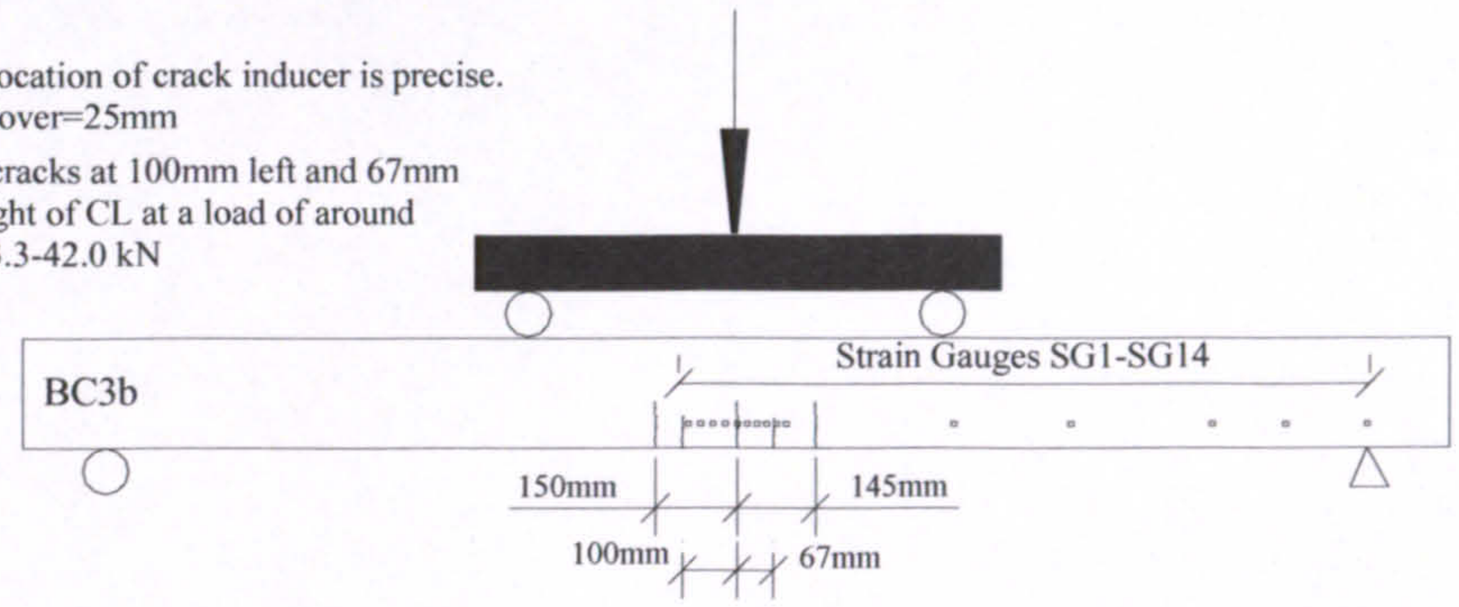

Cracks Around Centre

SLAB SG1a

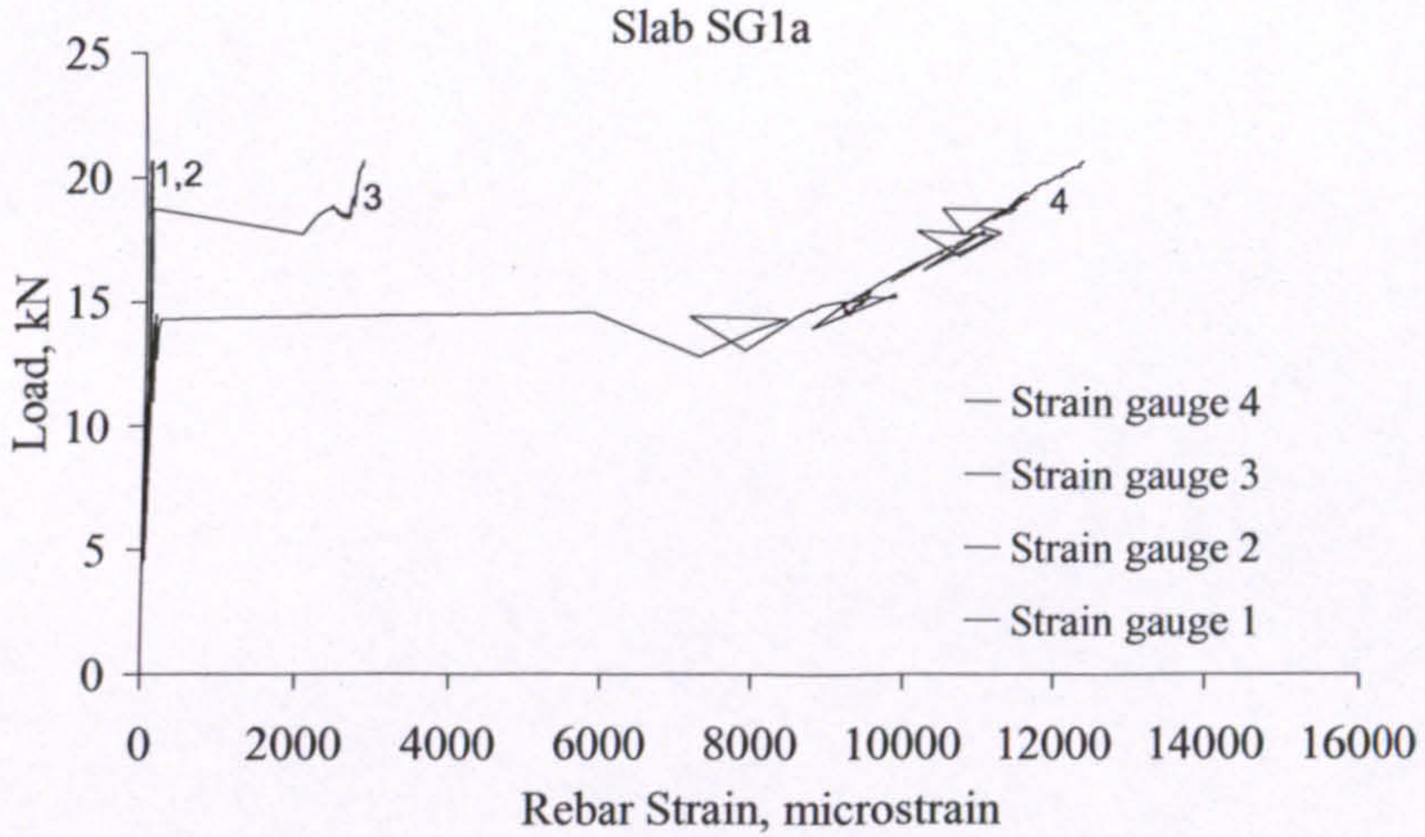
Slab SG1a
Load, kN
Rebar Strain, microstrain
1,2
3
4
Strain gauge 4
Strain gauge 3
Strain gauge 2
Strain gauge 1

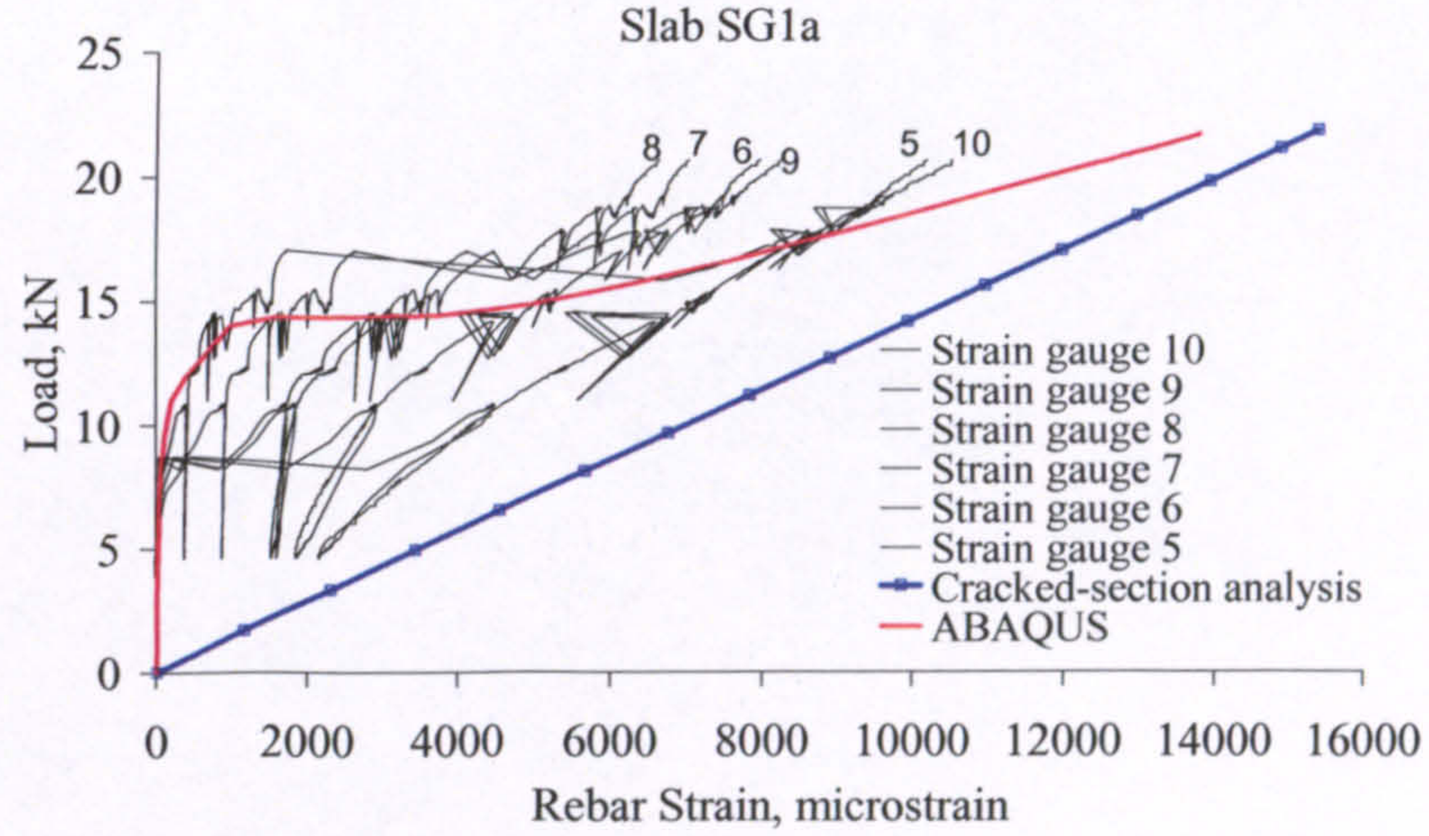
Slab SG1a
Load, kN
Rebar Strain, microstrain
8
7
6
9
5
10
Strain gauge 10
Strain gauge 9
Strain gauge 8
Strain gauge 7
Strain gauge 6
Strain gauge 5
Cracked-section analysis
ABAQUS

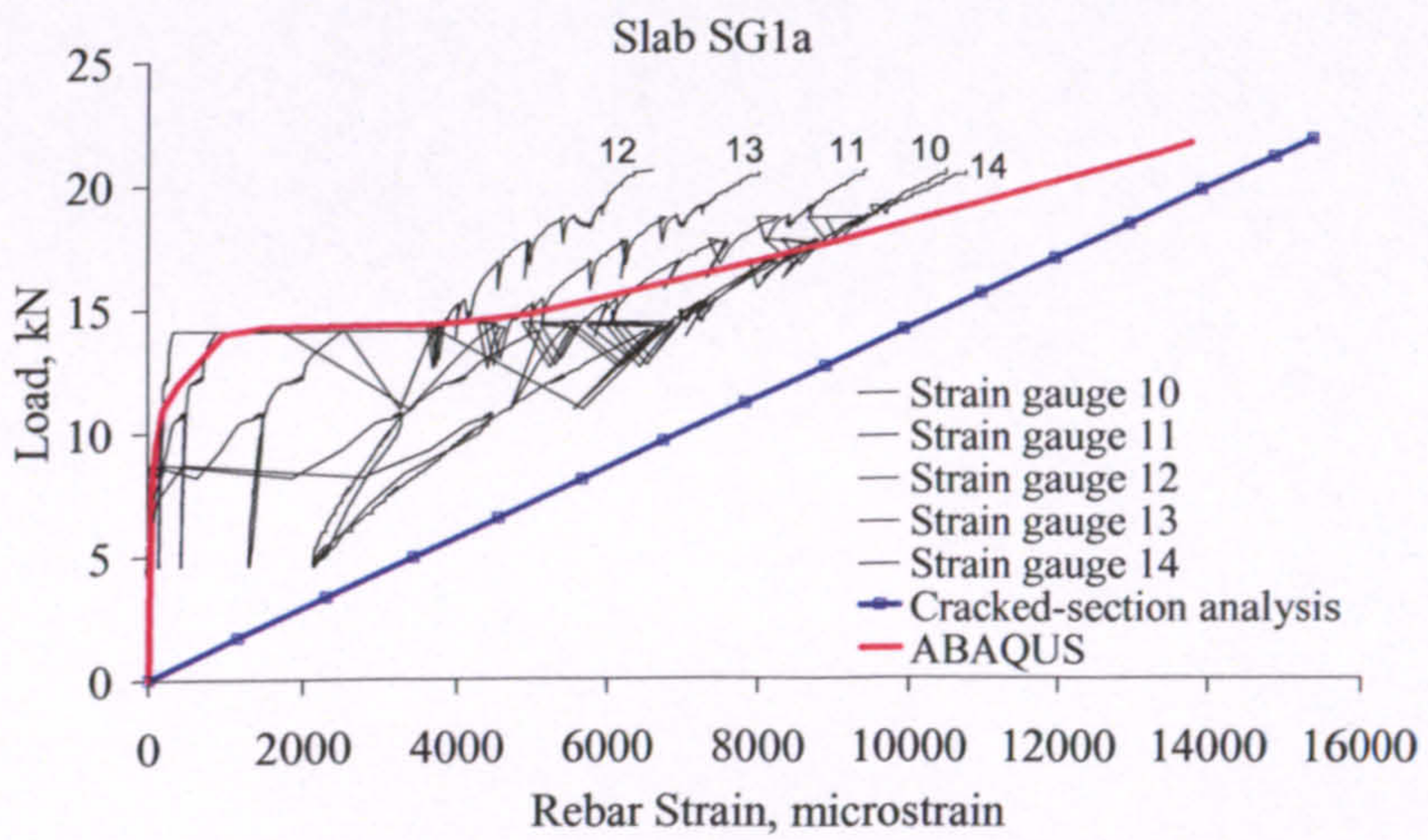
Slab SG1a
Load, kN
Rebar Strain, microstrain
12
13
11
10
14
Strain gauge 10
Strain gauge 11
Strain gauge 12
Strain gauge 13
Strain gauge 14
Cracked-section analysis
ABAQUS

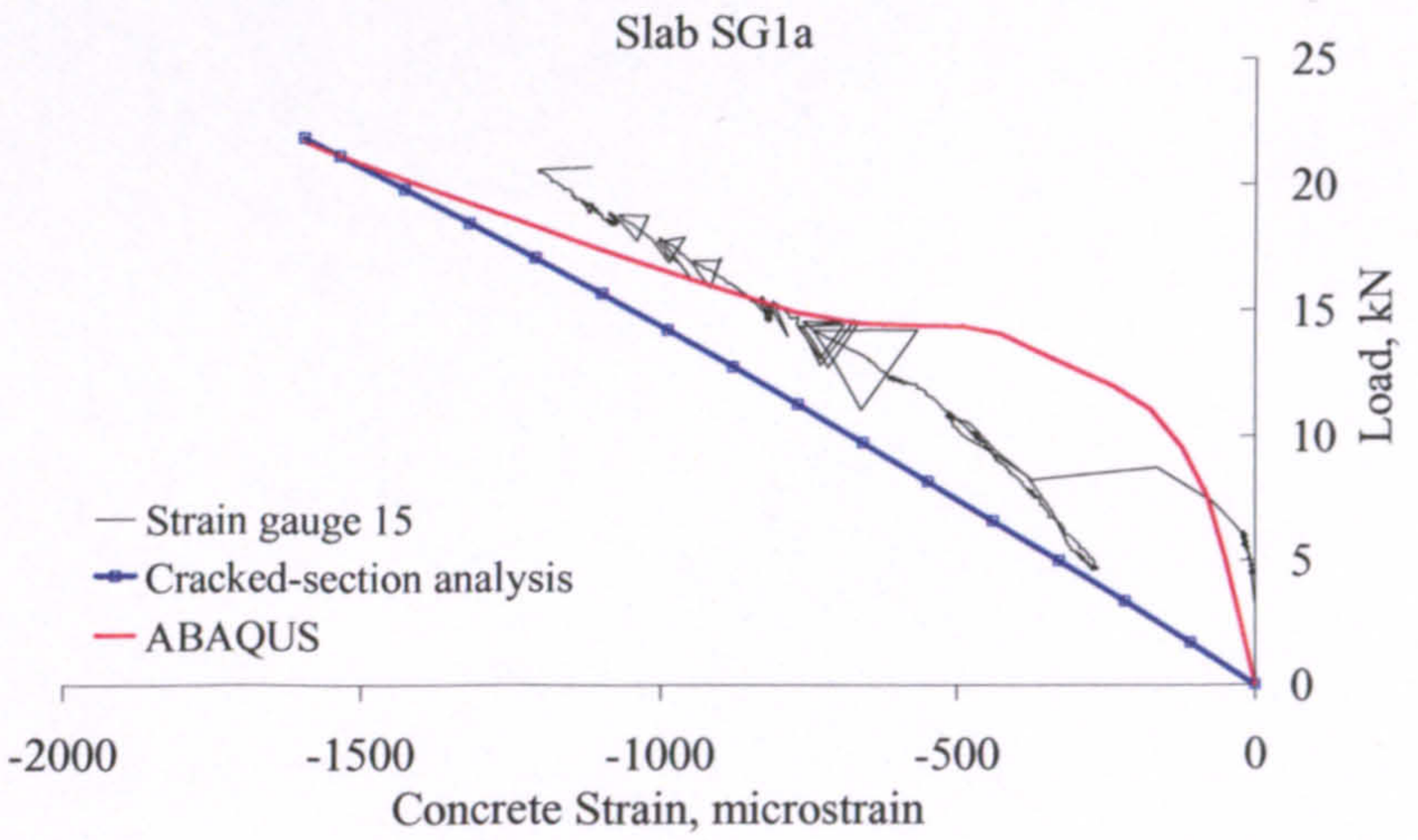
Slab SG1a
Load, kN
Concrete Strain, microstrain
Strain gauge 15
Cracked-section analysis
ABAQUS

SLAB SG1a

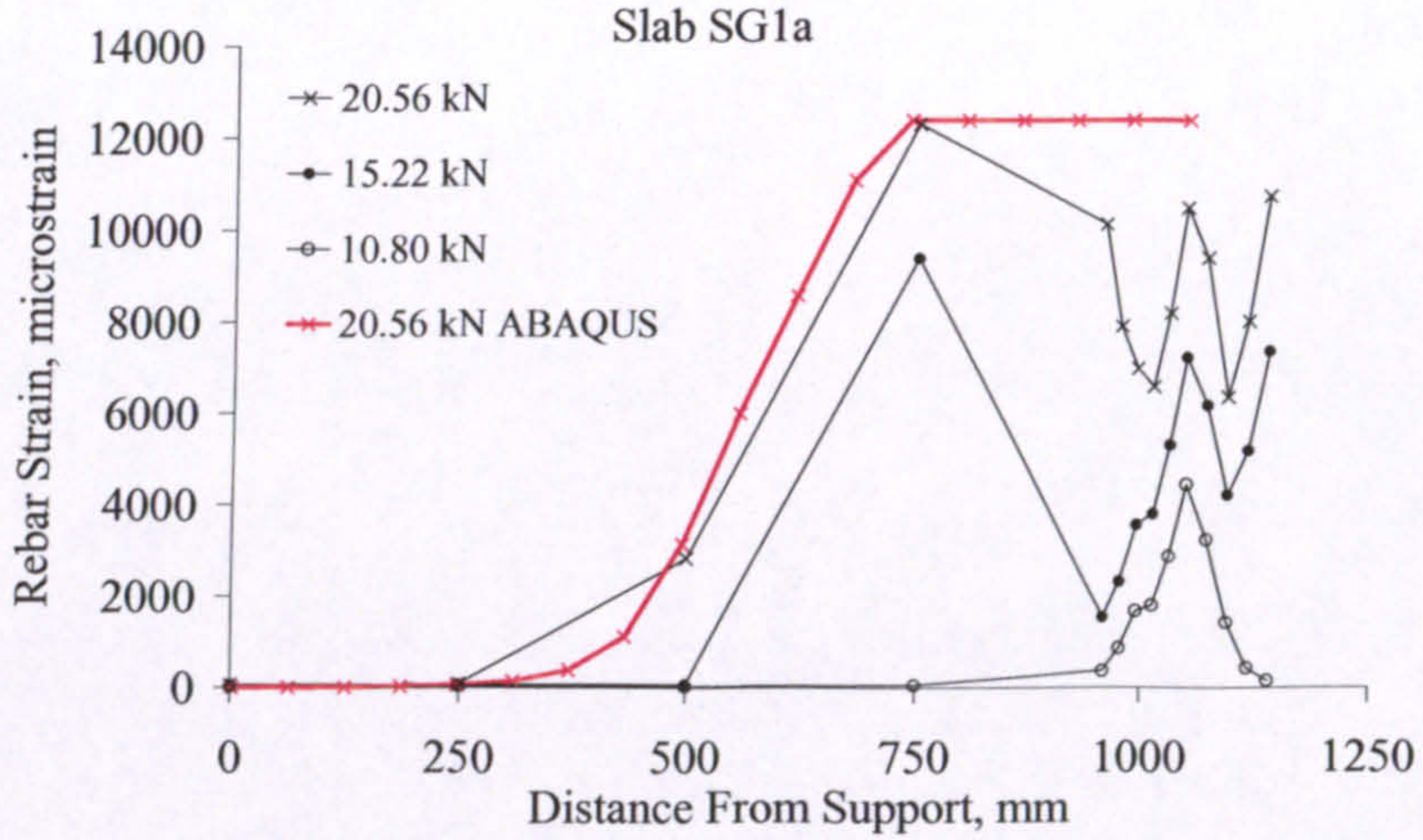
Slab SG1a
Rebar Strain, microstrain
14000
12000
10000
8000
6000
4000
2000
0
20.56 kN
15.22 kN
10.80 kN
20.56 kN ABAQUS
0
250
500
750
1000
1250
Distance From Support, mm

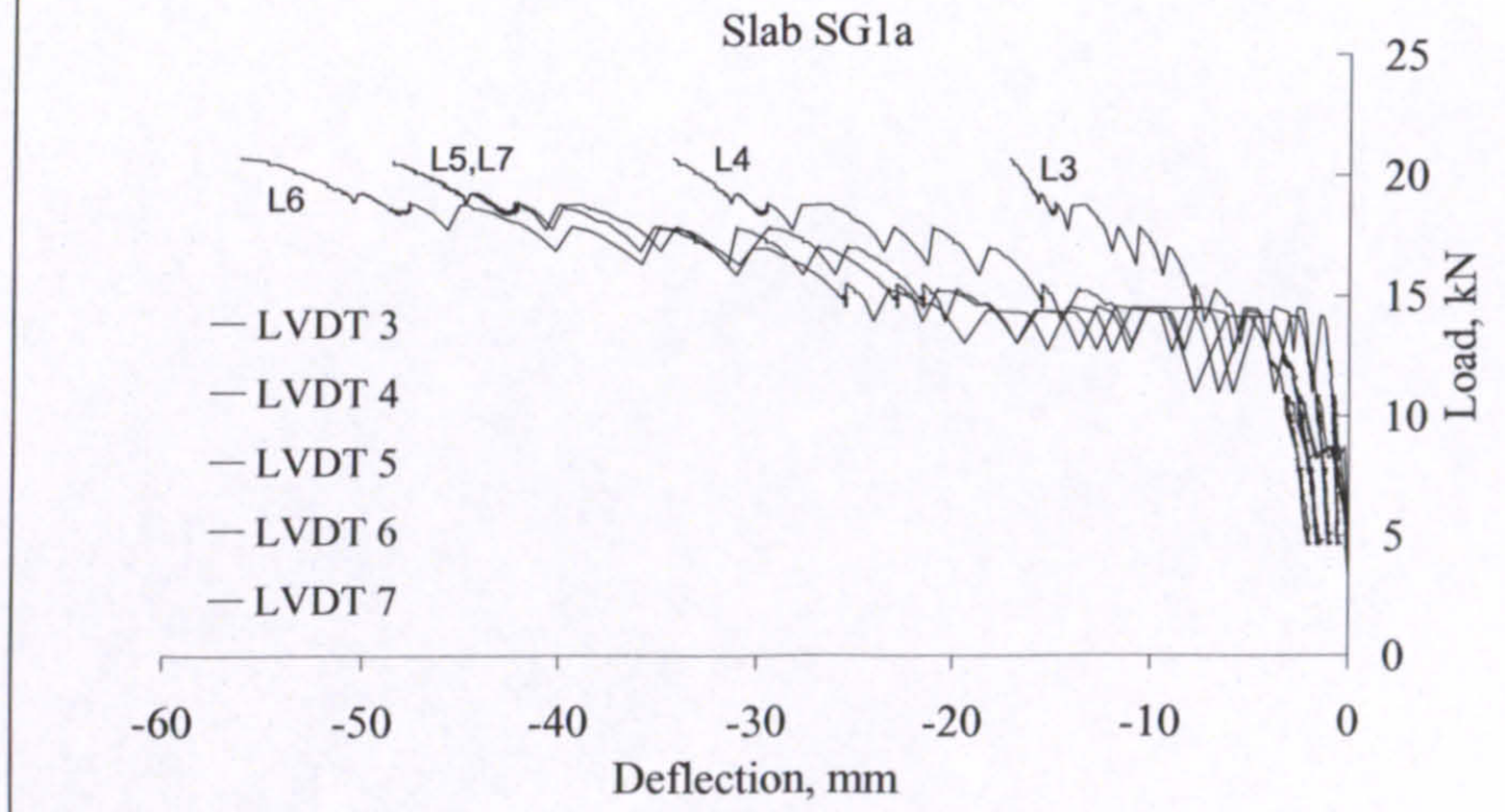
Slab SG1a
L6
L5,L7
L4
L3
LVDT 3
LVDT 4
LVDT 5
LVDT 6
LVDT 7
25
20
15
10
5
0
Load, kN
-60
-50
-40
-30
-20
-10
0
Deflection, mm

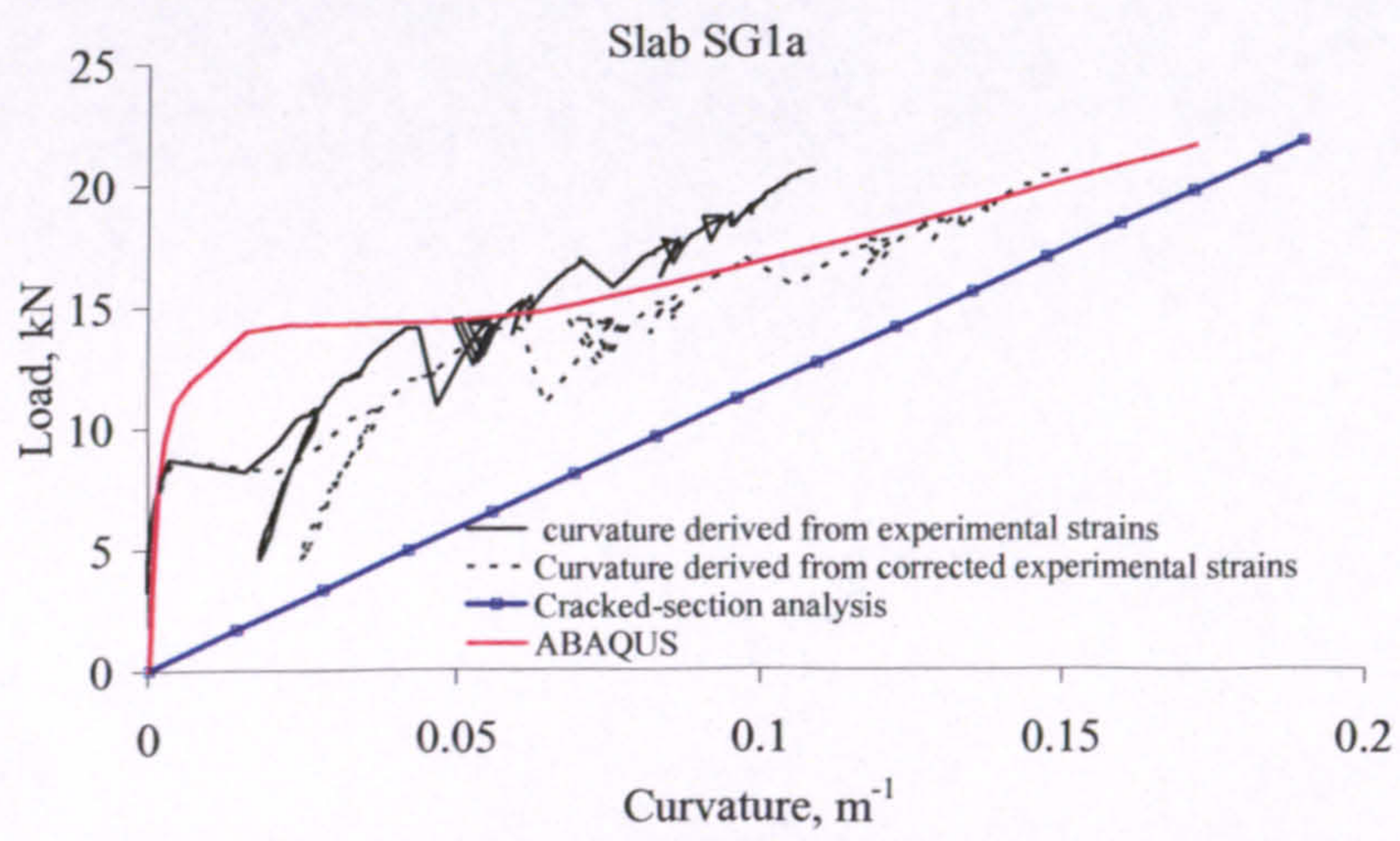
Slab SG1a
Load, kN
25
20
15
10
5
0
curvature derived from experimental strains
Curvature derived from corrected experimental strains
Cracked-section analysis
ABAQUS
0
0.05
0.1
0.15
0.2
Curvature, m-1

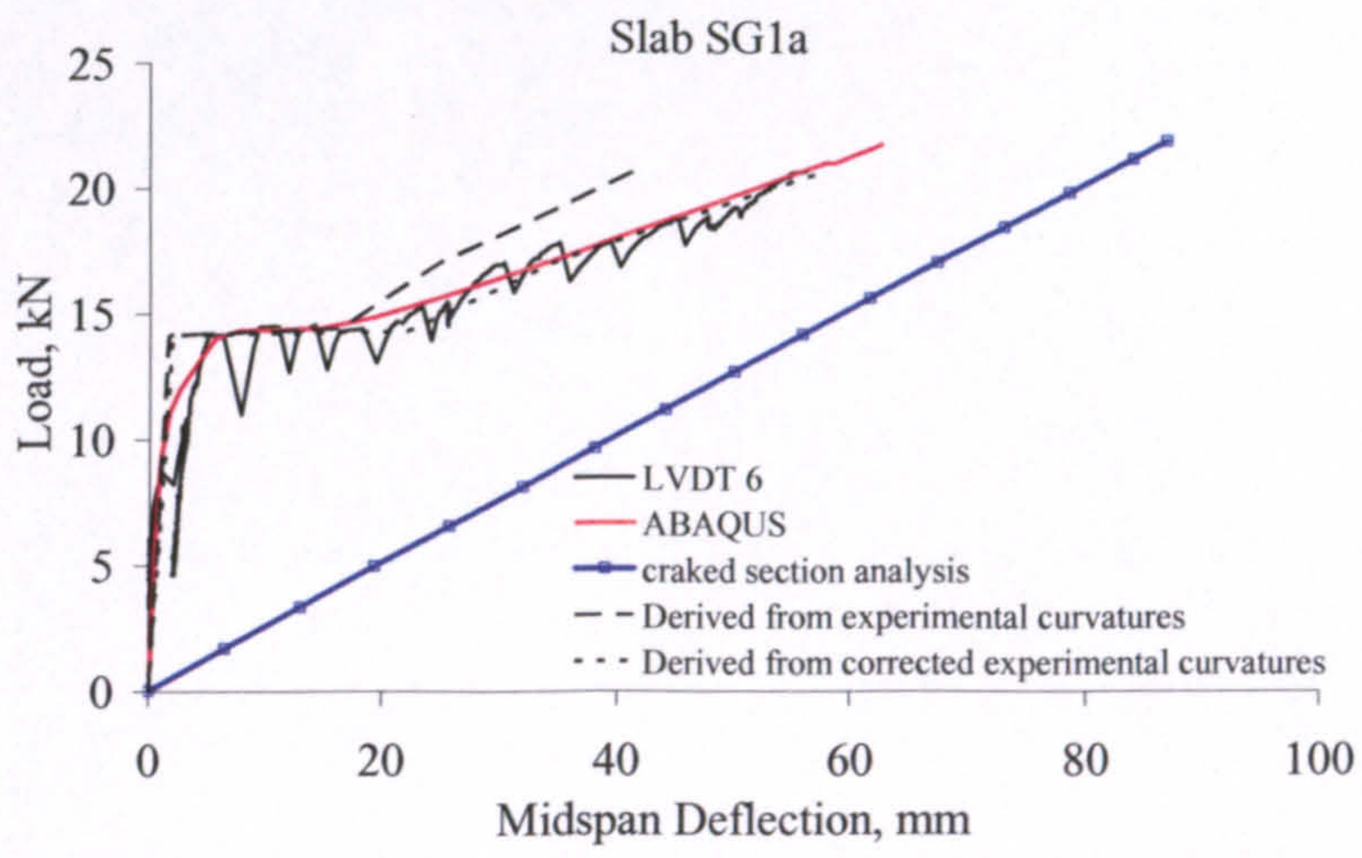
Slab SG1a
Load, kN
25
20
15
10
5
0
LVDT 6
ABAQUS
craked section analysis
Derived from experimental curvatures
Derived from corrected experimental curvatures
0
20
40
60
80
100
Midspan Deflection, mm

SLAB SG1a

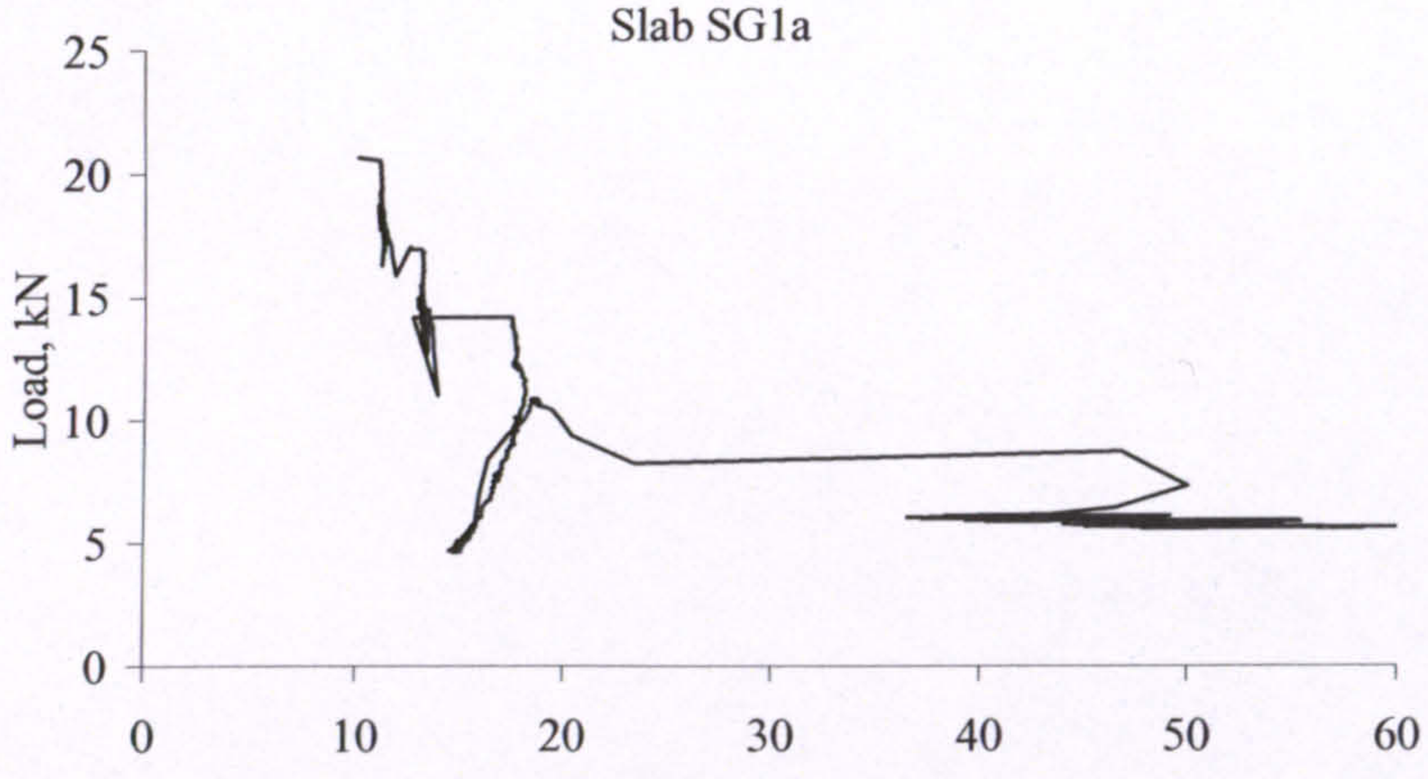
Slab SG1a
Load, kN
0
5
10
15
20
25
0
10
20
30
40
50
60
Average Neutral Axis Depth, mm

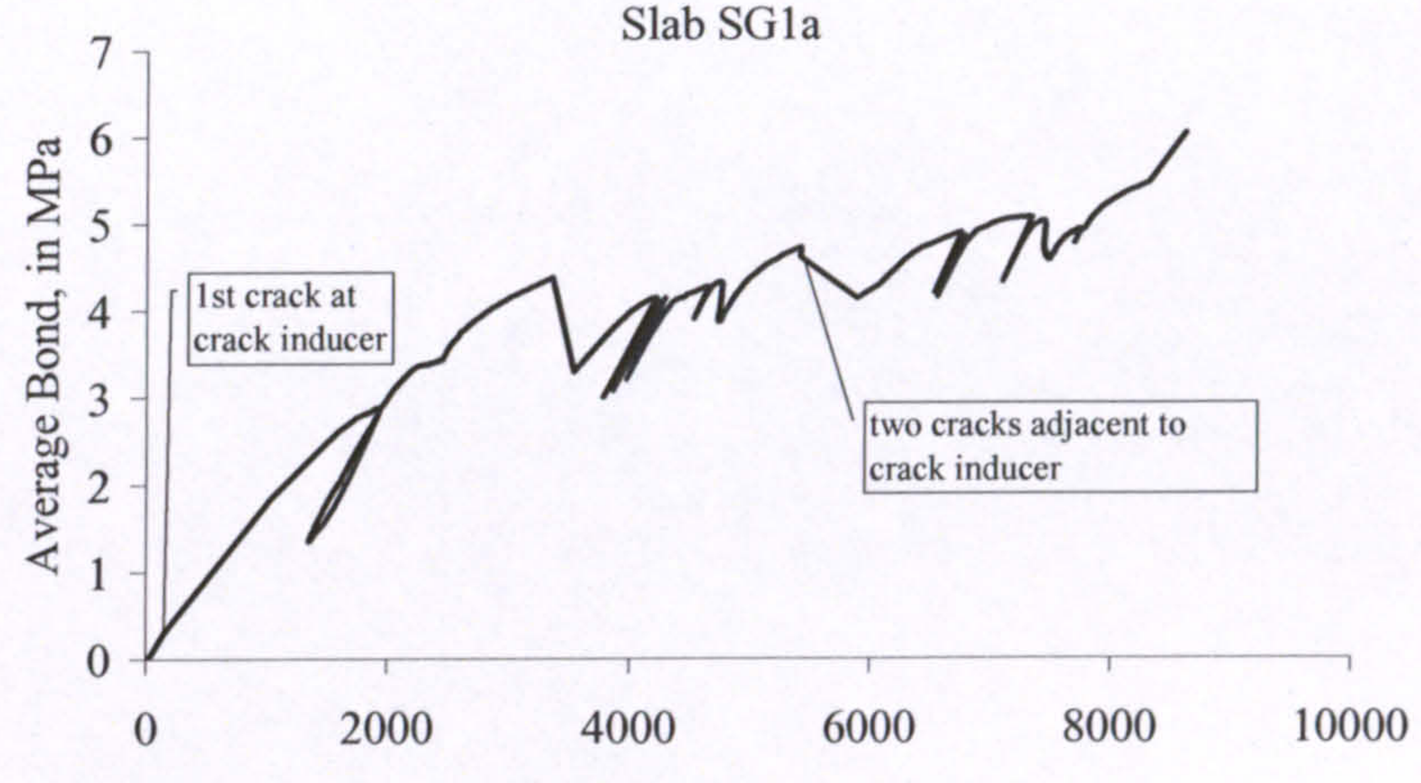
Slab SG1a
Average Bond, in MPa
0
1
2
3
4
5
6
7
1st crack at crack inducer
two cracks adjacent to crack inducer
0
2000
4000
6000
8000
10000
Average Strain Between Cracks, in microstrain

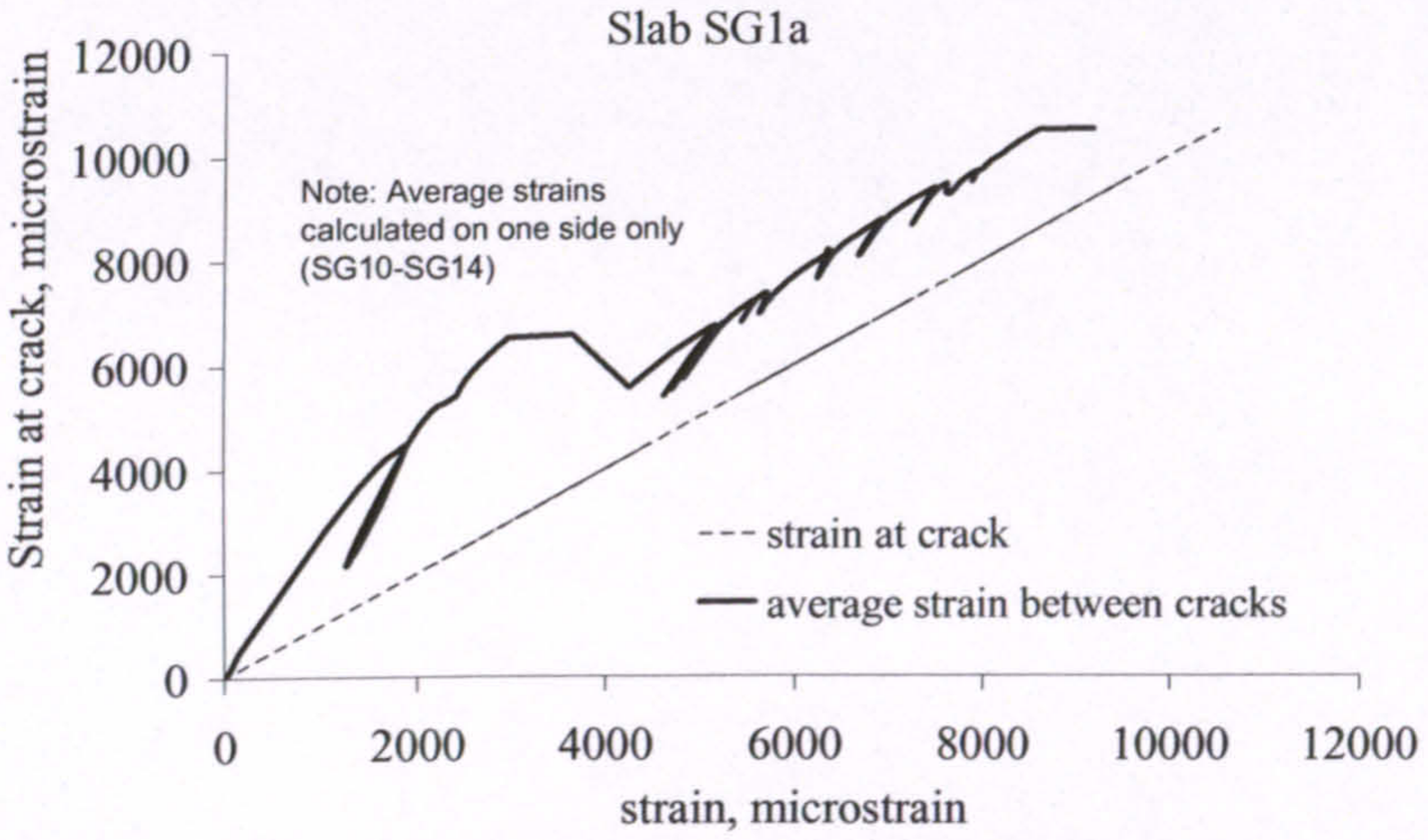
Slab SG1a
Strain at crack, microstrain
0
2000
4000
6000
8000
10000
12000
Note: Average strains calculated on one side only (SG10-SG14)
strain at crack
average strain between cracks
0
2000
4000
6000
8000
10000
12000
strain, microstrain

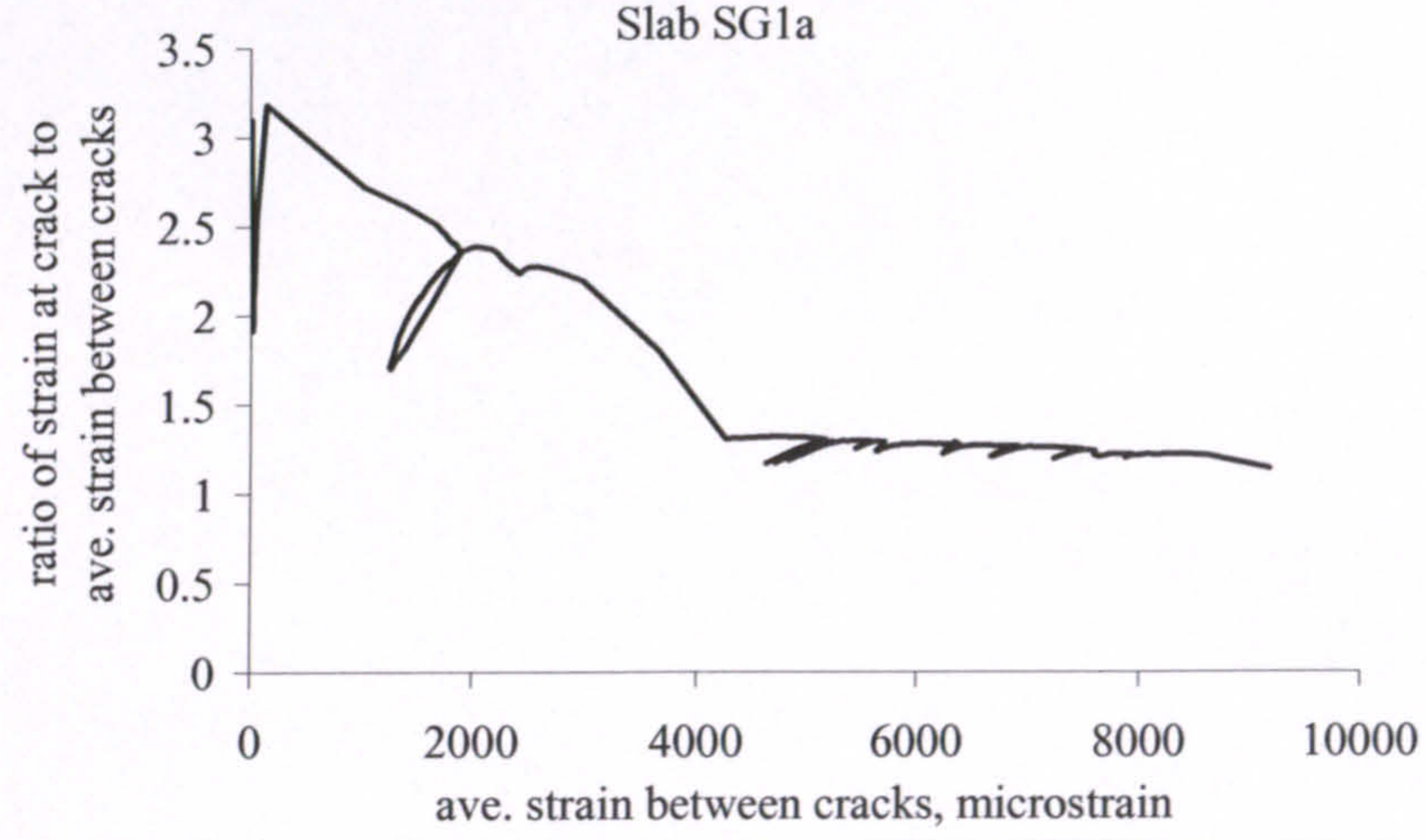
Slab SG1a
ratio of strain at crack to ave. strain between cracks
0
0.5
1
1.5
2
2.5
3
3.5
0
2000
4000
6000
8000
10000
ave. strain between cracks, microstrain

SLAB SG1a

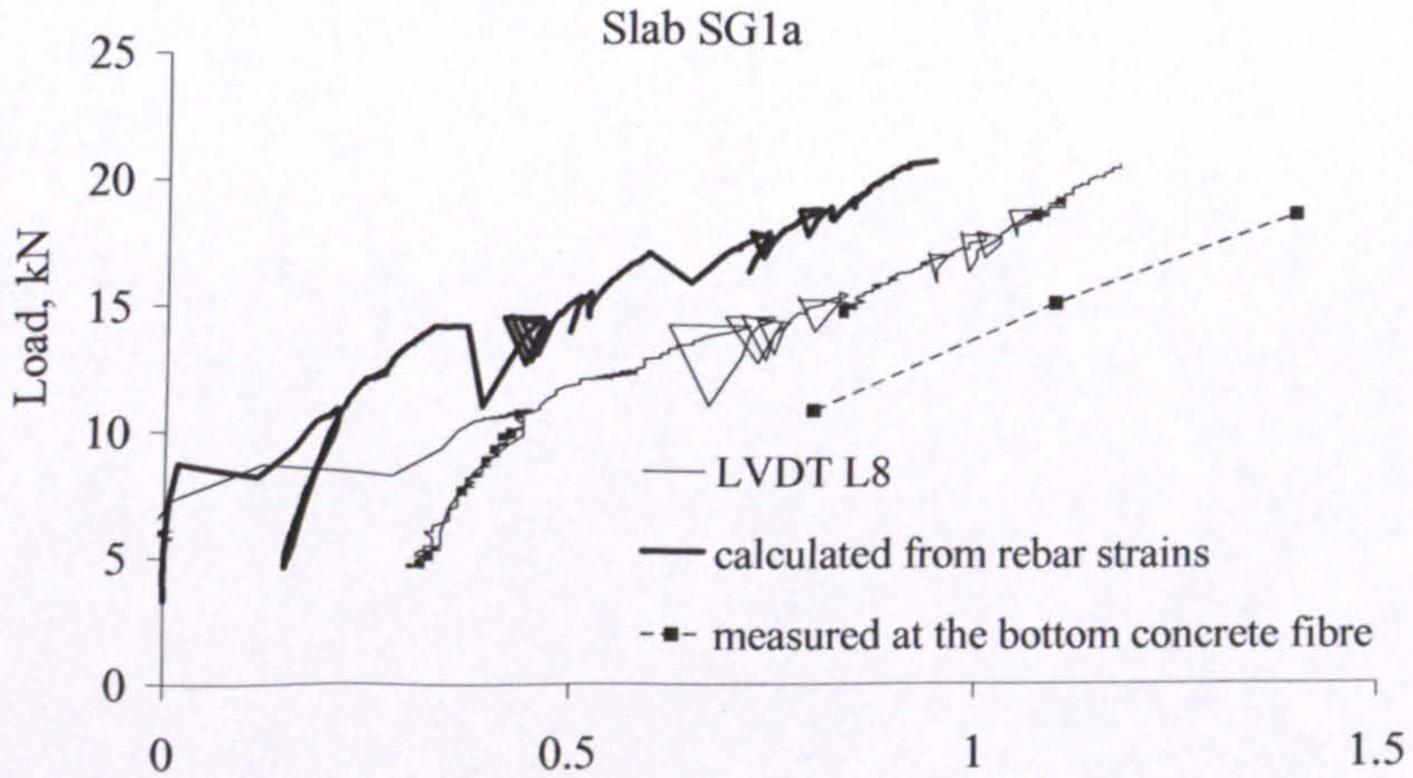

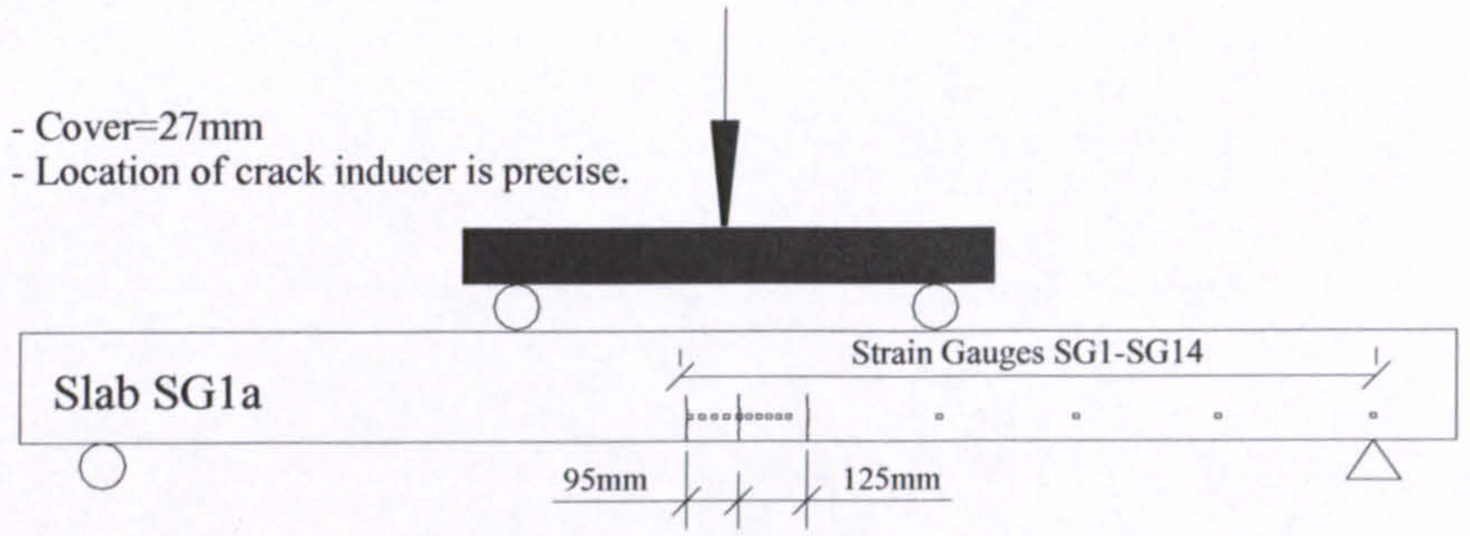

Cracks around Centre

Failure by rupture of rebars.

SLAB SG1b

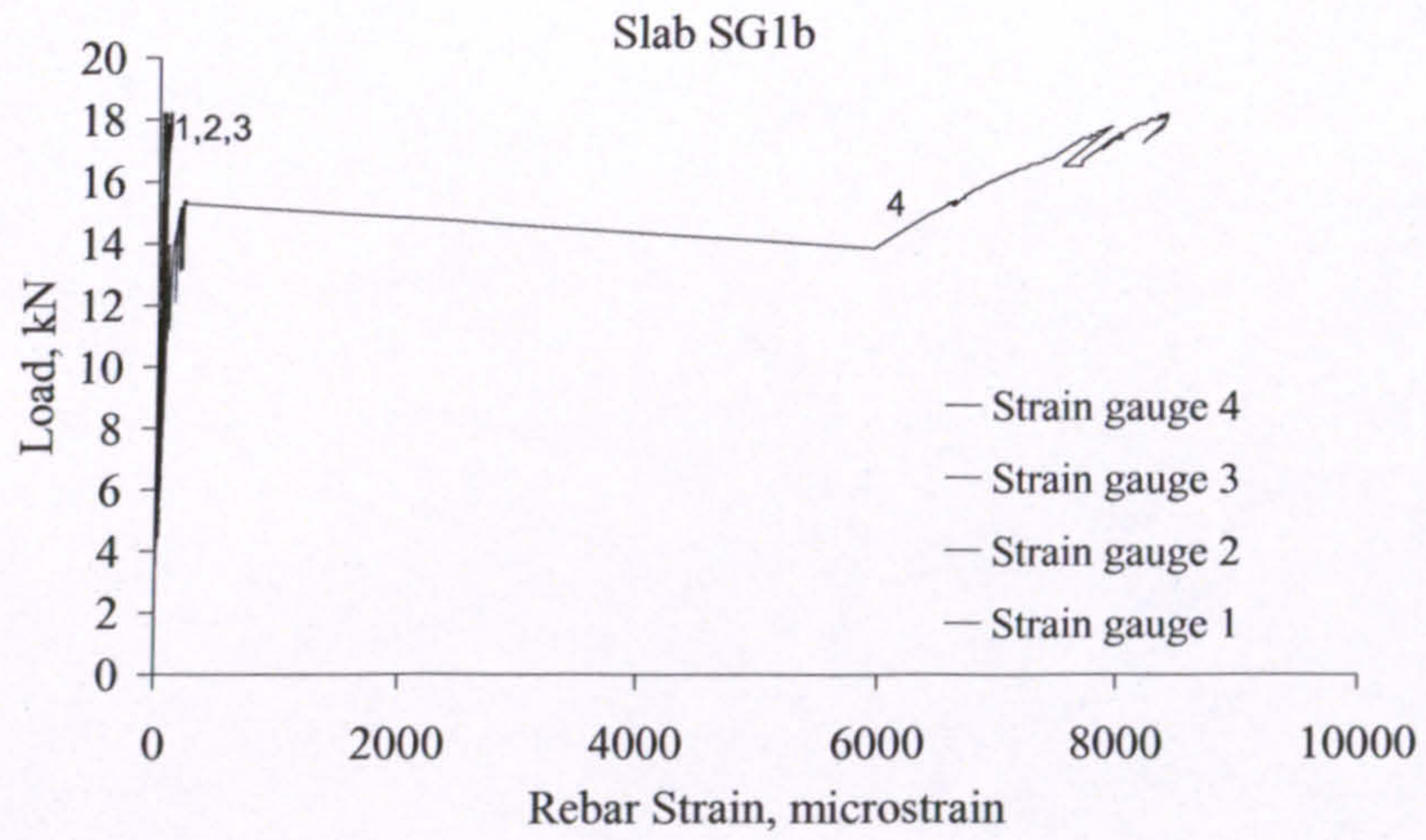
Slab SG1b
Load, kN
Rebar Strain, microstrain
1,2,3
4
Strain gauge 4
Strain gauge 3
Strain gauge 2
Strain gauge 1

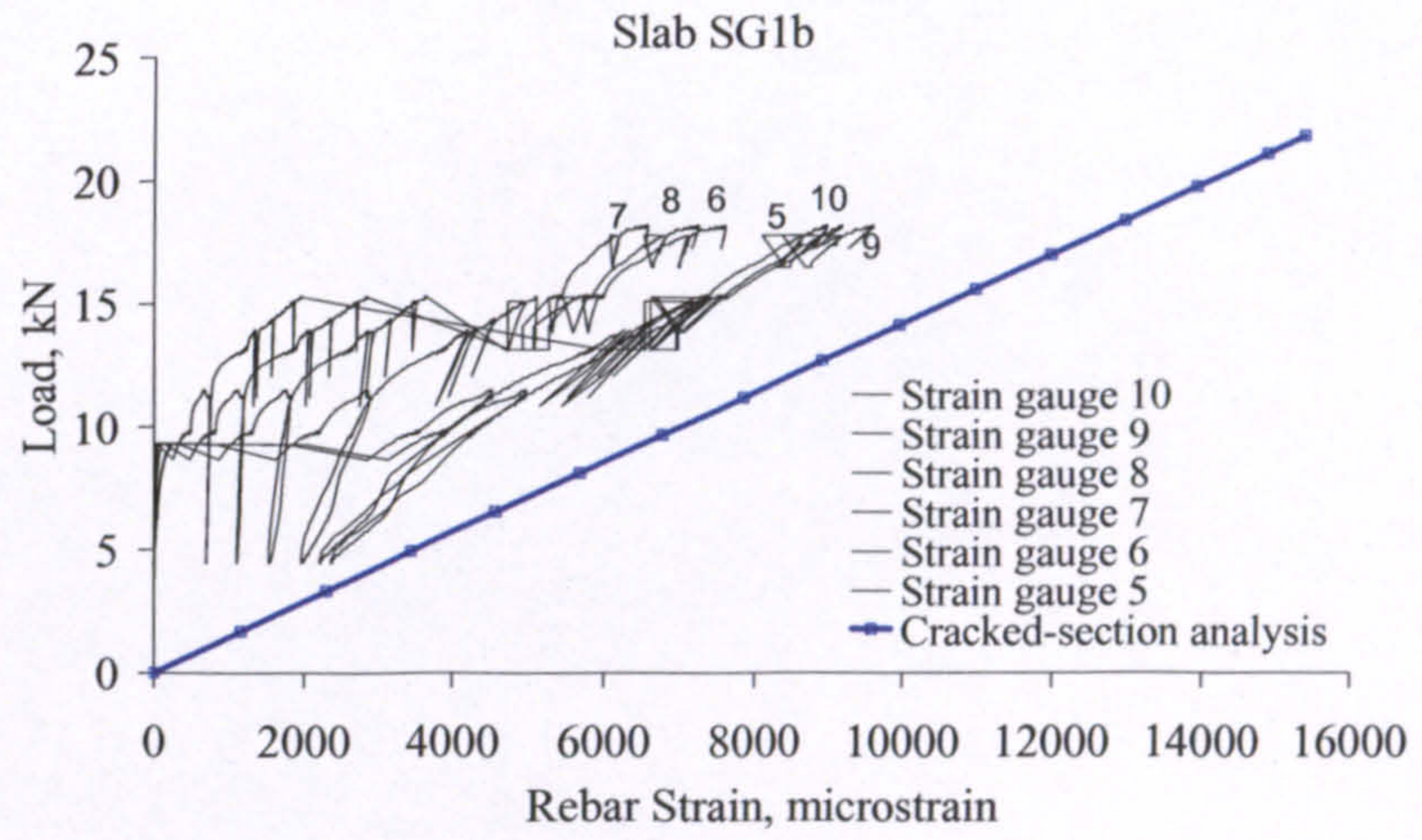
Slab SG1b
Load, kN
Rebar Strain, microstrain
7
8
6
5
10
9
Strain gauge 10
Strain gauge 9
Strain gauge 8
Strain gauge 7
Strain gauge 6
Strain gauge 5
Cracked-section analysis

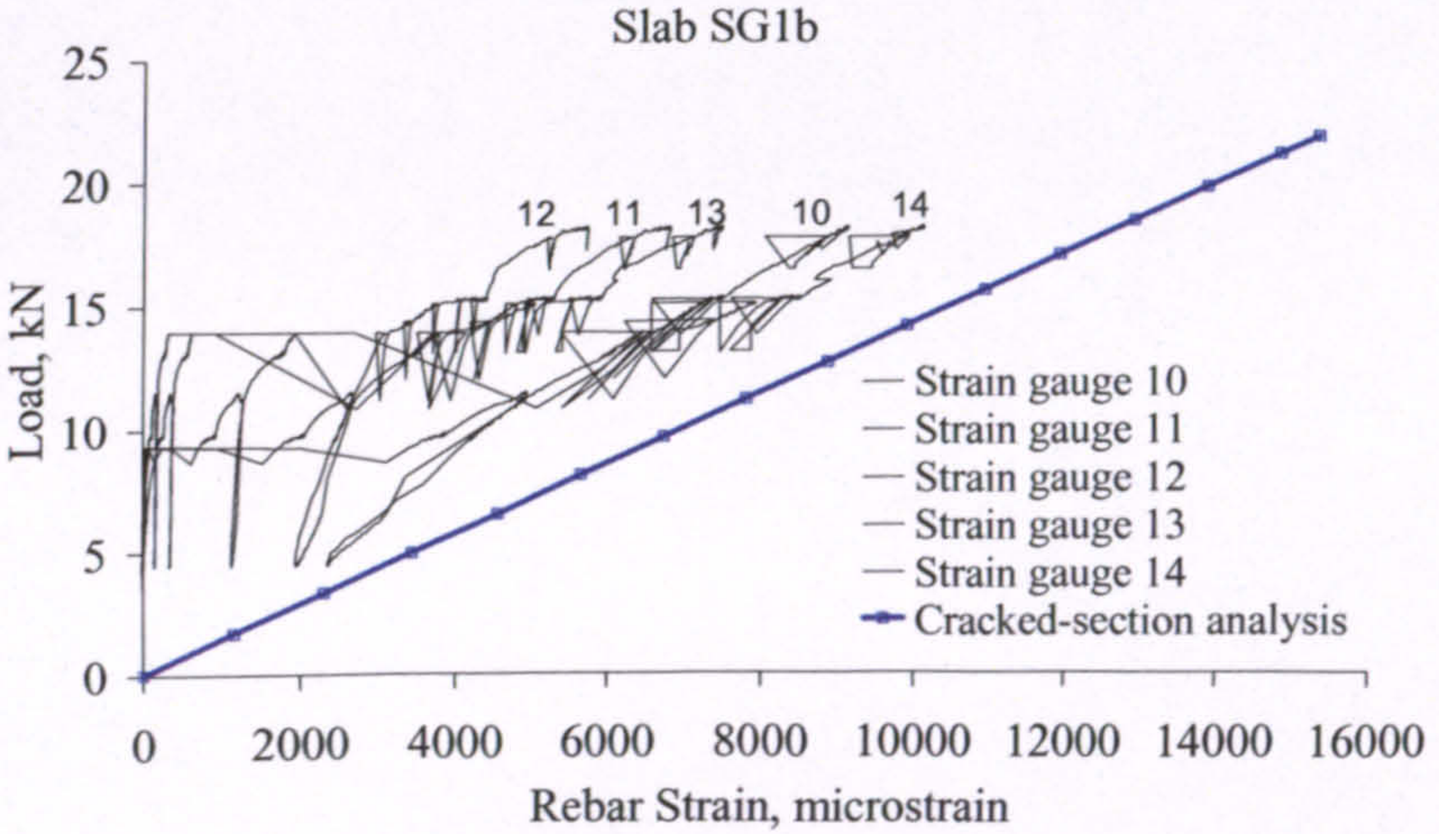
Slab SG1b
Load, kN
Rebar Strain, microstrain
12
11
13
10
14
Strain gauge 10
Strain gauge 11
Strain gauge 12
Strain gauge 13
Strain gauge 14
Cracked-section analysis

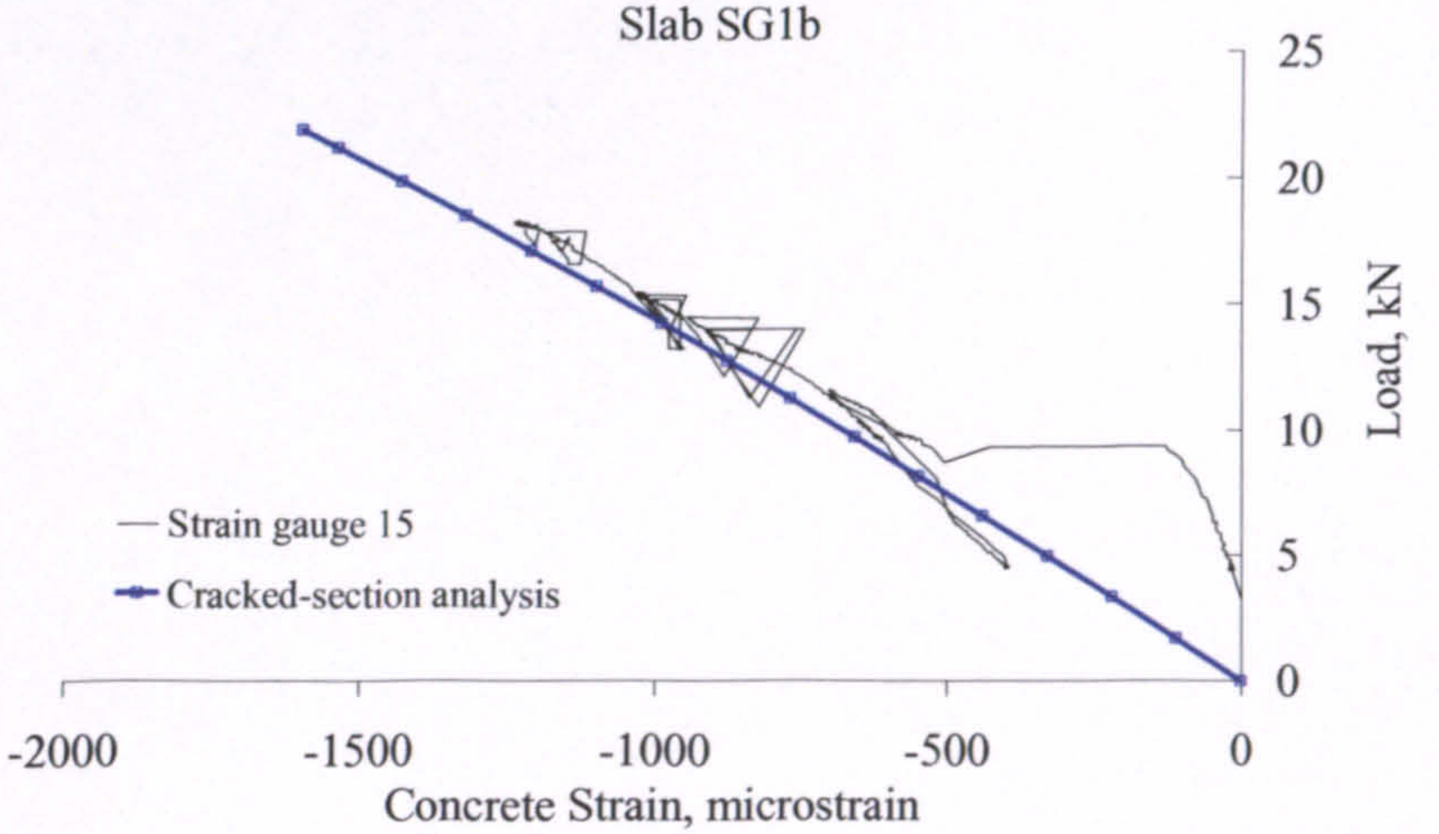
Slab SG1b
Load, kN
Concrete Strain, microstrain
Strain gauge 15
Cracked-section analysis

SLAB SG1b

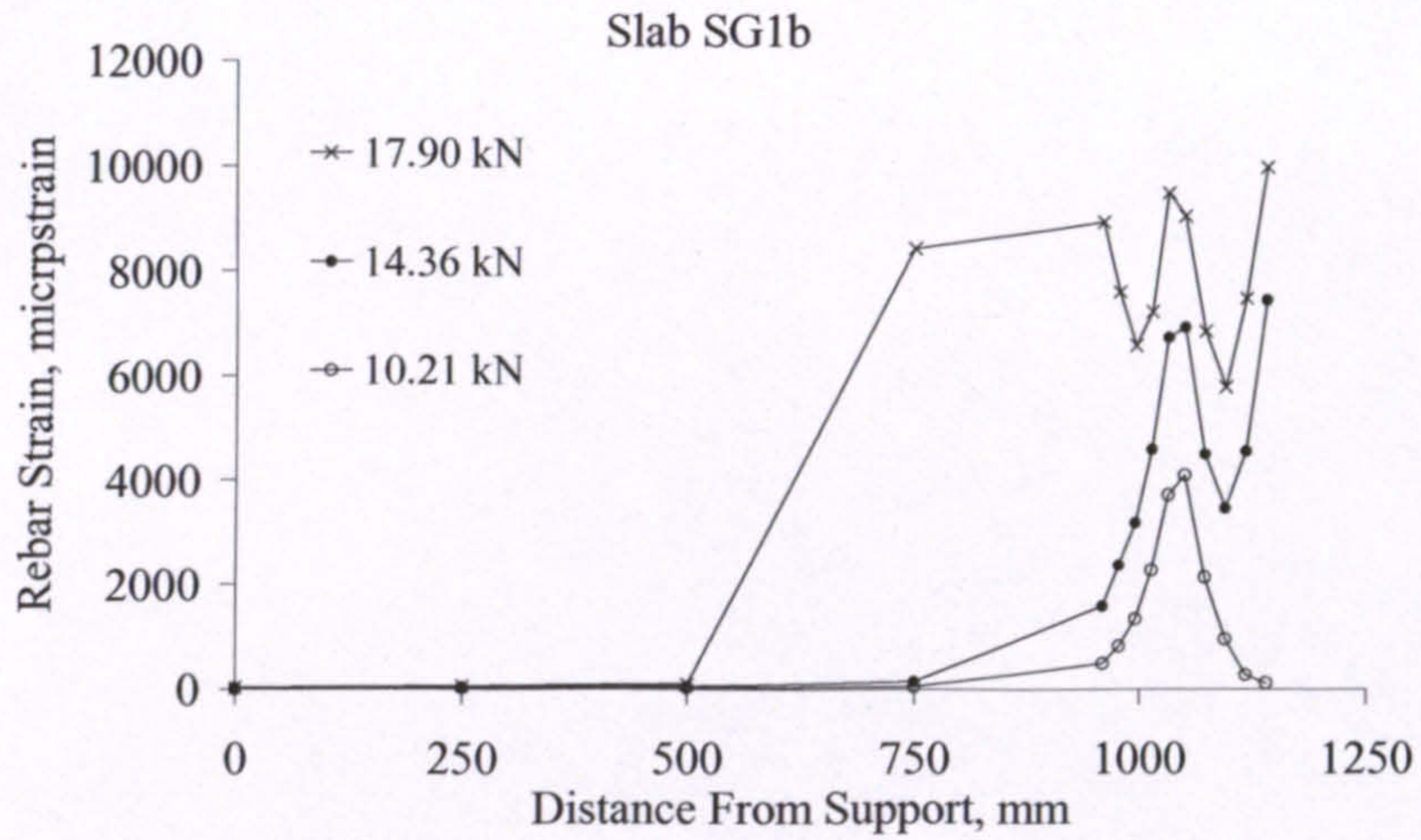
Slab SG1b
Rebar Strain, micrpstrain
12000
10000
8000
6000
4000
2000
0
17.90 kN
14.36 kN
10.21 kN
0
250
500
750
1000
1250
Distance From Support, mm

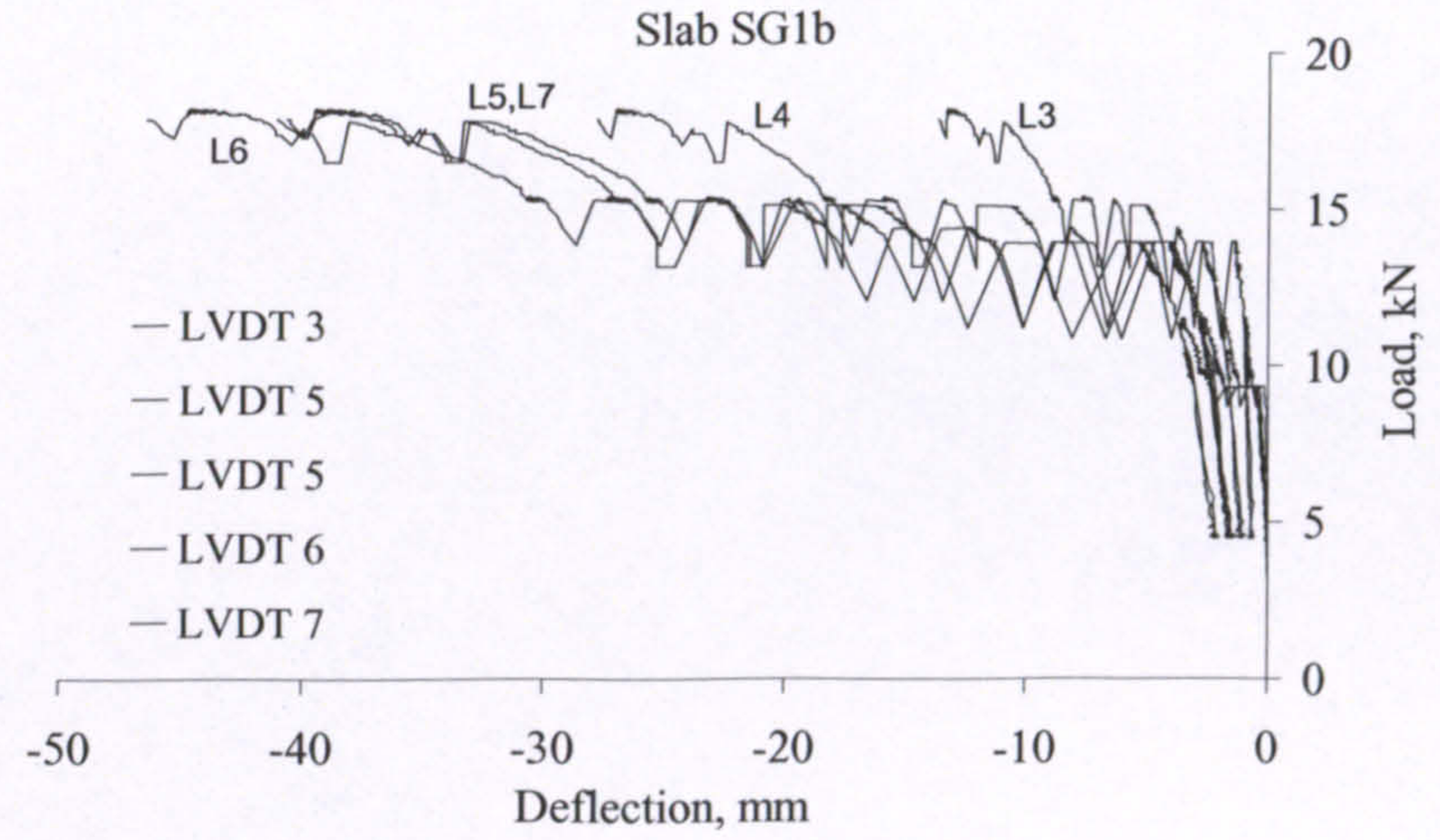
Slab SG1b
L6
L5,L7
L4
L3
LVDT 3
LVDT 5
LVDT 5
LVDT 6
LVDT 7
20
15
10
5
0
Load, kN
-50
-40
-30
-20
-10
0
Deflection, mm

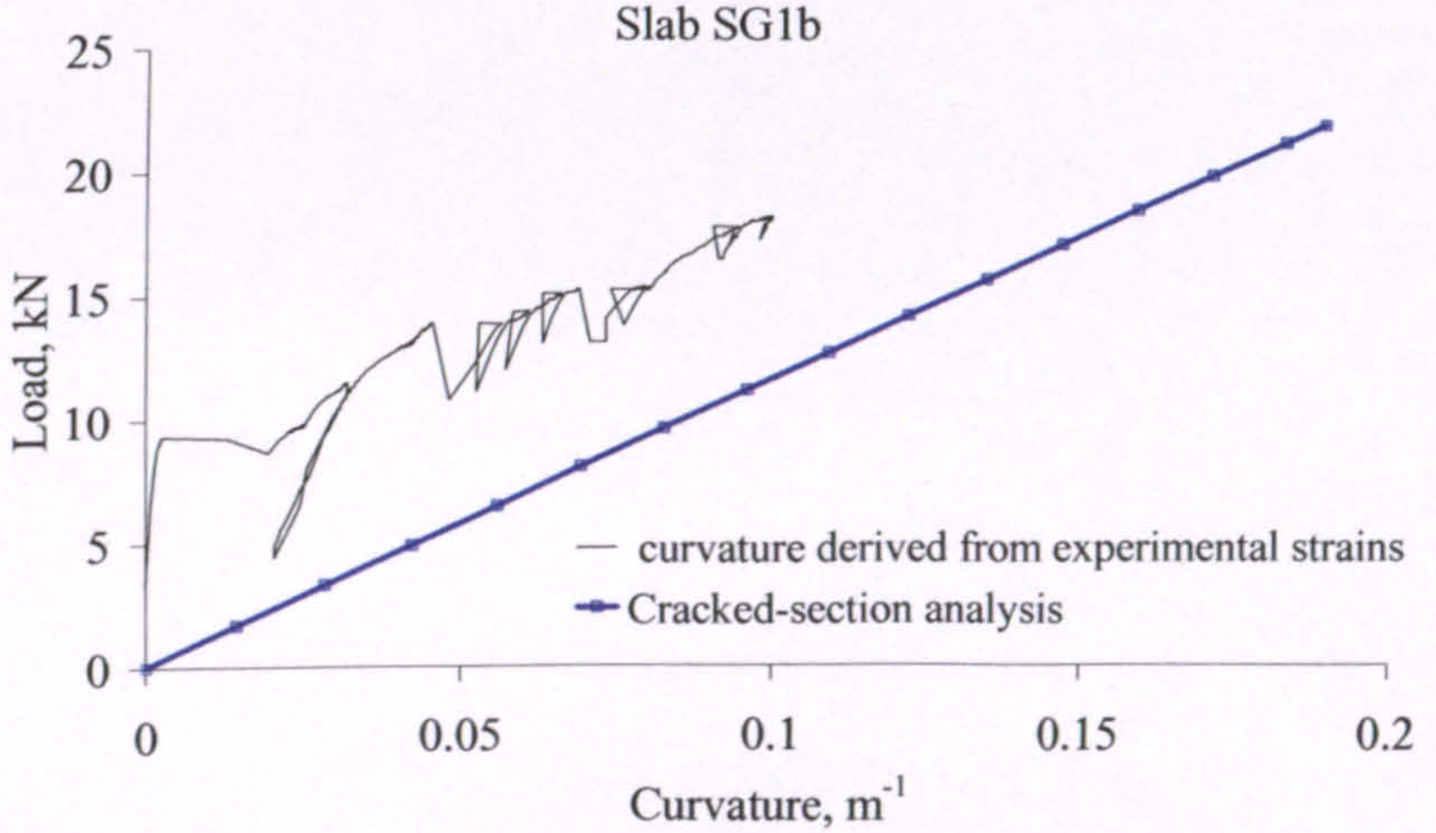
Slab SG1b
Load, kN
25
20
15
10
5
0
curvature derived from experimental strains
Cracked-section analysis
0
0.05
0.1
0.15
0.2
Curvature, m-1

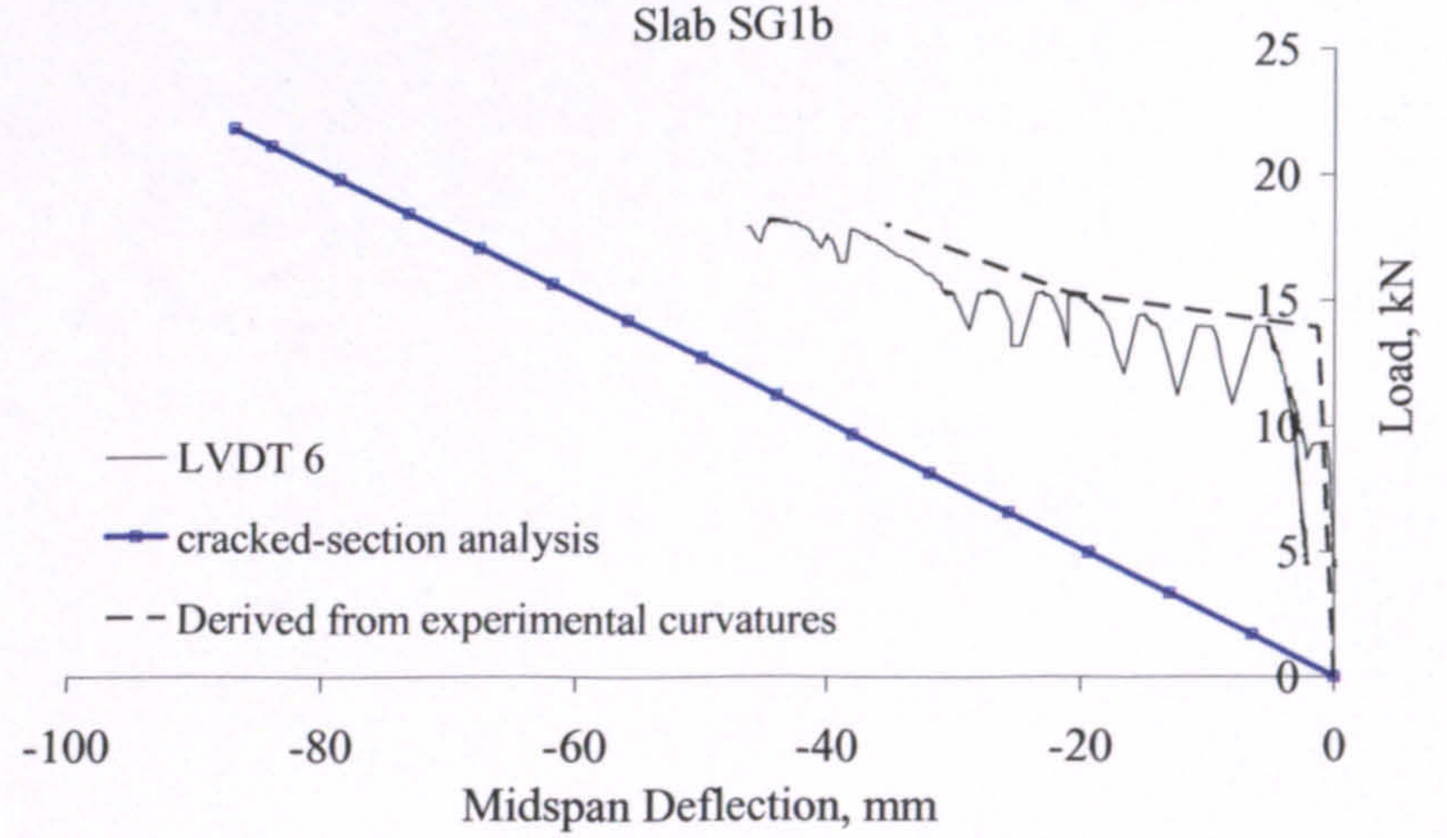
Slab SG1b
LVDT 6
cracked-section analysis
Derived from experimental curvatures
25
20
15
10
5
0
Load, kN
-100
-80
-60
-40
-20
0
Midspan Deflection, mm

SLAB SG1b

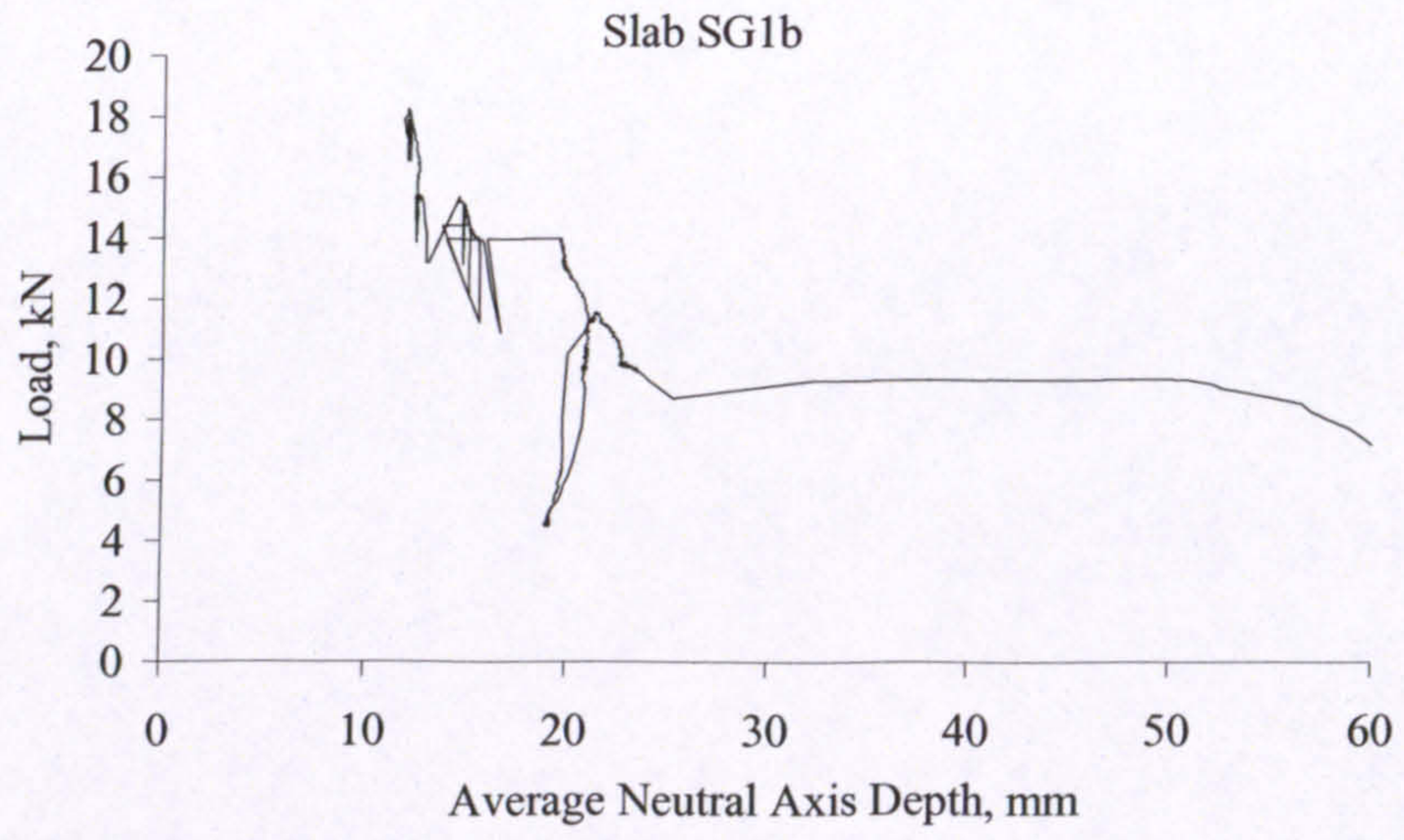
Slab SG1b
Load, kN
Average Neutral Axis Depth, mm

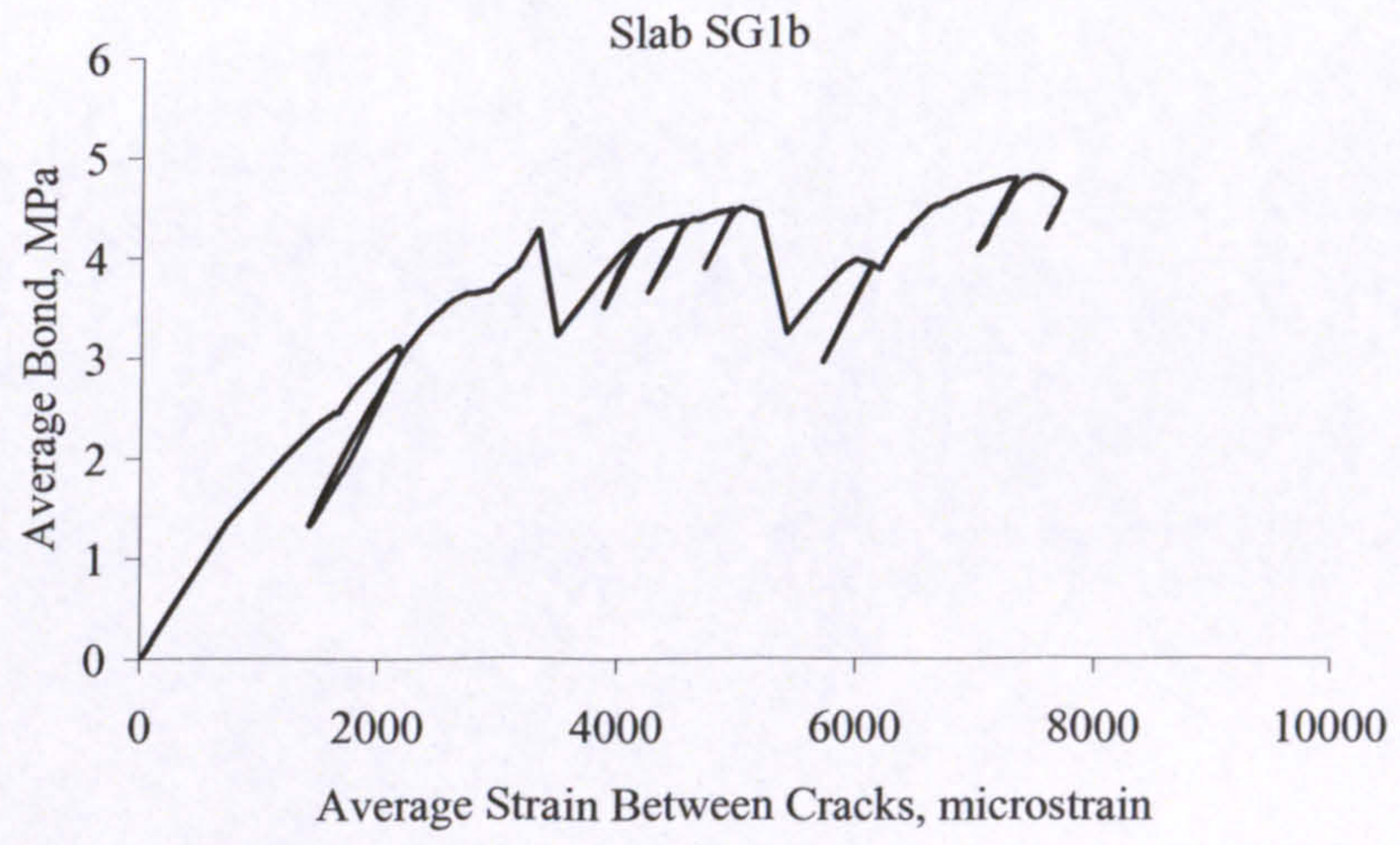
Slab SG1b
Average Bond, MPa
Average Strain Between Cracks, microstrain

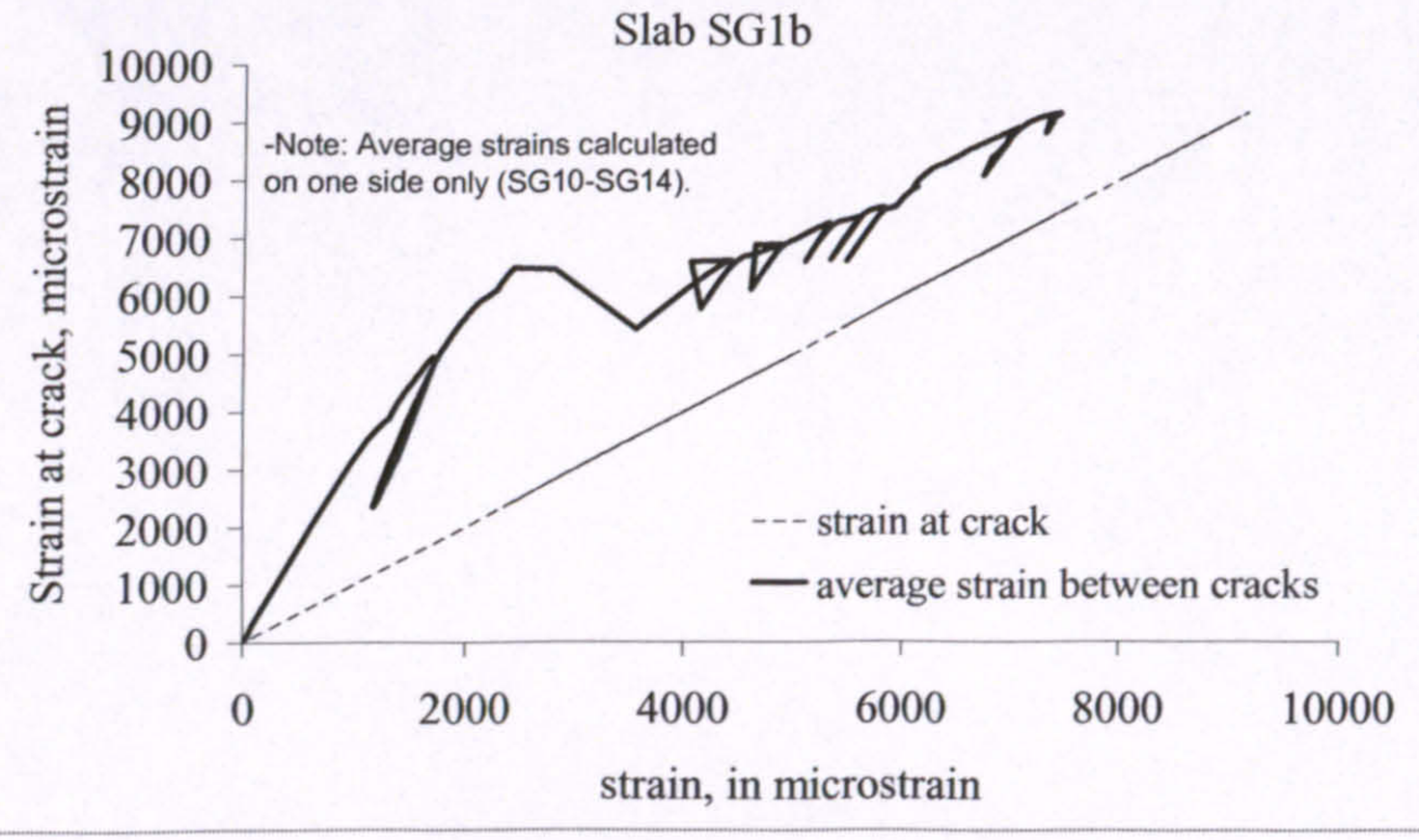
Slab SG1b
-Note: Average strains calculated on one side only (SG10-SG14).
Strain at crack, microstrain
strain at crack
average strain between cracks
strain, in microstrain

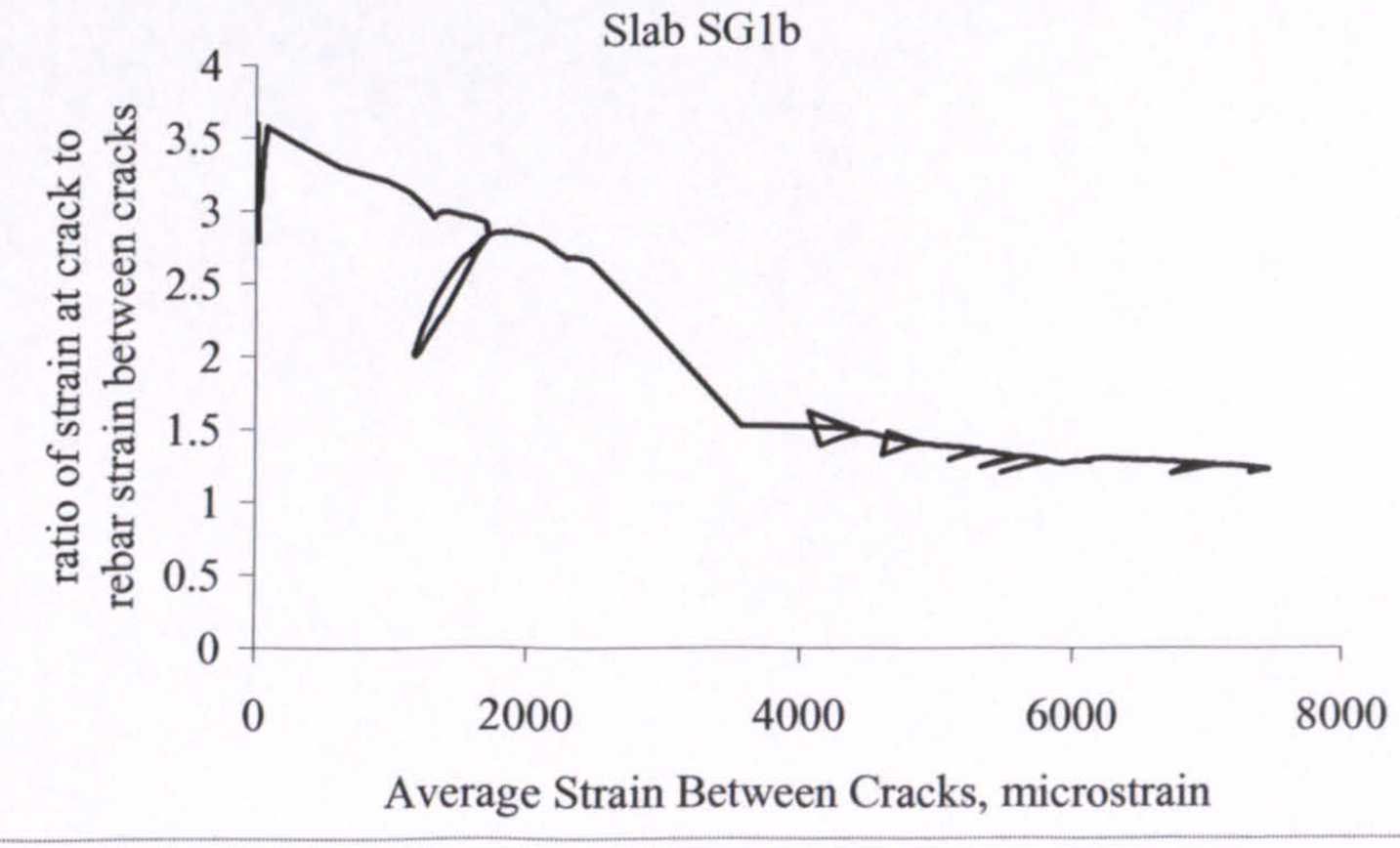
Slab SG1b
ratio of strain at crack to rebar strain between cracks
Average Strain Between Cracks, microstrain

SLAB SG1b

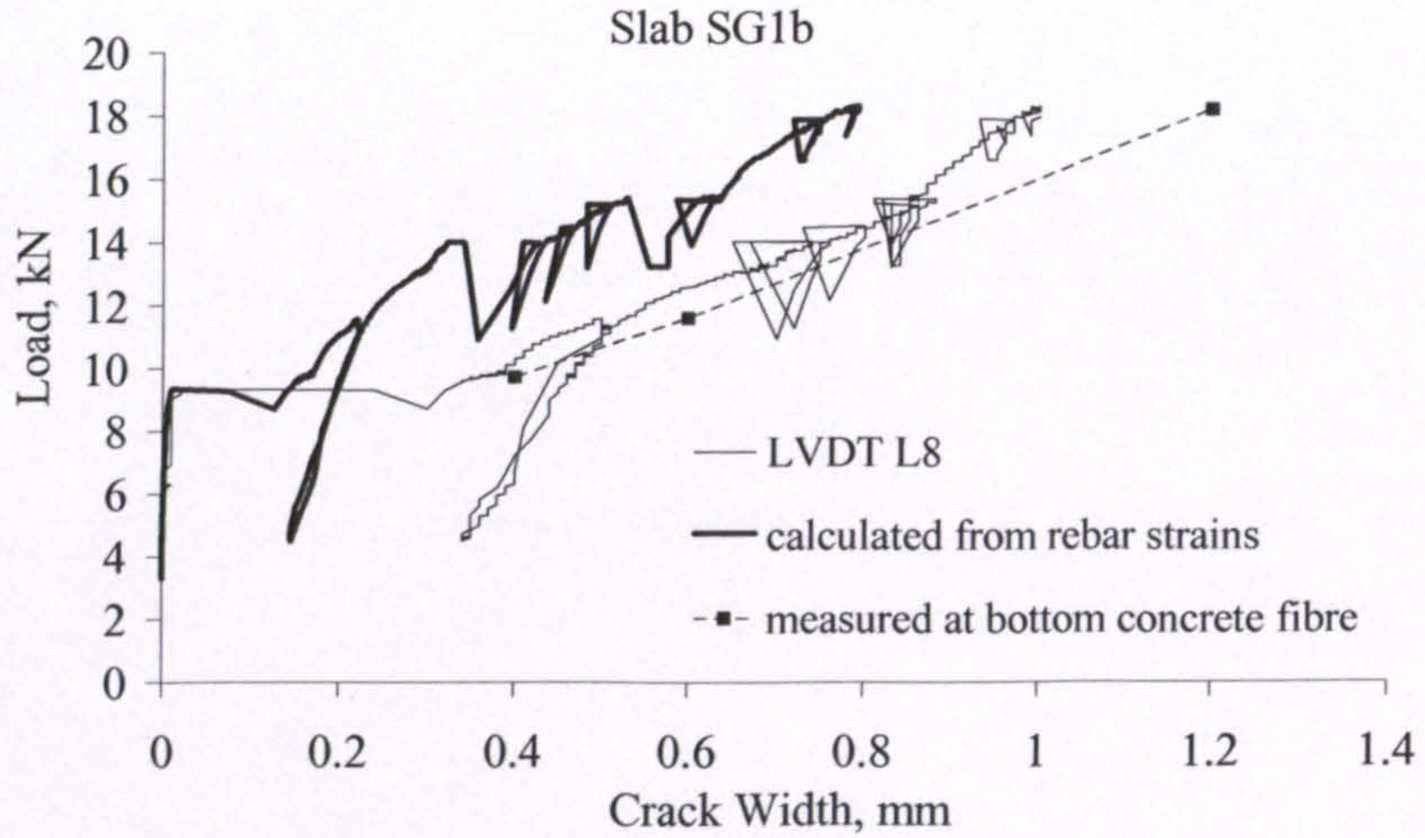

- Cover=28mm
- Location of crack inducer is precise.

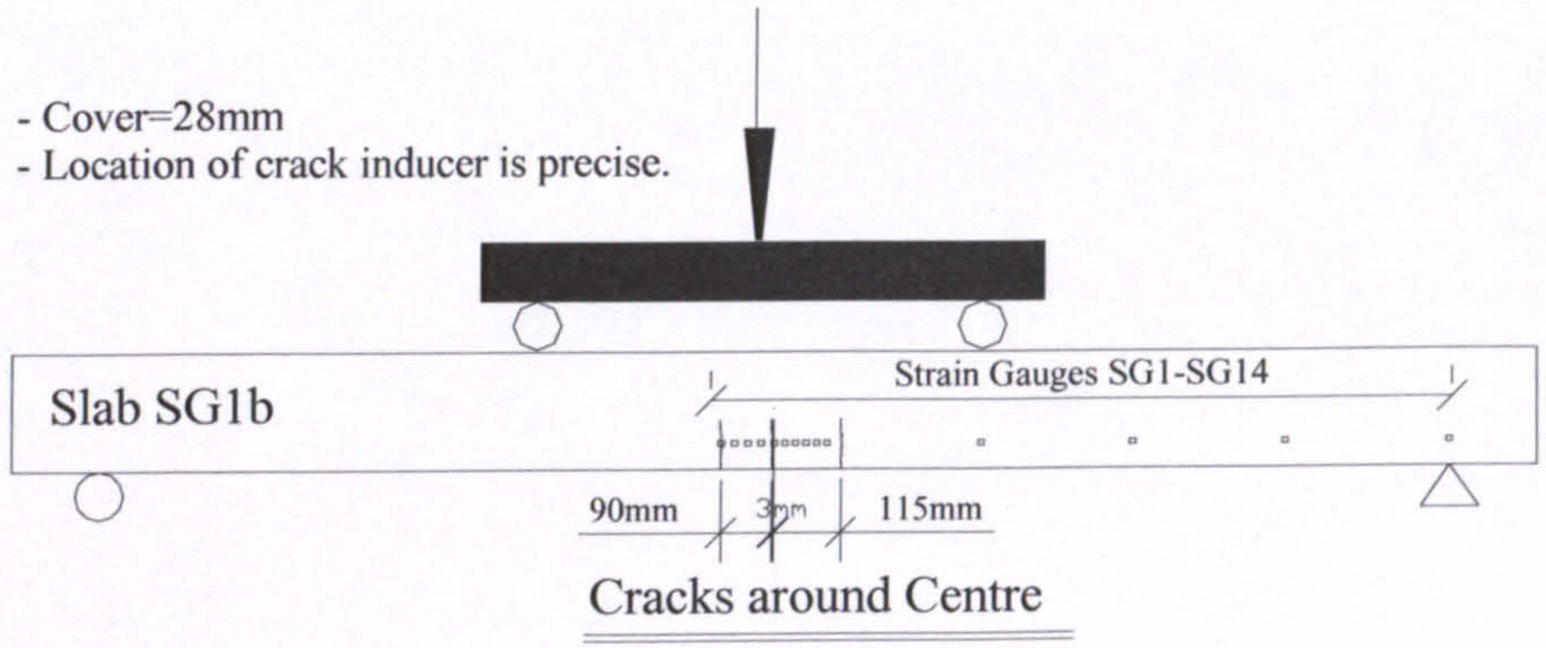

Cracks around Centre

Failure by rupture of rebars.

SLAB SG2a

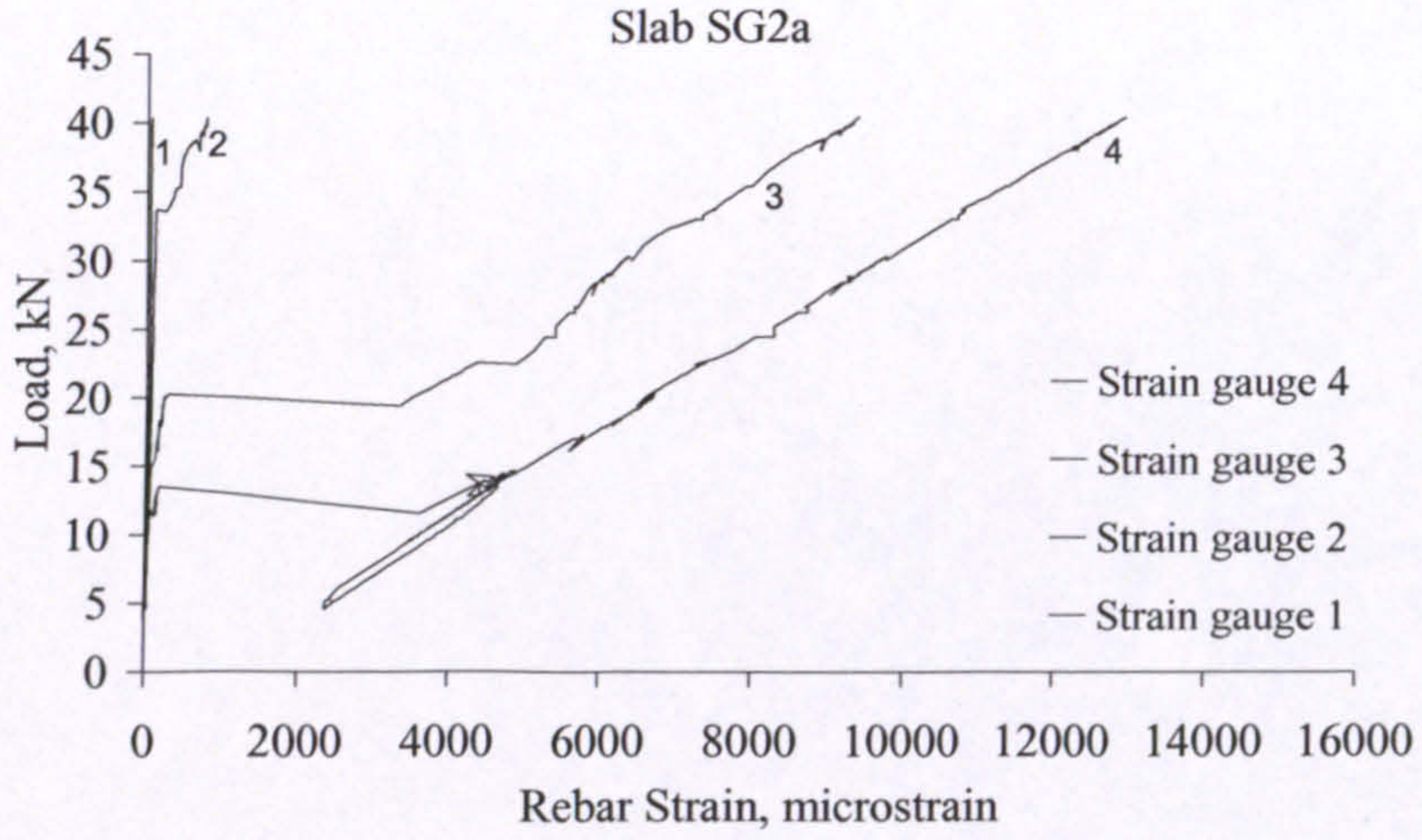
Slab SG2a
Load, kN
Rebar Strain, microstrain
1
2
3
4
Strain gauge 4
Strain gauge 3
Strain gauge 2
Strain gauge 1

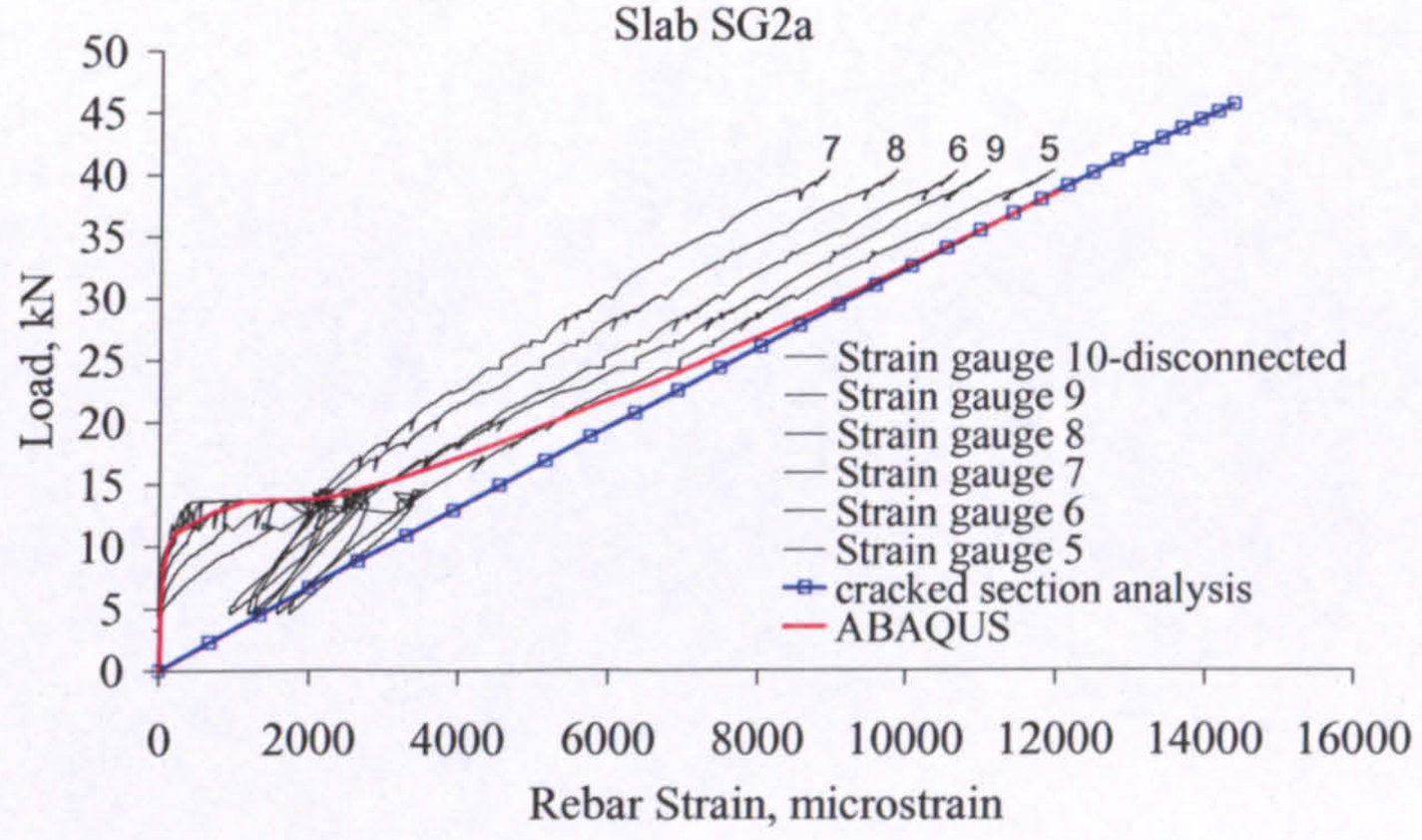
Slab SG2a
Load, kN
Rebar Strain, microstrain
7
8
6
9
5
Strain gauge 10-disconnected
Strain gauge 9
Strain gauge 8
Strain gauge 7
Strain gauge 6
Strain gauge 5
cracked section analysis
ABAQUS

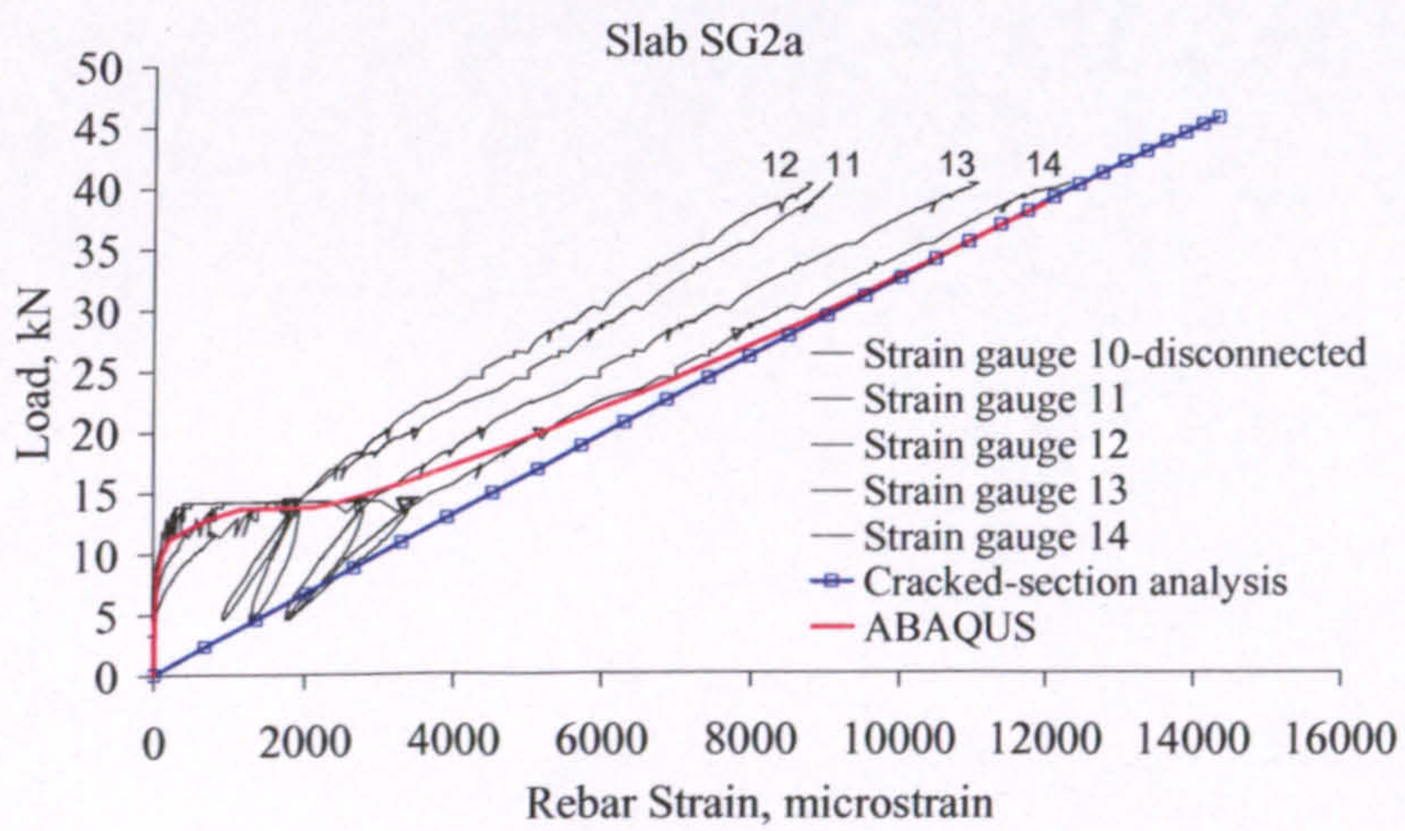
Slab SG2a
Load, kN
Rebar Strain, microstrain
12
11
13
14
Strain gauge 10-disconnected
Strain gauge 11
Strain gauge 12
Strain gauge 13
Strain gauge 14
Cracked-section analysis
ABAQUS

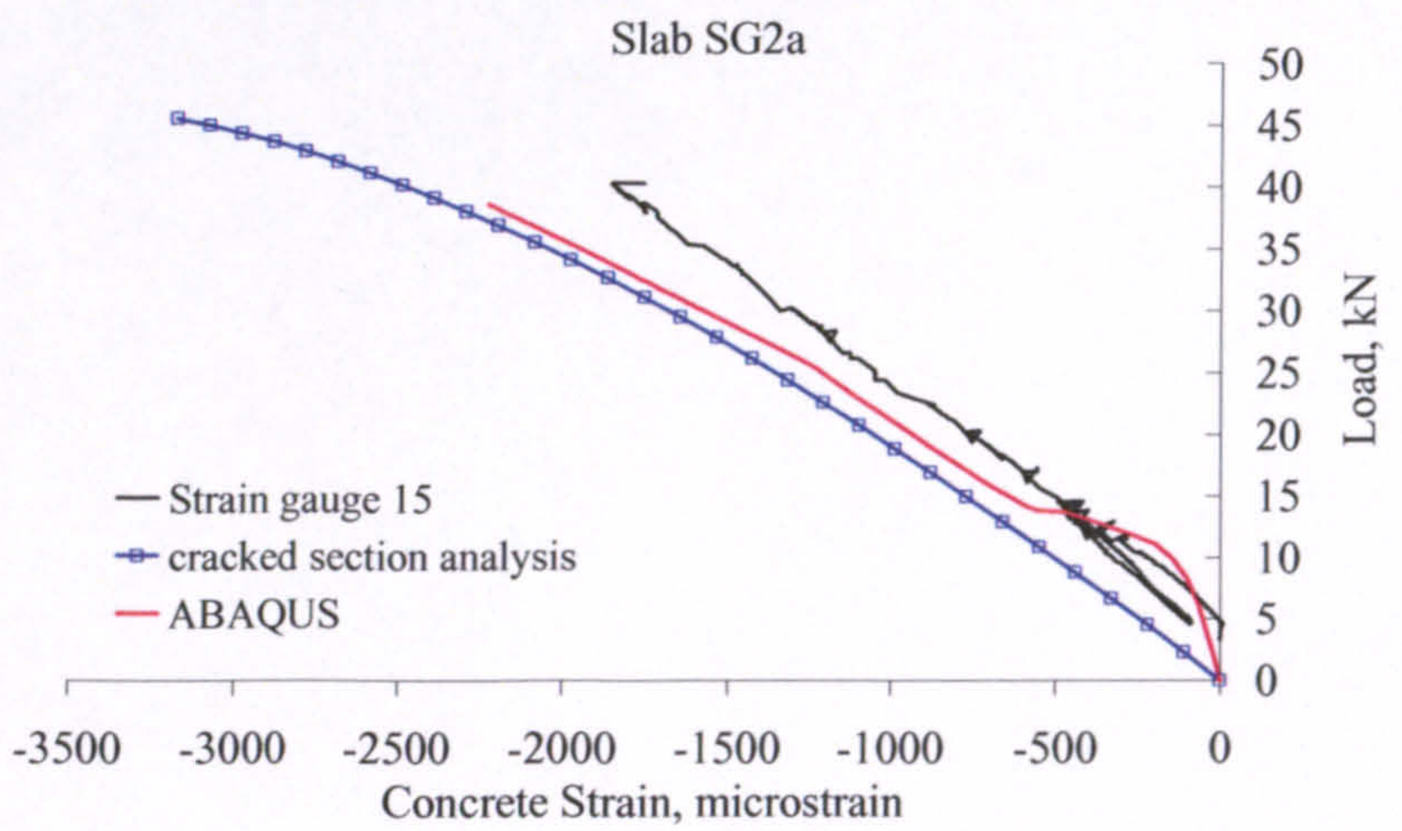
Slab SG2a
Load, kN
Concrete Strain, microstrain
Strain gauge 15
cracked section analysis
ABAQUS

SLAB SG2a

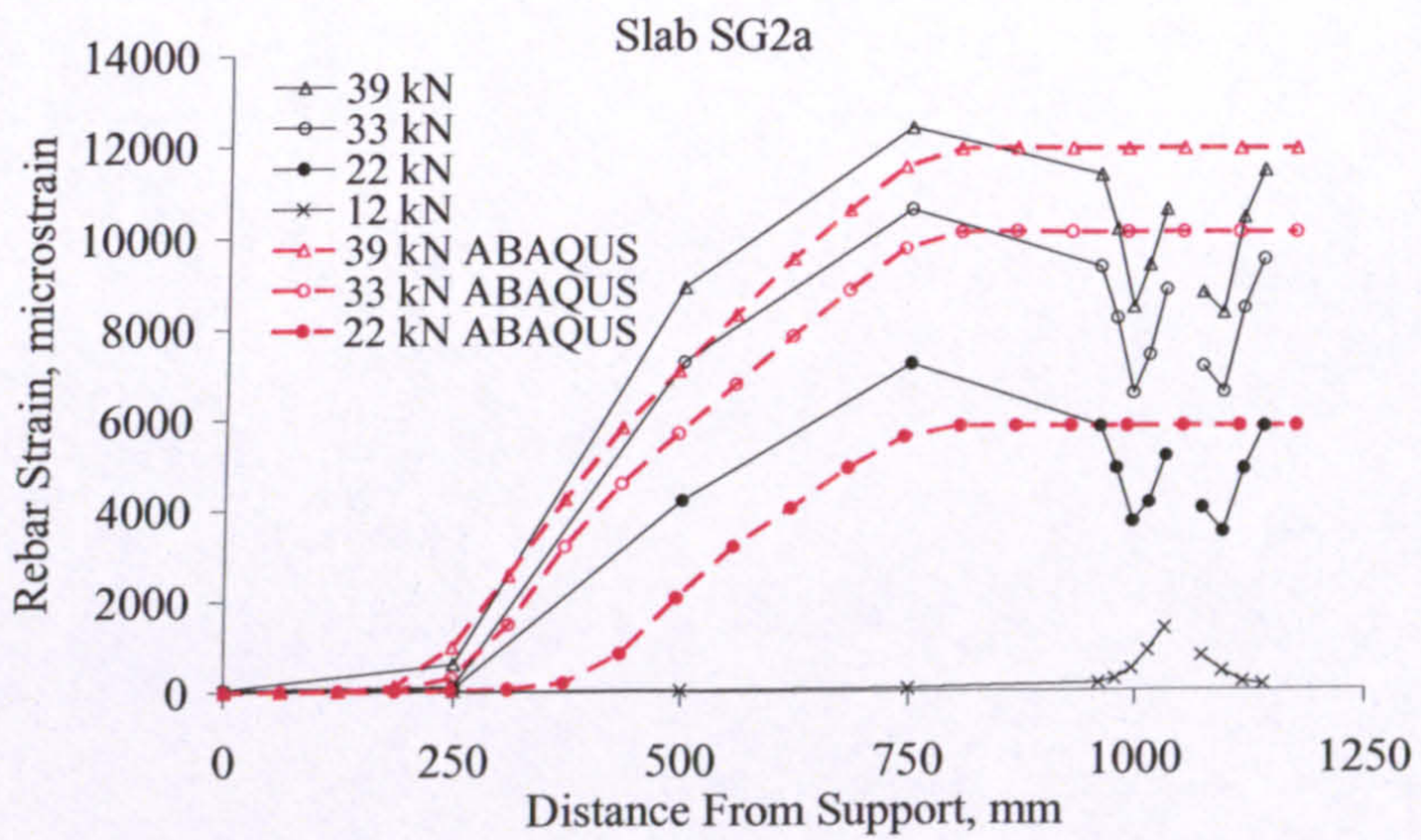
Slab SG2a
Rebar Strain, microstrain
14000
12000
10000
8000
6000
4000
2000
0
39 kN
33 kN
22 kN
12 kN
39 kN ABAQUS
33 kN ABAQUS
22 kN ABAQUS
0
250
500
750
1000
1250
Distance From Support, mm

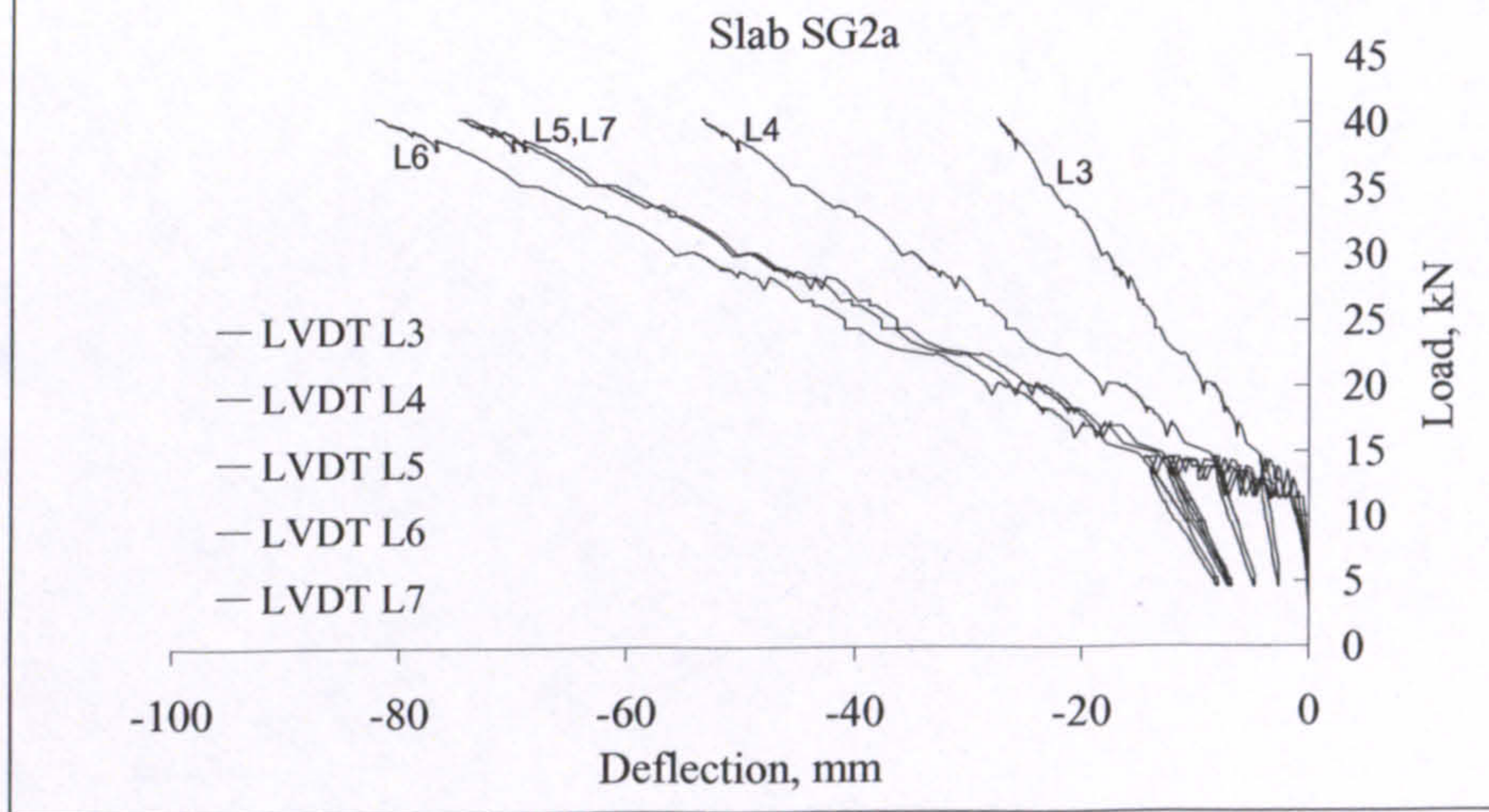
Slab SG2a
L6
L5,L7
L4
L3
LVDT L3
LVDT L4
LVDT L5
LVDT L6
LVDT L7
45
40
35
30
25
20
15
10
5
0
Load, kN
-100
-80
-60
-40
-20
0
Deflection, mm

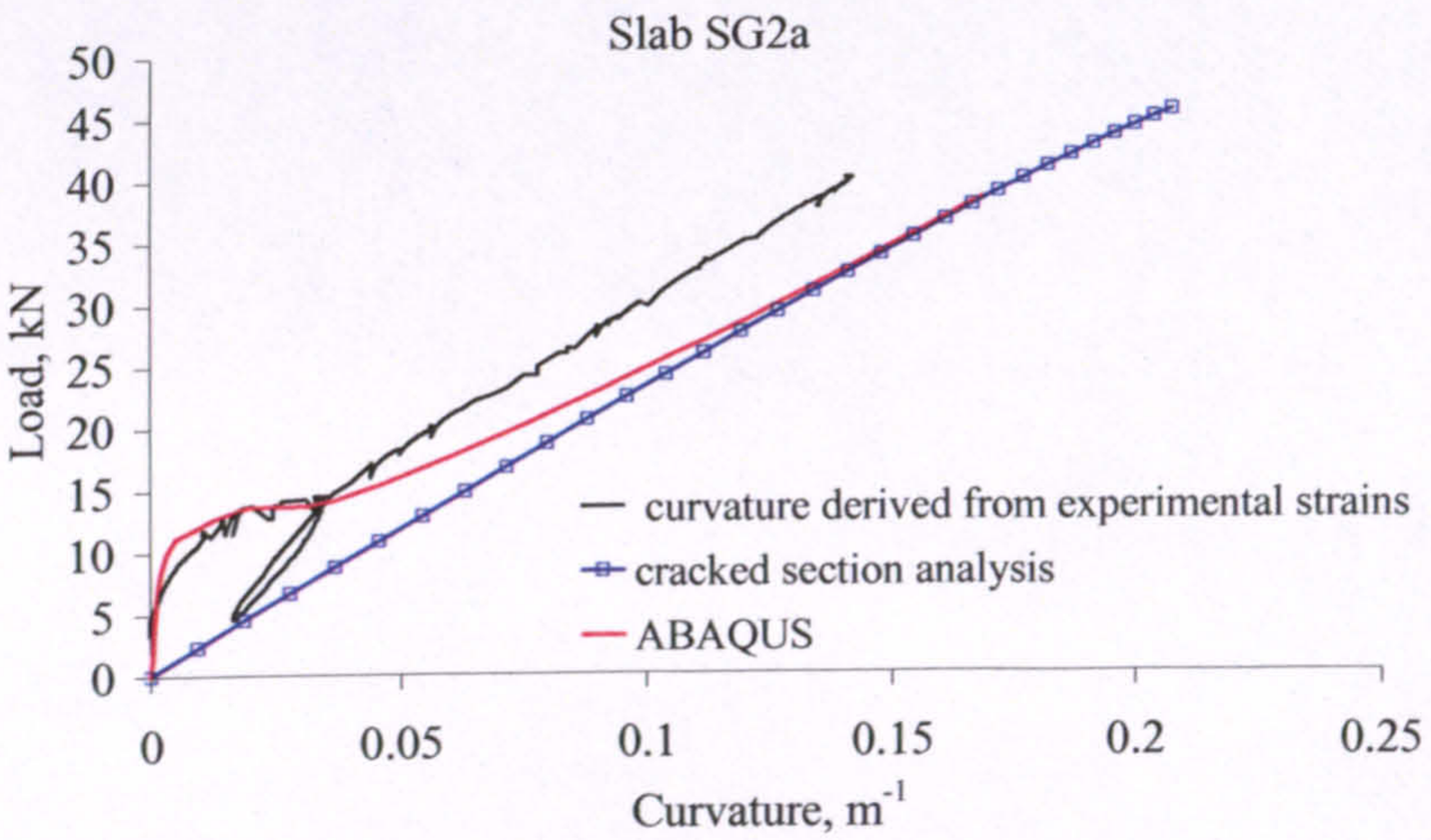
Slab SG2a
Load, kN
50
45
40
35
30
25
20
15
10
5
0
curvature derived from experimental strains
cracked section analysis
ABAQUS
0
0.05
0.1
0.15
0.2
0.25
Curvature, m-1

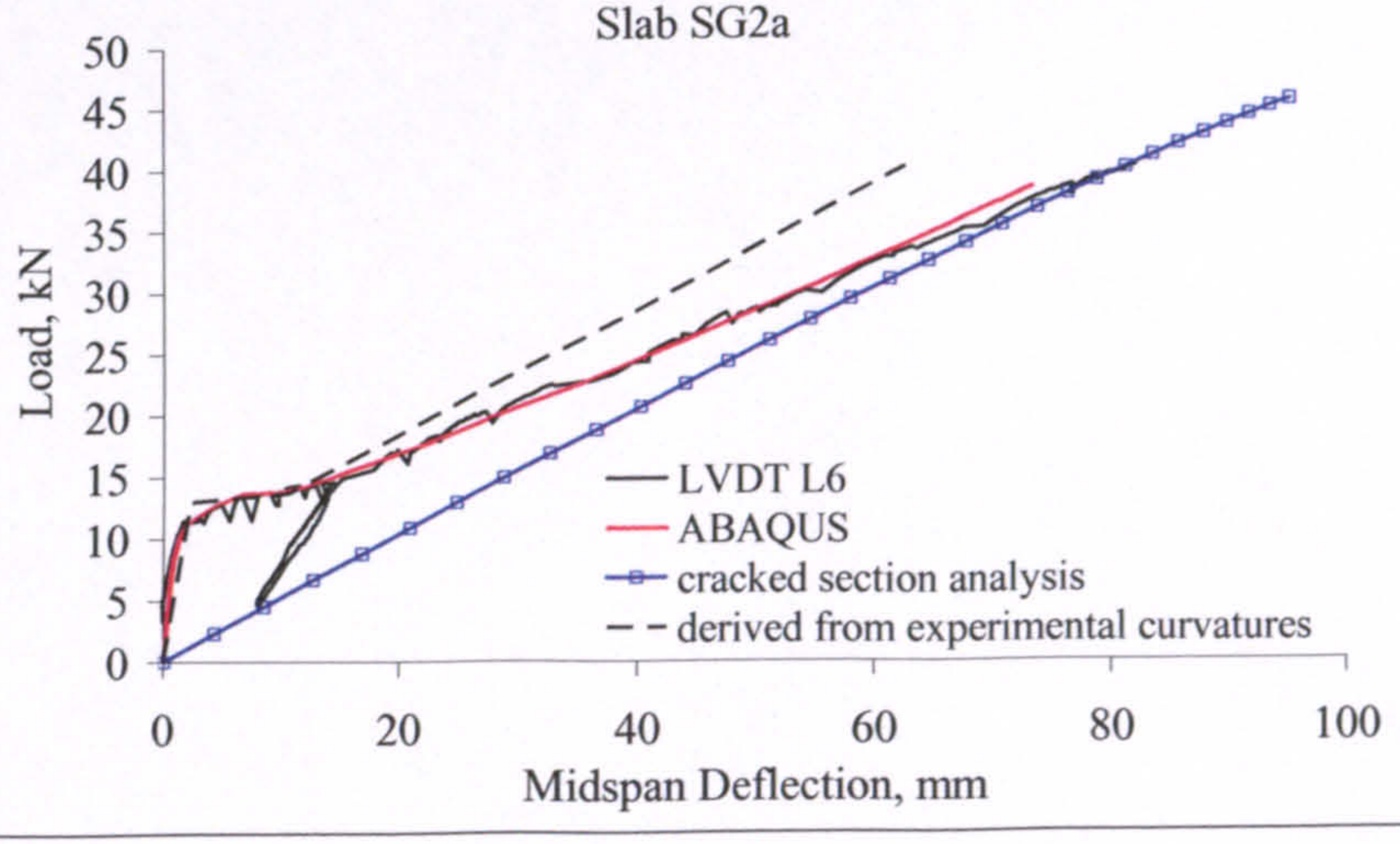
Slab SG2a
Load, kN
50
45
40
35
30
25
20
15
10
5
0
LVDT L6
ABAQUS
cracked section analysis
derived from experimental curvatures
0
20
40
60
80
100
Midspan Deflection, mm

SLAB SG2a

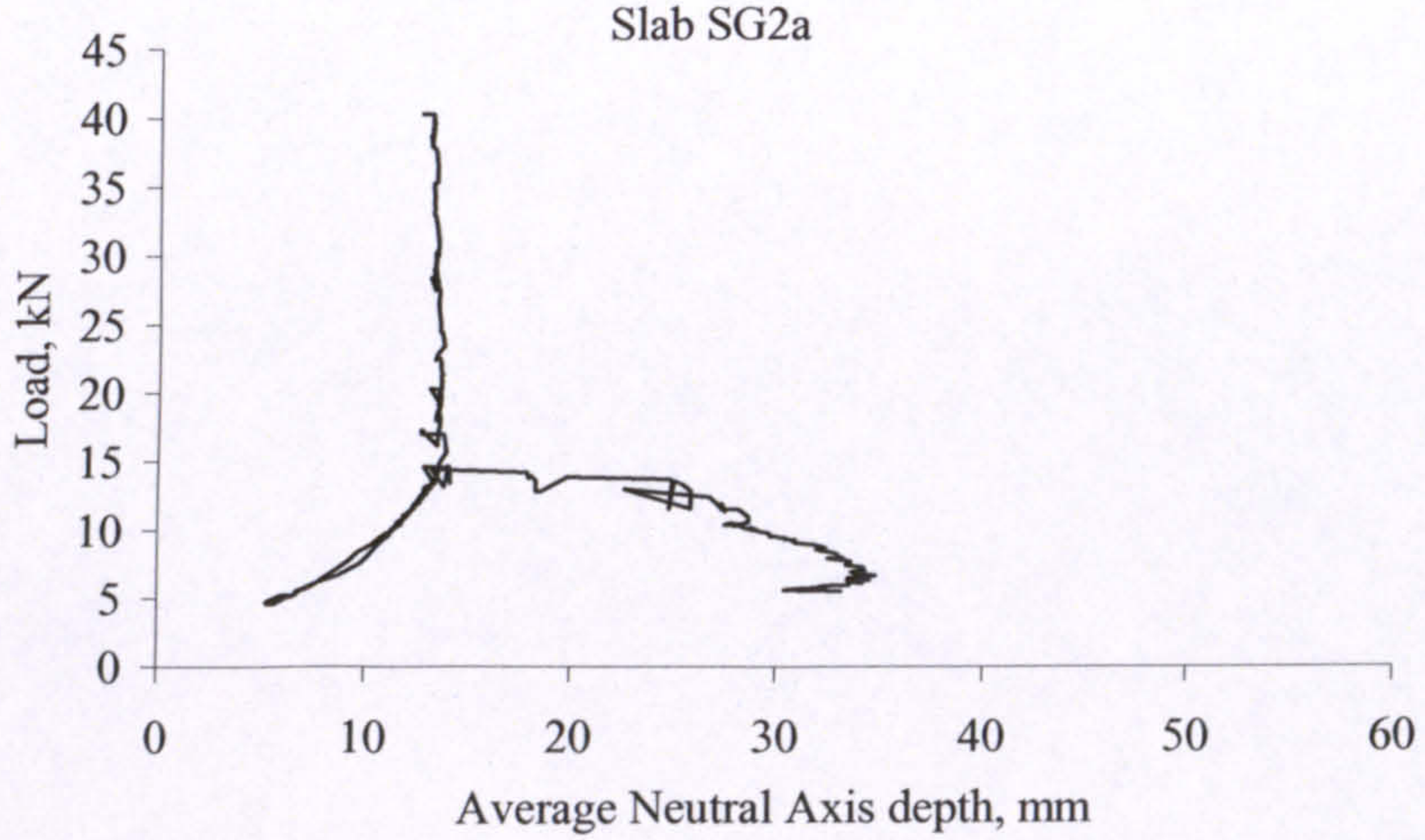
Slab SG2a
Load, kN
0
5
10
15
20
25
30
35
40
45
0
10
20
30
40
50
60
Average Neutral Axis depth, mm

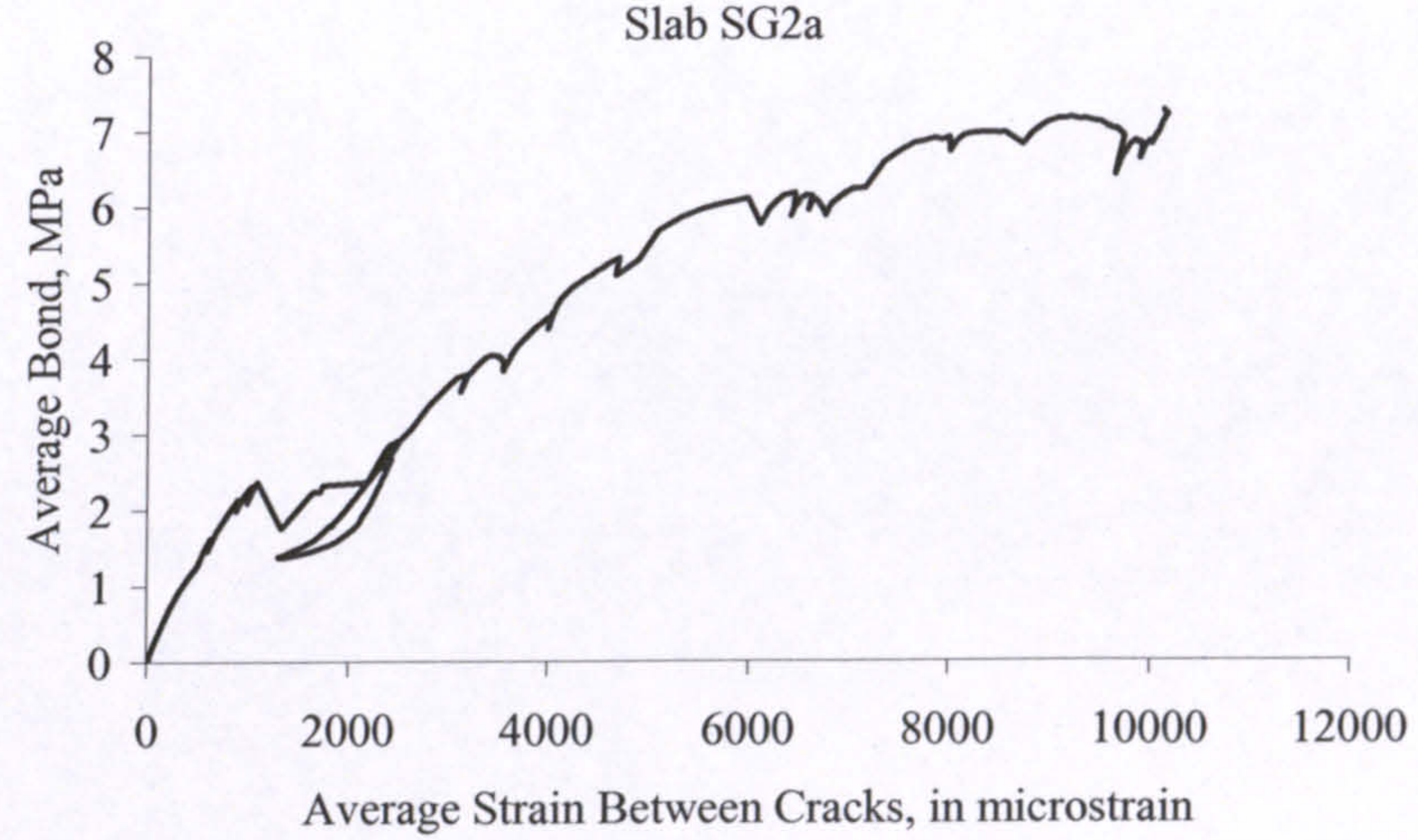
Slab SG2a
Average Bond, MPa
0
1
2
3
4
5
6
7
8
0
2000
4000
6000
8000
10000
12000
Average Strain Between Cracks, in microstrain

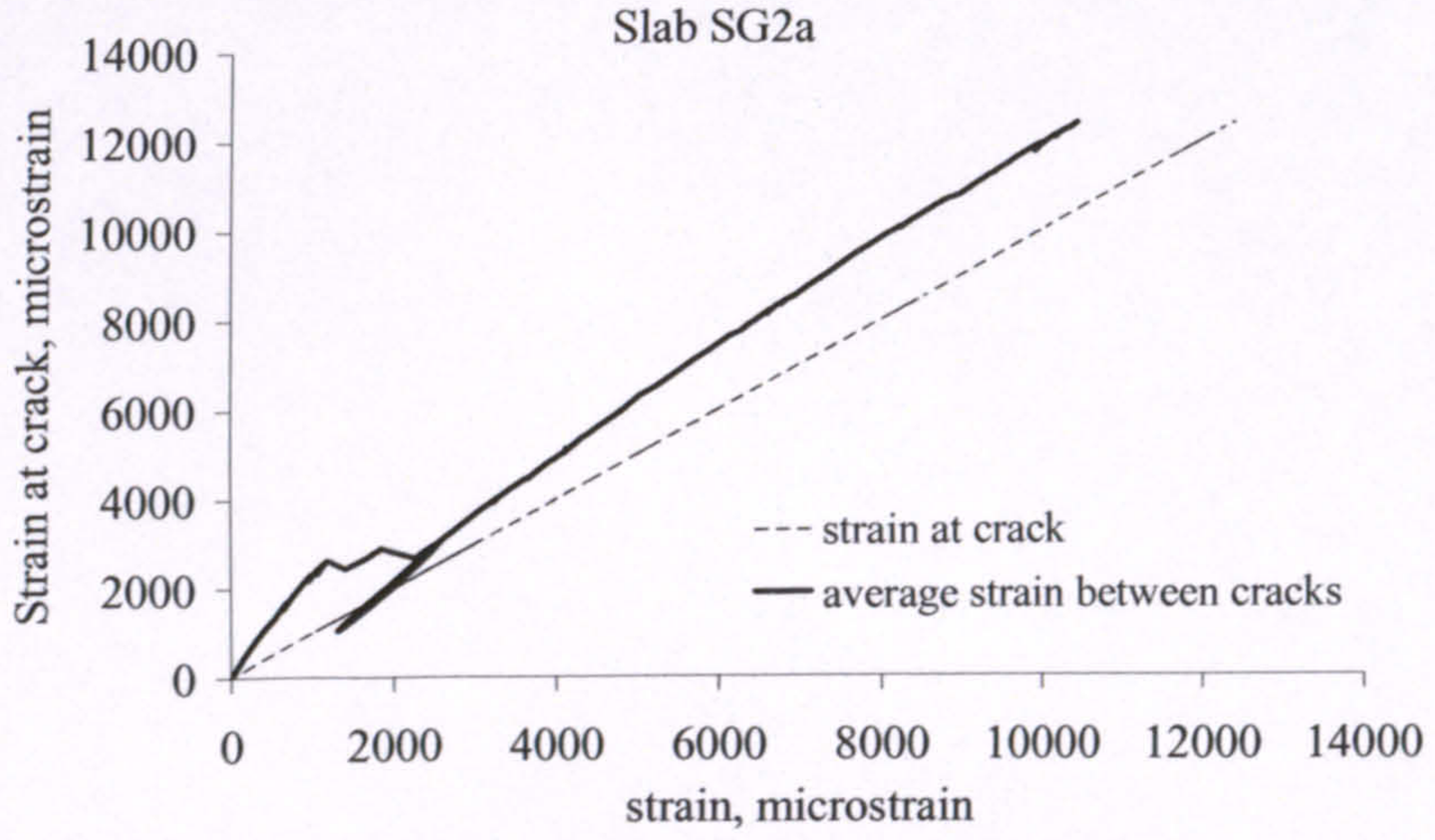
Slab SG2a
Strain at crack, microstrain
0
2000
4000
6000
8000
10000
12000
14000
strain at crack
average strain between cracks
0
2000
4000
6000
8000
10000
12000
14000
strain, microstrain

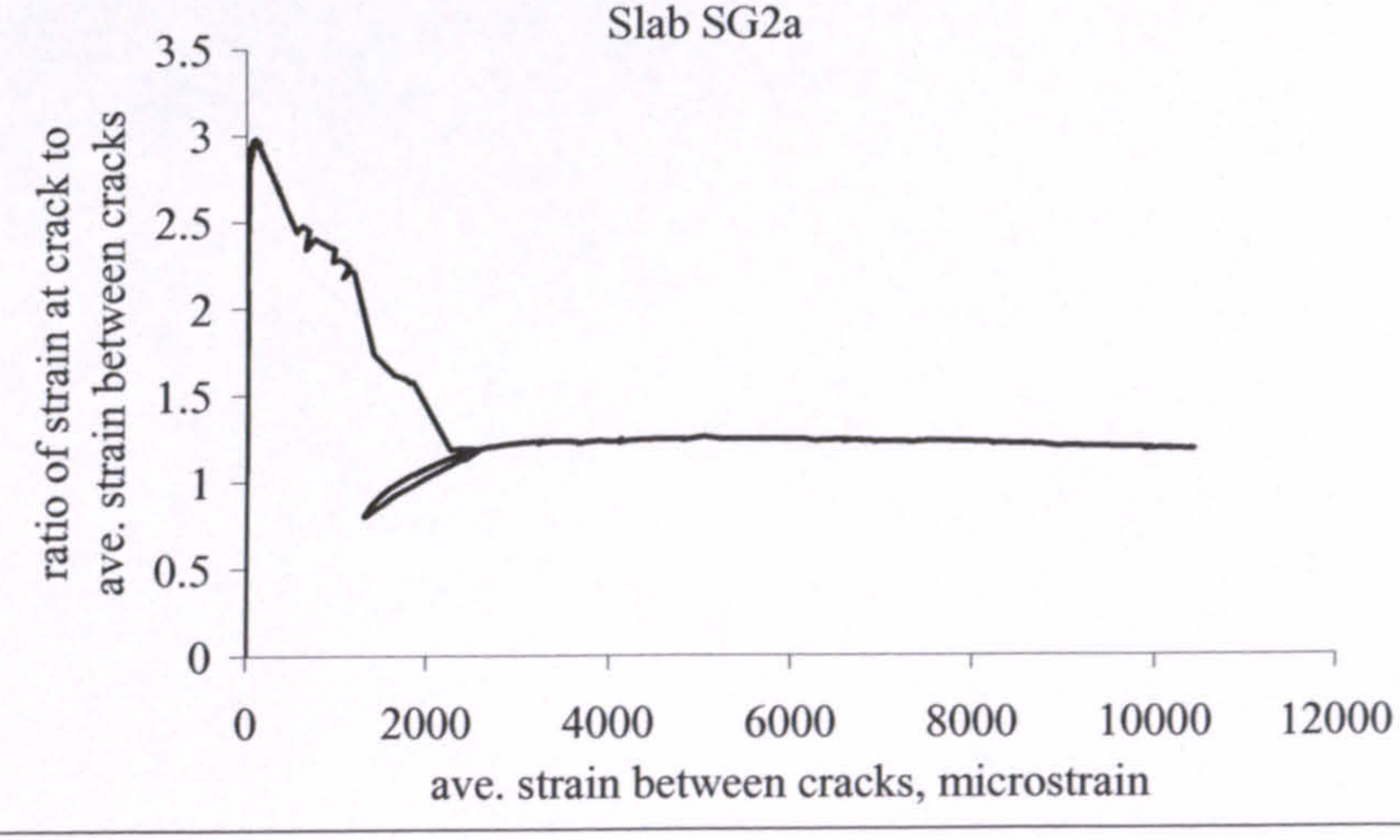
Slab SG2a
ratio of strain at crack to ave. strain between cracks
0
0.5
1
1.5
2
2.5
3
3.5
0
2000
4000
6000
8000
10000
12000
ave. strain between cracks, microstrain

SLAB SG2a

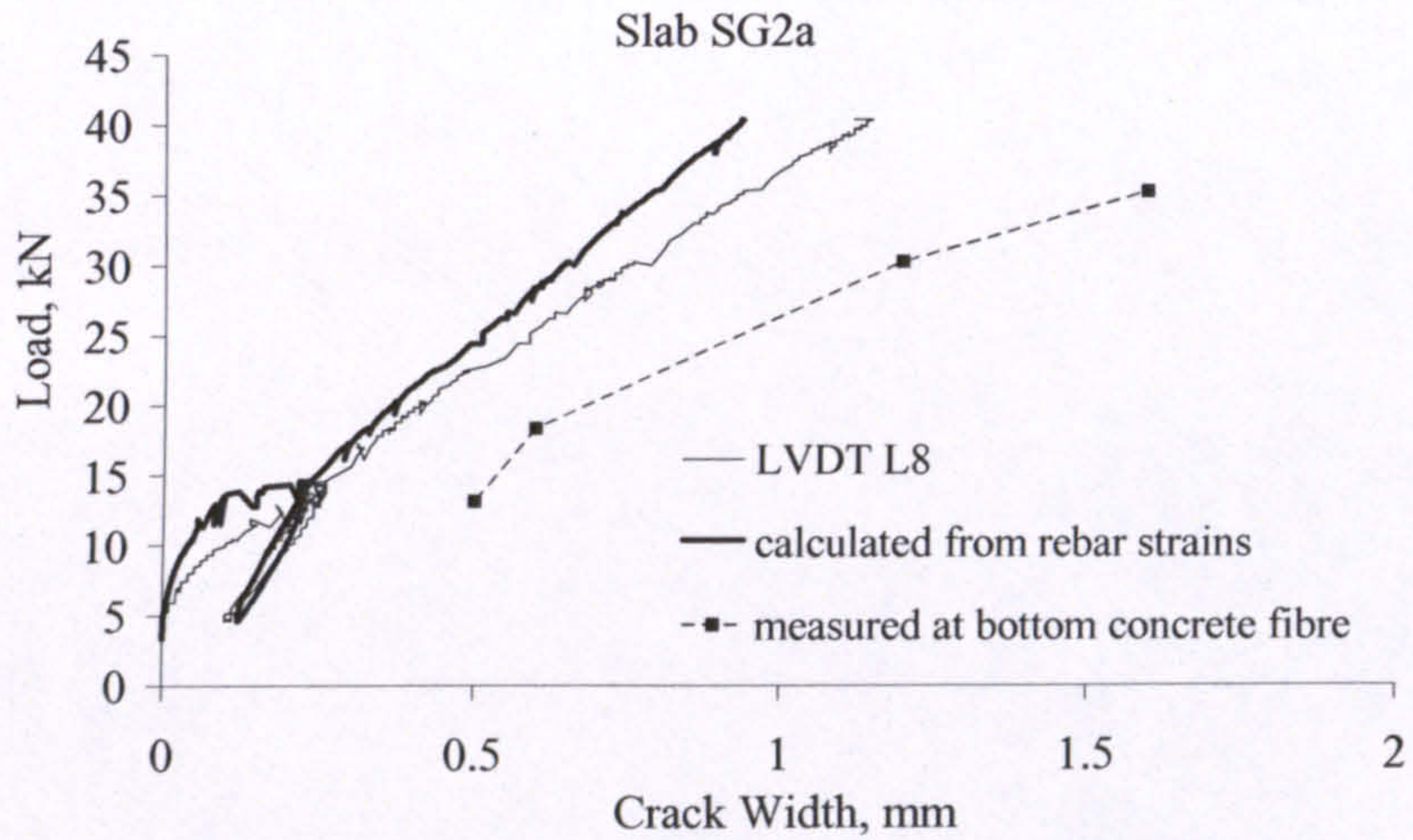

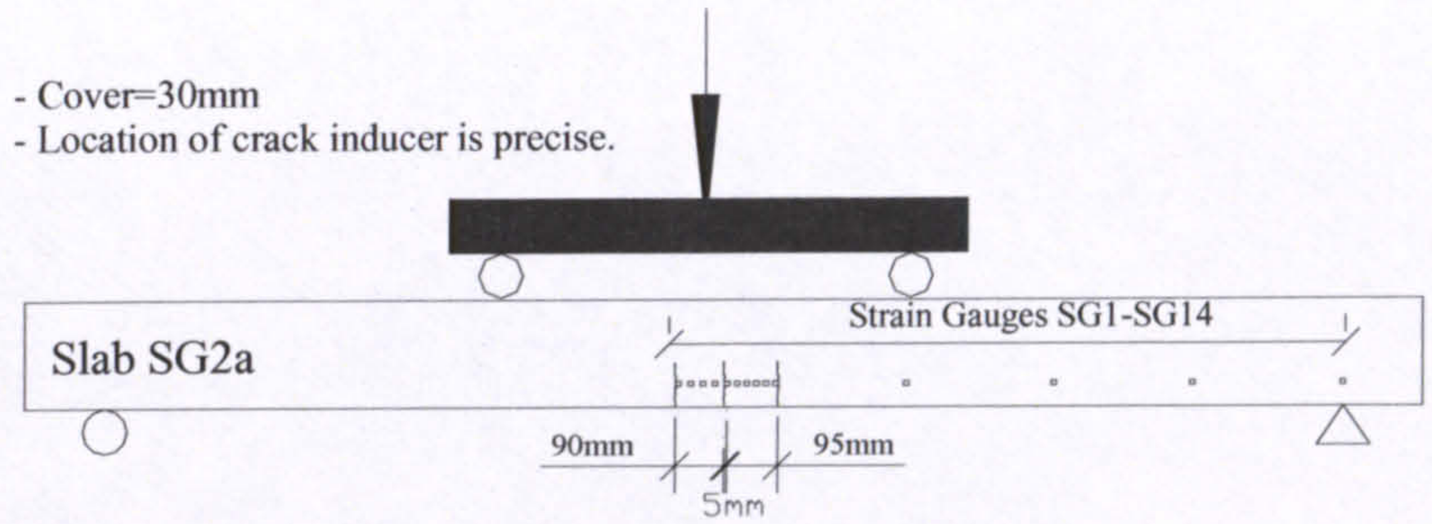

Cracks around Centre

Failure by rupture of rebars.

SLAB SG2b

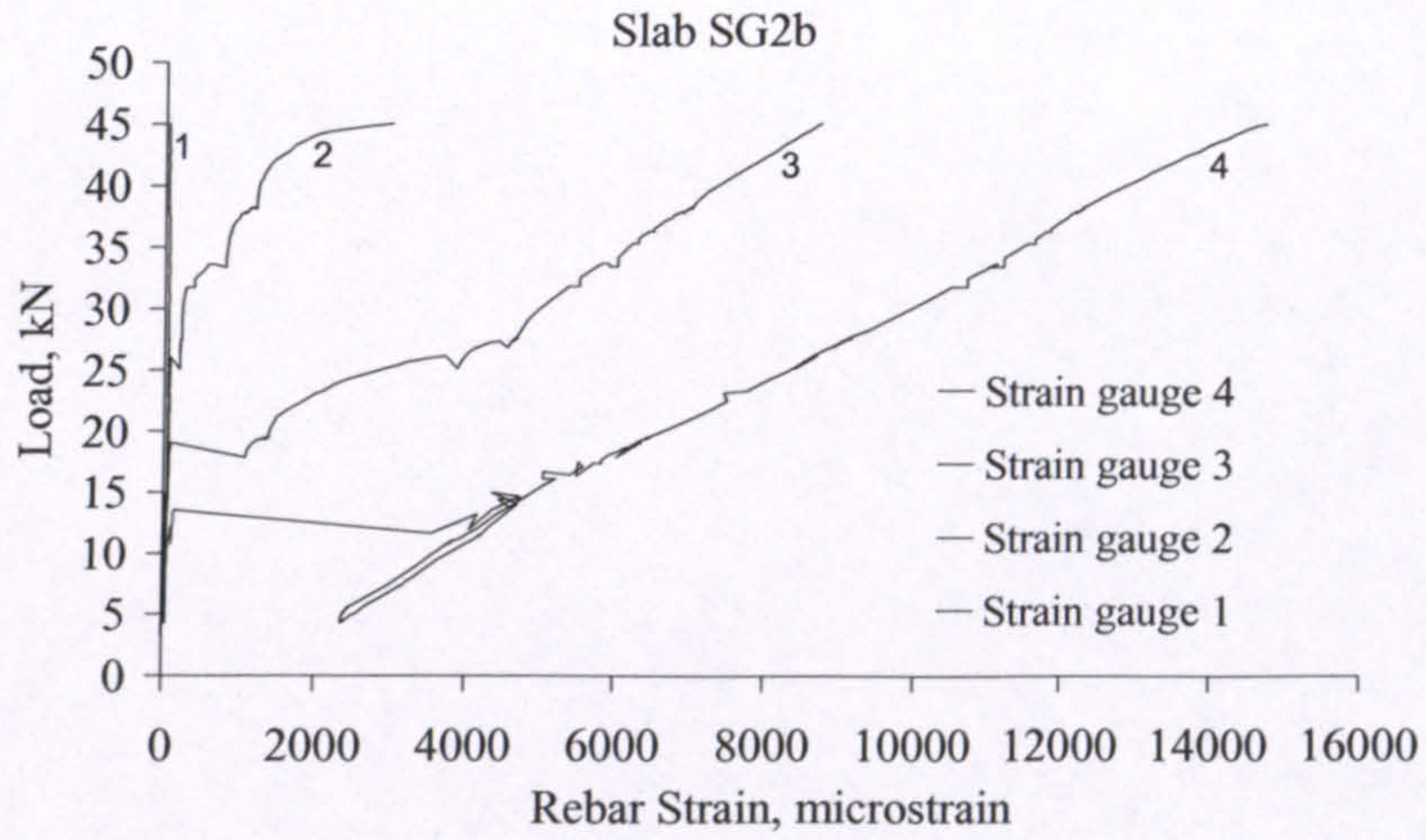
Slab SG2b
Load, kN
Rebar Strain, microstrain
1
2
3
4
Strain gauge 4
Strain gauge 3
Strain gauge 2
Strain gauge 1

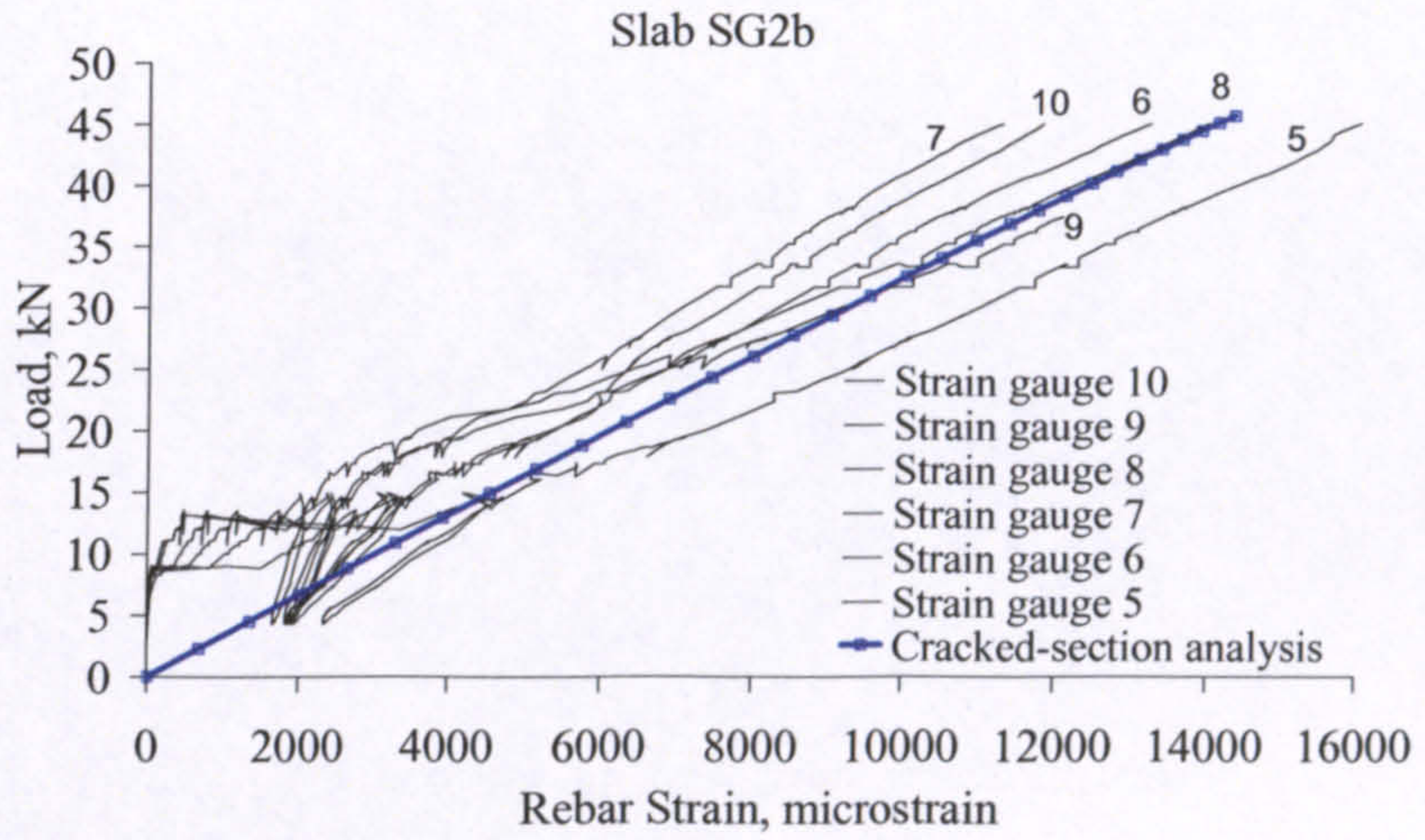
Slab SG2b
Load, kN
Rebar Strain, microstrain
5
6
7
8
9
10
Strain gauge 10
Strain gauge 9
Strain gauge 8
Strain gauge 7
Strain gauge 6
Strain gauge 5
Cracked-section analysis

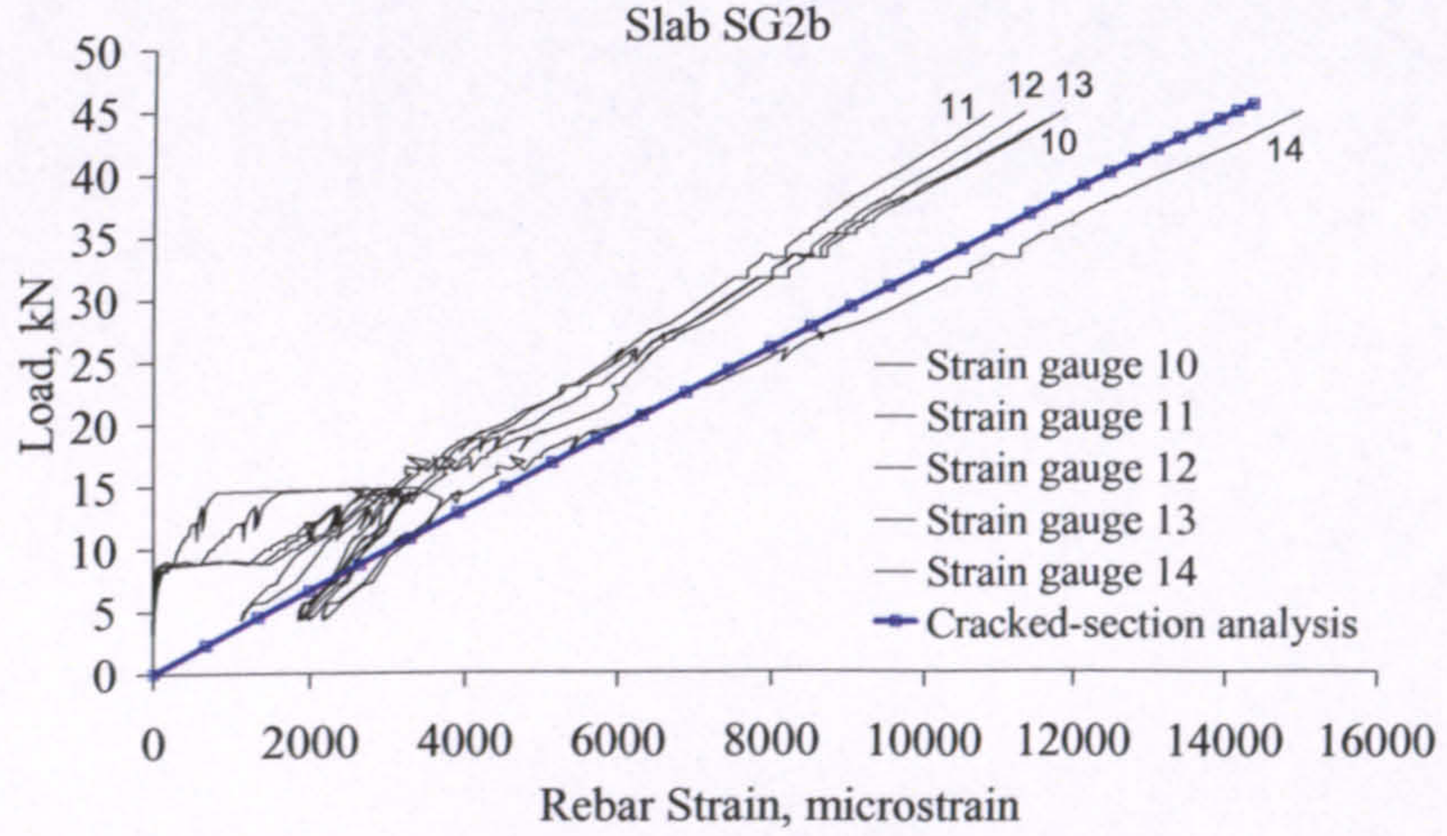
Slab SG2b
Load, kN
Rebar Strain, microstrain
10
11
12
13
14
Strain gauge 10
Strain gauge 11
Strain gauge 12
Strain gauge 13
Strain gauge 14
Cracked-section analysis

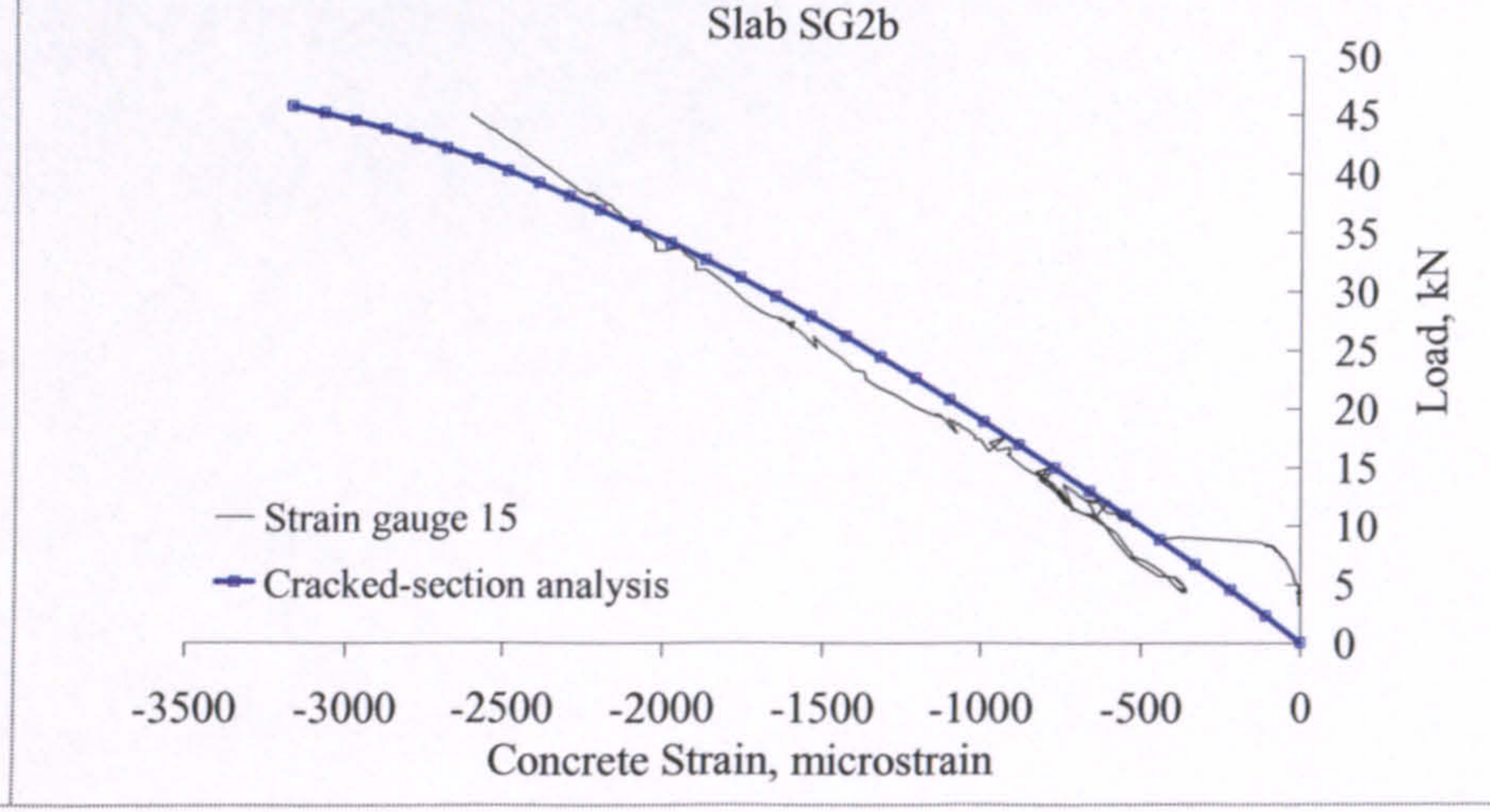
Slab SG2b
Load, kN
Concrete Strain, microstrain
Strain gauge 15
Cracked-section analysis

SLAB SG2b

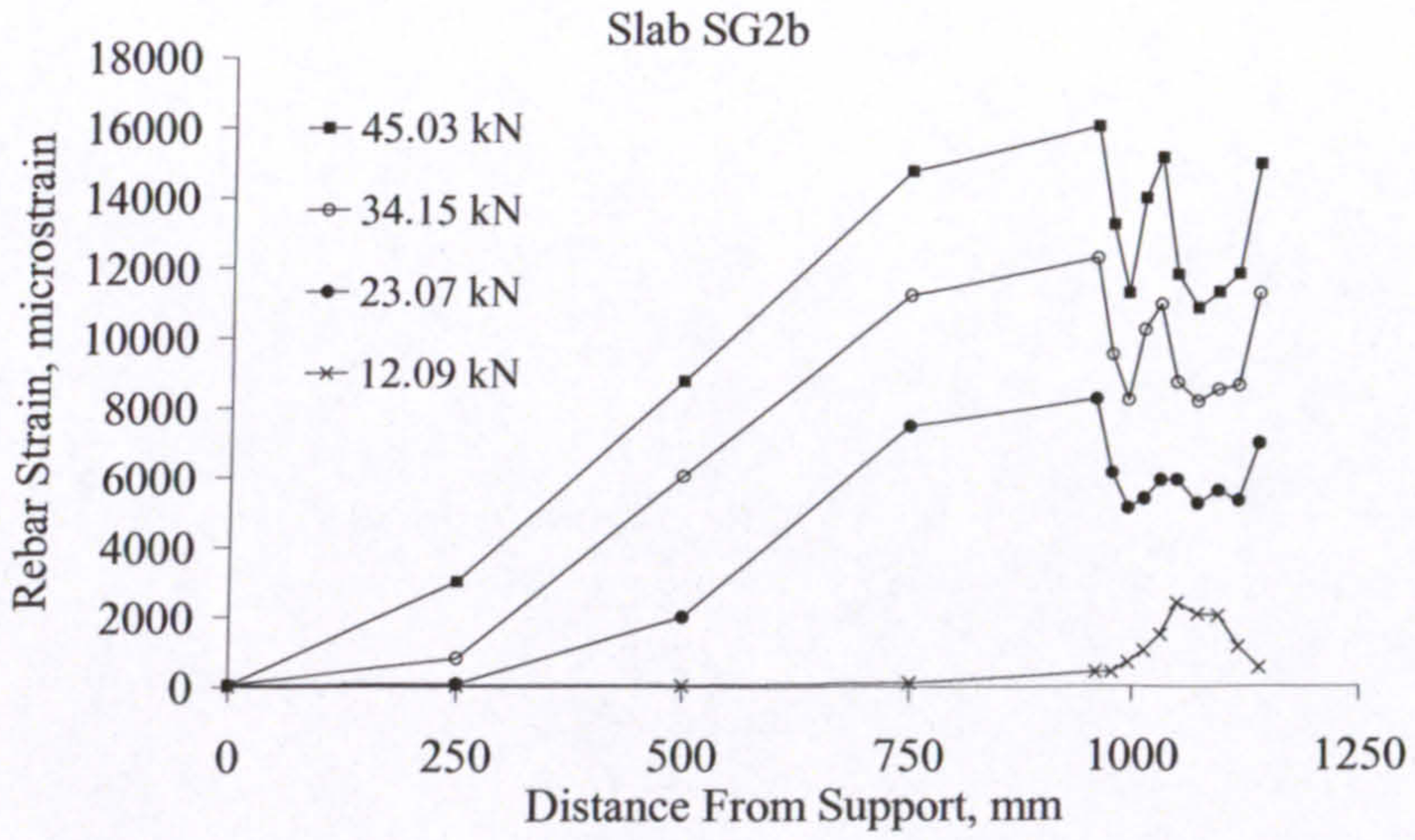
Slab SG2b
Rebar Strain, microstrain
18000
16000
14000
12000
10000
8000
6000
4000
2000
0
45.03 kN
34.15 kN
23.07 kN
12.09 kN
0
250
500
750
1000
1250
Distance From Support, mm

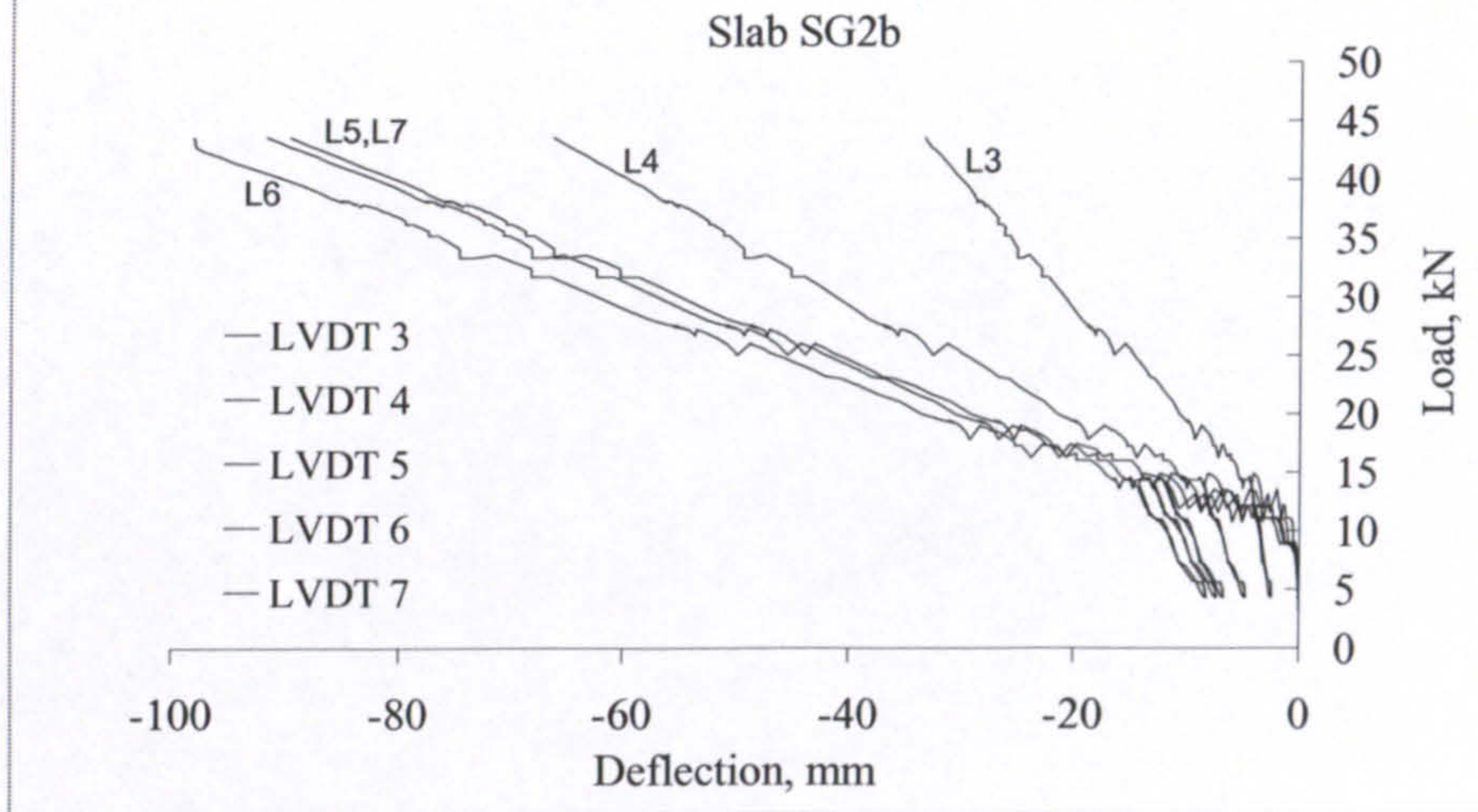
Slab SG2b
L5,L7
L4
L3
L6
LVDT 3
LVDT 4
LVDT 5
LVDT 6
LVDT 7
50
45
40
35
30
25
20
15
10
5
0
Load, kN
-100
-80
-60
-40
-20
0
Deflection, mm

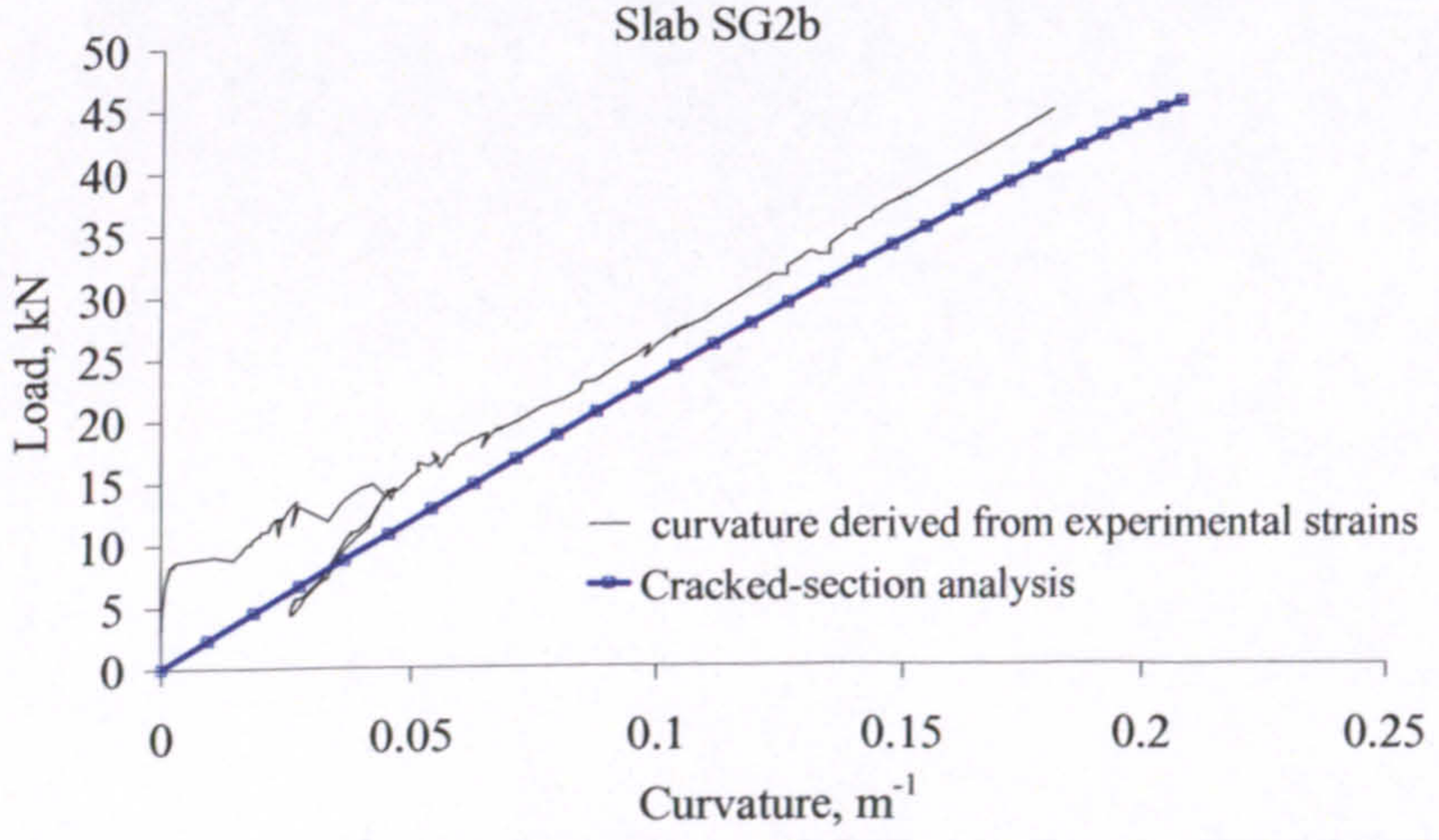
Slab SG2b
Load, kN
50
45
40
35
30
25
20
15
10
5
0
curvature derived from experimental strains
Cracked-section analysis
0
0.05
0.1
0.15
0.2
0.25
Curvature, m-1

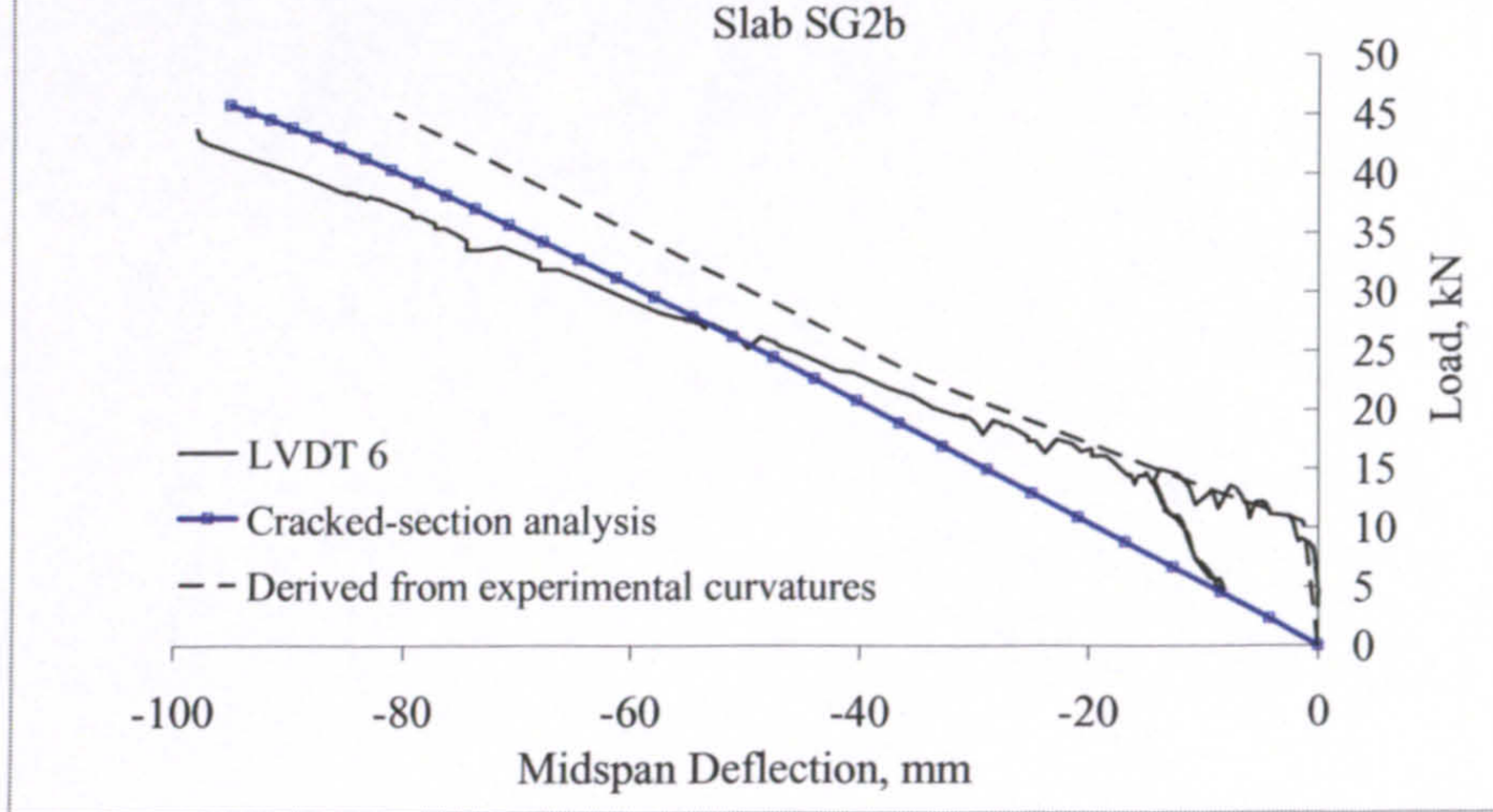
Slab SG2b
50
45
40
35
30
25
20
15
10
5
0
Load, kN
LVDT 6
Cracked-section analysis
Derived from experimental curvatures
-100
-80
-60
-40
-20
0
Midspan Deflection, mm

SLAB SG2b

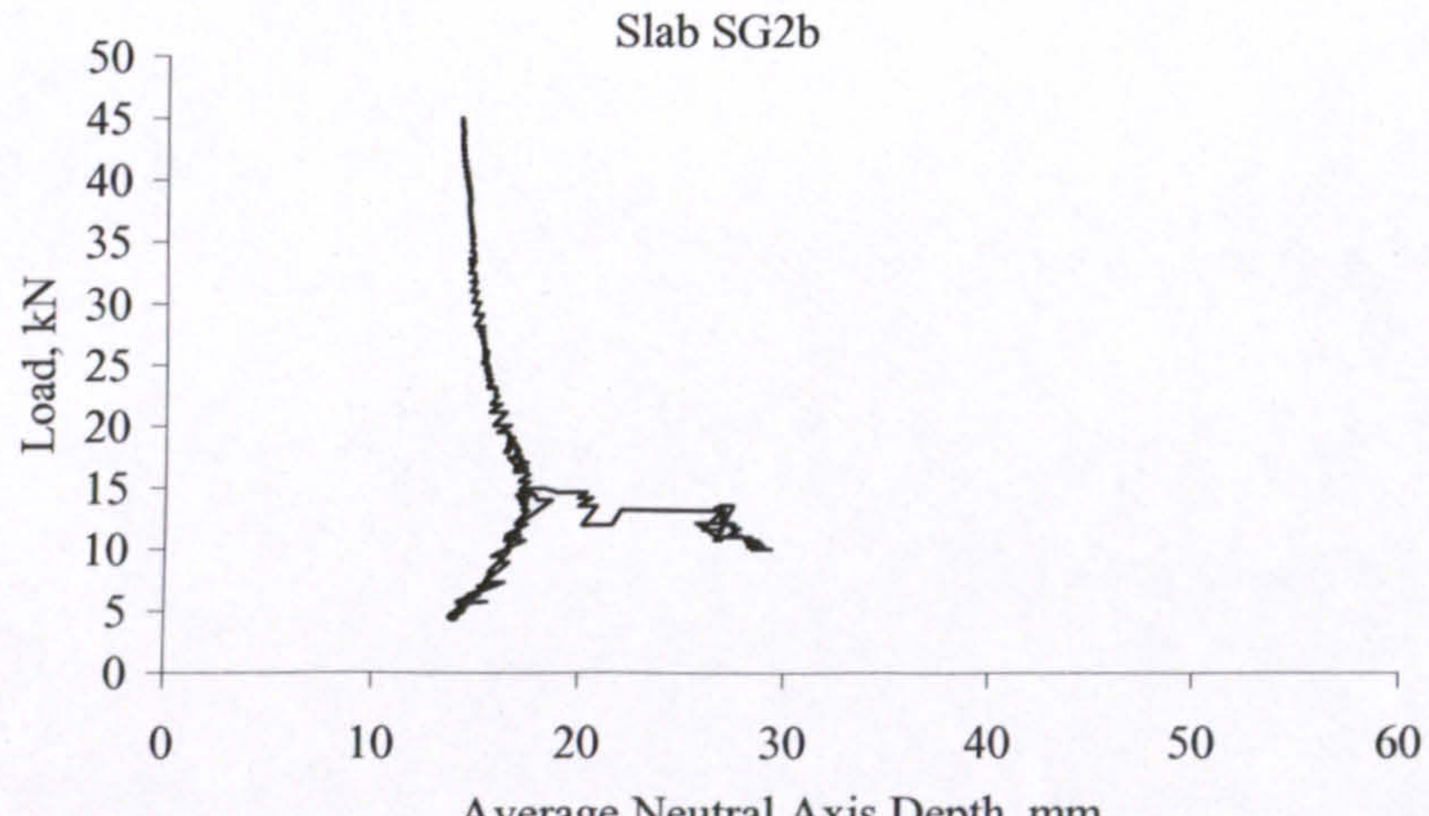
Slab SG2b
Load, kN
0
5
10
15
20
25
30
35
40
45
50
0
10
20
30
40
50
60
Average Neutral Axis Depth, mm

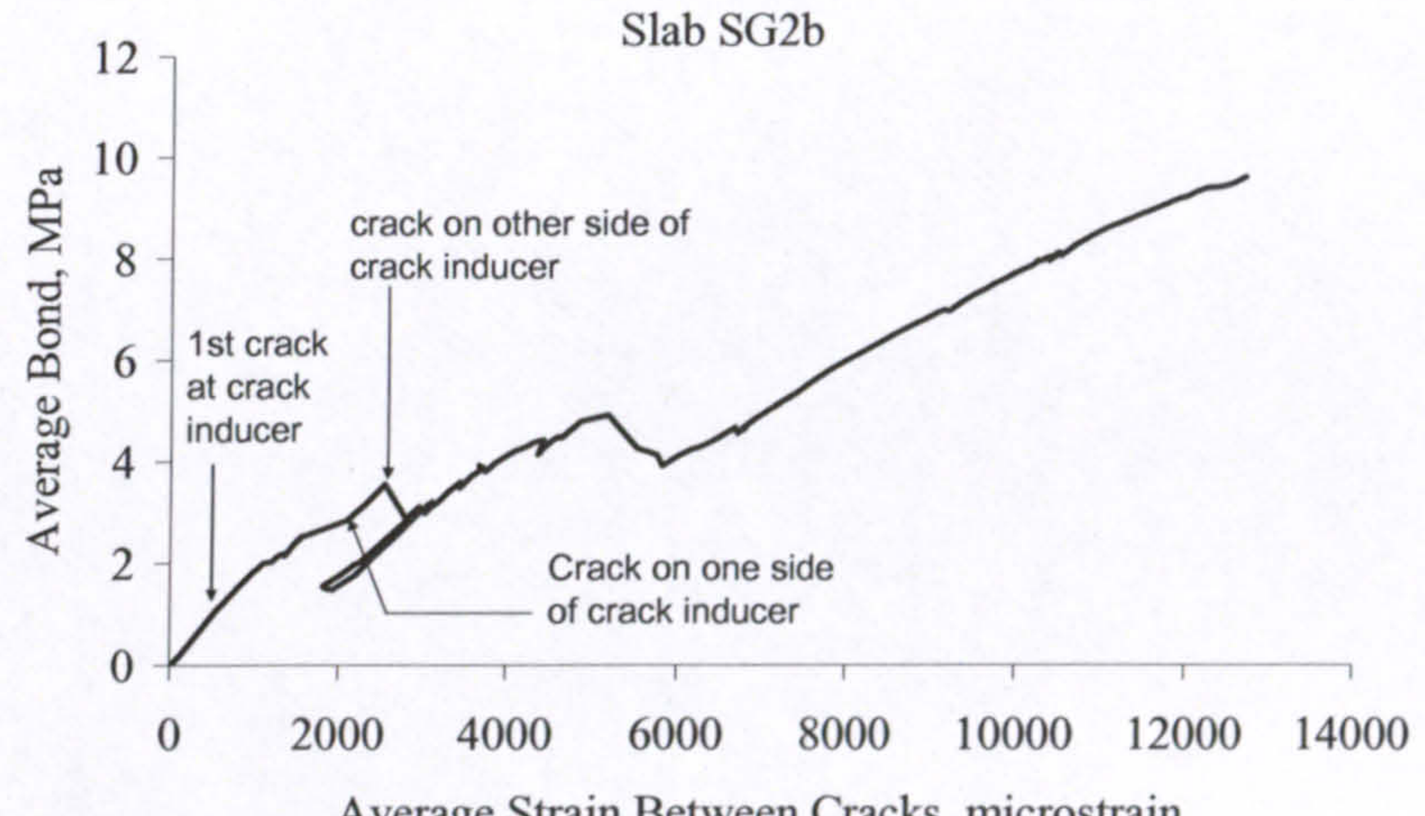
Slab SG2b
Average Bond, MPa
0
2
4
6
8
10
12
crack on other side of crack inducer
1st crack at crack inducer
Crack on one side of crack inducer
0
2000
4000
6000
8000
10000
12000
14000
Average Strain Between Cracks, microstrain

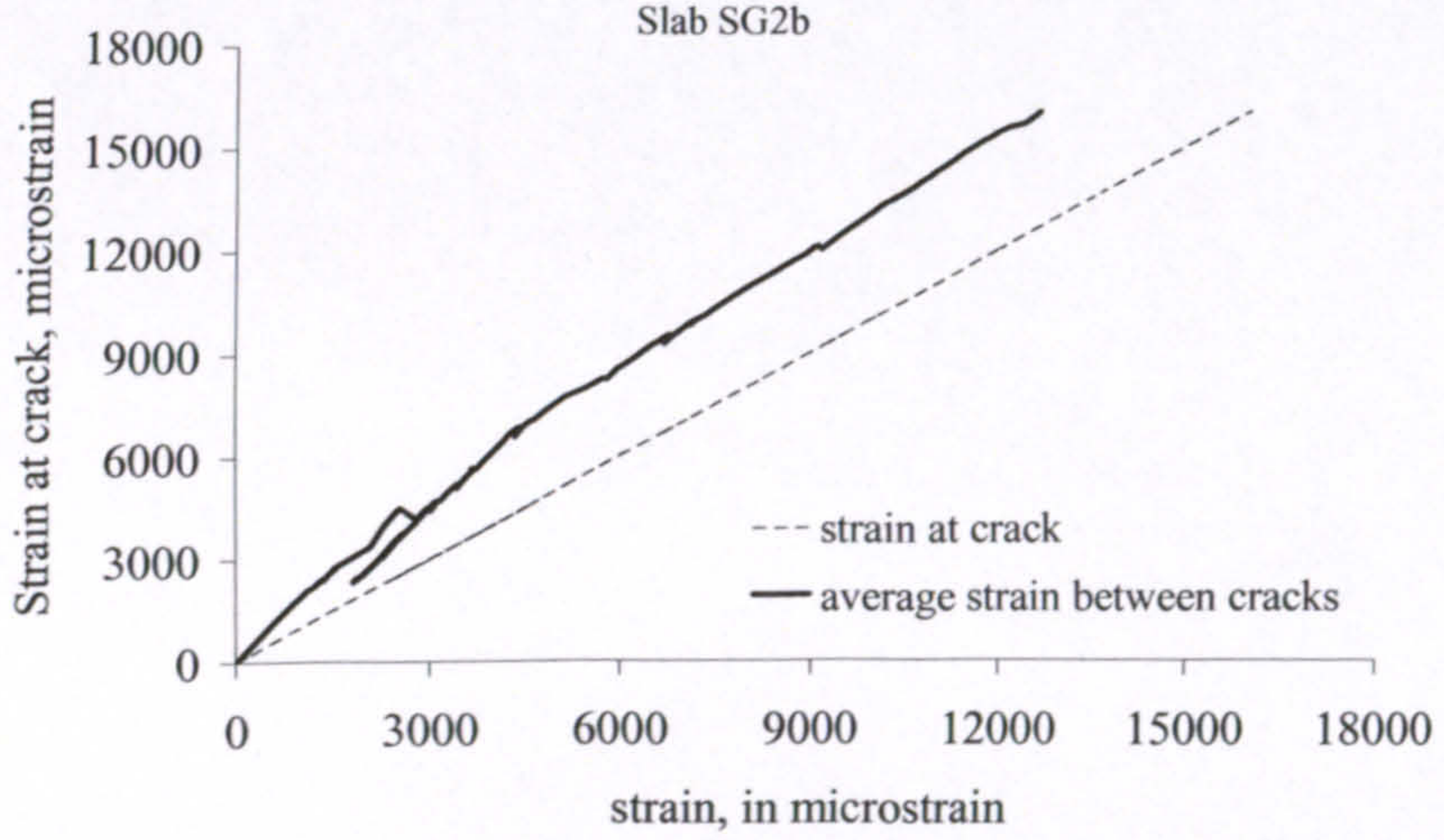
Slab SG2b
Strain at crack, microstrain
0
3000
6000
9000
12000
15000
18000
strain at crack
average strain between cracks
0
3000
6000
9000
12000
15000
18000
strain, in microstrain

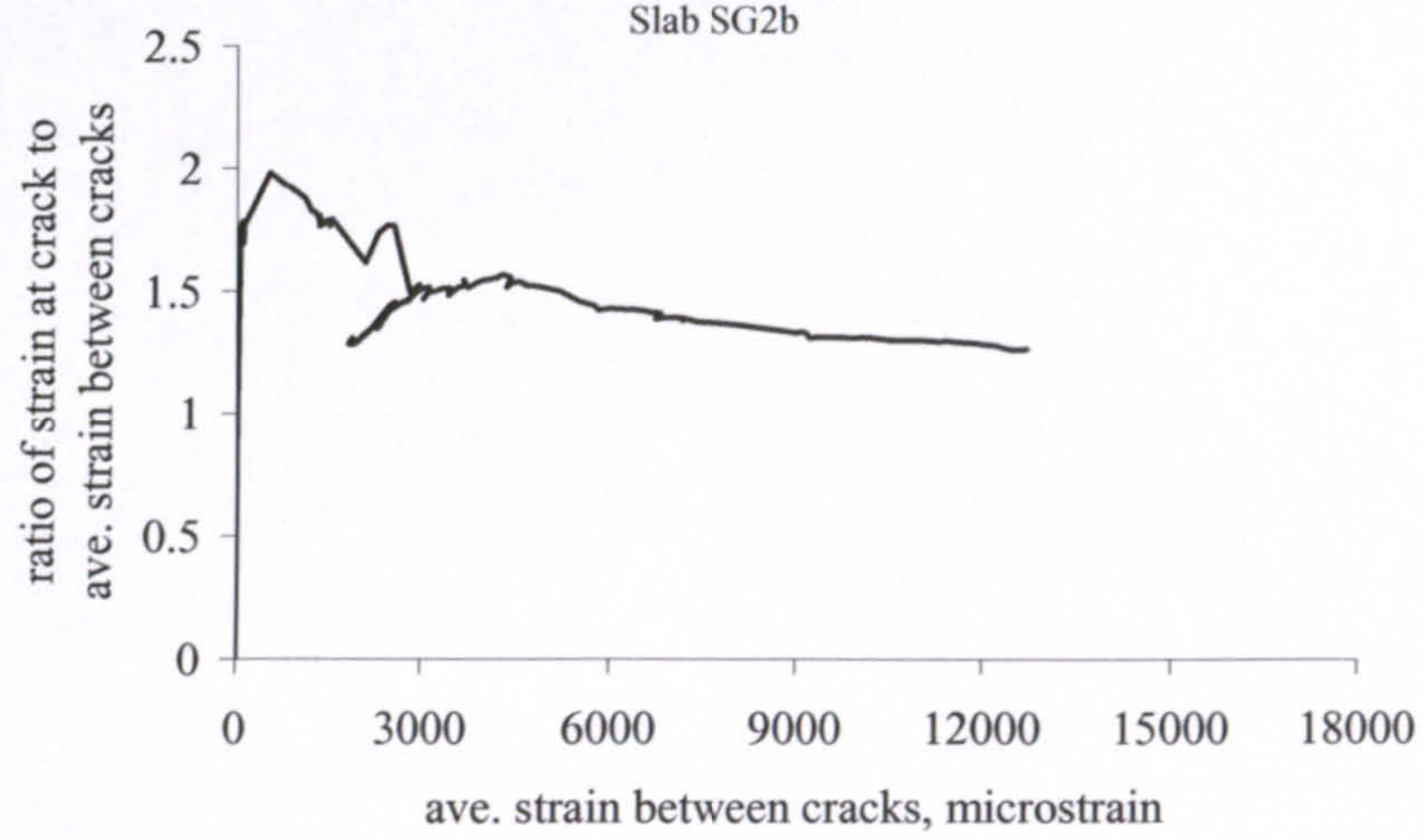
Slab SG2b
ratio of strain at crack to ave. strain between cracks
0
0.5
1
1.5
2
2.5
0
3000
6000
9000
12000
15000
18000
ave. strain between cracks, microstrain

SLAB SG2b

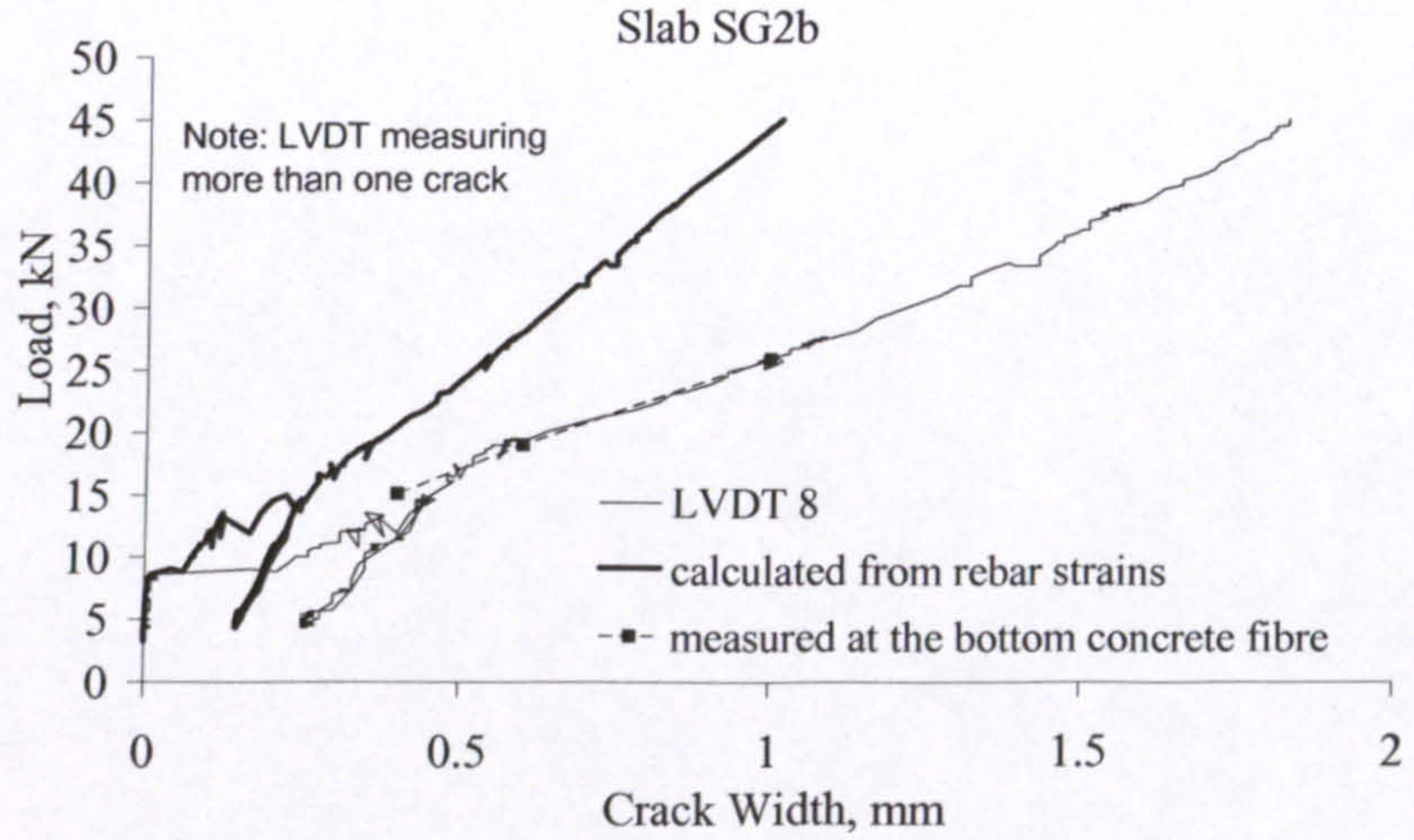

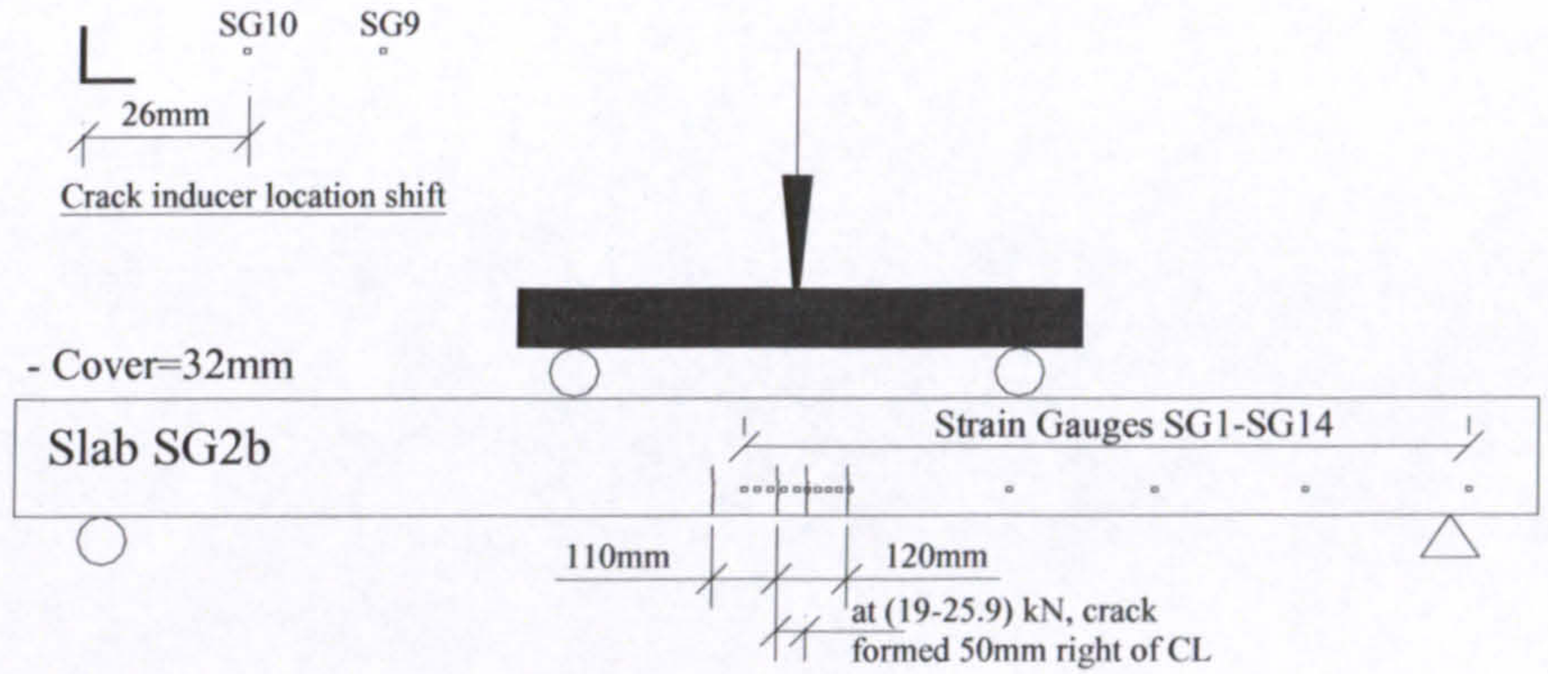

Cracks around Centre

Almost Balanced Failure.

SLAB SG3a

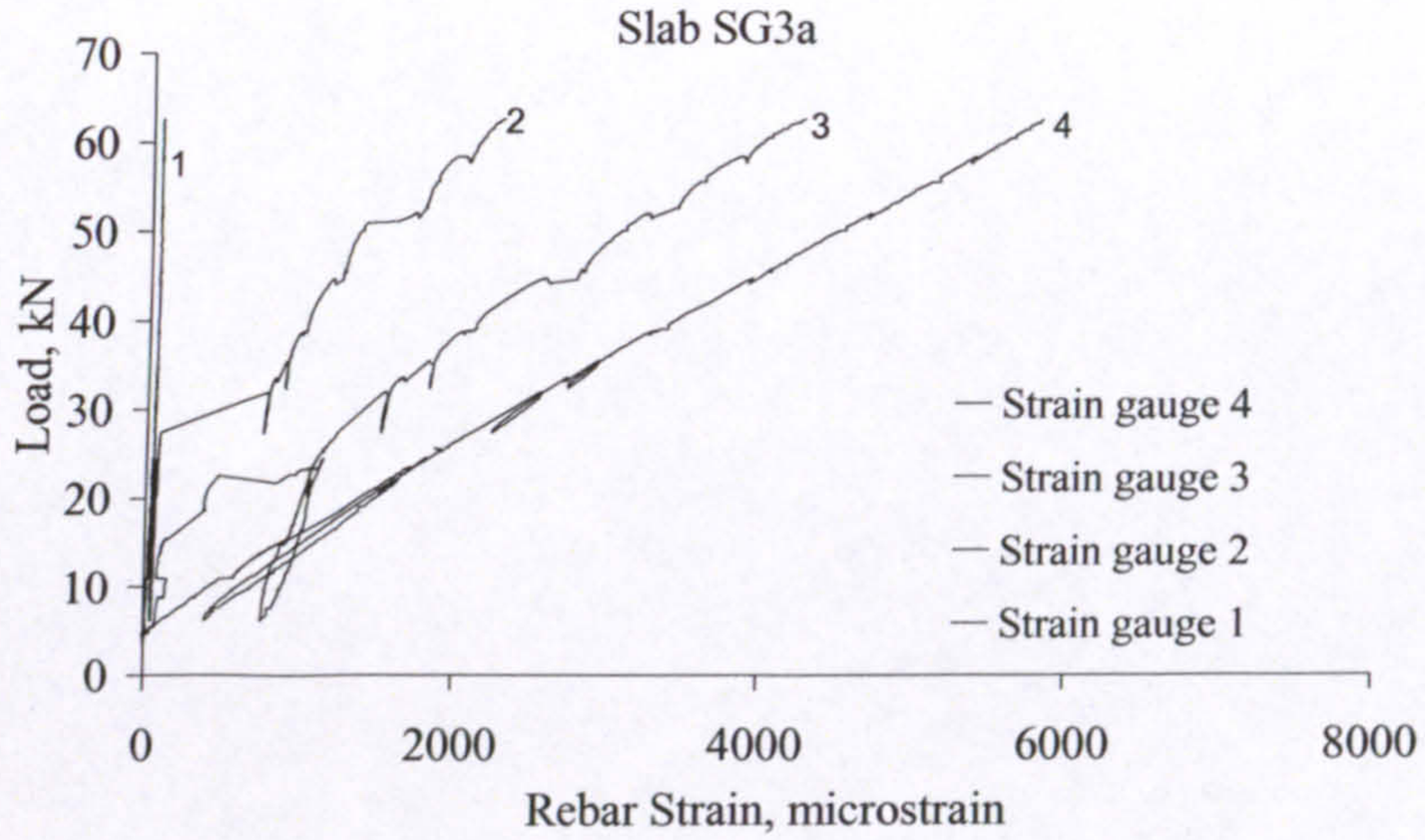
Slab SG3a
Load, kN
Rebar Strain, microstrain
Strain gauge 4
Strain gauge 3
Strain gauge 2
Strain gauge 1

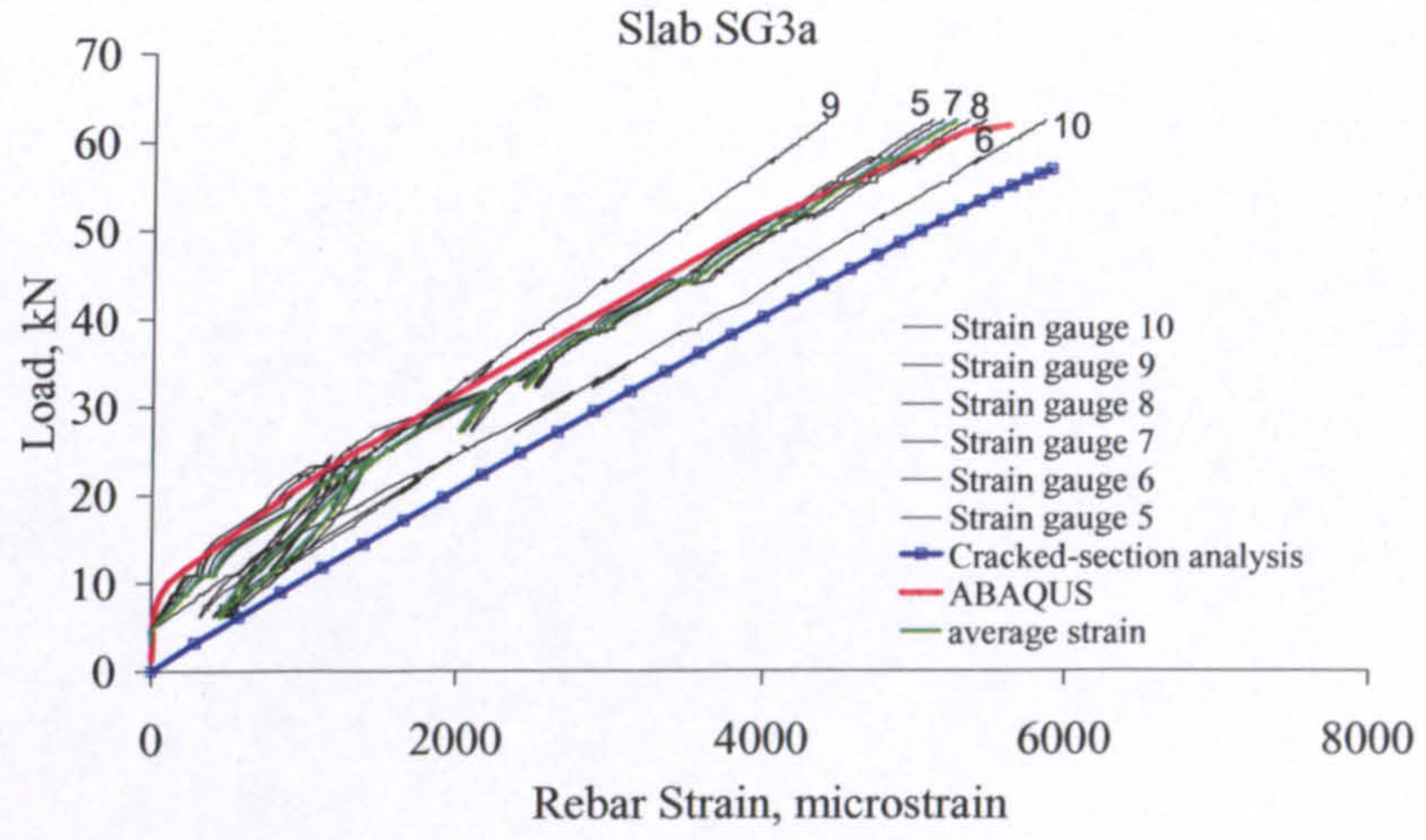
Slab SG3a
Load, kN
Rebar Strain, microstrain
Strain gauge 10
Strain gauge 9
Strain gauge 8
Strain gauge 7
Strain gauge 6
Strain gauge 5
Cracked-section analysis
ABAQUS
average strain

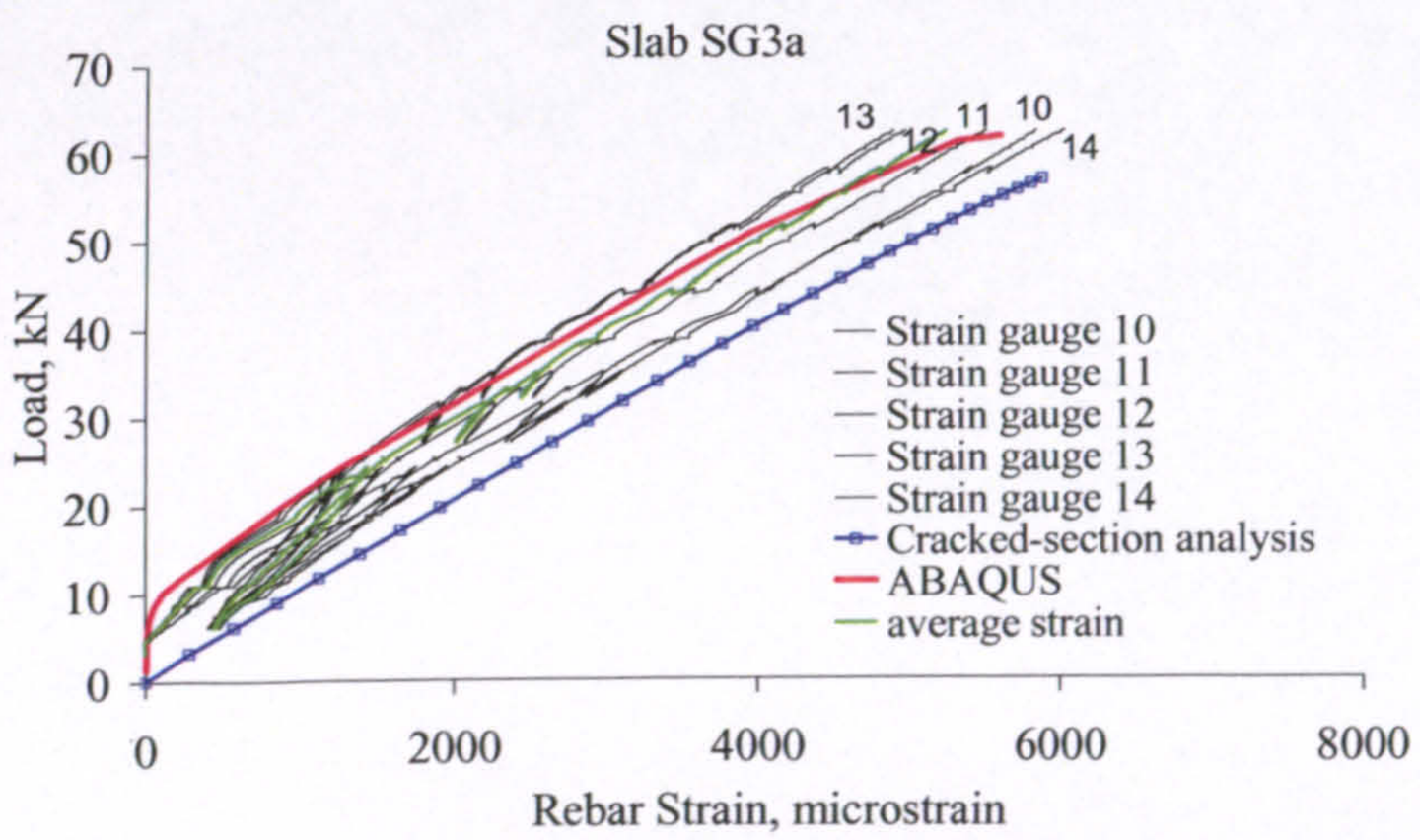
Slab SG3a
Load, kN
Rebar Strain, microstrain
Strain gauge 10
Strain gauge 11
Strain gauge 12
Strain gauge 13
Strain gauge 14
Cracked-section analysis
ABAQUS
average strain

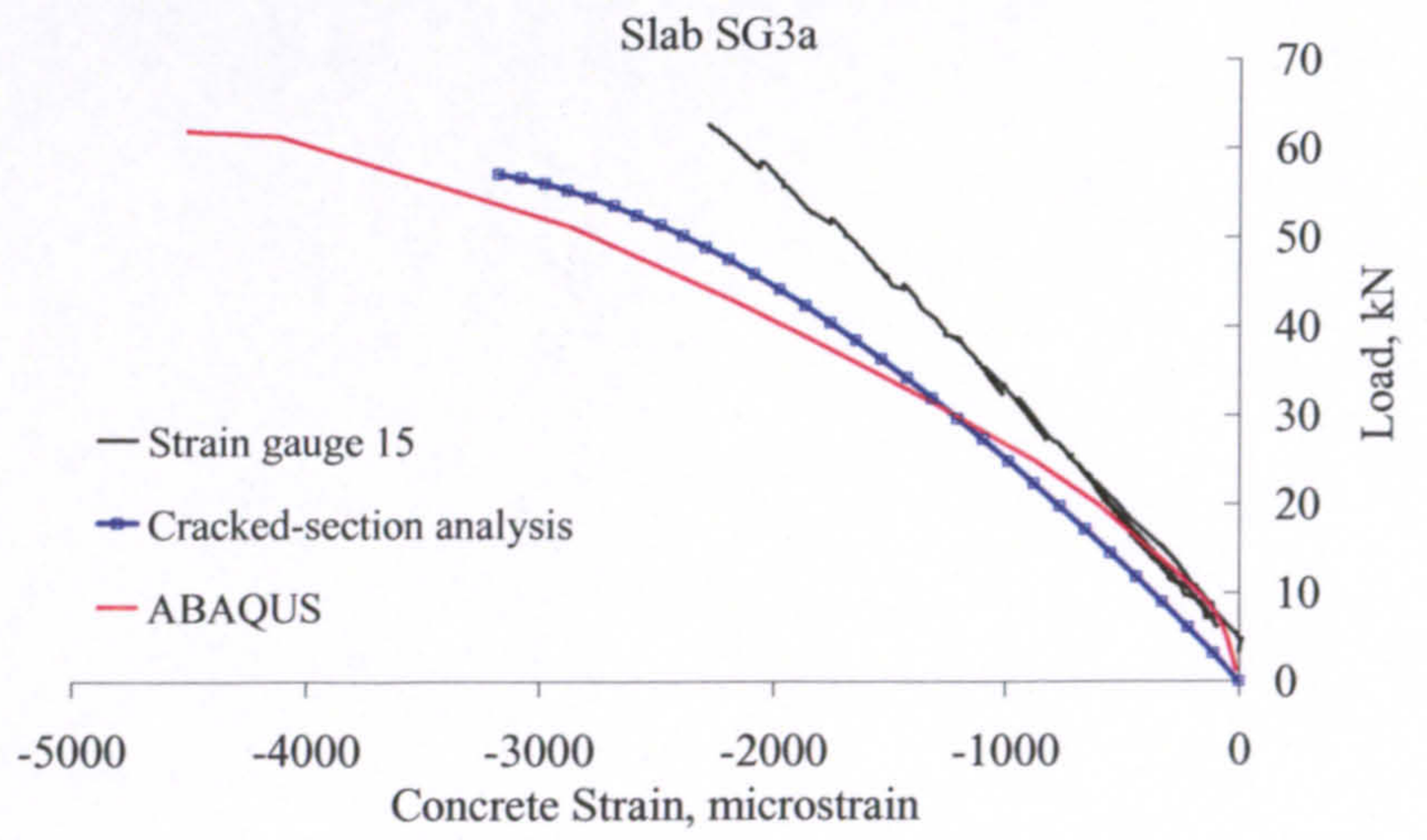
Slab SG3a
Load, kN
Concrete Strain, microstrain
Strain gauge 15
Cracked-section analysis
ABAQUS

SLAB SG3a

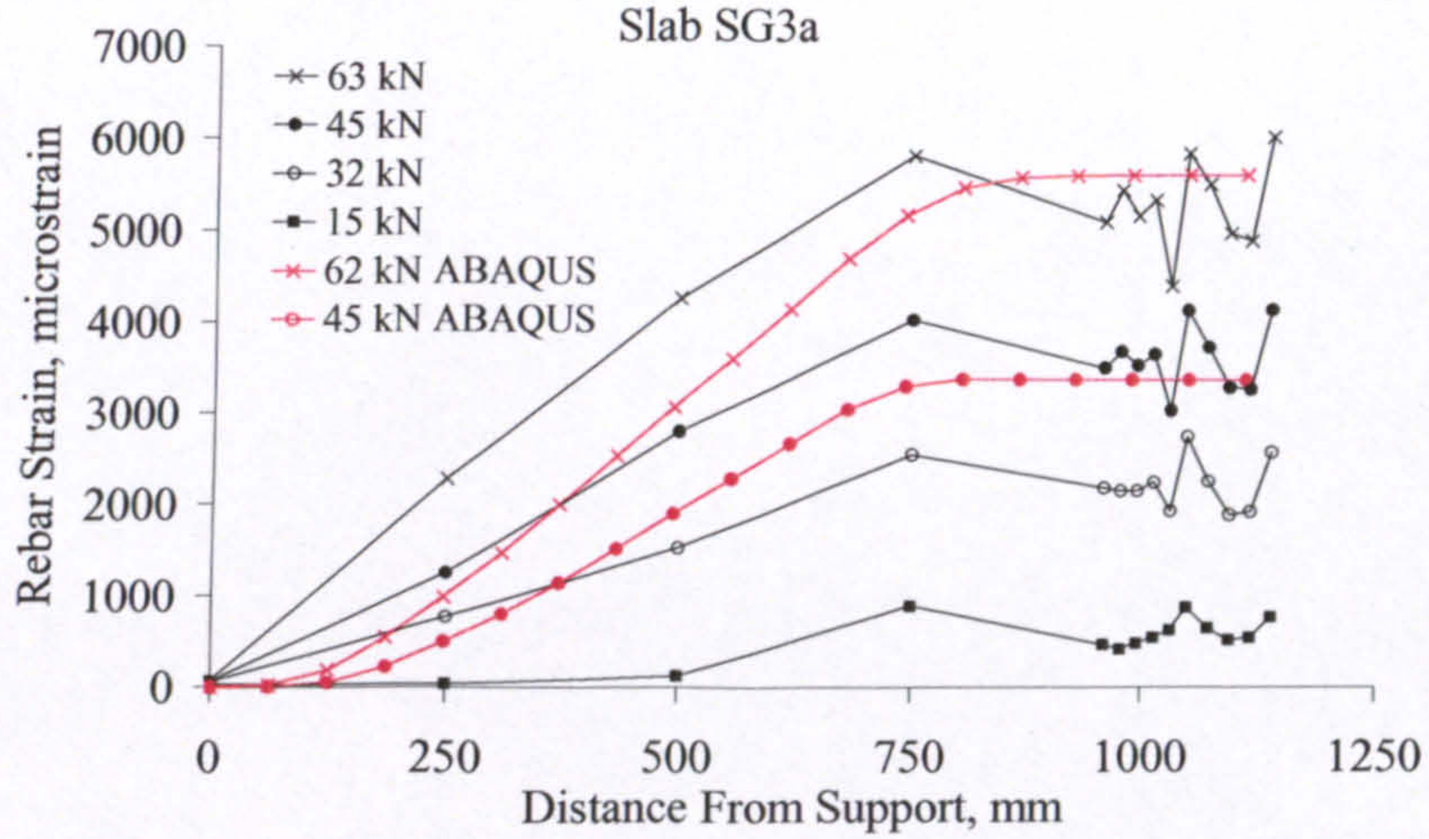
Slab SG3a
Rebar Strain, microstrain
7000
6000
5000
4000
3000
2000
1000
0
63 kN
45 kN
32 kN
15 kN
62 kN ABAQUS
45 kN ABAQUS
0
250
500
750
1000
1250
Distance From Support, mm

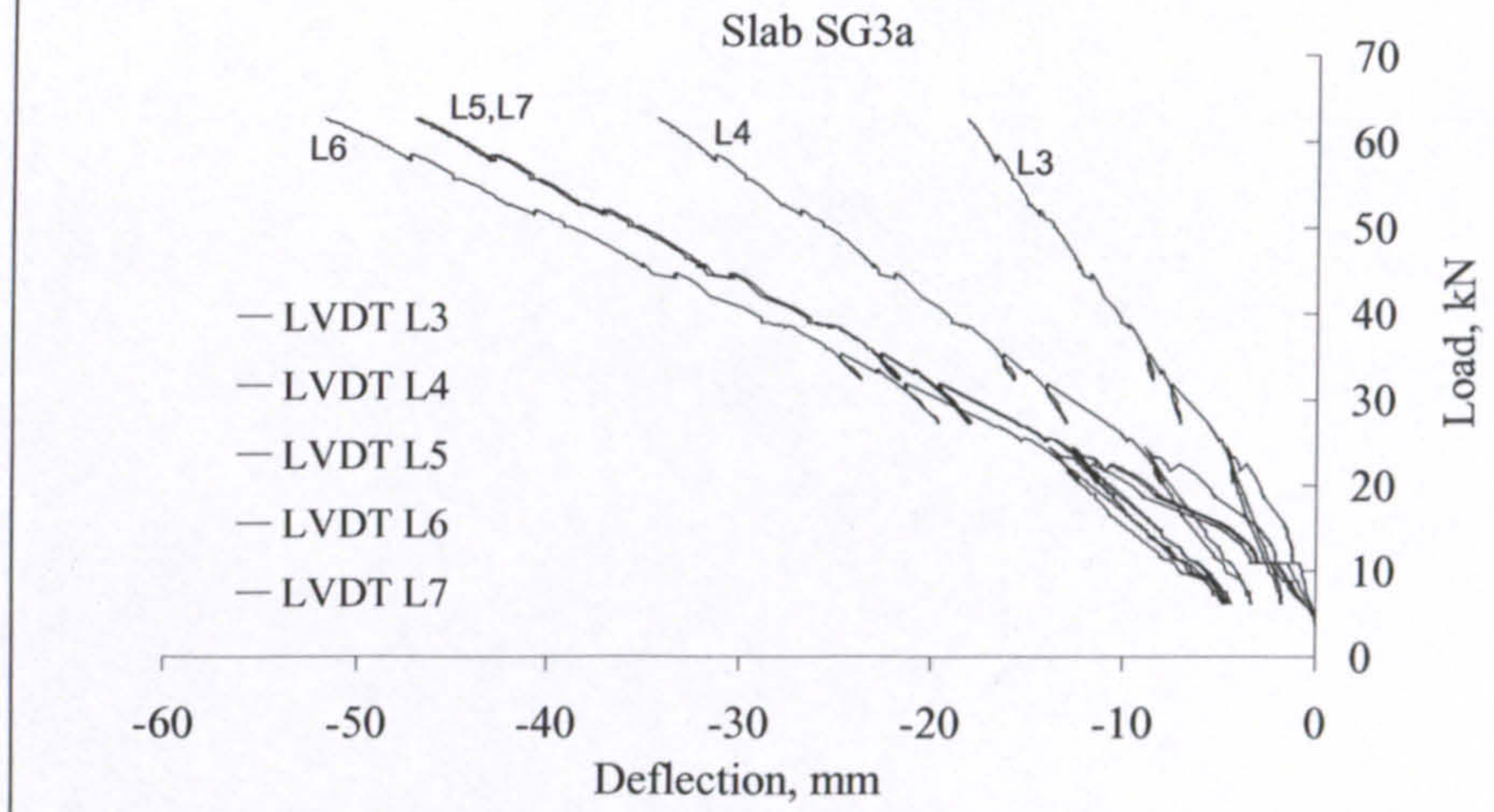
Slab SG3a
L6
L5,L7
L4
L3
LVDT L3
LVDT L4
LVDT L5
LVDT L6
LVDT L7
70
60
50
40
30
20
10
0
Load, kN
-60
-50
-40
-30
-20
-10
0
Deflection, mm

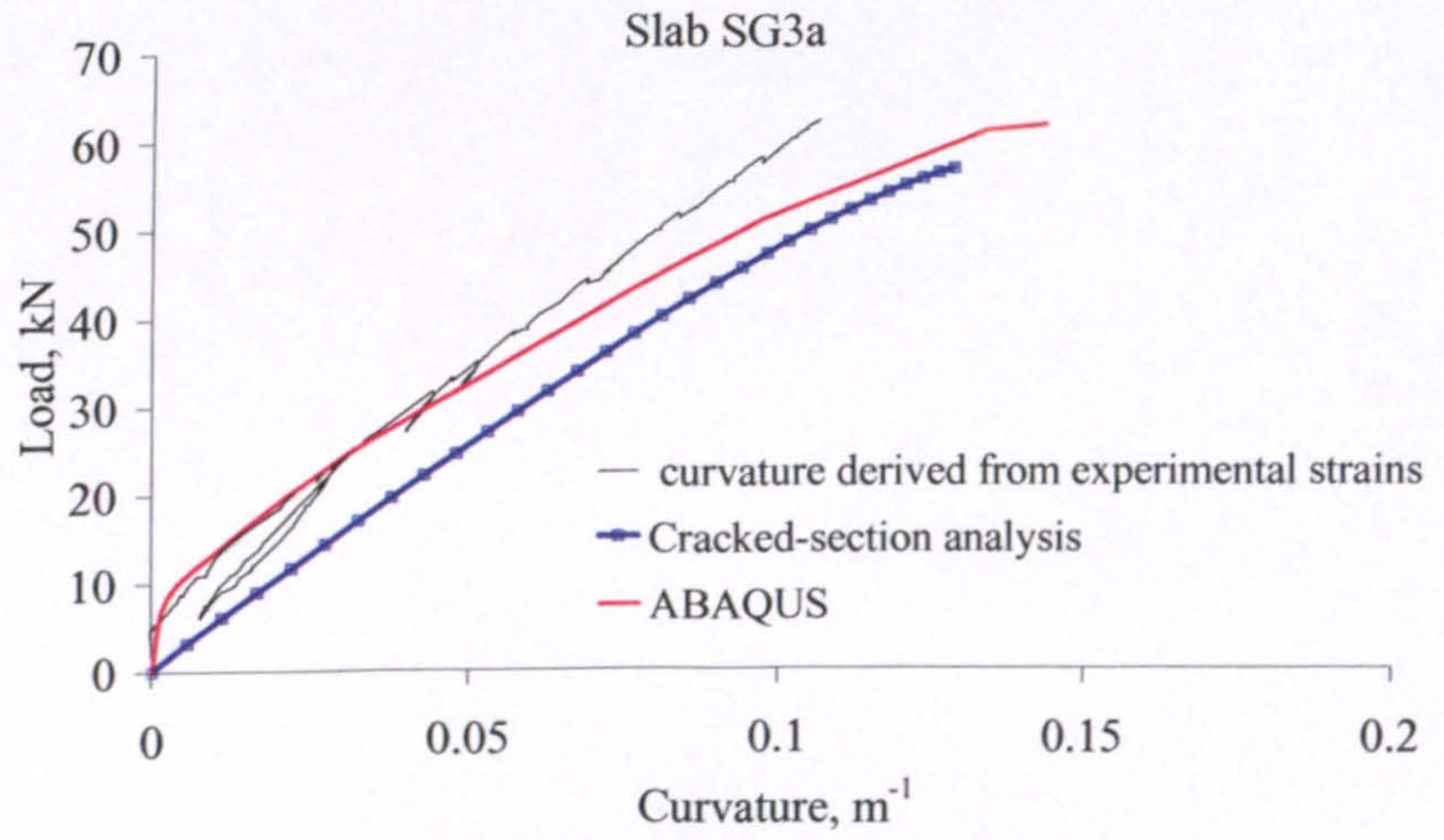
Slab SG3a
Load, kN
70
60
50
40
30
20
10
0
curvature derived from experimental strains
Cracked-section analysis
ABAQUS
0
0.05
0.1
0.15
0.2
Curvature, m-1

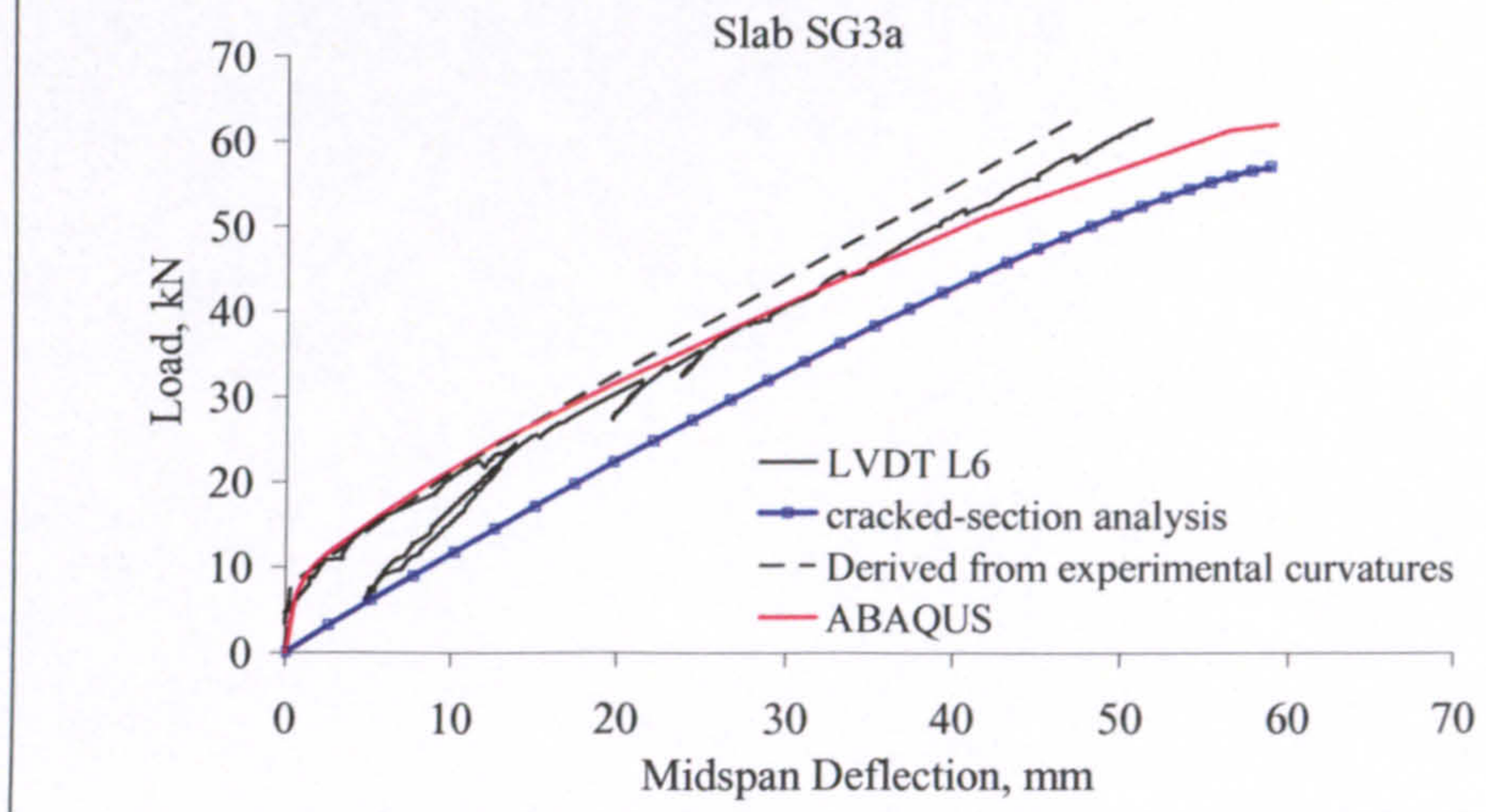
Slab SG3a
Load, kN
70
60
50
40
30
20
10
0
LVDT L6
cracked-section analysis
Derived from experimental curvatures
ABAQUS
0
10
20
30
40
50
60
70
Midspan Deflection, mm

SLAB SG3a

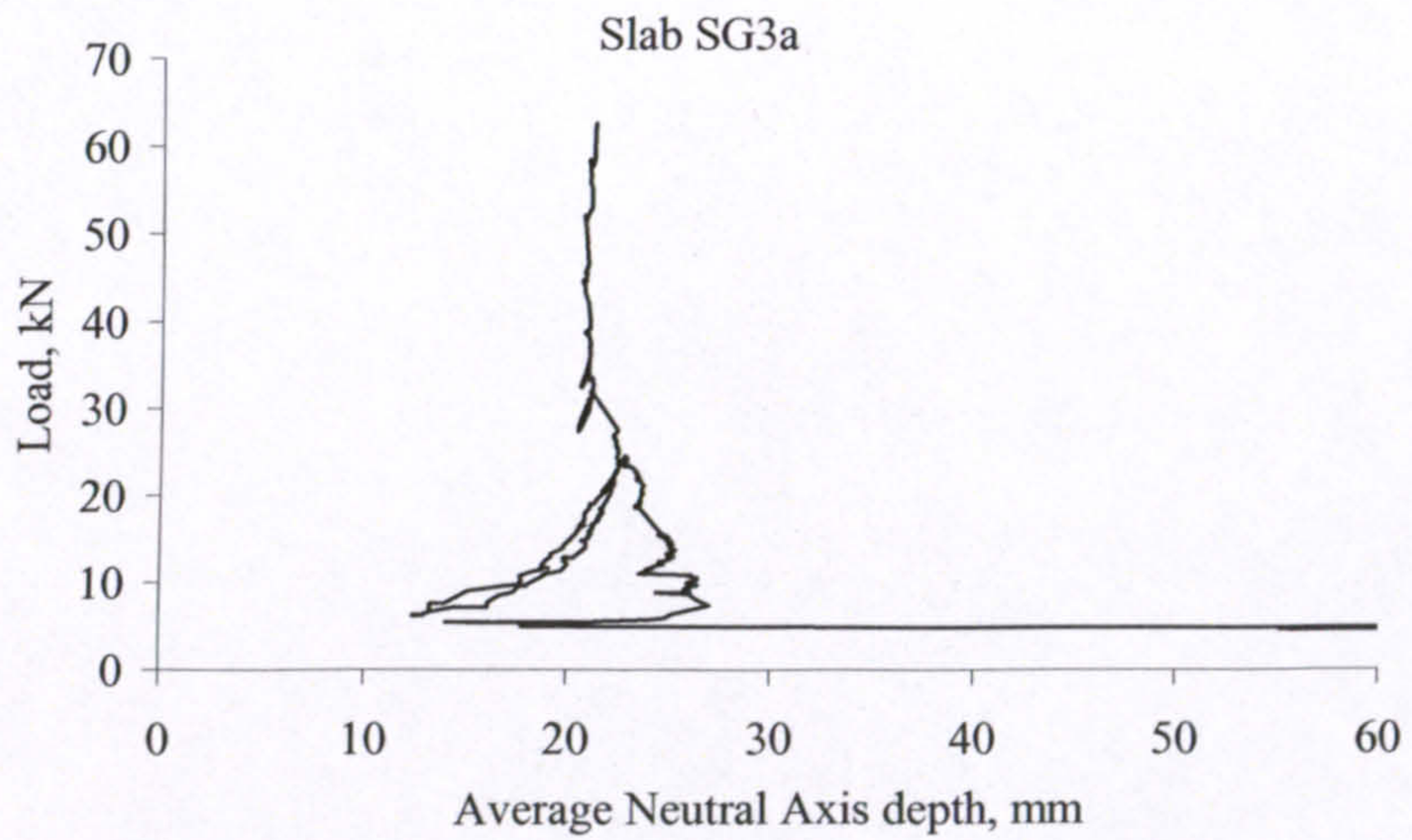
Slab SG3a
Load, kN
0
10
20
30
40
50
60
70
0
10
20
30
40
50
60
Average Neutral Axis depth, mm

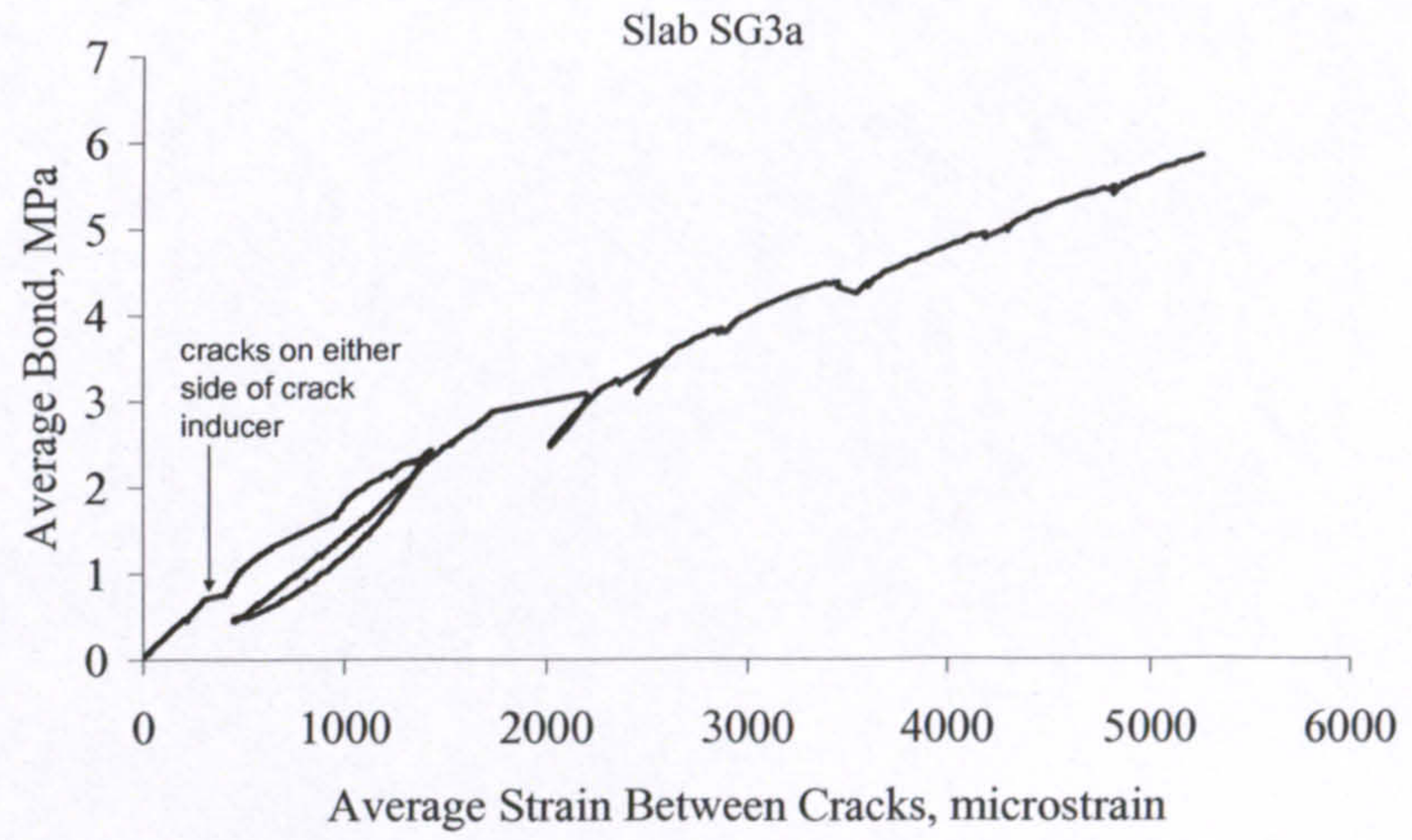
Slab SG3a
Average Bond, MPa
cracks on either side of crack inducer
0
1
2
3
4
5
6
7
0
1000
2000
3000
4000
5000
6000
Average Strain Between Cracks, microstrain

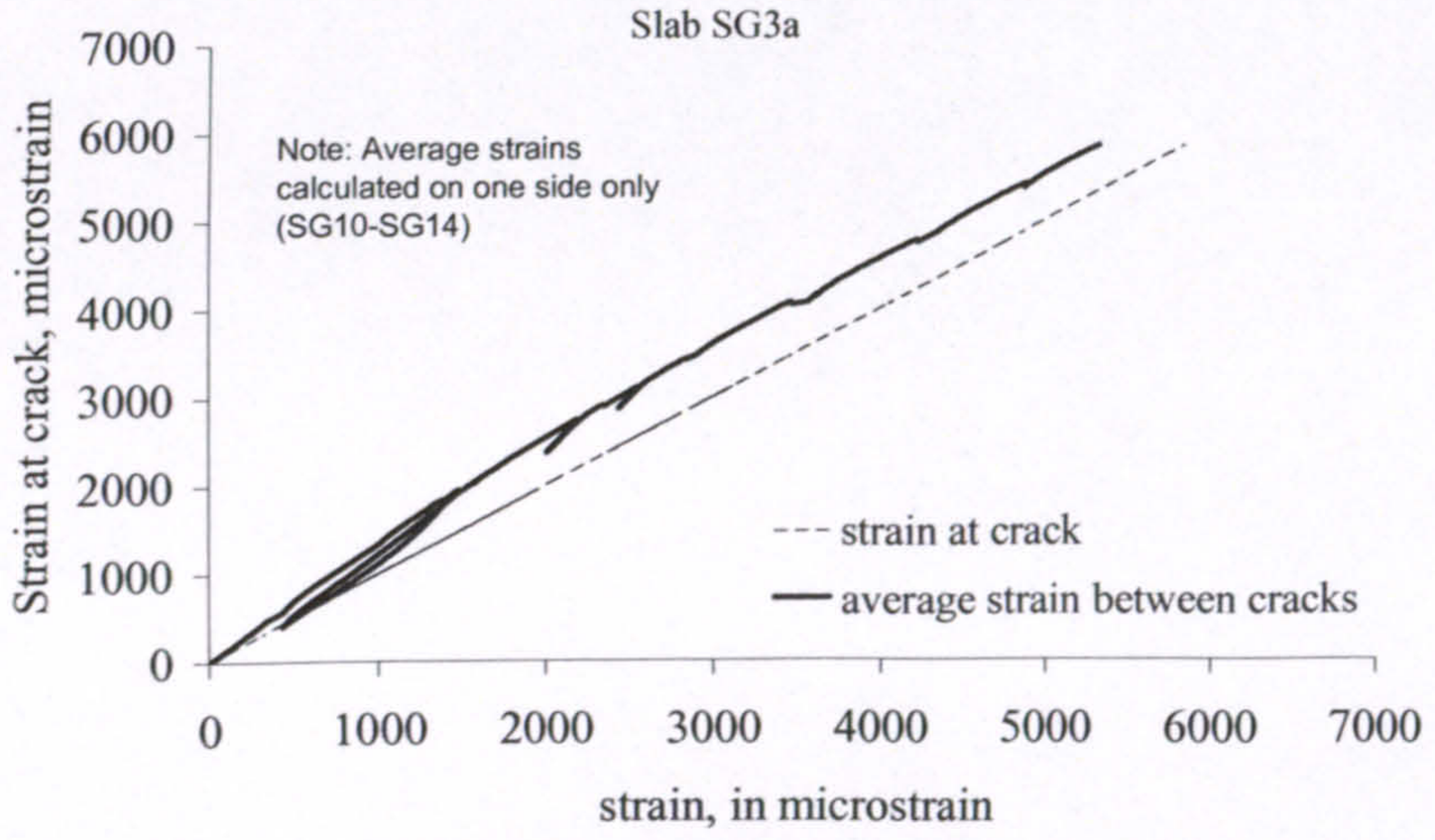
Slab SG3a
Strain at crack, microstrain
Note: Average strains calculated on one side only (SG10-SG14)
strain at crack
average strain between cracks
0
1000
2000
3000
4000
5000
6000
7000
strain, in microstrain

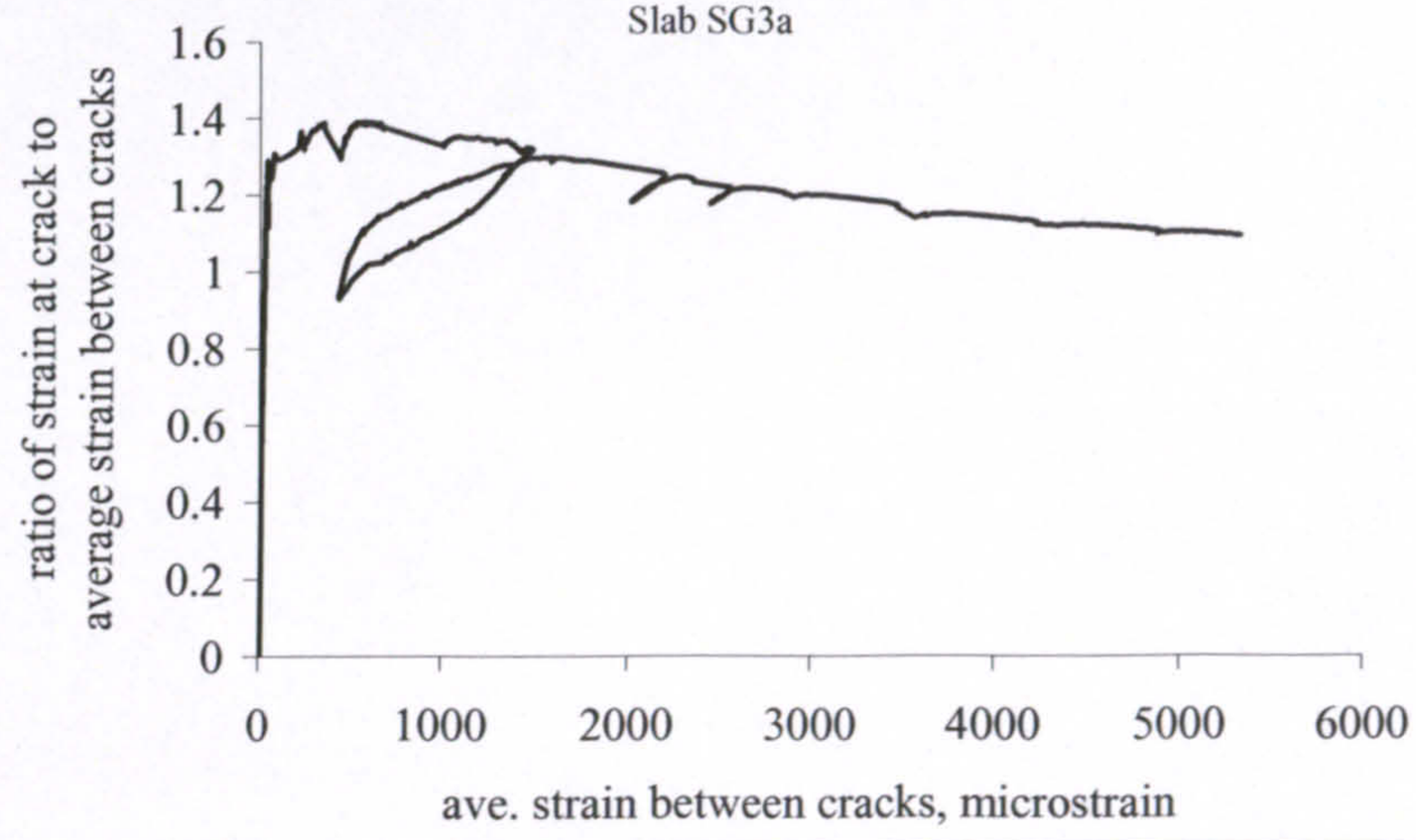
Slab SG3a
ratio of strain at crack to average strain between cracks
0
0.2
0.4
0.6
0.8
1
1.2
1.4
1.6
0
1000
2000
3000
4000
5000
6000
ave. strain between cracks, microstrain

SLAB SG3a

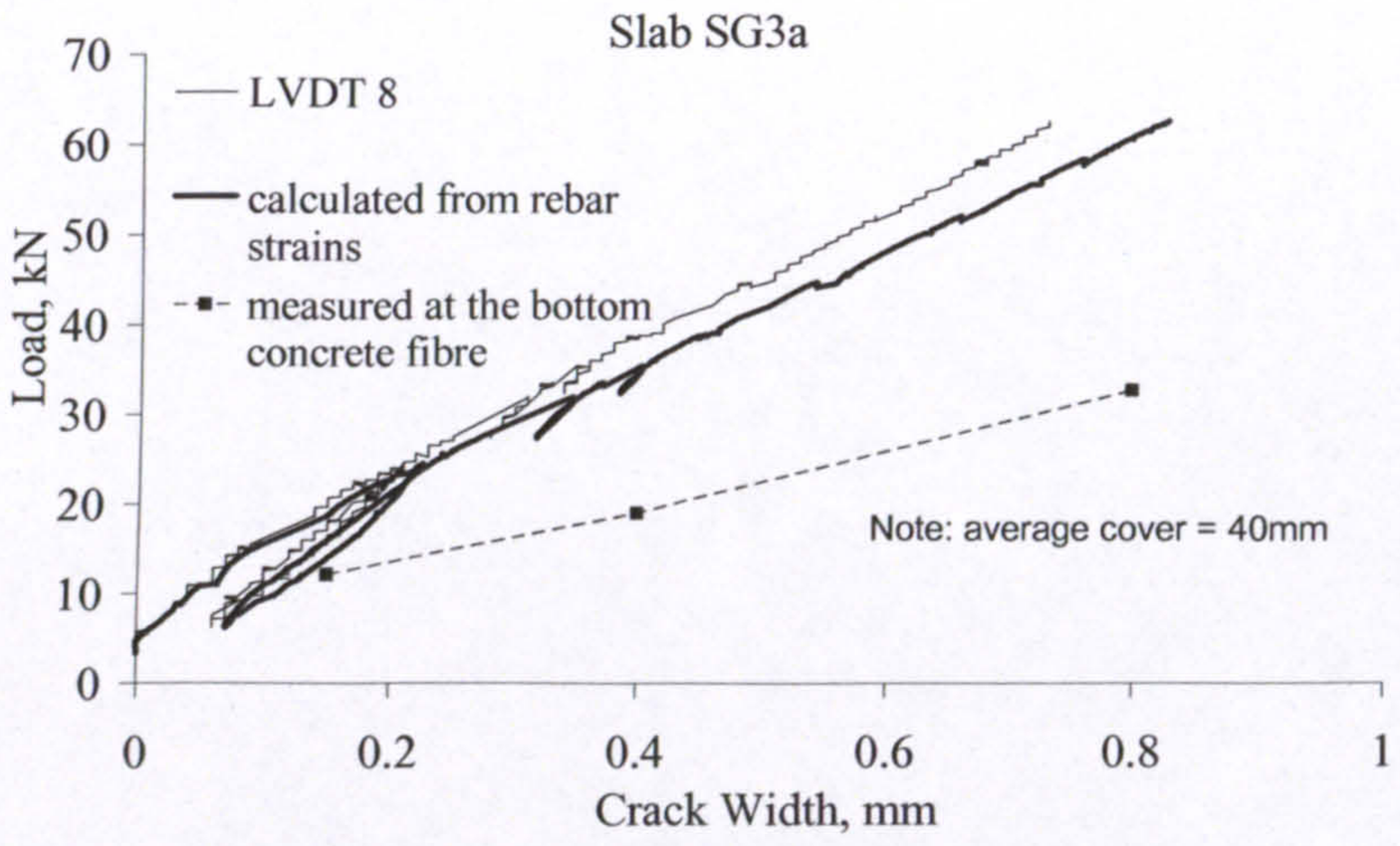

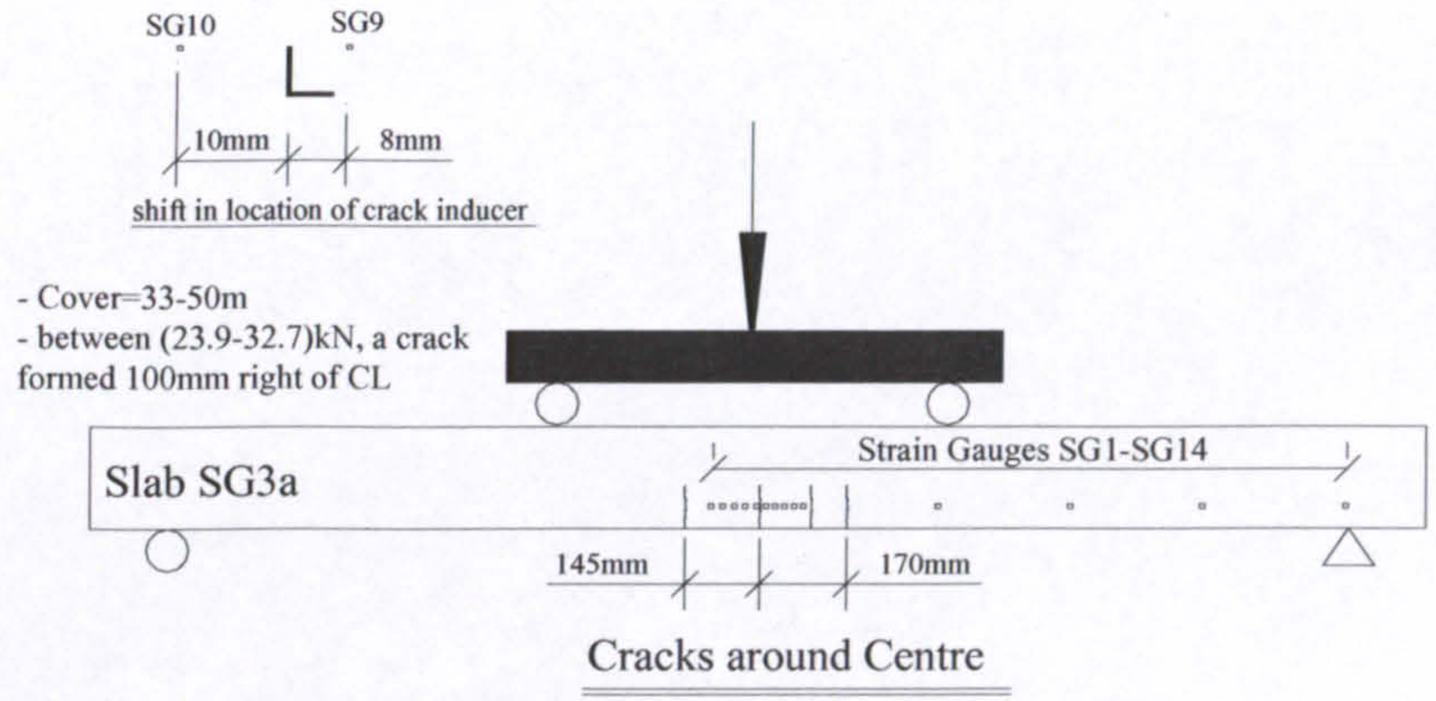

Cracks around Centre

Failure by concrete crushing.

SLAB SG3b

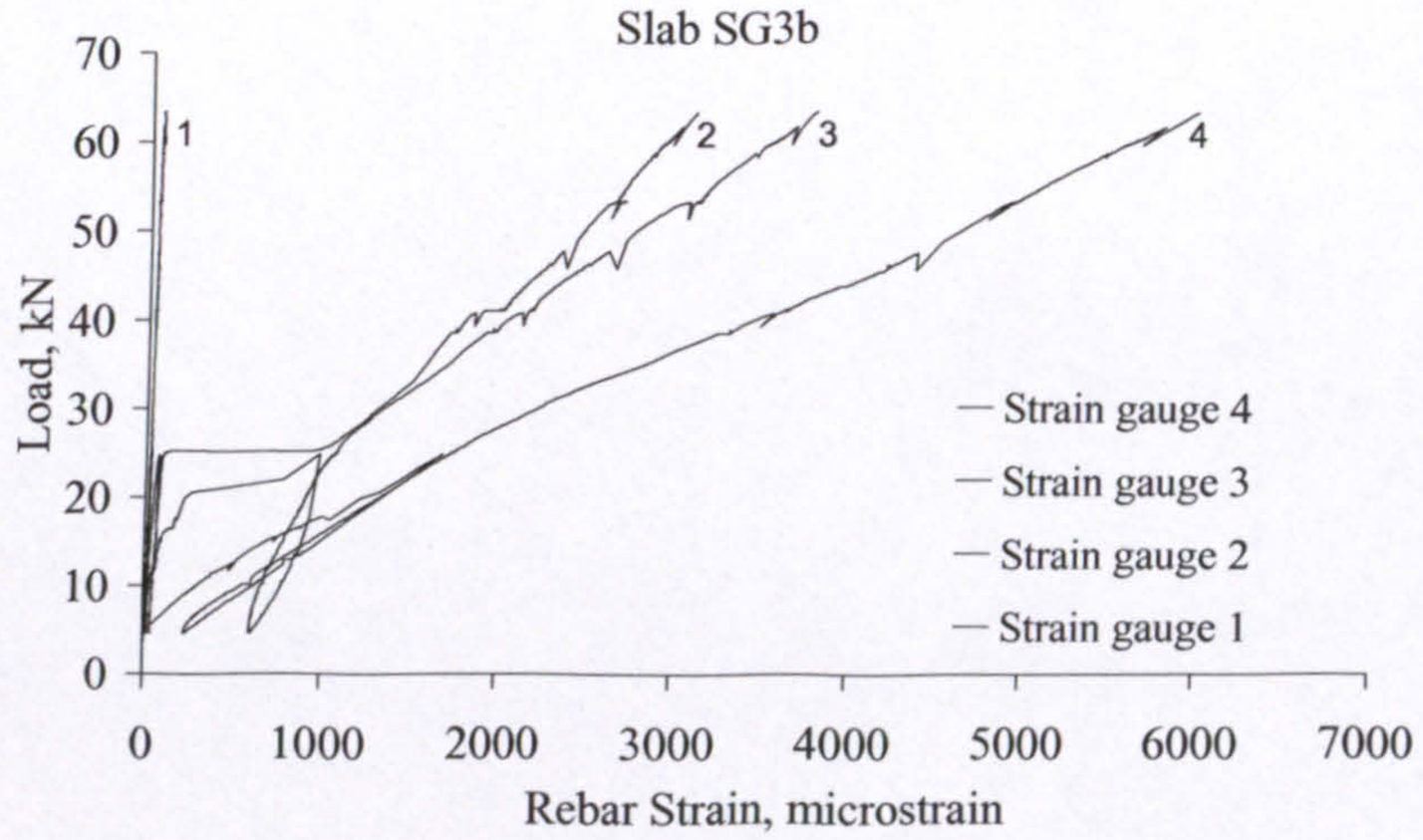
Slab SG3b
Load, kN
Rebar Strain, microstrain
1
2
3
4
Strain gauge 4
Strain gauge 3
Strain gauge 2
Strain gauge 1

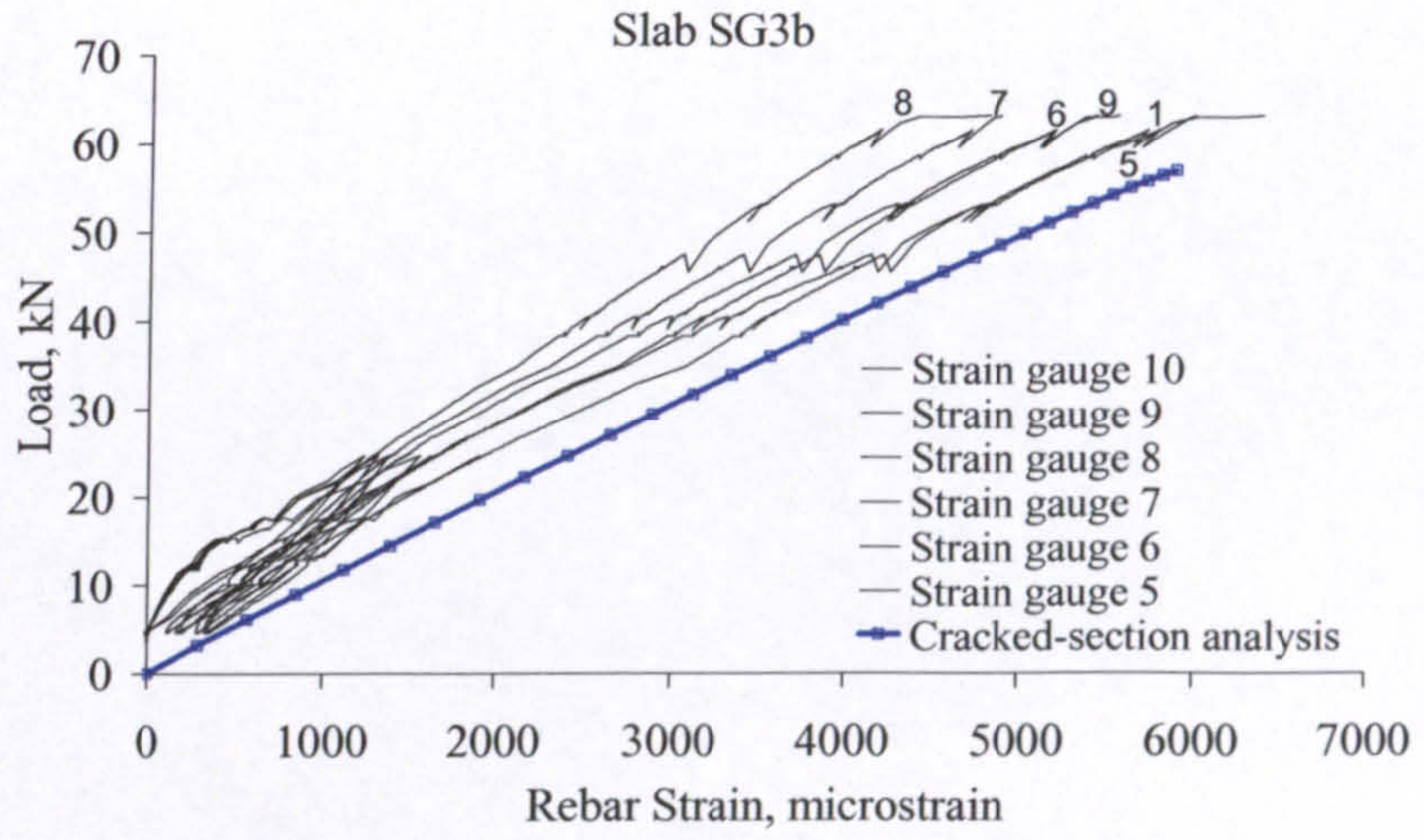
Slab SG3b
Load, kN
Rebar Strain, microstrain
8
7
6
9
1
5
Strain gauge 10
Strain gauge 9
Strain gauge 8
Strain gauge 7
Strain gauge 6
Strain gauge 5
Cracked-section analysis

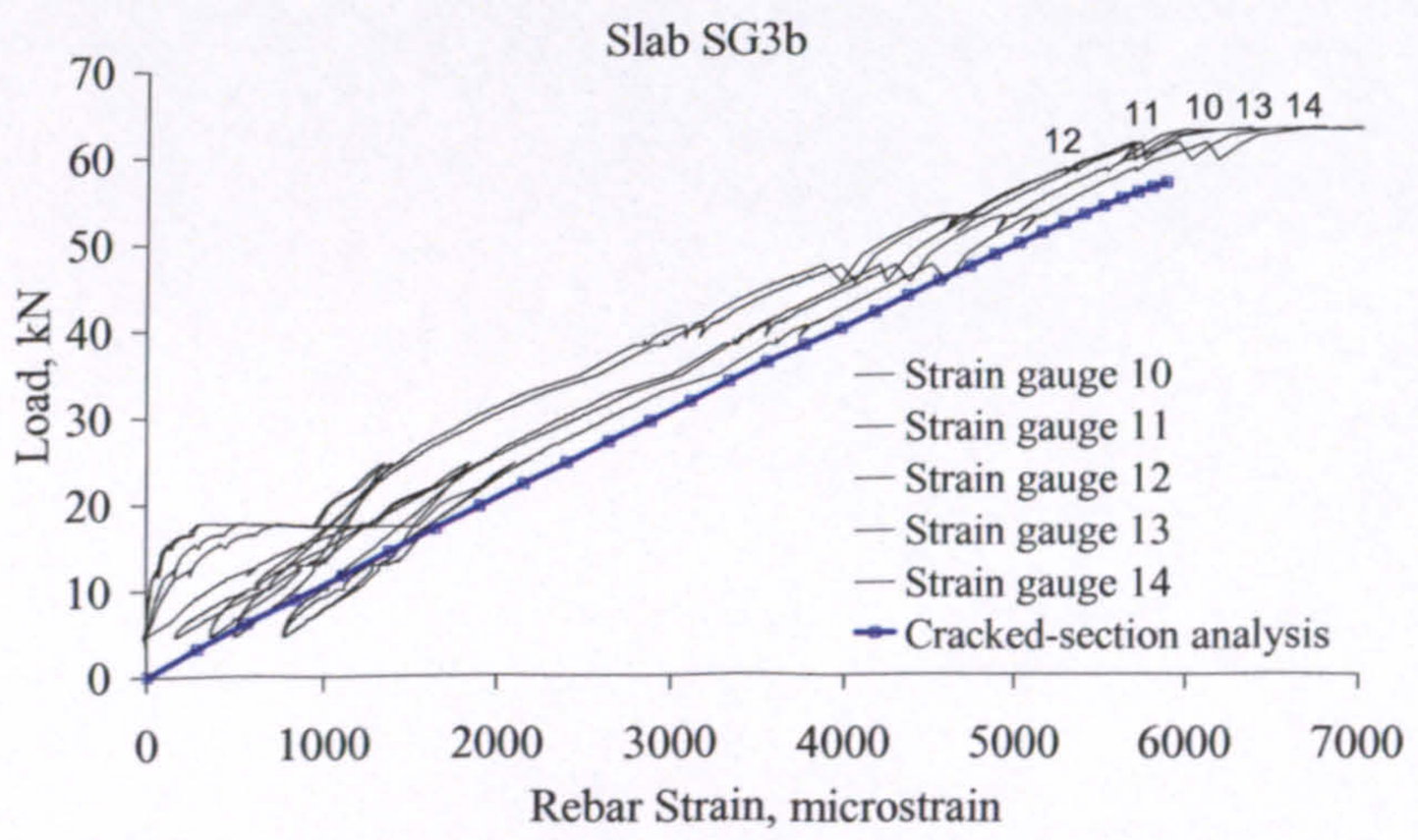
Slab SG3b
Load, kN
Rebar Strain, microstrain
12
11
10 13 14
Strain gauge 10
Strain gauge 11
Strain gauge 12
Strain gauge 13
Strain gauge 14
Cracked-section analysis

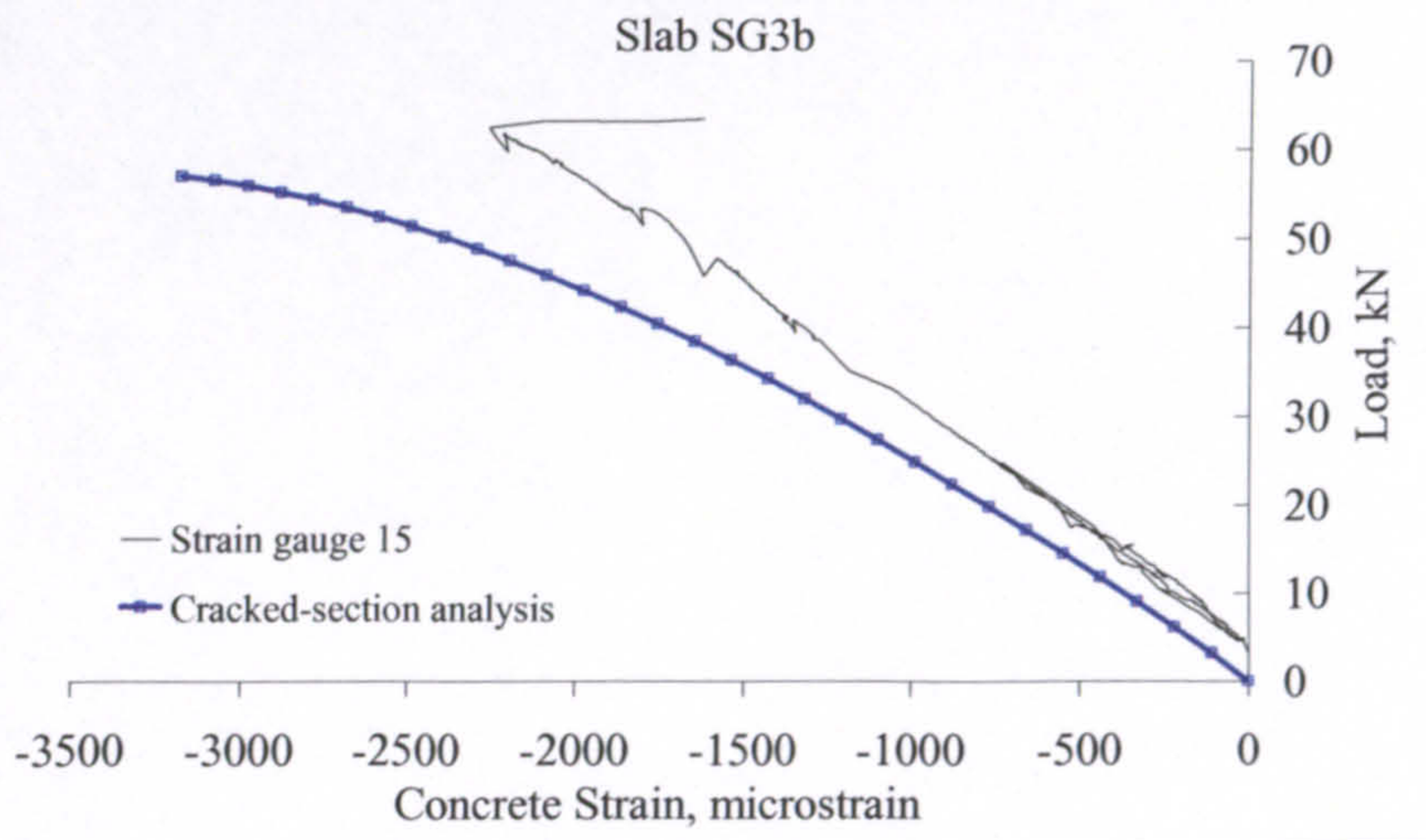
Slab SG3b
Load, kN
Concrete Strain, microstrain
Strain gauge 15
Cracked-section analysis

SLAB SG3b

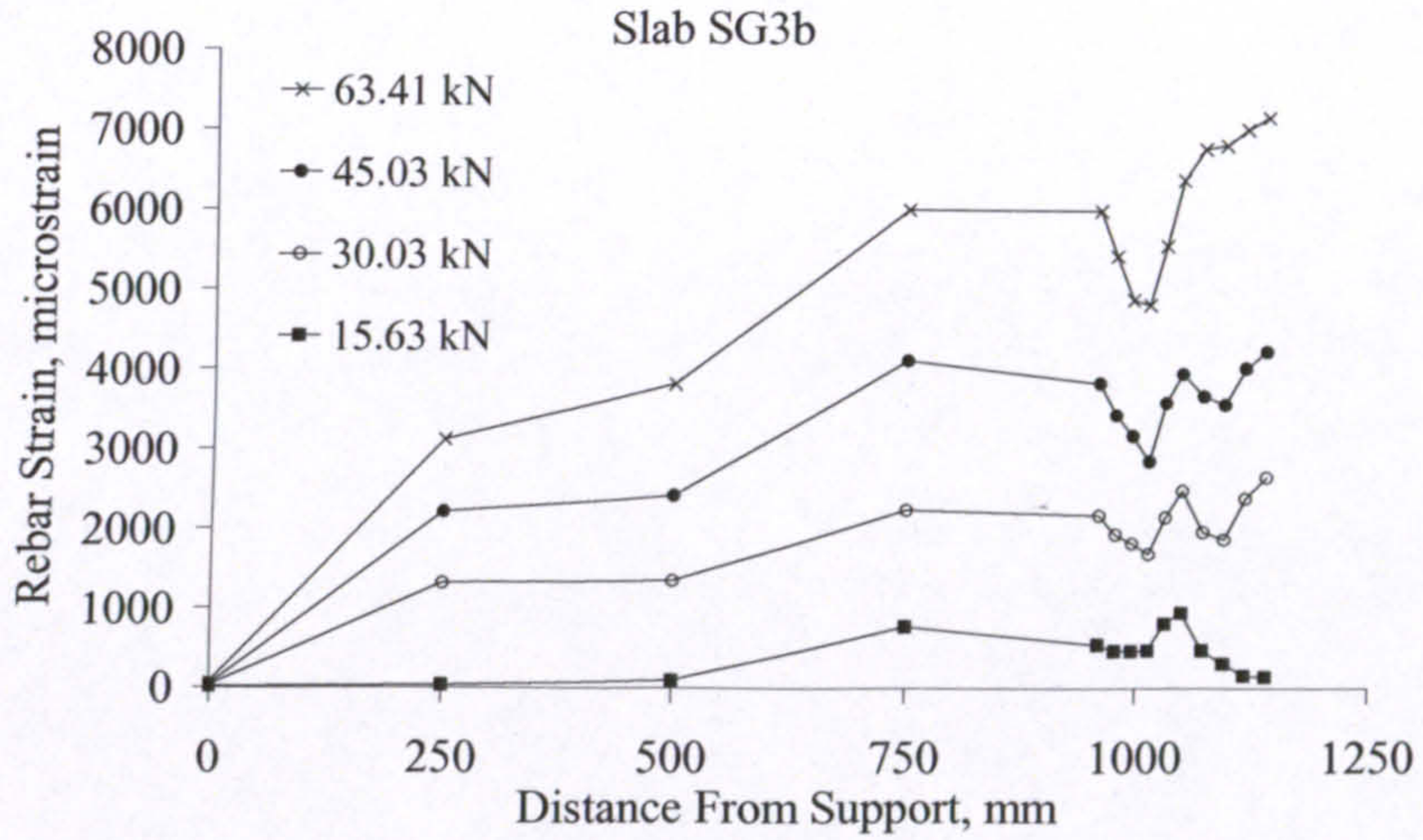
Slab SG3b
Rebar Strain, microstrain
8000
7000
6000
5000
4000
3000
2000
1000
0
63.41 kN
45.03 kN
30.03 kN
15.63 kN
0
250
500
750
1000
1250
Distance From Support, mm

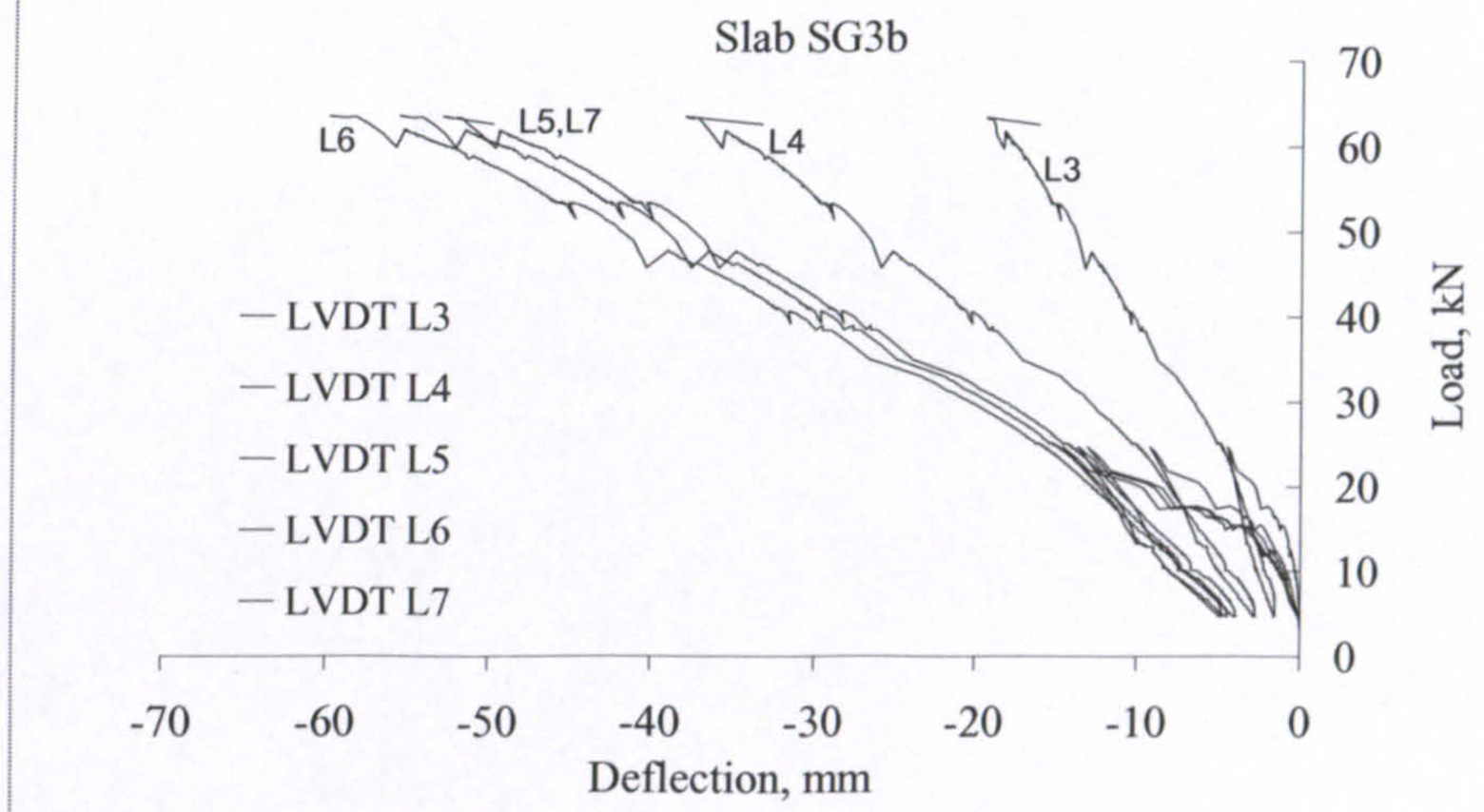
Slab SG3b
L6
L5,L7
L4
L3
LVDT L3
LVDT L4
LVDT L5
LVDT L6
LVDT L7
70
60
50
40
30
20
10
0
Load, kN
-70
-60
-50
-40
-30
-20
-10
0
Deflection, mm

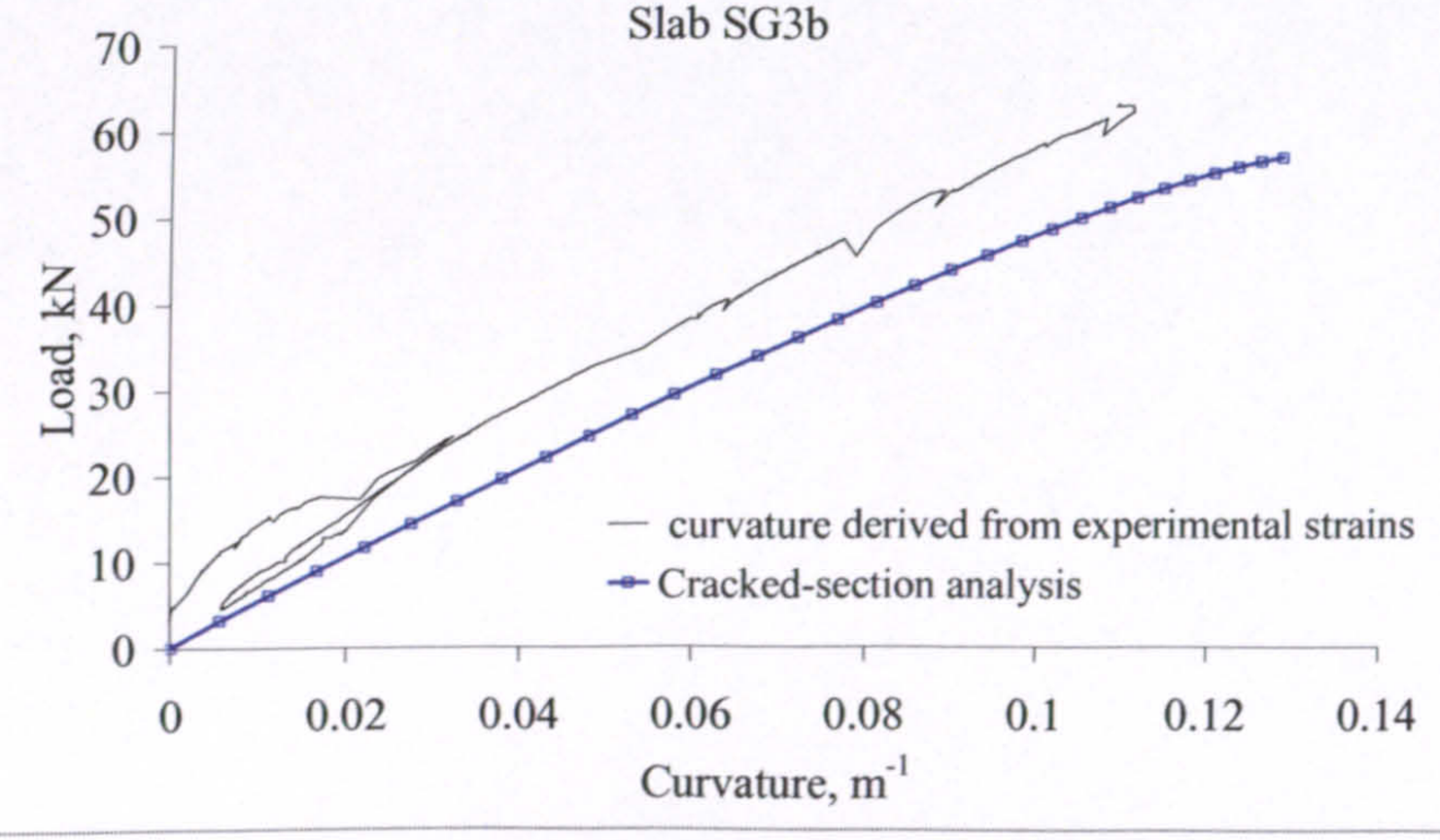
Slab SG3b
Load, kN
70
60
50
40
30
20
10
0
curvature derived from experimental strains
Cracked-section analysis
0
0.02
0.04
0.06
0.08
0.1
0.12
0.14
Curvature, m-1

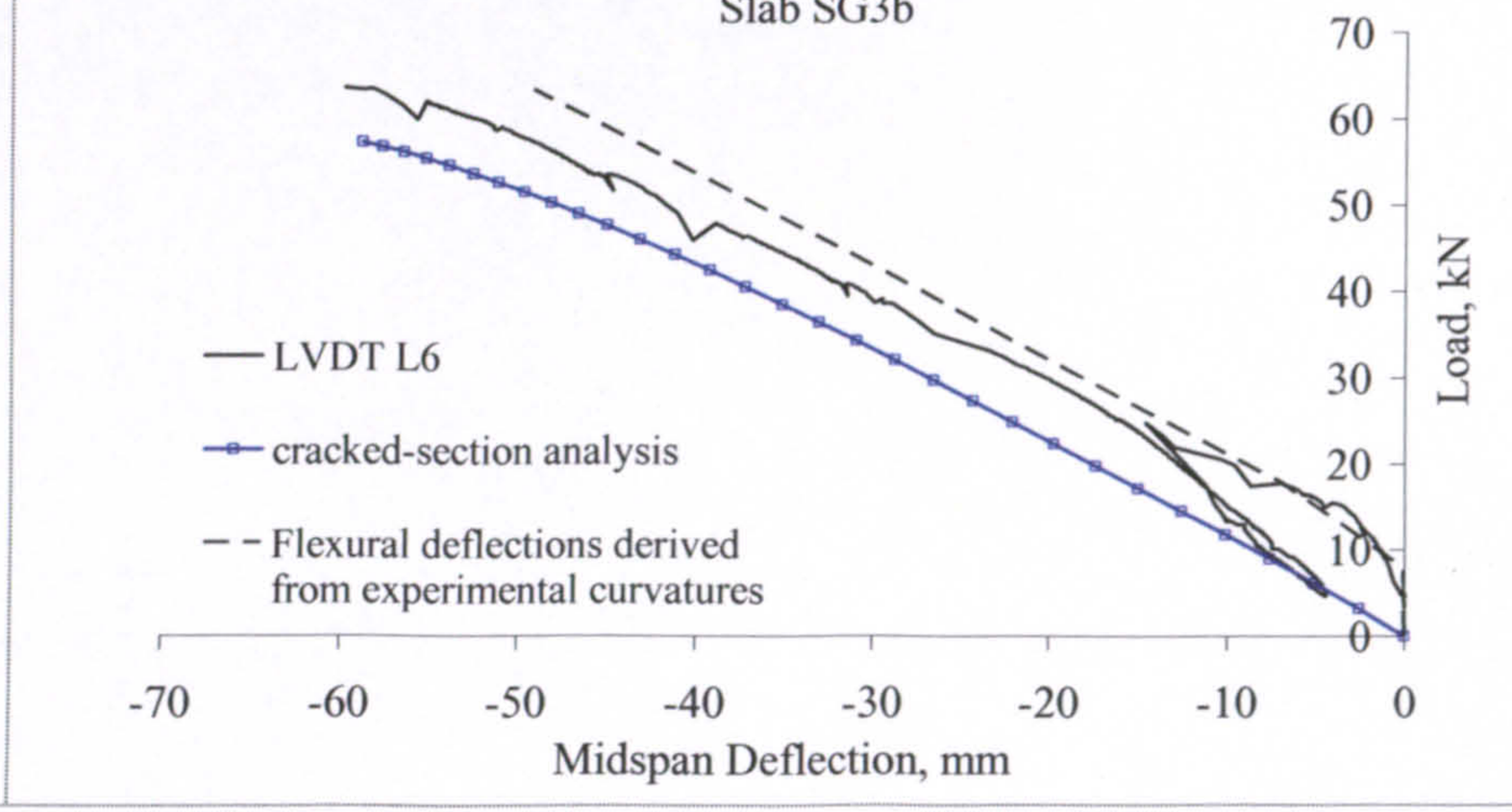
Slab SG3b
LVDT L6
cracked-section analysis
Flexural deflections derived
from experimental curvatures
70
60
50
40
30
20
10
0
Load, kN
-70
-60
-50
-40
-30
-20
-10
0
Midspan Deflection, mm

SLAB SG3b

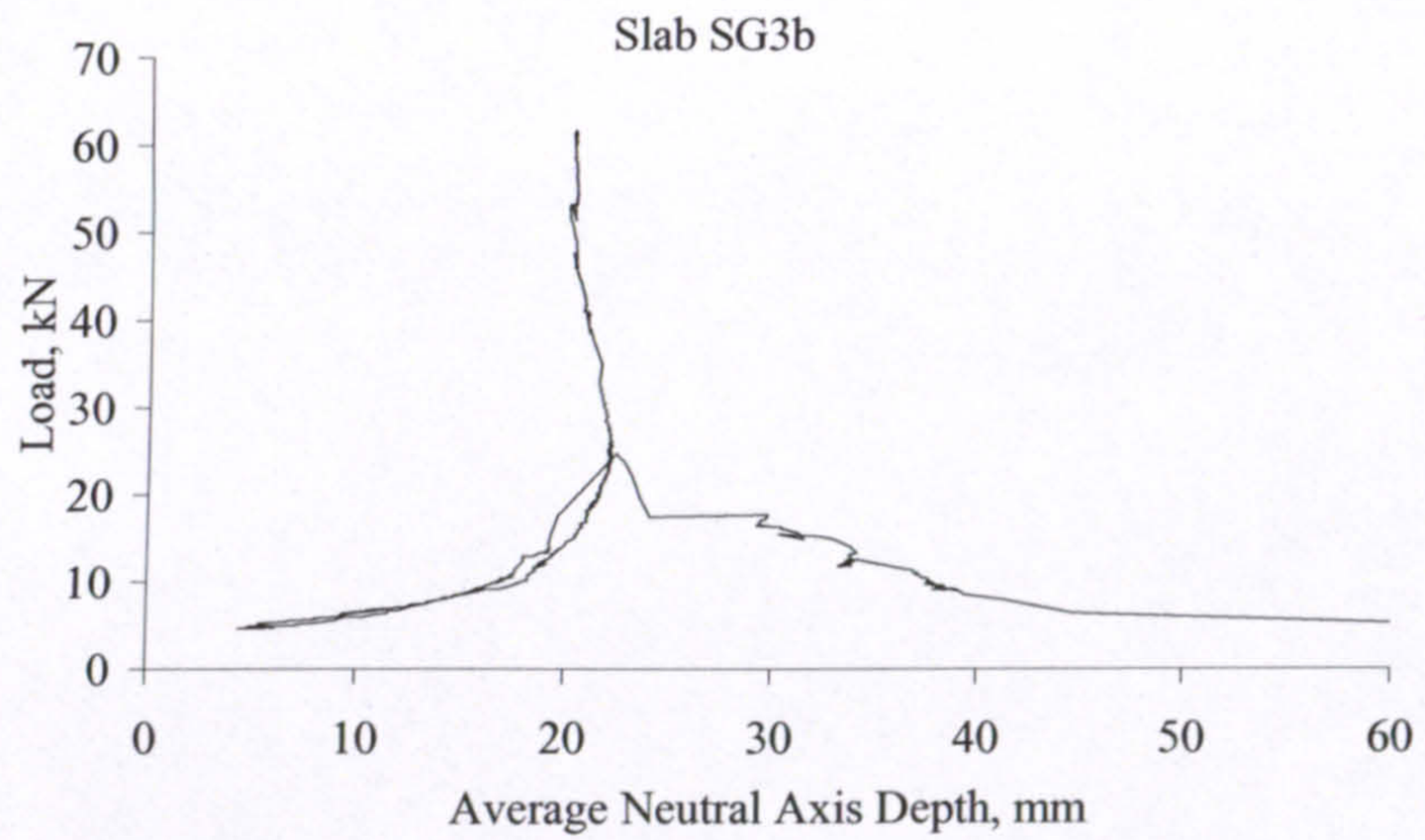
Slab SG3b
Load, kN
0
10
20
30
40
50
60
70
Average Neutral Axis Depth, mm

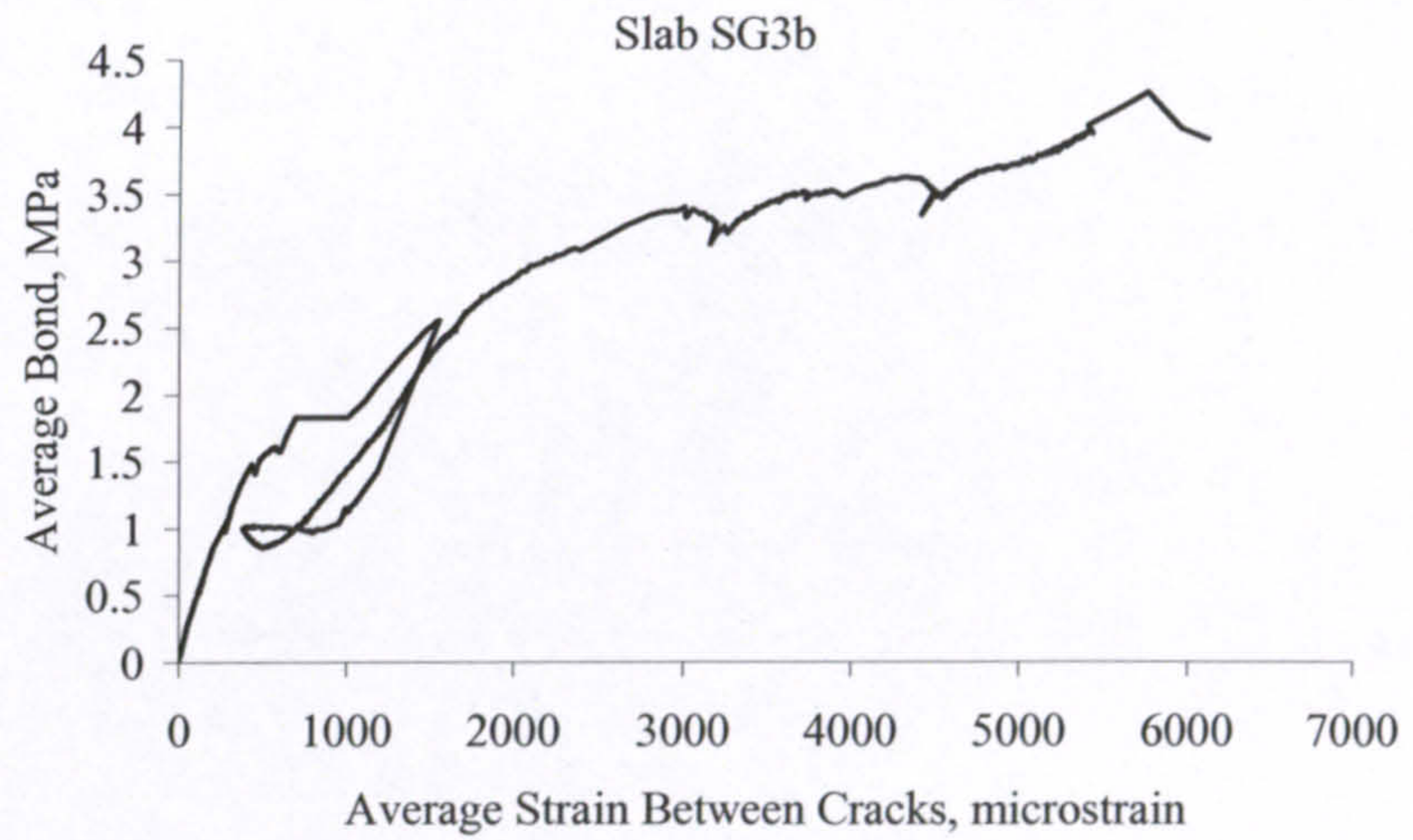
Slab SG3b
Average Bond, MPa
0
0.5
1
1.5
2
2.5
3
3.5
4
4.5
0
1000
2000
3000
4000
5000
6000
7000
Average Strain Between Cracks, microstrain

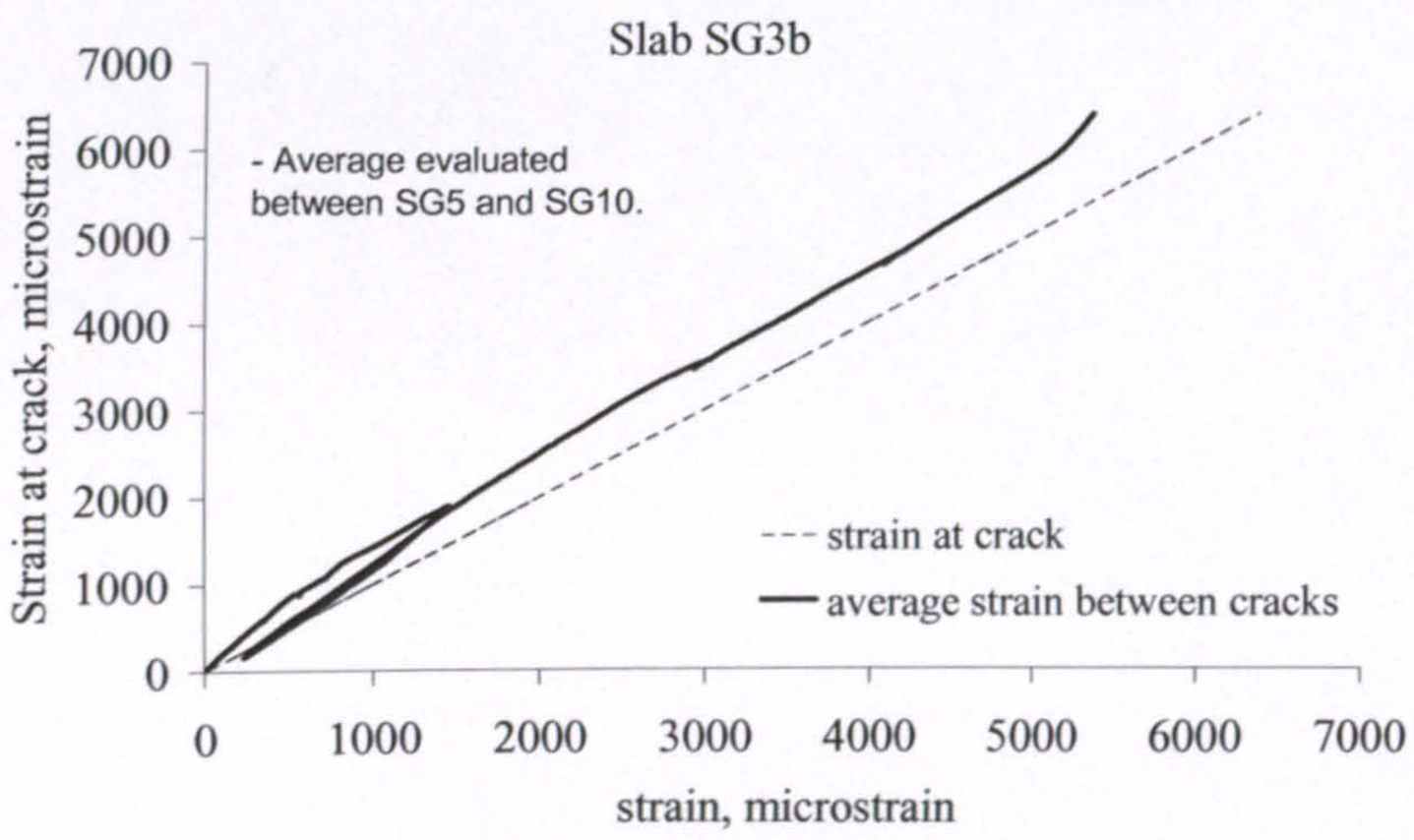
Slab SG3b
- Average evaluated between SG5 and SG10.
Strain at crack, microstrain
0
1000
2000
3000
4000
5000
6000
7000
strain at crack
average strain between cracks
strain, microstrain

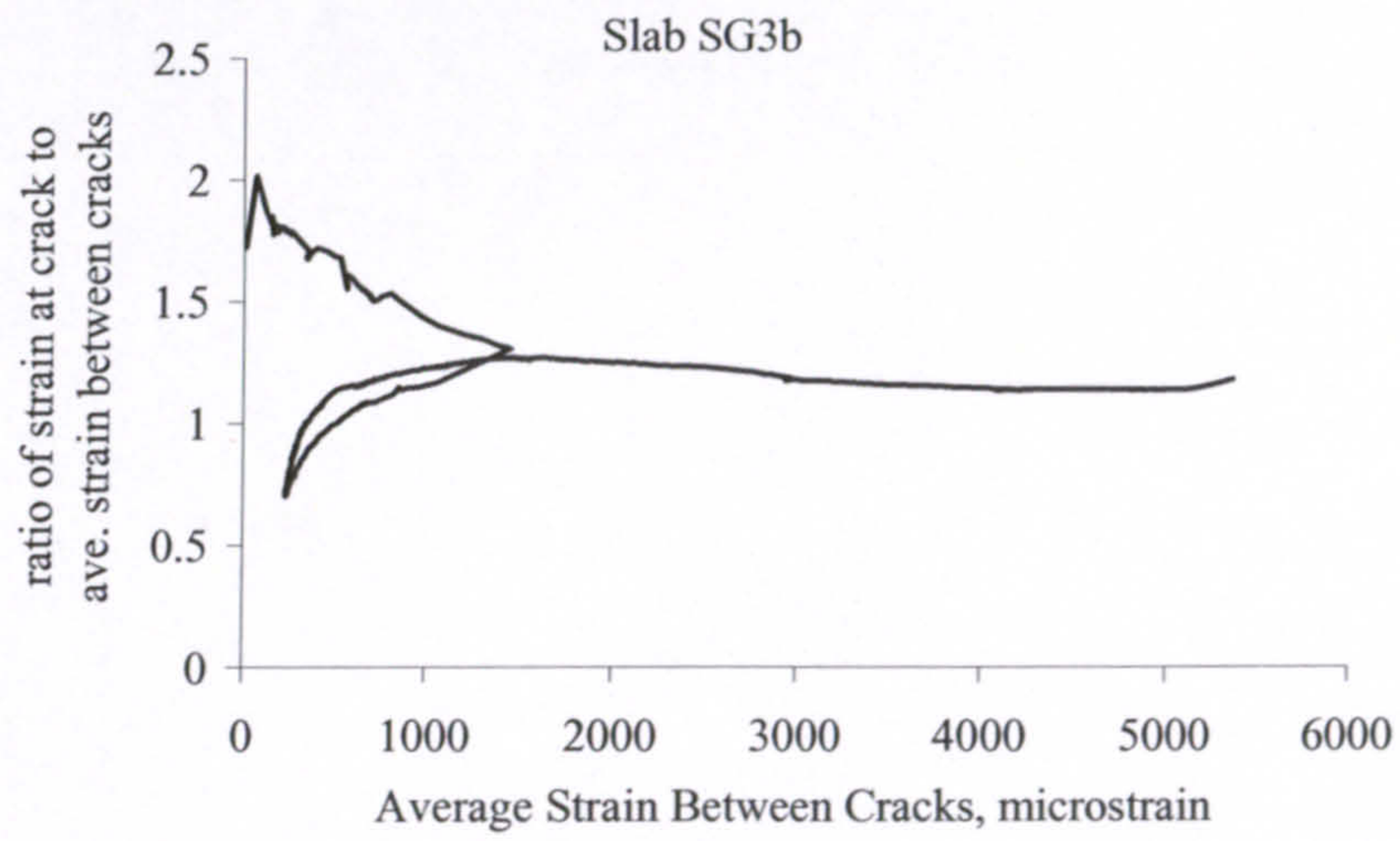
Slab SG3b
ratio of strain at crack to ave. strain between cracks
0
0.5
1
1.5
2
2.5
0
1000
2000
3000
4000
5000
6000
Average Strain Between Cracks, microstrain

SLAB SG3b

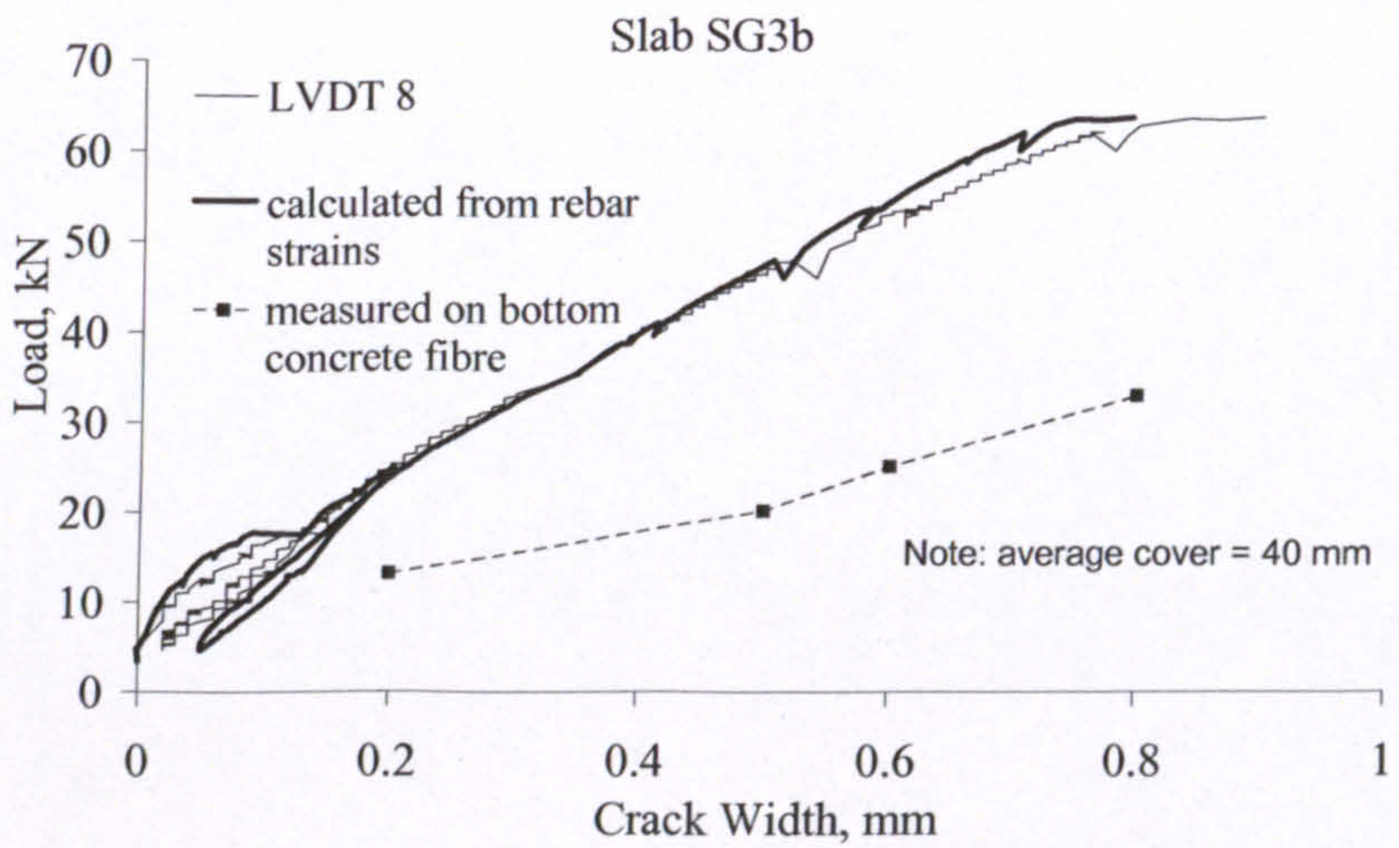

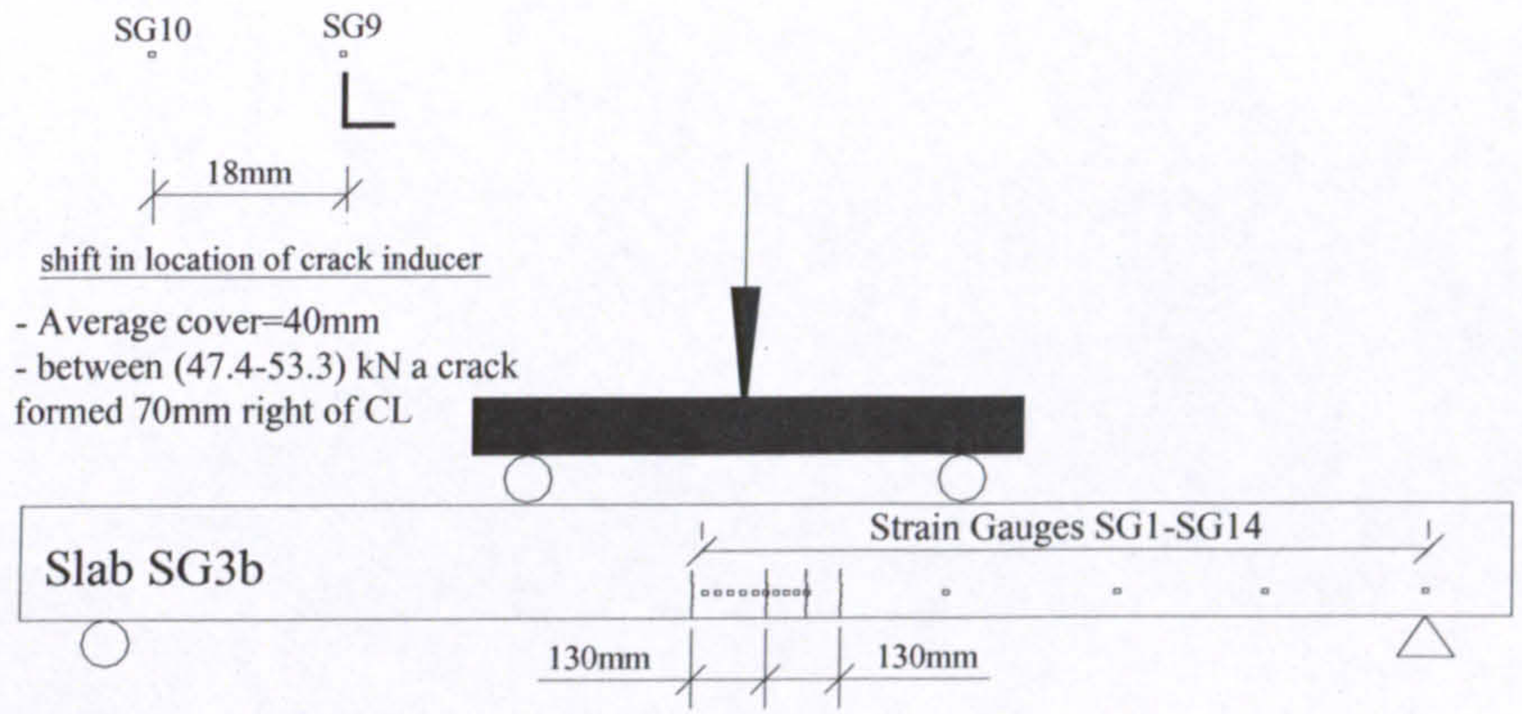

Cracks around Centre

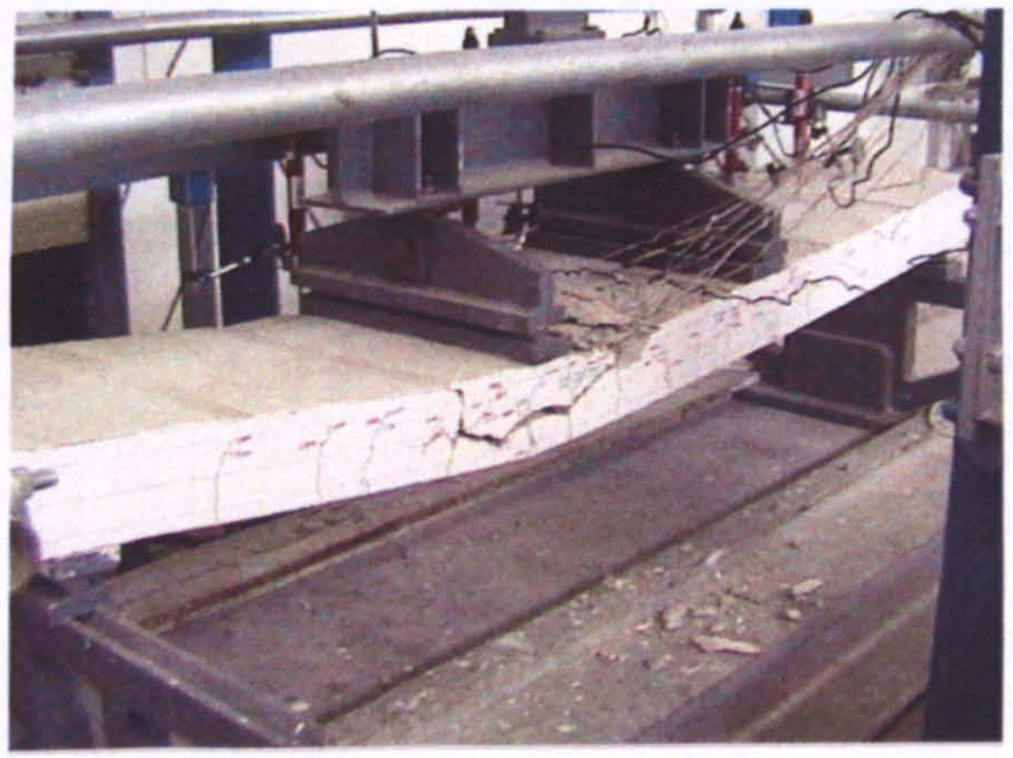

Failure by concrete crushing.

SLAB SC1a

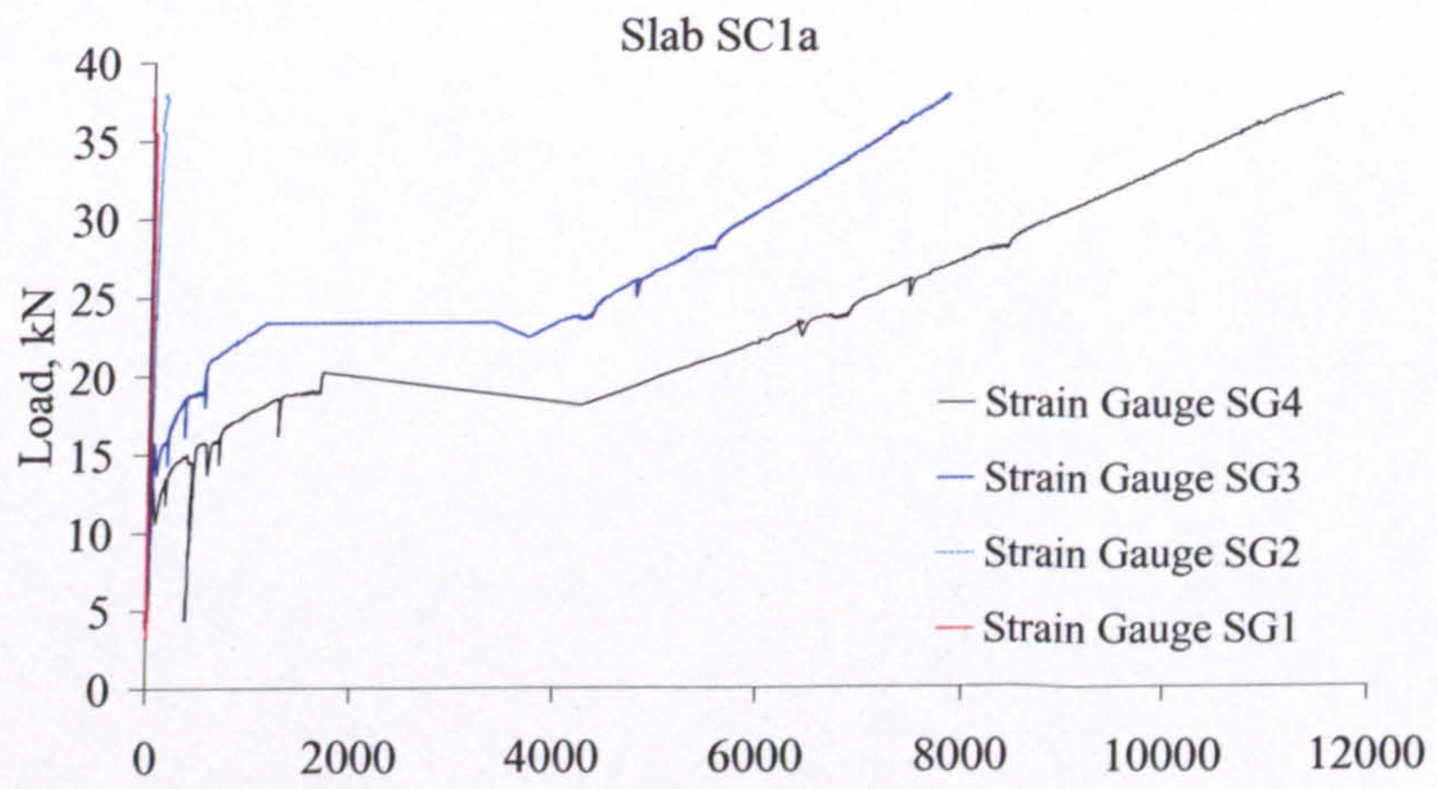
Slab SC1a
Load, kN
Rebar Strain, microstrain
Strain Gauge SG4
Strain Gauge SG3
Strain Gauge SG2
Strain Gauge SG1

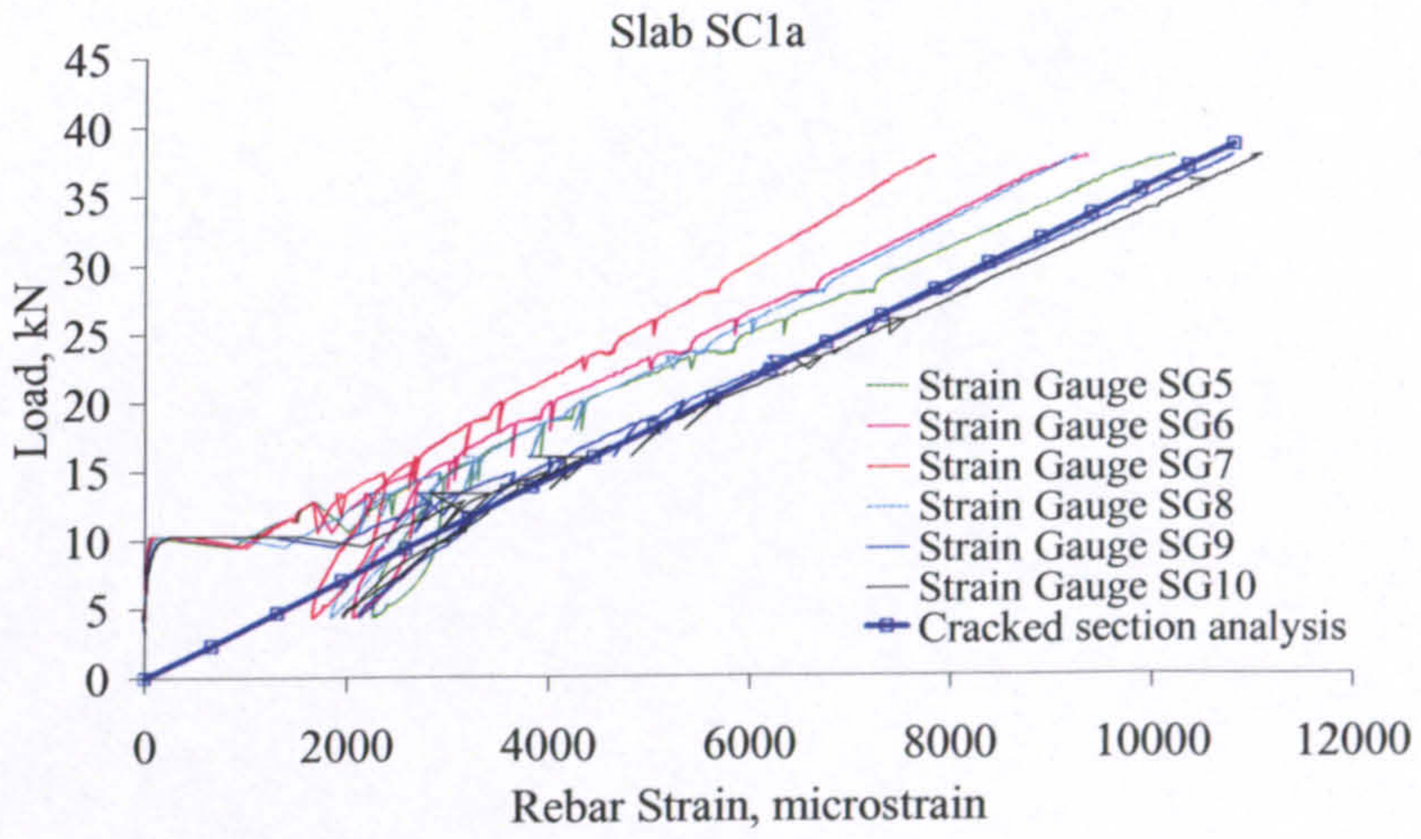
Slab SC1a
Load, kN
Rebar Strain, microstrain
Strain Gauge SG5
Strain Gauge SG6
Strain Gauge SG7
Strain Gauge SG8
Strain Gauge SG9
Strain Gauge SG10
Cracked section analysis

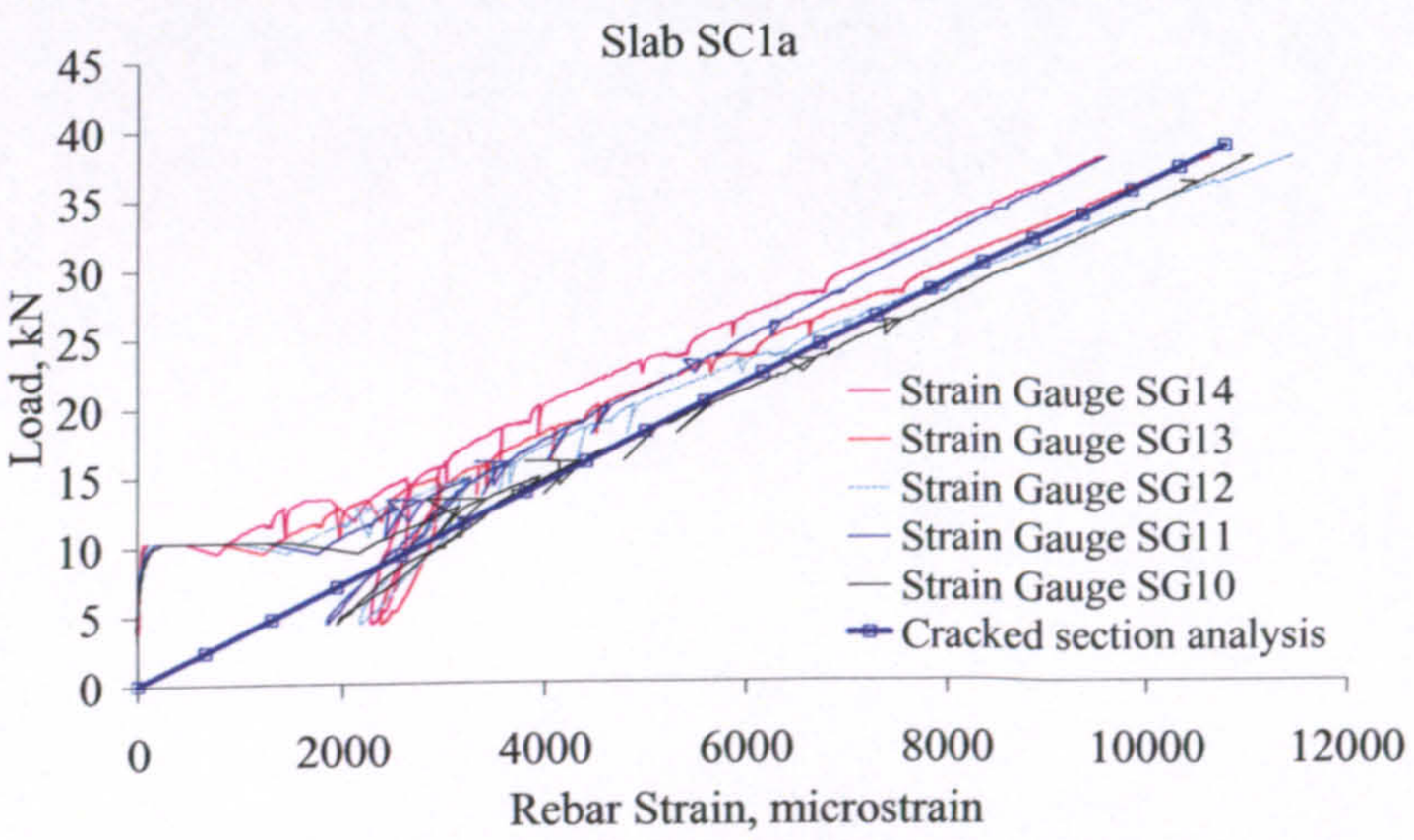
Slab SC1a
Load, kN
Rebar Strain, microstrain
Strain Gauge SG14
Strain Gauge SG13
Strain Gauge SG12
Strain Gauge SG11
Strain Gauge SG10
Cracked section analysis

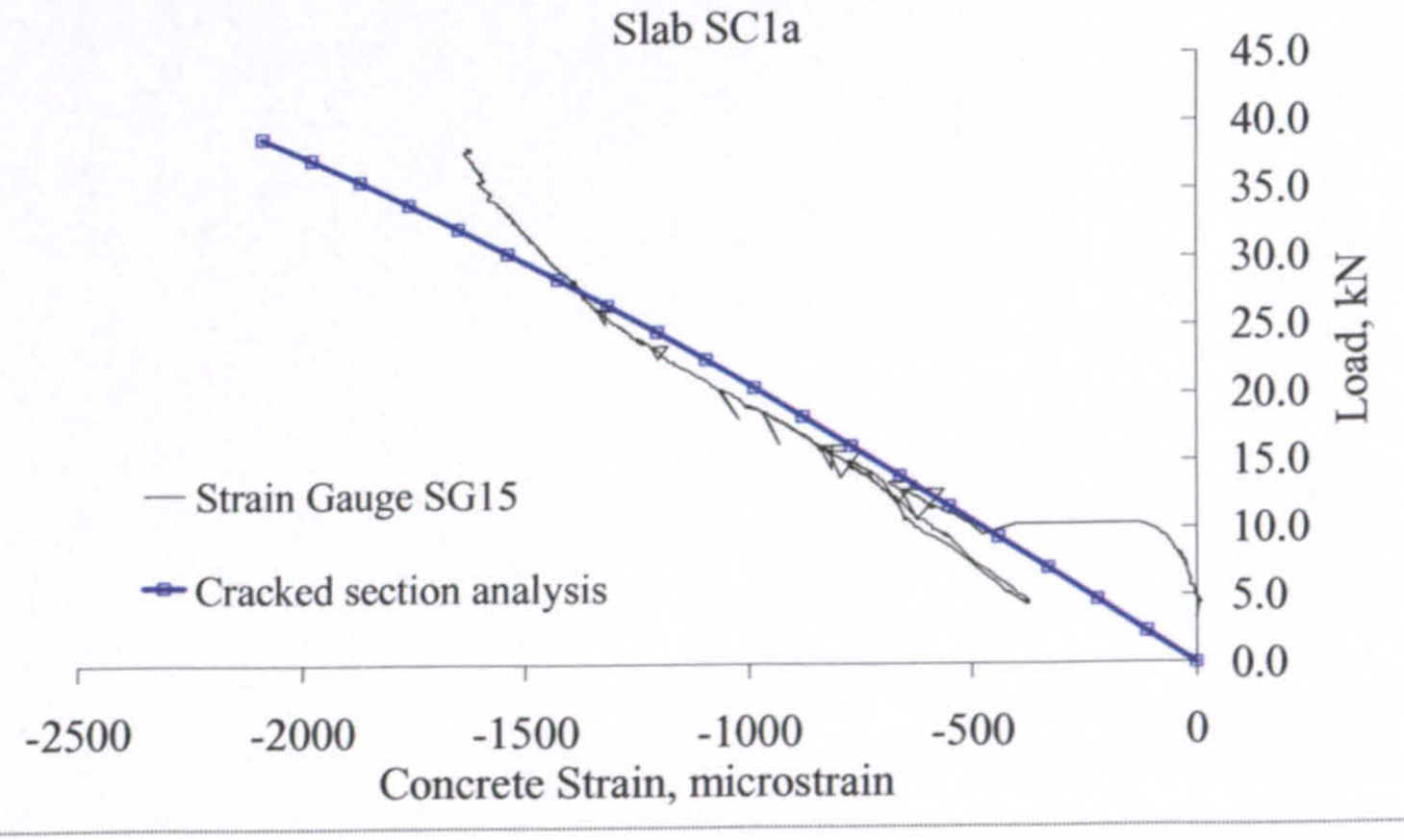
Slab SC1a
Load, kN
Concrete Strain, microstrain
Strain Gauge SG15
Cracked section analysis

SLAB SC1a

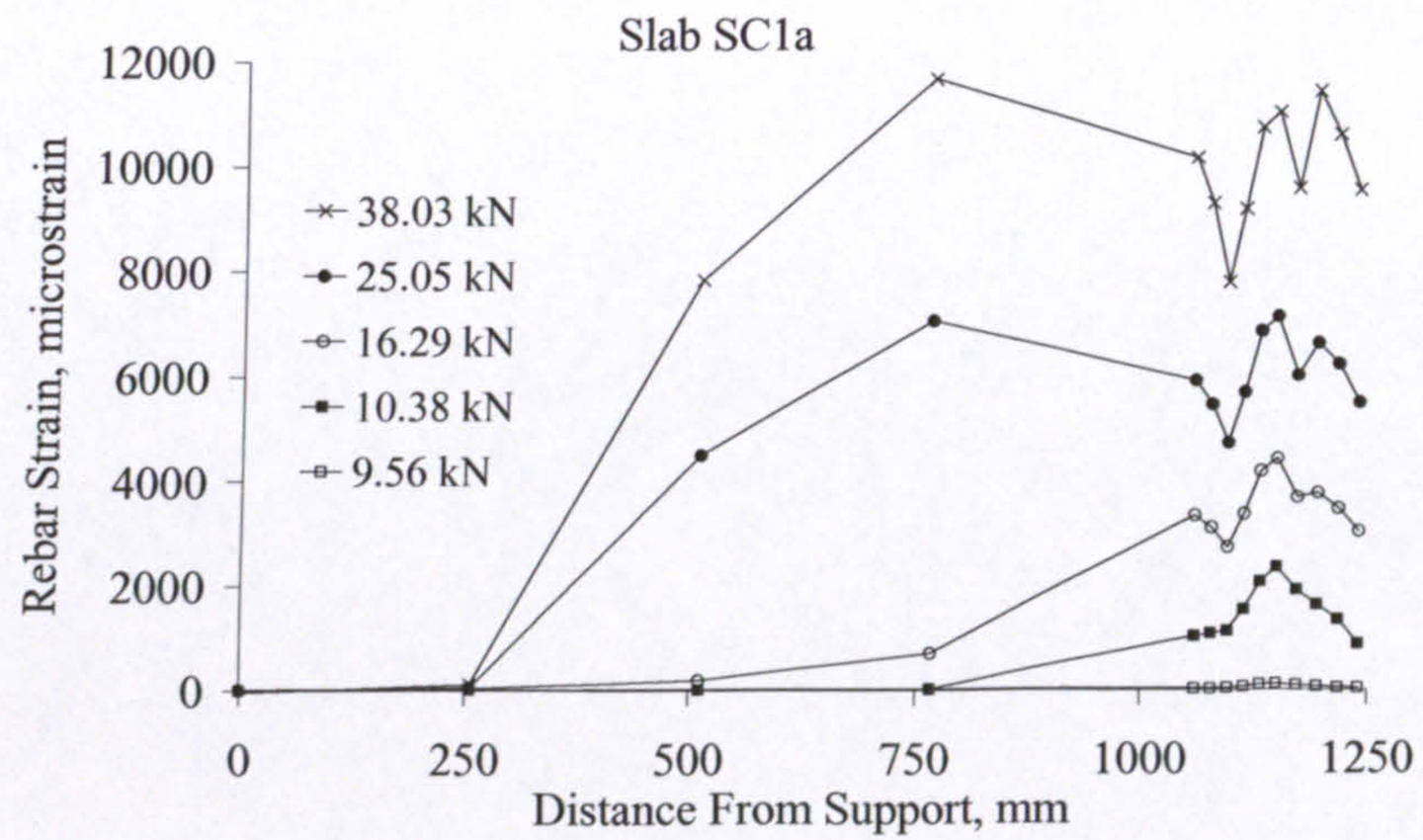
Slab SC1a
Rebar Strain, microstrain
12000
10000
8000
6000
4000
2000
0
38.03 kN
25.05 kN
16.29 kN
10.38 kN
9.56 kN
0
250
500
750
1000
1250
Distance From Support, mm

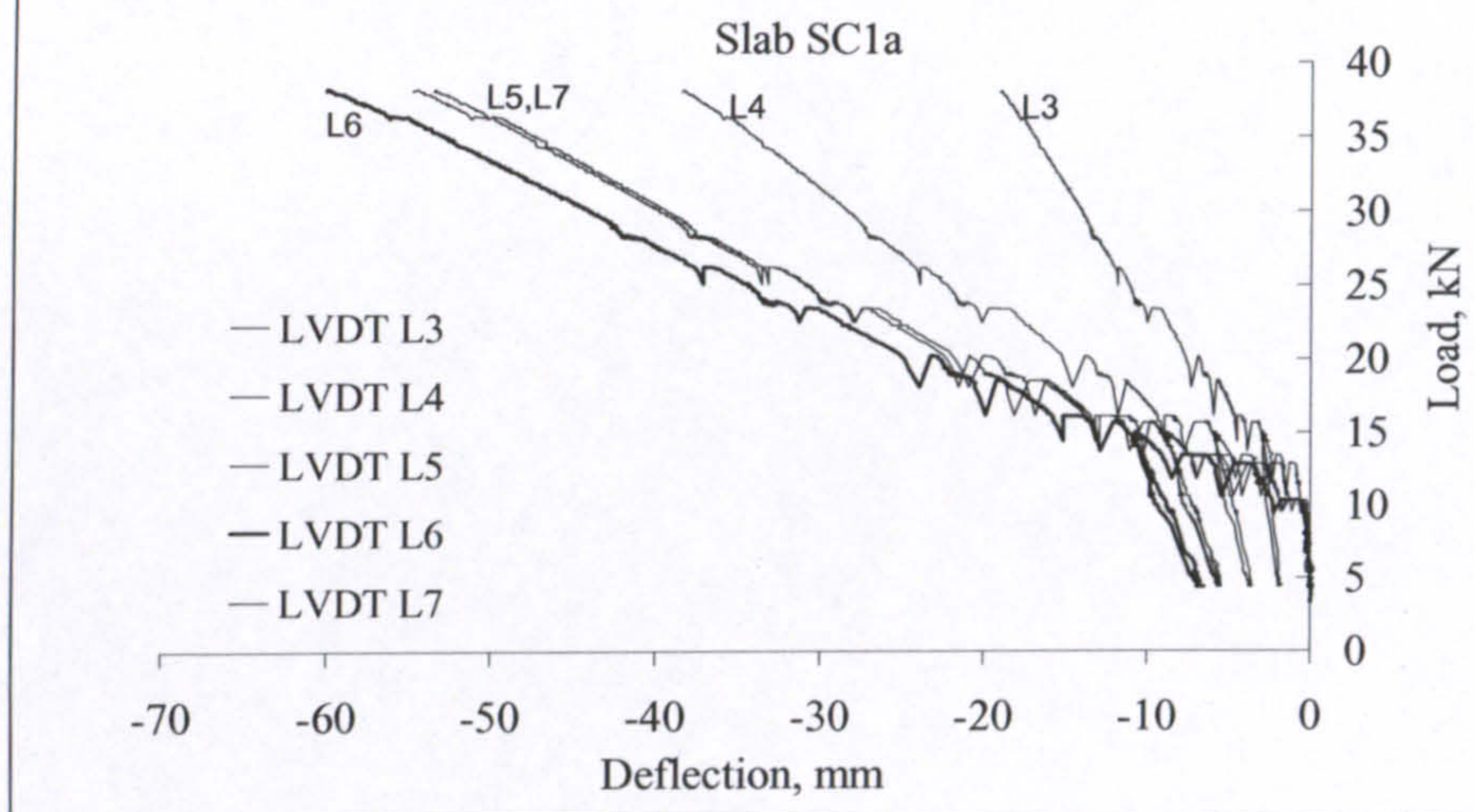
Slab SC1a
L6
L5,L7
L4
L3
LVDT L3
LVDT L4
LVDT L5
LVDT L6
LVDT L7
Load, kN
40
35
30
25
20
15
10
5
0
-70
-60
-50
-40
-30
-20
-10
0
Deflection, mm

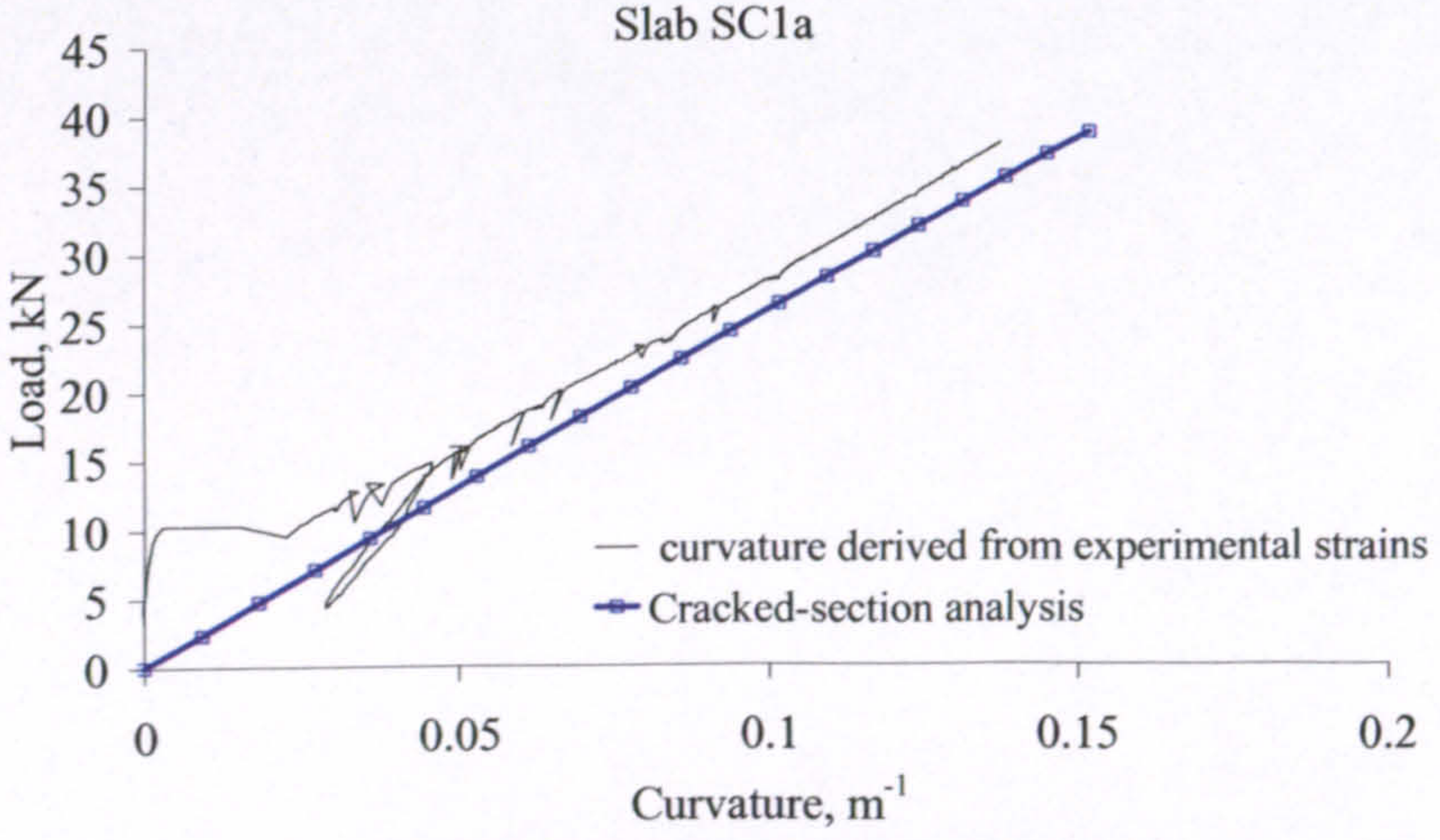
Slab SC1a
Load, kN
45
40
35
30
25
20
15
10
5
0
curvature derived from experimental strains
Cracked-section analysis
0
0.05
0.1
0.15
0.2
Curvature, m-1

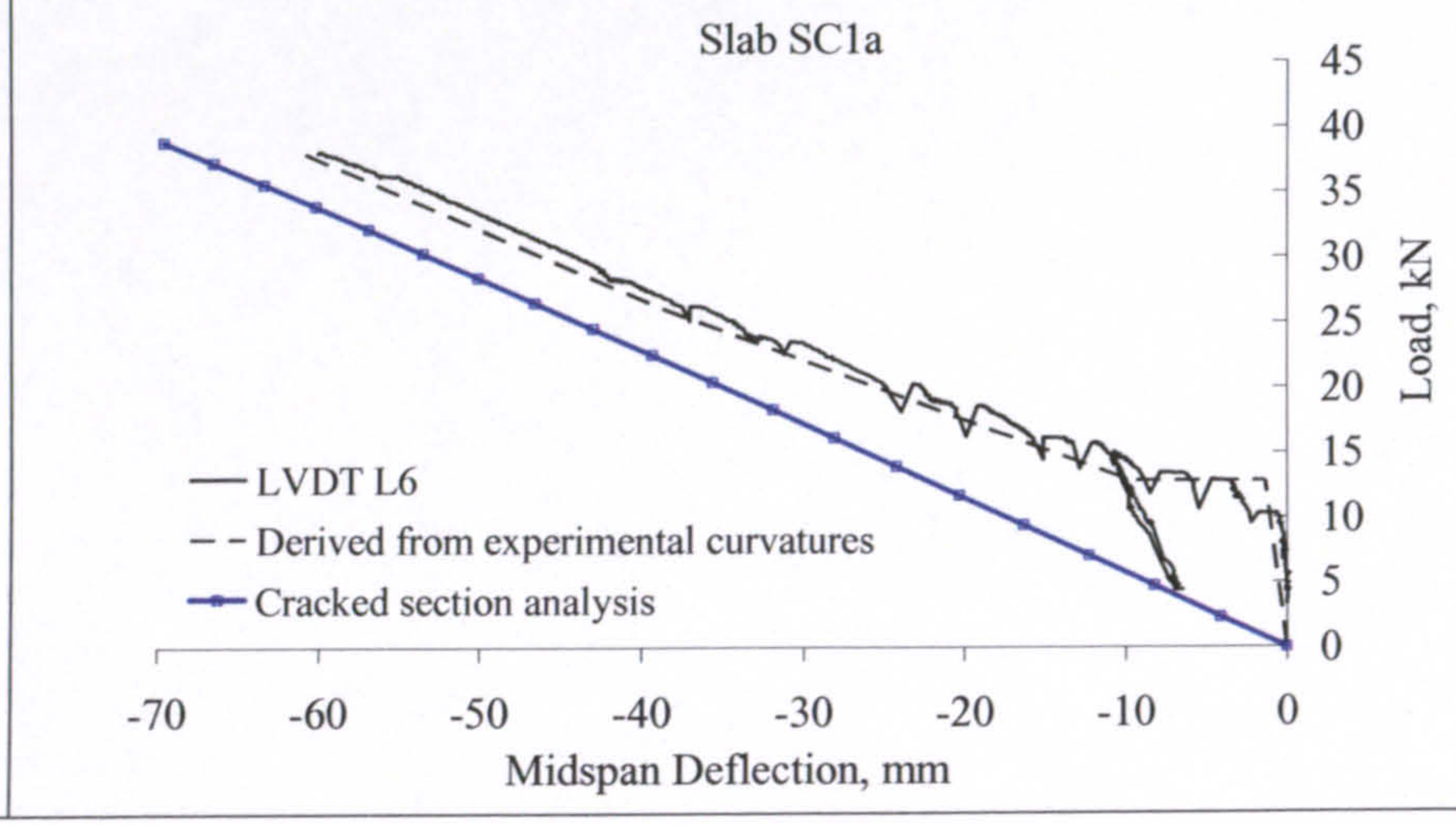
Slab SC1a
Load, kN
45
40
35
30
25
20
15
10
5
0
LVDT L6
Derived from experimental curvatures
Cracked section analysis
-70
-60
-50
-40
-30
-20
-10
0
Midspan Deflection, mm

SLAB SC1a

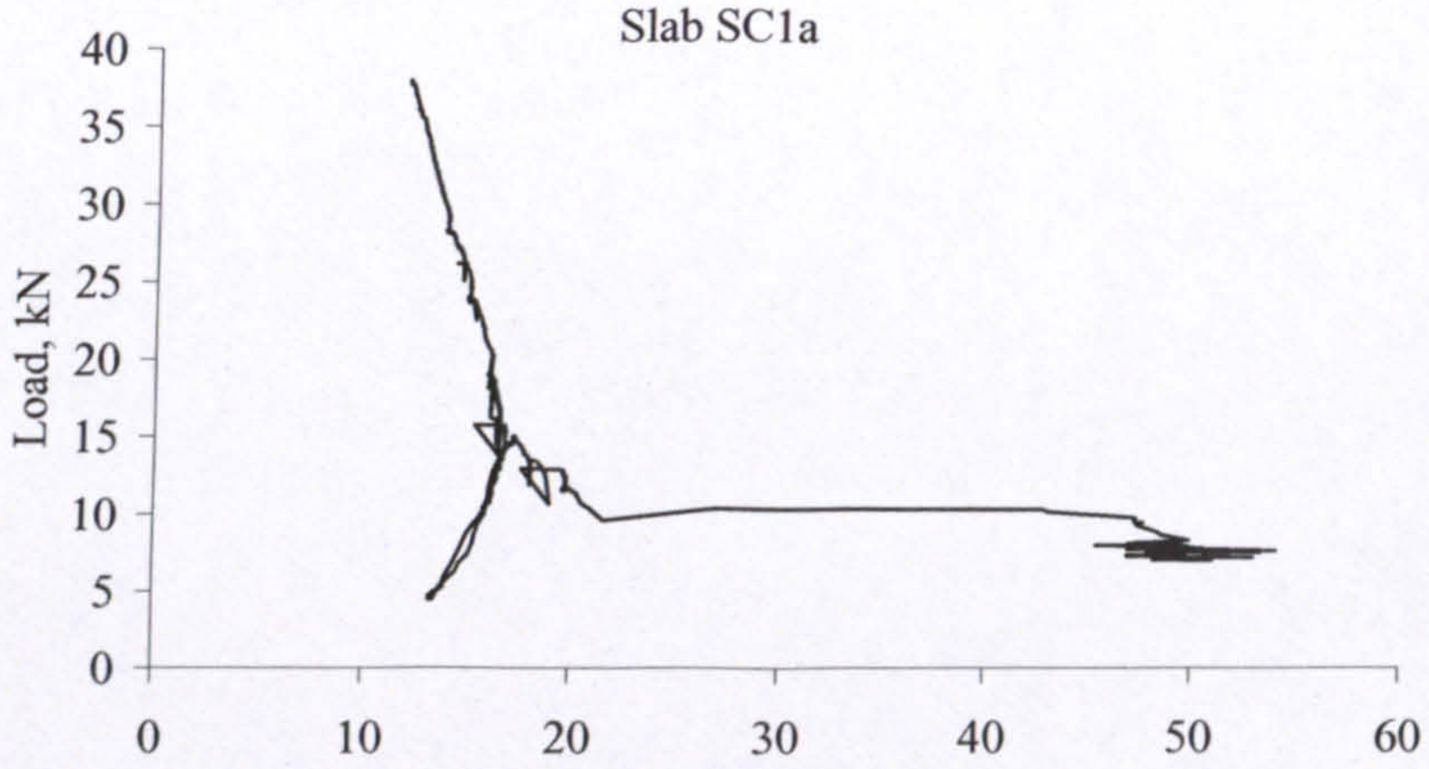
Slab SC1a
Load, kN
0
5
10
15
20
25
30
35
40
0
10
20
30
40
50
60
Average Neutral Axis depth, mm

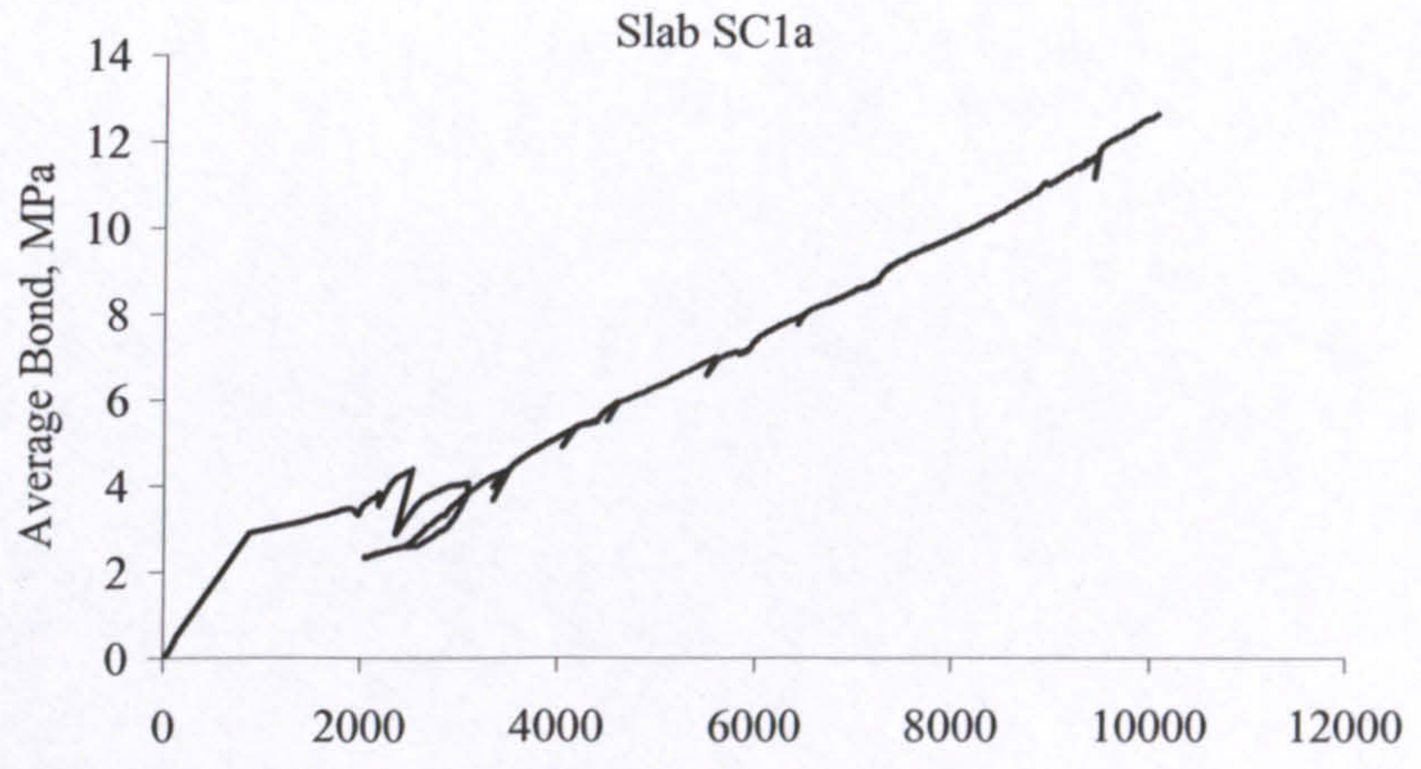
Slab SC1a
Average Bond, MPa
0
2
4
6
8
10
12
14
0
2000
4000
6000
8000
10000
12000
Average Strain Between Cracks, microstrain

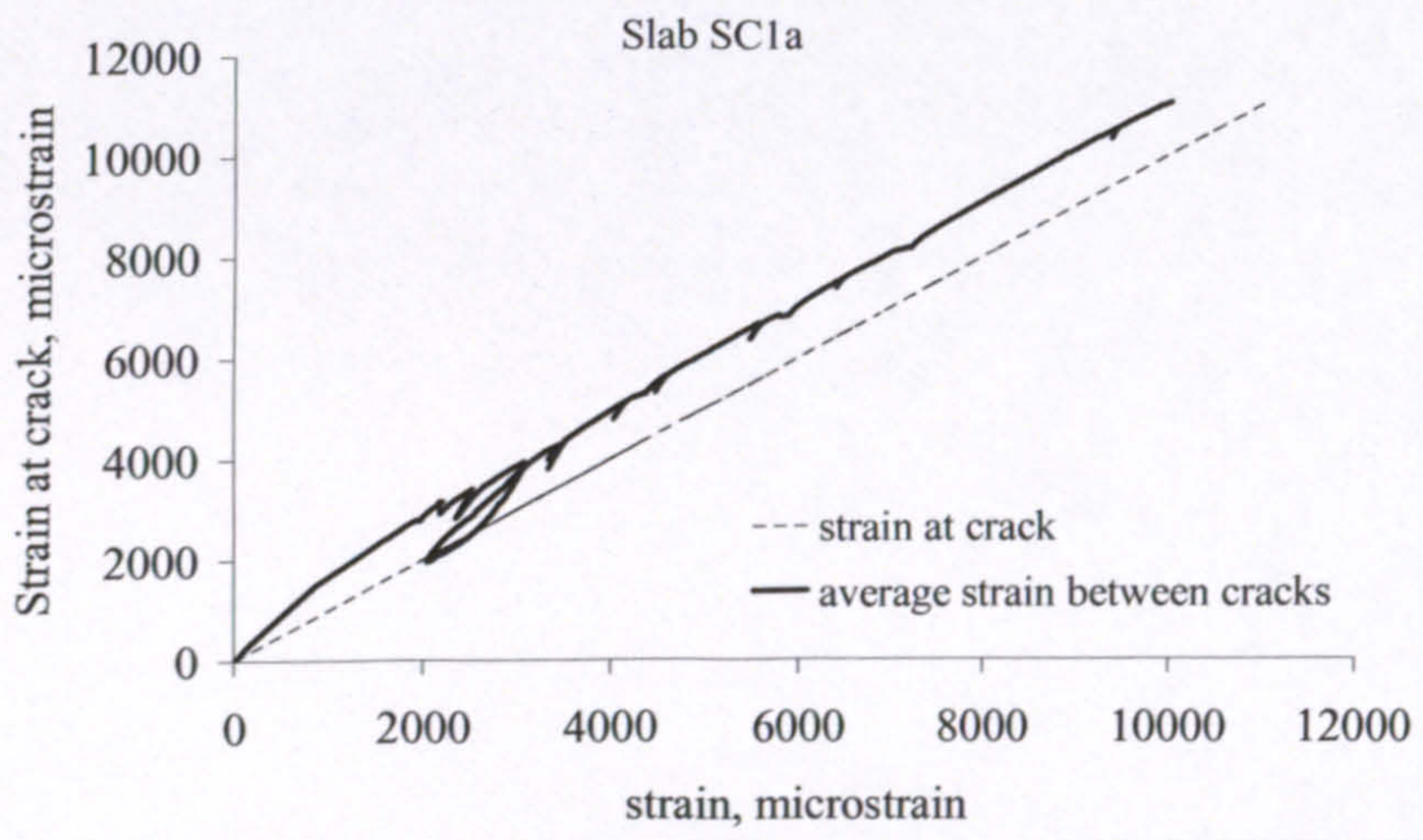
Slab SC1a
Strain at crack, microstrain
0
2000
4000
6000
8000
10000
12000
strain at crack
average strain between cracks
0
2000
4000
6000
8000
10000
12000
strain, microstrain

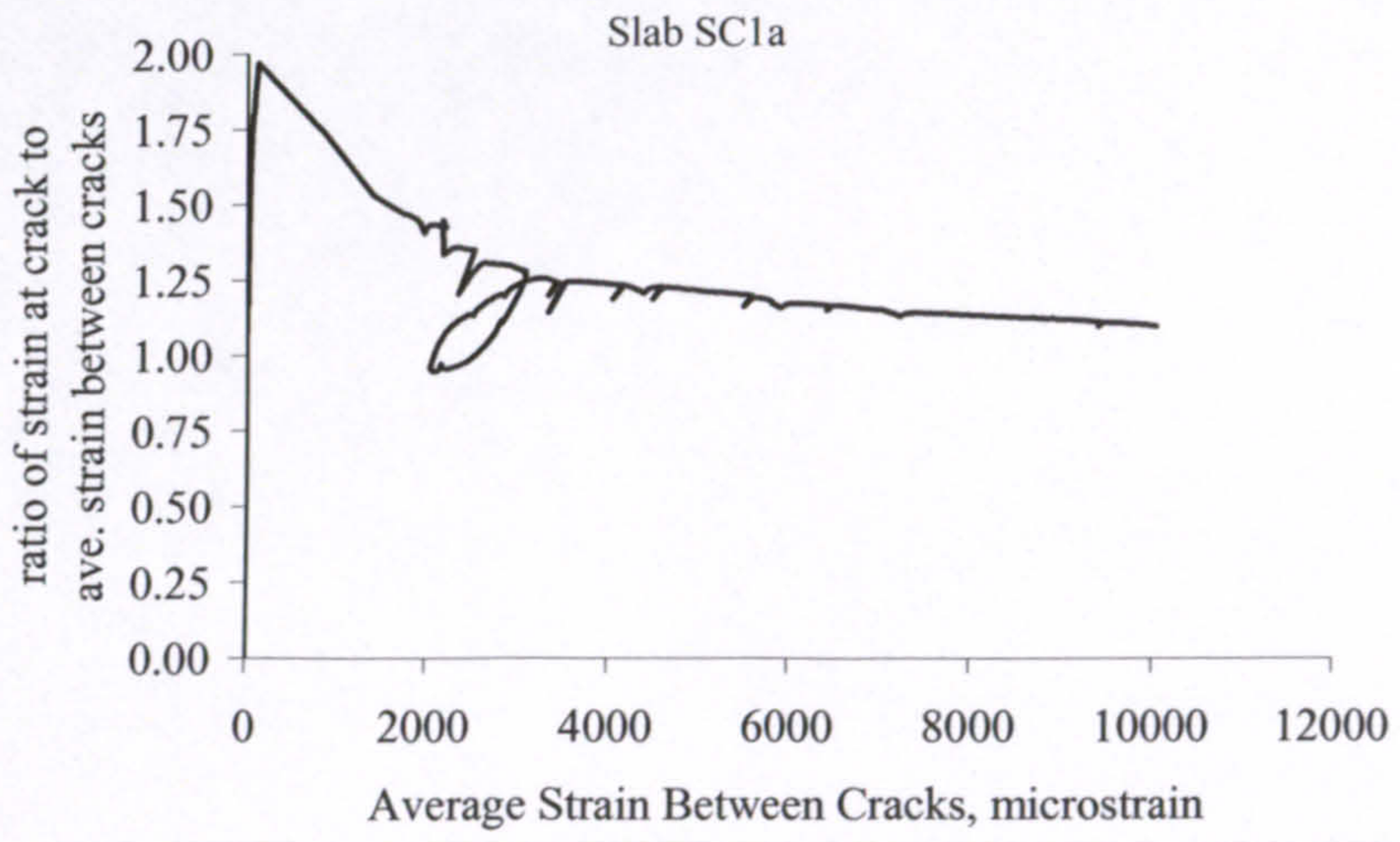
Slab SC1a
ratio of strain at crack to ave. strain between cracks
0.00
0.25
0.50
0.75
1.00
1.25
1.50
1.75
2.00
0
2000
4000
6000
8000
10000
12000
Average Strain Between Cracks, microstrain

SLAB SC1a

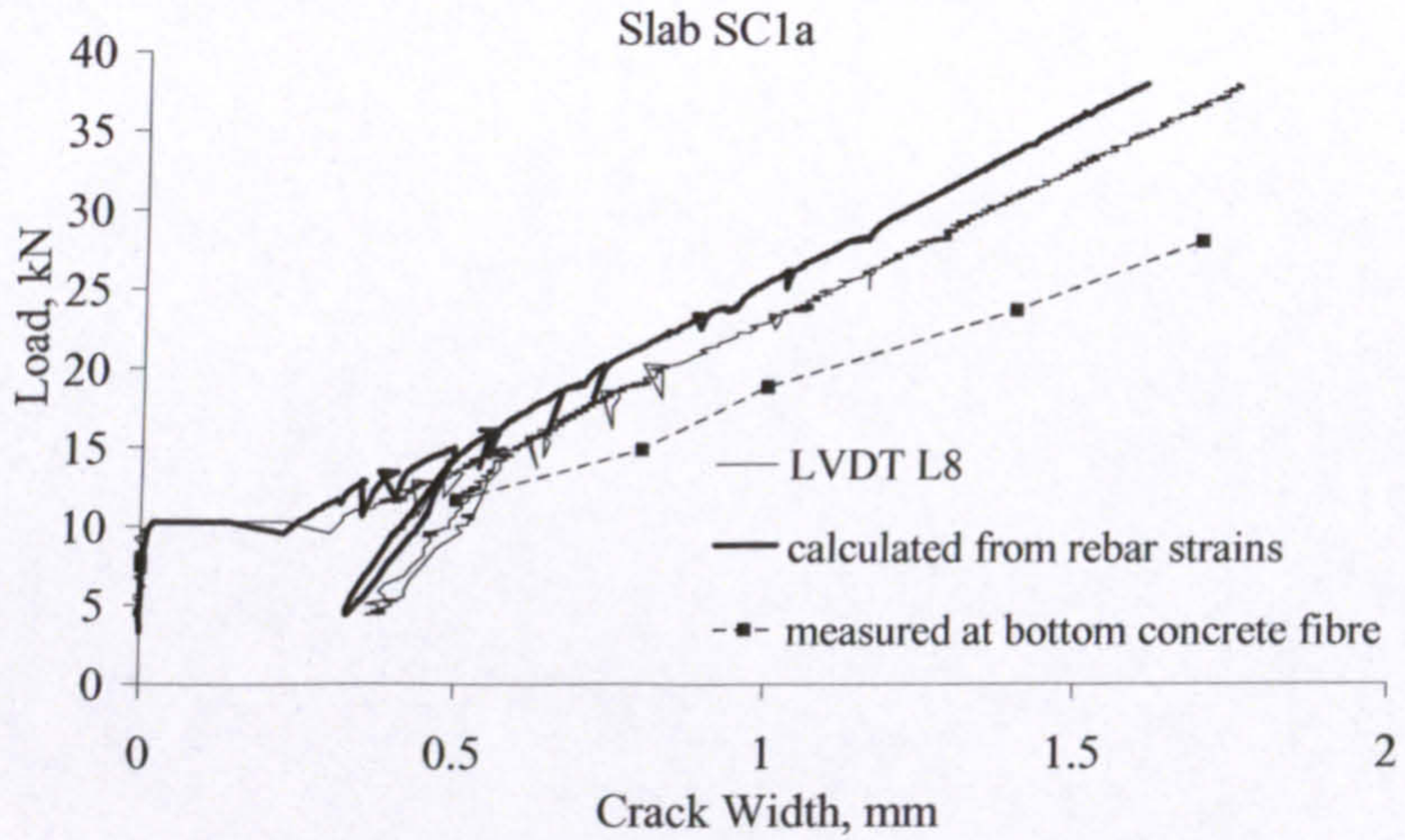

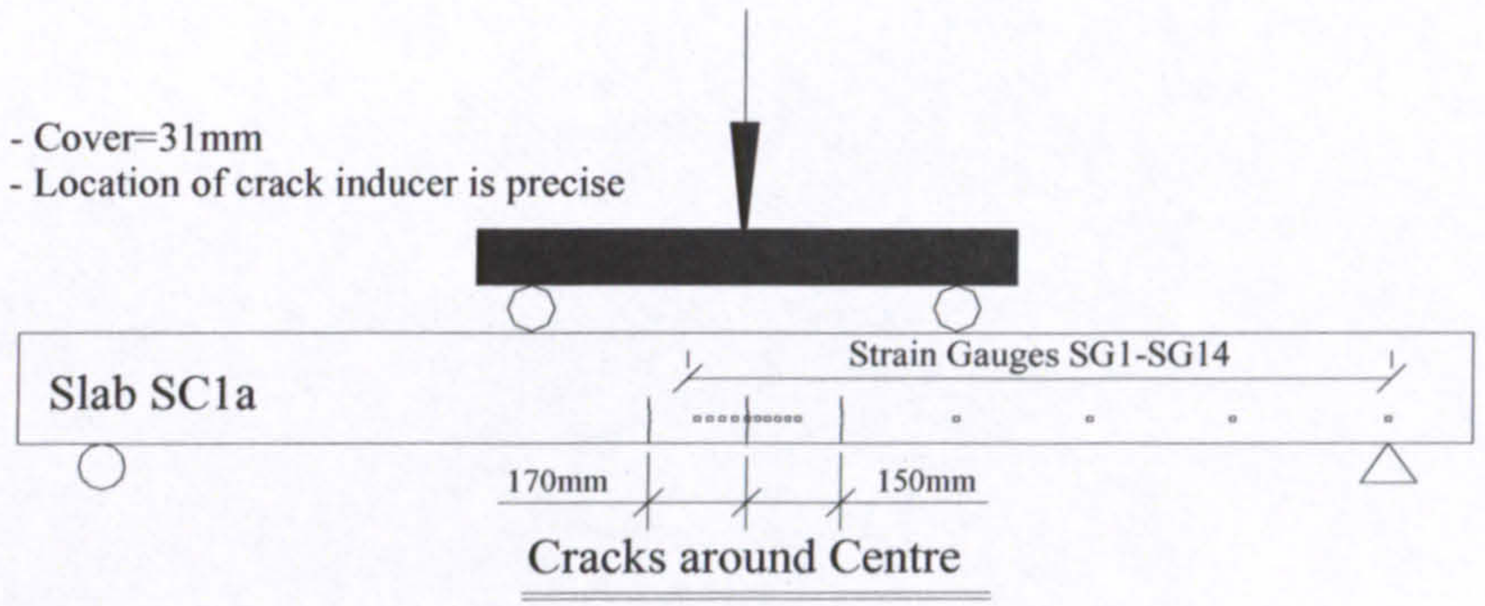

Failure by rupture of rebars.

SLAB SC1b

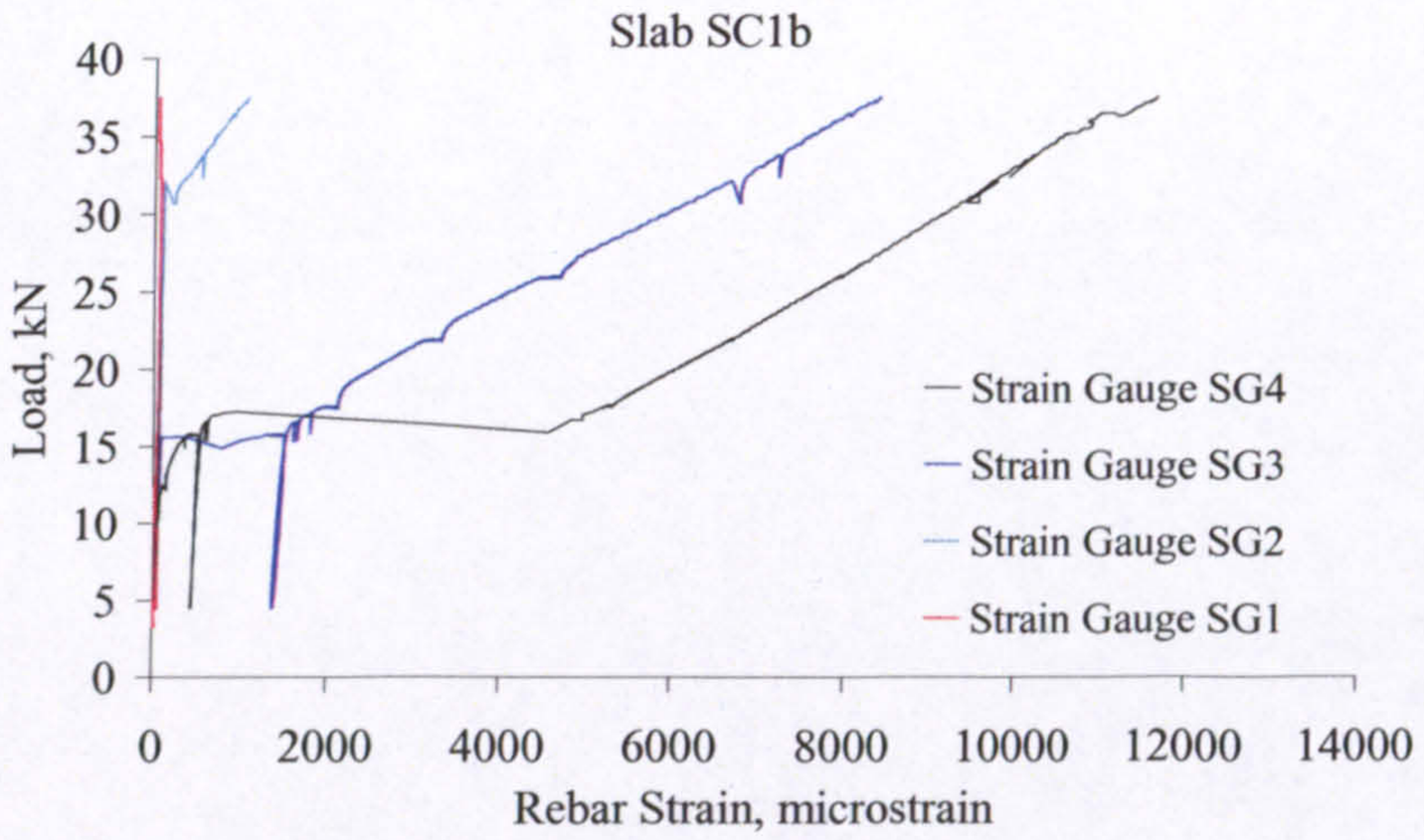
Slab SC1b
Load, kN
Rebar Strain, microstrain
Strain Gauge SG4
Strain Gauge SG3
Strain Gauge SG2
Strain Gauge SG1

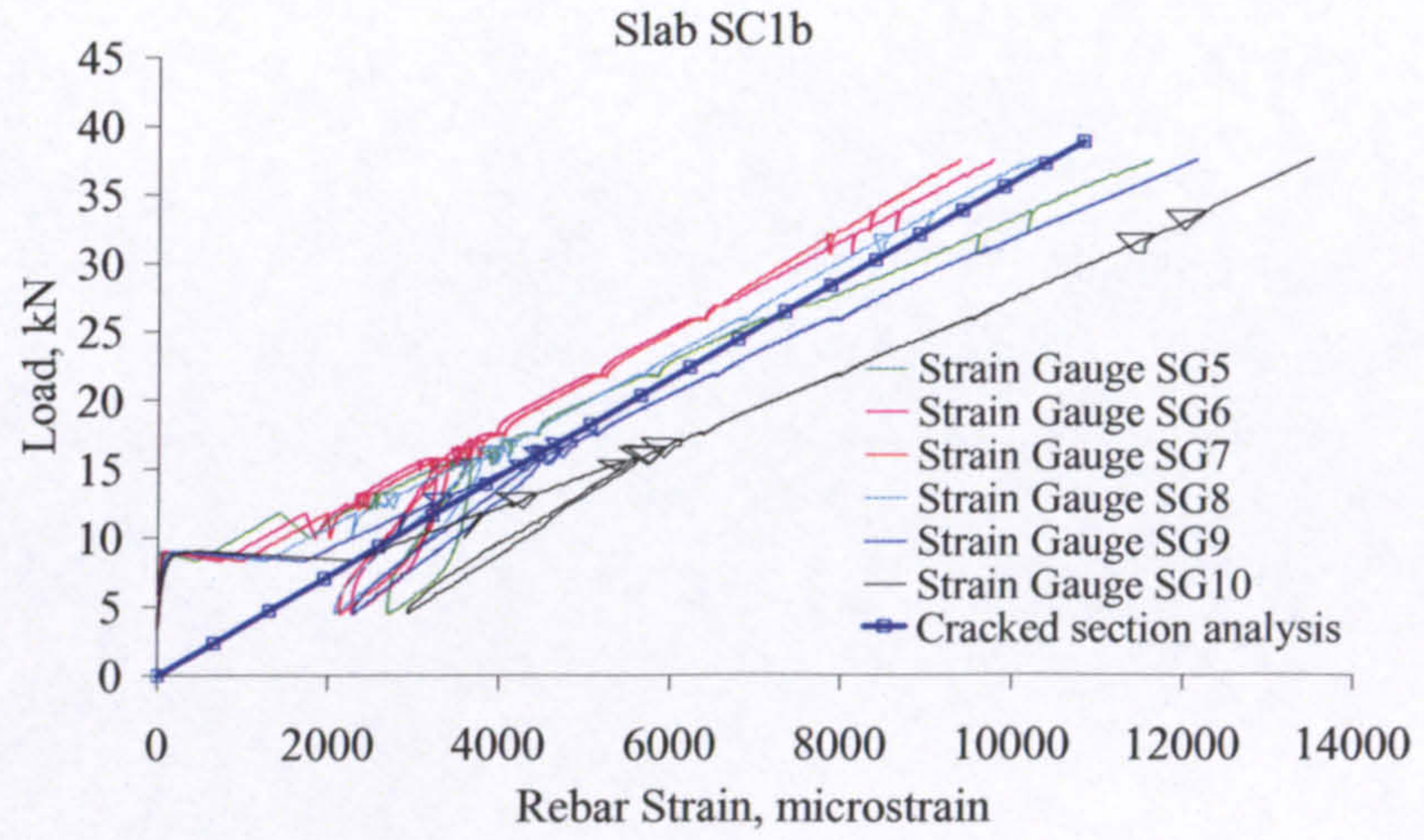
Slab SC1b
Load, kN
Rebar Strain, microstrain
Strain Gauge SG5
Strain Gauge SG6
Strain Gauge SG7
Strain Gauge SG8
Strain Gauge SG9
Strain Gauge SG10
Cracked section analysis

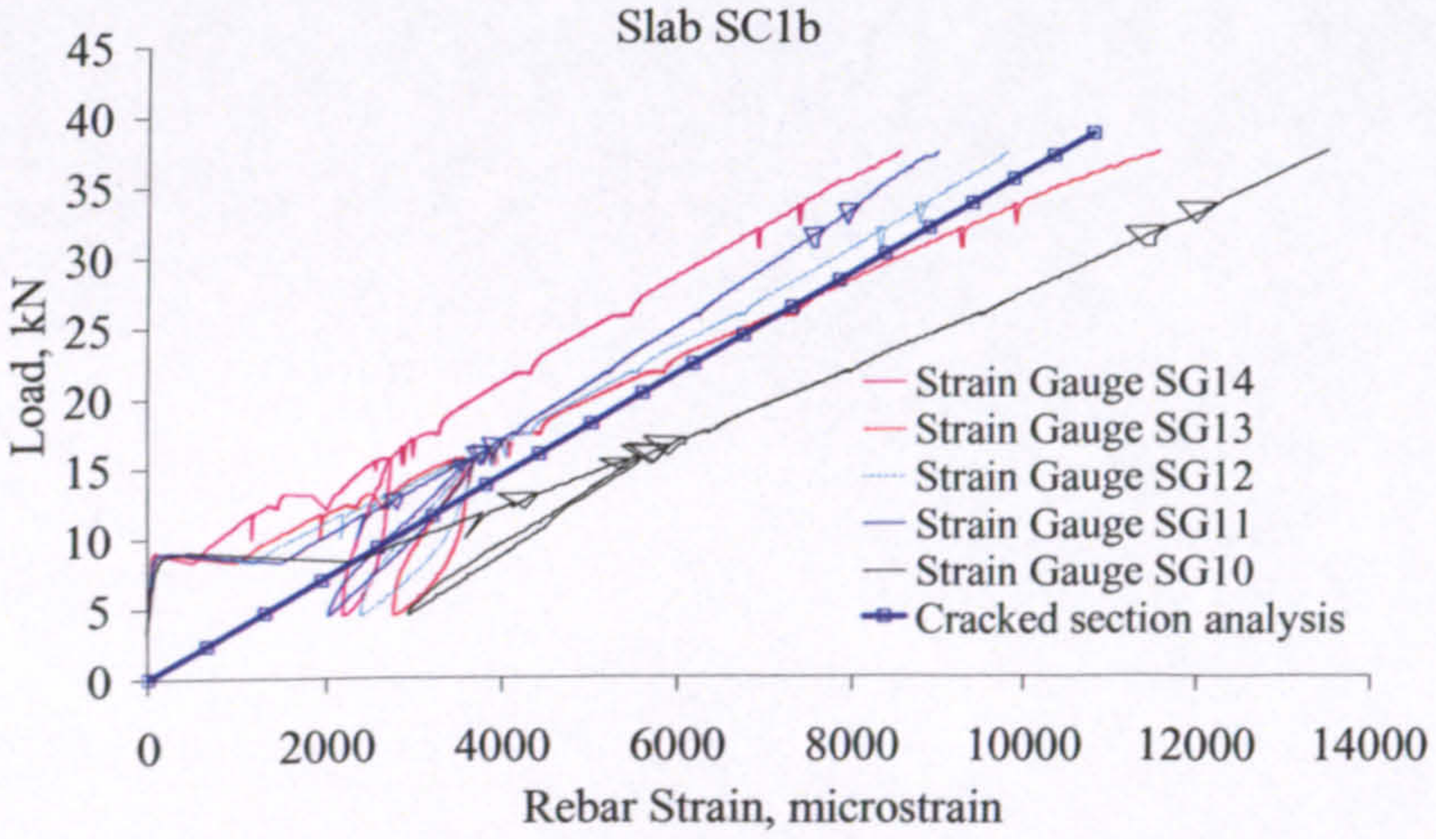
Slab SC1b
Load, kN
Rebar Strain, microstrain
Strain Gauge SG14
Strain Gauge SG13
Strain Gauge SG12
Strain Gauge SG11
Strain Gauge SG10
Cracked section analysis

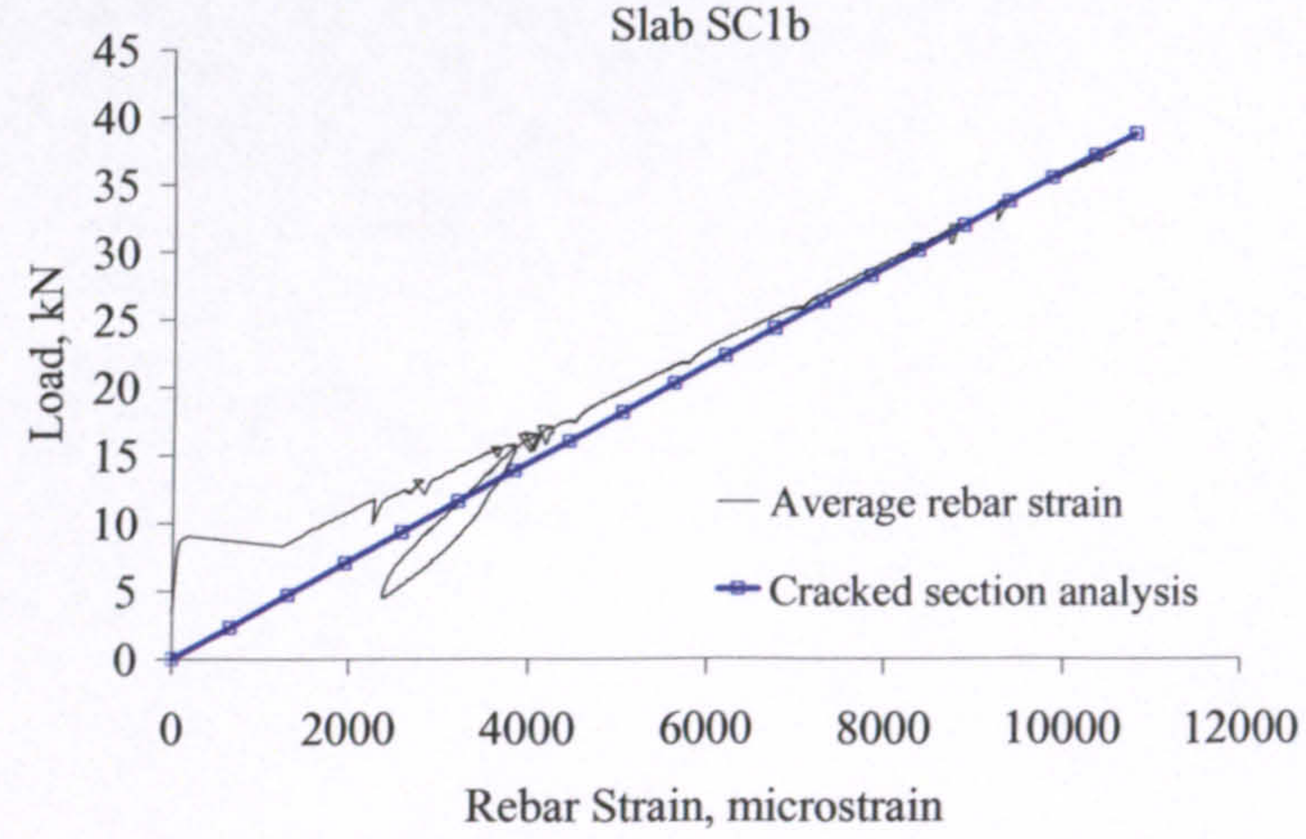
Slab SC1b
Load, kN
Rebar Strain, microstrain
Average rebar strain
Cracked section analysis

SLAB SC1b

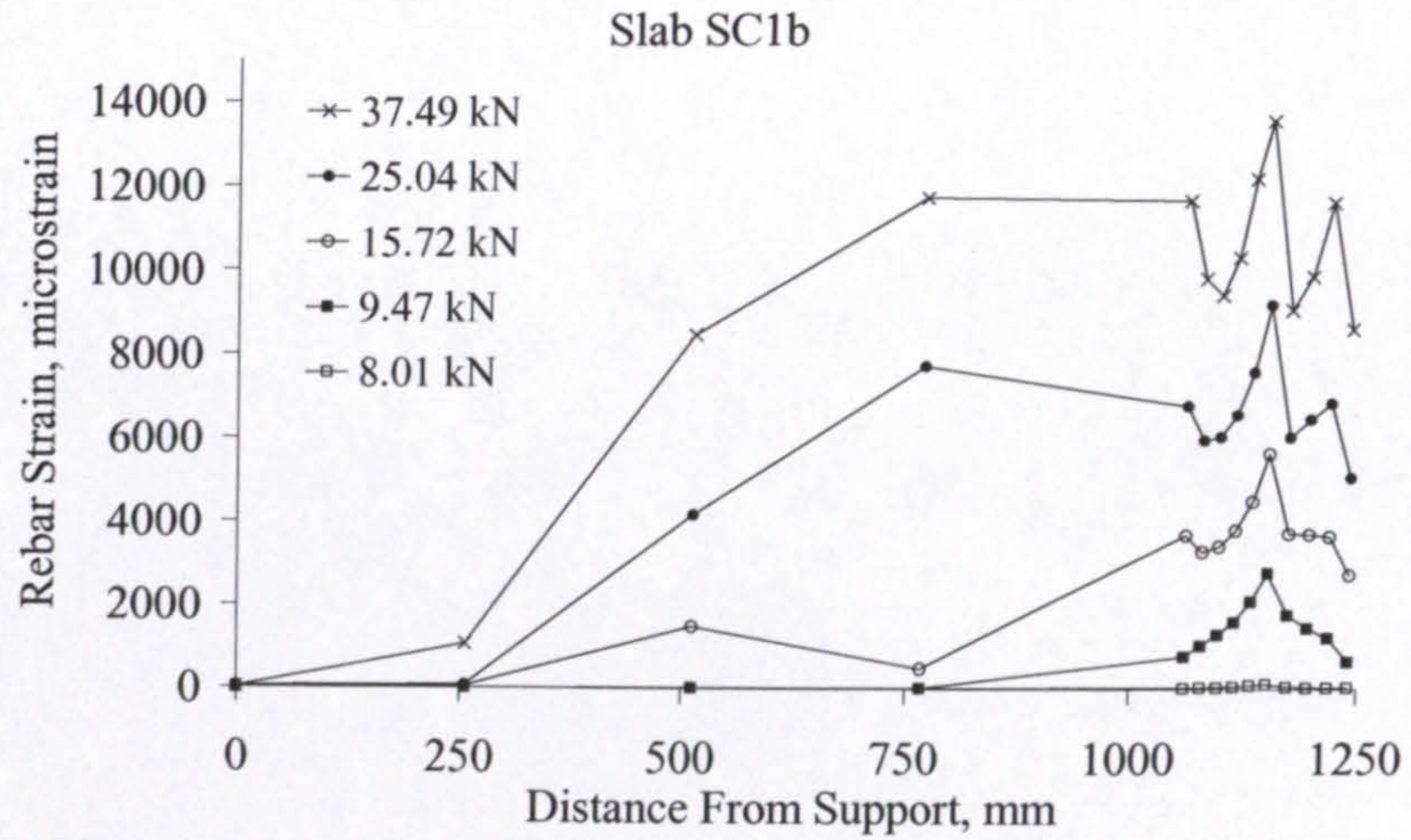
Slab SC1b
Rebar Strain, microstrain
14000
12000
10000
8000
6000
4000
2000
0
37.49 kN
25.04 kN
15.72 kN
9.47 kN
8.01 kN
0
250
500
750
1000
1250
Distance From Support, mm

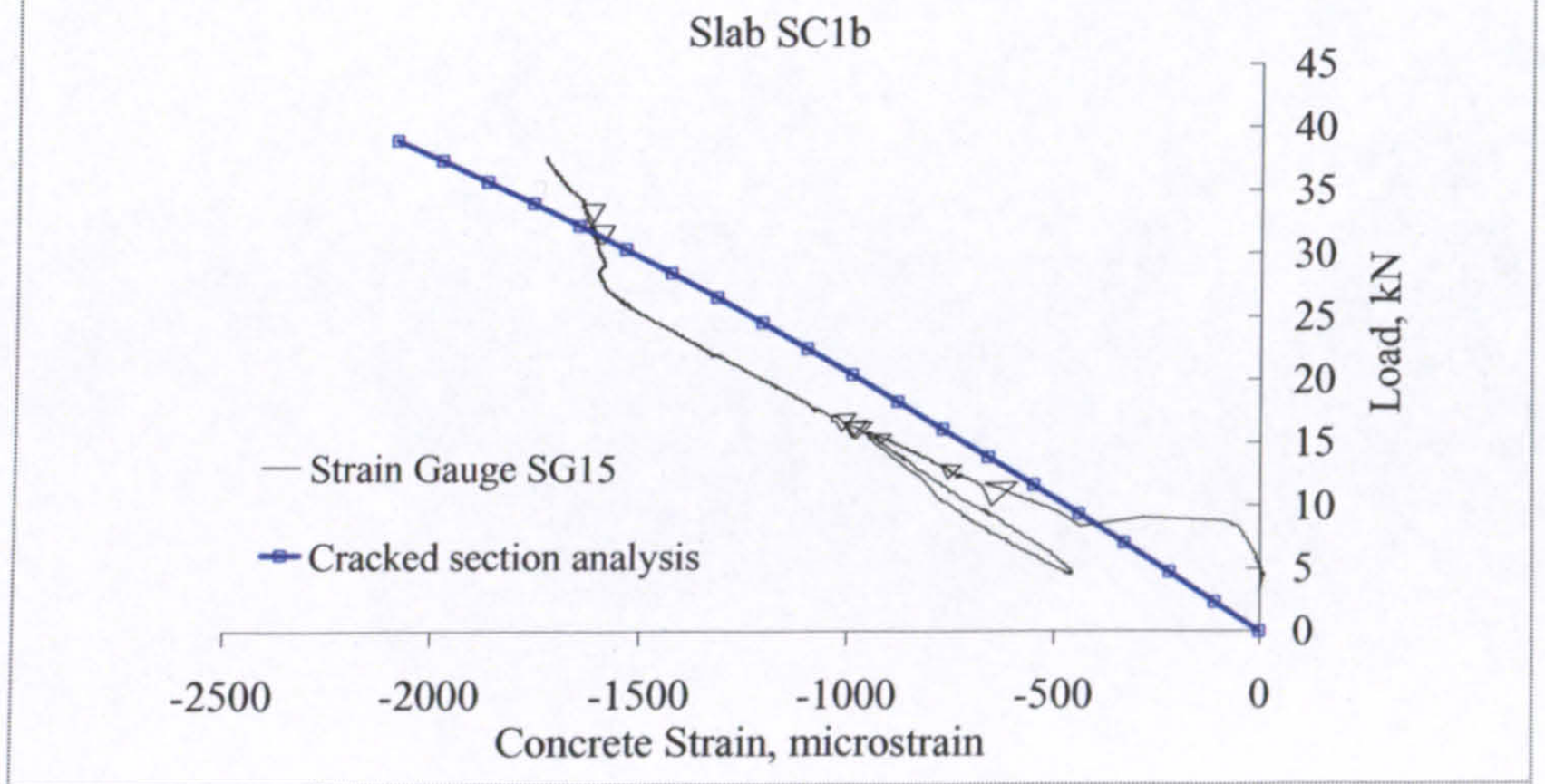
Slab SC1b
Load, kN
45
40
35
30
25
20
15
10
5
0
Strain Gauge SG15
Cracked section analysis
-2500
-2000
-1500
-1000
-500
0
Concrete Strain, microstrain

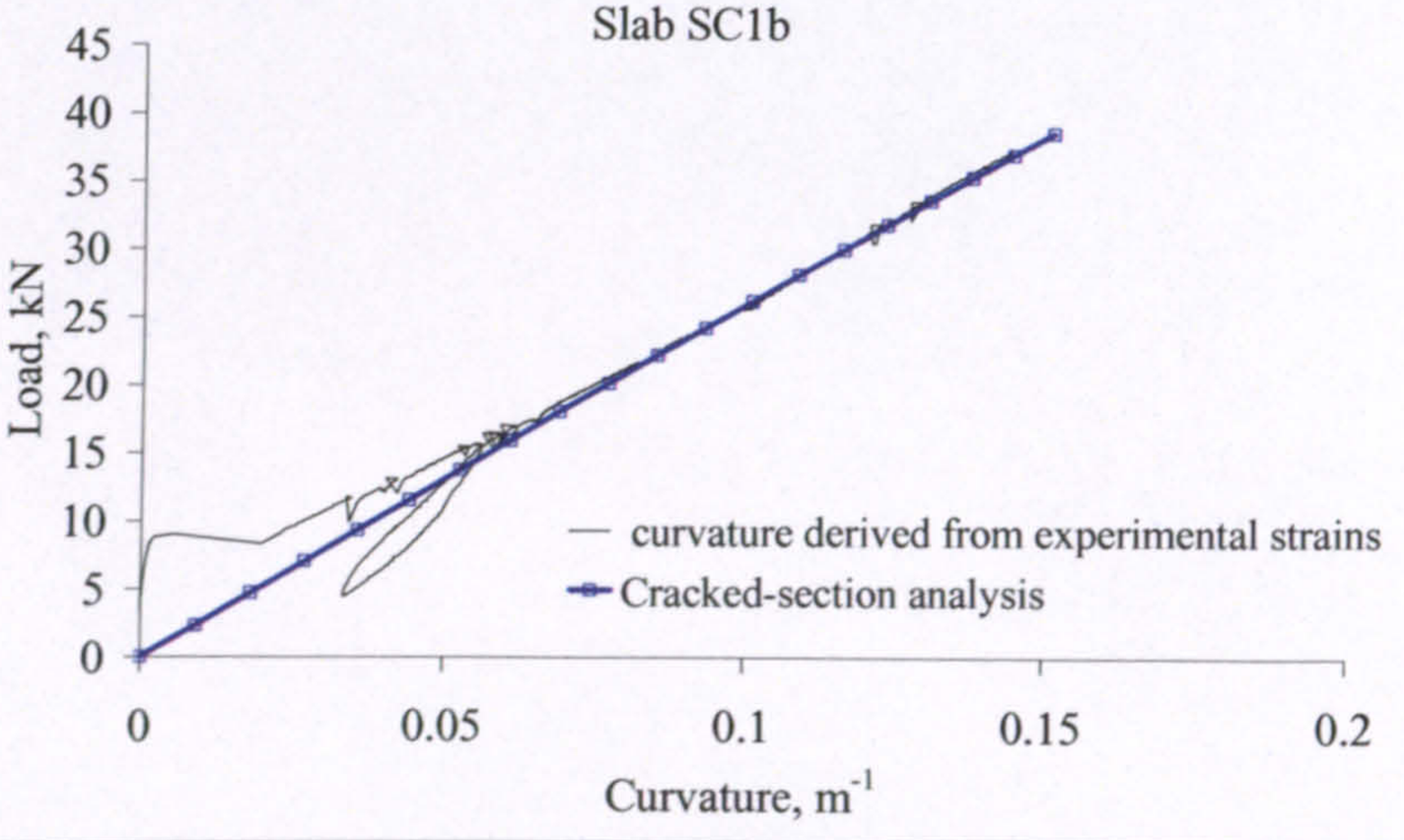
Slab SC1b
Load, kN
45
40
35
30
25
20
15
10
5
0
curvature derived from experimental strains
Cracked-section analysis
0
0.05
0.1
0.15
0.2
Curvature, m-1

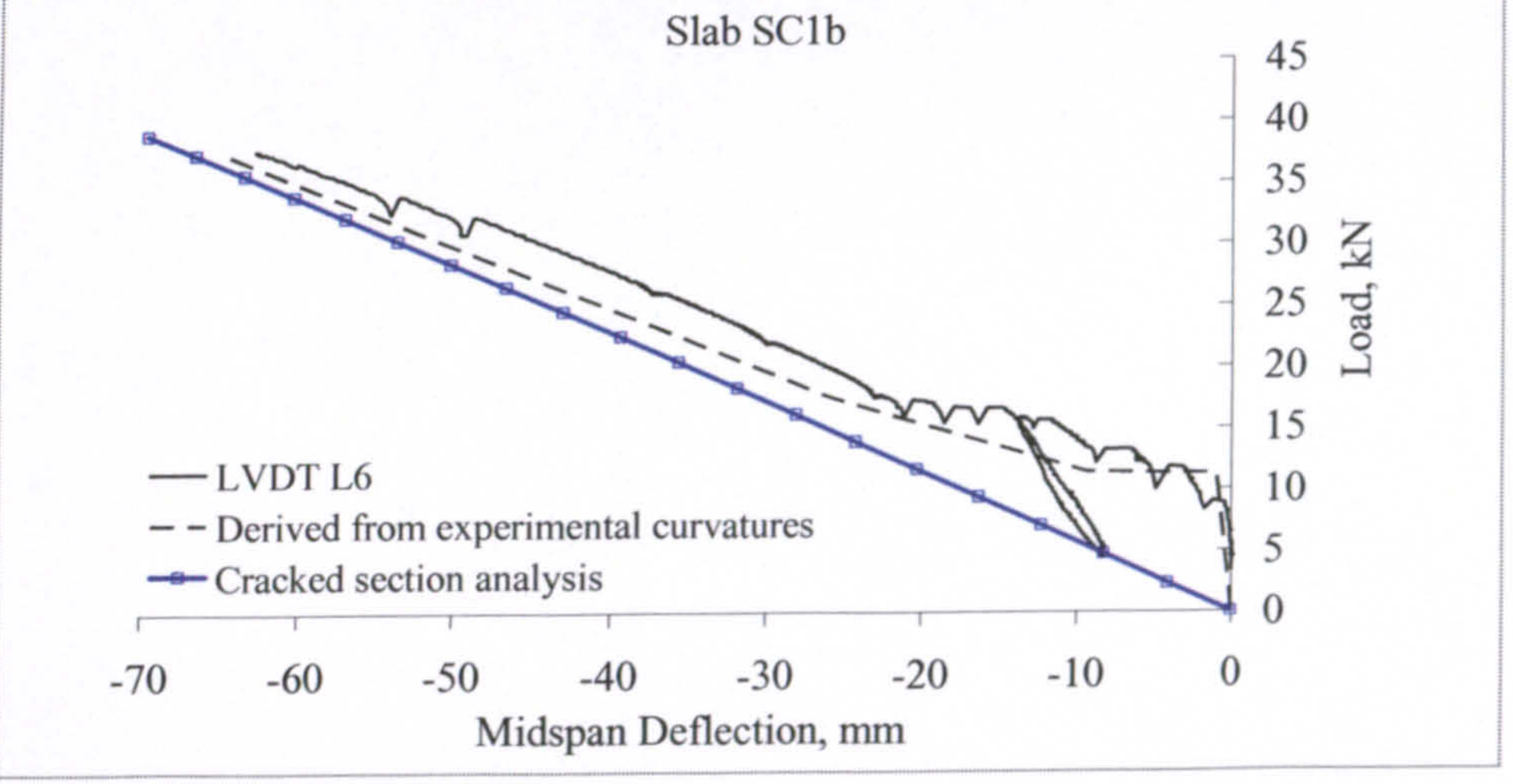
Slab SC1b
Load, kN
45
40
35
30
25
20
15
10
5
0
LVDT L6
Derived from experimental curvatures
Cracked section analysis
-70
-60
-50
-40
-30
-20
-10
0
Midspan Deflection, mm

SLAB SC1b

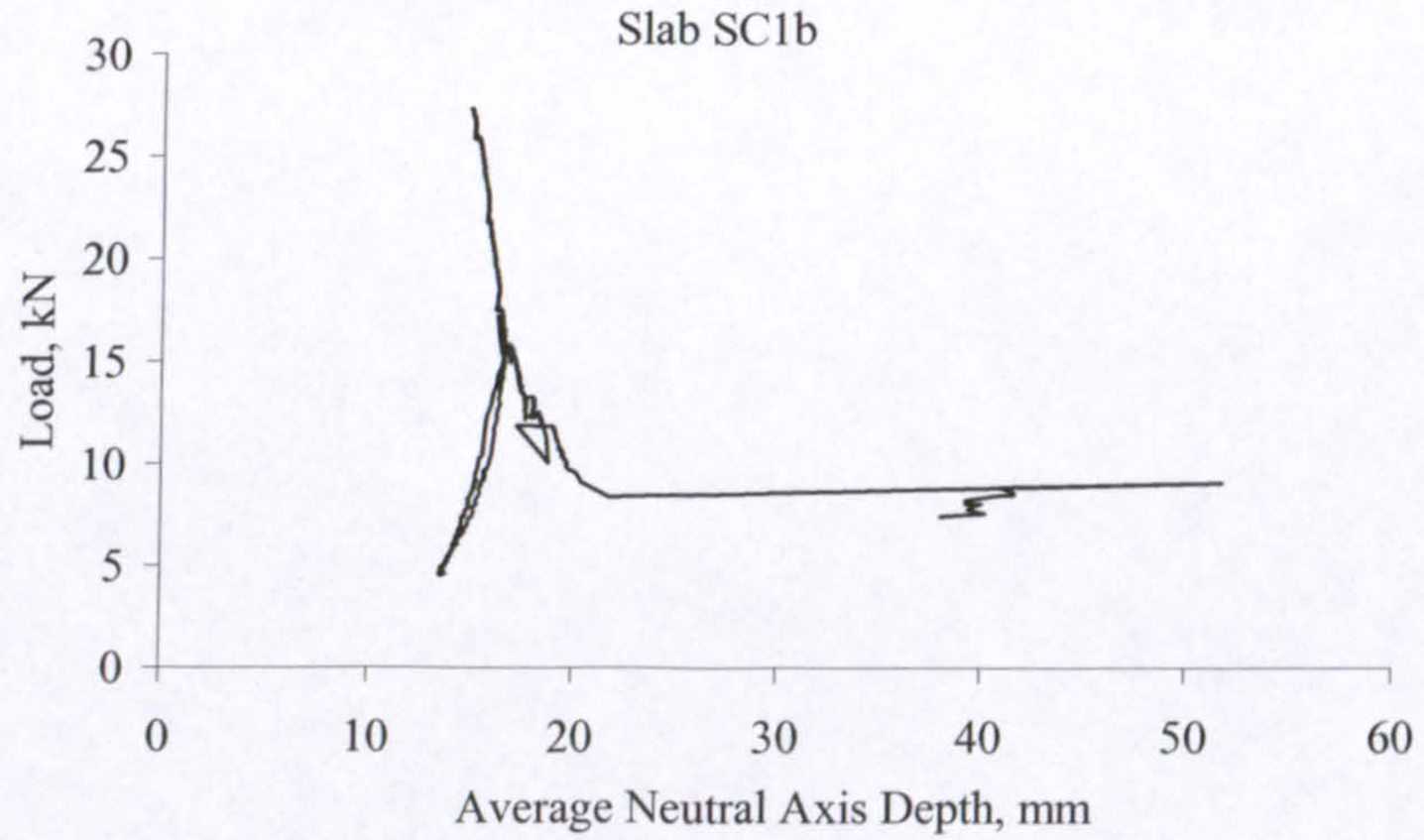
Slab SC1b
Load, kN
Average Neutral Axis Depth, mm
0
5
10
15
20
25
30
0
10
20
30
40
50
60

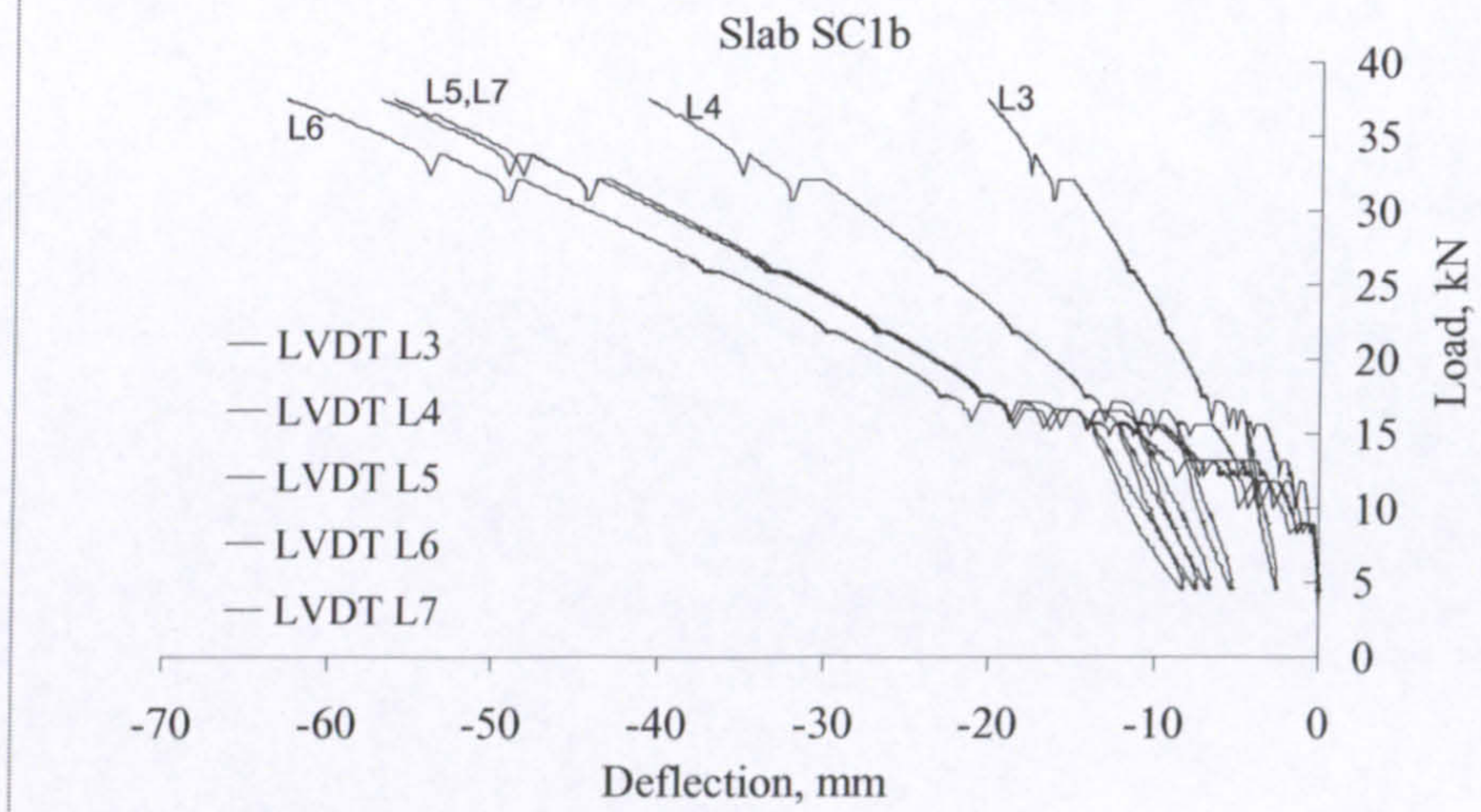
Slab SC1b
L6
L5,L7
L4
L3
LVDT L3
LVDT L4
LVDT L5
LVDT L6
LVDT L7
Load, kN
Deflection, mm
0
5
10
15
20
25
30
35
40
-70
-60
-50
-40
-30
-20
-10
0

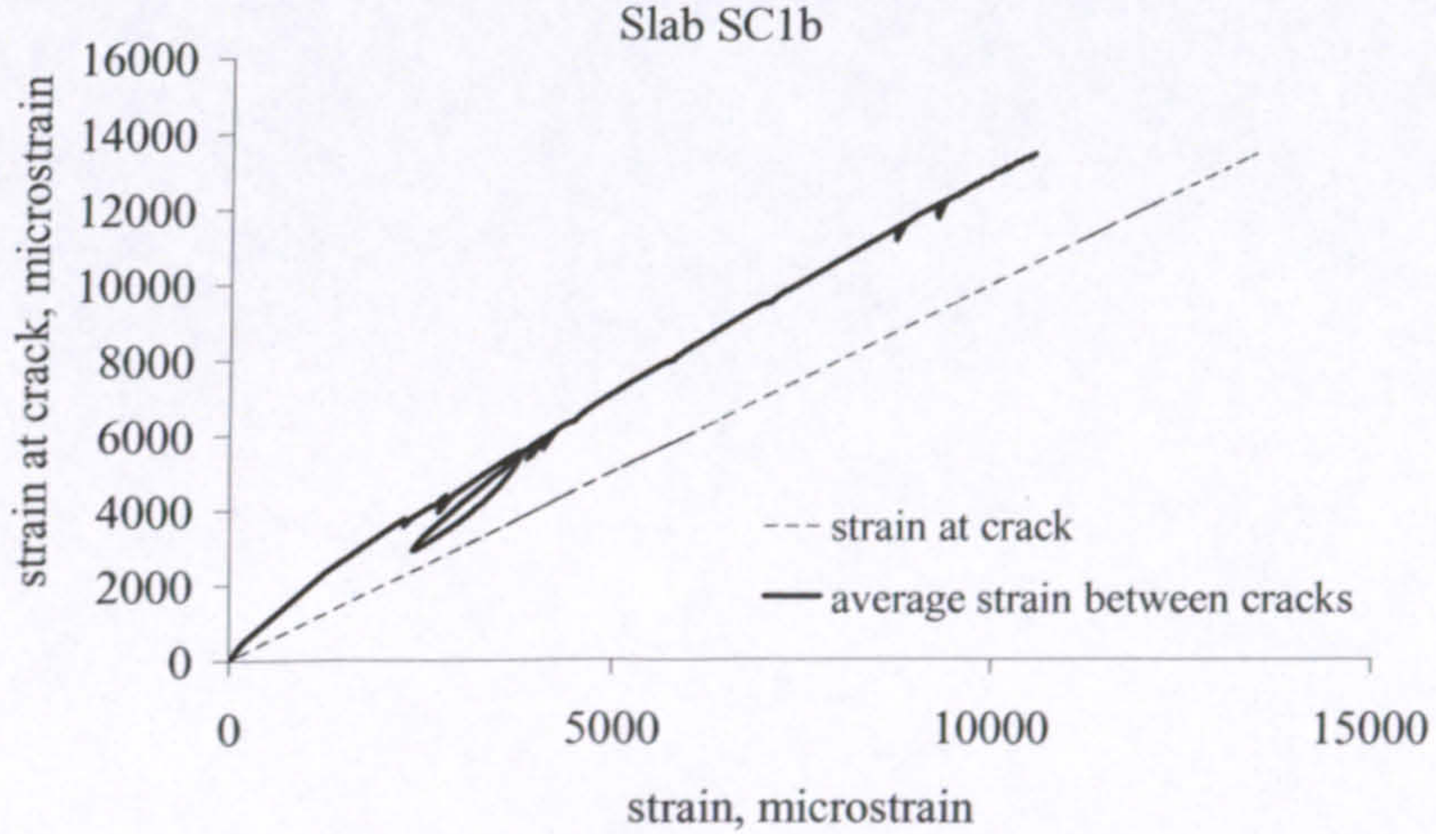
Slab SC1b
strain at crack, microstrain
strain, microstrain
strain at crack
average strain between cracks
0
2000
4000
6000
8000
10000
12000
14000
16000
0
5000
10000
15000

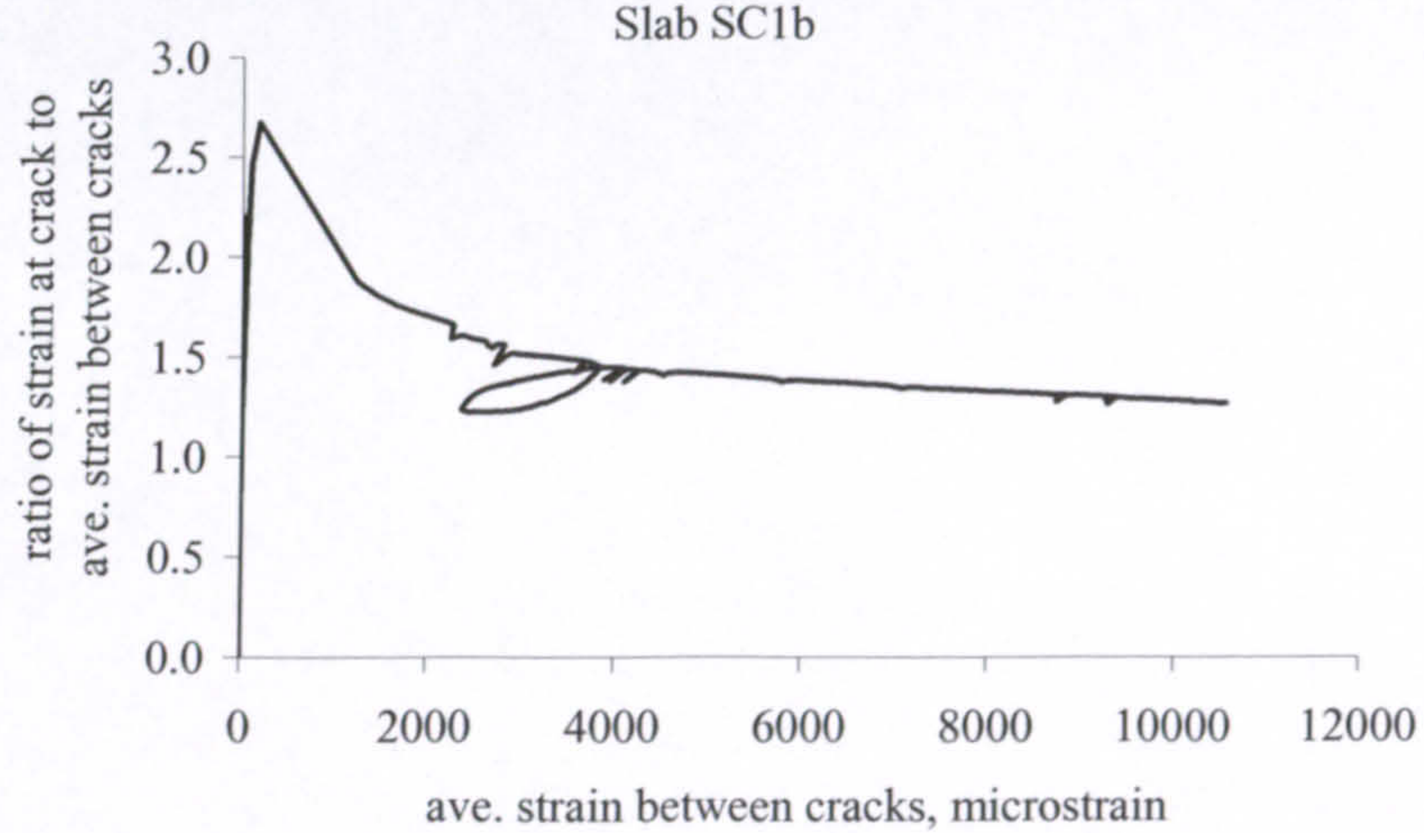
Slab SC1b
ratio of strain at crack to ave. strain between cracks
ave. strain between cracks, microstrain
0.0
0.5
1.0
1.5
2.0
2.5
3.0
0
2000
4000
6000
8000
10000
12000

SLAB SC1b

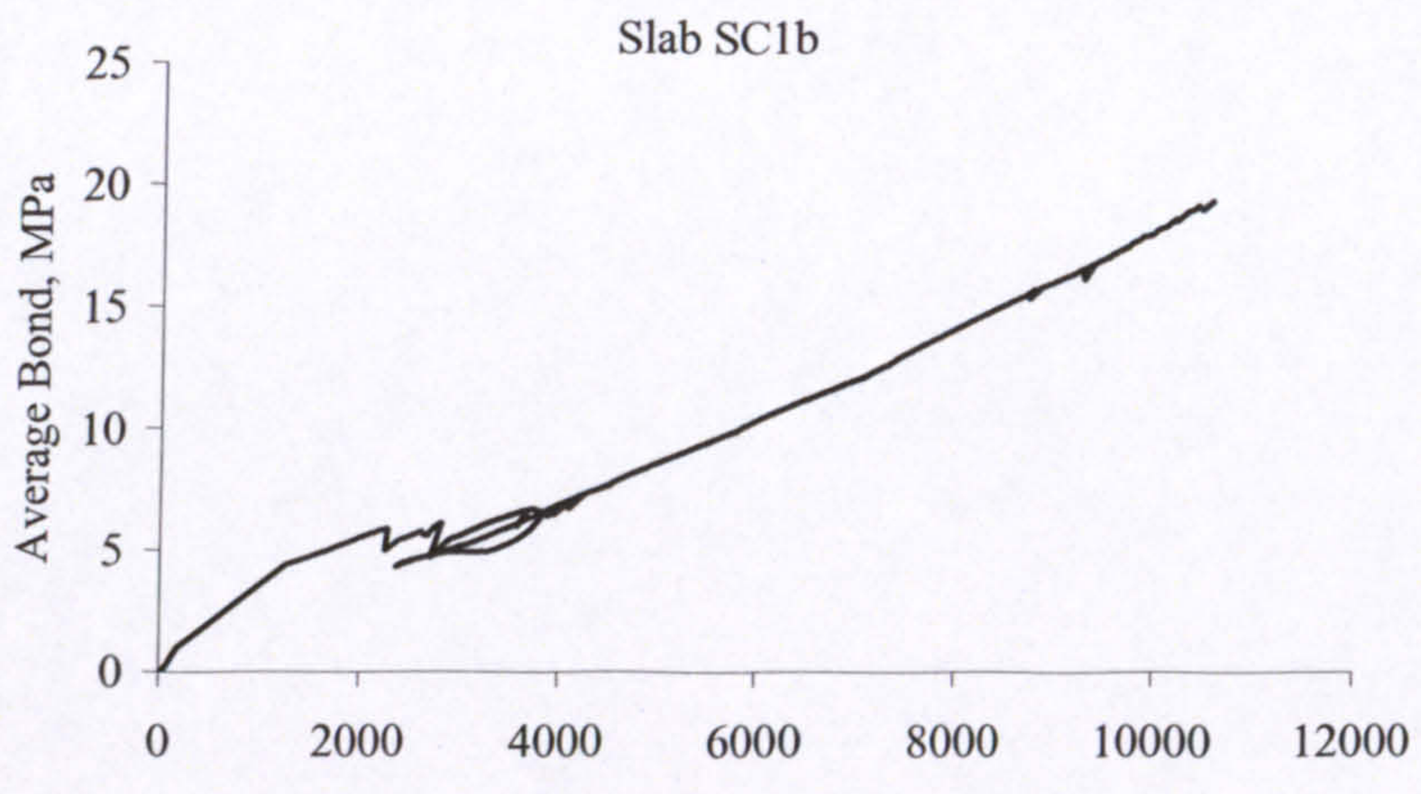

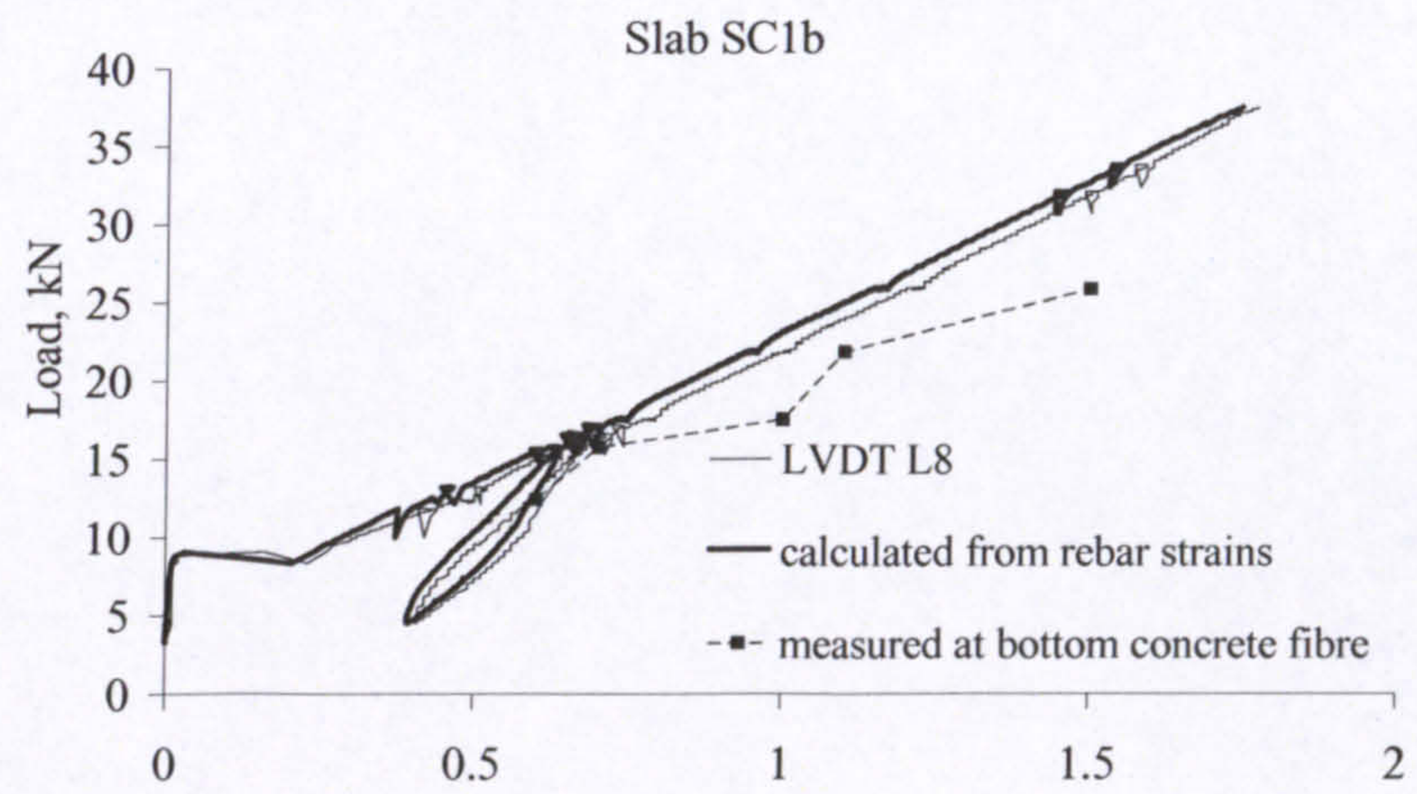

Failure by rupture of rebars.

- Cover=33mm
- Location of crack inducer is precise

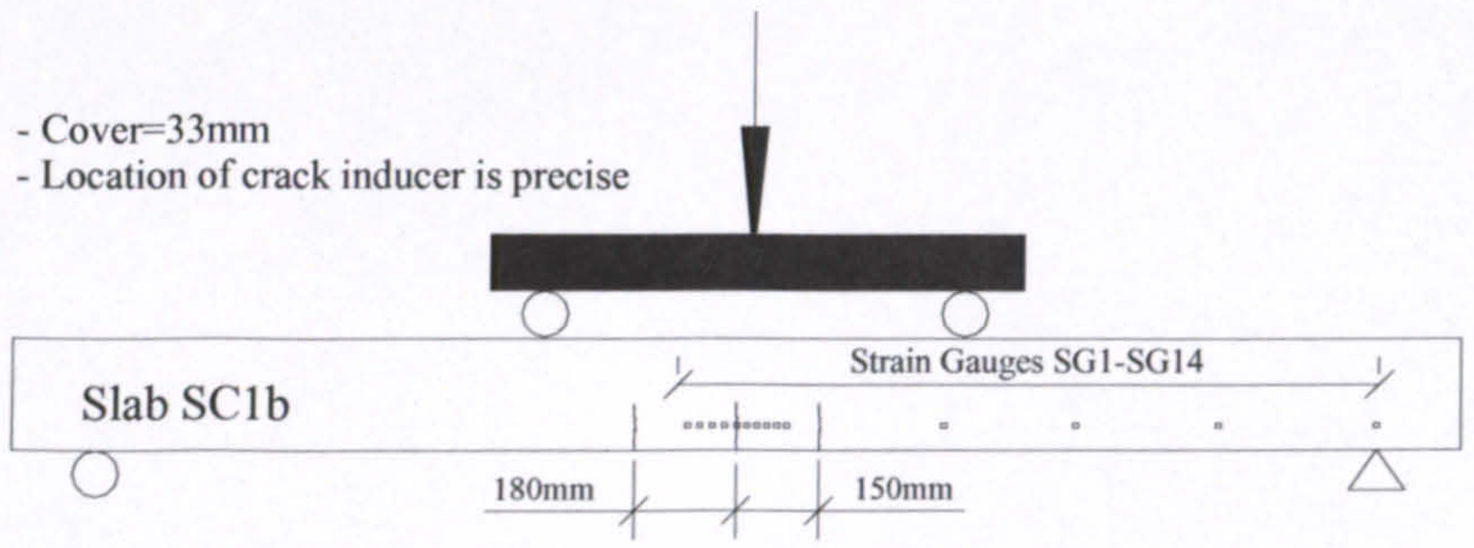

Cracks around Centre

SLAB SC2a

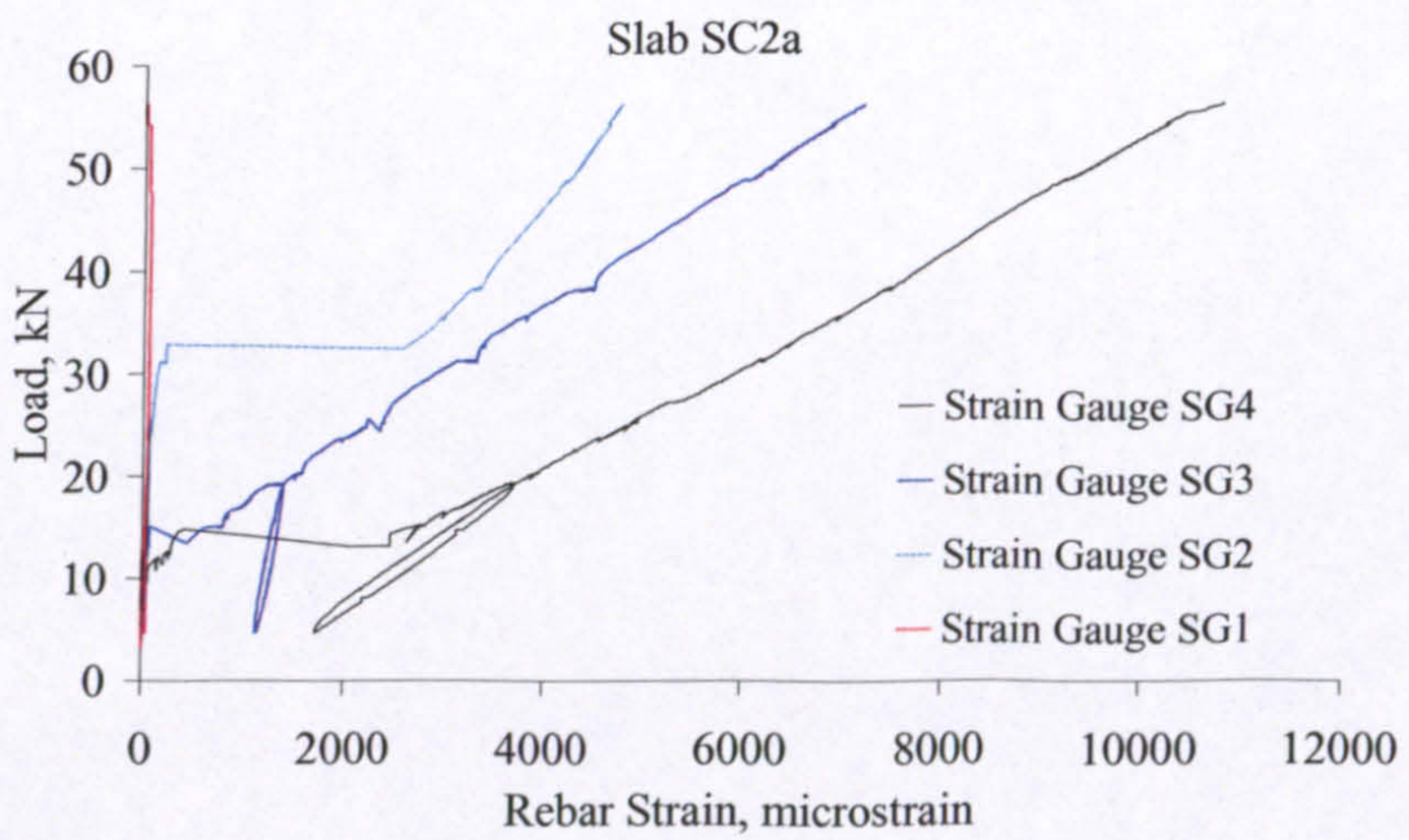
Slab SC2a
Load, kN
Rebar Strain, microstrain
Strain Gauge SG4
Strain Gauge SG3
Strain Gauge SG2
Strain Gauge SG1

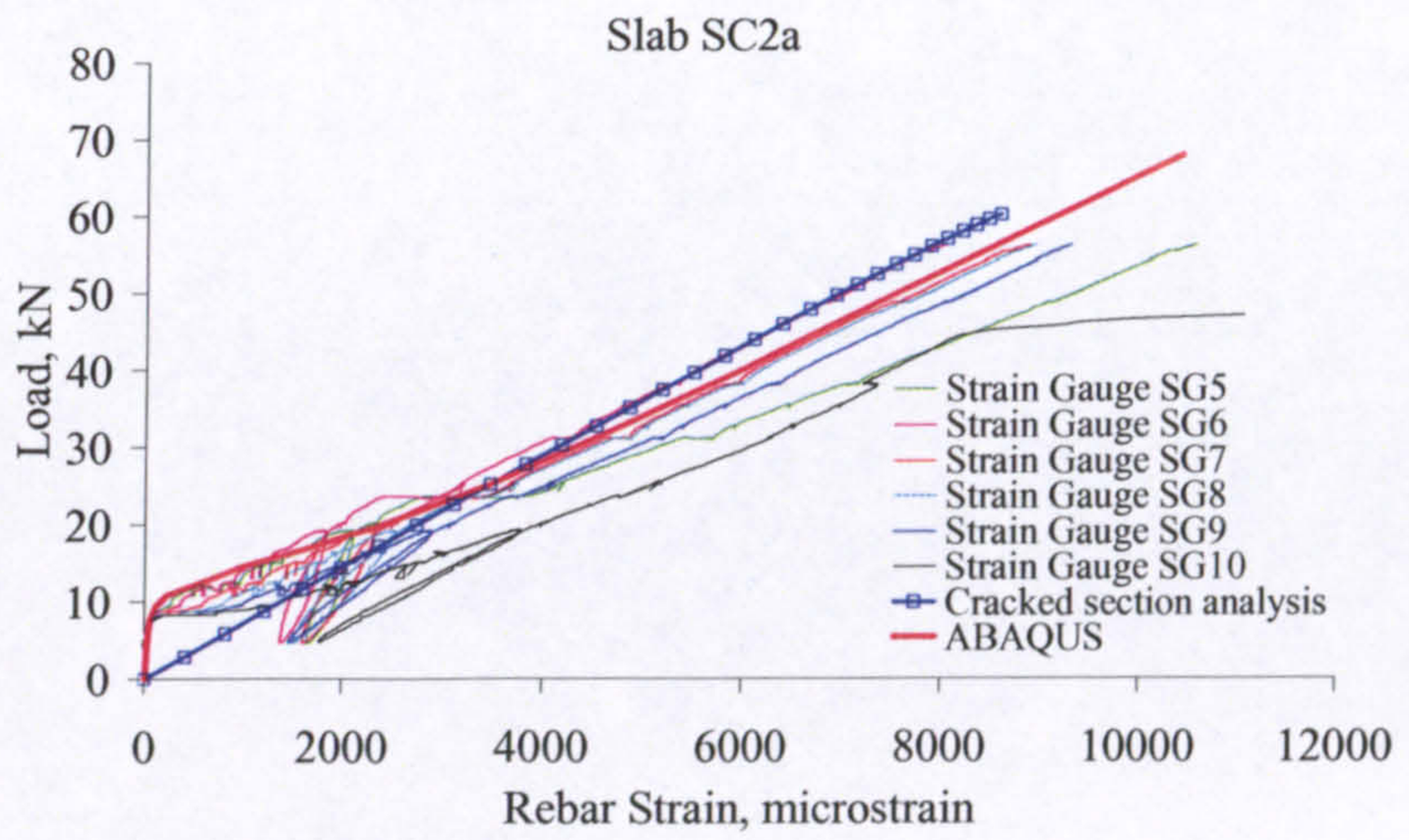
Slab SC2a
Load, kN
Rebar Strain, microstrain
Strain Gauge SG5
Strain Gauge SG6
Strain Gauge SG7
Strain Gauge SG8
Strain Gauge SG9
Strain Gauge SG10
Cracked section analysis
ABAQUS

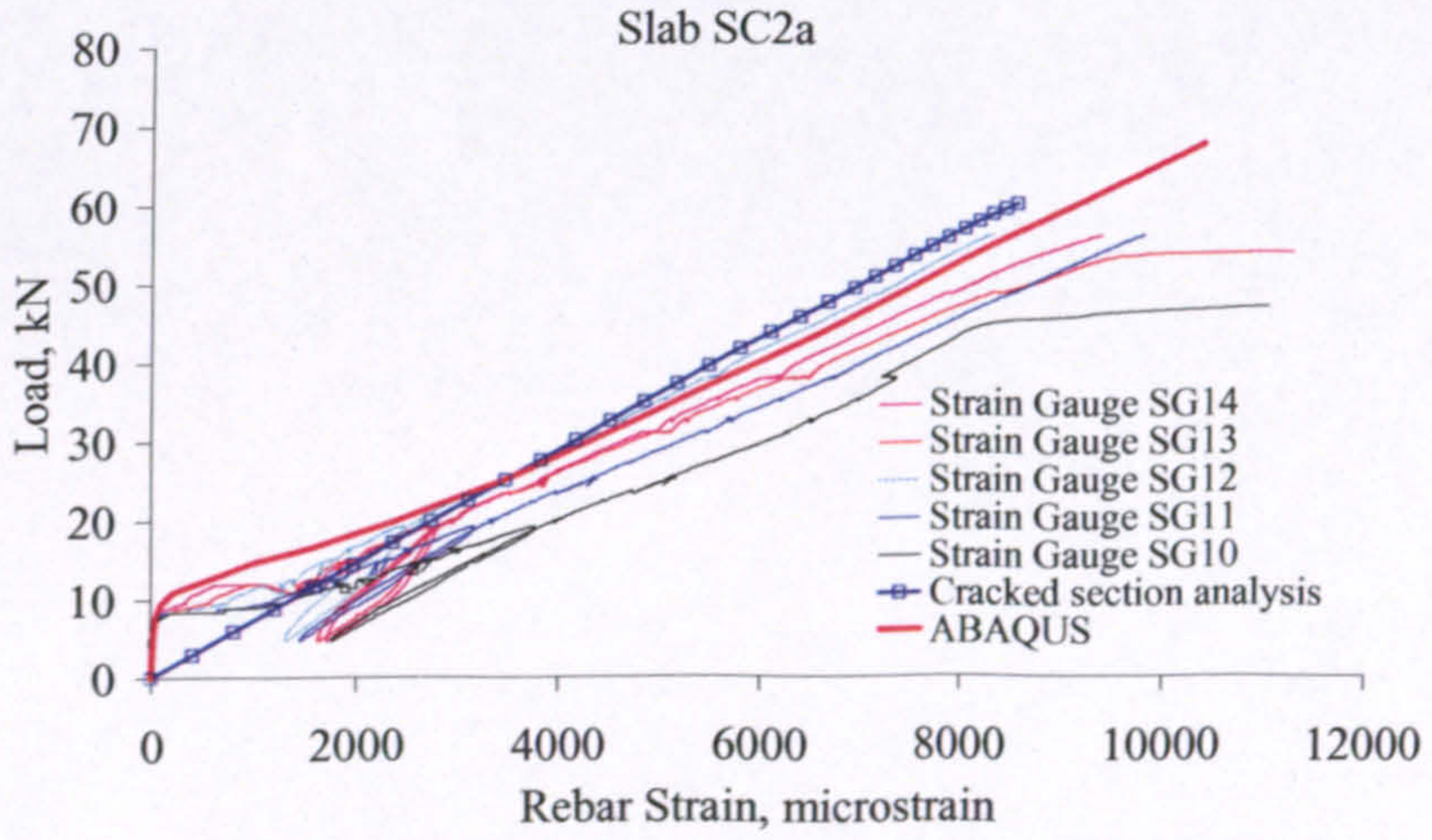
Slab SC2a
Load, kN
Rebar Strain, microstrain
Strain Gauge SG14
Strain Gauge SG13
Strain Gauge SG12
Strain Gauge SG11
Strain Gauge SG10
Cracked section analysis
ABAQUS

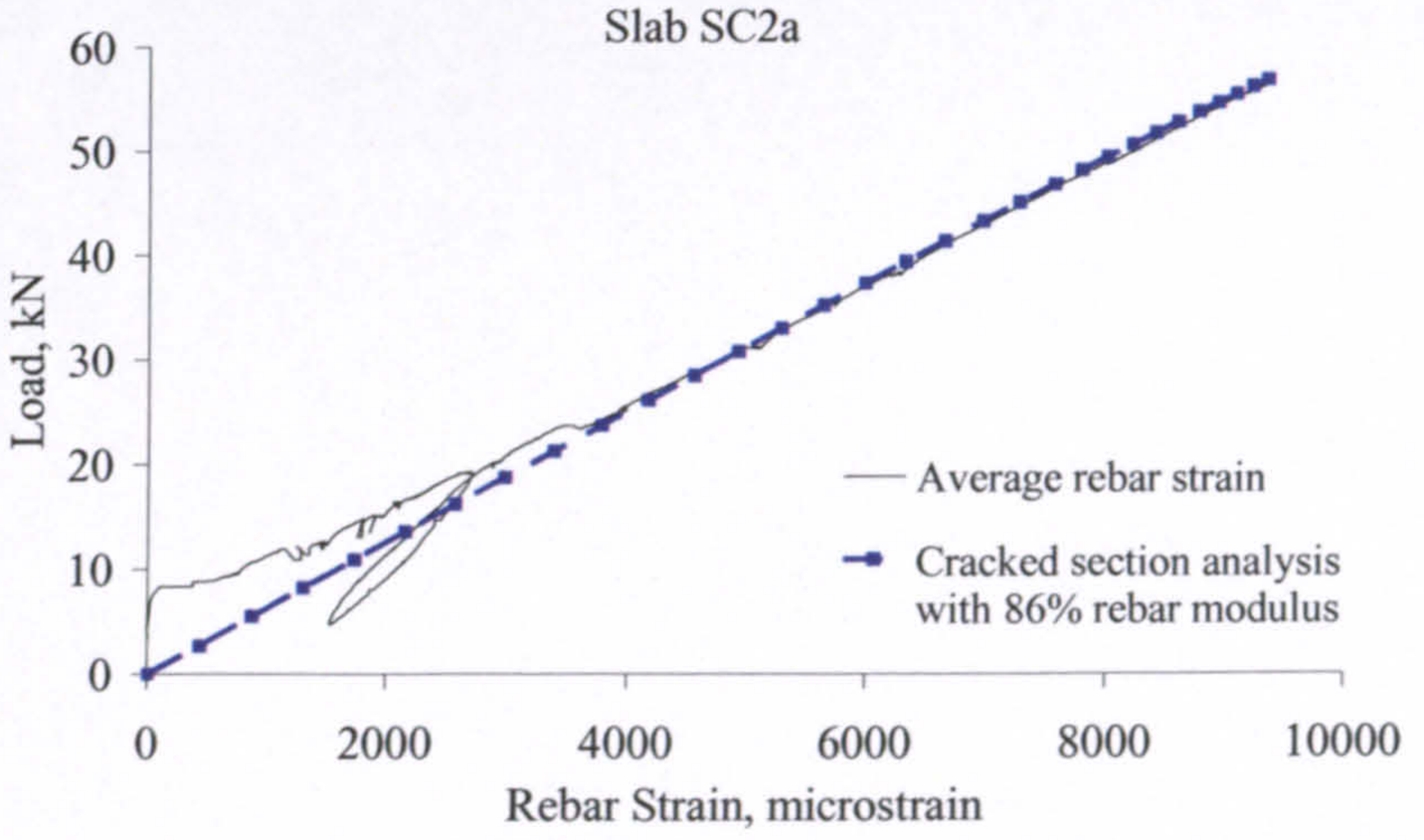
Slab SC2a
Load, kN
Rebar Strain, microstrain
Average rebar strain
Cracked section analysis
with 86% rebar modulus

SLAB SC2a

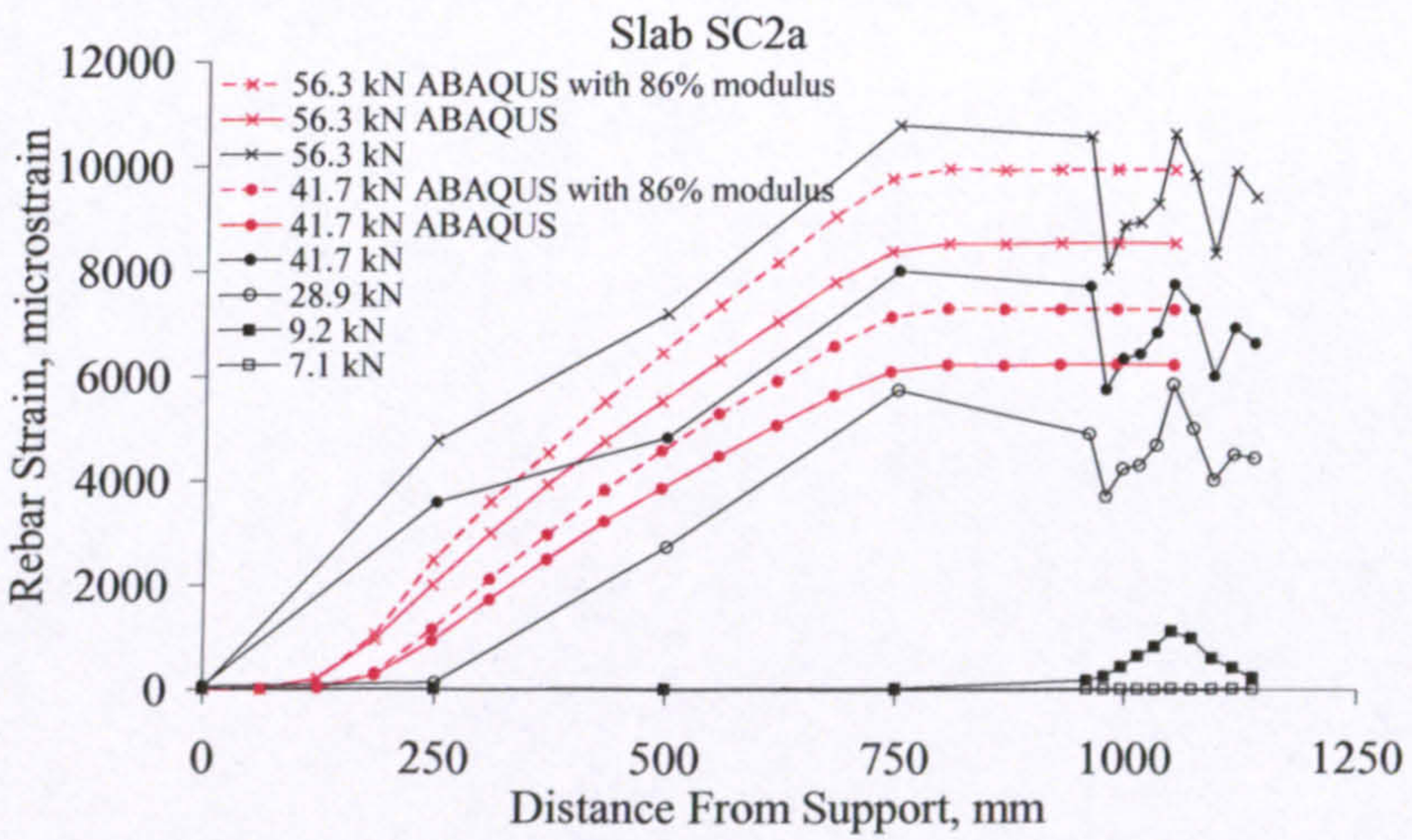
Slab SC2a
Rebar Strain, microstrain
12000
10000
8000
6000
4000
2000
0
56.3 kN ABAQUS with 86% modulus
56.3 kN ABAQUS
56.3 kN
41.7 kN ABAQUS with 86% modulus
41.7 kN ABAQUS
41.7 kN
28.9 kN
9.2 kN
7.1 kN
0
250
500
750
1000
1250
Distance From Support, mm

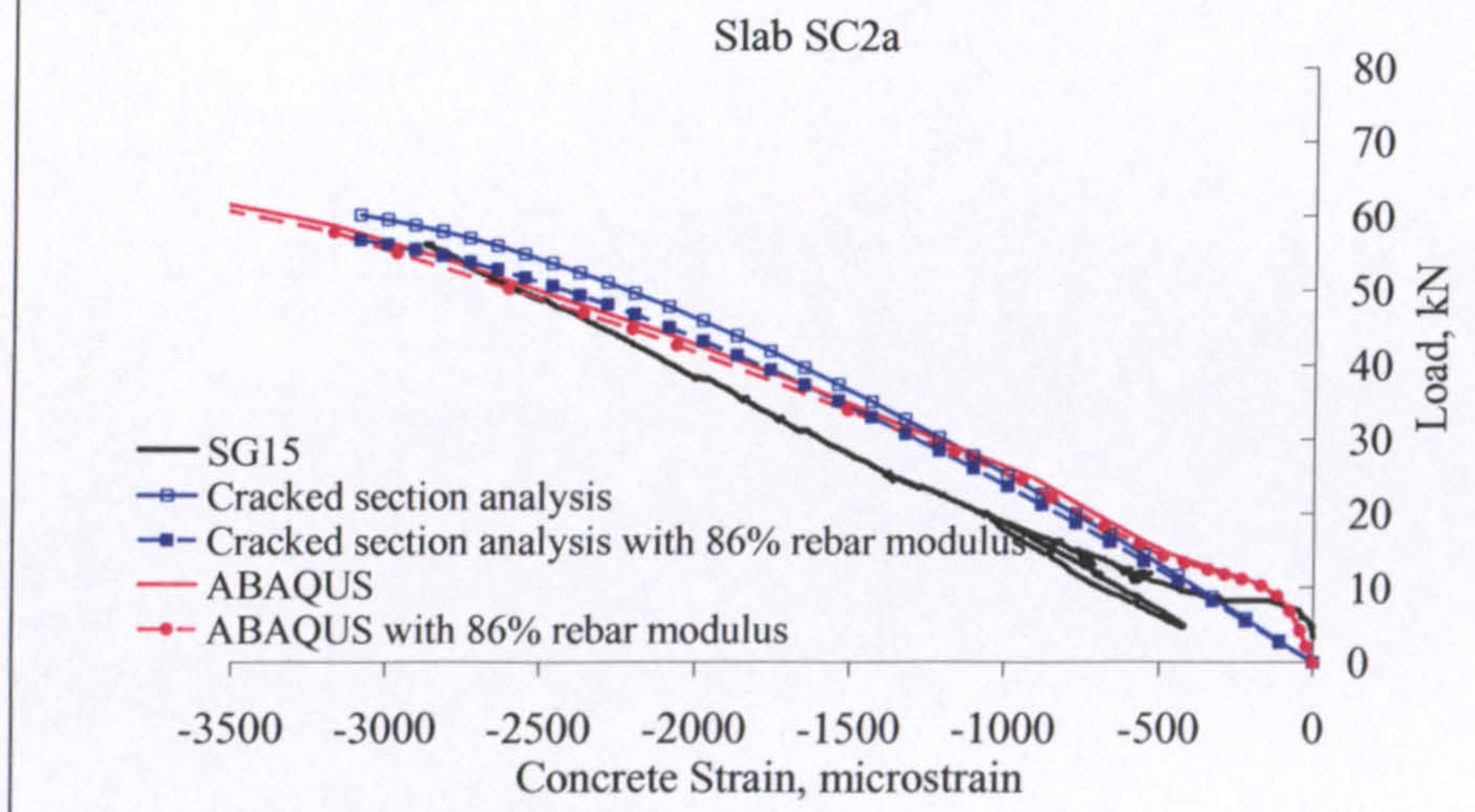
Slab SC2a
Load, kN
80
70
60
50
40
30
20
10
0
SG15
Cracked section analysis
Cracked section analysis with 86% rebar modulus
ABAQUS
ABAQUS with 86% rebar modulus
-3500
-3000
-2500
-2000
-1500
-1000
-500
0
Concrete Strain, microstrain

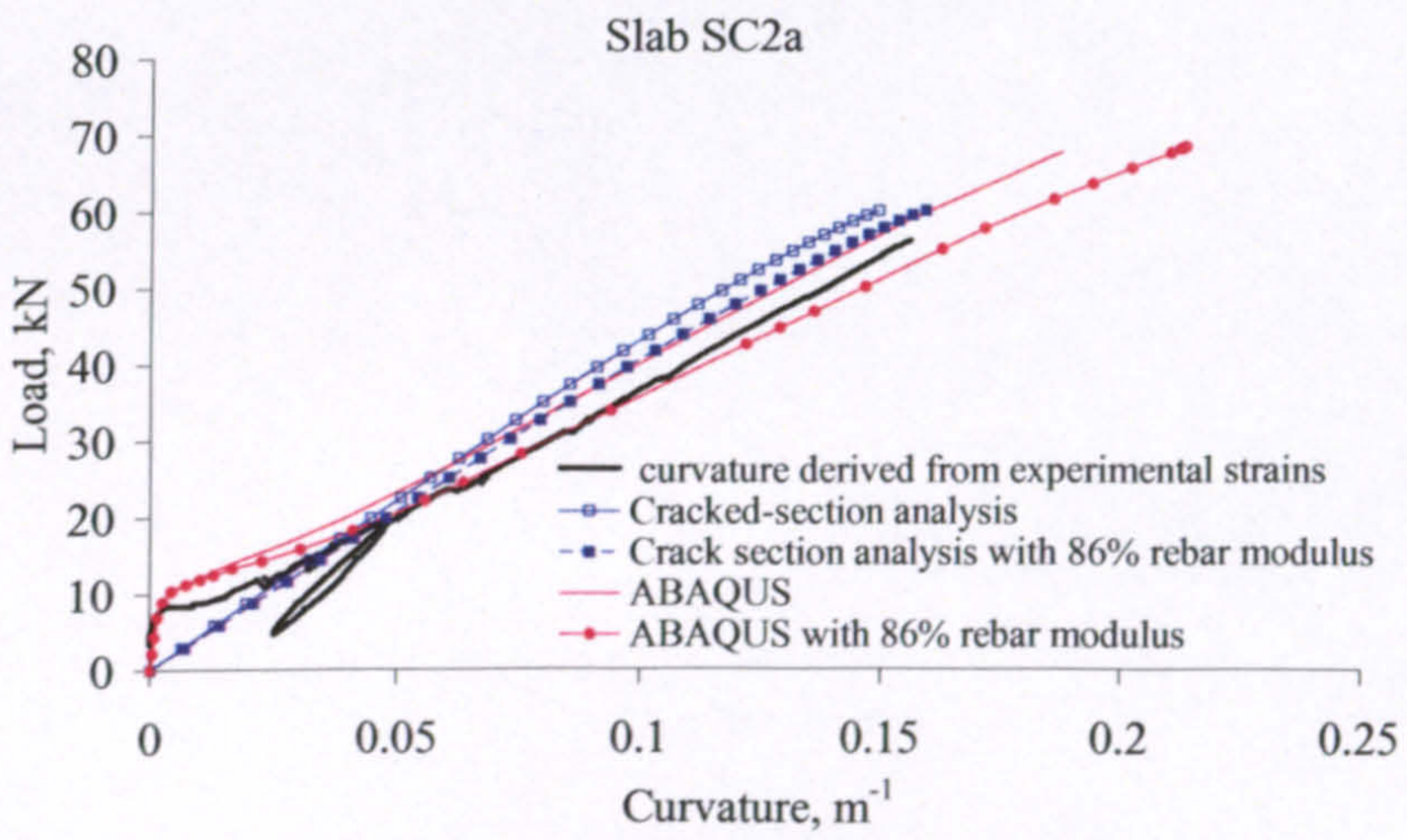
Slab SC2a
Load, kN
80
70
60
50
40
30
20
10
0
curvature derived from experimental strains
Cracked-section analysis
Crack section analysis with 86% rebar modulus
ABAQUS
ABAQUS with 86% rebar modulus
0
0.05
0.1
0.15
0.2
0.25
Curvature, m-1

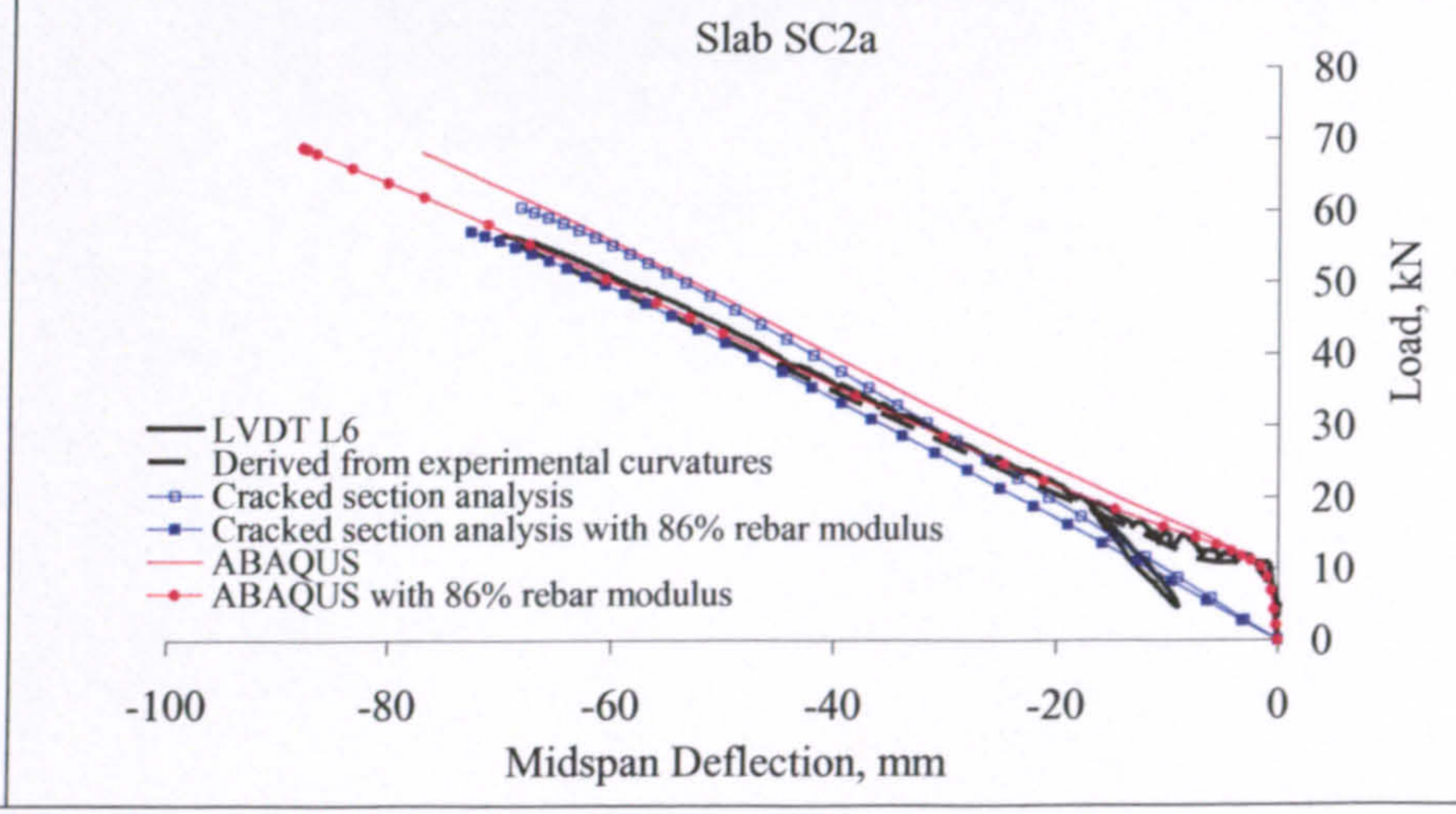
Slab SC2a
Load, kN
80
70
60
50
40
30
20
10
0
LVDT L6
Derived from experimental curvatures
Cracked section analysis
Cracked section analysis with 86% rebar modulus
ABAQUS
ABAQUS with 86% rebar modulus
-100
-80
-60
-40
-20
0
Midspan Deflection, mm

SLAB SC2a

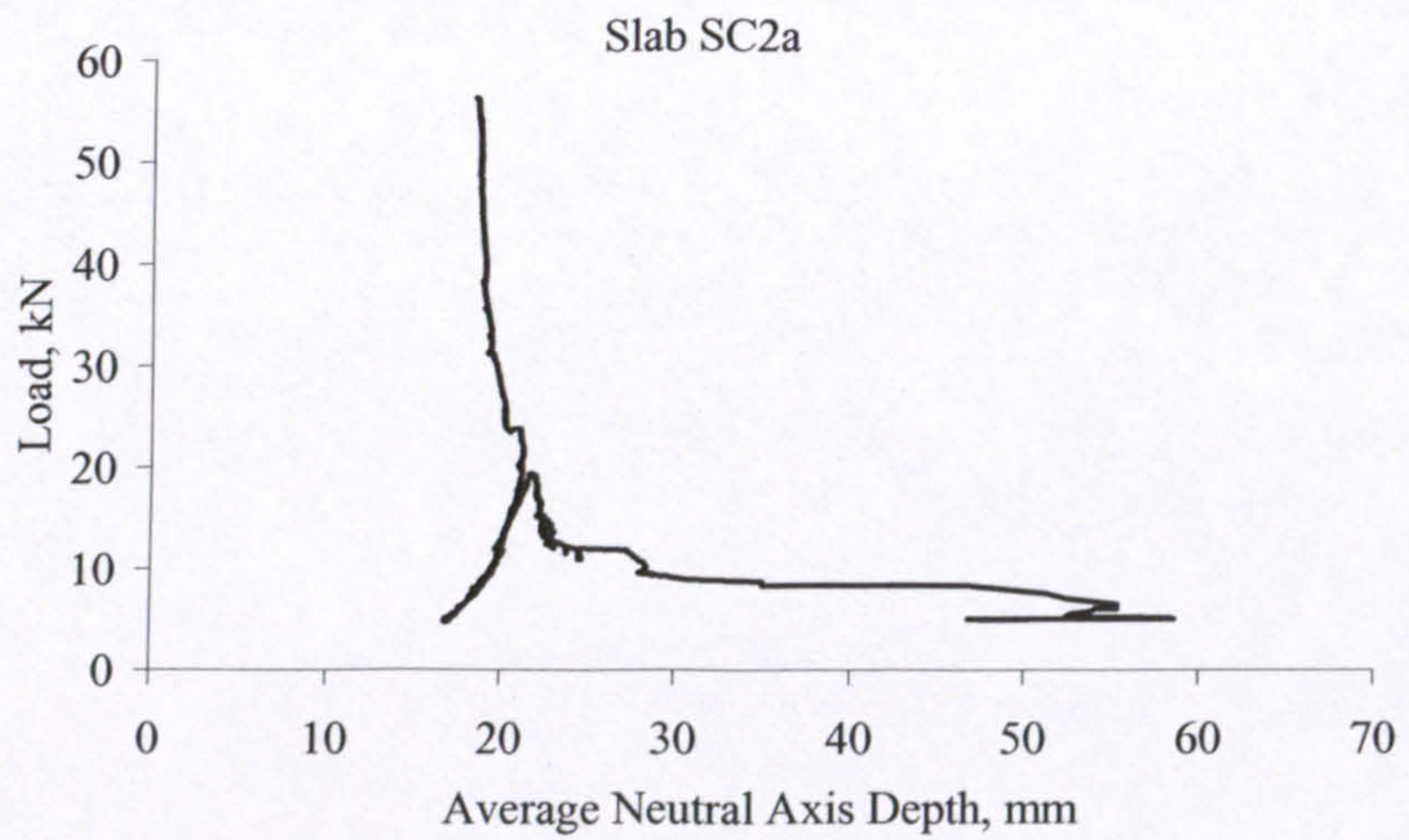
Slab SC2a
Load, kN
Average Neutral Axis Depth, mm
0
10
20
30
40
50
60
70

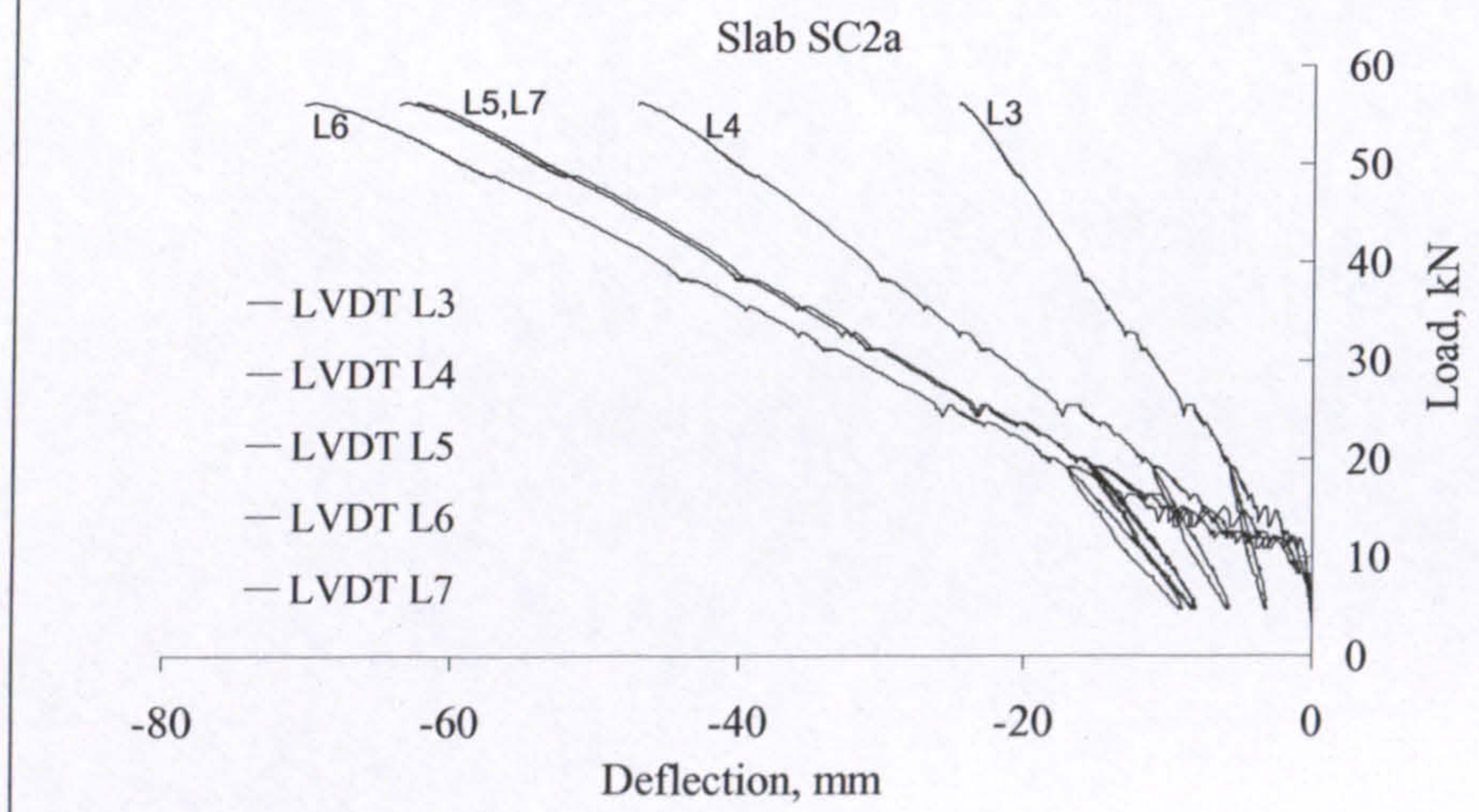
Slab SC2a
L6
L5,L7
L4
L3
LVDT L3
LVDT L4
LVDT L5
LVDT L6
LVDT L7
Load, kN
Deflection, mm
-80
-60
-40
-20
0

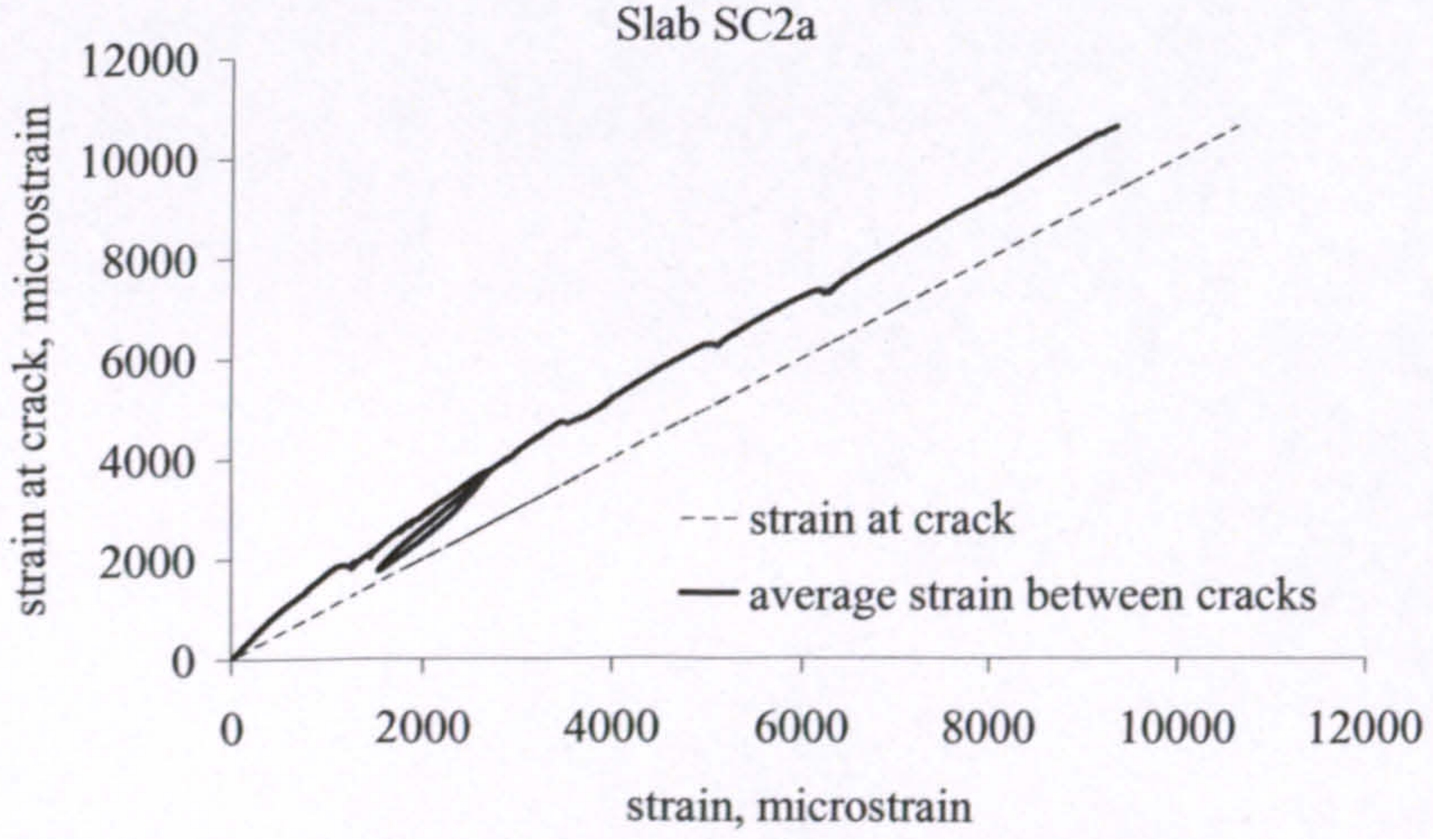
Slab SC2a
strain at crack, microstrain
strain, microstrain
strain at crack
average strain between cracks
0
2000
4000
6000
8000
10000
12000

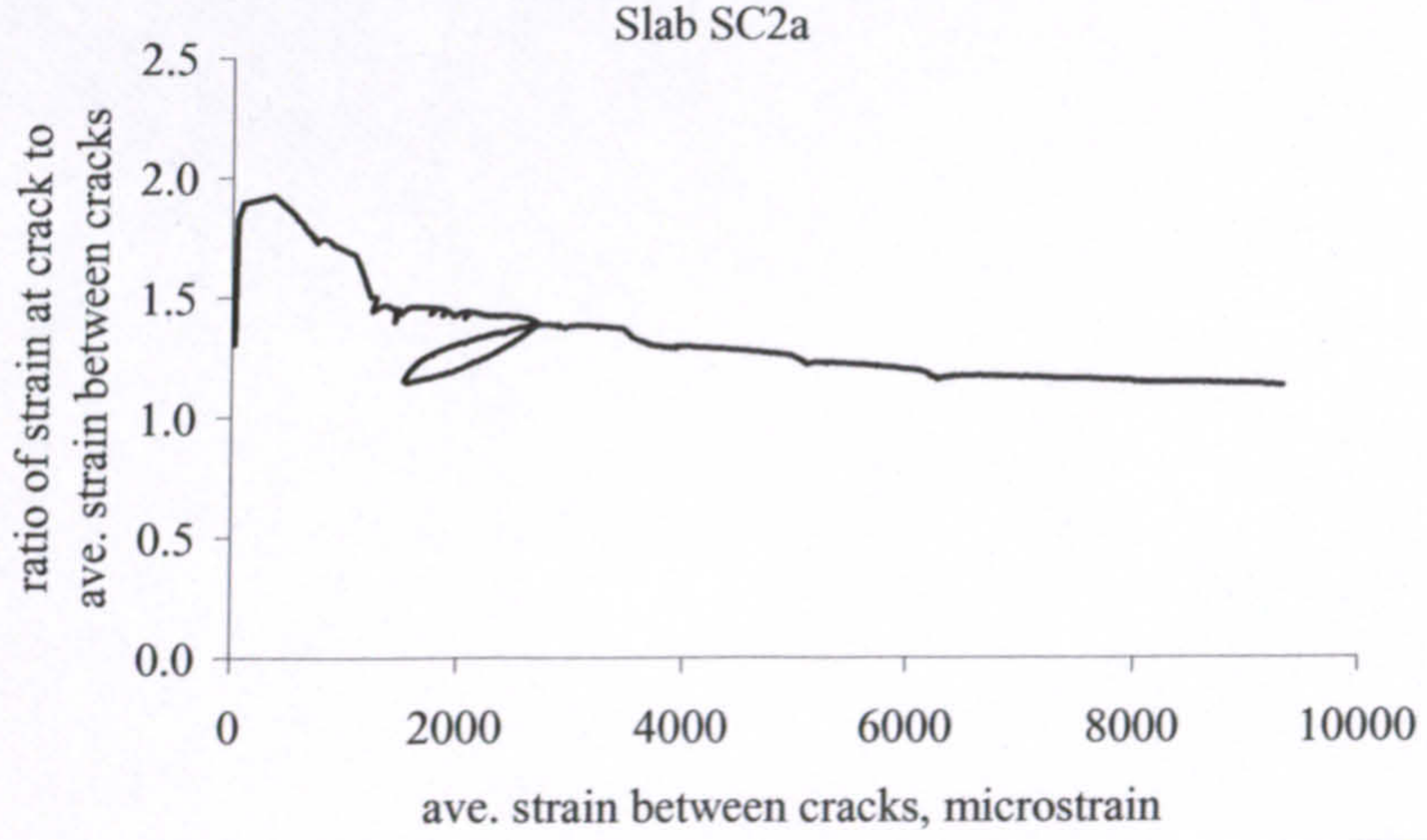
Slab SC2a
ratio of strain at crack to ave. strain between cracks
ave. strain between cracks, microstrain
0.0
0.5
1.0
1.5
2.0
2.5
0
2000
4000
6000
8000
10000

SLAB SC2a

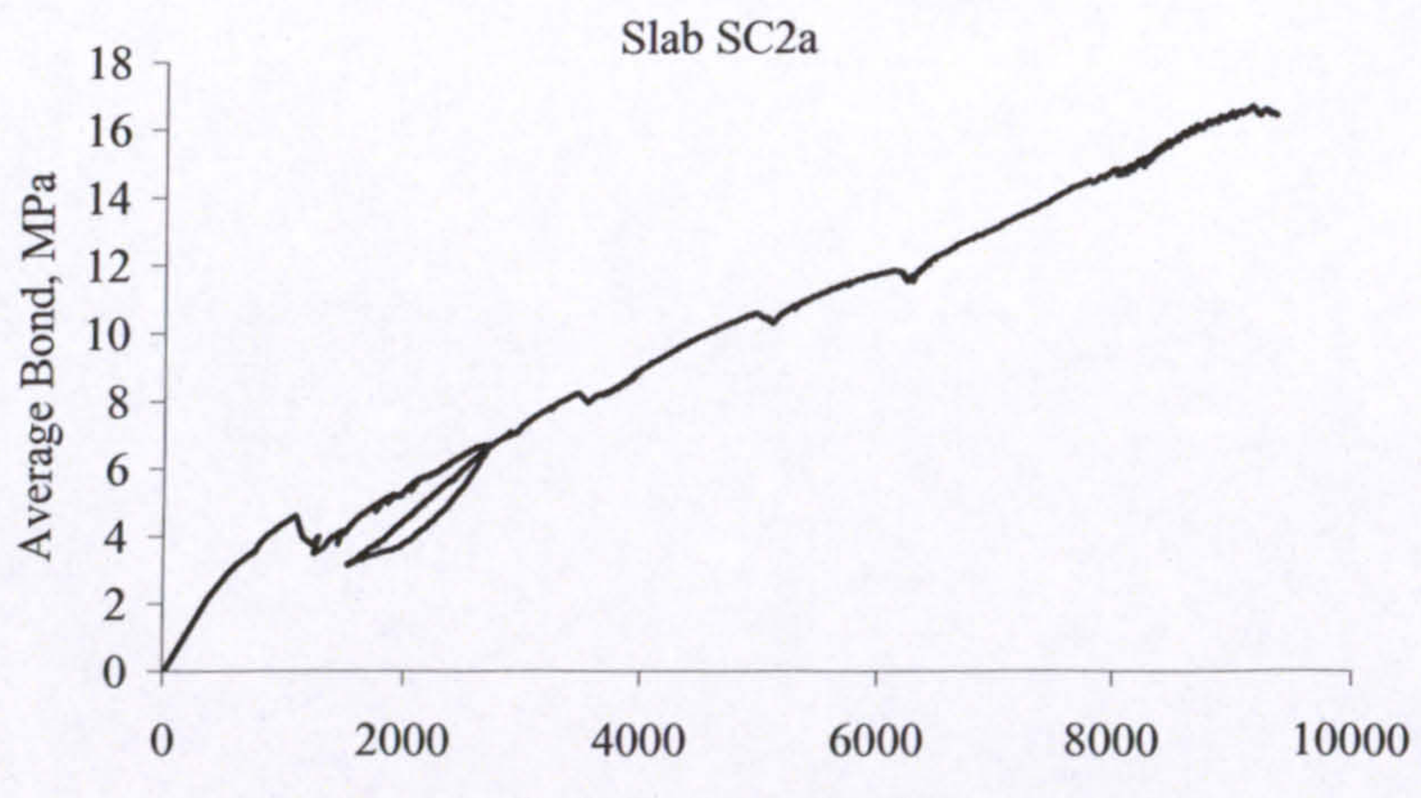

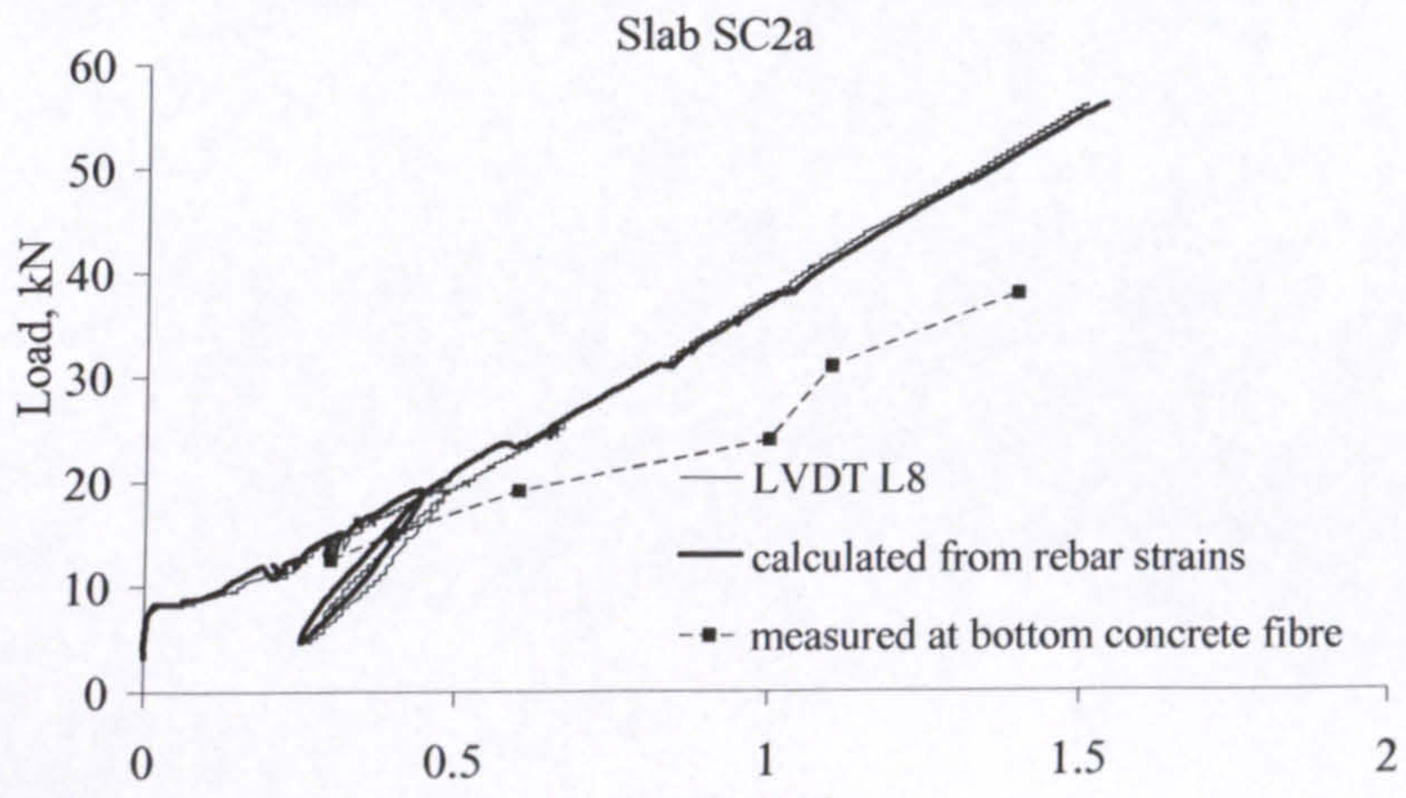

Almost Balanced Failure.

- Cover=36-40mm
- Location of crack inducer is precise
- at 24-31 kN, a crack formed 90mm right of CL.

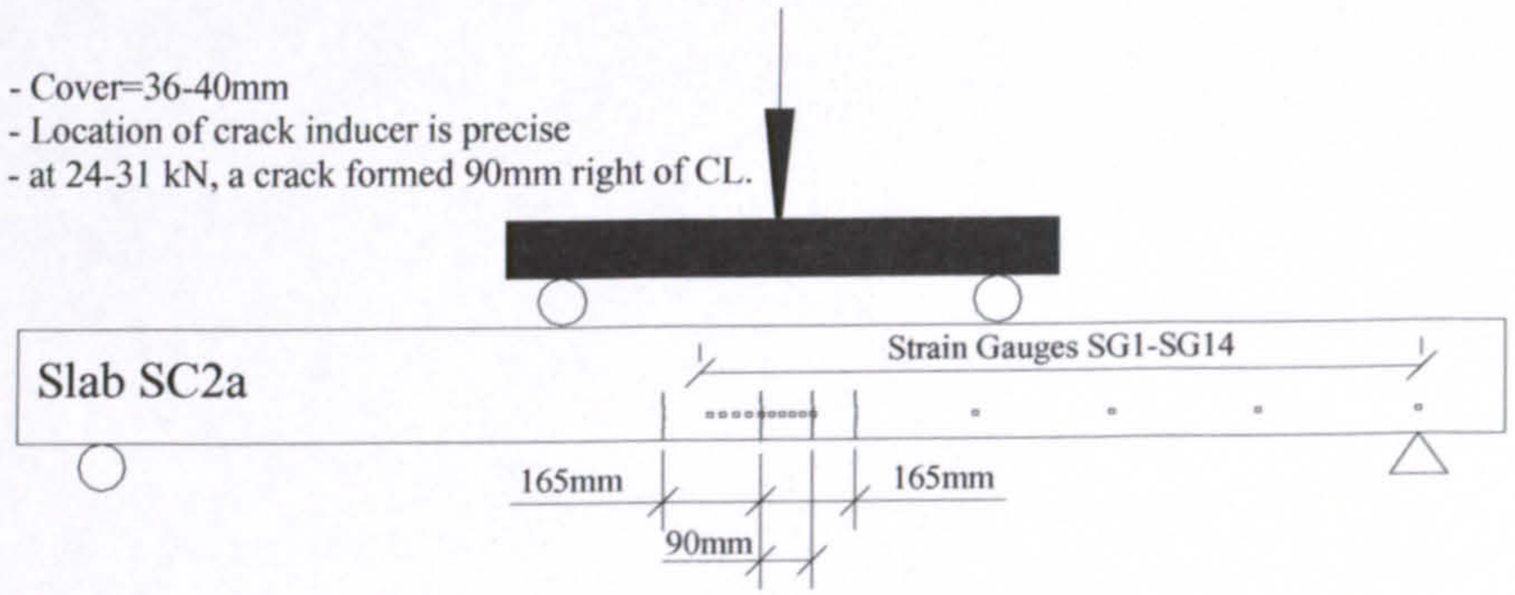

Cracks around Centre

SLAB SC2b

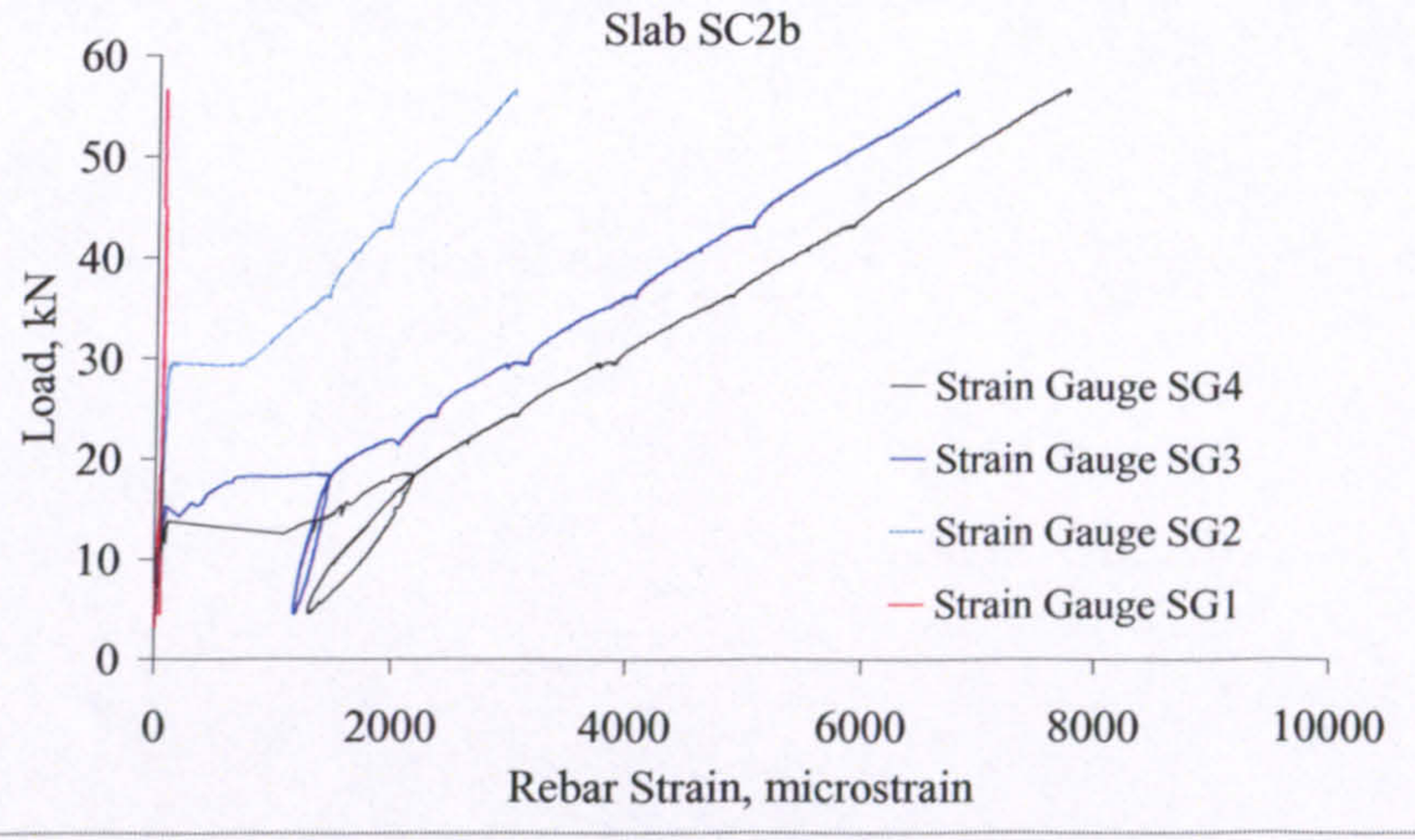
Slab SC2b
Load, kN
Rebar Strain, microstrain
Strain Gauge SG4
Strain Gauge SG3
Strain Gauge SG2
Strain Gauge SG1

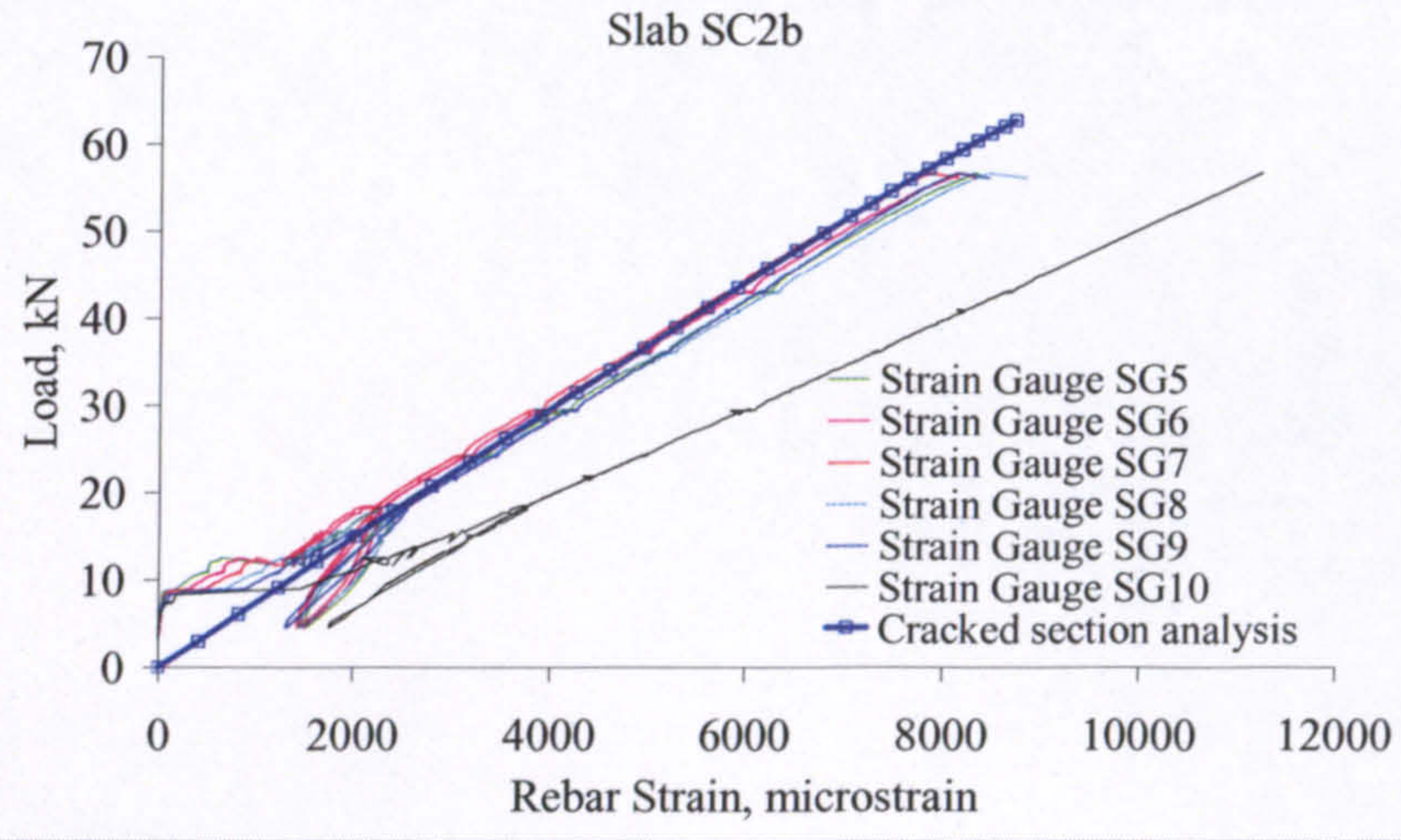
Slab SC2b
Load, kN
Rebar Strain, microstrain
Strain Gauge SG5
Strain Gauge SG6
Strain Gauge SG7
Strain Gauge SG8
Strain Gauge SG9
Strain Gauge SG10
Cracked section analysis

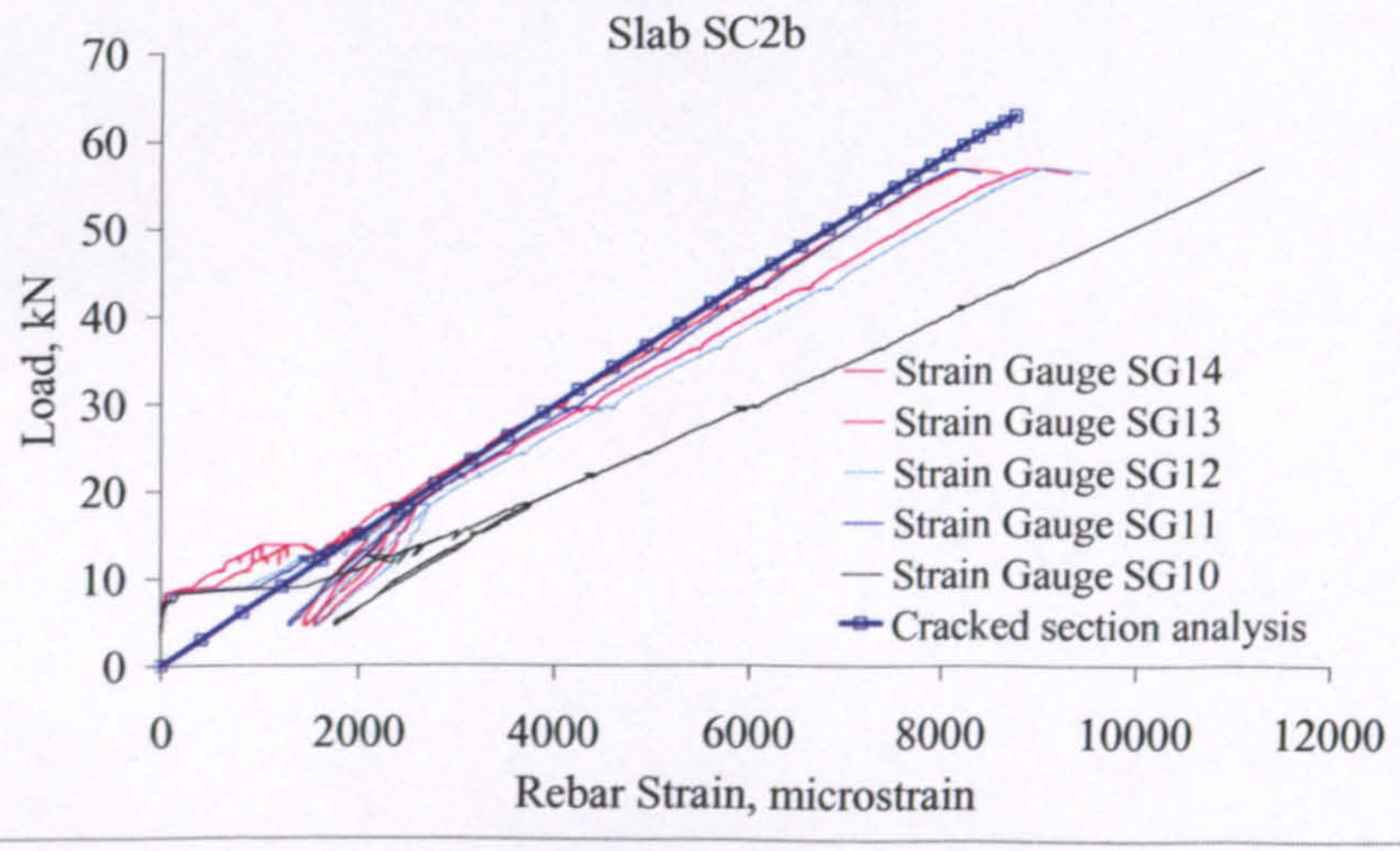
Slab SC2b
Load, kN
Rebar Strain, microstrain
Strain Gauge SG14
Strain Gauge SG13
Strain Gauge SG12
Strain Gauge SG11
Strain Gauge SG10
Cracked section analysis

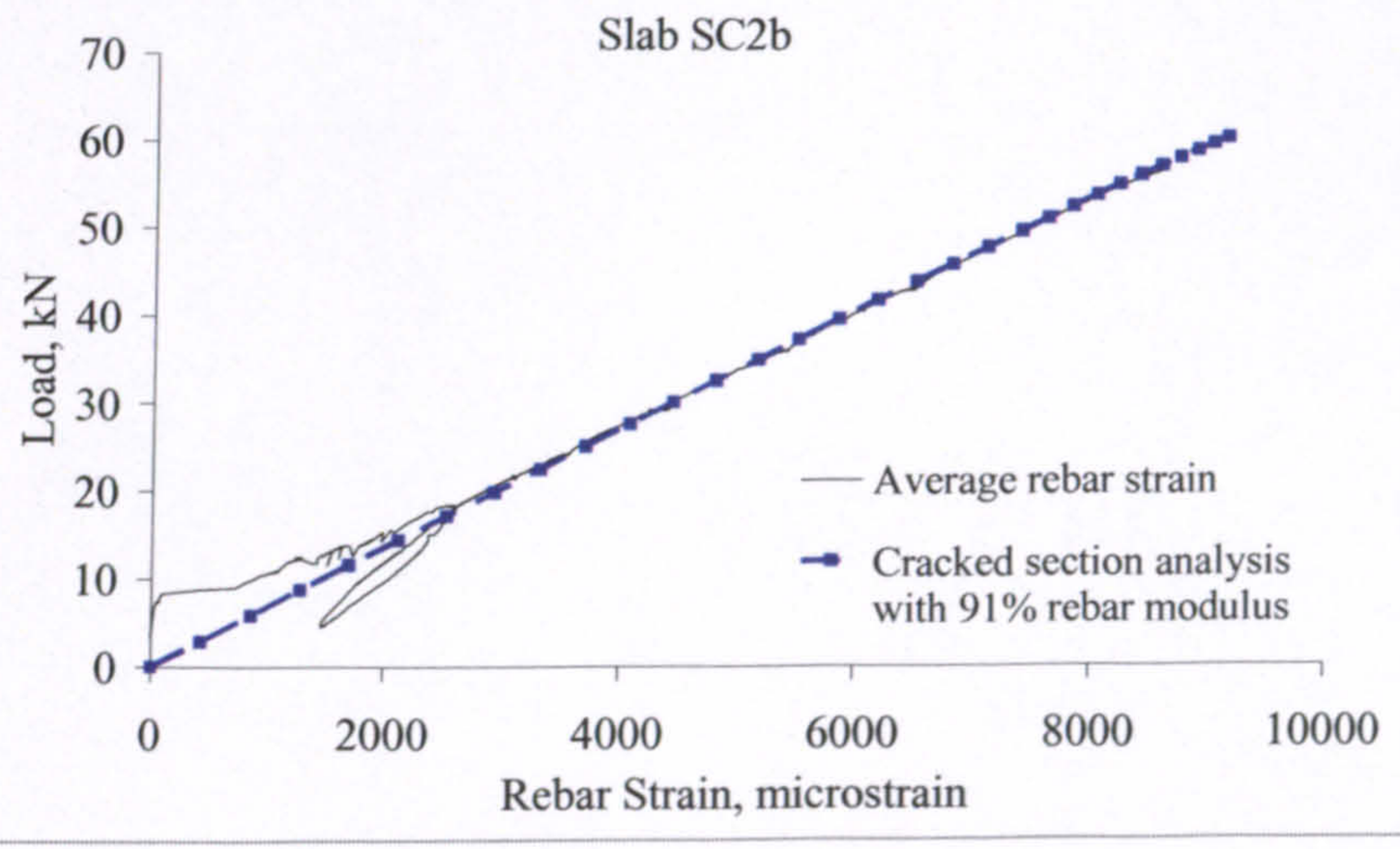
Slab SC2b
Load, kN
Rebar Strain, microstrain
Average rebar strain
Cracked section analysis
with 91% rebar modulus

SLAB SC2b

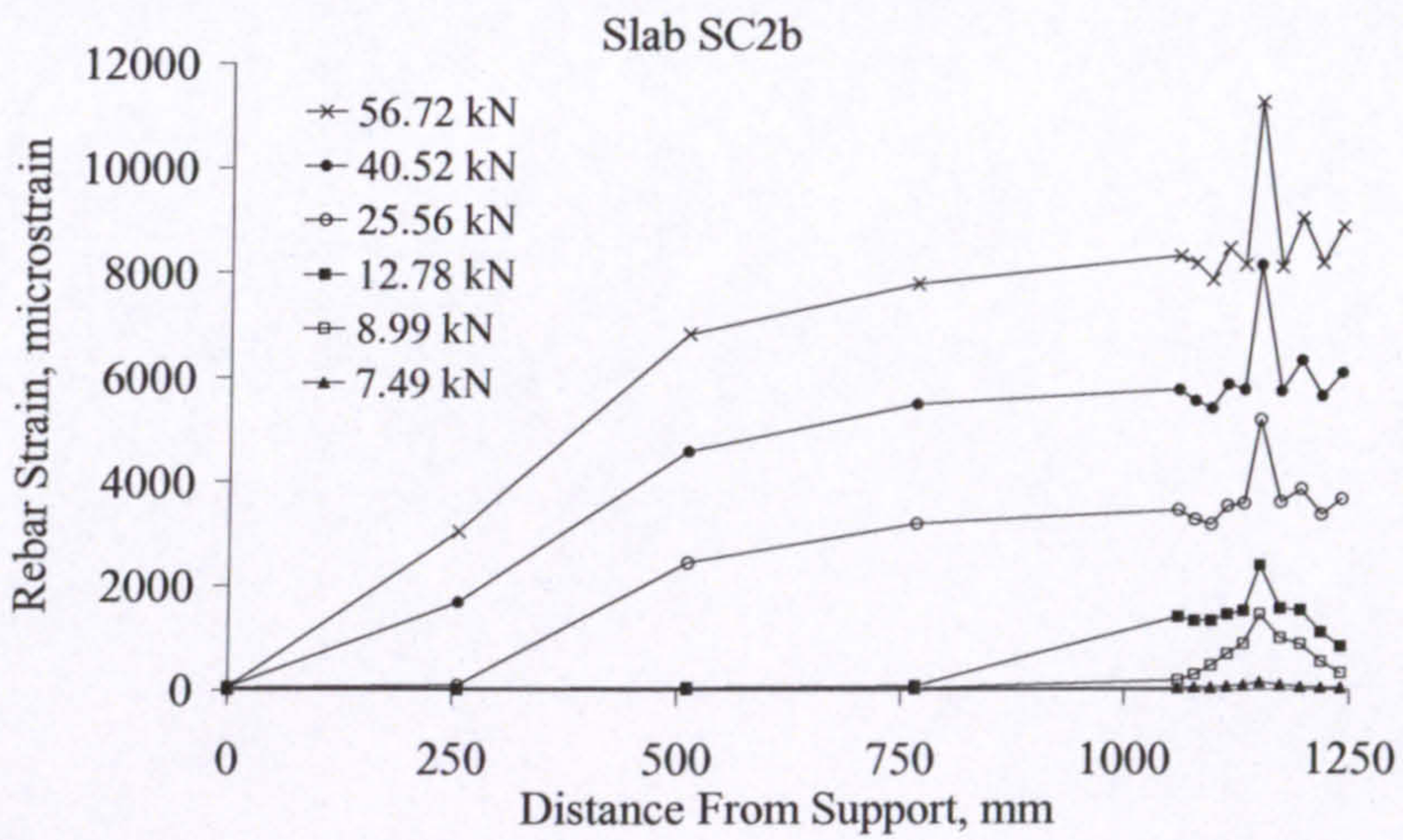
Slab SC2b
Rebar Strain, microstrain
12000
10000
8000
6000
4000
2000
0
56.72 kN
40.52 kN
25.56 kN
12.78 kN
8.99 kN
7.49 kN
0
250
500
750
1000
1250
Distance From Support, mm

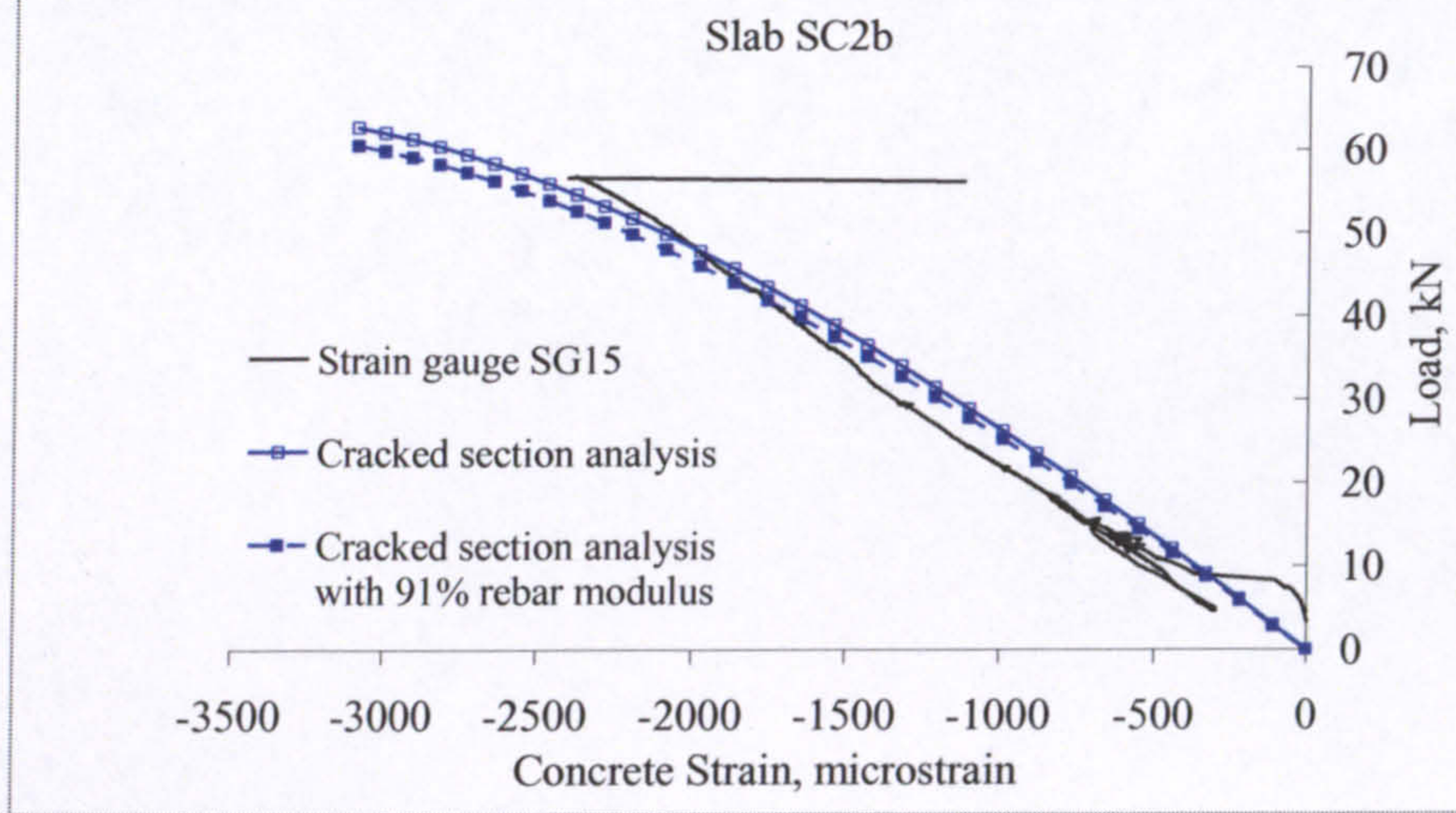
Slab SC2b
Load, kN
70
60
50
40
30
20
10
0
Strain gauge SG15
Cracked section analysis
Cracked section analysis with 91% rebar modulus
-3500
-3000
-2500
-2000
-1500
-1000
-500
0
Concrete Strain, microstrain

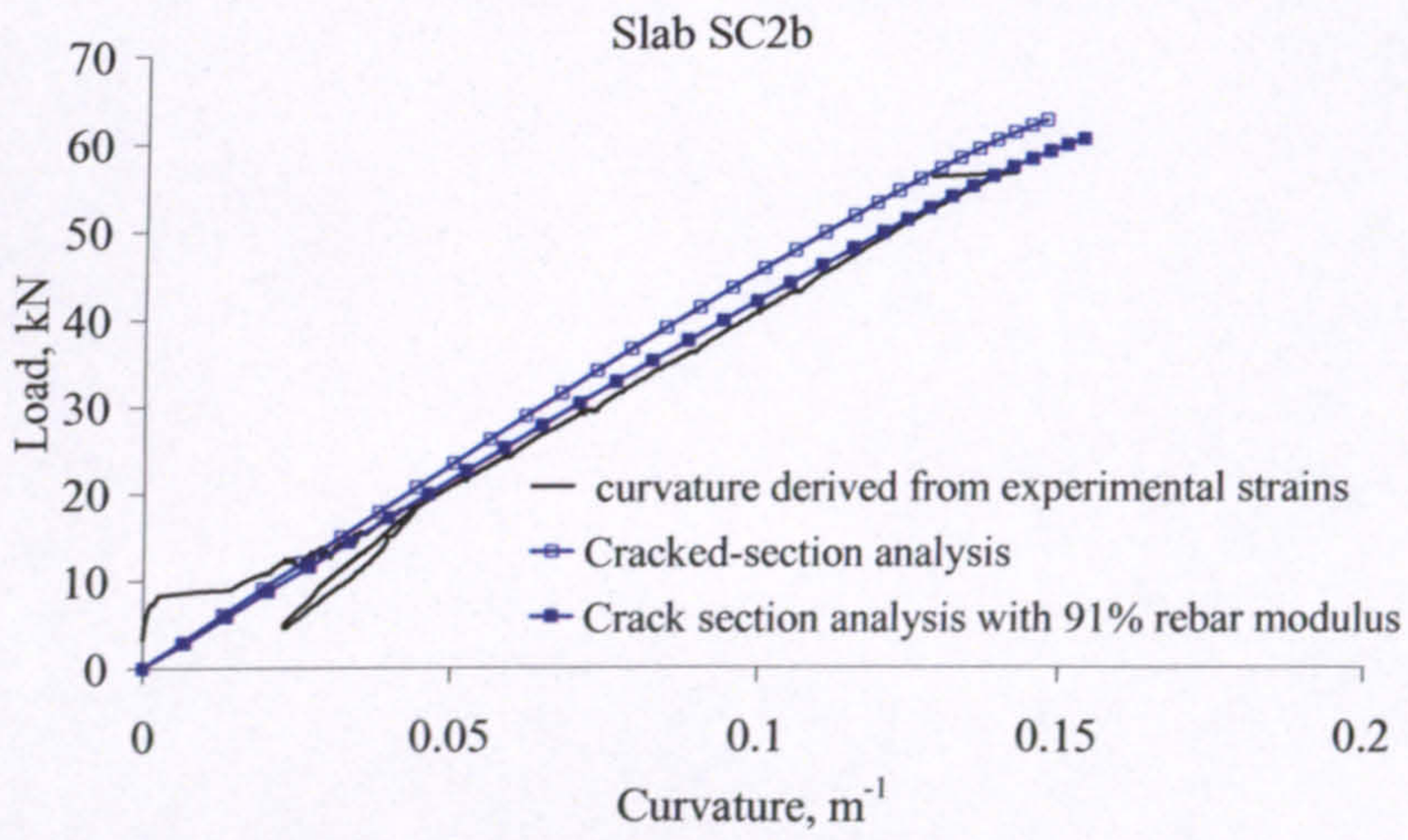
Slab SC2b
Load, kN
70
60
50
40
30
20
10
0
curvature derived from experimental strains
Cracked-section analysis
Crack section analysis with 91% rebar modulus
0
0.05
0.1
0.15
0.2
Curvature, m-1

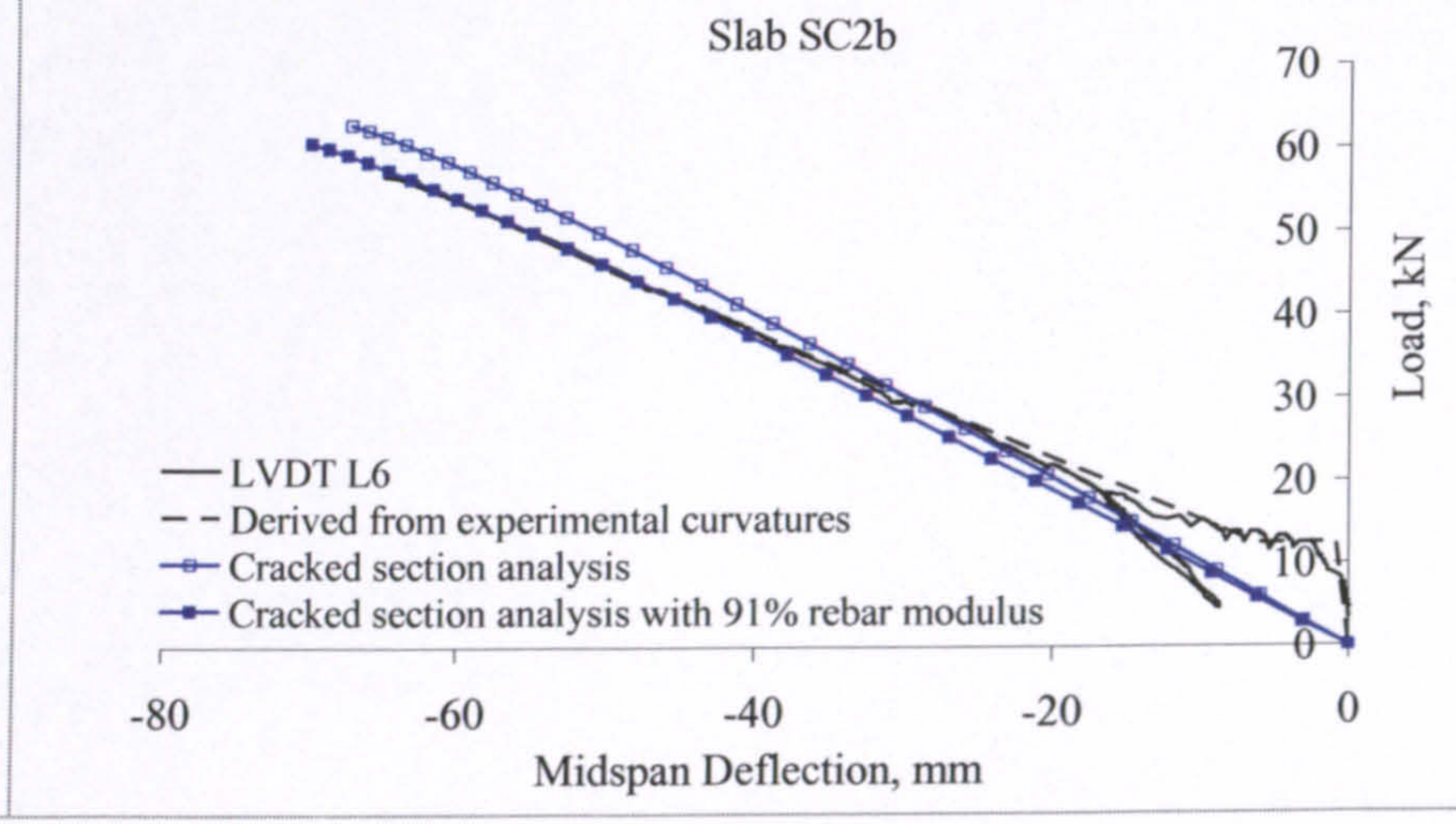
Slab SC2b
Load, kN
70
60
50
40
30
20
10
0
LVDT L6
Derived from experimental curvatures
Cracked section analysis
Cracked section analysis with 91% rebar modulus
-80
-60
-40
-20
0
Midspan Deflection, mm

SLAB SC2b

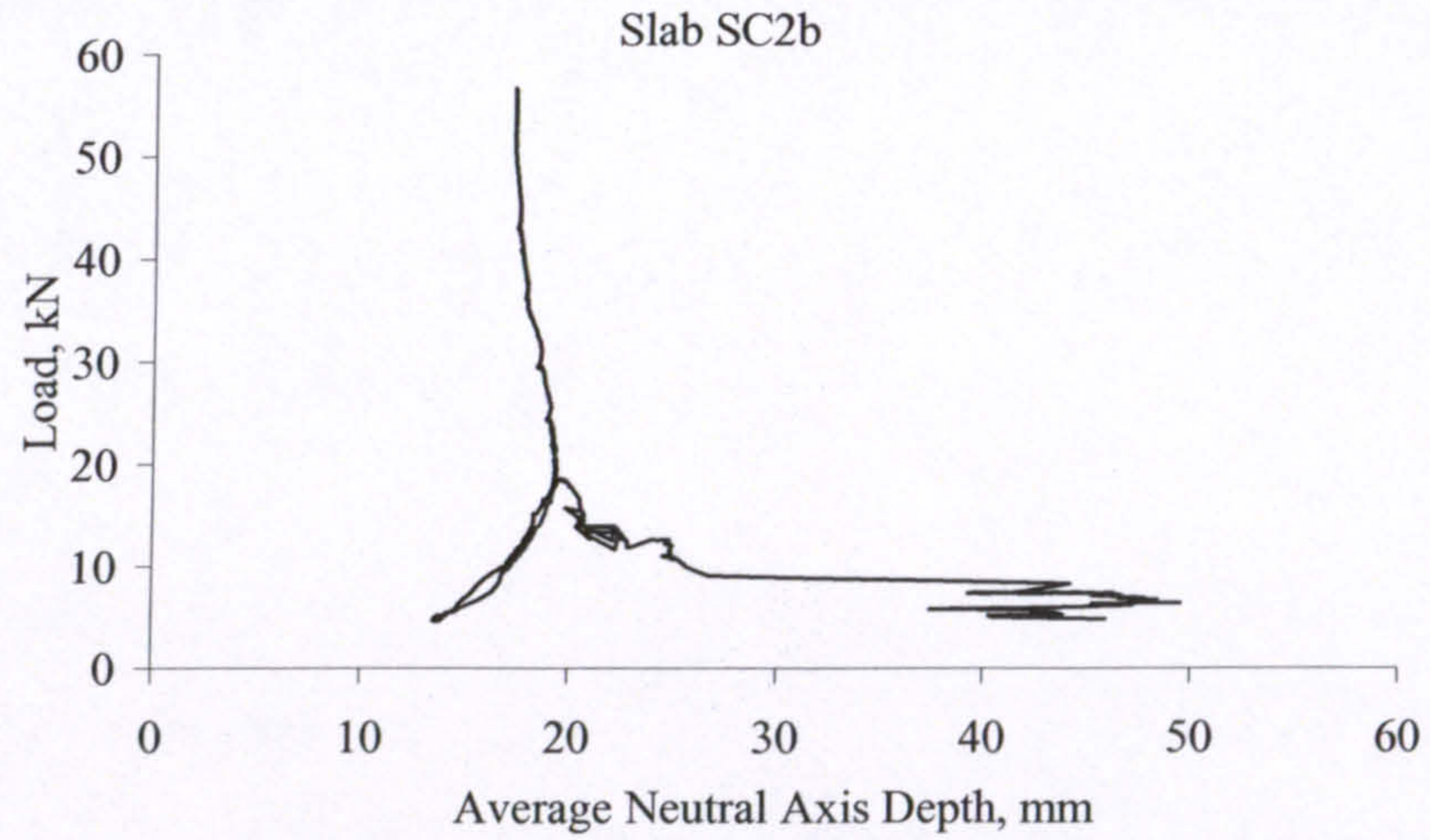
Slab SC2b
Load, kN
Average Neutral Axis Depth, mm
0
10
20
30
40
50
60

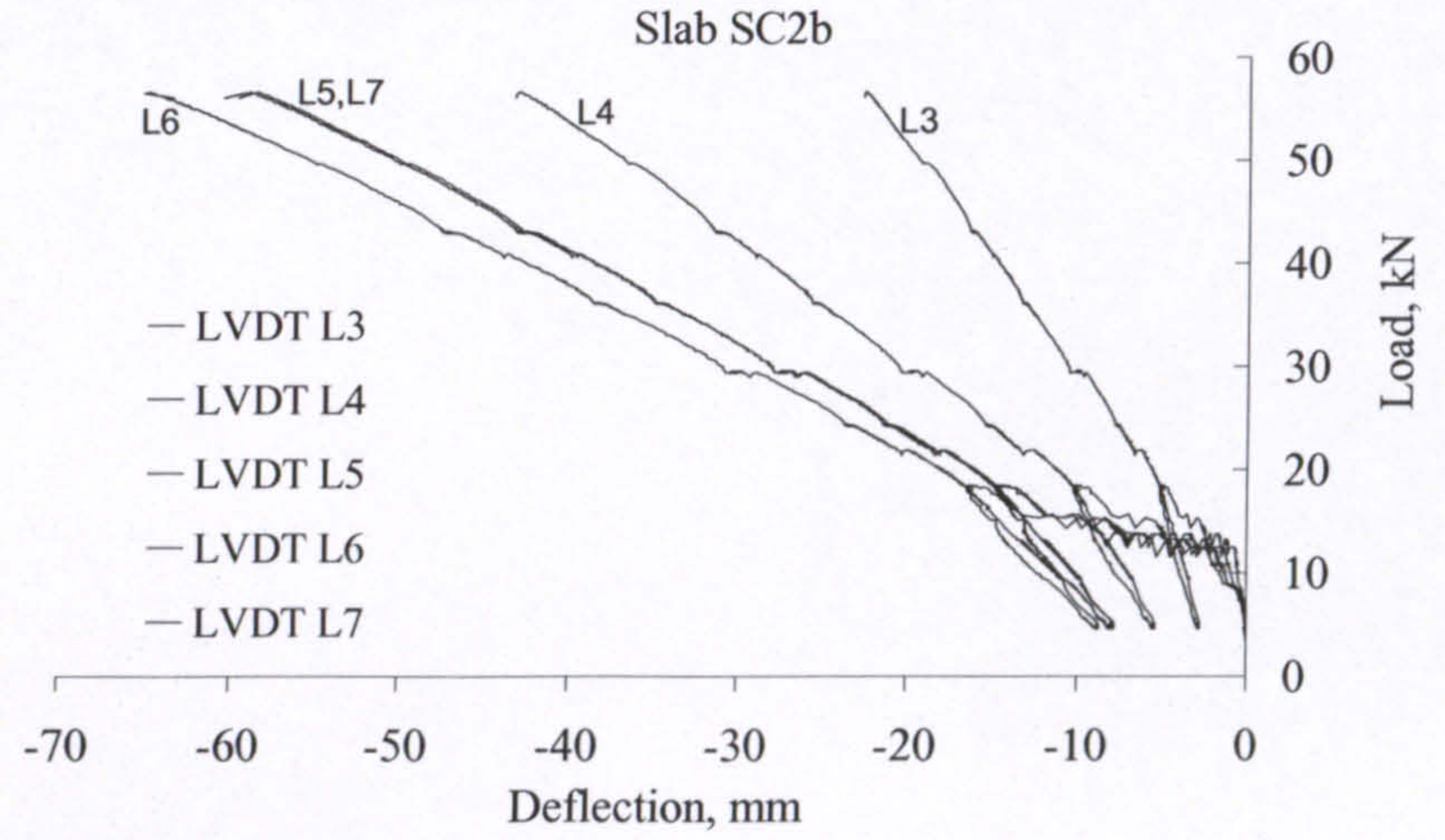
Slab SC2b
L6
L5,L7
L4
L3
— LVDT L3
— LVDT L4
— LVDT L5
— LVDT L6
— LVDT L7
Load, kN
Deflection, mm
-70
-60
-50
-40
-30
-20
-10
0

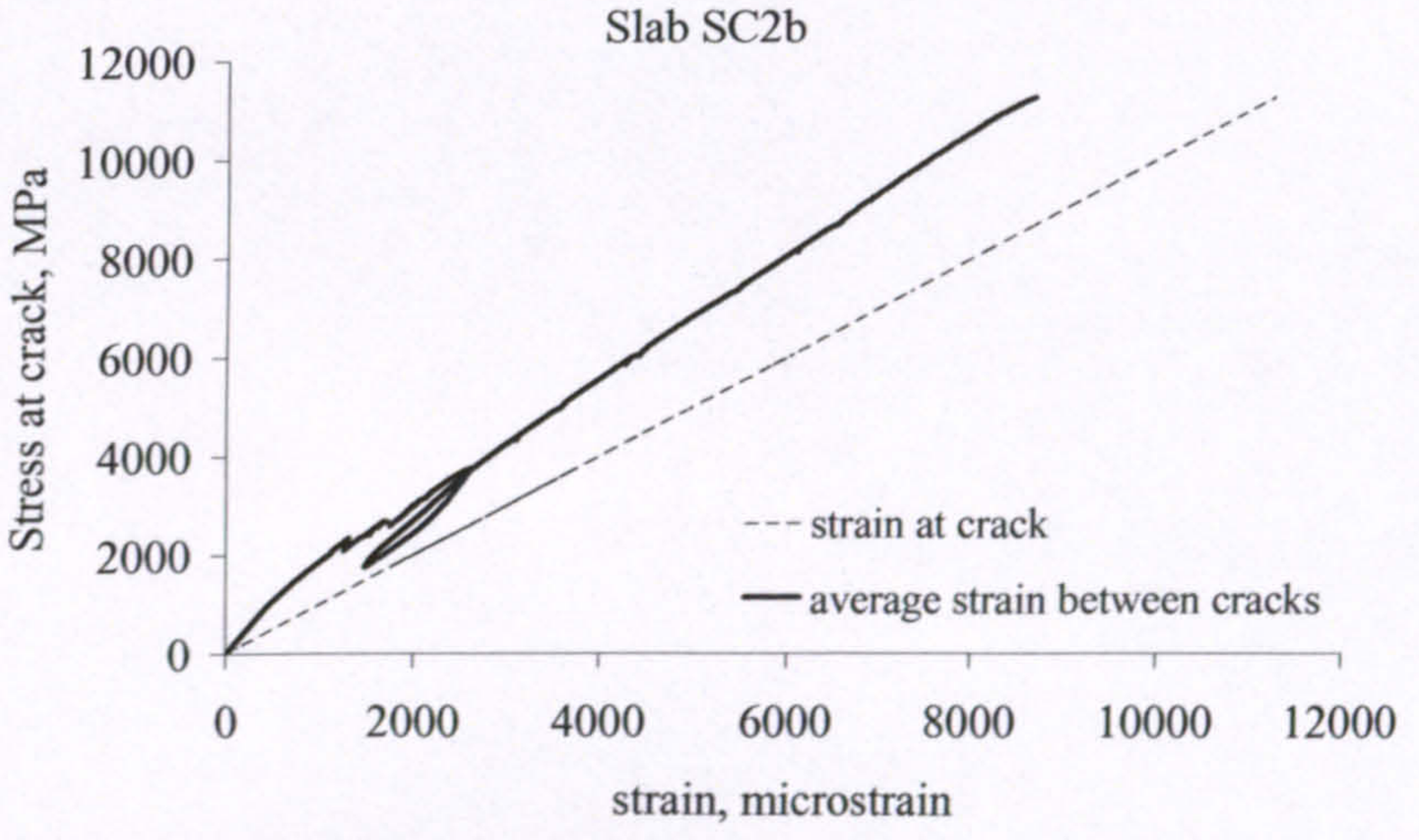
Slab SC2b
Stress at crack, MPa
strain, microstrain
strain at crack
average strain between cracks
0
2000
4000
6000
8000
10000
12000

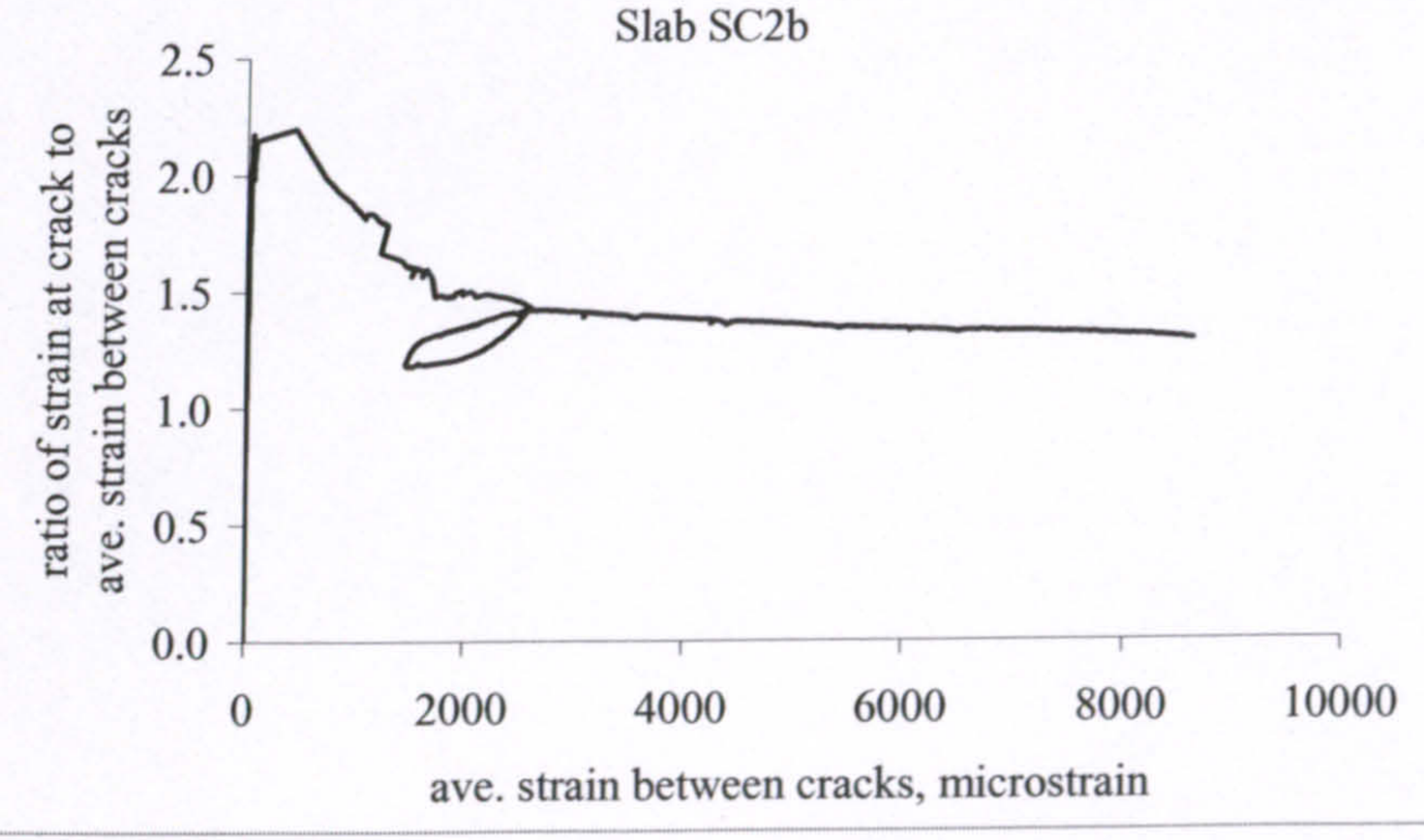
Slab SC2b
ratio of strain at crack to ave. strain between cracks
ave. strain between cracks, microstrain
0.0
0.5
1.0
1.5
2.0
2.5
0
2000
4000
6000
8000
10000

SLAB SC2b

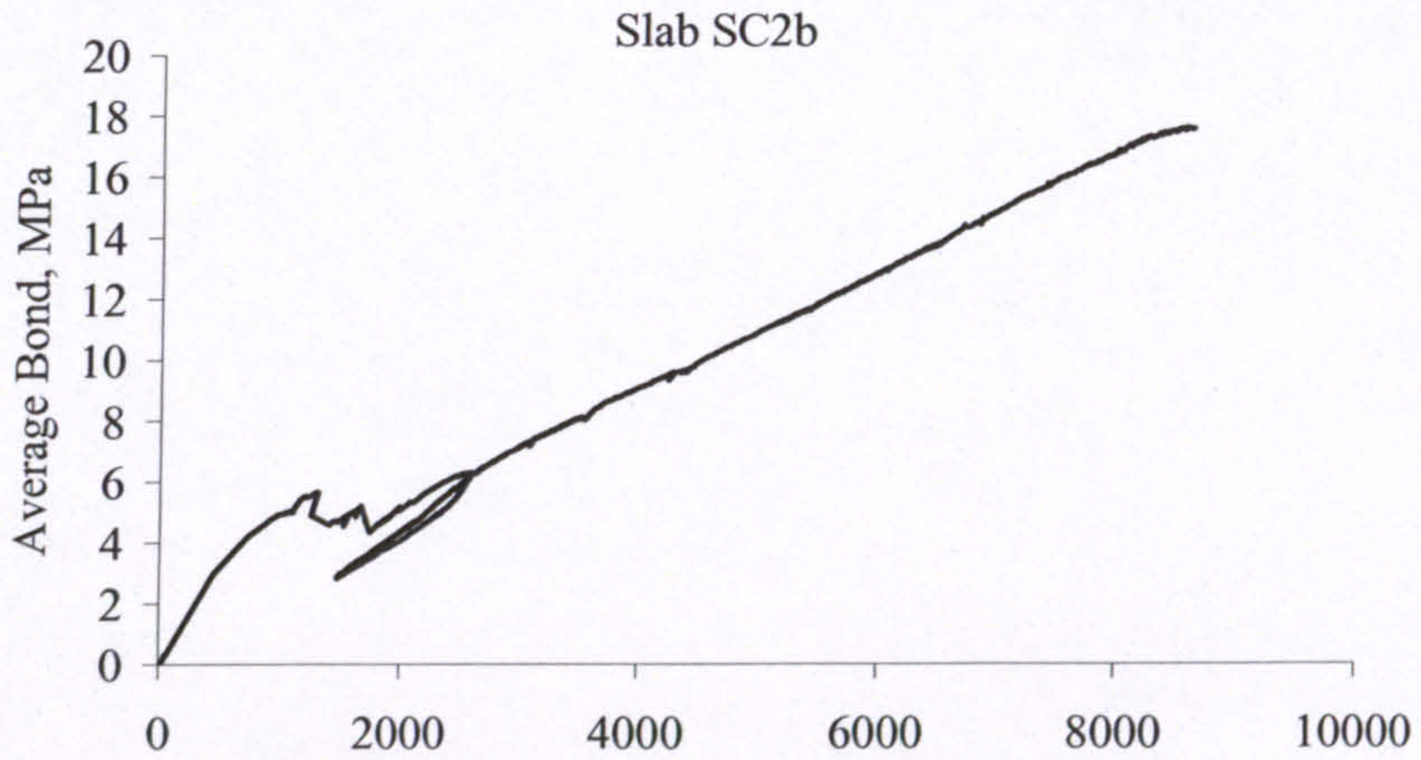

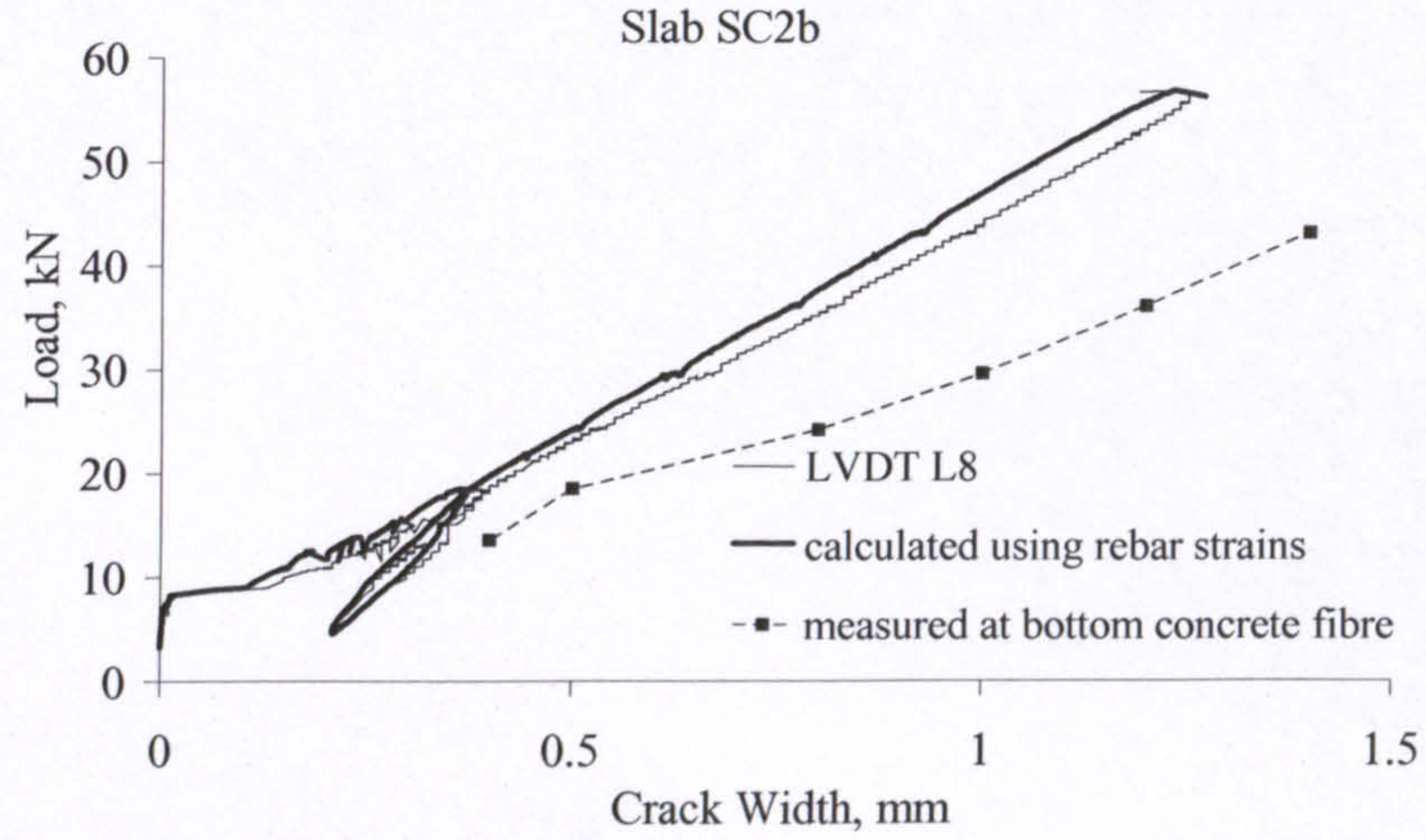

Almost Balanced Failure

- Cover=30-40mm
- Location of crack inducer is precise

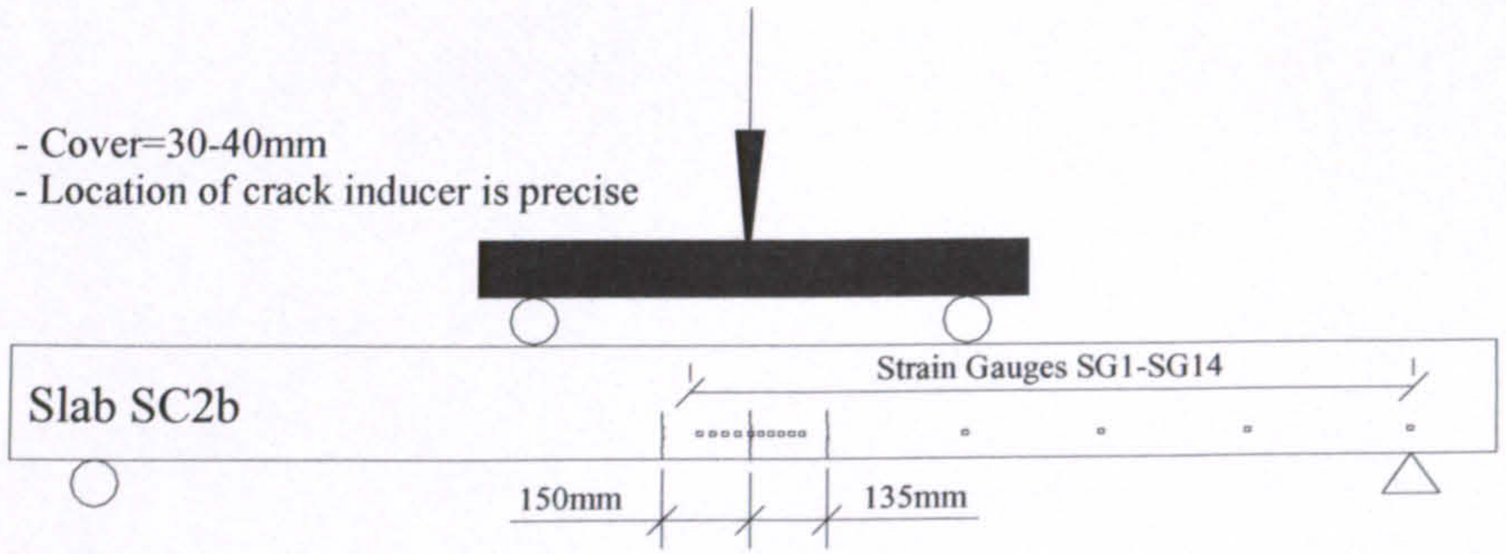

Cracks around Centre

SLAB SC3a

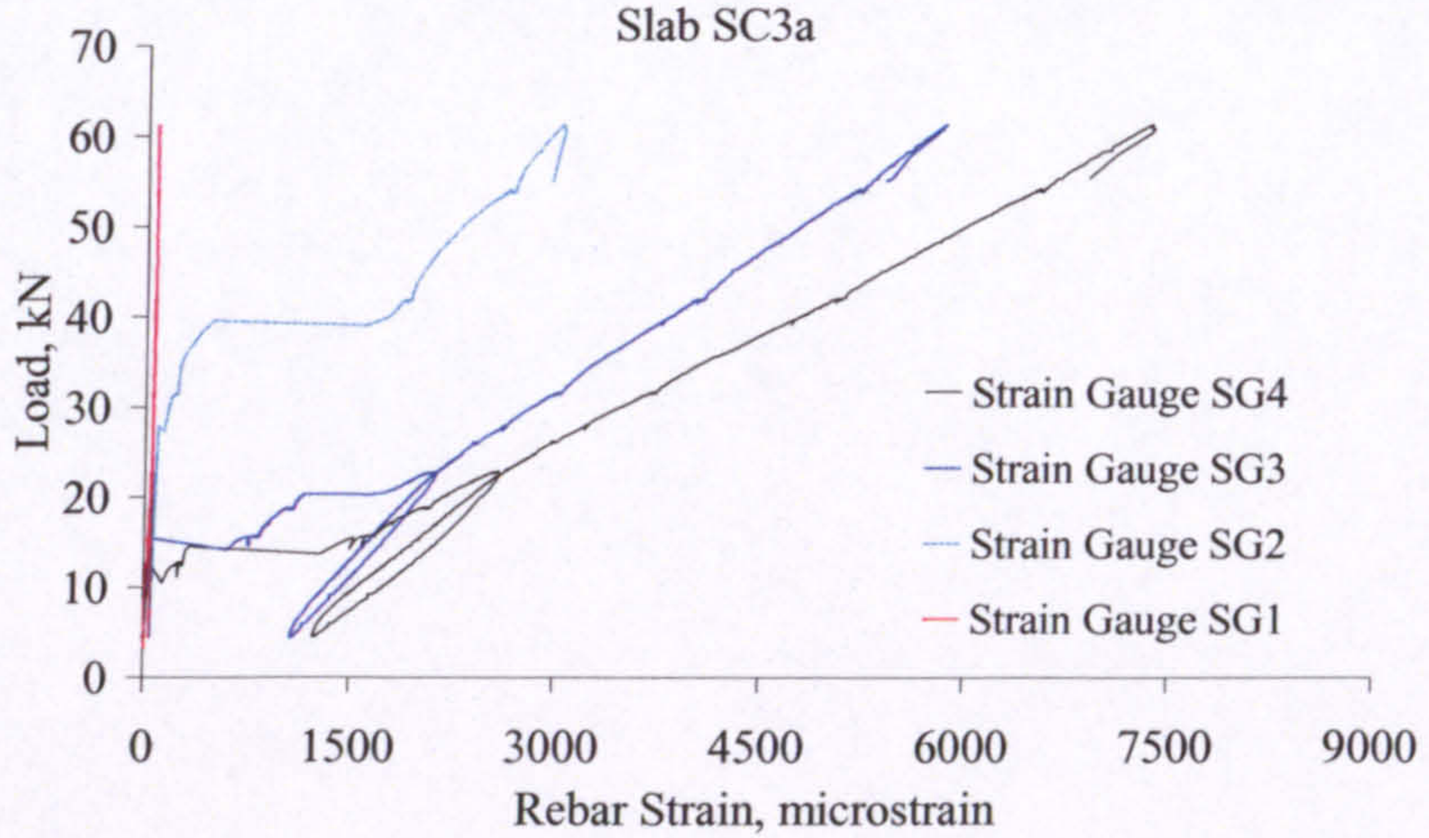
Slab SC3a
Load, kN
Rebar Strain, microstrain
Strain Gauge SG4
Strain Gauge SG3
Strain Gauge SG2
Strain Gauge SG1

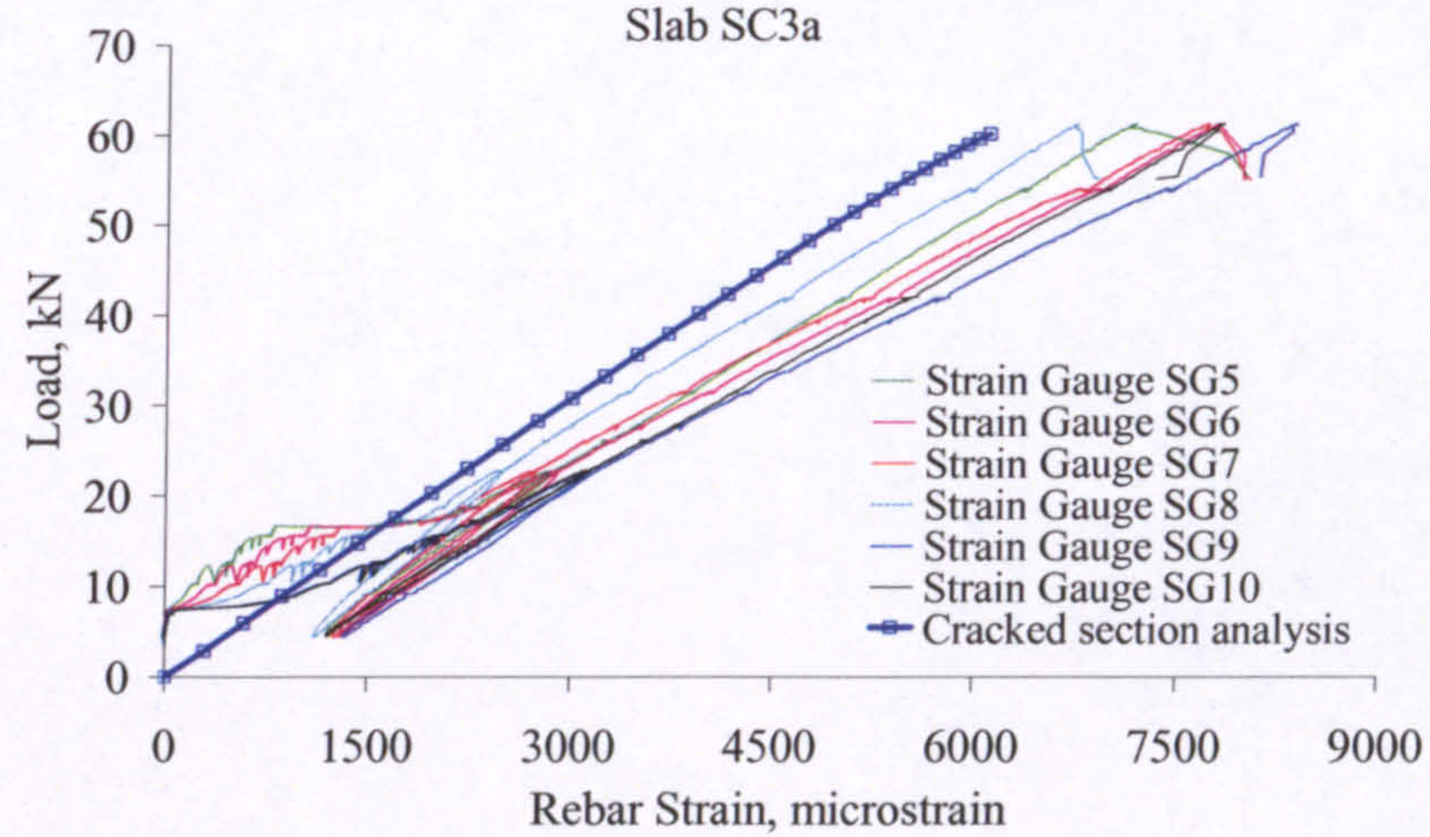
Slab SC3a
Load, kN
Rebar Strain, microstrain
Strain Gauge SG5
Strain Gauge SG6
Strain Gauge SG7
Strain Gauge SG8
Strain Gauge SG9
Strain Gauge SG10
Cracked section analysis

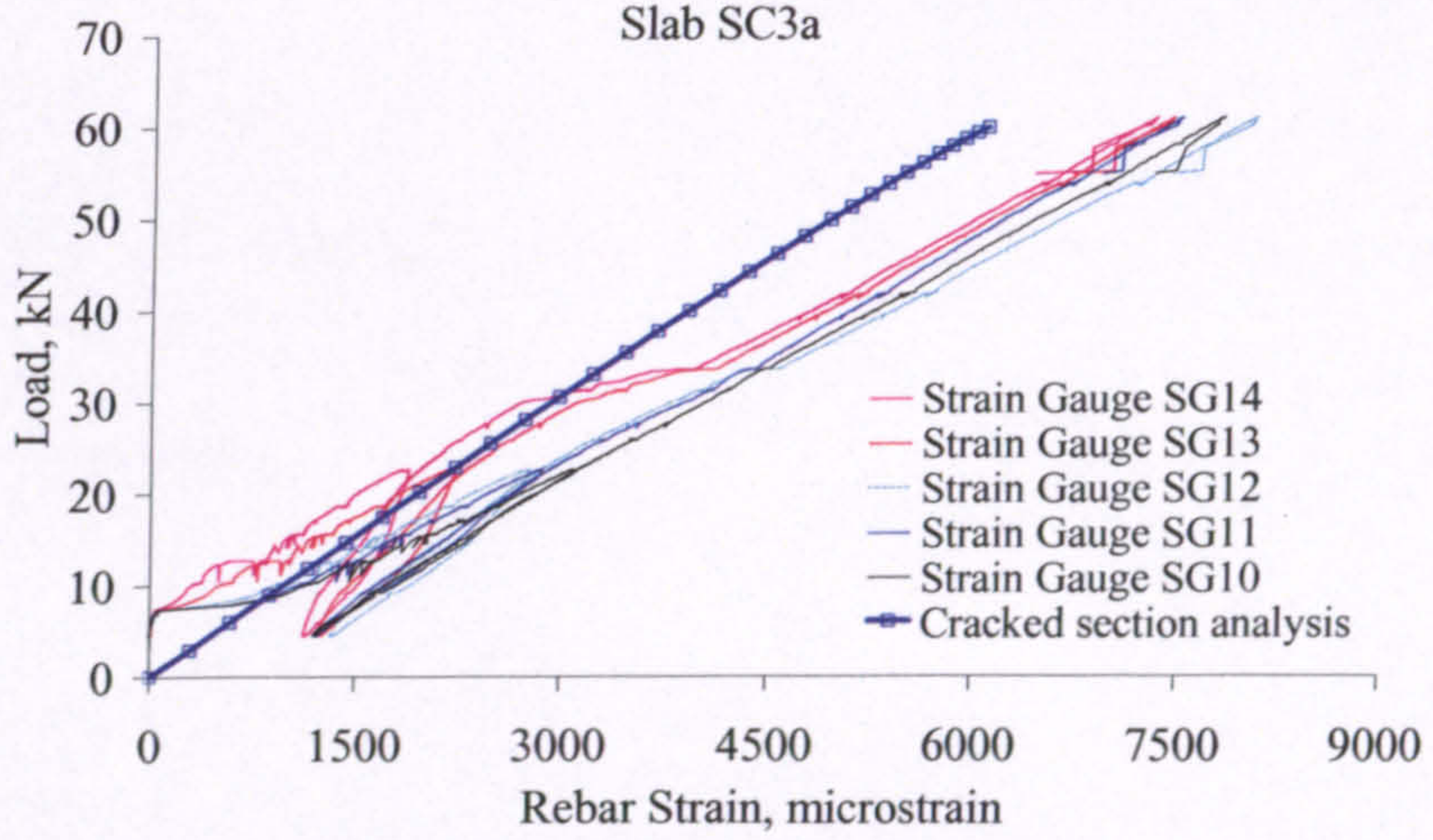
Slab SC3a
Load, kN
Rebar Strain, microstrain
Strain Gauge SG14
Strain Gauge SG13
Strain Gauge SG12
Strain Gauge SG11
Strain Gauge SG10
Cracked section analysis

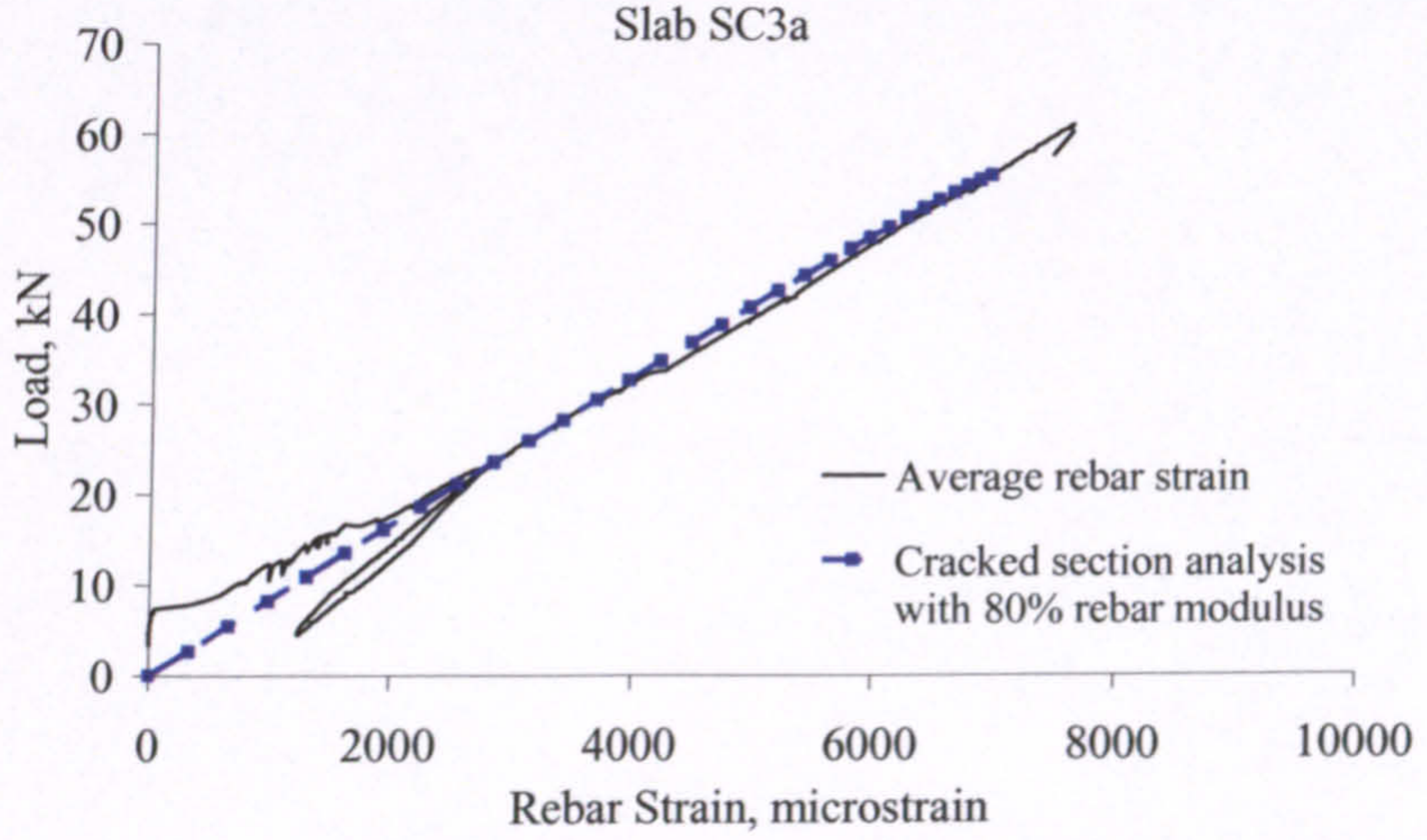
Slab SC3a
Load, kN
Rebar Strain, microstrain
Average rebar strain
Cracked section analysis
with 80% rebar modulus

SLAB SC3a

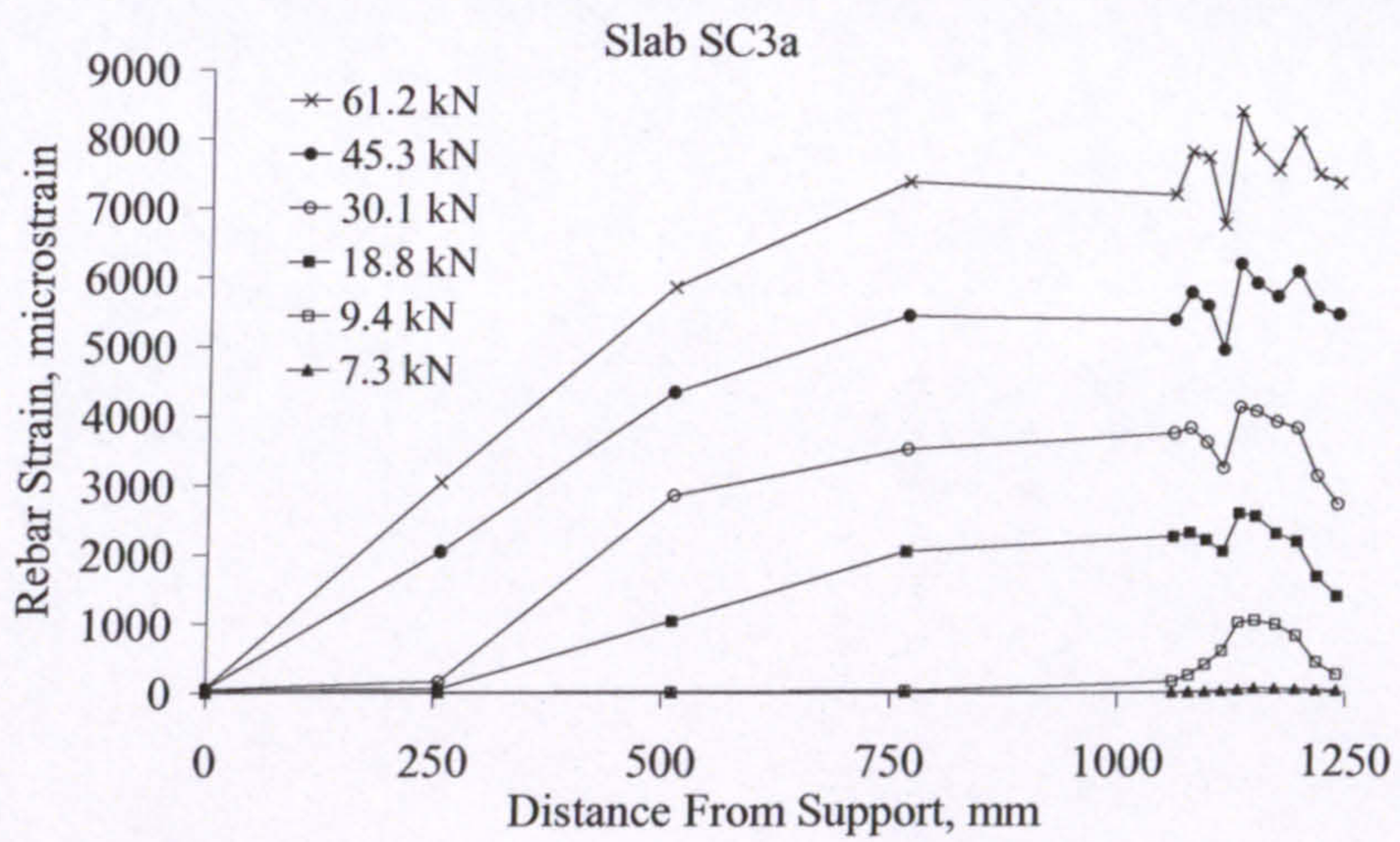
Slab SC3a
Rebar Strain, microstrain
9000
8000
7000
6000
5000
4000
3000
2000
1000
0
61.2 kN
45.3 kN
30.1 kN
18.8 kN
9.4 kN
7.3 kN
0
250
500
750
1000
1250
Distance From Support, mm

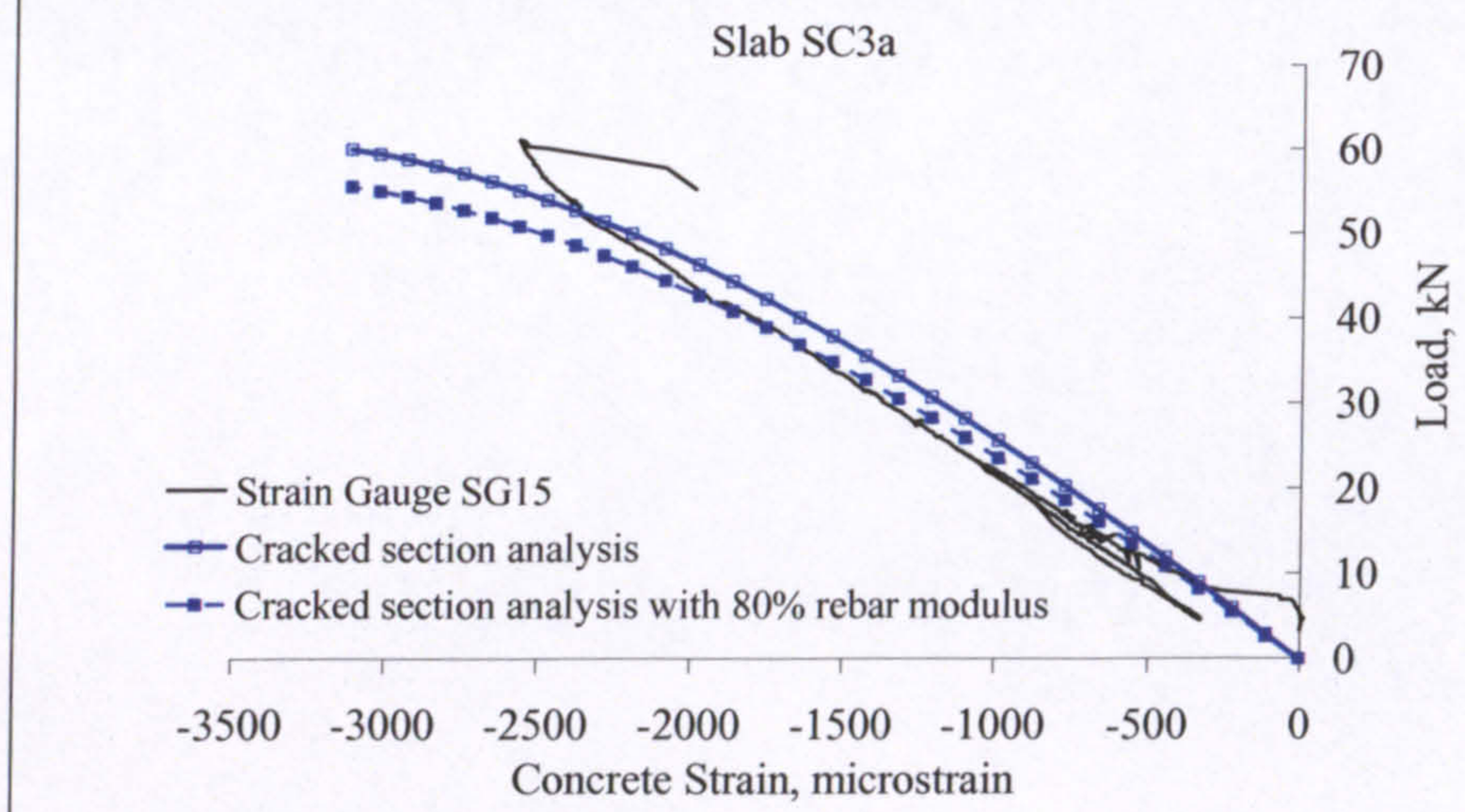
Slab SC3a
Load, kN
70
60
50
40
30
20
10
0
Strain Gauge SG15
Cracked section analysis
Cracked section analysis with 80% rebar modulus
-3500
-3000
-2500
-2000
-1500
-1000
-500
0
Concrete Strain, microstrain

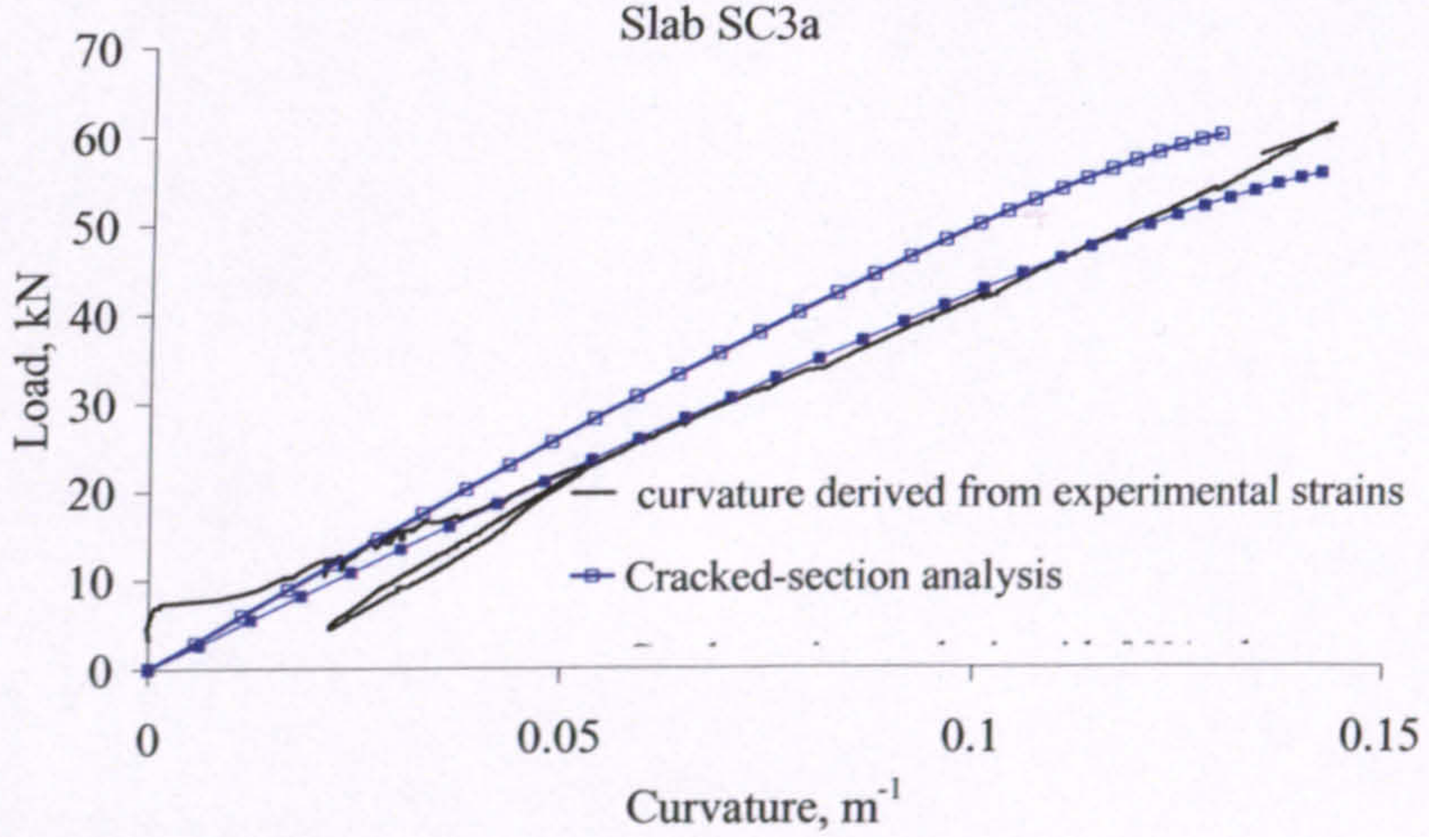
Slab SC3a
Load, kN
70
60
50
40
30
20
10
0
curvature derived from experimental strains
Cracked-section analysis
0
0.05
0.1
0.15
Curvature, m-1

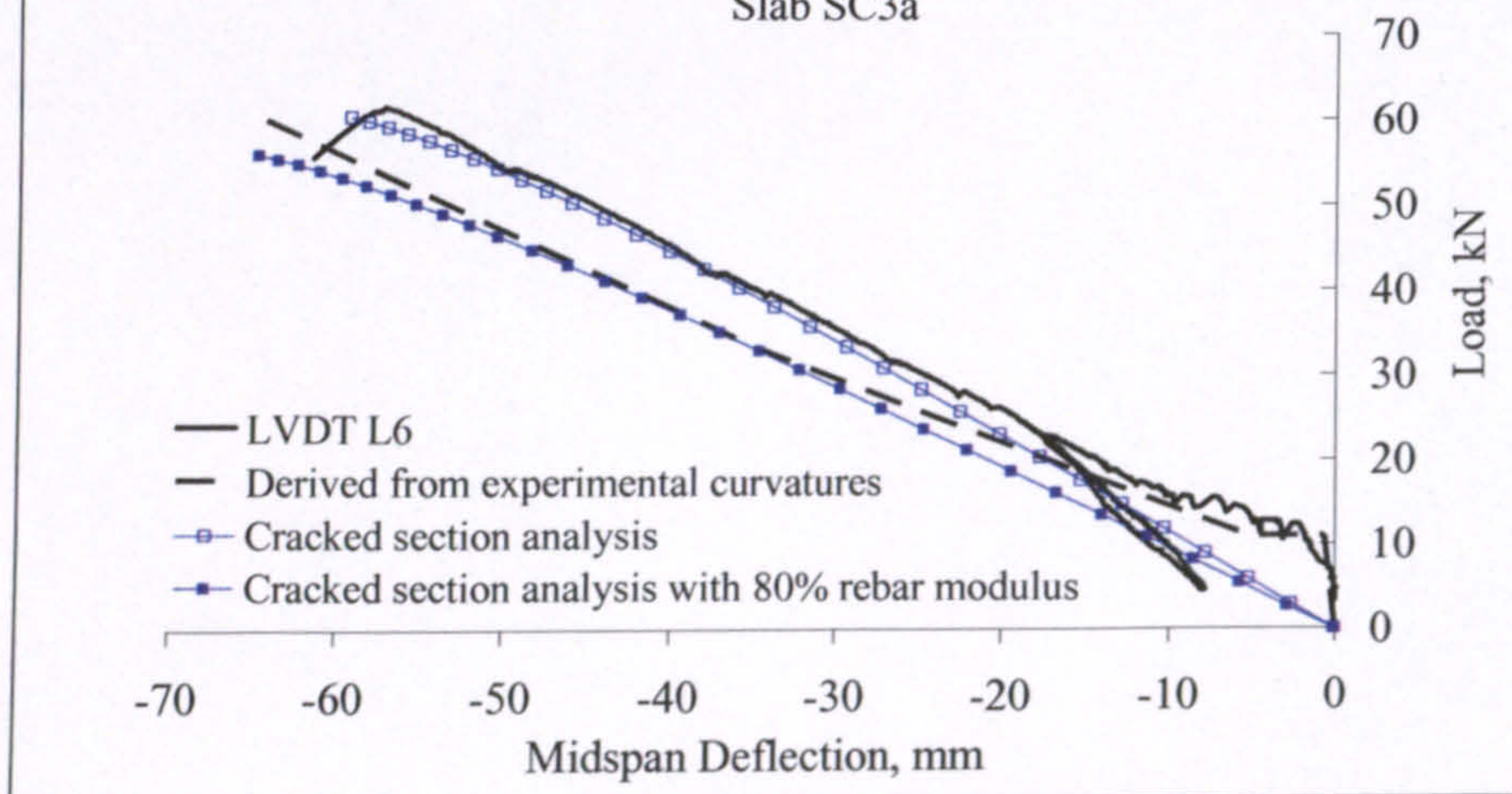
Slab SC3a
Load, kN
70
60
50
40
30
20
10
0
LVDT L6
Derived from experimental curvatures
Cracked section analysis
Cracked section analysis with 80% rebar modulus
-70
-60
-50
-40
-30
-20
-10
0
Midspan Deflection, mm

SLAB SC3a

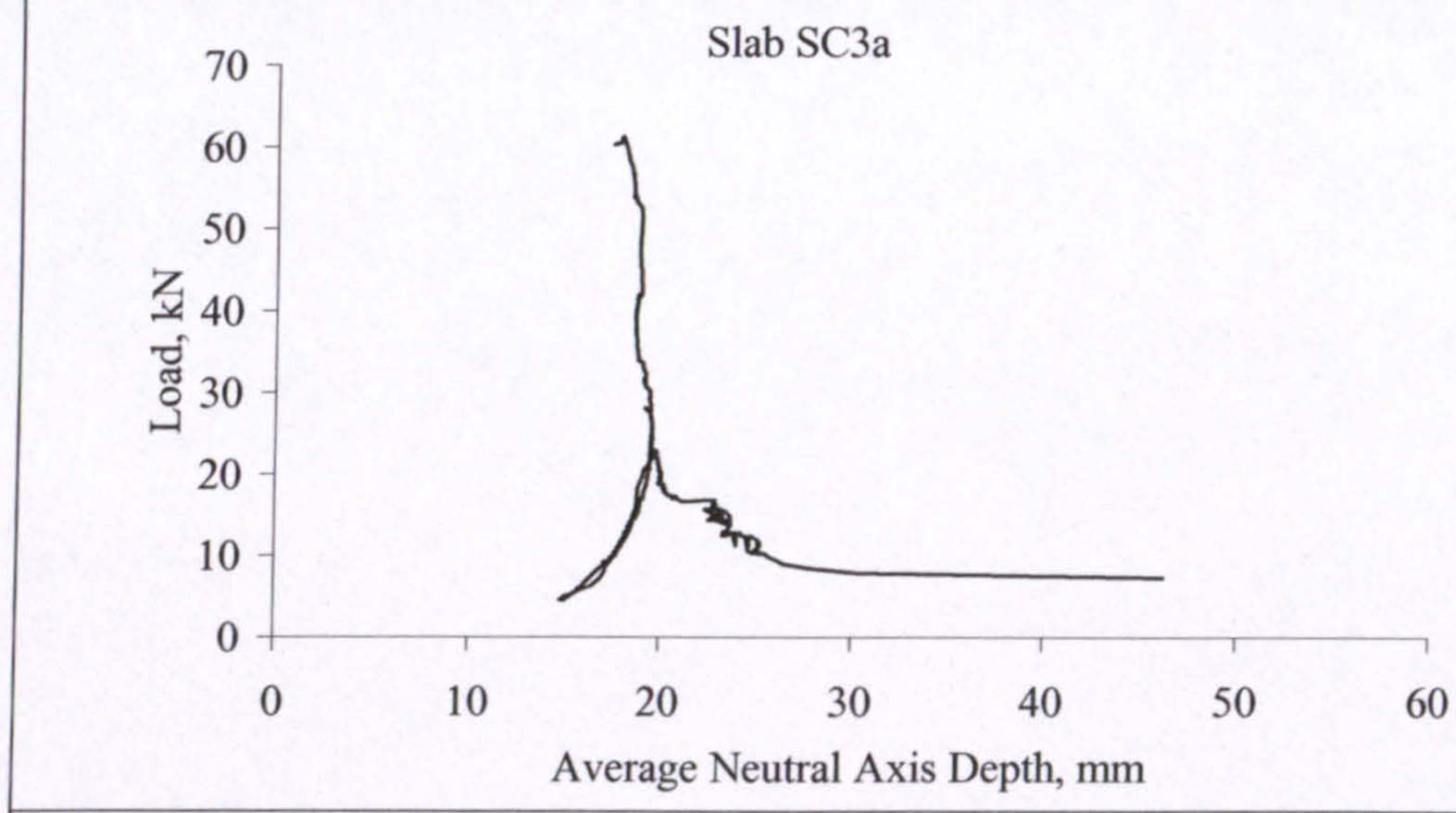
Slab SC3a
Load, kN
Average Neutral Axis Depth, mm
0
10
20
30
40
50
60
70

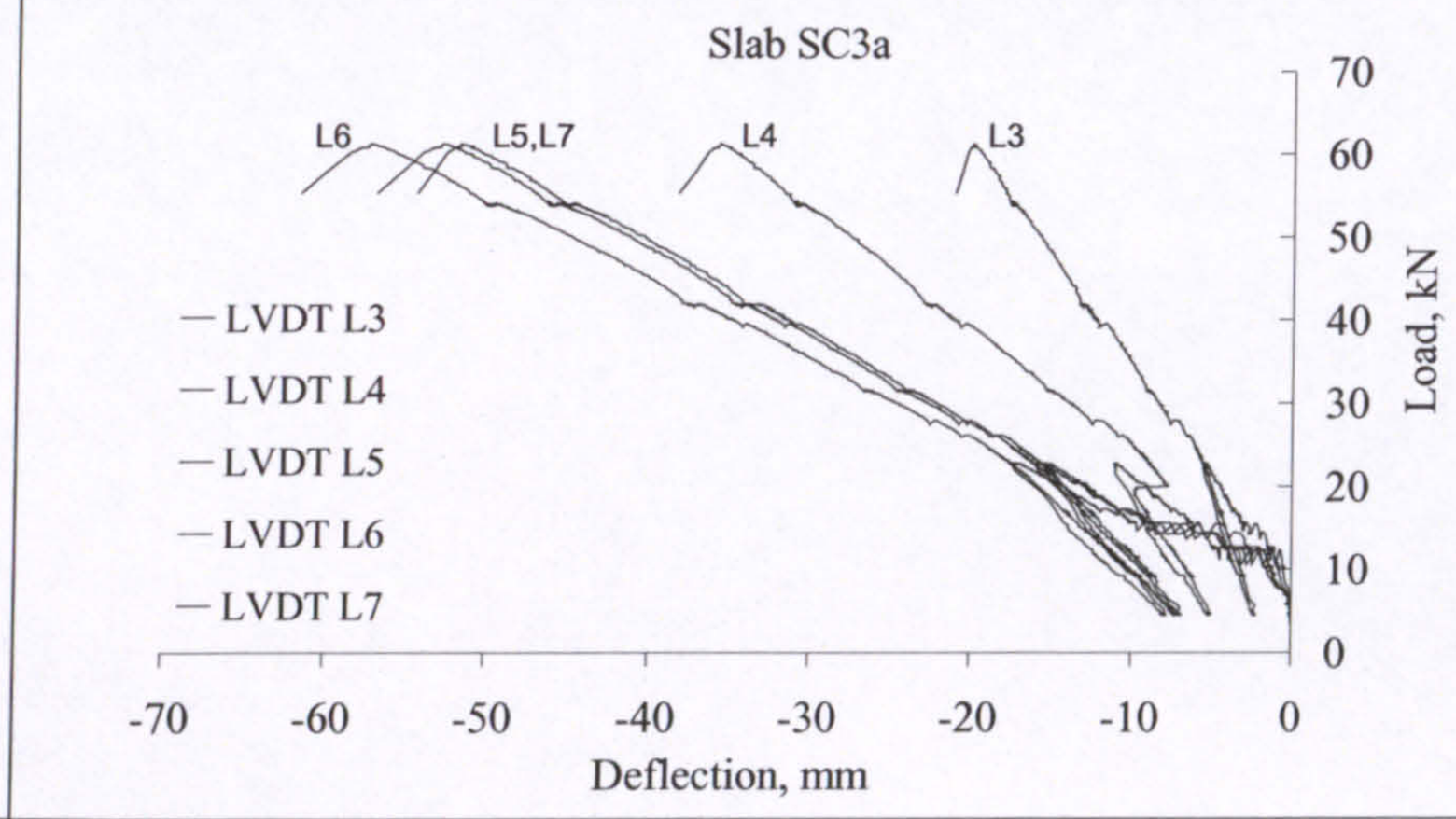
Slab SC3a
L6
L5,L7
L4
L3
LVDT L3
LVDT L4
LVDT L5
LVDT L6
LVDT L7
Load, kN
Deflection, mm
-70
-60
-50
-40
-30
-20
-10
0

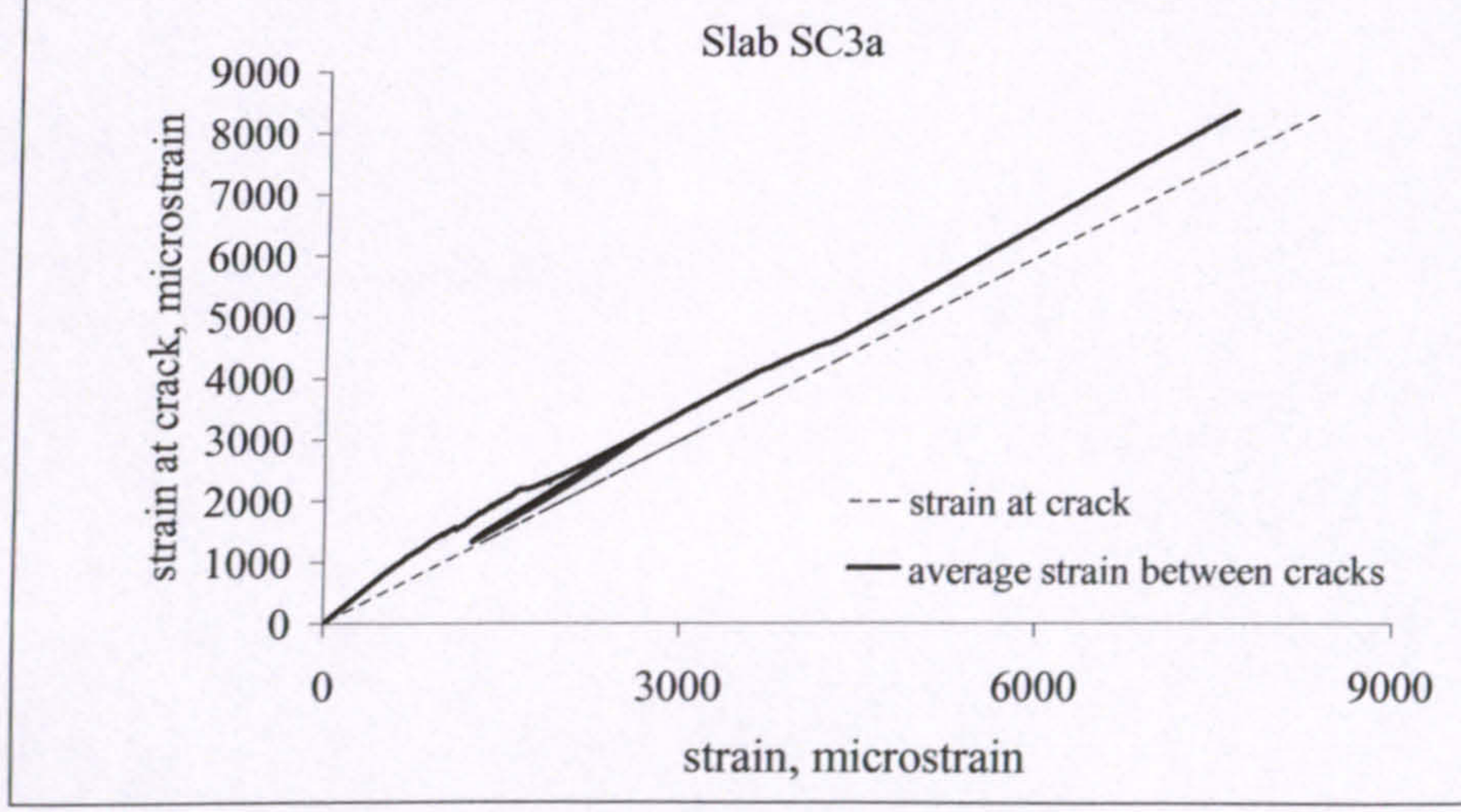
Slab SC3a
strain at crack, microstrain
strain, microstrain
strain at crack
average strain between cracks
0
1000
2000
3000
4000
5000
6000
7000
8000
9000

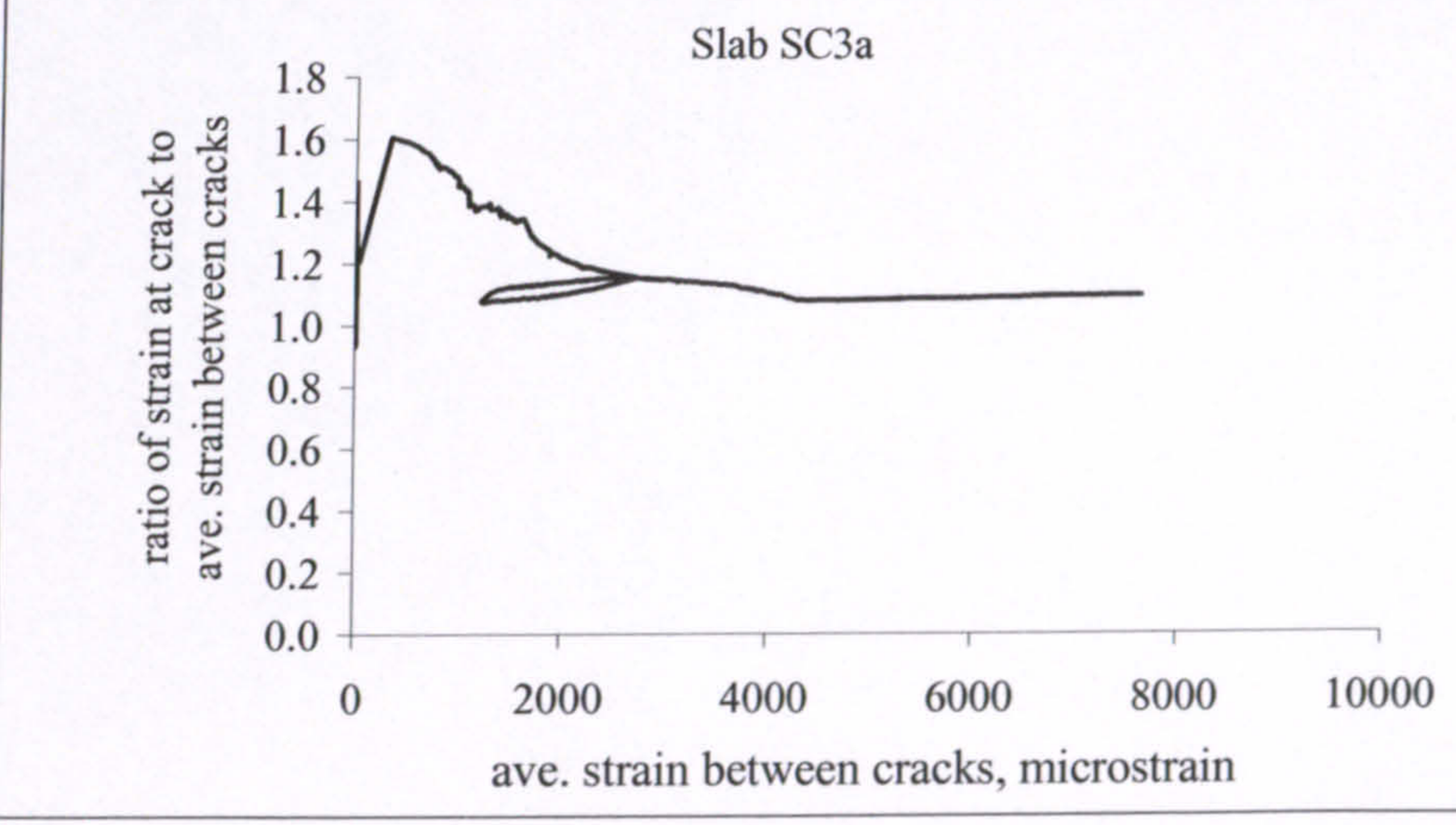
Slab SC3a
ratio of strain at crack to ave. strain between cracks
ave. strain between cracks, microstrain
0.0
0.2
0.4
0.6
0.8
1.0
1.2
1.4
1.6
1.8
0
2000
4000
6000
8000
10000

SLAB SC3a

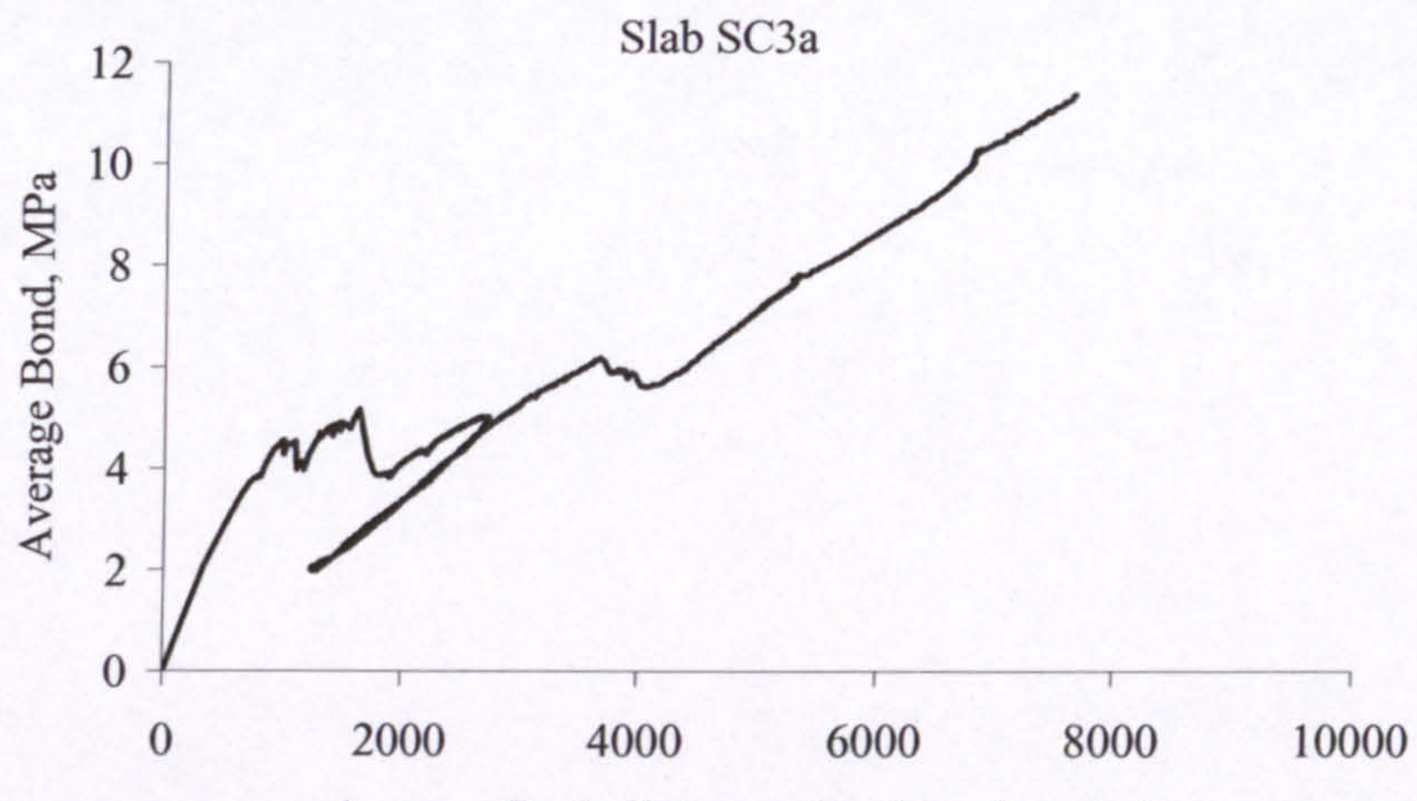

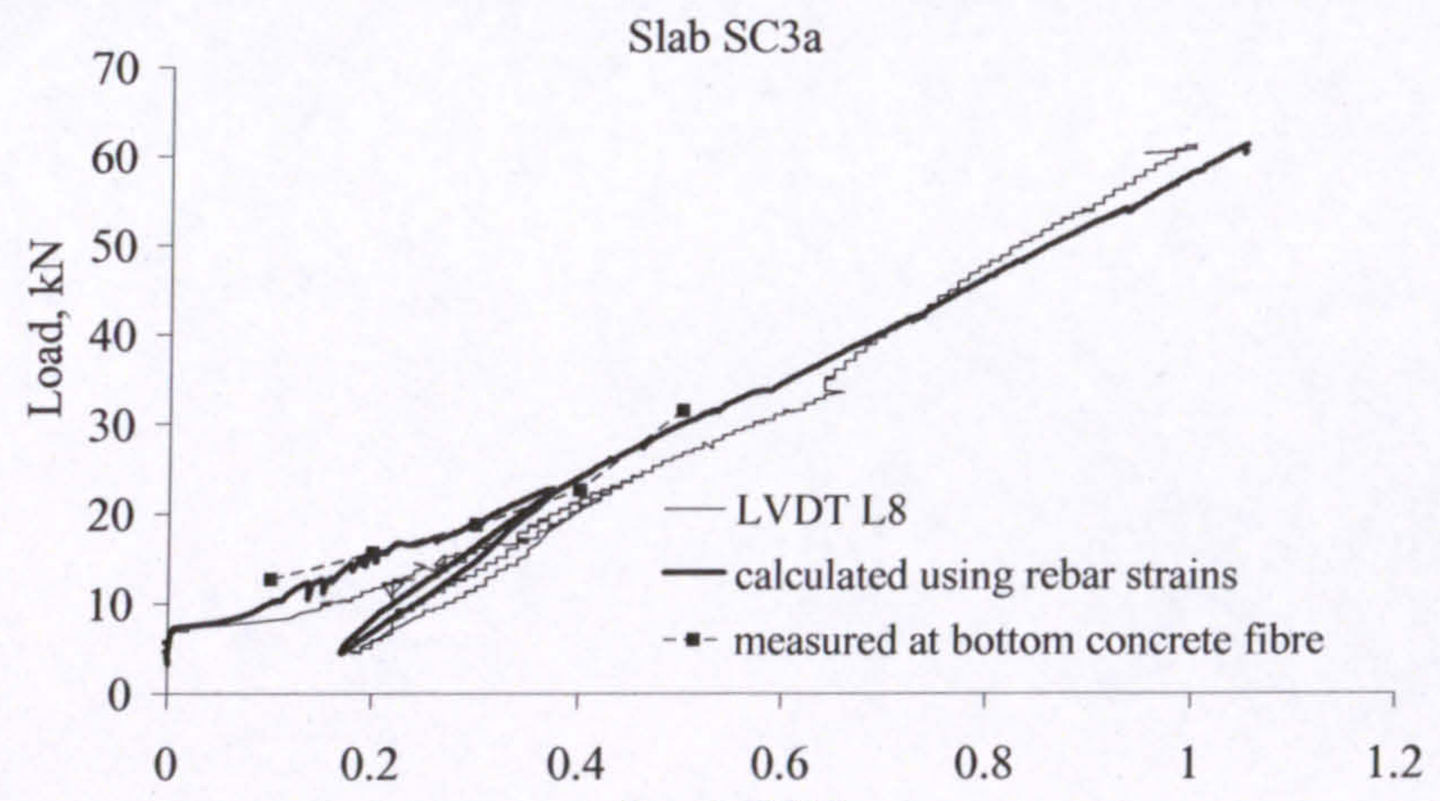

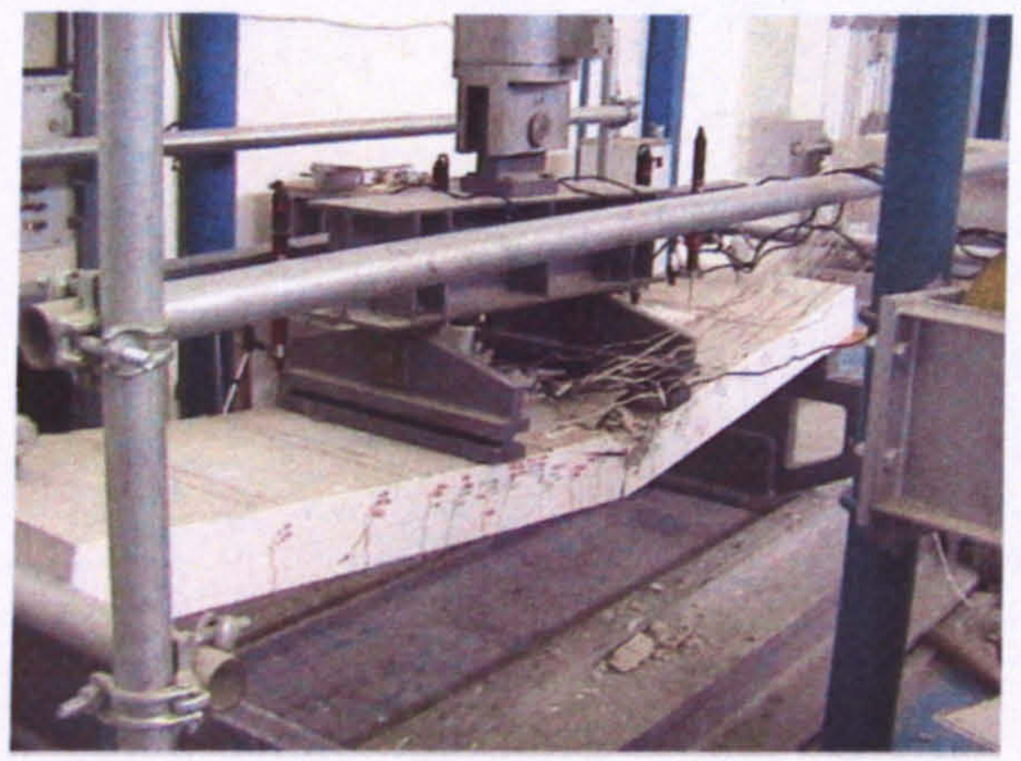

Failure by crushing of concrete

- Cover=35-50mm
- Location of crack inducer is precise
- at (22.7-31.6) kN, a crack formed 75mm left of CL.

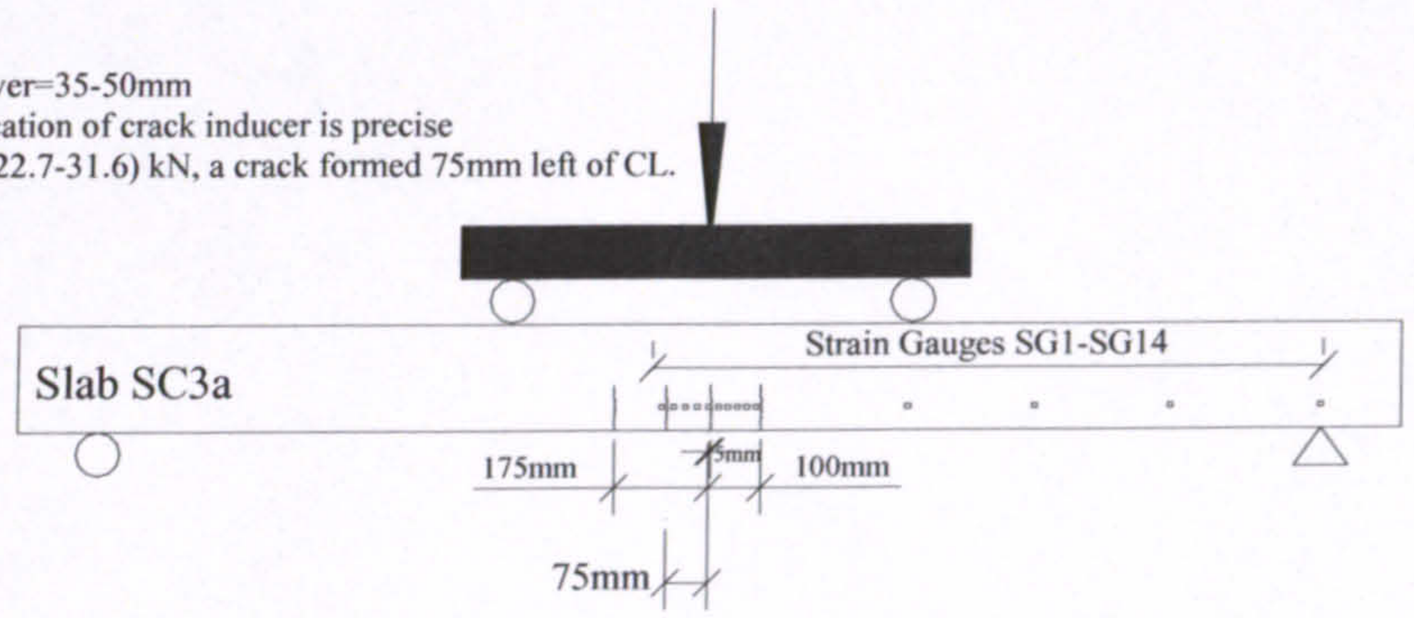

Cracks around Centre

SLAB SC3b

note: slab pre-cracked only at centre

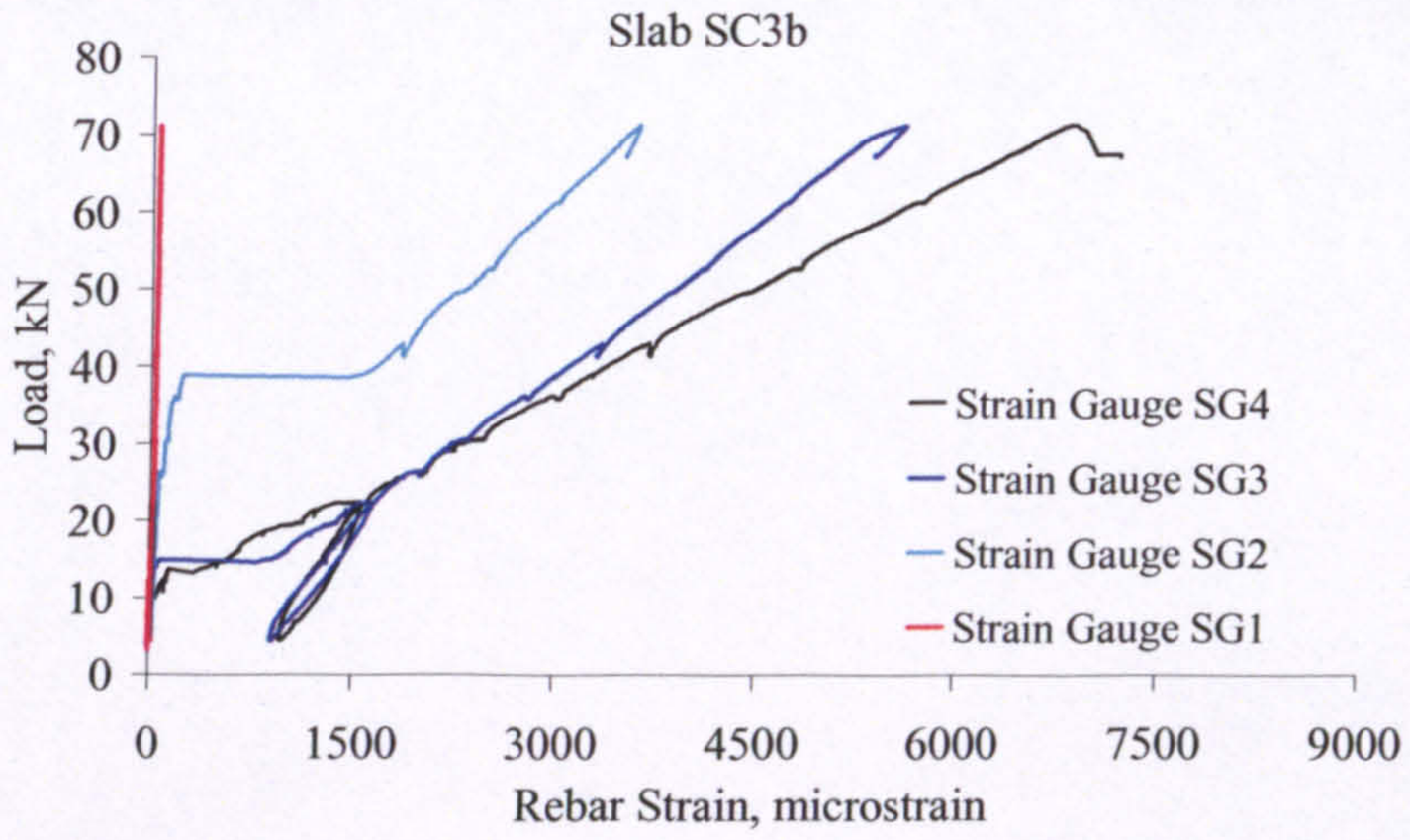

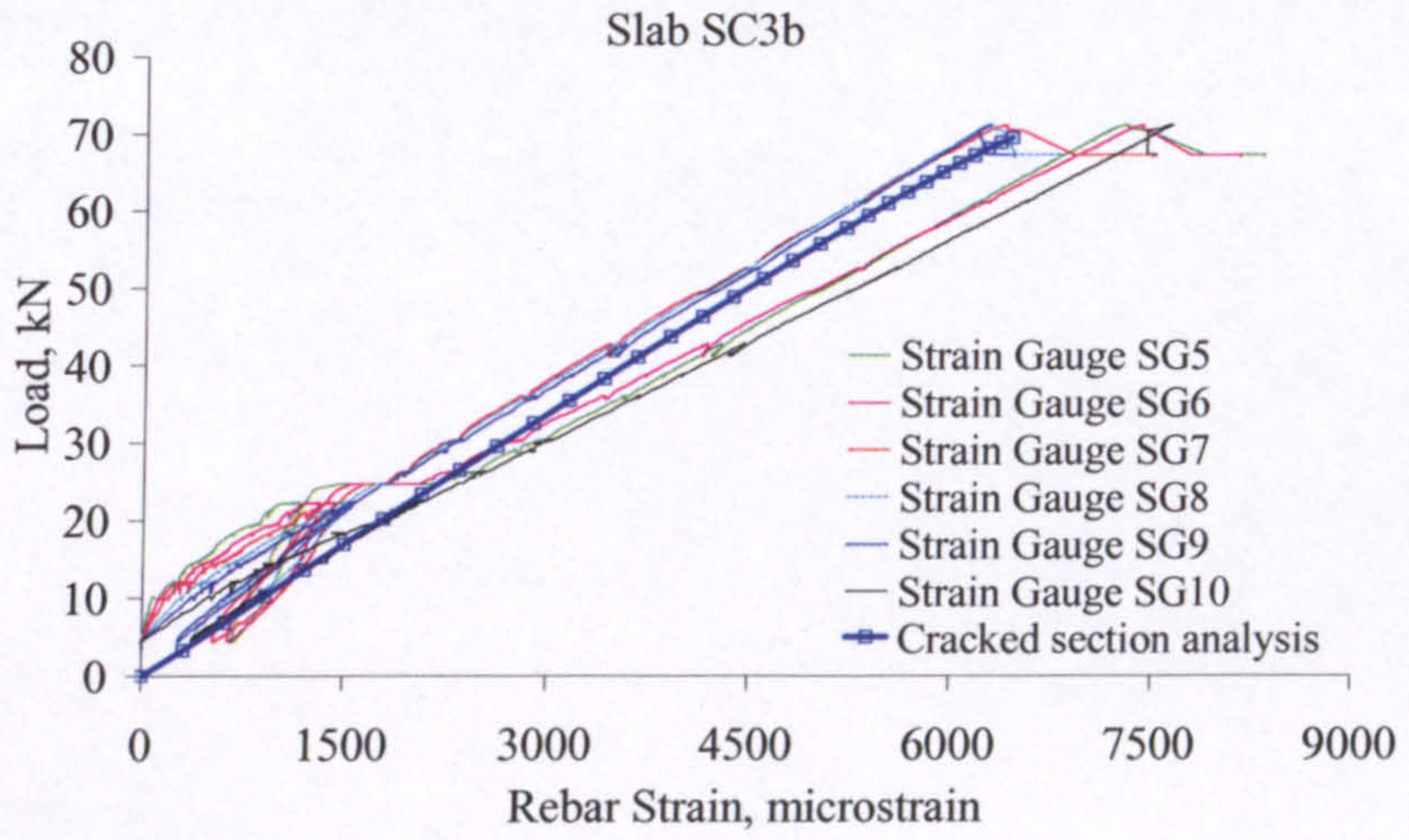

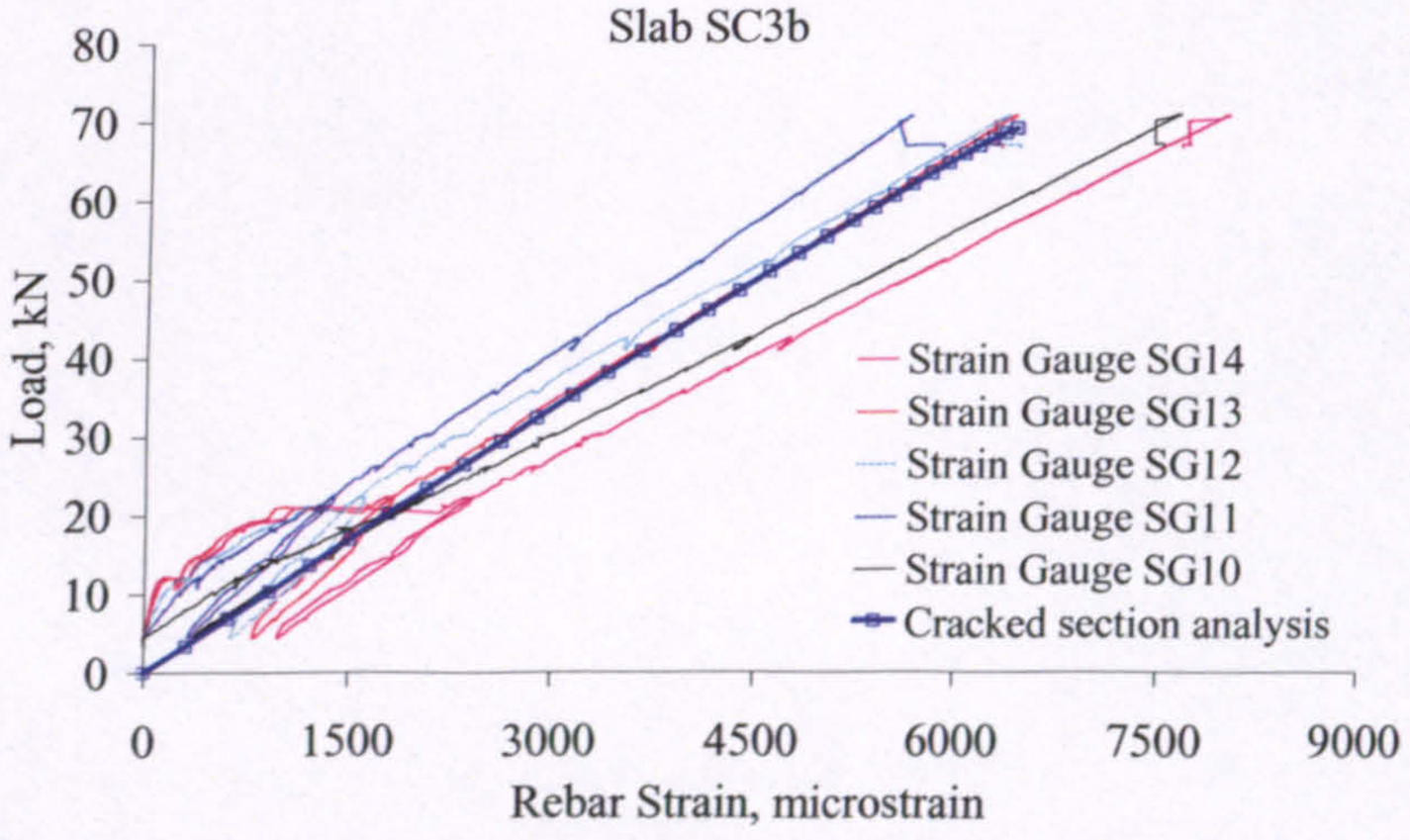

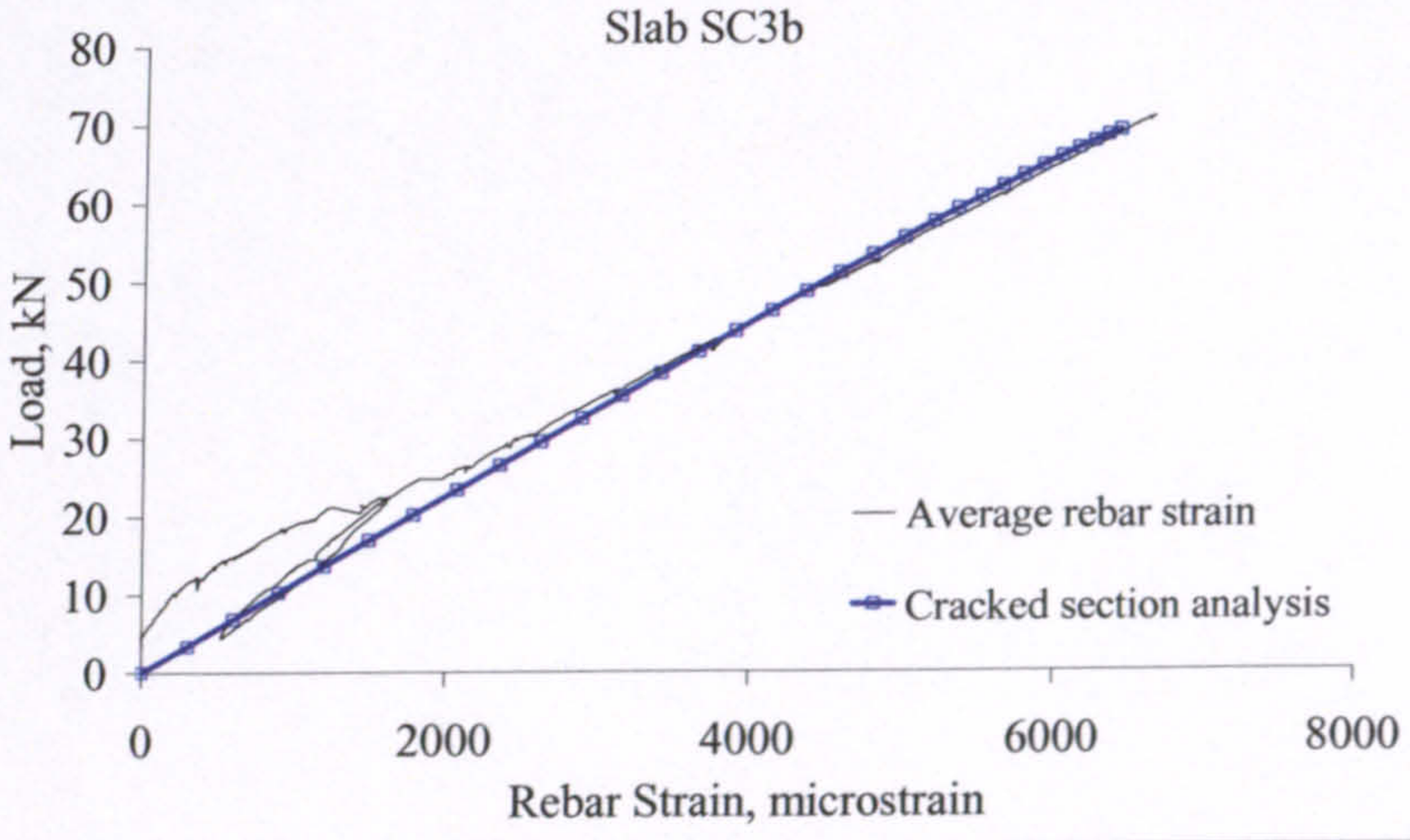

SLAB SC3b

note: slab pre-cracked only at centre

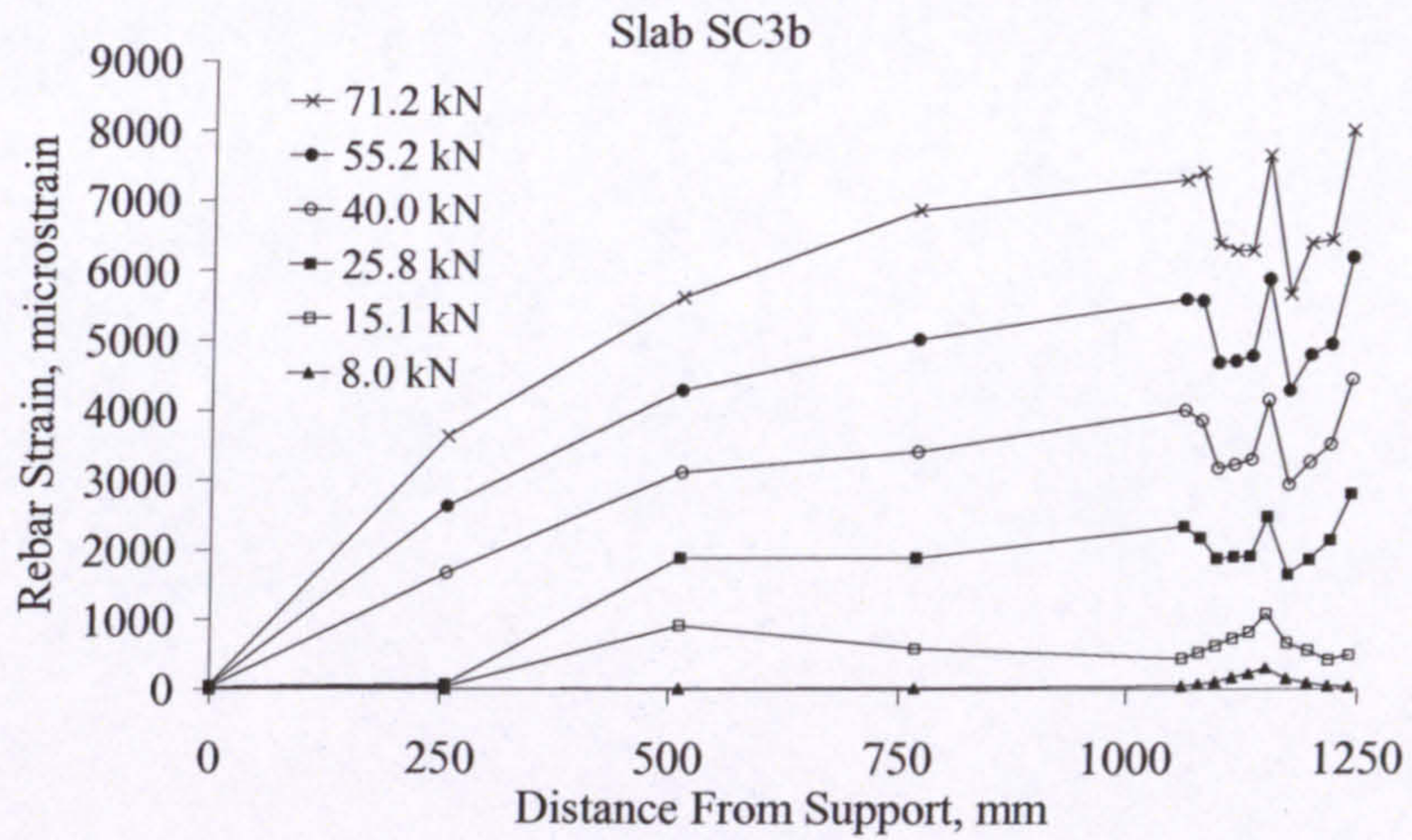

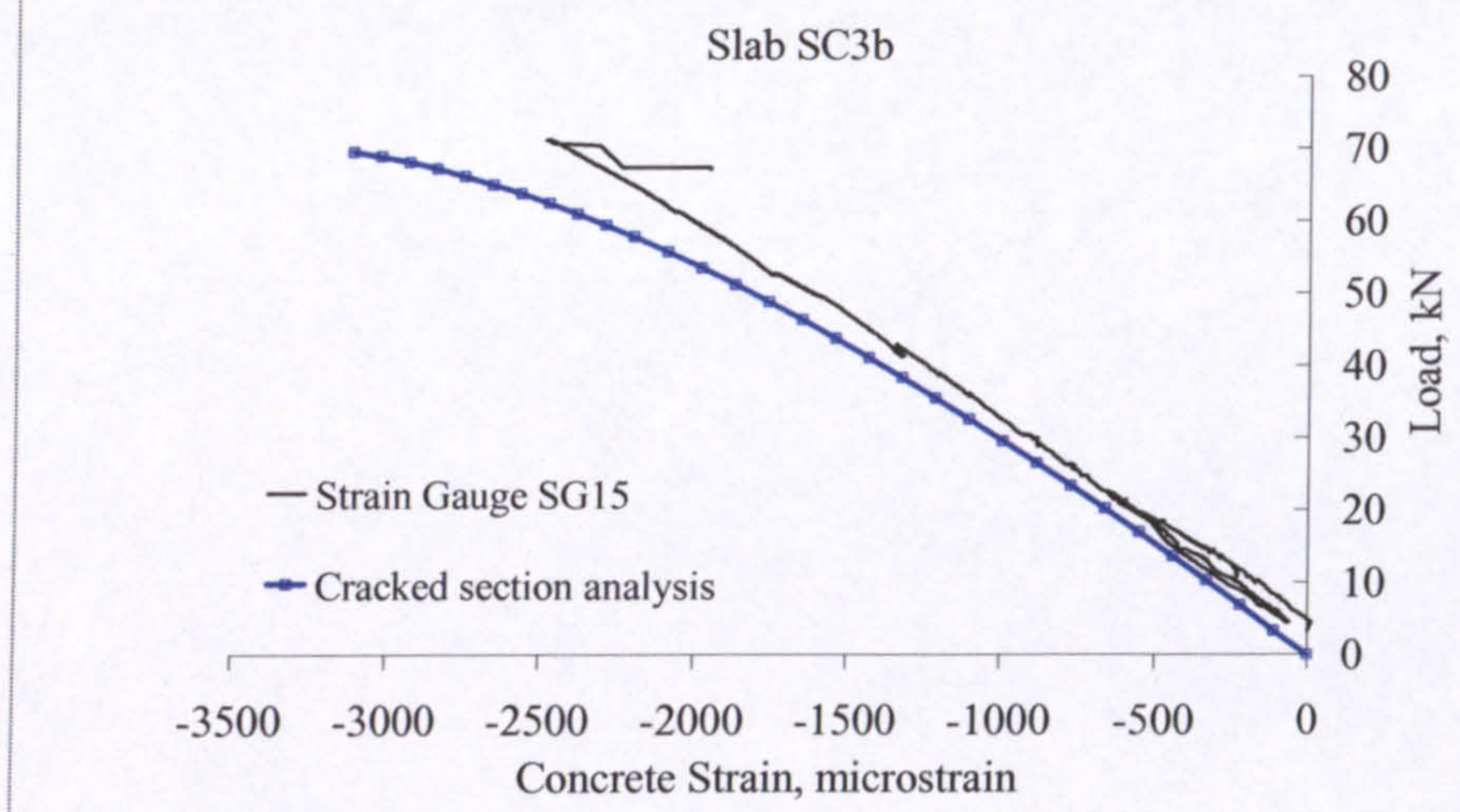

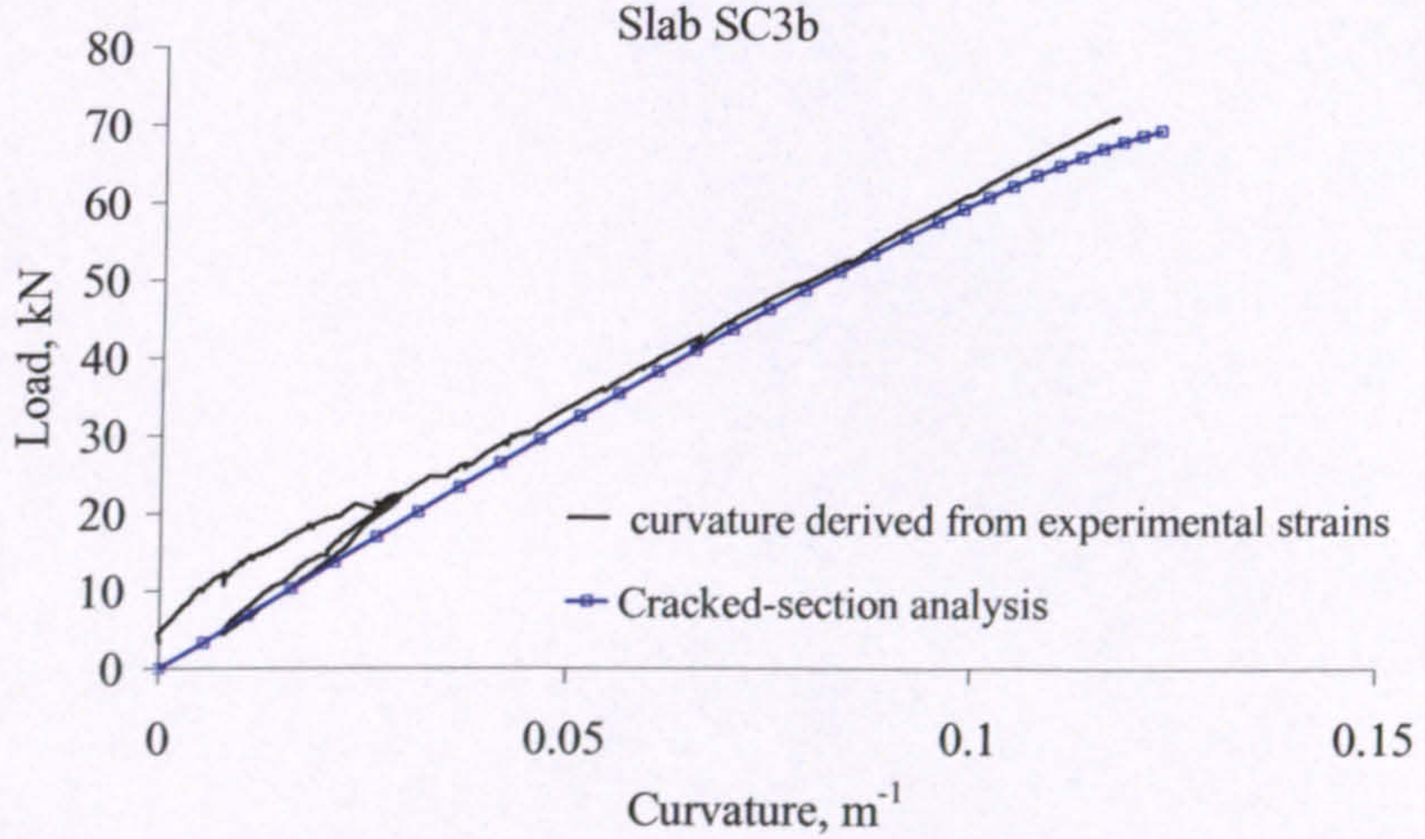

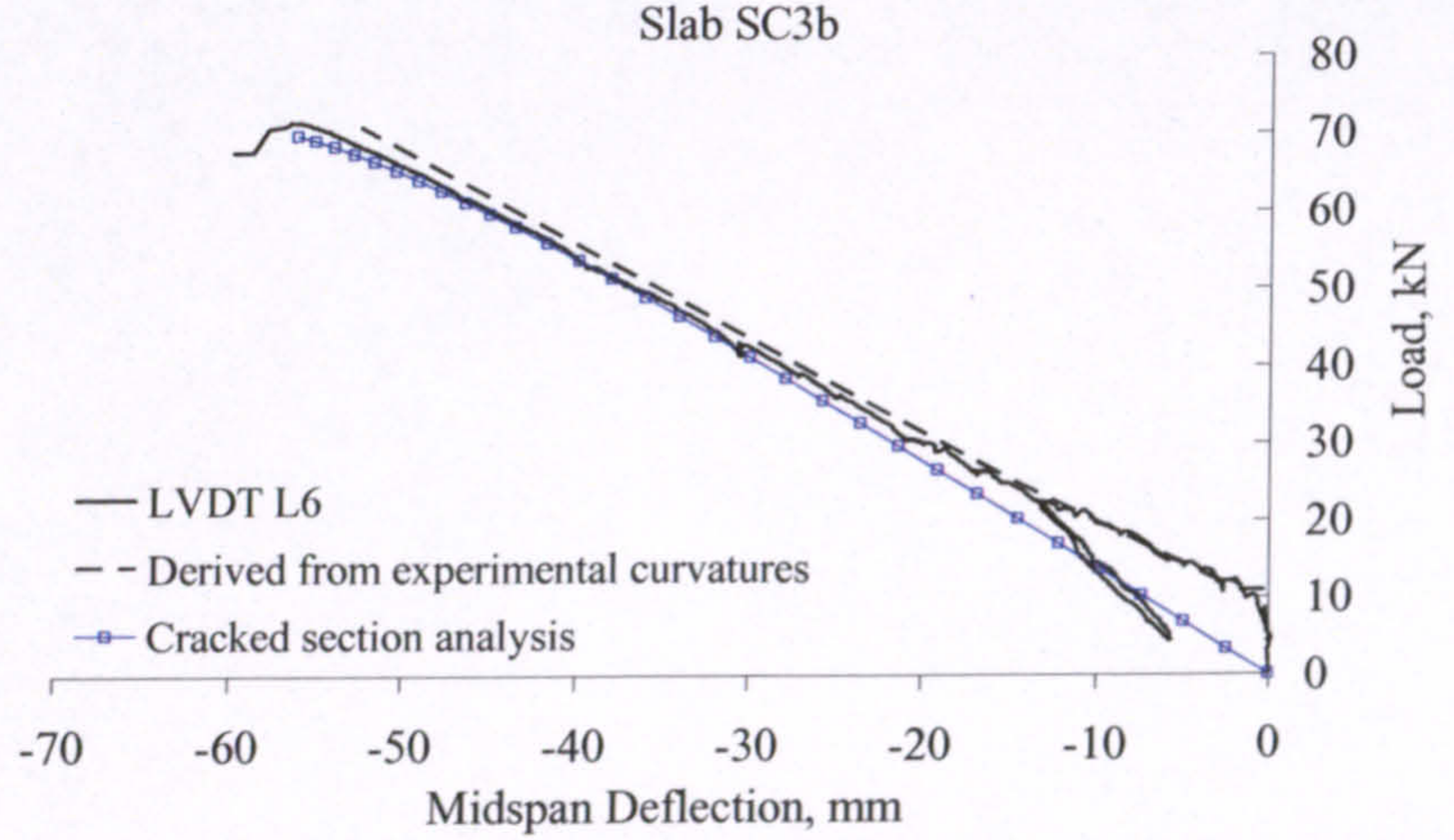

SLAB SC3b

note: slab pre-cracked only at centre

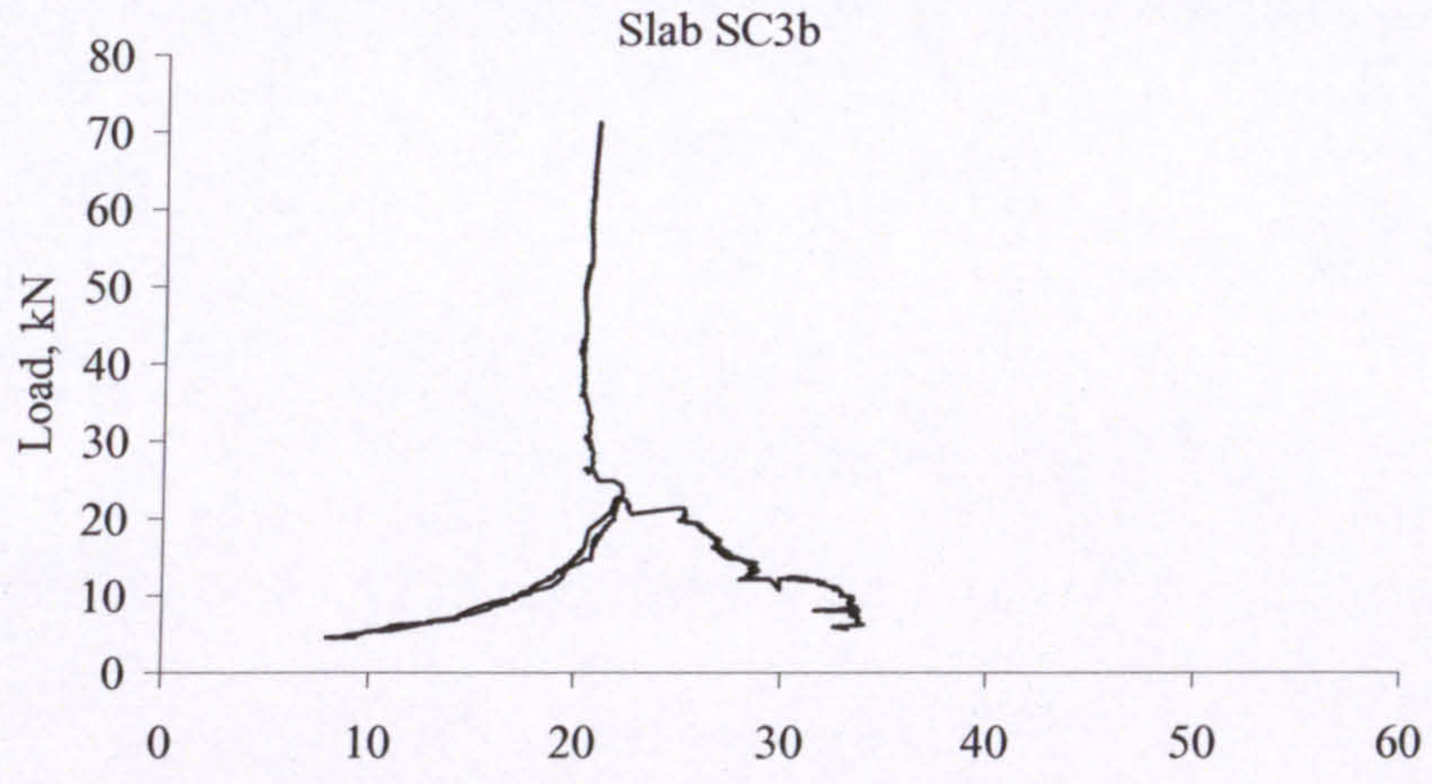

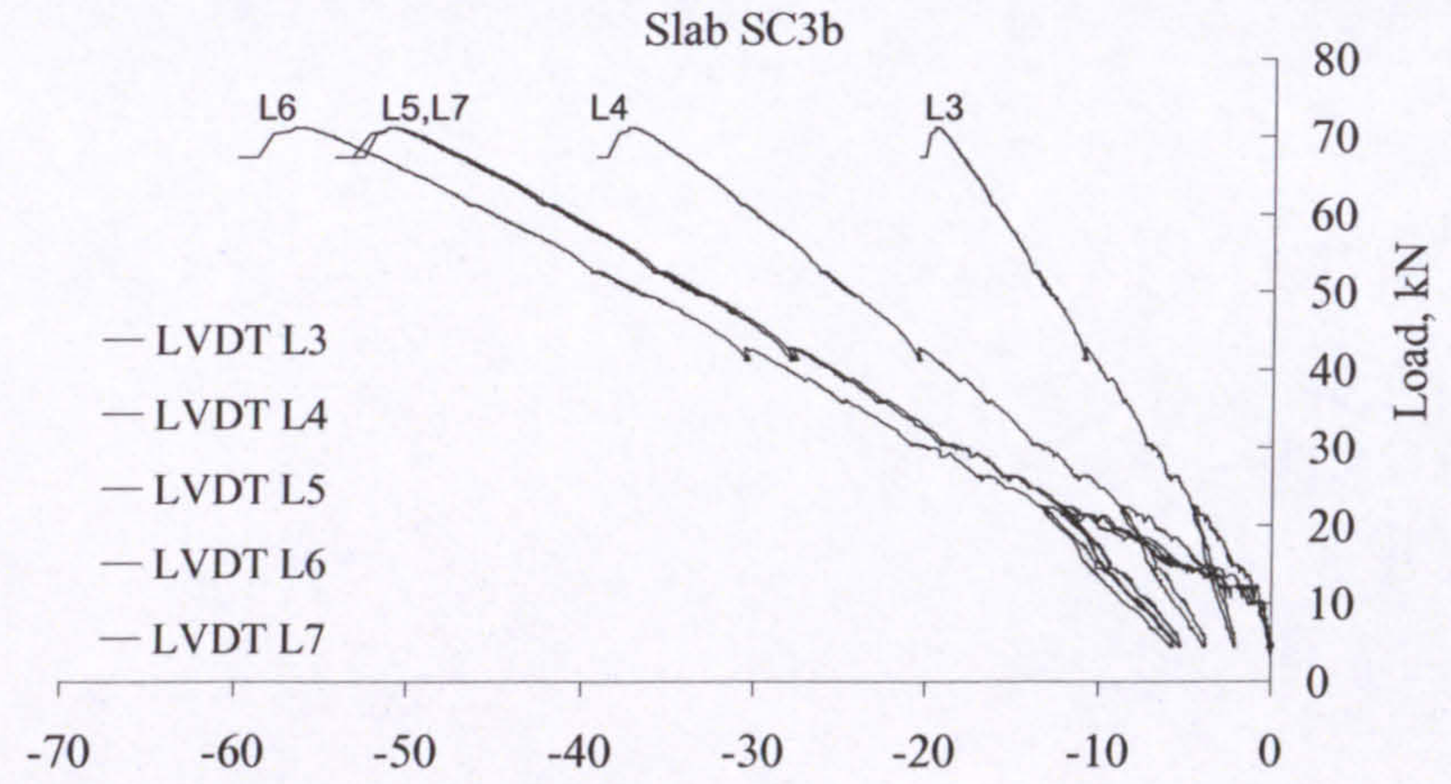

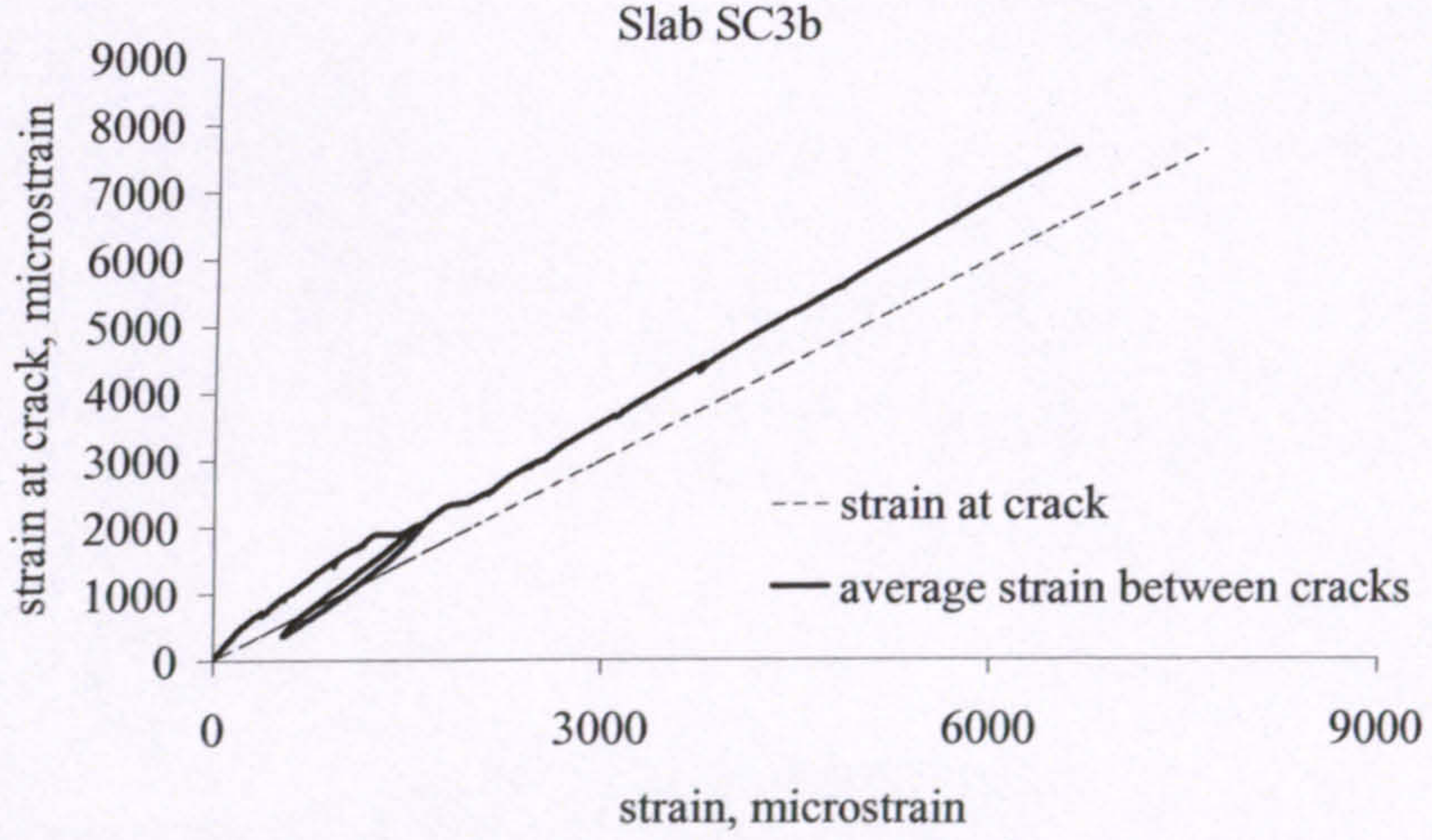

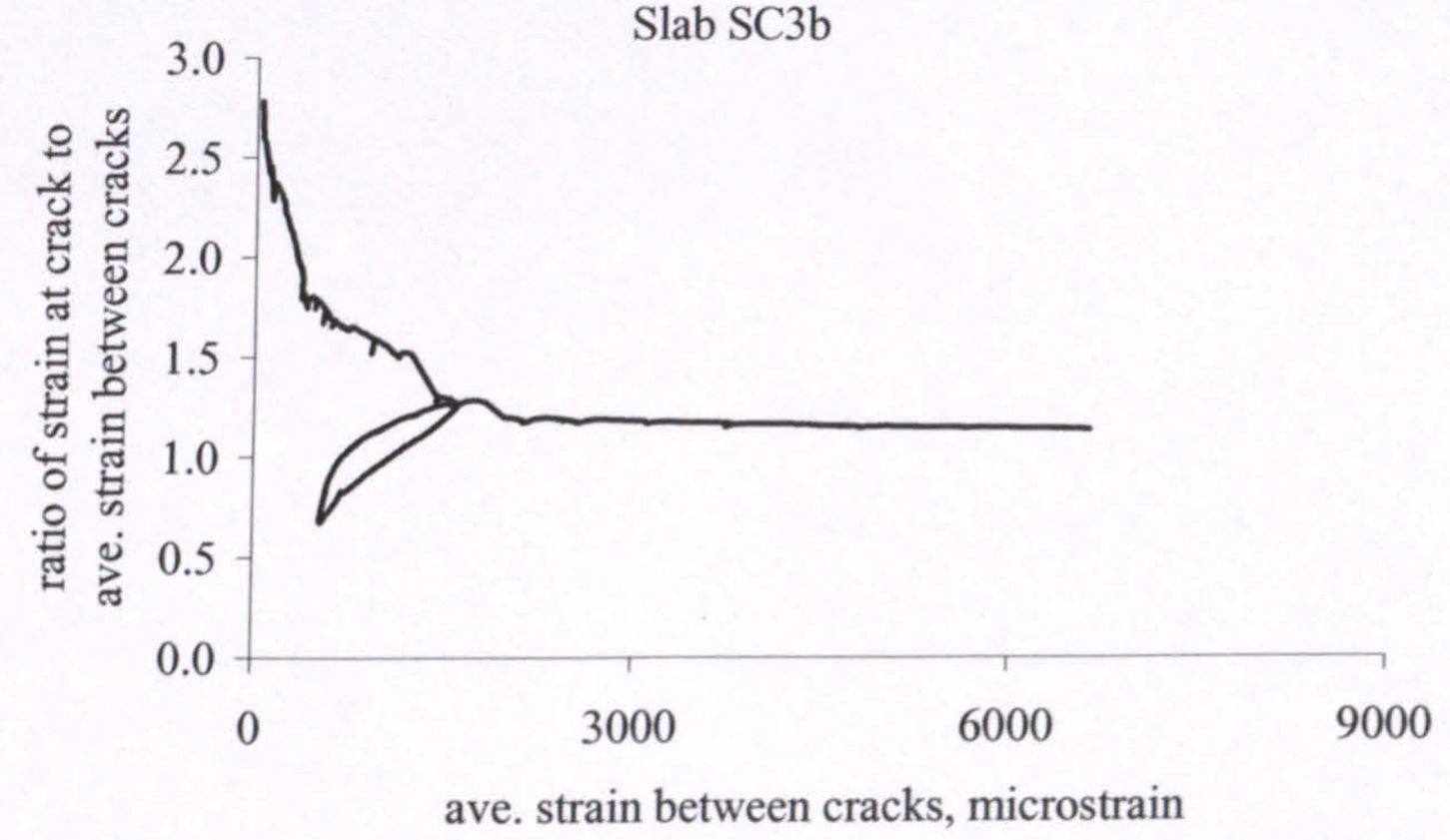

SLAB SC3b

note: slab pre-cracked only at centre

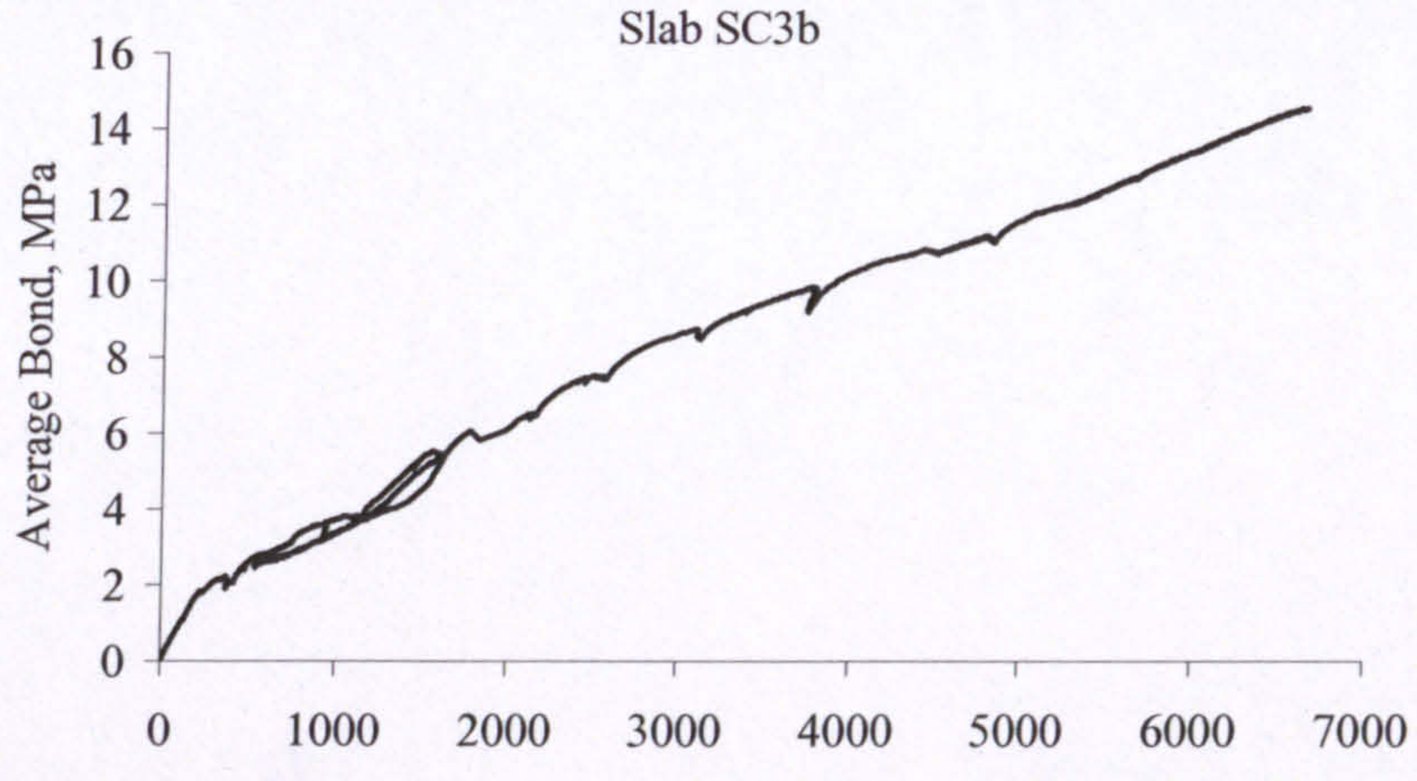

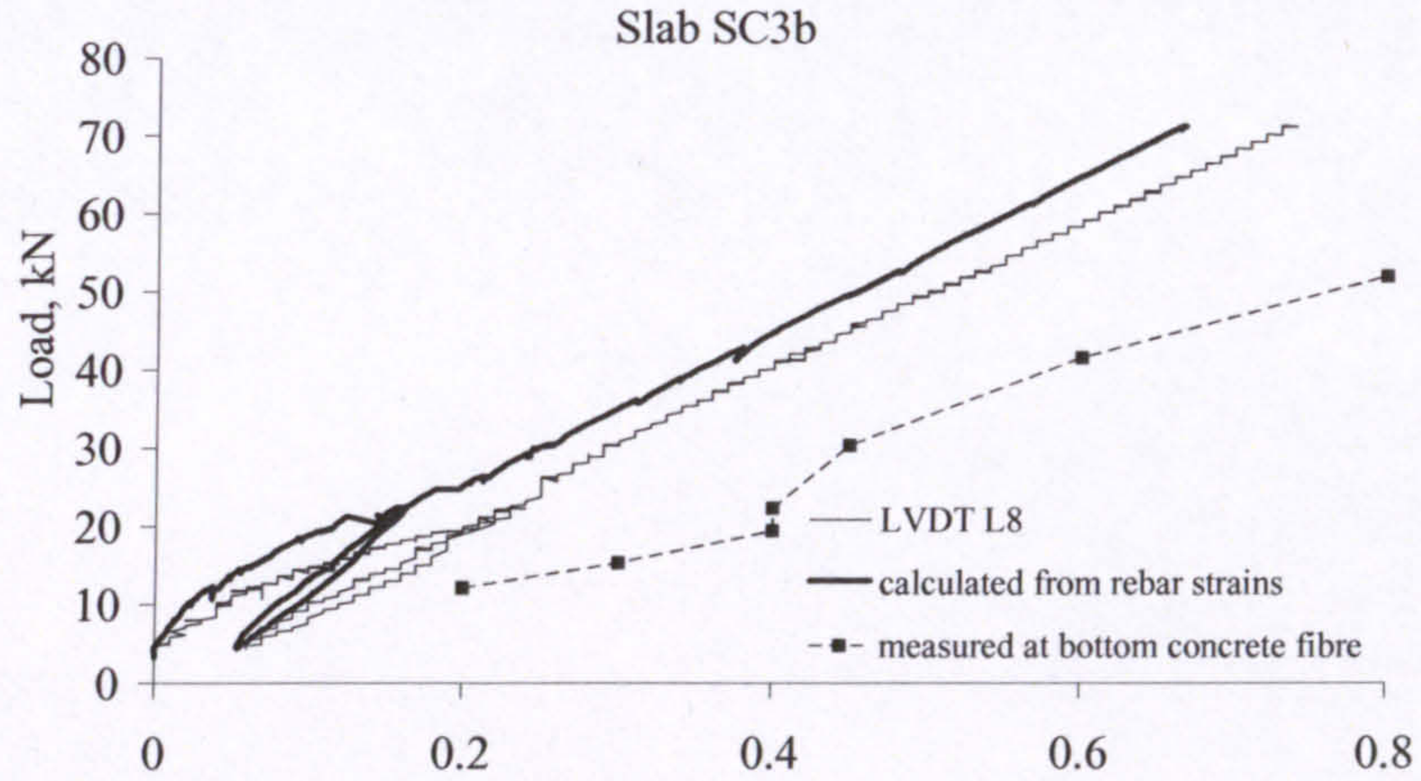

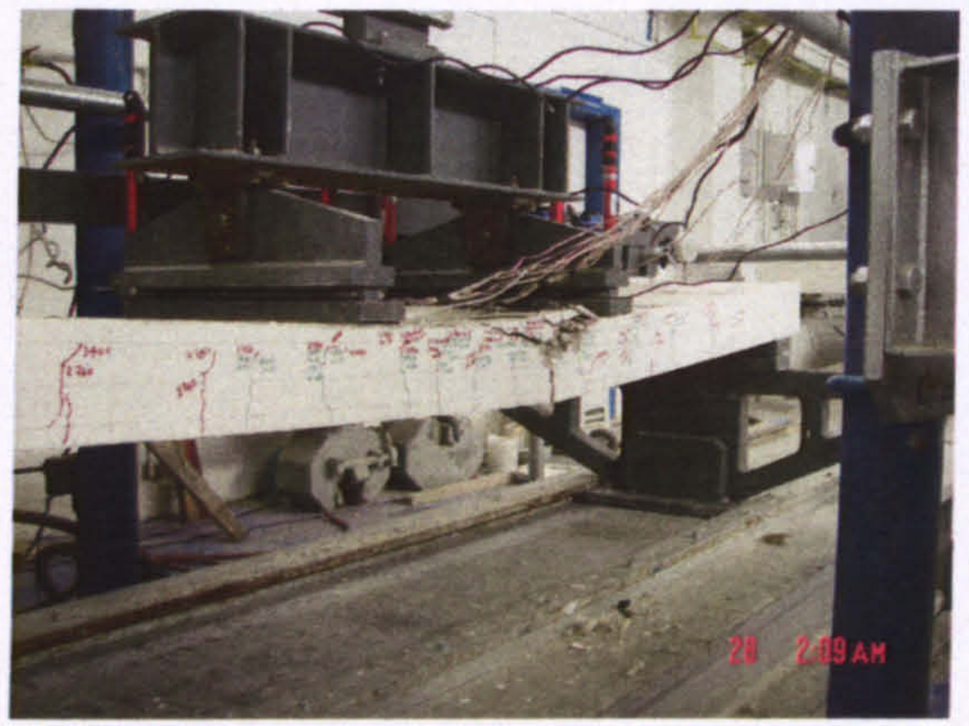

Failure by crushing of concrete

- Average cover=36mm
- Location of crack inducer is precise
- at (22.3-26.3) kN, a crack formed 90mm right of CL.

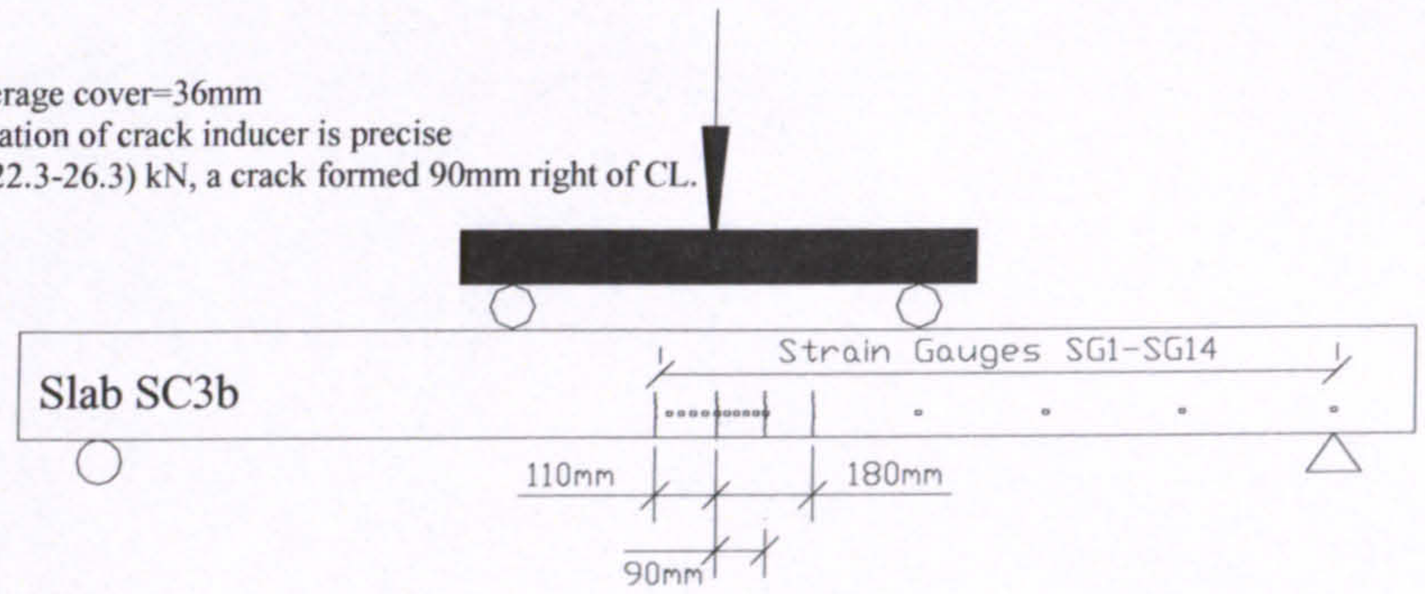

Cracks around Centre

Beam BSa

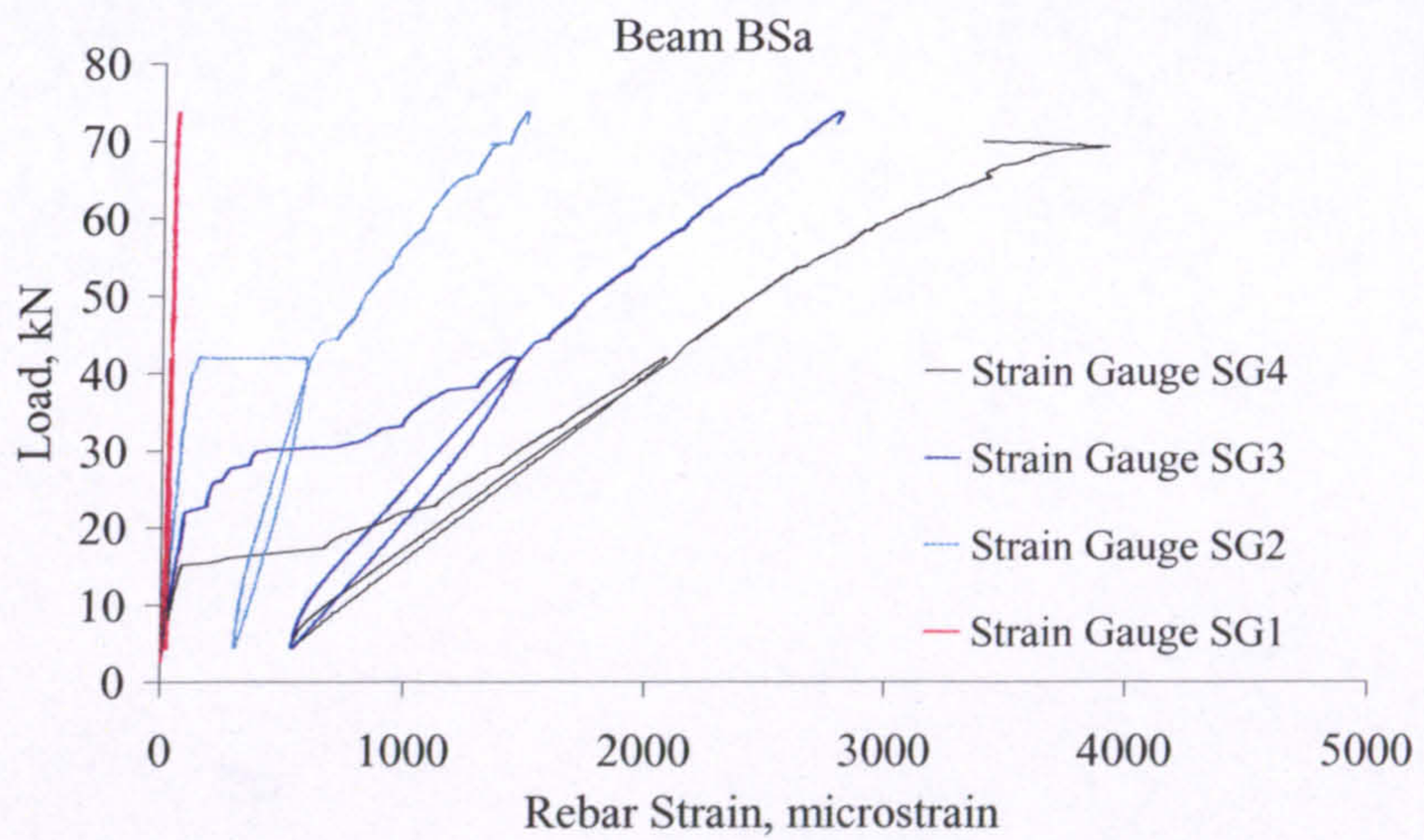
Beam BSa
Load, kN
Rebar Strain, microstrain
Strain Gauge SG4
Strain Gauge SG3
Strain Gauge SG2
Strain Gauge SG1

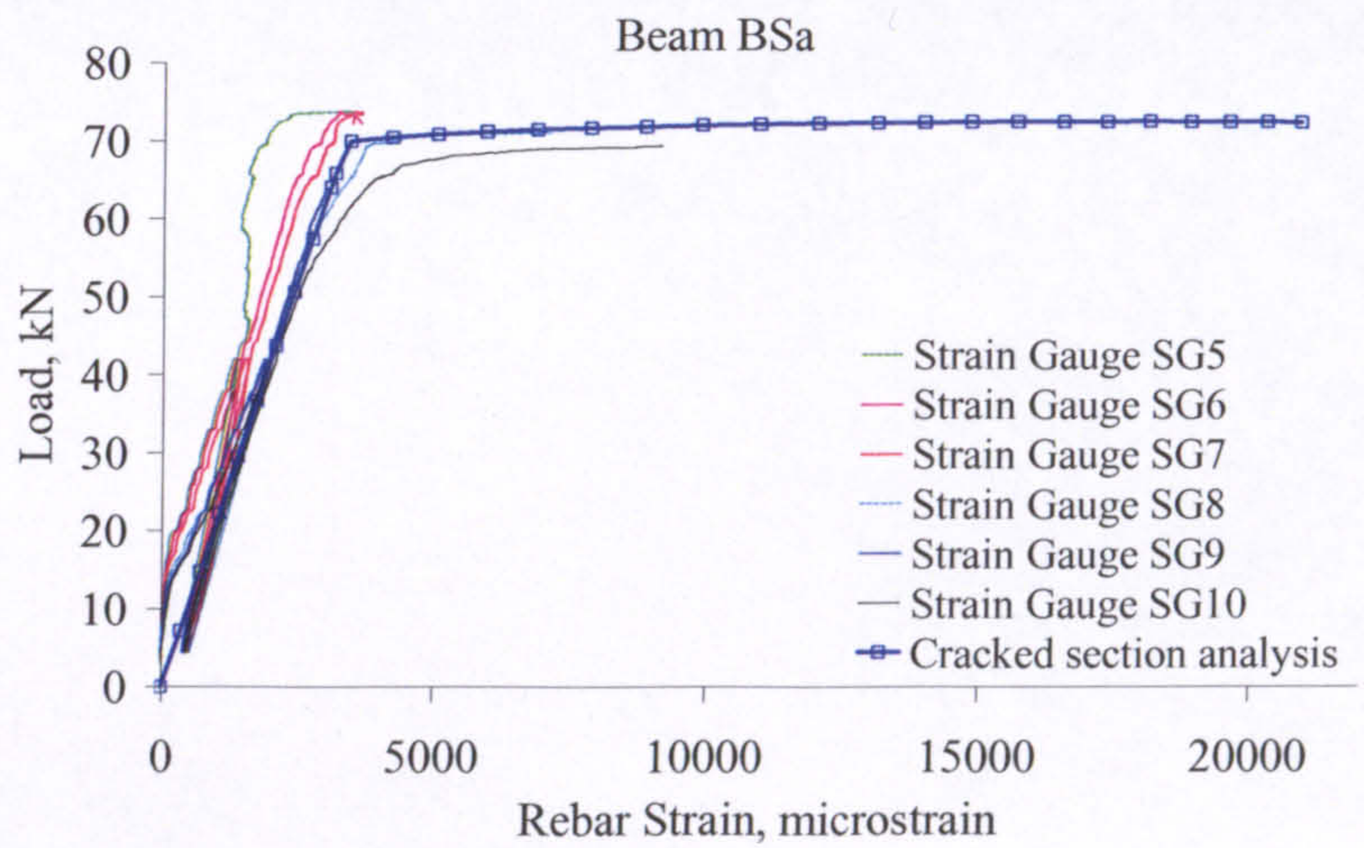
Beam BSa
Load, kN
Rebar Strain, microstrain
Strain Gauge SG5
Strain Gauge SG6
Strain Gauge SG7
Strain Gauge SG8
Strain Gauge SG9
Strain Gauge SG10
Cracked section analysis

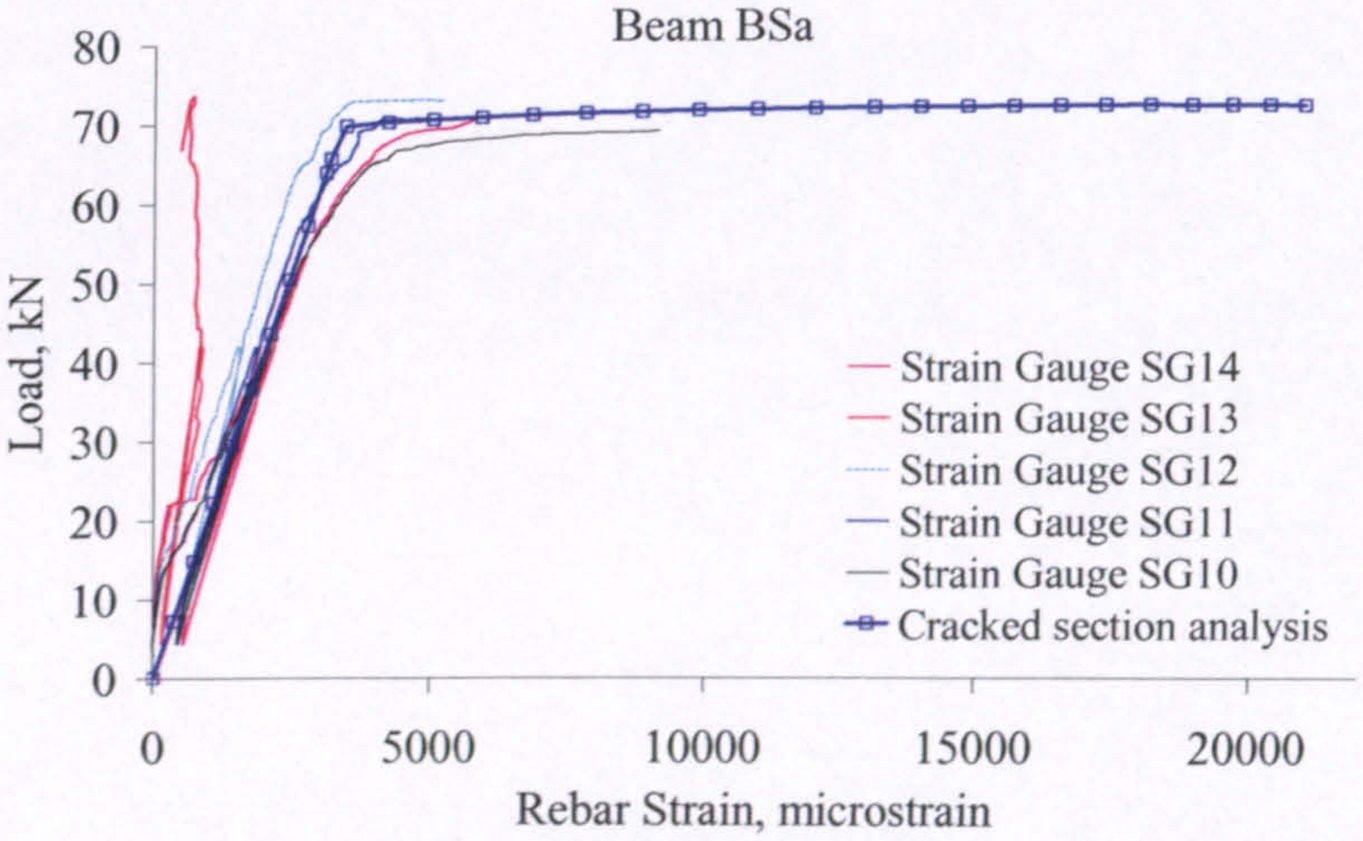
Beam BSa
Load, kN
Rebar Strain, microstrain
Strain Gauge SG14
Strain Gauge SG13
Strain Gauge SG12
Strain Gauge SG11
Strain Gauge SG10
Cracked section analysis

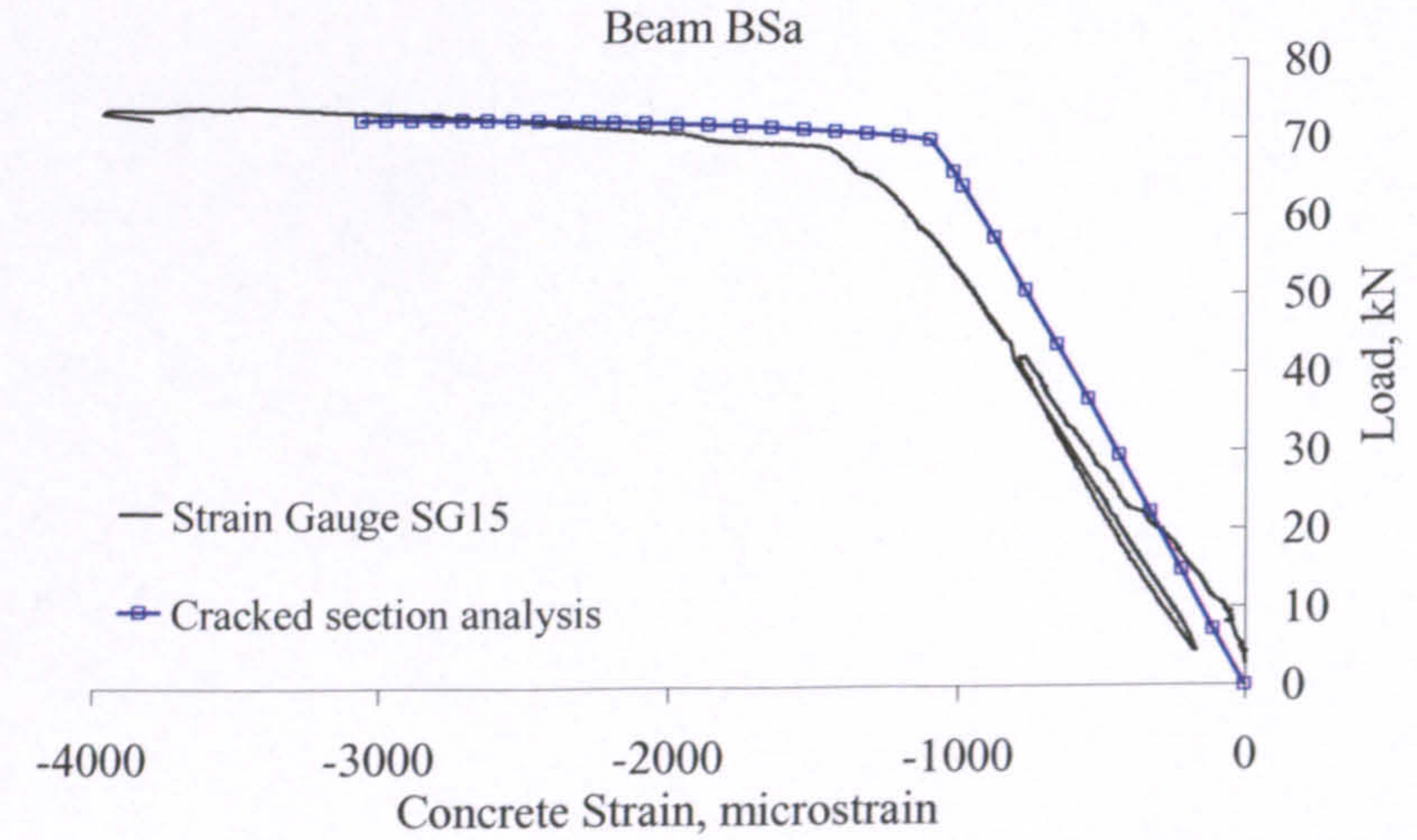
Beam BSa
Load, kN
Concrete Strain, microstrain
Strain Gauge SG15
Cracked section analysis

Beam BSa

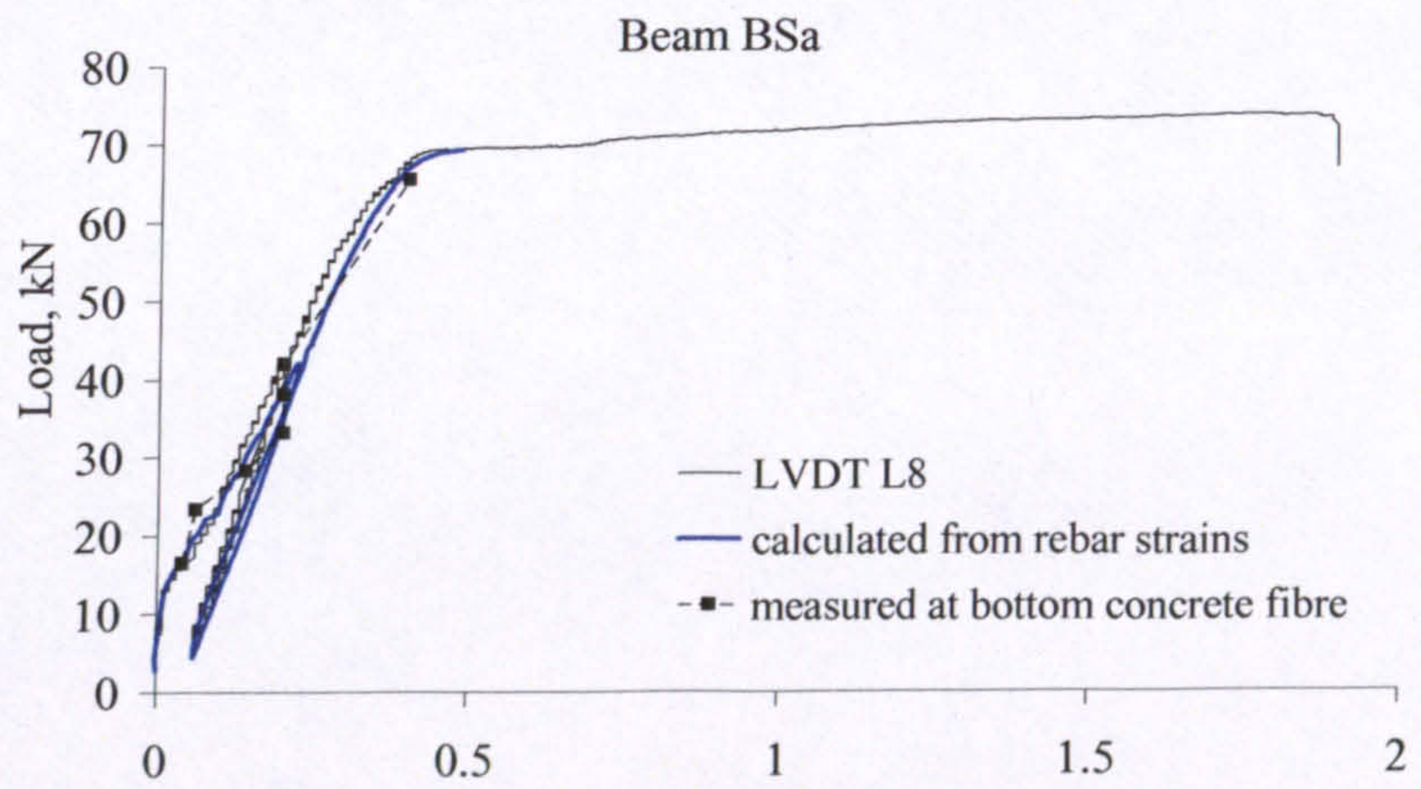
Beam BSa
Load, kN
Crack Width, mm
LVDT L8
calculated from rebar strains
measured at bottom concrete fibre

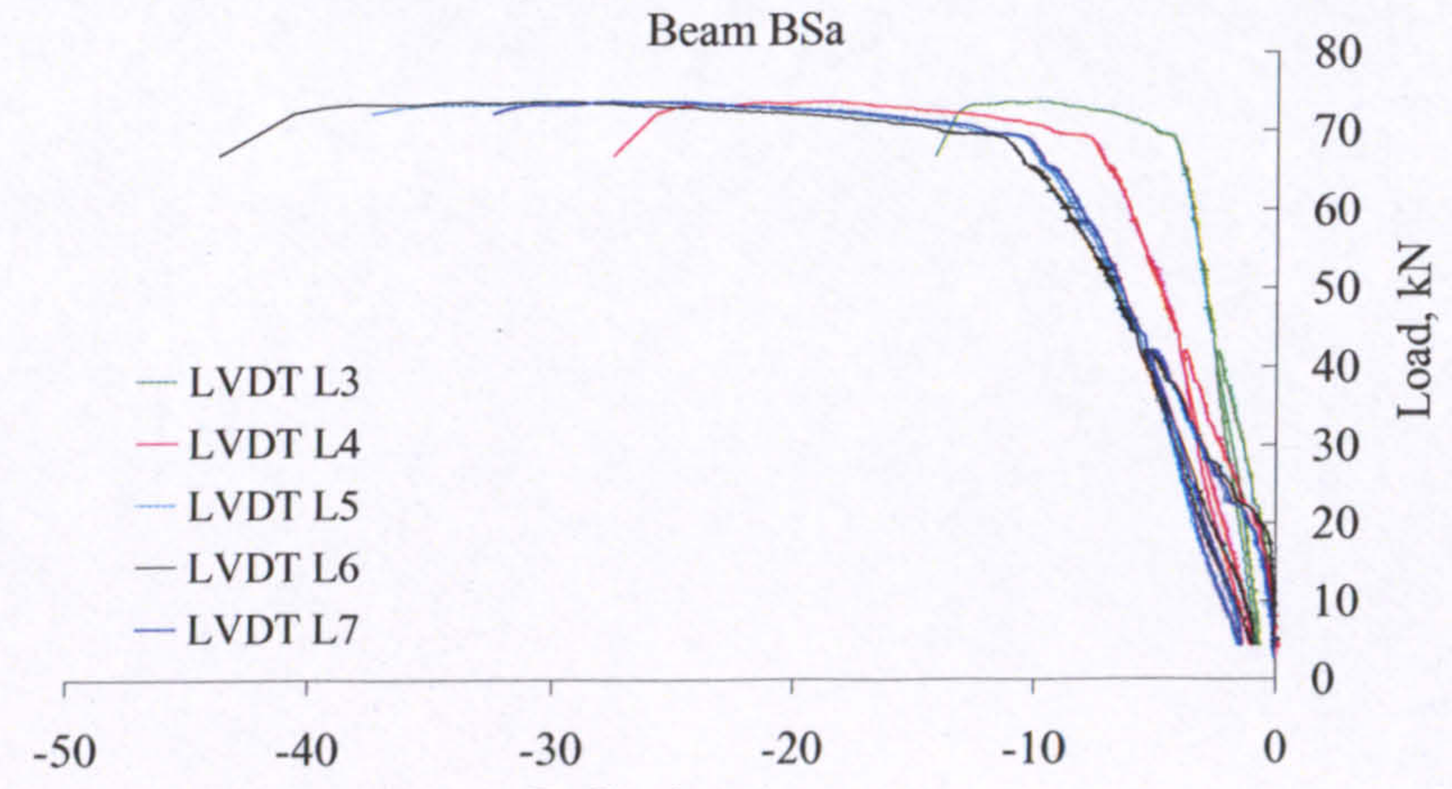
Beam BSa
LVDT L3
LVDT L4
LVDT L5
LVDT L6
LVDT L7
Load, kN
Deflection, mm

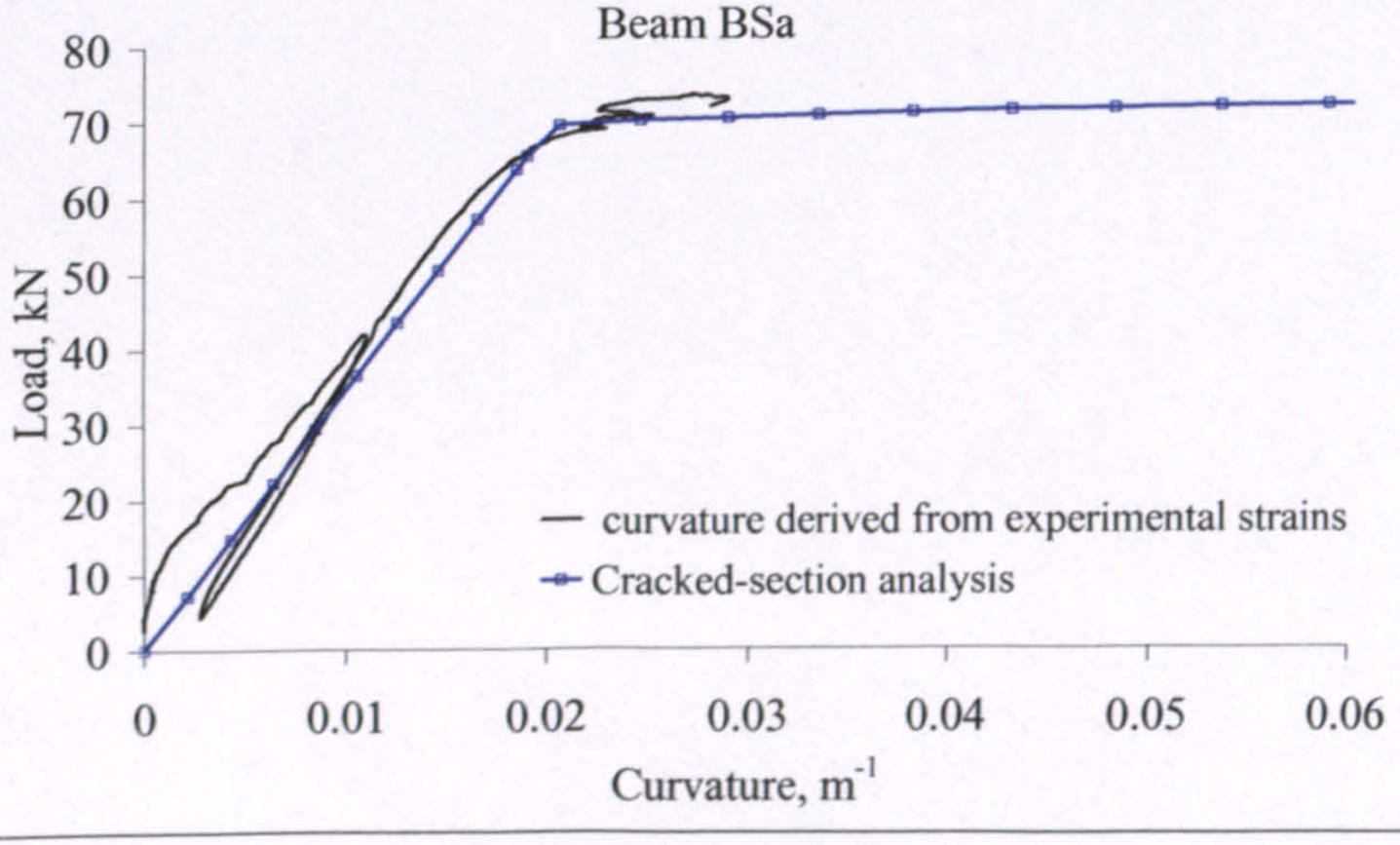
Beam BSa
Load, kN
Curvature, m-1
curvature derived from experimental strains
Cracked-section analysis

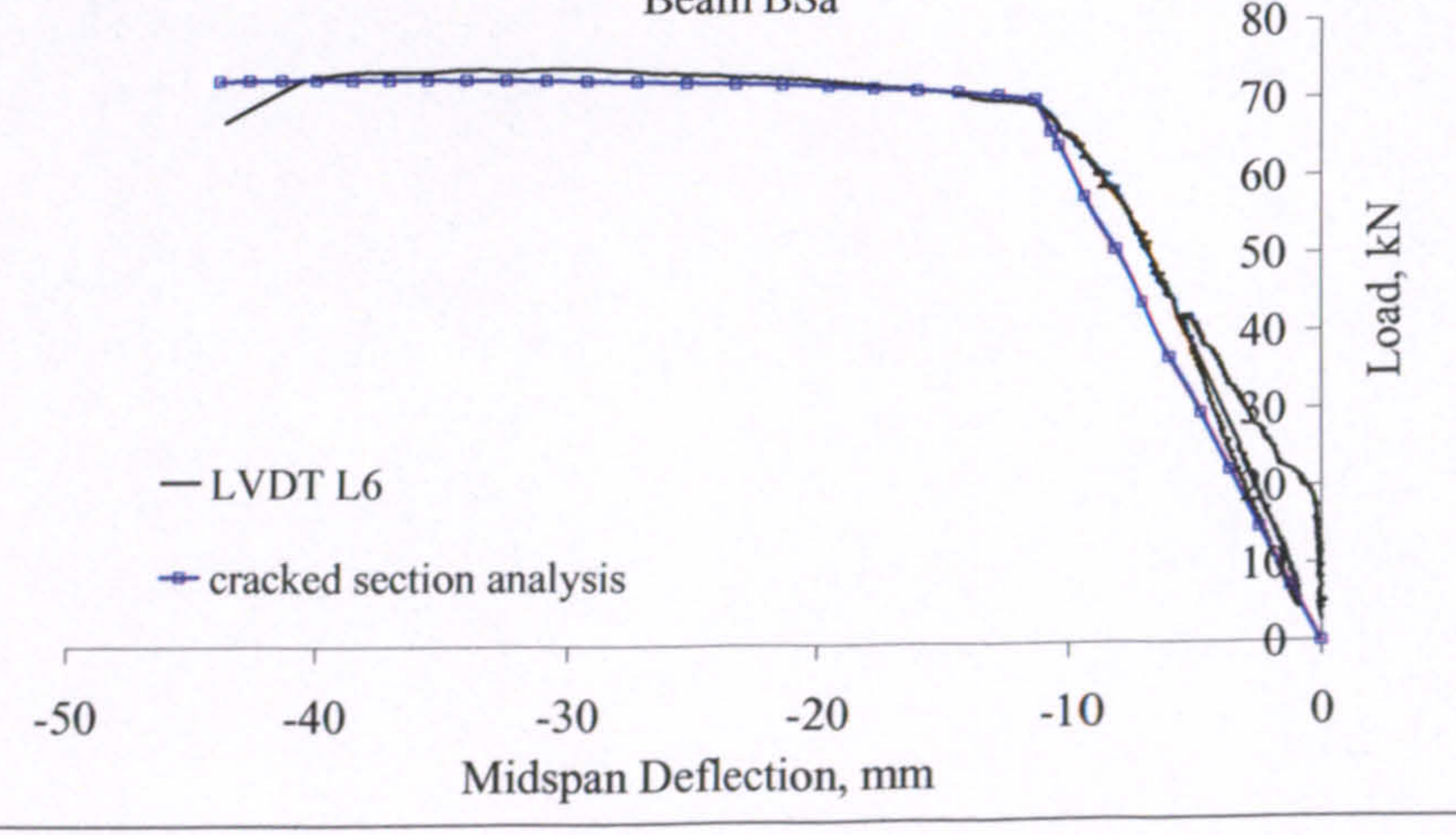
Beam BSa
LVDT L6
cracked section analysis
Load, kN
Midspan Deflection, mm

Beam BSa

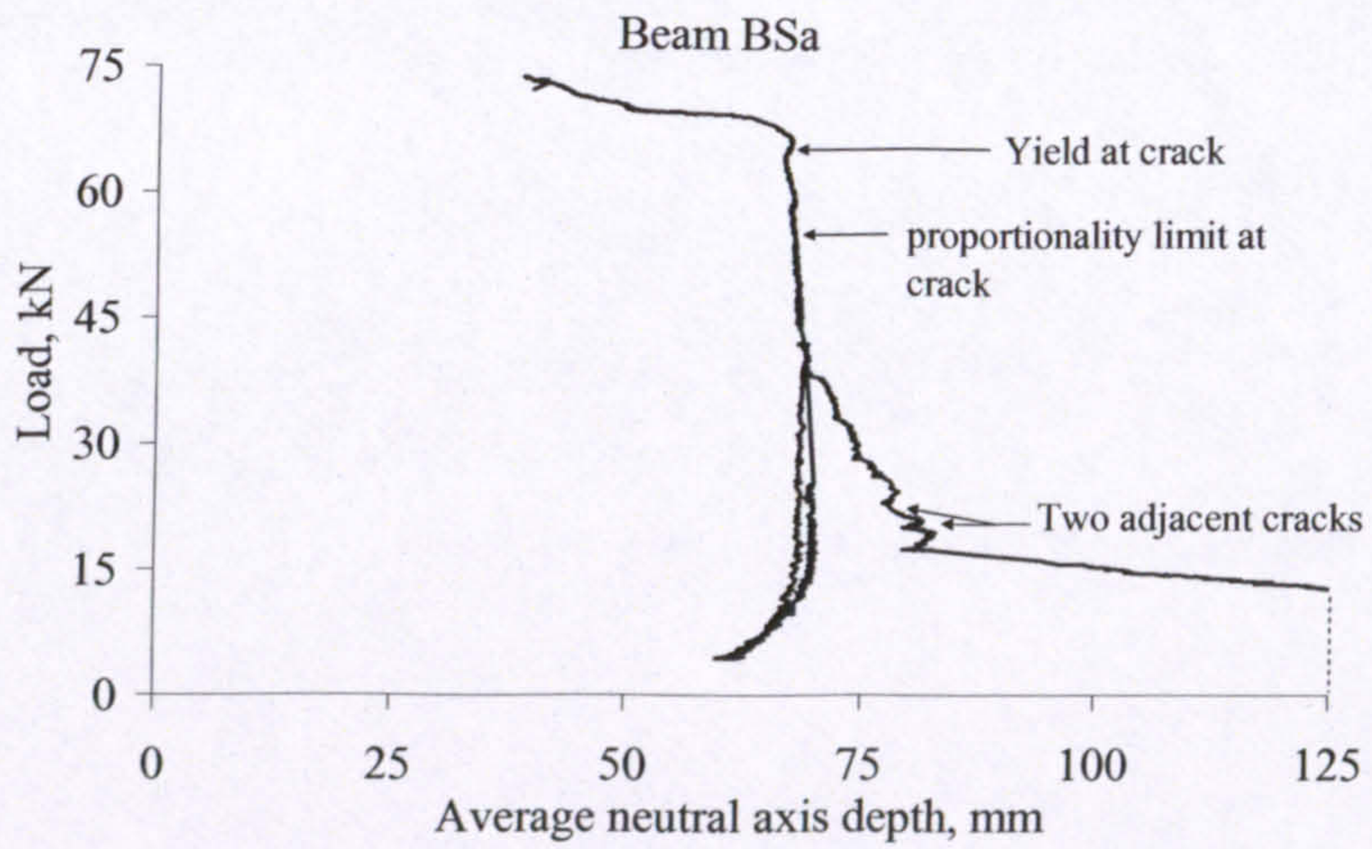
Beam BSa
Load, kN
75
60
45
30
15
0
0
25
50
75
100
125
Average neutral axis depth, mm
Yield at crack
proportionality limit at crack
Two adjacent cracks

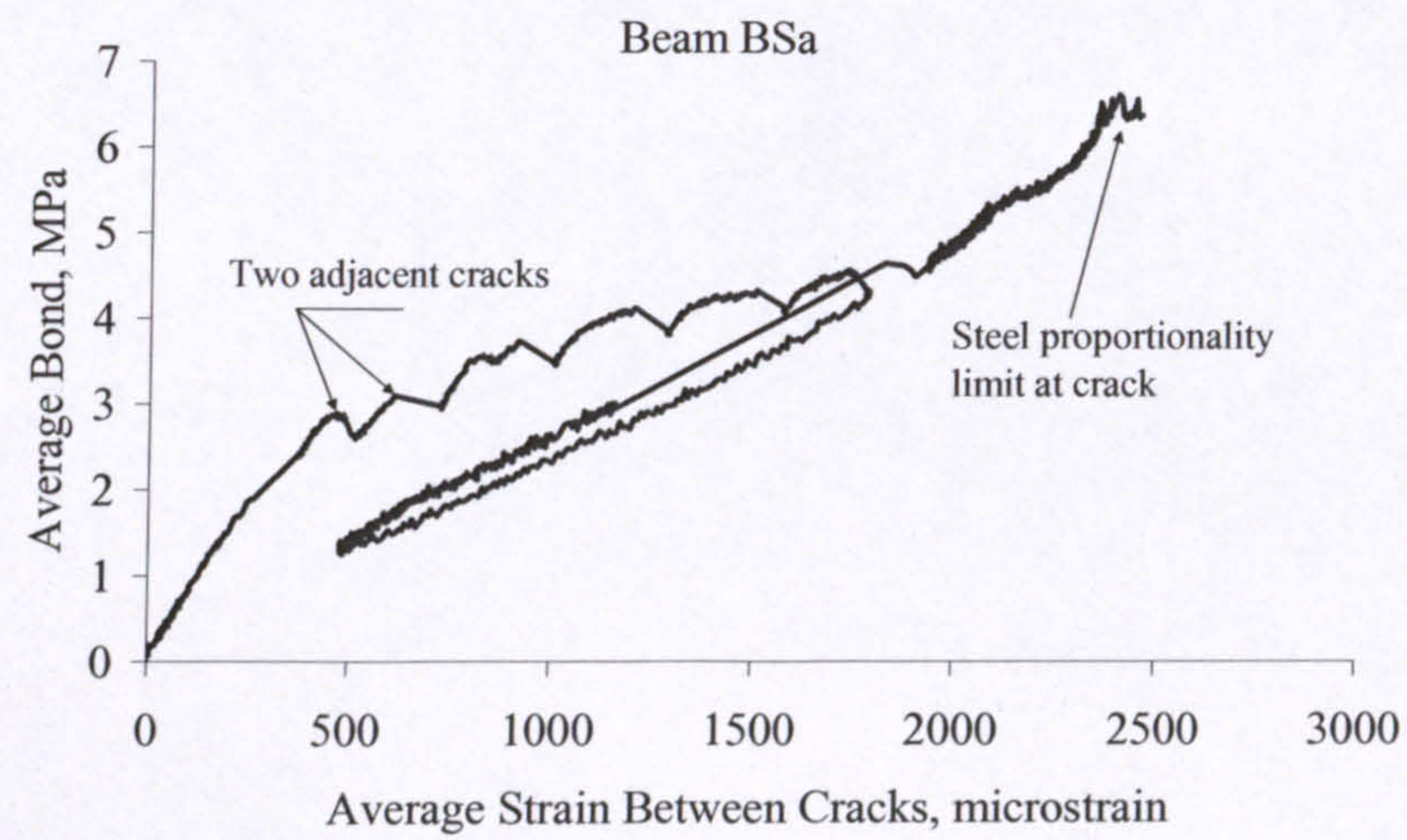
Beam BSa
Average Bond, MPa
7
6
5
4
3
2
1
0
0
500
1000
1500
2000
2500
3000
Average Strain Between Cracks, microstrain
Two adjacent cracks
Steel proportionality limit at crack

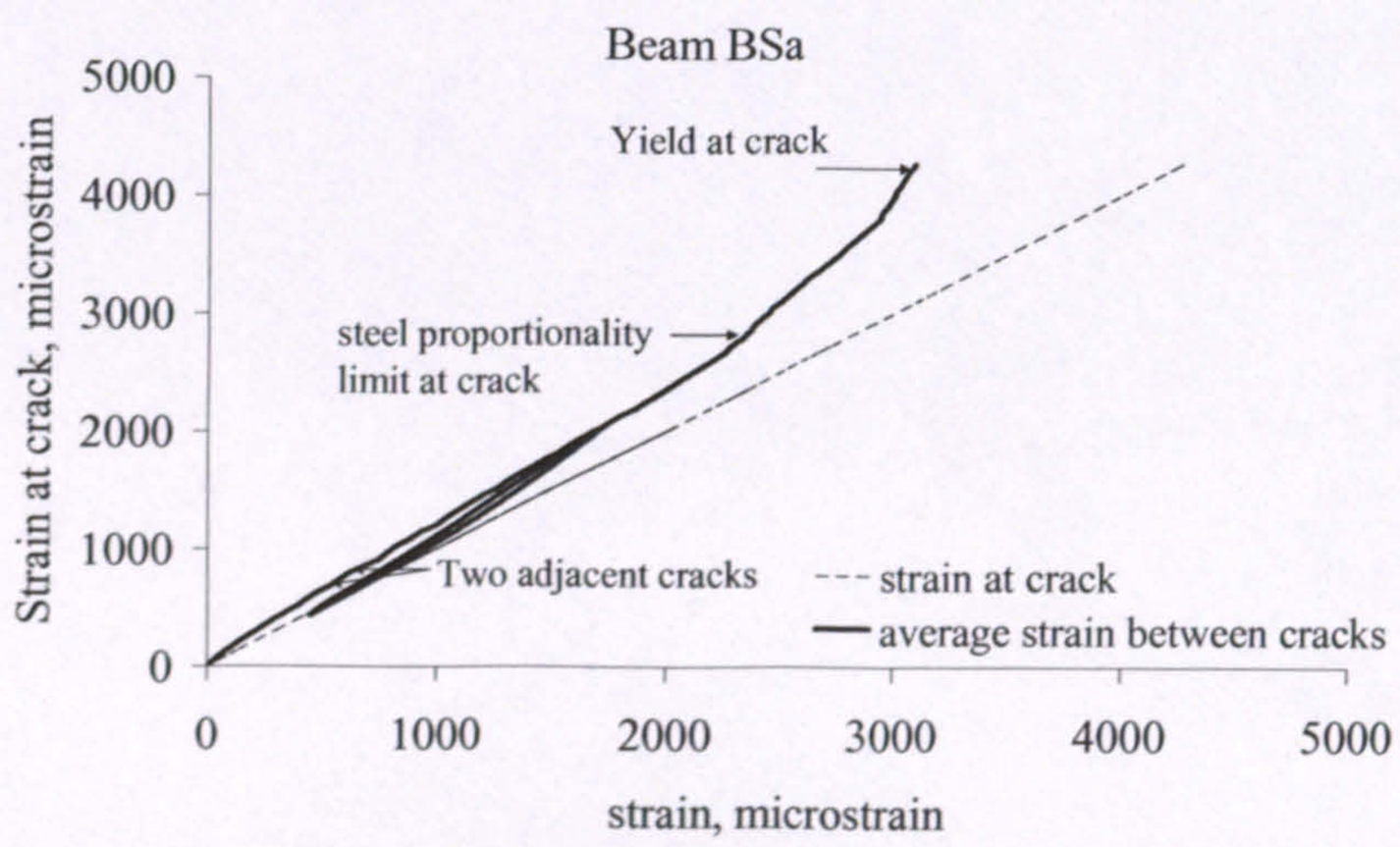
Beam BSa
Strain at crack, microstrain
5000
4000
3000
2000
1000
0
0
1000
2000
3000
4000
5000
strain, microstrain
Yield at crack
steel proportionality limit at crack
Two adjacent cracks
strain at crack
average strain between cracks

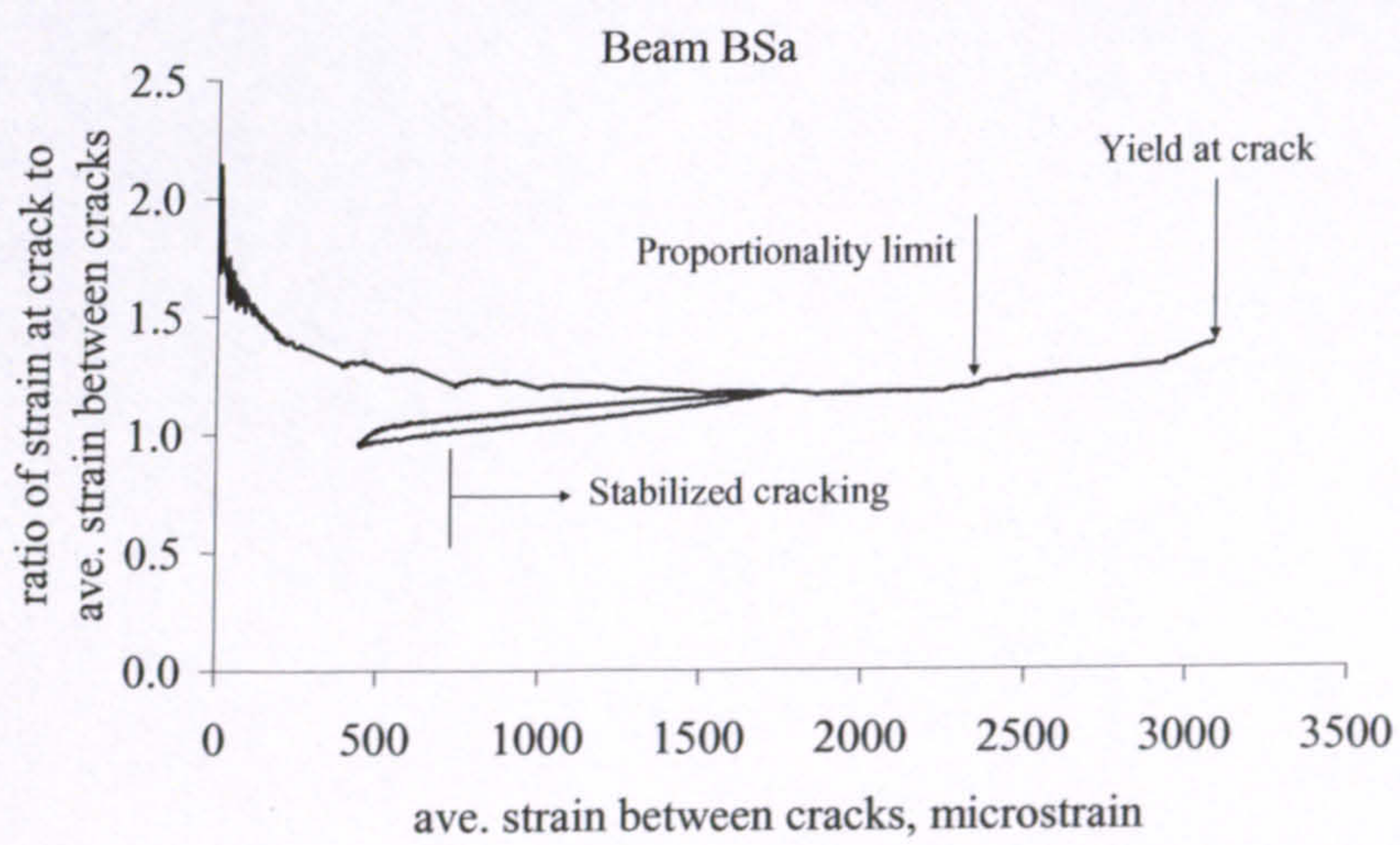
Beam BSa
ratio of strain at crack to ave. strain between cracks
2.5
2.0
1.5
1.0
0.5
0.0
0
500
1000
1500
2000
2500
3000
3500
ave. strain between cracks, microstrain
Yield at crack
Proportionality limit
Stabilized cracking

Beam BSa

- Cover=27mm
- location of crack inducer is precise.

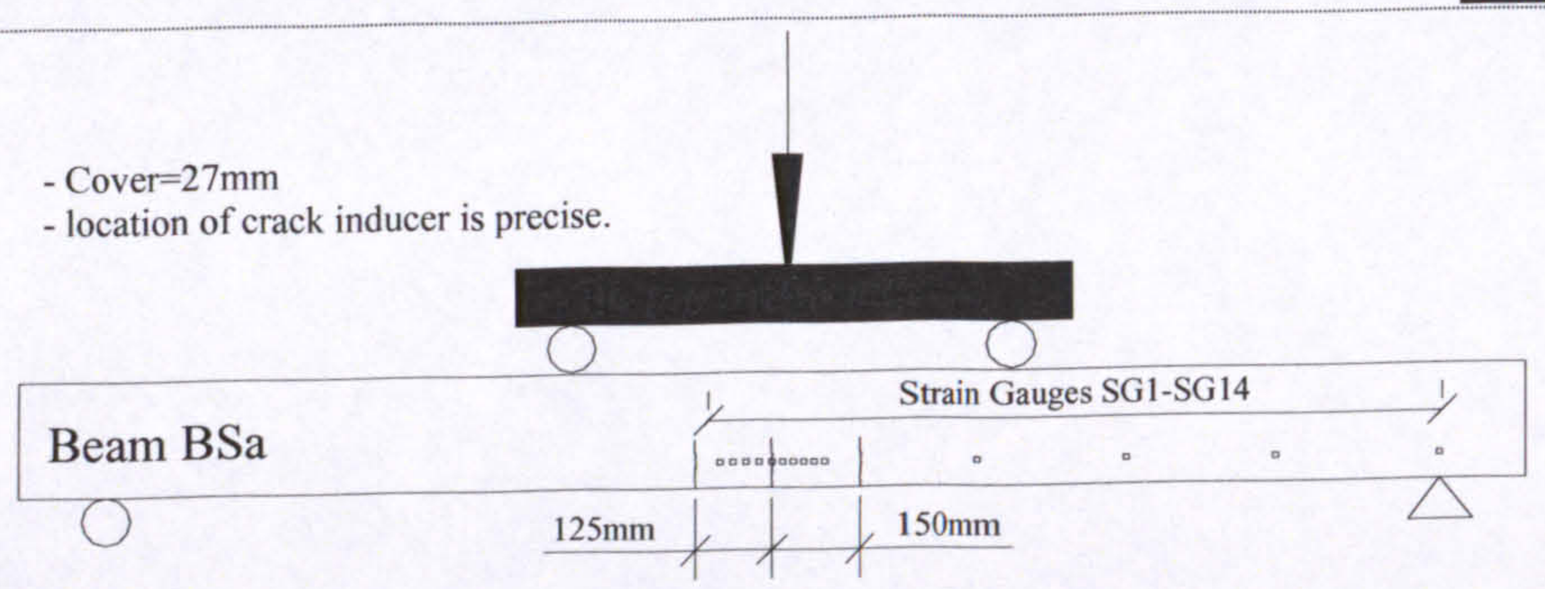

Cracks around Centre

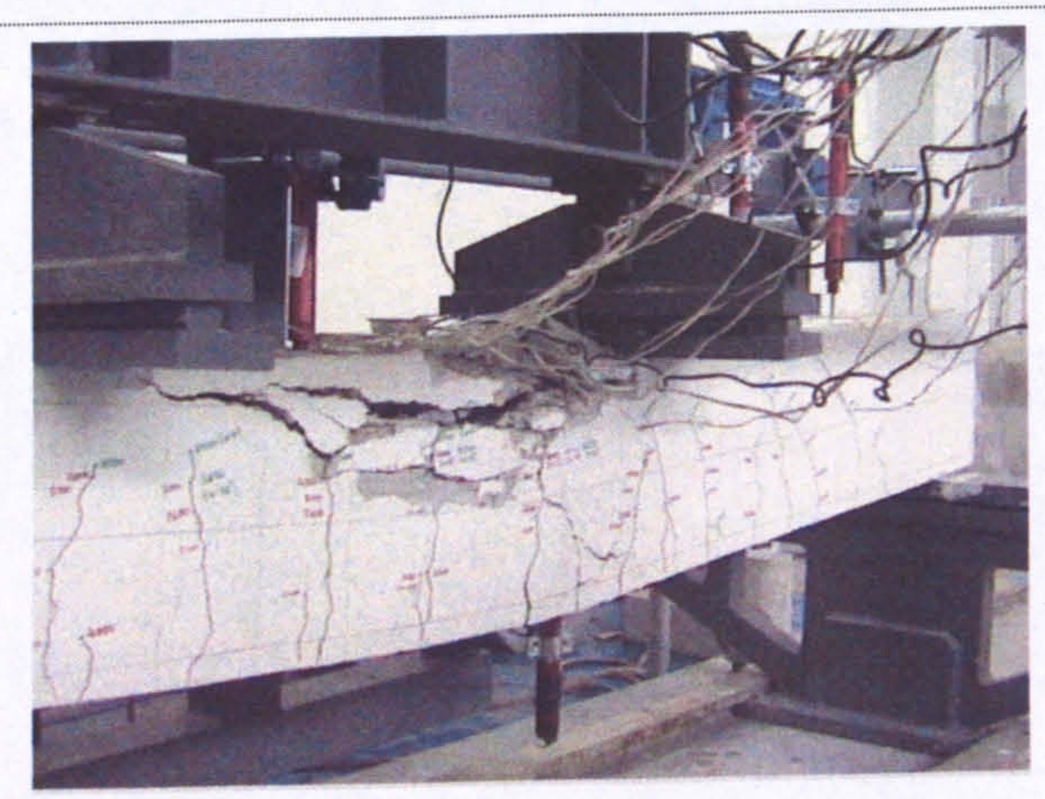

Crushing of concrete following yielding of steel.

Beam BSb

Beam pre-loaded and pre-cracked (a load of ~47kN)

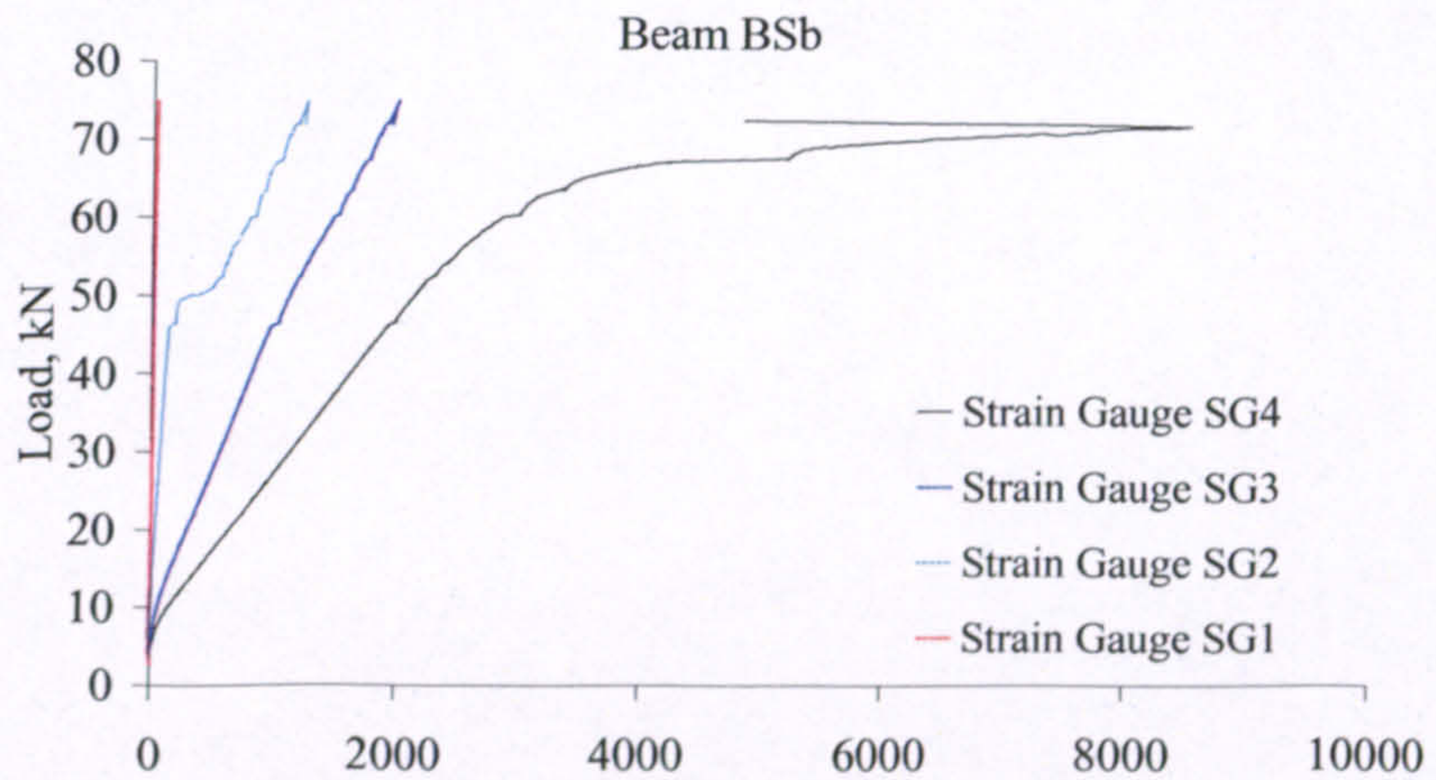

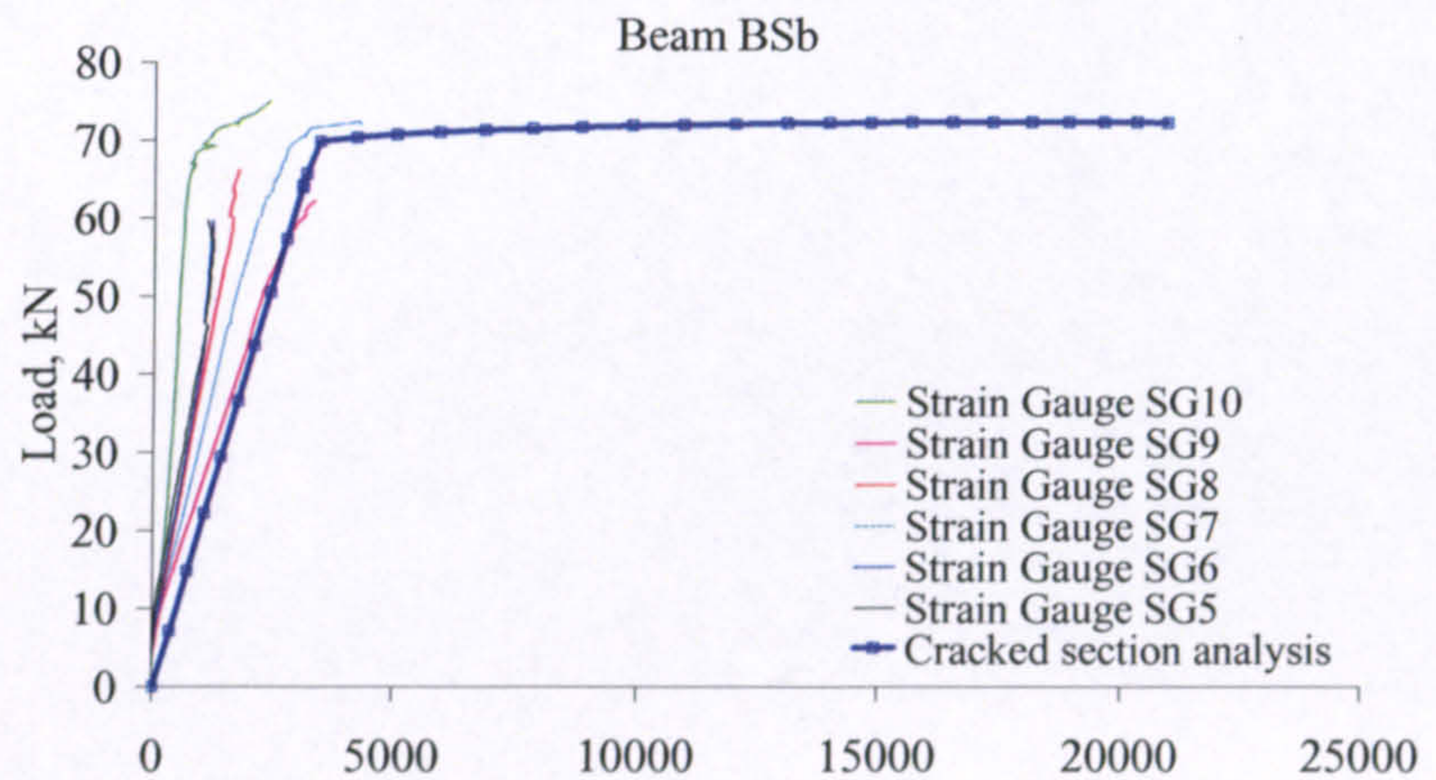

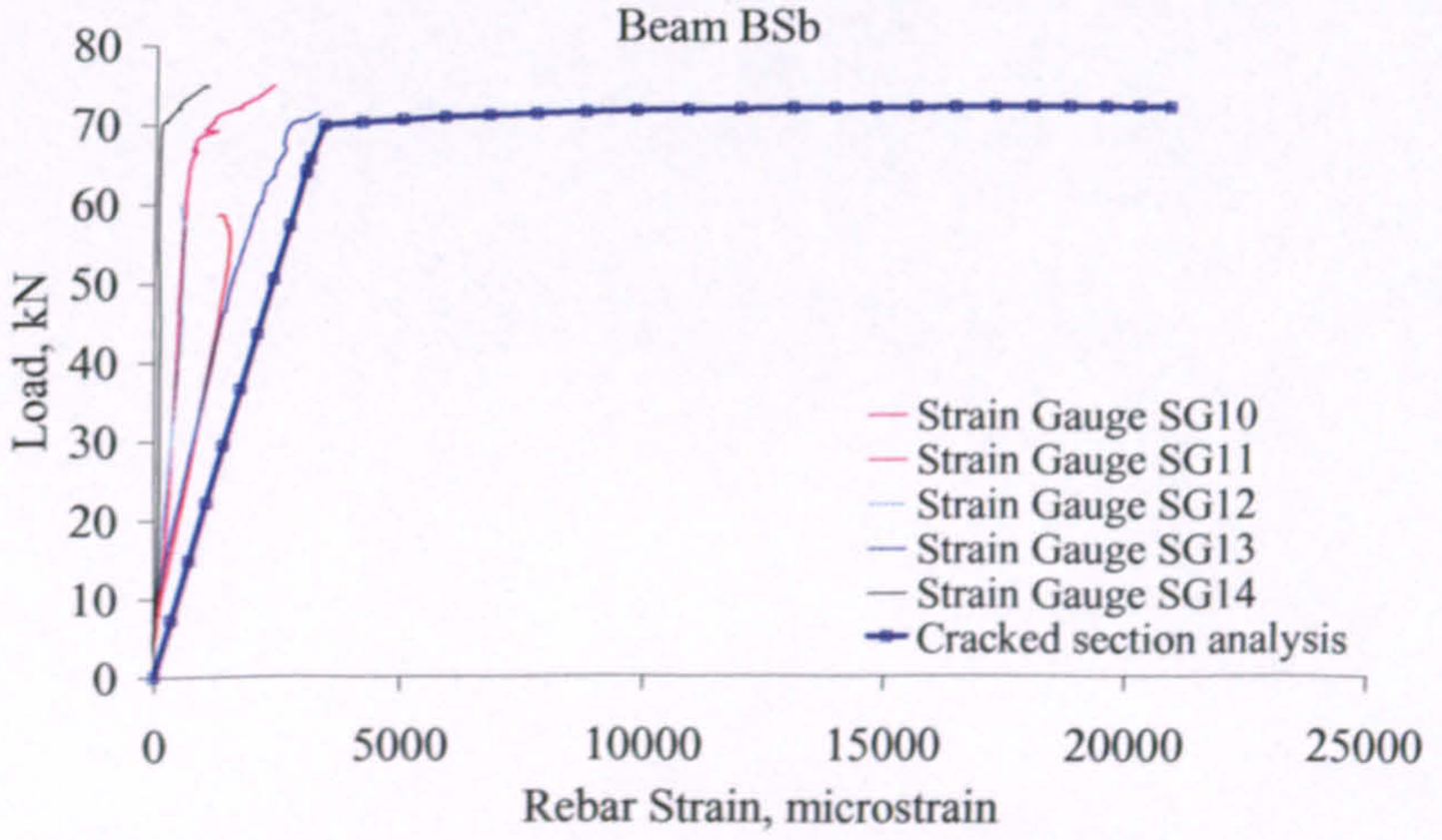

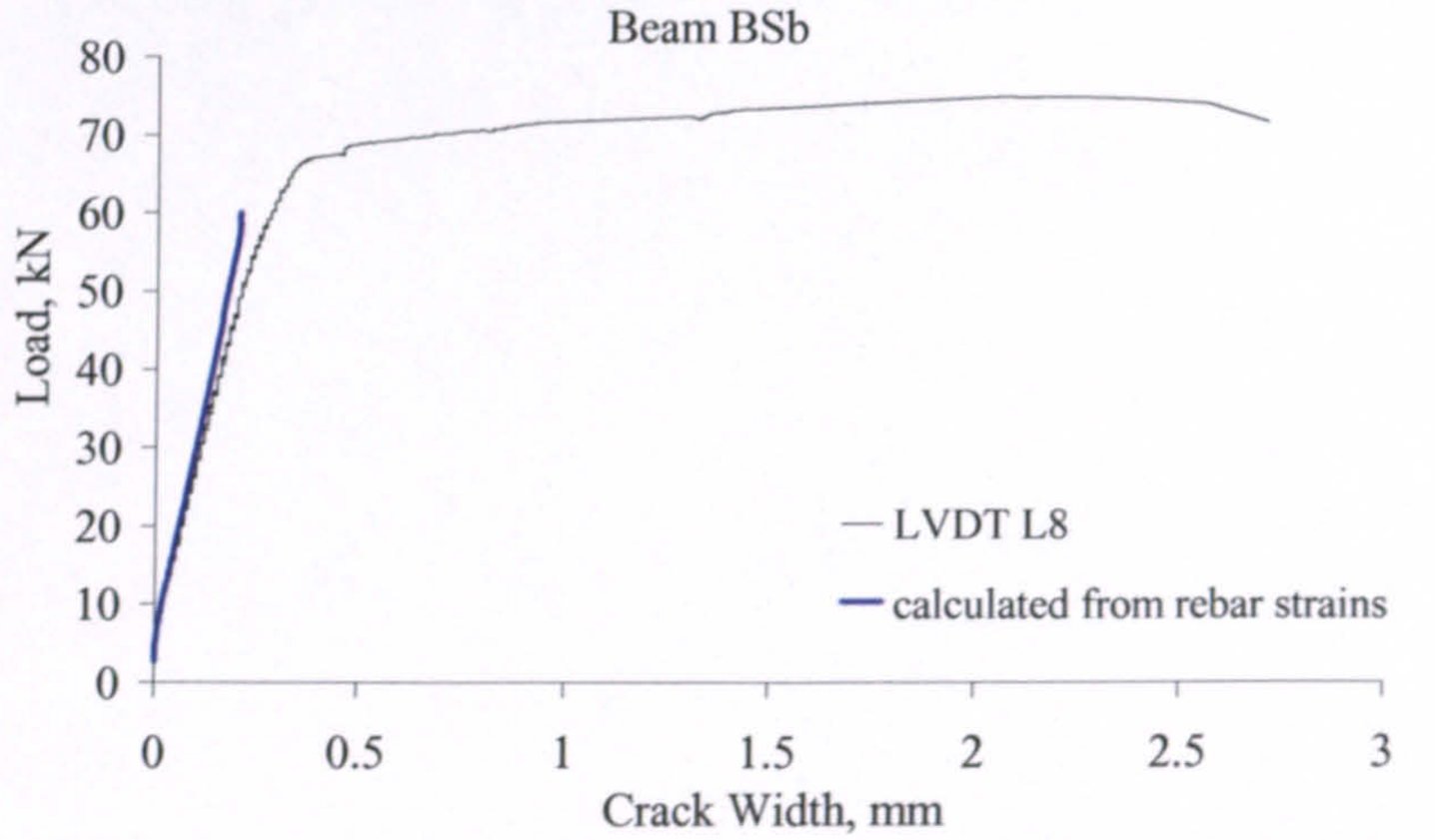

Beam BSb

Beam pre-loaded and pre-cracked (a load of ~47kN)

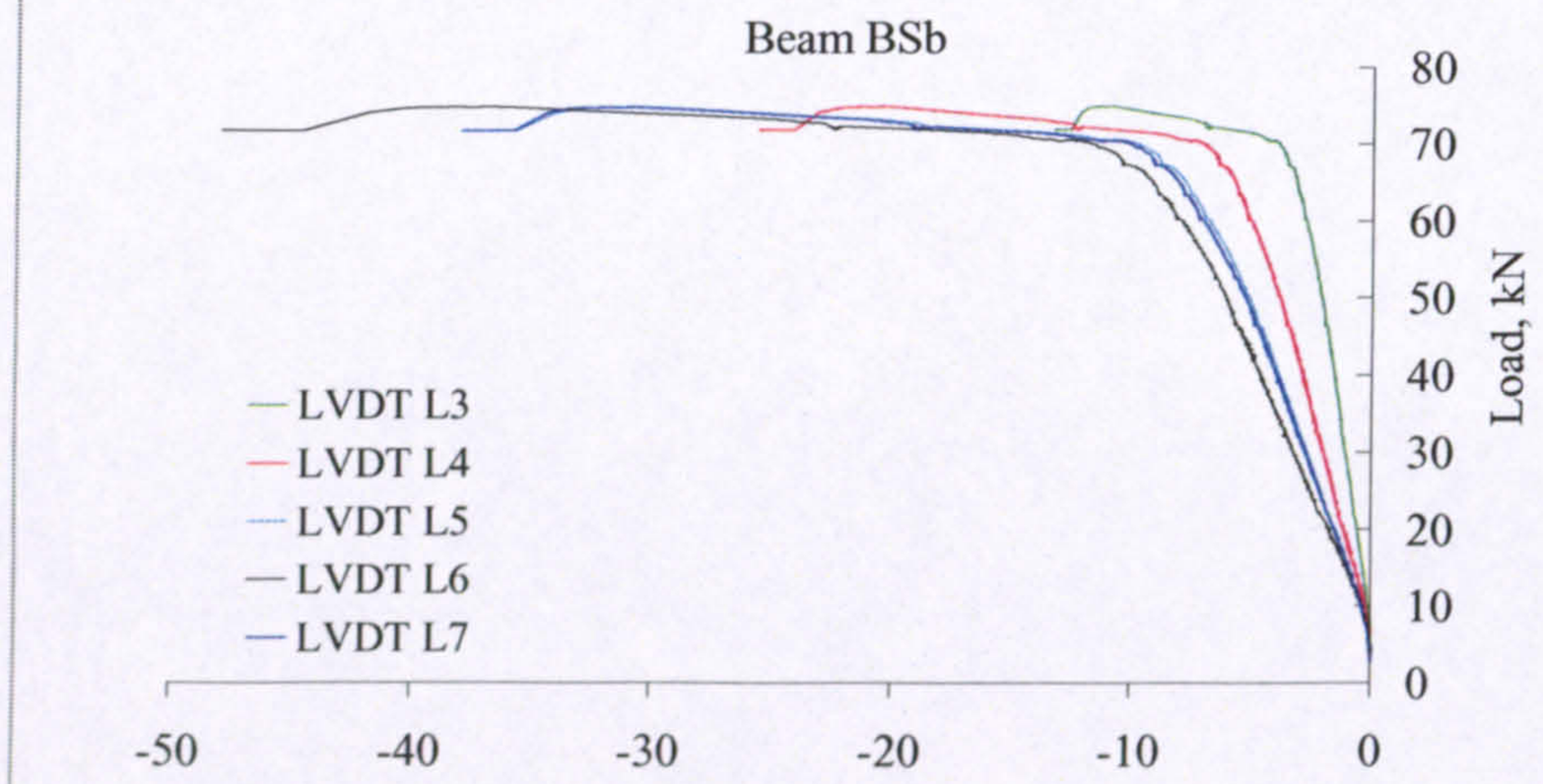

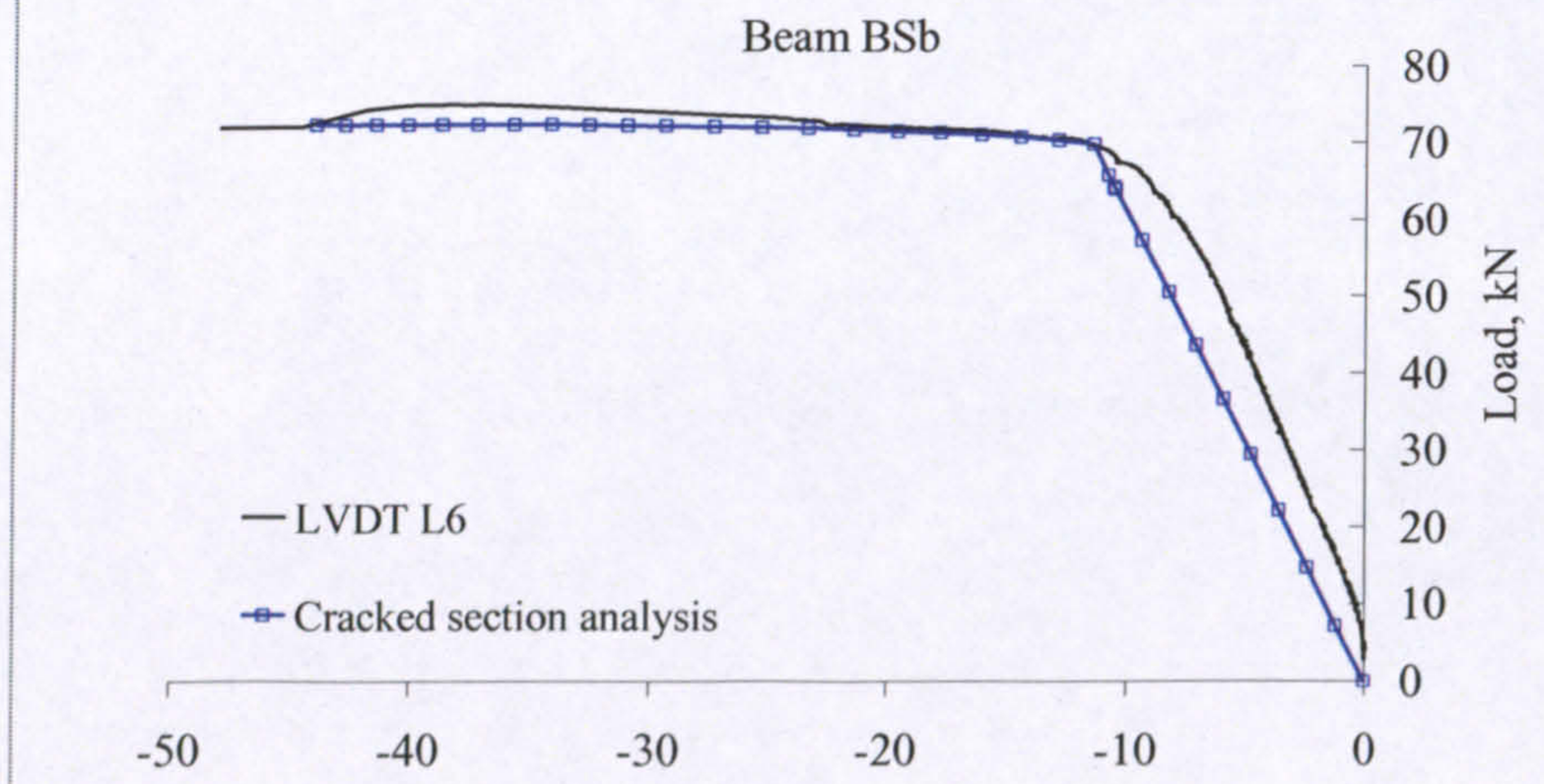

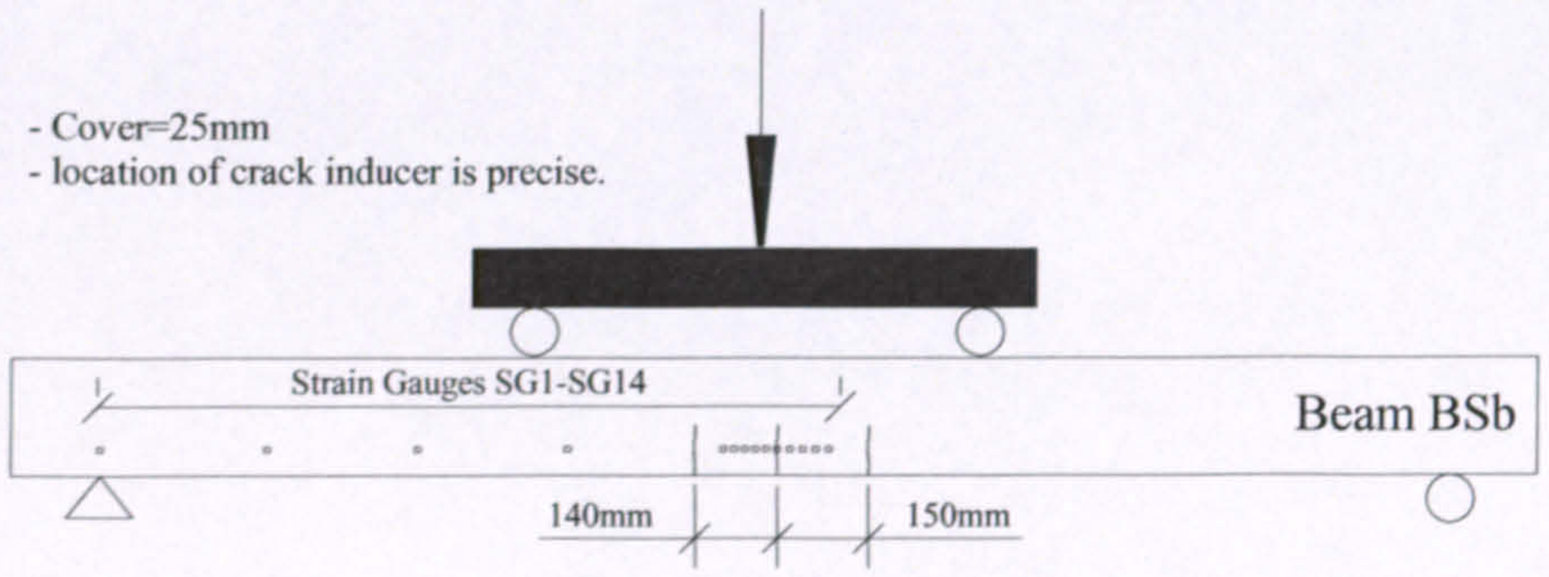

Cracks around Centre

Crushing of concrete following yielding of steel

Slab SSa

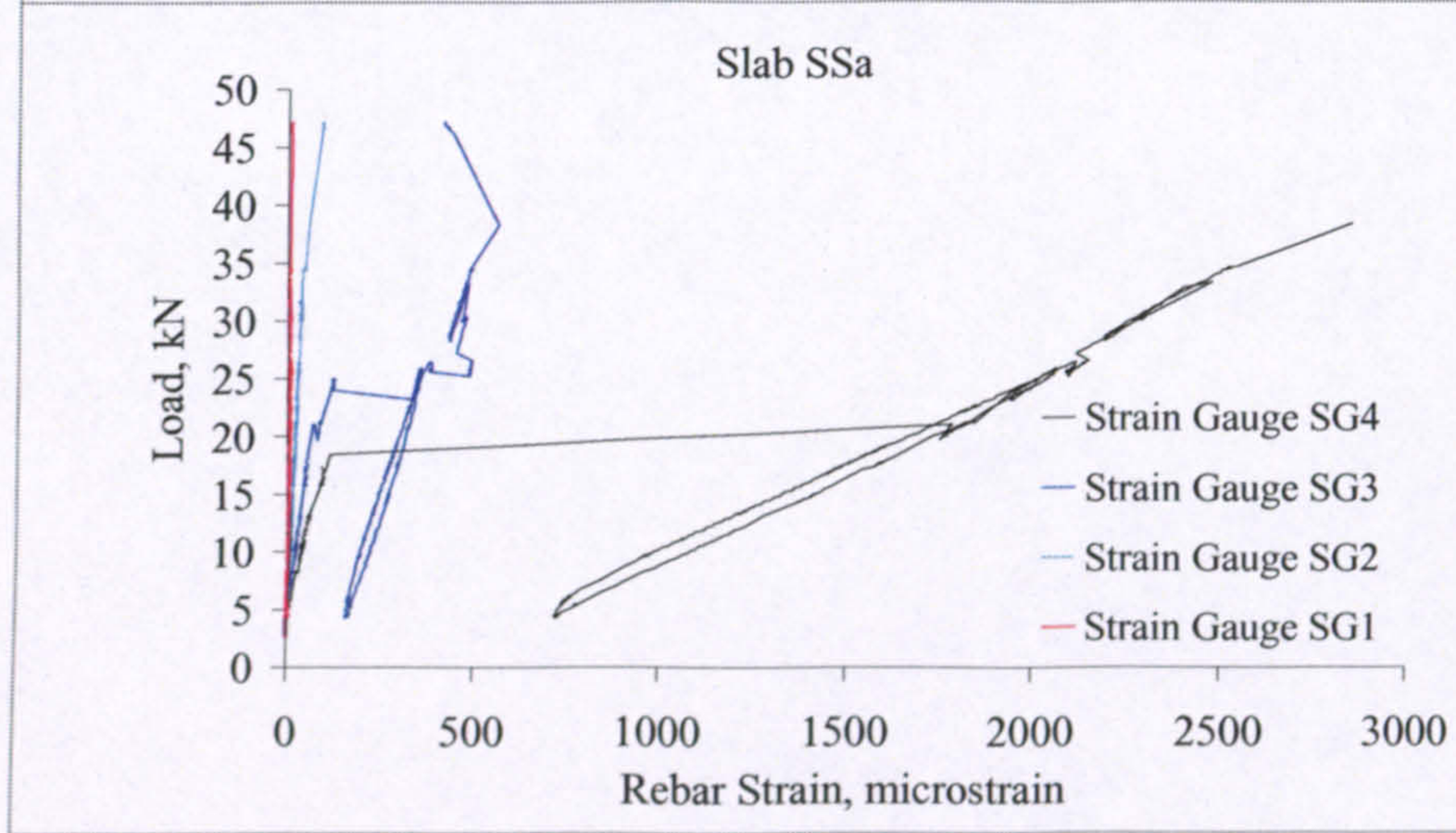
Slab SSa
Load, kN
Rebar Strain, microstrain
Strain Gauge SG4
Strain Gauge SG3
Strain Gauge SG2
Strain Gauge SG1

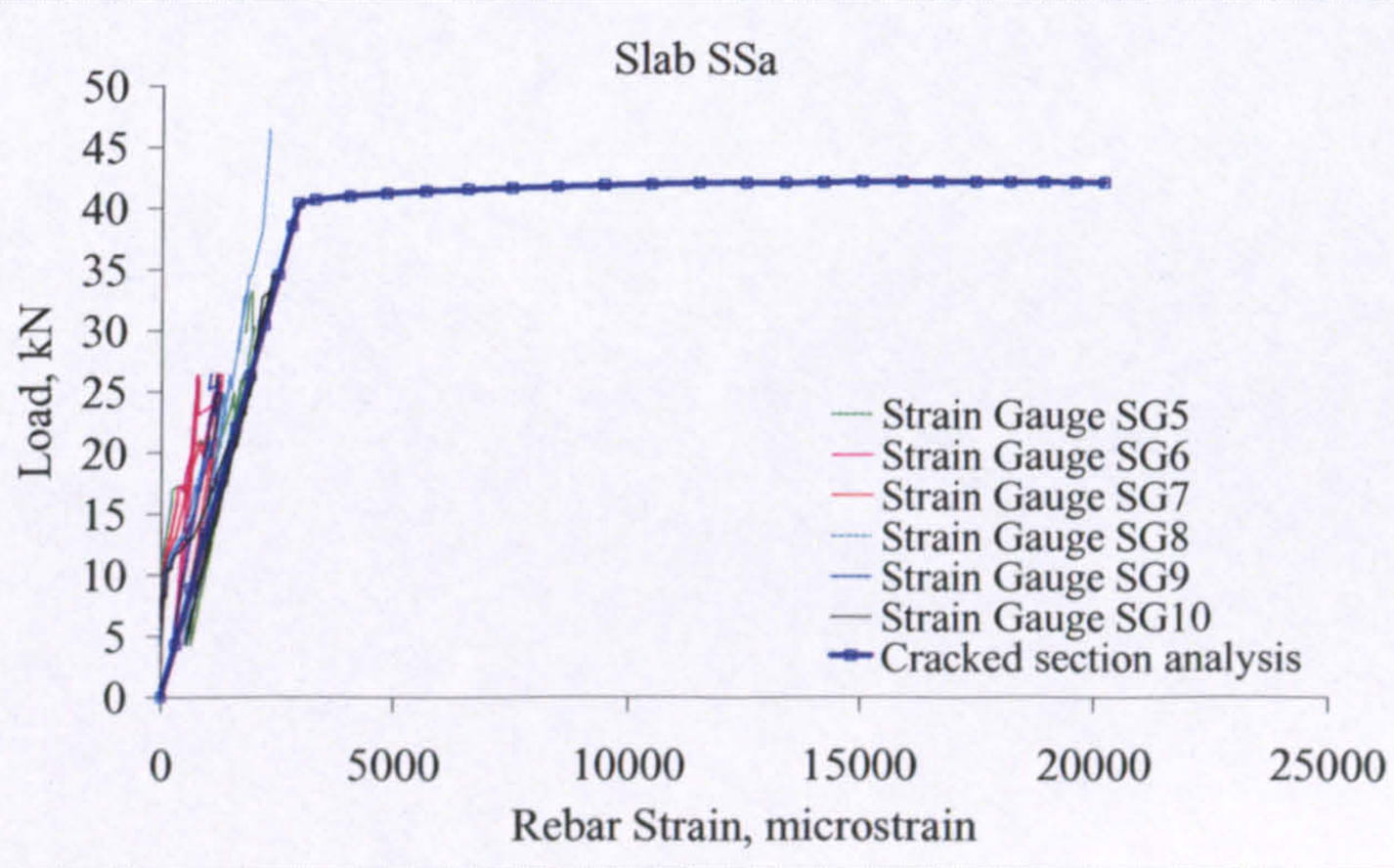
Slab SSa
Load, kN
Rebar Strain, microstrain
Strain Gauge SG5
Strain Gauge SG6
Strain Gauge SG7
Strain Gauge SG8
Strain Gauge SG9
Strain Gauge SG10
Cracked section analysis

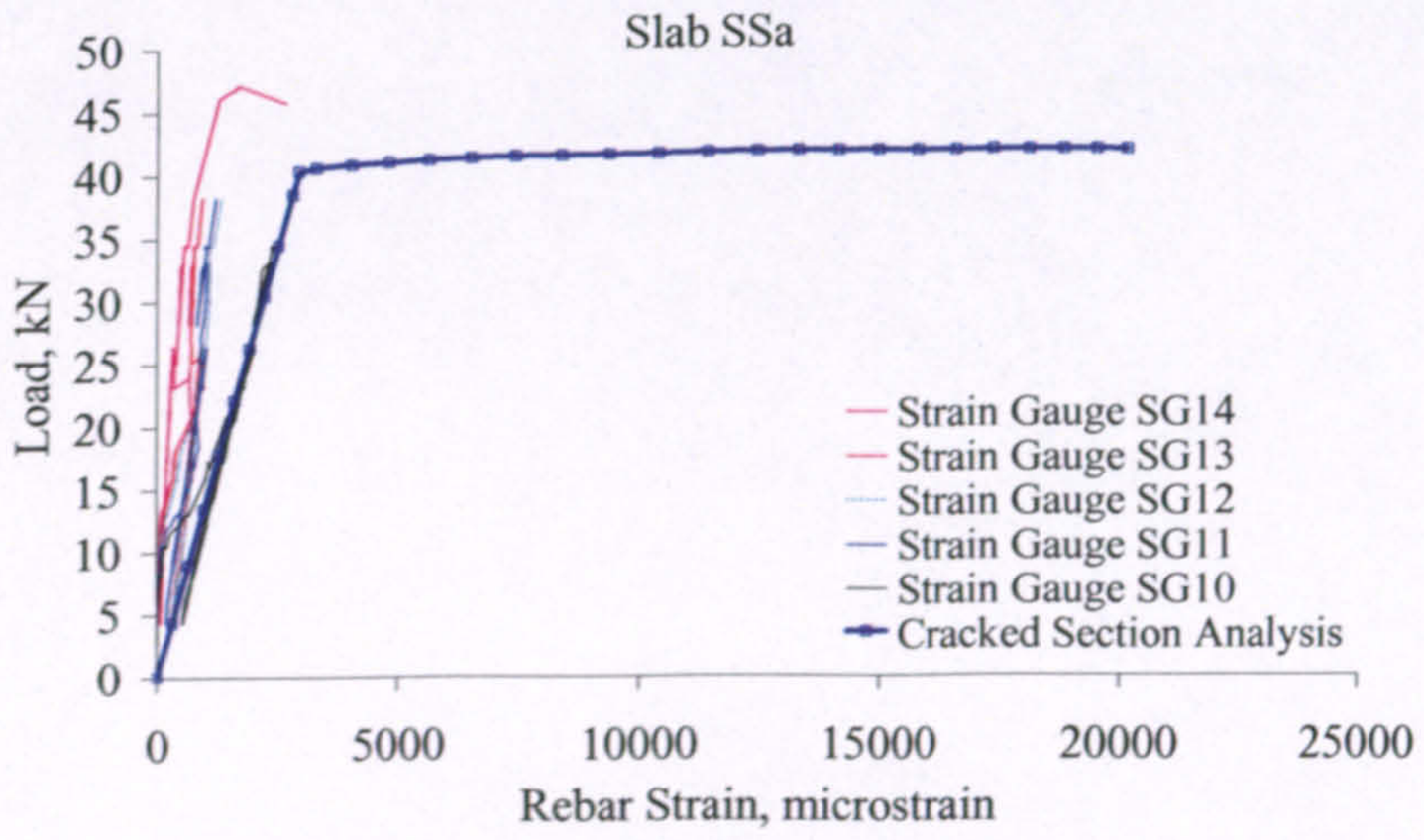
Slab SSa
Load, kN
Rebar Strain, microstrain
Strain Gauge SG14
Strain Gauge SG13
Strain Gauge SG12
Strain Gauge SG11
Strain Gauge SG10
Cracked Section Analysis

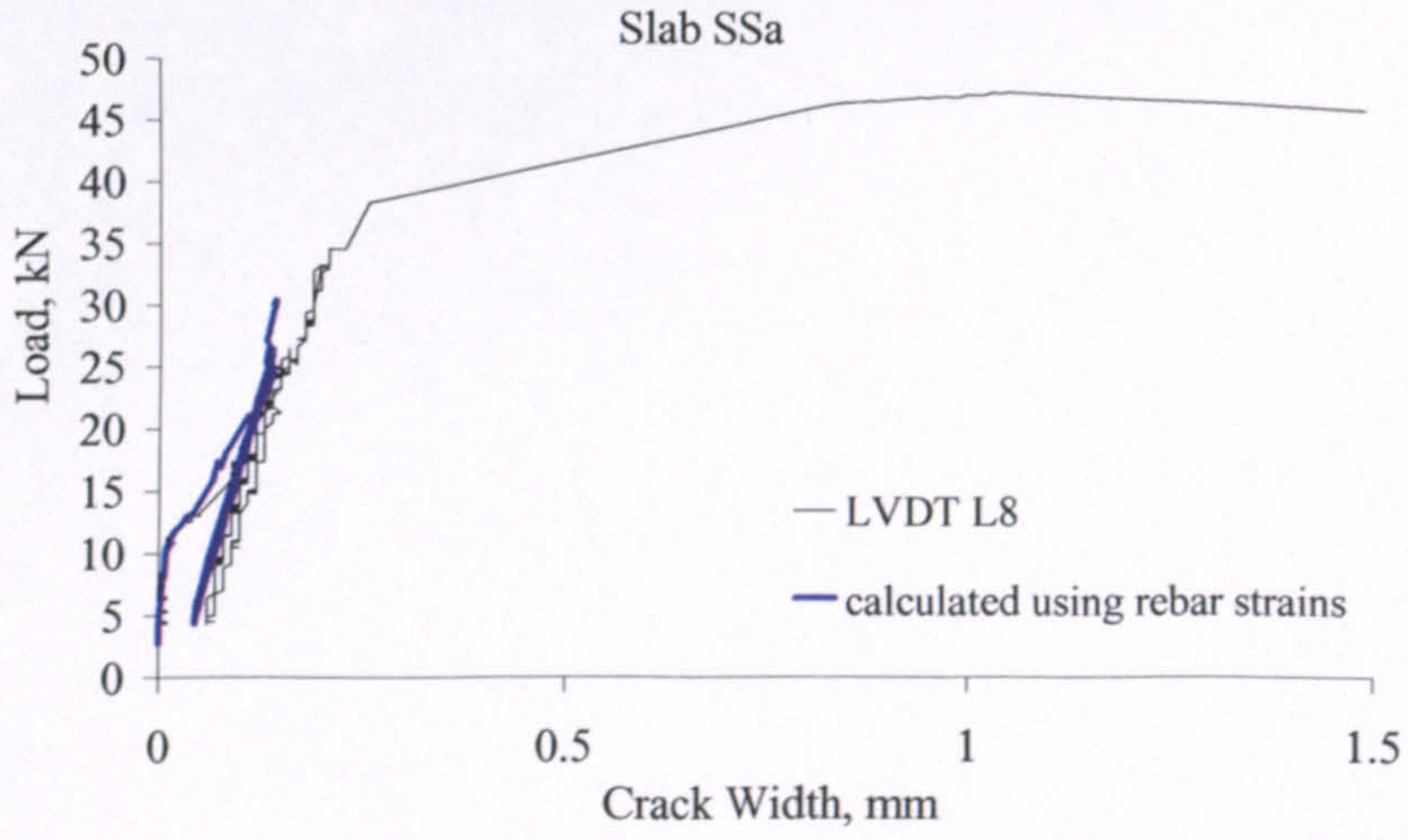
Slab SSa
Load, kN
Crack Width, mm
LVDT L8
calculated using rebar strains

Slab SSa

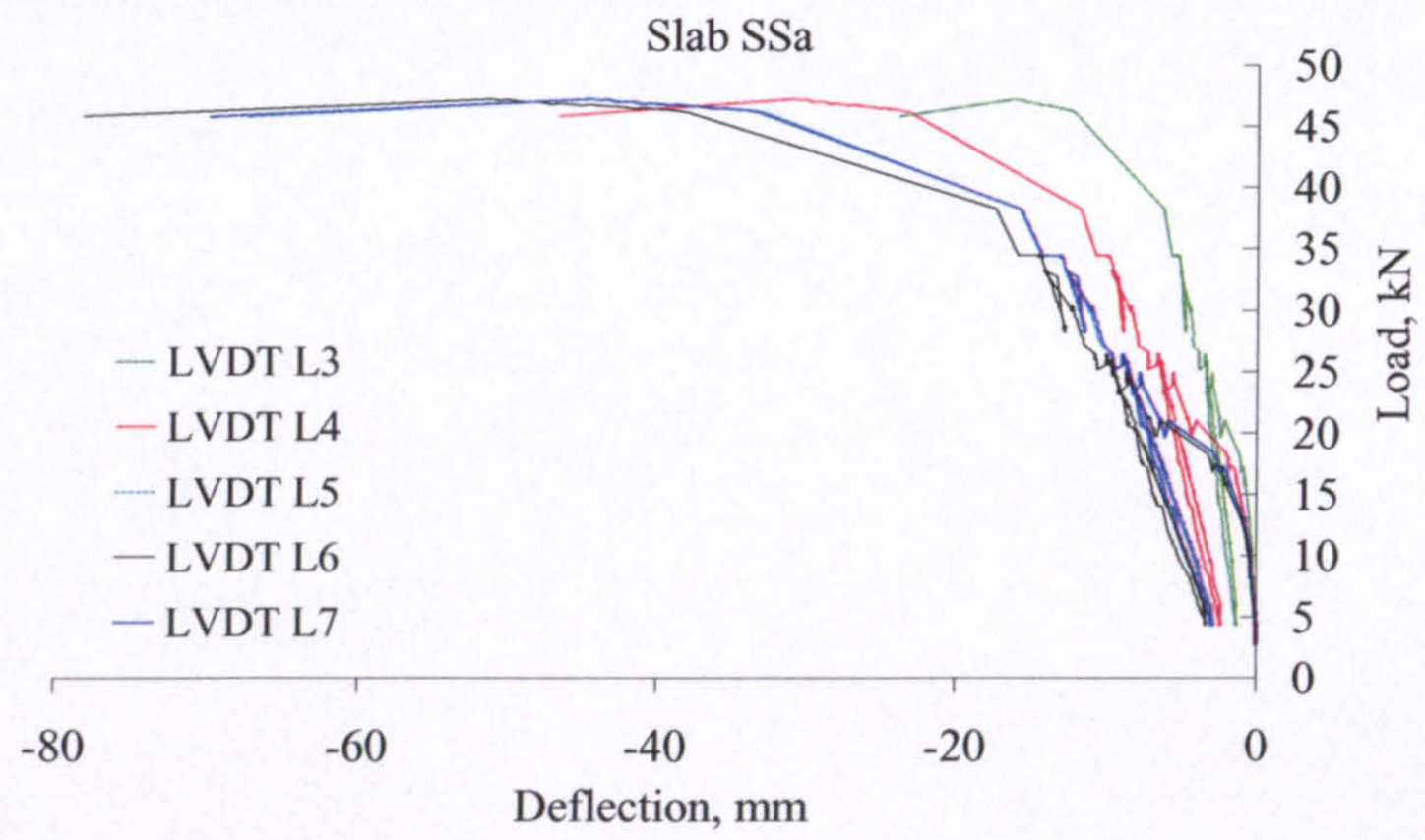

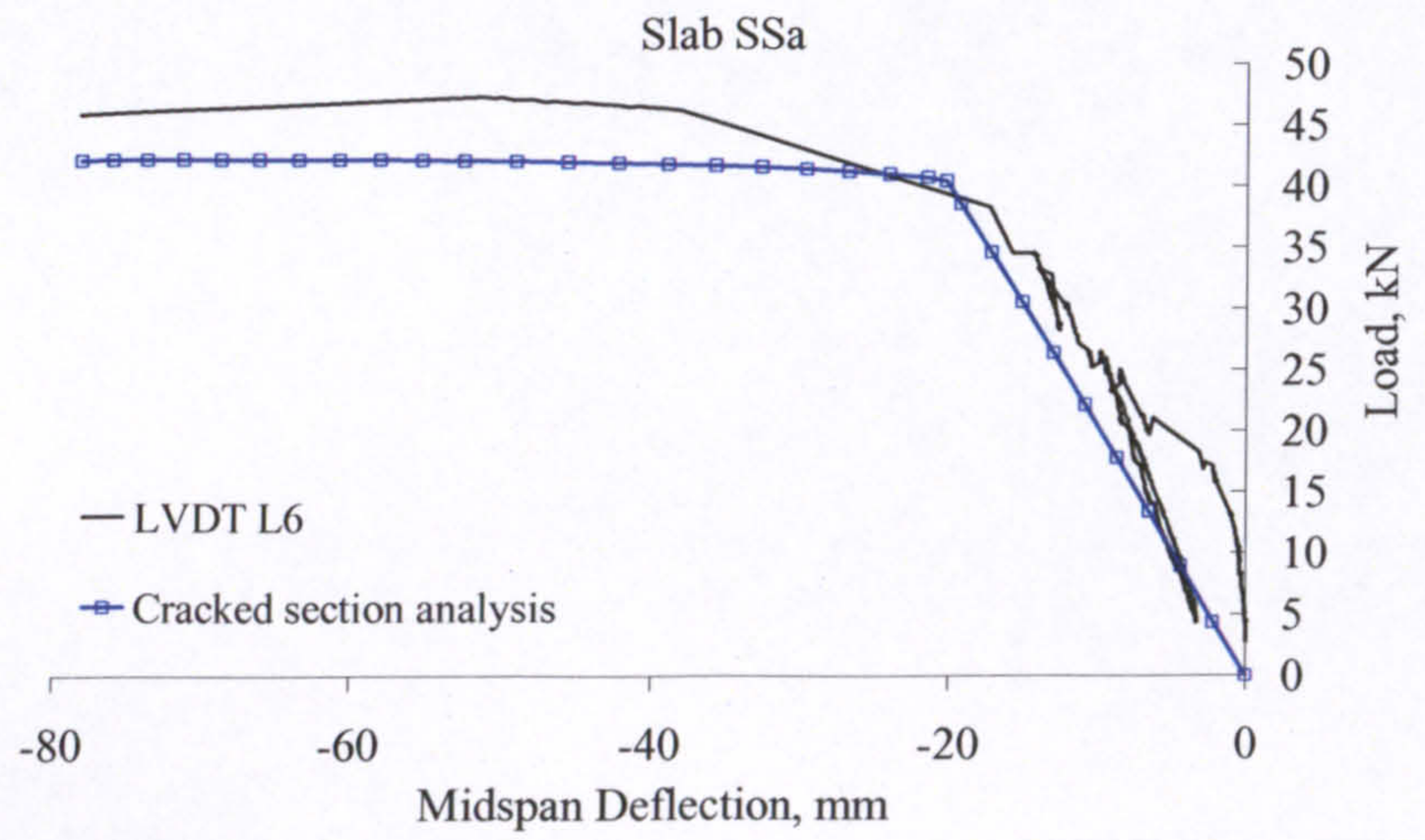

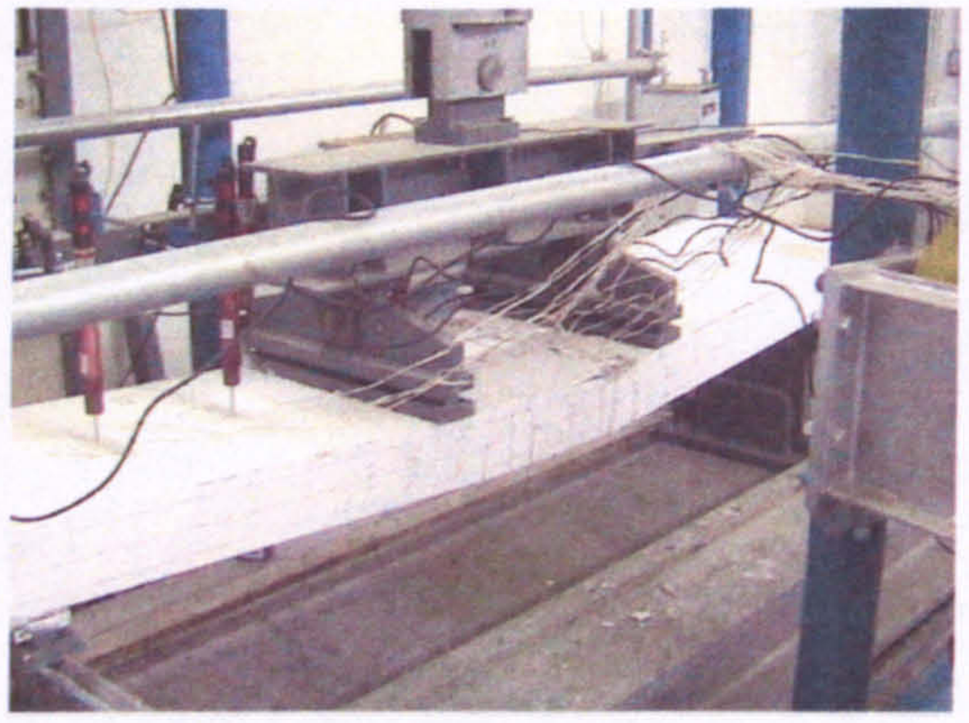

Crushing of concrete following steel yielding.

- Cover=25mm
- location of crack inducer is precise.

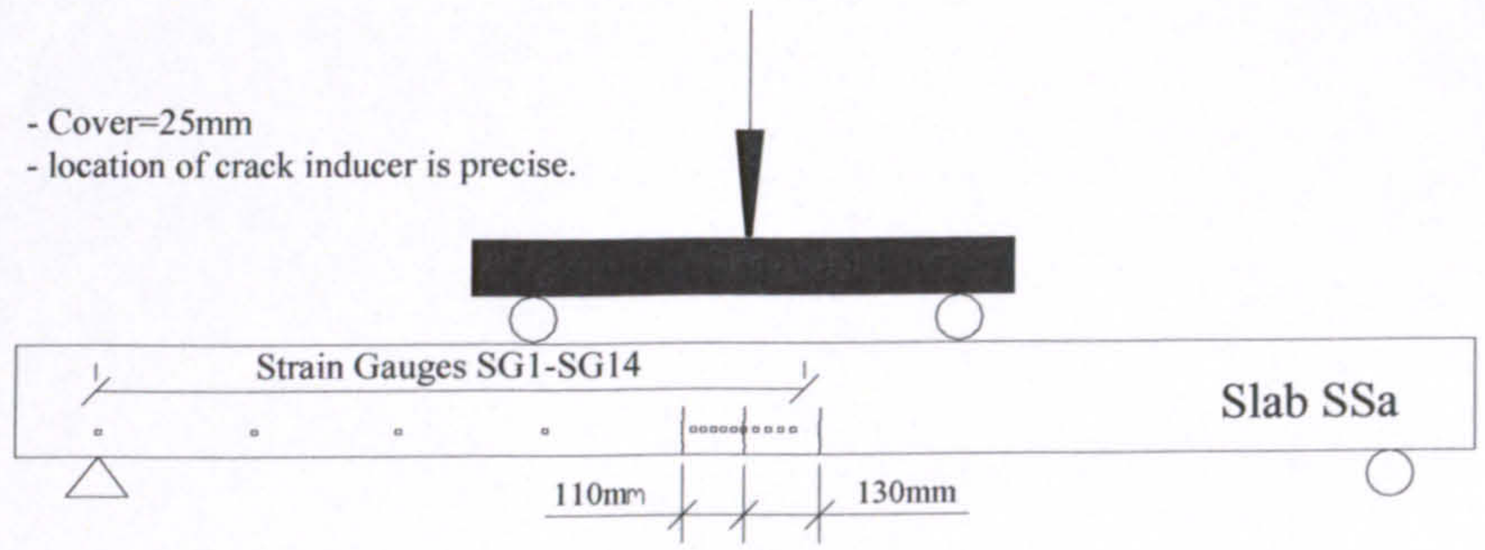

Cracks around Centre

Slab SSb

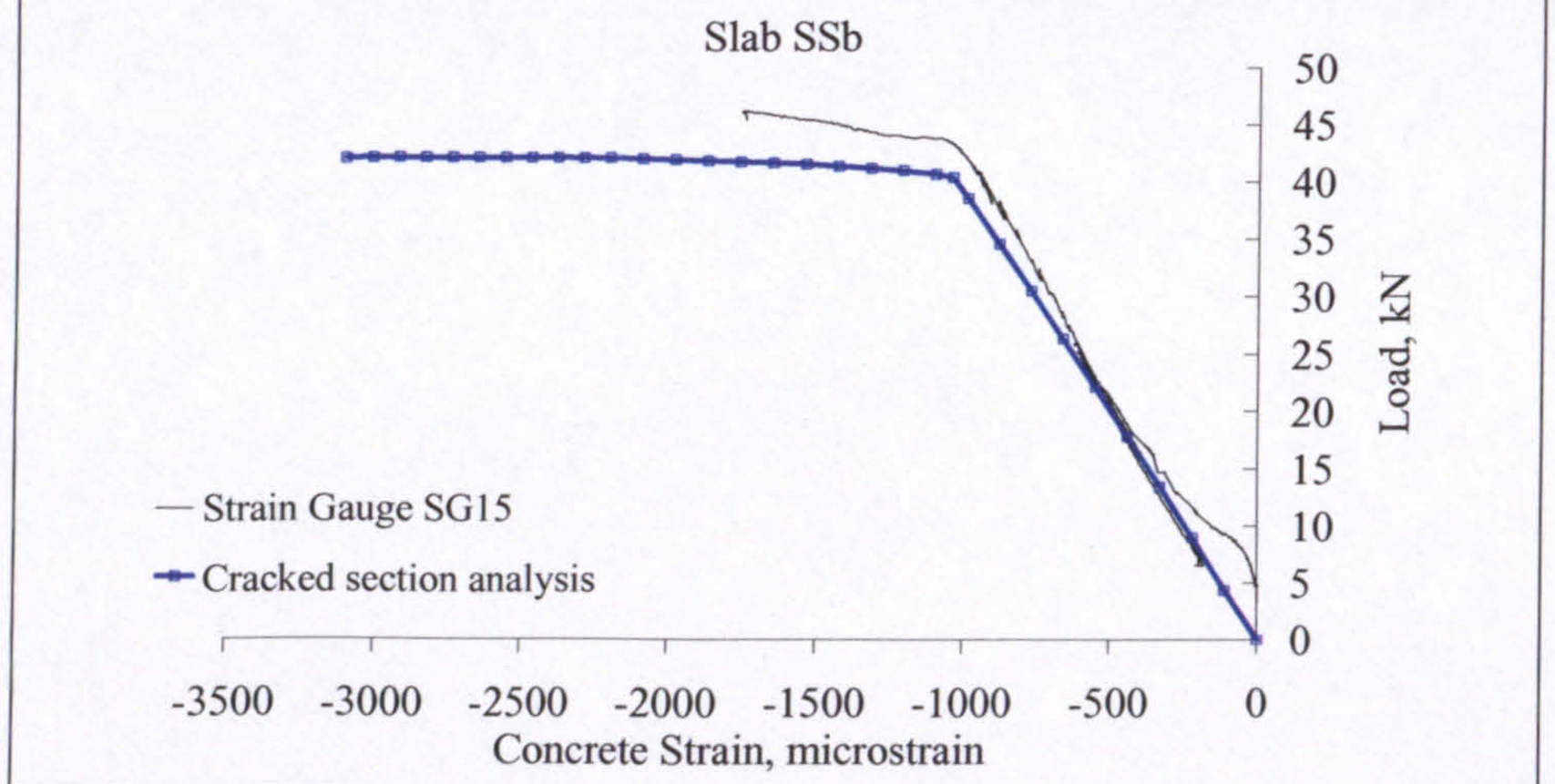
Slab SSb
Load, kN
50
45
40
35
30
25
20
15
10
5
0
Strain Gauge SG15
Cracked section analysis
-3500
-3000
-2500
-2000
-1500
-1000
-500
0
Concrete Strain, microstrain

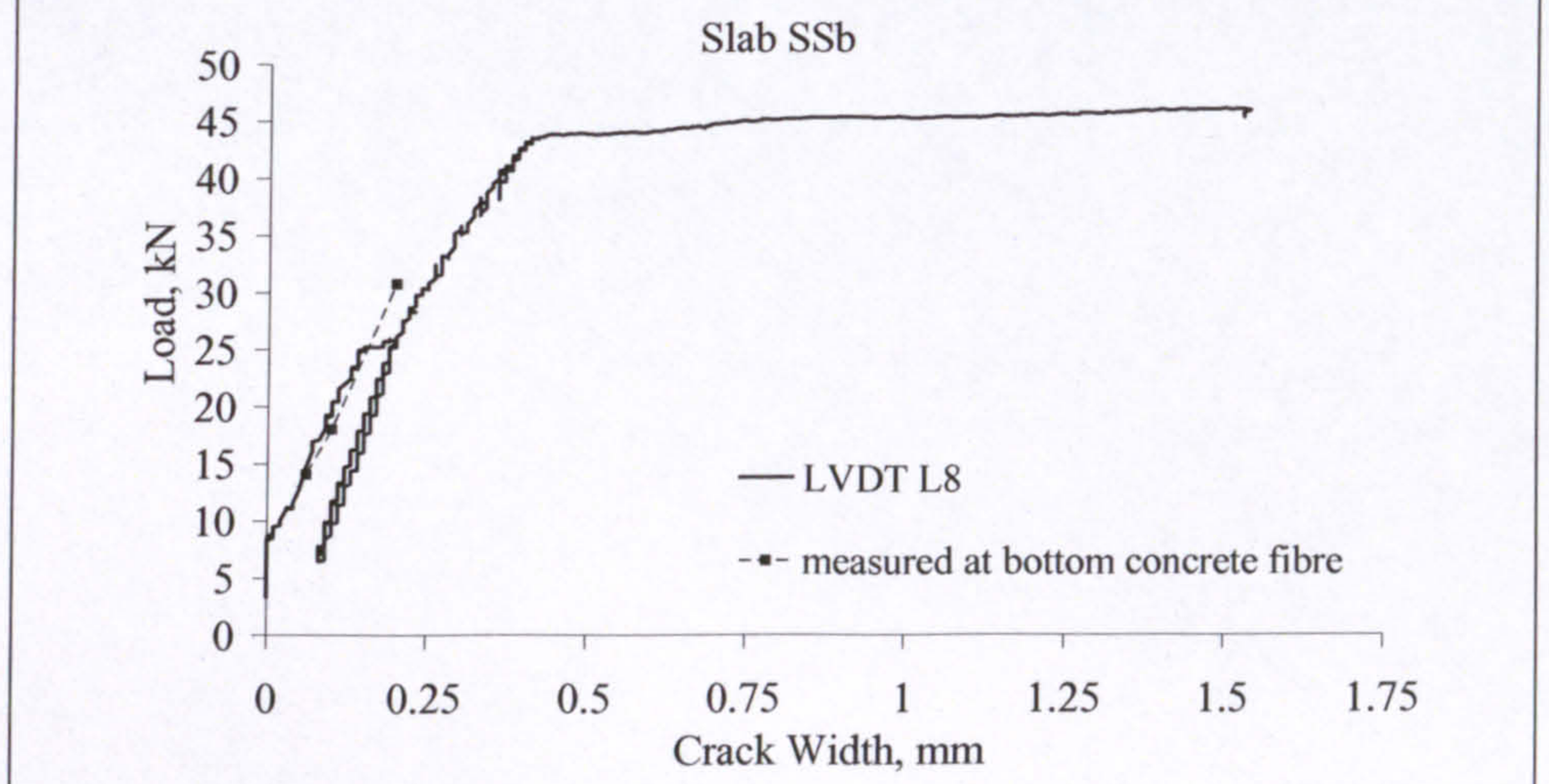
Slab SSb
Load, kN
50
45
40
35
30
25
20
15
10
5
0
LVDT L8
measured at bottom concrete fibre
0
0.25
0.5
0.75
1
1.25
1.5
1.75
Crack Width, mm

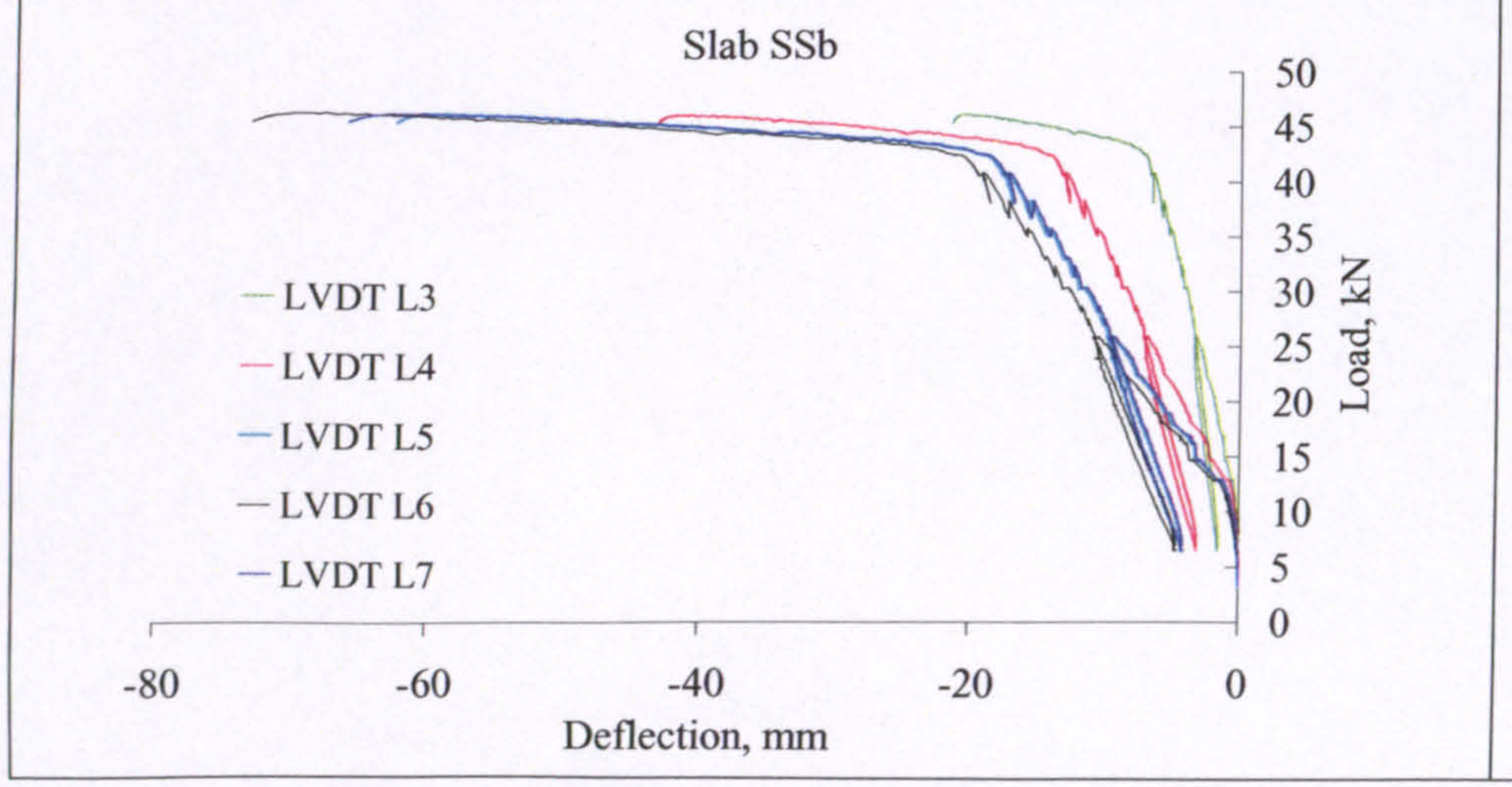
Slab SSb
Load, kN
50
45
40
35
30
25
20
15
10
5
0
LVDT L3
LVDT L4
LVDT L5
LVDT L6
LVDT L7
-80
-60
-40
-20
0
Deflection, mm

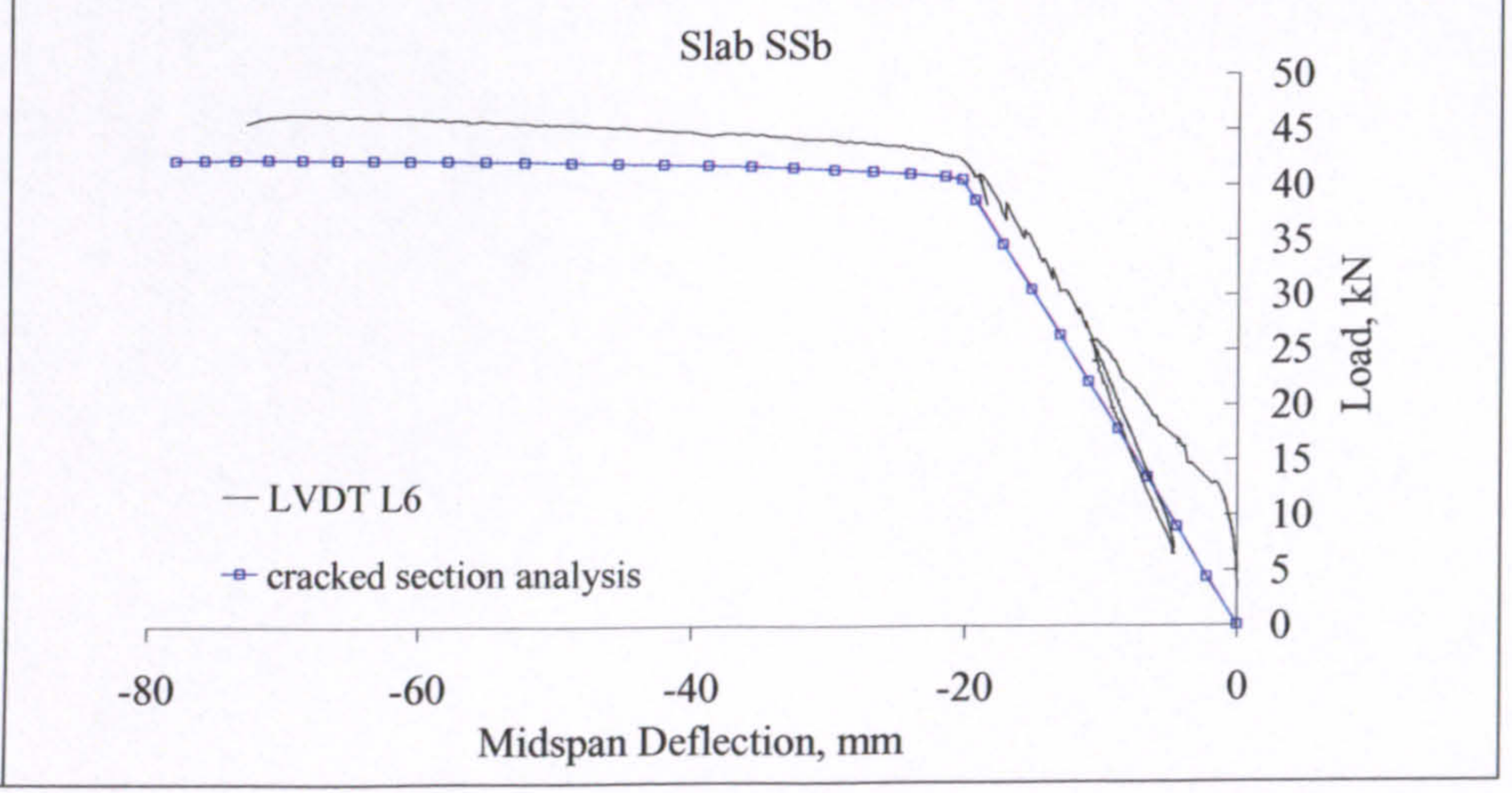
Slab SSb
Load, kN
50
45
40
35
30
25
20
15
10
5
0
LVDT L6
cracked section analysis
-80
-60
-40
-20
0
Midspan Deflection, mm

Slab SSb

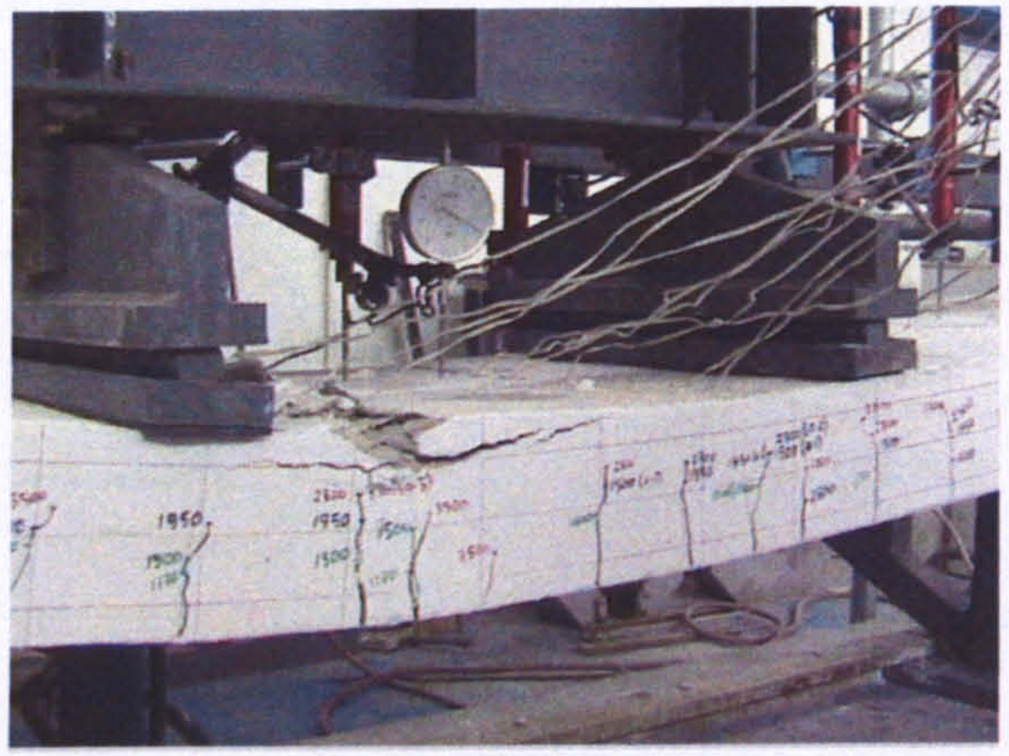

Crushing of concrete following steel yielding.

- Cover=25mm
- location of crack inducer is precise.

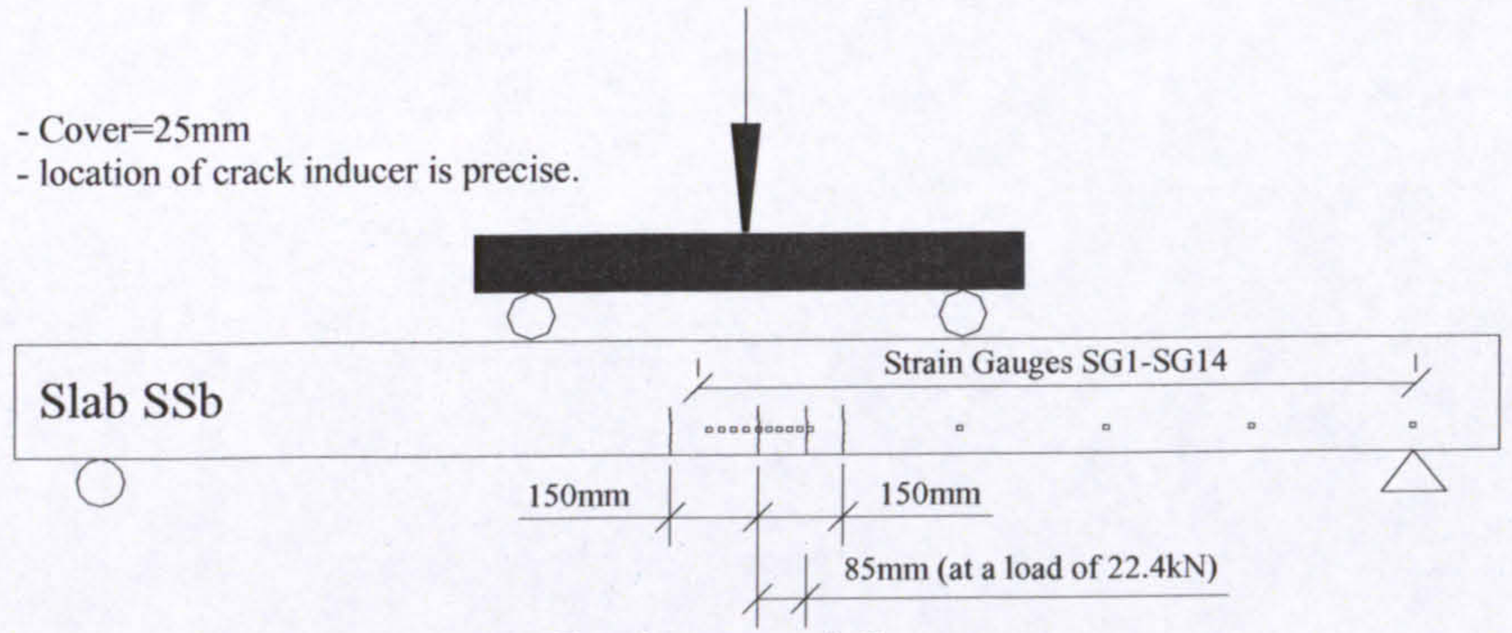

Cracks around Centre

Combined Midspan Deflection (LVDT L6) vs. Load

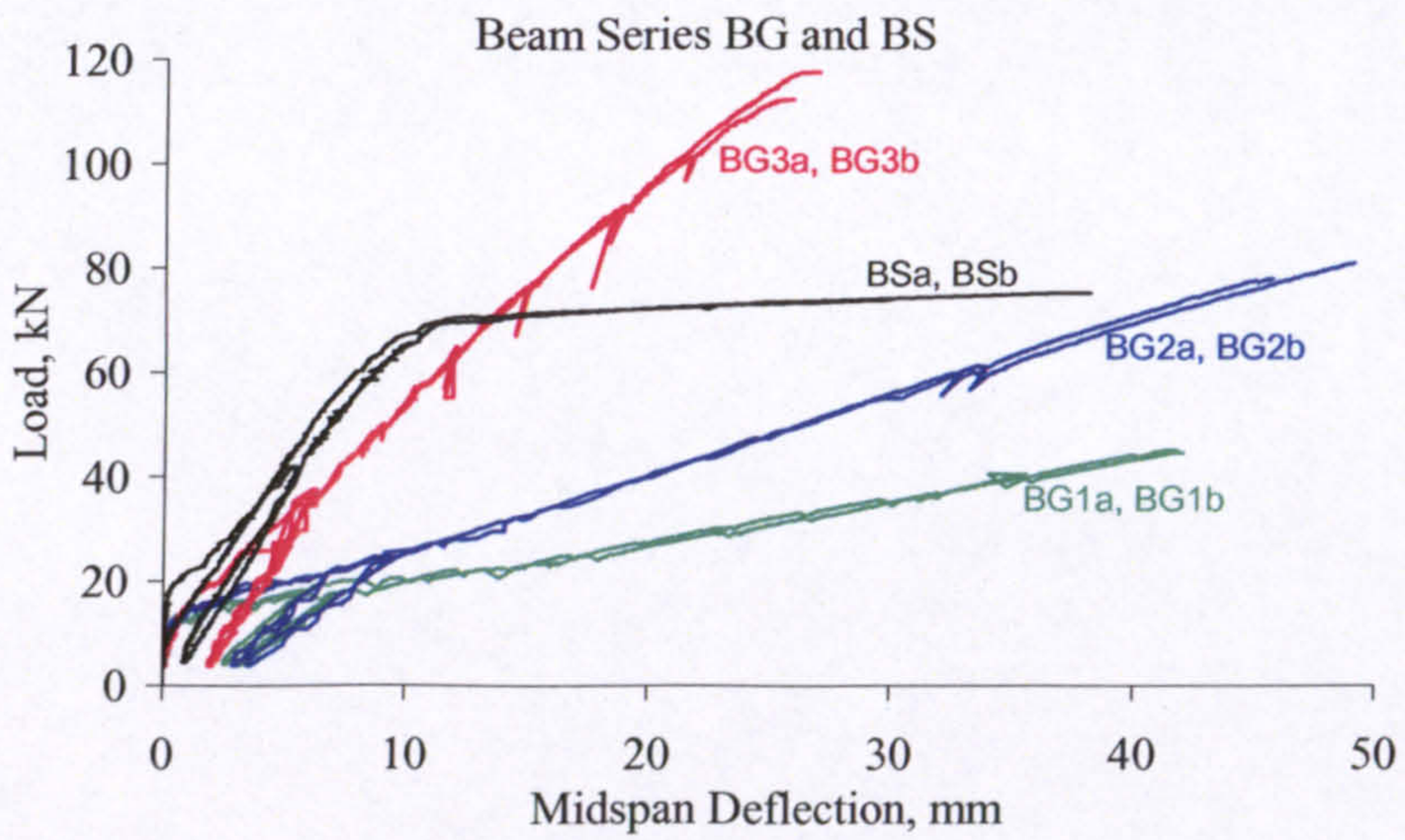

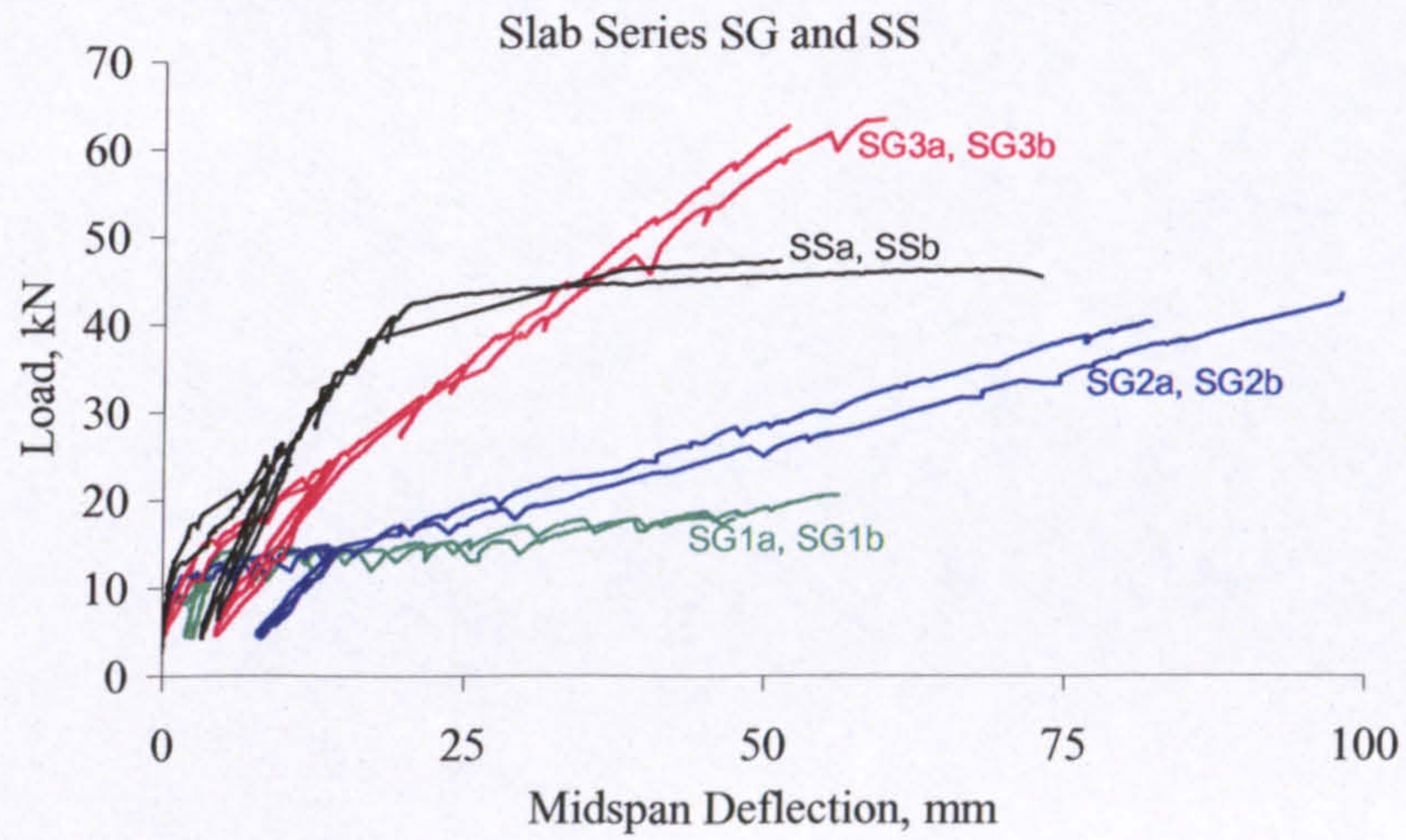

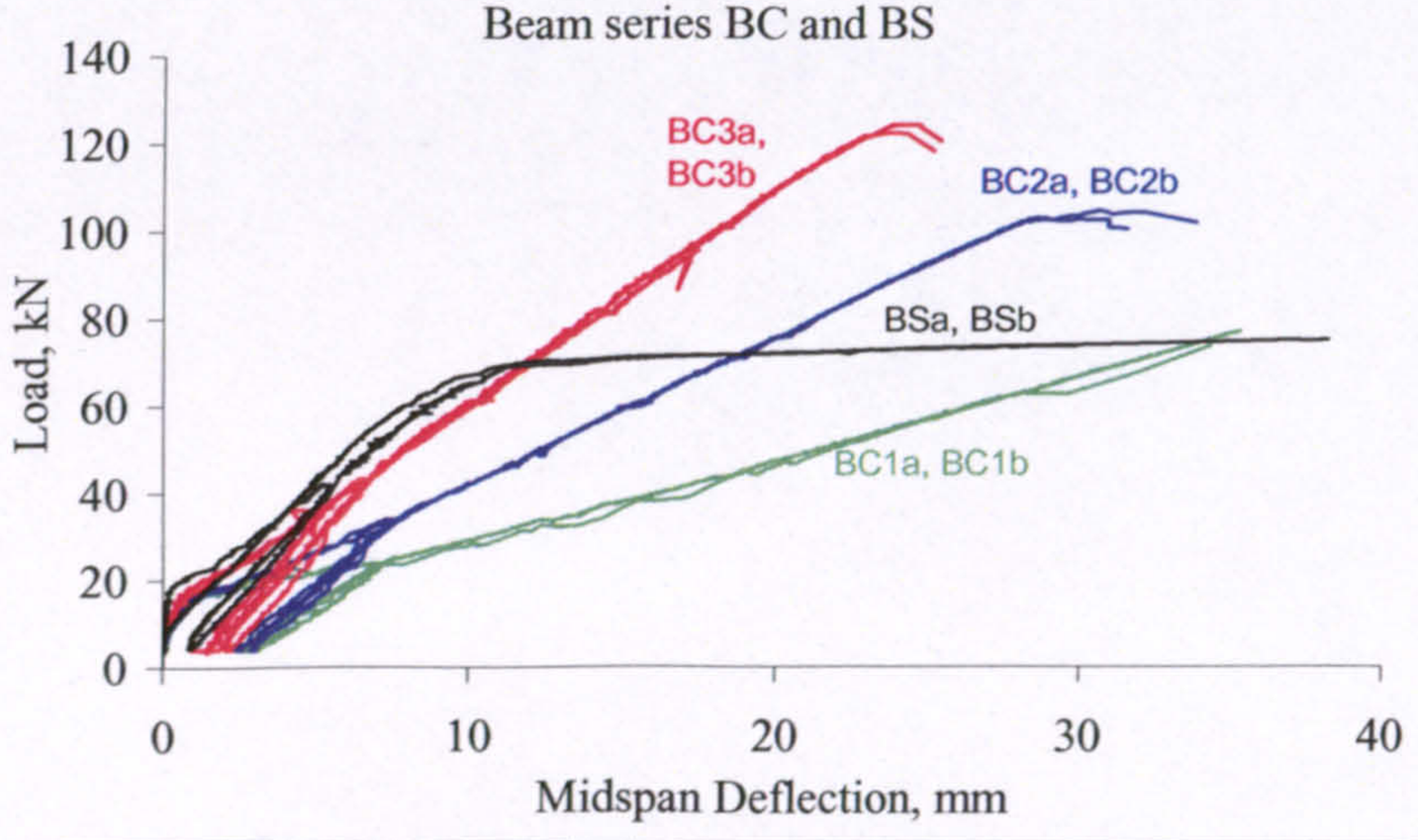

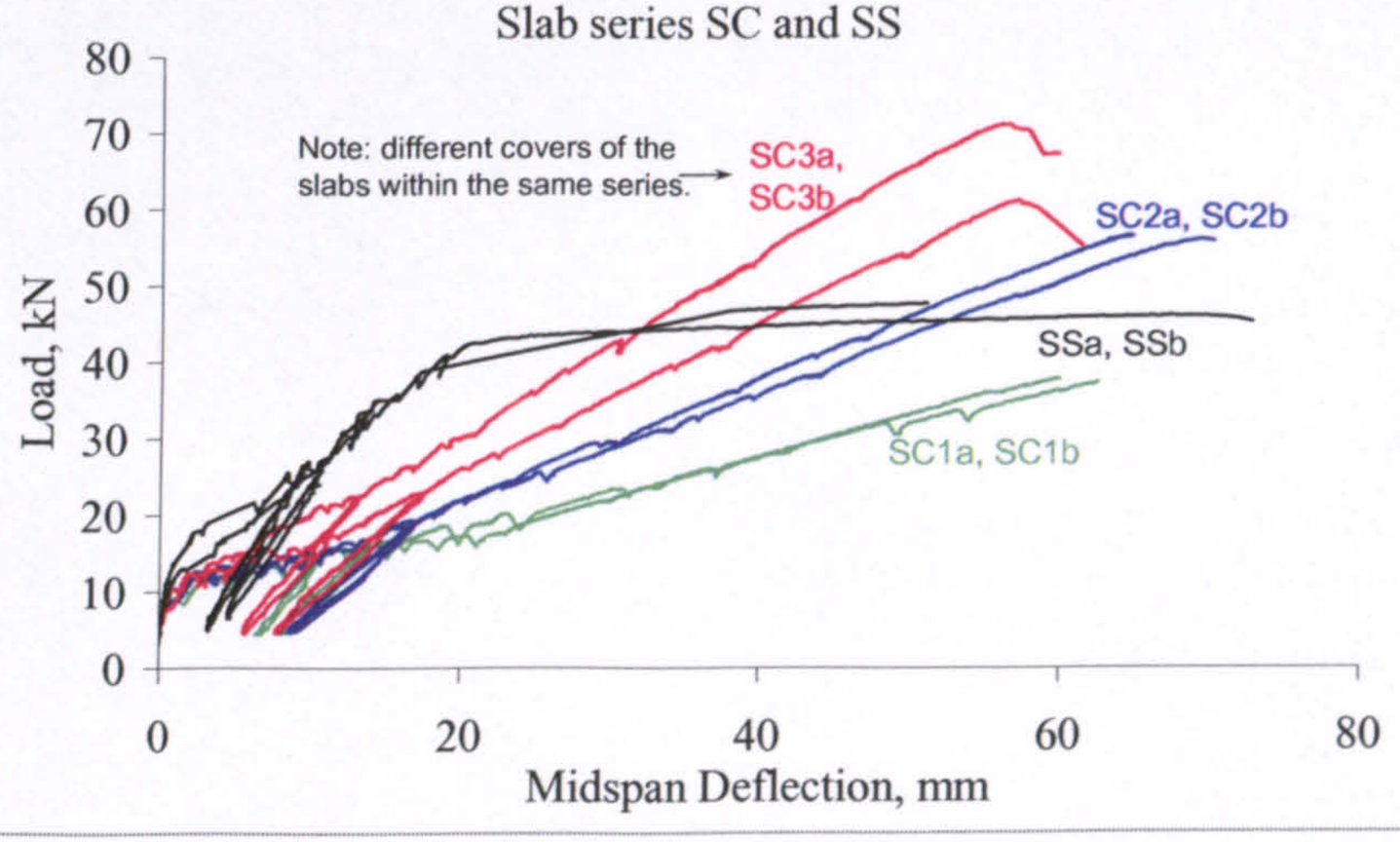

Combined Crack Width (LVDT L8) vs. Load

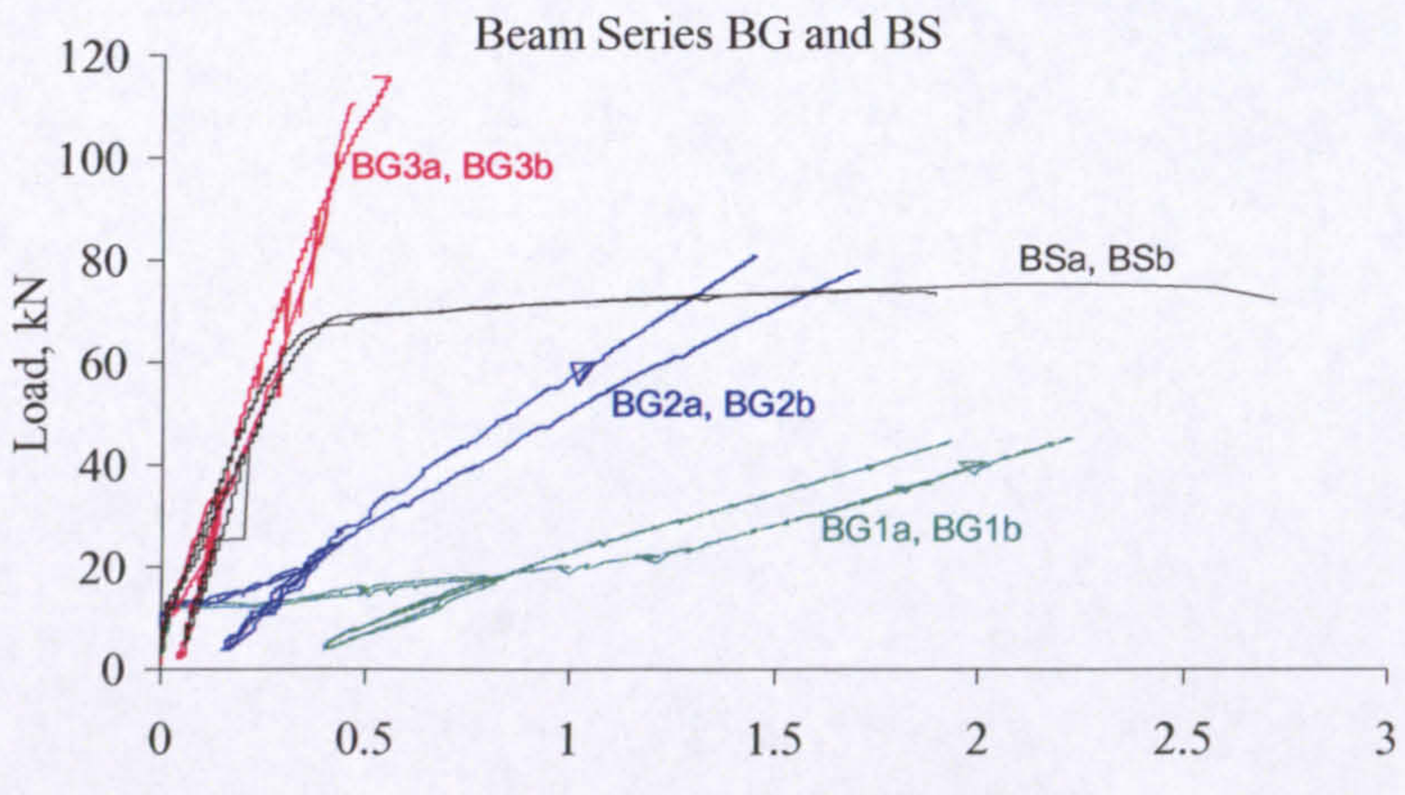

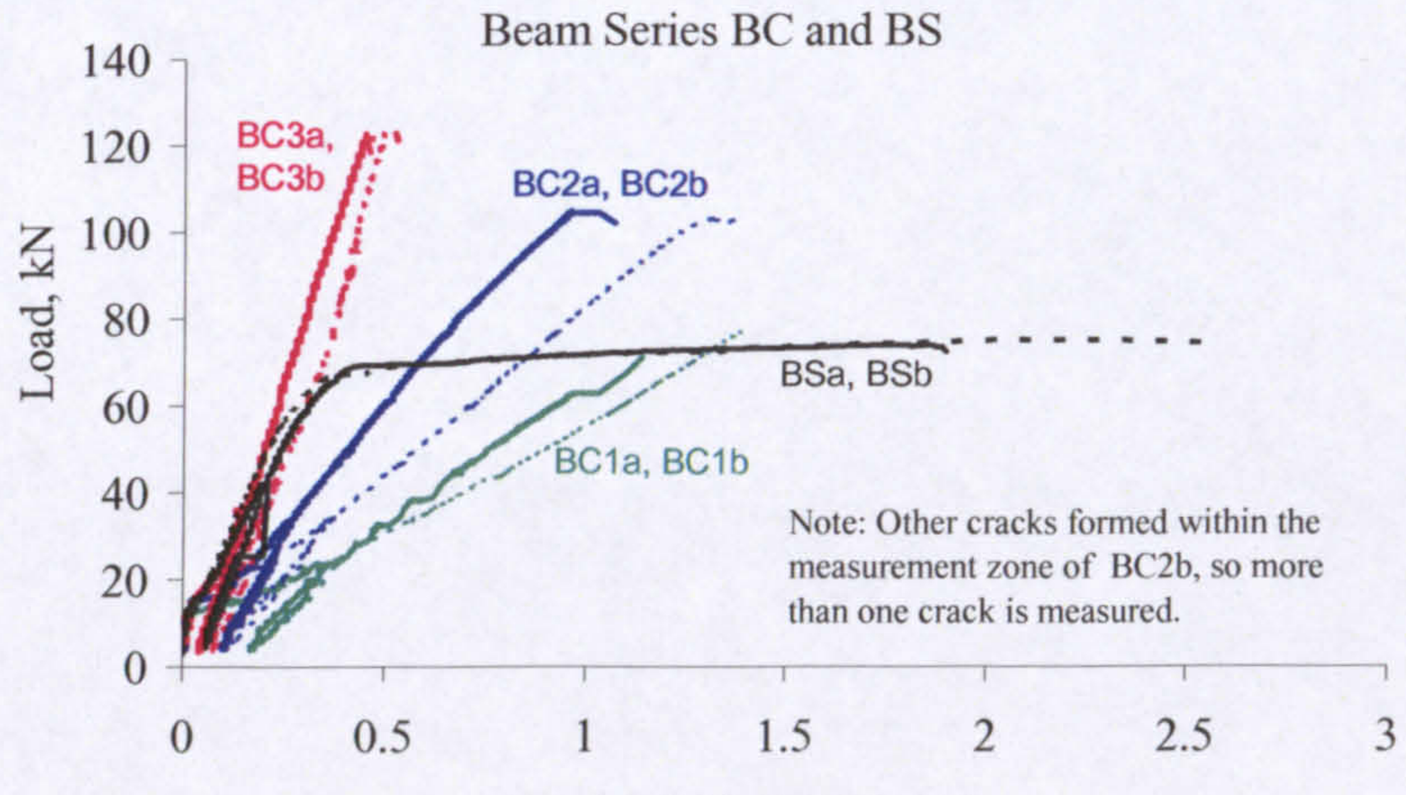

Appendix C

Prediction of Short-Term Deflection by ACI and Eurocode 2

Beams BG1

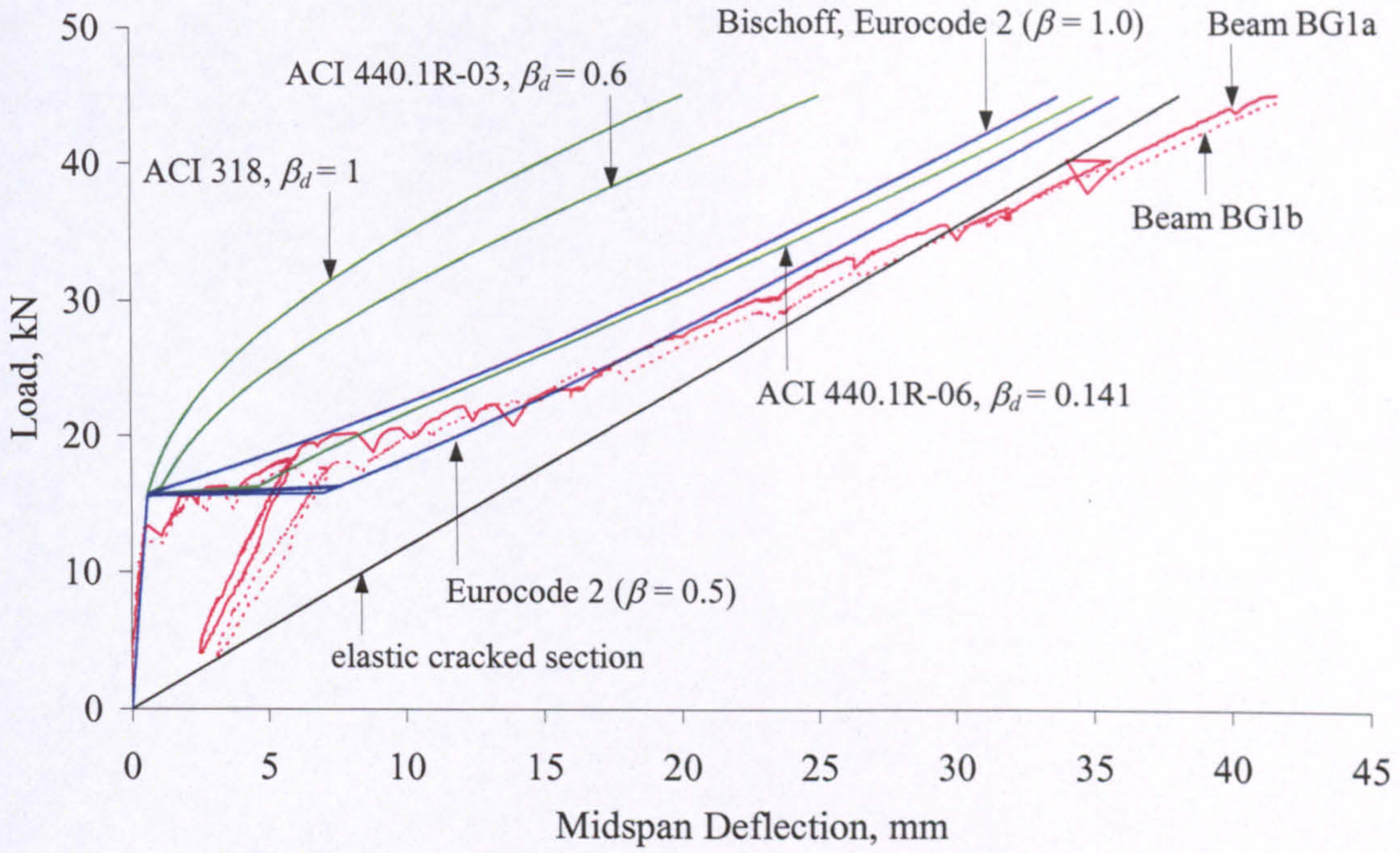

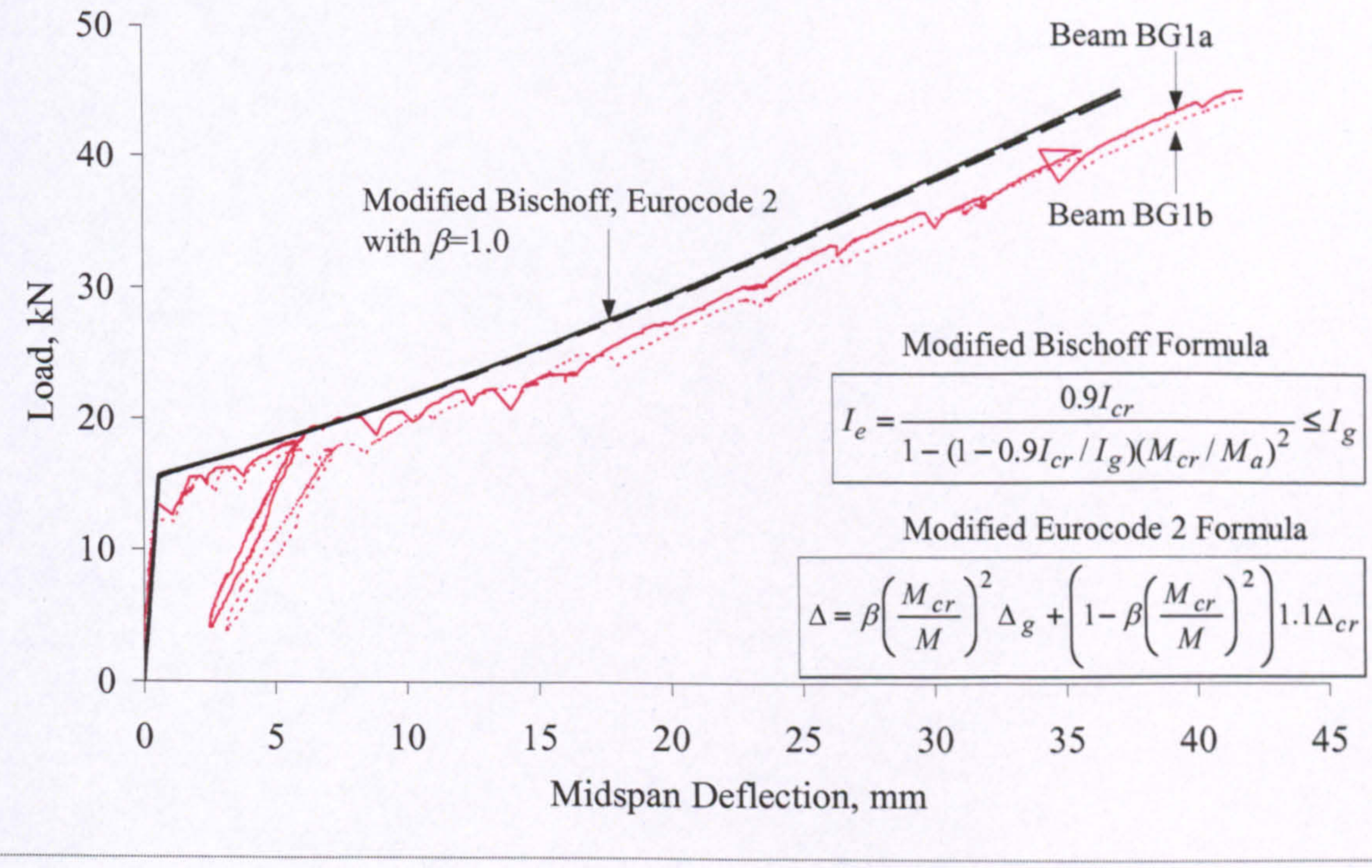

Modified Bischoff Formula

$$I_e = \frac{0.9 I_{cr}}{1 - (1 - 0.9 I_{cr} / I_g)(M_{cr} / M_a)^2} \le I_g$$

Modified Eurocode 2 Formula

$$\Delta = \beta \left(\frac{M_{cr}}{M} \right)^2 \Delta_g + \left(1 - \beta \left(\frac{M_{cr}}{M} \right)^2 \right) 1.1 \Delta_{cr}$$

Beams BG2

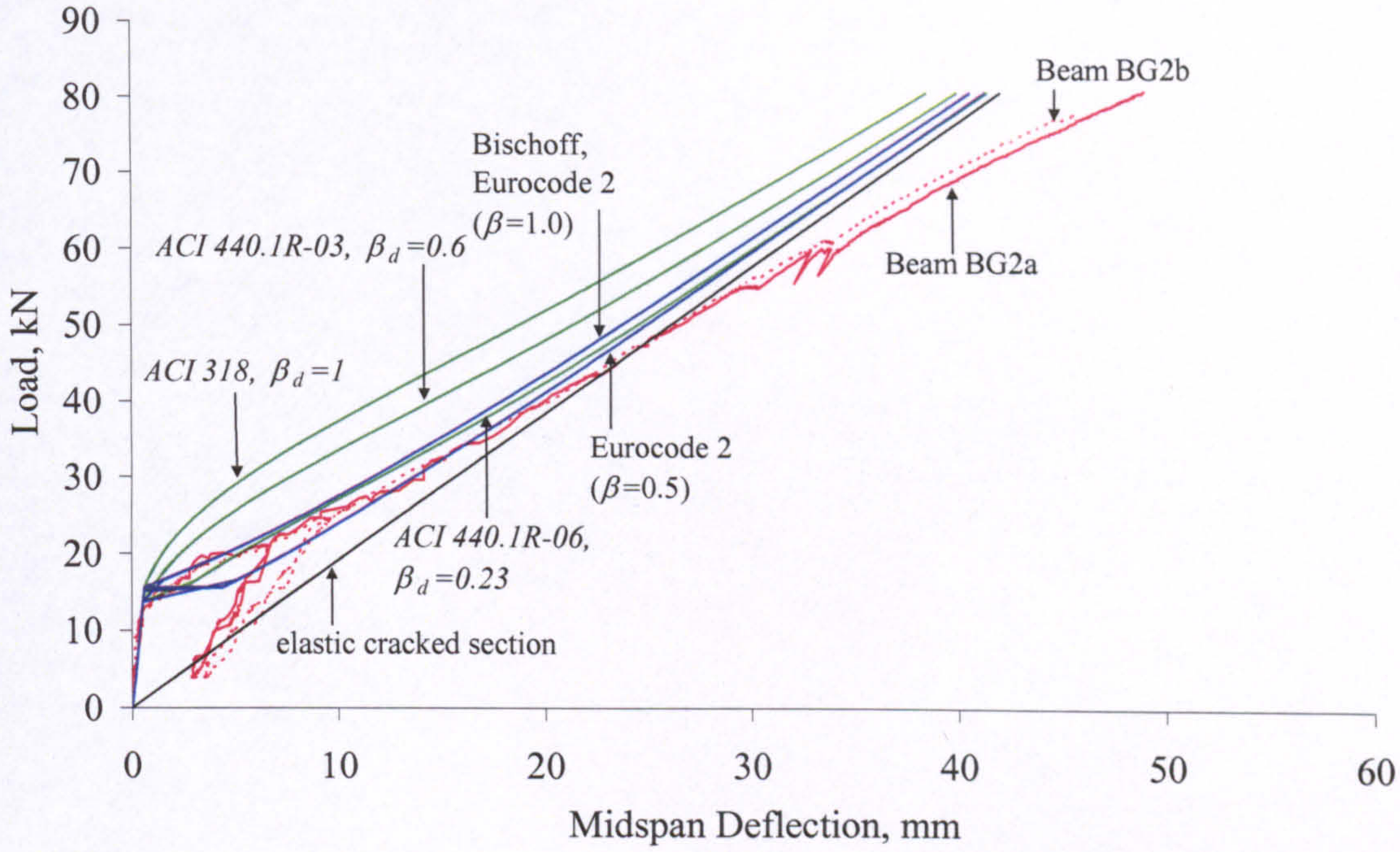
Load, kN
Midspan Deflection, mm
Beam BG2b
Beam BG2a
Bischoff, Eurocode 2 (β=1.0)
ACI 440.1R-03, β_d=0.6
ACI 318, β_d=1
Eurocode 2 (β=0.5)
ACI 440.1R-06, β_d=0.23
elastic cracked section

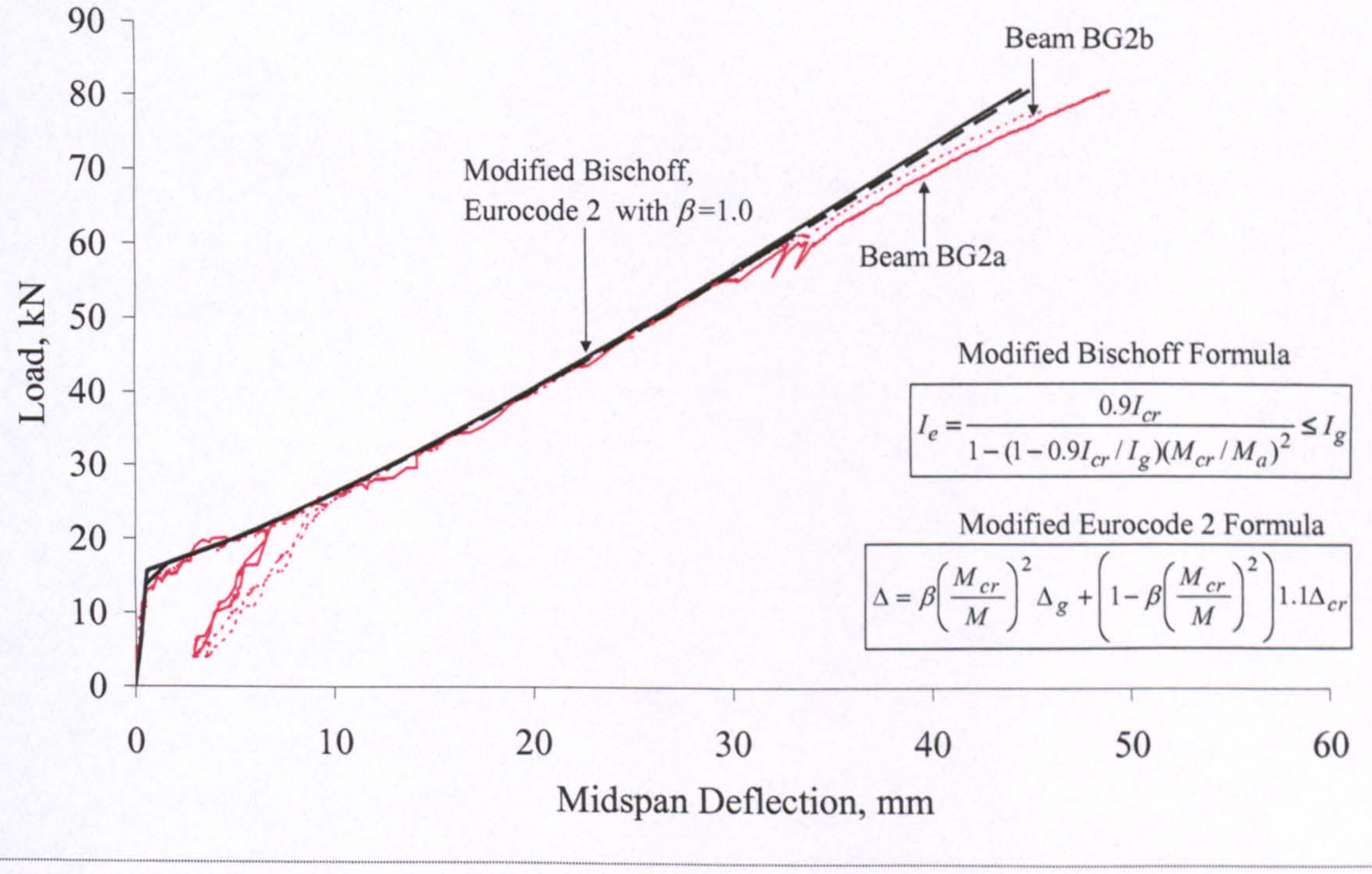
Load, kN
Midspan Deflection, mm
Beam BG2b
Beam BG2a
Modified Bischoff, Eurocode 2 with β=1.0
Modified Bischoff Formula
$I_e = \frac{0.9I_{cr}}{1-(1-0.9I_{cr}/I_g)(M_{cr}/M_a)^2} \le I_g$
Modified Eurocode 2 Formula
$\Delta = \beta\left(\frac{M_{cr}}{M}\right)^2 \Delta_g + \left(1-\beta\left(\frac{M_{cr}}{M}\right)^2\right) 1.1\Delta_{cr}$

Beams BG3

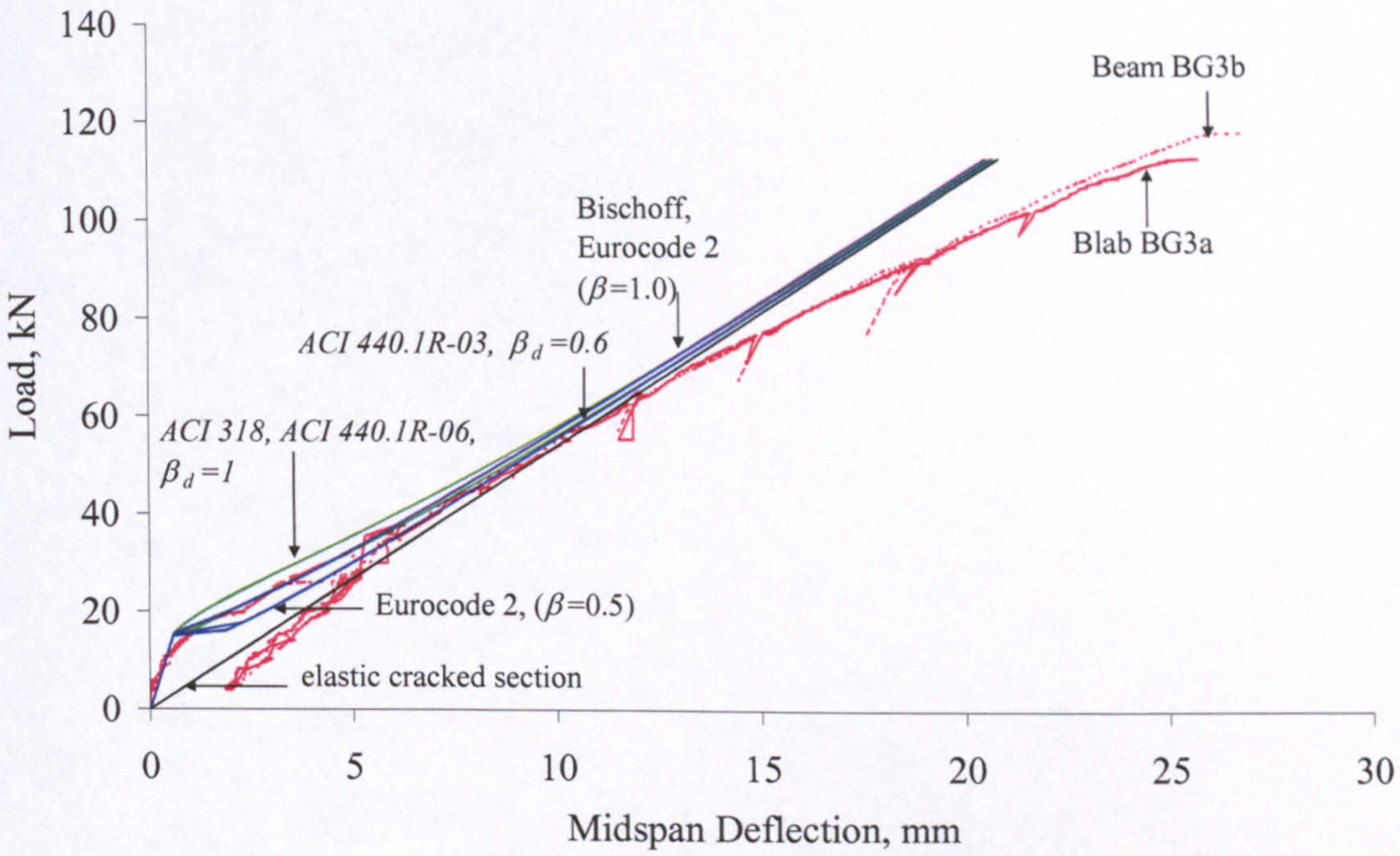
Load, kN
Midspan Deflection, mm
Beam BG3b
Blab BG3a
Bischoff,
Eurocode 2
(β=1.0)
ACI 440.1R-03, β_d=0.6
ACI 318, ACI 440.1R-06,
β_d=1
Eurocode 2, (β=0.5)
elastic cracked section

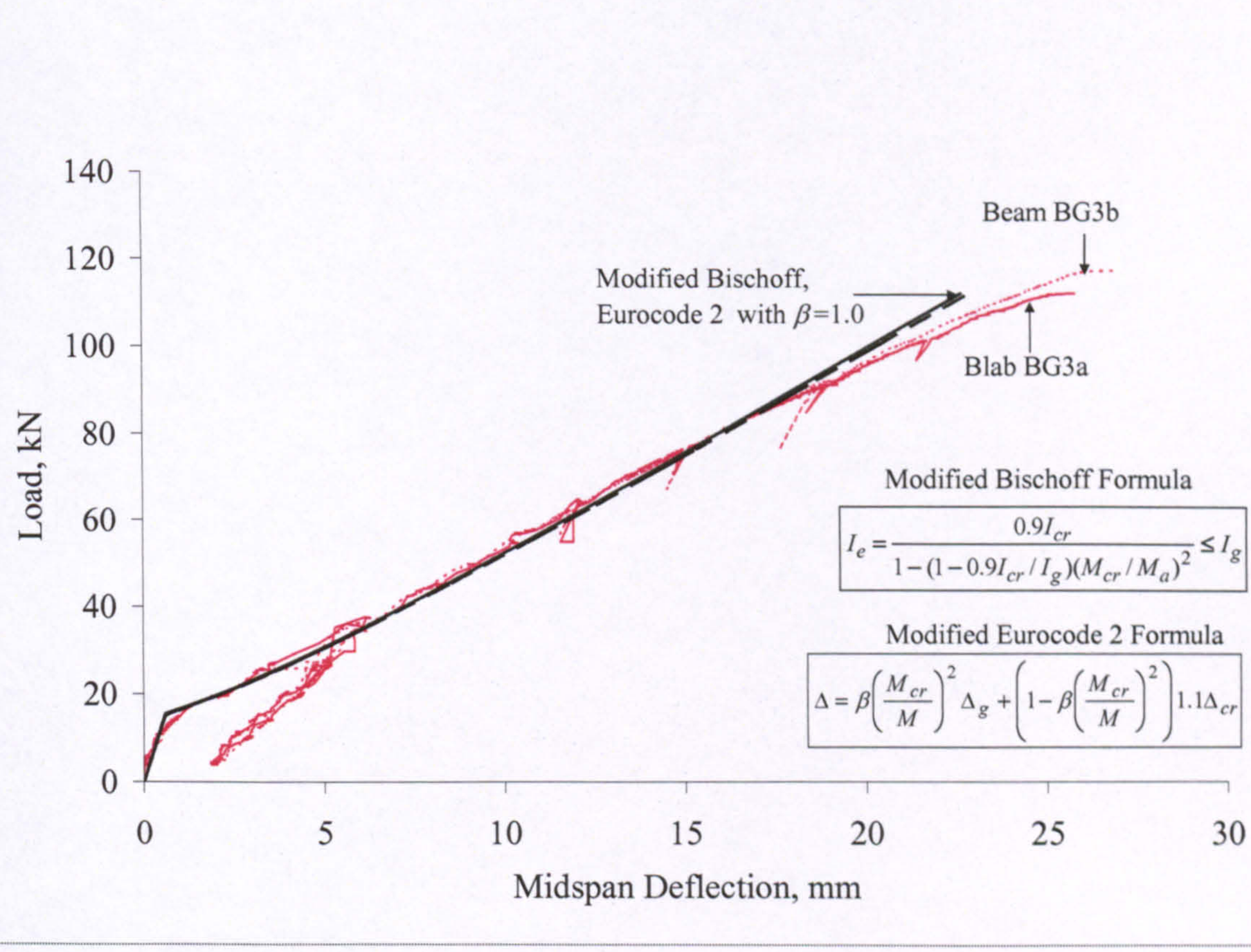
Load, kN
Midspan Deflection, mm
Beam BG3b
Blab BG3a
Modified Bischoff,
Eurocode 2 with β=1.0
Modified Bischoff Formula
$I_e = \frac{0.9 I_{cr}}{1-(1-0.9 I_{cr}/I_g)(M_{cr}/M_a)^2} \le I_g$
Modified Eurocode 2 Formula
$\Delta = \beta\left(\frac{M_{cr}}{M}\right)^2 \Delta_g + \left(1-\beta\left(\frac{M_{cr}}{M}\right)^2\right) 1.1\Delta_{cr}$

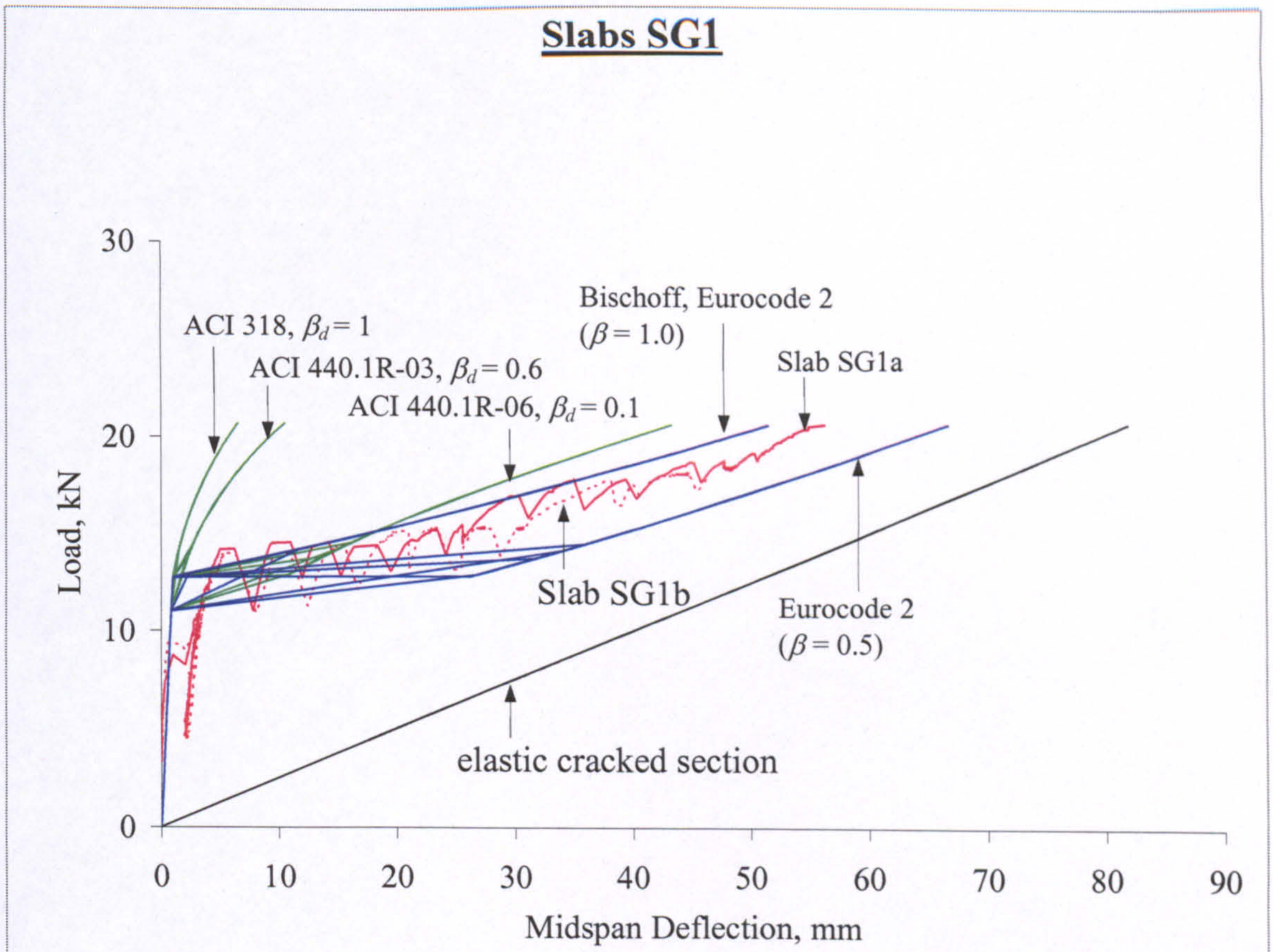
Slabs SG1
30
20
10
0
Load, kN
ACI 318, $\beta_d = 1$
ACI 440.1R-03, $\beta_d = 0.6$
ACI 440.1R-06, $\beta_d = 0.1$
Bischoff, Eurocode 2
($\beta = 1.0$)
Slab SG1a
Slab SG1b
Eurocode 2
($\beta = 0.5$)
elastic cracked section
0
10
20
30
40
50
60
70
80
90
Midspan Deflection, mm

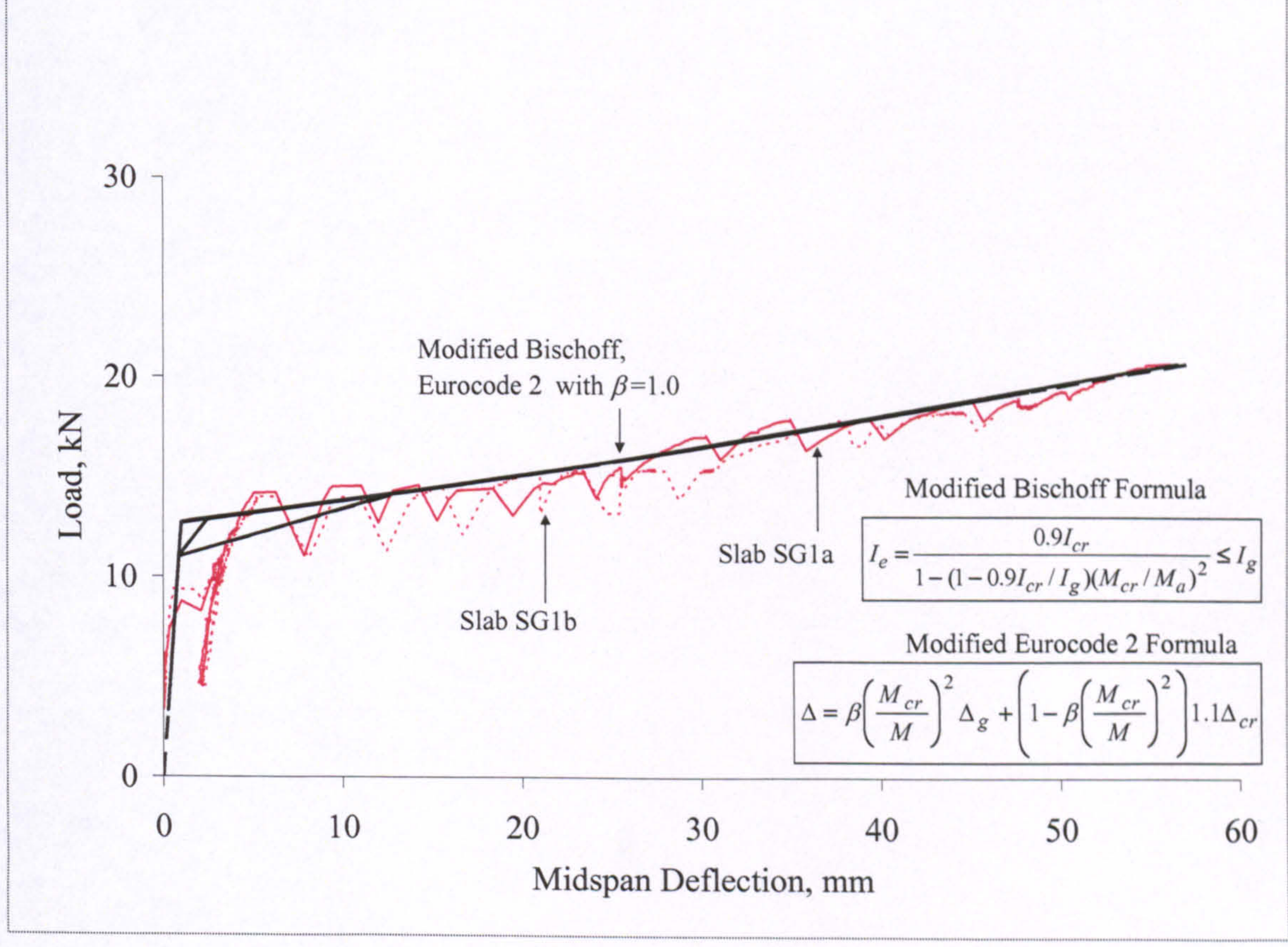
30
20
10
0
Load, kN
Modified Bischoff,
Eurocode 2 with β=1.0
Slab SG1a
Slab SG1b
Modified Bischoff Formula
$I_e = \frac{0.9I_{cr}}{1-(1-0.9I_{cr}/I_g)(M_{cr}/M_a)^2} \le I_g$
Modified Eurocode 2 Formula
$\Delta = \beta\left(\frac{M_{cr}}{M}\right)^2 \Delta_g + \left(1-\beta\left(\frac{M_{cr}}{M}\right)^2\right)1.1\Delta_{cr}$
0
10
20
30
40
50
60
Midspan Deflection, mm

Slabs SG2

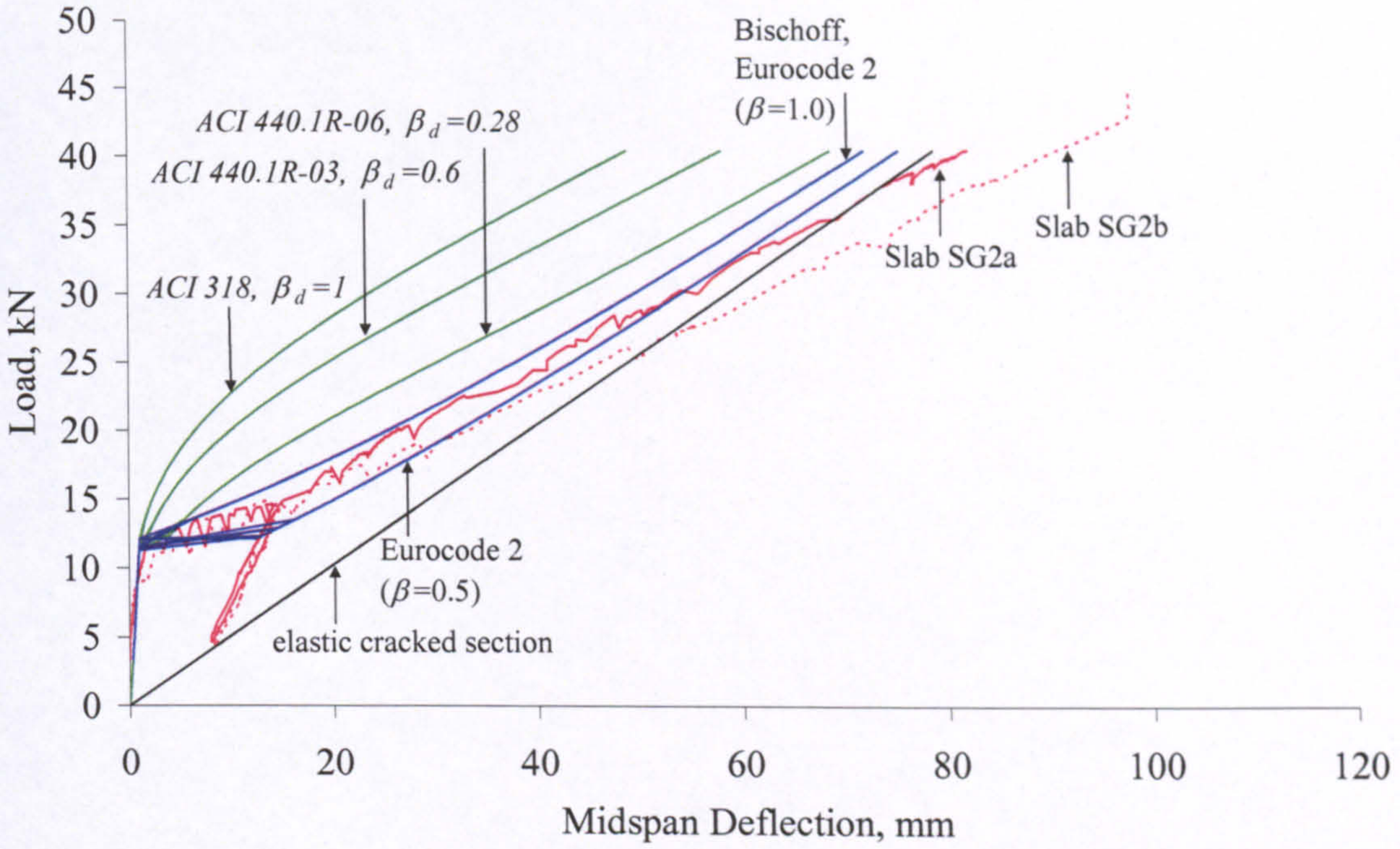
Load, kN
Midspan Deflection, mm
ACI 440.1R-06, β_d=0.28
ACI 440.1R-03, β_d=0.6
ACI 318, β_d=1
Bischoff, Eurocode 2 (β=1.0)
Eurocode 2 (β=0.5)
elastic cracked section
Slab SG2a
Slab SG2b

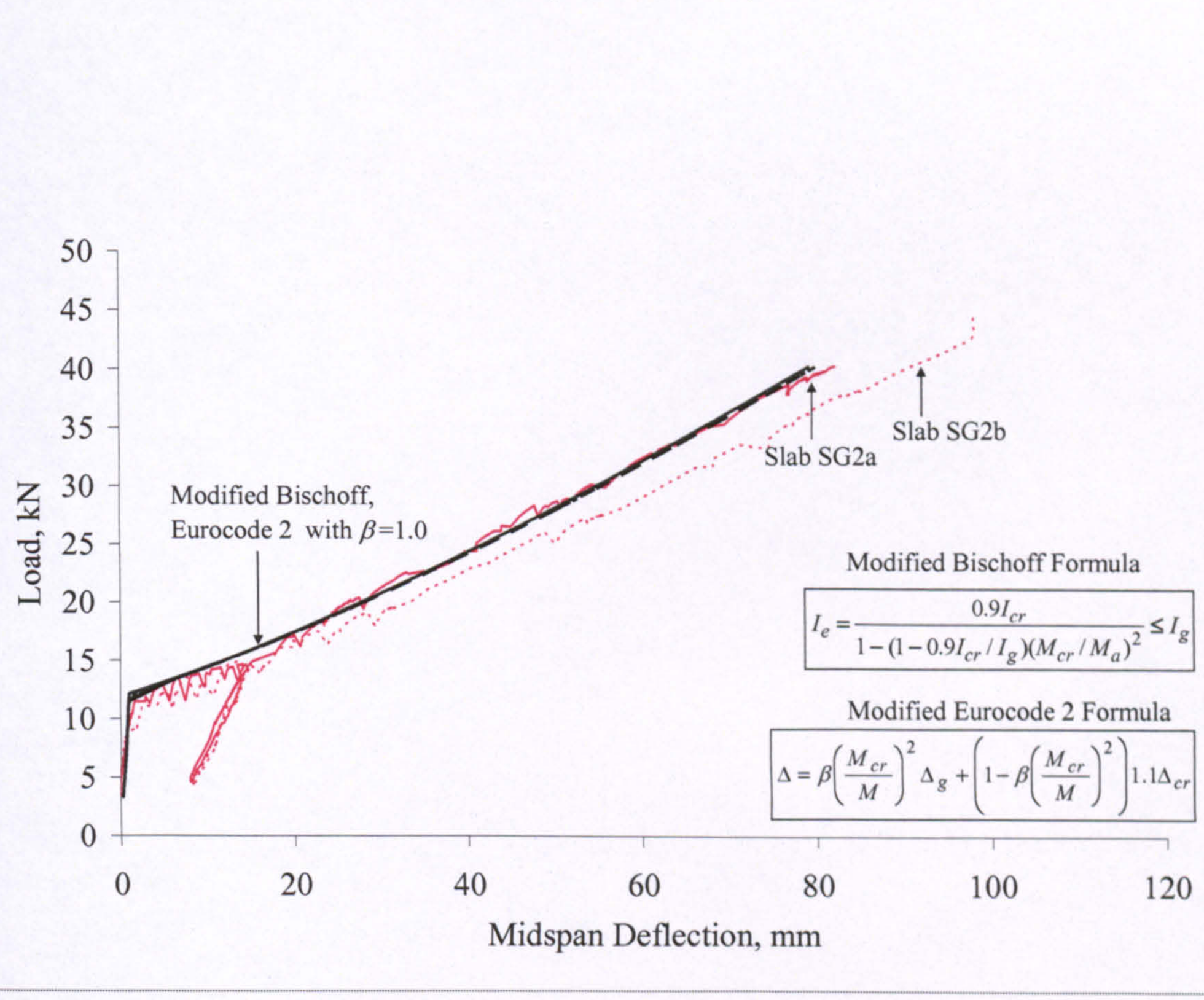
Load, kN
Midspan Deflection, mm
Modified Bischoff, Eurocode 2 with β=1.0
Slab SG2a
Slab SG2b
Modified Bischoff Formula
$I_e = \frac{0.9I_{cr}}{1-(1-0.9I_{cr}/I_g)(M_{cr}/M_a)^2} \le I_g$
Modified Eurocode 2 Formula
$\Delta = \beta\left(\frac{M_{cr}}{M}\right)^2 \Delta_g + \left(1-\beta\left(\frac{M_{cr}}{M}\right)^2\right)1.1\Delta_{cr}$

Slabs SG3

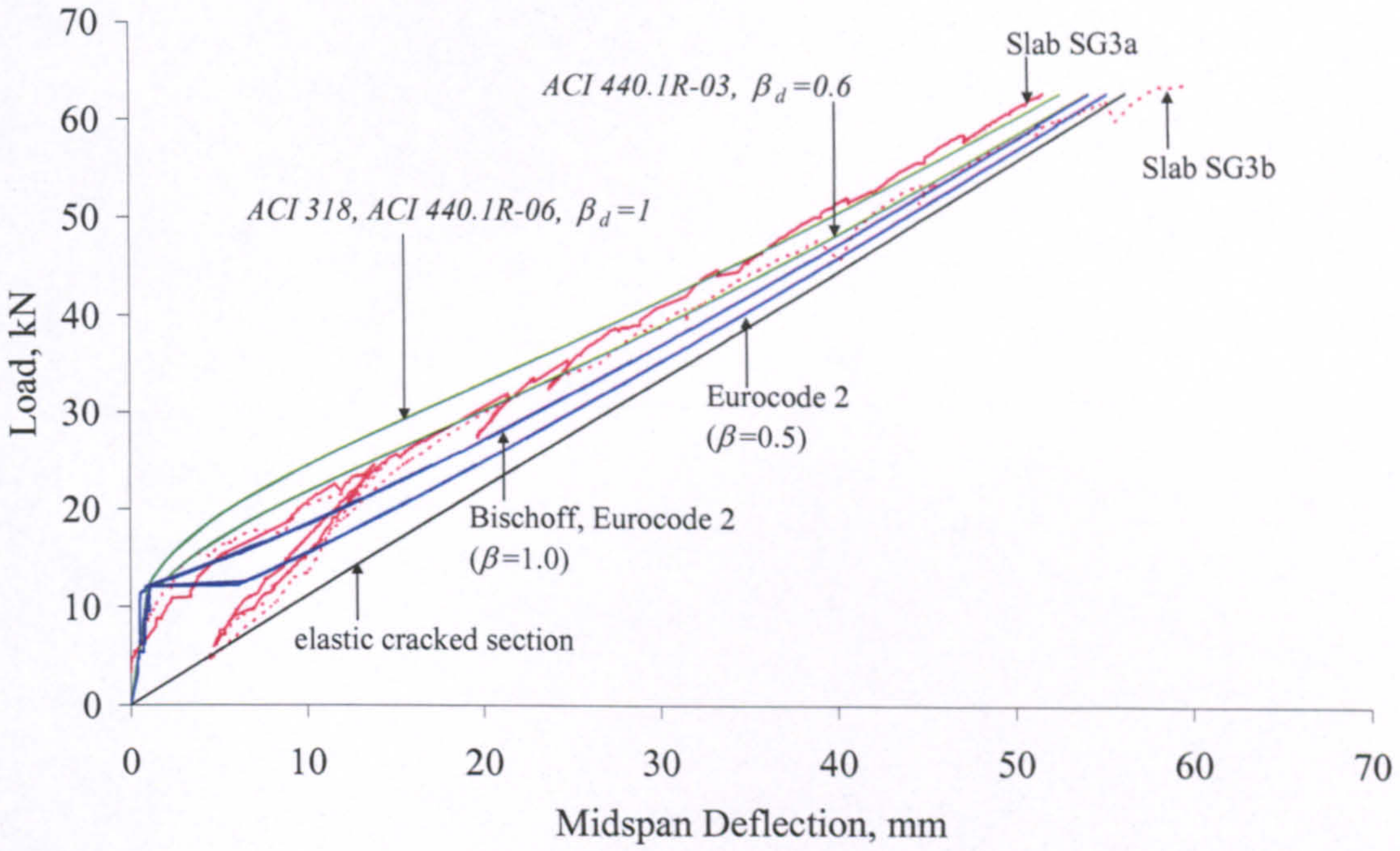
Load, kN
Midspan Deflection, mm
Slab SG3a
Slab SG3b
ACI 440.1R-03, β_d=0.6
ACI 318, ACI 440.1R-06, β_d=1
Eurocode 2
(β=0.5)
Bischoff, Eurocode 2
(β=1.0)
elastic cracked section

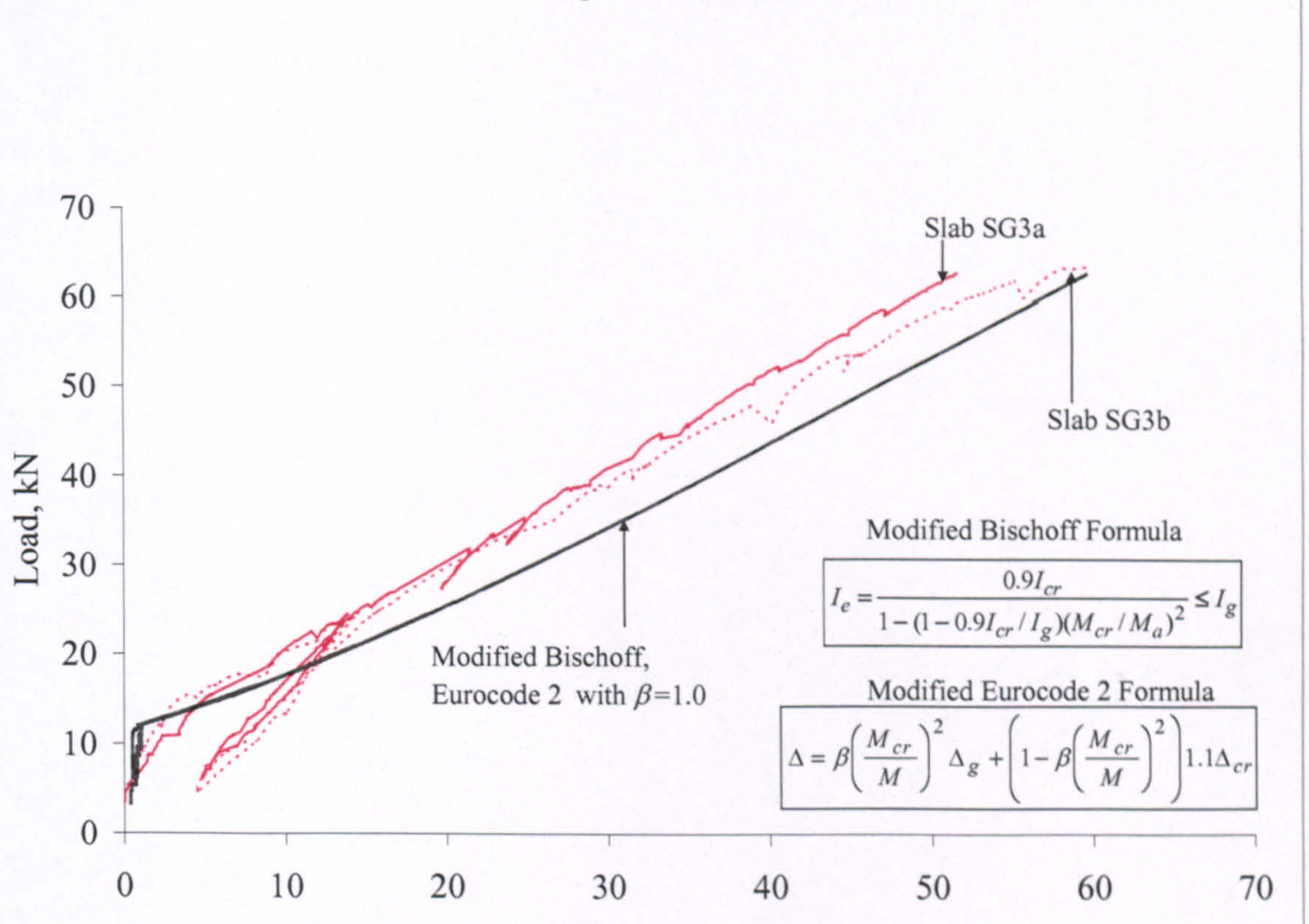
Load, kN
Midspan Deflection, mm
Slab SG3a
Slab SG3b
Modified Bischoff,
Eurocode 2 with β=1.0
Modified Bischoff Formula
$I_e = \frac{0.9I_{cr}}{1-(1-0.9I_{cr}/I_g)(M_{cr}/M_a)^2} \le I_g$
Modified Eurocode 2 Formula
$\Delta = \beta\left(\frac{M_{cr}}{M}\right)^2 \Delta_g + \left(1-\beta\left(\frac{M_{cr}}{M}\right)^2\right)1.1\Delta_{cr}$

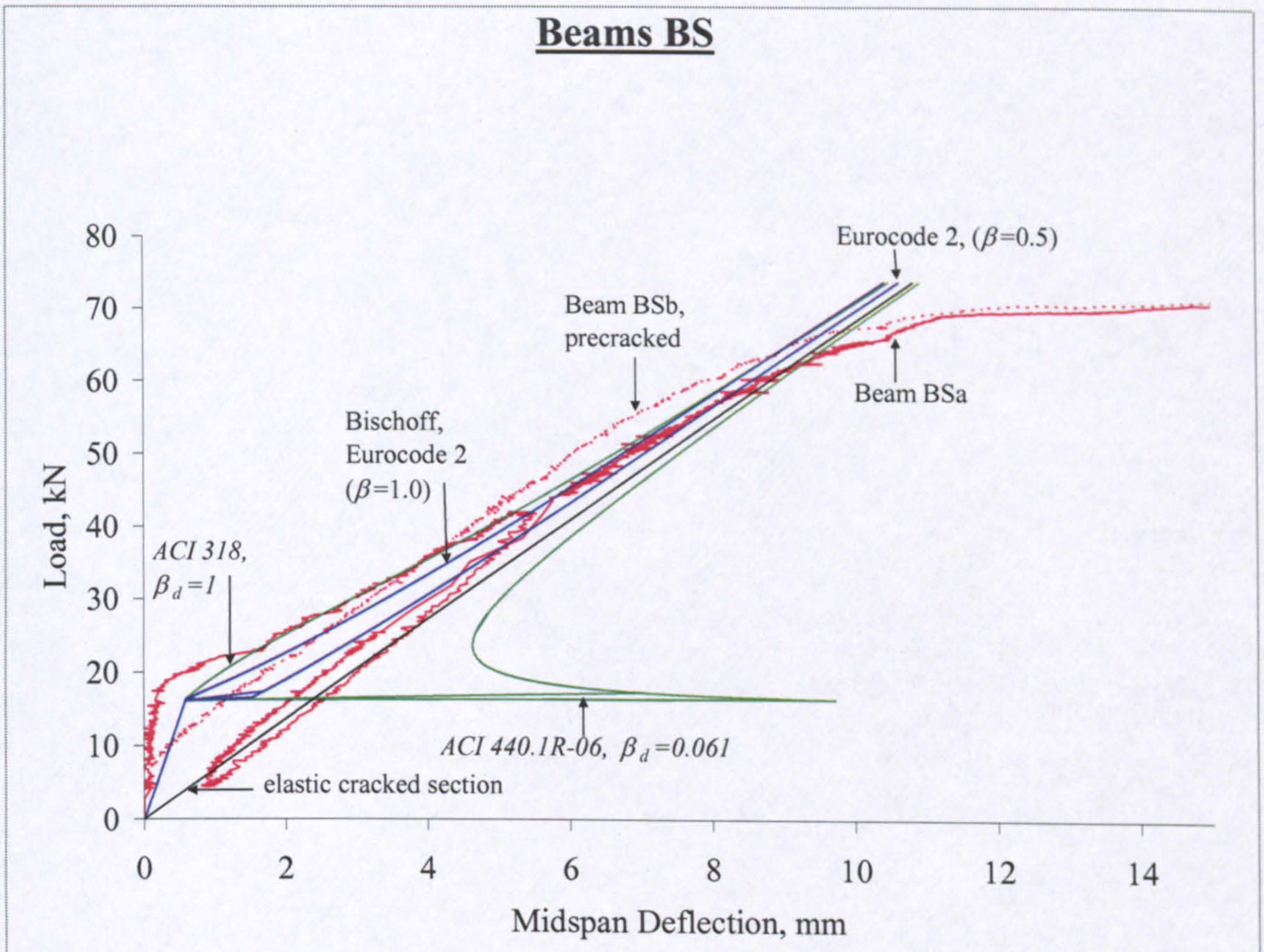
Beams BS
Load, kN
Midspan Deflection, mm
Eurocode 2, (β=0.5)
Beam BSb, precracked
Beam BSa
Bischoff, Eurocode 2 (β=1.0)
ACI 318, β_d=1
ACI 440.1R-06, β_d=0.061
elastic cracked section
0
10
20
30
40
50
60
0
2
4
6
8
10
12
14

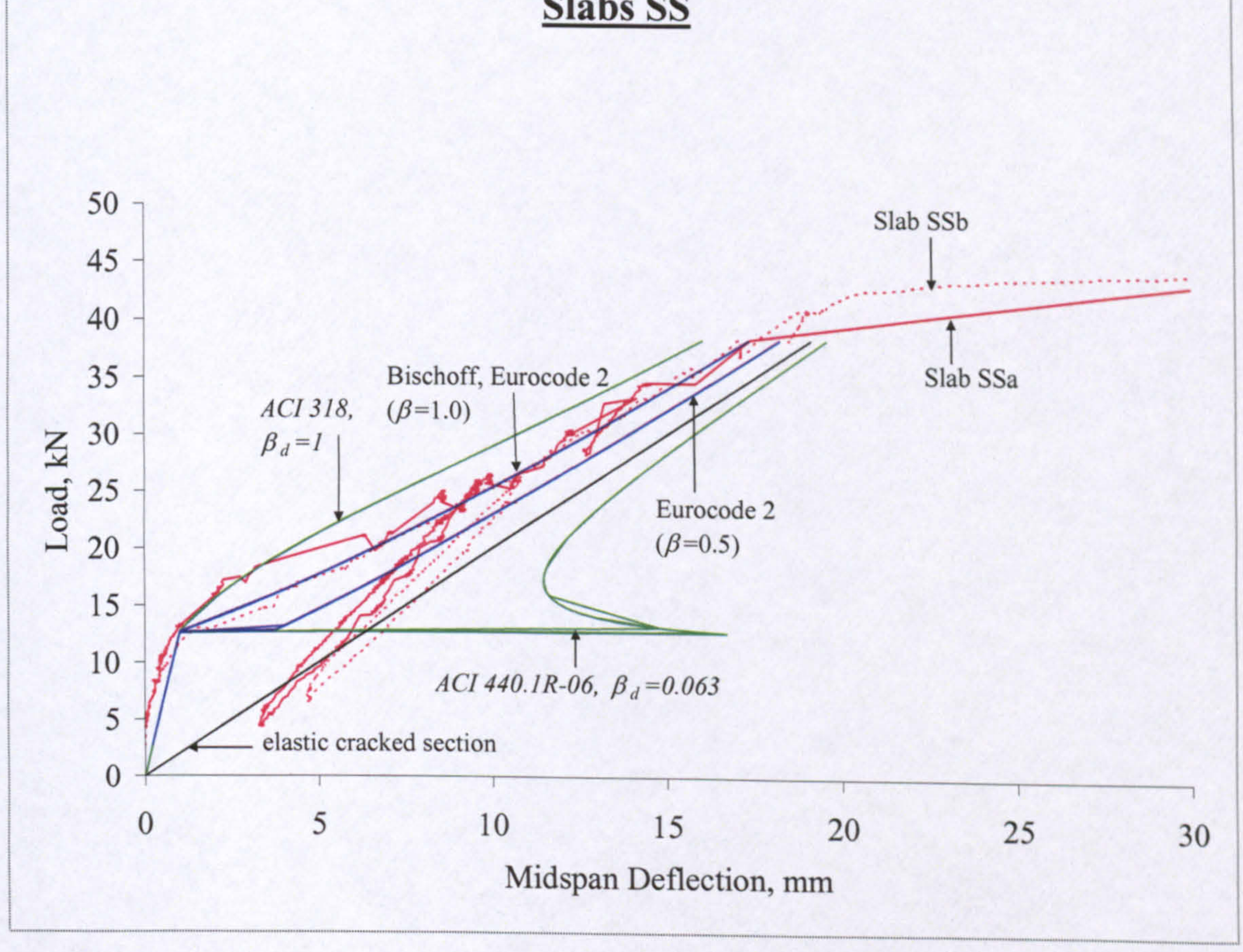
Slabs SS
Load, kN
Midspan Deflection, mm
Slab SSb
Slab SSa
Bischoff, Eurocode 2 (β=1.0)
ACI 318, β_d=1
Eurocode 2 (β=0.5)
ACI 440.1R-06, β_d=0.063
elastic cracked section
0
5
10
15
20
25
30
35
40
45
50
0
5
10
15
20
25
30